

THIS WEEK

EDITORIALS

HIGGS Would a boson by another name smell as sweet? **p.374**

WORLD VIEW Rio summit demands a different science approach **p.375**

TASTELESS Bottlenose dolphins get little flavour from food **p.377**



Incidental benefits

Scientists who screen the genes of volunteers for research should tell participants if they find information relevant to their health.

All research studies on humans can uncover facts relevant to a volunteer's health — at initial screening, during the study itself, or even after the study finishes, when other researchers review the data or conduct their own analyses.

For the most part, researchers have opted not to reveal these potentially important 'incidental findings' to participants. This has been to protect the research process, and to prevent coercing people into studies by unwittingly eliciting the 'therapeutic misconception' — the incorrect assumption on the individual's part that participating in a study will help their own health.

But the emergence of high-throughput genomics, with its ability to catalogue vast amounts of information that may have a bearing on a person's health, has prompted a rethink of this convention.

A working group funded by the US National Institutes of Health (NIH) in Bethesda, Maryland, has recommended that biobanks and archives that house large genetic data sets introduce policies to encourage the return of incidental findings to research subjects (see page 387).

The impact of these recommendations should not be underestimated. As genetics invades every branch of medicine, no field is likely to be exempt from ethical standards introduced to cover genetic data. The recommendations are likely to have their most immediate influence in discussions on the topic now under way at the US Department of Health and the NIH.

There is a precedent for returning information to the subjects of a study. In imaging studies, for instance, a radiologist often reviews patients' scans for incidental findings before they are analysed by researchers. Support is growing for the idea that genetics researchers should similarly review a selected set of genes with known impacts on health before undertaking their own research.

Implementing this will not be easy. Defining appropriate sets of genes is problematic, and any list will need to be constantly updated. And to return the information to an individual in a way that avoids unnecessary anxiety and medical expense is a huge issue. Opponents of the idea point out that it contravenes standard practice in medicine itself, because doctors do not routinely sift through patients' records for old test results that may carry new significance in the light of more recent research.

Perhaps the most visible example of the need for this debate comes not from science, but from commerce. Companies routinely mine vast quantities of consumer information to influence marketing decisions. Governments have not been able to keep pace with standard business practices, and most consumers are unaware of the breadth and depth of information that companies gather on them from Internet searches, social networks and supermarket purchases.

In testimony before the US Presidential Commission on Bioethics in February, John Wilbanks, who runs the project Consent to Research, noted that this pattern is likely to repeat itself in the era of electronic medical records and genomics. "My sad realization is that whether it's your genome or your health information, anyone who really wants to

screw you will probably be able to get a copy of the data they need to do so, and the people who are least likely to get a copy are the people who can do something amazing with it, like researchers," he said. Companies are lining up to market products to consumers on the basis

"No field is likely to be exempt from ethical standards introduced to cover genetic data."

of their genomes. Law-enforcement agencies already use DNA left at crime scenes to find suspects and their relatives, and are funding programmes to create physical profiles of suspects on the basis of their DNA. In other words, people now have incomplete protection for their own DNA, and this lack of privacy is likely to increase in the future.

In this free market, how sure can researchers be that they are truly doing no harm to their study participants when they take a cheek swab? People thinking of entering a study will assess the risks of how their volunteered genetic information might be used, and this might make them more reluctant to participate. Researchers could help to counter this by offering them medically relevant information back in exchange. ■

Flight risk

As the campaign against animal research intensifies, so must the response.

Picture a crowd of scientists waving placards plastered with photographs of stroke victims and sufferers of Parkinson's disease. They are demonstrating outside the corporate headquarters of British Airways, Lufthansa and Delta, demanding that the airlines stop impeding the biomedical research that could deliver big advances against these and other diseases.

Seem far-fetched? Maybe. But if scientists want continued access to animals as research models, they will have to appear on the front line with every bit as much visibility, determination, organization and persistence as animal-rights activists now muster.

In a renewed campaign targeting transportation companies, protestors have found a public pressure point so effective that only a few major airlines still agree to transport non-human primates bound for research labs (see page 381). Nor is the focus confined to primate transportation: earlier this year, the last ferry company that was willing to carry research rodents into the United Kingdom stopped doing so. Such blocks, scientists warn, could shift much animal work to countries where regulations are more lax.

But there is a silent majority for whom the activists do not speak.

This includes most scientists, many ordinary citizens and millions of patients and their families touched by disease and injury. This constituency must mobilize in the defence of human health if the gains enabled by future primate research — and, ultimately, all animal research — are not to be thrown away.

Scientists and their allies must, of course, continue to be open about the price animals pay in research. They must openly acknowledge, immediately correct and do everything they can to prevent lapses in the care of the animals in their charge. At the same time, scientists must make every effort to use lower animal, and non-animal, models where possible, as regulations already require. And alongside all of that, they must emphasize the tangible and compelling improvements to human life that animal research has made possible.

Consider stroke, which affects some 795,000 people in the United States alone each year — 1 person every 40 seconds — at a cost in excess of US\$40 billion. More than 1,000 experimental treatments aimed at protecting brain cells in acute stroke have been developed in cells and rodents; none has been effective in humans. So a possible advance in a paper published last month is significant (D. J. Cook *et al.* *Nature* **483**, 213–217; 2012). Using macaques — animals whose neuroanatomy, genetics and behaviour are far closer to humans than are those of rodents — the study showed that a drug called a PSD-95 inhibitor reduced the volume of brain tissue killed by the stroke and significantly preserved neurological function. It has now moved into human trials, where early results are promising.

Many other advances have been made possible by primate research. Trials of brain-machine interfaces that allow quadriplegics to control robotic limbs with their minds, for example, and of gene therapy for haemophilia B. And deep-brain stimulation to alleviate the symptoms

of advanced Parkinson's disease. Primates have also helped the development of antiviral therapies to prevent mother-to-child transmission of HIV; of Rituxan (rituximab), a key drug against non-Hodgkin's lymphoma; and of Benlysta (belimumab), the first new lupus treatment in 50 years. Primates are making possible strides towards a vaccine against Ebola, and they have affirmed that the diabetes drug pioglitazone can slow early Parkinson's disease — a therapy now being taken into human trials.

“Silence from the research community will mean lost access to research animals.”

zone can slow early Parkinson's disease — a therapy now being taken into human trials.

Future advances of this kind cannot be allowed to stall. The scientific community and its allies in patient and research advocacy groups should mount a vigorous, coordinated campaign to lobby major airlines. They should vocally support companies such as Air France

that continue to fly research primates. They should confront others with the human cost of their alignment with animal activists. And to those airlines that are wavering, they should make a pointed, persuasive case.

An apt target in the last category is United Airlines, which merged with Continental in 2010. Continental was the last major US airline carrying non-human primates for research. The now-merged airline, still under the name of United, says it is “in the process of integrating” the former United and Continental policies on transporting research primates, for publication this autumn. Only a powerful and visible public campaign urging United to transport research primates will give the firm the political cover it needs to take such a position.

Urgent and dramatic action is necessary. It is increasingly clear that silence and passivity from the research community will lead to only one result: lost access to research animals in the countries best equipped for their responsible, humane and justified use. ■

Mass appeal

As physicists close in on the Higgs boson, they should resist calls to change its name.

The naming of the Higgs boson as such is clearly a simplification — physicists besides Peter Higgs contributed to the theory that predicts it. But it is far from the most extreme example.

The relationship between the velocity of recession of galaxies and their distance from Earth that we call Hubble's law was first formulated by Belgian cosmologist Georges Lemaître. The quantity known as Avogadro's number was first calculated by Austrian chemist Johann Josef Loschmidt. Higgs, a physicist at the University of Edinburgh, UK, at least has the strongest claim to credit for the boson. And for the arcane world of particle physics, simplification is often a good thing.

In 1964, Higgs was the first to postulate the existence of a massive particle arising from the mechanism of electroweak symmetry breaking, in which a unification of electromagnetism and the weak nuclear force fails in such a way as to give some force-carrying particles masses while others remain without. Yet moves are afoot to rename the Higgs. Earlier this month, some speakers at the Moriond particle-physics conference in La Thuille, Italy, chose to describe progress on the search for the BEH scalar boson (after the physicists Robert Brout, François Englert and Higgs) or the SM scalar boson (where SM stands for standard model).

It is not hard to guess why. Experiments at the Large Hadron Collider at CERN, Europe's premier particle-physics laboratory near Geneva in Switzerland, have reported tentative signals of the Higgs. If these are real, data collected in 2012 should see CERN claim a discovery. A Nobel prize is in the offing, and one that should arguably go not just to the experimentalists, but also to the theorists whose efforts inspired the successful search. But who — besides Higgs — should be included?

The name Higgs boson was supposedly coined by Korean-born

physicist Ben Lee, some time between 1966 and 1972. According to journalist Ian Sample, Lee learned about the mass-giving mechanism from Higgs, and later coined the term as a shorthand. Yet several others played an important part in developing the theory that gives rise to the Higgs.

Belgian physicists Brout and Englert were the first to publish on the subject in 1964, building on ideas from condensed-matter physics developed by physics Nobel laureate Phil Anderson and others. Higgs published the same year; his paper contains the first mention of the boson. Tom Kibble, Gerald Guralnik and Carl Hagen followed with a third account that is generally considered more complete. One interpretation of this history is reflected in the American Physical Society's joint award, in 2010, of the J. J. Sakurai Prize for Theoretical Particle Physics to Brout, Englert, Higgs, Guralnik, Hagen and Kibble.

This provides plenty for physicists to argue about. In 2010, a row over credit erupted when Brout, Englert and Higgs were acknowledged in an advertisement for a conference on the particle but Guralnik, Hagen and Kibble were not (see *Nature* <http://doi.org/ctz988>; 2010). Meanwhile, 2011 saw a dispute over editing of the Wikipedia article ‘Higgs boson’ between one editor who supported Guralnik's view that his paper with Hagen and Kibble proposed a boson and another who was pro-Higgs.

Particle physicists should not rename the Higgs. And the reason would be obvious to anyone in business: branding. There are already relatively few concepts in their subject that have achieved widespread recognition without crossing one of them out. In business, it would be considered destructive to take a well-known name and replace it with a long-winded, technical-sounding alternative that no one has heard of.

Correct allocation of credit is important, and authoritative accounts of the history of science are useful and enlightening, but both must be balanced with science's need for consistent conventions, brevity, and public communication and outreach, especially when taxpayer's expenditures,

such as the US\$6.5 billion for the Large Hadron Collider, are at stake. Renaming the Higgs boson in the year when it is most likely to be found gets the balance wrong. (And anyway, Higgs is a better name than the God particle, isn't it?) ■

➤ NATURE.COM
To comment online,
click on Editorials at:
go.nature.com/xhunjv

CSIRO



Change the approach to sustainable development

Conventional environmental assessments are not enough — it is time for some joined-up global thinking, says **Mark Stafford Smith**.

As the world heads towards the next big environmental summit — the United Nations Conference on Sustainable Development (Rio+20) in Rio de Janeiro, Brazil, in June — officials and politicians are calling for further assessments of our global ecological plight.

In January, for example, a panel on global sustainability set up by UN secretary-general Ban Ki-moon recommended a “periodic global sustainable development outlook report that brings together information and assessments currently dispersed across institutions and analyses them in an integrated way”.

This is a response to research that shows how global society is increasingly interconnected and interdependent. The cascading effect on land availability and food security of a switch to biofuels, for example, demonstrates how actions to address carbon dioxide emissions can rebound on other goals.

But, in these difficult times, can the thinly stretched scientific community support a new assessment process? And is that really what policy-makers need from research?

Scientists are already busy on policy-makers' behalf. There is the Intergovernmental Panel on Climate Change (IPCC), the Millennium Ecosystem Assessment, assessments of international waters, mountains and fresh water, the Global Marine Assessment and the important new Intergovernmental Platform on Biodiversity and Ecosystem Services. Each has a crucial role in consolidating knowledge about individual sectors. But how to connect the dots?

In many areas, the rates of global environmental change are accelerating but decision-making processes are stuck in low gear. It is not clear that another conventional assessment will catalyse swifter action. So, although the research community should rally behind an integrated analysis, it must be done differently.

First, the focus must shift from documenting problems to supporting solutions. This requires strong and continual interaction between those working in strategic applied research and decision-makers in policy, industry and civil society, both on specific decisions (such as how to frame a particular trade agreement) and on the wider context (interactions between national well-being, environmental outcomes and economic flows).

Second, the process must promote responses at all scales, from national governments and regional groups to UN institutions. Appropriate solutions will differ from region to region, be they specific technologies for energy production or carbon sequestration, or analyses that jointly address water, energy and food.

Finally, the process must work across sectors, through simultaneous analysis of the impact of a

migration policy on environmental and social well-being, for example. To do this comprehensively, the research must also become more integrated, encompassing natural and social sciences and the humanities to understand the implications of changes.

How could this be done? Two proposals already on the table for Rio+20 could help: a UN Sustainable Development Council (UNSDC), directly answerable to the UN General Assembly, and a set of sustainable-development goals (SDGs).

A UNSDC could commission strategic analyses of global sustainability and set up and coordinate decision-specific panels — small mixed working groups that include non-scientific members, appointed to report quickly on specific issues. Such panels would work across sectors, independent from but jointly owned by global bodies such as the

Food and Agriculture Organization of the UN, the World Trade Organization, the UN Environment Programme and the World Bank.

This model must be replicated at regional and national levels, driven by local needs, with local ownership. Light-touch coordination by the UNSDC would ensure good communication and exchange of ideas, and would make sure that activities in one region did not lead to perverse global outcomes — perhaps by causing people to move, distorting prices or over-using resources.

The SDGs could ensure that these activities integrate the three pillars of sustainability — environmental, economic and social — instead of dealing with each in isolation, as the UN's current Millennium Development Goals do. They should connect sectors, aiming for example to improve well-being without environmental damage, ensure food security without undermining local livelihoods and develop habitable urban environments without increasing resource use.

All of this builds on existing trends in the activities of bodies such as the IPCC, but we need a rapid step change in the evolving relationship between science and decision-making.

Countries such as Australia already talk about ‘national innovation systems’ — the totality of their pure and applied research efforts and the interactions of these with decision-making in industry and government. It is time to embrace a global innovation system to support better-coordinated and more nimble decision-making on global sustainability at all scales. Much work needs to be done on the details, but if science is to be genuinely useful to society, this is what we must fight for. ■

Countries such as Australia already talk about ‘national innovation systems’ — the totality of their pure and applied research efforts and the interactions of these with decision-making in industry and government. It is time to embrace a global innovation system to support better-coordinated and more nimble decision-making on global sustainability at all scales. Much work needs to be done on the details, but if science is to be genuinely useful to society, this is what we must fight for. ■

THE FOCUS MUST
SHIFT FROM
**DOCUMENTING
PROBLEMS**
TO
**SUPPORTING
SOLUTIONS.**

➔ **NATURE.COM**
Discuss this article
online at:
go.nature.com/79fhuu

Mark Stafford Smith is science director of the Commonwealth Scientific and Industrial Research Organisation Climate Adaptation Flagship in Canberra, and co-chair of the Planet Under Pressure conference, which will be held in London next week.
e-mail: mark.staffordsmith@csiro.au

RESEARCH HIGHLIGHTS

Selections from the
scientific literature

CHEMISTRY

Hydrogen can be stored as acid

Hydrogen gas holds promise as a carbon-free fuel, but is difficult to store and transport because it is highly flammable, diffuse and has a low energy density. Jonathan Hull at Brookhaven National Laboratory in New York and his colleagues have found a possible way to store hydrogen as an aqueous solution of formic acid (HCOOH), which has a higher energy density.

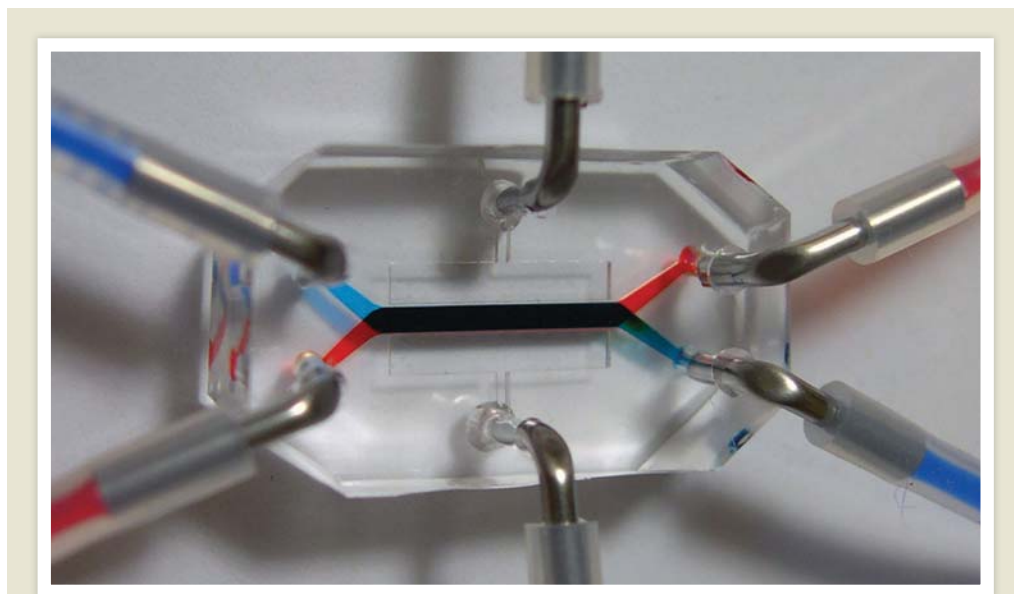
At ambient temperature and pressure, an iridium catalyst dissolved in water causes H₂ to react with carbon dioxide to form the acid under mildly basic conditions. Acidifying the solution triggers the release of pure pressurized H₂ gas. Because of the mild conditions needed for the reactions, the work could eventually lead to a mechanism for H₂ storage.

Nature Chem. <http://dx.doi.org/10.1038/nchem.1295> (2012)

MATERIALS

Slicing silicon with less waste

Cutting silicon blocks into thin wafers for solar cells and other applications generates a lot of wasted metal because



BIOENGINEERING

A pulsating gut on a chip

A coin-sized device created by a team at Harvard University mimics the structure and physiology of the human intestine by supporting gut microbes and imitating the organ's rhythmic motion.

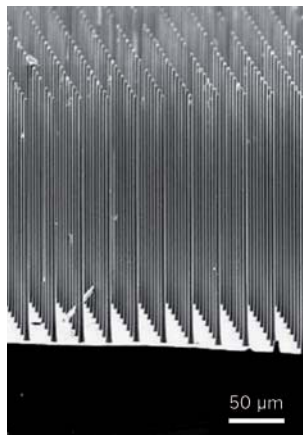
Donald Ingber and his colleagues at the Wyss Institute in Boston, Massachusetts, built the chip (**pictured**) out of a clear polymer. It contains two microscopic fluid channels separated by a porous, flexible membrane. Human gut epithelial cells, which line the gut's surface, cover the membrane and supported the growth of a common gut bacterium, *Lactobacillus rhamnosus*. The researchers

simulated gut contractions, or peristalsis, by applying suction through two side chambers. In response, the epithelial cells formed folds similar to the finger-like protrusions, or villi, that line the inner intestinal wall.

The gut tissue layer blocked the flow of small molecules between the channels, and this barrier function improved with the presence of the bacteria. The authors say that their device is a better intestinal mimic than cells in static culture and suggest that it could be used for drug screening and toxicity tests.

Lab Chip <http://dx.doi.org/10.1039/C2LC40074J> (2012)

AM. CHEM. SOC.



of the width and vibration of the mechanical sawing wire typically used. Sungho Jin at the University of California, San Diego, and his colleagues report a way to etch silicon into various intricate shapes that produces an order of magnitude less waste than conventional approaches.

The authors adapted a common etching technique, depositing a catalytic gold and iron layer on top of certain sections of a silicon wafer and using other

chemicals to dissolve those parts of the silicon away. Strong neodymium magnets guide the chemical etching, allowing the researchers to slice silicon in any desired direction, forming sheets, microneedles, nanowires (**pictured**) and tunnels. Magnetically guided chemical etching makes thinner cuts than mechanical sawing, thus reducing waste.

Nano Lett. <http://dx.doi.org/10.1021/nl300141k> (2012)

ZOOLOGY

All the better to see whales with

The giant eyes of the world's largest squid seem to be specially adapted to spot approaching predatory sperm whales.

Dan-Eric Nilsson at Lund University in Sweden and his colleagues examined a photograph of an adult giant squid (*Architeuthis* sp.) and a full-size colossal squid

R. SOC. CHEM.

(*Mesonychoteuthis hamiltoni*) specimen, and found both animals' eyes to measure about 27 centimetres in diameter — the largest eyes of any species. The researchers created a mathematical model relating eye size to vision. They found that the only advantage of such large eyes over smaller ones is an enhanced ability to detect large, luminous objects below ocean depths of about 500 metres.

The authors suggest that these squid evolved such eyes to detect the bioluminescence that can be created by the movement of hunting whales. *Curr. Biol.* <http://dx.doi.org/10.1016/j.cub.2012.02.031> (2012)

MICROBIOLOGY

Bacteria signal to survive

Bacterial cells that are genetically identical to members of their population that succumb to antibiotics can survive in a dormant state, thanks to chemical communication between bacteria.

Surviving 'persister' cells have been implicated in chronic infections such as tuberculosis. James Collins and his team at Boston University in Massachusetts gave *Escherichia coli* the chemical indole, which the bacteria produce as a signalling molecule. Indole-treated *E. coli* were able to withstand higher levels of several antibiotics than untreated bacteria. Moreover, the individual bacterial cells in a culture that were most responsive to indole were also those most resistant to antibiotics.

Indole activates genes involved in responding to stress, and *E. coli* strains lacking stress-response genes produce fewer persisters. *Nature Chem. Biol.* <http://dx.doi.org/10.1038/nchembio.915> (2012)

CLIMATE MODELLING

Predicting realistic rains

A high-resolution climate model has produced the most accurate representation yet of rainfall in the southern United Kingdom, bolstering confidence in the potential of detailed regional modelling.

A team led by Elizabeth Kendon at the Met Office Hadley Centre in Exeter, UK, used a regional model with a 1.5-kilometre grid to conduct detailed simulations from 1989 to 2008. The authors analysed the duration, extent and intensity of rainfall and compared the results of their model with those produced by a less-detailed 12-kilometre regional climate model.

The results suggest that the 1.5-kilometre model significantly improves the representation of heavy rains and reduces long-standing inaccuracies that produced too much light rain. *J. Clim.* <http://dx.doi.org/10.1175/JCLI-d-11-00562.1> (2012)

EVOLUTION

No sweetness for meat-eaters

Many meat-eating animals have lost their ability to taste sugars, having lost a working copy of a gene that encodes a taste receptor for sugar.

Peihua Jiang and Gary Beauchamp at the Monell Chemical Senses Center in Philadelphia, Pennsylvania, and their co-workers sequenced DNA from 12 members of the order Carnivora, including spotted hyenas and several sea mammals. Seven of the species carried a malfunctioning copy of the *Tas1r2* gene that encodes a sweet taste receptor. However, the exact mutations differed from one species

COMMUNITY CHOICE

The most viewed papers in science

BEHAVIOURAL SCIENCE

Testosterone hinders collaboration

HIGHLY READ
on rspsb.royalsocietypublishing.org in February

Women taking testosterone pills collaborate less effectively than those given a placebo.

Nicholas Wright and his colleagues at University College London asked 17 pairs of women to decide individually if a set of striped circles on one screen was brighter than those on a second screen. If the women within a pair disagreed, they had to collaborate to come up with a joint decision.

The team found that the women were generally more accurate when they collaborated than when working alone. However, testosterone decreased this boost in the women's performance compared with placebo, even though the hormone did not affect the accuracy of the decisions made individually. The authors suggest that the hormone causes individuals to place much more weight on their own judgment than on that of others.

Proc. R. Soc. B <http://dx.doi.org/10.1098/rspb.2011.2523> (2012)

to another, suggesting that carnivores have independently lost their ability to detect sugars during the course of evolution.

Furthermore, bottlenose dolphins (pictured) and sea lions lack working copies of the gene encoding receptors for tasting savoury flavours, or umami. Dolphins also seem

to have lost a receptor that senses bitter compounds. The authors say taste may not affect what these creatures eat as sea lions and dolphins tend to swallow their food whole. *Proc. Natl Acad. Sci. USA* <http://dx.doi.org/10.1073/pnas.1118360109> (2012) For a longer story on this research, see go.nature.com/y4tzk7

CLIMATE CHANGE

Coming surge in storm surges

As the climate warms and sea levels rise, the frequency of local extremes in storm surges will increase along much of the US coastline.

To assess changes in local

flood risk, Claudia Tebaldi at Climate Central in Princeton, New Jersey, and her colleagues combined projections from a model of global sea-level rise with long-term records from 55 tidal gauges around the United States. The team estimates that by 2050, one-third of gauge locations will see an increase in the frequency of extreme high-water levels that are currently expected to occur only about once a century. Some locations can expect to see these extremes, on average, every ten years, others even annually.

In a separate study, Benjamin Strauss, also at Climate Central, and his colleagues assessed US communities' topographic vulnerability to sea-level rise. Given that sea level could increase by one metre or more during this century, the team estimates that 3.7 million people live within one vertical metre of local mean high tide. *Environ. Res. Lett.* **7**, 014032; 014033 (2012)

► NATURE.COM

For the latest research published by Nature visit: www.nature.com/latestresearch



SEVEN DAYS

The news in brief

RESEARCH

No faster than light

Neutrinos don't travel faster than light, according to results from the ICARUS experiment at the Gran Sasso National Laboratory near L'Aquila, Italy. The experiment found no light-busting speed when it timed 7 neutrinos as they travelled about 730 kilometres from CERN, Europe's particle-physics lab near Geneva, Switzerland — contradicting last September's results from the OPERA experiment, also at the Gran Sasso lab. OPERA had recorded neutrinos travelling faster than light, but has since uncovered possible problems with its measurement. The ICARUS report was posted to the preprint server arXiv.org on 15 March (M. Antonello *et al.* <http://arxiv.org/abs/1203.3433>; 2012). See go.nature.com/go4247 for more.

Early drug screening

The newest centre at the US National Institutes of Health — the National Center for Advancing Translational Sciences (NCATS) in Bethesda, Maryland, which aims to speed new drugs to market — has announced its first major deal. NCATS will partner with drug firm Eli Lilly, based in Indianapolis, Indiana, to screen around 3,800 approved and investigational medicines to find potential new uses. The two organizations announced on 13 March that the screening will take place over the next 12–18 months and the results will be posted publicly at <http://tripod.nih.gov/npc>. See go.nature.com/rgudpy for more.

LHC restarts

The world's most powerful particle accelerator has begun warm-up stretches for its 2012 run. On 14 March, beams of protons again began to

circulate in the Large Hadron Collider (LHC) at CERN, Europe's particle-physics lab near Geneva, Switzerland. Full-scale collisions at 8 teraelectronvolts should begin in April, and scientists could confirm the detection of the long-sought-after Higgs particle by the end of the year.

Children's study row

Two advisers to the US National Children's Study — which aims to track environmental influences on the health of 100,000 children — have resigned in less than a fortnight. Ellen Silbergeld, an environmental scientist at Johns Hopkins Bloomberg School of Public Health in Baltimore, Maryland, resigned

on 5 March, followed on 16 March by biostatistician Jonas Ellenberg of the University of Pennsylvania's Perelman School of Medicine in Philadelphia. They and other scientists are complaining about an abrupt change in sampling design, in which the study will recruit subjects from the offices of physicians rather than taking a representative sample of the US population. See go.nature.com/wb9sh8 for more.

Biomedical awards

The Howard Hughes Medical Institute in Chevy Chase, Maryland, is investing US\$200 million to fund up to 30 US biomedical researchers for five years. The 15 March announcement marks the first

time the institute has held a general competition for its coveted investigator awards since 2007. See go.nature.com/j2a3xt for more.



E. SARKISOV/CORBIS

Scientists join protest over Spanish cuts

Scientists have warned Spain's government that its planned budget cuts and hiring freeze could be fatal for national research. Along with widespread general protests (pictured, in Madrid) this month against budget cuts and labour reforms, more than 36,000 people (including three Nobel laureates) and 65 organizations have signed an 'open letter

BUSINESS

Academic pharma

In the latest union between academia and industry, drug giant Merck has announced that it will create a non-profit research entity called the California Institute for Biomedical Research (Calibr), to be located in San Diego, California. The institute plans to hire about 150 scientists and will be headed by chemist and serial entrepreneur Peter Schultz, currently at the Scripps Research Institute in La Jolla, California.

D. GRAY/REUTERS Academics from around the world will be able to submit proposals for research at Calibr. See go.nature.com/26fij7 for more.

UK venture capital

The Wellcome Trust, the world's largest non-governmental funder of biomedical research, announced on 20 March that it would launch a £200-million (US\$371-million) business to invest in health-care and life-sciences companies. The charity — which awards around £600 million in research grants each year — says that in the past it has invested in biotech companies, and that £148 million of £2.7 billion it invested in venture-capital firms in the year to 30 September 2011 already goes to life-sciences and health-care businesses. But the new fund marks its largest direct effort to invest in biotech start-ups.

POLICY

Rare-earth trade

The United States, Europe and Japan have jointly complained to the World Trade Organization that China is restricting exports of rare-earth elements. The elements are quite plentiful, but miners in China (**pictured**, smelting lanthanum) produce more than 90% of the supply. They



are used as catalysts and in high-tech magnets, car batteries, wind turbines and mobile phones. The formal complaint — which could result in sanctions — was made on 13 March, and follows years of disputes about China's export quotas.

Misconduct in China

China's education ministry has launched an effort to curb scientific misconduct at universities. Rules announced on 14 March require universities to create mechanisms for inspecting original data, and for getting departing scientists to hand over materials produced in experiments. Universities must also create committees with five or more experts to investigate academic misconduct, and arrange ethics training. Various Chinese organizations have previously issued guidelines to stem scientific misconduct, but many scientists complain that the measures are not implemented and cheaters remain unpunished. A few

universities, notably Zhejiang University in Hangzhou, have stepped up efforts to be stringent (see *Nature* **481**, 134–136; 2012).

SESAME funding

A US\$110-million synchrotron is still on track for construction near Amman, Jordan, despite political upheaval in the Middle East. Iran and Israel announced on 13 March that they had joined Jordan and Turkey in committing funding to the project, known as SESAME (Synchrotron-light for Experimental Science and Applications in the Middle East). Partners have now promised \$20 million in total, and SESAME is looking for \$15 million more to complete its first four beamlines by 2015. See page 385 for more.

Animal shipments

UK scientists warned last week that pressure from animal-rights activists has led all ferry companies and many airlines to stop transporting research animals (including mice) into the United Kingdom. Less than 1% of UK experiments use animals from abroad. Science minister David Willetts said that the government is working with airlines and ferry companies to try to tackle the problem, perhaps by getting researchers and industry to agree on codes of conduct for

COMING UP

25–29 MARCH

The 'chemistry of life' — including topics such as the biochemical basis of epigenetics — is the key topic at the American Chemical Society's spring meeting in San Diego, California. go.nature.com/ystlb8

26–29 MARCH

'Planet under Pressure' will see scientists and policy-makers meet in London to discuss the latest research on ecosystems and planetary stewardship. go.nature.com/xtqrnh

28 MARCH

Swiss drug firm Novartis's six-year legal fight with India's government, which began when the firm was denied a patent on a cancer drug, goes to India's supreme court. The ruling could set precedents for patented drugs in India and many developing countries. go.nature.com/aliquor

animal transportation. For more on the issue of airlines and primate transport, see pages 373 and 381.

Indian budget

Researchers in India were not impressed by a moderate increase in the country's science budget, announced on 16 March. Rises varied between 2% and 18% for scientific departments, but, with inflation running at 7%, there will be little extra real spending power — even though Prime Minister Manmohan Singh had promised in January that there would be a "major increase" in research spending. See page 384 for more.

► NATURE.COM

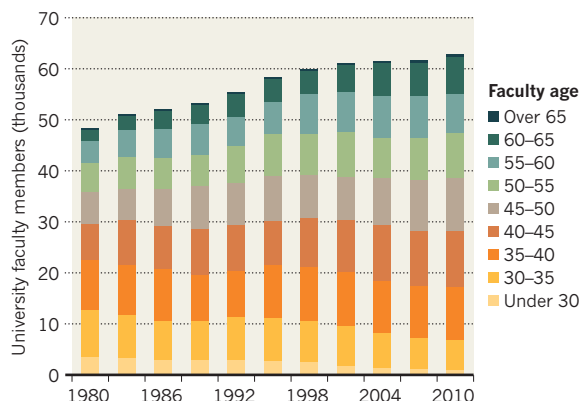
For daily news updates see: www.nature.com/news

TREND WATCH

Junior researchers are being squeezed out of Japanese universities by government policies that have trimmed hiring. The claim is made in a draft report on Japan's science and technology activities from the Council for Science and Technology Policy, the nation's top advisory body on science. It points out that the number of faculty members under 35 has plunged from more than 10,000 to 6,800 in the past 30 years (see chart). See go.nature.com/bide1g for more.

GOING GREY

Despite a growth in the number of university faculty members in Japan, there are fewer opportunities for young researchers.



NEWS IN FOCUS

CRYSTALLOGRAPHY Opioid receptors revealed in double exposure **p.383**

PHOTONIC CHIPS Giving researchers the right tools for the job **p.388**

TRANSLATIONAL MEDICINE Teaming mice and men for better clinical trials **p.389**

PROFILE Joe Thornton, the man who resurrects extinct proteins **p.390**



BY MEREDITH WADMAN

Each year, thousands of macaques and other monkeys are flown into Europe and North America to supply academic and industrial research labs — more than 18,000 to the United States in 2011 alone. But in a campaign that could affect scientists across the West, the few major air carriers that still transport non-human primates are coming under unprecedented pressure to halt the practice.

One key route under threat is from China, which last year shipped more than 70% of the research primates sent to the United States (see ‘Up in the air’). On 14 March, animal breeders in China met with officials of China Southern Airlines to implore them to resume flights into Los Angeles International Airport, the largest US port of entry for research primates. Last August, China Southern cancelled a shipment from Guangzhou of 80 crab-eating macaques (*Macaca fascicularis*) destined for Los Angeles, after a social media, e-mail and telephone campaign by pressure group People for the Ethical Treatment of Animals (PETA), based in Norfolk, Virginia. China Southern has not flown research primates into Los Angeles since then.

“This was part of our larger campaign to disrupt the flow of primates to US labs,” says Justin Goodman, associate director of the laboratory investigations department at PETA in Washington DC. The group complains that imports are supplementing an already-burgeoning primate population in US labs (see ‘Frequent flyers’).

Two other airlines are also in the public spotlight. Air France faces mounting pressure as the last major European carrier to transport research primates. And Air Canada is petitioning the Canadian Transportation Agency, the body that regulates Canadian air carriers, for the required permission to refuse to transport research primates in the future. With news breaking last week that ferry companies have entirely ceased transporting all research animals — including sophisticated mouse disease models — into the United Kingdom, researchers fear that this is the start of a larger trend.

Michael Hsu, president of animal-breeding company Shared Enterprises in Richlandtown, Pennsylvania, says that activism is affecting companies such as his, which maintains a macaque breeding colony in Shanghai and relies on flights into Los Angeles to get its animals to its clients. China Southern, he says, was easily the biggest carrier serving Los Angeles ▶



Protesters make their mark at an Animal Transportation Association meeting in Vancouver on 18 March.

ANIMAL RESEARCH

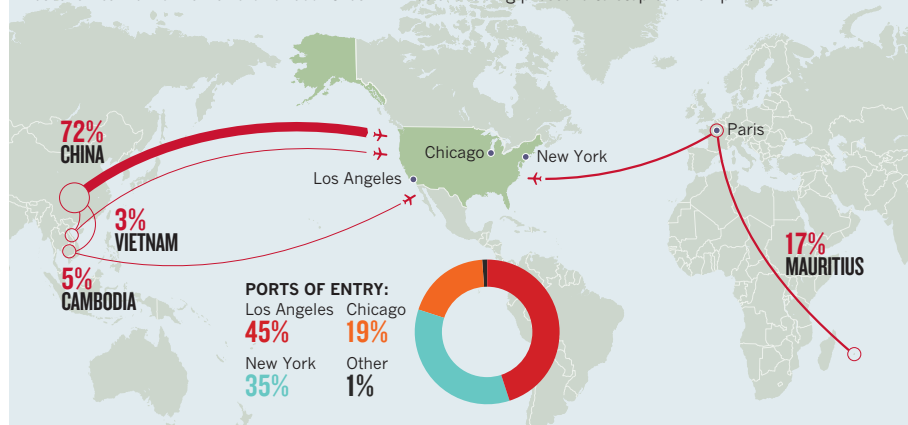
Activists ground primate flights

Supply of research monkeys to Western labs under threat as airlines react to animal-rights campaign.

CHRISTOPHER J. MORRIS/AP

UP IN THE AIR

In 2011, some 97% of the 18,044 non-human primates imported into the United States for use in research came from a handful of countries. Airlines are facing pressure to stop such shipments.



► airport. The other Chinese carriers serving the United States — Air China and China Eastern — have lower capacity, creating a bottleneck for breeders lining up to ship animals. The situation, says Hsu, “is causing a big backlog. It’s costing us money. We’ve been producing these animals for these markets, and if we can’t ship them, it’s very difficult for us to sustain them.”

Breeding the animals in the United States instead would be problematic: infrastructure and labour costs are much higher than they are in Asia, and colonies are much more likely to become the targets of animal activists. And moving the animals by sea is a non-starter because of the deleterious effects of the six-week trans-Pacific journey on the animals’ health.

Martin Paré, an associate professor at the Centre for Neuroscience Studies at Queen’s University in Kingston, Ontario, worries not only about his own access to primates, but about a slippery-slope effect. “If Air Canada was permitted to stop transporting non-human primates, what would be next? Stopping all animal transportation for research, which is what’s happening in the UK?”

Many airlines, including Lufthansa, British Airways and Virgin Atlantic, already refuse to carry research primates. In fact, the China Southern shutdown at Los Angeles resulted in part from PETA putting pressure on Lufthansa, which unloads planes for China Southern at the airport. Activists pointed out to Lufthansa that unloading research primates for the Chinese carrier was at odds with its policy on the transport of non-human primates. Within 24 hours, the China Southern macaque shipment was cancelled. Goodman speculates that “Lufthansa was anticipating a really bad PR situation”. Lufthansa says that it cannot comment on matters involving another carrier.

At the time that it merged with United Airlines in 2010, Continental Airlines was the last remaining US carrier that still transported research primates. United is preparing to publish a policy for the merged airline later this year.

“Nearly every major airline rejects the transport of primates to laboratories,” says Goodman. “The handful that are still doing it are facing more intense opposition and scrutiny than they ever have before. Because it’s not in their best interest to continue doing so, I am sure that they will stop.”

SEVERED LINKS

The next several months could prove crucial. After last week’s meeting, China Southern is still deciding whether it will resume transporting research primates through Los Angeles. If Air Canada’s petition to stop shipping primates is successful, Canadian researchers would be inconvenienced, but not entirely cut off — around 1,700 non-human primates were imported from the United States last year, mostly driven across the border. The Public Health Agency of Canada and Queen’s University are challenging the airline’s move, and a decision from the transportation agency is expected later this year.

“The research that Queen’s University performs has significant benefits for the health and welfare of Canadians,” says Steven Liss,

the university’s vice-principal for research. He adds that the humane treatment of the animals is “always” the university’s priority. “Air travel is simply the fastest and least stressful way of transporting them.”

Air France issued a statement last September declaring that “nothing allows the airline to decide on the merits of the use of animals in biomedical research,” which it called “important and scientifically justified”. Nonetheless, after it was bombarded with PETA-orchestrated e-mails, phone calls and Facebook postings, the airline cancelled a scheduled 1 February shipment from Mauritius of 60 monkeys bound for a private laboratory in Everett, Washington.

The apparent success of the public campaign has alarmed breeders, importers and biomedical researchers. “It’s unfortunate that some airlines have chosen to capitulate to a small number of individuals with an agenda who aren’t truly representative of the general public,” says Matthew Bailey, vice-president of the National Association for Biomedical Research in Washington DC, a trade organization that lobbies on lab-animal policy for drug firms and research universities.

Tipu Aziz, a professor of neurosurgery at the University of Oxford, UK, has used macaques

“More and more scientists will go elsewhere to do primate research.”

to study Parkinson’s disease. He believes that restricting transport of animals will not have the desired effect. “My gut feeling is that more and

more scientists will go elsewhere to do primate research,” he says. “I have no qualms about going abroad to do my work. There are quite a few countries that have good facilities: there are centres in India, Singapore, Malaysia, China.”

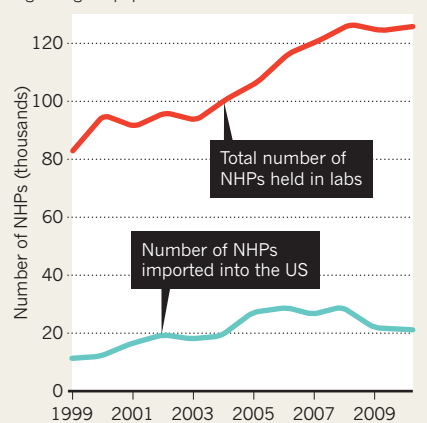
Others say that the drug industry — a major user of research primates — may also be inclined to relocate activities if the flight barrier becomes insurmountable.

“Let’s say [the activists] get their wish and no animal comes into the United States,” Hsu argues. “Merck is not going to say: ‘Okay, fine.’ They are going to go to other countries where animal care might not be as good, and start doing research there.”

Still, expert observers say that the pressure on the airlines is significant. “The public tide is turning against the use of non-human primates in general, and researchers must either find alternatives or convince the public there is a compelling reason to continue such research,” says Paul Root Wolpe, director of the Center for Ethics at Emory University in Atlanta, Georgia, which is home to the Yerkes National Primate Research Center. If scientists don’t make a louder, more persuasive public case, he says, “more companies — not only in transportation — will choose the side of animal-rights advocates”. ■ **SEE EDITORIAL P.373**

FREQUENT FLYERS

The United States has increased imports of non-human primates (NHPs) over the past decade, supplementing a growing lab population.



CRYSTALLOGRAPHY

Opioid receptors revealed

Two more structures join the parade of once-intractable proteins.

BY LIZZIE BUCHEN

On a small table in his office at the Scripps Research Institute in La Jolla, California, Ray Stevens spreads out a sheet of paper covered with colourful branched lines, each sprouting and thinning before terminating in an esoteric code.

"This is the dream," he declares.

The intricate diagram represents the largest family of receptor proteins encoded in the genome — the G-protein-coupled receptors (GPCRs), ubiquitous cell-surface molecules that are activated by light, odours, hormones and neurotransmitters. Stevens wants to determine the atomic structures of receptors on all branches of the tree. This week, that goal moved two receptors closer: Stevens's group has solved the atomic structure of the κ -opioid receptor (κ -OR)¹, and a team led by Brian Kobilka at Stanford University in California has solved the medically crucial μ -opioid receptor (μ -OR)². The structures, published in *Nature*, bring the tally of GPCR structures solved this year alone up to five.

Ten years ago, Stevens's dream would have seemed a hopeless fantasy — the complex, dynamic molecules had confounded relentless attempts to expose their atomic secrets by X-ray crystallography. But in 2007, several technological breakthroughs brought the drought to an end³, and the structures began to trickle out, with one or two solved nearly every year. Now, it seems the flood is approaching. Stevens's and Kobilka's groups each have another structure ready to go, on top of the five GPCRs they have already published this year^{4–6}. Stevens predicts several more from his lab by the end of the year.

The opioid receptors are hot targets. Opioid drugs, including morphine, codeine and oxycodone, are invaluable in medicine for their powerful painkilling and sedative effects. But they are also highly addictive, an enormous liability that limits their medical use. Their ability to produce a strong sense of euphoria also leads to rampant recreational use of prescription drugs and their more potent and deadly derivative, heroin. The majority of their effects, including analgesia, euphoria and sedation, are mediated by the μ -OR, although most opioid drugs are promiscuous, activating κ -OR and other opioid receptors as

well. Understanding the molecular structure of these receptors is crucial for designing drugs that exert the beneficial actions of opioids but lack the unwanted side-effects.

But opioid receptors, like other GPCRs, had long dodged the scrutiny of X-ray crystallography. The technique requires relatively

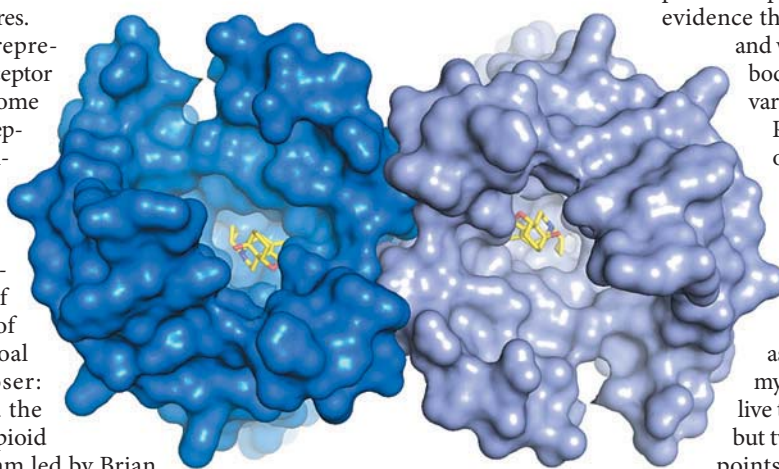
binding site may also explain why the actions of opioids can turn on so quickly and be rapidly reversed. Heroin overdoses, for example, can be quickly treated with opioid antagonists such as naloxone.

Kobilka and his colleagues also discovered that the μ -OR crystallized in tightly linked pairs, complementing several other lines of evidence that the receptor pairs with itself and with other opioid receptors in the body. These pairings may mediate the various effects of opioid drugs.

Philip Portoghese at the University of Minnesota in Minneapolis, who has been studying opioid receptors since the 1960s, is thrilled with the structures. "When I first started in the opioid field, crystallographic determination of any receptor was viewed as science fiction," he says. "Never in my wildest dreams did I think I would live to see the coordinates of not one, but two opioid receptors." Portoghese points out, however, that both receptors were crystallized in their inactivated states, which he says may limit the value of the structures in the hunt for safer painkillers.

Nor are crystal structures the be-all and end-all for rational drug design. GPCRs are not static; they writhe and twist, and crystal structures don't capture this crucial dynamism, which may be critical for designing drugs that can join in this dance. Kobilka, Stevens and many others are complementing crystallography with techniques that can capture protein movement, such as nuclear magnetic resonance and molecular-dynamics modelling.

On Stevens's website, where the tree of dreams is prominently displayed, 14 victorious red flags mark solved GPCRs, and more will follow very soon. It took at least 20 years of dogged devotion to solve the β_2 AR — but today, when someone visits Stevens's lab to learn about crystallography, he has them crystallize the once-uncrystallizable protein as an introductory exercise. It takes three days. ■



When crystallized with a ligand (yellow), μ -opioid receptors form an intimate pair.

large amounts of purified protein; for proteins nestled in cell membranes, such as GPCRs, that means carefully extracting the molecules from their fatty environment while maintaining their delicate shapes. Identical copies of the protein must then be packed so tightly that they form a crystal. This step is particularly difficult for GPCRs, which have floppy loops that are resistant to staying in place and conforming to a regular crystal lattice.

But one by one, the bottlenecks were circumvented. Kobilka, who had worked on crystallizing the β_2 -adrenergic receptor (β_2 AR) for more than 20 years, discovered that he could quiet the most restive loop by replacing it with a protein called T4L. In 2007, he and Stevens both crystallized the β_2 AR using T4L and a medium called the lipidic cubic phase^{7,8}. Since then, all but one of the solved GPCRs have been cracked using this approach.

The μ -OR and the κ -OR structures reveal that the binding pockets of both receptors are large and gaping, which Stevens suggests could explain how the κ -OR recognizes such a diverse set of molecules. Kobilka and his colleague Sébastien Granier, now a molecular pharmacologist at the French National Institute of Health and Medical Research in Montpellier, say that the openness of the μ -OR

1. Wu, H. *et al.* *Nature* <http://dx.doi.org/10.1038/nature10939> (2012).
2. Manglik, A. *et al.* *Nature* <http://dx.doi.org/10.1038/nature10954> (2012).
3. Buchen, L. *Nature* **476**, 387–390 (2011).
4. Haga, K. *et al.* *Nature* **482**, 547–551 (2012).
5. Kruse, A. C. *et al.* *Nature* **482**, 552–556 (2012).
6. Hanson, M. A. *et al.* *Science* **335**, 851–855 (2012).
7. Rosenbaum, D. M. *et al.* *Science* **318**, 1266–1273 (2007).
8. Cherezov, V. *et al.* *Science* **318**, 1258–1265 (2007).



Finance minister Pranab Mukherjee (centre, with other ministers) didn't deliver hoped-for increases.

past year, prompting a cautious budget. "Less funding for science agencies will mean fewer research grants for university scientists," says Ajay Sood, a physicist at the Indian Institute of Science in Bangalore, and president of the Bangalore-based Indian Academy of Sciences.

Vishwa Mohan Katoch, secretary for the Department of Health Research, says that although he had requested 30 billion rupees for 2012–13, his department had been allocated only 9 billion, an 18% increase on last year. Kanikaran Satyanarayana, deputy chief of the Indian Council of Medical Research, says that as a result, plans to increase funding for virology laboratories and establish a nationwide disease-surveillance network will have to be put on hold.

"If we want to bring in quality changes we need big money," says Katoch. "But what can the government do if they do not have resources?"

Thirumalachari Ramasami, secretary for the DST, is confident that the relative austerity of this year's budget will not set a precedent. "I am optimistic that funding will be restored [in 2013] once the 12th five-year plan, for 2012–17, is finalized by the planning commission," he says. That plan is expected by next month. Ramasami adds that the big DST projects outlined in Singh's speech should not be affected by the disappointing increases.

There is ample evidence that India's previous budgets have helped to advance science in the country, says Lingadahalli Shashidhara, a developmental biologist at the Indian Institute of Science Education and Research in Pune. "We have quadrupled the number of research faculty members in just ten years," he says. "The quality of projects coming to funding agencies is going up, and India is publishing research papers in high-impact journals more frequently."

But some researchers feel that Indian science needs reform much more than it needs extra cash. Rajesh Kochhar, a historian of science at the Indian Institute of Science Education and Research in Mohali, says that research institutions must be more strictly audited to divert funding away from poorly performing centres and give more to the most productive researchers. Increased funding cannot help to advance science "unless the weeds are ruthlessly removed so that the flowering plants can flourish," he says. ■

FUNDING

Indian budget disappoints

Downturn finally ends run of increases for science.

BY K. S. JAYARAMAN IN BANGALORE

India's remarkable growth in science funding — notching up annual increases of about 25% over the past five years — seems finally to have been hit by the global economic downturn.

Last week, the government's budget for 2012–13 promised increases of between 2% and 18% for most of its scientific departments, disappointing researchers who note that the country's 7% inflation rate will consume most of the extra cash (see table). An apparent increase of 52% in the space-science budget was actually caused by a roll-over of unused funds from last year.

Researchers had been expecting a major funding boost this year, after assurances from Prime Minister Manmohan Singh. In a speech at the annual Indian Science Congress in Bhubaneswar in January (see *Nature* <http://dx.doi.org/10.1038/nature.2012.9750>; 2012), Singh lamented that China's progress in science has overshadowed India's, and he promised a "major increase" in research and development spending, from the current 1% of the

gross domestic product to at least 2% by 2017. He also backed plans from the Department of Science and Technology (DST) for a 50-billion-rupee (US\$1-billion) supercomputing facility in Bangalore; a 13.5-billion-rupee neutrino observatory near Pudukkottai in Theni district, Tamil Nadu; and a 3.5-billion-rupee project to improve monsoon forecasting.

But on 16 March, finance minister Pranab Mukherjee's budget dashed scientists' hopes. The country's economic growth has slowed over the

DISCOURAGING RESULT

Budget allocations in billions of rupees.

	2011–12	2012–13	% increase
Atomic energy	67.24	76.51	13.8
Department of Health Research	7.70	9.08	17.9
Department of Science and Technology	26.06	28.73	10.3
Department of Scientific and Industrial Research	32.17	34.84	8.3
Department of Biotechnology	13.77	15.00	9.0
Department of Agricultural Research	50.08	53.92	7.7
Oceanographic research	6.99	7.13	1.8

PHYSICS

Clashing nations back SESAME

Participants put politics aside to find cash for construction of Middle-East synchrotron.

BY GEOFF BRUMFIEL

Israel and Iran can agree on little these days, but they have found common ground in a scientific project.

Despite brinkmanship over Iran's nuclear programme, the two nations have joined with Jordan and Turkey to commit crucial funding to the construction of Synchrotron-light for Experimental Science and Applications in the Middle East (SESAME). Under an agreement announced on 13 March, the partners have promised a total of US\$20 million towards the construction of the project. SESAME is now looking for a further \$15 million from other partner nations to complete the synchrotron's first four beamlines in 2015.

"The fact that we could get such an agreement given the political situation is kind of remarkable," says Chris Llewellyn Smith, the president of SESAME's governing council and a past director-general of CERN, Europe's particle-physics lab near Geneva, Switzerland.

Based in Allan, outside Amman, Jordan, SESAME aims to build scientific expertise in its member countries and bolster cultural ties between them. When completed, the \$110-million machine would be the Middle East's only source of high-intensity synchrotron X-rays, which are used in fundamental research ranging from molecular biology to materials science.

The project mirrors the organization of CERN, but Amman is a long way from Geneva — metaphorically as well as literally. In recent years, SESAME has had to contend with the assassination of two members of its Iranian delegation and huge political upheavals in partner countries including Egypt.

Despite the tensions, scientists involved with the project say that SESAME is succeeding because it has something to offer all the participants. Israel, for example, gets a world-class research facility on its doorstep and an opportunity to show its willingness to collaborate with neighbours, says Eliezer Rabinovici, director of the Institute for Advanced Studies

at the Hebrew University of Jerusalem, and a member of SESAME's council. Other member states see an opportunity to educate a young and rapidly growing science base. "Turkey is also interested in developing similar laboratories and SESAME would be a very good experience," says Zehra Sayers, a physicist at Sabanci University in Istanbul and head of SESAME's scientific advisory committee.

Llewellyn Smith is optimistic that the remaining money can be found. Now that local partners have committed funding, the project is more likely to gain support from outsiders such as the United States and the European Union. And other partners in the Middle East, notably Egypt, may yet provide cash, although political turmoil could make commitments difficult.

Rabinovici says that SESAME shows the strength of scientific collaboration, even under the most difficult circumstances. "This is an existence proof that scientists can, at least for a period of time, transcend the politics around them," he says. ■

BIOETHICS

DNA donor rights affirmed

NIH committee urges that genome study subjects be told of medically relevant results.

BY ERIKA CHECK HAYDEN

It is a familiar scenario in genetic research: a subject's DNA is collected for one study, deposited in a database or biobank and then analysed by other researchers for separate studies. But what happens when a later study stumbles on something that could be of significance for the donor, such as an allele for familial hypercholesterolaemia — a treatable genetic disorder that causes progressive atherosclerosis — or some other health-related variation? Do researchers conducting secondary studies and biobanks have a duty to share such revelations with the original research subjects?

They do, when possible, according to a detailed consensus statement from a working group funded by the US National Institutes of Health (NIH) in Bethesda, Maryland, and published this week (S. M. Wolf *et al. Gen. Med.* <http://dx.doi.org/10.1038/gim.2012.23>; 2012). The statement's 26 signatories consulted dozens of other researchers and biobank managers over a two-year period. They conclude that biobanks "shoulder significant responsibility" for addressing how to deal with 'incidental findings' — those research results that could have medical consequences for the donors of genetic material.

Genetics researchers are divided on the matter of incidental findings. Conventional research ethics holds that participants should not be told of their individual results, to keep them from expecting to benefit personally from the study. What's more, reporting such findings can be a logistical challenge because many studies strip identifying information from donated samples. But, increasingly, geneticists are embracing the idea that research participants have a right to know of any unwelcome surprises in their genome. "If

we really believe this is medically valuable and useful data, then we have to act on it," says Leslie Biesecker of the US National Human Genome Research Institute in Bethesda, who contributed to the discussions that led up to the consensus statement but is not a signatory.



Genetic testing is increasingly coming up with 'incidental findings'.

The need to establish policies for the return of results has grown with the proliferation of whole-genome sequencing, says James Evans, editor-in-chief of *Genetics in Medicine*, which is publishing an entire issue on the return of results in genetic research, along with the consensus statement.

In the past, says Evans, medically significant incidental findings were an exception in genetic studies, but "when you do whole-genome sequencing you will regularly come up with findings that have some medical import". Yet less than half of US biobanks return results to participants, according to a study done for the working group by Mao Thao of the University of Minnesota in Twin Cities and colleagues. The working group, coordinated by Susan Wolf of the University of Minnesota Law School in Minneapolis, urges biobanks to take the lead in changing that ethos. The group

recommends that each biobank sets up a committee to oversee the return of results and also that a single central advisory body be created that would foster consistency among biobank research systems. Wolf led a previous NIH working group that in 2008 published recommendations proposing that primary researchers — those responsible for collecting data — should report some incidental findings back to research participants (S. M. Wolf *et al. J. Law Med. Ethics* **36**, 219–248; 2008).

But some researchers warn that keeping track of incidental results and re-identifying participants so that they can be informed could prove costly and pose ethical and legal difficulties. "It's unfortunate that the authors of the consensus statement didn't discuss the cost implications of what they're proposing, because what they have in mind is going to be expensive and difficult, particularly at a time when funding success is as low as it's ever been," says Ellen

Wright Clayton, a paediatrician and lawyer at the Center for Biomedical Ethics and Society at Vanderbilt University in Nashville, Tennessee.

Wolf counters that some biobanks already do return results, so it does not need to be prohibitively costly or difficult. For instance, Biesecker runs a study called ClinSeq, which has enrolled around 900 people whose exomes (the protein-coding part of the genome) are being sequenced. The participants are told about any findings that could have implications for their health care. Biesecker says that there is an increasing tension in the field between studies such as his that underscore the usefulness of genetic medicine and an assumption that it is too costly and difficult to use the results of such studies to help improve patients' lives. "I don't think, as a field, that we can continue to say both things at the same time," Biesecker says. ■ **SEE EDITORIAL P.373**

MORE ONLINE

TOP STORY



One researcher's genome shows personalized genomic medicine in action go.nature.com/rwgs6z

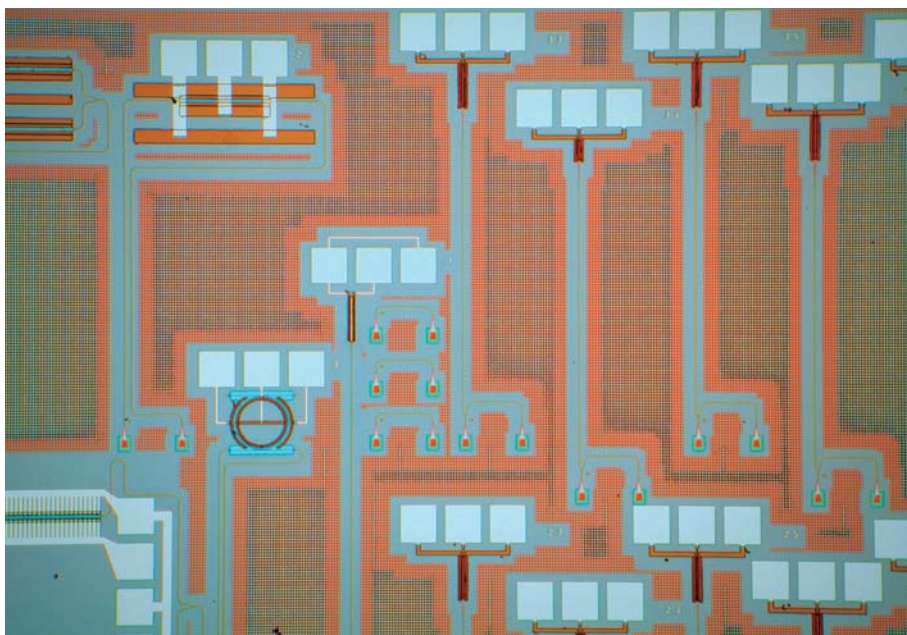
OTHER NEWS

- Satellites expose 8,000 years of civilization go.nature.com/2ejdri
- Rare autism spectrum disorder partially caused by faulty immune cells in the brain go.nature.com/oekimu
- Spurred flies turn to booze go.nature.com/oxshcm



VIDEO

The laser that can see around corners go.nature.com/is4lfx



Optical components including modulators, waveguides and photodetectors crowd a silicon chip.

TECHNOLOGY

Photonic chips made easier

Shared-production system aids academics and start-ups.

BY KATHERINE BOURZAC

If you want to speed up computers much more, you will need a faster messenger. That is the idea behind silicon photonics, which whizzes data around a silicon chip using light instead of sluggish old electrons.

Photons already carry data in fibre-optic cables for telecommunications. But using light in computing means carving transistors and lasers out of the same wafer of silicon, which needs an advanced manufacturing 'foundry'. Only large companies and a few research institutions with deep pockets have these facilities, and some researchers worry that lack of access is slowing progress in photonics.

A project called Optoelectronic Systems Integration in Silicon (OpSIS) now promises a solution. Based at the University of Washington in Seattle and at the University of Delaware in Newark, OpSIS provides design support for researchers in silicon photonics; organizes shared production runs; and arranges low-cost access to advanced foundries so that academics and start-up companies can create prototype devices. The US Air Force is the project's biggest funder, with more support coming from Intel, based in Santa Clara, California,

and design-automation company Mentor Graphics in Wilsonville, Oregon.

OpSIS will make its first batch of silicon photonics prototype chips at the Institute of Microelectronics' foundry in Singapore this month. Its customers are some 25 groups working on high-speed communications circuits, portable medical diagnostic devices and photonics basic research.

Users will pay US\$1,500 for one square millimetre of wafer space, with projects requiring anywhere from 10 mm² to 40 mm². Researchers going it alone would have to pay for a complete production run at the foundry — at a cost many times higher. OpSIS offers much lower prices by putting many different projects into a single run and splitting the cost.

Michael Hochberg, a photonics researcher at the University of Delaware who co-founded and leads OpSIS, knows how expensive it can be to translate silicon photonics technology from university lab into product. In 2001, he co-founded

Luxtera, in Carlsbad, California, the first company to offer integrated electronics and optics on chips, which are now used commercially in

data centres and supercomputers. Luxtera spent more than \$100 million to develop and produce its first product, released in 2010. "I want to make it possible to do what Luxtera did for an order of magnitude less cost," says Hochberg. OpSIS will soon also have access to foundries owned by Luxtera and by UK aerospace company BAE Systems, headquartered in London.

The history of the silicon chip suggests that OpSIS could be hugely influential. Its shared-production model is based on the University of Southern California's Metal Oxide Semiconductor Implementation Service (MOSIS), which has been operating since 1981 in Marina del Rey and has helped the semiconductor industry to grow rapidly. Electronics pioneers, including Carver Mead at the California Institute of Technology in Pasadena, pushed for academics and small companies to gain access to fabrication facilities ('fabs') to build the integrated circuits they needed to test their ideas and train students. At the time, academics were restricted to making simple devices in the lab, doing theoretical work or — as Mead did — having friends at Intel sneak their students' designs into production runs. "You have to have access to a fab to build the real thing," says Mead.

Silicon photonics now is at a similar stage to the electronics industry in the early 1980s, says Mario Paniccia, director of the photonics technology lab at Intel. Today's photonics researchers have better access to foundries than Mead did decades ago, but most are still excluded from the cutting-edge facilities that can make more complicated devices.

A data-processing photonic chip, for example, must integrate lasers, waveguides and electrical transistors in complex systems that are completely reliable. Making such devices in advanced fabrication facilities ensures that they are of acceptable quality, says OpSIS user S. J. Ben Yoo, director of the Center for Information Technology Research in the Interest of Society at the University of California in Davis.

A service similar to OpSIS has been offered since 2008 by the ePIXfab initiative, funded in part by the European Union. But OpSIS has access to more advanced foundries, says Lukas Chrostowski, an electrical engineer at the University of British Columbia in Vancouver, Canada.

Chrostowski has 20 designs in the first OpSIS run. Several are prototype versions of optical sensors for a hand-held medical diagnostic device that could analyse blood samples to detect disease biomarkers. Previous versions of this system were far from being hand-held: Chrostowski had to attach an external laser and a detector to an optical chip he made using ePIXfab. Through OpSIS, he will now be able to integrate all the building blocks onto one chip in a more realistic prototype.

This sort of innovation cannot be left only to well funded companies, says Paniccia. "We need more people experimenting, learning, and innovating with silicon photonics." ■

➔ **NATURE.COM**
For more on silicon photonics, see Focus at:
go.nature.com/yqwdaa

TRANSLATIONAL RESEARCH

Mice guide human drug trial

Parallel approach to cancer study provides genetic insights.

BY HEIDI LEDFORD

The mouse hospital at the Dana-Farber Cancer Institute in Boston, Massachusetts, boasts resources rivalling those offered to human patients, including state-of-the-art medical-imaging facilities, round-the-clock nursing staff and access to cutting-edge cancer drugs. The goal is not to cure mice, of course, but to gain insight into clinical trials of those drugs in humans.

The roughly 5,000 rodent residents at Dana-Farber are pioneers in an approach known as a co-clinical trial, in which a human clinical trial is partnered with animal studies designed to reveal clues about why some patients respond to a treatment and others fail to do so. The first findings from the Dana-Farber project, published online on 18 March (Z. Chen *et al.* *Nature* <http://doi.org/hrr>; 2012), suggest that adding an experimental drug called selumetinib to standard chemotherapy may help to shrink lung tumours in patients with mutations in a gene called *KRAS*. The parallel study in the mouse revealed, however, that the drug may fail in those who also carry a mutation in a tumour-suppressor gene called *LKB1*.

"Normally, very little scientific interrogation occurs during the conduct of a human cancer trial," says David Tuveson, a cancer researcher at the University of Cambridge, UK, who was not involved in the study. "This is a logical and badly needed path forward."

It is standard for new drugs to undergo animal studies before they reach the clinic. But early-stage animal trials can be misleading because they often fail to mimic the conditions of subsequent human trials, says Andrew Kung, an oncologist at Dana-Farber and an author on the mouse study. By contrast, a co-clinical trial is designed to closely match a parallel trial in human subjects.

Selumetinib, developed by Array BioPharma of Boulder, Colorado, and London-based AstraZeneca, is a member of a hotly pursued class of cancer drug that inhibits a crucial biochemical step promoting tumour-cell proliferation and survival. Full results of the human trial, which enrolled 87 patients with *KRAS* mutations, have yet to be published. Array BioPharma announced last year that, when given with standard chemotherapy, the drug slowed the progress of the cancer. Effects on overall patient survival were not statistically significant.

➔ NATURE.COM
For ways to fix the clinical trial, see:
go.nature.com/wy6bns



SAM OGDEN

A genetically engineered mouse lung-cancer model offers clues to its human analogue.

Like the human subjects, the hundreds of mice used for the co-clinical trial carried a mutated form of *Kras*, but some also contained mutations in the tumour-suppressor genes *p53* and *Lkb1*. Mice treated with selumetinib and standard chemotherapy benefited if they had the additional mutation in *p53* alone, but the *Lkb1* mutation seemed to render the drugs ineffective. Outcomes of the mouse trials were measured using methods similar to those for the human subjects, which meant relying on non-invasive imaging techniques, rather than simply killing the animals and measuring tumour volume, as is often done in animal studies.

"It is a new way to use mice as a looking glass into the human condition."

Overall, the mouse study suggests that, in future trials of selumetinib, patients should be screened for the presence of *LKB1* mutations, says Kung. That would allow researchers to determine whether a genetically identifiable subset of patients resistant to the drug may be affecting their results.

The results in mice also suggest that an imaging technique called FDG-PET can measure short-term tumour responses to selumetinib. The method could be a boon for human studies, because patients generally cannot be subjected to repeated tumour biopsies.

The co-clinical approach could speed up drug development as oncology increasingly embraces complex treatment regimens involving multi-drug cocktails and tailored

for specific genotypes, says Hugues de Thé, a cancer researcher at the Paris Diderot University. He has used a similar approach in a trial of drugs for a form of leukaemia, but says that the new work is a "technical tour de force" because of the genetic complexity of the tumours studied.

Many other centres are developing facilities for co-clinical trials, but the experiments can be prohibitively expensive. The drugs often need to be given daily, which requires more personnel to handle the animals, and the technology used to image tumours in living animals can be costly. Mouse hospitals will probably have to invest heavily in generating trial-specific mouse models of cancer, cautions Tuveson, who has been using the approach to tackle pancreatic cancer. "You need the infrastructure to breed these animals and then to follow them just like you would in a hospital, and most laboratories do not have that."

But funders are aware of the approach's promise. In 2009, the US National Cancer Institute in Bethesda, Maryland, awarded US\$4.2 million to Pier Paolo Pandolfi, a cancer researcher at Harvard Medical School in Boston who is a co-author on the *Nature* study, to establish the co-clinical trial project in lung and prostate cancer. Additional grants from Stand Up To Cancer, a project of the Entertainment Industry Foundation charity, based in Los Angeles, California, are funding co-clinical trials in breast and ovarian cancer. It is a new way, says Tuveson, "to use mice as a looking glass into the human condition". ■

RAISING THE DEAD

To dissect evolution, Joe Thornton resurrects proteins that have been extinct for many millions of years. His findings rebut creationists and challenge polluters.

BY HELEN PEARSON



Halfway through breakfast, Joe Thornton gets a call from his freezer. A local power cut has triggered an alarm on the -80°C appliance in his lab at the University of Oregon in Eugene, and it has sent out an automatic call. Thornton breaks off our conversation and calls his senior research scientist, Jamie Bridgham, to make sure that the back-up generator has kicked in. If the freezer starts warming up, a lot could be lost — not least a valuable collection of proteins that had been extinct for hundreds of millions of years until Thornton and his team brought them back from the dead.

One deep-frozen vial holds the more-than-600-million-year-old ancestor of the receptors for oestrogen, cortisol and other hormones, which Thornton brought to life¹ nine years ago. Other tubes house proteins more than 400 million years old, which Thornton resurrected a few years later to show how an ancient receptor had changed its preferences — and how the march of evolution cannot be reversed²⁻⁴. In another corner of the freezer rest the ancient protein components of a sophisticated cellular machine that acquired a more complex form through random mutations rather than selection for superior function, as the group showed in *Nature* this January⁵. The sheer awe of working with long-dead proteins doesn't fade, says Thornton. "It's amazing. The ability to do this type of time travel is fantastic."

Thornton is a leader in a movement to do for proteins what the scientists in *Jurassic Park* did for dinosaurs: bring ancient forms back to life, so that they can be studied in the flesh. "Instead of passively observing things as most evolutionary biologists do, you actively go in and test the hypotheses experimentally," says Antony Dean, a molecular biologist at the University of Minnesota in St Paul who heads another major group in the field. "His is one of the leading labs, no doubt." And Thornton is tackling some important questions, says Kenneth Miller, a

molecular biologist at Brown University in Providence, Rhode Island. "He's helping to put some flesh on the bones of speculation about how complexity arises."

What isn't so widely known is that evolutionary biology is Thornton's second career: in his first, he was an activist for Greenpeace, campaigning vigorously against the release of toxic chemicals. He wrote a controversial book on organochlorines: industrial chemicals that include dioxins, polychlorinated biphenyls (PCBs) and pesticides such as DDT. That activist legacy bleeds into his work today, for example in his focus on the oestrogen receptor, which is corrupted by many pollutants. The grubby, sea-green tiles under Thornton's lab benches were carefully sourced to be free of polyvinyl chloride (PVC), one of the organochlorines that worries him most. His activist past also helps to explain why he has been fearless — almost enthusiastic — about highlighting the challenge that his work presents to a creationist argument called intelligent design: the claim that complex molecular systems can only have been created by a divine force. Thornton shows how evolution did the job, leaving no need for a designer.

ENVIRONMENT TO EVOLUTION

Thornton says that his activist days — during which he saw that many risk-assessment models were shot through with assumptions and biases — left him "intensely committed to methodological reductionism and experimentalism", which he now uses to break evolution down into detailed steps that he can test. "If you're doing science, I think it ought to be as strong and decisive as possible," he says. "If you're doing politics, go ahead, but don't try to disguise it as science."

Thornton's unconventional career path started with an obsession with *Moby Dick*, which led him to study English at Yale University in New

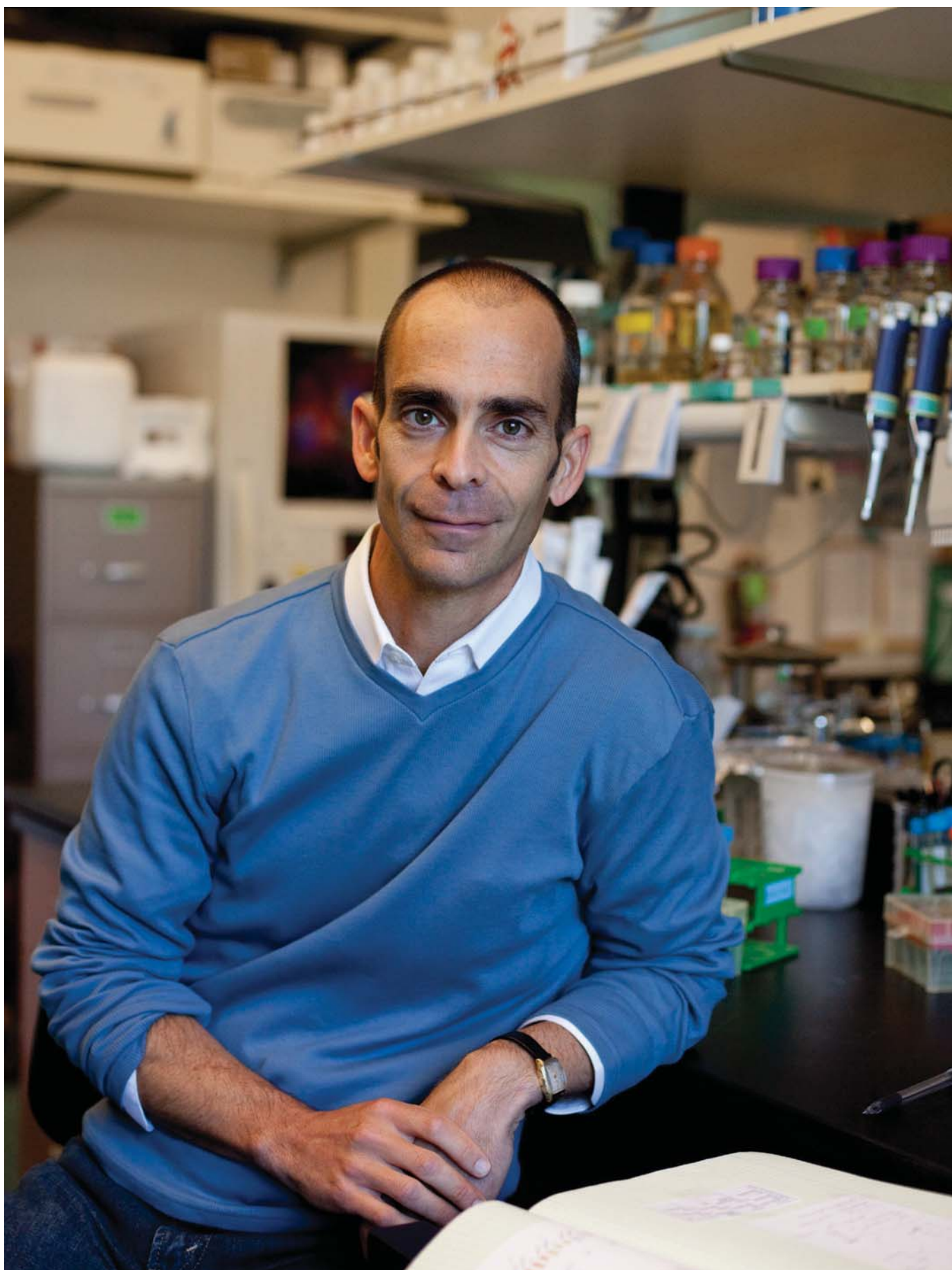
Haven, Connecticut. But the course, with its focus on the philosophy of criticism rather than literary texts, left him with a hunger for reality, and nothing seemed more real than politics and activism. He dropped out of college, signed up with Greenpeace and spent several months doorstepping to canvass people for money and support.

In the early 1990s, Greenpeace was campaigning against sources of toxic pollution, and Thornton was drawn in. He became the 'science guy', translating the scientific literature into reports and other material that communities and Greenpeace could use to make their case. "You could rely on Joe when you didn't have enough knowledge of an issue," says Charlie Cray, a research specialist at Greenpeace in Washington DC, who worked with Thornton. His reports "put a challenge out there that industry couldn't answer". One campaign that Thornton helped to organize, against plans to build more than 100 hazardous-waste incinerators across the United States, climaxed in May 1993 when Greenpeace parked a truck dressed up as an incinerator outside the White House and some 60 people chained themselves to it. The next day, the Environmental Protection Agency announced a moratorium on new hazardous waste incinerators.

But Thornton was growing older, and yearning to "develop my own body of work". His time with Greenpeace had taught him the power of science to influence society, and his ambitions turned to research. First, he had to deal with the small matter of graduating from Yale. Then living in New York, he did that by accruing course credits at Columbia University — attending his first molecular-biology classes aged 30 — only to find himself rejected from almost every graduate programme he applied to, in part because of his unusual CV.

Of the seven friends and colleagues of Thornton's who spoke to *Nature*, six called him intense. The seventh described him as "beyond intense". But only a little of that

► NATURE.COM
Hear more about
protein resurrection
on *Nature's* podcast:
go.nature.com/5tlcza



intensity is apparent at his Wednesday morning lab meeting in Eugene. The freezer crisis has blown over: the power came back after half an hour and the thermometer rose to only -76°C . Now graduate student Dave Anderson gets a friendly grilling during a practice talk outlining his thesis proposal: to trace the evolution of the DNA-binding domain of an ancient hormone receptor. The meeting stretches on for 2.5 hours — not uncommon in this lab, everyone says.

A BINDING FASCINATION

Since his Greenpeace days, Thornton has been fascinated by the steroid hormone receptors: in vertebrates, six proteins that sit in the cell nucleus and control the activity of genes. By binding specific 'ligands' — hormones ranging from oestrogens and androgens to cortisol — the receptors trigger "these remarkable cascades of biological activity during development and physiology", Thornton says. "Their affinity for their hormones is just stunning. A drop of hormone in a railroad tank car of serum is enough" — and yet, as Thornton learned at Greenpeace, they can be waylaid by toxic substances. "I wanted to know where that system came from," he says.

When he was finally accepted for a PhD at Columbia, he set about comparing receptor genes from living organisms to piece together a detailed history of how the receptor family had evolved⁶.

Just as Thornton completed his first year of graduate study, however, MIT Press called to ask if he would write a book on organochlorine pollution. He worked in the lab during the day and wrote at night, in a tiny room in his Brooklyn apartment, encircled by towers of papers that eventually formed the nearly 1,200 references and 611 pages of *Pandora's Poison*, which came out in 2000. "I was shocked when I saw the book," says Rob DeSalle, who studies molecular evolution at the American Museum of Natural History in New York, and co-supervised Thornton's PhD. "He could've been writing *War and Peace* and I wouldn't have known it."

The book caused a stir. Drawing on arguments that he had formulated at Greenpeace, Thornton made the case that regulatory policy should focus on managing classes of toxic chemicals rather than tens of thousands of substances, one by one — and that the priority should be organochlorines. These substances, generated by the use of chlorine gas in the chemical and paper-making industries, have properties of stability and solubility that make them desirable to industry but problematic to the environment because they are long-lived and accumulate in animal tissues. *Nature's* review called *Pandora's Poison* a "landmark" and another review compared it to Rachel Carson's famous 1962 treatise on pollutants, *Silent Spring*. The Chlorine Chemistry Council in Washington DC, however, decried Thornton's "hyperbole and faulty risk analysis".

But Thornton was already gearing up to make a different kind of splash, with his first paper in *Science*¹. He and his team trampled the assumption that only vertebrates have steroid hormone receptors by cloning one from the sea slug *Aplysia californica*. The finding implied that the origin of the receptor gene was far more ancient than anyone had realized. "I would've hated to be a fellow grad student. He was writing a book and publishing in *Science* and having two children at the same time," says Darcy Kelley, a biologist at Columbia and Thornton's other PhD co-supervisor.

The approach that Thornton took in the 2003 study is one that he has loosely followed ever since. Starting with the genes for steroid hormone receptors from a slew of living organisms, he clambered backwards through the evolutionary tree to deduce the most likely sequence of the common ancestor of all such receptors, which existed some 600 million to 800 million years ago, in the common ancestor of "you and a snail", as he puts it. Instead of stopping there, as most evolutionary biologists would have done, he then built the gene and inserted it into cells that could manufacture the ancient protein.

Resurrecting the protein, says Thornton, allowed his team "to experimentally test hypotheses about evolution that would otherwise be just speculation". They went on to show¹ that the ancestral receptor was sensitive to oestrogens but not to related hormones — supporting the idea that the family of receptors evolved through a series of gene duplications

"HE'S HELPING TO PUT SOME FLESH ON THE BONES OF SPECULATION ABOUT HOW COMPLEXITY ARISES."

and that the copies gradually evolved affinities for other ligands (see 'Receptors, resurrected').

By the time his paper came out in *Science*, Thornton had taken a faculty position in Eugene, an old hippy town that pays as much homage to bicycles as it does to cars. He built a house (no PVC, sustainable bamboo floors) and set to work building up his protein-resurrection lab.

Thornton wanted to delve deeper into the puzzle of how complex systems with tightly interacting molecular parts evolve. It was a long-standing conundrum. As Charles Darwin wrote in *On the Origin of Species*: "If it could be demonstrated that any complex organ existed which could not possibly have been formed by

numerous, successive, slight modifications, my theory would absolutely break down." And what was an evolutionary puzzle to biologists was a target for evolution's critics. Michael Behe, a biochemist at Lehigh University in Bethlehem, Pennsylvania, and a senior fellow at the Discovery Institute in Seattle, Washington, proposed in the 1990s that such systems — the blood-clotting cascade, for example, or the molecular motor called the flagellum — are so "irreducibly complex" that they could not have evolved step by step, and can only be the product of intelligent design.

Thornton says that he didn't set out to refute intelligent design, but the prospect of a fight hardly put him off. "Been there, enjoyed that," he says. He chose to explore a pair of steroid hormone receptors: the mineralocorticoid receptor (MR), which binds the hormone aldosterone and regulates salt and water balance; and the closely related glucocorticoid receptor (GR), which binds cortisol and controls stress response. A gene duplication more than 450 million years ago produced the two receptors — but aldosterone didn't arise until many millions of years later. The timing seemed to make the MR a textbook example of irreducible complexity: how could selection drive the evolution of a lock (the MR) to fit a key (aldosterone) that didn't yet exist?

EVOLUTION AT WORK

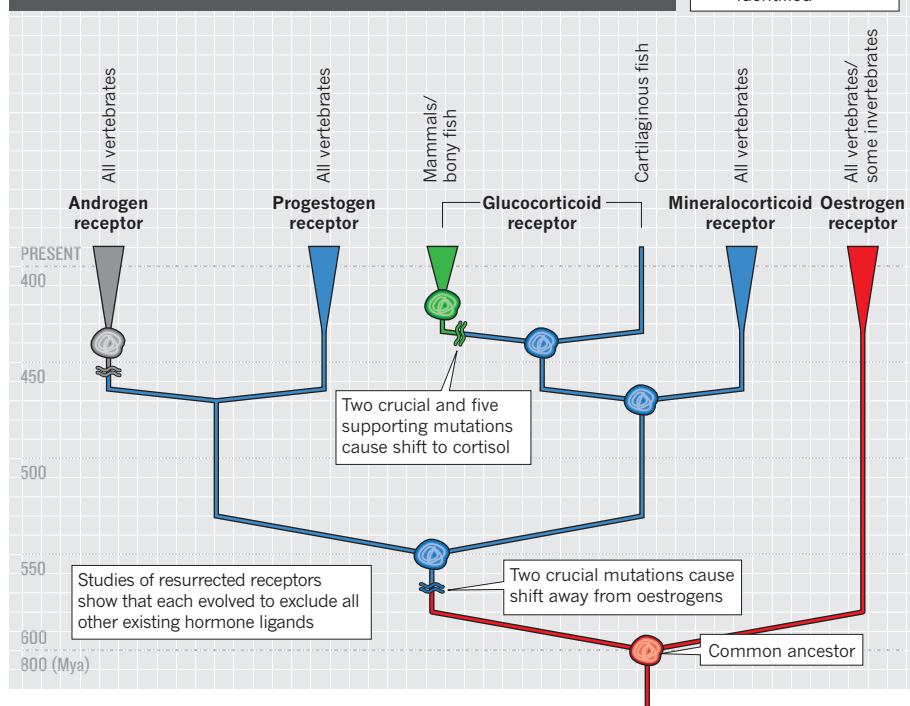
Led by Bridgham, Thornton's team found the answer by resurrecting the ancestor of both receptors. To their surprise, it was sensitive to aldosterone, suggesting that it had been activated by an ancient ligand with a similar structure². Once aldosterone had evolved, the team proposed, evolution was able to take advantage of the existing receptor to control a new biological function — a process that Thornton termed molecular exploitation. They also showed how its sister receptor, the GR, was evolving functions of its own.

"Such studies solidly refute all parts of the intelligent design argument," wrote Christoph Adami, an evolutionary biologist at the Keck Graduate Institute of Applied Life Sciences in Claremont, California, in an article entitled 'Reducible complexity'⁷. But Behe dismissed the result. The receptor and ligand are not irreducibly complex, he says, and evolution did not give them any truly new function. "I think his results are quite consistent with my own view that Darwinian processes are poor ones to explain the complexity found in life," Behe told *Nature*.

Thornton turned up more clues to the workings of evolution when his team explored the history of the GR, which became sensitive only to cortisol over the course of about 20 million years. Working with structural biologists at the University of North Carolina, Chapel Hill, the group determined the crystal structure of the common ancestor of the GR and MR. They showed³ that two crucial mutations together

RECEPTORS, RESURRECTED

The vertebrate steroid hormone receptors evolved from a common ancestor that existed 600 million to 800 million years ago (Mya). Resurrecting ancient proteins on its family tree has revealed key events in their evolution.



to simulate the movements of every atom in the ancestral receptors, showing how just two mutations drove the transformation. When Harms hits play, an oestrogen molecule snuggles its way into the binding pocket of a receptor roughly 550 million years old. But when he runs a simulation of the same receptor with those two mutations, the oestrogen never finds a comfortable spot.

This evolutionary story also sheds light on why the oestrogen receptor is now vulnerable to the threats against which Thornton campaigned in his former life. The team worked out that each steroid receptor evolved to be only as specific as it had to be to bind its target ligand and exclude all others that existed at the time. The oestrogen receptor achieves this by binding substances that contain a chemical structure called an aromatized A ring. Because oestrogens are the only steroid hormones to have such a ring, that criterion was enough to ensure that the receptor bound only oestrogens for many millions of years. Until, that is, the chemical industry started pumping out hundreds of substances containing such aromatized rings, which the oestrogen receptor unwittingly bound. "The endocrine disrupters are taking advantage, unfortunately, of the promiscuity that is the result of the evolutionary history of receptors," Thornton says.

Thornton does see progress on the issues on which he once campaigned. Production of toxic chemicals in the United States has fallen since his days with Greenpeace, and in 2007 the European Union enacted REACH (Registration, Evaluation, Authorisation and Restriction of Chemicals), which emphasizes elimination of the most dangerous substances. That law puts the onus on the chemical industry to show that a chemical is safe rather than on regulators to prove it is dangerous — the approach for which Thornton argued in *Pandora's Poison*.

Does he miss having something to campaign against? Yes and no. "I'm less able to convince myself that the world has to be exactly as I envision it. So it's harder for me to occupy that activist persona." Besides, he says, "My kids take all that energy now."

Or almost. His creations need tending too. Back in his office, we listen to the tinny voice-mail message left by the freezer on his phone earlier that day. "The past is calling," Thornton says. ■

Helen Pearson is Nature's chief features editor.

1. Thornton, J. W., Need, E. & Crews, D. *Science* **301**, 1714–1717 (2003).
2. Bridgman, J. T., Carroll, S. M. & Thornton, J. W. *Science* **312**, 97–101 (2006).
3. Örtlund, E. A., Bridgman, J. T., Redinbo, M. R. & Thornton, J. W. *Science* **317**, 1544–1548 (2007).
4. Bridgman, J. T., Örtlund, E. A. & Thornton, J. W. *Nature* **461**, 515–519 (2009).
5. Finnigan, G. C., Hanson-Smith, V., Stevens, T. H. & Thornton, J. W. *Nature* **481**, 360–364 (2012).
6. Thornton, J. W. *Proc. Natl Acad. Sci. USA* **98**, 5671–5676 (2001).
7. Adami, C. *Science* **312**, 61–63 (2006).

altered the binding pocket of the ancestral receptor so that it preferred to bind cortisol — and identified another five mutations that finished the job.

In a final chapter to the story, Thornton tried to run that evolutionary sequence backwards. But when the researchers reversed the seven mutations in the ancient cortisol-specific form, they could not transform it back into a protein that worked like the common ancestor of the GR and MR. They instead engineered a dud, unable to respond to any hormone⁴. That was because a handful of other mutations had also cropped up on the way to making a cortisol-specific receptor. They played little part in the receptor's new function, but acted as an evolutionary ratchet, preventing it from regaining its old one.

Thornton showed that it was necessary to undo those mutations too, to reverse the change. To him, the work was a powerful demonstration that the path of evolution can be contingent on random events. "Chance plays a very large role in determining what evolutionary outcomes are possible," he says. The study captivated the scientific press — and beyond. "Evolution opens gateways into the future. But it appears to close them — firmly — behind it as well," read an editorial in the *New York Times*.

In the *Nature* article that was published this year⁵, Thornton took a break from hormone receptors, and instead collaborated with Tom Stevens, a geneticist at Eugene, to dissect the evolution of V-ATPase, a molecular machine that pumps protons across membranes to acidify compartments inside cells. The group

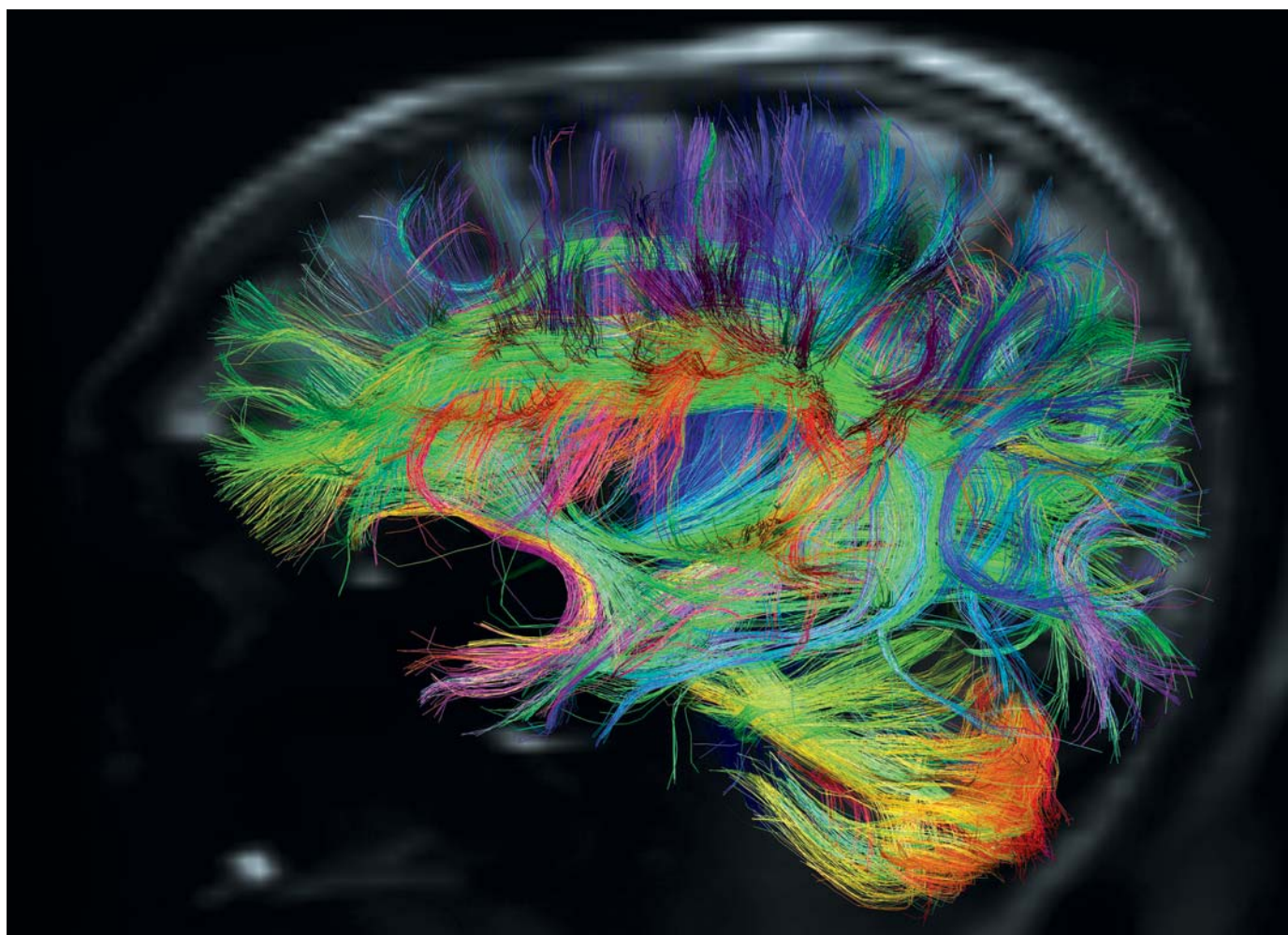
wanted to know how an essential part of the machine — a ring of proteins that spans cell membranes — evolved from an ancestral form with two components to one with three.

With their protein-resurrection toolbox, the researchers showed that, around 800 million years ago, the ancestral gene coding for one protein component was duplicated, and the daughter genes then picked up two vital mutations. The changes meant that the proteins could no longer sit anywhere in the ring, but instead had to occupy a specific spot. Suddenly, the ring could function only with all three parts. What surprised Thornton was that the three-component ring seemed to work no better than its two-component counterpart. Random mutations that actually corrupted proteins had led to 'irreducible complexity'.

COMPUTING COMPLEXITY

The study flipped another finger to intelligent-design proponents — but "I'm sort of bored with them," Thornton says. He is more excited by the next scientific story that is about to come out of the lab. His group wanted to explore how the ancestor of the entire steroid hormone receptor family, which was sensitive only to oestrogens, evolved into forms sensitive to other hormones. And this time, he found no clues in the crystal structures of resurrected proteins from before and after the change.

The answer can be found on a computer screen at the end of Thornton's lab. Mike Harms, a postdoc who joined the lab three years ago, used his expertise in biophysics and some immense computational power



MGH HUMAN CONNECTOME PROJECT ACQUISITION TEAM

Making connections

Is a project to map the brain's full communications network worth the money?

BY JON BARDIN

A building that once housed a Second World War torpedo factory seems an unlikely location for a project aiming to map the human brain. But the Martinos Center for Biomedical Imaging — an outpost of the Massachusetts General Hospital in an industrialized stretch of Boston's riverfront — is home to an impressive collection of magnetic resonance imaging machines. In January, I slid into the newest of these, head first. The operator ran a few test sequences to see whether I experienced any side effects from the unusually rapid changes in this machine's magnetic field. And, when I didn't — no involuntary muscle twitches or illusory flashes of light in my peripheral

vision — we began. The machine hummed, then started to vibrate. For 90 minutes, I held still as it scanned my brain.

That scan would be one of the first carried out by the Human Connectome Project (HCP), a five-year, US\$40-million initiative funded by the National Institutes of Health (NIH) in Bethesda, Maryland, to map the brain's long-distance communications network. The network, dubbed the 'connectome', is a web of nerve-fibre bundles that criss-cross the brain in their thousands and form the bulk

of the brain's white matter. It relays signals between specialized regions devoted to functions such as sight, hearing, motion and memory, and ties them together into a system that perceives, decides and acts as a unified whole.

The connectome is bewilderingly complex and poorly understood. The HCP proposes to resolve this by using new-generation magnetic resonance imaging (MRI) machines, like that used to scan my brain, to trace the connectomes of more than 1,000 individuals. The hope is that this survey will establish a baseline for what is normal, shed light on what the variations might mean for qualities such as intelligence or sociability, and possibly reveal what

The nerve fibres of the author's brain were traced by diffusion spectrum imaging, and coloured to represent their direction.

happens if the network goes awry. “We increasingly believe that brain disorders — from schizophrenia to depression to post-traumatic stress disorder — are disorders of connectivity,” says Thomas Insel, director of the National Institute of Mental Health (NIMH) in Bethesda and a strong supporter of the HCP. “So it is of vital importance that we have ways of detecting and quantifying these connections.”

Yet many wonder whether the NIH is making a mistake. Researchers have yet to prove that MRI techniques can produce a reliable picture of normal connectivity, never mind the types of abnormal connection likely to be found in brain disorders, and some researchers argue that the techniques have not been adequately validated. “I would do the basic neuroscience before I started running lots of people through MRI scanners,” says David Kleinfeld, a physics and neurobiology researcher at the University of California, San Diego.

THE GRAND CHALLENGE

Proponents counter that the HCP is a calculated risk. “No one thinks this is going to produce a wiring diagram like you might have for the electricity in your house,” says Insel. But so little is known about the connectome, he says, that even crude maps would represent a major scientific advance.

The decision to take that risk was made by the NIH's Blueprint for Neuroscience Research, set up in 2004 as a collaboration among the 15 NIH institutes, centres and offices with an interest in nervous-system research. In 2009, after five years of funding smaller projects, the group asked officials from across the NIH to submit ideas for ‘grand challenges’ in neuroscience: large-scale programmes that, Insel says, “would be both extremely high-impact, and virtually impossible with traditional grant mechanisms”.

The Blueprint group received a dozen submissions, including one from Michael Huerta, then a programme officer at the NIMH and a member of a Blueprint subcommittee. Huerta, now at the NIH's National Library of Medicine, began his research career studying the organization of mammalian brains using old-school anatomical and neural-tracing techniques, which typically require the injection of a tracer compound that migrates along nerve fibres and reveals their routes. So he was all too familiar with the barriers to such studies in humans. For ethical reasons, tracers can only be used post-mortem — when they don't migrate far enough to trace a fibre's full length. “The studies just never panned out,” says Huerta.

In 2007, Huerta became fascinated by two new non-invasive imaging methods that might finally allow researchers to study the finer details of connectivity in the brains of living

humans. The first was diffusion-spectrum imaging (DSI), developed in 2005 by Van Wedeen, a radiologist at the Martinos Center, and his colleagues¹. DSI is a refinement of the two-decades-old diffusion tensor imaging technique, which exploits MRI's ability to detect the direction in which water molecules are moving at each point in the brain. Because most of those molecules move along the lengths of nerve fibres, like water through a pipe, the data can be used to reconstruct each fibre's location and trajectory. What DSI adds is a more sophisticated form of signal analysis that allows researchers to continue tracing fibre bundles even when one

“We increasingly believe that brain disorders are disorders of connectivity.”

seems to pass behind another, a situation that posed serious problems for the older technique.

The second method that caught Huerta's attention was resting-state functional MRI (rs-fMRI), in which people think about nothing in particular while their brain activity is measured. This is quite different from conventional functional-imaging studies, in which participants are asked to carry out a specific cognitive task and researchers look for the brain regions that are activated in the process. In rs-fMRI, there is no task, and researchers look for correlations among the activity levels in different areas. The presumption is that any two regions with a consistently high correlation are linked — perhaps by an actual bundle of nerve fibres, but certainly by working together in some way.

The application of both DSI and rs-fMRI had already led to a number of high-profile publications. But Huerta realized that few groups were applying both methods in the same subjects, and most studies used small samples, limiting their generalizability. So he proposed that the Blueprint group fund a Human Connectome Project that would apply both methods to hundreds of people. This would allow the first large-scale comparison to be made between structural connectivity, as determined by DSI, and functional connectivity, as determined by rs-fMRI. “No single neuroimaging approach would give you the type of gold-standard connectivity data you need,” says Huerta, recalling his argument for the dual data sets.

The Blueprint group was intrigued, but was not blind to the problems inherent in these techniques. One obvious issue is DSI's spatial resolution: each fibre bundle in the image contains thousands of neurons, meaning that it would miss a great deal of structure on smaller scales.

Partha Mitra, a neuroscientist at Cold Spring Harbor Laboratory in New York, illustrated the problem to me by displaying a series of high-resolution digital pictures of mouse brain slices, each of which had some of its neurons coloured with a dark brown dye. On one such

slice, he showed neurons that originated in the left cortex, then branched out and sent fibres to areas on both the left and the right side of the brain. “The brain is not made up of point-to-point connections,” he said. “It's made up of trees.”

This level of connectome structure is invisible to even the most advanced diffusion-imaging methods, says Mitra, who heads the Mouse Brain Architecture Project, a parallel version of the HCP, funded by the NIH and the W. M. Keck Foundation of Los Angeles, that seeks to generate a whole-brain wiring diagram for the mouse using staining techniques. And the problem is

made even worse when the data are converted into a ‘connectivity matrix’, which seeks to quantify how much every point in the brain is connected to every other point — but can't tell the difference between, say, two separate fibres and one fibre with two branches.

The Blueprint group was also aware of concerns about resting-state scans. As with the more familiar form of fMRI, what is actually measured isn't neural activity itself, but blood flow. The general presumption is that the two quantities are closely related — that blood flow increases in a region of the brain whenever the neurons there are active and need to be supplied with more oxygen. But recently, Kleinfeld points out, several studies have called that assumption into question, showing that some increases in blood flow in the brain occur without an increase in neuronal activity². “There is no simple one-to-one relationship,” he says.

A REMAINING CONCERN

That makes rs-fMRI studies particularly hard to interpret, Kleinfeld adds, if only because the brain's resting-state activity may fluctuate on the same timescales that its blood vessels do. A recent review³ of rs-fMRI admits that this vascular fluctuation “remains a concern”. Other studies show that even something as simple as a subject's pattern of breathing⁴ or slight movements of the head⁵ can significantly confound rs-fMRI measurements.

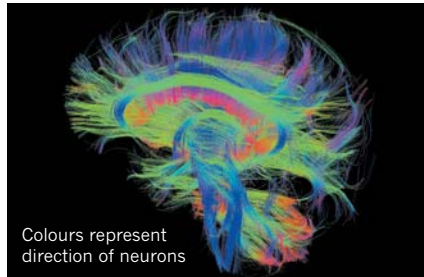
Even leaving the technical challenges aside, there was no assurance that collecting the connectomes of hundreds of individuals would lead to interesting generalizations. “You could certainly imagine situations in which everyone's wiring diagrams are quite different,” says Gregory Farber, the programme officer at the NIMH who manages the connectome project. Nonetheless, the Blueprint group was swayed by the argument that imperfect data are better than no data. “The committee asked, ‘Will we have better methods in five years?’” recalls Huerta. “I'm sure we would. But if we followed

SCANNING THE CONNECTOME

The Human Connectome Project aims to trace the brain's long-range communication network using two main techniques, both of which rely on magnetic resonance imaging (MRI) to obtain data from living people.

Mapping structure

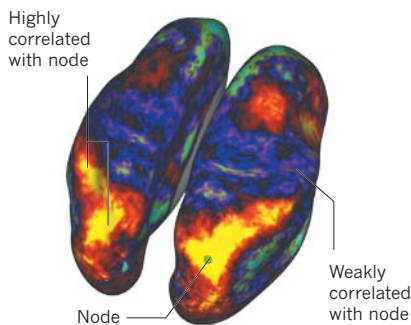
Diffusion spectrum imaging detects the movement of water molecules that flow along nerve fibres in the brain. The result is a map of the brain's neuronal network.



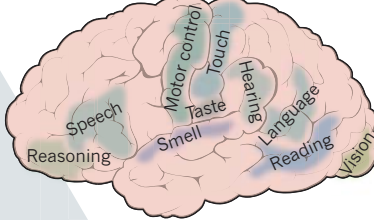
Colours represent direction of neurons

Mapping function

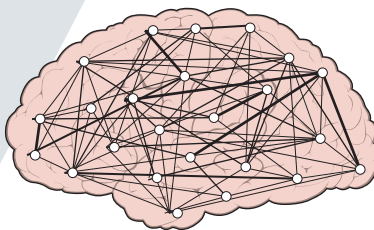
Resting-state functional MRI maps resting brain activity, then looks for correlations between one area and another. Highly correlated areas are thought to have some kind of functional link.



The brain has many areas specialized for specific functions, some of which are shown here.



Data on structure and function can be combined and analysed using tools such as network theory.



The connectome ties these areas together, allowing the brain to function as a coherent whole. The project's goal is to understand how the connectome works.

that rule, no science would ever get done."

The group also liked the fact that the findings would be broadly applicable to clinical, as well as scientific, questions. "We thought we could do something like what we did with the Human Genome Project," Insel says, "because once you have that map of the brain you can compare it to similar maps across development, or to maps of subjects with different disorders of brain circuitry."

A BLUEPRINT FOR THE BRAIN

In July 2009, the Blueprint group announced its choice of the HCP as one of three grand challenges — the other two focused on pain and on drugs for nervous-system disorders — and simultaneously put out a request for proposals. On 15 September 2010, the NIH announced that it would be funding two HCP proposals.

The larger of the two is a 5-year, \$30-million effort led by David Van Essen, a neurobiologist at Washington University in St Louis, Missouri, and Kamil Ugurbil, an fMRI pioneer at the University of Minnesota in Minneapolis. (Another collaborator is Olaf Sporns, a neuroscientist at Indiana University in Bloomington, a co-author on the 2005 review article that coined the term 'connectome'.⁶) During phase one, now nearing completion in Minneapolis, this

team has developed a scanner that will be able to double the resolution of standard MRI.

Once complete, that scanner will be moved to Washington University, where it will immediately begin high-throughput scanning. The plan is to use both DSI and rs-fMRI (see 'Scanning the connectome') to study 1,200 people: 300 identical twins, 300 non-identical twins and 600 non-twin siblings. This will allow researchers to explore how much of the brain's connectivity is mapped out by genes. Volunteers will also complete behavioural tests and other fMRI, magnetoencephalogram and electroencephalogram protocols, so that brain structure can be further correlated with function. All these data will be made public, allowing unaffiliated researchers to answer their own questions, and Van Essen's group plans to release a set of new data-analysis tools. Connectomics, Van Essen says, "has been a cottage industry. But we expect this project to allow for a much richer, more unified approach".

The smaller HCP project — a 3-year, \$8.5-million effort led by Bruce Rosen, a radiologist at the Massachusetts General Hospital, and Arthur Toga, a neurologist at the University of California, Los Angeles — involved building a new fMRI scanner optimized for the collection of fibre-tracking data. The idea

was to massively increase the gradient strength of the machine — a measure of how rapidly the MRI's magnetic field varies from point to point in the brain. A more intense gradient is like "a bigger mirror in a telescope", says Wedeen, who is director of connectomics at the Martinos Center. It simultaneously makes the instrument more sensitive to faint signals, and gives it a higher resolution. The machine has now been built — it is the one that collected images of my brain in January — but will require much more tweaking and testing before it is optimized for routine use. But the researchers have already achieved a tenfold increase in sensitivity to the water-diffusion signal, allowing their scanner to trace connections much more precisely than the best off-the-shelf machines.

In a press release announcing the launch of the HCP in July 2009, Insel said that the project would "map the wiring diagram of the entire, living human brain" and that this map could be linked to "the full spectrum of brain function in health and disease". Such lofty ambitions may or may not succeed in five years. But the project still has its place, says Sebastian Seung, a computational neuroscientist at the Massachusetts Institute of Technology in Cambridge, who studies brain connectivity at the cellular level. "I think it is a mistake to think we have to look at every cell in every region of the brain to make scientific progress," says Seung, who is not involved in the HCP.

But he also emphasizes that the HCP's connectivity map will be, at best, a beginning. "That is just going to tell us where to look," he says. "Then we need to study actual cells to learn more", to figure out how the brain's networks actually transmit information.

A week after my visit to the Martinos Center, I received my DSI data. Using free software from the centre, it is easy to explore the architecture of my brain. I can clearly see my hippocampus, and the vast array of fibres projecting from the midbrain sensory hubs up to my cerebral cortex. I am overwhelmed by the visible detail and obvious organization. At present, it is just a pretty picture — a novelty to show friends. But, I wonder: once scientists know what 'average' looks like, and once they understand the variations, what, if anything, will this rainbow-coloured highway map of my brain say about me? ■

Jon Bardin is a freelance writer based in New York.

1. Wedeen, V. J., Hagmann, P., Tseng, W. Y., Reese, T. G. & Weisskoff, R. M. *Magn. Reson. Med.* **54**, 1377–1386 (2005).
2. Sirotni, Y. B. & Das, A. *Nature* **457**, 475–479 (2009).
3. Kelly, C., Biswal, B. B., Craddock, R. C., Castellanos, F. X. & Milham, M. P. *Trends Cogn. Sci.* **16**, 181–188 (2012).
4. Di, X., Kannurpatti, S. S., Rypma, B. & Biswal, B. B. *Cerebral Cortex* <http://dx.doi.org/10.1093/cercor/bhs001> (2012).
5. Power, J. D., Barnes, K. A., Snyder, A. Z., Schlaggar, B. L. & Petersen, S. E. *Neuroimage* **59**, 2142–2154 (2012).
6. Sporns, O., Tononi, G. & Kötter, R. *PLoS Comput. Biol.* **1**, e42 (2005).

COMMENT

MARINE CONSERVATION A broader concept for protecting ocean reserves **p.399**

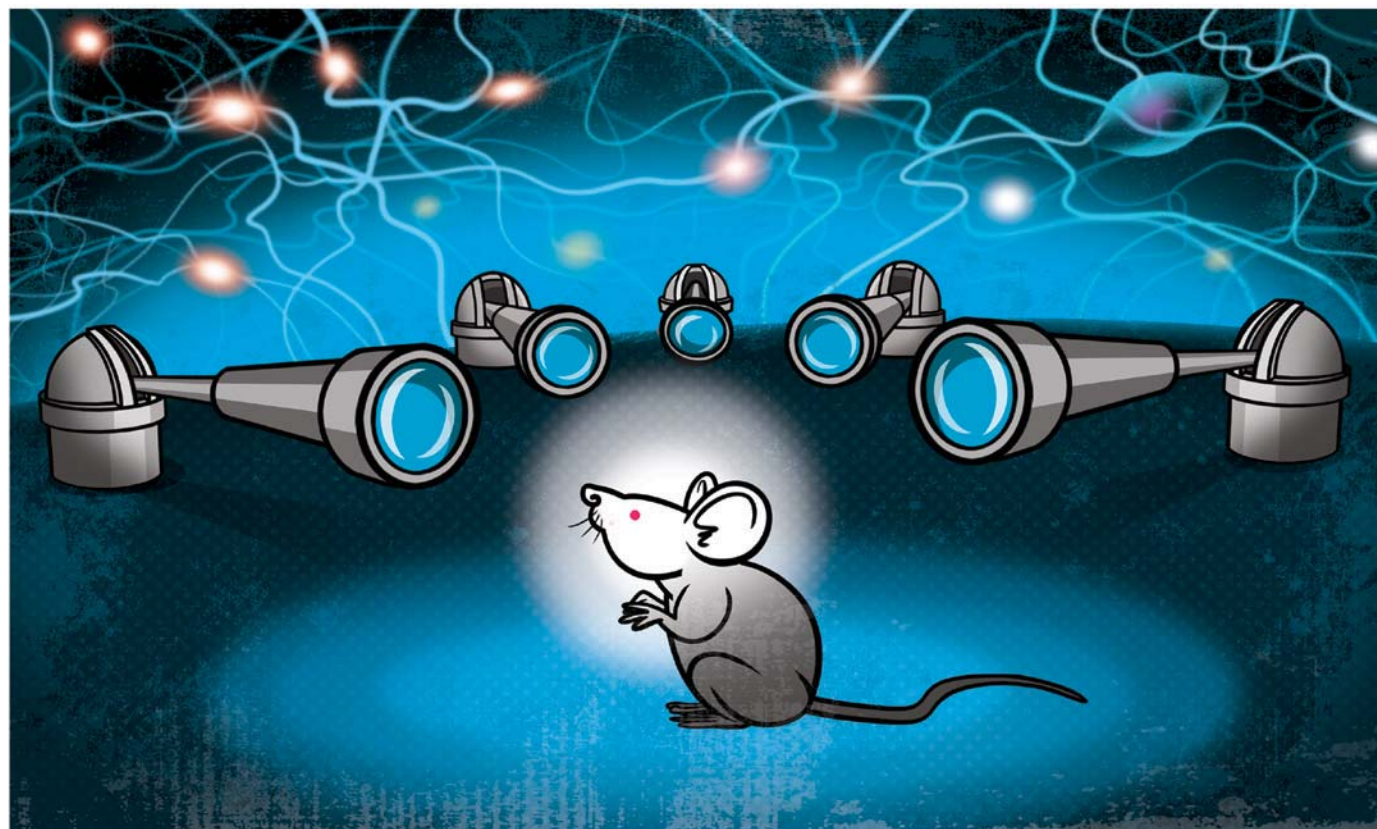
PHYSICS How the discovery of cosmic rays a century ago seeded particle physics **p.400**



EXHIBITION Transgenic sushi and the future of food **p.404**

OBITUARY Renato Dulbecco, elegant pioneer of cancer biology **p.408**

ILLUSTRATION BY PETE ELLIS, DRAWGOOD.COM



Observatories of the mind

An ambitious project to map the mouse brain at the Allen Institute for Brain Science is a huge undertaking that may unify neuroscience, argue **Christof Koch** and **R. Clay Reid**.

Neuroscience is a splintered field. Some 10,000 laboratories worldwide are pursuing distinct questions about the brain across a panoply of spatio-temporal scales and in a dizzying variety of animal species, behaviours and developmental time-points. At any large neuroscience meeting, one is struck by the pace of discovery, with 50,000 or more practitioners heading away from each other in all directions, in a sort of scientific Big Bang.

Although this independence is necessary, it has prevented neuroscience from entering a more mature phase, which would involve

developing common standards and collaborative projects. Neurophysiologists are more likely to use each other's toothbrushes than each other's data and software; physiological results are hoarded and rarely made accessible online; molecular compounds and transgenic animals are shared only after publication. All of this has made comparisons across laboratories difficult and has slowed progress.

At the Allen Institute for Brain Science in Seattle, Washington, we and our colleagues are initiating an experiment in the sociology of neuroscience — a huge endeavour

that will involve several hundred scientists, engineers and technicians at the institute. Philanthropist Paul G. Allen, who founded the institute in 2003, has pledged US\$300 million for the first four years of an ambitious ten-year plan that will accelerate progress in neuroscience, bringing his total commitment so far to \$500 million. Our goal is to attract the best young scientists and build a series of 'brain observatories', with the aim of identifying, recording and intervening in the mouse cerebral cortex, the outermost layer of the brain. Unlike the telescopes that peer at remote events in space ▶

► and time, our instruments will track the flow of information in complex, interbraided neural circuits within a layer of tissue one millimetre thick.

The goal is to synthesize knowledge from all relevant disciplines — from genomics, anatomy and physiology to computer modelling — into a comprehensive theory of how the mouse uses its cortex to see. Following Allen's founding mandate for the institute, we will curate and publicly share all data and other resources (such as transgenic animals, probes and neuronal morphologies) for free, even before publication.

We believe that this initiative signals the arrival of large-scale science in a field that is populated by small groups. It will require rewarding the team, rather than a few lead investigators, for its collective effort. We envisage a time in the future when sophisticated, well-equipped brain observatories — 'mindscopes' — will complement the many academic neuroscience labs that will continue to make the bulk of discoveries.

Although the institute's project will focus on visual stimuli in mice, it will capture fundamental aspects of higher brain functions: perception, conscious awareness and decision-making, and how they lead to action. Once neuroscientists know the basic mechanisms in the mouse, they may start to understand more-complex forms of perception in other animals, including humans. In short, we believe that this project has the potential to revolutionize our understanding of the mammalian brain.

2020 VISION

The brain observatories initiative focuses on the cerebral cortex — the proverbial 'grey matter' that is one of the hallmarks of mammals, and the seat of cognition and intelligence. For its size, the cortex is the most complex piece of organized matter in the known Universe. But given a grain of cortex, it is not easy to tell from which mammal it came. We all have the same basic hardware — humans just happen to have a thousand times more of it than mice (see 'Man versus mouse').

The project will start with the anatomy of cortical neurons, using molecular techniques to count and catalogue the diverse array of cells that transmit information into and out of the visual cortex, as well as those that lie solely within the cortex. Then we will observe and measure the electrical activity of a sizeable fraction of those neurons to learn how the function of the cortex follows from its structure. It is a big question, but less daunting if one considers the cortex as being composed of many copies of a basic local circuit.

Studies of the human brain have been revolutionized by magnetic resonance

► **NATURE.COM**

For more on the European Human Brain Project: go.nature.com/fjcdtt

MAN VERSUS MOUSE

Comparing the human and mouse brain reveals why mapping the mouse brain is easier.

	Human	Mouse
Mass of brain	1,500 grams	0.5 grams
Number of brain neurons	86 billion	70 million
Number of cortical neurons	16 billion	14 million
Fraction of cortex that is visual	20%	~10%
Cortical regions involved in vision	30	10
Number of neurons in these areas	5 billion	1 million–2 million
Axons in optic nerve	1 million	45,000

SOURCE: REFS 3–5

imaging, which reveals brain regions activated in real time. However, the underlying signals are slow and fuzzy, and brain regions are not the building blocks of the mind — neurons, in their immense complexity, are the atoms of perception and thought.

Fortunately, scientists can now study individual mammalian neurons in living brains, by making neurons fluoresce using genetic engineering. Neurons can be made to emit flashes of light when they are active or, using the most recent optogenetics techniques, can be controlled with light (named Method of the Year in 2010 by *Nature Methods*¹). In this way, researchers can transiently and reversibly control certain events in specific cell types at defined times. Perturbing the nervous system lets neuroscience move from correlation to causation, from observing that a given circuit is activated whenever the animal makes a decision to inferring that this circuit is necessary for decision-making.

Other technological advances enable neuroscientists to visualize every axon, dendrite and synapse in a circuit using three-dimensional electron microscopy. Another observatory in the visual-brain programme is designed to record the electrical activity of thousands of neurons simultaneously. When all of these techniques are stitched together, one can imagine a full physiological and structural characterization of entire brain regions.

Finally, we will use all of this information to generate realistic and dynamic computer models of the mouse cortex and its associated structures, and use these to build theories of how the visual cortex behaves. The modelling facility will be next door to the labs so that collaborators can mingle easily. This should shorten the time between prediction and experimental validation, a virtuous circle that will be iterated until the model faithfully reproduces the data.

A CALCULATED RISK

Even though neuroscientists have spent the past 120 years uncovering the constitutive elements of the mammalian brain, we are far from understanding how any higher brain function comes about. Yet such knowledge is vital, especially because of the toll that

nervous-system injuries and disorders take on individuals, families and society at large.

Although the challenge may seem daunting, we are not the first to propose such a huge undertaking. For example, the European Human Brain Project, under the leadership of Henry Markram at the Swiss Federal Institute of Technology in Lausanne, hopes to bring together some 150 principal investigators in 22 countries to create working computer models of the mouse, rat, monkey and human brains². The brain observatories programme at the Allen Institute differs in that we are focusing on a single sense, in a single species, in one institution.

We know that such an expensive project will have critics: the resources required could fund hundreds of other projects, so why focus them in this way? Our response is that funding agencies are already spending billions of dollars on many smaller projects across all areas of biomedical research, and the Allen Institute wants to pioneer a new approach. We want to understand one piece of brain tissue by integrating knowledge across techniques and scales, rather than distributing the funds more widely.

There is a risk that this project will not work out as we anticipate, and that the various brain observatories — looking at anatomy, physiology and modelling, for example — will not synergize to form a sophisticated understanding of the mouse visual cortex. There is no guarantee that neuroscience is ready to become big science — but the only way to find out is to try. ■

Christof Koch is at the Allen Institute for Brain Science, Seattle, Washington 98103, USA, and at the California Institute of Technology, Pasadena, California 91125, USA. **R. Clay Reid** is at Harvard Medical School, Boston, Massachusetts 02115, USA, and will join the Allen Institute this summer. e-mail: christofk@alleninstitute.org

1. *Nature Methods* **8**, 1 (2011).
2. Waldrop, M. M. *Nature* **482**, 456–458 (2012).
3. Herculano-Houzel, S. *Front. Hum. Neurosci.* **3**, 31 (2009).
4. Herculano-Houzel, S., Mota, B. & Lent, R. *Proc. Natl Acad. Sci. USA* **103**, 12138–12143 (2006).
5. Wang, Q. & Burkhalter, A. J. *Comp. Neurol.* **502**, 339–357 (2007).

Think big for marine conservation

Err on the side of caution and protect the widest-possible areas of ecologically important deep sea, say **Phil Weaver** and **David Johnson**.

Marine protected areas are key tools for conservation, but they have some serious shortcomings. The Convention on Biological Diversity (CBD) has called for these areas to cover 10% of each of the world's marine and coastal eco-regions by the end of 2020. Even this modest target is proving elusive. So far, less than 2% of the ocean has been designated as protected, and nearly all of these areas are in coastal and continental-shelf regions. This is partly the result of a lack of data from the open ocean, and partly because of pressures from various interest groups, which may resist the management of ocean areas with valuable resources.

There is now an additional option for protecting the marine environment. In 2010, the CBD created a process to officially endorse Ecologically or Biologically Significant Areas (EBSAs) and to convey information to competent intergovernmental organizations, such as the United Nations General Assembly, for further action. The point of EBSAs is to allow scientists to identify areas that are particularly important to the function of marine ecosystems without the requirement for an accompanying detailed management plan. This 'softer' procedure opens the door to labelling a larger swathe of the ocean as important to ecosystem functioning.

An EBSA is defined by a set of criteria established by the CBD in 2008: the area should contain unique, rare or endemic creatures and/or habitats; have a special role in the survival of a given species; be important for the survival or recovery of threatened species; be vulnerable, fragile or slow to recover once harmed; have high biological productivity; and/or have high biological diversity. These are good criteria. Unfortunately, there are vast swathes of ocean about which very little is known, for which these criteria can be hard to prove.

This lack of knowledge is not preventing fishing, deep-sea mining and other exploitation from expanding, however; nor should it stand in the way of designating EBSAs. We believe that EBSAs should be made as large as possible, encompassing all areas within which the criteria are likely to be substantively met, even before that can be proven.

This approach should be widely adopted by the scientific community now, while proposed EBSAs are being drawn up for a first technical evaluation at a CBD meeting in Montreal, Canada, at the end of April, before their political endorsement.

ATLANTIC BEGINNINGS

The first CBD regional workshop to identify EBSAs was held in September 2011 to consider the northeast Atlantic, which already hosts a number of marine protected areas

Fortunately, the eventual consensus of this meeting was to propose large EBSAs: eight extensive areas (averaging 362,097 square kilometres each) and two smaller international bird areas. For Hatton–Rockall, that meant drawing a line around the entire banks region, measuring 264,322 km². This stands in stark contrast to the average size of the 276 protected areas in this ocean's national waters, which average just 1,040 km² each, and the 6 high-seas protected areas, at 47,718 km² each.

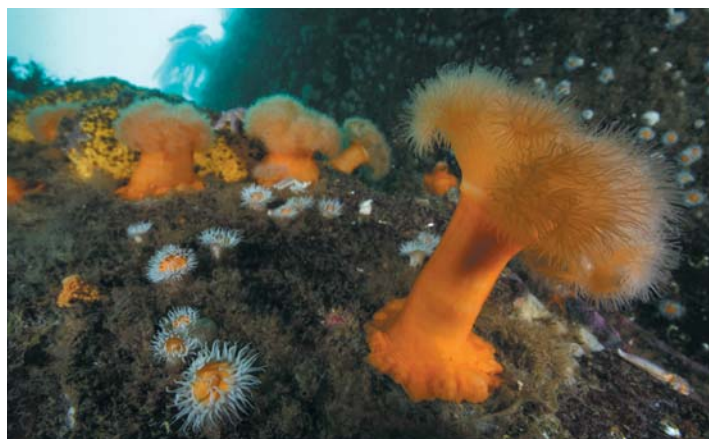
What should happen once an EBSA is defined? We suggest that a marine spatial plan be drawn up for each EBSA and regularly updated. This will articulate a vision, show what activity is taking place in the region (from commercial fishing to tourism) and study the impacts of those activities. In terms of management, we support a three-tier approach whereby areas that historically have been heavily fished and are now degraded remain unprotected; areas with light historical fishing are given full protection; and moderately fished areas are subject to further scrutiny. Marine protected

areas could sit comfortably within EBSAs, giving protection to the most critical ecosystems. The main benefit of this system is that it appeals to many different stakeholders: for example, it legitimizes existing fishing activities while preventing them from spreading to vulnerable ecosystems in future.

As scientists meet to rationalize what exactly EBSAs should look like in different parts of the world, we urge them to err on the side of caution and to make the areas large rather than small. This will open the door to broader conservation measures and to sustainable development in future. ■

Phil Weaver is science coordinator of the Global Ocean Biodiversity Initiative and is at the National Oceanography Centre, Southampton, UK. **David Johnson** is executive secretary for the Convention for the Protection of the Marine Environment of the North-East Atlantic (OSPAR) in London. e-mail: ppew@noc.ac.uk

Further reading accompanies this article online at go.nature.com/soxziu



Species such as North Atlantic anemones deserve conservation attention.

and precautionary bottom-fisheries closures. This ocean includes the Hatton and Rockall banks and basin area, to the west of Ireland and Scotland. This area, parts of which are heavily fished, hosts many discrete habitats and supports a wide range of animals, including fragile cold-water coral reefs and sponges. It provides feeding grounds for birds such as shearwaters and petrels. And it may harbour turtles and the endangered blue whale (*Balaenoptera musculus*) as well as the critically endangered North Atlantic right whale (*Eubalaena glacialis*). The exact boundaries of any of the habitats and species distributions are yet to be established.

Initially, there was considerable support among the 25 participating scientists for the designation of small, discrete EBSAs, such as isolated seamounts, in the northeast Atlantic. Experts were focused on their particular specialist habitat or species group, and were conscious that their expert judgement would be scrutinized by their peers. Under such circumstances, it can be difficult to support a large EBSA that extends beyond one's expertise and into areas where there are little data.

A century of cosmic rays

High-energy nuclei coming from far beyond the Solar System, and the exotic particles they produce, remain our best window onto the extreme Universe.

Michael Friedlander reflects on what we have learned.

“Coming out of space and incident on the high atmosphere, there is a thin rain of charged particles known as the primary cosmic radiation.” With these words on the nature of cosmic rays, British physicist Cecil Powell began his Nobel prize lecture in 1950.

Powell's prize was awarded for his development of the photographic method of identifying high-speed and short-lived particles that were turning up unexpectedly in cosmic-ray studies as the products of high-energy collisions. At the same time, that photographic method was being used to discover new components of Powell's ‘thin rain’: heavy atomic nuclei. These two strands — the study of primary cosmic rays and the products of their collisions — continue to be woven into the fabric of today's research.

Although particle collisions are now studied mainly through the use of giant particle accelerators, the only window into the behaviour of the very highest-energy particles comes from examining cosmic rays. The study of the primary cosmic radiation is a part of current astrophysics: by comparing the composition of cosmic rays with that of stars, we can identify their sources and use them to investigate violent stellar processes.

This year, we celebrate the centenary of the discovery of cosmic rays by Austrian-American physicist Victor Hess. Over the decades, cosmic-ray research has spread in directions that he could never have imagined, from the discovery of antimatter to the use of carbon dating in archaeology. It has even played a crucial part in the origins of ‘big science’.

RADIATION SOURCE

Hess's research was carried out in the heady days following the discovery of radioactivity and the electron. In the early 1900s, a prime research tool in the study of radioactivity was the electroscope, a sensitive device for measuring the ionization produced by radiation. It was soon found that the radioactive components of some rocks produced ionization, and most researchers believed that Earth's crust was the source of background levels of radiation. To investigate, scientists lowered electroscopes into lakes and oceans, carried them up mountains and took them to even greater heights in open baskets underneath hydrogen-filled balloons. The

results were conflicting, with some showing a decrease in ionization with altitude, others an increase. It was during this confusing time that Hess, in 1911, started his own series of balloon flights.



Physicist Victor Hess on a balloon flight in 1912.

Hess found that the ionization rate at first decreased with altitude, but then started to increase up to a height of 5.3 kilometres, the greatest height he reached. That flight took place from northern Bohemia (now part of the Czech Republic) on 17 April 1912, when a partial solar eclipse was visible from many parts of Europe. Hess detected no decrease in ionization during the eclipse, indicating that whatever the main source of the ionizing radiation coming from above, it was not the Sun.

Born in Austria in 1883 and educated at the University of Graz, Hess was a young assistant at the Radium Institute of the Austrian Academy of Sciences at the time of the flights. His discovery brought him a series of increasingly senior positions and growing professional recognition, culminating

in a shared Nobel prize in 1936. With the deteriorating political situation in Europe, Hess was dismissed from his post at the University of Innsbruck in 1938 because he had a Jewish wife. He managed to escape from Austria, taking up a faculty post at Fordham University in New York.

For some years after these legendary beginnings, the nature of cosmic rays was strenuously debated by physicists. Robert Millikan (who coined the term ‘cosmic rays’ in 1925) continued to insist that they were electromagnetic ‘rays’, even after Arthur Compton had established that they were really ‘particles’, as revealed by the way in which they were deflected by Earth's magnetic field.

The experimental study of cosmic rays has often moved ahead of theory, yielding a host of unpredicted discoveries. One of the most dramatic was the observation of particles of antimatter. Paul Dirac's relativistic quantum theory had foretold the existence of antiparticles, and Dirac speculated that anti-atoms with anti-electrons might exist in distant anti-stars. But he made no predictions as to where to look for them on Earth: certainly not among cosmic rays.

In 1911, a tool for the study of cosmic rays had been developed by Scottish physicist C. T. R. Wilson. Wilson realized that water droplets were formed in the atmosphere by condensation of vapour on ions (an observation inspired by watching mist form on the summit of Ben Nevis in Scotland). He converted this insight into a powerful laboratory-scale device — the cloud chamber — in which the passage of charged particles was made visible by their trails of liquid droplets. In 1932, Carl Anderson was using a Wilson cloud chamber with a large magnet to study cosmic rays when he observed a particle that had the mass of an electron, but a positive charge. The discovery of the positron, as Anderson named the particle, was recognized when Anderson shared the 1936 Nobel prize with Hess.

During the period 1947–56, when cosmic-ray studies resumed after the Second World War, a host of unpredicted subatomic particles including hyperons, pions and kaons was found using photographic emulsions and Wilson cloud chambers. This complex mix of particles, called the particle zoo, forced a complete upheaval in particle theory.

Meanwhile, the study of the primary

cosmic radiation itself was advancing, and nuclei much heavier than helium were discovered. With further recent improvements to experimental techniques, the relative proportions of different cosmic-ray nuclei, and even some of their isotopes, have been precisely determined.

The proportions of the different chemical elements among cosmic rays can be compared with their abundances in the Solar System, in the atmospheres of distant stars and among the remnants of supernova explosions, to identify objects and regions where cosmic rays originate. Researchers also seek to identify the regions in which cosmic rays are accelerated to enormous energies, producing particles that travel close to the speed of light. The largest corresponding kinetic energy measured for a single cosmic-ray particle is comparable to that of a cricket ball or baseball travelling at 160 kilometres per hour. This energy is more than 100 million times larger than that of protons accelerated in the Large Hadron Collider at CERN, Europe's particle-physics laboratory near Geneva, Switzerland.

These ultra-high-energy particles are rare — only a few arrive each century over each square kilometre of Earth. Through their collisions in the atmosphere they generate billions of particles, requiring many detectors spread out over large areas. High-energy γ -rays, also produced in cosmic-ray sources, can similarly be detected by large-area arrays. Their arrival directions can point back to their sources, such as supernova remnants and active galaxies. Continued exploration of these highest-energy particles and photons might tell us about conditions in the early and very hot stages of our Universe.

Cosmic-ray studies have expanded in unanticipated directions. For example, cosmic rays have been identified as the source of

the radioactive isotope carbon-14, produced by collisions with atmospheric nitrogen. The amount of carbon-14 produced in the atmosphere depends on the numbers of cosmic rays reaching Earth, which in turn depends on the 11-year cycle of solar activity. Measurement of carbon-14 has revolutionized archaeology by enabling the ages of ancient organic matter to be determined.

COSMIC CONSEQUENCES

Hess's discovery came from observing the effects of ionization produced by cosmic rays. That same effect is taking place in our bodies as cosmic rays pass through them. Over our lifetimes, we accumulate a radiation dose that causes biological damage, presumably contributing to a basic level of cancer production. Unshielded by the atmosphere, astronauts accumulate radiation doses from cosmic rays that may well exceed those considered safe. This could limit the distances to which astronauts can go as they explore the Solar System.

Today, the scale of physics research has expanded to the point at which it is not unusual for a single scientific paper to have hundreds of authors, crossing international boundaries and using internationally funded equipment. The origin of this revolution can be traced to cosmic rays. The cost and manpower demands of cosmic-ray research in the 1950s, although modest by today's standards, were beyond the capacity of any single group. The 'G-stack' collaboration, for example, of which I was a part (in Powell's research group at the University of Bristol, UK), was created to undertake the flight of a 'giant' stack of photographic detectors beneath a balloon. The special photographic emulsions, made by the photo company Ilford, were processed in Bristol; the balloon was flown in northern

Italy; and the measurements and analysis were carried out by groups in Bristol, Brussels, Copenhagen, Dublin, Genoa, Milan and Padua. Our results, including many examples of new and very short-lived particles, were reported in a 1955 paper (J. H. Davies *et al.* *Il Nuovo Cimento* **2**, 1063–1103; 1955) that carried the names of 36 scientists, by far the largest number of co-authors up to that time.

This style of large international collaborations is today exemplified by CERN, which was founded in 1954 and houses the largest particle accelerator ever built. Prominent among CERN's founders were many cosmic-ray scientists, including Powell and Edoardo Amaldi, its first director of research.

"After 100 years, cosmic-ray research is mature but still open to producing surprises."

One lesson to be learned from cosmic-ray research is the need to examine carefully any rare but apparently strange observations, and not to discard them as part of the background noise that many particle-physics

experiments accumulate. The discovery of antimatter rested on the detection of a single track of a lone positron. Similarly, the discovery of some kaons was based on observations of single events. Although some discoveries may emerge from the statistical analysis of large quantities of data, we should remember that important discoveries can still be established by a single observation.

After 100 years, cosmic-ray research is mature but still open to producing surprises. Cosmic rays continue to be studied from balloons, Earth-orbiting satellites and long-range space probes as well as ground-based detectors that cover enormous areas, seeking the sources of the highest-energy cosmic rays. Antiparticles might also be identified. Longer flights and larger areas are permitting the accumulation of more data on particles and cosmic γ -rays, thus increasing the detection of yet more of the rarest events.

There are already suggestions that some of the highest-energy particles and γ -rays come from well-known objects such as some supernova remnants. More data might locate, more firmly, the directions in which their sources are located and should define the acceleration processes. Perhaps the physical conditions are even more exotic than we can imagine at present. This field of astroparticle physics seems sure to produce future Nobel prizewinners. ■

Michael Friedlander is emeritus professor in the Department of Physics, Washington University, St Louis, Missouri, USA. His most recent book is *A Thin Cosmic Rain* (Harvard University Press, 2000). e-mail: mwf@wuphys.wustl.edu



Cosmic-ray collisions create showers of particles, requiring detectors spread out over a vast area.



Michael Mann has been harassed personally and politically over his work on climate change.

CLIMATE SCIENCE

At the storm front

Simon Lewis gets to grips with a climate scientist's account of a conflict that began with a graph.

How would you feel if a powerful politician demanded, with apparent legal authority, that you supply him with every piece of scientific data you had ever collected, every computer program you had written, and every detail that would allow his staff to replicate your work? How would you feel if an envelope of suspicious white powder was posted to you — and the police sealed your office? And if your family was threatened with violence?

Michael Mann knows how he would feel: he experienced all this after publishing a

scientific paper. His *The Hockey Stick and the Climate Wars* tells the story of one of the most harassed scientists in the United States.

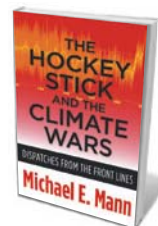
The book begins slowly, moving from happy anecdotes of childhood computer programming to the joys of responsibility-free postdoctoral research. But it becomes riveting when we reach what was in retrospect the turning point in Mann's life: his 1998 paper 'Global-scale temperature patterns and climate forcing over the past six centuries' (M. E. Mann *et al. Nature* **392**, 779–787; 1998).

Mann's study used proxy climate records, such as tree-ring growth and the ratios of oxygen isotopes in corals, to make estimates of surface air temperature extending back to AD 1400 — long before direct thermometer measurements were available. The results showed that in the Northern Hemisphere, temperatures were higher in the last years of the twentieth century than at any time in the previous 600 years, and that the suspected dominant cause was anthropogenic carbon dioxide emissions.

Mann's result came to be known as the hockey stick, because the key graph showed a flat 'handle' — the low-level natural oscillations in temperature in the centuries before humans began to create large quantities of greenhouse gases — and a 'blade' representing the sharp uptick in surface air temperature in the twentieth century. The work invoked the ire of lobby groups opposed to political action on climate change, who launched an astonishing decade of attacks on the veracity of the result. The bulk of Mann's book documents this ugly debate.

Mann ably dissects how ideologically driven, industry-funded campaigns attack climate scientists and their work to obstruct the formulation and implementation of policies restricting CO₂ emissions. We learn about Mann's bemusement when he is first assailed, and later his resigned anger. After telling how, in 2006, a US National Academy of Sciences panel found no evidence that Mann's hockey stick was flawed, he notes dryly that one "might think that this would have ended such charges once and for all. One would be wrong."

The influence of lobby groups on public perception of scientific issues is covered in more scholarly detail in the 2010 book *Merchants of Doubt* (Bloomsbury) by historians Naomi Oreskes and Erik Conway. However, Mann's shocking first-hand testimony of the repeated attempts to discredit him and his work gives his book power. Mann reports his 'highs', such as when more than 30 scientific organizations declared their support for him after Senator Joe Barton (Republican, Texas) sent him an aggressive letter demanding, among other things, copies of his records. And we get the 'lows' of what Mann calls the "most malicious of the assaults": the publication in November 2009 of a cache of e-mails, including some from Mann, that had been stolen from the University of East Anglia in Norwich, UK.



The Hockey Stick and the Climate Wars: Dispatches from the Front Lines

MICHAEL E. MANN
Columbia Univ. Press:
2012. 384 pp. \$28.95,
£19.95

Although there is little in the book with which I seriously disagree, it left me uneasy. Many scientists will agree with Mann's three basic points: that climate change is a major societal problem; that there are campaigns to convince the public that this is not the case; and that scientists should engage with society and not allow the public to be "confused and misled by industry-funded propaganda".

However, I am unconvinced that presenting the attacks as a "climate war" waged by a "corporate-funded denial machine" is the best way to help scientists to counter misinformation. It makes good copy, but the war metaphor, with its talk of battle scars and front lines, is unlikely to be an ideal communication strategy: it is, by definition, polarizing. Because denial that climate change poses a problem for society is associated mainly with right-wing political views, science communication needs to transcend ideological divides, not reinforce them.

Last year saw the end of a similarly ugly climate-change spat, following an ideology-transcending innovation that Mann does not mention. After years of bitter dispute about estimates of the warming documented by direct thermometer measurements, the Berkeley Earth Surface Temperature project

"Science communication needs to transcend ideological divides, not reinforce them."

in California brought together vocal critics of past analyses and experts who were unconnected with those previous studies. They collated, processed and published raw data, results and associated computer code.

Unsurprisingly, the results confirmed previous analyses. This reminded the public of an important result, provided a well-publicized vindication of it and, by involving key critics, dealt deftly with those who choose to confuse the public. A comparable effort to estimate the past millennium's surface air temperature could be similarly decisive.

An influential Editorial in *Nature*, cited by Mann, noted that climate scientists are in a "street fight" (*Nature* 464, 141; 2010) — imagery that I think is more apt than that of war. Street fighting is not about taking sides, and the metaphor describes well the 'anything goes' attacks that scientists can face when publishing or speaking about climate change.

Mann's story is important. However, it is also important to step back from the conflict. Emphasizing a binary war might not be the best way to end it. ■

Simon L. Lewis is a reader in global change science at University College London, UK, and the University of Leeds, UK.
e-mail: s.l.lewis@leeds.ac.uk

Books in brief



Opium: Reality's Dark Dream

Thomas Dormandy YALE UNIVERSITY PRESS 376 pp. \$40 (2012)

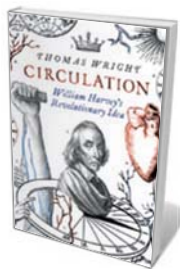
'Poppy tears' — the sap of the opium poppy — are aptly named: the drug has enslaved multitudes and sparked violence for 6,000 years. Yet opium and derivatives such as morphine and heroin have been stars of medicine and inspired greats such as the Romantic poet Samuel Taylor Coleridge and, more arguably, surgeon William Stewart Halsted. Those stories are threaded through medical historian Thomas Dormandy's engrossing chronicle, but we're never far from the shadows — the dosing of infants in Victorian England, the torments of addiction, and wars in Afghanistan and China.



Megachange: The World in 2050

Edited by Daniel Franklin and John Andrews PROFILE/WILEY 320 pp. £15/\$34.95 (2012)

The *Economist* editors Daniel Franklin and John Andrews give the "helicopter view" of where the world will be by mid-century. Aiming to pin down the trends forcing "megachange", they offer 20 chapters that make predictions in everything from public health and women's welfare to social networking, climate change and, inevitably, economics. This succinct, pithy resource has surprises: by 2050, China's gross domestic product will be 80% more than the United States's, for instance; and the world's total fertility rate could stabilize.



Circulation: William Harvey's Revolutionary Idea

Thomas Wright CHATTO & WINDUS 272 pp. £16.99 (2012)

It is easy to forget that William Harvey's great theory on the circulation of blood was as groundbreaking as Copernicus's on the Solar System. Working mainly from dissections and vivisections, Harvey also drew insight from his observations of networks and systems in transport and technology. Author Thomas Wright's account has a brilliant cast — including John Donne, the great metaphysical poet and dean of St Paul's Cathedral, London, whose interest in anatomy and the human heart drew him to Harvey's work. A classic example of how great science affects culture, language and politics.



Learning from the Octopus: How Secrets from Nature Can Help Us Fight Terrorist Attacks, Natural Disasters, and Disease

Rafe Sagarin BASIC BOOKS 320 pp. \$26.99 (2012)

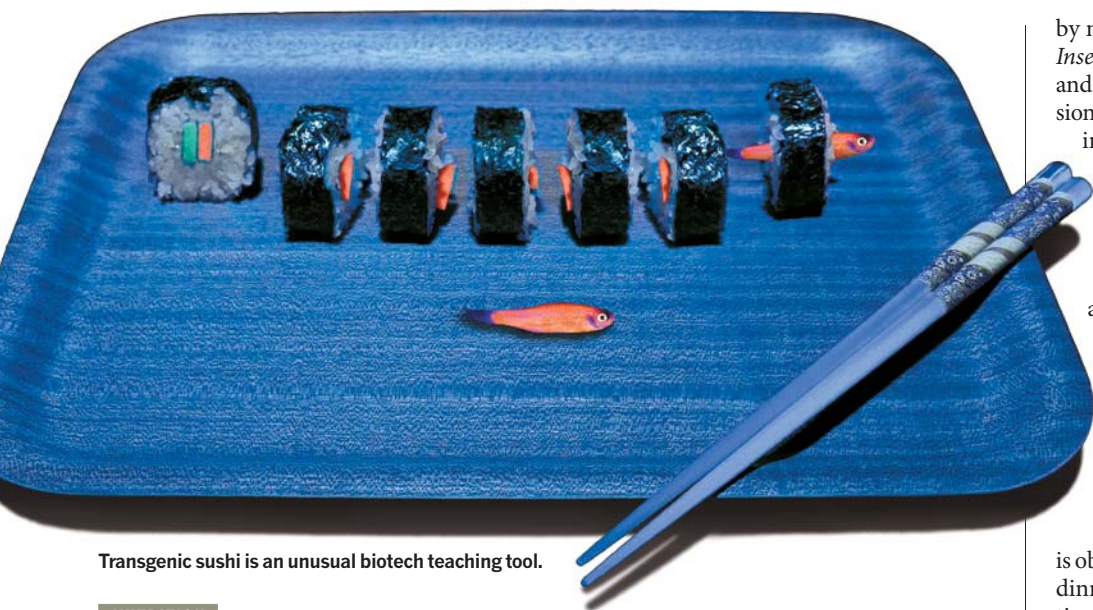
How are tide pools linked to national security? Ecologist Rafe Sagarin says that adaptability in nature — particularly in the octopus — exemplifies key defence principles. For example, the cephalopod has both attack and defence capabilities, with a powerful bite and inky camouflage, and its flair for escapology in the lab shows that it can handle a change in environment. Drawing on life science and evidence from the military and emergency services, Sagarin defines adaptability as the "sweet spot" between reaction and prediction.



Clouds That Look Like Things: From the Cloud Appreciation Society

Gavin Pretor-Pinney SCEPTRE 112 pp. £12.99 (2012)

Anyone who has spent long minutes staring idly into the blue will relish these bingo moments gathered by Gavin Pretor-Pinney, author of *The Cloudspotter's Guide* and *The Wavewatcher's Companion*, which won the 2011 Royal Society Winton prize for Science Books. From Alfred Hitchcock to flying saucers and a menagerie of beasts, Pretor-Pinney's gallery of evanescence is a reminder of the simple joy of perception.



Transgenic sushi is an unusual biotech teaching tool.

NUTRITION

Chew on this

Anthony King savours a surreally varied show on food, from glowing sushi to 1,001 uses for a pig carcass.

Fifty billion chickens are heading to the slaughter at any one time on Earth. What humans eat determines which crops are grown and which animals are reared, with big implications for science, agriculture, the environment and society.

Edible, an exhibition at Dublin's Science Gallery, probes our cultivation and consumption choices and their effects in the contexts of time, place, technology and taste. There are serious messages, but much of what is on offer has a zany flavour.

The increasingly globalized agricultural system gets more than a look-in. Artist Christien Meindertsma's photobook on 'pig parts' is a compellingly graphic exploration of the afterlife of a pig carcass. For *PIG 05049* (the number denotes the animal's ear tag), Meindertsma spent three years tracing the products derived from a single animal raised in the Netherlands to build a visual chronicle of the carcass's incredible global journey.

The pig's skin was used for tattoos, chewing gum, injectable collagen, safety gloves and cheesecake, while its bones went into paper, X-ray films, book covers and train brakes. Cigarettes, cooked ham, mink feed and photodynamic therapy accounted for some of its blood, and its gelatine eased cordite into bullets. Meindertsma dissects the pig all over again, depicting the products to scale.

Humanity's over-

NATURE.COM
For more on attitudes to food:
go.nature.com/gtmfxy

EDIBLE: The Taste of Things to Come
Science Gallery, Trinity College Dublin.
Until 5 April 2012.

50% of what we eat. The exhibition's curators, Cat Kramer and Zack Denfeld — artists with the mobile research institute the Center for Genomic Gastronomy — point out that new crops could gain dominance within a century: "The future of food is much more complex than we can predict," they write.

One aspect of that complexity is the need to maintain species diversity as insurance in case of disease; the Food and Agriculture Organization of the United Nations in Rome estimates that crop genetic diversity has fallen by 75% since 1900. *The Edible Heritage Lab* features 12 historically and scientifically important varieties of potato. Part of a haul collected by the Irish Seed Savers Association, which champions non-commercial Irish heritage varieties, they include the lumper potato, which succumbed to successive attacks by the fungal blight *Phytophthora infestans* in the mid-nineteenth century, triggering the great Irish potato famine.

Close by, a stuffed grey squirrel illustrates the question of whether we should eat invasive species. A recipe for Guinness and grey squirrel stew is provided for the brave. Insects give more food for thought; eaten over much of the world, they are seen

reliance on a handful of crops is explored in an infographic revealing how rice, wheat, maize (corn) and potatoes make up

by many as a part of future food security. *Insects Au Gratin* by designer Susana Soares and her colleagues consists of three-dimensional sculptural shapes printed using milled insect flour. Crickets, we're told, are more efficient than cattle in converting vegetation to protein: 100 kilograms of feed produces 40 kg of the insects, but only 10 kg of beef.

Given the current fashion for foodism and molecular gastronomy, the science of taste inevitably plays its part. You can learn whether you are a supertaster by gauging the bitterness of a disc infused with bitter compounds, or pinpoint where particular taste buds are concentrated by sprinkling droplets of five solutions onto your tongue.

But with taste, the proof of the pudding is obviously in the eating. A ticketed 'curated dinner' — a molecular-gastronomy evocation of the spirit of Dublin — by chef-for-the-night Pete Williams proved a sensory treat. The recipes, by local company Designgoat, featured a contemporary take on the traditional Irish coddle, involving a poached pork-mousse sausage with a mashed-potato gel, set carrot foam and a bacon and pork sausage broth in a test tube.

The diners themselves learned to whip up a gin and tonic with a difference. Spheres of cucumber, lime juice and salt were mixed with sodium alginate and sodium citrate, then set in a bath of calcium chloride. The resulting chewable spheres went into the drinks.

Back at the exhibition, a "mutagenic mist" reminds the audience that radiation has been used since the mid-twentieth century to induce mutations in crops. The mist, a palate-cleansing puff of peppermint oil, is made from a varietal approved in the 1970s and bred for disease resistance. Most peppermint oil consumed today is from this variety.

Elsewhere, you can watch *The Glowing Sushi Cooking Show*, a video of Kramer and

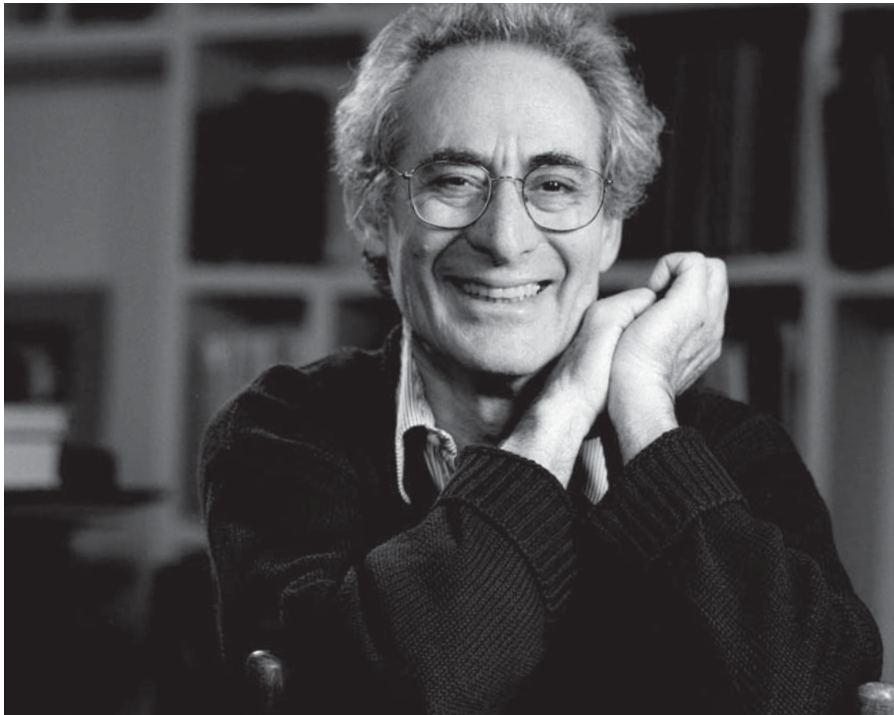
"The future of food is much more complex than we can predict."

Denfeld creating an even more startling treat: transgenic, bioluminescent zebrafish sushi. It is an intriguing way to absorb cutting-edge biotechnology. "This will be

fun at parties," quips Denfeld.

There is much more to this feast, from smog tasting to the fun inflated-stomach sculpture *Gas Bag* by artists Andy Best and Merja Puustinen. *Edible* offers a menu of appetizing morsels on the evolution of gastronomy and its influence on our ecological, technological, commercial and political world — something to chew on even if you're not yet ready to snack on a cricket. ■

Anthony King is a writer based in Dublin.
e-mail: anthonyjking@gmail.com



Barry Mazur believes that maths and literature are driven by the same imaginative impulse.

Q&A Barry Mazur

The maths raconteur

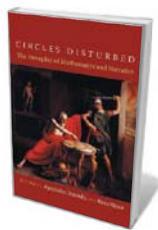
Barry Mazur, a mathematician at Harvard University in Cambridge, Massachusetts, has explored the literary side of mathematics. With the publication this month of *Circles Disturbed*, a collection of essays on mathematics and narrative that he edited with writer Apostolos Doxiadis, he talks about the overlapping realms of mathematics and the imagination.

How did you get into mathematics?

Through electronics. At school I read popular works on electromagnetism. I found it baffling that there could be action at a distance that let energy travel through a medium you couldn't touch. As a student at the Massachusetts Institute of Technology in Cambridge, I saw mathematics as a gateway to a more philosophical understanding of electronics. I wanted to understand physical principles, such as conservation of energy, from a Euclidean standpoint: rarified and axiomatic. I later saw that this was impossible, but I became riveted by mathematics. I came to Harvard in 1959, starting in topology then moving to algebraic geometry, which has led me to number theory.

What inspired you to write your 2003 book, *Imagining Numbers*?

It began as a letter to a friend. We had been chatting about the difficulties of imagining certain things and he said that he would like to know what imaginary numbers were. It took more than 200 years for mathematicians to



Circles Disturbed: The Interplay of Mathematics and Narrative

EDITED BY
APOSTOLOS DOXIADIS
AND BARRY MAZUR
Princeton University
Press: 2012. 552 pp.
\$49.50, £34.95

become comfortable with them, so I thought it might be instructive not to directly teach this to my friend, but to help him to arrive at his own familiarity with them. I wrote him a letter inviting him to do just that. It expanded, circulated among literary friends, and eventually became the book.

And *Circles Disturbed*?

The concept came from Apostolos Doxiadis. His 1992 novel *Uncle Petros and Goldbach's Conjecture* marries literature and mathematical themes, and his 2008 graphic novel *Logicomix* is about the mathematicians Gottlob Frege, David Hilbert, Henri Poincaré, Ludwig Wittgenstein and Kurt Gödel, and the early-twentieth-century crisis in

the foundations of mathematics. Apostolos invited mathematicians, historians and literary scholars to write about mathematics and narrative. They met in Greece in 2007 to discuss their work; this was the origin of *Circles Disturbed*. They interviewed one another to make their contributions more accessible. These interviews are available at www.thalesandfriends.org.

How can historians tell the story of maths?

You can recount mathematical lives, as Peter Galison does in the book. His essay contrasts the biographies of John Archibald Wheeler — whose mechanical illustrations of mathematical operations were influenced by his upbringing on a Vermont farm — and Nicolas Bourbaki, the pseudonym of a group of Parisian mathematicians whose vision of mathematical progress was monolithic and structural. Or you can take the meta-historical approach, as Amir Alexander does in his essay, which discusses how the transformation in mathematics in the eighteenth and nineteenth centuries was partly guided by the stories told about it. You can do a close reading of dramatic mathematical texts, as in Federica La Nave's examination of a work on imaginary numbers by sixteenth-century Italian mathematician Rafael Bombelli, who laboured for decades over the question of whether these numbers are fictitious.

And is it possible to use mathematics for literary purposes?

Yes, you can reverse roles. A mathematical sensibility is useful for illuminating patterns and structures — such as the structure of narrative, as in our book. A seminal example is French literary theorist Gérard Genette's 1972 modelling of the tangled layers of time in the writings of Marcel Proust.

Is there a place for dreams in mathematics?

In Michael Harris's chapter on intuition in *Circles Disturbed*, he recounts how mathematician Robert Thomason had a dream in which a dead friend (not a mathematician) made a mathematical claim. Although the claim was false, it inspired Thomason, once awake, to successfully complete his mathematical project, and to include his friend as a co-author in the published paper.

What do the pursuits of maths and literature have in common?

The common thread is urgency. Mathematicians are impelled by an urgent desire to understand. In literature, there is a similar impulse to engage in an all-absorbing imaginative experience. When it comes to mathematical inspiration, the imagination could be considered the ghost in the rational machine of proof-making. ■

INTERVIEW BY JASCHA HOFFMAN

Correspondence

Mixed media policies of US federal agencies

You cite two US government agencies that interact openly with the media (*Nature* **483**, 6; 2012): the National Oceanic and Atmospheric Administration (NOAA) and the National Science Foundation (NSF). Yet these are rare exceptions in my experience as editor of *FDA Webview* and *FDA Review*.

Take the US Department of Health and Human Services (DHHS), which last September proclaimed a repressive media guidelines policy. All journalists are now referred to its press office, which permits access only to selected personnel and may monitor and record interviews (see go.nature.com/xczin6).

Another large US government entity, the Department of Justice, has gone even further. Barely a month after the DHHS move, it proposed a rule that directs federal law-enforcement agencies to respond to requests for particularly sensitive documents under the Freedom of Information Act “as if the excluded records did not exist” (see go.nature.com/gfd8pn).

Recent guidelines on openness from the NSF and NOAA are modest steps in the right direction — albeit on a tiny scale, given the size, scope and complexity of the US federal government.

James G. Dickinson *Camp Hill, Pennsylvania, USA.*
jim@fdaweb.com

China: a cultural shift for science

I disagree that the ancient cultural influences of Confucius and Zhuang Zhou are to blame for the problems pervading China's academic research today (*Nature* **481**, 411; 2012). Neither sage encouraged isolation or inhibited intellectual curiosity. I believe that China's problems are exacerbated by insufficient

respect for these cultural traditions, which promote such values as objectivity and high moral standards.

China's scientists should be devoting themselves to the advance of research that abides by international scientific standards. Misconduct and other flaws undermine the Chinese government's increased investment in higher education and scientific research.

It is time for the research community in China to rekindle its respect for cultural traditions and to take responsibility for creating a healthy, transparent academic system.

Keqian Xu *Nanjing Normal University, Jiangsu, China.*
xukeqian@njnu.edu.cn

China: philosophers sparked good science

Peng Gong misrepresents the thoughts of Chinese philosophers Confucius and Zhuang Zhou by suggesting that they hinder scientific advancement in modern China (*Nature* **481**, 411; 2012).

Confucius encouraged curiosity and practice in teaching and learning. His thoughts are universal and timeless, and have influenced many other Asian countries — including Japan, where sound science thrives.

Zhuang advocated harmony so that we could fulfil our essential connection with nature. This view is pertinent in today's China, where the environment and human health are being damaged by explosive and unbalanced development.

Moreover, Confucius, Zhuang and other ancient Chinese philosophers made significant advances in science, technology, medicine, mathematics, astronomy and architecture, with inventions such as paper and the compass having a large impact on civilization.

Jianxin Su *Fujian University of*

Technology, Fuzhou, China.
jianxinsu@gmail.com
Cheng Lu *Newark, Delaware, USA.*

Work together to crack wildlife trade

There is no single solution to monitoring illegal wildlife trade (L. F. Toledo *et al.* *Nature* **483**, 36; 2012), which is widespread, adaptive and sophisticated.

Extensive reforms are needed to expand government monitoring and reporting, and to include a wider range of detection strategies and non-government stakeholders (J. Phelps *et al.* *Science* **330**, 1752–1753; 2010).

Government agencies are largely limited to regulating wildlife trade through monitoring and enforcement, mainly confined to checkpoints such as airports. More resourceful research strategies are crucial for keeping up with wildlife trading (see, for example, M. Gastañaga *et al.* *Bird Conserv. Int.* **21**, 76–85; 2011).

Improving regulation will require broadening collaborations, for example through resource monitoring by local communities, engaging the private sector in point-of-harvest reporting, and forming partnerships with non-governmental organizations and academics. Local networks and expertise would encourage pooling of resources and give governments access to new techniques and methodological support.

Such cooperation would help to resolve taxonomic uncertainties and offer independent review of contentious trade decisions. This is especially relevant to countries where the technical and administrative authorities of the Convention on International Trade in Endangered Species lie within the same government institution.

Jacob Phelps, David P. Bickford, Edward L. Webb *National University of Singapore, Singapore.*
jacob.phelps@gmail.com

Colorado methane study not clear-cut

As a partner of the US National Oceanic and Atmospheric Administration, we at Western Energy Alliance provided much of the data for the reported study on methane emissions from a natural-gas field in Colorado's Denver-Julesburg Basin (*Nature* **482**, 139–140; 2012). However, uncertainties remain over the extent of methane leakage from these operations.

For example, this study (G. Pétron *et al.* *J. Geophys. Res.*, in the press) relied heavily on data from mobile-laboratory samples taken in summer 2008, before regulations reduced emissions of volatile organic compounds to 90%, and before low-bleed pneumatic devices were implemented to reduce methane emissions from the field. Much of the data were collected in an operating environment that no longer exists. Also, the venting you describe is at odds with industry practices.

The authors acknowledge that methane emissions from agriculture are of “comparable magnitude to the estimate from natural gas systems” in Colorado, but do not consider these.

Pétron *et al.* should have noted that methane readings were lower at the Boulder observation tower than at a tower in a Wisconsin forest that is far removed from significant industrial activity.

Kathleen M. Sgamma *Western Energy Alliance, Denver, Colorado, USA.*
ksgamma@westernenergyalliance.org

CORRECTION

A declaration of competing financial interests was omitted from the Correspondence ‘Sugar: fruit fructose is still healthy’ (*Nature* **482**, 470; 2012). This has been added at <http://go.nature.com/xudf1i>.

Renato Dulbecco

(1914–2012)

Molecular biologist who proved that virus-derived genes can trigger cancer.

Renato Dulbecco, a giant of cancer biology, passed away peacefully on 19 February, just three days shy of his 98th birthday. Through a decade-long series of experiments that began in the late 1950s — first at the California Institute of Technology (Caltech) in Pasadena and then at the Salk Institute in La Jolla, California — he and his co-workers demonstrated that the behaviour of cancer cells could be traced directly to acquired genes. Some viruses can integrate their genomes into host cell DNA, inducing uncontrolled cell growth — the hallmark of a cancer cell. For these early clues to the genetic origins of cancer, Dulbecco shared the 1975 Nobel prize with the late Howard Temin, his former student, and with David Baltimore, my former mentor.

Born in Catanzaro, Italy, on 22 February 1914, Dulbecco grew up during the First World War and its aftermath with his mother and siblings. He entered the University of Turin in 1930 at the age of 16 to study medicine. His interests quickly shifted to biology and he became a laboratory assistant for Giuseppe Levi, learning from him the cell-culture techniques that had a dominant role in Dulbecco's later scientific work. His fellow students included two other future Nobel laureates — microbiologist Salvador Luria and neurobiologist Rita Levi-Montalcini.

After obtaining his doctorate in 1936, Dulbecco was drafted into the Italian army as a physician. He was called to action in 1939, at the outset of the Second World War, to serve first in France and then in Russia. Disaffected by the war and its consequences, he deserted the army and hid in a small village near Turin, becoming physician to the local partisan units resisting the German occupation. After the end of the war, following a short stint as an elected city councillor in Turin in 1945, he returned to scientific research at the University of Turin.

In 1946, Luria invited Dulbecco to join his research group at the University of Indiana in Bloomington to work on bacteriophages

— the viruses of bacteria. Dulbecco shared his laboratory with a graduate student, James Watson, who was later to determine the structure of DNA with Francis Crick. Dulbecco's finding that visible light can reactivate phages previously rendered inactive by exposure to ultraviolet light — with repercussions for experimental methods

fame. He and Vogt continued their research collaborations on tumour viruses, definitively proving the essential role of the viral genes in transforming cells into cancer cells. During this highly productive period, Dulbecco trained some of the top virologists in the world. In 1972, he moved to the Imperial Cancer Research Fund (now Cancer

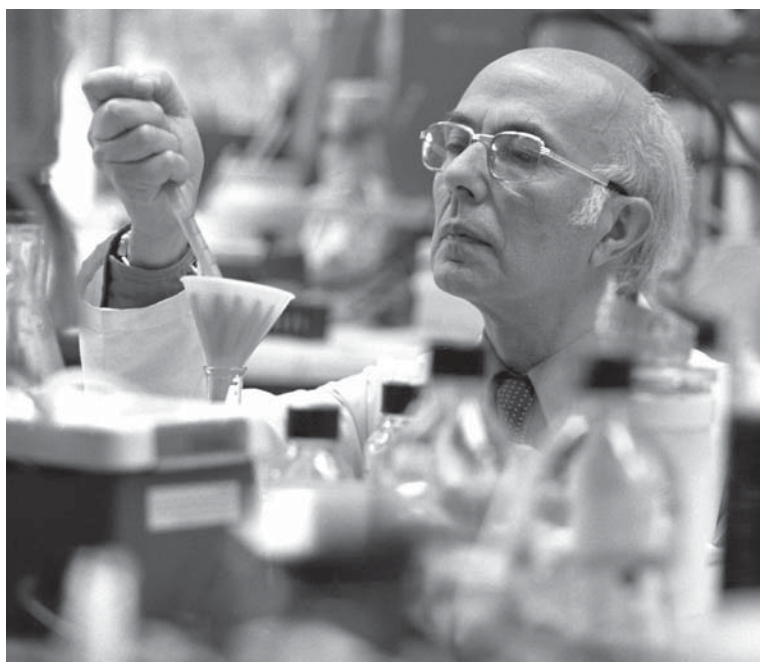
Research UK) in London, where he initiated studies of breast cancer — a subject he continued to pursue after moving back to California in 1977. His last scientific paper, published in 2004, identified tumour-initiating cells in rat mammary cancers. In 1988, Dulbecco assumed the presidency of the Salk Institute, following the illness of long-term president Frederic de Hoffmann, and brought stability during a difficult time.

An experimentalist at heart, Dulbecco loved to work in the laboratory. He was a quiet man, yet did not shy away from making bold visionary statements: in a classic 1986 perspective in *Science* (R. Dulbecco *Science* **231**, 1055–1056; 1986), he argued that the best way to understand cancer would be

to sequence the human cancer genome. In 1992, Dulbecco stepped down from the Salk presidency to organize the Italian contribution to the Human Genome Project. He spent a good part of his time in Italy, where he was much revered and helped the careers of many young scientists.

Dulbecco was an elegant man: a dapper dresser, soft spoken, with an ever-present smile. He was comfortable among the nobility, yet adept at changing the oil in his car; at once distant yet approachable. He was a charming host at dinners organized by his wife Maureen, which my wife and I often had the pleasure of attending. In short, he was always the perfect gentleman. ■

Inder M. Verma is the Irwin and Joan Jacobs Chair in Exemplary Life Science and an American Cancer Society professor of molecular biology at the Salk Institute, La Jolla, California 92037, USA.
e-mail: verma@salk.edu



SALK INST.

at the time — brought him to wider attention. Phage geneticist Max Delbrück invited Dulbecco to join him at Caltech in 1949 as a research fellow.

Dulbecco felt that research into animal viruses would benefit hugely from improved quantitative techniques. In 1952, he developed the plaque assay for Western equine encephalomyelitis virus: a system that allowed researchers to determine the number of biologically active viral particles in a sample by counting the number of discrete plaques, or clear spots, where a single virus and its progeny had killed host cells. Soon Dulbecco was joined by Marguerite Vogt, a German émigré. Their fruitful collaborations led to quantitative assays for the poliomyelitis virus, a scourge at the time, and later for the polyoma virus — a DNA virus that causes many different types of tumours.

In 1963, Dulbecco left Caltech to become one of the first fellows of the Salk Institute, founded by Jonas Salk of polio vaccine

EVOLUTIONARY BIOLOGY

Life imperfectly imitates life

Some species evolve to resemble another species so as to protect themselves from predation, but this mimicry is often imprecise. An analysis of hoverflies suggests why imperfect imitation persists in the face of natural selection. [SEE LETTER P.461](#)

DAVID W. PFENNIG & DAVID W. KIKUCHI

One hundred and fifty years ago, the English naturalist Henry Walter Bates¹ discovered a phenomenon that he regarded as “a most powerful proof of the theory of natural selection”. Charles Darwin and Alfred Russel Wallace, who had proposed natural selection as the engine of evolution only a few years earlier, agreed. Indeed, Darwin² considered Bates’s manuscript to be “one of the most remarkable and admirable papers I ever read”.

Bates had uncovered a spectacular type of adaptation, now known as Batesian mimicry³, in which a species (the mimic) that is edible to predators evolves to resemble a conspicuous, inedible species (the model) that predators avoid. These lookalikes are selectively favoured, Bates argued¹, because predators confuse them for the inedible model and thereby avoid them. This idea was so persuasive that Batesian mimicry is still widely used to illustrate the power of natural selection for producing adaptations^{3,4}. However, mimics are often poor replicas of their model, and this inexact mimicry poses a challenge for evolutionary theory³. On page 461 of this issue, Penney *et al.*⁵ discuss possible explanations for why mimics are frequently imprecise.

As Penney and colleagues describe, several non-mutually exclusive hypotheses have been proposed to explain imperfect mimicry. They include: the ‘eye-of-the-beholder’ or sensory-limitation hypothesis, which asserts that imprecise mimicry is an artefact of human perception; the ‘jack-of-all-trades’ or multimodel hypothesis, which posits that imperfect mimics persist because they are under selection pressure to resemble more than one model; and the ‘kin-selection’ hypothesis, which asserts that imperfect mimicry is maintained because it provides benefits for genetically related individuals. Specifically, if mimics are imperfect, then predators will be more discriminatory and occasionally spare a mimic by mistaking it for a model. This will also spare relatives that share the same imperfect trait.

Another theory to explain imperfect mimicry is the ‘relaxed-selection’ hypothesis, which holds that there is little selective benefit in refining mimetic resemblance beyond a certain



M. COLE/FLPA

Figure 1 | A fly in wasp's clothing. The harmless marmalade hoverfly, *Episyrphus balteatus*, shown here, resembles stinging wasps. Although some species of hoverfly closely resemble wasps or bees, others are poor lookalikes. Penney and colleagues⁵ show that the lower selection pressures that come with decreasing abundance and small body size may provide the explanation for how such imprecise mimicry can persist.

point, for example if the model is common or especially noxious. Finally, the ‘constraints’ hypothesis proposes that either imperfect mimics lack the genes to produce refined mimicry, or that a selective trade-off exists between predator-mediated selection favouring more precise mimicry on the one hand and other agents of selection (such as mate choice) favouring divergence on the other.

Until now, no study had rigorously evaluated these multiple hypotheses within a single system. Penney and colleagues⁵ did precisely this by comparing the degree of mimicry in dozens of species of hoverfly. Mimicry is a dominant feature of this large family of harmless Diptera (Fig. 1). About 5,600 species have been described, at least a quarter of which resemble stinging wasps and bees (Hymenoptera)⁶. Although some hoverflies are remarkably accurate mimics, converging both morphologically and behaviourally on their hymenopteran model, many others seem to bear poor resemblance⁶. This variation in mimetic

fidelity makes hoverflies ideal for studying imperfect mimicry.

The authors report that birds (which are hoverfly predators) and humans seem to agree on the resemblances between hoverflies and hymenopterans. Thus, in this case, the eye-of-the-beholder hypothesis does not hold. Furthermore, Penney and colleagues’ statistical analysis reveals that the mimics’ characteristics do not fall somewhere between those of different models, so the jack-of-all-trades hypothesis receives no support either. The kin-selection hypothesis predicts that mimetic precision should decrease with an increasing abundance of mimics, but the authors observed the opposite trend. In fact, this finding is consistent only with the constraints and relaxed-selection hypotheses. In addition to predicting that mimics’ precision should increase with their abundance, these two hypotheses predict that mimetic precision should increase with the body size of the mimic, and this is exactly what the authors find.

To understand how the relaxed-selection hypothesis applies when both the abundance and body size of mimics increase, let us consider the problem of discriminating between tasty mimics and nasty models from the predators' perspective. If not all mimics are equally deceptive, a predator must take risks when attacking its prey — if it strikes a mimic, it will reap more reward than regret. When mimics are abundant, the likelihood of attacking a model by mistake decreases. In such conditions, predators should be willing to sample all but the best mimics, which will push selection towards more precise mimicry.

By the same token, when mimics have a larger body size, their potential benefit to predators is greater (larger prey are generally more profitable for predators), so there will be greater selection pressure on them than on their smaller counterparts to become better mimics. Although other studies have found that mimetic precision increases when mimics are abundant⁷, Penny and colleagues' demonstration that this pattern also holds when mimics increase in size is an

elegant affirmation of an old idea.

We still do not know whether hoverfly mimicry is imprecise because of an absence of selection for refinement once mimicry is 'good enough' (as in the relaxed-selection hypothesis), or whether there is active selection pressure against further refinement because of the costs of producing better mimicry (as in the constraints hypothesis). For example, constraints may be imposed by competition between mimics and their models (over shared resources⁸ or reproductive opportunities⁹), which would favour divergence between them and, hence, imprecise mimicry¹⁰. Future studies are needed to tease apart these two hypotheses.

As we celebrate the 150th anniversary of Bates's discovery of mimicry¹, the topic continues to fascinate the public and scientists alike^{3,4}. Penny and colleagues' findings help us to understand why selection sometimes produces precise mimicry, but often does not, and further clarification of this puzzle promises to provide additional insight into the evolutionary process. ■

David W. Pfennig and David W. Kikuchi are in the Department of Biology, University of North Carolina, Chapel Hill, North Carolina 27599, USA.

e-mails: dpfennig@unc.edu; dkikuchi@live.unc.edu

1. Bates, H. W. *Trans. Linn. Soc.* **23**, 495–556 (1862).
2. Burkhardt, F., Evans, S. & Pearn, A. M. (eds) *Evolution: Selected Letters of Charles Darwin 1860–1870* (Cambridge Univ. Press, 2008).
3. Ruxton, G. D., Sherratt, T. N. & Speed, M. P. *Avoiding Attack: The Evolutionary Ecology of Crypsis, Warning Signals & Mimicry* (Oxford Univ. Press, 2004).
4. Forbes, P. *Dazzled and Deceived: Mimicry and Camouflage* (Yale Univ. Press, 2009).
5. Penney, H. D., Hassall, C., Skevington, J. H., Abbott, K. R. & Sherratt, T. N. *Nature* **483**, 461–464 (2012).
6. Gilbert, F. in *Insect Evolutionary Ecology* (eds Fellowes, M. D. E., Holloway, G. J. & Rolff, J.) 231–288 (CABI, 2005).
7. Harper, G. R. Jr & Pfennig, D. W. *Proc. R. Soc. Lond. B* **274**, 1955–1961 (2007).
8. Alexandrou, M. A. *et al. Nature* **469**, 84–88 (2011).
9. Estrada, C. & Jiggins, C. D. *J. Evol. Biol.* **21**, 749–760 (2008).
10. Pfennig, D. W. & Kikuchi, D. W. *Curr. Zool.* (in the press).

BIOLOGICAL PHYSICS

Swarming microtubules

An artificial system of microtubules propelled by dynein motor proteins self-organizes into a pattern of whirling rings. This observation may provide insight into collective motion in biological systems. SEE LETTER P.448

TAMÁS VICSEK

The spectacle of animals moving en masse is arguably one of the most fascinating phenomena in biology. For example, schools of fish can move in an orderly manner, and then change direction abruptly or, if under pressure from a nearby predator, swirl like a vigorously stirred fluid. The non-living world also has examples of collective motion, in systems that consist of units ranging from macromolecules to metallic rods, or even robots. On page 448 of this issue, Sumino *et al.*¹ describe another, until now unobserved, example of such behaviour: the coordinated motion of hundreds of thousands of subcellular structures known as microtubules, which spontaneously self-organize into a lattice-like structure of vortices. When considered in the context of about half a dozen known universal classes of collective-motion pattern², this new structure poses challenges in terms of explaining how it can arise and its relevance to applications.

If two or more moving units such as

self-propelled rods interact, their direction of motion is likely to change. When pairwise interactions dominate over multiparty ones, the process of two units approaching each other, then adopting a new direction and leaving the area of interaction, can be interpreted as a collision. In closed systems at equilibrium, such collisions conserve energy and momentum, whereas, for example, when two birds interact and decide which way to fly in the open expanses of the sky, the concept of conservation of momentum is not applicable.

Typically, local interactions between organisms result in a consensus: fish or mammals tend to adopt a common direction of motion. Such 'polar' interactions are widespread and have been observed even for bacteria³ and locusts⁴. Nonetheless, it was a great achievement when, in 2010, two groups^{5,6} observed motional patterns associated with polar interactions on a molecular scale — that is, for a huge number of actin filaments on a layer of immobilized myosin protein heads.

In addition to polar interactions, 'nematic' interactions also occur. In this case, if the

directions of motion of two units approaching one another form an angle smaller than 90°, both parts will take the same direction after the approach. But if the units come towards one another from directions that differ by more than 90°, they will leave in opposite directions.

Sumino *et al.*¹ have constructed a biological system in which nematic collisions take place (Fig. 1). The authors achieved this by choosing an assay of moving microtubules propelled by modified motor proteins (one-headed dynein molecules) in which the microtubules cannot, for the most part, cross each other's trajectories and maintain their own trajectory's direction and curvature. The authors find that, in this setting, and for relatively high densities (typically 5 microtubules in 100 square micrometres), the moving microtubules self-organize into a semiregular pattern of whirling rings, or vortices, within which they move either clockwise or anticlockwise. Furthermore, as time goes on, the microtubules jump from one vortex to another and change their rotational direction. The size of the observed pattern is large compared with the 15-micrometre length of each microtubule: the system shows regularities on a millimetre scale.

One of the strengths of the present study is the authors' ability to explain the main features of the microtubules' intricate motion with a simple model. The model draws on studies aimed at understanding the rich, large-scale behaviour that results from simple bilateral interactions between point-like, self-propelled particles.

But Sumino and colleagues' results also prompt several questions. For example, is the observation that individual microtubules have a slight preference to rotate anticlockwise

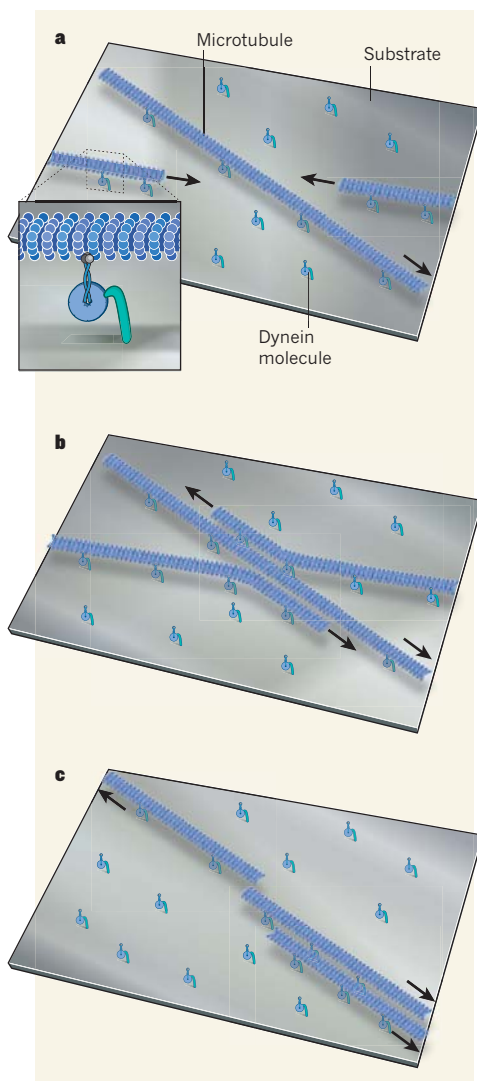


Figure 1 | Nematic collisions. Sumino *et al.*¹ have studied a system of microtubules in which nematic collisions occur. The microtubules are propelled by one-headed dynein molecules attached to the surface of a substrate. Three microtubules are shown here: **a**, approaching one another; **b**, colliding; and **c**, after the collision has taken place. Their final direction of motion depends on the angles at which they approach one another. In this case, the two leftmost microtubules adopt the same direction, whereas the rightmost microtubule leaves in the opposite direction.

a necessary condition for the observed semi-regular pattern of vortices? How is the persistence of the curvature of the microtubules' trajectories relevant? Furthermore, it would be interesting to investigate why actin filaments undergo polar interactions, whereas microtubules undergo nematic ones.

Whether the authors' observations are system specific or belong to a new class of collective-motion pattern remains to be seen. But one possibility is that the observed lattice-like structure falls within the group of patterns of vortex formation seen in many systems made up of self-propelled units. Typically, vortex

formation can be closely related to the geometry of the confined area within which the collective motion occurs. In the current case, it seems that, owing to the persistence of curvature in the individual microtubules' motion, curved 'walls' of microtubules are spontaneously formed and enforce the formation of the vortices. Indeed, it has been shown⁷ that, without such curvature persistence, nematic interactions in a system of self-propelled rods do not result in a similar arrangement of vortices.

Potential applications of Sumino and colleagues' study remain, for the time being, in the realm of speculation. But it is conceivable that the complex fluid currents generated in the stems of various plants relate to the collective motion of microtubules observed by the authors¹. The streams of energy-supplying and waste materials in a stem have to fulfil a number of criteria, which could be best met

through a coordinated action of motor molecules. The authors' demonstration that such action can be attained in a relatively simple assay is a step towards a better understanding of the role of collective motion in plants and other biological systems. ■

Tamás Vicsek is in the Department of Biological Physics, Eötvös University, 1117 Budapest, Hungary.
e-mail: vicsek@hal.elte.hu

1. Sumino, Y. *et al.* *Nature* **483**, 448–452 (2012).
2. Vicsek, T. & Zafeiris, A. *Phys. Rep.* (in the press); preprint at arxiv.org/abs/1010.5017 (2012).
3. Ingham, C. J. & Jacob, E. B. *BMC Microbiol.* **8**, 36 (2008).
4. Buhl, J. *et al.* *Science* **312**, 1402–1406 (2006).
5. Schaller, V. *et al.* *Nature* **467**, 73–77 (2010).
6. Butt, T. *et al.* *J. Biol. Chem.* **285**, 4964–4974 (2010).
7. Ginelli, F., Peruani, F., Bär, M. & Chaté, H. *Phys. Rev. Lett.* **104**, 184502 (2010).

MOLECULAR BIOLOGY

How to duplicate a DNA package

Cells replicate half of their genome as short fragments that are put together later on. The way in which this process is linked to the formation of DNA–protein complexes called nucleosomes is now becoming clearer. [SEE ARTICLE P.434](#)

**ALYSIA VANDENBERG
& GENEVIÈVE ALMOUZI**

In a typical human cell, about two metres of DNA is wrapped around proteins to form nucleosomes, the basic units of chromatin. When this DNA is duplicated, the nucleosomes that lie ahead of the replication machinery are displaced, or disassembled into their component histone proteins. And after the machinery has passed by, the nucleosomes are reassembled on the two resulting 'daughter' strands, which requires the addition of new histones¹. To make things more complicated, one of the two DNA strands can be replicated only in short pieces — called Okazaki fragments — that are joined together afterwards, and so its replication lags behind that of the other strand (Fig. 1). This elaborate mechanism is needed because DNA synthesis is unidirectional, whereas the sequences of the two DNA strands run in opposite directions. However, the links between DNA replication and nucleosome dynamics have previously been studied without distinguishing between the two strands. On page 434 of this issue, Smith and Whitehouse² uncover the interplay between nucleosome assembly and the synthesis of the lagging strand.

The authors² analysed Okazaki fragments

from baker's yeast, a unicellular fungus commonly used as a model for eukaryotic cells — those found in organisms such as animals, plants and fungi. Smith and Whitehouse took advantage of an available large catalogue of defined yeast mutants, together with well annotated genomic information that included recently defined nucleosome positions³. The researchers developed an elegant method for purifying Okazaki fragments from yeast, then sequenced the fragments and mapped them on the yeast genome. The result is the first high-resolution, genome-wide analysis of Okazaki fragments from live eukaryotic cells. The analysis is a major achievement, as our knowledge of lagging-strand synthesis has been based largely on model studies⁴ of the replication of non-chromosomal DNA molecules such as viral DNA.

Smith and Whitehouse discovered that, strikingly, the Okazaki fragments' size and location in the genome depend on where the nucleosomes are located. More specifically, the ends of the Okazaki fragments fall near the nucleosome's dyad axis, which corresponds to the midpoint of the DNA segment wrapped around the chromatin unit. This result contrasts with a common assumption that, during lagging-strand replication, a nucleosome would form as soon as the Okazaki fragment

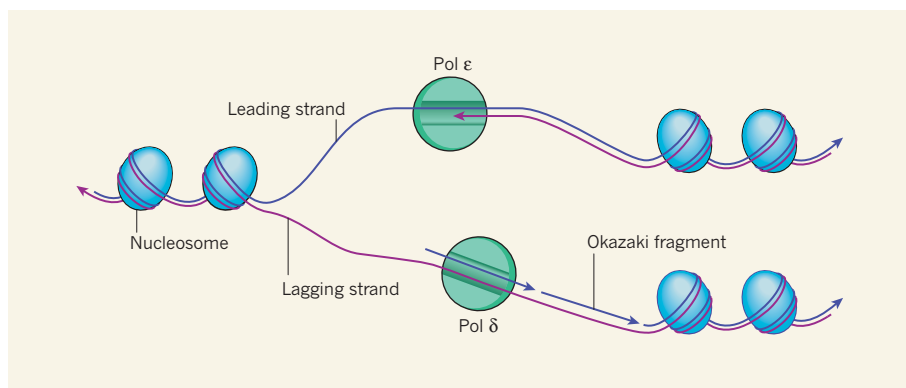


Figure 1 | Asymmetric DNA replication. The sequences of the two strands of a DNA molecule run in opposite directions, but during replication the new DNA molecules are synthesized in only one direction. Each strand is therefore duplicated differently. The leading strand is used as a template by a polymerase enzyme (Pol ϵ , top), which makes a new molecule in a continuous manner. By contrast, duplication of the lagging strand is discontinuous and requires another polymerase (Pol δ , bottom), which synthesizes short DNA pieces known as Okazaki fragments. These fragments are then joined together with the help of other enzymes to form a continuous molecule. During the process, nucleosomes — protein complexes around which DNA is coiled — disassemble from parental DNA to then reassemble, along with additional nucleosome proteins as needed, allowing both DNA duplication and chromatin reorganization. Smith and Whitehouse's analysis² of Okazaki fragments illuminates the link between nucleosome assembly and the synthesis of the lagging strand.

was long enough, and then the next fragment would be synthesized. This assumption tallies with the observation that the average length of Okazaki fragments is similar to that of the DNA wound around a nucleosome.

The authors² propose an alternative model in which the presence of a nascent nucleosome acts as a roadblock to an advancing polymerase enzyme (Pol δ), which is synthesizing the lagging strand. According to their model, Pol δ and other associated enzymes can invade the nascent nucleosome up to its dyad axis, but then the nucleosome mediates the dissociation of all of these enzymes from the DNA — by doing so, the nucleosome determines the length of the Okazaki fragment.

To test the model, Smith and Whitehouse used yeast strains in which the physiological balance between polymerases and nucleosomes was altered, either because the polymerases were less active or because nucleosome assembly was impaired. For example, they observed² that the Okazaki fragments were longer in mutant strains defective in CAF-1, a protein complex known⁵ to act as a histone chaperone, which promotes histone deposition on newly synthesized DNA. Therefore, the tight balance between the capacity to form a new nucleosome on the lagging strand and the polymerase's ability to advance is what sets the length of the Okazaki fragment. These findings also suggest that the efficiency of the replication machinery's progression may depend on where the nucleosome forms.

The authors' work provides the basis for research on how other factors involved in histone dynamics and nucleosome movement on DNA — such as histone chaperones⁵ and chromatin remodeller enzymes — can affect Okazaki-fragment size and, overall, DNA

replication. Moreover, additional proteins involved in chromatin assembly could be identified by screening the available collection of yeast mutants for changes in Okazaki-fragment length. And the technique used for mapping Okazaki fragments offers a means to identify the genomic sites at which DNA replication starts.

It is tempting to postulate that the inherent asymmetry of nucleosome dynamics during DNA replication could contribute to

a mechanism for asymmetric cell division, a process by which two different cell types are generated. This hypothesis is supported by the finding⁶ that CAF-1 has a role in asymmetric cell division in the worm *Caenorhabditis elegans*. In addition, histones in nucleosomes exist in different forms associated with specific genomic regions, and can be 'marked' with various chemical modifications that reflect functional states, such as activation or repression of gene expression. Whereas some of these modifications are transient, others may be inherited during cell division in an epigenetic fashion — that is, independently of the DNA sequence. But to understand how the chemical modifications of nucleosomes can be inherited during cell division, we must first determine how nucleosomal organization is reproduced during DNA replication. So Smith and Whitehouse's study paves the way for a deeper exploration of the intimate relationship between genetics and epigenetics. ■

Alysia Vandenberg and Geneviève Almouzni are in Unit UMR218, Institut Curie/Centre National de la Recherche Scientifique, Paris F-75248, France.
e-mail: genevieve.almouzni@curie.fr

1. Saha, A., Wittmeyer, J. & Cairns, B. R. *Nature Rev. Mol. Cell Biol.* **7**, 437–447 (2006).
2. Smith, D. J. & Whitehouse, I. *Nature* **483**, 434–438 (2012).
3. Jiang, C. & Pugh, B. F. *Genome Biol.* **10**, R109 (2009).
4. Anderson, S. & DePamphilis, M. L. *J. Biol. Chem.* **254**, 11495–11504 (1979).
5. Corpet, A. & Almouzni, G. *Trends Cell Biol.* **19**, 29–41 (2009).
6. Nakano, S., Stillman, B. & Horvitz, H. R. *Cell* **147**, 1525–1536 (2011).

GEOCHEMISTRY

Bubbles from the deep

A study suggests that hydrocarbons released from sedimentary basins formed part of a climatic feedback mechanism that exacerbated global warming during the Eocene epoch.

HENRIK SVENSEN

Gas released from sedimentary basins has been proposed to be a key player in many of the rapid climate changes that occurred in the past 250 million years. The types and sources of the released gases are still debated, but they probably included gases formed by the heating of organic matter around hot magma¹, and gases released by the dissociation of gas hydrates (solid compounds that trap gas molecules) found in deep-ocean sediments². The influence of hydrates is greater in a warming world because higher ocean temperatures can melt methane-bearing gas hydrates, releasing the gas. The methane can

then be oxidized to carbon dioxide, causing ocean acidification, and can contribute to global warming because both methane and carbon dioxide are greenhouse gases. Writing in *Geophysical Research Letters*, Kroeger and Funnell³ suggest another way in which global warming can lead to increased gas emissions from the sea floor.

Sedimentary basins have large accumulations of biological, inorganic and clastic deposits (which consist of fragments of pre-existing rocks), and are host to more than 99.9% of the organic carbon in Earth's crust. This amounts to a staggering 15,000,000 gigatonnes (Gt) of carbon; for comparison, 3,300 Gt of carbon are stored in all known hydrocarbon and

coal reserves⁴. Any viable mechanism for transferring significant quantities of sediment-bound carbon to the atmosphere on a short timescale may thus perturb the global carbon cycle and lead to global warming.

A series of such perturbations has been suggested^{5,6} to have happened in the Eocene epoch (which ran from 55.8 million to 33.9 million years ago) to explain several short-lived climatic anomalies that occurred during a period of otherwise steady warming from 58 to 50 Myr ago (Fig. 1). The most prominent of these events was the Palaeocene–Eocene thermal maximum (PETM), which was characterized by global warming of 5–10 °C and subtropical conditions in the Arctic. One cause of the PETM is commonly assumed to have been methane release to the atmosphere that was triggered either by the melting of gas hydrates⁷ or by the heating of rocks rich in organic material in sedimentary basins (caused by widespread volcanic activity in the northeast Atlantic region^{1,7}).

The extended period of warming during the Eocene culminated in the Early Eocene Climatic Optimum (EECO) 52 to 50 Myr ago, the hottest prolonged climatic episode since the Cretaceous period 145.5 to 65.5 Myr ago. Kroeger and Funnell³ focus on the EECO in their work. Using computer models of four sedimentary basins in the southwest Pacific, they simulated the increase in hydrocarbon generation in the basins as the warming Eocene oceans transferred heat to the sea floor and to deep-seated, organic-rich rocks.

The sedimentary basins studied by the authors all contained rocks that could produce petroleum given the right temperature conditions and sufficient time. Organic matter within the sedimentary rocks can convert into petroleum at temperatures of 60–120 °C (the oil window), or into predominantly natural gas at temperatures of 100–200 °C (the gas window). On the basis of their models, Kroeger and Funnell estimate that the warming ocean during and after the PETM eventually raised the temperature of a 300-metre-thick layer of sediments into the oil and gas windows. A marked rise in hydrocarbon production would therefore have occurred in the 4 to 5 Myr following the PETM, peaking during the EECO.

The authors' results help us to understand the dynamics and temperature-dependence of hydrocarbon (petroleum and gas) generation in sedimentary basins. But there is more to the story than that. If oil and gas generated during the Eocene somehow escaped the sedimentary basins and leaked out to the ocean and the atmosphere in sufficient quantities, this may have contributed to global warming at the time. In other words, Kroeger and Funnell propose a climate feedback mechanism: global warming causes increased hydrocarbon production that leads to prolonged global warming.

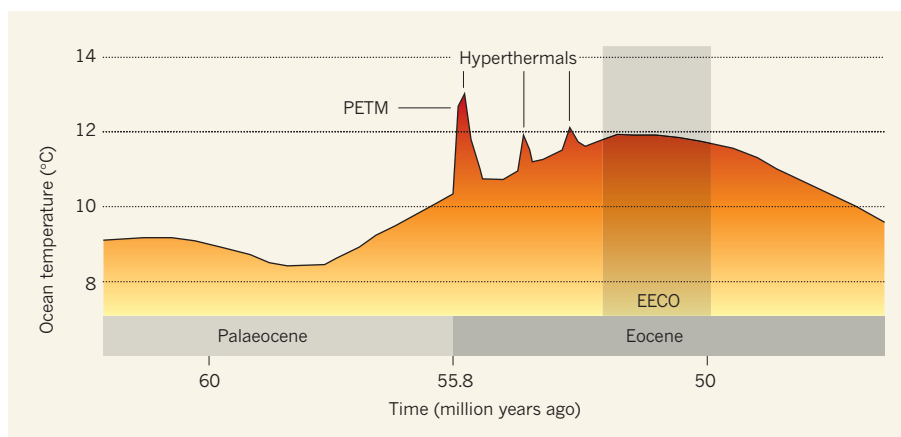


Figure 1 | Ancient climate change. The graph depicts ocean temperatures during the Palaeocene and early Eocene epochs, estimated from the abundance of oxygen isotopes in microfossils^{5,6}. A warming trend from about 58 to 50 Myr ago was punctuated by short-lived climatic anomalies known as hyperthermals, of which the Palaeocene–Eocene Thermal Maximum (PETM) was the greatest. The warmest climate occurred during the Early Eocene Climatic Optimum (EECO) about 52 to 50 Myr ago, after which climate cooling occurred. The PETM may have been caused in part by the release of methane to the atmosphere, triggered by the melting of gas hydrates (solids that trap gases in ocean sediments) and/or by the heating of organic matter by intruding magma in sedimentary basins. Kroeger and Funnell³ propose that the production of hydrocarbons (petroleum and natural gas) in sedimentary basins increased during and after the PETM, and that seepage of hydrocarbons from such basins into the ocean and atmosphere contributed to global warming.

The idea that the conversion of organic matter into petroleum following a temperature increase in sedimentary basins may form part of a climate feedback mechanism was first posited⁸ by Kroeger and colleagues last year. The modelling in Kroeger and Funnell's present work³ remarkably predicts and quantifies a peak in hydrocarbon production that overlaps in time with the EECO. The authors' results show that about 37 Gt of oil and 8 Gt of gas were generated from the four basins during this period, which is 50% more than would have occurred in the absence of extra ocean warming. This alone would not have been sufficient to affect the Eocene climate⁹, but many other basins around the world would presumably have increased in temperature at the same time. The mass of hydrocarbons generated globally could therefore have been considerably higher than that predicted in the authors' study, although the exact amount is difficult to quantify.

Is hydrocarbon seepage at the sea floor on a climate-changing scale a realistic possibility? Kroeger and Funnell argue that it is, because more oil and gas are generated in sedimentary basins than are trapped¹⁰. Studies¹¹ of sedimentary basins around the globe have shown that gas seepage is currently a common phenomenon, and there is no reason why this should not have been the case earlier in Earth's history¹².

But did the hydrocarbons predicted³ to have been generated during the Eocene really leak out to the ocean and atmosphere, or did they stay trapped in the subsurface? A way to test this is to search for carbonate deposits in old sea-floor sediments, because sea-floor hydrocarbon seepage leaves behind deposits that

have distinct geochemical signals that can be attributed to their origin¹³. Unfortunately, the carbonate record is currently too poorly investigated to confirm the extent of seepage from sedimentary basins during the Eocene, and so more studies are needed. Nevertheless, one thing seems clear: the transfer of carbon from sedimentary rocks to the atmosphere is an important component of climate change, both past and future. ■

Henrik Svensen is at the Centre for Physics of Geological Processes, University of Oslo, PO Box 1048, Blindern, 0316 Oslo, Norway. e-mail: hensven@fys.uio.no

1. Svensen, H. *et al.* *Nature* **429**, 542–545 (2004).
2. Dickens, G. R., O'Neil, J. R., Rea, D. K. & Owen, R. M. *Paleoceanography* **10**, 965–971 (1995).
3. Kroeger, K. F. & Funnell, R. H. *Geophys. Res. Lett.* <http://dx.doi.org/10.1029/2011GL050345> (2012).
4. www.grida.no/publications/other/ipcc_tar
5. Zachos, J. C., Pagani, M., Sloan, L., Thomas, E. & Billups, K. *Science* **292**, 686–693 (2001).
6. Sluijs, A., Bowen, G. J., Brinkhuis, H., Lourens, L. J. & Thomas, E. in *Deep Time Perspectives on Climate Change: Marrying the Signal from Computer Models and Biological Proxies* (eds Williams, M., Haywood, A., Gregory, J. & Schmidt, D.) 267–293 (Geol. Soc. Lond., 2007).
7. Storey, M., Duncan, R. A. & Swisher, C. C. III *Science* **316**, 587–589 (2007).
8. Kroeger, K. F., di Primio, R. & Horsfield, B. *Earth Sci. Rev.* **107**, 423–442 (2011).
9. Cui, Y. *et al.* *Nature Geosci.* **4**, 481–485 (2011).
10. Kvenvolden, K. A. & Cooper, C. K. *Geo-Mar. Lett.* **23**, 140–146 (2003).
11. Serié, C. S., Huuse, M. & Schødt, N. H. *Geology* <http://dx.doi.org/10.1130/G32690> (2012).
12. Berndt, C. *Phil. Trans. R. Soc. A* **363**, 2855–2871 (2005).
13. Mazzini, A., Aloisi, G., Akhmanov, J., Parnell, B. & Murphy, P. J. *Geol. Soc. Lond.* **162**, 815–827 (2005).

VIROLOGY

Influenza's tale of tails

Epigenetics is a hot new research field, but it seems that the influenza virus already has it figured out. By mimicking epigenetic regulation in human cells, one flu strain suppresses the expression of antiviral genes. [SEE ARTICLE P.428](#)

ALEXEI L. KRASNOSELSKY
& MICHAEL G. KATZE

Influenza virus infections are sometimes severe, or even deadly, but most people recover within a few days, helped by their body's immune system. Yet this apparently simple interaction between the virus and its host is deceptive. Influenza viruses are, in fact, masters at circumventing their hosts' defences — they co-opt cellular protein-synthesis pathways to produce viral proteins, for example, and antagonize aspects of the immune response. On page 428 of this issue, Marazzi *et al.*¹ describe another viral evasion tactic. They show that an influenza protein called NS1 mimics a host-cell histone protein that is involved in regulating gene expression. By hijacking this regulatory machinery, the virus inhibits the cell's production of antiviral proteins*.

Cells tightly regulate the expression of specific genes according to an organism's developmental stage and physiological state, and in response to environmental stimuli such as infection. Gene expression can be altered in various ways, including by transcription-factor proteins, which bind to DNA and regulate the transcription of certain genes, or through epigenetic modification — heritable chemical changes to DNA and associated proteins that do not affect the DNA sequence but alter the rate of transcription. Epigenetics has rapidly become a much-studied topic since these regulatory mechanisms were first reported around 20 years ago.

A common epigenetic alteration is the addition of methyl or acetyl groups to histone proteins, which are the 'building blocks' of chromatin, the scaffold that packages DNA into chromosomes. The four main histone proteins (H2A, H2B, H3 and H4) consist of a globular domain and an unstructured amino-terminal tail region that is dominated by the positively charged amino acids lysine and arginine. These amino acids can be modified by enzymes that add or remove methyl or acetyl groups². Such modifications alter the histone–DNA interaction, which in turn leads

to dynamic changes in chromatin that allow specific areas of the chromatin to unfold, or other proteins to be recruited to the site. Thus, by regulating the accessibility of a particular region of DNA, epigenetic modifications can regulate gene expression.

Some epigenetic changes are generally associated with a site of active gene transcription³. An example of such a change is methylation at the lysine residue (K) of the amino acid sequence designated ARTK in histone H3 (known as the H3K4 modification). Marazzi *et al.*¹ found that the H3N2 influenza virus contains an amino-acid sequence (ARSK) very similar to the histone's ARTK sequence (Fig. 1). This mimic sequence is found in the virus's NS1 protein, which is not essential for viral structure but is known to have other roles in evading the host's immune system⁴. The authors also show that this sequence similarity is functional — the NS1 tail can serve as a substrate for the histone-modifying enzyme Set1, a lysine methyltransferase.

Marazzi and colleagues also demonstrate that H3N2's histone-mimic tail binds directly

to the transcription-elongation complex PAF1C (Fig. 1). PAF1C accompanies the transcription enzyme RNA polymerase II during the formation of messenger RNA, and is thought to recruit the Set1 enzyme that leads to H3K4 methylation⁵. The authors propose that NS1 binding to PAF1C interferes with gene transcription in the host cell. Indeed, the researchers found that when cells from human lung tissue were infected with the H3N2 virus, transcription of rapidly inducible genes was halted. But when the cells were infected with H3N2 viruses that had been mutated so that they could no longer bind PAF1C, transcription of these genes was unaffected. Furthermore, the authors provide compelling evidence that it is specifically the transcription of antiviral genes that is interfered with by the interaction between NS1's histone-like tail and PAF1C. Thus, histone mimicry seems to support viral infection, and may give a selective advantage to viruses that have this ability.

Is this mechanism unique to H3N2 viruses, and could it be a recent evolutionary adaptation? Moreover, does possession of this mechanism have a role in the variation in infectivity and disease severity that is seen among influenza strains? The H3N2 virus is an emerging influenza subtype that has caused only a limited number of human infections during the 2011–12 flu season. However, they seem to cause illness of around the same severity as that induced by standard seasonal influenza viruses, which do not contain the NS1 histone-mimic tail¹. It will be necessary to assess other emerging influenza strains for histone mimicry to determine whether this mechanism is evolutionarily new, and to study more influenza cases to predict its

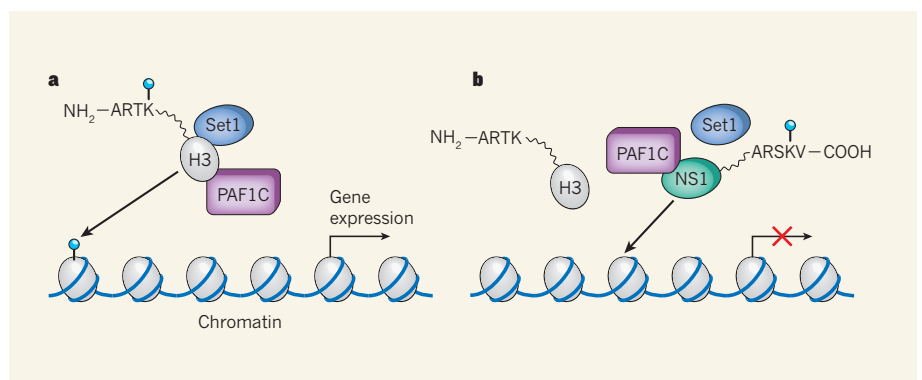


Figure 1 | Interfering influenza. Histones are the building-block proteins around which DNA is wound to form chromatin. Epigenetic changes to histones, such as the addition of methyl groups (blue circles), can affect the rate of gene transcription at specific DNA sequences. **a**, The amino-terminal (NH₂) 'tail' of the human H3 histone protein contains a string of amino acids (ARTK) that can be methylated at the lysine (K) residue by a methyltransferase enzyme, Set1. This enzyme is recruited by a protein complex called PAF1C, which also promotes elongation of RNA molecules during gene transcription. Methylation of the lysine in ARTK of the H3 histone tail is associated with active gene transcription. **b**, Marazzi and colleagues¹ show that the NS1 protein of the H3N2 influenza virus contains an amino-acid sequence (ARSK, close to the protein's carboxy (COOH) terminus) that mimics the H3 ARTK sequence. Using this sequence, viral NS1 can bind directly to PAF1C, which might direct Set1's methylation activity to NS1 rather than to the H3 histone. The authors also show that NS1 is deposited at the promoter regions of the host's DNA to which methylated H3K4 would typically bind, and that this interference suppresses the expression of antiviral genes.

*This article and the paper¹ under discussion were published online on 14 March 2012.

potential impact on public health. Even if histone mimicry is not widespread and does not dramatically alter disease severity, Marazzi and colleagues' discovery may provide a novel target for antiviral drugs aimed at modulating the host's antiviral response.

The finding raises another intriguing question: what would happen if a person is concurrently infected with H3N2 virus and a more virulent influenza virus, such as the highly pathogenic avian H5N1? Or what might occur if an H5N1 virus acquires the NS1 sequences required for the protein to function as a histone mimic? The combined effect of a suppressed antiviral response and a highly virulent virus might lead to devastating

consequences for the host. Alternatively, if an overly active host response is itself the main culprit in causing severe influenza, as has been suggested⁶, a suppressed antiviral response could actually reduce disease pathology.

Research aimed at addressing these questions may be hampered by an increasing wariness about generating recombinant H5N1 viruses⁷. But ongoing influenza research remains essential. Although epigenetic gene regulation is new to scientists, other mechanisms of gene regulation no doubt remain to be discovered, and we can be certain that viruses have already evolved to interfere with these regulatory processes, and to use them to their advantage. ■

Alexei L. Krasnoselsky and Michael G. Katze are in the Department of Microbiology and Washington National Primate Research Center, University of Washington, Seattle, Washington 98195-8070, USA.
e-mails: akrasnos@u.washington.edu; honey@u.washington.edu

1. Marazzi, I. *et al. Nature* **483**, 428–433 (2012).
2. Berger, S. L. *Nature* **447**, 407–412 (2007).
3. Ng, S. S., Yue, W. W., Oppermann, U. & Klose, R. J. *Cell Mol. Life Sci.* **66**, 407–422 (2009).
4. García-Sastre, A. *Virus Res.* **162**, 12–18 (2011).
5. Jaehning, J. A. *Biochim. Biophys. Acta* **1799**, 379–388 (2010).
6. Kash, J. C. *et al. Nature* **443**, 578–581 (2006).
7. Kawaoka, Y. *Nature* **482**, 155 (2012).

MICROSCOPY

Plasmons go quantum

Observations of collective electron waves in metal nanoparticles challenge our understanding of how light interacts with matter on small scales and underscore the need to factor quantum effects into nanophotonics. [SEE ARTICLE P.421](#)

F. JAVIER GARCÍA DE ABAJO

Just as water ripples travel along the surface of a pond after a stone is thrown into it, collective oscillations of conduction electrons called plasmons can be produced in a metal and propagate along its surface. Like pond ripples, plasmons can generally be explained in terms of a classical theory — electromagnetism. But if the metal structure on which they reside is very small (less than about 10 nanometres across), quantum-mechanical effects emerge and become relevant, changing the plasmons' oscillation frequency and lifetime. Such changes have so far been poorly understood, particularly on the experimental front. On page 421 of this issue, Scholl *et al.*¹ describe an experiment, and an accompanying theoretical analysis, that addresses this issue.

When light is shone on nanometre-sized particles made of silver and gold, it creates plasmons that have frequencies in the optical and near-infrared parts of the spectrum. The intense colours of the Lycurgus Cup, which dates back to fourth-century Rome and is on display at the British Museum in London, are an example of nanoparticle plasmons at work. Plasmons are unique in their ability to enhance the intensity of incident light and to concentrate the light down to regions much smaller than its wavelength. These features are the main reason that plasmons are finding use in a wide range of applications, including improved photovoltaic devices², cancer therapy³ and catalysis⁴.

Much effort is being invested in engineering small metallic structures so as to manipulate

plasmons and optimize their performance. As a result, a plasmon taxonomy has been developed that is mostly based on the classical electromagnetic description of structured metals. This classical approach is useful for accurately describing plasmons in structures larger than about 10 nm. But it fails for smaller structures, which are of utmost importance for the applications mentioned above.

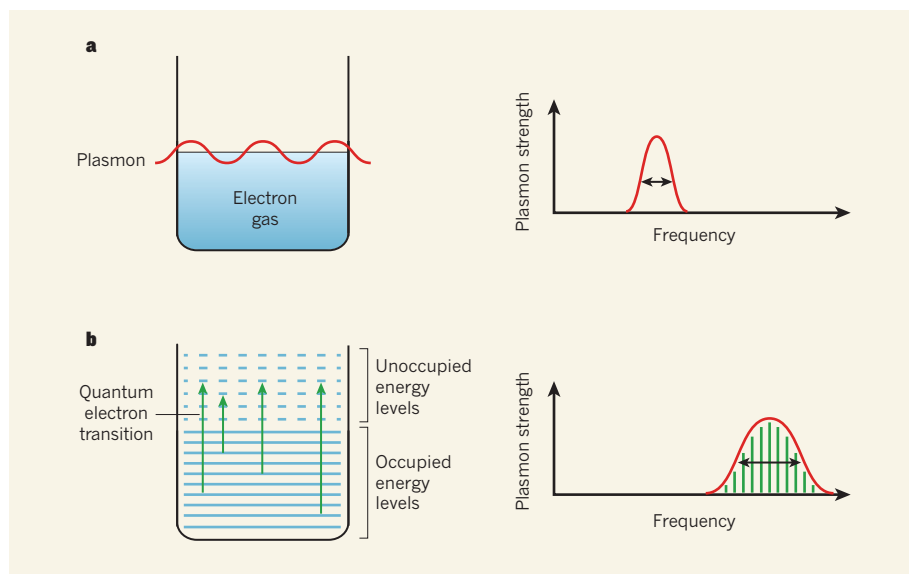


Figure 1 | Quantum effects in nanoparticle plasmons. **a**, In particles larger than about 10 nanometres, plasmons emerge as collective oscillations of a gas of conduction electrons, and have a frequency that is uncertain (double-headed arrow) because of collisions among the electrons and between the electrons and the particles' atomic lattice. **b**, In particles smaller than 10 nanometres, plasmons are associated with quantum electron transitions between occupied and unoccupied energy levels. As a result, the plasmon frequency and its uncertainty, which Scholl *et al.*¹ accurately measured, are larger than those for bigger particles.

the interaction of light with plasmons. Using state-of-the-art electron energy-loss spectroscopy, the authors have measured the plasmon frequencies with sufficient accuracy to separate surface- and bulk-plasmon components and also to resolve tiny changes in the frequency of surface plasmons with particle size. In classical electrodynamics, no size dependence is expected. However, Scholl and colleagues have observed a sizeable increase (about 15%) in the plasmon frequency of their smallest nanoparticles (roughly 2 nm across) compared with larger ones (larger than 10 nm), accompanied by a decrease in the plasmon lifetime of about 50%.

In a simple model, conduction electrons moving at about one million metres per second take approximately 10^{-14} seconds to travel across a 10-nm silver particle. This is comparable to the observed plasmon lifetime of such particles, which is about 10 plasmon periods. Under the assumption that reflections of the electrons at the surface contribute to the reduction in the plasmon lifetime, a model has been formulated⁵ that is widely used and accounts for the observed lifetime reduction in assemblies of sub-10-nm particles. But the increase in plasmon frequency observed by Scholl *et al.*¹ in their individual sub-10-nm silver particles cannot be explained by this model, and requires quantum-mechanical effects to be understood in detail and carefully accounted for.

In nanoparticles larger than 10 nm, the conduction electrons respond to electromagnetic fields as a classical electron gas. In this gas, the contribution of each electron to the plasmons cannot be observed, and the plasmon frequency is uncertain because of collisions of the electrons with each other and with the metal's atomic lattice (Fig. 1a).

By contrast, in nanoparticles smaller than 10 nm, because there are relatively few conduction electrons participating in the plasmons (about 250 electrons in a 2-nm particle), the electrons appear at a discrete set of energy levels, which are increasingly separated from one another as the particle size is reduced. This produces individual electron transitions between occupied and unoccupied electron energy levels. The frequency jumps of these transitions are centred around a value that is higher than the plasmon frequency of large nanoparticles (Fig. 1b), and the finite separation between the frequency jumps increases the uncertainty about the plasmon frequency and therefore reduces plasmon lifetime⁶. In fact, individual transitions cannot in general be resolved owing to the uncertainty produced by the collisions mentioned previously. Using a simplified model that incorporates the effects of individual electron transitions, Scholl *et al.*¹ have successfully explained their data.

By measuring the plasmon-frequency increase and lifetime reduction in sub-10-nm particles, and by modelling these effects

in terms of quantum transitions, Scholl and co-workers¹ have shown that the quantum nature of conduction electrons emerges in plasmons of small nanoparticles. So far, their study has focused on spherical nanoparticles. But it is expected that quantum effects should also have a role in nanometre-sized gaps between metallic nanoparticles and in sharp metal tips. These gaps and tips can create localized plasmon 'hotspots' that are relevant for applications such as nonlinear optics⁷ and ultrasensitive, single-molecule detection (for example, through an effect known as surface-enhanced Raman scattering⁸).

Prospects for using plasmons to fabricate quantum-optics devices in robust solid-state systems also depend on the interaction between molecules and plasmon hotspots⁹. In such systems, quantum effects such as non-locality cannot be ignored because they produce sizeable plasmon-frequency shifts and reduced plasmon lifetimes. There are,

of course, unknowns on the long road to understanding plasmons at the nanometre scale, but Scholl and colleagues' study is a step in that direction. ■

F. Javier García de Abajo is at the *Instituto de Química Física "Rocasolano", CSIC, Serrano 119, 28006 Madrid, Spain.*
e-mail: j.g.deabajo@csic.es

- Scholl, J. A., Koh, A. L. & Dionne, J. A. *Nature* **483**, 421–427 (2012).
- Atwater, H. A. & Polman, A. *Nature Mater.* **9**, 205–213 (2010).
- Gobin, A. M. *et al.* *Nano Lett.* **7**, 1929–1934 (2007).
- Hirakawa, T. & Kamat, P. V. *J. Am. Chem. Soc.* **127**, 3928–3934 (2005).
- Kreibig, U. & Vollmer, M. *Optical Properties of Metal Clusters* (Springer, 1995).
- Thongrattanasiri, S., Manjavacas, A. & García de Abajo, F. J. *ACS Nano* **6**, 1766–1775 (2012).
- Danckwerts, M. & Novotny, L. *Phys. Rev. Lett.* **98**, 026104 (2007).
- Stiles, P. L., Dieringer, J. A., Shah, N. C. & Van Duyne, R. P. *Annu. Rev. Anal. Chem.* **1**, 601–626 (2008).
- Akimov, A. V. *et al.* *Nature* **450**, 402–406 (2007).

NEURODEGENERATION

Trouble in the cell's powerhouse

Studies of rare hereditary disorders are intended to find treatments, but they can also bring other discoveries. One such study links the dysfunction of a protein to that of the cell's energy producers, the mitochondria.

DEREK P. NARENDRA & RICHARD J. YOULE

In Greek, 'ataxic' (ατάξιος) means 'disordered'. In neurological diseases known as ataxias, the lack of order is mainly one of movement: patients cannot coordinate voluntary movements because of the loss of certain neural circuits, making it difficult for them to walk, reach for objects and speak. Increasingly, researchers are finding^{1,2} that the underlying cause of some hereditary ataxias is another sort of disorder — that of mitochondria, the intracellular organelles that act as the cell's powerhouses. However, we know very little about the mechanisms that trigger certain other hereditary ataxias, such as the condition known as autosomal recessive spastic ataxia of Charlevoix–Saguenay, or ARSACS. The disease is caused by mutations in the SACS gene³, but the link between the mutations and the neuronal loss has been unclear. Writing in *Proceedings of the National Academy of Sciences*, Girard *et al.*⁴ find that mitochondrial dysfunction is just such a link, and in the process provide clues about the cellular role of the SACS-encoded protein, saccin*.

*This News & Views article was published online on 7 March 2012.

The ataxia in ARSACS is due to a progressive loss of neurons called Purkinje cells, which are found in the cerebellum⁵, a part of the brain involved in muscle coordination. Affected patients carry mutations in both chromosomal copies of SACS, so that their cells lack functional saccin^{3,6}. The disorder was first described⁶ in 1978 in patients from the Charlevoix and Saguenay regions of Quebec, Canada, where it is much more common than in the rest of the world. One in 22 of the regions' residents carries a mutation in one of their two copies of SACS — probably brought by French immigrants four centuries ago.

To understand saccin's functions, Girard *et al.*⁴ analysed the location of saccin within various types of cells, including neurons, in culture and observed that the protein co-localizes with mitochondria. Moreover, mitochondria in mouse cells in which saccin expression had been inhibited, and in cells from patients with ARSACS, had markedly abnormal shapes: they were larger and formed more clumps than mitochondria in normal cells. The authors then generated mice that lacked the protein. These animals progressively lost Purkinje cells as they aged, making them potential models

for studying at least some aspects of ARSACS. Taken together, Girard and colleagues' results suggest that saccin deficiency results in unusually shaped, large mitochondria, and that this in turn leads to Purkinje-cell loss.

The shape of mitochondria is dynamically controlled by their fission and fusion. But why do unusually shaped mitochondria harm Purkinje cells more than other cells? Each Purkinje cell has many long, branching projections that form an extensive tree-like structure (Fig. 1a), establishing about 150,000 synaptic connections with other neurons⁵. The synapses are energy-demanding because of the need for continual pumping of ions through the cell membrane — to keep the 'lines' clear for neural transmission — and thus they require functional mitochondria to be located nearby. To enter the narrow neuronal projections, small mitochondria need to be pinched off by fission from large ones⁷ (Fig. 1b). Moreover, fission has a role in preserving mitochondrial health by eliminating organelles that become damaged by oxidative molecules produced during normal mitochondrial activity⁸. Purkinje cells seem to be highly dependent on the quality and efficient distribution of mitochondria throughout the cell, because their robust activity carries a high oxidative burden and they have a higher number of narrow prolongations than other cells. Indeed, Girard *et al.*⁴ find that the clumped, fused mitochondria in saccin-deficient neurons fail to distribute into the cellular prolongations (Fig. 1c), and that damaged mitochondria seem to be more abundant than in normal cells.

The authors' findings⁴ raise several questions. For example, how does saccin affect the size and distribution of mitochondria? Girard and colleagues propose that the protein may be needed for efficient fission of the organelle. In addition to the abnormal mitochondrial shapes in saccin-deficient cells, the researchers⁴ report that saccin binds to the Drp1 protein, which is essential for mitochondrial division. During fission, Drp1 polymerizes to form a spiral around the outside of the organelle, constricting it and facilitating its division^{9,10}.

The hypothesis that saccin is required for full Drp1 activity is consistent with previous research^{11,12} showing that mice with brain-specific Drp1 deficiency display features similar to those observed by Girard *et al.*⁴ in saccin-deficient mice — a loss of Purkinje cells, together with the presence of oversized mitochondria that fail to spread into the neuronal projections. And it has been reported⁸ that damaged mitochondria are not efficiently degraded in cultured cells in which Drp1 activity is inhibited. Therefore, the dependence of Purkinje cells on the shape and health of mitochondria may explain why they are preferentially lost in Drp1- and saccin-deficient mice, and in patients with ARSACS.

Additional questions remain, such as why saccin binds to Drp1 and how this binding

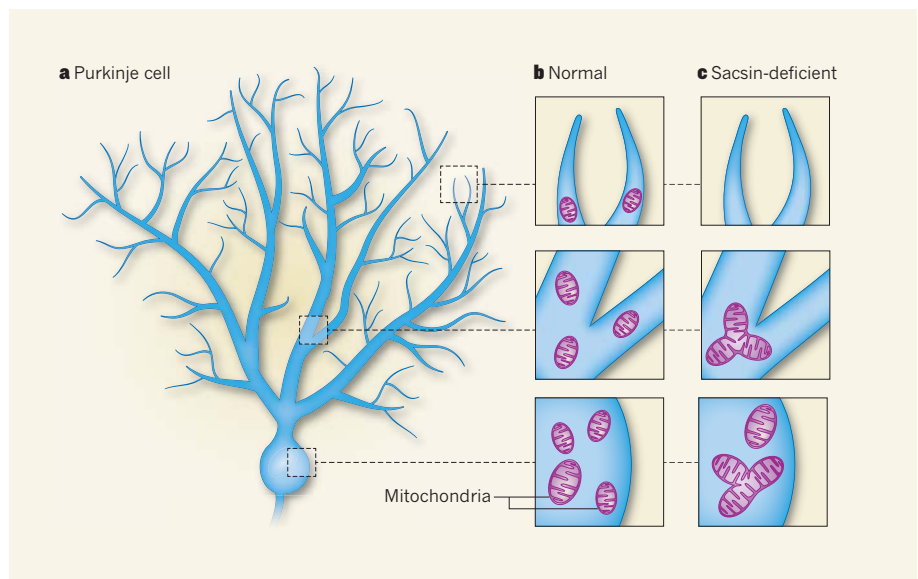


Figure 1 | Out-of-shape organelles lead to disease. **a**, Neurons known as Purkinje cells have many long, branching prolongations and are found in the cerebellum, an area of the brain that controls movement. These cells progressively die off in patients with a neurological disease called autosomal recessive spastic ataxia of Charlevoix–Saguenay (ARSACS), which is caused by mutations in the gene encoding the protein saccin. **b**, Mitochondria are usually found throughout the body of normal neurons, including in the narrow cellular prolongations. **c**, Girard *et al.*⁴ find that mitochondria in saccin-deficient mouse cells and in cells from patients with ARSACS are larger than those in normal cells and accumulate in clumps. Such large mitochondria do not distribute into the cellular prolongations in saccin-lacking neurons. These results, together with other data from saccin-deficient mice, suggest that mitochondrial dysfunction is involved in the death of Purkinje cells in patients with ARSACS.

may affect mitochondrial shape. Some portions of the saccin protein are similar to chaperones (proteins that help other proteins to fold efficiently), so it is tempting to speculate that saccin may be needed for Drp1 or other proteins involved in mitochondrial division to assume their proper conformation. The link between saccin and Drp1 also raises the possibility that saccin regulates the division of peroxisomes, another type of intracellular organelle. Drp1 elimination in mice results in abnormally long peroxisomes¹¹, and so it would be interesting to test whether the cells of patients with ARSACS contain longer peroxisomes.

Girard and colleagues' study of ARSACS strikes a common theme in research into neurodegenerative disorders: insight from clinical studies reveals new perspectives for cell biology, and vice versa. For instance, the study of families affected by optic atrophy type 1 revealed the protein OPA1 as being essential for mitochondrial fusion^{12,13}. And research in the fruitfly revealed that the parkin protein — the dysfunction of which is the leading cause of recessive Parkinson's disease — regulates mitochondrial shape¹⁴. These examples demonstrate the importance of fostering interaction between the clinic and the lab. Thus, we can continue to learn about neurological disease from model organisms such as the fruitfly, and about mitochondrial biology from people in Quebec who have ataxia. With further collaboration between clinicians and

scientists, this understanding might translate into treatments for these devastating disorders in the not-too-distant future. ■

Derek P. Narendra and Richard J. Youle are in the Biochemistry Section, Surgical Neurology Branch, National Institute of Neurological Disorders and Stroke, National Institutes of Health, Bethesda, Maryland 20892, USA.
e-mail: youler@ninds.nih.gov

1. Babcock, M. *et al. Science* **276**, 1709–1712 (1997).
2. Van Goethem, G. *et al. Neurology* **63**, 1251–1257 (2004).
3. Engert, J. C. *et al. Nature Genet.* **24**, 120–125 (2000).
4. Girard, M. *et al. Proc. Natl Acad. Sci. USA* **109**, 1661–1666 (2012).
5. Kandel, E. R., Schwartz, J. H. & Jessell, T. M. *Principles of Neural Science* (McGraw-Hill, 2000).
6. Bouchard, J. P., Barbeau, A., Bouchard, R. & Bouchard, R. W. *Can. J. Neurol. Sci.* **5**, 61–69 (1978).
7. Li, Z., Okamoto, K., Hayashi, Y. & Sheng, M. *Cell* **119**, 873–887 (2004).
8. Twig, G. *et al. EMBO J.* **27**, 433–446 (2008).
9. Ingberman, E. *et al. J. Cell Biol.* **170**, 1021–1027 (2005).
10. Labrousse, A. M., Zappaterra, M. D., Rube, D. A. & van der Bliek, A. M. *Mol. Cell* **4**, 815–826 (1999).
11. Ishihara, N. *et al. Nature Cell Biol.* **11**, 958–966 (2009).
12. Delettre, C. *et al. Nature Genet.* **26**, 207–210 (2000).
13. Alexander, C. *et al. Nature Genet.* **26**, 211–215 (2000).
14. Greene, J. C. *et al. Proc. Natl Acad. Sci. USA* **100**, 4078–4083 (2003).

Quantum plasmon resonances of individual metallic nanoparticles

Jonathan A. Scholl¹, Ai Leen Koh² & Jennifer A. Dionne¹

The plasmon resonances of metallic nanoparticles have received considerable attention for their applications in nanophotonics, biology, sensing, spectroscopy and solar energy harvesting. Although thoroughly characterized for spheres larger than ten nanometres in diameter, the plasmonic properties of particles in the quantum size regime have been historically difficult to describe owing to weak optical scattering, metal–ligand interactions, and inhomogeneity in ensemble measurements. Such difficulties have precluded probing and controlling the plasmonic properties of quantum-sized particles in many natural and engineered processes, notably catalysis. Here we investigate the plasmon resonances of individual ligand-free silver nanoparticles using aberration-corrected transmission electron microscope (TEM) imaging and monochromated scanning TEM electron energy-loss spectroscopy (EELS). This technique allows direct correlation between a particle's geometry and its plasmon resonance. As the nanoparticle diameter decreases from 20 nanometres to less than two nanometres, the plasmon resonance shifts to higher energy by 0.5 electronvolts, a substantial deviation from classical predictions. We present an analytical quantum mechanical model that describes this shift due to a change in particle permittivity. Our results highlight the quantum plasmonic properties of small metallic nanospheres, with direct application to understanding and exploiting catalytically active and biologically relevant nanoparticles.

The remarkable growth of nanotechnology has been driven by the ability to alter material properties as dimensions are reduced towards the atomic scale. Nanomaterials exhibit physical and chemical properties very different from those of their bulk counterparts, often resulting from enhanced surface interactions or quantum confinement. In the past decade, attention has focused on nanoparticles composed of noble metals, because they support localized surface plasmon resonances (LSPRs). These collective oscillations of the conduction band electrons enable strong optical absorption and scattering in subwavelength structures, with spectral properties dependent on the nanoparticle's material, size, shape, electronic charge and surrounding medium^{1,2}. LSPRs have enabled applications including photothermal ablation of cancer cells³ and light concentration in thin-film photovoltaics⁴. Furthermore, the sensitivity of LSPRs to changes in the particle's environment has enabled ultrafine sensing, with applications including biomolecular and gas detection^{5–8}, catalytic monitoring of reactant adsorption^{9,10} and sensing of electron charge-transfer events¹¹.

Although the plasmon resonances of nanospheres with diameters exceeding 10 nm have been well characterized¹², LSPRs of nanoparticles below this size are poorly understood. In this smaller size regime, plasmon resonances become more sensitive to the quantum nature of the conduction electrons. Experimentally probing this transition has been extremely challenging: optical detection in the far-field is hampered by these particles' diminishing scattering and absorption intensities, which scale as the sixth and third power of a particle's diameter, respectively¹³. Furthermore, the LSPR peaks become broadened and damped as the dimensions of the particle decrease well below the electron mean free path (52 nm for silver¹⁴). The difficulty in observing such weak signals has led to conflicting results from experiments involving quantum-sized plasmonic particles, with multiple reports of LSPR 'redshifts' or 'blueshifts' as the sphere dimensions are reduced¹⁵. For example, ensemble studies of glass-embedded silver spheres with sizes ranging from 10 nm to 2 nm have indicated a

plasmon resonance blueshift of 0.1 eV (ref. 16). In contrast, ensembles of monodisperse silver nanospheres stabilized with oleylamine ligands have indicated significant LSPR redshifts of 0.3 eV (from 3.1 eV to 2.8 eV) as the mean particle diameter decreases from 18 nm to 2 nm (ref. 17).

To eliminate ensemble heterogeneity effects, other recent experiments have examined single metallic nanoparticles. Confocal heterodyne¹⁸ and photothermal¹⁹ techniques were used to observe the absorption of nanoparticles as their diameter decreased. Citrate-stabilized gold spheres with diameters ranging from 30 nm to 5 nm have exhibited a plasmon-resonance blueshift of approximately 0.05 eV, indicating a transition to quantum-confined effects. However, direct correlation between individual particle geometry, size and spectra was not achieved because the specimens were substantially below the optical diffraction limit.

With such difficulty in experimentally determining the plasmonic properties of small metallic particles, theoretical models to explain the nanospheres' deviations from bulk permittivity values have been equally challenging to develop and validate. Classical approaches have included the addition of size-dependent electron scattering terms in the Drude permittivity model, but the use of these alone results in predictions of redshifts and imperceptible plasmon resonances at small size scales¹⁴ that conflict with experimental findings^{16,18,19}. *Ab initio* density functional theory (DFT) approaches have also been used to predict metallic cluster properties^{20,21}, but are currently limited to particles smaller than 1–2 nm, owing to their high computational demands²².

If the plasmon resonances of such quantum-sized particles could be understood and used, they would offer unprecedented opportunities in biology, catalysis and quantum optics. For example, their reduced dimensions would enable improved nanoparticle integration into cells for bio-plasmonic imaging or therapeutics^{23–26}. Simultaneously, their increased surface-to-volume ratios would make them ideal catalytic centres or sensors²⁷. Quantum-sized plasmonic particles would be

¹Department of Materials Science and Engineering, Stanford University, Stanford, California 94305, USA. ²Stanford Nanocharacterization Laboratory, Stanford University, Stanford, California 94305, USA.

particularly sensitive to single-molecule adsorbates⁶ or to few-photon or few-electron transfer events²⁸, with potentially profound applications for quantum information transfer²⁹.

In this Article, we examine the plasmonic properties of individual nanospheres with diameters ranging from 20 nm to less than 2 nm, extending from the classically described regime to the quantum size regime. Rather than relying on optical observation, we use aberration-corrected TEM imaging in conjunction with monochromated scanning transmission electron microscopy (STEM) EELS. Combined, these techniques allow direct morphological and spectral analysis of individual nanoparticles, addressing many of the ambiguities of previous investigations. STEM EELS has recently yielded unprecedented insight into the plasmonic resonances of nanoscale hemispheres³⁰ as well as larger spheres³¹ and prisms³². Here, we explore the plasmon modes of silver nanoparticles as their size is reduced to dimensions well below the electron mean free path. To minimize any surface chemical interface effects, the particles are synthesized without ligands. Our experimental results indicate a significant 0.5-eV blueshift in the plasmon resonance as the particle size approaches the quantum regime, with only slight linewidth broadening. The results indicate an increasingly substantial change in nanoparticle permittivity as the diameter is reduced below 10 nm, which can be well described with a computationally light analytical model based on fundamental quantum mechanical principles.

Nanoparticle synthesis and electron spectroscopy

Figure 1 presents high-resolution micrographs of our particles. The Ag nanospheres were synthesized in solution using silver nitrate as the metallic precursor and sodium borohydride as both the reducing agent and electrostatic stabilizer to prevent agglomeration (see Methods)³³. The absence of surface ligands on the silver nanoparticles is important to reduce the chemical interface effects on the plasmon resonance, but does present some synthetic challenges: ligands are typically used to prevent particle aggregation and reduce surface energy to counterbalance thermodynamic driving forces, allowing particle size to be more directly controlled. In this synthesis, electrostatic repulsion is used as a substitute for surface ligands to prevent agglomeration. The resulting silver nanoparticles have a mean diameter of 8 nm with sizes ranging from 1 nm up to 20 nm. They retain spherical-like symmetry for diameters just below 2 nm.

Spectroscopic analysis of our silver nanoparticles was performed with a FEI Titan transmission electron microscope at 300 kV in STEM mode, with an imaging spatial resolution of 0.27 nm, a spectral dispersion of 0.01 eV per pixel, and an EELS zero-loss peak (ZLP) full-width at half-maximum of 0.15 eV. Particles were deposited and well-dispersed on ultrathin (3 nm) carbon films to minimize the signal from the substrate during EELS. As a control, we also investigated the plasmon resonances of nanoparticles on 8-nm-thick SiO₂ substrates, which yielded very similar results (see Supplementary Information).

During EELS collection, electrons that interact with the particle exhibit an energy loss corresponding to the electromagnetic modes of the structure^{32,34–37}. However, not all incident electrons will excite plasmons. In fact, the vast majority of source electrons are able to pass through the sample with minimal energy loss, resulting in a dominant ZLP on the detector. Owing to its relative magnitude and intrinsic Gaussian-like shape, the ZLP contributes a substantial background spanning several electronvolts in energy loss. To extract the plasmon contribution, techniques must be implemented either to deconvolve the ZLP from the collected spectra or to subtract the signal entirely. The former was accomplished through the Richardson–Lucy deconvolution algorithm, using the spectra of the substrate alone as the point spread function and deconvolving it from the particle spectra³⁸. Alternatively, the ZLP subtraction was accomplished through two techniques: the ‘reflected tail’ method and Gaussian plus Lorentzian ZLP curve fitting (see Methods)³¹. Each of the above three strategies separately yielded consistent results in the plasmonic spectra.

Multiple energy loss spectra were collected for each particle, both near the sphere’s edge to observe the surface plasmon resonance modes and through its centre to observe the bulk modes. When the electron beam is directed in close proximity to the edge of a particle, the surface electrons collectively oscillate and the LSPR modes are excited³⁷. The energy of this resonance is dependent on not only the material’s permittivity function but also its size, shape and surrounding medium. The bulk plasmon resonance, in contrast, is the collective oscillation of all the electrons in the material. It indicates the frequency of a metal-to-dielectric transition and is affected solely by the material’s permittivity. Although the higher-energy bulk resonance peak can be observed with electron excitation, it cannot be seen in optical measurements, owing to the symmetry of the mode³⁶.

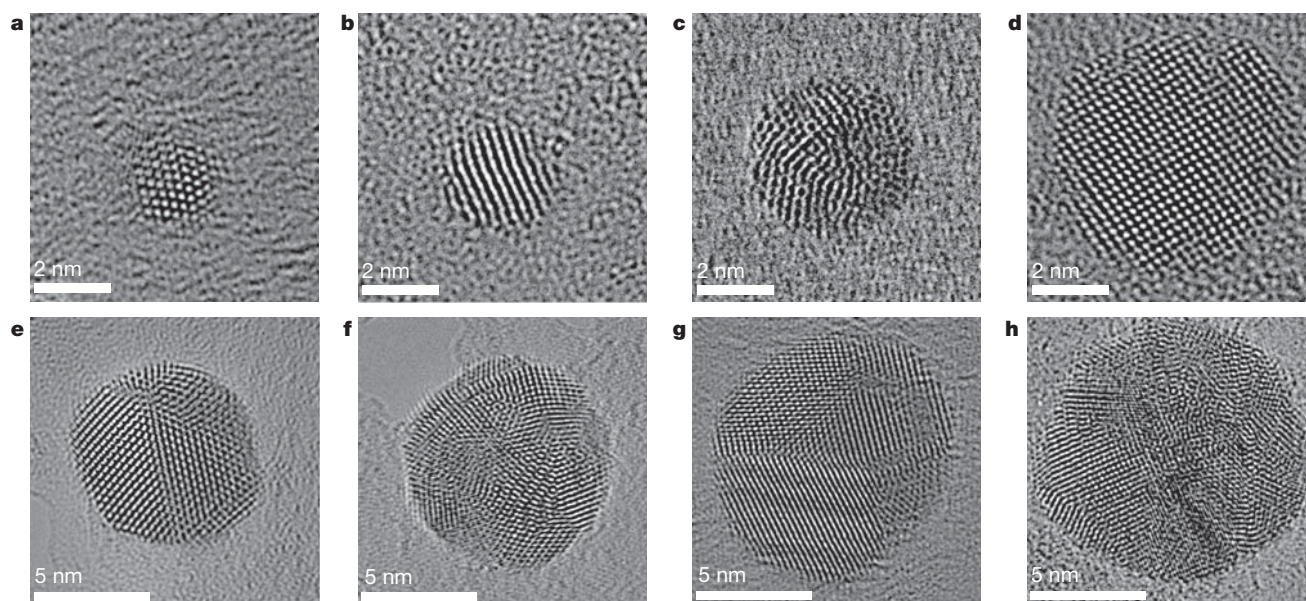


Figure 1 | Aberration-corrected TEM images of silver nanoparticles synthesized free of stabilizing ligands. Particles with diameters of 2 nm (a), 3 nm (b), 4.5 nm (c), 6 nm (d), 7.5 nm (e), 9 nm (f), 10.5 nm (g), and 12 nm (h) are shown. Scale bars: a–d, 2 nm; e–h, 5 nm.

First, we used STEM EELS to measure the plasmon resonances of larger, classically described nanoparticles that have been well characterized³¹. Figure 2 illustrates a 20-nm-diameter nanosphere that was excited with the electron beam along the edge and through the bulk of the particle. Both the STEM-acquired particle image and spectra are included. As can be seen, exciting the particle at the edge (position (i)) results in a single spectral peak at 3.3 eV, corresponding to the particle's LSPR. Electron excitation near the particle's interior (positions (ii) and (iii)) results in development of a second spectral peak at 3.85 eV, corresponding to the bulk plasmon of silver. The spectral positions of the surface and bulk plasmon resonances remain unchanged with the location of the electron source. However, the relative weight of the peaks varies, corresponding to the efficiency with which each mode is excited.

We repeated these techniques for individual nanoparticles with diameters ranging from 20 nm down to 1.7 nm. Figure 3a illustrates the STEM image and energy loss spectra of six individual particles with diameters of 11 nm, 8.5 nm, 5.5 nm, 3.5 nm, 2.5 nm and 1.7 nm. These spectra were generated by directing the electron beam at the edge of the particles to excite the LSPR selectively. As the nanosphere diameter is decreased, several trends can be noted. First, signal

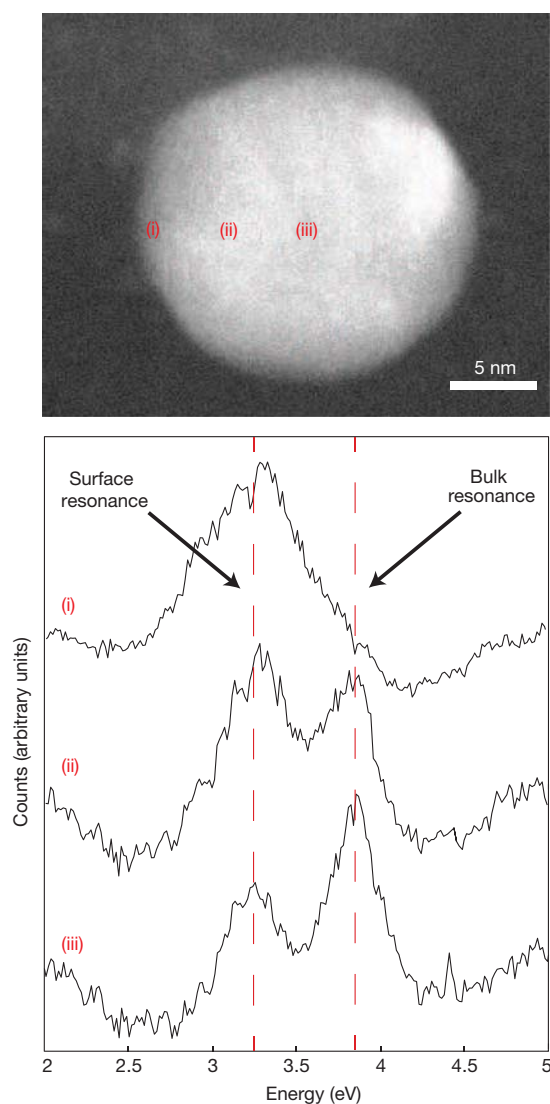


Figure 2 | STEM image of a 20-nm-diameter silver particle and the associated deconvoluted EELS data. Spectra were collected by directing the electron beam to different locations on the particle, from the edge (i) through the bulk (iii). Based on the excitation location, surface or bulk resonances can be selectively observed.

strength from larger particles is stronger than from smaller spheres, as would be expected on the basis of particle volume. However, even with the smallest observed particles, the plasmon resonance is still significantly above the noise level. Second, the spectral peak widths do show some expansion as particle size is decreased, with a full-width at half-maximum increasing from 0.4 eV to 0.6 eV as the diameter is reduced from 11 nm to 1.7 nm. Nevertheless, this broadening is substantially less than would be expected from ensemble measurements for similarly sized small particles, where the resonance peak becomes so dampened as to be nearly unrecognizable¹⁴. Finally, and most significantly, the energy of the surface plasmon resonance exhibits a notable increase as the particle size decreases.

Figure 3b plots this plasmon resonance energy shift over a collection of particle sizes, with surface resonance peaks increasing from 3.3 eV to 3.8 eV as the particle size decreases. In contrast, classical Mie theory would predict only a 0.03-eV blueshift over the same size range. Interestingly, the trend towards higher energy resonances is not purely monotonic in the EELS data, with a greater variety in peak locations occurring at the smallest sizes.

In Fig. 3b, two standard deviation (95%) confidence intervals are included, generated by analysing the particle's spectra and fitted peak location data with a bootstrapping technique (see Methods). The confidence intervals indicate that the observed surface resonance peak shift is indeed real and is due to alterations in the permittivity as the particles enter the quantum size regime.

Figure 3b also includes a plot of the bulk plasmon shift with decreasing particle diameter, generated by directing the electron source through the particle's interior. For large particle dimensions, the bulk plasmon peak remains unaltered around 3.85 eV. For diameters smaller than 10 nm, however, a slight blueshift of 0.1 eV can be noticed. Bulk plasmon resonances distinct from LSPRs were observed for particles as small as 6 nm in diameter. Smaller particles exhibited a nearly indistinguishable spectral response for electron excitation both at the edge and at the centre of the particle. As shown below, this small-particle response can ostensibly be assigned to the LSPR.

Modelling the classical-to-quantum transition

To understand the EELS data of Figs 2 and 3, we have developed an analytic model to describe size-dependent changes in plasmon resonances. The model is rooted in quantum calculations of the metal's electric permittivity ϵ as particle dimensions are reduced towards the atomic scale. Though completely analytic, the results are complementary to both *ab initio* DFT calculations³⁹ and recent developments in predicting a system's electromagnetic response with nonlocal dielectric functions^{40–42}.

According to the quasistatic approximation of Mie theory for small particles^{13,43}, the LSPR peak occurs when the particle's polarizability is maximized. For a spherical particle, this condition is satisfied when $|\epsilon_{\text{particle}} + 2\epsilon_{\text{medium}}|$ is minimized. The bulk plasmon resonance occurs when the real component of the metal permittivity crosses zero. Thus, the spectral properties of plasmonic nanoparticles depend very sensitively on their dielectric function.

Classically, the frequency-dependent permittivity of metals can be described with a Drude model which determines the material's dielectric response by considering the motion of the free electrons against a background of positive ion cores. The general Drude permittivity is expressed as:

$$\epsilon(\omega) = \epsilon_{\infty} - \frac{\omega_p^2}{\omega^2 + i\gamma\omega} \quad (1)$$

where ω is the angular frequency of the light, ω_p is the plasma frequency, a material property that is based on the number density of conduction electrons, ϵ_{∞} is a corrective constant that accounts for the background electron screening at high frequency, and γ represents the scattering frequency of the electron as it travels through the metal. To increase the energy range across which the Drude model matches the

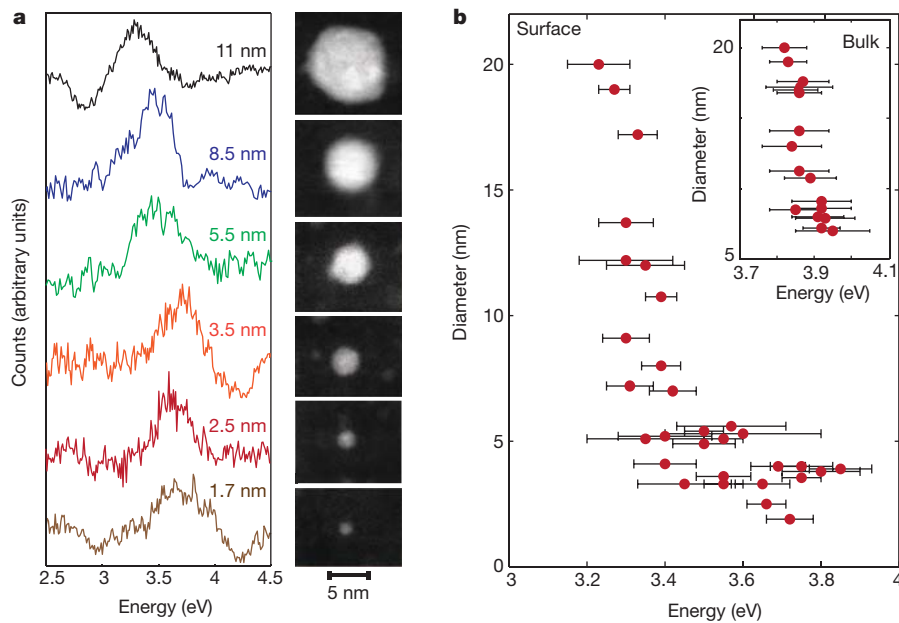


Figure 3 | Correlating Ag nanoparticle geometry with plasmonic EELS data. **a**, Collection of normalized, deconvoluted EELS data from particles ranging from 11 nm to 1.7 nm in diameter and the corresponding STEM image of each specimen. The electron beam was directed onto the edge of the particles so that only the surface resonance is shown. **b**, Plot of the surface plasmon resonance

energy versus particle diameter, with the inset depicting bulk resonance energies. Horizontal error bars indicating 95% confidence intervals were generated with a curve fitting and bootstrapping technique (see Methods). Vertical error bars are contained within the size of the data points.

empirical literature data⁴⁴, we replace the corrective constant ε_{∞} with the frequency-dependent term ε_{IB} . This component accounts for the contribution of d-band valence electrons that undergo an interband transition at high energies (see Supplementary Information).

Although Drude-like permittivity models accurately predict the plasmon spectra for larger nanoparticles (diameters greater than 10 nm), error significantly increases for reduced particle sizes. For nanostructures composed of only a few hundred to a few thousand atoms, both increased surface interactions and quantum confinement will affect the motion of electrons. Surface interactions will cause the scattering frequency γ to increase owing to the increased number of electron collisions. Existing classical models of small-particle Drude-based permittivities have described this change with the expression:

$$\gamma = \gamma_{\text{bulk}} + \frac{A v_F}{R} \quad (2)$$

where R is the particle radius and v_F is the Fermi velocity (approximately $1.4 \times 10^6 \text{ m s}^{-1}$ in silver⁴⁵). The variable A is a fitting coefficient whose value is still much debated in the literature, spanning an order of magnitude from 0.1 to 2 depending on the experimental data and physical model^{15,46,47}. The discrepancies in reported values for this coefficient may indicate that by itself, the classical surface scattering approach is insufficient to model the plasmon resonances of quantum-sized particles accurately. In fact, in contrast to our experimental results, solely increasing the γ value with decreasing particle size results in a slight redshift of the plasmon resonance¹⁴.

To fully model small plasmonic particles (diameters of 2–10 nm), quantum mechanical effects must also be considered. For such particles, the energy levels in the conduction band become discretized and only certain electronic or plasmonic transitions are allowed. To account for these transitions, we start with the Drude model of equation (1), but include Lorentzian terms that can be defined quantum mechanically. Following the example of Genzel¹⁶ and Kraus⁴⁸, we model the conduction electrons as a free electron gas constrained by infinite potential barriers at the physical edges of the particle. Transition frequencies ω_{if} thus correspond to the allowed quantum energies of transitions of conduction electrons from occupied states i within the k-space Fermi sphere to unoccupied states f immediately outside it.

The relative magnitude of each of these Lorentzian perturbations is based on the well-established Thomas–Reiche–Kuhn energy-weighted sum rule (also known as the f-sum rule) that are commonly used for absorption processes. Encapsulating significant information about the energy spectrum and eigenfunctions of a system in a compact form, they have enabled experimental confirmation of early quantum theory and have since been widely used in solid-state physics as well as atomic and nuclear spectroscopy⁴⁹. Here, the technique is employed in the form of oscillator strengths (S_{if}) that correspond to each transition frequency.

In total, the particle permittivity can be expressed as:

$$\varepsilon(\omega) = \varepsilon_{IB} + \omega_p^2 \sum_i \sum_f \frac{S_{if}}{\omega_{if}^2 - \omega^2 - i\gamma\omega} \quad (3)$$

where the sum is taken over all initial and final states of the electrons. The frequency of the transitions from the occupied to excited states can be described as:

$$\omega_{if} = \frac{E_f - E_i}{\hbar} \quad (4)$$

where the energy levels E_f and E_i depend on the geometry and potential of the system. We assume that the nanocrystal's physical shape closely approximates a sphere and thus treat the conduction electrons as particles in an infinite spherical well:

$$E = \frac{\hbar^2 \pi^2}{8MR^2} (2n + l + 2)^2 \quad (5)$$

Here, M is the mass of the electron, and n and l are the principal and azimuthal quantum numbers respectively. (This assumption of a 'spherical well' potential is justified on the basis of the geometry of the particles seen in Fig. 1.)

The oscillator strength terms, as dictated by the Thomas–Reiche–Kuhn sum rule, collectively sum to unity and are described using the standard harmonic oscillator quantum mechanical definition:

$$S_{if} = \frac{2M\omega_{if}}{\hbar N} |\langle f | z | i \rangle|^2 \quad (6)$$

where N is the number of conduction electrons in the nanoparticle. The matrix element term $\langle f | z | i \rangle$ is determined by the allowed

wavefunctions of the spherical well model. Further details can be found in the Supplementary Information.

Figure 4a illustrates the real and imaginary components of the permittivity, accounting for both quantum mechanical effects and surface scattering. Here, the electron scattering term γ was allowed to vary in accordance with equation (2), using $A = 0.25$. This value was chosen based on fits from single-particle experiments of larger spheres on glass substrates¹⁹ and DFT simulations of silver nanoparticles³⁹, both of which are free of the complicating effects of heterogeneity in ensemble measurements.

As can be seen, the permittivity is highly dependent on the specific size of the spherical particle. For small particle diameters (<10 nm), the Lorentzian oscillations occur at higher energies as a result of the allowed electron transition frequencies. These have an R^{-2} dependence according to the allowed energies in a spherical well (equation (5)). As the particle diameter increases beyond the quantum size range (>10 nm), the conduction electron transition frequencies decrease into the infrared, and the magnitude of the perturbations, as dictated by the oscillator strength, also decrease. Accordingly, larger particle permittivities converge to bulk experimental data and the classical Drude model based on bulk parameters (see Fig. 4). The choice of a larger A coefficient would result in increased plasmon peak broadening, but does not significantly affect the general energy trends.

Using the permittivity values shown in Fig. 4a as an input to electromagnetic Mie theory, the absorption efficiencies (absorption cross-sections divided by physical cross-sections) of spheres with diameters of 2, 4, 6 and 8 nm are determined. The energies of the dipolar resonances that dominate the particles' optical spectra are the same as when generated through EELS^{35,36}, allowing direct comparison with our experimental data (see Supplementary Information). Figure 4b illustrates the results, revealing decreasing absorption efficiency and blueshifting LSPR peaks as particle size decreases that agree with experimental findings.

The full trend of calculated LSPR energy versus particle diameter is shown in Fig. 5a. Particle diameter values are displayed in gradations of full metallic monolayers (each adding approximately 0.5 nm), and the corresponding absorption spectra for each size is normalized to the same intensity colour scale. An effective medium refractive index of $n = 1.3$ is used as a weighted average of the carbon substrate ($n = 2$) and the surrounding vacuum ($n = 1$). The precise value of the index was determined by fitting the theory to the resonances of the largest particles (diameters about 20 nm) outside the quantum size regime. For comparison at smaller sizes, the full range of experimental EELS data was then overlaid, showing excellent agreement with the analytic quantum model. Both empirical values and calculations point to

quantum size effects beginning to appear at diameters below 10 nm, resulting in a strong blueshift of the LSPR peaks compared to classical Mie theory predictions (dashed line).

The increased variability in experimental resonance energies in this quantum size regime additionally matches the non-monotonic trend in theoretical absorption. In the model, these perturbations are caused by higher-order conduction electron transitions (from deeper within the Fermi sphere to immediately outside it). Although these resonances have a weaker influence on the permittivity than the lowest-order transitions that dominate in Fig. 4a, their effects can be more pronounced for particles of certain diameters: when the radius-dependent transition frequencies overlap the overall dipolar resonance condition of the particle in its environment (that is, $|\epsilon_{\text{particle}} + 2\epsilon_{\text{medium}}|$ is minimized), additional spectral resonance peaks may appear and result in apparent shifts in the LSPR. These higher-order transitions have an increasing role for smaller particles because their oscillator strengths are relatively greater than those of larger spheres.

Our analytic model provides a straightforward method of understanding changes in the metal permittivity as nanomaterials approach the quantum size regime. It remains a relatively coarse approximation, however, because three simplifying assumptions are necessary to make the model tractable. First, the wavefunctions and allowed energies are based on an infinite potential barrier model. In experimental systems that involve colloidal particles with stabilizing ligands, the barrier may behave in a more finite manner with spill-out effects¹⁴. The nanospheres used in this experiment, however, were synthesized without ligands to minimize this phenomenon. Second, the quantum model assumes an essentially spherical particle, which becomes increasingly difficult to synthesize at sizes below 1.5 nm when there are fewer than a hundred atoms. For this reason, we limit the present model and experimental study to particles larger than 1.5 nm in diameter. However, it should be noted that high-symmetry structures approximating spheres can be attained at certain 'magic number' collections of atoms even down to the smallest cluster sizes³⁹. Lastly, the model assumes that there is no interaction between the conduction electrons, a common assumption in many analytical quantum models. For a complete understanding of nanoparticle properties, *ab initio* techniques are required.

Comparing analytic and *ab initio* predictions

As a means of comparison, we have also used Ag permittivities derived from a rigorous DFT model employing a local density approximation³⁹ to calculate plasmon resonances. In ref. 39, the particle dielectric functions were generated through the analysis of

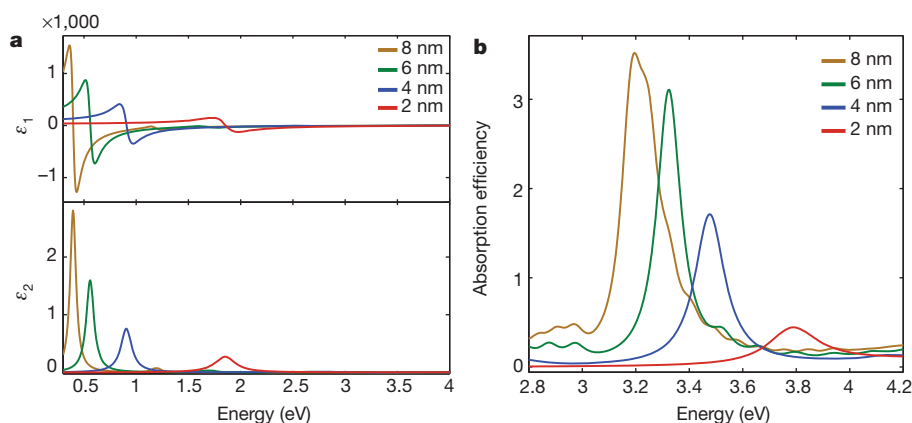


Figure 4 | Analytic quantum theory of particle permittivity and spectra. **a**, The real (ϵ_1) and imaginary (ϵ_2) components of the dielectric functions of silver nanoparticles with diameters of 2, 4, 6 and 8 nm, calculated using the analytic quantum model of equation (3). **b**, The corresponding absorption

spectra of the particles generated by Mie theory. The refractive index of the surrounding medium was set to 1.3. As particle size decreases, reduced absorption efficiencies and blueshifted surface plasmon peak energies are predicted.

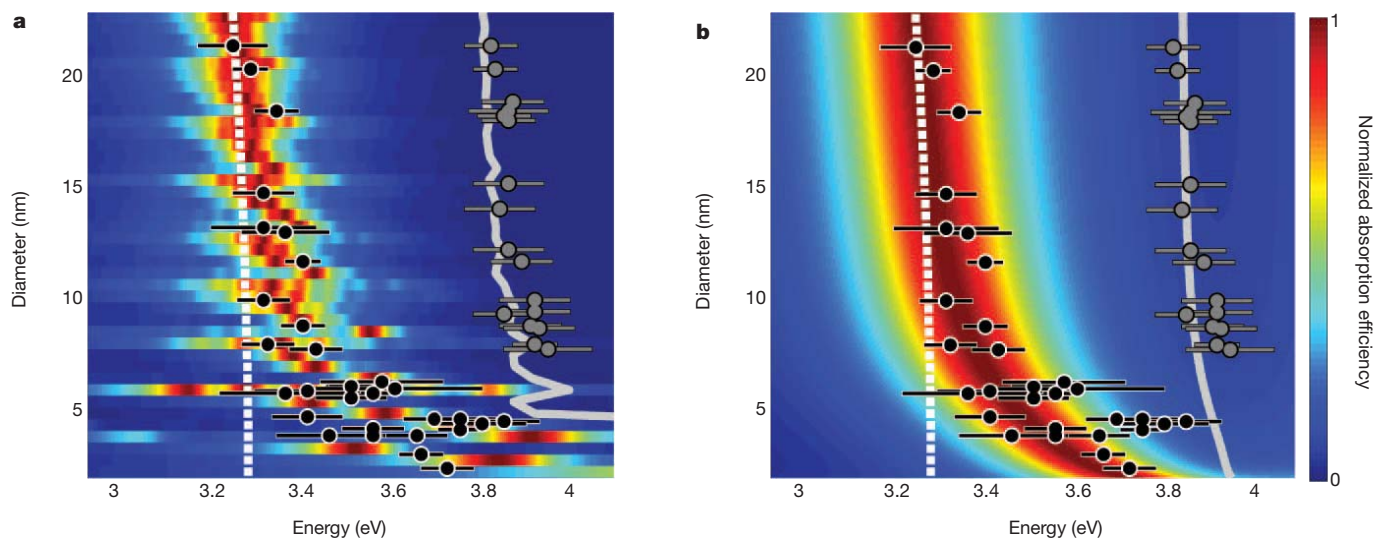


Figure 5 | Comparison of experimental data with quantum theory. Experimental, EELS-determined localized surface plasmon resonance energies of various Ag particle diameters are overlaid on the absorption spectra generated from the analytic quantum permittivity model (a) and the DFT-derived permittivity model (b). The experimental bulk resonance energies are

high-symmetry silver clusters spanning from Ag_{13} to Ag_{586} . Interband (d-band) and intraband (conduction) electron contributions were separated, and it was shown that interband effects on permittivity remain consistent with those seen in bulk while the particles exceed 2 nm in diameter, thus validating our use of a constant ϵ_{IB} term in the analytic model. In ref. 39, the intraband contributions to the DFT-calculated permittivities were smoothed by single Gaussians to fit the relevant Drude model parameters, including the plasma frequency ω_p , scattering frequency γ and a single resonance frequency ω_{if} . Given that particle sizes larger than Ag_{586} (diameter 2.7 nm) become increasingly computationally demanding using DFT techniques, the trends in these parameters were extrapolated to bridge the quantum to classically described size span.

Using this DFT permittivity model and inserting the values into Mie theory, we similarly generated the absorption efficiency spectra for comparison to our experimental EELS data, as seen in Fig. 5b. The empirical and DFT-derived resonances again exhibit excellent agreement, with blueshifts of 0.5 eV observed as the particle decreases below 10 nm in diameter. It is additionally worth noting that when only the lowest-order electron transitions are allowed in our quantum analytic approach, it presents a trend nearly identical to that seen in the DFT-derived model (see Supplementary Information).

Predictions of the bulk plasmonic resonance energies using the quantum analytic and DFT-derived permittivity data have also been calculated by monitoring the frequency of the metal-to-dielectric transition (where $\epsilon_1 = 0$). Note that this bulk frequency differs from the plasma frequency ω_p that is calculated by the simple Drude model, owing to the additional influence of the interband transitions on the permittivity.

The theory data for the bulk frequency, plotted as lines in Fig. 5a and b, shows strong consistency with the experimental values. Both show a blueshift for particles below 10 nm because the permittivity is altered by quantum size effects. We note that the predicted bulk resonance energy is greater than that of the corresponding surface resonance at all particle sizes throughout the modelled range. As the sphere diameter decreases, however, the LSPR frequency experiences a greater shift and the two peaks become harder to distinguish empirically. Additionally, with these smallest-sized particles, the relative surface-to-volume ratio greatly increases and the probability of bulk excitation decreases through a documented *begrenzung* effect^{32,34,37}. We therefore predict that the surface resonance peak will dominate the peak from the bulk.

also included (grey dots) along with the theory prediction (grey line). Classical Mie theory peak prediction is given by the dashed white line. The experimental data begin to deviate significantly from classical predictions for particle diameters smaller than 10 nm. Horizontal error bars represent 95% confidence intervals, as calculated through curve fitting and bootstrapping techniques.

Discussion

We have, for the first time, systematically observed and thoroughly analysed the plasmonic properties of individual silver nanospheres with sizes entering the quantum size regime. Using STEM EELS in an aberration-corrected electron microscope, we correlate the exact nanoparticle size and geometry with its spectra for colloidal synthesized particles devoid of the surface damping effects of ligands. A substantial blueshift in LSPR resonances is observed as particle size decreases, indicating a transition into the quantum-influenced regime. We develop an analytical quantum model to describe these resonances, which, despite its approximations and relative simplicity, agrees remarkably well with DFT methods. This straightforward theoretical framework can be directly applied to other metals with only the adjustment of the bulk material parameters γ_{bulk} , ω_p and ϵ_{IB} . Additional particle geometries such as rectangular prisms, cylinders and spherical shells can also be analysed through modification of the analytic quantum wavefunctions⁴⁸.

The combination of this versatile analytic model with direct plasmon observation in STEM EELS presents numerous opportunities for exploiting the plasmonic properties of quantum-sized particles. We anticipate a number of *in situ* STEM EELS experiments on both metallic and semiconducting plasmonic quantum dots⁵⁰. In particular, real-time EELS monitoring of quantum plasmon resonances may yield dynamic insight into multi-electron redox reactions catalysed by small metallic particles, such as in artificial photosynthesis. Moreover, these quantum plasmon resonances may enable novel quantum devices based on excitation and detection of single photons or plasmons. Ultimately, EELS of quantum plasmonic systems should facilitate new understanding of electronic-scale processes, powerfully complemented by the atomic-scale resolution of aberration-corrected TEM.

METHODS SUMMARY

Ligand-free silver nanospheres were synthesized according to a previously described technique³³. 5 ml of 1 mM AgNO_3 (>99% Alfa Aesar) were added dropwise over 3 min to 15 ml of 2 mM NaBH_4 (Fisher Scientific) that had been chilled in an ice bath. The sodium borohydride solution was stirred during the silver addition to ensure a homogeneous distribution.

Particles were dispersed on either ultrathin carbon or silicon dioxide suspended films. Spectra were collected by directing the electron beam onto the edge and centre of the particle, with ten acquisitions of 30 ms each to prevent saturation of the charge-coupled device (CCD) detector. These collections were aligned

according to their ZLP and summed in post-processing. To reduce the background from the dominant ZLP and improve the energy resolution, the Richardson–Lucy deconvolution algorithm was employed. The point spread function, which indicates the energy spread of the electron source and aberrations in the spectrometer and CCD, was estimated by the acquisition of ten aligned spectra from the nearby substrate alone.

ZLP subtraction can also be used to reveal the plasmon resonance and was accomplished through two different techniques. In the first, ‘reflected tail’ method, the negative tail of the ZLP was reflected about the 0-eV axis and subtracted from the positive side³¹. In the second method, the ZLP was fitted to the sum of a Gaussian and Lorentzian curve and subtracted from the spectra. We separately applied each ZLP-removal method, which yielded consistent results in the plasmonic spectra.

Confidence intervals for resonance peak energies were generated using a bootstrapping method in which a locally weighted scatterplot smoothing (LOWESS) algorithm was applied to the summed EELS data of each particle. Each curve-fitting relies on a randomly selected subset of the spectral data, producing slight variations in the calculated peak energy. Using 20 iterations of the algorithm, 95% confidence intervals could be generated.

Full Methods and any associated references are available in the online version of the paper at www.nature.com/nature.

Received 12 October 2011; accepted 26 January 2012.

- Willems, K. A. & Van Duyne, R. P. Localized surface plasmon resonance spectroscopy and sensing. *Annu. Rev. Phys. Chem.* **58**, 267–297 (2007).
- Juluri, B. K., Zheng, Y. B., Ahmed, D., Jensen, L. & Huang, T. J. Effects of geometry and composition on charge-induced plasmonic shifts in gold nanoparticles. *J. Phys. Chem. C* **112**, 7309–7317 (2008).
- Lal, S., Clare, S. E. & Halas, N. J. Nanoshell-enabled photothermal cancer therapy: impending clinical impact. *Acc. Chem. Res.* **41**, 1842–1851 (2008).
- Catchpole, K. R. & Polman, A. Design principles for particle plasmon enhanced solar cells. *Appl. Phys. Lett.* **93**, 191113 (2008).
- Bingham, J. M., Anker, J. N. & Kreno, L. E. Gas sensing with high-resolution localized surface plasmon resonance spectroscopy. *J. Am. Chem. Soc.* **132**, 17358–17359 (2010).
- Anker, J. N. *et al.* Biosensing with plasmonic nanosensors. *Nature Mater.* **7**, 442–453 (2008).
- Stiles, P. L., Dieringer, J. A., Shah, N. C. & Van Duyne, R. P. Surface-enhanced Raman spectroscopy. *Ann. Rev. Anal. Chem.* **1**, 601–626 (2008).
- Jeanmaire, D. L. & Van Duyne, R. P. Surface Raman spectroelectrochemistry. Part I. Heterocyclic, aromatic, and aliphatic amines adsorbed on the anodized silver electrode. *J. Electroanal. Chem. Interf. Electrochem.* **84**, 1–20 (1977).
- Larsson, E. M., Langhammer, C., Zorić, I. & Kasemo, B. Nanoplasmonic probes of catalytic reactions. *Science* **326**, 1091–1094 (2009).
- Liu, N., Tang, M. L., Hentschel, M., Giessen, H. & Alivisatos, A. P. Nanoantenna-enhanced gas sensing in a single tailored nanofocus. *Nature Mater.* **10**, 631–636 (2011).
- Novo, C., Funston, A. M. & Mulvaney, P. Direct observation of chemical reactions on single gold nanocrystals using surface plasmon spectroscopy. *Nature Nanotechnol.* **3**, 598–602 (2008).
- Link, S. & El-Sayed, M. A. Spectral properties and relaxation dynamics of surface plasmon electronic oscillations in gold and silver nanodots and nanorods. *J. Phys. Chem. B* **103**, 8410–8426 (1999).
- Bohren, C. F. & Huffman, D. R. *Absorption and Scattering of Light by Small Particles* (Wiley, 1983).
- Kreibig, U. & Vollmer, M. *Optical Properties of Metal Clusters* (Springer, 1995).
- Kreibig, U. & Genzel, L. Optical absorption of small metallic particles. *Surf. Sci.* **156**, 678–700 (1985).
- Genzel, L., Martin, T. P. & Kreibig, U. Dielectric function and plasma resonances of small metal particles. *Z. Phys. B* **21**, 339–346 (1975).
- Peng, S., McMahon, J. M., Schatz, G. C., Gray, S. K. & Sun, Y. Reversing the size-dependence of surface plasmon resonances. *Proc. Natl Acad. Sci. USA* **107**, 14530–14534 (2010).
- Lindfors, K., Kalkbrenner, T., Stoller, P. & Sandoghdar, V. Detection and spectroscopy of gold nanoparticles using supercontinuum white light confocal microscopy. *Phys. Rev. Lett.* **93**, 037401 (2004).
- Berciaud, S., Cognet, L., Tamarat, P. & Lounis, B. Observation of intrinsic size effects in the optical response of individual gold nanoparticles. *Nano Lett.* **5**, 515–518 (2005).
- Bakr, O. M. *et al.* Silver nanoparticles with broad multiband linear optical absorption. *Angew. Chem.* **48**, 5921–5926 (2009).
- Zhu, M., Aikens, C. M., Hollander, F. J., Schatz, G. C. & Jin, R. Correlating the crystal structure of a thiol-protected Au₂₅ cluster and optical properties. *J. Am. Chem. Soc.* **130**, 5883–5885 (2008).
- Sholl, D. S. & Steckel, J. A. *Density Functional Theory: A Practical Introduction* (Wiley-Interscience, 2009).
- Cognet, L. *et al.* Single metallic nanoparticle imaging for protein detection in cells. *Proc. Natl Acad. Sci. USA* **100**, 11350–11355 (2003).
- Hu, M. *et al.* Gold nanostructures: engineering their plasmonic properties for biomedical applications. *Chem. Soc. Rev.* **35**, 1084–1094 (2006).
- Jain, P. K., Huang, X., El-Sayed, I. H. & El-Sayed, M. A. Noble metals on the nanoscale: optical and photothermal properties and some applications in imaging, sensing, biology, and medicine. *Acc. Chem. Res.* **41**, 1578–1586 (2008).
- Sperling, R. A., Gil, P. R., Zhang, F., Zanella, M. & Parak, W. J. Biological applications of gold nanoparticles. *Chem. Soc. Rev.* **37**, 1896–1908 (2008).
- Templeton, A. C., Pietron, J. J., Murray, R. W. & Mulvaney, P. Solvent refractive index and core charge influences on the surface plasmon absorbance of alkanethiolate monolayer-protected gold clusters. *J. Phys. Chem. B* **104**, 564–570 (2000).
- Hirakawa, T. & Kamat, P. V. Charge separation and catalytic activity of Ag@TiO₂ core-shell composite clusters under UV-irradiation. *J. Am. Chem. Soc.* **127**, 3928–3934 (2005).
- Akimov, A. V. *et al.* Generation of single optical plasmons in metallic nanowires coupled to quantum dots. *Nature* **450**, 402–406 (2007).
- Qiyang, F., Batson, P. E. & Isaacson, M. Quantum size effects in the surface-plasmon excitation of small metallic particles by electron-energy-loss spectroscopy. *Phys. Rev. B* **46**, 15421–15425 (1992).
- Koh, A. L. *et al.* Electron energy-loss spectroscopy (EELS) of surface plasmons in single silver nanoparticles and dimers: influence of beam damage and mapping of dark modes. *ACS Nano* **3**, 3015–3022 (2009).
- Nelayah, J. *et al.* Mapping surface plasmons on a single metallic nanoparticle. *Nature Phys.* **3**, 348–353 (2007).
- Solomon, S. D. *et al.* Synthesis and study of silver nanoparticles. *J. Chem. Educ.* **84**, 322–325 (2007).
- Ritchie, R. H. Plasma losses by fast electrons in thin films. *Phys. Rev.* **106**, 874–881 (1957).
- Ferrell, T. L. & Echenique, P. M. Generation of surface excitations on dielectric spheres by an external electron beam. *Phys. Rev. Lett.* **55**, 1526–1529 (1985).
- García de Abajo, F. J. Optical excitations in electron microscopy. *Rev. Mod. Phys.* **82**, 209–275 (2010).
- Egerton, R. F. Electron energy-loss spectroscopy in the TEM. *Rep. Prog. Phys.* **72**, 016502 (2009).
- Gloter, A., Douiri, A., Tence, M. & Colliex, C. Improving energy resolution of EELS spectra: an alternative to the monochromator solution. *Ultramicroscopy* **96**, 385–400 (2003).
- He, Y. & Zeng, T. First-principles study and model of dielectric functions of silver nanoparticles. *J. Phys. Chem. C* **114**, 18023–18030 (2010).
- García de Abajo, F. J. Nonlocal effects in the plasmons of strongly interacting nanoparticles, dimers, and waveguides. *J. Phys. Chem. C* **112**, 17983–17987 (2008).
- McMahon, J. M., Gray, S. K. & Schatz, G. C. Nonlocal optical response of metal nanostructures with arbitrary shape. *Phys. Rev. Lett.* **103**, 097403 (2009).
- David, C. & García de Abajo, F. J. Spatial nonlocality in the optical response of metal nanoparticles. *J. Phys. Chem. C* **115**, 19470–19475 (2011).
- Mie, G. Beiträge zur optik trüber medien, speziell kolloidaler metallösungen. *Ann. Phys.* **330**, 377–445 (1908).
- Johnson, P. B. & Christy, R. W. Optical constants of the noble metals. *Phys. Rev. B* **6**, 4370–4379 (1972).
- Kreibig, U. & Frangstein, C. V. The limitation of electron mean free path in small silver particles. *Z. Phys.* **224**, 307–323 (1969).
- Alvarez, M. M. *et al.* Optical absorption spectra of nanocrystal gold molecules. *J. Phys. Chem. B* **101**, 3706–3712 (1997).
- Hövel, H., Fritz, S., Hilger, A., Kreibig, U. & Vollmer, M. Width of cluster plasmon resonances: bulk dielectric functions and chemical interface damping. *Phys. Rev. B* **48**, 18178–18188 (1993).
- Kraus, W. A. & Schatz, G. C. Plasmon resonance broadening in small metal particles. *J. Chem. Phys.* **79**, 6130–6139 (1983).
- Palik, E. D. *Handbook of Optical Constants of Solids* (Elsevier, 1998).
- Luther, J. M., Jain, P. K., Ewers, T. & Alivisatos, A. P. Localized surface plasmon resonances arising from free carriers in doped quantum dots. *Nature Mater.* **10**, 361–366 (2011).

Supplementary Information is linked to the online version of the paper at www.nature.com/nature.

Acknowledgements We thank S. Sheikholeslami, A. Atre, A. García-Etxarri and A. Baldi for discussions. This research was supported by the National Science Foundation Graduate Research Fellowship Program. J.A.D. acknowledges support from a Stanford Terman Fellowship and a Robert N. Noyce Family Faculty Fellowship.

Author Contributions J.A.S. performed the experiment, analysed the data, and developed the model. A.L.K. provided substantial assistance with the STEM EELS procedure. J.A.D. guided and supervised the experiments and analysis. All authors contributed to writing and editing the manuscript.

Author Information Reprints and permissions information is available at www.nature.com/reprints. The authors declare no competing financial interests. Readers are welcome to comment on the online version of this article at www.nature.com/nature. Correspondence and requests for materials should be addressed to J.A.D. (jdionne@stanford.edu) or J.A.S. (jscholl@stanford.edu).

METHODS

Chemicals and synthesis. Ligand-free silver nanospheres were synthesized according to a previously described technique³³. 5 ml of 1 mM AgNO₃ (>99% Alfa Aesar) were added drop-wise over 3 min to 15 ml of 2 mM NaBH₄ (Fisher Scientific) that had been chilled in an ice bath. Both solutions were prepared with Milli-Q deionized water (18 MΩ cm⁻¹). The sodium borohydride solution was stirred vigorously during the silver addition to ensure a homogeneous distribution. The metallic particles remained separated owing to the charge on the surrounding BH₄⁻ ions.

Electron energy-loss spectroscopy. The Ag nanospheres were dispersed on ultrathin (3 nm) carbon films (Ted Pella, Inc.) for optimal TEM imaging and minimal signal from the substrate. To control for any carbon background effects in the EELS data, the nanoparticles were also examined on 8-nm-thick SiO₂ substrates (Ted Pella, Inc.). Silver spheres on both support films exhibited nearly identical blueshifts with decreasing particle dimensions (see Supplementary Information).

A FEI Titan 80-300 environmental (scanning) transmission electron microscope was employed for particle imaging and EELS collection at 300 kV. EELS experiments were performed in scanning, monochromated mode, allowing an imaging resolution of 0.27 nm and a EELS zero-loss peak (ZLP) full-width at half-maximum of 0.15 eV. The Gatan Tridiem 866 spectrometer achieved a spectral dispersion of 0.01 eV per channel. A 50 μm C3 aperture, camera length of 48 mm, and a spectrometer entrance aperture of 2.5 mm were used during the data acquisition. This corresponds to a convergence semi-angle of 9.2 mrad and a collection semi-angle of 16.8 mrad.

Spectra were collected by directing the beam onto the edge and centre of the particle, with ten acquisitions of 30 ms each to prevent saturation of the charge-coupled device (CCD) detector. These collections were aligned according to their ZLP and summed in post-processing. To reduce the background from the dominant ZLP and improve the energy resolution, the Richardson–Lucy deconvolution algorithm was employed. The point spread function, which indicates the energy spread of the electron source and aberrations in the spectrometer and CCD, was estimated by the acquisition of ten aligned spectra from the nearby substrate alone. The deconvolution algorithm was iterated five times to maximize peak visibility while minimizing the introduction of artefacts.

A ZLP subtraction can also be used to reveal the plasmon resonance and was here accomplished through two different techniques. In the first, ‘reflected tail’ method, the negative tail of the ZLP was reflected about the 0-eV axis and subtracted from the positive side³¹. The second method involved fitting the ZLP to the sum of a Gaussian and Lorentzian curve and subtracting the fit from the spectra. We separately applied each ZLP-removal method on the collected EELS data, with all methods yielding consistent results in the plasmonic spectra.

Confidence intervals for resonance peak energies were generated using a bootstrapping method in which a locally weighted scatterplot smoothing (LOWESS) algorithm was applied to the summed energy loss spectra of each particle. Each curve fitting relies on a randomly selected subset of the spectral data, producing slight variations in the calculated peak energy. Using 20 iterations of the algorithm, 95% confidence intervals could be generated.

Suppression of the antiviral response by an influenza histone mimic

Ivan Marazzi¹, Jessica S. Y. Ho¹, Jaehoon Kim², Balaji Manicassamy^{3,4}, Scott Dewell⁵, Randy A. Albrecht^{3,4}, Chris W. Seibert³, Uwe Schaefer¹, Kate L. Jeffrey¹, Rab K. Prinjha⁶, Kevin Lee⁶, Adolfo García-Sastre^{3,4,7}, Robert G. Roeder² & Alexander Tarakhovskiy¹

Viral infection is commonly associated with virus-driven hijacking of host proteins. Here we describe a novel mechanism by which influenza virus affects host cells through the interaction of influenza non-structural protein 1 (NS1) with the infected cell epigenome. We show that the NS1 protein of influenza A H3N2 subtype possesses a histone-like sequence (histone mimic) that is used by the virus to target the human PAF1 transcription elongation complex (hPAF1C). We demonstrate that binding of NS1 to hPAF1C depends on the NS1 histone mimic and results in suppression of hPAF1C-mediated transcriptional elongation. Furthermore, human PAF1 has a crucial role in the antiviral response. Loss of hPAF1C binding by NS1 attenuates influenza infection, whereas hPAF1C deficiency reduces antiviral gene expression and renders cells more susceptible to viruses. We propose that the histone mimic in NS1 enables the influenza virus to affect inducible gene expression selectively, thus contributing to suppression of the antiviral response.

Histones are essential regulators of genome function in eukaryotic cells^{1,2}. The amino-terminal domain of histones (the histone tail) provides a scaffold for the assembly of protein complexes controlling gene activity³. This role of a histone tail is achieved largely by post-translational histone modifications, catalysed by distinct modifying enzymes⁴. The combination of diversely modified histone tails establishes gene-region-specific patterns that, upon recognition by histone-binding proteins, contribute to the regulation of gene replication⁵, repair⁶ and transcription⁷.

The ability of histone tails to guide gene function indicates the possibility of targeted control of gene expression by artificial or naturally occurring molecules that can structurally and/or functionally mimic the histone tail. The former possibility has been demonstrated by studies that show the ability of synthetic compounds to interfere with inducible gene expression by abolishing the interaction between the acetylated histone H4 and the BET family of transcriptional regulators^{8,9}. Histone binding to transcriptional regulators could also be interrupted by exogenous cell-permeable histone peptides^{10,11}. This approach underscores the possibility of a competition between endogenous and exogenous histone tails for the common binding partners. Indeed, the histone H3 tail-like sequence (histone mimic) within histone methyltransferase G9a can compete, in a modification-dependent fashion, for binding to the histone-bound heterochromatin protein 1 (HP1)¹². Overall, the 3–5-amino-acid-long sequences that match various parts of the histone tail can be found in numerous eukaryotic and prokaryotic proteins; however, the role of these presumptive histone mimics in the regulation of gene activity remains unknown.

Influenza virus NS1 carries a histone H3-like sequence

Pathogens have a known ability to interfere with vital processes in the host cells by mimicking regulatory components of host protein networks¹³. In searching for naturally occurring histone mimics with a gene regulatory capability, we screened *in silico* for pathogen-derived proteins that have

a known or predicted capacity to accumulate within the nuclei of infected cells, and bear a histone-tail-like unstructured domain at the amino or carboxy termini. One of these proteins was found to be the influenza A virus NS1 protein that suppresses host response to influenza virus¹⁴.

Depending on the viral subtype, NS1 is a 219–237-amino-acid-long protein¹⁴. NS1 is not essential for formation of the viral particle but is critical for counteracting the antiviral cell response^{14,15}. In the absence of NS1, influenza is greatly attenuated¹⁵. Suppression of antiviral host response by NS1 relies partly on the ability of NS1 to interfere with cytosolic signalling processes that regulate the expression of type I interferon genes^{16–19}. Additionally, the NS1 protein can affect host gene expression by interfering with RNA splicing and messenger RNA export^{20–23}.

We found that NS1 of influenza A (H3N2) virus carries a sequence that resembles the histone H3 tail. Similar to the histone tail, the C terminus of NS1 comprises a non-structured and potentially highly interactive domain^{24,25} (Fig. 1a). Although this unstructured C-terminal domain is present in most of the human influenza A variants (Fig. 1a), only NS1 from H3N2 subtype (hereafter defined as NS1) possesses the ARSK sequence (amino acids 226–229) that is chemically analogous to the ¹ARTK⁴ sequence that comprises the lysine 4 site (H3K4) of histone H3 (Fig. 1a). The similarity between histone H3 and NS1 tails is further strengthened by the ability of the NS1 tail to serve as a substrate for histone-modifying enzymes *in vitro*. Incubation of the NS1 tail peptide with lysine methyltransferase Set1 complex or Set7/9 in the presence of S-adenosylmethionine resulted in incorporation of the methyl mark into the peptide (Fig. 1b, upper panel). Accordingly, substitution of lysine 229 to arginine (K229R) prevented methylation. These results, as well as the ability of histone acetyltransferase TIP60—which acetylates histone H3 lysine 4 in yeast²⁶—to acetylate the NS1 peptide at K229 (Fig. 1b, upper panel), support the histone mimicry by NS1. The ability of the H3K4-like sequence within the NS1 tail to serve as a substrate

¹Laboratory of Immune Cell Epigenetics and Signaling, The Rockefeller University, 1230 York Avenue, New York, New York 10065, USA. ²Laboratory of Biochemistry and Molecular Biology, The Rockefeller University, 1230 York Avenue, New York, New York 10065, USA. ³Department of Microbiology, Mount Sinai School of Medicine, One Gustave L. Levy Place, Box 1124, New York, New York 10029, USA. ⁴Global Health and Infectious Pathogens Institute, Mount Sinai School of Medicine, One Gustave L. Levy Place, Box 1124, New York, New York 10029, USA. ⁵Genomics Resource Center, The Rockefeller University, 1230 York Avenue, New York, New York 10065, USA. ⁶Epinova DPU, Immuno-Inflammation Centre of Excellence for Drug Discovery, GlaxoSmithKline, Medicines Research Centre, Gunnels Wood Road, Stevenage SG1 2NY, UK. ⁷Department of Medicine, Division of Infectious Diseases, Mount Sinai School of Medicine, One Gustave L. Levy Place, Box 1124, New York, New York 10029, USA.

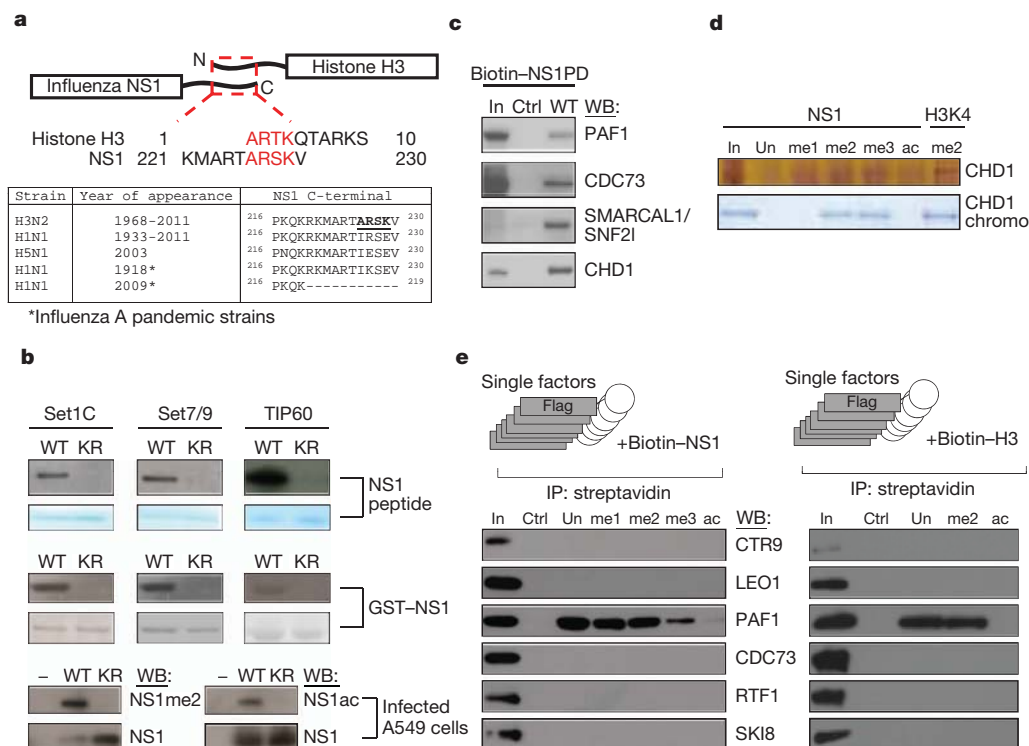


Figure 1 | Influenza NS1 contains a histone mimic. **a**, The homologous carboxy-terminal NS1 and the amino-terminal histone H3 sequences are shown (red letters). The table displays C-terminal NS1 sequences of the influenza A subtypes. **b**, Methylation or acetylation of the NS1 peptide (top panel), the GST-NS1 protein (middle panel) or of the viral NS1 in A549 infected cells (bottom panel) are shown. KR, NS1 substrates where K229 is replaced by arginine. **c**, Association of the NS1 histone mimic with the hPAF1C

subunits and CHD1 in nuclear extracts. In, input material. **d**, NS1 histone mimic binds to CHD1. Unmodified or methylated NS1 (K229) or methylated H3 (K4) peptides were incubated with the recombinant CHD1 or the CHD1 double-chromodomain. Binding to NS1 was revealed by silver or Coomassie staining (top and bottom panel, respectively). **e**, Binding of Flag-tagged hPAF1C subunits to NS1 or histone H3 peptides was assessed by western blotting (left and right panels, respectively). IP, immunoprecipitation.

for chosen histone-modifying enzymes has been further confirmed by using recombinant GST fusion NS1 protein (Fig. 1b, middle panel). Finally, the H3K4-like site within NS1 could be methylated or acetylated in virally infected cells. Using a custom-made antibody against dimethylated lysine 229 in NS1 (NS1me2; Supplementary Fig. 1), or acetyl-specific antibody²⁷, we found the presence of methylated and acetylated NS1 in infected human cells (Fig. 1b, lower panel). Point mutation of the NS1 gene that causes K229R substitution prevented modification (Fig. 1b, lower panel). It is likely that members of the H3K4 methyltransferase and acetyltransferase enzymes, that can modify NS1 *in vitro*, are responsible for NS1 modification *in vivo*. However, in view of the known redundancy between multiple H3K4 modifying complexes^{4,28–30}, identification of a sole NS1 modifying enzyme seems unlikely.

NS1 interacts with transcript-elongating proteins

Our experiments show the presence of a histone mimic within the NS1 tail. In histones, the unmodified or modified histone tail contributes to the assembly of chromatin protein complexes^{31–33}. The nature of the histone-tail-binding proteins is commonly revealed by the identification of nuclear proteins that bind to immobilized histone peptides during affinity purification³⁴. Using this approach (Supplementary Fig. 2), we searched for human nuclear proteins that bind to the NS1 tail peptide (amino acids 220–230). To control for the specificity of binding we used a scrambled peptide with an amino acid composition identical to NS1. Mass-spectrometry analysis of NS1-tail-bound proteins revealed the association of the NS1 tail with polypeptides that belong to the human PAF1 transcription elongation (hPAF1C) and CHD1 chromatin remodelling complexes (Supplementary Fig. 2). Binding of the NS1 tail to human PAF1, parafibromin (CDC73), SNF21 and CHD1 were validated by western blotting (Fig. 1c). In

support of the histone mimicry by the NS1 tail, we observed the histone-H3-like pattern of the NS1 tail binding to CHD1 *in vitro*. The chromodomain of human CHD1 binds specifically to di- or trimethylated lysine 4 of histone H3 (ref. 35). Similarly, the full-length CHD1 or the purified double-chromodomain binds selectively to di- or trimethylated NS1 peptide, but not to unmodified or acetylated NS1 tail (Fig. 1d).

To start assessing the role of the NS1 histone mimic in the regulation of chromatin complexes, we focused our attention on hPAF1C. We chose this on the basis of several factors. First, hPAF1C is a potent regulator of RNA elongation³⁶, a co-transcriptional process that contributes significantly to pathogen-induced gene expression^{11,37}. Second, PAF1C has been implicated in the regulation of stress-induced genes in yeast³⁸ that could be functionally equated to pathogen-induced genes in mammalian cells. Third, opposite to CHD1 that binds to the NS1 tail in a methyl-dependent fashion, purified hPAF1C binds to unmodified as well as modified NS1 tail (Supplementary Fig. 3a, left panel), thus making this interaction potentially more versatile. The interaction of hPAF1C with the NS1 tail is sequence-dependent. Neither NS1 tail of the H5N1 influenza virus, the scrambled NS1 peptide, nor the truncated NS1 tail that lacks the H3K4-like sequence were able to bind to hPAF1C (Supplementary Fig. 3b).

hPAF1C consists of six distinct subunits (PAF1, LEO1, CDC73 (also called parafibromin), SKI8 (also called WDR61), CTR9, RTF1) that have different roles in the interaction between hPAF1C and its binding partners, including RNA polymerase II (RNA Pol II)^{36,39,40}. To identify the primary NS1-tail-interacting hPAF1C subunit(s), we tested binding of the NS1 tail to purified recombinant individual hPAF1C subunits. We found that human PAF1 is the primary binder of the unmodified or methylated NS1 tail, but not the control peptide that lacks the histone mimic (Fig. 1e, left panel). PAF1 does not bind to

acetylated NS1 tail, thus pointing to a possible *in vivo* regulation of NS1 binding to PAF1 by a methyl/acetyl-switch mechanism. Finally, NS1 interacts with PAF1 *in vivo*. Immunoprecipitation of NS1 or PAF1 from infected cell extract revealed the existence of an NS1–PAF1 complex (Supplementary Fig. 3c). Our findings show that direct binding of the NS1 histone mimic to PAF1 is responsible for the association of NS1 with hPAF1C.

Interaction of hPAF1C with the NS1 histone mimic raised the possibility of hPAF1C binding to the histone H3 tail. Although the interaction of hPAF1C with RNA Pol II and other transcriptional regulators is well established^{36,39,40}, the direct association between hPAF1C and histone H3 has not been documented. We found that unmodified and methylated histone H3 tail peptides, but not the scrambled control peptide, bind to hPAF1C (Supplementary Fig. 3a, right panel) or to purified PAF1 protein (Fig. 1e, right panel). Similar to the NS1 histone mimic, the acetylated histone H3 tail did not bind to either hPAF1C components.

The ability of homologous tails of NS1 and histone H3 to interact directly with hPAF1C indicated a possibility of virus-mediated hijacking of the transcription elongation machinery from the host genes. We found that NS1 accumulates in the nuclei of the infected human cells (Supplementary Fig. 4a), where it reaches approximately 5×10^5 molecules per nucleus within 12 h after infection (Supplementary Fig. 4b). The salt-extraction profile of NS1 from nuclei of infected cells showed association of NS1 with chromatin (Supplementary Fig. 4c). To assess the position of NS1 on chromatin during viral infection, we generated a recombinant virus (Flag–NS1) that expresses Flag-tagged NS1 protein (Supplementary Fig. 5a, b). Genome-wide analysis of the Flag–NS1 binding at 12 h after infection revealed the presence of NS1 on induced antiviral gene promoters (Supplementary Tables 1 and 2).

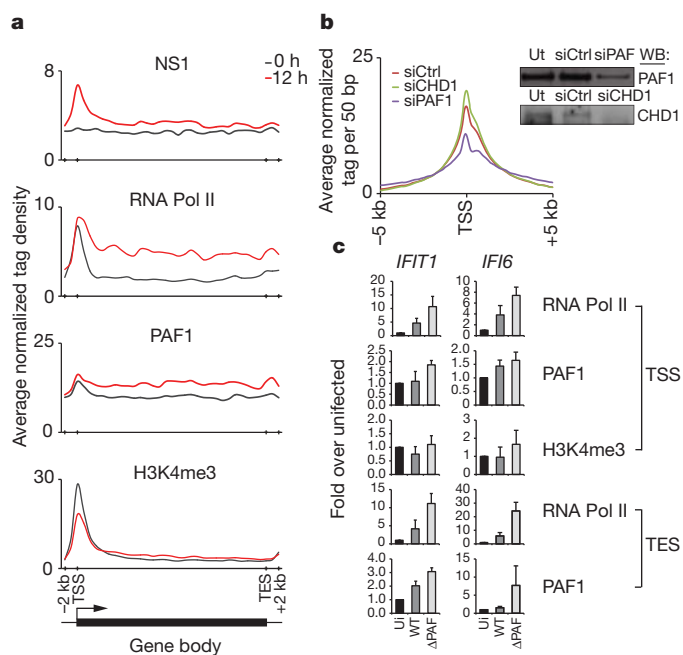


Figure 2 | Functional interaction between NS1 and PAF1 in infected cells. **a**, The ChIP-seq profiles show the distribution of indicated proteins at inducible genes before (black line) and after (red line) infection. The induced genes were revealed by RNA-seq and ChIP-seq analysis of infected A549 cells (Supplementary Tables 1 and 2). TSS and TES, the transcriptional start and end sites, respectively. **b**, The NS1 levels at gene promoters in PAF1- or CHD1-deficient cells (blue and green lines, respectively). The scrambled siRNA-treated cells (red line) were used as control. The insert shows knockdown of PAF1 or CHD1 in A549 cells. **c**, PAF1, RNA Pol II and H3K4me3 levels at the TSS and TES of the induced genes in uninfected (ui) cells, cells infected with the wild-type (WT) or PAF1-binding mutant virus (Δ PAF). Data are representative of three independent experiments; error bars show the s.e.m.

In infected cells, NS1 is enriched at promoters characterized by the presence of H3K4me3 and RNA Pol II (Fig. 2a). The pattern of NS1 distribution on its targets parallels the distribution of hPAF1C (Fig. 2a). Collectively, these data revealed a strategic position of NS1 at sites of active antiviral gene transcription.

NS1 histone mimic controls antiviral gene expression

The interaction between the NS1 tail and hPAF1C has two complementary functions that may support viral infection. The virus probably uses the NS1–hPAF1C interaction to target sites of active transcription. The short interfering RNA (siRNA)-mediated PAF1 deficiency resulted in 30% reduction of NS1 levels at the transcriptional start sites of the NS1-bound genes in infected cells (Fig. 2b). The specific role of PAF1 in recruitment of NS1 was supported by unaltered NS1 binding to its gene targets in cells treated with CHD1-specific siRNA (Fig. 2b). These findings revealed a previously unknown ability of the influenza virus to use host PAF1 to position viral NS1 protein at sites of active gene transcription.

Once targeted to transcriptionally active loci, as defined by RNA Pol II levels cross-referenced to the infected cell transcriptome (Supplementary Tables 1 and 2), NS1 interferes with PAF1 and RNA Pol II abundance at target genes. As exemplified by virus-induced *IFIT1* and *IFI6* genes, infection with the wild-type influenza virus resulted in decreased PAF1 and RNA Pol II levels at the transcriptional end sites (TES) and to a lesser extent at the transcriptional start sites (TSS) of the genes, as compared with PAF1-binding mutant virus (Δ PAF) (Fig. 2c). This pattern of PAF1, RNA Pol II and H3K4me3 distribution is indicative of impaired transcriptional elongation.

To determine the impact of the NS1 tail on the dynamics of antiviral gene transcription, we conducted a genome-wide nuclear ‘run-on’ analysis (global run-on sequencing, GRO-seq)⁴¹ of cells infected with the wild-type or mutant viruses that cannot bind to human PAF1 (Δ PAF). In the absence of infection, we observed accumulation of RNA species that map to the TSS of antiviral genes and low levels of RNAs that map to the gene body (Fig. 3a). Accumulation of TSS-associated short RNAs is a common feature of rapidly inducible genes that maintain a paused/poised state in the absence of an inducer⁴¹.

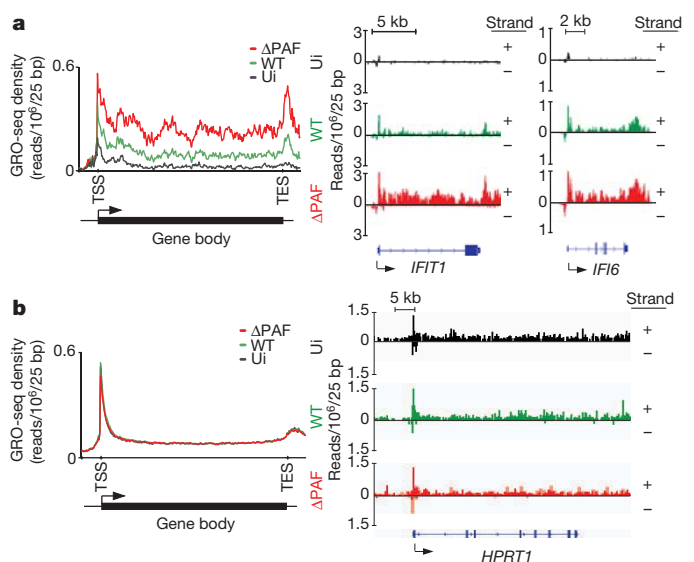


Figure 3 | NS1 suppresses antiviral gene transcription in infected cells. **a**, Left: the GRO-seq profile of inducible RNA transcripts in uninfected (ui) A549 cells (black line) or cells infected with wild-type or Δ PAF virus (green and red lines, respectively). Right: GRO-seq profile of *IFIT1* and *IFI6* genes in uninfected and infected cells. **b**, GRO-seq profile of A549-expressed genes that are not affected by virus infection (left panel) or of the *HPRT1* gene (right panel). Reads from either DNA strands are indicated as +/–. The y axes display reads per million mapped reads per 25 bp.

Infection with the Δ PAF virus resulted in a marked increase in levels of RNA transcripts that map to the TSS as well as to the downstream gene region. The high abundance of transcripts associated within the gene body is indicative of effective RNA elongation, which has an essential role in regulation of the pathogen-driven host response^{11,37}. Compared to cells infected with Δ PAF virus, the cells infected with wild-type virus displayed slightly reduced levels of TSS-associated RNAs but greatly diminished levels of transcripts associated with the gene body and 3' end region (Fig. 3a). This pattern is indicative of impaired transcriptional elongation and is consistent with defective elongation in other experimental settings^{42,43}. The differences between the impact of Δ PAF and wild-type viruses on the global dynamics of antiviral gene transcription are exemplified by differences in transcription of selected antiviral genes (Fig. 3a, right panel). Infection with either wild-type or Δ PAF virus has no effect on transcriptional dynamics of housekeeping genes and genes not affected by viral infection (Fig. 3b).

The ability of NS1 to control directly hPAF1C-dependent transcriptional elongation was further supported by the analysis of the impact of the NS1 tail on hPAF1C-driven RNA elongation *in vitro*. In this assay, a chromatinized DNA template, supplemented with selected transcription factors and histone-modifying enzymes, supports hPAF1C-mediated transcription in a fashion that faithfully reproduces transcriptional elongation *in vivo*³⁶ (Fig. 4a). We found that NS1 has a negative impact on hPAF1C function (Fig. 4b). The comparison between the amount of *in vitro* synthesized RNA in the absence or presence of hPAF1C shows the ability of hPAF1C to boost RNA synthesis (Fig. 4b). Addition of purified NS1 (Supplementary Fig. 5c) to the transcription reaction reduced the amount of synthesized RNA to background levels (Fig. 4b). Addition of purified NS1 that lacks the PAF1-binding sequence had no effect on RNA synthesis (Fig. 4b). Both wild-type NS1 and NS1 that lacks the PAF1 binding sequence have no impact on transcription of non-chromatinized template *in vitro* (Supplementary Fig. 6). This selective and direct impact of NS1 on virus-induced gene expression has been further supported by a lack of NS1 requirement for the association between the viral and the host RNA polymerases in infected cells^{44,45} (Supplementary Fig. 7).

Our findings provide unambiguous proof for the ability of the NS1 tail to interfere directly with hPAF1C-driven transcription of antiviral genes.

hPAF1C controls antiviral gene expression and infection

The significance of NS1–hPAF1C interaction during infection was evaluated by two independent experimental approaches. Deletion of the hPAF1C binding sequence in NS1 resulted in reduced viral titres of the Δ PAF virus as compared to those of the virus carrying full-length NS1 (Supplementary Fig. 8). This finding is in agreement with the previously reported positive role of the NS1 carboxy terminus in influenza A virulence⁴⁶.

We also revealed the central role of hPAF1C in transcriptional response induced by various viruses, as well as by the viral RNA analogue poly(I:C) and type I interferon. To study the impact of PAF1 on influenza-induced antiviral gene expression we used the

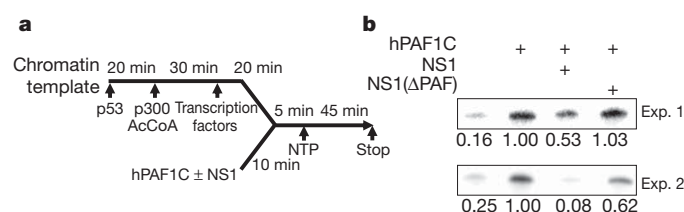


Figure 4 | NS1 inhibits transcriptional elongation *in vitro*. **a**, The full-length NS1 protein (NS1) or NS1 lacking the PAF1-binding sequence (NS1(Δ PAF)) (Supplementary Fig. 5c) was added to the RNA elongation reaction as indicated. **b**, The amount of the 390-nt RNA elongation product was quantified by ImageJ. The results of two independent experiments are shown.

NS1-deficient influenza virus (PR8/ Δ NS1) that elicits an extremely potent antiviral response and is therefore particularly useful to study host factors that regulate the antiviral response^{14,15}. Infection with PR8/ Δ NS1 of control siRNA-treated cells resulted in a strong upregulation of numerous antiviral genes (Fig. 5a). This response was reduced in PAF1-deficient cells (Fig. 5a, Supplementary Fig. 9, left panel, and Supplementary Table 3). The negative effect of PAF1 deficiency on antiviral response is not a consequence of impaired virus life-cycle caused by a reduction in viral gene expression (Supplementary Fig. 10).

PAF1 deficiency also attenuated the transcriptional response to wild-type influenza A H1N1 (Supplementary Fig. 11, left panel). The general positive role of PAF1 in antiviral gene expression was underscored by reduced expression of antiviral genes in PAF1-deficient cells infected with vesicular stomatitis virus (VSV) as well as cells treated with poly(I:C) (Supplementary Fig. 11 and Supplementary Tables 4–6). PAF1 deficiency also downregulates the transcriptional response to type I interferon that governs the antiviral immunity (Fig. 5b, Supplementary Fig. 9, right panel and Supplementary Table 7). The impaired antiviral response by PAF1-deficient cells contributes to a nearly tenfold increase of NS1-deficient PR8/ Δ NS1 virus replication,

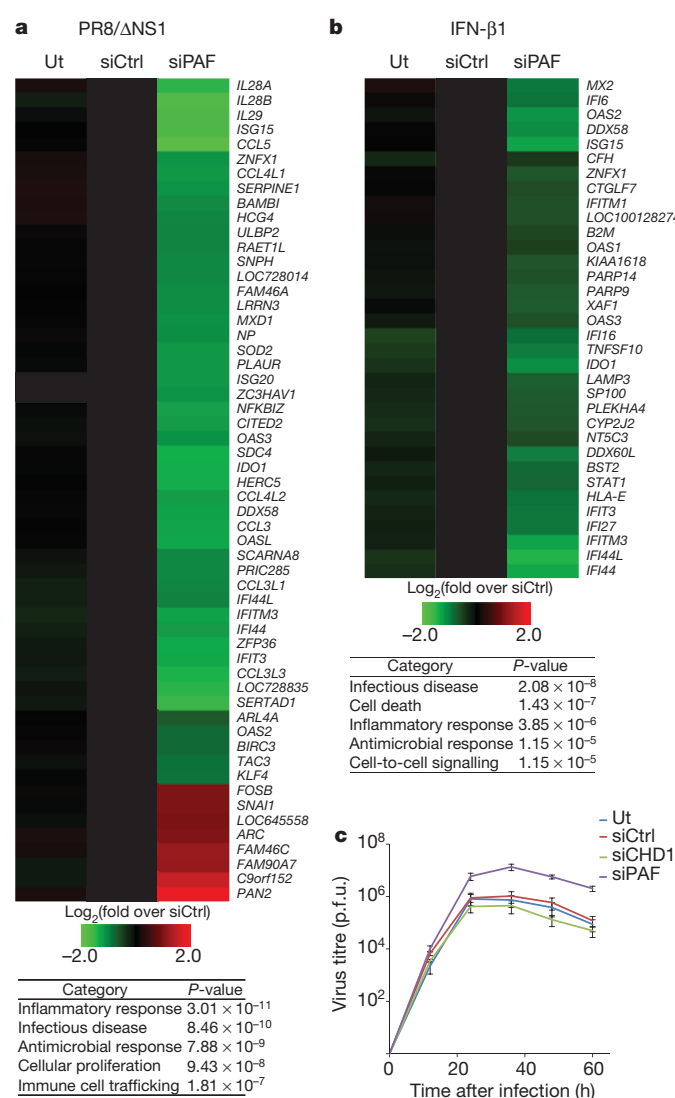


Figure 5 | PAF1 controls antiviral response. **a**, **b**, The expression levels of mRNAs in influenza infected (**a**) or IFN- β 1-treated (**b**) control (siCtrl) or PAF1-deficient (siPAF) A549 cells. The tables show the siPAF-affected gene categories. Ut, untreated with siRNA. **c**, Dynamics of virus replication in control or PAF1-deficient A549 cells. p.f.u. plaque-forming units. Data are representative of three independent experiments. Error bars show the s.e.m.

as compared to infected control cells (Fig. 5c). The impact of PAF1 deficiency on antiviral gene expression is selective. PAF1 deficiency does not alter the expression of housekeeping genes (Supplementary Fig. 12 and Supplementary Table 8).

Concluding remarks

We have shown that H3N2 influenza A virus interferes with host gene expression by exploiting the very basic principles of the epigenetic control of gene regulation. By mimicking the histone H3K4 sequence, which has a key role in positive regulation of gene transcription, the influenza virus gains access to histone-interacting transcriptional regulators that govern inducible antiviral gene expression. The histone-like unstructured NS1 tails are present in the majority of human influenza A isolates, but their primary sequence differs between viruses. The presence of potentially reactive amino acid residues within the unstructured NS1 tails and the nuclear localization of NS1 predict a multitude of nuclear proteins interacting with influenza NS1 in a sequence- and/or modification-specific fashion. In extension of the histone code that has provided a conceptual framework for understanding chromatin-based gene regulation^{47–49}, we propose the existence of the ‘NS1 code’ that guides influenza virus interference with host chromatin. The interference with chromatin function may complement other immunosuppressive functions of NS1 and provide the influenza virus with an opportunity to affect host gene expression in a highly selective fashion by recognizing and using epigenetic patterns of the host cells. This mechanism may contribute to the influenza-variant-specific pathogenesis and disease progression that differ between viruses carrying the histone-like NS1 tail and those viruses, such as human H1N1 (including pandemic 2009 virus), that lack the NS1 tail⁵⁰. It is possible that by targeting the actively transcribed antiviral genes, the NS1 tail helps influenza to balance its virulence against the preservation of the infected cell function. Such a mechanism could help the virus to maintain its long-term presence within the human population. Our findings could also be applied to the development of novel anti-influenza therapies that will interfere in a highly selective fashion with the NS1 tail binding to its chromatin partners. Finally, identification of hPAF1C as a key mediator of antiviral and pro-inflammatory gene response may pave the way for the development of anti-inflammatory therapies that—similar to the recently described ‘epigenetic’ therapies^{8,9}—will interfere selectively with hPAF1C binding to its partners.

METHODS SUMMARY

The methylation and acetylation *in vitro* has been performed as described previously^{12,26}. The analysis of NS1 methylation or acetylation *in vivo* has been done by using custom-made methyl-specific or commercial acetyl-specific antibodies²⁷. Isolation of the NS1 binding proteins, their analysis by mass-spectrometry and western blotting were performed according to a protocol used to identify histone-bound proteins³⁴. The recombinant hPAF1C and its individual components were prepared as described before³⁶. Interaction between hPAF1C and its individual components with peptides were performed as reported^{32,33}. The transcriptional assays have been performed as described³⁶. Genome-wide distribution of NS1 and other chromatin-bound proteins were accessed by ChIP-sequencing as previously described⁹, and analysed using standard bioinformatic approaches. Recombinant influenza viruses were generated using standard reverse genetics approaches^{15,17}. Infection of cells with viruses was performed according to the standard methods^{17,46} and viral titres were quantified by plaque assay. Gene expression analysis has been done by microarray using Illumina Human HT-12 v4 Expression BeadChips or by RNA-sequencing and verified by quantitative real-time PCR⁹. GRO-sequencing was performed as described⁴¹. All methodological details are additionally outlined in Supplementary Information.

Received 7 September 2011; accepted 23 January 2012.

Published online 14 March 2012.

- Kornberg, R. D. & Thomas, J. O. Chromatin structure—oligomers of histones. *Science* **184**, 865–868 (1974).
- Campos, E. I. & Reinberg, D. Histones: annotating chromatin. *Ann. Rev. Genet.* **43**, 559–599 (2009).

- Taverna, S. D., Li, H., Ruthenburg, A. J., Allis, C. D. & Patel, D. J. How chromatin-binding modules interpret histone modifications: lessons from professional pocket pickers. *Nature Struct. Mol. Biol.* **14**, 1025–1040 (2007).
- Kouzarides, T. Chromatin modifications and their function. *Cell* **128**, 693–705 (2007).
- Kelly, A. E. *et al.* Survivin reads phosphorylated histone H3 threonine 3 to activate the mitotic kinase Aurora B. *Science* **330**, 235–239 (2010).
- Fernandez-Capetillo, O. *et al.* DNA damage-induced G2-M checkpoint activation by histone H2AX and 53BP1. *Nature Cell Biol.* **4**, 993–997 (2002).
- Li, B., Carey, M. & Workman, J. L. The role of chromatin during transcription. *Cell* **128**, 707–719 (2007).
- Filippakopoulos, P. *et al.* Selective inhibition of BET bromodomains. *Nature* **468**, 1067–1073 (2010).
- Nicodemus, E. *et al.* Suppression of inflammation by a synthetic histone mimic. *Nature* **468**, 1119–1123 (2010).
- Nishiyama, A. *et al.* Intracellular delivery of acetyl-histone peptides inhibits native bromodomain-chromatin interactions and impairs mitotic progression. *FEBS Lett.* **582**, 1501–1507 (2008).
- Hargreaves, D. C., Horng, T. & Medzhitov, R. Control of inducible gene expression by signal-dependent transcriptional elongation. *Cell* **138**, 129–145 (2009).
- Sampath, S. C. *et al.* Methylation of a histone mimic within the histone methyltransferase G9a regulates protein complex assembly. *Mol. Cell* **27**, 596–608 (2007).
- Elde, N. C. & Malik, H. S. The evolutionary conundrum of pathogen mimicry. *Nature Rev. Microbiol.* **7**, 787–797 (2009).
- Hale, B. G., Randall, R. E., Ortin, J. & Jackson, D. The multifunctional NS1 protein of influenza A viruses. *J. Gen. Virol.* **89**, 2359–2376 (2008).
- Garcia-Sastre, A. *et al.* Influenza A virus lacking the NS1 gene replicates in interferon-deficient systems. *Virology* **252**, 324–330 (1998).
- Lu, Y., Wambach, M., Katze, M. G. & Krug, R. M. Binding of the influenza-virus NS1 protein to double-stranded-RNA inhibits the activation of the protein-kinase that phosphorylates the Elf-2 translation initiation-factor. *Virology* **214**, 222–228 (1995).
- Gack, M. U. *et al.* Influenza A Virus NS1 targets the ubiquitin ligase TRIM25 to evade recognition by the host viral RNA sensor RIG-I. *Cell Host Microbe* **5**, 439–449 (2009).
- Pichlmair, A. *et al.* RIG-I-mediated antiviral responses to single-stranded RNA bearing 5'-phosphates. *Science* **314**, 997–1001 (2006).
- Hale, B. G., Jackson, D., Chen, Y. H., Lamb, R. A. & Randall, R. E. Influenza A virus NS1 protein binds p85b and activates phosphatidylinositol-3-kinase signaling. *Proc. Natl Acad. Sci. USA* **103**, 14194–14199 (2006).
- Krug, R. M., Yuan, W. M., Noah, D. L. & Latham, A. G. Intracellular warfare between human influenza viruses and human cells: the roles of the viral NS1 protein. *Virology* **309**, 181–189 (2003).
- Nemeroff, M. E., Barabino, S. M. L., Li, Y. Z., Keller, W. & Krug, R. M. Influenza virus NS1 protein interacts with the cellular 30 kDa subunit of CPSF and inhibits 3' end formation of cellular pre-mRNAs. *Mol. Cell* **1**, 991–1000 (1998).
- Das, K. *et al.* Structural basis for suppression of a host antiviral response by influenza A virus. *Proc. Natl Acad. Sci. USA* **105**, 13093–13098 (2008).
- Satterly, N. *et al.* Influenza virus targets the mRNA export machinery and the nuclear pore complex. *Proc. Natl Acad. Sci. USA* **104**, 1853–1858 (2007).
- Luger, K., Mader, A. W., Richmond, R. K., Sargent, D. F. & Richmond, T. J. Crystal structure of the nucleosome core particle at 2.8 Å resolution. *Nature* **389**, 251–260 (1997).
- Hale, B. G., Barclay, W. S., Randall, R. E. & Russell, R. J. Structure of an avian influenza A virus NS1 protein effector domain. *Virology* **378**, 1–5 (2008).
- Khemalce, B. & Kouzarides, T. A chromodomain switch mediated by histone H3 Lys 4 acetylation regulates heterochromatin assembly. *Genes Dev.* **24**, 647–652 (2010).
- Becker, P. B. *et al.* Site-specific acetylation of ISWI by GCN5. *BMC Mol. Biol.* **8** (2007).
- Ruthenburg, A. J., Allis, C. D. & Wysocka, J. Methylation of lysine 4 on histone H3: intricacy of writing and reading a single epigenetic mark. *Mol. Cell* **25**, 15–30 (2007).
- Wang, P. F. *et al.* Global analysis of H3K4 methylation defines MLL family member targets and points to a role for MLL1-mediated H3K4 methylation in the regulation of transcriptional initiation by RNA polymerase II. *Mol. Cell Biol.* **29**, 6074–6085 (2009).
- Guillemette, B. *et al.* H3 lysine 4 is acetylated at active gene promoters and is regulated by H3 lysine 4 methylation. *PLoS Genet.* **7** (2011).
- Lachner, M., O'Carroll, N., Rea, S., Mechtler, K. & Jenuwein, T. Methylation of histone H3 lysine 9 creates a binding site for HP1 proteins. *Nature* **410**, 116–120 (2001).
- Shi, X. B. *et al.* ING2 PHD domain links histone H3 lysine 4 methylation to active gene repression. *Nature* **442**, 96–99 (2006).
- Lan, F. *et al.* Recognition of unmethylated histone H3 lysine 4 links BHC80 to LSD1-mediated gene repression. *Nature* **448**, 718–722 (2007).
- Wysocka, J. Identifying novel proteins recognizing histone modifications using peptide pull-down assay. *Methods* **40**, 339–343 (2006).
- Sims, R. J. *et al.* Human but not yeast CHD1 binds directly and selectively to histone H3 methylated at lysine 4 via its tandem chromodomains. *J. Biol. Chem.* **280**, 41789–41792 (2005).
- Kim, J., Guermah, M. & Roeder, R. G. The human PAF1 complex acts in chromatin transcription elongation both independently and cooperatively with SII/TFIIS. *Cell* **140**, 491–503 (2010).
- Ramirez-Carrozzi, V. R. *et al.* A unifying model for the selective regulation of inducible transcription by CpG islands and nucleosome remodeling. *Cell* **138**, 114–128 (2009).

38. Kim, K. Y. & Levin, D. E. Mpk1 MAPK association with the Paf1 complex blocks Sen1-mediated premature transcription termination. *Cell* **144**, 745–756 (2011).
39. Chen, Y. X. *et al.* DSIF, the Paf1 complex, and Tat-SF1 have nonredundant, cooperative roles in RNA polymerase II elongation. *Genes Dev.* **23**, 2765–2777 (2009).
40. Jaehning, J. A. The Paf1 complex: platform or player in RNA polymerase II transcription? *Biochim. Biophys. Acta* **1799**, 379–388 (2010).
41. Core, L. J., Waterfall, J. J. & Lis, J. T. Nascent RNA sequencing reveals widespread pausing and divergent initiation at human promoters. *Science* **322**, 1845–1848 (2008).
42. Min, I. M. *et al.* Regulating RNA polymerase pausing and transcription elongation in embryonic stem cells. *Gene Dev.* **25**, 742–754 (2011).
43. Mapendano, C. K., Lykke-Andersen, S., Kjems, J., Bertrand, E. & Jensen, T. H. Crosstalk between mRNA 3' end processing and transcription initiation. *Mol. Cell* **40**, 410–422 (2010).
44. Loucaides, E. M. *et al.* Nuclear dynamics of influenza A virus ribonucleoproteins revealed by live-cell imaging studies. *Virology* **394**, 154–163 (2009).
45. Engelhardt, O. G., Smith, M. & Fodor, E. Association of the influenza A virus RNA-dependent RNA polymerase with cellular RNA polymerase II. *J. Virol.* **79**, 5812–5818 (2005).
46. Jackson, D., Hossain, M. J., Hickman, D., Perez, D. R. & Lamb, R. A. A new influenza virus virulence determinant: The NS1 protein four C-terminal residues modulate pathogenicity. *Proc. Natl Acad. Sci. USA* **105**, 4381–4386 (2008).
47. Strahl, B. D. & Allis, C. D. The language of covalent histone modifications. *Nature* **403**, 41–45 (2000).
48. Turner, B. M. Histone acetylation and an epigenetic code. *Bioessays* **22**, 836–845 (2000).
49. Jenuwein, T. & Allis, C. D. Translating the histone code. *Science* **293**, 1074–1080 (2001).
50. Yang, Y. *et al.* The transmissibility and control of pandemic influenza A (H1N1) virus. *Science* **326**, 729–733 (2009).

Supplementary Information is linked to the online version of the paper at www.nature.com/nature.

Acknowledgements We thank P. deGross and A. Rudensky for the mass spectroscopy analysis of the NS1 binding proteins. A. Rojas Soto, D. Reinberg, M. Dobenecker and T. Zhanyun provided us with recombinant CHD1 (A.R.S., D.R.), recombinant Set7/9 (M.D.) and Set1C (T.Z.). F. Casadio, P. Lewis, O. Binda, O. Gozani, N. Levenkova, A. Mele, R. Darnell, L. Core, J. Lis and P. Palese gave us valuable technical advice and help with data analysis. We acknowledge the Rockefeller University Genomics Resource Center for technical support. We thank R. Cadagan, A. Santana, W. Huang, R. Chandramouli and H. Zebrowsky for technical assistance, R. Rizzo for help with manuscript preparation and C. Nathan for discussion. L.M.K. for artwork. B.M. is supported by NIH/NIAID K99 Pathway to Independence award (1K99AI095320-01). A.G.-S. is partially supported by NIAID grants R01AI046954, U19AI083025 and by CRIP (Center for Research in Influenza Pathogenesis), an NIAID funded Center of Excellence for Influenza Research and Surveillance, HHSN266200700010C. R.G.R. is supported by NIH grant CA129325. J.K. is supported by Charles H. Revson Foundation. I.M. is supported by American Italian Cancer Foundation. J.H. is supported by the Agency for Science, Technology and Research (A*STAR), Singapore. A.T. is supported by the NIH grant R01AI068058 and by Starr Cancer Consortium.

Author Contributions I.M. contributed to design, execution, analysis of the experiments and manuscript preparation. J.S.Y.H. studied the role of PAF1 in viral infection and assisted in manuscript preparation. J.K. and R.R. studied the impact of NS1 on hPAF1C and transcriptional elongation. B.M., R.A.A. engineered the recombinant influenza viruses and studied viral infectivity. U.S. was involved in gene expression studies. S.D. performed bioinformatic analysis. C.W.S. generated antibody against viral polymerase. K.L.J. gave technical assistance. R.K.P. and K.L. contributed to manuscript preparation and enabled ChIP-seq and RNA-seq. A.G.-S. supervised and discussed the work with infectious influenza viruses. A.T. conceived and supervised this study and wrote the final manuscript.

Author Information Reprints and permissions information is available at www.nature.com/reprints. The authors declare competing financial interests: details accompany the full-text HTML version of the paper at www.nature.com/nature. Readers are welcome to comment on the online version of this article at www.nature.com/nature. Correspondence and requests for materials should be addressed to I.M. (imarazzi@rockefeller.edu) or A.T. (tarakho@rockefeller.edu).

Intrinsic coupling of lagging-strand synthesis to chromatin assembly

Duncan J. Smith¹ & Iestyn Whitehouse¹

Fifty per cent of the genome is discontinuously replicated on the lagging strand as Okazaki fragments. Eukaryotic Okazaki fragments remain poorly characterized and, because nucleosomes are rapidly deposited on nascent DNA, Okazaki fragment processing and nucleosome assembly potentially affect one another. Here we show that ligation-competent Okazaki fragments in *Saccharomyces cerevisiae* are sized according to the nucleosome repeat. Using deep sequencing, we demonstrate that ligation junctions preferentially occur near nucleosome midpoints rather than in internucleosomal linker regions. Disrupting chromatin assembly or lagging-strand polymerase processivity affects both the size and the distribution of Okazaki fragments, suggesting a role for nascent chromatin, assembled immediately after the passage of the replication fork, in the termination of Okazaki fragment synthesis. Our studies represent the first high-resolution analysis—to our knowledge—of eukaryotic Okazaki fragments *in vivo*, and reveal the interconnection between lagging-strand synthesis and chromatin assembly.

During eukaryotic chromosome replication, both genetic and epigenetic information must be accurately duplicated. For chromatin architecture and modifications to be truly epigenetic—that is, heritable despite not being genetically encoded—complete disruption and dissociation of nucleosomes from the replication fork must be prevented to allow the rapid re-deposition of precisely located and appropriately modified histones on the nascent DNA. Histone chaperone complexes govern both nucleosome disassembly and assembly at the replication fork¹.

DNA replication is inherently asymmetric. Okazaki fragment synthesis on the lagging strand necessitates the repeated production of single-stranded DNA and polymerization in the opposite direction to fork progression. Given the delay in lagging-strand synthesis and the rapidity of histone deposition behind the replication fork², these two processes may be interlinked. A coordinated series of events occurs each time an Okazaki fragment is synthesized³. Each fragment is initiated via an RNA primer⁴ and up to 30 nucleotides of DNA, both synthesized by DNA polymerase α (Pol α)-primase⁵; subsequently, the clamp loading factor RFC mediates the replacement of Pol α by the sliding clamp PCNA and the processive polymerase Pol δ (ref. 6). Pol δ extends the nascent DNA chain through the 5' end of the preceding Okazaki fragment^{7,8}; this strand-displacement synthesis generates a 5' RNA or DNA flap that is cleaved by nucleases such as the flap endonuclease Fen1 (ref. 9). Repeated cycles of extension and DNA cleavage followed by Pol δ idling¹⁰ produce a nick that migrates away from the replication fork and can be sealed by DNA ligase I¹¹. Little to no DNA synthesized by the error-prone Pol α remains in the genome after replication¹², suggesting that strand displacement generally replaces at least 30 nucleotides of DNA, but it remains unclear how the replication machinery coordinates the transition from Pol δ to DNA ligase. Indeed, despite their fundamental importance in replication, comparatively little is known about the *in vivo* properties of eukaryotic Okazaki fragments: although they are widely accepted to be shorter than the 1–2 kilobases (kb) observed in prokaryotes, a clear consensus has not emerged^{11,13–15}. Moreover, we have little information about how nucleosome assembly may interact with lagging-strand synthesis. A plausible explanation for the difference in size between eukaryotic and prokaryotic Okazaki fragments is that eukaryotic DNA replication occurs within the context of chromatin.

To investigate the relationship between lagging-strand processing and chromatin assembly, we have developed strategies to analyse Okazaki fragments purified from *S. cerevisiae*. We find that Okazaki fragments are heterogeneously sized with a repeat length corresponding to that of nucleosomes. In addition, we find that ligation junctions occur preferentially around known nucleosome midpoints, and that these relationships can be altered by interfering with chromatin assembly or Pol δ processivity. Our data suggest an integrated model whereby nascent chromatin structure facilitates Okazaki fragment processing, which may provide a means to monitor nucleosome assembly behind the replication fork.

Nucleosome-sized Okazaki fragments

To enrich for ligation-competent Okazaki fragments, we constructed strains of *S. cerevisiae* in which DNA ligase I¹¹ (CDC9) expression is driven from a doxycycline-repressible promoter and the encoded protein tagged with a temperature-sensitive degron¹⁶. The inability to ligate Okazaki fragments should result in the accumulation of nicked DNA that, after purification, can be radiolabelled using DNA polymerase and α -³²P dCTP. Ligase inactivation in an asynchronous culture resulted in the accumulation of short heterogeneous DNA species whose abundance increased with duration of ligase inhibition (Fig. 1a). Notably, these fragments displayed an underlying periodicity reminiscent of the nucleosome repeat. Indeed, comparison of the nicked DNA to a nucleosome ladder indicated that a significant fraction of fragments seem to be sized according to the 165-bp nucleosomal repeat length in *S. cerevisiae* (Fig. 1b).

To clarify that we were observing Okazaki fragments, we confirmed that they did not appear in a G1-arrested culture until S-phase release (Fig. 1c). Additionally, we treated purified DNA with recombinant DNA ligase; this repaired the nicks and severely diminished our ability to label fragments (Fig. 1d), showing that our assay predominantly detects nicked DNA rather than species containing single-stranded gaps or flaps resulting from incomplete Okazaki fragment processing. Unrelated control experiments indicated that a 125-nucleotide species previously reported to be Okazaki fragments^{14,17} is 5S ribosomal RNA (Supplementary Fig. 2). Thus, we demonstrate that the mono-, di- and

¹Molecular Biology Program, Memorial Sloan-Kettering Cancer Center, 1275 York Avenue, New York, New York 10065, USA.

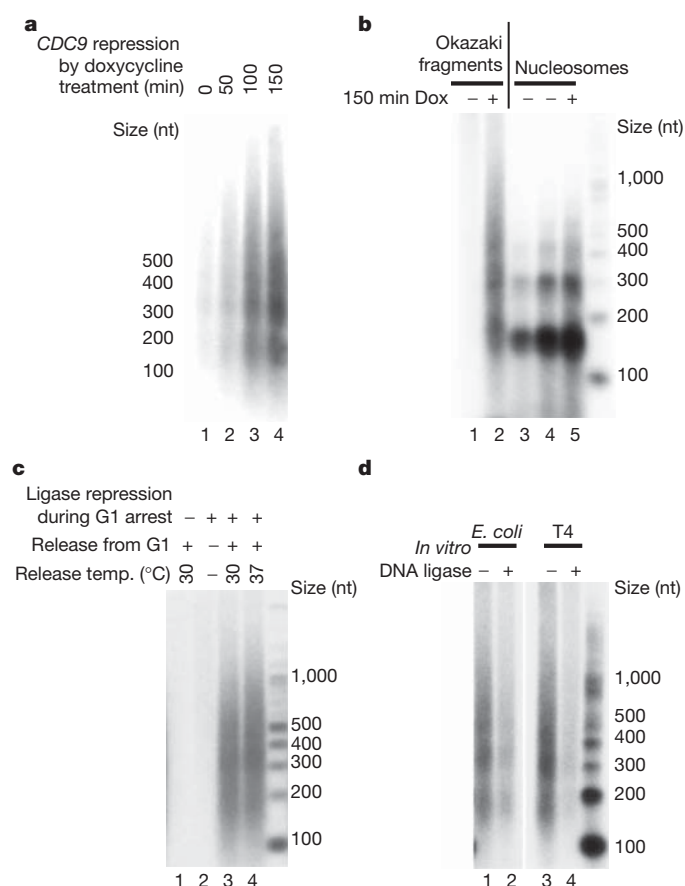


Figure 1 | DNA ligase I depletion in *S. cerevisiae* leads to the accumulation of Okazaki fragments sized similarly to the nucleosome repeat.

a, Transcriptional repression of DNA ligase I (*CDC9*) results in the accumulation of nicked DNA. Cells carrying a doxycycline-repressible allele of the *CDC9* gene were treated with doxycycline (Dox) for the indicated time. Purified genomic DNA was labelled using exonuclease-deficient Klenow fragment and α - 32 P dCTP and separated in a denaturing agarose gel. nt, nucleotides. **b**, The size of labelled Okazaki fragments mirrors the nucleosome repeat. Okazaki fragments (lane 2) were labelled as in Fig. 1a; nucleosomes were prepared from wild-type (lane 3) or repressible *CDC9* strains (lanes 4 and 5) by *in vivo* micrococcal nuclease (MNase) digestion. The chromatin digestion patterns in lanes 4 and 5 indicate that *CDC9* repression does not alter global chromatin structure. **c**, Okazaki fragments accumulate during S phase. Cells were arrested in G1 using α -factor, during which time *CDC9* transcription was inhibited by the addition of doxycycline, and degradation of the protein stimulated by activation of the degon system using galactose and 37 °C. Okazaki fragments appear upon release of the culture into S phase (lanes 3 and 4). **d**, Okazaki fragments are bordered by ligatable nicks. Purified DNA was treated (lanes 2 and 4) or mock-treated (lanes 1 and 3) with the indicated ligase, and then labelled as in Fig. 1a. The inability to label fragments after ligase treatment confirms that labelled Okazaki fragments are flanked by ligatable nicks.

trinucleosome-sized fragments observed on ligase inhibition are generated in S phase and bordered by ligatable nicks—the essential properties of ligation-competent Okazaki fragments.

Global distribution of Okazaki fragments

To explore further the relationship between Okazaki fragments and nucleosomes, we developed a deep sequencing approach to map the strand, position and abundance of fragments across the *S. cerevisiae* genome. To allow yeast to complete S phase in the presence of nicked DNA we inactivated the DNA damage checkpoint by deleting the *RAD9* gene. Additionally, to deplete ligase activity further we deleted the second DNA ligase (*DNL4*). *DNL4* or *RAD9* deletion does not affect Okazaki fragment size (Supplementary Fig. 3). Okazaki fragments were harvested from an asynchronous culture after a ~2.5 h

ligase inactivation. Small single-stranded fragments were purified by anion exchange chromatography in alkaline conditions and sequencing primers were ligated directly to each end¹⁸ (Supplementary Fig. 4). Importantly, this method preserves strand identity.

After paired-end deep sequencing, we aligned the data to the *S. cerevisiae* genome and found that use of a single asynchronous culture was sufficient to attain complete coverage (a representative chromosome is shown in Fig. 2a, and a comparison of replicates in Supplementary Fig. 5). Sequencing reads aligning to the Watson or Crick strands showed a complementary distribution with strand bias being particularly pronounced close to replication origins¹⁹; such asymmetry is expected, given that replication forks proceed bidirectionally from origins (Fig. 2b). The strong strand bias observed around experimentally validated replication origins mapped at high resolution (Fig. 2c)²⁰ demonstrates preferential sequencing of nascent lagging strands, unequivocally confirming that the DNA species enriched after ligase repression are Okazaki fragments. Detailed analysis of global Okazaki fragment distributions can provide mechanistic insight into replication-fork dynamics (S. McGuffee, D.J.S. and I.W., manuscript in preparation).

Okazaki fragments terminate within nucleosomes

The periodic size of Okazaki fragments observed in Fig. 1 led us to investigate how the ends of Okazaki fragments relate to nucleosome positions found within the yeast genome. We aligned Okazaki fragment termini to a reference list of all consensus nucleosome midpoints (dyads) in *S. cerevisiae*²¹. Inherent bias towards smaller fragments during purification, library amplification and sequencing result in size distributions that differ substantially between starting material and sequenced fragments (Supplementary Fig. 6); therefore, we randomly selected fragments from our sequencing data to approximate the mononucleosome-sized fragments we detected by electrophoresis (Supplementary Fig. 6). Aligning both the 5' and 3' ends of mature (Fig. 3a) mononucleosome-sized fragments against the dyads of

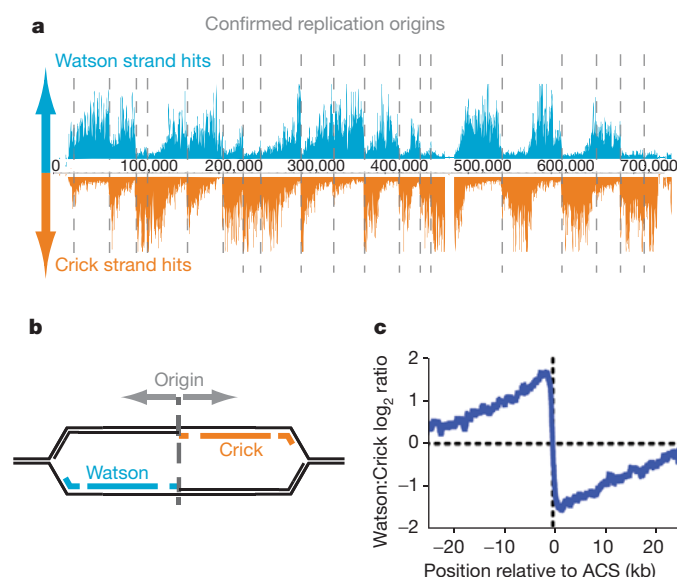


Figure 2 | Sequenced Okazaki fragments show a pronounced bias towards the lagging strand. **a**, Distribution of paired-end sequencing hits mapping to either the Watson (blue, above the axis) or Crick (orange, below) strands across *S. cerevisiae* chromosome 10. The locations of replication origins¹⁹ are indicated as grey dashed lines. Data are unsmoothed. **b**, The anticipated distribution of Okazaki fragments surrounding an efficient origin. **c**, Sequenced Okazaki fragments are strongly enriched in regions predicted to be replicated as the lagging strand. Log₂ ratio of Watson strand: Crick strand fragments across a 50-kb window around ARS consensus sequences (ACS) confirmed previously²⁰ to correspond to active origins. Data are smoothed to 200 bp.

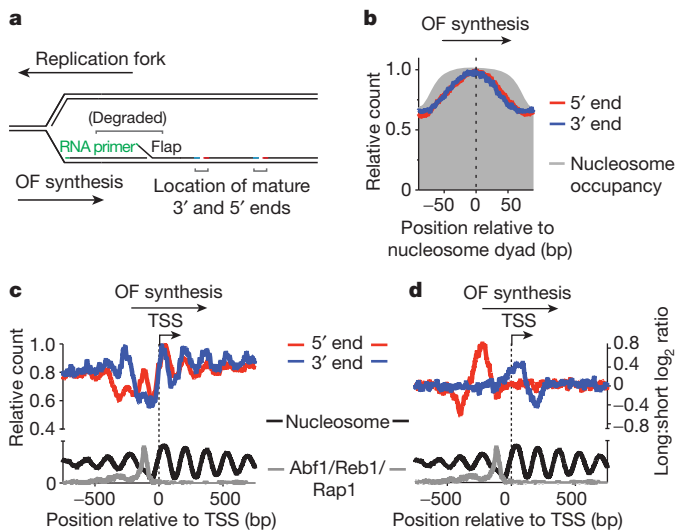


Figure 3 | Okazaki fragment termini are preferentially located at nucleosome dyads. **a**, Schematic indicating the mature Okazaki fragment termini sequenced in this study. **b**, Okazaki fragment termini are enriched around nucleosome dyads. The distribution of termini from mononucleosome-sized Okazaki fragments around the top 50% consensus *S. cerevisiae* nucleosome dyad locations²¹ is shown. Unless otherwise indicated, all analyses use unsmoothed data normalized to the maximum signal in the analysed range, and area aligned such that Okazaki fragment (OF) synthesis by Pol δ proceeds from left to right. **c**, The distribution of Okazaki fragment termini correlates with nucleosome occupancy²⁸ around TSSs. Data are aligned to TSSs such that the direction of transcription is from left to right: only Okazaki fragments synthesized in the same direction as transcription are analysed here; equivalent analyses for fragments synthesized in the opposite direction can be found in Supplementary Fig. 7. Data are smoothed to 5 bp. **d**, Okazaki fragments at nucleosome-depleted regions are disproportionately likely to be long. Equal numbers of reads were selected from the top (long), and the bottom three (short) length quartiles of sequenced fragments. The log₂ ratio of long to short fragments is plotted. Data are smoothed to 5 bp.

high-confidence nucleosomes indicated that the highest density of ends occurs at the dyad (Fig. 3b). Alignment of unfiltered data and dinucleosome-sized fragments is comparable to the mononucleosome size-selected subset (Supplementary Fig. 6). Therefore, rather than being overrepresented in the accessible internucleosomal linker DNA, we find that Okazaki fragment termination is most likely to occur at locations corresponding to nucleosome dyads.

DNA-bound proteins dissociate Pol δ

To confirm that the observed correspondence between nucleosome occupancy and Okazaki fragment end density was not biased by a small subset of nucleosomes, we analysed transcription start sites (TSSs), at which nucleosome positioning follows a well-defined pattern²². Alignment of Okazaki fragment termini around ~4,500 TSSs indicated a marked correlation between nucleosome occupancy and the density of Okazaki fragment ends (Fig. 3c and Supplementary Fig. 7) across a broad region surrounding TSSs. Precise nucleosome positioning around TSSs is determined by chromatin remodelling^{22,23}, allowing us to infer that the correlation refers to remodelled, rather than intrinsically preferred, nucleosome locations.

If the ends of Okazaki fragments are dictated by nucleosomes then nicks should always be in register with positioned nucleosomes, regardless of internucleosomal spacing. Thus, nucleosomes separated by long linker DNA should be associated with longer Okazaki fragments. We took advantage of the differential nucleosome spacing surrounding the nucleosome-depleted region (NDR) at TSSs, comparing the distribution of equal numbers of randomly selected long and short fragments (defined, respectively, as the top quartile of sequenced fragments by length, and the bottom three quartiles).

When the ratio of long to short fragments is plotted across this region (Fig. 3d and Supplementary Fig. 7), we find that fragments whose ends map within nucleosomes bordering the NDR are disproportionately long. Thus, Okazaki fragment length reflects nucleosome spacing.

As well as correlating with nucleosome occupancy, Okazaki fragment termini were enriched around known transcription factor binding sites (Fig. 3c)^{24,25}. This suggested that, in addition to nucleosomes, sequence-specific DNA binding factors might directly influence the ends of Okazaki fragments. Such correlations would be expected if, following replication-fork passage, some transcription factors rapidly bound to replicated DNA and impeded Pol δ during strand-displacement synthesis, causing the polymerase to dissociate and leave a nick close to the site of collision. Furthermore, this model would also provide an explanation for the observed link between nucleosome occupancy and Okazaki fragment termination: nucleosomes contain numerous weak protein–DNA interactions, whose cumulative strength peaks around the dyad²⁶. Polymerases can invade nucleosomes, but experience increasing resistance as they approach the dyad^{27,28}. Therefore, if nucleosomes are rapidly re-established on the lagging strand behind the replication fork, and Pol δ invades them during strand-displacement synthesis, the likelihood of polymerase stalling and/or dissociation will increase with proximity to the dyad (see model in Supplementary Fig. 1), producing Okazaki fragments sized according to the nucleosome repeat. Other models that invoke biased Okazaki fragment initiation due to replisome pausing on encountering nucleosomes would produce distinct correlations around NDRs (Supplementary Fig. 8).

If polymerization by Pol δ is inhibited by sequence-specific DNA-bound transcription factors, Okazaki fragment ends should accumulate on the side of the factor that is first encountered by Pol δ . Aligning all transcription factor binding sites²⁵ indicated a significant enrichment of precisely juxtaposed Okazaki fragment 5' and 3' termini around the replication-fork-proximal side of the binding site (Fig. 4a). However, when the Abf1, Reb1 and Rap1 binding sites were considered separately we found that, among transcription factors, these proteins most strongly biased the positioning of Okazaki fragment ends (Fig. 4b, c and Supplementary Fig. 9). Abf1, Reb1 and Rap1 have essential roles in chromatin organization^{24,29}, and may therefore bind more rapidly and tightly to newly replicated DNA than the majority of transcription factors. We observed a strand-dependent enrichment of Okazaki fragment termini around the 3' ends of tRNA genes, as well as transcription factor TFIIB binding sites (Supplementary Fig. 10). Thus, it seems that diverse DNA binding proteins can influence the processing of Okazaki fragments and probably facilitate the dissociation of Pol δ , with tightly bound protein complexes stimulating termination more precisely than those, such as nascent histones, that have more diffuse binding regions.

Chromatin assembly dictates nick location

Two testable predictions arise from the model that Pol δ dissociates via interaction with nascent nucleosomes: (1) disrupting nucleosome

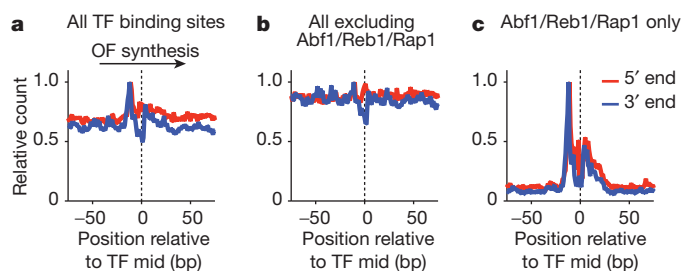


Figure 4 | Transcription factors with roles in nucleosome positioning stimulate dissociation of Pol δ . **a**, Okazaki fragment termini are enriched on the replication-fork-proximal side of known transcription factor (TF) binding sites²⁵. Mid, midpoint of TF binding site. **b**, **c**, The enrichment of Okazaki fragment termini around transcription factor binding sites can be attributed almost entirely to three factors—Abf1, Reb1 and Rap1—known to have roles in nucleosome positioning.

assembly will impair nucleosome-mediated Okazaki fragment termination and should, therefore, alter the size distribution of the fragments; and (2) reducing Pol δ processivity will result in a shift of Okazaki fragment termination sites away from the dyad, towards the replication-fork-proximal side of nucleosomes.

The deposition of (H3H4)₂ tetramers on nascent DNA—the first stage in nucleosome assembly—is mediated in part by CAF-1, a multi-subunit histone chaperone complex associated with the replisome via PCNA³⁰. We deleted each subunit of CAF-1 individually, and compared the length of Okazaki fragments in the deletion strains to those with wild-type CAF-1 (Fig. 5a). Loss of any CAF-1 subunit abrogated the periodic sizing of Okazaki fragments, significantly increasing their average length. These data are consistent with a global delay in (H3H4)₂ deposition following replication, with the resulting paucity of tetrasomes/nucleosomes on the lagging strand leading to increased strand displacement by Pol δ and thus to longer Okazaki fragments.

In *S. cerevisiae*, Pol δ is a heterotrimer whose Pol32 subunit increases processivity and PCNA binding affinity³¹; Pol δ lacking Pol32 shows decreased strand-displacement synthesis *in vitro* and probably *in vivo*³². Labelled Okazaki fragments from a *pol32* Δ strain were more heterogeneous but were still generally sized according to the nucleosome repeat (Fig. 5b). When the positions of the 5' and 3' termini of mononucleosome-sized fragments (165 ± 15 nucleotides, as per Fig. 3b) from the *pol32* Δ strain were aligned against nucleosome midpoints, a clear shift was observed towards the first edge of the nucleosome encountered by the polymerase (Fig. 5c and Supplementary Fig. 11). Therefore, when Pol δ processivity is perturbed, the polymerase dissociates more rapidly due to an inability to invade nascent nucleosomes assembled on Okazaki fragments. The new maximum end density occurs ~ 35 –40 nucleotides from the dyad, consistent with the extent of DNA protected by (H3H4)₂ tetramers³³; nucleosome assembly occurs step-wise, with assembly of (H3H4)₂ tetramers preceding recruitment of H2A/H2B³⁴; it is therefore possible that the histone-DNA species encountered by Pol δ is a tetrasome rather than a nucleosome, although our data do not allow us to distinguish between these possibilities. Importantly, the distribution of Okazaki fragment termini around transcription factor binding sites was identical between wild-type and *pol32* Δ strains (Supplementary Fig. 9), allowing us to conclude that the shift towards the edge of nucleosomes does not simply

represent a constant decrease of ~ 35 –40 bp in the extent of strand displacement.

Discussion

Our data suggest a mechanism by which Pol δ may reliably remove DNA synthesized by Pol α while avoiding excessive strand-displacement synthesis. Repeated cycles of extension and cleavage can occur during the synthesis of a single Okazaki fragment. After removal of the RNA primer, all DNA flap structures generated by Pol δ are biochemically indistinguishable from one another, and an external mechanism is therefore required to measure the extent of strand displacement already carried out by Pol δ on each fragment. The removal of Pol δ by newly deposited histones represents a simple way to constrain Pol δ extension, and might allow nucleosome assembly to stimulate replication-fork progression directly. Although our data imply that nucleosomes strongly impede Pol δ , we note that both Fen1 and DNA ligase I can act efficiently on nucleosomal substrates^{35,36}. We speculate that carrying out Okazaki fragment processing in the context of nucleosomes rather than DNA allows the ligation reaction to outcompete further strand displacement by Pol δ .

CAF-1 is not essential in *S. cerevisiae*, suggesting that other histone chaperones such as Asf1, Rtt106 and HIR³⁷ allow sufficient replication-coupled or post-replicative nucleosome assembly for viability. Nevertheless, our results are consistent with a temporal delay in nucleosome assembly in CAF-1 mutants, which may give rise to previously reported silencing defects³⁸. The importance of replication-coupled chromatin assembly in metazoa is illustrated by the severe phenotypes of CAF-1 or ASF1 disruption in human cell lines: ASF1 depletion leads to replication-fork stalling³⁹, and CAF-1 depletion also precludes progression through S phase⁴⁰.

Our studies demonstrate that the location of Okazaki fragment termini can be determined by interactions between the lagging-strand polymerase and nascent nucleosomes. This observation provides the first direct mechanistic evidence for the coupling of DNA replication to chromatin assembly on the newly replicated daughter genomes. Such coupling is fundamentally important given the part played by chromatin in the regulation of gene expression, as well as the potential for the epigenetic inheritance of precisely located modified nucleosomes. In addition, transcription factors known to have roles in the establishment of chromatin structure are apparently able to re-bind to DNA immediately after replication-fork passage. Unlike histones, which are present in sufficient number to be distributed to both daughter genomes, DNA-bound transcription factors are present at only one local copy per two daughters. Regulation of transcription factor re-binding could thus have a key role in asymmetric epigenetic inheritance.

METHODS SUMMARY

Genomic DNA was prepared from spheroblasts essentially as described for medium resolution DSB mapping⁴¹, labelled using exo-Klenow fragment (NEB) and α -³²P dCTP and separated in 1.3% denaturing agarose gels.

Okazaki fragments were purified by binding heat-denatured genomic DNA to Source 15Q (GE Healthcare) at pH 12, 300 mM NaCl, and eluting in 50 mM steps to 1 M. Primers for paired-end Illumina TruSeq sequencing were directly ligated to each end. Following second-strand synthesis and size selection by gel purification, libraries were amplified by PCR, purified from two sequential 2.5% native agarose gels, and sequenced directly. Full details are in Supplementary Fig. 4 and Methods.

Full Methods and any associated references are available in the online version of the paper at www.nature.com/nature.

Received 21 November 2011; accepted 24 January 2012.

Published online 14 March 2012.

1. Corpet, A. & Almouzni, G. Making copies of chromatin: the challenge of nucleosomal organization and epigenetic information. *Trends Cell Biol.* **19**, 29–41 (2009).

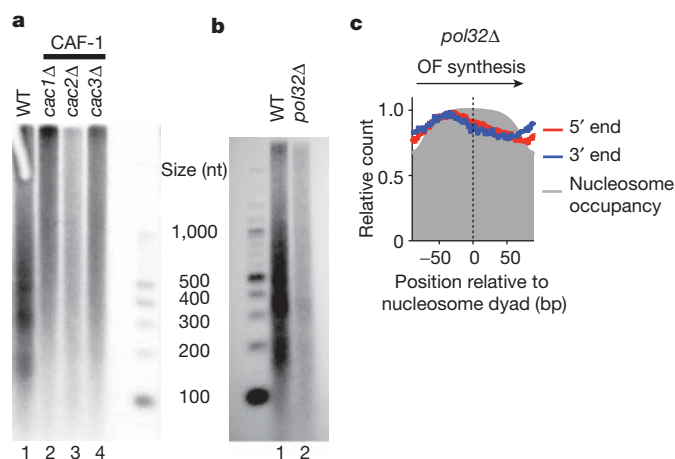


Figure 5 | Impaired chromatin assembly and Pol δ processivity affect the size of Okazaki fragments and the location of their termini, respectively. **a**, Deletion of any component of the CAF-1 complex (lanes 2–4) results in Okazaki fragments that are no longer sized according to nucleosomes. WT, wild type. **b**, Deletion of the *pol32* subunit of Pol δ (lane 2) does not abrogate the chromatin-like size distribution of Okazaki fragments. **c**, In the absence of Pol32, the termini of mononucleosome-sized Okazaki fragments are shifted towards the replication-fork-proximal edge of the nucleosome: peak density occurs at a location consistent with the predicted edges of (H3H4)₂ tetramers. See also Supplementary Fig. 11.

2. Sogo, J. M., Stahl, H., Koller, T. & Knippers, R. Structure of replicating simian virus 40 minichromosomes. The replication fork, core histone segregation and terminal structures. *J. Mol. Biol.* **189**, 189–204 (1986).
3. Burgers, P. M. Polymerase dynamics at the eukaryotic DNA replication fork. *J. Biol. Chem.* **284**, 4041–4045 (2009).
4. Kaufmann, G. & Falk, H. H. An oligoribonucleotide polymerase from SV40-infected cells with properties of a primase. *Nucleic Acids Res.* **10**, 2309–2321 (1982).
5. Nethanel, T. & Kaufmann, G. Two DNA polymerases may be required for synthesis of the lagging DNA strand of simian virus 40. *J. Virol.* **64**, 5912–5918 (1990).
6. Waga, S. & Stillman, B. Anatomy of a DNA replication fork revealed by reconstitution of SV40 DNA replication *in vitro*. *Nature* **369**, 207–212 (1994).
7. Ayyagari, R., Gomes, X. V., Gordenin, D. A. & Burgers, P. M. Okazaki fragment maturation in yeast. I. Distribution of functions between FEN1 and DNA2. *J. Biol. Chem.* **278**, 1618–1625 (2003).
8. Bae, S. H., Bae, K. H., Kim, J. A. & Seo, Y. S. RPA governs endonuclease switching during processing of Okazaki fragments in eukaryotes. *Nature* **412**, 456–461 (2001).
9. Kao, H. I., Veeraraghavan, J., Polaczek, P., Campbell, J. L. & Bambara, R. A. On the roles of *Saccharomyces cerevisiae* Dna2p and Flap endonuclease 1 in Okazaki fragment processing. *J. Biol. Chem.* **279**, 15014–15024 (2004).
10. Garg, P., Stith, C. M., Sabouri, N., Johansson, E. & Burgers, P. M. Idling by DNA polymerase δ maintains a ligatable nick during lagging-strand DNA replication. *Genes Dev.* **18**, 2764–2773 (2004).
11. Johnston, L. H. & Nasmyth, K. A. *Saccharomyces cerevisiae* cell cycle mutant *cdc9* is defective in DNA ligase. *Nature* **274**, 891–893 (1978).
12. Pavlov, Y. I. *et al.* Evidence that errors made by DNA polymerase α are corrected by DNA polymerase δ . *Curr. Biol.* **16**, 202–207 (2006).
13. Anderson, S. & DePamphilis, M. L. Metabolism of Okazaki fragments during simian virus 40 DNA replication. *J. Biol. Chem.* **254**, 11495–11504 (1979).
14. Bielinsky, A. K. & Gerbi, S. A. Discrete start sites for DNA synthesis in the yeast *ARS1* origin. *Science* **279**, 95–98 (1998).
15. Blumenthal, A. B. & Clark, E. J. Discrete sizes of replication intermediates in *Drosophila* cells. *Cell* **12**, 183–189 (1977).
16. Dohmen, R. J. & Varshavsky, A. Heat-inducible degron and the making of conditional mutants. *Methods Enzymol.* **399**, 799–822 (2005).
17. Bielinsky, A. K. & Gerbi, S. A. Chromosomal *ARS1* has a single leading strand start site. *Mol. Cell* **3**, 477–486 (1999).
18. Ng, P. *et al.* Gene identification signature (GIS) analysis for transcriptome characterization and genome annotation. *Nature Methods* **2**, 105–111 (2005).
19. Nieduszynski, C. A., Hiraga, S., Ak, P., Benham, C. J. & Donaldson, A. D. OriDB: a DNA replication origin database. *Nucleic Acids Res.* **35**, D40–D46 (2007).
20. Eaton, M. L., Galani, K., Kang, S., Bell, S. P. & MacAlpine, D. M. Conserved nucleosome positioning defines replication origins. *Genes Dev.* **24**, 748–753 (2010).
21. Jiang, C. & Pugh, B. F. A compiled and systematic reference map of nucleosome positions across the *Saccharomyces cerevisiae* genome. *Genome Biol.* **10**, R109 (2009).
22. Whitehouse, I., Rando, O. J., Delrow, J. & Tsukiyama, T. Chromatin remodelling at promoters suppresses antisense transcription. *Nature* **450**, 1031–1035 (2007).
23. Hartley, P. D. & Madhani, H. D. Mechanisms that specify promoter nucleosome location and identity. *Cell* **137**, 445–458 (2009).
24. Badis, G. *et al.* A library of yeast transcription factor motifs reveals a widespread function for Rsc3 in targeting nucleosome exclusion at promoters. *Mol. Cell* **32**, 878–887 (2008).
25. MacIsaac, K. D. *et al.* An improved map of conserved regulatory sites for *Saccharomyces cerevisiae*. *BMC Bioinformatics* **7**, 113 (2006).
26. Hall, M. A. *et al.* High-resolution dynamic mapping of histone–DNA interactions in a nucleosome. *Nature Struct. Mol. Biol.* **16**, 124–129 (2009).
27. Bondarenko, V. A. *et al.* Nucleosomes can form a polar barrier to transcript elongation by RNA polymerase II. *Mol. Cell* **24**, 469–479 (2006).
28. Churchman, L. S. & Weissman, J. S. Nascent transcript sequencing visualizes transcription at nucleotide resolution. *Nature* **469**, 368–373 (2011).
29. Bai, L., Ondracka, A. & Cross, F. R. Multiple sequence-specific factors generate the nucleosome-depleted region on *CLN2* promoter. *Mol. Cell* **42**, 465–476 (2011).
30. Shibahara, K. & Stillman, B. Replication-dependent marking of DNA by PCNA facilitates CAF-1-coupled inheritance of chromatin. *Cell* **96**, 575–585 (1999).
31. Johansson, E., Garg, P. & Burgers, P. M. The Pol32 subunit of DNA polymerase δ contains separable domains for processive replication and proliferating cell nuclear antigen (PCNA) binding. *J. Biol. Chem.* **279**, 1907–1915 (2004).
32. Stith, C. M., Sterling, J., Resnick, M. A., Gordenin, D. A. & Burgers, P. M. Flexibility of eukaryotic Okazaki fragment maturation through regulated strand displacement synthesis. *J. Biol. Chem.* **283**, 34129–34140 (2008).
33. Dong, F. & van Holde, K. E. Nucleosome positioning is determined by the (H3–H4)₂ tetramer. *Proc. Natl Acad. Sci. USA* **88**, 10596–10600 (1991).
34. Smith, S. & Stillman, B. Stepwise assembly of chromatin during DNA replication *in vitro*. *EMBO J.* **10**, 971–980 (1991).
35. Chafin, D. R., Vitolo, J. M., Henricksen, L. A., Bambara, R. A. & Hayes, J. J. Human DNA ligase I efficiently seals nicks in nucleosomes. *EMBO J.* **19**, 5492–5501 (2000).
36. Huggins, C. F. *et al.* Flap endonuclease 1 efficiently cleaves base excision repair and DNA replication intermediates assembled into nucleosomes. *Mol. Cell* **10**, 1201–1211 (2002).
37. Ray-Gallet, D. *et al.* Dynamics of histone H3 deposition *in vivo* reveal a nucleosome gap-filling mechanism for H3.3 to maintain chromatin integrity. *Mol. Cell* **44**, 928–941 (2011).
38. Zhang, Z., Shibahara, K. & Stillman, B. PCNA connects DNA replication to epigenetic inheritance in yeast. *Nature* **408**, 221–225 (2000).
39. Groth, A. *et al.* Regulation of replication fork progression through histone supply and demand. *Science* **318**, 1928–1931 (2007).
40. Hoek, M. & Stillman, B. Chromatin assembly factor 1 is essential and couples chromatin assembly to DNA replication *in vivo*. *Proc. Natl Acad. Sci. USA* **100**, 12183–12188 (2003).
41. Murakami, H., Borde, V., Nicolas, A. & Keeney, S. Gel electrophoresis assays for analyzing DNA double-strand breaks in *Saccharomyces cerevisiae* at various spatial resolutions. *Methods Mol. Biol.* **557**, 117–142 (2009).

Supplementary Information is linked to the online version of the paper at www.nature.com/nature.

Acknowledgements We thank S. McGuffee for assistance with data processing; S. Keeney, K. Mariani, D. Remus, T. Tsukiyama, members of the Molecular Biology Program and Whitehouse laboratory for discussions and comments on the manuscript. This work was supported by a Louis V. Gerstner Jr Young Investigator Award and an Alfred Bressler Scholars Endowment Award to I.W. D.J.S. is an HHMI fellow of the Damon Runyon Cancer Research Foundation (DRG-#2046-10).

Author Contributions D.J.S. and I.W. designed experiments; D.J.S. performed experiments and analysed data; D.J.S. and I.W. interpreted results; the manuscript was drafted by D.J.S. and edited by D.J.S. and I.W.

Author Information Raw sequencing data and processed data are available at the Gene Expression Omnibus (<http://www.ncbi.nlm.nih.gov/geo/query/acc.cgi?acc=GSE33786>) under accession number 33786. Reprints and permissions information is available at www.nature.com/reprints. The authors declare no competing financial interests. Readers are welcome to comment on the online version of this article at www.nature.com/nature. Correspondence and requests for materials should be addressed to I.W. (whitehoi@mskcc.org).

METHODS

DNA purification. Yeast strains carrying degon-tagged, doxycycline-repressible alleles of *CDC9* and a galactose-inducible *UBR1* allele (see Supplementary Table 1 for a list of strains) were grown at 30 °C in YEP supplemented with 2% raffinose. At optical density (OD) 0.4, galactose and doxycycline were added to final concentrations of 2% and 40 mg l⁻¹, respectively, and the culture shaken at 37 °C for 2.5 h. Fifty-millilitre cultures were used for labelling experiments, and 250-ml cultures for purification and library generation.

Genomic DNA was prepared from spheroblasts as described for medium resolution DSB mapping⁴¹. Following ligase repression, cells were collected by centrifugation, washed in SCE buffer (1 M sorbitol, 100 mM sodium citrate, 60 mM EDTA, pH 7.0) and spheroblasted for 3 min with 5 mg zymolyase 20T (USB) per 50-ml culture. Spheroblasts were washed with SCE, and resuspended in 480 µl lysis buffer (50 mM Tris-HCl, pH 8.0, 50 mM EDTA, 100 mM NaCl, 1.5% sarkosyl) containing 150 µg proteinase K (Fisher). Digestion was carried out for 2–16 h at 37 °C. After digestion, residual proteins and peptides were precipitated by adding 200 µl 5 M KOAc and spinning at 16,000g for 30 min at 4 °C. Nucleic acids were precipitated from the supernatant by addition of 500 µl isopropanol and centrifugation at 16,000g for 10 min. Pellets were washed twice with 500 µl 70% ethanol, resuspended in 200 µl STE buffer (10 mM Tris-HCl, pH 8.0, 1 mM EDTA, 100 mM NaCl) and digested with 25 µg RNase A (Sigma) and/or 10 U RIBoshredder RNase blend (Epicentre) at 37 °C for 30 min. Genomic DNA was precipitated by addition of 20 µl NaOAc, pH 5.5 and 800 µl ethanol followed by centrifugation at 5,000g for 10 min at room temperature (25 °C). Pellets were washed with 70% ethanol and resuspended in 1 µl TE (10 mM Tris:Cl pH 7.5, 0.1 mM EDTA) per ml original culture volume. DNA was stored at 4 °C and never frozen.

DNA labelling. Two microlitres of DNA (corresponding to the genomic DNA content of 2 ml cultured cells) was used in 20 µl labelling reactions containing 5 U Klenow (exo-)polymerase (NEB) and α -dCTP (Perkin Elmer) at a final concentration of 33 nM. Free label was removed using Illustra microspin G-50 columns (GE healthcare). Labelled DNA was separated in 1.3% denaturing agarose gels (50 mM NaOH, 1 mM EDTA). After electrophoresis, the gel was neutralized and DNA transferred to an uncharged nitrocellulose membrane (Hybond-N; GE healthcare) via capillary transfer. Membranes were exposed to phosphor screens or film.

Okazaki fragment purification. Genomic DNA purified as described earlier was denatured by heating to 95 °C for 5 min, rapidly cooled on ice and brought to 300 mM NaCl, pH 12. Purification was carried out in batch using 400 µl Source 15Q (GE healthcare), binding at 300 mM NaCl, pH 12 and eluting in 50 mM steps to 1 M NaCl, pH 12. As determined by purification of fragments pre-labelled as above (see also Supplementary Fig. 4), fractions from 800–900 mM NaCl contained the majority of fragments of interest. DNA was ethanol precipitated and treated with 10 U Riboshredder RNase blend for 30 min at 37 °C to remove residual, undigested RNA: digestion products were removed using Illustra microspin G-50 columns to leave essentially pure Okazaki fragments.

Sequencing library generation. Adaptor primer pairs with single-stranded overhangs (shown schematically in Supplementary Fig. 4) were annealed by cooling from 95 °C and purified from 12% native polyacrylamide gels via standard methods. Sequences of the adaptor pairs are as follows. 5' top, ACACTCTTTCCCTACACG ACGCTCTTCCGATCT; 5' bottom, NNNNNNAGATCGGAAGAGCGTCGTGT AGGGAAAGAGTGT; 3' top, /Phos/AGATCGGAAGAGCGGTTCAGCAGGAA TGCCGAG; 3' bottom, CTCGGCATTCTCTGCTGAACCGCTCTTCCGATCTN NNNNN.

Up to 200 ng denatured purified Okazaki fragments were incubated at 16 °C overnight in a ligation reaction containing 1 µg of each primer pair and 1,000 U T4 DNA ligase (NEB). Unligated adaptors were removed using Illustra microspin S-300 columns (GE healthcare) and a second strand-synthesis reaction carried out at 72 °C using Taq polymerase (NEB). Products from ~200–1,000 bp were purified from 2.5% agarose gels run in TBE using Qiaquick kits (Qiagen). Purified libraries were amplified (16 cycles) using Illumina Truseq primers according to Illumina protocols, except that KOD hot start polymerase (Novagen) was used. Amplified libraries were purified from two sequential 2.5% agarose gels. Subsequent steps in the sequencing workflow were carried out according to standard procedures.

Nucleosome dyad and occupancy data. The top 50% of nucleosome dyads (by confidence score), taken from a meta-analysis²¹, were used in our analysis; nucleosome occupancy data (Fig. 3b) were from the YPD data set detailed previously⁴².

42. Kaplan, N. *et al.* The DNA-encoded nucleosome organization of a eukaryotic genome. *Nature* **458**, 362–366 (2009).

Resonant quantum transitions in trapped antihydrogen atoms

C. Amole¹, M. D. Ashkezari², M. Baquero-Ruiz³, W. Bertsche^{4,5,6}, P. D. Bowe⁷, E. Butler⁸, A. Capra¹, C. L. Cesar⁹, M. Charlton⁴, A. Deller⁴, P. H. Donnan¹⁰, S. Eriksson⁴, J. Fajans^{3,11}, T. Friesen¹², M. C. Fujiwara^{12,13}, D. R. Gill¹³, A. Gutierrez¹⁴, J. S. Hangst⁷, W. N. Hardy^{14,15}, M. E. Hayden², A. J. Humphries⁴, C. A. Isaac⁴, S. Jonsell¹⁶, L. Kurchaninov¹³, A. Little³, N. Madsen⁴, J. T. K. McKenna¹⁷, S. Menary¹, S. C. Napoli⁴, P. Nolan¹⁷, K. Olchanski¹³, A. Olin^{13,18}, P. Pusa¹⁷, C. Ø. Rasmussen⁷, F. Robicheaux¹⁰, E. Sarid¹⁹, C. R. Shields⁴, D. M. Silveira^{20†}, S. Stracka¹³, C. So³, R. I. Thompson¹², D. P. van der Werf⁴ & J. S. Wurtele^{3,11}

The hydrogen atom is one of the most important and influential model systems in modern physics. Attempts to understand its spectrum are inextricably linked to the early history and development of quantum mechanics. The hydrogen atom's stature lies in its simplicity and in the accuracy with which its spectrum can be measured¹ and compared to theory. Today its spectrum remains a valuable tool for determining the values of fundamental constants and for challenging the limits of modern physics, including the validity of quantum electrodynamics and—by comparison with measurements on its antimatter counterpart, antihydrogen—the validity of CPT (charge conjugation, parity and time reversal) symmetry. Here we report spectroscopy of a pure antimatter atom, demonstrating resonant quantum transitions in antihydrogen. We have manipulated the internal spin state^{2,3} of antihydrogen atoms so as to induce magnetic resonance transitions between hyperfine levels of the positronic ground state. We used resonant microwave radiation to flip the spin of the positron in antihydrogen atoms that were magnetically trapped^{4–6} in the ALPHA apparatus. The spin flip causes trapped anti-atoms to be ejected from the trap. We look for evidence of resonant interaction by comparing the survival rate of trapped atoms irradiated with microwaves on-resonance to that of atoms subjected to microwaves that are off-resonance. In one variant of the experiment, we detect 23 atoms that survive in 110 trapping attempts with microwaves off-resonance (0.21 per attempt), and only two atoms that survive in 103 attempts with microwaves on-resonance (0.02 per attempt). We also describe the direct detection of the annihilation of antihydrogen atoms ejected by the microwaves.

Magnetostatic trapping of neutral atoms⁷ or anti-atoms is accomplished by creating a local minimum of the magnetic field magnitude in free space. The confining force results from interaction of the atomic magnetic moment μ with the non-uniform magnetic field. Figure 1 shows the expected Breit–Rabi hyperfine level diagram for the ground state of the antihydrogen atom in a magnetic field. We label the four eigenstates $|a\rangle$, $|b\rangle$, $|c\rangle$ and $|d\rangle$ in order of increasing energy. Trapping is possible when the atom is in a ‘low-field seeking’ quantum state ($|c\rangle$ or $|d\rangle$ in Fig. 1). We employ the Ioffe–Pritchard⁷ configuration: the superposition of a magnetic multipole (an octupole) field that confines atoms in the transverse directions and two ‘mirror coil’ fields for axial confinement⁸.

Working at the Antiproton Decelerator⁹ facility at CERN, we recently demonstrated magnetic confinement of cold antihydrogen

atoms⁴ and showed that—once trapped—these atoms end up in their ground state, where they can be held⁵ for up to 1,000 s. Here we use the same apparatus, modified to enable injection of microwaves into the trapping volume (Fig. 2a). Antihydrogen atoms are produced near the field minimum (about 1 T, Fig. 2b) by mixing cold plasmas of antiprotons and positrons for about 1 s (Methods). Atoms having kinetic energies corresponding to less than 0.5 K can be trapped. Mixing about two million positrons and 20,000 antiprotons yields approximately 6,000 anti-atoms; on average, approximately one anti-atom is trapped. The trapping field currents can be ramped down with a time constant of 9 ms, releasing trapped atoms in a well-defined time window⁴. The trapping volume is surrounded by a three-layer, 30,720-channel imaging silicon detector¹⁰, which can locate the spatial positions—vertices—of antiproton annihilations.

Our approach was to subject trapped antihydrogen atoms to resonant microwaves to eject them from the trap. A tuned, oscillating magnetic field B_1 applied perpendicularly to the trapping field can drive positron spin-flip transitions between the trappable and the untrappable states, that is, $|c\rangle \rightarrow |b\rangle$ and $|d\rangle \rightarrow |a\rangle$. Untrapped atoms escape and annihilate on the surrounding apparatus. A single experimental cycle or ‘trapping attempt’ involves producing anti-atoms in

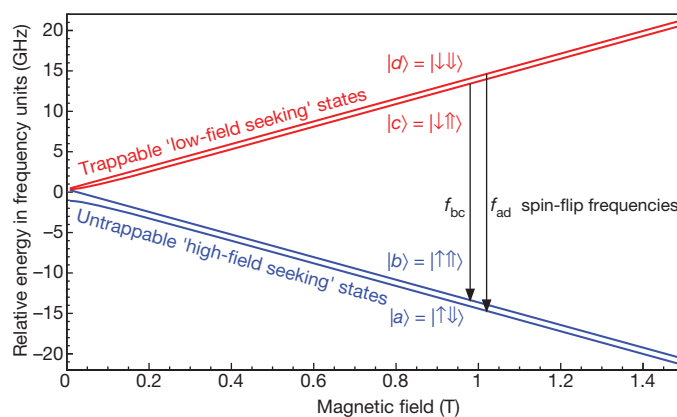


Figure 1 | Hyperfine energy levels. The Breit–Rabi diagram, showing the relative hyperfine energy levels of the ground state of the hydrogen (and antihydrogen, assuming CPT invariance) atom in a magnetic field. In the state vectors shown (for the high-field limit), the single arrow refers to the positron spin and the double arrow refers to the antiproton spin.

¹Department of Physics and Astronomy, York University, Toronto, Ontario, M3J 1P3, Canada. ²Department of Physics, Simon Fraser University, Burnaby, British Columbia, V5A 1S6, Canada. ³Department of Physics, University of California, Berkeley, California 94720-7300, USA. ⁴Department of Physics, Swansea University, Swansea SA2 8PP, UK. ⁵School of Physics and Astronomy, University of Manchester, M13 9PL Manchester, UK. ⁶The Cockcroft Institute, WA4 4AD Warrington, UK. ⁷Department of Physics and Astronomy, Aarhus University, DK-8000 Aarhus C, Denmark. ⁸CERN, Department PH, CH-1211 Geneva 23, Switzerland. ⁹Instituto de Física, Universidade Federal do Rio de Janeiro, Rio de Janeiro 21941-972, Brazil. ¹⁰Department of Physics, Auburn University, Auburn, Alabama 36849-5311, USA. ¹¹Lawrence Berkeley National Laboratory, Berkeley, California 94720, USA. ¹²Department of Physics and Astronomy, University of Calgary, Calgary, Alberta T2N 1N4, Canada. ¹³TRIUMF, 4004 Wesbrook Mall, Vancouver, British Columbia V6T 2A3, Canada. ¹⁴Department of Physics and Astronomy, University of British Columbia, Vancouver, British Columbia V6T 1Z1, Canada. ¹⁵The Canadian Institute of Advanced Research, Toronto M5G-1Z8, Canada. ¹⁶Department of Physics, Stockholm University, SE-10691, Stockholm, Sweden. ¹⁷Department of Physics, University of Liverpool, Liverpool L69 7ZE, UK. ¹⁸Department of Physics and Astronomy, University of Victoria, Victoria, British Columbia V8W 3P6, Canada. ¹⁹Department of Physics, NRCN-Nuclear Research Center Negev, Beer Sheva, IL-84190, Israel. ²⁰Atomic Physics Laboratory, RIKEN, Saitama 351-0198, Japan. †Present address: Instituto de Física, Universidade Federal do Rio de Janeiro, Rio de Janeiro 21941-972, Brazil.

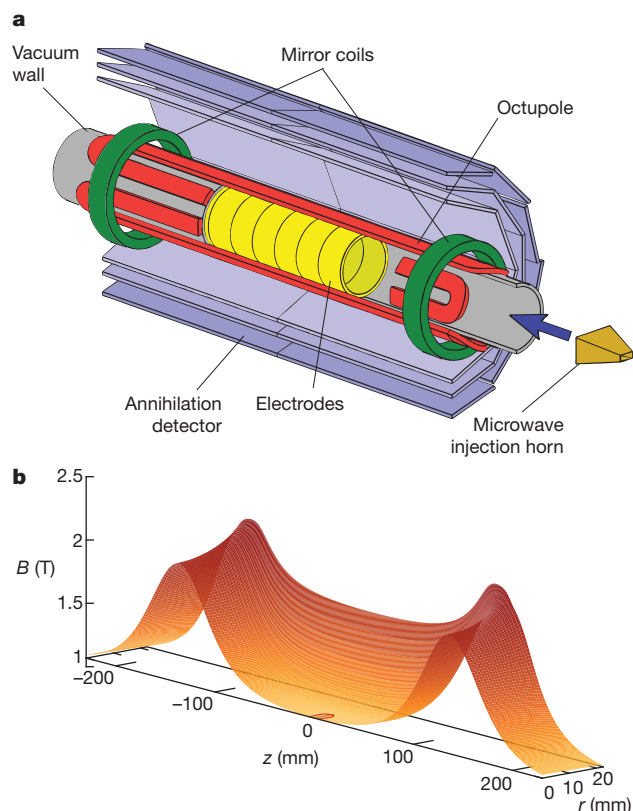


Figure 2 | The ALPHA device. **a**, Cut-away, schematic drawing of the antihydrogen synthesis and trapping region of the ALPHA apparatus. The superconducting atom-trap magnets, the annihilation detector, and some of the Penning trap electrodes are shown. An external solenoid (not shown) provides a 1-T magnetic field for the Penning trap. The drawing is not to scale. The inner diameter of the Penning trap electrodes is 44.5 mm and the minimum- B trap has an effective length of 274 mm. Microwaves are injected along the axis of the trapping volume using a horn antenna, which is located about 130 cm from the trap axial midpoint. **b**, Map of magnetic field strength in the ALPHA antihydrogen trap. The red contour bounds a region up to 0.35 mT (or 10 MHz in microwave frequency equivalent) above the minimum field, to roughly indicate the size of the resonant volume.

the magnetic trap, holding any trapped atoms first for 60 s (during which the magnetic field may be changed) and then for 180 s (during which microwaves may be introduced), and then intentionally releasing any remaining atoms to detect their annihilation.

To select the proper microwave frequencies and magnetic field configurations, we consider (Fig. 3a) the calculated positron spin resonance lineshapes for equal numbers of trapped $|c\rangle$ and $|d\rangle$ state atoms exposed to microwaves. The abrupt low-frequency onsets are associated with the minimum in the static magnetic field near the trap centre; the high-frequency tails reflect the highly inhomogeneous nature of the trapping fields elsewhere. We choose the resonance condition such that transitions are induced as atoms pass close to the magnetic minimum (Fig. 2b). This choice yields higher transition rates than elsewhere in the trap, and it localizes the position in space where transitions occur, and whence the resulting high-field seeking atoms are ejected. We do not know a priori the hyperfine level in which atoms are trapped; for a given magnetic field configuration we need to alternately irradiate the trap at two frequencies (details in Fig. 3 legend) separated by the zero-field hyperfine splitting of 1,420.4 MHz.

We collect two distinct, complementary types of annihilation data. First, at the end of every trapping attempt, we rapidly turn off the confining fields and watch for annihilation events in a 30-ms window from the start of the magnet shutdown. This allows us to determine an effective trapping rate. The ejection of trapped atoms by resonant microwaves will reduce this rate. Rates for application of resonant

microwaves, off-resonant microwaves and no microwaves can be compared: these are ‘disappearance mode’ data. The second data set comes from monitoring annihilation events throughout the entire time that antihydrogen atoms are held in the trap. We look for events from ejected atoms during the time that resonant microwave fields are applied: these are ‘appearance mode’ data.

Because the duration of the observation window differs significantly between these two modes, we rely on two different cosmic background rejection algorithms (Methods). In the 30-ms ‘disappearance window’ we use the algorithm developed earlier⁴ (the ‘default criteria’). The rate at which cosmic ray events are interpreted as annihilations by this selection scheme is $(4.7 \pm 0.2) \times 10^{-2} \text{ s}^{-1}$. For the much longer ‘appearance mode’ observation (180 s), we rely on an alternative set of acceptance criteria that, compared to the default criteria, reduces annihilations by 25% but lowers the cosmic background by an order of magnitude. To avoid experimenter bias, the two sets of criteria are optimized and cross-checked using control samples^{4,6}; cosmic ray events and annihilation events collected independently of the trapping experiments described here.

We conducted six series of measurements. For series 1, we set the minimum on-axis trapping field $B_{\text{min}}^{\text{axis}}$ to some value B^A (Methods), and then applied resonant microwave fields at frequencies f_{bc}^A and f_{ad}^A (Fig. 3b; see the legend for microwave frequency drive details) during the 180-s hold portion of the cycle. For series 2, we shifted $B_{\text{min}}^{\text{axis}}$ to $B^B > B^A$ by increasing the mirror coil currents such that microwave fields oscillating at f_{bc}^A and f_{ad}^A are detuned by 100 MHz and are no longer resonant with atoms at the centre of the trap (Fig. 3c). The field was shifted (in about 1 s) after the mixing and initial trapping phase of each trapping attempt, and a waiting period of 59 s was imposed to allow the field to stabilize before microwave introduction. This configuration should eliminate $|d\rangle \rightarrow |a\rangle$ transitions and reduce the rate of $|c\rangle \rightarrow |b\rangle$ transitions. The latter can still occur as atoms pass through regions of space in which the local magnetic field brings them into resonance with microwave fields applied at frequency f_{ad}^A . Series 3 involved operating at the higher field B^B and shifting the microwave frequencies so as to bring both transitions back into resonance (Fig. 3d). Series 4 field and frequency conditions were identical to those of series 2, but series 4 attempts were interleaved with those of series 3. This repetition attempts to minimize possible systematic effects due to time variations in the experimental conditions. Antiproton beam and plasma conditions—and thus the initial trapping rate—can vary from day to day, so on- and off-resonance experiments were interspersed. Thus, series 1 and 2 were taken under very similar conditions, and series 3 and 4 constitute a second, complementary set of measurements. In concert with series 1–4, we measured trapping and annihilation rates with $B_{\text{min}}^{\text{axis}}$ set to B^A or B^B when no microwaves are injected into the apparatus (series 5 and 6, respectively). Apart from changes in magnetic field or microwave conditions, the experimental procedure was identical for each of the six series.

A summary of ‘disappearance mode’ data appears in Tables 1 and 2. The errors quoted are based on counting statistics only. By comparing the Poisson rate of the process of interest with the rate of the control process, we evaluate the probability (P -value) that the observed number of outcomes, or a more extreme one, could have been produced by background fluctuations¹¹. We observe a clear decrease in the survival rate for the cases in which microwaves are injected on-resonance, as compared to the equivalent off-resonance measurements, with a P -value of 1.0×10^{-5} .

The two measurement sets (series 1–2; series 3–4) could have different systematic uncertainties. For example, in the former, the mirror field shift might affect the orbit dynamics of the trapped antihydrogen (a hypothesis not supported by numerical simulations), while the latter could suffer from different microwave field characteristics between on- and off-resonance frequencies (again, this is not supported by our detailed off-line measurements with electron plasmas; see Methods). However, both data sets show decreases in the on-resonance rate

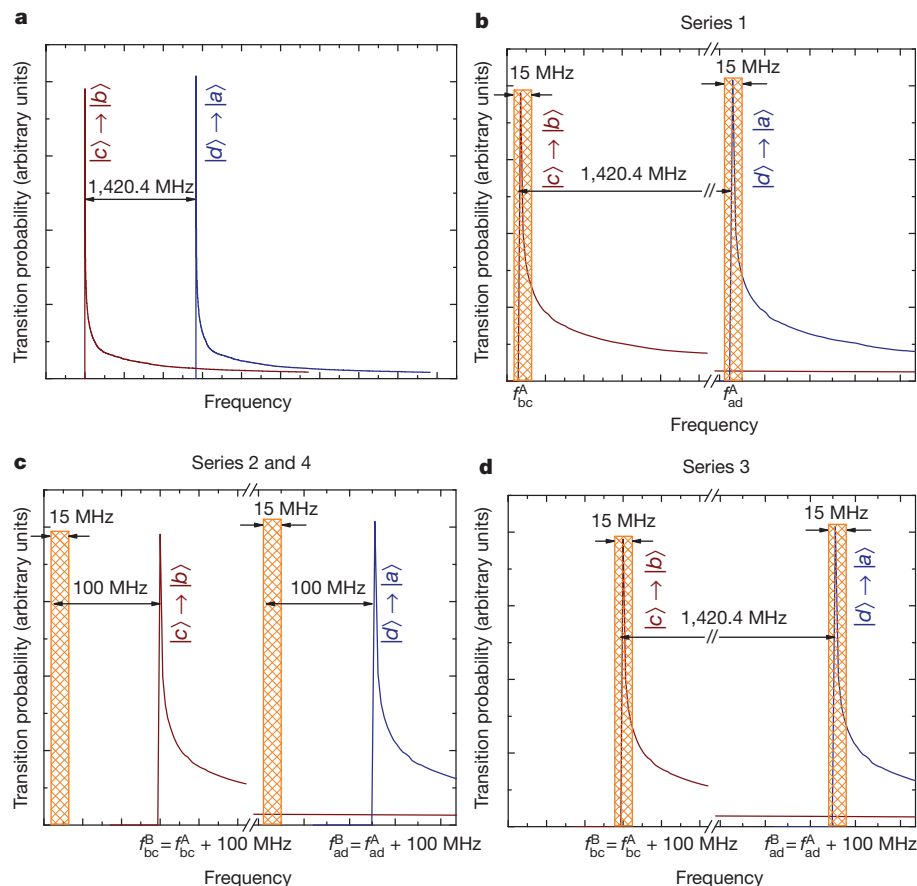


Figure 3 | Transition lineshapes and resonance conditions. **a**, Calculated spin-flip transition lineshapes in the ALPHA antihydrogen trap. Transition probability (arbitrary units) is plotted versus microwave frequency. Only the trapping field inhomogeneity is considered in calculating the lineshape. **b**, Schematic representation of the experimental situation for the on-resonance experiments at magnetic field B^A (series 1). The yellow bands represent the frequency ranges over which the microwaves are scanned. **c**, The situation for off-resonance experiments at magnetic field B^B (series 2 and 4). **d**, The situation

for on-resonant experiments at magnetic field B^B (series 3). A two-segment frequency sweep lasting 30 s was used to apply microwave fields. This sweep was repeated six times in each trapping attempt for a total microwave application time of 180 s, beginning 60 s after the end of antihydrogen formation. In each case, the first 15-s scan covers the lower yellow band and the second 15-s scan covers the upper yellow band. The bands span -5 MHz to $+10$ MHz about the target frequency.

measurements, compared to the associated off-resonance measurements, with P -values of 1.6×10^{-4} and 1.5×10^{-2} , respectively, supporting the hypothesis that the difference is due to spin flip.

We note that the survival rates for the no-microwave measurements are higher than for those in which microwaves are present but off-resonance (the P -value is 6×10^{-3}). This difference could be explained by far off-resonance interactions with the $|c\rangle$ state, assuming there is sufficient microwave power to induce spin flips in the long tails of the resonance lineshape (Fig. 3c). (See the discussion of the appearance mode data below.)

We also directly searched for annihilation signals of anti-atoms that are ejected from the trap after a spin-flip transition—the ‘appearance mode’ described above. Figure 4a shows the time history of events satisfying the alternative acceptance criteria and having $|z| < 6$ cm (Methods). In the first frequency sweep ($0 < t < 30$ s) we observe a significant excess of counts ($P = 2.8 \times 10^{-5}$) in on-resonance (series 1

plus series 3) compared to off-resonance attempts (series 2 plus series 4). Seven of the 19 events appearing in $0 < t < 15$ s (microwaves probing f_{bc}) occur in the first second; for $15 < t < 30$ s (probing f_{ad}) the first second has seven of 18 events. This suggests that the microwave power is sufficient to flip most of the spins during the first 30-s sweep, in agreement with numerical simulations of the transition rate (Methods). An investigation of power dependence indicated that a level as low as one-sixteenth of the nominal 700 mW injected (Methods) was still enough to eject the trapped atoms in the first 30-s sweep, again consistent with the simulations.

In the off-resonant experiments, we observe a mild excess of counts above the no-microwave case (series 5 plus series 6) with an associated $P = 5.6 \times 10^{-2}$. We interpret this excess to be due to the above-mentioned off-resonance interaction with the $|c\rangle$ state. This conclusion is supported by the fact that the events are in $15 < t < 30$ s (Fig. 4a), when the microwaves are probing the upper 15-MHz

Table 1 | Series summaries for the ‘disappearance mode’ analysis

Series	Relative microwave frequency	Relative magnetic field	Number of attempts	Antihydrogen detected at trap shutdown	Rate	Comment
1	0 MHz	0 mT ($B_{\min}^{\text{axis}} = B^A$)	79	1	0.01 ± 0.01	On resonance (Fig. 3b)
2	0 MHz	+3.5 mT ($B_{\min}^{\text{axis}} = B^B$)	88	16	0.18 ± 0.05	Off resonance (Fig. 3c)
3	+100 MHz	+3.5 mT ($B_{\min}^{\text{axis}} = B^B$)	24	1	0.04 ± 0.04	On resonance (Fig. 3d)
4	0 MHz	+3.5 mT ($B_{\min}^{\text{axis}} = B^B$)	22	7	0.32 ± 0.12	Off resonance (Fig. 3c)
5	Off	0 mT ($B_{\min}^{\text{axis}} = B^A$)	52	17	0.33 ± 0.08	No microwaves
6	Off	+3.5 mT ($B_{\min}^{\text{axis}} = B^B$)	48	23	0.48 ± 0.10	No microwaves

Table 2 | Totals for all ‘disappearance mode’ series

	Number of attempts	Detected antihydrogen	Rate
On resonance (1 + 3)	103	2	0.02 ± 0.01
Off resonance (2 + 4)	110	23	0.21 ± 0.04
No microwaves (5 + 6)	100	40	0.40 ± 0.06

frequency band (Fig. 3c), and by indications that the nominal power should be sufficient to drive off-resonant transitions. Taken together, the disappearance and appearance analyses constitute a consistent picture of the fate of the trapped antihydrogen atoms.

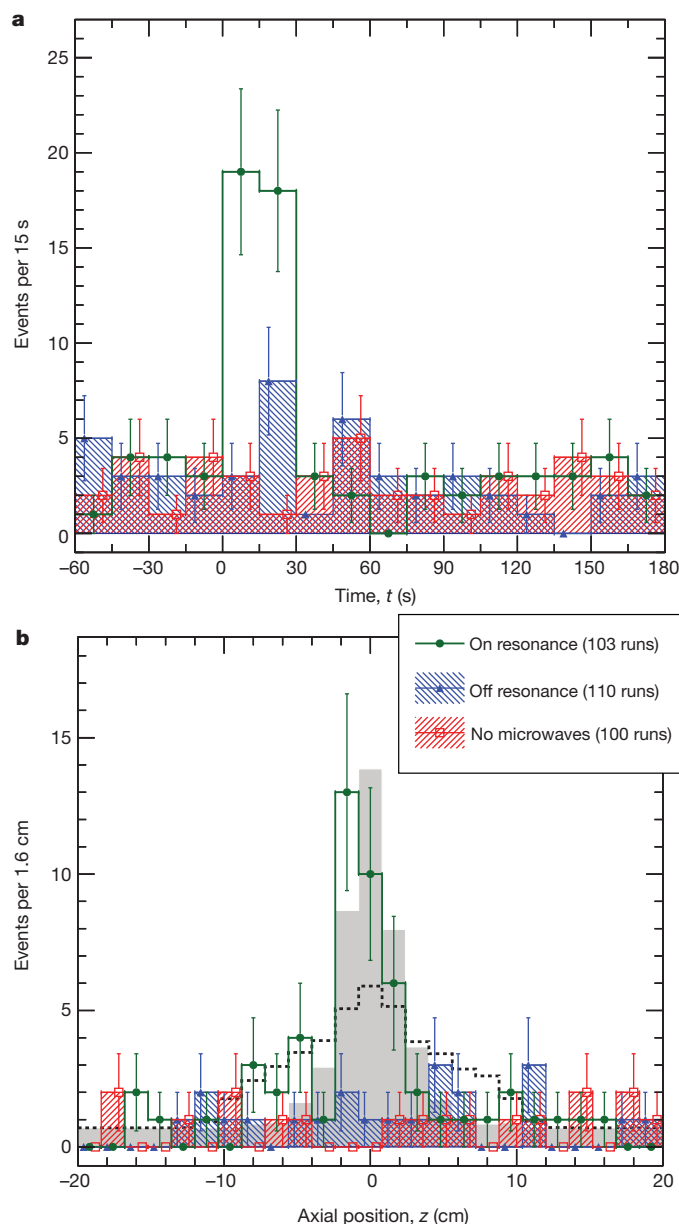


Figure 4 | Appearance mode data. **a**, The number of ‘appearance mode’ annihilation events satisfying the alternative selection criteria and $|z| < 6$ cm (Methods) as a function of time between the end of antihydrogen production and the trap shutdown. Microwave power is first applied at time $t = 0$. The expected cosmic background per bin per run is 0.026 ± 0.005 events. The error bars are due to counting statistics. **b**, The z -distribution of annihilation vertices in ‘appearance mode’ for $0 < t < 30$ s. The grey histogram is the result of a numerical simulation of the motion of spin-flipped atoms ejected from the trap. The dashed black curve is the result of a simulation of trapped antihydrogen annihilating on the residual gas (Methods). Both simulations are normalized to the on-resonant data.

We have considered other processes that could lead to antihydrogen loss in the presence of microwaves but that could not be due to a spin-flip. The only plausible candidate is heating of the trap electrodes by the microwaves, causing desorption from the surfaces of cryo-pumped material, which could then scatter or annihilate the trapped anti-atoms. Indeed, we observe a slight electrode temperature increase from about 8 K to at most 11 K during the 180-s microwave cycle. However, any such thermal effect on the vacuum should be the same for series 1 and 2, which differ only by a slight change in the trapping magnetic field. Further evidence against vacuum deterioration comes from Fig. 4b, which shows the z -distribution of appearance-type events (in $0 < t < 30$ s). The distribution is highly localized around the trap centre, as we expect from simulations of how spin-flipped atoms are lost from the trap (Methods). Annihilation or collisional loss of trapped anti-atoms in a compromised vacuum could occur anywhere in the 274-mm-long trapping volume.

We thus conclude that we have observed resonant interaction of microwave radiation with the internal quantum states of trapped antihydrogen atoms. This is a proof-of-principle experiment; we have not yet attempted to accurately localize a resonance or determine a spectroscopic lineshape. We have bounded the resonance between the off-resonance scan value and the maximum of the on-resonance sweep. Roughly speaking, the observed resonance is within 100 MHz of the resonance frequency expected for hydrogen, corresponding to a relative precision of about 4×10^{-3} . This experiment marks the advent of antimatter spectroscopy and takes a preliminary step towards precision comparison of the spectra of hydrogen and antihydrogen as a test of CPT symmetry. Importantly, it also demonstrates the viability of performing fundamental measurements on small numbers of trapped anti-atoms by combining resonant interaction with the long trapping times and sensitive annihilation detection in ALPHA. In future experiments, the transition $|c\rangle \leftrightarrow |d\rangle$ could be probed by double resonance; the frequency of this transition goes through a broad maximum¹² at a field of 0.65 T, allowing a precision measurement of hyperfine parameters without requiring precise knowledge of the absolute value of B (see Supplementary Information).

METHODS SUMMARY

The ALPHA apparatus traps antihydrogen atoms synthesized from cold plasmas of positrons and antiprotons. Microwaves from a frequency synthesizer were amplified and injected into the magnetic atom trap using a horn antenna. We use electron cyclotron frequency measurement techniques to set the magnetic field in the device, and to characterize microwave field patterns. We perform numerical simulations of trapped antihydrogen dynamics to model microwave resonant lineshapes and transition rates, atom ejection dynamics, and the spatial distribution of residual gas annihilation. Two distinct analysis methods are used to reduce cosmic ray background in the annihilation detector.

Full Methods and any associated references are available in the online version of the paper at www.nature.com/nature.

Received 9 January; accepted 7 February 2012.

Published online 7 March 2012.

- Hänsch, T. W. Nobel lecture: Passion for precision. *Rev. Mod. Phys.* **78**, 1297–1309 (2006).
- Martin, A. G., Helmerson, K., Bagnato, V. S., Lafyatis, G. P. & Pritchard, D. E. RF spectroscopy of trapped neutral atoms. *Phys. Rev. Lett.* **61**, 2431–2434 (1988).
- Fujiwara, M. C. *et al.* Towards antihydrogen confinement with the ALPHA antihydrogen trap. *Hyperfine Interact.* **172**, 81–89 (2006).
- Andresen, G. B. *et al.* Trapped antihydrogen. *Nature* **468**, 673–676 (2010).
- Andresen, G. B. *et al.* Confinement of antihydrogen for 1,000 seconds. *Nature Phys.* **7**, 558–564 (2011).
- Andresen, G. B. *et al.* Search for trapped antihydrogen. *Phys. Lett. B* **695**, 95–104 (2011).
- Pritchard, D. E. Cooling neutral atoms in a magnetic trap for precision spectroscopy. *Phys. Rev. Lett.* **51**, 1336–1339 (1983).
- Bertsche, W. *et al.* A magnetic trap for antihydrogen confinement. *Nucl. Instrum. Meth. A* **566**, 746–756 (2006).
- Maury, S. The antiproton decelerator: AD. *Hyperfine Inter.* **109**, 43–52 (1997).
- Andresen, G. B. *et al.* The ALPHA detector: module production and assembly. *J. Instrum.* **7**, C01051 (2012).

11. Przyborowski, J. & Wilenski, H. Homogeneity of results in testing samples from Poisson series. *Biometrika* **31**, 313–323 (1939).
12. Hardy, W. N. *et al.* Magnetic resonance studies of gaseous atomic hydrogen at low temperatures. *Phys. Rev. Lett.* **42**, 1042–1045 (1979).

Supplementary Information is linked to the online version of the paper at www.nature.com/nature.

Acknowledgements This work was supported by CNPq, FINEP/RENAFAE (Brazil), ISF (Israel), MEXT (Japan), FNU (Denmark), VR (Sweden), NSERC, NRC/TRIUMF, AITF, FQRNT (Canada), DOE, NSF (USA), EPSRC, the Royal Society and the Leverhulme Trust (UK). We thank them for their generous support. We are grateful to the AD team (T. Eriksson, P. Belochitskii, B. Dupuy, L. Bojtar, C. Oliveira, B. Lefort and G. Tranquille) for the delivery of a high-quality antiproton beam. We thank the following individuals for help: M. Harrison, J. Escallier, A. Marone, M. Anerella, A. Ghosh, B. Parker, G. Ganetis, J. Thornhill, D. Wells, D. Seddon, F. Butin, H. Brueker, K. Dahlerup-Pedersen, J. Mourao, T. Fowler, S. Russenschuck, R. De Oliveira, N. Wauquier, J. Hansen, M. Polini, J. M. Geisser, L. Deparis, P. Frichot, J. M. Malzacker, A. Briswalter, P. Moyret, S. Mathot, G. Favre, J. P. Brachet, P. Mésenge, S. Sgobba, A. Cherif, J. Bremer, J. Casas-Cubillos, N. Vauthier, G. Perinic, O. Pirotte, A. Perin, G. Perinic, B. Vullierme, D. Delkaris, N. Veillet, K. Barth, R. Consentino, S. Guido, L. Stewart, M. Malabaila, A. Mongelluzzo, P. Chiggiato, G. Willering, E. Mahner, A. Froton, C. Lasseur, F. Hahn, E. Søndergaard, F. Mikkelsen, W. Carlisle, A. Charman, J. Keller, P. Amaudruz, D. Bishop, R. Bula, K. Langton, P. Vincent, S. Chan, D. Rowbotham, P. Bennet, B. Evans, J.-P. Martin, P. Kowalski, A. Read, T. Willis, J. Kivell, H. Thomas, W. Lai, L. Wasilenko, C. Kolbeck, H. Malik, P. Genoa, L. Posada, R. Funakoshi, M. Okeane, S. Carey and N. Evetts. We thank former collaborators M. J. Jenkins, G. B. Andresen, R. Hydromako, S. Chapman, A. Povilus, R. Hayano, L. V. Jørgensen and Y. Yamazaki. We are grateful to the CERN Summer Student Program for funding the participation of undergraduate students (C.Ø.R. and S.C.N.) in our experiment.

Author Contributions W.B., P.D.B., J.F., M.C.F., J.S.H., N.M. and D.M.S. conceived, designed and constructed the central ALPHA apparatus and participated in all aspects

of the experimental and physics programme. The microwave hardware was designed and fabricated by M.D.A., E.B., W.N.H. and M.E.H., who also participated in all aspects of the experimental programme. T.F. developed the electron cyclotron resonance diagnostic and participated actively in all aspects of the experimental programme. S.S. developed the alternative event analysis and participated actively in the experimental and analysis efforts. C.A., M.B.-R., A.C., A.G., A.J.H., J.T.K.M., E.S. and C.S. participated actively in the experimental runs, data taking, on- and offline analysis, and maintenance and modification of the apparatus. D.R.G. and A.O. contributed to all aspects of the detector systems and participated actively in the experimental shift work and analysis efforts. M.C. designed and built the positron accumulator and participated in the experimental shift work, the physics planning effort, and the strategic direction of the experiment. D.P.v.d.W. designed and built the positron accumulator, contributed to the magnetic design of the atom trap, and participated in the experimental programme. F.R., with help from P.H.D., performed the spin-flip simulations reported in this paper and supported the design and experimental programme with simulations and calculations. P.N. led the design of the ALPHA silicon detector. P.P. was responsible for implementing the silicon detector at CERN and participated in the experimental and analysis programme. A.D., C.A.I., C.Ø.R., S.C.N., A.L. and C.R.S. contributed to the experimental shift work. S.J. and J.S.W. contributed theoretical support in the form of atomic or plasma physics calculations and simulations and contributed to the experimental shift work. C.L.C., S.E., S.M. and R.I.T. participated in the experimental programme and the physics planning effort. L.K. and K.O. provided offsite support for detector electronics and database management systems, respectively, and contributed to the experimental shift work. E.B., J.S.H. and M.E.H. wrote the initial manuscript, which was edited, improved and approved by the entire collaboration.

Author Information Reprints and permissions information is available at www.nature.com/reprints. The authors declare no competing financial interests. Readers are welcome to comment on the online version of this article at www.nature.com/nature. Correspondence and requests for materials should be addressed to J.S.H. (hangst@phys.au.dk) or M.E.H. (mhayden@sfu.ca).

METHODS

Antihydrogen synthesis and trapping. The ALPHA techniques for synthesizing trappable anti-atoms are described extensively elsewhere^{4–6}. Antihydrogen atoms are produced near the trap minimum by mixing cold plasmas of antiprotons and positrons for about 1 s in a Penning–Malmberg¹³ trap. The mixing makes use of the evaporative cooling¹⁴ (for both positrons and antiprotons) and autoresonant injection¹⁵ techniques developed for our initial demonstration of trapping. At the end of the 1-s synthesis stage the magnetic trap fields are on and the trapping region has been cleared of any remaining charged particles. The anti-atoms are then held in the trap for 240 s before being released. During the first 1 s of this time period we either ramp the mirror coil currents from 650 A to 692 A (adding 3.5 mT to $B_{\text{min}}^{\text{axis}}$ to attain B^{B}), or do nothing (to remain at B^{A}). During the next 59 s we wait to ensure that the currents in the mirror coils have stabilized. Finally, during the last 180 s we either inject microwaves or not, depending on the measurement type.

Microwave injection. Ka-band microwaves from an Agilent 8257D PSG Signal Generator are amplified and injected down the axis of the apparatus via a waveguide-fed horn antenna. The maximum power used was about 700 mW, measured at the vacuum transition.

Electron cyclotron resonance diagnostics. We measure the electron cyclotron resonance frequency by loading an electron plasma in the centre of the trap. A series of 4- μ s microwave pulses is injected, at frequencies scanned across the cyclotron resonance; these pulses heat the plasma. Between each pulse we allow the plasma to return to its equilibrium temperature. Simultaneously, we monitor the quadrupole vibrational mode of the plasma by applying an oscillating potential at 26.5 MHz to an electrode adjacent to the plasma and measuring the plasma response on another. The frequency of this mode shifts approximately linearly with changes in temperature¹⁶. When the microwave frequency matches the cyclotron frequency, the heating of the plasma and the quadrupole frequency shift will be maximized. This method allows us to determine and to set the trapping magnetic field and to ensure field stability between trapping attempts.

Using the quadrupole frequency shift diagnostic, we can also infer the *in situ* amplitude of the microwave electric fields near the trap centre. We adjust the solenoid field so that the electron cyclotron resonance frequency is equal to one of the spin-flip transition frequencies and inject resonant microwave pulses to heat the plasma. From the temperature increase we can infer that the peak electric field amplitudes for 700 mW injected power are about $E(f_{\text{bc}}^{\text{A}}) = 110 \text{ V m}^{-1}$, $E(f_{\text{ad}}^{\text{A}}) = 150 \text{ V m}^{-1}$, $E(f_{\text{bc}}^{\text{B}}) = 130 \text{ V m}^{-1}$, $E(f_{\text{ad}}^{\text{B}}) = 100 \text{ V m}^{-1}$.

In yet another mode of operation, we fix the microwave frequency and apply an axial magnetic field gradient across a long (about 4 cm) electron plasma so that only a narrow slice of the plasma is in resonance. The external solenoid field is then swept through resonance to generate a map of electric field strength along the length of the plasma, reflecting the underlying standing-wave pattern. This provides another check of the similarity of microwave field distributions at the four frequencies, as well as of variations over the 15-MHz frequency sweeps. We see no evidence for significant differences in the microwave environment at the two pairs of frequencies ($f_{\text{bc}}^{\text{A}}, f_{\text{ad}}^{\text{A}}$ and $f_{\text{bc}}^{\text{B}}, f_{\text{ad}}^{\text{B}}$) or within the sweeps.

Magnetic field settings. The background solenoid field of about 1 T is the same as that used previously⁴. We use the electron cyclotron resonance technique to quantify the contributions of the solenoid and trap magnets to $B_{\text{min}}^{\text{axis}}$ and to determine the field change necessary to achieve the 100 MHz offset for off-resonant operation. The microwave frequencies used for driving ($f_{\text{bc}}^{\text{A}}, f_{\text{ad}}^{\text{A}}$) were (28.276, 29.696) GHz and for ($f_{\text{bc}}^{\text{B}}, f_{\text{ad}}^{\text{B}}$) were (28.376, 29.796) GHz. The electron cyclotron resonance measurements were used to monitor field stability from attempt to attempt; any necessary corrections were done by adjusting the background solenoid field. The reproducibility of the field-setting procedure translates to ± 2 MHz in microwave frequency.

Numerical simulations of antihydrogen dynamics. We use a mixture of quantum and classical mechanics to simulate the effect of the microwaves on the trapped antihydrogen, and to calculate spatial distributions, both for ejected atoms, and for atoms lost by annihilation on the residual gas. The simulated anti-atoms⁴ are in a low-field seeking state and are launched from the region of the positron plasma with a 50 K thermal distribution; only those with kinetic energy less than about 0.5 K are trapped. The atomic motion is calculated classically using a smooth fit to the magnetic field to obtain the centre-of-mass force.

The spatial structure of the microwave field in the electrode stack is complex, but an order-of-magnitude estimate of spin-flip transition rates can be obtained

by assuming that the microwave magnetic fields \mathbf{B}_1 are those of a plane wave propagating in free space. During each simulation time step, we check whether the spin-flip resonance condition was met. If it was, we compute the transition probability from the standard Landau–Zener approximation for a two state system using a three-point time fit to the energy and coupling parameters. In the strong trapping field, the coupling matrix element between the states is approximately $B_1 \mu/4$. The resonance condition is met twice each time the atom passes through the centre of the trap, and we allow for the unlikely possibility of the spin flipping twice. The coupling matrix element V can be related to the Rabi frequency, $\Omega = V/\hbar$. For a microwave electric field of 100 V m^{-1} (giving a vacuum intensity of 1.3 mW cm^{-2}), B_1 is about $0.33 \mu\text{T}$ and the Rabi frequency is approximately $1.5 \times 10^4 \text{ rad s}^{-1}$. Simulations do not lead to a simple exponential decay of trapped population when the microwaves are present, because antihydrogen trajectories differ in how they pass through the resonance volume. As a rough estimate, a microwave intensity of 2 mW cm^{-2} gives a flip rate of the order of 1 s^{-1} .

Default criteria for annihilation event identification. The detector tracks the trajectories of charged pions that are produced when released antihydrogen atoms encounter matter in the Penning trap electrodes and annihilate. A reconstruction algorithm that considers track topology is then used to discriminate between pion tracks and cosmic ray events, and ultimately to locate the spatial position ('vertex') of each annihilation event¹⁷. The detector and the 'default criteria' for the event discrimination procedure have been extensively described previously^{6,17}.

Alternative criteria for annihilation event identification. We use a bagged decision tree classifier, in the random forest approach^{18–20}, to separate antiproton annihilations on the trap walls from cosmic ray events. Nine variables are used for classification: (1) the radial and (2) the azimuthal coordinates of the reconstructed annihilation vertex, if present, (3) the total number of channels registering 'hits' by charged particles, (4) the number of three-hit combinations used as track candidates, (5) the number of reconstructed tracks, (6) the sum of the squared residual distances of hits from a fitted straight line, and three topological variables. The topological variables comprise (7) a sphericity variable, (8) the cosine of the angle between the event axis and the detector axis, and (9) the angle between the vertical and the projection of the event axis onto the transverse (x – y) plane.

The sphericity variable is defined as the quantity $\frac{3}{2}(\lambda_2 + \lambda_3)$. Here $\lambda_1 \geq \lambda_2 \geq \lambda_3$ are the eigenvalues of the tensor $S^{\alpha\beta} = \left(\sum_i^N p_i^\alpha p_i^\beta |\mathbf{p}_i|^{-2} \right) / N$, where p_i^α is the component α (where $\alpha = x, y, z$) of the momentum associated with the i th track.

The event axis is defined as the line passing through the centre of the detector and oriented along the eigenvector associated with λ_1 .

The random forest event-selection criteria have been determined by maximizing a sensitivity figure of merit²¹. Compared to the 'default' selection, this method is about ten times more effective in rejecting cosmic background, while retaining 75% of the signal. For Fig. 4a, based on dynamical simulations, we require the event's axial position z to be less than 6 cm away from the trap centre. This requirement affects the signal only marginally and further suppresses the background by a factor of three, resulting in a cosmic rate of $(1.7 \pm 0.3) \times 10^{-3} \text{ s}^{-1}$. For Fig. 4b we select an annihilation candidate if it falls within $0 < t < 30 \text{ s}$ (the first microwave sweep).

- Dehmelt, H. Nobel lecture: experiments with an isolated subatomic particle at rest. *Rev. Mod. Phys.* **62**, 525–530 (1990).
- Andresen, G. B. *et al.* Evaporative cooling of antiprotons to cryogenic temperatures. *Phys. Rev. Lett.* **105**, 013003 (2010).
- Andresen, G. B. *et al.* Autoresonant excitation of antiproton plasmas. *Phys. Rev. Lett.* **106**, 025002 (2011).
- Tinkle, M. D., Greaves, R. G., Surko, C. M., Spencer, R. L. & Mason, G. W. Low-order modes as diagnostics of spheroidal non-neutral plasmas. *Phys. Rev. Lett.* **72**, 352–355 (1994).
- Andresen, G. B. *et al.* Antihydrogen annihilation reconstruction with the ALPHA silicon detector. *Nucl. Instrum. Meth. A* (submitted).
- Breiman, L. Random forests. *Mach. Learn.* **45**, 5–32 (2001).
- Narsky, I. StatPatternRecognition: a C++ package for statistical analysis of high energy physics data. Preprint at <http://arxiv.org/abs/physics/0507143> (2005).
- Narsky, I. Optimization of signal significance by bagging decision trees. Preprint at <http://arxiv.org/abs/physics/0507157> (2005).
- Punzi, G. Sensitivity of searches for new signals and its optimization. In *Proc. PHYSTAT2003: Statistical Problems in Particle Physics, Astrophysics, and Cosmology* 79–83 Preprint at <http://arxiv.org/abs/physics/0308063> (2003).

Electron tomography at 2.4-ångström resolution

M. C. Scott^{1*}, Chien-Chun Chen^{1*}, Matthew Mecklenburg^{1*}, Chun Zhu¹, Rui Xu¹, Peter Ercius², Ulrich Dahmen², B. C. Regan¹ & Jianwei Miao¹

Transmission electron microscopy is a powerful imaging tool that has found broad application in materials science, nanoscience and biology^{1–3}. With the introduction of aberration-corrected electron lenses, both the spatial resolution and the image quality in transmission electron microscopy have been significantly improved^{4,5} and resolution below 0.5 ångströms has been demonstrated⁶. To reveal the three-dimensional (3D) structure of thin samples, electron tomography is the method of choice^{7–11}, with cubic-nanometre resolution currently achievable^{10,11}. Discrete tomography has recently been used to generate a 3D atomic reconstruction of a silver nanoparticle two to three nanometres in diameter¹², but this statistical method assumes prior knowledge of the particle's lattice structure and requires that the atoms fit rigidly on that lattice. Here we report the experimental demonstration of a general electron tomography method that achieves atomic-scale resolution without initial assumptions about the sample structure. By combining a novel projection alignment and tomographic reconstruction method with scanning transmission electron microscopy, we have determined the 3D structure of an approximately ten-nanometre gold nanoparticle at 2.4-ångström resolution. Although we cannot definitively locate all of the atoms inside the nanoparticle, individual atoms are observed in some regions of the particle and several grains are identified in three dimensions. The 3D surface morphology and internal lattice structure revealed are consistent with a distorted icosahedral multiply twinned particle. We anticipate that this general method can be applied not only to determine the 3D structure of nanomaterials at atomic-scale resolution^{13–15}, but also to improve the spatial resolution and image quality in other tomography fields^{7,9,16–20}.

Since its introduction in 1968, electron tomography has been primarily used to determine the 3D structure of biological samples^{7,9}. In the past decade, electron tomography has been increasingly applied in materials science and nanoscience through the use of scanning transmission electron microscopy (STEM)^{8,10,11}. The highest resolution at present achieved by STEM tomography is around 1 nm in three dimensions^{10,11}, although slightly higher resolution has been obtained in a study of fullerene-like nanostructures with bright-field electron tomography²¹. A general electron tomography method with atomic-scale resolution, however, has not been demonstrated for several reasons. First, aligning the projections of a tomographic tilt series to a common axis with atomic level precision is technically challenging. Second, radiation damage limits the number of projections that can be acquired from a single object^{13,22}. Last, specimens cannot usually be tilted beyond $\pm 79^\circ$, preventing acquisition of data from the 'missing wedge'^{7–11}. Here we demonstrate that these limitations can be overcome or alleviated by applying a novel alignment approach and an iterative tomographic reconstruction method to a tilt series obtained via annular dark field (ADF)-STEM^{23,24}.

The conventional alignment approach used in electron tomography either relies on fiducial markers such as colloidal gold beads or is based on the cross-correlation between neighbouring projections^{7,9}. To our

knowledge, neither of these alignment approaches can achieve atomic-level precision. To overcome this limitation, we have developed a method based on the centre of mass, which is able to align the projections of a tilt series at atomic-level accuracy even with noise (Methods). To address the other two difficulties mentioned above, we have implemented a data acquisition and tomographic reconstruction method, termed equally sloped tomography^{16,18–20,25} (EST). Compared to conventional tomography, which reconstructs a 3D object from a tilt series of projections with constant angular increments, EST acquires a tilt series with equal slope increments, and then iterates back and forth between real and reciprocal space (Methods). In each iteration, constraints such as the sample boundary (that is, the support) and positivity of the Coulomb potential are applied in real space, while the measured projectional slices (that is, the Fourier transform of the projections) are enforced in reciprocal space. Each iteration is monitored by an error metric, and the algorithm is terminated after reaching a maximum number of iterations.

To test the feasibility of achieving a high-resolution tomographic reconstruction by the centre-of-mass and EST methods, we conducted numerical simulations on an ~ 5 -nm gold nanoparticle with icosahedral symmetry and a total of 3,871 atoms (Supplementary Figs 3a, 4a, c, e). A tilt series of 55 projections was obtained from the particle using multislice STEM calculations²⁶ (energy, 300 keV; spherical aberration, 1.2 mm; illumination semi-angle, 7.98 mrad; defocus, 48.6 nm; detector inner and outer angles, 13 and 78 mrad). To minimize nonlinear intensity contributions caused by dynamical scattering and electron channelling²⁷, projections along zone axis orientations were avoided. The tilt angles range from -72.6° to $+72.6^\circ$ with equal slope increments. To more closely approximate realistic experimental conditions, several additional modifications were made to generate the simulated data. First, the tilt angles were continuously shifted from 0° to 0.5° over the process of the tilt series and the magnification of the images was continuously changed from 0 to 0.2%. Second, each projection in the tilt series was arbitrarily shifted along the x and y axes, where the electron beam direction is parallel to the z axis. Last, Poisson noise was added to the projections of the tilt series with a total electron dose of $6.1 \times 10^6 \text{ e} \text{ \AA}^{-2}$. Supplementary Fig. 3 shows a linear projection of the model at 0° and the corresponding multislice STEM projection. The apparent increase of the atom size in the multislice projection was mainly caused by the nonlinear and diffraction effects in the nanoparticle.

The 55 projections were aligned to a common tilt axis with the centre-of-mass method, and were then reconstructed with the EST algorithm. Supplementary Fig. 4b, d, f shows three 2.5-Å-thick central slices of the 3D reconstruction in the x - y , z - x and z - y planes. Although the missing wedge problem is not completely solved (the top and bottom parts in Supplementary Fig. 4f) and the size of the reconstructed atoms is increased mainly due to the nonlinear and diffraction effects, the atomic positions and grain boundaries in the 3D reconstruction are consistent with the model. The simulation results indicate that the centre-of-mass and EST methods can be used

¹Department of Physics and Astronomy and California NanoSystems Institute, University of California, Los Angeles, California 90095, USA. ²National Center for Electron Microscopy, Lawrence Berkeley National Laboratory, Berkeley, California 94720, USA.

*These authors contributed equally to this work.

to achieve an atomic-scale resolution reconstruction from a tilt series of 55 projections with a missing wedge, nonlinear effects, Poisson noise and experimental errors.

Next, the centre-of-mass and EST methods were applied to experimental tilt series acquired from gold nanoparticles. Nanoparticles are an important class of materials with properties different from either molecules or bulk solids^{13–15}, and nano-gold is among the most widely studied of this class of material owing to its broad applications in chemistry, biology, materials science, nanoscience and nanotechnology²⁸. In this study, we imaged gold particles with a diameter of ~ 10 nm because smaller particles are not as stable under an electron beam^{13,22}. To reduce the electron dose, we used a low-exposure data acquisition scheme with a 300-keV ADF-STEM (Methods). When focusing an image, a nearby nanoparticle was first viewed (not the particle of interest), thus reducing the unnecessary radiation dose to the particle under study. Using this scheme, we acquired several tomographic tilt series of gold nanoparticles. Supplementary Fig. 5 shows a tilt series of 69 projections and their Fourier transforms, with a total electron dose of $\sim 7.6 \times 10^6 \text{ e} \text{ \AA}^{-2}$. Supplementary Fig. 6 shows three 0° projections and their Fourier transforms measured during the acquisition of this tilt series to monitor the effects of radiation damage. Although some minor shape changes occurred, the crystal lattice structure of the particle remained consistent throughout the experiment.

To investigate the nonlinear effects in the experiment, we simulated an ~ 10 -nm gold particle with icosahedral symmetry and performed multislice STEM calculations on an 11.5- \AA -thick slab of this particle²⁶ (Supplementary Fig. 7). Although the atom size was increased, mainly owing to the nonlinear diffraction and dynamical scattering effects, the multislice STEM projection exhibits a crystal lattice structure consistent with the model. We then calculated a tilt series for a 2.5- \AA central slice using the multislice simulations. The tilt series consists of 69 projections with a tilt range of $\pm 72.6^\circ$. Supplementary Fig. 8 shows the model and reconstructed slices. The atomic positions and the

internal grain boundaries are resolved, except in a very few places owing to the nonlinear effects in the projections.

After investigating the nonlinear effects, we performed post data analysis of the experimental tilt series (Methods), and aligned the projections with the centre-of-mass method. To reconstruct the 3D structure, we first estimated a loose 3D support, defined to be larger than the particle boundary. After 500 iterations of the EST algorithm, the reconstruction was used to determine a tight support (that is, close to the true boundary of the particle). Using the tight support, we ran another 500 iterations and obtained a final 3D structure. To examine the quality of the reconstruction, we calculated 69 projections from the final 3D structure and found the average normalized discrepancy with the measured projections to be 6.7% (Supplementary Methods and Supplementary Table 1). Representative measured and calculated projections at different particle orientations are shown in Fig. 1 and Supplementary Fig. 9. Although there are some minor differences between the two projections, the overall shape and lattice structure agree well. To more rigorously examine the accuracy of the reconstruction, an EST reconstruction was performed from 68 experimental projections by removing the 7.1° projection. The 3D reconstruction was then projected back to calculate the projection at 7.1° , which is consistent with the experimentally measured one (Supplementary Fig. 10).

To estimate the resolution achieved in the reconstruction, we chose a 3.36- \AA -thick central slice in the x - y plane. Figure 2a, b shows the slice and its Fourier transform, in which the distance between two neighbouring atom columns and the location of the Bragg peaks indicate that a resolution of 2.4 \AA was achieved in the x and y directions. To estimate the resolution along the z axis (beam direction), we selected a 3.36- \AA -thick slice with the horizontal axis along the z axis (Fig. 2c, d). The resolution close to the z axis was determined to be 2.4 \AA . Individual atoms are visible in some regions of the slices, but not all atoms can be identified in the slices. Supplementary Fig. 11 shows two 3.36- \AA -thick slices of the nanoparticle in a different orientation,

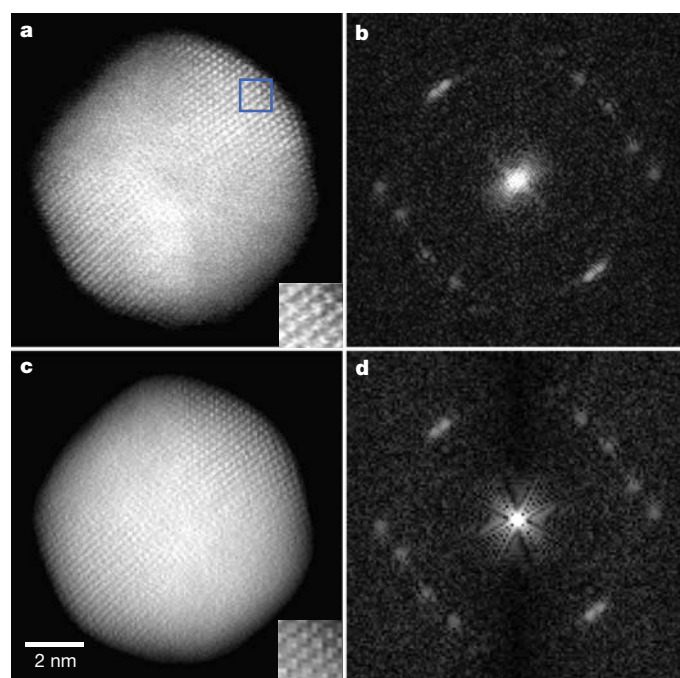


Figure 1 | Evaluation of the 3D reconstruction quality. a–d, Representative measured (a) and calculated (c) projections and their Fourier transforms (respectively b, d) at tilt angle 7.1° . Insets in a and c show the projected atomic positions inside the blue square in the main panel. The overall shape of the nanoparticle and the location of the Bragg peaks agree well, indicating a good quality 3D reconstruction. This gold nanoparticle is the same as studied in Figs 2–4.

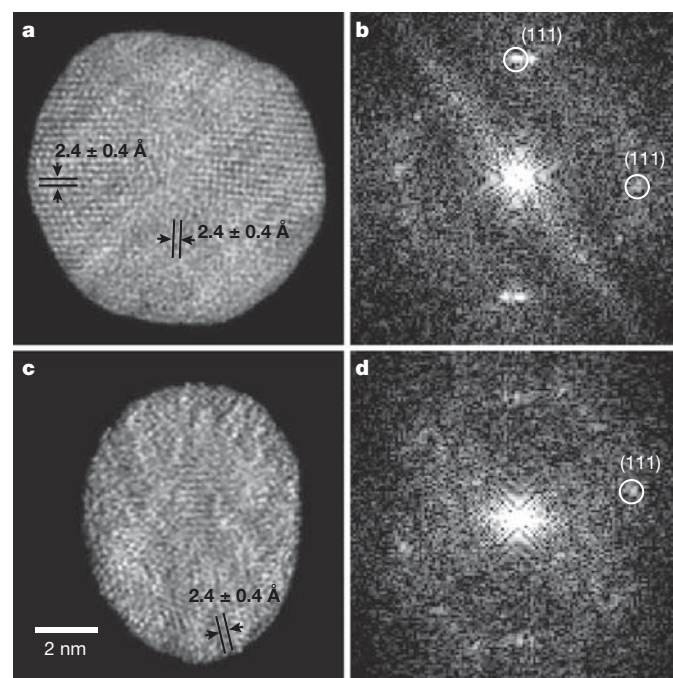


Figure 2 | Estimation of the 3D resolution of the reconstruction of the gold nanoparticle. a, b, A 3.36- \AA thick central slice in the x - y plane (a) and its Fourier transform (b), indicating that a resolution of 2.4 \AA corresponding to the gold (111) lattice was achieved along the x and y axes. c, d, A 3.36- \AA -thick slice in the z - y plane (c) and its Fourier transform (d) where the horizontal axis is along the z axis (beam direction). The resolution in the z axis was estimated to be 2.4 \AA . Individual atoms are visible in some regions of the slices, but not all atoms can be identified in the slices.

exhibiting crystal lattice structure that is not present in Fig. 2a and c. The apparent flattening of the particle along the beam axis was also observed in the 3D reconstructions (Fig. 2 and Supplementary Movie 1), and was probably caused by the interaction between the nanoparticle and the Si substrate.

To visualize the internal structure and the morphology of the gold nanoparticle, we generated 3D volume and iso-surface renderings of the reconstruction, in which both surface and internal lattice structures are visible (Supplementary Movies 1 and 2). Figure 3a, b shows volume renderings of the nanoparticle and their Fourier transforms (insets) at the two- and three-fold symmetry orientations. The corresponding iso-surface renderings at the same orientations are shown in Fig. 3c and d. The overall 3D shape and facets of the nanoparticle are consistent with an icosahedron (insets in Fig. 3c and d). To identify internal 3D grains, we applied the 3D Fourier transform to the reconstruction. By identifying the Bragg peaks of each major grain and applying the 3D inverse Fourier transform to the selected Bragg peaks, we determined four major 3D grains inside the gold nanoparticle (Methods). Figure 4 and Supplementary Movie 3 show a volume rendering of the four grains in three dimensions, in which grains 1, 2 and grains 3, 4 are related by mirror-reflection across the horizontal interfaces marked by dotted lines. The angle enclosed by close-packed planes across these interfaces was measured to be $69.9^\circ \pm 0.8^\circ$ between grains 1 and 2, and $71.3^\circ \pm 0.8^\circ$ between grains 3 and 4, both of which are consistent with the angle for a face-centred-cubic twin boundary (70.53°). By applying the same method to some other Bragg peaks, we identified 3D grains in the top and bottom parts of the particle (Supplementary Fig. 12). The surface morphology and the internal lattice structures suggest that this is a distorted icosahedral multiply twinned particle, typically found for nano-gold in the size range above 10 nm (ref. 29).

By combining the centre-of-mass alignment technique and the EST reconstruction method with an ADF-STEM, we have determined the 3D structure of a ~ 10 -nm gold nanoparticle at 2.4 Å resolution from a tilt series of 69 projections with a missing wedge. Several grains are identified inside the nanoparticle in three dimensions. Although individual

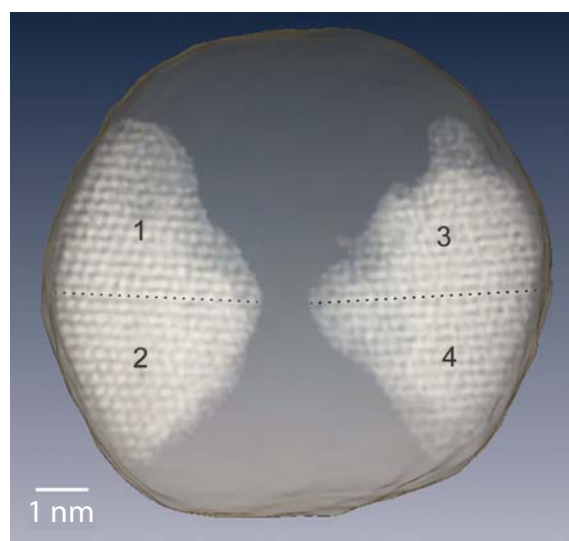


Figure 4 | Identification of four major grains inside the gold nanoparticle in three dimensions. Grains 1, 2 and grains 3, 4 are related by mirror-reflection across the horizontal interfaces marked by dotted lines. The angle enclosed by close-packed planes across these interfaces was measured to be $69.9^\circ \pm 0.8^\circ$ between grains 1 and 2, and $71.3^\circ \pm 0.8^\circ$ between grains 3 and 4, both of which are consistent with the angle for a face-centred cubic twin boundary (70.53°).

atoms are visible in some regions of the nanoparticle, we cannot definitively locate all of the atoms inside the particle. In order to identify all the atoms in the particle (estimated to be $\sim 23,800$) without using atomicity and bond information, a resolution higher than 2.4 Å is needed, which requires future developments. With aberration-corrected STEM^{4,23,24}, better 3D resolution and image quality should be achievable, but extended depth-of-field techniques may have to be applied to the tilt series before the EST reconstruction can be performed. Compared to atom-probe tomography³⁰, this non-destructive technique can not only handle isolated nanoparticles, but also provide the 3D local structure of complex nanomaterials at high resolution.

METHODS SUMMARY

Gold nanoparticles with a size of ~ 10 nm (Ted Pella) were supported on 5-nm-thick Si membranes (TEMwindows.com), which can withstand plasma cleaning for a longer period than carbon substrates to alleviate carbon contamination. Tomographic tilt series with equal slope increments were acquired from the gold nanoparticles by using an ADF-STEM (FEI Titan 80-300). The tilt angles (θ) were determined by^{16,25} $\theta = -\tan^{-1}[(N+2-2n)/N]$ for $n = 1, \dots, N$ and $\theta = \pi/2 - \tan^{-1}[(3N+2-2n)/N]$ for $n = N+1, \dots, 2N$ with $N = 32$ or 64 in this experiment. The angles beyond $\pm 72.6^\circ$ were not accessible owing to the geometry of the support grid. To monitor the radiation induced stability effect, several projections at the same particle orientation were measured during the acquisition of each tilt series (Supplementary Fig. 6). To improve the 3D reconstruction and enhance the signal to noise ratio, the background of the projections was subtracted and 2×2 pixel binning was performed for each projection. After post data analysis, the tilt series was aligned with the centre-of-mass method (Methods). The reconstruction of the aligned tilt series was conducted using the EST method, which iterated back and forth between real and reciprocal space with constraints enforced in real space and measured data in reciprocal space (Methods, Supplementary Methods and Supplementary Fig. 2). To examine the reconstruction quality, the reconstructed 3D structure was projected back to obtain 69 projections, which were compared to the corresponding measured ones. An average R_{real} (Supplementary Methods) was calculated to be 6.7%, indicating a good quality reconstruction (Fig. 1, Supplementary Table 1).

Full Methods and any associated references are available in the online version of the paper at www.nature.com/nature.

Received 18 April 2011; accepted 9 February 2012.

1. Williams, D. B. & Carter, C. B. *Transmission Electron Microscopy: A Textbook for Materials Science* 2nd edn (Springer, 2009).

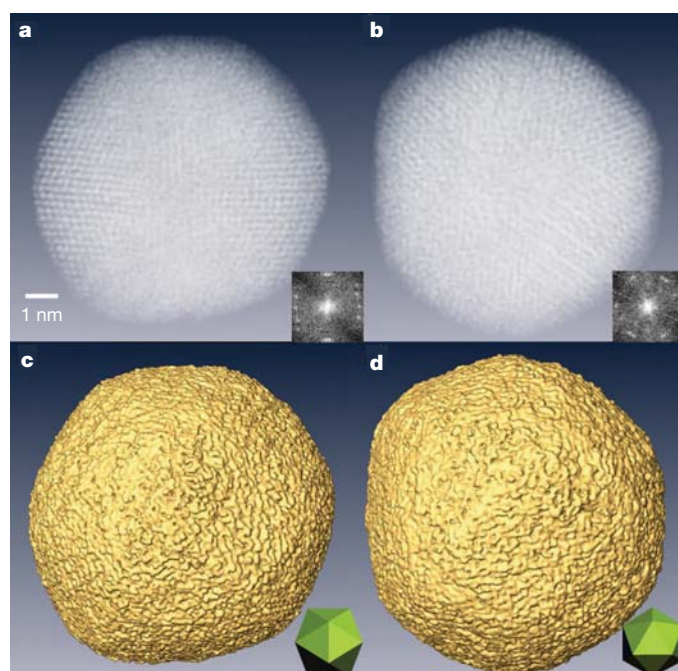


Figure 3 | 3D structure of the reconstructed gold nanoparticle. a, b, 3D volume renderings of the nanoparticle and their Fourier transforms (insets) at the two-fold (a) and three-fold (b) symmetry orientations. c, d, Iso-surface renderings of the nanoparticle at the two-fold (c) and three-fold (d) symmetry orientations. Insets show a model icosahedron at the same orientations.

2. Spence, J. C. H. *Experimental High-Resolution Electron Microscopy* 3rd edn (Oxford Univ. Press, 2003).
3. Frank, J. *Three-Dimensional Electron Microscopy of Macromolecular Assemblies* (Oxford Univ. Press, 2006).
4. Batson, P. E., Dellby, N. & Krivanek, O. L. Sub-ångström resolution using aberration corrected electron optics. *Nature* **418**, 617–620 (2002).
5. Haider, M. *et al.* Electron microscopy image enhanced. *Nature* **392**, 768–769 (1998).
6. Erni, R., Rossell, M. D., Kisielowski, C. & Dahmen, U. Atomic-resolution imaging with a sub-50-pm electron probe. *Phys. Rev. Lett.* **102**, 096101 (2009).
7. Frank, J. *Electron Tomography* (Plenum, 1992).
8. Midgley, P. A. & Weyland, M. 3D electron microscopy in the physical sciences: the development of Z-contrast and EFTEM tomography. *Ultramicroscopy* **96**, 413–431 (2003).
9. Lucić, V., Förster, F. & Baumeister, W. Structural studies by electron tomography: from cells to molecules. *Annu. Rev. Biochem.* **74**, 833–865 (2005).
10. Midgley, P. A. & Dunin-Borkowski, R. E. Electron tomography and holography in materials science. *Nature Mater.* **8**, 271–280 (2009).
11. Arslan, I., Yates, T. J. V., Browning, N. D. & Midgley, P. A. Embedded nanostructures revealed in three dimensions. *Science* **309**, 2195–2198 (2005).
12. Van Aert, S., Batenburg, K. J., Rossell, M. D., Erni, R. & Van Tendeloo, G. Three-dimensional atomic imaging of crystalline nanoparticles. *Nature* **470**, 374–377 (2011).
13. Marks, L. D. Experimental studies of small particle structures. *Rep. Prog. Phys.* **57**, 603–649 (1994).
14. Billinge, S. J. L. & Levin, I. The problem with determining atomic structure at the nanoscale. *Science* **316**, 561–565 (2007).
15. Yacamán, M. J., Ascencio, J. A., Liu, H. B. & Gardea-Torresdey, J. Structure shape and stability of nanometric sized particles. *J. Vac. Sci. Technol. B* **19**, 1091–1023 (2001).
16. Lee, E. *et al.* Radiation dose reduction and image enhancement in biological imaging through equally sloped tomography. *J. Struct. Biol.* **164**, 221–227 (2008).
17. Kak, A. C. & Slaney, M. *Principles of Computerized Tomographic Imaging* (SIAM, Philadelphia, 2001).
18. Fahimian, B. P., Mao, Y., Cloetens, P. & Miao, J. Low dose X-ray phase-contrast and absorption CT using equally-sloped tomography. *Phys. Med. Biol.* **55**, 5383–5400 (2010).
19. Mao, Y., Fahimian, B. P., Osher, S. J. & Miao, J. Development and optimization of regularized tomographic reconstruction algorithms utilizing equally-sloped tomography. *IEEE Trans. Image Process.* **19**, 1259–1268 (2010).
20. Jiang, H. *et al.* Quantitative 3D imaging of whole, unstained cells by using X-ray diffraction microscopy. *Proc. Natl Acad. Sci. USA* **107**, 11234–11239 (2010).
21. Bar Sadan, M. *et al.* Toward atomic-scale bright-field electron tomography for the study of fullerene-like nanostructures. *Nano Lett.* **8**, 891–896 (2008).
22. Bovin, J.-O., Wallenberg, R. & Smith, D. J. Imaging of atomic clouds outside the surfaces of gold crystals by electron microscopy. *Nature* **317**, 47–49 (1985).
23. Muller, D. A. Structure and bonding at the atomic scale by scanning transmission electron microscopy. *Nature Mater.* **8**, 263–270 (2009).
24. Pennycook, S. J. & Nellist, P. D. *Scanning Transmission Electron Microscopy: Imaging and Analysis* 1st edn (Springer, 2011).
25. Miao, J., Förster, F. & Levi, O. Equally sloped tomography with oversampling reconstruction. *Phys. Rev. B* **72**, 052103 (2005).
26. Kirkland, E. J. *Advanced Computing in Electron Microscopy* 2nd edn (Springer, 2010).
27. Howie, A. Diffraction channelling of fast electrons and positrons in crystals. *Phil. Mag.* **14**, 223–237 (1966).
28. Daniel, M. C. & Astruc, D. Gold nanoparticles: assembly, supramolecular chemistry, quantum-size-related properties, and applications toward biology, catalysis, and nanotechnology. *Chem. Rev.* **104**, 293–346 (2004).
29. Barnard, A. S., Young, N. P., Kirkland, A. I., van Huis, M. A. & Xu, H. Nanogold: a quantitative phase map. *ACS Nano* **3**, 1431–1436 (2009).
30. Arslan, I., Marquis, E. A., Homer, M., Hekmaty, M. & Bartelt, N. C. Towards better 3-D reconstructions by combining electron tomography and atom-probe tomography. *Ultramicroscopy* **108**, 1579–1585 (2008).

Supplementary Information is linked to the online version of the paper at www.nature.com/nature.

Acknowledgements We thank E. J. Kirkland for help with multislice STEM calculations, R. F. Egerton, Z. H. Zhou and J. A. Rodríguez for discussions and I. Atanasov for assistance in data acquisition. The tomographic tilt series were acquired at the Electron Imaging Center for NanoMachines of the California NanoSystems Institute. This work was partially supported by UC Discovery/TomoSoft Technologies (IT107-10166).

Author Contributions J.M. conceived the overall project; M.C.S., M.M., C.Z., B.C.R. and J.M. designed and conducted the experiments; C.Z., R.X., C.-C.C., P.E. and J.M. did multislice STEM calculations; C.-C.C. and J.M. performed the data analysis and image reconstruction; U.D., J.M., C.-C.C., M.C.S., M.M. and B.C.R. interpreted the results, and J.M., M.C.S., C.-C.C. and M.M. wrote the manuscript. All authors commented on the manuscript.

Author Information Reprints and permissions information is available at www.nature.com/reprints. The authors declare no competing financial interests. Readers are welcome to comment on the online version of this article at www.nature.com/nature. Correspondence and requests for materials should be addressed to J.M. (miao@physics.ucla.edu).

METHODS

Sample preparation. Gold nanoparticle solution with an average particle size of ~ 10 nm (Ted Pella) was sonicated for ~ 10 min to prevent aggregation. Five-nm-thick Si membranes (TEMwindows.com) were used as the particle substrates in the experiment. The thin membrane, with a size of $100 \times 1,500 \mu\text{m}$, is supported on a $100\text{-}\mu\text{m}$ -thick Si frame, allowing for a maximum tilt range of $\pm 83^\circ$. To avoid breaking the membrane, a micromanipulator was used to place a small drop of solution onto the outer frame of the Si grid. After gently moving the drop onto the membrane, it was removed and not allowed to dry and leave excessive gold particles and contaminants. The Si grids were cleaned pre-deposition in a Gatan Solarus plasma cleaner (Model 950) for 20 s using a standard H_2/O_2 recipe. To further ensure removal of contaminant sources, the sample holder (Fischione Model 2020) was plasma-cleaned for an hour before data acquisition using the same recipe.

ADF-STEM. STEM images of gold nanoparticles were acquired on a FEI Titan 80-300 (energy, 300 keV; spherical aberration, 1.2 mm; illumination semi-angle, 7.98 mrad; and defocus, 48.6 nm). The 70 pA electron beam was focused to a probe with a $50 \mu\text{m}$ probe-forming aperture (C2) and rastered over the sample. The scattered electrons were captured by a Fischione Model 3000 ADF detector with angles between 13 mrad and 78 mrad from the optical axis. The use of ADF angles was to improve the signal to noise ratio with a low current electron beam. The effects of nonlinear image intensities and diffraction contrast were carefully determined by multi-slice simulations. The maximum tilt angles were limited by the holder to $\pm 75^\circ$.

Low-exposure acquisition of tomographic tilt series. In order to reduce vibration and drift during data acquisition, the sample holder was allowed to settle for one hour after insertion into the microscope, and also for several minutes after moving to each new angle. Tilt series were acquired by manually changing the angle with equal slope increments. The tilt angles (θ) were determined by^{16,25} $\theta = -\tan^{-1}[(N+2-2n)/N]$ for $n = 1, \dots, N$ and $\theta = \pi/2 - \tan^{-1}[(3N+2-2n)/N]$ for $n = N+1, \dots, 2N$ with $N = 32$ or 64 in this experiment. To focus each projectional image during data acquisition, a nearby particle was used (rather than the particle of interest) to reduce the radiation dose to the particle. By using this low-exposure data acquisition scheme, we have obtained several tomographic tilt series. Supplementary Fig. 5 shows the tilt series used in this reconstruction with 69 projections and a tilt range of $\pm 72.6^\circ$. A representative sinogram of the tilt series is shown in Supplementary Fig. 13. The probe current was ~ 70 pA with a dwell time of $45 \mu\text{s}$ per pixel, and the magnification of each projection was 5.2×10^6 . Since the pixel size in STEM mode can vary, a calibration image of the particle was taken in TEM mode, and the STEM pixel size was determined to be 0.42 \AA . The total electron dose of the tilt series was estimated to be $\sim 7.6 \times 10^6 \text{ e}^- \text{ \AA}^{-2}$. Supplementary Fig. 6 shows three 0° projections measured during the acquisition of this tilt series. Although some minor shape changes occurred, the crystal lattices of the particle remained consistent throughout the experiment.

Post data analysis. In order to apply the EST method, the background surrounding the nanoparticle in each projection has to be subtracted. To systematically eliminate the background, we first projected all the projections onto the tilt axis and obtained a set of 1D curves. We then determined the optimal cut-off value for background subtraction in each projection by maximizing the cross-correlation among these 1D curves. After background subtraction, we binned 2×2 pixels into 1 pixel, which was used to enhance the signal to noise ratio in the projections and improve the EST reconstruction. The background subtracted and binned projections with pixel size of 0.84 \AA were aligned using the centre-of-mass approach and reconstructed with the EST method.

The centre-of-mass alignment method. To achieve an atomic scale resolution reconstruction, the projections in a tilt series have to be aligned to a common axis (not necessarily the true tilt axis) with atomic level precision in both the x and y axes, where the y axis represents the tilt axis and the z axis the beam direction. To align the tilt series along the y axis, the projections were first projected onto the y axis and a set of 1D curves was generated. We then chose a 1D curve at 0° as a reference, and aligned the remaining curves to the reference. To align the projections along the x axis, we developed a method based on the centre of mass. When a 3D object is tilted around the y axis from 0° to 360° , the centre-of-mass of the object forms a circle. However, in the special geometry where the centre of mass coincides with the origin of the x axis, this circle becomes a point. To determine the centre of mass in this special geometry, we projected each 2D projection onto the x axis, chose a pixel as the origin and calculated the centre of mass (CM) along the x axis, $x_{\text{CM}} = \sum_i x_i \rho(x_i) / \sum_i \rho(x_i)$, where $\rho(x_i)$ is the Coulomb potential at position x_i . We then shifted this projection to set x_{CM} as the new origin of the x axis. Through repeating this process for all projections, we aligned the tilt series to the common axis that coincides with the new origin. Both our simulation and experimental results indicate that the centre-of-mass alignment is a general method and can align the projections of a tilt series at atomic level accuracy, even

with relatively high noise and the nonlinear effects (Fig. 1, Supplementary Figs 4 and 8, and Supplementary Table 1).

The EST method. When the projections of a tilt series use equal slope increments, it has been shown that a direct fast Fourier transform, the pseudopolar fast Fourier transform (PPFFT)³¹, exists between a pseudopolar grid and a Cartesian grid. Supplementary Fig. 1 shows a pseudopolar grid and the PPFFT. For an $N \times N$ Cartesian grid, the corresponding pseudopolar grid is defined by a set of $2N$ lines, each line consisting of $2N$ grid points mapped out on N concentric squares. The $2N$ lines are subdivided into a horizontal group (in blue) defined by $y = sx$, where s is the slope and $|s| \leq 1$, and a vertical group (in red) defined by $x = sy$, where $|s| \leq 1$; the horizontal and vertical groups are symmetric under the interchange of x and y , and $\Delta s = 2/N$. When these conditions are met, the PPFFT and its inverse algorithm are mathematically faithful³¹. Note that the PPFFT and its inverse algorithm were originally developed to interpolate tomographic projections from a polar to a Cartesian grid in reciprocal space. The idea of acquiring tomographic tilt-series at equal slope increments and then combining the PPFFT with iterative algorithms for 3D image reconstructions was first suggested in 2005 (ref. 25).

Compared to other data acquisition approaches, such as the Saxton scheme³², the EST data acquisition approach is different in that it acquires projections with equal slope increments in order to use the PPFFT. Although the PPFFT and its inverse provide an algebraically faithful way to do the fast Fourier transform between the Cartesian and pseudopolar grids, three difficulties limit its direct application to electron tomography. First, the tilt range has to be from -90° to $+90^\circ$. Second, the number of projections in a tilt series needs to be $2N$ for an $N \times N$ object. Third, the grid points past the resolution circle (dashed circle in Supplementary Fig. 1) cannot be experimentally determined. We overcame these limitations by combining the PPFFT with an iterative process^{16,18–20,25}. Supplementary Fig. 2 shows the schematic layout of the iterative EST method. We first convert the electron micrograph projections to Fourier slices in the pseudopolar grid. As illustrated in Supplementary Fig. 1, the distance between the sampling points on the individual $2N$ lines of the pseudopolar grid varies from line to line. In order to calculate the Fourier slices from the projections, the fractional Fourier transform is used to vary the output sampling distance of the Fourier slices³³. By applying the inverse PPFFT, we obtain a 3D image in real space. A 3D support is defined to separate the object from a zero region where the size of the zero region is proportional to the over-sampling of the projections³⁴. The negative-valued voxels inside the support and the voxel values outside the support are set to zero, and a new 3D image is obtained. The forward PPFFT is applied to the new image and a set of calculated Fourier slices is obtained. We then replace the corresponding calculated Fourier slices with the measured ones, and the remaining slices are kept unchanged. The iterative process is then repeated with each iteration monitored by an R_{recip} (Supplementary Methods). The algorithm is terminated after reaching a maximum number of iterations. A more detailed description of the EST method is presented in Supplementary Methods. Compared to phase retrieval in coherent X-ray/electron diffraction imaging^{20,35–37}, the EST method aims to solve the missing data by combining an iteration process with the PPFFT algorithm.

Identification of the major 3D grains inside the nanoparticle. The following procedures were used to determine the major 3D grains inside the gold nanoparticle. (1) Apply the 3D Fourier transform to the reconstructed nanoparticle and identify the Bragg peaks corresponding to a major grain. (2) Use small spheres with soft edges to select these Bragg peaks and set other values to zero. (3) Apply the 3D inverse Fourier transform to the selected Bragg peaks and obtain a 3D image. (4) Convolve the 3D image with a Gaussian filter and choose a cut-off value to determine the 3D shape of the grain. (5) Use the 3D shape to identify the corresponding 3D grain in the reconstructed nanoparticle. (6) Repeat steps 1–5 to determine other major grains.

1. Averbuch, A., Coifman, R. R., Donoho, D. L., Israeli, M. & Shkolnisky, Y. A framework for discrete integral transformations I — the pseudopolar Fourier transform. *SIAM J. Sci. Comput.* **30**, 785–803 (2008).
2. Saxton, W. O., Baumeister, W. & Hahn, M. Three-dimensional reconstruction of imperfect two-dimensional crystals. *Ultramicroscopy* **13**, 57–70 (1984).
3. Bailey, D. H. & Swartztrauber, P. N. The fractional Fourier transform and applications. *SIAM Rev.* **33**, 389–404 (1991).
4. Miao, J., Sayre, D. & Chapman, H. N. Phase retrieval from the magnitude of the Fourier transform of non-periodic objects. *J. Opt. Soc. Am. A* **15**, 1662–1669 (1998).
5. Miao, J., Charalambous, P., Kirz, J. & Sayre, D. Extending the methodology of X-ray crystallography to allow imaging of micrometre-sized non-crystalline specimens. *Nature* **400**, 342–344 (1999).
6. Miao, J., Ohsuna, T., Terasaki, O., Hodgson, K. O. & O'Keefe, M. A. Atomic resolution three-dimensional electron diffraction microscopy. *Phys. Rev. Lett.* **89**, 155502 (2002).
7. Zuo, J. M., Vartanyants, I., Gao, M., Zhang, R. & Nagahara, L. A. Atomic resolution imaging of a carbon nanotube from diffraction intensities. *Science* **300**, 1419–1421 (2003).

Large-scale vortex lattice emerging from collectively moving microtubules

Yutaka Sumino^{1*}, Ken H. Nagai^{2*}, Yuji Shitaka³, Dan Tanaka^{4‡}, Kenichi Yoshikawa⁵, Hugues Chaté⁶ & Kazuhiro Oiwa^{3,7}

Spontaneous collective motion, as in some flocks of bird and schools of fish, is an example of an emergent phenomenon. Such phenomena are at present of great interest^{1–5} and physicists have put forward a number of theoretical results that so far lack experimental verification^{6–8}. In animal behaviour studies, large-scale data collection is now technologically possible, but data are still scarce and arise from observations rather than controlled experiments. Multicellular biological systems, such as bacterial colonies or tissues^{9,10}, allow more control, but may have many hidden variables and interactions, hindering proper tests of theoretical ideas. However, in systems on the subcellular scale such tests may be possible, particularly in *in vitro* experiments with only few purified components^{11–13}. Motility assays, in which protein filaments are driven by molecular motors grafted to a substrate in the presence of ATP, can show collective motion for high densities of motors and attached filaments. This was demonstrated recently for the actomyosin system^{14,15}, but a complete understanding of the mechanisms at work is still lacking. Here we report experiments in which microtubules are propelled by surface-bound dyneins. In this system it is possible to study the local interaction: we find that colliding microtubules align with each other with high probability. At high densities, this alignment results in self-organization of the microtubules, which are on average 15 μm long, into vortices with diameters of around 400 μm . Inside the vortices, the microtubules circulate both clockwise and anticlockwise. On longer timescales, the vortices form a lattice structure. The emergence of these structures, as verified by a mathematical model, is the result of the smooth, reptation-like motion of single microtubules in combination with local interactions (the nematic alignment due to collisions)—there is no need for long-range interactions. Apart from its potential relevance to cortical arrays in plant cells^{16,17} and other biological situations, our study provides evidence for the existence of previously unsuspected universality classes of collective motion phenomena.

Our experimental *in vitro* motility assay consisted of dynein motor proteins grafted to a glass surface at a density of 750–2,500 molecules per square micrometre and to fluorescently labelled, stabilized microtubules (details can be found in Supplementary Methods). We used inner-arm dynein subspecies c (dynein c) purified from *Chlamydomonas* flagella. This drove the microtubules, with their plus ends leading, at a mean velocity of $\sim 12 \mu\text{m s}^{-1}$ *in vitro* at 23 °C in the presence of 1 mM ATP, while rotating them around their longitudinal axis in a clockwise direction as viewed from their minus ends^{18,19}. ('Plus' and 'minus' here refer to microtubule polarity.) When introduced in a flow cell, the microtubules did not move and bound to the dynein-c-coated glass surface in the absence of ATP^{18,19}. On addition of 1 mM Mg-ATP, they started moving smoothly on the surface at a fairly constant speed. No preferred direction of isolated microtubule motion was observed. The

smoothness and isotropy of motion reflect the fact that relatively many, randomly oriented, dyneins were attached at any time to a given microtubule.

Using microtubules at a concentration of 40 $\mu\text{g ml}^{-1}$, which is a few times greater than in conventional assays¹⁸, we found the density of attached microtubules to be $0.05 \mu\text{m}^{-2}$ (there were five microtubules, $15.6 \pm 7.3 \mu\text{m}$ in length (mean \pm s.d., $n = 257$), per 100 μm^2). On addition of ATP (at 0 min), we observed many aligning collisions (discussed further below) that gradually led to streams along which dozens of microtubules moved in both directions. The size of a stream increased in time (by more than 10 μm in width and more than 100 μm in length) (12 min; Fig. 1a). The streams started to meander over the surface typically after 10 min. At 10–20 min, some vortices appeared (17 min; Fig. 1a and Supplementary Movie 1) and eventually covered the flow cell almost entirely, except for the area less than 500 μm away from the boundaries (Fig. 1b). The shape of the vortices gradually changed over time but their diameters were almost constant, at 400 μm (major axis, $443 \pm 64 \mu\text{m}$ (s.d., $n = 40$); minor axis, $390 \pm 59 \mu\text{m}$ (s.d., $n = 40$)). At this late stage, the vortices showed a tendency to arrange their positions into a hexagonal lattice, although not perfectly. A given vortex consists of a sparse core and a dense peripheral annulus inside which microtubules move both clockwise and anticlockwise in small streams and slide past each other (Fig. 2 and Supplementary Movie 2). That is, the streams show nematic rather than polar order. Microtubules were never trapped in a vortex: they would circulate inside one vortex for some time before moving to a neighbouring one or travelling farther and starting to revolve around a more distant core.

As the first step in understanding vortex formation, we examined the interactions between microtubules. We decreased their density to 0.5–1 $\mu\text{g ml}^{-1}$ to focus on pair interactions between isolated microtubules. We examined 393 pair collision events. No significant interaction was detected until the pair collided, indicating that long-range, 'hydrodynamic' effects are negligible. On collision, strong interactions due to volume exclusion occurred overwhelmingly (80% of events), leading either to alignment or anti-alignment (70%; Fig. 3a, b) or to the stoppage of one microtubule to prevent it from hitting the other (10%; Fig. 3c). In the remaining fraction of events (20%), the microtubules crossed each other with little effect on their trajectories (Fig. 3d, e; see also Supplementary Movie 3). In aligning and anti-aligning collisions, the trajectory of one microtubule undergoes a sharp turn (Fig. 3a, b) and alignment was observed to be near perfect. We believe that this is due to the leading end of the microtubule being relatively free from attached dyneins by comparison with rest of it: on meeting an obstacle, the tip of the microtubule can then bend more easily. Thus, the outgoing angle is near 0 or π in aligning events, irrespective of the value of the incoming angle, ϕ . In stoppage and crossing events, the orientations of both microtubules remain roughly unchanged. (During stoppage events, one microtubule simply 'waits'

¹Faculty of Education, Aichi University of Education, Aichi 448-8542, Japan. ²Department of Physics, Graduate School of Science, The University of Tokyo, Tokyo 113-0033, Japan. ³Advanced ICT Research Institute, National Institute of Information and Communications Technology, Kobe 651-2492, Japan. ⁴Department of Complex Systems Science, Graduate School of Information Science, Nagoya University, Nagoya 464-8601, Japan. ⁵Department of Physics, Graduate School of Science, Kyoto University and ICORP, JST, Kyoto 606-8502, Japan. ⁶Service de Physique de l'Etat Condensé, CEA-Saclay, 91191 Gif-sur-Yvette, France. ⁷Graduate School of Life Science, University of Hyogo, Harima Science Park City, Hyogo 678-1297, Japan.

*These authors contributed equally to this work.

‡Deceased.

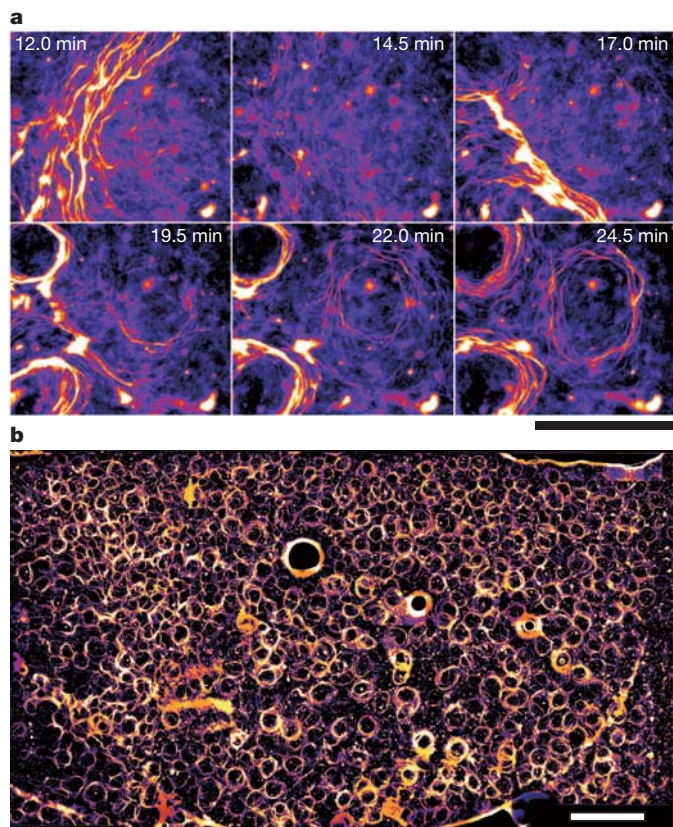


Figure 1 | Emergence of vortices of microtubules. False-colour images. **a**, Formation process of vortex pattern: 0 min corresponds to the time of injection of ATP. Streams appeared around 5 min after this injection. At 12 min, streams started to meander. Vortices started to appear around 17 min, when meandering streams contacted one another. Once vortices had formed, they grew steadily (22 min). Scale bar, 500 μm . **b**, Large-scale lattice of vortices. Vortices can be observed everywhere on the surface of the flow cell. Three air bubbles in the flow cell can be seen distinctively owing to their greater size and thicker edges. Scale bar, 2 mm.

until the other has passed (Fig. 3c.) Given that the outcome of each type of collision is well defined, we represented the complete collision statistics in terms of the probability of each collision type as a function of ϕ only (Fig. 3d). We observe an overall symmetry around $\phi = \pi/2$, with alignment and anti-alignment occurring mainly for small ($\phi \approx 0$) and large ($\phi \approx \pi$) angles, respectively, whereas stoppage and crossing dominate for $\phi \approx \pi/2$. Thus, we conclude that near-perfect *nematic* alignment is induced by direct collision.

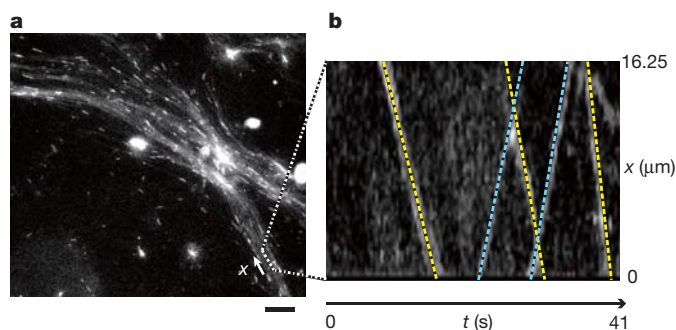


Figure 2 | Nematic order inside a vortex stream. In this experiment, the microtubules were all stained fluorescent but approximately 0.1% of microtubules were stained to be more fluorescent than the rest. **a**, Close-up of vortex. Scale bar, 20 μm . **b**, Spatiotemporal diagram of a magnified region of the vortex shown in **a**. Yellow lines indicate microtubules travelling from top to bottom, and blue lines indicate microtubules travelling from bottom to top.

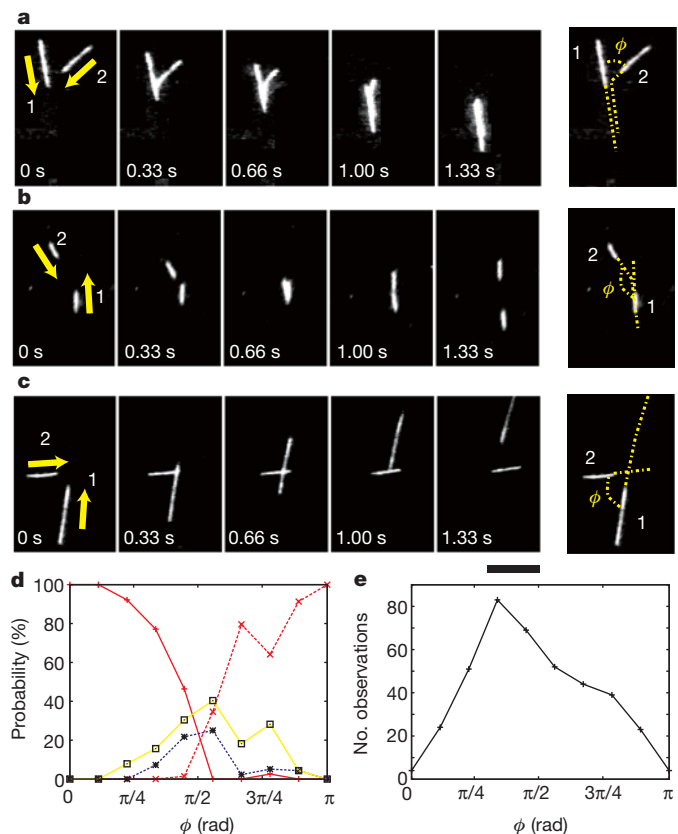


Figure 3 | Collision between microtubules. **a–c**, Three different types of collision between two microtubules. In **a** and **b**, microtubule 2 collides with the side of microtubule 1 and changes its direction of motion abruptly, leading to almost perfect alignment (**a**) or anti-alignment (**b**). In **c**, microtubule 2 stops until microtubule 1 has passed. Scale bar, 10 μm . **d**, Probability of each interaction type as a function of ϕ (see right-most images in **a–c**). We analysed 393 events. Red lines represent alignment (solid) and anti-alignment (dotted) events; blue dotted lines represent stopping events; yellow solid lines represent crossing-over events. **e**, Total number of observations in each angular bin.

Constant-speed particles aligning nematicly in the presence of noise have been studied recently in mathematical models of self-propelled rods, which were shown to give rise to unexpected collective dynamics but not to vortical structures²⁰. Our motility assay has properties not present in simple models of colliding rods. One such feature is the nature of the motion of isolated microtubules: as already mentioned, their reptation-like movement yields smooth but constantly turning trajectories, unlike both straight ballistic motion and the ragged behaviour of random walkers submitted to rotational diffusion, the individual dynamics adopted in rods models^{20–22}. We analysed the trajectories of isolated microtubules for durations of up to 350 s (Fig. 4a, left). Here we further decreased their concentration, to 4.8 ng ml^{-1} . The speed (tangential velocity) of the microtubules fluctuated in time, with a mean of $v_0 = 8.75 \mu\text{m s}^{-1}$. We also measured the direction of motion, θ (where $\theta = 0$ and $\pi/2$ correspond to the direction of the x and y axes, respectively), and the instantaneous angular velocity, and found them to have no significant correlation with the instantaneous speed. This allowed us to neglect the speed fluctuations and focus on θ .

A closer look at a representative trajectory (Fig. 4a, right) reveals small-amplitude transverse oscillations, which might be caused by the rotation of the microtubule around its axis¹⁸. After an appropriate filtering, based on the Savitzky–Golay method, to eliminate these oscillations (Supplementary Methods), we obtained the variation of curvature, $\kappa = d\theta/ds$, as a function of distance, s , along the trajectory and calculated its autocorrelation (Fig. 4b). (With this definition, κ can be positive

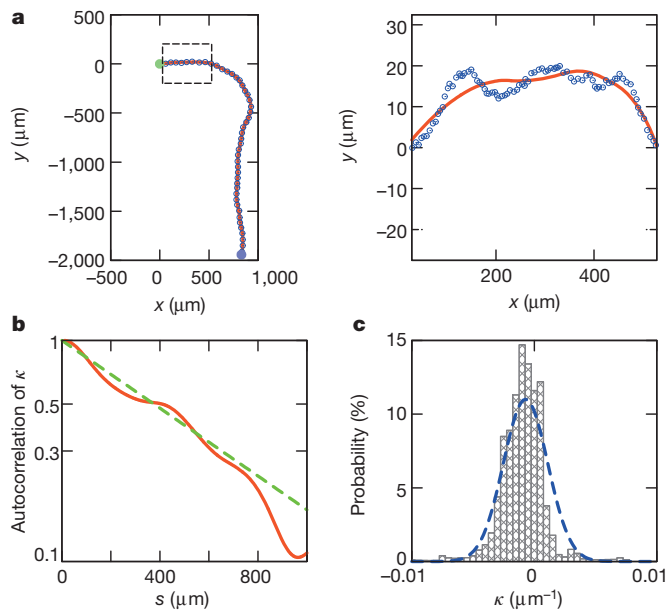


Figure 4 | Motion of isolated microtubules. **a**, Left: trace of an isolated microtubule. Right: enlarged image of boxed area on left. The green and blue filled circles correspond to the start and end points of the observation. The open blue dots represent the position of the microtubule, and the red solid line corresponds to the smoothed curve. **b**, Autocorrelation of the trajectory curvature, κ , with respect to the distance along a trajectory, s (red solid line). The green dotted line is an exponential fit with the correlation length $s_0 = 542 \pm 4 \mu\text{m}$. **c**, Distribution of κ values observed (bars) and Gaussian fit (dashed blue line): mean, $\kappa_0 = -7.1 \times 10^{-4} \mu\text{m}^{-1}$; s.d., $\sigma_\kappa = 1.8 \times 10^{-3} \mu\text{m}^{-1}$.

(anticlockwise motion) or negative (clockwise motion). Fitting the result with the exponential function $\exp(-s/s_0)$, we found the persistent length, s_0 , of curvature to be of the order of $500 \mu\text{m}$. The distribution of κ values observed is roughly Gaussian with mean $\kappa_0 = -7.1 \times 10^{-4} \mu\text{m}^{-1}$ and standard deviation $\sigma_\kappa = 1.8 \times 10^{-3} \mu\text{m}^{-1}$ (Fig. 4c). We note that these numbers correspond to length scales that are rather large and of the same order as the vortex diameter, and that the small negative value of κ_0 indicates a preference for clockwise turning in single-microtubule trajectories, which is probably a consequence of the clockwise rotation around of the microtubules around their axes while in motion²³. A detailed molecular-level study should confirm this.

We constructed a mathematical model for the collective motion of microtubules in our experimental motility assay by incorporating the few ingredients uncovered in our analysis of the trajectories of single microtubules and of pair collisions. A deliberate choice of minimality was made, to stress that with only these very few features all observed collective phenomena are reproduced, and to allow for numerical simulations of millions of objects: for instance, the dynein motors driving the microtubules are not modelled explicitly; the hydrodynamic interactions induced by the fluid are neglected, in agreement with our observation that only direct contact modifies the microtubules' motion. The microtubules themselves are not represented as flexible polymers: here, in the spirit of ref. 6, they are identical point particles moving at constant speed, v_0 (the speed fluctuations are also neglected). In direct agreement with the observations reported in Fig. 4, the free motion of particle i , with position \mathbf{x}_i and orientation θ_i , is a biased Ornstein–Uhlenbeck process, $\omega_i(t)$, with correlation time $\tau = s_0/v_0$, acting on the particle's instantaneous angular velocity, $d\theta_i/dt$:

$$\begin{aligned} \frac{d\mathbf{x}_i}{dt} &= v_0(\mathbf{e}_x \cos \theta_i + \mathbf{e}_y \sin \theta_i) \\ \frac{d\theta_i}{dt} &= \omega_i \end{aligned} \quad (1)$$

$$\frac{d\omega_i}{dt} = -\frac{1}{\tau}(\omega_i - \omega_0) + \xi(t) \quad (2)$$

where \mathbf{e}_x and \mathbf{e}_y are respectively unit vectors in the x and y directions, $\xi(t)$ is a Gaussian white noise with zero mean and variance $\sigma^2 = 2v_0^2\sigma_\kappa^2/\tau = 2v_0^3\sigma_\kappa^2/s_0$, and $\omega_0 = v_0\kappa_0$ is the preferred non-zero angular velocity induced by the mean curvature, κ_0 . This ensures that all correlation properties of the curvature measured in the experiment are reproduced (Supplementary Methods).

These equations must be complemented with an interaction term. Only the nematic alignment collisions are modelled (because stoppage and crossings do not substantially modify the microtubule orientations). As they were observed to induce much sharper turns in the trajectories (Fig. 3a, b) than the spontaneous curvature changes of free microtubules (Fig. 4a), these collisions are modelled as a nematic alignment term acting directly on the particle orientation θ_i , that is, in equation (1), and not on the angular velocity, ω_i . Following previous studies^{6,20}, we replaced explicit pair collisions by an effective alignment within an interaction range, l , which is naturally chosen to be the typical microtubule length. Equation (1) is thus replaced by

$$\begin{aligned} \frac{d\mathbf{x}_i}{dt} &= v_0(\mathbf{e}_x \cos \theta_i + \mathbf{e}_y \sin \theta_i) \\ \frac{d\theta_i}{dt} &= \omega_i + \frac{\alpha}{n_i(t)} \sum_{j \sim i} \sin(2(\theta_j - \theta_i)) \end{aligned} \quad (3)$$

where α is a parameter and the sum is over the $n_i(t)$ particles j within distance l of particle i at time t .

Numerical simulations of equations (2) and (3) using experimentally obtained parameters (Supplementary Methods) show the emergence, from disordered initial conditions, of large-scale vortices with a diameter of the same order as those observed in experiments (Fig. 5a and Supplementary Movie 4).

Inside vortices, the simulated particles revolved both clockwise and anticlockwise, with the majority moving clockwise, as expected from the non-zero value of ω_0 used. The number of vortices increased over time and saturated, leading eventually to a regular hexagonal lattice structure. As in our experimental observations, vortices did not form at low densities. To see this more clearly, we calculated $u^2(n)$, the variance of the local density in small boxes containing n_a particles on average, as a function of the rescaled average density, ρ_a (the actual density multiplied by l^2 ; Supplementary Methods), the other parameters being kept fixed (Fig. 5b). For $\rho_a < 0.4$, the system remains disordered and $u^2(n)/n_a$ is almost constant, indicating the absence of density structures (Fig. 5b, right, images (i) and (ii)). However, $u^2(n)/n_a$ increased with ρ_a for $\rho_a > 0.4$, indicating the appearance of a density pattern, which we checked visually to be a vortex lattice (Fig. 5b, right, images (iii) and (iv)). This result is consistent with our experimental observation that the vortex pattern disappears when the density of microtubules is halved (compare with Supplementary Fig. 1). We also performed numerical simulations in which we varied the rescaled correlation time, $\lambda = v_0\tau/l$ (Supplementary Methods), but kept all the other parameters fixed. Global nematic order without a density pattern was observed for $\lambda < 60$, but the system showed vortex formation for $\lambda > 60$ (Fig. 5c). Thus, the large persistence length and time of single-microtubule motion is necessary for the emergence of the vortices. Further information on the phase diagram of our mathematical model can be found in Supplementary Methods and Supplementary Fig. 2.

The study of our mathematical model thus shows that smooth trajectories of single microtubules and their direct collisions inducing sharp bends and nematic alignment—both experimentally observed—are sufficient, when associated with self-propulsion, to account for all observed collective properties. In particular, there is no theoretical reason to invoke, nor is experimental evidence of, long-range ‘hydrodynamic’ interactions or other ‘collective effects’ in our system. By

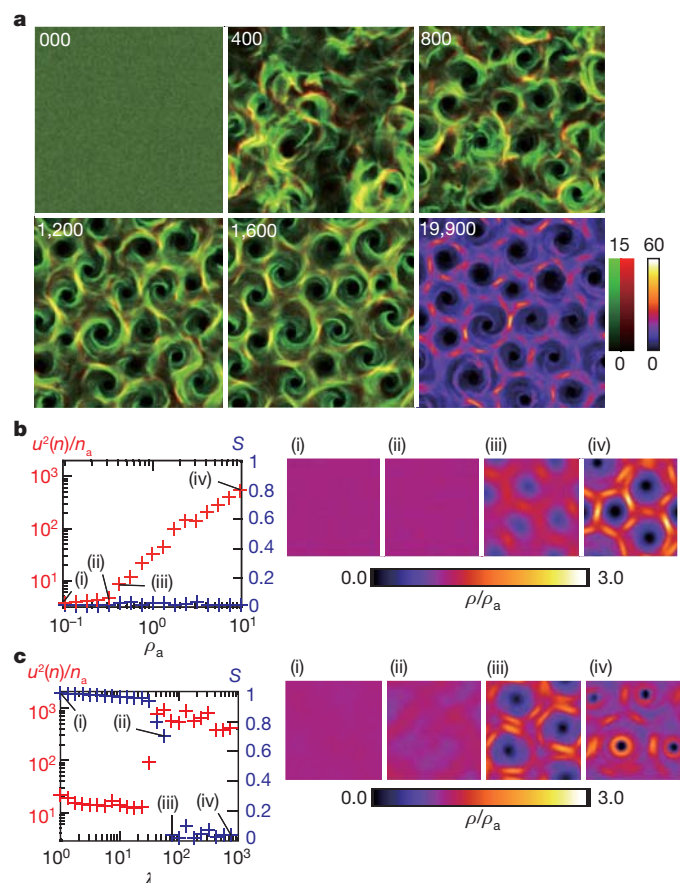


Figure 5 | Collective dynamics of mathematical model of interacting, self-propelled particles. See equations (2) and (3). **a**, Spontaneous formation of a vortex reproduced by our model. Each image is averaged for $\Delta T = 10$, where T is simulation time rescaled by l/v_0 . The brightest area corresponds to a density of 15 particles per unit area. Green and red respectively correspond to the densities of particles moving clockwise ($\omega < 0$) and anticlockwise ($\omega > 0$). Yellow regions indicate areas with clockwise and anticlockwise motion in approximately equal proportions. The area of the figure is 512×512 simulation cells. The last snapshot, at $T = 19,900$, shows the particle densities without differentiating between clockwise and anticlockwise motion, to make comparison with experimental results easy. **b**, Global nematic order parameter, S , and variance of the local density, $u^2(n)$ (calculated over boxes 4 simulation cells in linear size and $\Delta T = 10$), divided by the average density for the box, n_a , plotted against ρ_a . Corresponding density distributions are shown in images (i)–(iv) (each corresponds to a different value of ρ_a , as shown, and is a sum over 5,000 snapshots taken at intervals of $\Delta T = 1$ in a 256×256 system). Here we set the rescaled correlation time, $\lambda = v_0 \tau / l$, to $\lambda = 100$. **c**, Same as **b**, but plotted against λ with $\rho_a = 10$. The density distributions correspond to different values of λ , as shown.

contrast, such interactions were relied on to explain some of the collective phenomena observed in the actomyosin system¹⁴. We believe that our observations are a consequence of using dynein c motors; in fact, when kinesin was used instead of dynein, microtubules mostly crossed each other and vortex formation could not be observed (Supplementary Fig. 3). With dynein, collisions are frequent enough to induce large-scale order. We suppose that this is due to the mechanical properties of dynein molecules and the asymmetry of their molecular structure. The formation of vortices arises from the smoothness and the curvature persistence of trajectories of single microtubules, both of which properties are, we believe, the consequence of having a relatively large number of motors attached at any time (we estimate it to be of the order of 100).

The vortices observed in our motility assay possess unique features: their large scale (relative to the length of microtubules), the irrelevance of hydrodynamic interactions and the dominantly nematic order

inside them distinguish them from the polar, small-scale vortices formed by swimming sperm cells confined in quasi-two-dimensional conditions²⁴. Their stability in time, and their well-defined diameters also distinguish them from the unstable ‘swirling patterns’ reported in the actomyosin assay¹⁴. From a theoretical viewpoint, we are not aware of other models showing a large-scale vortex pattern of the type found here. In our model, the crucial feature introduced is the combination of smooth, reptation-like motion and sharp nematic alignment. This combination can be seen as the signature of a new class in the emerging landscape of universality classes of collective motion phenomena.

Returning to the biological relevance of our findings, we believe that they stress further the message, in various *in vivo* situations and in particular in plant cell cortical arrays^{16,17,25,26}, that simple physical collisions can induce the reorientation of microtubules, creating large-scale structures even in the absence, here, of crosslinkers^{27,28}. Furthermore, there is a striking analogy between our analysis of microtubule collisions and that performed in plant cell cortex^{17,26,29}, although there is only treadmilling and no actual displacement of microtubules in the cortex. As shown in Fig. 3d, in our system the probability of aligning collisions is high at small incoming angles ($\phi = 0 \bmod \pi$) and decreases monotonically from 0 to $\pi/2$, as for ‘zippering’ (positive-end entrapment) of cortical microtubules.

Well-controlled *in vitro* experiments of the type reported here present crucial advantages due to the simplicity of the objects involved and the relative ease of collecting large amounts of data: not only can theoretical ideas be tested, but such experiments can reveal the importance of mechanisms previously ignored, and allow for quantitative analysis of features also present *in vivo*. They are and will remain invaluable tools for our understanding of active matter and biological organization processes.

METHODS SUMMARY

We prepared inner-arm dynein and tubulin using standardized protocols¹⁹. Cy3-labelled microtubules were polymerized from a mixture of Cy3-tubulin and non-fluorescent tubulin and were stabilized using Taxol. Fractionated dynein c was diluted at various concentrations ($27\text{--}90 \mu\text{g ml}^{-1}$) in buffer solution containing 30 mM HEPES/KOH (pH 7.4), 5 mM MgSO_4 , 1 mM DTT, 1 mM EGTA and 1 mg ml^{-1} bovine serum albumin. The flow cell was flushed with the diluted dynein solution, incubated for 5 min and then washed using the buffer solution. Solution containing microtubules as well as 1 mM ATP and 1 mM DTT was introduced into the flow cell. Microtubules were visualized on an epifluorescence microscope. The vortex pattern, binary collisions and individual trajectories were observed with solutions of microtubules with respective concentrations of $40 \mu\text{g ml}^{-1}$, $0.5\text{--}1 \mu\text{g ml}^{-1}$ and 4.8 ng ml^{-1} . For single-trajectory analysis, the position of a microtubule was measured every $\Delta t = 0.68 \text{ s}$.

Received 14 October 2011; accepted 17 January 2012.

1. Ballerini, M. *et al.* Interaction ruling animal collective behavior depends on topological rather than metric distance: evidence from a field study. *Proc. Natl Acad. Sci. USA* **105**, 1232–1237 (2008).
2. Buhl, J. *et al.* From disorder to order in marching locusts. *Science* **312**, 1402–1406 (2006).
3. Katz, Y., Tunström, K., Ioannou, C. C., Huepe, C. & Couzin, I. D. Inferring the structure and dynamics of interactions in schooling fish. *Proc. Natl Acad. Sci. USA* **108**, 18720–18725 (2011).
4. Lukeman, R., Li, Y.-X. & Edelstein-Keshet, L. Inferring individual rules from collective behavior. *Proc. Natl Acad. Sci. USA* **107**, 12576–12580 (2010).
5. Sumpter, D. J. T. *Collective Animal Behavior* (Princeton Univ. Press, 2010).
6. Vicsek, T., Czirók, A., Ben-Jacob, E., Cohen, I. & Shochet, O. Novel type of phase transition in a system of self-driven particles. *Phys. Rev. Lett.* **75**, 1226–1229 (1995).
7. Toner, J., Tu, Y. & Ramaswamy, S. Hydrodynamics and phases of flocks. *Ann. Phys.* **318**, 170–244 (2005).
8. Ramaswamy, S. The mechanics and statistics of active matter. *Annu. Rev. Condens. Mat. Phys.* **1**, 323–345 (2010).
9. Zhang, H. P., Be'er, A., Florin, E.-L. & Swinney, H. L. Collective motion and density fluctuations in bacterial colonies. *Proc. Natl Acad. Sci. USA* **107**, 13626–13630 (2010).
10. Poujade, M. *et al.* Collective migration of an epithelial monolayer in response to a model wound. *Proc. Natl Acad. Sci. USA* **104**, 15988–15993 (2007).
11. Nédélec, F. J., Surrey, T., Maggs, A. C. & Leibler, S. Self-organization of microtubules and motors. *Nature* **389**, 305–308 (1997).

12. Surrey, T., Nédélec, F., Leibler, S. & Karsenti, E. Physical properties determining self-organization of motors and microtubules. *Science* **292**, 1167–1171 (2001).
13. Loose, M., Fischer-Friedrich, E., Ries, J., Kruse, K. & Schwille, P. Spatial regulators for bacterial cell division self-organize into surface waves *in vitro*. *Science* **320**, 789–792 (2008).
14. Schaller, V., Weber, C., Semmrich, C., Frey, E. & Bausch, A. R. Polar patterns of driven filaments. *Nature* **467**, 73–77 (2010).
15. Butt, T. *et al.* Myosin motors drive long range alignment of actin filaments. *J. Biol. Chem.* **285**, 4964–4974 (2010).
16. Yuan, M., Shaw, P. J., Warn, R. M. & Lloyd, C. W. Dynamic reorientation of cortical microtubules, from transverse to longitudinal, in living plant cells. *Proc. Natl Acad. Sci. USA* **91**, 6050–6053 (1994).
17. Wasteneys, G. O. & Ambrose, J. C. Spatial organization of plant cortical microtubules: close encounters of the 2D kind. *Trends Cell Biol.* **19**, 62–71 (2009).
18. Kagami, O. & Kamiya, R. Translocation and rotation of microtubules caused by multiple species of *Chlamydomonas* inner-arm dynein. *J. Cell Sci.* **103**, 653–664 (1992).
19. Sakakibara, H., Kojima, H., Sakai, Y., Katayama, E. & Oiwa, K. Inner-arm dynein c of *Chlamydomonas flagella* is a single-headed processive motor. *Nature* **400**, 586–590 (1999).
20. Ginelli, F., Peruani, F., Bär, M. & Chaté, H. Large-scale collective properties of self-propelled rods. *Phys. Rev. Lett.* **104**, 184502 (2010).
21. Kudrolli, A., Lumay, G., Volfson, D. & Tsimring, L. S. Swarming and swirling in self-propelled polar granular rods. *Phys. Rev. Lett.* **100**, 058001 (2008).
22. Peruani, F., Deutsch, A. & Bär, M. Nonequilibrium clustering of self-propelled rods. *Phys. Rev. E* **74**, 030904(R) (2006).
23. Kikushima, K. & Kamiya, R. Clockwise translocation of microtubules by flagellar inner-arm dyneins. *Biophys. J.* **94**, 4014–4019 (2008).
24. Riedel, I. H., Kruse, K. & Howard, J. A self-organized vortex array of hydrodynamically entrained sperm cells. *Science* **309**, 300–303 (2005).
25. Tindemans, S. H., Hawkins, R. J. & Mulder, B. M. Survival of the aligned: ordering of the plant cortical microtubule array. *Phys. Rev. Lett.* **104**, 058103 (2010).
26. Allard, J. F., Ambrose, J. C., Wasteneys, G. O. & Cytrynbaum, E. N. A mechanochemical model explains interactions between cortical microtubules in plants. *Biophys. J.* **99**, 1082–1090 (2010).
27. Hess, H. *et al.* Molecular self-assembly of “nanowires” and “nanospools” using active transport. *Nano Lett.* **5**, 629–633 (2005).
28. Schaller, V., Weber, C., Hammerich, B., Frey, E. & Bausch, A. R. Frozen steady states in active systems. *Proc. Natl. Acad. Sci. USA* **108**, 19183–19188 (2011).
29. Dixit, R. & Cyr, R. Encounters between dynamic cortical microtubules promote ordering of the cortical array through angle-dependent modifications of microtubule behavior. *Plant Cell* **16**, 3274–3284 (2004).

Supplementary Information is linked to the online version of the paper at www.nature.com/nature.

Acknowledgements We thank H. Sakakibara, Y. Uchida and R. Nakamori for the preparation of the material and observations. They as well as H. Kitahata are also thanked for discussions. Y. Sumino is supported by a Grant-in-Aid for Research Activity Start-up (no. 23840019), Grant-in-Aid for Scientific Research (B) (no. 21340023) and Grant-in-Aid for Scientific Research (A) (no. 20244067). K.H.N. would like to acknowledge the support of a fellowship from the JSPS (no. 23-1819).

Author Contributions K.O. discovered the phenomenon of vortex lattice formation described here and conceived and performed the experiments with Y. Shitaka. Y. Sumino, K.H.N., D.T. and H.C. conceived and designed the simulations. Y. Sumino, K.H.N. and H.C. performed and analysed the simulations. *In vitro* motility assays were carried out under the directions of K.O. Y. Sumino, K.H.N., Y. Shitaka, H.C., K.Y. and K.O. interpreted the data. Y. Sumino, K.H.N., H.C. and K.O. wrote the paper.

Author Information Reprints and permissions information is available at www.nature.com/reprints. The authors declare no competing financial interests. Readers are welcome to comment on the online version of this article at www.nature.com/nature. Correspondence and requests for materials should be addressed to K.O. (oiwa@nict.go.jp).

Collapse of polar ice sheets during the stage 11 interglacial

Maureen E. Raymo¹ & Jerry X. Mitrovica²

Contentious observations of Pleistocene shoreline features on the tectonically stable islands of Bermuda and the Bahamas have suggested that sea level about 400,000 years ago was more than 20 metres higher than it is today^{1–4}. Geochronologic and geomorphic evidence indicates that these features formed during interglacial marine isotope stage (MIS) 11, an unusually long interval of warmth during the ice age^{1–4}. Previous work has advanced two divergent hypotheses for these shoreline features: first, significant melting of the East Antarctic Ice Sheet, in addition to the collapse of the West Antarctic Ice Sheet and the Greenland Ice Sheet^{1–3}; or second, emplacement by a mega-tsunami during MIS 11 (ref. 4, 5). Here we show that the elevations of these features are corrected downwards by ~10 metres when we account for post-glacial crustal subsidence of these sites over the course of the anomalously long interglacial. On the basis of this correction, we estimate that eustatic sea level rose to ~6–13 m above the present-day value in the second half of MIS 11. This suggests that both the Greenland Ice Sheet and the West Antarctic Ice Sheet collapsed during the protracted warm period while changes in the volume of the East Antarctic Ice Sheet were relatively minor, thereby resolving the long-standing controversy over the stability of the East Antarctic Ice Sheet during MIS 11.

The stability of ice sheets in the face of continuing global warming is an issue of significant societal concern. Satellite gravity measurements indicate that the Greenland Ice Sheet (GIS) and the West Antarctic Ice Sheet (WAIS), the two ice sheets most susceptible to climate change, are experiencing a net mass loss^{6–9}, with evidence of an accelerating pace^{9–12}. In contrast, the current mass balance of the much larger East Antarctic Ice Sheet (EAIS) is uncertain, even in sign^{6,9}, though a recent study¹¹ has inferred EAIS mass loss localized to coastal regions. This uncertainty about the stability of the EAIS in a progressively warming world has been a key motivation for studies of the palaeoclimate record during past warm intervals.

One such study, a statistical analysis of widely distributed sea-level markers related to the last interglacial (MIS 5e; about 120,000 years ago), concluded with 95% confidence that eustatic sea level (ESL; defined as the globally averaged sea-level change) was >6.6 m higher during MIS 5e than at the present day, and with 66% confidence that ESL was >8.0 m higher¹³. (This inference, higher than earlier estimates¹⁴, is supported by a recent analysis of MIS 5e sea-level records from Florida¹⁵.) Estimates of the ESL rise associated with collapse of polar ice sheets range from 3.4 m (ref. 16) to 7 m for the GIS, and from 3.2 m (ref. 17) to 5 m for the WAIS, where the upper bounds refer to the complete disappearance of the ice sheet. Thus, whereas the estimate of peak ESL during MIS 5e implies significant collapse of both the GIS and the WAIS, it also implies that the EAIS remained relatively stable.

It is within this context of assessing potential future instability of the EAIS that the sea-level highstand features found at ~20 m (here and elsewhere, height above present-day sea level is meant) in Bermuda and the Bahamas, and which formed during the MIS 11 interglacial (~424–395 kyr ago), have taken on great significance. MIS 11 spanned two precession cycles and was the longest interglacial of the past

500 kyr (refs 18, 19), including the current interglacial MIS 1 (Fig. 1) and MIS 5e (Supplementary Fig. 4). If the ESL during the MIS 11 interglacial peaked at a level 20 m higher than today^{1–3}, then at least 8 m of that rise must have come from melting of the EAIS. Geologic evidence for a ~20-m sea-level highstand in Bermuda and the Bahamas is convincing. In Bermuda, reasonably well-dated deposits with thalassinidean shrimp burrows, foraminifera, and gastropods characteristic of littoral and intertidal environments constrain relative sea level at 21.3 ± 1.0 m during MIS 11 (refs. 2, 3). On Eleuthera, in the Bahamas, a gently sloping erosion surface capped with fenestrae-rich intertidal beach deposits provides a maximum sea-level estimate of 20 ± 3 m, and the occurrence of pendant fibrous cements suggests a minimum sea level of 17 ± 2 m (we will henceforth quote a sea-level estimate of 18.5 ± 3.6 m for this site); multiple dating methods suggest that these deposits were formed during MIS 11 (ref. 1).

How do these observations compare to other MIS 11 sea-level indicators or proxies? In a recent survey of MIS 11 sea-level records worldwide (most of which are located in tectonically active regions), Bowen⁵ estimated peak MIS 11 sea level using a range of tectonic uplift

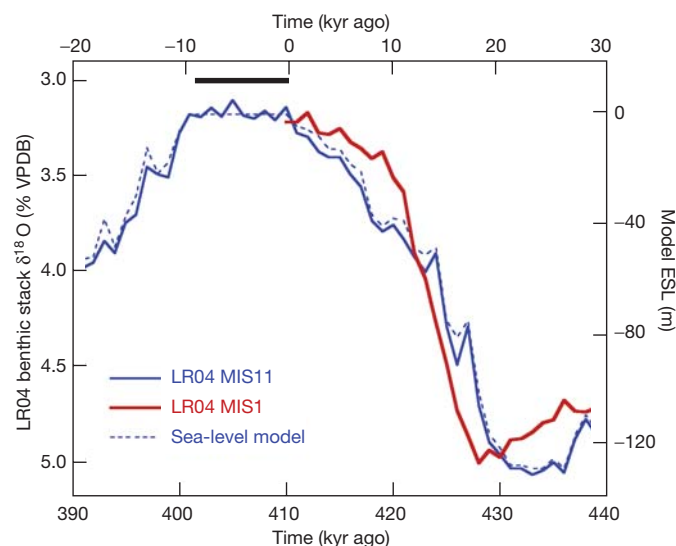


Figure 1 | Comparison of the duration of the MIS 11 and MIS 1 interglacials. Plot of the LR04 benthic oxygen isotope stack²⁸ (left-hand vertical axis) over a time window spanning the MIS 11 (blue; bottom time scale) and MIS 1 (red; top time scale) interglacials. The mean standard error on $\delta^{18}\text{O}$ in the LR04 stack is 0.06‰ with an age error of ± 4 kyr for the intervals considered here. The juxtaposition illustrates the significantly longer duration of maximum interglacial conditions during MIS 11 relative to MIS 1. ESL associated with the model ice history used to calculate GIA effects during MIS 11 is shown by dashed line (right-hand vertical axis). Note the hiatus in model ice volume changes from 410 to 401 kyr ago (black bar). An analogous comparison between the duration of MIS 11 with MIS 5e can be found in Supplementary Fig. 4.

¹Lamont-Doherty Earth Observatory, Columbia University, PO Box 1000, 61 Route 9W, Palisades, New York 10964, USA. ²Department of Earth and Planetary Sciences, Harvard University, 20 Oxford Street, Cambridge, Massachusetts 02138, USA.

corrections based on different assumed ages and elevations of MIS 5e sea-level markers. If we adopt Kopp *et al.*'s¹³ recent inference of the age and peak magnitude of ESL during MIS 5e as a constraint on the latter, then Bowen's estimates from far-field sites imply that peak sea level during MIS 11 was 6–9 m above the present-day value, an estimate consistent with marine $\delta^{18}\text{O}$ isotopic anomalies²⁰. However, Bowen excluded a number of outliers, including the well-studied Bermuda and Bahamas sites, and following McMurtry *et al.*⁴, he attributed the anomalously high elevation of shoreline features at those sites to deposition by storms or a mega-tsunami.

The two explanations for the MIS 11 highstand features in Bermuda and the Bahamas—global sea-level rise associated with significant EAIS melting^{1–3}, or mega-tsunami deposition^{4,5}—ignore the potential signal from glacial isostatic adjustment (GIA). The GIA signal may be significant at the two sites, as they both are located on the peripheral bulge of the ancient Laurentian ice complex. As a consequence, they would be subject to local crustal subsidence and sea-level rise of amplitude $\sim 1\text{--}2\text{ mm yr}^{-1}$ during any interglacial²¹.

To explore the potential contribution from GIA to MIS 11 highstand elevations, we compute global sea-level variations over the past 500 kyr using a gravitationally self-consistent theory valid for spherically symmetric, linear viscoelastic Earth models²² (see Supplementary Information). As an illustration of the physics of interglacial sea-level trends, we plot the predicted change in sea level across the warmest, most stable interval in MIS 11 (as implied by $\delta^{18}\text{O}$ records), a 9-kyr period spanning 410–401 kyr ago that occurred during the second half of MIS 11 (Fig. 2). The predictions adopt an Earth model with upper-mantle and lower-mantle viscosities of $5 \times 10^{20}\text{ Pa s}$ and $5 \times 10^{21}\text{ Pa s}$, respectively (model LM^{23,24}; see Supplementary Information).

In the near-field of the former MIS 12 ice sheets, the predicted sea-level change is dominated by radial crustal motions. For example, in regions once covered by ice sheets, post-glacial rebound of the crust produces a sea-level fall of amplitude up to $\sim 1\text{--}2\text{ cm yr}^{-1}$, leading to a net fall over 9 kyr that can exceed 100 m (these amplitudes are well off the scale of Fig. 2). Surrounding these regions of uplift are peripheral bulges predicted to subside at rates of up to $0.2\text{--}0.3\text{ cm yr}^{-1}$ during the interglacial. This subsidence accounts for the (red) zones of sea-level rise in Fig. 2, with maximum amplitude of $\sim 20\text{ m}$, that encircle the Laurentian, Fennoscandian and Antarctic ice complexes. In contrast, a sea-level fall of 2–3 m is predicted across most of the far-field of the former ice sheets during MIS 11. This fall is due to a combination of two processes: (1) deglaciation-induced ocean loading effects, which act, near continental margins, to tilt the crust such that continents are deformed upward (that is, sea level falls) and offshore regions downward^{21,25}; and (2) the redistribution—or syphoning—of water from ocean basins towards regions of peripheral bulge and offshore subsidence²¹.

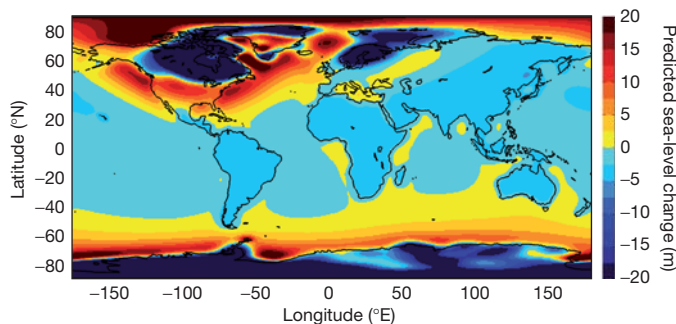


Figure 2 | Predicted sea-level change across the hiatus in ice volume changes (410–401 kyr ago) spanned by the model MIS 11 interglacial. The GIA calculation is based on the ice history discussed in Supplementary Information and the LM^{23,24} viscosity model. The colour scale saturates in regions within the near-field of the late Pleistocene ice sheets.

Following Fig. 2, we conclude that in the absence of interglacial ice volume changes and steric effects, sea-level highstands will date to the end of the interglacial at sites within the subsiding peripheral bulge of major ice centres, and to the beginning of the interglacial over most of the far-field (Fig. 3). (Of course, any sea-level signal associated with interglacial ice volume variations and with ocean temperature and salinity changes will be superimposed on these predicted GIA trends.) Consider Bermuda: the predicted relative sea-level history for this site (Fig. 3 and Supplementary Fig. 1, solid red line) exhibits a monotonic rise across MIS 11, reaching a level 11.9 m above the present-day value. The predicted highstand for the Bahamas (dashed red line, Fig. 3), lying on the outer flank of the same peripheral bulge, is 7.4 m. It is clear that the amplitude of highstands at Bermuda or the Bahamas, indeed at all sites within a peripheral bulge, will be a strong function of the duration of the interglacial highstand. In this regard, the protracted length of MIS 11, relative to the Holocene (Fig. 1) or MIS 5e (Supplementary Fig. 4), should be manifested by highstands of particularly large magnitude. From this it also follows that simple field comparisons of the relative elevations of Holocene, MIS 5e and MIS 11 sea-level markers on these islands would lead to an erroneous assessment of the difference in ESL between those times.

This result may be stated with more generality. The elevation of an ancient interglacial highstand at any site within a peripheral bulge will be governed by the difference in the state of isostatic disequilibrium at the end of the ancient interglacial relative to the disequilibrium at the present day in that same location. As the MIS 11 interglacial was significantly longer than the current interglacial (or MIS 5e), more subsidence had occurred by the time the final MIS 11 shoreline indicators were emplaced on those islands than during the current (or MIS 5e) interglacial. Further, as the current interglacial proceeds, sites like Bermuda and the Bahamas will be subject to a continuing sea-level rise as the present peripheral bulge continues to subside. Thus, the height of these ancient MIS 11 highstand features will progressively fall as time progresses (even in the absence of any future change in ice volume).

By contrast, the highstand amplitude at sites located in the far field will depend on the difference in isostatic disequilibrium at the beginning of the interglacial relative to the disequilibrium at the present day.

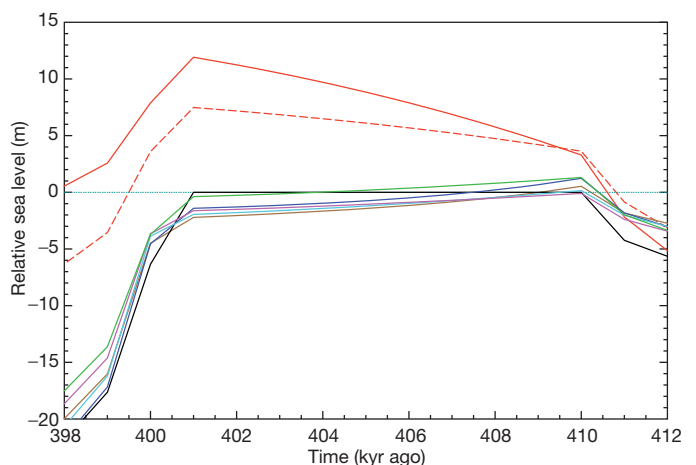


Figure 3 | Predicted relative sea-level changes across the model MIS 11 interglacial. The calculations are based on the ice history discussed in Supplementary Information and the LM viscosity model. The top two curves are predictions for Bermuda (solid red line) and the Bahamas (dashed red line) at locations of published data discussed in text. The lower coloured curves, predictions for a number of far-field sites, are included for comparison: the Gulf of Aden, Red Sea (brown), Curacao (green), Coorong, South Australia (magenta), Oahu, Hawaii (blue) and Cape Town, South Africa (cyan). The black line shows the ESL variation associated with the adopted ice history (as in the dashed blue line in Fig. 1 and the black line in Supplementary Fig. 1) and the thin horizontal dashed line references to present-day sea level.

Thus, perhaps counter-intuitively, the current elevation of these highstands does not depend on the duration of the ancient interglacial.

Global predictions of current MIS 11 shoreline elevations within each of the two zones discussed above are shown in Fig. 4a and b: Fig. 4a encompasses sites where the highstand occurred at the end of the modelled interglacial hiatus in ice mass change (for example, 401 kyr ago) whereas Fig. 4b encompasses sites where the highstand occurs at the beginning of the modelled hiatus (410 kyr ago). These results represent the predicted contribution to observed MIS 11 highstands from GIA alone; this contaminating signal should be removed from geological observations before they are used to infer the difference in ESL (or ice volume) between MIS 11 and the present.

As noted above, the GIA contribution to the MIS 11 shoreline elevations in Bermuda and the Bahamas is predicted to be 11.9 m and 7.4 m, respectively (Fig. 3). Correcting the published highstand estimates at these sites for these GIA predictions yields residual MIS 11 sea-level elevations of 9.4 ± 1 m for Bermuda and 11.1 ± 3.6 m in Eleuthera (Supplementary Table 1). Although additional field observations in the Bahamas could greatly decrease the multi-metre error associated with these sea-level estimates, we conclude that no significant contribution from melting of the EAIS is required to explain the geologic observations at the two sites.

In our analysis, we implicitly assume that melting of the WAIS and the GIS occurred towards the end of the MIS 11 interglacial, such that the contribution of the melt event to sea level at Bermuda and the Bahamas could be added to a coeval GIA-induced highstand. This timing for ice sheet collapse is strongly supported by at least two arguments. First, if the collapse took place at the beginning of the hiatus in MIS 11 melting (that is, at ~ 410 kyr ago), then the associated ESL rise would have had to be close to 20 m in order to fit the observed highstand elevations at Bermuda and the Bahamas. However, in this case, the predicted highstand elevation at far-field sites would have been even greater than 20 m (that is, an ~ 20 -m melt signal added to the GIA-induced highstand of a few metres; Fig. 3), a situation apparently ruled out by far-field observations⁵. Second, GIA calculations predict a submergence of up to several metres for far-field sites by 401 kyr ago (Fig. 3) and an average submergence of ~ 1 m at the specific far-field

sites considered by Bowen⁵. Therefore, correcting an inferred sea-level peak of 6–9 m for this GIA-induced contamination yields a predicted ESL ~ 1 m higher (that is, 7–10 m), in accord with the residual highstand elevations at Bermuda and the Bahamas cited above (Supplementary Table 1).

In the Supplementary Information we present results of sensitivity tests related to GIA predictions. First, we extend the duration of the MIS 11 hiatus in ice mass change from 9 to 14 kyr. In this case, the GIA-induced elevation of MIS 11 shorelines at sites within the Laurentian peripheral bulge are predicted to increase by ~ 1 –2 m when viscosity model LM is adopted, yielding residual MIS 11 highstand elevations of 7.0 ± 1 m for Bermuda and 9.9 ± 3.6 m in Eleuthera (Supplementary Table 1), and thus lowering the inferred peak ESL during MIS 11 by ~ 1 –2 m. Second, we considered an alternative viscosity profile, VM2 (ref. 26), characterized by a lower-mantle viscosity that is a factor of two smaller than model LM. In this case, the predicted GIA contribution to MIS 11 highstand elevations within the peripheral bulge is reduced by a factor of ~ 2 . This reduction yields residual (GIA-corrected) MIS 11 elevations of 15.0 ± 1 m and 14.3 ± 3.6 m at Bermuda and the Bahamas, respectively, values that appear to be at odds with lower far-field estimates⁵. Last, we performed a Monte Carlo parameter search in which we varied mantle viscosity, lithospheric thickness, and the duration of the modelled hiatus in MIS 11 ice volume changes, and tested for the consistency of the GIA-corrected highstand elevations. This exercise yields a preferred bound on the peak ESL during MIS 11 of 6–13 m.

In summary, observations of MIS 11 highstand features in Bermuda and the Bahamas must be corrected for the significant contaminating signal of GIA before these data are used to infer peak ESL during the MIS 11 interglacial. We conclude that ESL reached ~ 6 –13 m above the present-day value in the late stages of MIS 11. It is unlikely that ocean thermal expansion contributed more than ~ 1 m to this inference^{13,27}. Therefore, although this estimate of peak ESL indicates significant collapse of both the WAIS and GIS during the MIS 11 interglacial, it rules out any significant melting of the EAIS during this unusually prolonged period of ice age warmth.

Received 30 September 2011; accepted 23 January 2012.

Published online 14 March 2012.

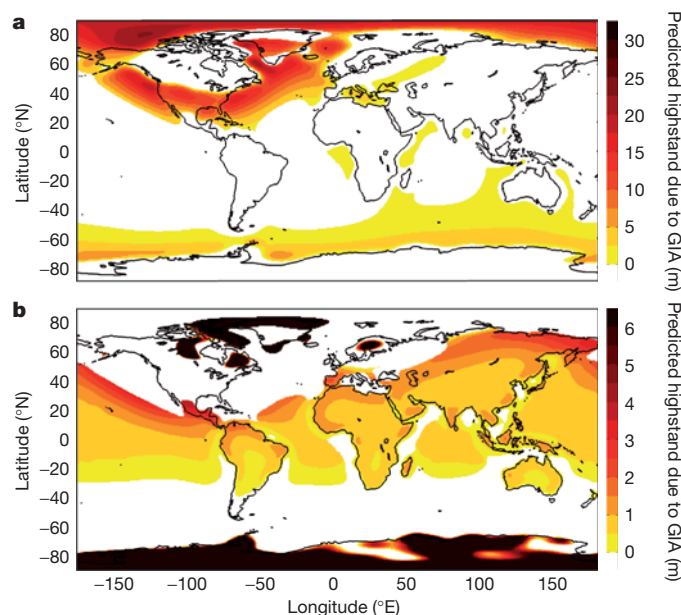


Figure 4 | Plot of the predicted GIA-induced present-day elevation of MIS 11 highstands that are currently greater than zero. Elevation is shown for all sites in which sea-level peaks either at the end of the hiatus in ice volume changes spanned by the model MIS 11 interglacial (a; that is, at 401 kyr ago; see also Supplementary Fig. 1) or at the beginning of that hiatus (b; that is, at 410 kyr ago).

1. Hearty, P. J., Kindler, P., Cheng, H. & Edwards, R. L. A +20 m middle Pleistocene sea level highstand (Bermuda and the Bahamas) due to partial collapse of Antarctic ice. *Geology* **27**, 375–378 (1999).
2. Olson, S. L. & Hearty, P. J. A sustained +21 m sea level highstand during MIS 11 (400 ka): direct fossil and sedimentary evidence from Bermuda. *Quat. Sci. Rev.* **28**, 271–285 (2009).
3. van Hengstum, P., Scott, D. B. & Javaux, E. Foraminifera in elevated Bermudian caves provide further evidence for +21 m eustatic sea level during Marine Isotope Stage 11. *Quat. Sci. Rev.* **28**, 1850–1860 (2009).
4. McMurtry, G. M. *et al.* Elevated marine deposits in Bermuda record a late Quaternary megatsunami. *Sedim. Geol.* **200**, 155–165 (2007).
5. Bowen, D. Q. Sea level ~ 400000 years ago (MIS 11): analogue for present and future sea-level? *Clim. Past* **6**, 19–29 (2010).
6. Velicogna, I. & Wahr, J. Measurements of time-variable gravity show mass loss in Antarctica. *Science* **311**, 1754–1756 (2006).
7. Luthcke, S. B. *et al.* Recent Greenland ice mass loss by drainage system from satellite gravity observations. *Science* **314**, 1286–1289 (2006).
8. Shepherd, A. & Wingham, D. Recent sea-level contributions of the Antarctic and Greenland ice sheets. *Science* **315**, 1529–1532 (2007).
9. Rignot, E. *et al.* Recent Antarctic ice mass loss from radar interferometry and regional climate modelling. *Nature Geosci.* **1**, 106–110 (2008).
10. Thomas, R. *et al.* Accelerated sea level rise from West Antarctica. *Science* **306**, 255–258 (2004).
11. Chen, J. L., Wilson, C. R., Blankenship, D. & Tapley, B. D. Accelerated Antarctic ice loss from satellite gravity measurements. *Nature Geosci.* **2**, 859–862 (2009).
12. Velicogna, I. Increasing rates of ice mass loss from the Greenland and Antarctic ice sheets revealed by GRACE. *Geophys. Res. Lett.* **36**, L19503, <http://dx.doi.org/10.1029/2009GL040222> (2009).
13. Kopp, R. E., Simons, F. J., Mitrovica, J. X., Maloof, A. C. & Oppenheimer, M. Probabilistic assessment of sea level during the last interglacial stage. *Nature* **462**, 863–867 (2009).
14. Jansen, E. *et al.* in *Climate Change 2007: The Physical Science Basis* (eds Solomon, S. *et al.*) 433–498 (Cambridge Univ. Press, 2007).

15. Muhs, D. R., Simmons, K. R., Schumann, R. R. & Halley, R. B. Sea-level history of the past two interglacial periods: new evidence from U-series dating of reef corals from south Florida. *Quat. Sci. Rev.* **30**, 570–590 (2011).
16. Otto-Bliesner, B. *et al.* Simulating Arctic climate warmth and ice field retreat in the last interglaciation. *Science* **311**, 1751–1753 (2006).
17. Bamber, J. L., Riva, R. E. M., Vermeersen, L. L. A., & LeBrocq, A. M. Reassessment of the potential sea level rise from a collapse of the West Antarctic Ice Sheet. *Science* **324**, 901–903 (2009).
18. Loutre, M. F. & Berger, A. Marine isotope stage 11 as an analogue for the present interglacial. *Glob. Planet. Change* **36**, 209–217 (2003).
19. Rohling, E. J. *et al.* Comparison between Holocene and Marine Isotope Stage-11 sea level histories. *Earth Planet. Sci. Lett.* **291**, 97–105 (2010).
20. McManus, J., Oppo, D., Cullen, J. & Healey, S. in *Earth's Climate and Orbital Eccentricity: The Marine Isotope Stage 11 Question* (eds Droxler, A. W., Poore, R. Z. & Burckle, L. H.) 69–85 (AGU Geophys. Monogr. Ser. 137, 2003).
21. Mitrovica, J. X. & Milne, G. A. On the origin of postglacial ocean syphoning. *Quat. Sci. Rev.* **21**, 2179–2190 (2002).
22. Kendall, R. A., Mitrovica, J. X. & Milne, G. A. On post-glacial sea level: II. Numerical formulation and comparative results on spherically symmetric models. *Geophys. J. Int.* **161**, 679–706 (2005).
23. Lambeck, K., Smither, C. & Johnston, P. Sea level change, glacial rebound and mantle viscosity for northern Europe. *Geophys. J. Int.* **134**, 102–144 (1998).
24. Mitrovica, J. X. & Forte, A. M. A new inference of mantle viscosity based upon a joint inversion of convection and glacial isostatic adjustment data. *Earth Planet. Sci. Lett.* **225**, 177–189 (2004).
25. Nakada, M. & Lambeck, K. Late Pleistocene and Holocene sea-level change in the Australian region and mantle rheology. *Geophys. J. Int.* **96**, 497–517 (1989).
26. Peltier, W. R. Global glacial isostasy and the surface of the ice-age Earth: the ICE-5G (VM2) model and GRACE. *Annu. Rev. Earth Planet. Sci.* **32**, 111–149 (2004).
27. McKay, N. P., Overpeck, J. T. & Otto-Bliesner, B. L. The role of ocean thermal expansion in Last Interglacial sea level rise. *Geophys. Res. Lett.* **38**, L14605, <http://dx.doi.org/10.1029/2011GL048280> (2011).
28. Lisiecki, L. E. & Raymo, M. E. A. Pliocene-Pleistocene stack of 57 globally distributed benthic $\delta^{18}\text{O}$ records. *Paleoceanography* **20**, PA1003, <http://dx.doi.org/10.1029/2004PA001071> (2005).

Supplementary Information is linked to the online version of the paper at www.nature.com/nature.

Acknowledgements We thank P. Hearty and D. Bowen for discussions of MIS 11 field data, and J. L. Davis for suggestions regarding data analysis. Support for this research was provided by NSF-OCE-0825293 and OCE-1202632 (M.E.R.), Harvard University (J.X.M.) and the Canadian Institute for Advanced Research (J.X.M.).

Author Contributions This study was planned, undertaken and written jointly.

Author Information Reprints and permissions information is available at www.nature.com/reprints. The authors declare no competing financial interests. Readers are welcome to comment on the online version of this article at www.nature.com/nature. Correspondence and requests for materials should be addressed to M.E.R. (raymo@ldeo.columbia.edu).

Adaptive radiation of multituberculate mammals before the extinction of dinosaurs

Gregory P. Wilson¹, Alistair R. Evans², Ian J. Corfe³, Peter D. Smits^{1,2}, Mikael Fortelius^{3,4} & Jukka Jernvall³

The Cretaceous–Paleogene mass extinction approximately 66 million years ago is conventionally thought to have been a turning point in mammalian evolution^{1,2}. Prior to that event and for the first two-thirds of their evolutionary history, mammals were mostly confined to roles as generalized, small-bodied, nocturnal insectivores³, presumably under selection pressures from dinosaurs⁴. Release from these pressures, by extinction of non-avian dinosaurs at the Cretaceous–Paleogene boundary, triggered ecological diversification of mammals^{1,2}. Although recent individual fossil discoveries have shown that some mammalian lineages diversified ecologically during the Mesozoic era⁵, comprehensive ecological analyses of mammalian groups crossing the Cretaceous–Paleogene boundary are lacking. Such analyses are needed because diversification analyses of living taxa^{6,7} allow only indirect inferences of past ecosystems. Here we show that in arguably the most evolutionarily successful clade of Mesozoic mammals, the Multituberculata, an adaptive radiation began at least 20 million years before the extinction of non-avian dinosaurs and continued across the Cretaceous–Paleogene boundary. Disparity in dental complexity, which relates to the range of diets, rose sharply in step with generic richness and disparity in body size. Moreover, maximum dental complexity and body size demonstrate an adaptive shift towards increased herbivory. This dietary expansion tracked

the ecological rise of angiosperms⁸ and suggests that the resources that were available to multituberculates were relatively unaffected by the Cretaceous–Paleogene mass extinction. Taken together, our results indicate that mammals were able to take advantage of new ecological opportunities in the Mesozoic and that at least some of these opportunities persisted through the Cretaceous–Paleogene mass extinction. Similar broad-scale ecomorphological inventories of other radiations may help to constrain the possible causes of mass extinctions^{9,10}.

Multituberculate mammals were a taxonomically rich^{3,11} and numerically abundant¹² clade that had originated by the Middle Jurassic epoch (approximately 165 million years (Myr) ago) and went extinct in the late Eocene (approximately 35 Myr ago)^{3,11}. They were nearly globally distributed¹³ and had a distinctive dentition consisting of procumbent incisors, blade-like premolars, molars with longitudinal rows of cusps (Fig. 1) and a predominantly posteriorly directed (palinal) chewing motion^{14,15}.

Palaeontologists have agreed for a long time that the success of multituberculate mammals was at least partly related to their highly derived dentition. Despite this, there is little consensus on the interpretations of their feeding ecology, perhaps owing to the limitations of previous approaches. For example, toothwear analysis is time intensive

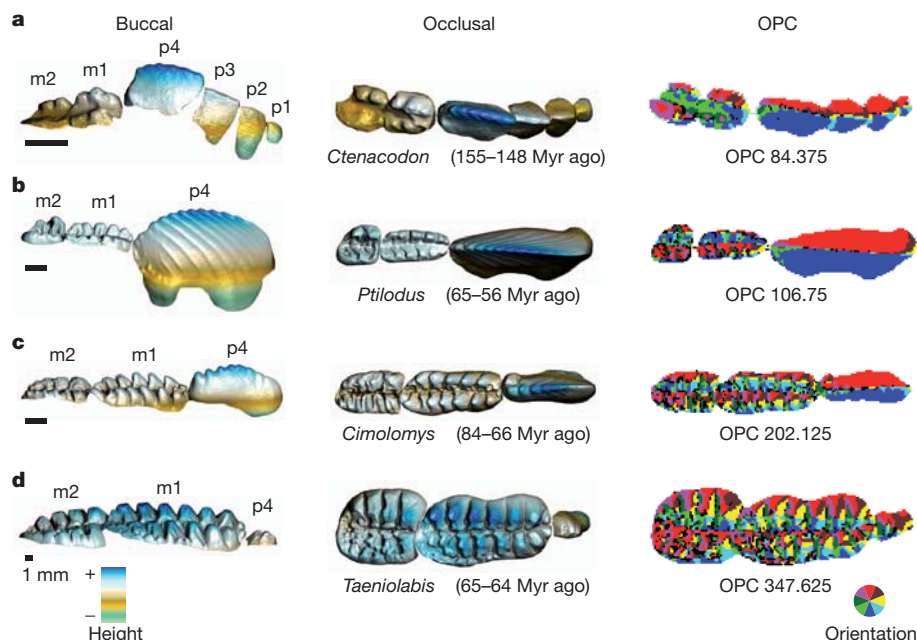


Figure 1 | Dental and dietary diversity in multituberculate mammals. a–d, Three-dimensional buccal–occlusal and occlusal reconstructions of multituberculate lower-right cheek tooth rows for GIS analysis: Late Jurassic plagiaulacid *Ctenacodon serratus* (a), Paleocene ptilodontoid *Ptilodus kummae* (b), Late

Cretaceous cimolomyid *Cimolomys gracilis* (c), Paleocene taeniolabidid *Taeniolabis taoensis* (d). Surface orientation map of each three-dimensional reconstruction (colour wheel indicates orientation) for OPC measurements (shown by the number of coloured patches). Clumps that are smaller than three grid points (black) are ignored. p, premolar; m, molar. Scale bars, 1 mm.

¹Department of Biology, University of Washington, Seattle, Washington 98195-1800, USA. ²School of Biological Sciences, Monash University, Victoria 3800, Australia. ³Developmental Biology Program, Institute of Biotechnology, University of Helsinki, PO Box 56, FIN-00014, Helsinki, Finland. ⁴Department of Geosciences and Geography, University of Helsinki, PO Box 64, FIN-00014, Helsinki, Finland.

and requires high-quality preservation¹⁵, and multituberculates lack living descendants and this hampers comparative studies. Interpretations of multituberculate feeding ecology therefore vary widely; they have been proposed to be broad herbivores, frugivores, granivores, root- and bark-eaters, egg-eaters, insectivores, carnivores and omnivores^{15–17}.

To obtain a robust and comprehensive view of multituberculate ecomorphological diversity through time, we quantified dental complexity in 41 genera using geographic information systems (GIS) analyses¹⁸ of three-dimensional crown surfaces of lower cheek teeth (Fig. 1; Supplementary Table 1). These analyses do not require cusp and facet homologies to be established, which can be a challenging task

when comparing morphologically and phylogenetically divergent taxa. Orientation patch count (OPC), a measure of dental complexity, was calculated as the number of discrete surfaces on the cheek tooth row distinguished by differences in orientation (for example, north, southwest; Fig. 1). Extant rodents, carnivorans and bats demonstrate a robust correlation between OPC and feeding ecology; OPC increases across the dietary spectrum from carnivores to omnivores to herbivores, despite many differences in specific tooth components, body size and chewing mechanics among these taxa^{18,19}. For a given clade, the standard deviation of OPC is an effective proxy for the dietary diversification and divergence in feeding function: higher standard deviation means greater dental disparity and a broader range of diets. OPC thus offers promise as a powerful tool for quantifying overall tooth shape and inferring diet in extinct taxa, such as multituberculates, that have highly derived dentitions with uncertain homology with living mammals and imprecise functional analogy.

Among the earliest multituberculates, the ‘Plagiaulacida’ are a paraphyletic assemblage of taxa with up to four simple blade-like premolars and two multi-cusped molars (Fig. 1a). OPC analyses of ‘plagiaulacids’ from the Late Jurassic through to the Early Cretaceous epoch (from 156–100 Myr ago) show low and tightly constrained dental complexity (Fig. 2a; OPC, 84–125). Their OPC values correspond to carnivory and the low end of animal-dominated omnivory among extant mammals (for example, eating both insects and fruits). Multituberculates in the early Late Cretaceous (100–84 Myr ago), which include mostly basal members of the suborder Cimolodonta, had a slightly higher mean OPC than did the ‘plagiaulacids’ but retained the low standard deviation of OPC (Fig. 2a), indicating low morphological disparity. A distinct break occurred 84–66 Myr ago, in the latest Cretaceous, when the mean OPC rose and peaked within the Campanian (mean OPC, 145) and maximum OPC and disparity sharply increased as well (Fig. 2a; OPC, 70–230). Of the 17 taxa for this interval, 5 have OPC values that are greater than 160 and 2 have OPC values that are greater than 200, corresponding to values for plant-dominated omnivory and herbivory among extant mammals, respectively (Fig. 2a).

Finally, in the early Paleocene (66–62 Myr ago) multituberculates maintained high OPC (mean OPC, 138) and disparity peaked (Fig. 2a; OPC, 70–348). The early Paleocene *Taeniolabis* from North America (Fig. 1d) had the highest OPC among multituberculates (OPC, 348), which exceeded OPC values of extant herbivorous rodents and carnivorans¹⁸. Of the 16 other early Paleocene taxa, 4 have OPC values greater than 160 and 1 has an OPC value greater than 200 (Fig. 2a). Mean OPC and disparity of OPC declined during the remainder of the Paleocene and in the early Eocene (62–49 Myr ago). *Ectypodus*, the only known genus from the middle to late Eocene (49–35 Myr ago), has a low OPC (109), corresponding to the high end of the range for extant mammalian carnivores. This sharp drop in dental ecomorphological

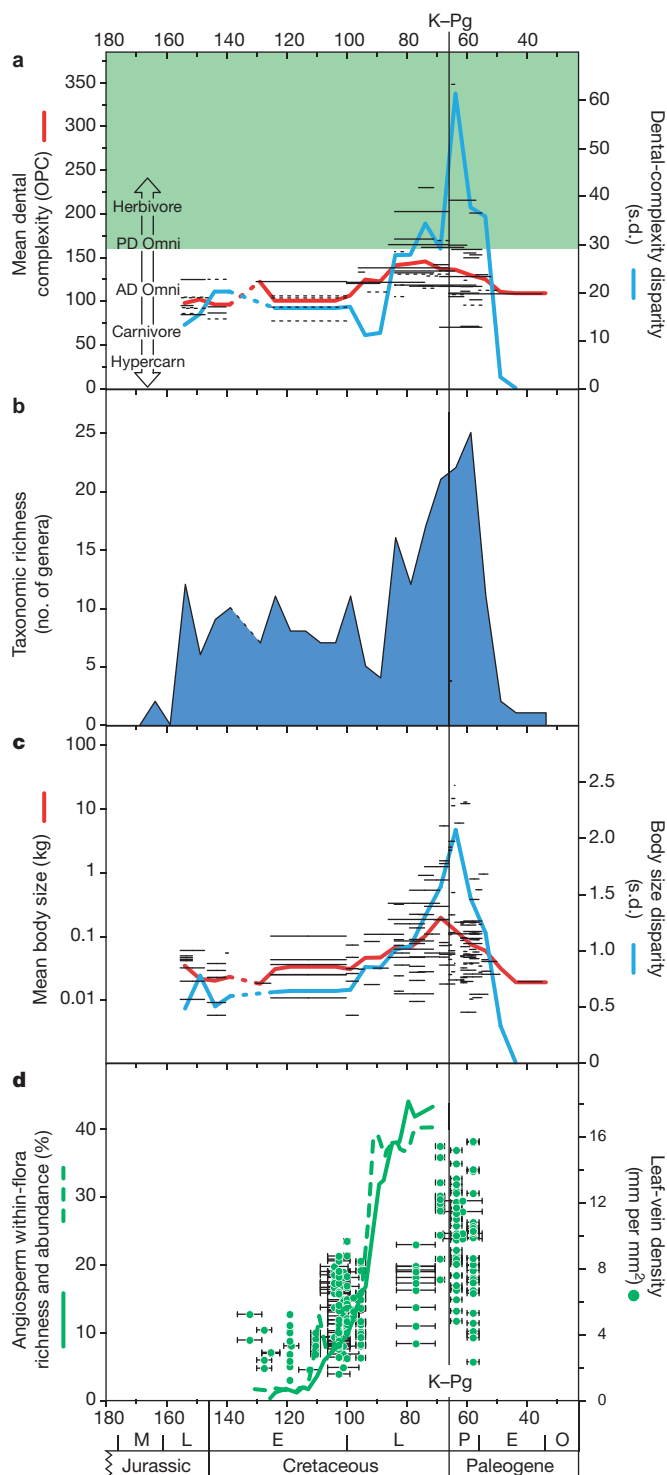


Figure 2 | Temporal patterns of multituberculate dental complexity, taxonomic richness, body size and angiosperm ecological diversification. **a**, Dental complexity (measured by OPC) for 41 multituberculate genera (solid black lines) and estimated for 24 additional genera (dashed black lines; see Supplementary Information) with mean dental complexity (OPC; red line) and disparity as standard deviations of OPC (blue line) in 5-Myr bins. Lengths of horizontal lines represent temporal ranges of taxa or uncertainties in ages of fossil localities. Labels for dietary classes are positioned at the lower end of their range based on OPC values in modern mammals¹⁸. Green shaded area represents plant-dominated omnivory (PD omni) and herbivory. **b**, Taxonomic richness is equal to the number of genera per 5-Myr bin (blue shaded area). **c**, Body-mass estimates for 156 multituberculate species (solid black lines) with geometric means (red line) and disparity (blue line) for each 5-Myr bin. **d**, Angiosperm within-flora richness (solid green line) and relative abundance (dashed green line) from ref. 24 (± 7.5 -Myr moving averages). Leaf hydraulic capacity of angiosperms as leaf-vein density (green circles) from ref. 25. The 136–131-Myr bin was excluded from all analyses (Supplementary Information). AD omni, animal-dominated omnivory; E, early; Hypercarn, hypercarnivory; M, middle; L, late; O, Oligocene; P, Paleocene.

disparity is intriguing in light of the hypothesis that some late Paleocene to early Eocene eutherian lineages (for example, rodents) competitively displaced multituberculates¹².

Variable sampling of fossils through time may influence our inferred patterns of multituberculate radiation. In particular, the relatively depauperate Jurassic and Early Cretaceous taxonomic richness of multituberculates may be partly due to the limited fossil record³. To test whether the changes in OPC through time might be sensitive to uneven sampling of fossils, we randomized the OPC value assignments for each genus. The results of 5,000 randomized mean OPC profiles through time indicate that even with additional fossil discoveries, the OPC patterns and ecological inferences that are presented here are likely to be robust (see Supplementary Fig. 8).

The overall trend of increasing multituberculate dental complexity was driven by increases in the number of cusps per molar and the relative size of molars in the cheek tooth row (Supplementary Fig. 1). This evolutionary pathway differs from that taken by ungulates, primates, rodents and lagomorphs, which responded to increased mechanical processing demands (that is, greater plant component) by evolving multi-cusped, molar-like premolars in addition to complex molars²⁰. Among several other mammalian lineages with blade-like premolars (for example, carpolestid primates and potoroid marsupials), only shenurine marsupials re-evolved multi-cusped premolars²¹. Developmental, functional or structural constraints that are associated with the evolution of a blade-like premolar may have inhibited later evolution of more cuspidate premolars.

Patterns of generic richness and conservative estimates of body size for multituberculates (see Methods Summary) mirror the pattern of initially low dental complexity for most of the Mesozoic followed by a marked increase just before the end of the Cretaceous (84–66 Myr ago; Fig. 2b, c). From the Late Jurassic to the early Late Cretaceous, multituberculate generic richness fluctuated between 4 and 16 genera, and body mass ranged between 9 g and 105 g. A marked shift occurred near the end of the Cretaceous, with generic richness increasing from 16 to 21 genera and average body mass increasing from 67 g to 194 g, in particular, *Bubodens magnus* reached an estimated 5.25 kg (for a comparison, the alpine marmot weighs 3–8 kg). Similarly, Cenozoic generic richness and body size patterns parallel changes in dental complexity (Fig. 2b, c). However, it should be noted that body size and dental complexity are not interchangeable as predictors of diet because small multituberculates can have high OPC values, and large multituberculates can have low OPC values (Supplementary Information), conforming to previous analyses of extant taxa¹⁸. Furthermore, variation in the amount of available fossil-bearing rock through the studied interval could contribute to the pattern of generic richness²².

It is worth noting that increases in dental complexity (OPC of greater than 160) occurred in five multituberculate lineages: in the Asian Djadochtheroidea, the North American Eucosmodontidae and Cimolomyidae (just before the end of the Cretaceous), the North American and Asian Taeniolabidae, and the North American Microcosmodontidae (in the early Paleocene). In the absence of a robust multituberculate phylogeny, it is unclear whether this represents a single evolutionary increase in tooth complexity, with multiple reversals to low complexity, or parallel increases in individual lineages or clades. This increase differs from the more commonly observed pattern, in which increased morphologic disparity precedes taxonomic diversification²³, as this increase occurred in step with an increase in multituberculate body size and taxonomic richness.

Overall, the pattern of increasing dental complexity in multituberculate mammals that pre-dates the Cretaceous–Paleogene mass extinction event contrasts with conventional ideas that mammalian evolution was suppressed during the Mesozoic era by selective pressures imposed by dinosaurs. Instead, multituberculates, the mammalian clade that co-existed for the longest time with non-avian dinosaurs, initiated an evolutionary radiation during the acme of dinosaur diversity, approximately 20 Myr before the Cretaceous–Paleogene boundary²².

This is consistent with the highly specialized adaptations that are found among several new, exceptionally well-preserved Mesozoic mammal specimens⁵ and with the timing of increased molecular divergence rates among extant mammalian lineages^{6,7}, but the multituberculates also show broad taxonomic and ecomorphologic diversification at the intraordinal level.

This adaptive response post-dated the taxonomic radiation of angiosperms but coincided broadly with increases in ecological diversity, abundance and leaf hydraulic capacities of angiosperms in the Late Cretaceous (in the Campanian and Maastrichtian)^{8,24,25} (Fig. 2d), suggesting that there is a causal link. Many angiosperms during this time were herbaceous, and had a rapid life cycle and less-effective herbivore defences compared to other seed plants and would consequently have been an attractive, protein-rich food source for herbivores²⁶. Some angiosperms had begun inhabiting a broader range of niches (trees, herbs and epiphytes) than most other plant groups and this may have enabled greater partitioning of the herbivore niche. Therefore, the multituberculate adaptive radiation, suggested by the increasing dental complexity, may have been triggered mainly by new niche space that was generated through the evolutionary and ecological radiations of angiosperms, but may have also been influenced by parallel radiations of associated non-angiosperm clades (for example, ferns²⁷), insect pollinators, dispersers and herbivores²⁸. A trophic link between angiosperms and some multituberculates is supported by our inferred dietary trend towards increased plant-dominated omnivory and herbivory among multituberculates just before the end of the Cretaceous and in the early Paleocene.

Our data also show that the dietary range of multituberculates did not decrease in response to the Cretaceous–Paleogene mass extinction event (Fig. 2a). Despite substantial taxonomic turnover of multituberculates at the Cretaceous–Paleogene boundary²⁹, they seem to have experienced little change in available food resources during one of the most severe extinction events in Earth's history. This apparent indifference of the multituberculate radiation to the Cretaceous–Paleogene event underscores the ecological selectivity of extinctions and suggests that broad-scale ecomorphological inventories of radiations may help to constrain the possible causes of extinction for other groups at the Cretaceous–Paleogene boundary^{9,10}.

METHODS SUMMARY

We scanned 48 dentitions from 41 genera of multituberculates. The three-dimensional scans of lower cheek tooth rows were analysed using GIS to quantify the number of discrete orientation patches using eight orientation directions. The mean of repeated measurements for eight rotations at multiples of 5.625° was used to reduce the effect of slight variations in the orientation of teeth. We compiled generic richness data from recent compendia and the primary literature. We estimated body mass from skull length, whenever available, and a tooth size to skull length regression formula. Detailed methods and calculations of dental complexity, generic richness and estimated body mass, data sets, measurements, calculations, randomization analyses and additional references are provided in the Supplementary Information.

Received 26 September 2011; accepted 20 January 2012.

Published online 14 March 2012.

1. Alroy, J. The fossil record of North American mammals: evidence for a Paleocene evolutionary radiation. *Syst. Biol.* **48**, 107–118 (1999).
2. Smith, F. A. *et al.* The evolution of maximum body size of terrestrial mammals. *Science* **330**, 1216–1219 (2010).
3. Kielan-Jaworowska, Z., Cifelli, R. L. & Luo, Z.-X. *Mammals from the Age of Dinosaurs: Origins, Evolution, and Structure* (Columbia Univ. Press, 2004).
4. Van Valen, L. M. & Sloan, R. E. Ecology and the extinction of the dinosaurs. *Evol. Theory* **2**, 37–64 (1977).
5. Luo, Z.-X. Transformation and diversification in early mammalian evolution. *Nature* **450**, 1011–1019 (2007).
6. Bininda-Emonds, O. R. P. *et al.* The delayed rise of present-day mammals. *Nature* **446**, 507–512 (2007).
7. Meredith, R. W. *et al.* Impacts of the Cretaceous terrestrial revolution and KPg extinction on mammal diversification. *Science* **334**, 521–524 (2011).
8. Wing, S. L. & Boucher, L. D. Ecological aspects of the Cretaceous flowering plant radiation. *Annu. Rev. Earth Planet. Sci.* **26**, 379–421 (1998).

9. Archibald, J. D. *et al.* Cretaceous extinctions: multiple causes. *Science* **328**, 973 (2010).
10. Schulte, P. *et al.* The Chicxulub asteroid impact and mass extinction at the Cretaceous–Paleogene boundary. *Science* **327**, 1214–1218 (2010).
11. Weil, A. & Krause, D. W. in *Evolution of Tertiary Mammals of North America* Vol. 2 (eds Janis, C. M., Gunnell, G. F. & Uhen, M. D.) 19–38 (Cambridge Univ. Press, 2008).
12. Krause, D. W. in *Vertebrates, Phylogeny, and Philosophy* (eds Flanagan, K. M. & Lillegraven, J. A.) 119–130 (Contributions to Geology, 1986).
13. Rich, T. H. *et al.* An Australian multituberculate and its palaeobiogeographic implications. *Acta Palaeontol. Pol.* **54**, 1–6 (2009).
14. Gingerich, P. D. in *Patterns of Evolution* (ed. Hallam, A.) 469–500 (Elsevier, 1977).
15. Krause, D. W. Jaw movement, dental function, and diet in the Paleocene multituberculate *Ptilodus*. *Paleobiology* **8**, 265–281 (1982).
16. Cope, E. D. The tertiary Marsupialia. *Am. Nat.* **18**, 686–697 (1884).
17. Simpson, G. G. The “plagiaulacoid” type of mammalian dentition. *J. Mamm.* **14**, 97–107 (1933).
18. Evans, A. R., Wilson, G. P., Fortelius, M. & Jernvall, J. High-level similarity of dentitions in carnivorans and rodents. *Nature* **445**, 78–81 (2007).
19. Santana, S. E., Strait, S. & Dumont, E. R. The better to eat you with: functional correlates of tooth structure in bats. *Funct. Ecol.* **25**, 839–847 (2011).
20. Jernvall, J., Gilbert, C. C. & Wright, P. C. in *Elwyn Simons: A Search for Origins* (eds Fleagle, J. G. & Gilbert, C. C.) 335–342 (Springer, 2008).
21. Prideaux, G. J. Systematics and evolution of the sthenurine kangaroos. *Univ. Calif. Publ. Geol. Sci.* **146**, 1–622 (2004).
22. Barrett, P. M., McGowan, A. J. & Page, V. Dinosaur diversity and the rock record. *Proc. R. Soc. B* **276**, 2667–2674 (2009).
23. Foote, M. The evolution of morphological diversity. *Annu. Rev. Ecol. Syst.* **28**, 129–152 (1997).
24. Lupia, R., Lidgard, S. & Crane, P. R. Comparing palynological abundance and diversity: implications for biotic replacement during the Cretaceous angiosperm radiation. *Paleobiology* **25**, 305–340 (1999).
25. Feild, T. S. *et al.* Fossil evidence for Cretaceous escalation in angiosperm leaf vein evolution. *Proc. Natl Acad. Sci. USA* **108**, 8363–8366 (2011).
26. Wing, S. L. & Tiffney, B. H. in *The Origins of Angiosperms and Their Biological Consequences* (eds Friis, E. M., Chaloner, W. G. & Crane, P. R.) 203–224 (Cambridge Univ. Press, 1987).
27. Schneider, H. *et al.* Ferns diversified in the shadow of angiosperms. *Nature* **428**, 553–557 (2004).
28. Grimaldi, D. The co-radiations of pollinating insects and angiosperms in the Cretaceous. *Ann. Mo. Bot. Gard.* **86**, 373–406 (1999).
29. Wilson, G. P. Mammalian faunal dynamics during the last 1.8 million years of the Cretaceous in Garfield County, Montana. *J. Mamm. Evol.* **12**, 53–76 (2005).

Supplementary Information is linked to the online version of the paper at www.nature.com/nature.

Acknowledgements We thank museums, institutions and individuals that made specimens available for this study (full list is available in Supplementary Information). Funding was provided by the National Science Foundation, Denver Museum, the University of Washington (G.P.W. and P.D.S.), the Australian Research Council, Monash University (A.R.E.), the Academy of Finland (A.R.E., M.F. and J.J.) and the EU SYNTHESYS program (project GB-TAF-4779) (I.J.C.).

Author Contributions G.P.W., A.R.E., J.J. and M.F. designed the study. G.P.W., A.R.E., I.J.C. and P.D.S. collected and analysed the data. G.P.W., A.R.E. and J.J. wrote the manuscript. G.P.W., A.R.E., I.J.C., P.D.S., M.F. and J.J. discussed results and commented on the manuscript at all stages.

Author Information The three-dimensional scans for this study are deposited in the MorphoBrowser database (<http://morphobrowser.biocenter.helsinki.fi/>). Reprints and permissions information is available at www.nature.com/reprints. The authors declare no competing financial interests. Readers are welcome to comment on the online version of this article at www.nature.com/nature. Correspondence and requests for materials should be addressed to G.P.W. (gpwilson@u.washington.edu).

A comparative analysis of the evolution of imperfect mimicry

Heather D. Penney¹, Christopher Hassall¹, Jeffrey H. Skevington^{1,2}, Kevin R. Abbott¹ & Thomas N. Sherratt¹

Although exceptional examples of adaptation are frequently celebrated, some outcomes of natural selection seem far from perfect. For example, many hoverflies (Diptera: Syrphidae) are harmless (Batesian¹) mimics of stinging Hymenoptera². However, although some hoverfly species are considered excellent mimics, other species bear only a superficial resemblance to their models³ and it is unclear why this is so. To evaluate hypotheses that have been put forward to explain interspecific variation in the mimetic fidelity of Palearctic Syrphidae we use a comparative approach. We show that the most plausible explanation is that predators impose less selection for mimetic fidelity on smaller hoverfly species because they are less profitable prey items. In particular, our findings, in combination with previous results, allow us to reject several key hypotheses for imperfect mimicry: first, human ratings of mimetic fidelity are positively correlated with both morphometric measures and avian rankings, indicating that variation in mimetic fidelity is not simply an illusion based on human perception⁴; second, no species of syrphid maps out in multidimensional space as being intermediate in appearance between several different hymenopteran model species, as the multimodel hypothesis⁵ requires; and third, we find no evidence for a negative relationship between mimetic fidelity and abundance, which calls into question the kin-selection⁶ hypothesis. By contrast, a strong positive relationship between mimetic fidelity and body size supports the relaxed-selection hypothesis^{7,8}, suggesting that reduced predation pressure on less profitable prey species limits the selection for mimetic perfection.

Much of evolutionary theory relating to mimicry has been based on the assumption that the fidelity of mimicry in any given system is extremely high (reviewed in ref. 9). Of course, if mimicry were poor, one might intuitively expect that signal receivers would learn to be able to distinguish mimics from their models and (depending on context) accept or reject them. In reality, however, there are many examples of inaccurate or low-fidelity mimics^{3,5,6,8,10}. For example, the relative compositions of key odour compounds of specific non-rewarding orchids differ markedly from the bees they have evolved to resemble¹⁰. Similarly, although mimetic spiders of the genus *Cosmophasis* bear some resemblance to ants, they are readily visually discriminated by the human observer¹¹. Perhaps the best examples of imperfect mimics are found in hoverflies (Diptera: Syrphidae), which are considered Batesian (harmless) mimics of hymenopteran models² but seem to vary markedly across species in the degree of mimetic perfection^{3,12} (see Supplementary Fig. 1).

Numerous hypotheses have been proposed to explain the evolution and maintenance of 'imperfect' mimicry, but despite calls for study there have been no comparative tests of their validity^{6,13}. Common (and interrelated) explanations include the following: first, 'eye of the beholder', such that poor mimics to human eyes remain good mimics to natural predators⁴; second, 'multimodel', such that mimics gain most benefit from imperfect similarity to multiple models⁵; third, kin selection, such that imperfect mimicry is maintained through its benefit to conspecifics carrying the same trait⁶; fourth, constraints such

that some factor limits the evolution of more perfect mimicry¹⁴ including trade-offs (for example mimetic perfection versus thermoregulation¹⁴ or camouflage¹⁵), phylogenetic constraints on body plan, or lack of genetic variation; and fifth, relaxed selection, such that selection for mimicry gradually weakens to a point at which it is readily counteracted by weak selection or mutation^{7,8} (see Supplementary Information for additional hypotheses). Here we describe new comparative morphological and genetic data that allow us to evaluate which of these hypotheses are best able to explain the range of mimetic perfection seen in hoverflies.

A long-standing challenge in elucidating the ultimate causes of imperfect mimicry is that of quantifying the extent of mimetic fidelity between mimics and models, which frequently differ in multiple trait dimensions ranging from colour to shape. Previous measures of mimetic fidelity have used human rankings¹⁶, pigeon responses^{12,17}, pixel mapping¹², neural networks¹⁶ and multivariate analyses¹⁸. We employed subjective human rankings of mimetic fidelity (hereafter f_{HR} ; see Methods) across a range of species that were compared for consistency against a measure derived from a multivariate analysis of trait values (hereafter f_{MD} ; see Methods).

Overall, our morphological analysis of 38 syrphid species and 10 hymenopteran model species indicated that there was a clear statistical difference in appearance between the two taxa (Syrphidae and Hymenoptera) (nested multivariate analysis of variance: taxon, $F_{1,427} = 797.77$, $P < 0.001$; species, $F_{47,427} = 11.03$, $P < 0.001$). The first three canonical variates in a generalized canonical discriminant analysis (GCDA) explained 80.6% of the variance between the species in terms of their morphological features (individually: 41.1%, 20.4% and 19.2%). The Mahalanobis distances between each of the syrphid species and each of the Hymenoptera groups were calculated from these three canonical variates. This measure was multiplied by -1 to give a quantity, f_{MD} , that is positively related to mimetic fidelity. Syrphids and hymenopterans tend to cluster with their respective orders, largely on the basis of relative length of antennae (L_{ant}), a feature that is thought to be used in discrimination by birds¹⁶. The multimodel hypothesis⁵ would predict that mimics fall between several models, gaining greater benefit from multiple, weaker associations. Our analysis clearly indicates that there are no mimetic phenotypes in our sample that could be considered to be falling morphologically between two or more distinct model phenotypes (Fig. 1).

The eye-of-the-beholder hypothesis recognizes that the natural predators of mimics (such as birds) and humans differ in both their perception and cognitive abilities, and argues that the apparent variation in mimetic perfection is therefore illusory and/or misleading. However, our multivariate measure of mimetic fidelity correlated well with our human ranking ($r = 0.555$, d.f. = 36, $P < 0.001$; Fig. 2), whereas similar work indicates that trained pigeons rank mimetic fidelity of hoverfly species in much the same way as humans do (Supplementary Fig. 2). Additional results suggest that behavioural mimicry (antenna waving, mock stinging, wing wagging) occurs only in species that humans classify as high-fidelity mimics (H.D.P., C.H.,

¹Department of Biology, Carleton University, 1125 Colonel By Drive, Ottawa, K1S 5B6, Canada. ²Agriculture and Agri-Food Canada, Canadian National Collection of Insects, Arachnids and Nematodes, K.W. Neatby Building, 960 Carling Avenue, Ottawa, K1A 0C6, Canada.

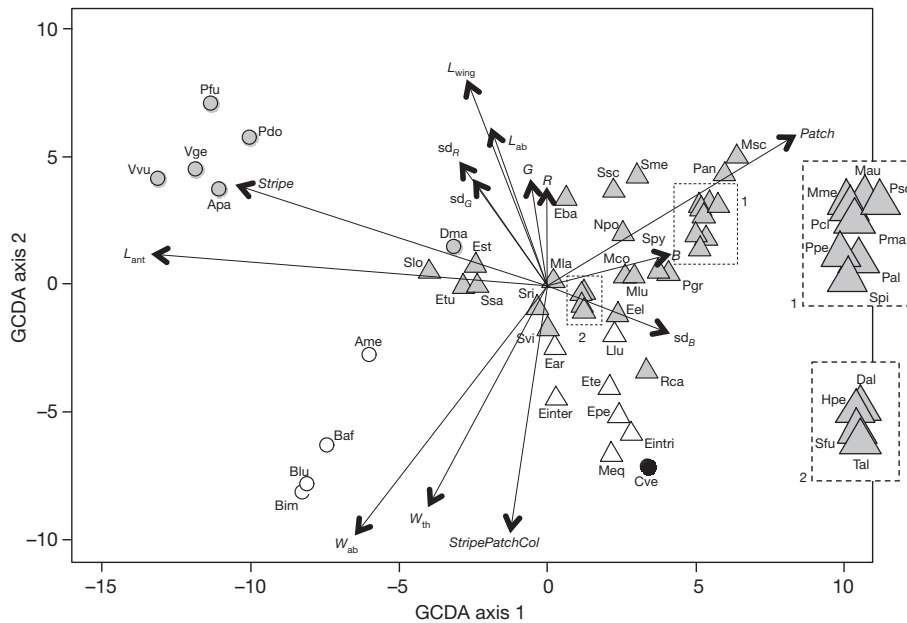


Figure 1 | GCDA plot of biometrical measurements. Circles are models (hymenopterans); triangles are mimics (syrphids); grey symbols are wasps or wasp mimics. Open symbols are bees or bee mimics, and the solid black circle is

the non-mimetic syrphid *Cheilosia vernalis*. Species codes can be found in Supplementary Table 2; other abbreviations are described in Methods.

J.H.S. and T.N.S., unpublished observations), further suggesting that the human-based quantification of mimetic perfection is ecologically relevant. Taken together, these findings suggest that we can discount the eye-of-the-beholder hypothesis as an explanation for interspecific variation in hoverfly fidelity.

It has been stated frequently that, within hoverflies at least, poor mimics tend to occur at higher population densities than good mimics^{3,5,12}. Although this relationship is plausible, it remains entirely anecdotal. The kin-selection hypothesis for imperfect mimicry not only assumes a degree of family grouping (which is unlikely in hoverflies³) but also predicts that the evolved degree of mimetic perfection will be lowest when mimics are relatively common and/or relatively beneficial to attack in comparison with their models⁶. This prediction arises from the assumption that predators that are largely unable to distinguish mimics from models will sample those high-fidelity mimics at a greater rate when the incentive to attack is greater. The constraints^{14,15} and

relaxed-selection^{7,8} hypotheses predict the opposite, namely that the evolved degree of perfection will be highest when mimics are relatively common and/or relatively beneficial to attack as a result of the increased selection pressure to avoid predation through mimicry. A meta-analysis of 11 independent studies (Supplementary Table 1) demonstrated no evidence of a strong correlation between relative abundance and either measure of mimetic fidelity in our 38 focal species, either before controlling for phylogenetic autocorrelation (f_{HR} , $\bar{r} = 0.065$ (95% confidence interval (CI), -0.052 to 0.181); f_{MD} , $\bar{r} = 0.001$ (95% CI, -0.149 to 0.152)) or after controlling for phylogeny by using phylogenetic generalized least-squares regression for a subset of 31 species (Fig. 3) (f_{HR} , $\bar{r} = -0.083$ (95% CI, -0.031 to 0.198); f_{MD} , $\bar{r} = 0.223$ (95% CI, 0.058 – 0.389)). Note that this latter correlation between f_{MD} and abundance was significant (the 95% CI did not overlap zero) and positive, indicating that in this case poor mimics tend to be less common. Therefore, on the basis of our sample of species (that is, those sufficiently common to appear regularly in systematic field surveys) we found no evidence that good mimics tend to be rarer (Supplementary Figs 3 and 4).

The constraints^{14,15} and relaxed-selection^{7,8} hypotheses suggest that smaller-bodied (and thus less nutritionally profitable¹⁹) species will endure low levels of predation, even if they are poor mimics, which produces weaker selection for improved mimicry; the kin-selection hypothesis predicts the opposite (see above). Therefore the relationship between the body size of hoverfly species and their mimetic fidelity was assessed. There was a highly significant relationship between body size (principal component 1; $-PC1$) and f_{HR} both before controlling for phylogeny (Pearson's correlation, $r = 0.680$, d.f. = 36, $P < 0.001$) and after controlling for phylogeny (phylogenetic generalized least-squares regression, $t = 4.693$, $P < 0.001$). The relationship between body size and f_{MD} was also highly significant before controlling for phylogeny ($r = 0.632$, d.f. = 36, $P < 0.001$) and after controlling for phylogeny ($t = 3.005$, $P = 0.005$); see Fig. 4. Finally, our meta-analysis indicates that the relative abundance of hoverfly species was only weakly (negatively) correlated with their body size before controlling for phylogeny ($\bar{r} = -0.132$ (95% CI, -0.239 to -0.024)) and after controlling for phylogeny ($\bar{r} = -0.240$ (95% CI, -0.476 to -0.005)), and it is clear that this relationship is not consistent across studies (Supplementary Fig. 5).

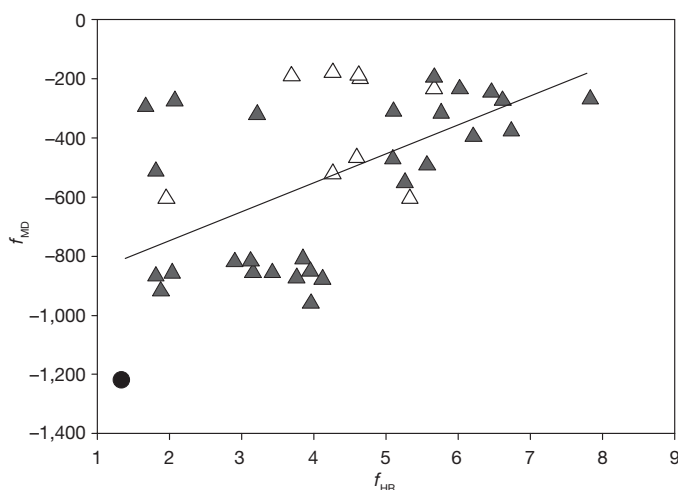


Figure 2 | The relationship between Mahalanobis distances (f_{MD}) and human rankings (f_{HR}) measures of mimetic fidelity in hoverflies. The line shows the fitted linear regression. Filled triangles, wasp mimics; open triangles, bee mimics; filled circle, the non-mimetic syrphid *Cheilosia vernalis*.

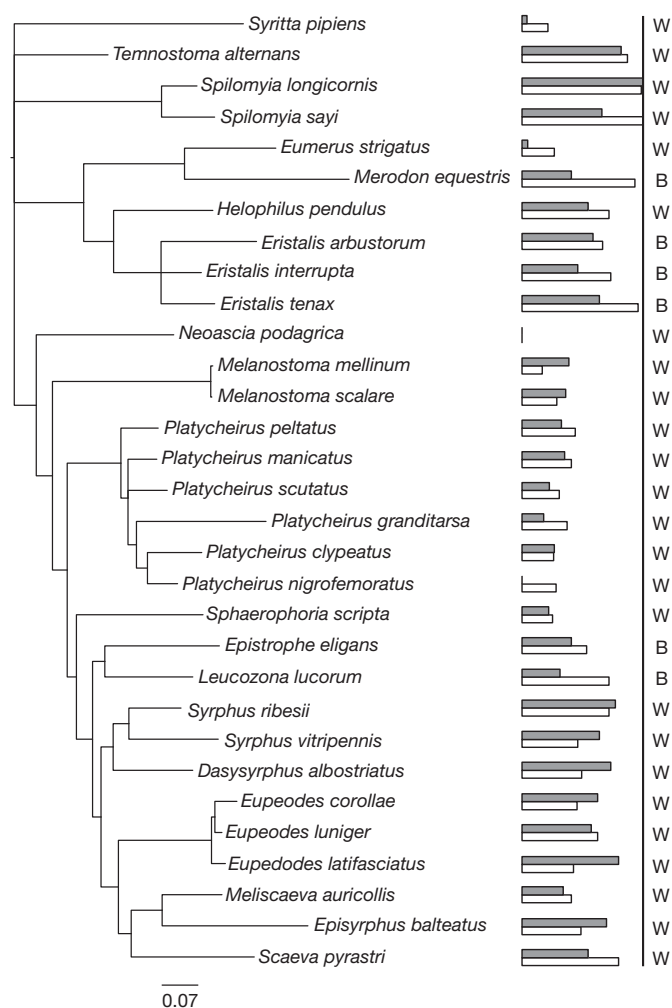


Figure 3 | Phylogenetic relationships between the 31 hoverfly species (Diptera: Syrphidae) for which fidelity and body-size data exist. Shaded bars show the species' mimetic fidelity (f_{HR}), and open bars show the species body size ($-PC1$). In both cases, the length of the bars is scaled from smallest to the largest score for the species shown. The model for each hoverfly species is shown at the right (W, wasp; B, bee). See the text for details of the tree construction methods, and Supplementary Fig. 6 for the phylogeny of all 81 species for which the cytochrome oxidase c subunit I (COI) gene has been sequenced.

The constraints and relaxed-selection hypotheses both suggest that larger, more profitable species will tend to achieve a higher degree of mimetic fidelity at equilibrium, as a result of the greater underlying incentive on predators to attack them. Other factors influencing profitability might include evasive flight behaviour, but predation of hoverflies by birds takes place largely on flowers³. Of course, the predicted evolutionary trajectory for small and large mimics is less obvious if larger-bodied species are rarer than smaller-bodied species^{18,20}; however, as noted above, there is no consistent evidence that this is true. Similarly, our expectation that selection might be less intense on small species because they are less valuable prey might not hold if predators rely heavily on body size as a trait to distinguish mimics from models²¹ (hymenopteran models tend to be larger). Thus, if predators were highly sensitive to difference in body size, then depending on conditions there might be a complete relaxation of selection on mimicry in small species (because they are always attacked regardless of mimetic fidelity), leading to the same general outcome we have observed, or even stronger selection mimetic fidelity in small species as a way to counteract size-based discrimination. Nevertheless, there is evidence that predators cannot discriminate perfectly between

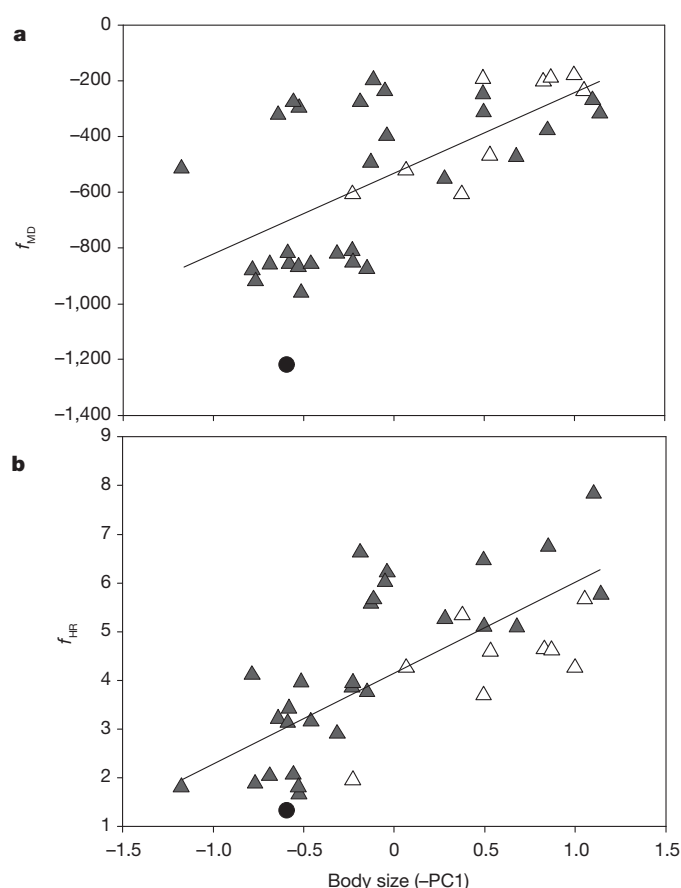


Figure 4 | Relationship between body size (estimated as $-PC1$) and two measures of mimetic fidelity. a, A measure of mimetic fidelity based on Mahalanobis distances (f_{MD}). b, Human ratings of mimetic fidelity (f_{HR}). Lines show the fitted linear regressions. Filled triangles, wasp mimics; open triangles, bee mimics; filled circle, the non-mimetic syrphid *Cheilosia vernalis*.

mimics and models on the basis of body size²¹, and so our profitability interpretation seems the most reasonable.

Mimicry provides a textbook example of adaptation, but researchers have long debated why the fidelity of many imperfect mimics is not further improved by natural selection. Our study represents the first attempt to evaluate multiple hypotheses for imperfect mimicry in the group best known for it, and the first to reveal a significant pattern. Of the five primary hypotheses that we evaluated, our comparative study is only consistent with the constraints and relaxed-selection hypotheses while questioning the assumptions and predictions of the kin-selection, eye-of-the-beholder and multimodel hypotheses. Our revelation of a strong positive relationship between body size and mimetic fidelity is readily explained if body size influences predation behaviour and thereby the intensity of selection for more perfect mimicry. Indeed, relationships between body size and the evolution of aposematic coloration in dendrobatid frogs²² and putative snake mimicry in Lepidoptera²³ may also be explained by the kinds of processes we have invoked. The fact that we can explain the variation in mimetic fidelity on the basis of a relaxation of selection on mimetic fidelity alone, without the need to invoke a specific constraint to generate counter-selection, renders the relaxed-selection hypothesis entirely sufficient to explain the variation we have documented, but we cannot discount the constraints hypothesis. Whether the patterns we have revealed are observed in other mimicry complexes remains to be seen. However, it is clear that the comparative method will be important in evaluating the various explanations not only for imperfect mimicry but for limits to adaptation in general.

METHODS SUMMARY

We focused on 35 hoverfly species recorded in the most extensive multiannual abundance data set available²⁴ (see Supplementary Table 2) and three additional high-fidelity mimics. Phenotypic characters relevant to avian perception were measured from photographs of the 38 species. These characters included antenna length (L_{ant}), abdomen length (L_{ab}), abdomen width (W_{ab}), thorax width (W_{th}), wing length (L_{wing}), all expressed relative to head width (W_{head}). The mean red, green and blue colours (R , G and B) of the abdomen and associated standard deviations (sd_R , sd_G and sd_B) were estimated. Finally, the number and colour of patches and/or stripes were recorded (*Stripe*, *Patch*, *StripePatchCol*). The Mahalanobis distances between species' centroids when these multivariate data were plotted in multivariate space gave a measure of mimetic fidelity, f_{MD} , and a principal components analysis of linear dimensions gave a measure of body size ($-PC1$, because the first principal component was negatively correlated with size). A sample of the photographs, all dorsal view and of the same apparent size, representing two different individuals of each of the 38 syrphid species, were rated by human volunteers ($n = 21$) for similarity (from 1 (very poor mimic) to 10 (excellent mimic)) to photographs of a wasp, honeybee and bumblebee. The highest average rating provided a second measure of mimetic fidelity, f_{HR} .

We calculated the relative abundance of our species from 11 independent studies on the basis of a range of trapping and survey methods. The *COI* gene was sequenced for 77 species of 21 genera of Syrphidae, including 31 species for which we have morphological data, and phylogenetic trees were constructed by using Bayesian methods. Relationships between variables were evaluated with control for phylogenetic autocorrelation (using phylogenetic generalized least-squares regression) and without control for phylogenetic autocorrelation (using Pearson correlations). For the abundance analysis, weighted-mean correlations (\bar{r}) and 95% confidence intervals were calculated across all 11 studies.

Full Methods and any associated references are available in the online version of the paper at www.nature.com/nature.

Received 21 December 2011; accepted 17 February 2012.

1. Bates, H. Contribution to an insect fauna of the Amazon Valley, Lepidoptera: Heliconidae. *Trans. Linn. Soc. Lond.* **23**, 495–566 (1862).
2. Mostler, G. Observations on the question of wasp mimicry. *Z. Morphol. Oekol. Tiere* **29**, 381–454 (1935).
3. Gilbert, F. in *Insect Evolutionary Ecology* (eds Fellowes, M. D. E., Holloway, G. J. & Rolff, J.) 231–288 (CABI Publishing, 2005).
4. Cuthill, I. C. & Bennett, A. T. D. Mimicry and the eye of the beholder. *Proc. R. Soc. Lond. B* **253**, 203–204 (1993).
5. Edmunds, M. Why are there good and poor mimics? *Biol. J. Linn. Soc.* **70**, 459–466 (2000).
6. Johnstone, R. A. The evolution of inaccurate mimics. *Nature* **418**, 524–526 (2002).
7. Duncan, C. J. & Sheppard, P. M. Sensory discrimination and its role in the evolution of Batesian mimicry. *Behaviour* **24**, 269–282 (1965).
8. Sherratt, T. N. The evolution of imperfect mimicry. *Behav. Ecol.* **13**, 821–826 (2002).
9. Ruxton, G. D., Sherratt, T. N. & Speed, M. P. *Avoiding Attack: The Evolutionary Ecology of Crypsis, Warning Signals, and Mimicry* (Oxford Univ. Press, 2004).

10. Vereecken, N. J. & Schiestl, F. P. The evolution of imperfect floral mimicry. *Proc. Natl Acad. Sci. USA* **105**, 7484–7488 (2008).
11. Edmunds, M. Do Malaysian *Myrmarachne* associate with particular species of ant? *Biol. J. Linn. Soc.* **88**, 645–653 (2006).
12. Dittrich, W., Gilbert, F., Green, P., McGregor, P. & Grewcock, D. Imperfect mimicry—a pigeon's perspective. *Proc. R. Soc. Lond. B* **251**, 195–200 (1993).
13. Chittka, L. & Osorio, D. Cognitive dimensions of predator responses to imperfect mimicry. *PLoS Biol.* **5**, e339 (2007).
14. Holen, Ø. H. & Johnstone, R. A. The evolution of mimicry under constraints. *Am. Nat.* **164**, 598–613 (2004).
15. Speed, M. P. & Ruxton, G. D. Imperfect Batesian mimicry and the conspicuousness costs of mimetic resemblance. *Am. Nat.* **176**, E1–E14 (2004).
16. Bain, R. S., Rashed, A., Cowper, V. J., Gilbert, F. S. & Sherratt, T. N. The key mimetic features of hoverflies through avian eyes. *Proc. R. Soc. B* **274**, 1949–1954 (2007).
17. Green, P. R. *et al.* Conditioning pigeons to discriminate naturally lit insect specimens. *Behav. Processes* **46**, 97–102 (1999).
18. Iserbyt, A. *et al.* Frequency-dependent variation in mimetic fidelity in an intraspecific mimicry system. *Proc. R. Soc. B* **278**, 3116–3122 (2011).
19. Sutherland, W. J. Do oystercatchers select the most profitable cockles? *Anim. Behav.* **30**, 857–861 (1982).
20. Harper, G. R. & Pfennig, D. W. Mimicry on the edge: why do mimics vary in resemblance to their model in different parts of their geographical range? *Proc. R. Soc. B* **274**, 1955–1961 (2007).
21. Marples, N. M. Do wild birds use size to distinguish palatable and unpalatable prey types? *Anim. Behav.* **46**, 347–354 (1993).
22. Hagman, M. & Forsman, A. Correlated evolution of conspicuous coloration and body size in poison frogs (Dendrobatidae). *Evolution* **57**, 2904–2910 (2003).
23. Janzen, D. H., Hallwachs, W. & Burns, J. M. A tropical horde of counterfeit predator eyes. *Proc. Natl Acad. Sci. USA* **107**, 11659–11665 (2010).
24. Gilbert, F. S. & Owen, J. Size, shape, competition and community structure in hoverflies (Diptera: Syrphidae). *J. Anim. Ecol.* **59**, 21–39 (1990).

Supplementary Information is linked to the online version of the paper at www.nature.com/nature.

Acknowledgements We thank W. Knee for help with the Bayesian analysis, and R. Laird, G. Ruxton and M. Speed for comments on the manuscript. The human aspect of this research was approved by the Carleton University Research Ethics Committee and conducted according to the guidelines set out in the Tri-Council Policy Statement on Ethical Conduct for Research Involving Humans; subjects gave informed consent. The work was supported by grants to T.N.S. from the Natural Sciences and Engineering Research Council of Canada (NSERC), the Canada Foundation for Innovation and the Ontario Innovation Trust, and to J.H.S. from Agriculture and Agri-Food Canada, the Canadian Centre for DNA Barcoding and NSERC Canpolin. C.H. was supported by an Ontario MRI Fellowship.

Author Contributions H.D.P. photographed and measured specimens, and collected data on human rankings. J.H.S. provided the novel molecular phylogeny. C.H. analysed the data. C.H., K.R.A. and T.N.S. wrote the paper. T.N.S. conceived the project. All authors discussed the results and provided comments on the manuscript.

Author Information All new genetic sequences are deposited in GenBank and are listed in Supplementary Table 4. Reprints and permissions information is available at www.nature.com/reprints. The authors declare no competing financial interests. Readers are welcome to comment on the online version of this article at www.nature.com/nature. Correspondence and requests for materials should be addressed to T.N.S. (sherratt@connect.carleton.ca).

METHODS

Mimetic fidelity. Specimens. We focused on the hoverfly species recorded in the most extensive (more than 40,000 specimens) multiannual (15 years) abundance data set available²⁴; see Supplementary Table 2 for a species list. We took photographs of the dorsal and lateral aspects of pinned specimens of 35 species that were included in this focal data set and present in sufficient numbers at the Canadian National Collection of Insects and Arachnids, Ottawa, Canada. Three additional hoverfly species were included to increase the number of high-fidelity mimics, and ten hymenopteran species representing a broad array of potential models (vespid wasps, polistine wasp, honeybee and bumble bees) were also photographed. Photographs were taken of ten individuals (five males, five females) for each of the 38 syrphid species, and ten individuals of each hymenopteran species (all female). All the photographs were taken with a Canon EO5 50D camera with macro lens (100 mm) and microtwin light (MT-243X).

Human rankings. A sample of the photographs, all dorsal view, representing two different individuals of each of the 38 syrphid species were collated. Human volunteers ($n = 21$) were shown each photograph in random order on a projector screen for 20 s, alongside the same images of a wasp (*Vespula vulgaris*), honeybee (*Apis mellifera*) and bumblebee (*Bombus impatiens*). Each hoverfly and model image was presented at magnifications such that they had the same projected body length. Human subjects were asked to rank each syrphid on a scale of 1 (very poor mimic) to 10 (excellent mimic) for each of the three potential models (wasp, honeybee and bumble bee). The human rank of mimetic fidelity identified the model type to which the potential mimic bore the closest resemblance (based on overall mean score for images of that species) and provided a measure of mimetic fidelity, f_{HR} .

Multivariate ratings. A range of attributes were extracted from individual photographs of specimens of the syrphids and hymenopterans described above, using ImageJ (<http://imagej.nih.gov/ij/>). Specimen phenotypic characters were selected on the basis of their relevance to avian perception (taken from ref. 16). Body dimensions comprised antenna length (L_{ant}), abdomen length (L_{ab}), abdomen width (W_{ab}), thorax width (W_{th}) and wing length (L_{wing}), all expressed relative to head width (W_{head}). Mean red, green and blue colours (R, G and B) and the standard deviation of RGB (sd_R , sd_G , sd_B) of the abdomen were also measured with Corel PhotoPaint X3. Finally, the number and colour (classified by the observer as white, grey, silver, yellow, orange or brown) of patches and/or stripes were also recorded (*Stripe*, *Patch*, *StripePatchCol*). Note that our RGB estimates were unstandardized and we did not transform our measurements into avian (or any other potential predator's) colour space. However, our estimates do capture (albeit coarsely) some of the variation in colour that is likely to be perceived by humans, birds and insects. Moreover, we note that the relationship we presented between human and multivariate measures of mimetic fidelity (see the text) remains significant (albeit weaker) even when we remove RGB and the number of stripes and patches, retaining only measurements of the physical dimensions of specimens ($r = 0.369$, d.f. = 36, $P = 0.023$).

A GCDA was used to identify combinations of variables that serve to discriminate between one or more groups of data on the basis of differences between them using the candisc library²⁵ in R (ref. 26). Each potential mimic species is represented by a centroid in multivariate space representing the mean GCDA variates of the individual specimens of that species. Typically, each model species centroid clustered closely around its taxonomic group centroid. The distance between species' centroids (the Mahalanobis distance) represents a multidimensional measure of the morphological similarity between species. Although we cannot confidently assign specific hymenopteran models to each mimic, it is possible to distinguish bee mimics from wasp mimics. Therefore, the average of the distances between each mimic centroid and the centroids of the bee and wasp models was calculated to give a score for mimetic fidelity for each mimic to its putative model group. The smallest mean Mahalanobis distance from the hoverfly species to its potential model type (bee or wasp) again provided a measure of mimetic fidelity. Because Mahalanobis distances were negatively related to mimetic fidelity, we invert those distances to give a measure of mimetic fidelity that is easier to interpret: f_{MD} .

Quantification of body size. The body size of each of the 38 syrphid species photographed was quantified by conducting a principal components analysis on body dimensions (expressed in absolute terms) mentioned above. The first principal component (PC1) explained 82.9% of the variation in the data, was strongly negatively correlated with all six body dimensions ($r < -0.81$, $P < 0.001$ in all cases), and was taken as a composite measure of body size. Because PC1 was negatively correlated to body size measures, we refer to $-PC1$, which is positively correlated with body size, in the results as an aid to interpretation.

Abundance. We identified 11 independent studies that provide estimates of relative hoverfly abundance based on a range of trapping and survey methods (see

Supplementary Table 1 for full details). These studies included between 3 and 35 species for which we had detailed morphological data (hence estimates of mimetic fidelity). Where multiple years of data were presented, this was based on the arithmetic mean count of each species trapped per year over the whole period of recording. These data were considered reasonably indicative of abundance, as there was a general tendency for the relative abundance of hoverfly species to correlate between studies based on a range of trapping methods (see Supplementary Table 3).

Phylogenetic analysis. A total of 77 species of 21 genera of Syrphidae are included in the ingroup (Supplementary Table 4), including 31 species for which we have morphological data (Fig. 3 and Supplementary Table 2). To encompass a range of genetic variation, we included multiple exemplars from each genus used in our mimicry analysis. These specimens represent most major syrphid clades. Four species of *Microdon*, the putative sister group to the rest of the syrphids^{27,28}, were used as outgroup taxa.

The 5' region of the gene encoding cytochrome oxidase c subunit I (*COI*) was sequenced for each specimen in accordance with the methods outlined in ref. 29. DNA extraction and sequencing were performed in house and at the Canadian Centre for DNA Barcoding. The resultant sequences, as well as images and related data, can be accessed through the Barcode of Life Data Systems (BOLD) (<http://www.barcodinglife.org/>) in the public project 'Mimicry—Skevington (MIMSK)' (<http://www.boldsystems.org/views/projectmenu.php?&>). In addition, all sequences were deposited in GenBank (Supplementary Table 4).

Bayesian analyses were conducted with MrBayes 3.1.2 (ref. 30) with a Markov Chain Monte Carlo (MCMC) method as submitted remotely to the CIPRES computing cluster (<http://www.phylo.org/>)³¹. MrModeltest v2.3 (ref. 32) was used to determine the best model (GTR+I+G) for analysis. Four chains (three hot, one cold) were run simultaneously for 5 million generations. Trees were sampled every 1,000 generations and each simulation was run twice. At 5 million generations the standard deviation was 0.03195. After the discard of the first 500,000 samples as burn-in, 9,002 trees were used to generate a majority-rule consensus tree, posterior probabilities for each node, and branch length estimates. The resulting phylogeny is largely congruent with other published results that used nuclear loci²⁷ and contains multiple taxa per genus, which acts as a major control for the single mitochondrial marker. Reassuringly, the resulting phylogeny supported monophyly for all genera apart from identifying two paraphyletic genera that have been suggested as such in the literature (*Cheilosia*^{33,34} and *Eupeodes*³⁴; Supplementary Fig. 6). Finally, using additional 28S sequences for a subset of 15 species (see Supplementary Table 4 for accession numbers), we find a significant correlation between the phylogenetic distances of the *COI*+28S and *COI*-only trees (Mantel test for phylogenetic distances, $r = 0.680$, $P < 0.0001$), suggesting that our *COI* phylogeny is an adequate representation of the phylogenetic relationships between the species in our analysis.

Relationships between variables were first evaluated without control for phylogenetic autocorrelation by using Pearson correlations. Autocorrelation was incorporated into a second analysis by using the corGrafen function in the ape library³⁵ in R (ref. 26) to create a covariance matrix based on species from the tree structure described above. The gls function in the nlme package³⁶ was then used to perform the test. For the abundance analysis, Pearson correlations between variables were used in the MetaTable function in the psychometric package³⁷ in R to calculate the weighted-mean correlation, \bar{r} , for all 11 studies. This statistic does not have an associated P value, but 95% confidence intervals for the coefficient were calculated and can be used to determine significance. To control for phylogenetic autocorrelation, t -statistics from the generalized least-squares regression analyses of abundance were converted to Pearson correlation coefficients, where $r = t/\sqrt{(n-2+t^2)}$, followed by the calculation of the weighted-mean correlation.

25. Friendly, M. & Fox, J. Candisc: generalized canonical discriminant analysis. R package version 0. 5-19, (<http://CRAN.R-project.org/package=candisc>) (2010).
26. R Development Core Team. *R: A Language and Environment for Statistical Computing* (R Foundation for Statistical Computing, 2010).
27. Skevington, J. H. & Yeates, D. K. Phylogeny of the Syrphoidea (Diptera) inferred from mtDNA sequences and morphology with particular reference to classification of the Pipunculidae (Diptera). *Mol. Phylogenet. Evol.* **16**, 212–224 (2000).
28. Ståhls, G., Hippa, H., Rotheray, G., Muona, J. & Gilbert, F. Phylogeny of Syrphidae (Diptera) inferred from combined analysis of molecular and morphological characters. *Syst. Entomol.* **28**, 433–450 (2003).
29. Gibson, J. F., Skevington, J. H. & Kelso, S. Placement of the Conopidae (Diptera) within the Schizophora based on ten mtDNA and nrDNA gene regions. *Mol. Phylogenet. Evol.* **56**, 91–103 (2010).
30. Ronquist, F. & Huelsenbeck, J. P. MrBayes 3: Bayesian phylogenetic inference under mixed models. *Bioinformatics* **19**, 1572–1574 (2003).
31. Miller, M. A., Pfeiffer, W. & Schwartz, T. In *Proceedings of the Gateway Computing Environments Workshop (GCE)* (IEEE, 2010).

32. Nylander, J. A. A. *MrModeltest* v.2 (Evolutionary Biology Centre, Uppsala Univ., 2004).
33. Rotheray, G. & Gilbert, F. Phylogeny of Palaearctic Syrphidae (Diptera): evidence from larval stages. *Zool. J. Linn. Soc.* **127**, 1–112 (1999).
34. Mengual, X., Ståhls, G. & Rojo, S. First phylogeny of predatory flower flies (Diptera, Syrphidae, Syrphinae) using mitochondrial COI and nuclear 28S rRNA genes: conflict and congruence with the current tribal classification. *Cladistics* **24**, 543–562 (2008).
35. Paradis, E., Claude, J. & Strimmer, K. APE: analyses of phylogenetics and evolution in R language. *Bioinformatics* **20**, 289–290 (2004).
36. Pinheiro, J., Bates, D., DebRoy, S., Sarkar, D., R Development Core Team. nlme: linear and nonlinear mixed effects models. R package version 3. 1-98, (<http://CRAN.R-project.org/package=nlme>) (2011).
37. Fletcher, T. D. Psychometric: applied psychometric theory. R package version 2. 2, (<http://CRAN.R-project.org/package=psychometric>) (2010).

MEGF10 and MEGF11 mediate homotypic interactions required for mosaic spacing of retinal neurons

Jeremy N. Kay¹, Monica W. Chu¹ & Joshua R. Sanes¹

In many parts of the nervous system, neuronal somata display orderly spatial arrangements¹. In the retina, neurons of numerous individual subtypes form regular arrays called mosaics: they are less likely to be near neighbours of the same subtype than would occur by chance, resulting in 'exclusion zones' that separate them^{1–4}. Mosaic arrangements provide a mechanism to distribute each cell type evenly across the retina, ensuring that all parts of the visual field have access to a full set of processing elements². Remarkably, mosaics are independent of each other: although a neuron of one subtype is unlikely to be adjacent to another of the same subtype, there is no restriction on its spatial relationship to neighbouring neurons of other subtypes⁵. This independence has led to the hypothesis that molecular cues expressed by specific subtypes pattern mosaics by mediating homotypic (within-subtype) short-range repulsive interactions^{1,4–9}. So far, however, no molecules have been identified that show such activity, so this hypothesis remains untested. Here we demonstrate in mouse that two related transmembrane proteins, MEGF10 and MEGF11, have critical roles in the formation of mosaics by two retinal interneuron subtypes, starburst amacrine cells and horizontal cells. MEGF10 and 11 and their invertebrate relatives *Caenorhabditis elegans* CED-1 and *Drosophila* Draper have hitherto been studied primarily as receptors necessary for engulfment of debris following apoptosis or axonal injury^{10–14}. Our results demonstrate that members of this gene family can also serve as subtype-specific ligands that pattern neuronal arrays.

The retina contains over 70 neuronal subtypes, divided into broad categories of photoreceptors, interneurons and retinal ganglion cells¹⁵. To seek molecules involved in cell–cell recognition events during retinal circuit assembly, we purified 13 subtypes of retinal neurons from transgenic mice and used microarrays to inventory the genes they expressed^{16,17}. We collected cells at postnatal day (P)6, a time at which synapse formation and mosaic refinement are underway. From this data set we identified genes selectively expressed by specific subtypes, including starburst amacrine cells (SACs), an interneuronal subtype that has critical roles in motion detection¹⁸. The approximately 100 genes that met our criteria for selective SAC expression included most known SAC markers as well as potential new markers (Fig. 1a and Supplementary Table 1). Thirty-one of the novel genes were tested by *in situ* hybridization or immunohistochemistry in combination with SAC markers such as choline acetyltransferase (ChAT) or calbindin¹⁹. This secondary screen yielded 26 genes (Supplementary Table 1), among which were two homologues, *Megf10* and *Megf11*. These genes encode transmembrane proteins with multiple epidermal growth factor (EGF)-like domains, a single membrane-spanning region, and a cytoplasmic domain with several binding sites for signal transduction components^{10,13} (Supplementary Fig. 1). At P5–6, both genes were strongly expressed in SACs (Fig. 1a–c). Both were also expressed in horizontal cells (HCs), which were not part of the data set.

SACs are present in both the inner nuclear and ganglion cell layers, and form independent mosaics in each⁵. These mosaics develop during late embryonic stages, as newborn SACs migrate from the site of their

birth, the outer neuroblast layer, to their final laminar locations. SACs begin to exhibit mosaic spacing upon arrival at their destinations, presumably due to contacts with their homotypic neighbours^{8,9}. As

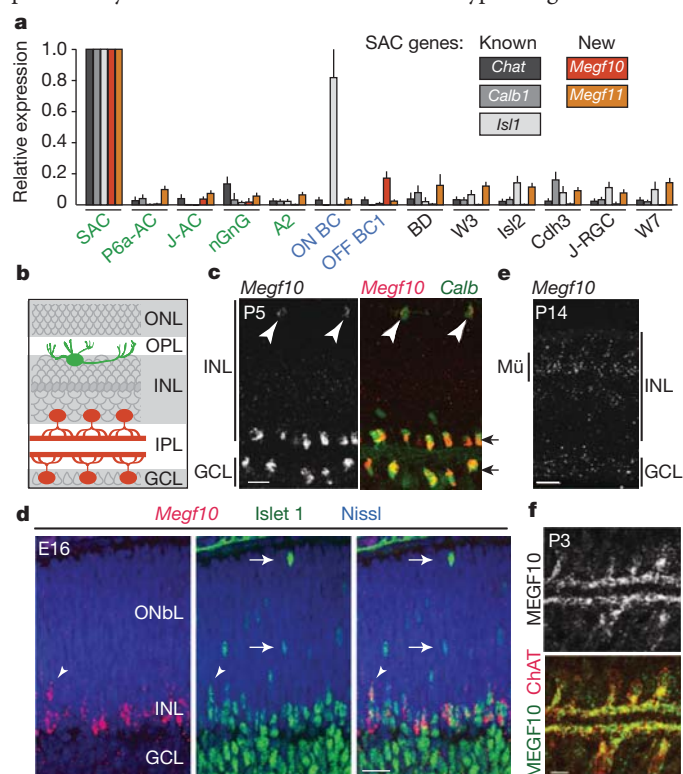


Figure 1 | Expression of *Megf10* and *Megf11* in SACs and HCs. **a**, Relative expression level of *Megf10*, *Megf11* and the known SAC markers *Chat*, *Calb1* (encoding calbindin) and *Isl1* (islet 1) in 13 amacrine (green), bipolar (blue) and retinal ganglion cell (black) subtypes analysed with microarrays. Level in SACs set to 1 for each gene. *Isl1* was also detected in ON bipolar cells as previously reported²¹. Abbreviations for subtypes are defined in Supplementary Table 2. **b**, Schematic of retina. INL, inner nuclear layer with horizontal, bipolar, amacrine, and Müller glial cells; IPL, inner plexiform layer with synapses among bipolar, amacrine and ganglion cells; GCL, ganglion cell layer including displaced amacrine cells; ONL, outer nuclear layer containing photoreceptors; OPL, outer plexiform layer with photoreceptor synapses. SACs (red), HCs (green) and Müller cells (dark grey row) are indicated. **c**, *In situ* hybridization for *Megf10* (left panel; red in right panel) combined with anti-calbindin immunohistochemistry (green in right panel) at P5 shows expression in SACs (black arrows) and HCs (arrowheads). **d**, *Megf10* (red) in E16 retina. *Islet 1* (green) marks SACs migrating through the outer neuroblast layer (ONbL) and in the INL. *Megf10* (red) is expressed by migrating SACs as they arrive in the INL (arrowhead), but not at earlier stages of their migration through the ONbL (arrows). **e**, *Megf10* expression appears in Müller glia (Mü) and is lost from SACs and HCs by P14. **f**, Double-label immunostaining for MEGF10 (green) and ChAT (red). MEGF10 protein localizes to the somata and processes of developing SACs (also see Supplementary Fig. 1). Scale bars, 20 µm (c–e) or 10 µm (f).

¹Center for Brain Science and Department of Molecular and Cellular Biology, Harvard University, 52 Oxford Street, Cambridge, Massachusetts 02138, USA.

new SACs are added to the array, local cellular rearrangements maintain mosaic spacing^{1,4,9}. Mosaic spacing is maintained even as SAC dendrites grow to overlap with those of their neighbours²⁰; thus, mosaicism is distinct from the phenomenon called tiling, which minimizes dendritic overlap¹⁵. Co-staining at embryonic day (E)16 with the early SAC marker islet 1 (refs 9, 21) demonstrated that newborn SACs activated *Megf10* expression as they finished their migration and became integrated into mosaics (Fig. 1d). *Megf10* expression persisted in SACs from E16 to the first postnatal week, and began in HCs at P0 (Supplementary Fig. 1 and data not shown). In the second postnatal week, *Megf10* was downregulated in neurons but appeared in Müller glia (Fig. 1e), consistent with previous reports that *Megf10* is expressed by brain glia²². To determine the subcellular localization of MEGF10 in neurons, we generated an antibody to recombinant protein (Supplementary Fig. 1). MEGF10 was present both on the somata of SACs and HCs and on their processes (Fig. 1f and Supplementary Fig. 1). As expected, immunoreactivity levels on SACs and HCs were highest during the first postnatal week, and then declined (data not shown). Thus, *Megf10* is expressed by SACs and MEGF10 protein is present on SAC processes during the time that mosaics form. Because *Megf11* expression was not observed in retina until after SAC mosaics had formed (see later), we focused first on *Megf10*.

To investigate whether MEGF10 is required for SAC development, we generated mutant mice (Supplementary Fig. 2). *Megf10* mutants were viable and fertile and their retinas exhibited no gross abnormalities.

Mutant SACs migrated to the inner nuclear and ganglion cell layers as in controls, they were present in normal numbers, and their dendrites projected to appropriate sublaminae of the inner plexiform layer (Fig. 2a–c). Examination of whole mounts showed, however, a marked loss of regular spacing among SAC somata, suggesting that their mosaic arrangement had been disrupted (Fig. 2a and Supplementary Fig. 3).

To assess the degree to which SAC mosaics were disrupted, we measured the exclusion zone—the region surrounding each SAC in which other SACs are rarely found. This parameter is calculated from the density recovery profile, a plot of cell density as a function of distance from each SAC in the array²³ (Fig. 2d). The SAC exclusion zone in mutants was smaller than in wild-type littermates, and was approximately equal to the diameter of a SAC soma (Fig. 2e). As the only limitation on proximity was soma size, SACs seem to be positioned randomly in *Megf10* mutants. This conclusion was supported by two additional measurements of spatial order: the packing factor²³, another index of regularity calculated from the density recovery profile; and an independent measure, the Voronoi domain regularity index, which quantifies variations in the area of the territories nearest to each cell in an array^{20,24}. In each case the index calculated for SAC arrays in *Megf10* mutants was similar to that measured for computer-generated random arrays, whereas SAC arrays from wild-type littermates were highly ordered (Fig. 2f, g); heterozygotes showed a mild disorganization (Supplementary Fig. 4). Together these results suggest that MEGF10 acts in SACs to impose a minimal intercellular spacing; in

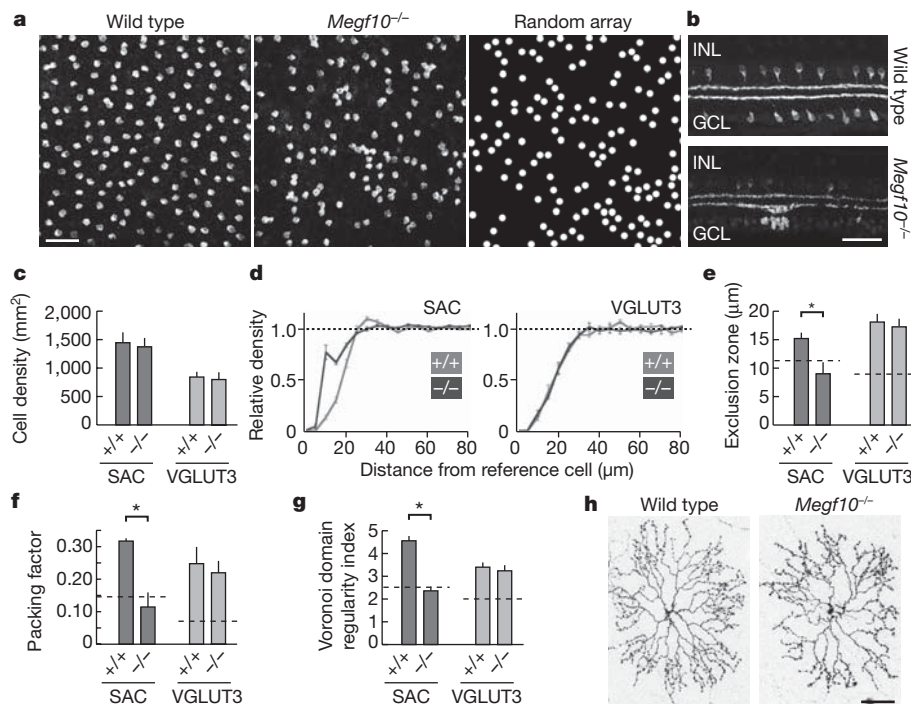


Figure 2 | Loss of SAC mosaic spacing in *Megf10* mutant mice. **a**, SAC mosaic in inner nuclear layer (INL) of wild-type (left) and *Megf10*^{-/-} (centre) retina, revealed by whole-mount staining with anti-ChAT. Wild-type mice have evenly spaced SAC somata, whereas mutants exhibit clumps and gaps similar to those seen in a simulation of a random cellular array (right). See Supplementary Fig. 3 for similar results in ganglion cell layer (GCL) SACs. **b**, ChAT-stained retinal sections from wild-type and *Megf10* mutant animals. Laminal positions of SAC somata and processes are normal in mutants, even in regions where somata are clumped. **c**, Density of SACs and VGLUT3⁺ amacrine cells is similar in wild-type (+/+) and *Megf10* mutant (-/-) retina. **d**, Density recovery profiles (DRPs) for the SAC (INL) and VGLUT3⁺ amacrine arrays. Graphs show the density of cells in a ring of radius *x*, relative to the density of cells in the image as a whole. Dashed line, DRP of random point array. The exclusion zone characteristic of mosaic spacing is measured as a dip below this line. **e**, Exclusion zone radius measured from **d**. Dashed line,

expected result for an array of cells distributed randomly; that is, the diameter of a single cell. Increases above this minimum indicate spatial order. The mutant SAC exclusion zone radius was similar in size to a SAC cell diameter, and was significantly smaller than wild type (**P* < 0.0001). VGLUT3⁺ amacrine exclusion zones were unaffected. **f**, **g**, SAC packing factor (**f**) and Voronoi domain regularity index (**g**) were significantly lower in *Megf10*^{-/-} mice than in wild-type littermates (**P* < 0.0001). Dashed line, mean for arrays of cells distributed randomly. Wild-type SACs and VGLUT3⁺ cells of both genotypes were non-randomly arrayed. The SAC array in mutants was not significantly different from random arrays (**f**, *P* = 0.16; **g**, *P* = 0.48). **h**, Morphology of single GCL SACs, labelled with adeno-associated virus driving membrane-targeted Cherry fluorescent protein, showed no gross abnormalities in *Megf10* mutants (*n* ≥ 8 cells each genotype). Data from P15 (**a–g**) or P80 (**h**) mice. Scale bars, 50 μm. Error bars, s.e.m.

its absence SACs assume random positions relative to each other. By contrast, other amacrine cell types examined (VGLUT3- (also known as SLC17A8) and tyrosine hydroxylase-positive) as well as bistratified direction-selective retinal ganglion cells, which are prominent synaptic targets of SACs¹⁸, showed normal mosaic spacing (Fig. 2d–g and Supplementary Fig. 3).

In mice lacking the adhesion molecules DSCAM or DSCAML1, certain retinal cell mosaics form normally, then degrade secondary to hyperfasciculation of their neurites^{25,26}. To investigate whether MEGF10 acts in a similar indirect fashion, we labelled individual SACs in mutants. Lack of MEGF10 had no obvious effect on SAC dendritic morphology (Fig. 2h). Moreover, soma disorganization was already evident by P0 (Supplementary Fig. 5), shortly after mosaics form, indicating that MEGF10 affected formation of SAC mosaics.

Next we asked whether MEGF10 is also essential for formation of the HC mosaic. Loss of MEGF10 had only a modest effect on HC regularity (Fig. 3). We therefore considered that MEGF11 might have a redundant role. *Megf11* was not expressed in embryonic retina, but it appeared in HCs and SACs during the first postnatal week and persisted into adulthood (Fig. 3a–d). Importantly, SAC mosaics begin to form before P0, but HC mosaics are established postnatally^{4,6,9}. We therefore generated *Megf11* mutant mice (Supplementary Fig. 2), which, like *Megf10* mutants, showed no gross retinal abnormalities (Supplementary Fig. 6). Examination of HC arrays in *Megf11* mutants revealed a modest decrease in regularity similar to that in *Megf10* mutants, whereas in *Megf10*^{−/−}; *Megf11*^{−/−} double-mutant animals, the HC mosaic was severely disrupted (Fig. 3e–m and Supplementary Fig. 7). By contrast, SACs were unaffected by loss of *Megf11* function, and were no more affected in double mutants than in *Megf10* single mutants (Supplementary Figs 6 and 8). Thus, *Megf11*

is dispensable for SAC arrangement, but acts together with *Megf10* to shape the HC mosaic.

To elucidate the cellular mechanisms by which *Megf10* and *Megf11* act, we used a gain-of-function approach in which we introduced MEGF10 into the retina by electroporation of plasmid DNA at P0. We first tested the hypothesis that MEGF10 can act as a signal that repels SACs, creating the exclusion zone that defines mosaic spacing. The electroporation method predominantly transfects dividing cells, leading to expression in neurons that exit the cell cycle postnatally, such as bipolar cells, Müller glia, photoreceptors and late-born amacrine cells²⁷. Because SACs and HCs are born embryonically, they are rarely transduced²⁷, allowing us to surround wild-type SACs and HCs with cells ectopically expressing excess MEGF10. Indeed, electroporation of plasmid encoding a fluorescent protein (FP) or a MEGF10–FP fusion produced retinal patches in which a large fraction of neurons, but no SACs or HCs, were FP⁺ (Fig. 4a and Supplementary Fig. 9). Expression of MEGF10–FP (but not FP alone) resulted in exclusion of SACs and HCs from a swath at the edge of the electroporated patch, whereas spacing of these cells was essentially normal in patch centres (Fig. 4a, b and Supplementary Fig. 10). A truncated MEGF10 lacking the cytoplasmic domain produced an identical phenotype (Supplementary Fig. 10), ruling out the possibility that MEGF10 acts indirectly by triggering production of a repellent factor by the transfected cells. Thus, MEGF10 can act as a ligand that signals to SACs and HCs.

Because MEGF10 relatives have been implicated in cell engulfment^{10–13}, we asked whether its overexpression formed an exclusion zone by eliminating cells. We found no evidence for cell death at patch edges (no pyknotic nuclei or activated caspase-3 immunoreactivity; data not shown). Instead, cell density was increased at the outer edge of the cell-free swath, indicating that SACs had exited the patch to create the

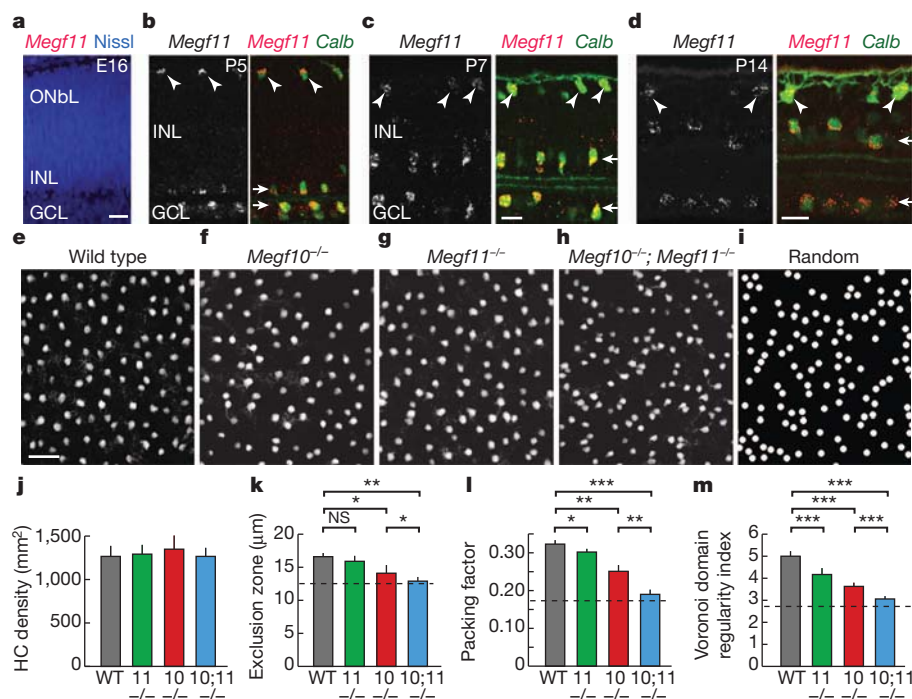


Figure 3 | HC mosaic spacing requires *Megf10* and *Megf11*. a–d, *In situ* hybridization for *Megf11* at ages indicated. *Megf11* (red) was not expressed at E16 (a). Calbindin immunostaining (green) labels SACs and HCs, which co-express *Megf11* at P5 (b), P7 (c) and P14 (d). See Fig. 1 for abbreviations. e–i, Retinal whole mounts stained for calbindin to reveal the HC array. In wild-type mice (e), HCs are distributed evenly. *Megf10*^{−/−} mutants (f) and *Megf11*^{−/−} mutants (g) show subtle changes in the regular spacing of HCs, whereas double *Megf10*^{−/−}; *Megf11*^{−/−} mutants (h) show marked HC disorganization similar to a simulation of a random HC array (i). j–m, Quantification of HC spacing regularity in *Megf10*^{−/−} (red) or *Megf11*^{−/−} (green) single mutants; *Megf10*^{−/−};

Megf11^{−/−} double mutants (blue); and wild-type (WT) siblings (grey). In all genotypes, HCs were present at normal density (j) but were less regularly spaced relative to wild type based on exclusion zone radius (k), packing factor (l) and Voronoi domain regularity (m) measurements as in Fig. 2. Double mutants showed significantly less order than single *Megf10*^{−/−} or *Megf11*^{−/−} mutants and approach random arrangement, indicated by dashed lines (k, mean HC soma diameter; l, m, computed values for random arrays). *P* values: **P* < 0.01, ***P* < 0.001, ****P* < 0.0001. NS, not significant. Error bars give s.e.m. Data in e–m from P15 animals. Scale bars, 20 μm (a–d; b, c share scale) or 50 μm (e–i).

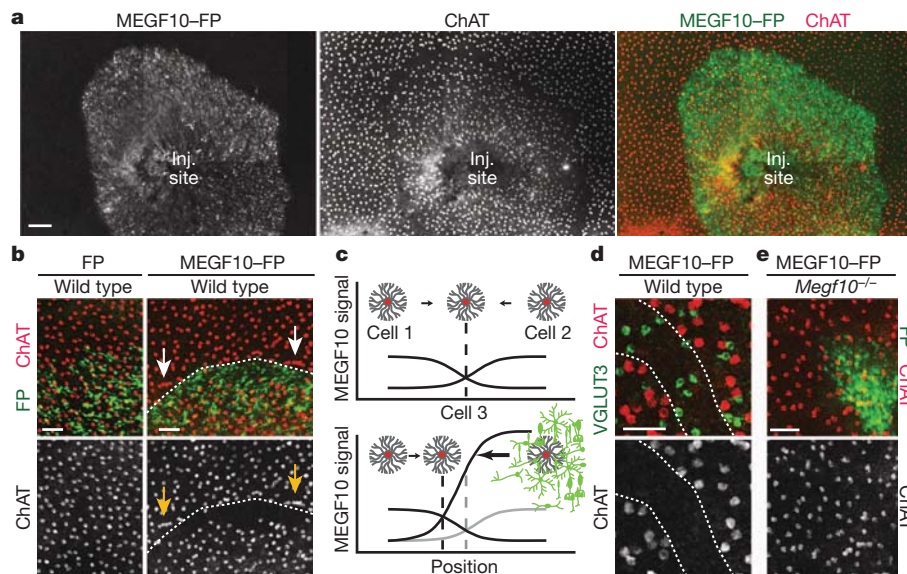


Figure 4 | MEGF10 acts as both ligand and receptor to trigger SAC repulsion. **a**, A retinal patch transfected by electroporation with plasmid encoding MEGF10-FP fusion protein, viewed in flat mount. SAC somata in INL, stained with anti-ChAT, are excluded from a swath at the patch edge. SACs are evenly spaced elsewhere, except where the retina was pierced to inject DNA (Inj. site). **b**, Higher-magnification views of patch edges. FP misexpression (left) did not affect SAC spacing, but MEGF10-FP (right) produced a SAC-free zone just inside the transfected region and induced apparent crowding of SACs immediately outside it (arrows). Dashed line, patch edge. See Supplementary Fig. 11 for quantification of cell distribution at patch edges. **c**, Hypothesis for MEGF10 function based on **a**, **b**. In wild-type retina

(top), SACs use MEGF10 as a ligand to signal their location to neighbouring SACs. Cell 3 positions itself at the point where repulsive signals on either side (from Cell 1 and Cell 2) are equal. In MEGF10-FP overexpression (bottom), that location is now outside the patch. **d**, MEGF10-FP transfected whole-mount immunostained for ChAT and VGLUT3. Dashed lines mark SAC-free zone (see Supplementary Fig. 10). VGLUT3⁺ amacrine cells are present in this zone. **e**, MEGF10-FP is incapable of generating a SAC-free zone when misexpressed in *Megf10* mutant retina, indicating that MEGF10 is needed for SAC responses to MEGF10. See Supplementary Fig. 11 for quantification. Scale bars, 100 μ m (**a**); 50 μ m (**b–e**). All retinas are from P10–P15 animals.

SAC-free zone (Fig. 4b and Supplementary Fig. 11). Our interpretation is that SACs and HCs are repelled by MEGF10, but that within MEGF10-FP patches the concentration of MEGF10 is similar in all directions, resulting in no net movement (Fig. 4c). Consistent with this view, SACs and HCs were entirely excluded from small patches (≤ 5 –6 cell diameters; Supplementary Fig. 10). Together these results suggest that MEGF10 can act as a repellent ligand.

We next asked which cells are sensitive to MEGF10 ligand. In *Megf10* mutants, SACs and HCs are selectively affected; this might be because they are uniquely sensitive to MEGF10 or because only these cells encounter endogenous MEGF10 at high concentration. Ectopic expression allowed us to distinguish between these possibilities. None of 13 other amacrine, bipolar or retinal ganglion cell subtypes assayed with cell-type-specific markers was detectably affected by MEGF10-FP (Fig. 4d and Supplementary Table 3). Thus, MEGF10 appears to act as a cell-surface ligand for a receptor specifically expressed by SACs and HCs.

This led us to ask whether MEGF10 might be the MEGF10 receptor. We used cultured epithelial cells (HEK293) to seek evidence for a MEGF10-dependent homotypic interaction. Whereas FP-expressing cells overlapped, MEGF10-FP-expressing cells formed sharp borders with narrow gaps (Supplementary Fig. 12a), consistent with previous results¹⁴. This 'jigsaw' pattern reflected suppression or elimination of filopodia at points of intercellular apposition (Supplementary Fig. 12b). Jigsaw formation and loss of filopodia required the MEGF10 cytoplasmic domain and did not occur when a MEGF10-FP-expressing cell contacted an untransfected or FP-transfected cell (Supplementary Fig. 12b, c). Although we have been unable to demonstrate MEGF10 homophilic binding using biochemical methods (data not shown), these results suggest that a MEGF10-containing signalling complex mediates a homotypic interaction resulting in intercellular repulsion.

Finally, we tested the idea that MEGF10 serves as both ligand and receptor *in vivo*. To this end, we electroporated MEGF10 into *Megf10* mutant retina. Mutant SACs did not exit MEGF10-FP patches (Fig. 4e

and Supplementary Fig. 11b), indicating that *Megf10* gene function is required for SACs to respond to MEGF10 repulsive signals. Together these results suggest a model in which SACs and HCs use MEGF10 as part of a receptor complex that detects MEGF10 on their homotypic neighbours. This repulsive signal positions their somata so as to equalize MEGF10 signals on all sides, thereby creating exclusion zones (Fig. 4c).

The phenomenon of retinal mosaicism implies a molecular system for cell-type-specific recognition. Several potential mechanisms have been proposed, based on imaging and computational studies, one being that short-range repulsive signals regulate tangential movements to establish each cell's territory^{3,4,6–9}. So far, however, direct mediators of this phenomenon have not been described. Here we provide evidence that, for SACs and HCs, mosaic spacing requires repellent homotypic interactions mediated by MEGF10 and 11. Signals initiated by MEGF10/11 in growing neurites could lead to repositioning of the soma within the cytoplasm, perhaps by mechanisms resembling those that direct soma translocation in response to signals at the leading process of migrating neurons²⁸. The finding that MEGF10 and 11 facilitate formation of three independent mosaics (two for SACs and one for HCs) appears at first to contradict the idea that mosaics are independent of each other and must therefore be regulated by distinct molecules^{1,3–5}. However, because the three mosaics occupy distinct cellular planes, they may be exempt from the requirement for molecular individuation. Different molecules are likely to mediate homotypic interactions in other retinal subtypes, some of which may lead to soma translocation and others to the death of cells that violate minimal spacing²⁴.

We note two broader implications of our results. First, Draper/CED-1/MEGF10 homologues have until now been studied predominantly as receptors for cell engulfment^{10–14}. Here we show that they also mediate cell–cell repulsion and can act as ligands as well as receptors, thereby expanding the roles for this gene family. Second, although mosaic arrangements have so far been studied formally only in retina, regularly arranged neuronal arrays are common features of central neural

organization^{1,29}. Mechanisms similar to those described here could be involved in promoting this regularity.

METHODS SUMMARY

Retinal neurons expressing fluorescent proteins were purified and used to generate amplified RNA for hybridizing Affymetrix microarrays as described previously^{16,17}. SAC-specific genes were identified using dChip software. *Megf10* and *Megf11* mutant mice were produced from constructs generated by the Knockout Mouse Project and European Conditional Mouse Mutagenesis program (EUCOMM)³⁰. Histological methods^{16,17} and methods for electroporation of plasmid DNA *in vivo*^{17,27} were described previously. HEK293 cells (ATCC) were cultured and transfected by standard methods.

For analysis of spatial statistics, we sampled a 635.9 μm square at 3–4 locations per retina. X–Y cell coordinates, marked manually, were used to calculate Voronoi domain areas (Fiji) or DRP statistics such as the effective radius (that is, exclusion zone) and packing factor (WinDRP). We generated random arrays matched in density and soma size to real data; these were analysed in parallel with data from mutants. For measurement of SAC crowding in gain-of-function experiments, the Delaunay triangulation⁸ was used to define each cell's nearest neighbours.

Full Methods and any associated references are available in the online version of the paper at www.nature.com/nature.

Received 8 October 2011; accepted 17 January 2012.

Published online 11 March 2012.

- Cook, J. E. & Chalupa, L. M. Retinal mosaics: new insights into an old concept. *Trends Neurosci.* **23**, 26–34 (2000).
- Wässle, H. & Riemann, H. J. The mosaic of nerve cells in the mammalian retina. *Proc. R. Soc. Lond. B* **200**, 441–461 (1978).
- Eglen, S. J. Development of regular cellular spacing in the retina: theoretical models. *Math. Med. Biol.* **23**, 79–99 (2006).
- Reese, B. E. & Galli-Resta, L. The role of tangential dispersion in retinal mosaic formation. *Prog. Retin. Eye Res.* **21**, 153–168 (2002).
- Rockhill, R. L., Euler, T. & Masland, R. H. Spatial order within but not between types of retinal neurons. *Proc. Natl Acad. Sci. USA* **97**, 2303–2307 (2000).
- Huckfeldt, R. M. *et al.* Transient neurites of retinal horizontal cells exhibit columnar tiling via homotypic interactions. *Nature Neurosci.* **12**, 35–43 (2009).
- Poché, R. A. *et al.* Somal positioning and dendritic growth of horizontal cells are regulated by interactions with homotypic neighbors. *Eur. J. Neurosci.* **27**, 1607–1614 (2008).
- Galli-Resta, L. Local, possibly contact-mediated signalling restricted to homotypic neurons controls the regular spacing of cells within the cholinergic arrays in the developing rodent retina. *Development* **127**, 1509–1516 (2000).
- Galli-Resta, L., Resta, G., Tan, S. S. & Reese, B. E. Mosaics of islet-1-expressing amacrine cells assembled by short-range cellular interactions. *J. Neurosci.* **17**, 7831–7838 (1997).
- Wu, H.-H. *et al.* Glial precursors clear sensory neuron corpses during development via Jedi-1, an engulfment receptor. *Nature Neurosci.* **12**, 1534–1541 (2009).
- MacDonald, J. M. *et al.* The *Drosophila* cell corpse engulfment receptor Draper mediates glial clearance of severed axons. *Neuron* **50**, 869–881 (2006).
- Reddien, P. W. & Horvitz, H. R. The engulfment process of programmed cell death in *Caenorhabditis elegans*. *Annu. Rev. Cell Dev. Biol.* **20**, 193–221 (2004).
- Hamon, Y. *et al.* Cooperation between engulfment receptors: the case of ABCA1 and MEGF10. *PLoS ONE* **1**, e120 (2006).
- Suzuki, E. & Nakayama, M. MEGF10 is a mammalian ortholog of CED-1 that interacts with clathrin assembly protein complex 2 medium chain and induces large vacuole formation. *Exp. Cell Res.* **313**, 3729–3742 (2007).
- Sanes, J. R. & Zipursky, S. L. Design principles of insect and vertebrate visual systems. *Neuron* **66**, 15–36 (2010).
- Kay, J. N. *et al.* Retinal ganglion cells with distinct directional preferences differ in molecular identity, structure, and central projections. *J. Neurosci.* **31**, 7753–7762 (2011).
- Kay, J. N., Voinescu, P. E., Chu, M. W. & Sanes, J. R. Neurod6 expression defines new retinal amacrine cell subtypes and regulates their fate. *Nature Neurosci.* **14**, 965–972 (2011).
- Demb, J. B. Cellular mechanisms for direction selectivity in the retina. *Neuron* **55**, 179–186 (2007).
- Haverkamp, S. & Wässle, H. Immunocytochemical analysis of the mouse retina. *J. Comp. Neurol.* **424**, 1–23 (2000).
- Keeley, P. W., Whitney, I. E., Raven, M. A. & Reese, B. E. Dendritic spread and functional coverage of starburst amacrine cells. *J. Comp. Neurol.* **505**, 539–546 (2007).
- Elshatory, Y. *et al.* Islet-1 controls the differentiation of retinal bipolar and cholinergic amacrine cells. *J. Neurosci.* **27**, 12707–12720 (2007).
- Cahoy, J. D. *et al.* A transcriptome database for astrocytes, neurons, and oligodendrocytes: a new resource for understanding brain development and function. *J. Neurosci.* **28**, 264–278 (2008).
- Rodiek, R. W. The density recovery profile: a method for the analysis of points in the plane applicable to retinal studies. *Vis. Neurosci.* **6**, 95–111 (1991).
- Raven, M. A., Eglen, S. J., Ohab, J. J. & Reese, B. E. Determinants of the exclusion zone in dopaminergic amacrine cell mosaics. *J. Comp. Neurol.* **461**, 123–136 (2003).
- Fuerst, P. G., Koizumi, A., Masland, R. H. & Burgess, R. W. Neurite arborization and mosaic spacing in the mouse retina require DSCAM. *Nature* **451**, 470–474 (2008).
- Fuerst, P. G. *et al.* DSCAM and DSCAML1 function in self-avoidance in multiple cell types in the developing mouse retina. *Neuron* **64**, 484–497 (2009).
- Matsuda, T. & Cepko, C. L. Electroporation and RNA interference in the rodent retina *in vivo* and *in vitro*. *Proc. Natl Acad. Sci. USA* **101**, 16–22 (2004).
- Solecki, D. J., Model, L., Gaetz, J., Kapoor, T. M. & Hatten, M. E. Par6 α signaling controls glial-guided neuronal migration. *Nature Neurosci.* **7**, 1195–1203 (2004).
- Budry, L. *et al.* Related pituitary cell lineages develop into interdigitated 3D cell networks. *Proc. Natl Acad. Sci. USA* **108**, 12515–12520 (2011).
- Skarnes, W. C. *et al.* A conditional knockout resource for the genome-wide study of mouse gene function. *Nature* **474**, 337–342 (2011).

Supplementary Information is linked to the online version of the paper at www.nature.com/nature.

Acknowledgements We thank B. Tilton, P. Rogers, J. Couget, and the Harvard Genome Modification Facility for technical assistance; S. Sarin and M. Yamagata for critical discussions; the National Institutes of Health (NS029169 and EY022073 to J.R.S.) and Life Sciences Research Foundation (J.N.K.) for funding.

Author Contributions J.N.K. and J.R.S. designed experiments and wrote the paper. J.N.K. and M.W.C. performed experiments. J.N.K. performed data analysis. J.R.S. supervised the project.

Author Information Data have been deposited at the Gene Expression Omnibus (<http://www.ncbi.nlm.nih.gov/geo/>) under accession code GSE35077. Reprints and permissions information is available at www.nature.com/reprints. The authors declare no competing financial interests. Readers are welcome to comment on the online version of this article at www.nature.com/nature. Correspondence and requests for materials should be addressed to J.R.S. (sanesj@mcb.harvard.edu).

METHODS

Animals. CD1 and C57BL/6 mice were obtained from Charles River and Jackson Labs. All experiments were carried out in accordance with protocols approved by the Harvard University Standing Committee on the Use of Animals in Research and Teaching.

Megf10 mutant mice were produced from a construct provided by the Knockout Mouse Project³⁰ (CHORI). Embryonic stem (ES) cell electroporation and chimera production were performed by the Harvard Genome Modification Facility. ES cell clones were screened for integration by PCR using primers listed in Supplementary Table 4 (also see Supplementary Fig. 2). *Megf11* mutant mice were generated from gene-targeted ES cells provided by the European Conditional Mouse Mutagenesis program (EUCOMM). In both cases germline transmission was obtained from two chimeric mice generated from independent ES cell clones; each had indistinguishable phenotypes. The primers used for genotyping *Megf10* and *Megf11* mice are listed in Supplementary Table 4. *Drd4-GFP* mice³¹ were obtained from the Mutant Mouse Regional Resource Center.

Cell sorting and expression profiling. Retinal neurons expressing fluorescent proteins were purified as described^{16,17}. Briefly, P6 retinas were dissociated, live-stained with antibodies recognizing cell surface antigens (if required for purification), and then passed through a flow cytometer (Mo Flo; Dako). Positive cells were then either: (1) plated, fixed, stained with cell-type-specific markers and counted to assess purity; or (2) sorted directly into RNA lysis buffer (PicoPure Kit; MDS). Gene expression was profiled using Affymetrix Mouse 430 2.0 arrays, following two rounds of linear amplification (MessageAmp II; Applied Biosystems). Using these methods we generated a gene-expression database for 13 specific retinal neuron subtypes (five amacrine, two bipolar and six retinal ganglion cell types; see Supplementary Table 2). SAC-specific genes (Supplementary Table 1) were identified using dChip software using fold-change over other cell types as filtering criteria.

Histology and staining. Fixation and preparation of retinal cryosections was performed as described¹⁷. For whole-mount retinal stains, the retina was dissected out of the eyecup in a dish of phosphate buffered saline (PBS), transferred to an Eppendorf tube (up to four retinas per tube), and incubated at room temperature (20–25 °C) for 1 h with agitation in blocking solution (PBS + 0.3% Triton-X-100 + 3% donkey serum; Jackson ImmunoResearch). Primary antibody, diluted in blocking solution, was then applied to the sample; incubation was for 6 days at 4 °C with agitation. Following a 2–3 h wash in 2–3 changes of PBS, secondary antibodies (Jackson ImmunoResearch) were applied overnight at 4 °C with agitation. After at least 4 h of washing in PBS with agitation, retinas were flattened onto nitrocellulose membranes (Millipore) and mounted on slides (Fluoromount G; Southern Biotech). Images were acquired with a FV1000 confocal microscope (Olympus).

The following antibodies were used for immunostaining: rabbit anti-calbindin (Swant); goat anti-ChAT (Millipore); goat anti-VACHT (Promega); guinea pig anti-VGLUT3 (Millipore); mouse anti-islet 1/2 (clone 39.4D5, Developmental Studies Hybridoma Bank (DSHB)); mouse anti-SYT2 (DSHB); chicken anti-green fluorescent protein (GFP; Aves labs); rabbit anti-DsRed (Clontech); rabbit anti-β-galactosidase³²; mouse anti-glutamine synthetase (BD); sheep anti-tyrosine hydroxylase (Millipore); mouse anti-PKC (Abcam); rabbit anti-DAB1 (Millipore); rabbit anti-CART (Phoenix); mouse anti-Kv4.2 (Neuromabs); rabbit anti-SOX9 (Millipore); rabbit anti-cleaved-caspase 3 (Cell Signaling Technology); rabbit anti-bNOS (Sigma); rabbit anti-EBF3 (ref. 17); rabbit anti-GAD65/67 (Millipore); goat anti-GLYT1 (Millipore); mouse anti-BRN3A (Millipore); mouse SMI-32 (Sternberger). MEGF10 antibody was raised in rabbits against a His-tagged peptide corresponding to amino acids 879–1130 of mouse MEGF10 (Millipore).

In situ hybridization was performed according to previously reported methods¹⁷. To make the template for the *Megf10* antisense probe, we obtained an IMAGE clone (BC075647) containing full-length mouse *Megf10* and linearized with ClaI. *Megf11* template, in pGEM-T Easy (Promega), was generated by PCR from brain cDNA using primers TGTCTTCTCTGCAAGCTGCTCT and ATTCCACAAGT GCCTGGTGAGTGT. Antisense riboprobes were transcribed using the DIG RNA labelling kit (Roche). Calbindin immunostaining was used to label SACs and HCs—at P0–P7 it is a selective marker for these two cell types, showing additional expression in only a small subset of amacrine and retinal ganglion cells (Fig. 1 and Supplementary Fig. 9, and data not shown).

Labelling of single SACs and HCs was performed by intraocular injection of low-titre adeno-associated virus, as described³³.

Quantification of mosaic regularity. For analysis of mutant phenotypes, confocal z-stacks through the GCL and INL were acquired from P14–17 retinas stained with antibodies to ChAT, calbindin, tyrosine hydroxylase, and/or VGLUT3. Each retina was sampled in 3–4 locations (sample size was a square, 635.9 μm on each side). Stacks in which mounting artefacts introduced large local z-axis displacement of the SAC or HC array were not used. We sampled from both central and peripheral

retina; despite differences in cell density between these locations the spatial organization of SAC, HC and VGLUT3 arrays did not appear to differ systematically. We therefore pooled data from central and peripheral retina for subsequent analysis. Using Fiji software, the centre of each cell was marked manually to generate X–Y coordinates. The point array was flattened to a single plane without correction for local curvature, but as we only used very flat images for analysis, the spatial distortions introduced by this procedure were minor. Density recovery profiles (DRPs) were computed from these X–Y coordinates using WinDRP software³⁴. Voronoi domain areas were computed in Fiji and Microsoft Excel from the X–Y coordinate data. SAC, HC and VGLUT3⁺ amacrine cell density and cell diameters were determined from these same images using Fiji to perform measurements.

We calculated three measures of regularity for each image. First, from the DRP, we obtained the effective radius. Effective radius gives the size of the exclusion zone—the zone in which another cell is less likely to be found than would be expected for a random array²³. Second (also from the DRP), we computed the packing factor—a regularity index that ranges between 0 (for a random array) and 1 (for a perfect hexagonal array). Third, we calculated the Voronoi domain regularity index (VDRI) by dividing the mean Voronoi domain area for a given cellular array by the standard deviation of those areas^{20,24,35}.

To ascertain how the measured packing factor and VDRI compared to those that would be observed in cell arrays lacking mosaic spacing, we generated random simulations of HC, SAC, and VGLUT3⁺ amacrine cell arrays. These simulations placed cells randomly in a 635.9 μm square following a Poisson point process, until the density of the array equalled the mean density of the cell type in question. The only constraint on cell location in these simulations was soma diameter, which was calculated for each cell type as described earlier. The soma diameters used to constrain the simulations were 9.0 μm (VGLUT3⁺ amacrine cells), 11.0 μm (SACs) and 12.2 μm (HCs). Programita software³⁶ was used to generate the simulations ($n = 10$ for each cell type). Packing factor and VDRI were then calculated as described above, and the means were plotted as dashed lines in Figs 2 and 3. The VDRI for our random simulations were similar to those calculated previously³⁵.

For analysis of SAC cell position in MEGF10-misexpressing retina, we acquired images at the edge of FP⁺ or MEGF10–FP⁺ misexpressing patches, and used the above method to obtain X–Y coordinates of all SACs in the field of view. SACs inside the patch, outside the patch, and at the edge of the patch were marked separately. ‘Edge’ cells were defined as those outside the FP⁺ region for which the shortest line drawn from that cell to the edge of the FP⁺ region did not pass the soma of another SAC. To ask whether SACs were present at higher density at patch edges, we calculated the distance from each SAC to its nearest neighbours. Neighbours were defined in an unbiased manner by computing the Delaunay triangulation for the X–Y location data set (Fiji), thereby defining line segments from each cell to its nearest neighbours.

Statistical analysis. For analysis of exclusion zone radius, packing factor, VDRI and cell density, the significance of measured differences between genotypes was evaluated by the Mann–Whitney U test. Sample sizes were ≥9 images from ≥3 retinas per genotype (SAC and HC analysis) or 6 images from 2 retinas per genotype (VGLUT3 analysis). In double-mutant experiments on HCs, the Holm–Bonferroni correction for multiple comparisons (four different genotypes) was applied when determining significance level. For measurement of soma diameter, sample size was ≥150 cells for each genotype.

Gain-of-function experiments. A *Megf10* expression construct was generated by PCR amplifying the open reading frame (ORF), with stop codon deleted, from the IMAGE clone described earlier. The open reading frame, which was predicted to encode a protein equivalent to the *Megf10* RefSeq sequence (NP_115822.1), was TA-cloned into the Gateway entry vector pCR8GW-Topo (Invitrogen). Primers used for cloning were CGATTGTCTTCTACAGAACATGGCG and TTGAT GTGATTCAGTCTGCT. A cytoplasmic domain-deletion construct was made by amplifying with reverse primer TGATTCCTTCTCTTCTGCTT to generate a truncated protein carrying only the first nine amino acids of the intracellular domain. For expression, these constructs were transferred to a Gateway destination vector bearing the ubiquitin-C promoter and an in-frame C-terminal GFP or monomeric Cherry tag. Mouse *Megf11* was also cloned, but pilot experiments in HEK cells suggested a lack of surface expression, so we did not attempt *in vivo* experiments with mouse *Megf11*.

In vivo electroporation was performed as described^{17,27}. Briefly, plasmid DNA (at least 1.5 mg ml^{−1}) was injected into the subretinal space of neonatal mice (4–36 h postpartum), and current pulses (80 V) were applied across the head using paddle electrodes. We obtained identical results in MEGF10–GFP and MEGF10–Cherry misexpression experiments. Sample sizes were >20 animals each for MEGF10 misexpression and FP controls.

HEK 293 cells were cultured in DMEM with 10% fetal calf serum and transfected using TransIT reagent (Mirus). Cells were counterstained using Alexa

- dye-labelled cholera toxin B subunit ($10 \mu\text{g ml}^{-1}$; Invitrogen), added to media 30 min before fixation (4% paraformaldehyde/1× PBS for 20 min on ice).
31. Huberman, A. D. *et al.* Genetic identification of an On-Off direction-selective retinal ganglion cell subtype reveals a layer-specific subcortical map of posterior motion. *Neuron* **62**, 327–334 (2009).
 32. Gray, G. E. & Sanes, J. R. Lineage of radial glia in the chicken optic tectum. *Development* **114**, 271–283 (1992).
 33. Hong, Y. K., Kim, I.-J. & Sanes, J. R. Stereotyped axonal arbors of retinal ganglion cell subsets in the mouse superior colliculus. *J. Comp. Neurol.* **519**, 1691–1711 (2011).
 34. Euler, T. WinDRP website. <http://www.mpimf-heidelberg.mpg.de/~teuler/WinDRP/ReadMe.htm> (2003).
 35. Whitney, I. E., Keeley, P. W., Raven, M. A. & Reese, B. E. Spatial patterning of cholinergic amacrine cells in the mouse retina. *J. Comp. Neurol.* **508**, 1–12 (2008).
 36. Wiegand, T. & Moloney, K. A. Rings, circles, and null-models for point pattern analysis in ecology. *Oikos* **104**, 209–229 (2004).

Control of ground-state pluripotency by allelic regulation of *Nanog*

Yusuke Miyanari¹ & Maria-Elena Torres-Padilla¹

Pluripotency is established through genome-wide reprogramming during mammalian pre-implantation development, resulting in the formation of the naive epiblast. Reprogramming involves both the resetting of epigenetic marks and the activation of pluripotent-cell-specific genes such as *Nanog* and *Oct4* (also known as *Pou5f1*)^{1–4}. The tight regulation of these genes is crucial for reprogramming, but the mechanisms that regulate their expression *in vivo* have not been uncovered. Here we show that *Nanog*—but not *Oct4*—is monoallelically expressed in early pre-implantation embryos. *Nanog* then undergoes a progressive switch to biallelic expression during the transition towards ground-state pluripotency in the naive epiblast of the late blastocyst. Embryonic stem (ES) cells grown in leukaemia inhibitory factor (LIF) and serum express *Nanog* mainly monoallelically and show asynchronous replication of the *Nanog* locus, a feature of monoallelically expressed genes⁵, but ES cells activate both alleles when cultured under 2i conditions, which mimic the pluripotent ground state *in vitro*. Live-cell imaging with reporter ES cells confirmed the allelic expression of *Nanog* and revealed allelic switching. The allelic expression of *Nanog* is regulated through the fibroblast growth factor–extracellular signal-regulated kinase signalling pathway, and it is accompanied by chromatin changes at the proximal promoter but occurs independently of DNA methylation. *Nanog*-heterozygous blastocysts have fewer inner-cell-mass derivatives and delayed primitive endoderm formation, indicating a role for the biallelic expression of *Nanog* in the timely maturation of the inner cell mass into a fully reprogrammed pluripotent epiblast. We suggest that the tight regulation of *Nanog* dose at the chromosome level is necessary for the acquisition of ground-state pluripotency during development. Our data highlight an unexpected role for allelic expression in controlling the dose of pluripotency factors *in vivo*, adding an extra level to the regulation of reprogramming.

The development of the naive epiblast in the late blastocyst is orchestrated by pluripotency-associated transcription factors such as NANOG and OCT4. OCT4 is required for establishing and maintaining the pluripotent state³, and NANOG is essential for the acquisition of pluripotency^{1,6}. In ES cells, the pluripotent state is also governed by these core transcription factors. *Nanog* occupies a central position in this network, but the mechanisms regulating its expression are unclear.

To address how pluripotency-associated factors are regulated during reprogramming *in vivo*, we assayed the *de novo* gene expression of *Nanog* and *Oct4* in mouse pre-implantation embryos, by using RNA fluorescence *in situ* hybridization (RNA-FISH), which allows nascent transcripts to be visualized. We found that *Oct4* is actively expressed in a small proportion of 2-cell-stage embryos, but most blastomeres express *Oct4* at the 4- and 8-cell stage (Fig. 1a, b). We detected active *Nanog* expression in about half of all 4- and 8-cell-stage blastomeres, which is consistent with previous reports of heterogeneous *Nanog* expression⁷. Surprisingly, although all of the other genes that we analysed were expressed biallelically, *Nanog* invariably showed monoallelic expression in 2-, 4- and 8-cell-stage embryos (Fig. 1a, b and Supplementary Movie 1). We next addressed whether the monoallelic

expression of *Nanog* is random or imprinted, by using allele-specific, single-cell PCR with reverse transcription (RT-PCR) on 8-cell-stage embryos from C57BL/6J \times *Mus musculus castaneus* crosses. Consistent with our RNA-FISH results, most blastomeres expressed *Nanog* monoallelically (Fig. 1c and Supplementary Fig. 1). We observed no bias in *Nanog* expression from either the C57BL/6J or the *M. musculus castaneus* allele (Fig. 1c). We conclude that *Nanog* expression is monoallelic and random during early pre-implantation development.

Nanog expression becomes restricted to the inner cell mass (ICM) of the blastocyst^{1,2}, where it is needed for the naive epiblast to attain pluripotency⁶. As expected, the proportion of cells expressing *Nanog* and *Oct4* declined gradually as the expression of these genes became restricted to inner cells (Fig. 2a). Remarkably, the proportion of biallelicism in *Nanog*-expressing cells increased progressively from 2% at the 8-cell stage to 70% of the inner cells in the late blastocyst (Fig. 2b and Supplementary Movie 2). This switch to biallelicism of *Nanog* is in contrast to the consistent biallelic expression of *Oct4* and *Actb* (Fig. 2a). Sequential RNA-FISH and DNA-FISH confirmed the biallelic expression of *Nanog* (Supplementary Fig. 1). The ICM of the late blastocyst contains two lineages: the extra-embryonic primitive endoderm, and the ‘ground-state’ pluripotent epiblast^{6,8}, which gives rise to the embryo. Inner cells expressing *Nanog* biallelically also express *Oct4* but not *Gata4*, a primitive endoderm marker⁹, and therefore are epiblast cells (Fig. 2c). This finding suggests that *Nanog* is predominantly expressed from both alleles in the naive epiblast. Furthermore, *Nanog* expression gradually reversed to monoallelic expression after implantation (Supplementary Fig. 2), in line with the downregulation of *Nanog* and concomitant loss of

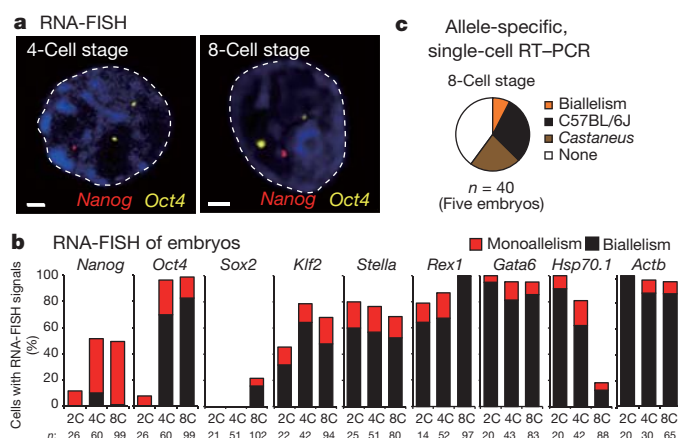


Figure 1 | *Nanog* expression is monoallelic in early embryos. **a**, RNA-FISH for *Nanog* and *Oct4* in 4- and 8-cell-stage nuclei. Scale bar, 2 μ m. **b**, Proportion of allelic expression for each gene in 2-cell-stage (2C), 4-cell-stage (4C) and 8-cell-stage (8C) blastomeres. *n*, number of cells analysed. **c**, Summary of single-cell RT-PCR data for *Nanog* in 8-cell-stage blastomeres, according to biallelic, monoallelic (C57BL/6J or *M. musculus castaneus* (*Castaneus*)) and no expression (none).

¹Institut de Génétique et de Biologie Moléculaire et Cellulaire, CNRS/INSERM U964, Université de Strasbourg, F-67404 Illkirch, Cité Universitaire de Strasbourg, France.

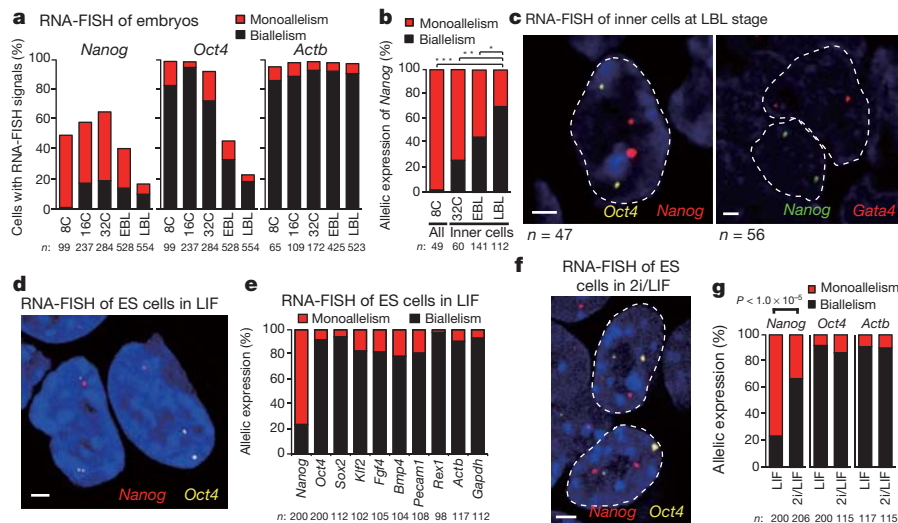


Figure 2 | *Nanog* shows biallelic expression in the naive, pluripotent epiblast. **a**, RNA-FISH for *Nanog*, *Oct4* and *Actb* in 8-cell-stage (8C), 16-cell-stage (16C) and 32-cell-stage (32C) embryos (before cavitation), and early blastocysts (EBLs; E3.5) and late blastocysts (LBLs; E4.25). Data are shown as the percentage of *Nanog*-expressing cells (or *Oct4*- or *Actb*-expressing cells) relative to all cells analysed. **b**, Quantification of cells showing monoallelic or biallelic *Nanog* expression in *Nanog*-expressing 8-cell-stage blastomeres and inner cells at the 32-cell, EBL and LBL stages. *, $P = 8.8 \times 10^{-5}$; **, $P = 3.1 \times 10^{-3}$; ***, $P < 1.0 \times 10^{-13}$ (Fisher's exact test). **c**, RNA-FISH in

ICM cells of the LBL. The dashed line delineates individual ICM cells. **d**, ES cells cultured with serum and LIF display primarily monoallelic *Nanog* expression. A representative RNA-FISH image of ES cells is shown. **e**, Distribution of monoallelic and biallelic expression of *Nanog* and the indicated genes in ES cells cultured with LIF. **f**, A representative RNA-FISH image of nuclei from ES cells cultured with 2i/LIF, showing biallelic expression of *Nanog*. **g**, Treatment of ES cells with 2i/LIF leads to increased biallelic *Nanog* expression. The proportion of allelic expression of *Nanog*, *Oct4*, and *Actb* is shown for ES cells cultured with LIF or 2i/LIF. **a**, **b**, **g**, n , number of cells analysed. **c**, **d**, **f**, Scale bars, 2 μ m.

pluripotency². Thus, *Nanog* expression switches transiently from monoallelic to biallelic during the formation of the pluripotent epiblast *in vivo*, coinciding with the completion of the reprogramming process.

We next investigated the allelic expression of *Nanog* in ES cells. When cultured in medium containing serum and LIF, 60–70% of ES cells express *Nanog* (refs 10, 11) (Supplementary Fig. 4). Under these conditions, *Nanog* is predominantly expressed from a single allele (Fig. 2d, e and Supplementary Movie 3). By contrast, all of the other genes analysed showed biallelic expression, including other pluripotency-associated genes (*Oct4*, *Sox2*, *Klf2* and *Fgf4*), heterogeneously expressed genes (*Pecam1*, *Bmp4* and *Rex1* (also known as *Zfp42*)) and housekeeping genes (*Actb* and *Gapdh*) (Fig. 2d, e). Allele-specific, single-cell RT-PCR with hybrid ES cells showed that *Nanog* expression is independent of parental origin, similarly to the early embryo (Supplementary Fig. 3). Thus, *Nanog* shows random monoallelic expression both in early pre-implantation embryos and in ES cells.

The proportion of monoallelic versus biallelic *Nanog* expression in the naive epiblast is significantly different from that in ES cells, the latter showing much lower biallelic expression (Fig. 2b, e). We hypothesized that this could reflect the more homogeneous expression of *Nanog* in the naive epiblast compared to ES cells^{6,8}. Ground-state pluripotency can be established *in vitro* through pharmacological inhibition (with two inhibitors (2i)) of MEK and GSK3 β ¹². ES cells cultured with 2i show increased levels of *Nanog* messenger RNA^{6,12} and homogeneous distribution of NANOG protein¹³ (Supplementary Fig. 4). Strikingly, we found that culturing ES cells in 2i resulted in a significant increase in biallelic *Nanog* expression (Fig. 2f, g, Supplementary Fig. 3 and Supplementary Movie 4). We confirmed *Nanog* biallelic expression with sequential RNA-FISH and DNA-FISH (data not shown). To address which signalling pathway(s) regulates the allelic expression of *Nanog*, we used combinations of pharmacological inhibitors^{6,12,14}. We found that blocking fibroblast growth factor (FGF)–extracellular regulated kinase (ERK) signalling was sufficient to trigger the biallelic expression of *Nanog* (Supplementary Fig. 4). The naive epiblast and ES cells are thought to be maintained in a ground state by preventing the differentiation that is induced through FGF–ERK signalling^{8,12}. Thus, collectively these results suggest that ground-state pluripotency might be achieved through the activation of the second allele of *Nanog*.

The above changes in *Nanog* allelic expression upon pharmacological treatment suggest that the *Nanog* alleles are dynamically regulated. To visualize the dynamics of activation of the two *Nanog* alleles in individual cells, we generated an ES-cell reporter in which a gene encoding destabilized Turbo green fluorescent protein (TurboGFP) was inserted immediately downstream of the NANOG-coding region in one *Nanog* allele and a gene encoding destabilized mCherry was inserted similarly into the other *Nanog* allele (Fig. 3a and Supplementary Fig. 5). Both fluorescent proteins dissociate from NANOG by self-cleavage of a 2A peptide and do not alter NANOG function. We observed heterogeneous distribution of TurboGFP or mCherry in ES cells grown in LIF, confirming that the monoallelic expression of *Nanog* is random (Fig. 3b). This is in contrast to the homogeneous distribution in ES cells grown in 2i, in which most cells expressed both fluorescent proteins, reflecting biallelic expression of *Nanog* (Fig. 3b). Using time-lapse analysis, we observed dynamic fluctuation of *Nanog* expression, in agreement with previous reports^{10,11} (Supplementary Fig. 6 and Supplementary Movie 5). Moreover, we found that *Nanog* expression can switch between alleles. In most cases, the allelic switch occurred through an intermediate state of biallelic *Nanog* expression or no *Nanog* expression over several cell cycles. In a minority of cases (2%), rapid allelic switching occurred during a single cell cycle (Fig. 3c and Supplementary Fig. 6). This switching is in contrast to other monoallelic genes, including imprinted genes, for which the inactive status of an allele is stably maintained¹⁵.

Given the potential importance of activation of the second *Nanog* allele in establishing ground-state pluripotency, we next addressed the chromatin signatures underlying biallelic activation. We asked whether the allelic expression of *Nanog* obeys any epigenetic feature. We found that *Nanog* replicated asymmetrically in ES cells cultured with LIF alone—a feature of monoallelically expressed genes—but changed its replication pattern towards symmetric replication in ES cells cultured with 2i and LIF (denoted 2i/LIF) (Fig. 3d, e). This pattern is in contrast to the invariable asymmetric replication of imprinted genes (*Snurf* and *H19*; Fig. 3d, e) and is consistent with changes in allelic *Nanog* expression. Replication timing is a distinctive epigenetic fingerprint^{5,16,17}, thus suggesting that the allelic regulation of *Nanog* could be associated with epigenetic signatures. Indeed, monoallelic expression is accompanied

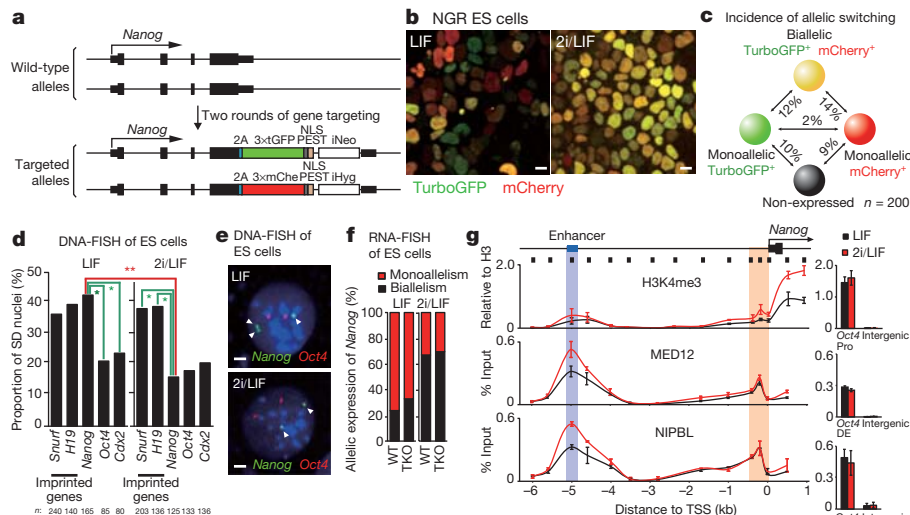


Figure 3 | The switch to biallelic expression of *Nanog* is accompanied by changes in replication timing and increased recruitment of mediator and cohesin. **a**, Schematic of the *Nanog* knock-in reporter NGR. A PEST motif in the carboxy terminus of the fluorescent proteins allows monitoring of dynamic *Nanog* expression. iHyg, internal ribosome entry site (IRES) hygromycin; iNeo, IRES neomycin; mChe, mCherry; NLS, nuclear localization signal; tGFP, TurboGFP. **b**, Representative image of NGR ES cells cultured with LIF or 2i/LIF. Scale bar, 10 μ m. **c**, The incidence of allelic switching of *Nanog* expression in ES cells. Cells were classified into four groups: monoallelic (TurboGFP-positive, green), monoallelic (mCherry-positive, red), biallelic (TurboGFP- and mCherry-positive, yellow) and no expression (black). The proportion of cells undergoing a transition between these four groups during a single cell cycle is indicated. Overall, 47% of cells showed a colour change in this period. *n*, number of cells analysed. **d**, The asymmetric replication of *Nanog* in ES cells cultured with LIF changes to symmetric replication upon treatment with 2i.

by allele-specific DNA methylation and/or histone modifications^{15,18}. However, we found that ES cells lacking all three DNA methyltransferases¹⁹ had similar *Nanog* allelic expression to wild-type ES cells (Fig. 3f), indicating that the allelic regulation of *Nanog* is independent of DNA methylation, unlike that of imprinted genes¹⁵.

Next, we assessed allelic histone modifications on *Nanog* by using chromatin immunoprecipitation (ChIP), taking advantage of the fact that ES cells grown in LIF express *Nanog* mainly in a monoallelic manner and those grown in 2i/LIF primarily have two active alleles. ChIP showed a significantly higher enrichment of H3K4me3, a modification of active chromatin, at the transcription start site (TSS) of *Nanog* in ES cells grown in 2i/LIF than those grown in LIF alone (Fig. 3g). This increase is in line with the higher biallelic expression in 2i/LIF than LIF alone. The H3K4me3 enrichment at the *Nanog* TSS was approximately twofold in 2i/LIF, possibly suggesting that H3K4me3 is enriched at the active *Nanog* allele but absent at the inactive one in ES cells expressing *Nanog* monoallelically. We observed significantly higher recruitment of the mediator subunit MED12, as well as the cohesin-loading factor NIPBL, to the *Nanog* enhancer in ES cells grown in 2i/LIF than in ES cells grown in LIF alone (Fig. 3g). This increased recruitment was accompanied by increased RNA polymerase II initiation and elongation upon 2i treatment (Supplementary Fig. 7). Indeed, changes in chromatin architecture mediated through simultaneous binding of mediator and cohesin to the *Nanog* locus facilitate looping between the enhancer and promoter, resulting in *Nanog* gene activation²⁰. Collectively, our data suggest that *Nanog* allelic expression might be actively regulated through chromosomal changes over the *Nanog* locus.

Mice that are heterozygous for *Nanog* (*Nanog*^{+/-}) are born at normal Mendelian ratios¹. We hypothesized that if *Nanog* biallelic expression is important for the formation of the ICM and/or for the acquisition of ground-state pluripotency, then *Nanog*^{+/-} embryos may show developmental defects at the onset of *Nanog* biallelic

The cell nuclei were classified as single/double (SD), single/single (SS) and double/double (DD) according to DNA-FISH signals⁵. *n*, number of nuclei analysed. *, $P < 4 \times 10^{-7}$; **, $P < 1.4 \times 10^{-3}$ (Fisher's exact test).

e, Representative image of DNA-FISH for *Nanog* (arrowheads) and *Oct4* in ES cells cultured with LIF or 2i/LIF. Scale bar, 2 μ m. **f**, *Nanog* allelic expression is unaffected in the absence of DNA methyltransferase activity. Quantification of RNA-FISH for *Nanog* in wild-type (WT) ES cells and ES cells lacking all three DNA methyltransferases (TKO) cultured with LIF or 2i/LIF. **g**, ChIP for H3K4me3, MED12 or NIPBL along the *Nanog* locus (black line, top) in ES cells cultured with LIF or 2i/LIF. The position of the ChIP amplicons is depicted by the thick boxes below the line, the TSS by an arrow, the first exon by the black box on the line, and the distal enhancer by the blue box on the line. The *Oct4* promoter region (*Oct4* Pro) and distal enhancer (*Oct4* DE) were positive controls (right)²⁰. The mean \pm s.d. of three independent biological replicates is shown.

expression. To address this, we counted ICM cells in individual *Nanog*^{+/-} blastocysts by using an anti-OCT4 antibody. Freshly collected embryonic day 3.5 (E3.5) *Nanog*^{+/-} and *Nanog*^{+/+} blastocysts had similar ICM cell numbers (Supplementary Fig. 8a). This finding is in agreement with previous reports^{6,21} and with our observations documenting *Nanog* monoallelic expression before this embryonic stage. By contrast, we found significantly fewer ICM cells in *Nanog*^{+/-} blastocysts as the embryo progressed through development to form the nascent epiblast (Fig. 4a), which also showed increased apoptosis in the ICM (Supplementary Fig. 8b). No significant difference in the number of NANOG-positive cells was observed between wild-type (*Nanog*^{+/+}) and heterozygous (*Nanog*^{+/-}) embryos (Fig. 4b, c). However, *Nanog*^{+/-} embryos showed delayed primitive endoderm formation (Fig. 4b, c). Indeed, primitive endoderm formation depends on a functional epiblast in a non-cell-autonomous manner²¹, suggesting that the epiblast in *Nanog*^{+/-} embryos is functionally impaired. It should be noted that the reduction in primitive endoderm cells does not fatally compromise development, owing to the regulatory capacity of the early post-implantation embryo. Thus, we conclude that the biallelic expression of *Nanog* is necessary for the timely maturation of the ICM into a functional epiblast and the accompanying primitive endoderm.

NANOG has a dose-sensitive action in reprogramming⁶. Overexpression of NANOG is sufficient to prevent ES-cell differentiation²; conversely, *Nanog*^{+/-} ES cells show spontaneous differentiation^{22,23}, suggesting that the tight regulation of *Nanog* levels is crucial for both reprogramming and differentiation. We found that this dose regulation occurs principally at the allelic level. Monoallelic expression is predominant during the early reprogramming phase in cleavage stages, but it switches to biallelic expression as the ICM matures into the pluripotent epiblast (Fig. 4d). Monoallelic *Nanog* expression in ES cells may be representative of the late ICM or the early post-implantation

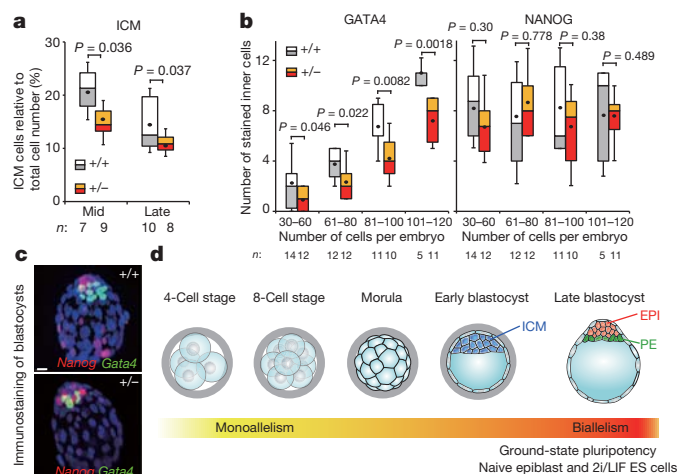


Figure 4 | Biallelic expression of *Nanog* is required for the timely maturation of the ICM derivatives. **a**, Reduced proportion of ICM derivatives in *Nanog*^{+/-} blastocysts compared to *Nanog*^{+/+} blastocysts. Mid and late blastocysts were staged according to their total cell number. Data are expressed as the percentage of ICM cells per embryo. The box plot represents the ninety-fifth, seventy-fifth, fiftieth (median), twenty-fifth and tenth percentiles, as well as the mean (black dot). **b**, Delayed primitive endoderm (PE) formation in *Nanog*^{+/-} blastocysts. Embryos were staged in groups according to their total cell number. The number of PE (GATA4-positive) and epiblast (EPI; NANOG-positive) cells was determined. **c**, Representative maximal confocal projections of late blastocysts, showing a reduced proportion of ICM derivatives in *Nanog*^{+/-} embryos. Scale bar, 10 μ m. **d**, Model for the allelic regulation of *Nanog* and the acquisition of ground-state pluripotency. *Nanog* is expressed monoallelically during the cleavage stages and up to the early blastocyst. Biallelic expression of *Nanog* accompanies the formation of the fully reprogrammed, pluripotent, epiblast. Biallelic expression of *Nanog* also occurs *in vitro* under conditions that mimic the ground-state pluripotency of the naive epiblast (ES cells cultured with 2i/LIF).

epiblast, in which there is a switch back to monoallelic expression. The expression of *Nanog* can switch between alleles, unlike most known monoallelic genes, raising the possibility that the regulation of *Nanog* allelic expression could be unique. Our evidence that such regulation is independent of DNA methylation and does not seem to involve typical repressive modifications (H3K27me3, H3K9me1, H3K9me2 and H3K9me3; data not shown) also supports this possibility. The ground-state pluripotency is facilitated by the suppression of FGF-ERK signalling^{8,12}. Our work suggests that the allelic regulation of *Nanog* is involved in this process and that the increased expression of *Nanog* that accompanies the establishment of ground-state pluripotency is achieved through activation of its second allele. The dose regulation of *Nanog* through allelic switching could also contribute to promoting heterogeneity, which could provide a window of opportunity both for establishing ground-state pluripotency in the epiblast and for lineage segregation towards the primitive endoderm. We propose that the regulation of *Nanog* at the allelic level provides a novel mechanism to establish ground-state pluripotency in the naive epiblast. Thus, our work has uncovered an unexpected role for the allelic regulation of key transcription factors, as a novel mechanism in stabilizing pluripotency.

METHODS SUMMARY

The embryos were from F₁ (C57BL/6J \times CBA/H) or C57BL/6J \times *M. musculus castaneus* crosses. The blastocysts from *Nanog*^{Gt1/+} \times C57BL/6J crosses²¹ were genotyped after immunostaining (47 *Nanog*^{+/+} and 49 *Nanog*^{+/-} were analysed). The ES-cell lines and culture conditions are described in the Methods. Briefly, when referring to LIF, ES cells were cultured in 15% FCS and LIF; when referring to 2i/LIF, ES cells were cultured in 15% FCS, LIF, 3 μ M CHIR99021 and 1 μ M PD0325901. Embryos and ES cells were fixed with 4% paraformaldehyde in PBS for immunostaining. Images were acquired on a TCS SP5 confocal microscope (Leica). Image analysis was performed with the programs ImageJ, LAS AF Lite (Leica) or Imaris (Bitplane). For single-cell RT-PCR analysis, individual 8-cell-stage

blastomeres were mechanically dissociated, and the cells were collected in 3.1 μ l Cell Lysis Buffer (Ambion) and processed for RT-PCR then digested with *Ava*II. All primer sequences are listed in Supplementary Table 1.

Full Methods and any associated references are available in the online version of the paper at www.nature.com/nature.

Received 22 June; accepted 19 December 2011.

Published online 12 February 2012.

- Mitsui, K. *et al.* The homeoprotein *Nanog* is required for maintenance of pluripotency in mouse epiblast and ES cells. *Cell* **113**, 631–642 (2003).
- Chambers, I. *et al.* Functional expression cloning of *Nanog*, a pluripotency sustaining factor in embryonic stem cells. *Cell* **113**, 643–655 (2003).
- Nichols, J. *et al.* Formation of pluripotent stem cells in the mammalian embryo depends on the POU transcription factor Oct4. *Cell* **95**, 379–391 (1998).
- Reik, W. Stability and flexibility of epigenetic gene regulation in mammalian development. *Nature* **447**, 425–432 (2007).
- Gribnau, J., Hochedlinger, K., Hata, K., Li, E. & Jaenisch, R. Asynchronous replication timing of imprinted loci is independent of DNA methylation, but consistent with differential subnuclear localization. *Genes Dev.* **17**, 759–773 (2003).
- Silva, J. *et al.* *Nanog* is the gateway to the pluripotent ground state. *Cell* **138**, 722–737 (2009).
- Dietrich, J. E. & Hiiragi, T. Stochastic patterning in the mouse pre-implantation embryo. *Development* **134**, 4219–4231 (2007).
- Nichols, J., Silva, J., Roode, M. & Smith, A. Suppression of Erk signalling promotes ground state pluripotency in the mouse embryo. *Development* **136**, 3215–3222 (2009).
- Morrisey, E. E., Ip, H. S., Lu, M. M. & Parmacek, M. S. GATA-6: a zinc finger transcription factor that is expressed in multiple cell lineages derived from lateral mesoderm. *Dev. Biol.* **177**, 309–322 (1996).
- Chambers, I. *et al.* *Nanog* safeguards pluripotency and mediates germline development. *Nature* **450**, 1230–1234 (2007).
- Kalmar, T. *et al.* Regulated fluctuations in *Nanog* expression mediate cell fate decisions in embryonic stem cells. *PLoS Biol.* **7**, e1000149 (2009).
- Ying, Q. L. *et al.* The ground state of embryonic stem cell self-renewal. *Nature* **453**, 519–523 (2008).
- Wray, J., Kalkan, T. & Smith, A. G. The ground state of pluripotency. *Biochem. Soc. Trans.* **38**, 1027–1032 (2010).
- Canham, M. A., Sharov, A. A., Ko, M. S. & Brickman, J. M. Functional heterogeneity of embryonic stem cells revealed through translational amplification of an early endodermal transcript. *PLoS Biol.* **8**, e1000379 (2010).
- Weaver, J. R., Susiarjo, M. & Bartolomei, M. S. Imprinting and epigenetic changes in the early embryo. *Mamm. Genome* **20**, 532–543 (2009).
- Shufaro, Y. *et al.* Reprogramming of DNA replication timing. *Stem Cells* **28**, 443–449 (2010).
- Jørgensen, H. F. *et al.* The impact of chromatin modifiers on the timing of locus replication in mouse embryonic stem cells. *Genome Biol.* **8**, R169 (2007).
- Magklara, A. *et al.* An epigenetic signature for monoallelic olfactory receptor expression. *Cell* **145**, 555–570 (2011).
- Tsumura, A. *et al.* Maintenance of self-renewal ability of mouse embryonic stem cells in the absence of DNA methyltransferases Dnmt1, Dnmt3a and Dnmt3b. *Genes Cells* **11**, 805–814 (2006).
- Kagey, M. H. *et al.* Mediator and cohesin connect gene expression and chromatin architecture. *Nature* **467**, 430–435 (2010).
- Messerschmidt, D. M. & Kemler, R. *Nanog* is required for primitive endoderm formation through a non-cell autonomous mechanism. *Dev. Biol.* **344**, 129–137 (2010).
- Hough, S. R., Clements, I., Welch, P. J. & Wiederholt, K. A. Differentiation of mouse embryonic stem cells after RNA interference-mediated silencing of OCT4 and *Nanog*. *Stem Cells* **24**, 1467–1475 (2006).
- Hatano, S. Y. *et al.* Pluripotential competence of cells associated with *Nanog* activity. *Mech. Dev.* **122**, 67–79 (2005).

Supplementary Information is linked to the online version of the paper at www.nature.com/nature.

Acknowledgements We thank M. Okano for providing the triple DNA methyltransferase knockout cells, P. Avner and P. Clerc for hybrid ES cells, H. Schöler for the *Oct4* probe (GOF6.1), J. Jaubert for *M. musculus castaneus* mice, R. Kemler and S. Rudloff for the *Nanog*^{Gt1} mice, G. Charvin for advice on time-lapse analysis. We also thank M. Koch, A. Dierich, M.-C. Birling, E. Heard and I. Okamoto for advice, and A. Burton, E. Heard and O. Pourquie for critical reading of the manuscript. M.-E.T.-P. acknowledges funding from AVENIR/INSERM, ANR-09-Blanc-0114, Epigenesys NoE and FRM Alsace. Y.M. is a recipient of an EMBO long-term fellowship (ALTF864-2008, 2009) and a JSPS postdoctoral fellowship (2010–2011).

Author Contributions Y.M. conceived, designed and performed the experiments in this study and analysed the data; M.-E.T.-P. conceived the project and designed and supervised the study. Y.M. and M.-E. T.-P. wrote the manuscript.

Author Information Reprints and permissions information is available at www.nature.com/reprints. The authors declare no competing financial interests. Readers are welcome to comment on the online version of this article at www.nature.com/nature. Correspondence and requests for materials should be addressed to M.-E.T.-P. (metp@igbmc.fr).

METHODS

Embryo collection and culture. Embryos were collected from ~6 week-old F₁ (C57BL/6J × CBA/H) superovulated females crossed with F₁ males. To obtain F₁ hybrid embryos, superovulated C57BL/6J females were crossed with *M. musculus castaneus* males. Embryos were collected at the following times after human chorionic gonadotrophin injection: the 2-cell stage (48 h), 4-cell stage (54 h), 8-cell stage (68 h), 16-cell stage (80 h), 32-cell stage (90 h), early blastocyst stage (98 h) and late blastocyst stage (114 h). To obtain late blastocysts, freshly collected early blastocysts were cultured in KSOM for 16 h. To obtain E4.5, E4.75 and E5.0 stage embryos, embryos were collected from naturally mated females. The analysis of *Nanog*^{+/-} embryos was done using the *Nanog*^{Gt1} line²¹. Blastocysts from *Nanog*^{+/-} × C57BL/6J (+/+) crosses were processed for immunostaining and reconstructed in three dimensions using Imaris software. Individual ICM cells were counted after immunostaining with an anti-OCT4 antibody. The number of primitive endoderm and epiblast cells was determined by counting individual cells after immunostaining for GATA4 and NANOG. The total number of cells was determined by counting nuclei stained with 4',6-diamidino-2-phenylindole (DAPI). Individual blastocysts were genotyped after confocal acquisition as described previously²¹. Primer sequences for genotyping are listed in Supplementary Table 1. All experiments were performed in accordance with the current legislation in France and the approval of the Regional Ethics Committee (ComEth's).

ES-cell culture. Mouse ES-cell lines, E14, BC1 and TKO (the latter of which lacked all three DNA methyltransferases), were cultured in DMEM with GlutaMAX (Invitrogen) containing 15% FCS, LIF, 1 mM sodium pyruvate, penicillin/streptomycin and 0.1 mM 2-mercaptoethanol. The treatment of ES cells with inhibitors was performed using 3 μM CHIR99021 (a GSK3β inhibitor), 1 μM PD0325901 (a MEK inhibitor), 5 μM PD173074 (an FGF receptor tyrosine kinase activity inhibitor) and 3 μM PD184352 (a MEK inhibitor). The hybrid ES-cell line (BC1) was derived from E3.5 embryos from C57BL/6 × *M. musculus castaneus* crosses as described previously¹².

Gene targeting. Mouse ES cells from the BD10 line (C57BL/6) were electroporated with a first targeting vector consisting of 2A-3×TurboGFP-NLS-PEST-IRES-Neo. The resultant G418-resistant ES-cell (*Nanog*^{GFP/+}) clone was subsequently subjected to a second targeting with a vector containing 2A-3×mCherry-NLS-PEST-IRES-Hyg. Genomic DNAs from both G418- and hygromycin-B-resistant colonies were screened for homologous recombination into each *Nanog* allele by PCR and Southern blotting.

Immunostaining. Embryos or ES cells were fixed with 4% paraformaldehyde in PBS for 20 min at room temperature. After washing with PBS, embryos were permeabilized with 0.5% Triton X-100 in PBS for 10 min and then incubated in blocking solution (0.2% BSA in PBS) for 30 min. Primary antibodies were anti-OCT4 (611202, BD Pharmingen), anti-NANOG (MLC-51, eBioscience) and anti-GATA4 (sc-1237, Santa Cruz Biotechnology). After incubation in blocking solution containing primary antibodies for 1 h, cells or embryos were washed three times with 0.01% Triton X-100 in PBS for 5 min each and then incubated in blocking solution containing secondary antibodies labelled with Alexa fluorophores (Invitrogen), Cy3, Cy5 (Jackson ImmunoResearch) or Kodak X-SIGHT 640 (Carestream Health). After washing with PBS, mounting was done in VECTASHIELD (Vector Labs). Images were collected on a TCS SP5 confocal microscope (Leica). For all images, DAPI is shown in blue. Image analysis was performed using the software ImageJ, LAS AF Lite (Leica) and Imaris (Bitplane).

Whole mount RNA-FISH. After removal of the zona pellucida by incubation in acidic Tyrode's solution (Sigma), embryos were washed twice with PBS and then incubated in fixative containing 4% paraformaldehyde/1×PBS for 20 min at room temperature. Embryos were permeabilized with 0.5% Triton X-100 in fixative for 10 min. After washing with PBS three times, embryos were pre-hybridized in a 2 μl drop of hybridization buffer covered with mineral oil on a 35-mm glass bottom dish for 30 min at 50 °C. The hybridization buffer consisted of 50% formamide, 10% dextran sulphate, 2×SSC, 1 μg μl⁻¹ Cot1 DNA, 1 μg μl⁻¹ yeast tRNA (Roche), 2 mM vanadyl ribonucleoside complex (New England BioLabs), 1 mg ml⁻¹ polyvinyl pyrrolidone (PVP), 1 mM EDTA, 0.1% Triton X-100 and 1 mg ml⁻¹ BSA. Embryos were then transferred to a 2 μl drop of hybridization buffer containing 5 ng μl⁻¹ fluorescent probes and incubated at 50 °C overnight. After washing three times with 2×SSC, 0.1% Triton X-100 and 1 mg ml⁻¹ PVP at 50 °C for 10 min, embryos were then subjected to a gradient series (20%, 40%, 60%, 80% and 100%) of VECTASHIELD containing DAPI. Images were acquired on a TCS SP5 confocal microscope with a 63× glycerol immersion objective lens. For RNA-FISH of ES cells, ES cells grown on gelatin-coated coverslips were fixed and permeabilized as described above. After briefly washing with PBS, the coverslip was dehydrated in 70% ethanol and 100% ethanol for 10 min each and was subsequently air dried. Hybridization buffer containing the corresponding probes was applied to the coverslip. Subsequent hybridization, washing and mounting were

performed as described above. The plasmids, BACs and fosmids used as probes for RNA-FISH were as follows: PBSII-Na1234 for *Nanog*, GOF6.1 for *Oct4*, G135P62831G1 and G135P630G2 for *Gata4*, RP23-476J7 or G135P6579H5 for *Actb*, G135P60852B4 for *Sox2*, G135P65370D8 for *Klf2*, G135P600983F2 for *Fgf4*, G135P60839B3 for *Bmp4*, RP23-129L1 for *Gata6*, G135P65026G5 for *Hsp70.1*, G135P604053D8 for *Pecam1*, G135P69364G7 for *Stella*, G135P602899G3 for *Rex1* and G135P60163E2 for *Gapdh*. The PBSII-Na1234 plasmid contains the NANOG-coding region without any repetitive sequences, as determined by RepeatMasker. BAC and fosmid probes were obtained from the BACPAC Resources Center. The specificity of all probes was confirmed by PCR using specific primers. Probes were labelled with handmade Alexa 488-dATP, TAMRA-dATP, ATTO 647N-dATP using a nick translation kit (Roche) and purified with a QIAquick PCR Purification Kit (QIAGEN). Images were analysed by the software ImageJ and LAS AF Lite. For all of the images, DAPI is shown in blue. It should be noted that the monoallelic expression of *Nanog* was independent of the genetic background, as it was reproducible in all of the mouse strains analysed (F₁ (C57BL/6J × CBA/H), F₁ (C57BL/6J × *M. musculus castaneus*), CD1 and C57BL/6J; data not shown).

Statistical analysis of RNA-FISH. Only interphase cells were taken into account for all of the analyses. Images were analysed across three-dimensional planes by using the software ImageJ and LAS AF Lite. The RNA-FISH signals, which were detected over three sequential Z-sections were judged as positive signals to distinguish background noise. Single RNA-FISH spots or two adjacent spots within 1 μm, which might result from DNA replication, were judged as monoallelism. Cells with two, three or four separate RNA-FISH spots were scored as biallelism. Statistical analysis was done using Fisher's exact test, and the number of cells analysed in all experiments is indicated in the corresponding figure.

DNA-FISH. DNA-FISH was performed as previously described²⁴. Probes for DNA-FISH were as follows: RP23-117I23 for *Nanog*, RP23-213M12 for *Oct4*, RP23-476J7 for *Actb*, RP23-106M4 for *Cdx2*, RP23-239M21 for *Snurf* and G135P602165C11 for *H19*. For all DNA-FISH images, DAPI is shown in blue.

Allele-specific, single-cell RT-PCR. Individual 8-cell-stage blastomeres from hybrid embryos or single hybrid BC1 ES cells were used for this assay. Embryos or ES cells were treated with 0.25% trypsin and 1 mM EDTA at 37 °C for 5 min with gentle pipetting. Single cells were manually collected by mouth pipette aided by a finely pulled glass tip, directly into 3.1 μl Cell Lysis Buffer (Ambion) containing RNase inhibitor (Invitrogen) and 73 nM specific primers for *Nanog* and *Actb*. The single-cell samples were snap frozen in liquid nitrogen and stored at -80 °C until use. Lysates were incubated at 65 °C for 5 min and placed on ice for 5 min. Reaction mixture (7 μl) (2 μl 5×RT buffer, 2 μl 2.5 mM dNTPs, 0.1 μl RNase inhibitor, 0.2 μl Transcriptor (Roche) and 2.7 μl water) was added to each tube. Reverse transcription was performed at 25 °C for 10 min, 37 °C for 15 min, 55 °C for 30 min and 85 °C for 5 min. The reaction mixtures were subjected to a first round of multiplex PCR with primer mixtures for *Nanog* and *Actb*. This first PCR reaction mixture (0.5 μl) was subsequently used for a second round of PCR with a specific primer set for *Nanog* or *Actb*. Pwo SuperYield DNA Polymerase (Roche) was used for PCR reactions. After the second PCR round, PCR products for *Nanog* were digested with the *Ava*II restriction enzyme and analysed by acrylamide gel electrophoresis. Primer sets for *Nanog*- and *Cdkn1*-flanking single nucleotide polymorphism (SNP) sites are listed in Supplementary Table 1. SNPs in the NANOG-coding region were identified by using The Jackson Laboratory's Mouse SNP database (<http://phenome.jax.org/SNP/>). SNPs in *Cdkn1* are described elsewhere²⁵. Primer sequences are listed in Supplementary Table 1.

Quantitative (real-time) PCR. RNA was extracted from ES cells with an RNeasy Mini Kit (QIAGEN) and reverse transcribed with Transcriptor (Roche). Real-time PCR was performed with SYBR Green JumpStart Taq ReadyMix (Sigma) on a LightCycler 480 Real-Time PCR System (Roche). The relative expression level of each gene was normalized to the *Gapdh* expression level. Primer sequences are listed in Supplementary Table 1.

ChIP assay. ChIP assays were performed with ES cells as previously described²⁶. Primer sequences are listed in Supplementary Table 1. The antibodies used were anti-histone H3 (ab1791, Abcam), anti-H3K4me3 (pAV-MEHAHS-024, Diagenode) anti-MED12 (A300-774A, Bethyl Laboratories), anti-NIPBL (301-779A, Bethyl Laboratories), anti-RNA polymerase II (PolII) (N-20, Santa Cruz Biotechnology), anti-PolII CTD Ser2P (ab5095, Abcam) and anti-PolII CTD Ser5P (ab5131, Abcam). The enrichment of histone modifications was quantified by real-time PCR as described above and normalized to histone H3. For MED12, NIPBL, PolII, PolII CTD Ser2P and PolII CTD Ser5P, the percentage input was calculated for each ChIP fraction.

Time-lapse imaging. NGR ES cells were cultured in Knockout DMEM (Invitrogen) supplemented with 15% Knockout Serum Replacement (Invitrogen), LIF, non-essential amino acids, glutamine, gentamicin and 2-mercaptoethanol, under conditions of 5% CO₂ and 95% air. The cells were grown on Culture-Insert (Ibidi) placed

on laminin-511 (Biolamina)-coated 3-cm glass-bottomed dishes (Mattek). The dishes were placed in an incubation chamber (Tokai Hit) on the microscope stage at 37 °C. An inverted microscope (Leica) attached to a Nipkow disk confocal microscope (Yokogawa Electric) and EMCCD camera (iXon, Andor Technology) was controlled with iQ software (Andor Technology). TurboGFP and mCherry were excited with 488-nm and 560-nm lasers, respectively. Images for each colour (green or red) were acquired across 17.5 µm (7 Z-planes) every 20 min for ~50 h.

Analysis of live-cell imaging data. Time-lapse data were analysed using the ImageJ software plug-in Circadian Gene Expression (CGE)²⁷. Fluorescent images were merged and used for the segmentation of nuclei. Cells ($n = 200$) were randomly selected, and the fluorescence intensities for TurboGFP and mCherry in each nucleus were measured in each time frame. Background intensity was subtracted from the mean fluorescence intensity and plotted as the expression level against time during a single cell cycle (~10 h) as shown in Supplementary Fig. 6. Cells that

were positive for TurboGFP, positive for mCherry, positive for both or negative for both were scored as monoallelic (green), monoallelic (red), biallelic (yellow) or non-expressed (black), respectively. Based on the kinetics of TurboGFP and mCherry during a single cell-cycle, the proportion of cells showing a transition between these four groups was calculated.

24. Bolzer, A. *et al.* Three-dimensional maps of all chromosomes in human male fibroblast nuclei and prometaphase rosettes. *PLoS Biol.* **3**, e157 (2005).
25. Lewis, A. *et al.* Epigenetic dynamics of the *Kcnq1* imprinted domain in the early embryo. *Development* **133**, 4203–4210 (2006).
26. Boyer, L. A. *et al.* Core transcriptional regulatory circuitry in human embryonic stem cells. *Cell* **122**, 947–956 (2005).
27. Sage, D., Unser, M., Salmon, P. & Dibner, C. A software solution for recording circadian oscillator features in time-lapse live cell microscopy. *Cell Div.* **5**, 17 (2010).

IDH mutation impairs histone demethylation and results in a block to cell differentiation

Chao Lu^{1,2}, Patrick S. Ward^{1,2}, Gurpreet S. Kapoor³, Dan Rohle^{4,5}, Sevin Turcan⁴, Omar Abdel-Wahab^{4,6}, Christopher R. Edwards⁷, Raya Khanin⁸, Maria E. Figueroa⁹, Ari Melnick⁹, Kathryn E. Wellen², Donald M. O'Rourke^{3,10}, Shelley L. Berger⁷, Timothy A. Chan⁴, Ross L. Levine^{4,6}, Ingo K. Mellinghoff^{4,5,11} & Craig B. Thompson¹

Recurrent mutations in isocitrate dehydrogenase 1 (IDH1) and IDH2 have been identified in gliomas, acute myeloid leukaemias (AML) and chondrosarcomas, and share a novel enzymatic property of producing 2-hydroxyglutarate (2HG) from α -ketoglutarate^{1–6}. Here we report that 2HG-producing IDH mutants can prevent the histone demethylation that is required for lineage-specific progenitor cells to differentiate into terminally differentiated cells. In tumour samples from glioma patients, IDH mutations were associated with a distinct gene expression profile enriched for genes expressed in neural progenitor cells, and this was associated with increased histone methylation. To test whether the ability of IDH mutants to promote histone methylation contributes to a block in cell differentiation in non-transformed cells, we tested the effect of neomorphic IDH mutants on adipocyte differentiation *in vitro*. Introduction of either mutant IDH or cell-permeable 2HG was associated with repression of the inducible expression of lineage-specific differentiation genes and a block to differentiation. This correlated with a significant increase in repressive histone methylation marks without observable changes in promoter DNA methylation. Gliomas were found to have elevated levels of similar histone repressive marks. Stable transfection of a 2HG-producing mutant IDH into immortalized astrocytes resulted in progressive accumulation of histone methylation. Of the marks examined, increased H3K9 methylation reproducibly preceded a rise in DNA methylation as cells were passaged in culture. Furthermore, we found that the 2HG-inhibitable H3K9 demethylase KDM4C was induced during adipocyte differentiation, and that RNA-interference suppression of KDM4C was sufficient to block differentiation. Together these data demonstrate that 2HG can inhibit histone demethylation and that inhibition of histone demethylation can be sufficient to block the differentiation of non-transformed cells.

The fact that IDH mutations were identified in multiple cancers with disparate tissues of origin suggests that 2HG-producing mutant enzymes probably affect some fundamental cellular processes that facilitate tumour progression. To study the effects of IDH mutations, we collected and performed gene expression microarray analysis on tumour specimens from patients with grade II–III oligodendroglioma. Sequencing results revealed a high frequency of IDH mutations in oligodendroglioma (33 of the samples had the R132 IDH1 mutation, 2 had the R172 IDH2 mutation and 6 were wild type for IDH1/2). Supervised analysis found a statistically enriched gene signature in IDH-mutant samples (q value <10%, fold change >2; Fig. 1a and Supplementary Table 1) that was independent of tumour grade and recurrence status and survived multiple testing corrections. Gene-ontology analysis identified the regulation of astrocyte and glial differentiation

as the top two functional categories enriched in differentially expressed genes (Supplementary Table 2). We previously reported that IDH mutation may promote leukaemogenesis by expanding the haematopoietic progenitor cell population and impairing haematopoietic differentiation⁷, and that such a phenotype could be attributed at least in part to mutant IDH-induced inhibition of TET2, an α -ketoglutarate (α KG)-dependent enzyme potentially involved in DNA demethylation^{7,8}. Although DNA hypermethylation has been associated with IDH mutation in glioma samples⁹, no mutations in TET family members have been found in this disease. We explored the possibility that IDH mutation may affect additional α KG-dependent enzymes that contribute to the regulation of cell differentiation.

Histone lysine methylation is an integral part of the post-translational modifications of histone tails that are important for chromatin organization and regulation of gene transcription^{10–13}. *In vitro* 2HG can competitively inhibit a family of α KG-dependent Jumonji-C domain histone demethylases (JHDMs)^{14,15}. To determine whether IDH-associated changes in histone methylation could be observed in cells, we ectopically expressed wild-type or mutant IDH1 or IDH2 in 293T cells and found that mutant IDH1 or IDH2 led to a marked increase in histone methylation compared to the wild-type enzymes. Transient transfection of wild-type IDH2 can also lead to increased 2HG production⁷. In all of the samples, the magnitude of increase in methylation correlated with the intracellular 2HG levels produced by IDH transfection (Fig. 1b and Supplementary Fig. 1). To test whether histone lysine methylation was dysregulated in gliomas with IDH mutation, immunohistochemistry analysis of patient oligodendroglioma samples was performed for several well-characterized histone marks. Compared to tumours with wild-type IDH, there was a statistically significant increase in the repressive trimethylation of H3K9 (H3K9me3) and an increasing trend in trimethylation of H3K27 (H3K27me3) in tumours with IDH1 mutation (Fig. 1c). No statistically significant difference was seen in trimethylation of H3K4 (H3K4me3), a mark associated with active transcription (data not shown). These data suggested that IDH mutations might preferentially affect the regulation of repressive histone methylation marks *in vivo*.

As IDH mutations were associated with glial tumours of the 'pro-neural' phenotype¹⁶, we sought to determine whether the persistence of histone repressive marks promoted by mutant IDH was sufficient to block the differentiation of non-transformed cells. Upon stimulation with a differentiation cocktail, immortalized murine 3T3-L1 cells undergo extensive chromatin remodelling, resulting in their maturation into adipocytes¹⁷. 3T3-L1 cells transduced with R172K mutant IDH2 produced 2HG whereas cells transduced with either wild-type IDH2 or vector alone did not (Fig. 2a). All three cell types were then

¹Cancer Biology and Genetics Program, Memorial Sloan-Kettering Cancer Center, New York, New York 10065, USA. ²Department of Cancer Biology, Perelman School of Medicine, University of Pennsylvania, Philadelphia, Pennsylvania 19104, USA. ³Department of Neurosurgery, Perelman School of Medicine, University of Pennsylvania, Philadelphia, Pennsylvania 19104, USA. ⁴Human Oncology and Pathogenesis Program, Memorial Sloan-Kettering Cancer Center, New York, New York 10065, USA. ⁵Department of Pharmacology, Weill Cornell Medical College, New York, New York 10065, USA. ⁶Leukemia Service, Department of Medicine, Memorial Sloan-Kettering Cancer Center, New York, New York 10065, USA. ⁷Department of Cell and Developmental Biology, Perelman School of Medicine, University of Pennsylvania, Philadelphia, Pennsylvania 19104, USA. ⁸Bioinformatics Core, Memorial Sloan-Kettering Cancer Center, New York, New York 10065, USA. ⁹Division of Hematology/Oncology, Weill Cornell Medical College, New York, New York 10065, USA. ¹⁰Department of Pathology & Laboratory Medicine, Perelman School of Medicine, University of Pennsylvania, Philadelphia, Pennsylvania 19104, USA. ¹¹Department of Neurology, Memorial Sloan-Kettering Cancer Center, New York, New York 10065, USA.

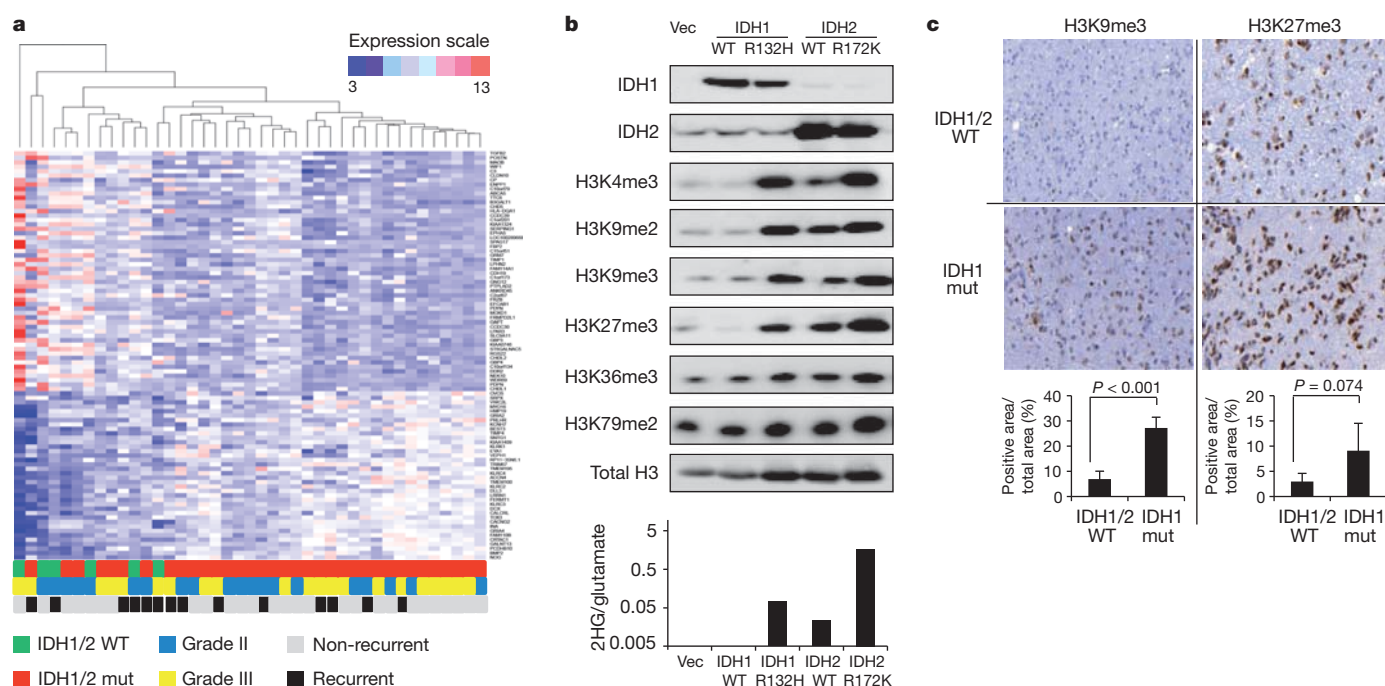


Figure 1 | IDH mutations are associated with dysregulation of glial differentiation and global histone methylation. **a**, Heatmap representation of a two-dimensional hierarchical clustering of genes identified as differentially expressed between IDH mutant (mut) patient oligodendroglioma samples and IDH wild-type (WT) samples. Each row represents a gene and each column represents a specimen. IDH mutational status, tumour grade and recurrence of each sample are listed. **b**, 293T cells transfected with empty vector (Vec), wild-type or R132H mutant IDH1, or wild-type or R172K mutant IDH2 for 3 days were lysed and assessed for expression levels of IDH1, IDH2 and histone lysine

induced to differentiate into adipocytes. After 7 days of differentiation induction, IDH mutant cells had visibly reduced lipid droplet accumulation compared to vector and IDH wild-type cells, as shown by Oil-Red-O staining (Fig. 2b). In separate experiments, stable transfection of R140Q mutant IDH2 also resulted in a block to adipocyte differentiation (data not shown). To determine whether 2HG was sufficient to mediate the effect of mutant IDH on cell differentiation, we synthesized cell-permeable 1-octyl-D-2-hydroxyglutarate (octyl-2HG; Supplementary Fig. 2). Treatment of 3T3-L1 cells with octyl-2HG led to a dose-dependent inhibition of lipid accumulation (Fig. 2c). Gene expression analysis showed that despite exposure to a well-standardized differentiation protocol¹⁸, IDH mutant cells or cells treated with octyl-2HG exhibited a profound defect in the expression of transcription factors essential for executing adipogenesis (*Cebpa* and *Pparg*) and an adipocytic lineage-specific gene (*Adipoq*) (Fig. 2d, e), suggesting that these cells failed to execute adipocyte differentiation.

Cells were harvested for a chromatin immunoprecipitation (ChIP) assay using antibodies against H3K9me3 and H3K27me3, before or after 4 days of differentiation induction. Quantitative polymerase chain reaction (PCR) with primers targeting promoters of *Cebpa* and *Adipoq* revealed that at day 4 there was a statistically significant increase in H3K9me3 and H3K27me3 at promoters of both genes in IDH mutant cells (Fig. 2f). These repressive marks also showed a modest but significant increase at gene promoters before differentiation induction. In contrast, quantitative assessment of DNA methylation at promoters of *Cebpa* and *Adipoq* by MassARRAY failed to reveal any significant difference between IDH wild-type and mutant cells (Supplementary Fig. 3). In addition to gene-specific changes, we detected a global increase in H3K9 methylation and a reciprocal decrease in H3 acetylation (Fig. 2g and Supplementary Fig. 4).

To determine whether IDH mutation was sufficient to induce enhanced repressive histone methylation in central nervous system

methylation by western blotting with specific antibodies. Total H3 was used as loading control. Quantification of band intensities is shown in Supplementary Fig. 1. Bottom panel provides quantification of intracellular 2HG to glutamate ratio (2HG/glutamate) as previously reported for these transfectants⁷.

c, Immunohistochemistry staining with antibodies against H3K9me3 and H3K27me3 in IDH1/2 wild-type and IDH1 mutant oligodendroglioma samples ($\times 40$ magnification). Image quantification was performed using Metamorph software (see Methods) and shown in bottom panels. Error bars represent standard deviation (s.d.) of at least three patient samples in each group.

(CNS)-derived cells and whether it was associated with altered neural gene expression, we retrovirally transduced immortalized normal human astrocytes (NHAs) with either wild-type or R132H mutant IDH1. Compared to parental cells, late-passage cells expressing mutant IDH exhibited elevated levels of a variety of histone methylation marks (Fig. 3a), and this correlated with an enhanced expression of the neural marker nestin (Fig. 3b). IDH mutations have been associated with CpG-island hypermethylation⁹ and consistent with this we observed that total CpG methylation was increased in IDH mutant cells (Supplementary Fig. 5). Because histone repressive marks can promote DNA methylation and vice versa¹³, we studied the temporal relationship of histone and DNA methylation in IDH-expressing astrocytes (Fig. 3c–e and Supplementary Fig. 5). The first observable change of the histone marks we examined was H3K9me3. H3K9me3 levels were significantly elevated by passage 12 after cells were infected with mutant IDH. Changes in other histone methylation marks were either delayed and of lower magnitude (H3K27me3 and H3K79me2) or were not observed (H3K4me3). Increases in DNA methylation were never observed before passage 17 and the difference in DNA methylation reached statistical significance only at passage 22.

To test whether the IDH1 R132H mutation could interfere with neural differentiation in the absence of prolonged adaptation in culture, primary neurosphere cultures established from the brains of *p16/p19*^{−/−} mice were infected with a retroviral construct containing IDH1 R132H mutant, wild-type IDH1 or the vector alone (Supplementary Fig. 6). After infection the cells were re-plated under conditions that promote astrocyte differentiation and induced to differentiate further by treatment with retinoic acid without further passaging. IDH mutant cells failed to induce expression of the astrocytic marker GFAP and exhibited expression of the neural marker β 3-tubulin (Fig. 3f). When the differentiation conditions were supplemented with retinoic acid, enhanced expression of the astrocytic marker GFAP was observed in

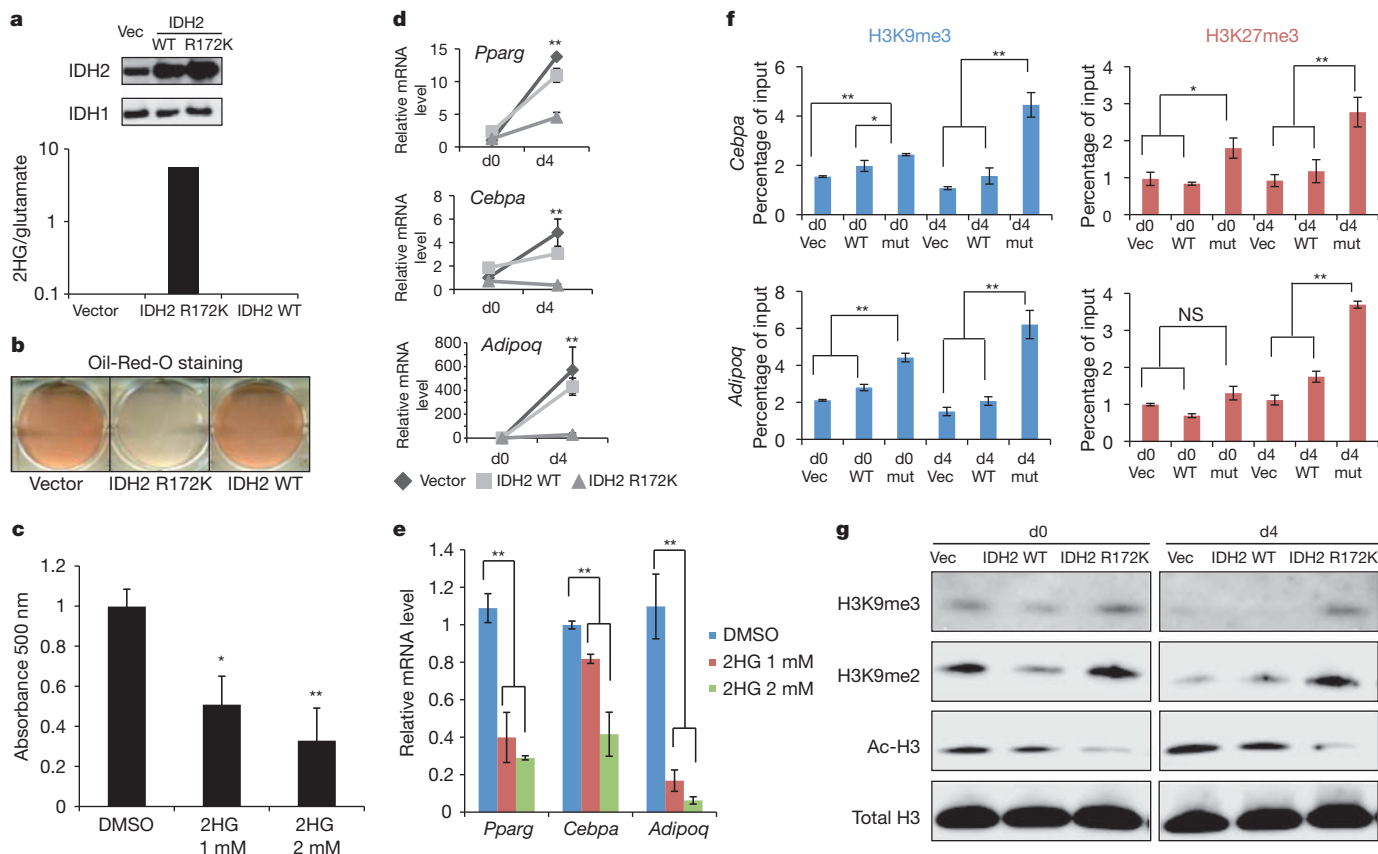


Figure 2 | Differentiation arrest induced by mutant IDH or 2HG is associated with increased global and promoter-specific H3K9 and H3K27 methylation. **a**, 3T3-L1 cells stably expressing empty vector, wild-type, or R172K mutant IDH2 were lysed and assessed for expression levels of IDH2 or IDH1 by western blotting. Cells were also extracted for intracellular metabolites, which were then MTBSTFA-derivatized (see Methods) and analysed by gas chromatography–mass spectrometry (GC–MS). The quantification of 2HG signal intensity relative to the intrasample glutamate signal is shown for a representative experiment. **b**, Cells were induced to differentiate into mature adipocytes for 7 days. The accumulation of lipid droplets was assessed by Oil-Red-O staining. Wells from a representative experiment from a total of four independent experiments are shown. **c**, 3T3-L1 cells were induced to differentiate for 7 days in the absence or presence of 1 mM or 2 mM octyl-2HG. Oil-Red-O staining was performed and quantified by measuring absorbance at 500 nm. DMSO, dimethylsulphoxide. **d**, Vector, wild-type or R172K mutant IDH2 transduced 3T3-L1 cells were induced to differentiate for 4 days. At days 0 and 4 (d0 and d4), RNA was extracted. Relative

IDH wild-type and vector cells but GFAP expression remained repressed in IDH mutant cells.

The enhancement of H3K9 methylation in mutant IDH-expressing cells from multiple tissues of origin led us to investigate whether this H3K9 methylation might be sufficient to block the ability of non-transformed cells to execute differentiation. Support for this hypothesis came with the discovery that KDM4C (also known as JMJD2C), an H3K9-specific JHDM, was induced in 3T3-L1 cells during differentiation (Fig. 4a). An *in vitro* histone demethylase assay with recombinant human GST-tagged KDM4C confirmed that KDM4C effectively removed H3K9me2 and H3K9me3 in the presence of α KG. Importantly, the demethylation reaction was inhibited by 2HG in a dose-dependent manner (Fig. 4b and Supplementary Fig. 7). Given the similarities between 2HG and α KG, the inhibition of KDM4C by 2HG would be predicted to be competitive. Consistently, increasing the concentration of α KG in the reaction mixture reversed the inhibition of H3K9 demethylation by 2HG (Fig. 4c).

Finally, to test the possibility that H3K9 demethylation is a required component of adipocyte differentiation, we examined whether blocking

expression of adipocyte-specific gene and transcription factors was assessed by quantitative PCR with reverse transcription (RT–qPCR). **e**, 3T3-L1 cells were induced to differentiate for 4 days in the absence or presence of 1 mM or 2 mM octyl-2HG. RNA was extracted. Relative expression of adipocyte-specific gene and transcription factors was assessed by RT–qPCR. **f**, Vector, wild-type or R172K mutant IDH2 transduced 3T3-L1 cells were induced to differentiate. At days 0 and 4 (d0 and d4), ChIP analysis was performed using antibodies against H3K9me3 and H3K27me3. Immunoprecipitated *Cebpa* and *Adipoq* promoter sequences were analysed by qPCR and shown as percentage of input. **g**, Vector, wild-type or R172K mutant IDH2 transduced 3T3-L1 cells were induced to differentiate for 4 days. At days 0 and 4 (d0 and d4), histones were acid-extracted and levels of H3K9me3, H3K9me2 and acetyl-H3 were assessed by western blotting with specific antibodies. Total H3 was used as loading control. Quantification of band intensities is shown in Supplementary Fig. 4. In **f**, error bars indicate s.d. from triplicate wells and a representative experiment from a total of two is shown. For all other experiments, error bars indicate s.d. from three independent experiments. * $P < 0.05$; ** $P < 0.01$; NS, not significant.

the induction of KDM4C was sufficient to impair the differentiation of 3T3-L1 cells. Treatment with three independent short interfering RNAs (siRNAs) against KDM4C reduced its expression and enhanced H3K9me3 in 3T3-L1 cells (Fig. 4d and Supplementary Fig. 8). After differentiation induction, cells treated with KDM4C siRNAs exhibited reduced ability to differentiate into adipocytes. Thus the inability to erase repressive H3K9 methylation can be sufficient to impair the differentiation of non-transformed cells.

Biochemical studies suggest that 2HG is a universal inhibitor of JHDM family members^{14,15}; therefore it was interesting to observe that H3K9 demethylation seemed to be more sensitive to mutant IDH-induced suppression than at least some other histone methylation marks. Future investigation of the sensitivity to 2HG inhibition among JHDM family members and/or cellular feedback mechanisms activated after defective histone demethylation will be needed. In addition to the data presented here, evidence is mounting for a direct role of histone methylation in stem cell maintenance, differentiation and tumorigenesis^{19–23} (see Supplementary Discussion). Our findings support a role for α KG-dependent demethylases in cell differentiation

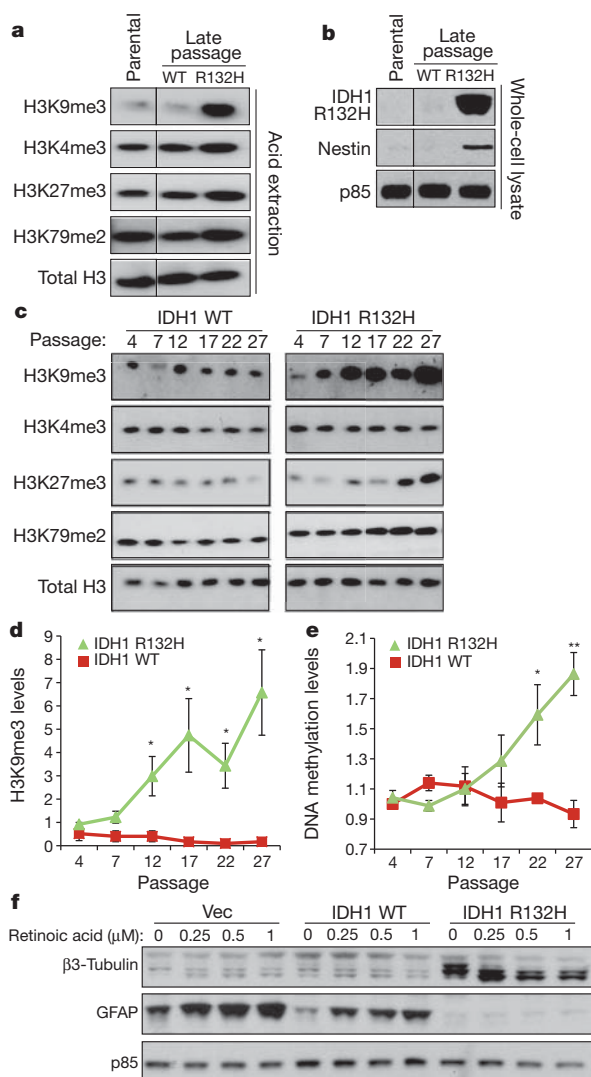


Figure 3 | IDH mutation induces histone methylation increase in CNS-derived cells and can alter cell lineage gene expression. **a**, Immortalized NHA cells were retrovirally transduced with constructs containing wild-type or R132H mutant IDH1. Histones were acid-extracted from parental cells or cells expressing wild-type or mutant IDH1 at late (>40) passages. Histone lysine methylation levels were assessed by western blotting with specific antibodies. Total H3 was used as loading control. Images presented are panels from different areas of the same gel. **b**, Parental, IDH1 wild-type and R132H mutant NHA cells at late passages were lysed and assessed for expression levels of nestin by western blotting. p85 was used as loading control. Images presented are panels from different areas of the same gel. **c**, NHA cells were retrovirally transduced with constructs containing wild-type or R132H mutant IDH1. Histones were acid-extracted at different time points as cells were passaged in culture. Histone lysine methylation levels were assessed by western blotting with specific antibodies. Total H3 was used as loading control. Images presented are panels from different areas of the same gel. **d**, Western blot band intensities of H3K9me3 in **c** and two additional independent experiments were quantified using Image J. Red squares indicate IDH1 wild-type cells. Green triangles indicate IDH1 R132H mutant cells. **e**, Total CpG methylation of IDH1 wild-type and R132H mutant NHA cells at various passages was measured by FACS using 5-methylcytosine-specific antibody and shown as normalized mean fluorescence intensity. FACS histograms from a representative experiment are shown in Supplementary Fig. 5. **f**, Neurosphere cultures established from the subventricular zone of brains of *p16/p19*^{-/-} mice were infected with a retroviral construct containing IDH1 R132H mutant, wild-type IDH1 or the vector alone and induced to differentiate. GFAP and β3-tubulin expression levels were assessed by western blotting. p85 was used as loading control. In **d** and **e**, error bars indicate standard error of the mean from three independent experiments. **P* < 0.05; ***P* < 0.01.

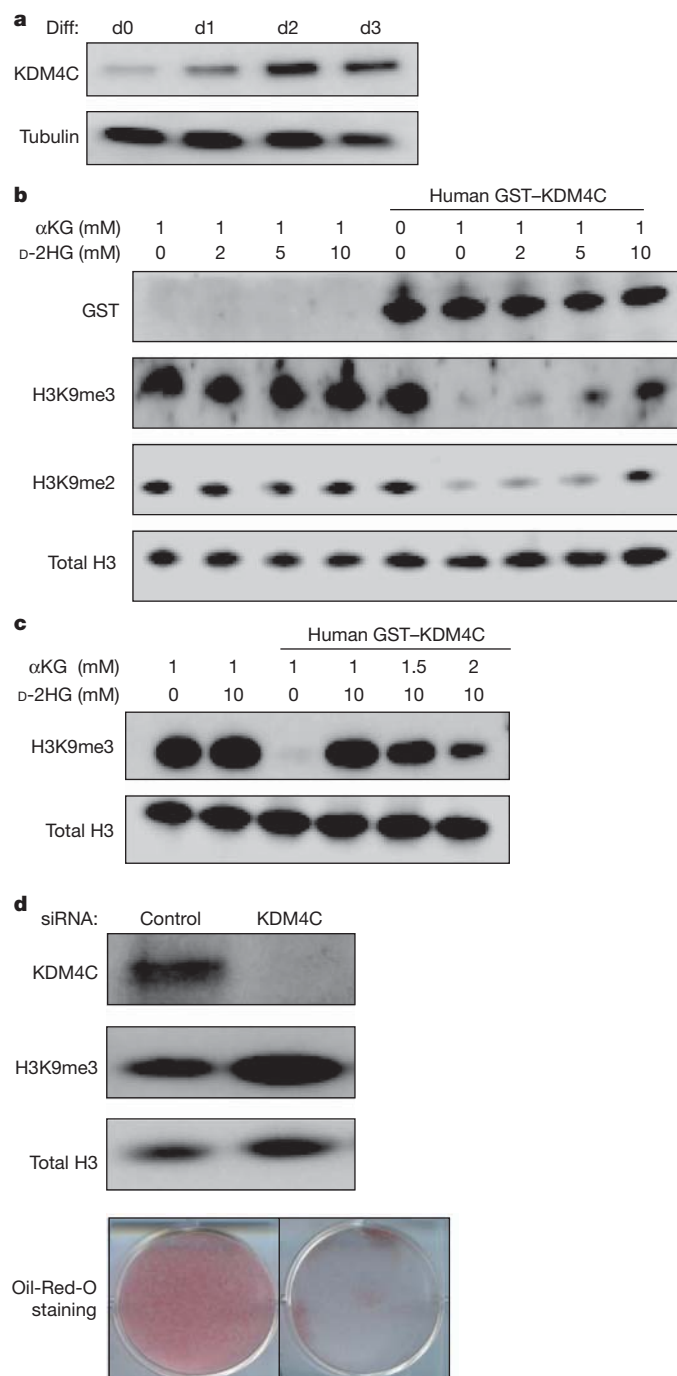


Figure 4 | 2HG-inhibitable H3K9 demethylase KDM4C is required for cell differentiation. **a**, 3T3-L1 cells were induced to differentiate (Diff) for 3 days. Before (d0) and each day after differentiation induction, cells were lysed and KDM4C protein levels were assessed by western blotting with specific antibody. Tubulin was used as loading control. **b**, Bulk histones were incubated with purified GST-tagged human KDM4C in the reaction mix with 1 mM αKG and increasing concentrations of D-2HG. Levels of GST tag, H3K9me3 and H3K9me2 were assessed by western blotting with specific antibodies. Total H3 was used as loading control. **c**, Bulk histones were incubated with purified GST-tagged human KDM4C in the reaction mix. 10 mM D-2HG was added to inhibit the demethylation reaction in the presence of increasing concentrations of αKG. Levels of H3K9me3 were assessed by western blotting with specific antibody. Total H3 was used as loading control. **d**, 3T3-L1 cells were transfected with control siRNA or siRNA specific for KDM4C. After 3 days, cells were lysed and assessed for expression levels of KDM4C and H3K9me3 by western blotting with specific antibodies. Total H3 was used as loading control. Cells from the same treatment were induced to differentiate for 7 days. The accumulation of lipid droplets was assessed by Oil-Red-O staining. Wells from a representative experiment from a total of three independent experiments are shown.

that can be impaired through the cellular accumulation of 2HG produced by IDH mutation.

METHODS SUMMARY

Details about histone extraction, GC-MS and ChIP assay can be found in Methods. In brief, 3T3-L1 cell differentiation, Oil-Red-O staining, and *in vitro* histone demethylase assay were performed as previously described^{24,25}.

Full Methods and any associated references are available in the online version of the paper at www.nature.com/nature.

Received 3 June 2011; accepted 16 January 2012.

Published online 15 February 2012.

- Parsons, D. W. *et al.* An integrated genomic analysis of human glioblastoma multiforme. *Science* **321**, 1807–1812 (2008).
- Yan, H. *et al.* IDH1 and IDH2 mutations in gliomas. *N. Engl. J. Med.* **360**, 765–773 (2009).
- Mardis, E. R. *et al.* Recurring mutations found by sequencing an acute myeloid leukemia genome. *N. Engl. J. Med.* **361**, 1058–1066 (2009).
- Amary, M. F. *et al.* IDH1 and IDH2 mutations are frequent events in central chondrosarcoma and central and periosteal chondromas but not in other mesenchymal tumours. *J. Pathol.* **224**, 334–343 (2011).
- Ward, P. S. *et al.* The common feature of leukemia-associated IDH1 and IDH2 mutations is a neomorphic enzyme activity converting α -ketoglutarate to 2-hydroxyglutarate. *Cancer Cell* **17**, 225–234 (2010).
- Dang, L. *et al.* Cancer-associated IDH1 mutations produce 2-hydroxyglutarate. *Nature* **462**, 739–744 (2009).
- Figuerola, M. E. *et al.* Leukemic IDH1 and IDH2 mutations result in a hypermethylation phenotype, disrupt TET2 function, and impair hematopoietic differentiation. *Cancer Cell* **18**, 553–567 (2010).
- Guo, J. U., Su, Y., Zhong, C., Ming, G. & Song, H. Hydroxylation of 5-methylcytosine by TET1 promotes active DNA demethylation in the adult brain. *Cell* **145**, 423–434 (2011).
- Noushmehr, H. *et al.* Identification of a CpG island methylator phenotype that defines a distinct subgroup of glioma. *Cancer Cell* **17**, 510–522 (2010).
- Taverna, S. D., Li, H., Ruthenburg, A. J., Allis, C. D. & Patel, D. J. How chromatin-binding modules interpret histone modifications: lessons from professional pocket pickers. *Nature Struct. Mol. Biol.* **14**, 1025–1040 (2007).
- Berger, S. L. The complex language of chromatin regulation during transcription. *Nature* **447**, 407–412 (2007).
- Bernstein, B. E. *et al.* A bivalent chromatin structure marks key developmental genes in embryonic stem cells. *Cell* **125**, 315–326 (2006).
- Estève, P. O. *et al.* Direct interaction between DNMT1 and G9a coordinates DNA and histone methylation during replication. *Genes Dev.* **20**, 3089–3103 (2006).
- Xu, W. *et al.* Oncometabolite 2-hydroxyglutarate is a competitive inhibitor of α -ketoglutarate-dependent dioxygenases. *Cancer Cell* **19**, 17–30 (2011).
- Chowdhury, R. *et al.* The oncometabolite 2-hydroxyglutarate inhibits histone lysine demethylases. *EMBO Rep.* **12**, 463–469 (2011).
- Verhaak, R. G. *et al.* Integrated genomic analysis identifies clinically relevant subtypes of glioblastoma characterized by abnormalities in *PDGFRA*, *IDH1*, *EGFR*, and *NF1*. *Cancer Cell* **17**, 98–110 (2010).
- MacDougald, O. A. & Lane, M. D. Transcriptional regulation of gene expression during adipocyte differentiation. *Annu. Rev. Biochem.* **64**, 345–373 (1995).
- Rubin, C. S., Hirsch, A., Fung, C. & Rosen, O. M. Development of hormone receptors and hormonal responsiveness *in vitro*. Insulin receptors and insulin sensitivity in the preadipocyte and adipocyte forms of 3T3-L1 cells. *J. Biol. Chem.* **253**, 7570–7578 (1978).
- Krivtsov, A. V. & Armstrong, S. A. MLL translocations, histone modifications and leukaemia stem-cell development. *Nature Rev. Cancer* **7**, 823–833 (2007).
- Hu, Z. *et al.* A novel nuclear protein, 5qNCA (LOC51780) is a candidate for the myeloid leukemia tumor suppressor gene on chromosome 5 band q31. *Oncogene* **20**, 6946–6954 (2001).
- van Haaften, G. *et al.* Somatic mutations of the histone H3K27 demethylase gene *UTX* in human cancer. *Nature Genet.* **41**, 521–523 (2009).
- Bilodeau, S., Kagey, M. H., Frampton, G. M., Rahl, P. B. & Young, R. A. SetDB1 contributes to repression of genes encoding developmental regulators and maintenance of ES cell state. *Genes Dev.* **23**, 2484–2489 (2009).
- Ceol, C. J. *et al.* The histone methyltransferase SETDB1 is recurrently amplified in melanoma and accelerates its onset. *Nature* **471**, 513–517 (2011).
- Wellen, K. E. *et al.* ATP-citrate lyase links cellular metabolism to histone acetylation. *Science* **324**, 1076–1080 (2009).
- Ingvarsdottir, K. *et al.* Histone H3K4 demethylation during activation and attenuation of *GAL1* transcription in *Saccharomyces cerevisiae*. *Mol. Cell. Biol.* **27**, 7856–7864 (2007).

Supplementary Information is linked to the online version of the paper at www.nature.com/nature.

Acknowledgements We thank members of the Thompson laboratory for technical help and critical reading of the manuscript. We thank T. A. Gocke and the genomic core of University of Pennsylvania for their assistance with the microarray study; the molecular cytology core facility of Memorial Sloan-Kettering Cancer Center (MSKCC) for technical help with the immunohistochemistry study; and O. Ouerfelli and M. K. Spassova at the organic synthesis core of MSKCC for the synthesis of octyl-2HG. This work was supported by grants from the National Cancer Institute and National Institutes of Health. R.L.L. is an Early Career Award recipient of the Howard Hughes Medical Institute and the Geoffrey Beene Junior Chair at MSKCC. D.M.O'R. is supported by the Betsy Cohen Fund of the Abramson Cancer Center at University of Pennsylvania. I.K.M. is supported by NCI-U54CA143798, the Doris Duke Charitable Foundation, and an Advanced Clinical Research Award in Glioma from the American Society of Clinical Oncology.

Author Contributions C.L., P.S.W. and C.B.T. designed the study. C.L., P.S.W., G.S.K., D.R. and M.E.F. performed research; S.T., D.R., T.A.C. and I.K.M. contributed research material; C.L., P.S.W., G.S.K., O.A.-W., C.R.E., R.K., M.E.F., A.M., K.E.W., D.M.O'R., S.L.B., R.L.L. and C.B.T. contributed to data analysis and interpretation; C.L., P.S.W. and C.B.T. wrote the manuscript.

Author Information Microarray data have been deposited with the ArrayExpress database under accession code E-MEXP-3239. Reprints and permissions information is available at www.nature.com/reprints. The authors declare competing financial interests: details accompany the full-text HTML version of the paper at www.nature.com/nature. Readers are welcome to comment on the online version of this article at www.nature.com/nature. Correspondence and requests for materials should be addressed to C.B.T. (thompsonc@mskcc.org).

METHODS

Patient samples, microarray, gene-ontology analysis. Primary oligodendroglioma samples were obtained with approval from the institutional review board at the University of Pennsylvania and were de-identified for the study. For microarray analysis, tumour sample RNA was extracted with Trizol and purified with Qiagen RNeasy, and then assayed on an Affymetrix Human Gene 1.0ST array. Significance Analysis of Microarrays (<http://www-stat.stanford.edu/~tibs/SAM/sam.pdf>) was applied to find differentially expressed genes (q value <10% and fold change >2). Functional analysis of differentially expressed genes was done using the DAVID tool (<http://david.abcc.ncifcrf.gov/home.jsp>) using all human genes as a background set.

3T3-L1 cell differentiation, Oil-Red-O staining. 3T3-L1 cell differentiation and Oil-Red-O staining were carried out as described previously²⁴. In brief, confluent 3T3-L1 cells were stimulated with a cocktail containing 0.5 mM isobutylmethylxanthine, 1 μ M dexamethasone, 5 μ g/ml insulin and 5 μ M troglitazone (all from Sigma) to induce differentiation. Cells were maintained in medium with insulin after 2 days of differentiation until ready to be harvested. For Oil-Red-O staining, cells were washed in PBS and then fixed for 20 min at room temperature (25 °C) with 3% paraformaldehyde. Cells were then washed with de-ionized water and stained with Oil-Red-O solution. For quantification, Oil-Red-O staining was dissolved in isopropanol and absorbance was measured at 500 nm.

In vitro histone demethylase assay. The histone demethylase assay was carried out as described previously²⁵. In brief, 4 μ g bulk calf thymus histones (Sigma) were incubated with GST-tagged KDM4C (1.42 μ g; BPS Bioscience) in a reaction mix containing 50 mM Tris-HCl pH 8.0, protease inhibitors cocktail, 1 mM α KG, 100 μ M FeSO₄ and 2 mM ascorbic acid at 37 °C for 4 h, in the absence or presence of various concentrations of D-2HG or L-2HG (Sigma). Reaction mixtures were analysed by western blotting using specific antibodies.

Cell culture, transfection and transduction, generation of cell lines. 293T cells, NHA cells immortalized by E6/E7/hTERT (provided by R. Pieper²⁶) and 3T3-L1 cells were cultured in Dulbecco's modified Eagle's medium (DMEM; Invitrogen) with 10% fetal bovine serum (FBS; CellGro). For expression of wild-type and mutant IDH1/2 in 293T cells, transfection was performed with Lipofectamine 2000 (Invitrogen) according to the manufacturer's instructions. For generation of IDH2 retrovirus and transduction of 3T3-L1 cells, supernatant from 293T cells transfected with pCL-Eco helper virus and plasmids was collected after 72 h, filtered and applied to cells overnight. For generating 3T3-L1 cell lines with stable expression of wild-type or mutant IDH2, cells were grown in 2.5 μ g ml⁻¹ puromycin for 7 days after retroviral transduction. Pooled populations of puromycin-resistant cells were obtained, and then continuously cultured in puromycin. For generation of IDH1 retrovirus and transduction of NHA cells, GP2-293 cells (Clontech, 631458) were calcium phosphate transfected with equal amounts of pVSV-G (Clontech, 631512) and plasmids. Virus was harvested at day 2 and day 3 after transfection and placed on logarithmically growing cells. After infection, cells were placed in 800 μ g ml⁻¹ G418 (Invitrogen) to generate stable cell lines. For siRNA knockdown of KDM4C, transfections were performed with Lipofectamine RNAiMAX (Invitrogen), using siRNAs targeting KDM4C (#1: sense, 5'-GCUUGAAUCUCCCAAGAUATT-3'; antisense, 5'-UAUCUU GGGGAUUAACAAGCTT-3'; #2: sense, 5'-CAAAGUAUCUUGGAUCAAATT-3'; antisense, 5'-UUUGAUCCAAGAUACUUUGCC-3'; #3: sense, 5'-GAGGAGUU UCGGGAGUUAACAAAU-3'; antisense, 5'-AUUUGUUGAACUCCCGAA ACUCCUC-3') or a non-targeting control (Dharmacon, #D-001810-01-20) at a concentration of 40 nM.

Mutational analysis. For IDH mutation analysis, tumour genomic DNA was extracted and the regions surrounding IDH1 codon 132 and IDH2 codons 140 and 172 were amplified by PCR followed by sequencing. IDH1 analysis used forward primer 5'-ACCAATGGCACCACATACGA-3' and reverse primer 5'-TTCATACC TTGCTTAATGGGTGT-3' for amplification, and primer 5'-CGGTCTTCAGAG AAGCATT-3' for sequencing¹. IDH2 analysis used forward primer 5'-CAG AGACAAGAGGATGGCTAGG-3' and reverse primer 5'-GTCTGCCTGTG TTGTTGCTTG-3' for amplification, and the same forward primer for sequencing²⁷. Out of the 42 tumours analysed, 41 had sufficient high quality genomic DNA for discerning IDH mutation status. The one sample unable to be classified as either IDH wild type or mutant was excluded from further analysis.

Plasmid construction. The cDNA clone of human IDH1 (BC012846.1) was purchased from the American Type Culture Collection in pCMV-Sport6, and human IDH2 (BC009244) was purchased from Invitrogen in pOTB7. Standard site-directed mutagenesis techniques were used to generate IDH1 R132H by introducing a G395A base-pair change in the IDH1 open reading frame (ORF). IDH2 R172K was made by introducing a G515A change in the IDH2 ORF, while IDH2 R140Q was made with a G419A alteration. Wild-type and mutant sequences were then subcloned into LPC vector. All sequences were confirmed by direct sequencing before expression in 293T cells and retrovirus generation. Retroviral constructs used for neurosphere infection were generated by excising wild-type

IDH1 and IDH1 R132H with NotI and PacI restriction enzymes from the previously made vectors and incorporating into the pQCXIH (Clontech, 631516) retroviral vector.

Histone extraction and western blotting. For histone acid extraction, cells were lysed in hypotonic lysis buffer (10 mM HEPES, 10 mM KCl, 1.5 mM MgCl₂, 0.5 mM DTT, protease inhibitors) for 1 h. H₂SO₄ was added to 0.2 N overnight at 4 °C with rotation. After spinning down and collecting supernatant, proteins were precipitated in 33% TCA, washed with acetone, and resuspended in de-ionized water. For whole-cell lysates, cells were lysed and sonicated in standard RIPA buffer (1% sodium deoxycholate, 0.1% SDS, 1% Triton X-100, 0.01 M Tris pH 8.0 and 0.14 M NaCl), and lysates were then centrifuged at 14,000g at 4 °C for 10 min. Supernatants were collected and measured for total protein concentration. For western blotting, lysates were separated by SDS-PAGE, transferred to nitrocellulose membrane, blocked in 5% non-fat milk in PBS containing 0.5% Tween-20, probed with primary antibodies and detected with horseradish-peroxidase-conjugated anti-rabbit or anti-mouse antibodies (GE Healthcare, NA934V and NA931V). Primary antibodies used were: anti-IDH1 (Proteintech, 12332-1-AP), anti-IDH2 (Abcam, ab55271), anti-GST tag (Millipore, 05-311), anti-H3K9me2 (Cell Signaling Tech, 9753), anti-H3K9me3 (Abcam, ab8898), anti-H3K36me3 (Abcam, ab9050), anti-H3K27me3 (Millipore, 17-622), anti-H3K4me3 (Millipore, 17-614), anti-H3K79me2 (Cell Signaling Tech, 9757), anti-KDM4C (Abcam, ab85454), anti-acetyl H3 (Upstate, 06-599), anti-H3 (Cell Signaling Tech, 4499), anti-tubulin (Sigma, T9026), anti-GFAP (Cell Signaling Tech, 3670), anti- β -tubulin (Cell Signaling Tech, 5666), anti-p85 (Millipore, 06-195), anti-nestin (Millipore, MAB5326), anti- β -actin (Sigma, A5316). Anti-IDH1 R132H mutant antibody was a gift from Agios Pharmaceuticals. Quantification of western blot band intensity was performed using Image J software according to the manufacturer's instructions.

Metabolite extraction, GC-MS. After gentle removal of culture medium, cells were rapidly quenched with ice-cold 80% methanol and incubated at -80 °C for 20 min. After sonication, extracts were then centrifuged at 14,000g for 20 min at 4 °C to remove precipitated protein and the aqueous metabolites in the supernatant layer were dried under nitrogen gas. For 293T cells, organic acids were further purified by redissolving the dried extract in de-ionized water, followed by elution from an AG-1 X8 100–200 anion exchange resin (Bio-Rad) in 3 N HCl after washing with five column volumes.

For GC-MS analysis, dried extracts were redissolved in a 1:1 mixture of acetonitrile and N-methyl-N-tert-butylidimethylsilyltrifluoroacetamide (MTBSTFA; Regis) and heated for 75 min at 70 °C to derivatize metabolites. Samples were then injected into an Agilent 7890A GC with an HP-5MS capillary column, connected to an Agilent 5975 C mass selective detector operating in splitless mode using electron impact ionization with ionizing voltage of -70 eV and electron multiplier set to 1,060 V. GC temperature was started at 100 °C for 3 min, ramped up to 230 °C at 4 °C min⁻¹ and held for 4 min, then ramped up to 300 °C and held for 5 min. Mass range of 50–500 AMU was recorded at 2.71 scans per second. Identification of the 2HG metabolite peak was confirmed using standards obtained from Sigma. The 2HG and glutamate signal intensities were quantified by integration of peak areas.

Quantitative real-time PCR. RNA was isolated using Trizol (Invitrogen). After incubating with DNase, cDNA was synthesized using Superscript II reverse transcriptase (Invitrogen). Quantitative PCR was performed on a 7900HT Sequence Detection System (Applied Biosystems) using Taqman Gene Expression Assays (Applied Biosystems). Gene expression data was normalized to 18S rRNA.

ChIP. ChIP was performed with the Millipore Magna ChIP G kit (Millipore, 17-611). In brief, 2,000,000 cells were cross-linked with 1% formaldehyde for 10 min at room temperature. After washing with cold PBS, cells were centrifuged and lysed in 500 μ l SDS lysis buffer for 10 min on ice. Lysate was then sonicated using Bioruptor sonicator (Diagenode) to shear DNA to approximately 200–600 bp. Samples were spun down and 50 μ l of the supernatant was used for each immunoprecipitation overnight with magnetic beads after 10 \times dilution. Primary antibodies (3 μ g per ChIP) used were: anti-H3K9me3 (Abcam, ab8898) and anti-H3K27me3 (Millipore, 17-622). Normal rabbit IgG (Millipore, 12-370) was used as control and showed minimal enrichment. The next day, samples were washed in low-salt immune complex buffer, high-salt immune complex buffer, LiCl immune complex buffer and TE buffer. Histone complexes were eluted in elution buffer plus proteinase K for 2 h at 65 °C. DNA was recovered using columns. Quantitative PCR was performed on purified DNA samples. Primers used are: *Adipoq* forward, 5'-ATGGCTGAACCACACAGCTTCA-3'; reverse, 5'-AGGGGTGAGGAGAG CCTCCCTTT-3'; *Cebpa* forward, 5'-CTGGAAGTGGGTGACTTAGAGG-3'; reverse, 5'-GAGTGGGGAGCATAGTGCTAG-3'. Data points (Ct) are converted to percentage to input.

Quantitative DNA methylation analysis. Matrix-assisted laser desorption/ionization time-of-flight mass spectrometry using EpiTyper by MassARRAY

(Sequenom) was performed on bisulphite-converted DNA extracted from 3T3-L1 cells. MassARRAY primer design was done as previously described^{28,29}.

Immunohistochemistry. Immunohistochemistry detection was performed using Discovery XT processor (Ventana Medical Systems). The tissue sections were blocked for 30 min in 10% normal goat serum in 0.2% BSA/PBS, followed by incubation for 5 h with 0.1 $\mu\text{g ml}^{-1}$ of the rabbit polyclonal anti-H3K9me3 (Abcam, ab8898) or 1 $\mu\text{g ml}^{-1}$ rabbit polyclonal anti-H3K27me3 (Millipore, 07-449) antibodies and incubation for 60 min with biotinylated goat anti-rabbit IgG (Vector labs, PK6101) at 1:200 dilution. The detection was performed with the DAB-MAP kit (Ventana Medical Systems). The entire slides were scanned by Zeiss Mirax Scan (Carl Zeiss) using a $\times 20/0.8$ objective. The scanned image was exported into image analysis software, Metamorph (Molecular Devices). The colour threshold for DAB-positive nuclei was determined and set for all images. Areas above the threshold for the DAB signal and for haematoxylin-counterstained total nuclei were measured in an automated fashion. The ratio between the two parameters were calculated and analysed for statistical significance.

Synthesis of 1-octyl-D-2-hydroxyglutarate. Commercial *R*(-)-tetrahydro-5-oxofuran-2-carboxylic acid (140 mg, 1.076 mmol) was dissolved in H_2O (1 ml), cooled to 0 °C and treated with 1 N KOH (2.16 ml, 2.15 mmol). The resulting solution was stirred at this temperature for 5 min and at ambient temperature for 2 h. It was then concentrated to dryness under reduced pressure and dried. The residue was dissolved in trifluoroacetic anhydride (8 ml) at 0 °C, stirred for 30 min at 0 °C, for 2 h at room temperature, then the volatiles were evaporated under reduced pressure. The residue was dried and dissolved in anhydrous tetrahydrofuran (6 ml). Octanol (0.3 ml, 2.1 eq.) was added to the solution at 0 °C and the mixture was stirred for an overnight period at ambient temperature. Water was added to quench the reaction, and the mixture extracted with EtOAc. The combined extracts were dried over MgSO_4 , concentrated and purified by Flash chromatography (EtOAc:hexane 1:3 and 1:1) to give 1-octyl-D-2-hydroxyglutarate (110 mg, 39%).

Neurosphere isolation, culture and differentiation. Six days postpartum *Ink4a/Arf* null (*p16/p19*^{-/-}) mice were killed, with the isolated subventricular zones subjected to chemical (Pronase E, Calbiochem 7433-2) and mechanical dissociation to obtain a single-cell suspension in full neurobasal medium (Neurobasal medium, GIBCO 21103; B27 supplement without retinoic acid, GIBCO 12587-010;

Glutamax, GIBCO 35050; 20 ng ml^{-1} EGF, R&D Systems 236-EG; 20 ng ml^{-1} basic FGF, Millipore GF003). On the next day the cells were spun down and re-suspended in fresh medium, and once neurospheres had formed in culture, the spheres were collected and chemically dissociated (Accumax, Innovative Cell Technologies AM105) back into single cells in fresh medium.

One day after final infection, infected neurospheres and a non-infected control were placed in 400 $\mu\text{g ml}^{-1}$ Hygromycin B (InvivoGen, ant-hg-1). Once selection was complete, isogenic cell lines maintained in full neurobasal medium were chemically dissociated into single cells and plated at the same density in full neurobasal medium with increasing concentrations of retinoic acid (Sigma-Aldrich, R2625). Seventy-two hours later cells were harvested, and expression of proteins was analysed by western blotting.

Measurement of total CpG methylation. DNA methylation was assessed as previously described³⁰. In brief, 1×10^6 NHA cells were washed with PBS and fixed with 2% paraformaldehyde for 10 min at room temperature and permeabilized with 0.5% Triton X-100 for 10 min. Cells were then treated with 2 N HCl for 20 min at room temperature and subsequently neutralized with 100 mM Tris-HCl, pH 8.0. Cells were incubated with anti-5-methylcytosine antibody (Calbiochem, NA 81) at 1:100 dilution for 30 min at room temperature. After washing with PBS, cells were incubated with secondary antibody coupled with ALEXA FLUOR 488 (Invitrogen) for 30 min in the dark. Flow cytometry was done using Becton Dickinson Calibur flow cytometer and analysed using FlowJo software.

Statistical analysis. All statistical analysis was performed using Student's *t*-test (two-sample equal variance; two-tailed distribution).

26. Sonoda, Y. *et al.* Formation of intracranial tumors by genetically modified human astrocytes defines four pathways critical in the development of human anaplastic astrocytoma. *Cancer Res.* **61**, 4956–4960 (2001).
27. Balss, J. *et al.* Analysis of the *IDH1* codon 132 mutation in brain tumors. *Acta Neuropathol.* **116**, 597–602 (2008).
28. Figueroa, M. E. *et al.* Genome wide epigenetic analysis delineates a biologically distinct immature acute leukemia with myeloid/T-lymphoid features. *Blood* **113**, 2795–2804 (2009).
29. Figueroa, M. E. *et al.* DNA methylation signatures identify biologically distinct subtypes in acute myeloid leukemia. *Cancer Cell* **17**, 13–27 (2010).
30. Habib, M. *et al.* DNA global hypomethylation in EBV-transformed interphase nuclei. *Exp. Cell Res.* **249**, 46–53 (1999).

IDH1 mutation is sufficient to establish the glioma hypermethylator phenotype

Sevin Turcan^{1*}, Daniel Rohle^{1,2*}, Anuj Goenka^{1,3*}, Logan A. Walsh¹, Fang Fang¹, Emrullah Yilmaz¹, Carl Campos¹, Armida W. M. Fabius¹, Chao Lu^{4,5}, Patrick S. Ward^{4,5}, Craig B. Thompson⁴, Andrew Kaufman¹, Olga Guryanova¹, Ross Levine¹, Adriana Heguy¹, Agnes Viale⁶, Luc G. T. Morris^{1,7}, Jason T. Huse^{1,8}, Ingo K. Mellinghoff^{1,2,9,10} & Timothy A. Chan^{1,2,3,10}

Both genome-wide genetic and epigenetic alterations are fundamentally important for the development of cancers, but the interdependence of these aberrations is poorly understood. Glioblastomas and other cancers with the CpG island methylator phenotype (CIMP) constitute a subset of tumours with extensive epigenomic aberrations and a distinct biology^{1–3}. Glioma CIMP (G-CIMP) is a powerful determinant of tumour pathogenicity, but the molecular basis of G-CIMP remains unresolved. Here we show that mutation of a single gene, isocitrate dehydrogenase 1 (*IDH1*), establishes G-CIMP by remodelling the methylome. This remodelling results in reorganization of the methylome and transcriptome. Examination of the epigenome of a large set of intermediate-grade gliomas demonstrates a distinct G-CIMP phenotype that is highly dependent on the presence of *IDH* mutation. Introduction of mutant *IDH1* into primary human astrocytes alters specific histone marks, induces extensive DNA hypermethylation, and reshapes the methylome in a fashion that mirrors the changes observed in G-CIMP-positive lower-grade gliomas. Furthermore, the epigenomic alterations resulting from mutant *IDH1* activate key gene expression programs, characterize G-CIMP-positive proneural glioblastomas but not other glioblastomas, and are predictive of improved survival. Our findings demonstrate that *IDH* mutation is the molecular basis of CIMP in gliomas, provide a framework for understanding oncogenesis in these gliomas, and highlight the interplay between genomic and epigenomic changes in human cancers.

The isocitrate dehydrogenase genes *IDH1* and *IDH2* are mutated in >70% of lower-grade gliomas (grades II and III), in some glioblastomas^{4,5}, and in leukaemias and several other cancers^{6,7}. The most common *IDH1* mutations in glioma (>95%) result in an amino acid substitution at arginine 132 (R132), which resides in the enzyme's active site. Mutation of *IDH* imparts the ability to produce 2-hydroxyglutarate (2-HG), a potential oncometabolite^{8–10}. Alterations in the methylation landscape have been shown to have important roles during oncogenesis¹¹. CIMP has emerged as a distinct molecular subclass of tumours in a number of human malignancies, including glioblastoma^{1–3}. This phenotype is associated with extensive, coordinated hypermethylation at specific loci^{1,2,12,13}. In glioblastomas, G-CIMP is associated with the proneural subgroup of tumours and *IDH* mutation¹. Exactly how mutant *IDH* promotes tumorigenesis and causes G-CIMP—or CIMP in any type of human cancer—is unknown.

To determine whether *IDH1* mutation directly causes G-CIMP, we used immortalized primary human astrocytes¹⁴ and constructed isogenic cells expressing either mutant *IDH1* (R132H), wild-type *IDH1*, or neither. These astrocytes are well characterized^{14–17}. Introduction of

wild-type *IDH1* and the R132H *IDH1* mutant resulted in equal expression of protein (modest threefold increase) (Fig. 1a). Expression of mutant but not wild-type *IDH1* in human astrocytes resulted in the production of 2-HG (Fig. 1b). To determine whether mutant *IDH1* altered the methylation landscape, we analysed genomic DNA from these cells using the Illumina Infinium HumanMethylation450 platform. The platform provides genome-wide coverage and is both well validated and highly reproducible^{18,19}.

Previous data demonstrated that *de novo* DNA methylation in *in vitro* models occurs over extended periods, requiring time to 'lock in' epigenomic changes^{12,20}. We thus analysed the methylomes of astrocytes expressing mutant or wild-type *IDH1* over successive passages (up to 50). Analysis using self-organizing maps demonstrated that mutant *IDH1* progressively remodelled the glial methylome over time (Fig. 1c, d), an effect that was not seen in control astrocytes. Expression of mutant *IDH1* caused a marked increase in hypermethylation at a large number of genes, although there was a small group of hypomethylated genes as well (Fig. 1e and Supplementary Fig. 1a and Supplementary Table 1). Surprisingly, expression of wild-type *IDH1* also reshaped the methylome but in a manner that differed from effects due to expression of mutant *IDH1* (Fig. 1f). Expression of wild-type *IDH1* caused hypomethylation at specific loci, suggesting that both the production of 2-HG and the levels of α -ketoglutarate can affect the methylome. Unsupervised hierarchical clustering of the methylome data showed that the hypermethylated genes included both genes that underwent *de novo* methylation as well as genes that originally possessed low levels of methylation but subsequently acquired high levels of methylation (Fig. 1e). Control astrocytes did not undergo these methylome changes (Fig. 1c, d). Mutant *IDH1*-induced remodeling of the methylome was progressive and reproducible, and resulted in significant changes in gene expression (Fig. 1f and Supplementary Fig. 1a, Supplementary Tables 2 and 3).

We sought to define the methylation targets of mutant *IDH* in astrocytes. Of the 44,334 CpG sites that were differentially methylated in mutant *IDH*-expressing cells, 30,988 sites were hypermethylated (3,141 unique genes with promoter CpG island methylation changes; Supplementary Table 1). Transcriptional module mapping showed that the genes undergoing methylation changes were highly enriched for polycomb complex 2 (PRC2)-targeted loci (Supplementary Fig. 1b and Supplementary Table 4)^{12,21}. These observations demonstrate that mutant *IDH1* is sufficient to reshape the epigenome by altering the global methylation landscape.

Lower-grade gliomas (LGGs; World Health Organization grades II and III) and secondary glioblastomas are biologically distinct from primary or *de novo* glioblastomas²². Present knowledge of G-CIMP

¹Human Oncology and Pathogenesis Program, Memorial Sloan-Kettering Cancer Center, New York, New York 10065, USA. ²Weill Cornell College of Medicine, New York, New York 10065, USA. ³Department of Radiation Oncology, Memorial Sloan-Kettering Cancer Center, New York, New York 10065, USA. ⁴Cancer Biology and Genetics, Memorial Sloan-Kettering Cancer Center, New York, New York 10065, USA. ⁵Department of Cancer Biology, University of Pennsylvania School of Medicine, Philadelphia, Pennsylvania 19104, USA. ⁶Genomics Core, Memorial Sloan-Kettering Cancer Center, New York, New York 10065, USA. ⁷Department of Surgery, Memorial Sloan-Kettering Cancer Center, New York, New York 10065, USA. ⁸Department of Pathology, Memorial Sloan-Kettering Cancer Center, New York, New York 10065, USA. ⁹Department of Neurology, Memorial Sloan-Kettering Cancer Center, New York, New York 10065, USA. ¹⁰Brain Tumor Center, Memorial Sloan-Kettering Cancer Center, New York, New York 10065, USA.

*These authors contributed equally to this work.

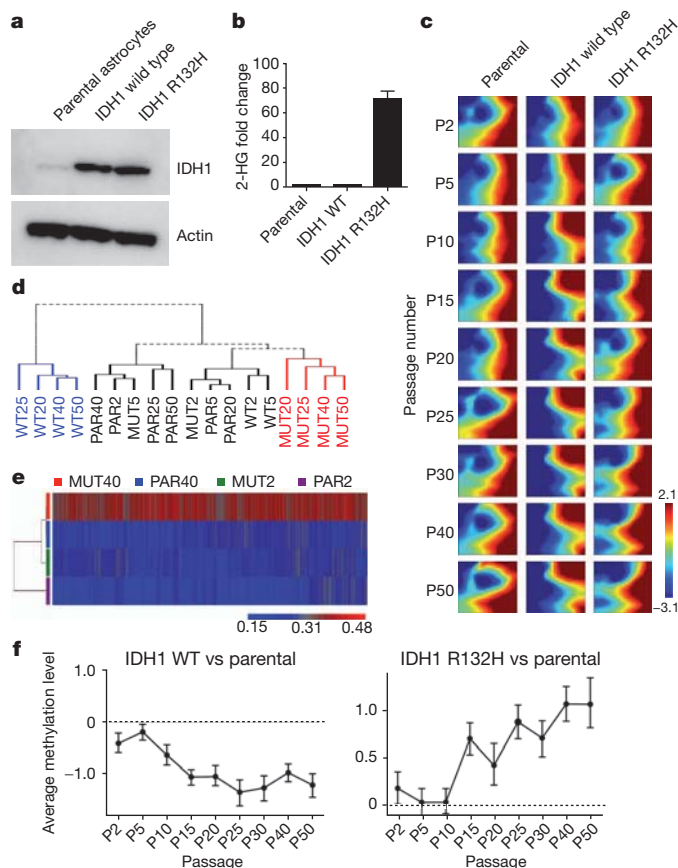


Figure 1 | Introduction of mutant IDH1 into human astrocytes remodels the methylome. **a**, Expression of wild-type and mutant IDH1 (R132H) in immortalized human astrocytes (passage 5). **b**, Overexpression of mutant IDH1 but not wild-type (WT) IDH1 in human astrocytes leads to production of 2-HG⁸. Error bars show 1 standard deviation (s.d.) ($n = 2$). **c**, Self-organizing map (SOM) analysis of methylome data for wild-type IDH1-expressing, mutant IDH1-expressing (R132H), and parental (control) cell lines shows changes in the methylome in mutant IDH1-expressing and wild-type IDH1-expressing astrocytes, compared to parental cells. Mosaic patterns are pseudo-coloured SOMs from different time points (P indicates passage number). Tile colours indicate methylation level of centroids. **d**, Hierarchical clustering showing divergence of the methylome of IDH1-expressing astrocytes from that of parental astrocytes. MUT, mutant; PAR, parental. **e**, Heatmap showing the 10,678 most significant differentially methylated probes (ANOVA) in IDH1 mutant astrocytes and parental astrocytes (passages 2 and 40). Colour scale indicates β values. **f**, Kinetics of differential methylation in mutant and wild-type-expressing astrocytes. Error bars indicate inter-quartile range ($n = 2$).

is based on the examination of primary glioblastomas in which IDH mutations are infrequent^{1,4,5}. To determine the impact of IDH mutation on the methylation landscape in primary LGGs, we generated a high-resolution, genome-wide set of LGG methylome data from patients with complete clinical follow-up using the same Infinium 450K platform as described earlier (72 WHO grade II and III gliomas; Fig. 2 and Supplementary Table 5). We first performed consensus clustering (Fig. 2a and Supplementary Fig. 2a) and unsupervised hierarchical clustering (Fig. 2b and Supplementary Fig. 2b) to identify LGG subgroups. We identified two robust DNA methylation clusters, one encompassing tumours with markedly high methylation levels (cluster 2) and another without the hypermethylated loci (cluster 1). Cluster 2 tumours demonstrated a characteristic DNA methylation profile with high-coordinate cancer-specific methylation at a subset of loci, concordant with the G-CIMP phenotype defined in glioblastomas (Supplementary Fig. 2b and Supplementary Table 6)¹. The composition of the G-CIMP group in these LGGs was confirmed by two independent clustering methods (K -means consensus and two-dimensional

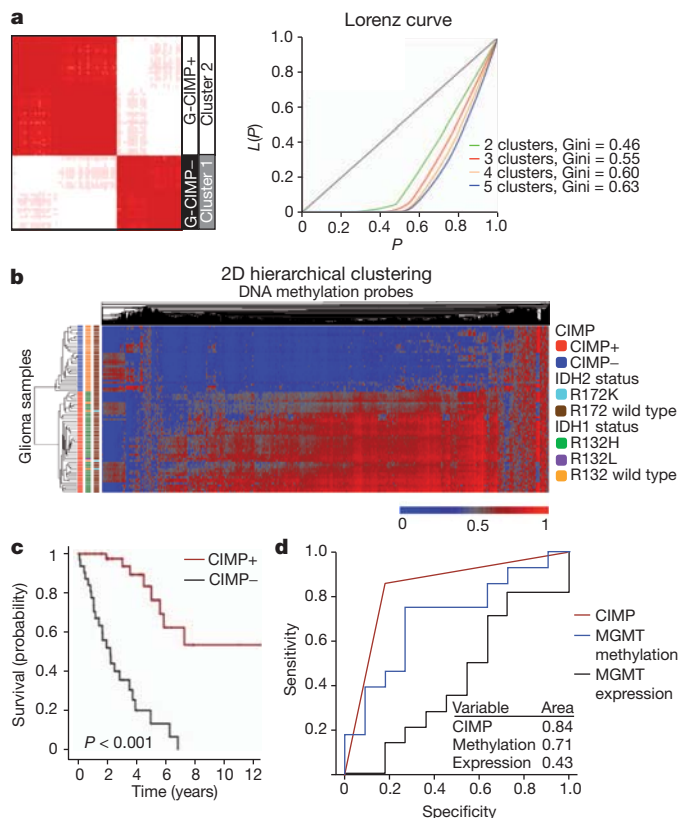


Figure 2 | Global epigenetic analysis of LGGs reveals dependence of G-CIMP on IDH mutation. **a**, Identification of G-CIMP by K -means consensus clustering of LGG samples. Unsupervised clustering was performed with the most variant probes (9,711 probes, top 2%). Tumours are listed in the same order along the x and y axes. G-CIMP status is indicated by the black and white bars. Consensus index values range from 0 to 1, with 0 being dissimilar (white) and 1 being similar (red). $K = 2$ is identified by the Lorenz curve. **b**, Two-dimensional (2D) hierarchical clustering of the same probes as in **a** identified the same two clusters. Each row represents a tumour and each column represents a probe. CIMP and IDH mutation status are indicated by the colour code. The level of DNA methylation (β value) for each probe is represented by colour scale (red, methylated; blue, non-methylated). Only cancer-specific events were used²⁷. **c**, Kaplan–Meier survival curve of Memorial Sloan-Kettering Cancer Center (MSKCC) patients ($n = 72$) with LGG (grade II and III). **d**, Receiver operating characteristic (ROC) curve comparing the sensitivity and specificity of G-CIMP status compared with MGMT methylation or MGMT expression status, in LGGs. Areas under the curve are noted in the inset. G-CIMP, MGMT methylation and MGMT expression were determined as described in Methods.

hierarchical clustering) (Fig. 2a, b). Probes defining CIMP in LGGs included those in CpG islands and shores (Supplementary Fig. 2c, d) and were enriched for PRC2-target genes (Supplementary Table 7). Global expression profiles showed that G-CIMP+ tumours possessed markedly different transcriptional profiles than G-CIMP- tumours (Supplementary Tables 8 and 9). EpiTYPER (Sequenom) mass spectrometry was used to validate the methylation status of loci in both the astrocyte model and in the tumours (Supplementary Fig. 2e–g)²³.

To determine the mutational status of *IDH1* and *IDH2*, we sequenced the entire coding sequence of the two genes in all the samples above (Fig. 2b). Ninety-eight per cent (49/50) of the G-CIMP+ tumours possessed either an *IDH1* mutation or *IDH2* mutation. Notably, none of the G-CIMP- tumours possessed mutant IDH (Supplementary Fig. 2h). These genomic data show that G-CIMP is highly dependent on the presence of IDH mutation and, in LGGs that are CIMP-, IDH mutations do not occur (0%). Currently, the methylation status of O-6-methylguanine DNA methyltransferase (MGMT) is a widely used molecular biomarker for glioblastoma prognosis and response to

temozolomide²⁴. In LGGs, G-CIMP associated with markedly better clinical endpoints (Fig. 2c and Supplementary Figs 3–6, Supplementary Tables 10 and 11). Importantly, G-CIMP was significantly superior to MGMT methylation or MGMT messenger RNA expression as a predictor of survival (Fig. 2d).

We next sought to define the nature of the methylome differences between IDH mutant and wild-type tumours and characterize the effects of these differences on the LGG transcriptome. Figure 3a shows a principal component analysis (PCA) of methylome and expression data from our tumours. PCA shows that G-CIMP+ and G-CIMP– LGGs methylome subgroups correlate with marked transcriptome differences (Fig. 3a). Of the 140,016 sites that were differentially methylated between IDH mutant and wild-type tumours, 121,660 were hypermethylated (Supplementary Table 6). There were 2,611 unique genes with alterations in promoter CpG islands represented in this group. Consistent with the results in Fig. 2b, a volcano plot showing differentially methylated genes between G-CIMP+ and G-CIMP– tumours was highly asymmetric (Fig. 3b). A starburst plot showing the relationship between DNA methylation and expression is shown in Fig. 3b. Integration of the normalized gene expression and DNA methylation gene sets identified 429 genes with both significant hypermethylation and downregulation and 176 genes that were hypomethylated and upregulated in G-CIMP+ LGGs (Supplementary Table 12). Among these genes are those known to be involved in glioma initiation and outcome, including *CDKN2C* and *GAP43* (refs 25, 26).

As a critical experiment to prove causality between IDH1 mutation and G-CIMP, we performed an in-depth comparison of methylation marks and gene expression alterations between human astrocytes expressing mutant IDH1 and the LGGs with endogenous IDH1 mutation. We first focused on the comparison of methylation marks and found that both sets of methylome alterations targeted similar loci. Gene set enrichment analysis (GSEA) of the mutant IDH1-induced methylation changes in the isogenic astrocyte system (Fig. 1) and the G-CIMP genes demonstrated very significant enrichment and concordance (Fig. 3c and Supplementary Table 13 and Supplementary Fig. 7). Importantly, the genes that were methylated after mutant IDH1 expression correctly classified LGG tumours into CIMP+ or CIMP– groups with very high accuracy (Fig. 3d and Supplementary Table 14). To confirm the impact of these alterations on glioma pathobiology, we used the transcriptomic footprint of mutant IDH to generate an expression signature (mutant IDH repression signature) composed of the most significantly methylated and downregulated genes in both the isogenic astrocyte system and the G-CIMP gene set (17 genes; Supplementary Table 15). As expected, this signature classified an independent LGG cohort (Rembrandt) into two distinct subgroups (Fig. 3e and Supplementary Figs 8–10 and Supplementary Table 16). Together, our findings show that introduction of mutant IDH reprograms the epigenome and generates the foundations of G-CIMP.

IDH mutation is highly enriched in the CIMP+, proneural subgroup of glioblastomas. Using data from The Cancer Genome Atlas (TCGA), we applied the mutant IDH repression signature as a classifier to the transcriptomes of all four subgroups of glioblastomas²⁷. The signature segregated IDH mutant and wild-type proneural glioblastomas into two distinct subgroups associated with very different prognoses, but did not do so in other glioblastoma subgroups (Supplementary Fig. 11a, b). These data demonstrate that mutant IDH-induced epigenomic alterations have profound biological implications within the proneural class of glioblastomas that are specific for this subclass. Comparison of gene expression programs that occur in astrocytes expressing mutant IDH1 to those in LGG tumours that harbour the IDH mutation showed remarkable similarity (Fig. 4a and Supplementary Fig. 12). Moreover, introduction of mutant but not wild-type IDH1 into astrocytes resulted in the upregulation of nestin (and other genes associated with stem cell identity) at the time of DNA methylation increase and the adoption of a neurosphere/stem-like phenotype (Fig. 4b and Supplementary

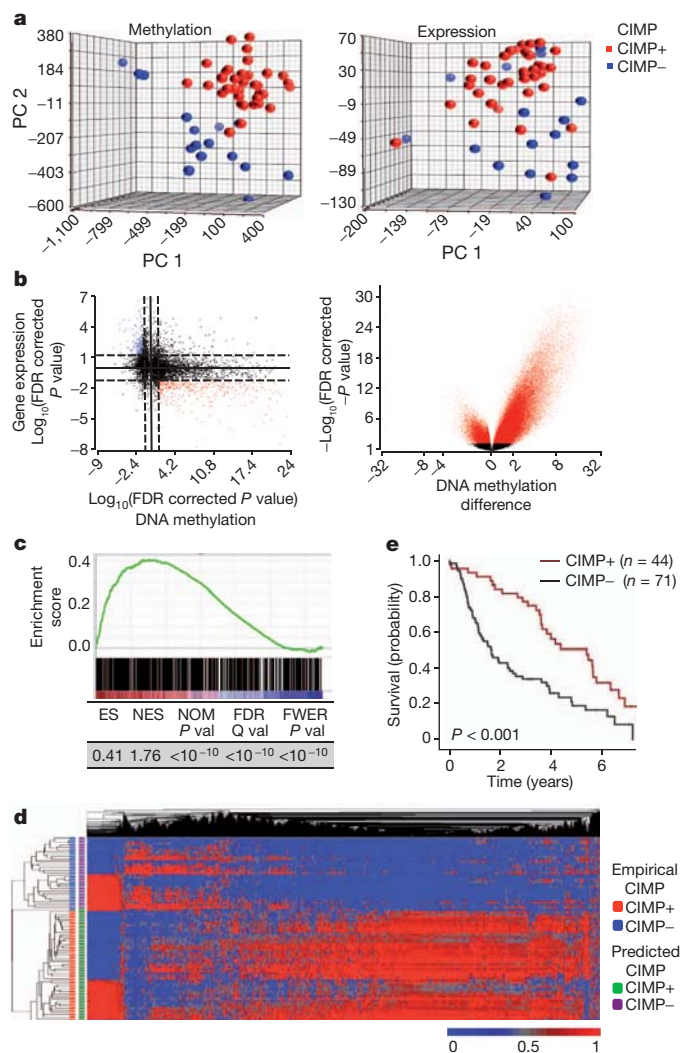


Figure 3 | IDH1 mutation directly generates the methylation patterns present in G-CIMP tumours. **a**, The methylomes and transcriptomes of LGGs are distinct. PCA plot of LGG tumours for all methylation probes (left) and expression probes (right) ($n = 52$). PC, principal component. **b**, Starburst plot (left) for comparison of DNA methylation and gene expression. The $\log_{10}(\text{FDR-corrected } P \text{ value})$ is plotted for β value for DNA methylation (x axis) and gene expression (y axis) for each gene. Black dotted line shows the FDR-adjusted P value of 0.05. Red points indicate downregulated and hypermethylated genes in G-CIMP+ LGGs versus G-CIMP– LGGs. Blue points show hypomethylated and upregulated genes. Volcano (right) plot of all CpG loci analysed for G-CIMP association. The β -value difference in DNA methylation between G-CIMP+ and G-CIMP– tumours is plotted along the x axis. The P value between G-CIMP+ and G-CIMP– tumours is plotted on the y axis ($-\log_{10}$ scale). Red indicates significantly different probes. **c**, Concordance between hypermethylated sites in mutant IDH1-expressing astrocytes and G-CIMP+ LGGs. GSEA shows significant enrichment between 730 hypermethylated unique CpG sites identified in IDH1 mutant astrocytes (ANOVA between passage 2 and 40) and those present in G-CIMP+ gliomas. GSEA correlation shown in colour scale. ES, enrichment score; FDR, false discovery rate; FEWR, familywise error rate; NES, normalized enrichment score; NOM, nominal P value. **d**, Differential methylation in IDH mutant astrocytes correctly classifies G-CIMP in the human LGGs. Two-dimensional-unsupervised hierarchical clustering of 81 human gliomas with top variant probes ($n = 10,000$) from mutant IDH1 astrocytes. Tumours are shown on the y axis, probes along the x axis. Methylation (β value) for each probe is represented with the colour scale. G-CIMP classification as determined by the astrocyte-derived data is denoted by the colour bars at the left. **e**, Kaplan–Meier survival curve of 115 patients with grade II or grade III gliomas in the Rembrandt Database grouped by CIMP status. P value calculated by log rank.

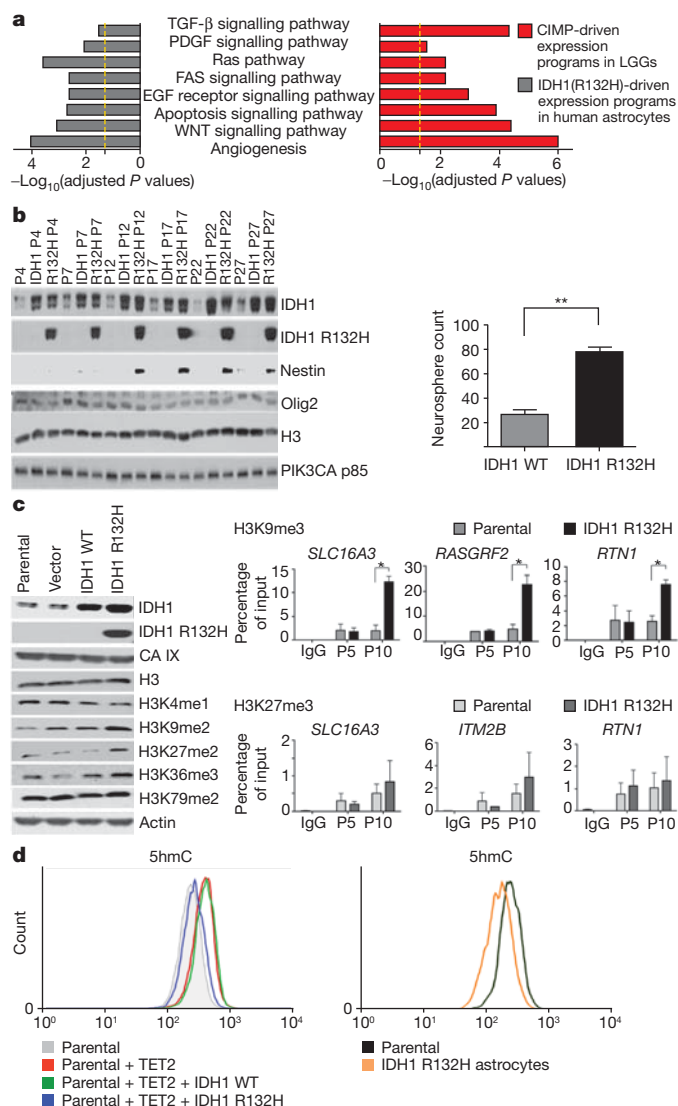


Figure 4 | Functional implications of IDH1-mutation-induced alterations in the glioma epigenome. **a**, Concordance of transcriptional programs regulated by mutant IDH1 in astrocytes and G-CIMP in LGGs. P value for significance is shown along the x axis. Yellow lines indicate threshold of significance ($P = 0.05$). **b**, Mutant IDH1 results in the expression of markers of self-renewal and stem cell identity. Left, mutant IDH1 results in expression of nestin. P indicates passage number. Right, expression of mutant IDH1 promotes the adoption of a neurosphere phenotype. Astrocytes (passage 15) that express IDH1 R132H or IDH1 wild type were used in the neurosphere assay. Error bars indicate 1 s.d. $^{**}P < 0.01$ (t -test). **c**, Alterations in histone marks in IDH1-mutant-expressing human astrocytes. Left, western blot results are shown using the indicated antibodies. Astrocytes are from passage 27. Right, ChIP of the indicated histone marks for representative hypermethylated genes. Error bars indicate 1 s.d. $^{*}P < 0.05$. **d**, Mutant IDH1 inhibits the production of 5hmC in human astrocytes. Left, mutant IDH inhibits TET2-dependent 5hmC production in astrocytes. Parental astrocytes were infected with lentivirus directing the expression of TET2 catalytic domain and green fluorescent protein (GFP) \pm mutant IDH1. FACS analyses are shown for 5hmC. Right, astrocytes expressing IDH R132H (passage 10) have less 5hmC than astrocytes that do not express the IDH mutant.

Fig. 13)²⁸. These data suggest that mutant IDH1 functions by interfering with differentiation state.

Our data show that IDH1 mutation is the mechanistic cause of G-CIMP. To gain further insight, we determined the effects of mutant IDH1 on histone alterations in our astrocyte system. Figure 4c (left) shows that expression of the IDH1 mutant increases levels of H3K9me2, H3K27me3 and H3K36me3, consistent with previous findings²⁹.

Chromatin immunoprecipitation (ChIP) experiments examining representative genes that undergo hypermethylation show H3K9 and H3K27 methylation are both enriched in cells expressing mutant IDH1 (Fig. 4c, right). As both of these marks can promote DNA methylation, alterations in histone marks may contribute to the accumulation of DNA methylation.

Next, we determined the effects the mutation had on TET2-dependent 5-hydroxymethylcytosine (5hmC) levels. We used a well-established assay^{9,29} and first confirmed that we were able to detect TET-dependent alterations in 5hmC (Supplementary Fig. 14). We found that expression of the IDH1 mutant in astrocytes resulted in a significant decrease in 5hmC (Fig. 4d, right). Expression of TET2 in the astrocytes produced 5hmC, which was inhibited by mutant but not wild-type IDH1 (Fig. 4d, left). Because TET-mediated production of 5hmC is a primary mode of DNA demethylation³⁰, inhibition of this activity in the IDH1-mutant-expressing astrocytes may be a mechanistic basis for accumulation of DNA methylation, ultimately leading to a CIMP pattern.

IDH mutation and the CIMP phenotype are two very common features in cancer, the underlying mechanisms for which are obscure. The fundamental questions regarding these features are (1) how the IDH mutation contributes to oncogenesis, and (2) what the root cause of CIMP is. Our data address these important questions by demonstrating that IDH mutation is the cause of CIMP and leads to the CIMP phenotype by stably reshaping the epigenome. This remodelling involves modulating patterns of methylation on a genome-wide scale, changing transcriptional programs and altering the differentiation state. Our observations suggest that the activity of IDH may form the basis of an 'epigenomic rheostat', linking alterations in cellular metabolism to the epigenetic state. In summary, these data provide a mechanistic framework for how IDH mutation leads to oncogenesis and the molecular basis of CIMP in gliomas. We believe our observations have critical implications for the understanding of gliomas and the development of novel therapies for this disease.

METHODS SUMMARY

Cell culture. Immortalized human astrocytes were a gift from R. O. Pieper (University of California, San Francisco) and were prepared as previously described¹⁴. Cells were cultured in Dulbecco's modified Eagle's medium (DMEM) plus 10% fetal bovine serum (FBS; Invitrogen). Expression of IDH was accomplished by cloning wild-type or mutant IDH1 (R132H) into the vector pLNCX2. These constructs were used to construct lentiviruses used for infection of target cells. Selection was performed using G418. All experiments were performed in duplicate.

Tumours. All tumours ($n = 81$) were obtained following surgical resection at the MSKCC as part of routine clinical care and snap frozen. Tumours were obtained in accordance with Institutional Review Board policies at the MSKCC. Each sample was examined histologically with haematoxylin-and-eosin-stained cryostat sections by a neuropathologist. Before analysis, tumours were sectioned and microdissected. Genomic DNA or RNA was extracted using the DNeasy kit (Qiagen) or RNeasy Lipid Tissue Mini kit (Qiagen) per the manufacturer's instructions.

Genomic analysis. Expression analysis of astrocytes and tumours was performed using the Affymetrix U133 2.0 microarray. Genome-wide methylation analysis was performed using the Illumina Infinium HumanMethylation450 bead array. Processing of the arrays was as per the manufacturer's protocol. Methylation data were extracted using GenomeStudio software (Illumina). Methylation values for each site are expressed as a β value, representing a continuous measurement from 0 (completely unmethylated) to 1 (completely methylated). This value is based on the following calculation: β value = (signal intensity of methylation-detection probe) / (signal intensity of methylation-detection probe + signal intensity of non-methylation detection probe).

Full Methods and any associated references are available in the online version of the paper at www.nature.com/nature.

Received 3 June 2011; accepted 17 January 2012.

Published online 15 February 2012.

- Noushmehr, H. *et al.* Identification of a CpG island methylator phenotype that defines a distinct subgroup of glioma. *Cancer Cell* **17**, 510–522 (2010).
- Fang, F. *et al.* Breast cancer methylomes establish an epigenomic foundation for metastasis. *Sci. Transl. Med.* **3**, 75ra25 (2011).

3. Toyota, M. *et al.* CpG island methylator phenotype in colorectal cancer. *Proc. Natl Acad. Sci. USA* **96**, 8681–8686 (1999).
4. Yan, H. *et al.* IDH1 and IDH2 mutations in gliomas. *N. Engl. J. Med.* **360**, 765–773 (2009).
5. Parsons, D. W. *et al.* An integrated genomic analysis of human glioblastoma multiforme. *Science* **321**, 1807–1812 (2008).
6. Sjöblom, T. *et al.* The consensus coding sequences of human breast and colorectal cancers. *Science* **314**, 268–274 (2006).
7. Mardis, E. R. *et al.* Recurring mutations found by sequencing an acute myeloid leukemia genome. *N. Engl. J. Med.* **361**, 1058–1066 (2009).
8. Dang, L. *et al.* Cancer-associated IDH1 mutations produce 2-hydroxyglutarate. *Nature* **462**, 739–744 (2009).
9. Figueroa, M. E. *et al.* Leukemic IDH1 and IDH2 mutations result in a hypermethylation phenotype, disrupt TET2 function, and impair hematopoietic differentiation. *Cancer Cell* **18**, 553–567 (2010).
10. Ward, P. S. *et al.* The common feature of leukemia-associated IDH1 and IDH2 mutations is a neomorphic enzyme activity converting α -ketoglutarate to 2-hydroxyglutarate. *Cancer Cell* **17**, 225–234 (2010).
11. Jones, P. A. & Baylin, S. B. The epigenomics of cancer. *Cell* **128**, 683–692 (2007).
12. Ohm, J. E. *et al.* A stem cell-like chromatin pattern may predispose tumor suppressor genes to DNA hypermethylation and heritable silencing. *Nature Genet.* **39**, 237–242 (2007).
13. Cheng, Y. W. *et al.* CpG island methylator phenotype associates with low-degree chromosomal abnormalities in colorectal cancer. *Clin. Cancer Res.* **14**, 6005–6013 (2008).
14. Sonoda, Y. *et al.* Formation of intracranial tumors by genetically modified human astrocytes defines four pathways critical in the development of human anaplastic astrocytoma. *Cancer Res.* **61**, 4956–4960 (2001).
15. Vivanco, I. *et al.* Identification of the JNK signaling pathway as a functional target of the tumor suppressor PTEN. *Cancer Cell* **11**, 555–569 (2007).
16. Sonoda, Y. *et al.* Akt pathway activation converts anaplastic astrocytoma to glioblastoma multiforme in a human astrocyte model of glioma. *Cancer Res.* **61**, 6674–6678 (2001).
17. Pieper, R. O. Defined human cellular systems in the study of glioma development. *Front. Biosci.* **8**, s19–s27 (2003).
18. Bibikova, M. *et al.* High density DNA methylation array with single CpG site resolution. *Genomics* **98**, 288–295 (2011).
19. Sandoval, J. *et al.* Validation of a DNA methylation microarray for 450,000 CpG sites in the human genome. *Epigenetics* **6**, 692–702 (2011).
20. Mutskov, V. & Felsenfeld, G. Silencing of transgene transcription precedes methylation of promoter DNA and histone H3 lysine 9. *EMBO J.* **23**, 138–149 (2004).
21. Bracken, A. P. *et al.* Genome-wide mapping of Polycomb target genes unravels their roles in cell fate transitions. *Genes Dev.* **20**, 1123–1136 (2006).
22. Furnari, F. B. *et al.* Malignant astrocytic glioma: genetics, biology, and paths to treatment. *Genes Dev.* **21**, 2683–2710 (2007).
23. Docherty, S. J. *et al.* Bisulfite-based epityping on pooled genomic DNA provides an accurate estimate of average group DNA methylation. *Epigenetics Chromatin* **2**, 3 (2009).
24. Hegi, M. E. *et al.* MGMT gene silencing and benefit from temozolomide in glioblastoma. *N. Engl. J. Med.* **352**, 997–1003 (2005).
25. Solomon, D. A. *et al.* Identification of p18^{INK4c} as a tumor suppressor gene in glioblastoma multiforme. *Cancer Res.* **68**, 2564–2569 (2008).
26. Etcheverry, A. *et al.* DNA methylation in glioblastoma: impact on gene expression and clinical outcome. *BMC Genomics* **11**, 701 (2010).
27. The Cancer Genome Atlas Network. Comprehensive genomic characterization defines human glioblastoma genes and core pathways. *Nature* **455**, 1061–1068 (2008).
28. Lendahl, U., Zimmerman, L. B. & McKay, R. D. CNS stem cells express a new class of intermediate filament protein. *Cell* **60**, 585–595 (1990).
29. Xu, W. *et al.* Oncometabolite 2-hydroxyglutarate is a competitive inhibitor of α -ketoglutarate-dependent dioxygenases. *Cancer Cell* **19**, 17–30 (2011).
30. He, Y. F. *et al.* Tet-mediated formation of 5-carboxylcytosine and its excision by TDG in mammalian DNA. *Science* **333**, 1303–1307 (2011).

Supplementary Information is linked to the online version of the paper at www.nature.com/nature.

Acknowledgements We thank A. Kayserian, K. Huberman, I. Dolgalev and S. Thomas for technical expertise. We thank C. Sawyers and E. Holland for helpful discussions. This grant was supported in part by the National Institutes of Health (R01CA154767-01) (T.A.C.), the National Cancer Institute (U54-CA143798) (I.K.M.), an Advanced Clinical Research Award in Glioma from the American Society of Clinical Oncology (I.K.M.), the Doris Duke Charitable Fund (I.K.M., T.A.C.), a National Brain Tumor Society Systems Biology Research Grant (I.K.M.), the MSKCC Brain Tumor Center (T.A.C.), the Louis Gerstner Foundation (T.A.C.), the STARR Cancer Consortium (T.A.C.) and the Sontag Foundation (T.A.C., I.K.M.).

Author Contributions T.A.C., S.T., A.G. and I.K.M. designed the experiments. S.T., A.G., F.F., D.R., A.H., L.A.W., C.C., E.Y., C.L., P.S.W., A.V., J.T.H., A.W.M.F. and L.G.T.M. performed the experiments. S.T., J.T.H., A.G., F.F., A.K., A.H., E.Y., A.V., P.S.W., C.B.T., T.A.C. and I.K.M. analysed the data. D.R., O.G., R.L. and I.K.M. contributed new reagents. T.A.C., S.T., I.K.M. and A.G. wrote the paper.

Author Information Data sets have been deposited in the Gene Expression Omnibus under accession number GSE30339. Reprints and permissions information is available at www.nature.com/reprints. The authors declare competing financial interests: details accompany the full-text HTML version of the paper at www.nature.com/nature. Readers are welcome to comment on the online version of this article at www.nature.com/nature. Correspondence and requests for materials should be addressed to T.A.C. (chant@mskcc.org) or I.K.M. (mellingi@mskcc.org).

METHODS

Cell culture. Immortalized human astrocytes were a gift from R. O. Pieper (University of California, San Francisco) and were prepared as previously described¹⁴. Cells were cultured in Dulbecco's modified Eagle's medium (DMEM) plus 10% fetal bovine serum (FBS; Invitrogen). Expression of IDH was accomplished by cloning wild-type or mutant IDH1 (R132H) into the vector pLNCX2. These constructs were used to construct retroviruses used for infection of target cells. The retroviral packaging cell line GP-293 was seeded in 10-cm-diameter dishes and (at 30–50% confluency) was transfected using Lipofectamine (Invitrogen) with pVSV-G (Clontech) and pLNCX2-IDH1 wild type or IDH1 R132H. Retroviral particles were collected, filtered through a 0.45- μ m syringe filter and polybrene was added (8 μ g ml⁻¹ final concentration) to infect the human astrocytes for 12 h. Stable transfectants were selected with G418 and pooled populations of G418-resistant cells expressing either wild-type IDH1 or IDH1 R132H were confirmed by western blot analysis with anti-IDH1 antibody (rabbit anti-IDH1; Cell Signaling). All experiments were performed in duplicate.

Tumours. All tumours ($n = 81$) were obtained following surgical resection at the MSKCC as part of routine clinical care, and snap frozen. Tumours were obtained in accordance with Institutional Review Board policies at the MSKCC. Each sample was examined histologically by a neuropathologist. Before analysis, tumours were sectioned and microdissected. Genomic DNA or RNA was extracted using the DNeasy kit (Qiagen) or Triazol (Invitrogen) as per the manufacturer's instructions. Data from TCGA tumours ($n = 173$) are publicly available²⁷. For the LGG validation set, expression data sets of 115 patients with grade II and grade III gliomas were identified from the NCI Repository for Molecular Brain Neoplasia Data (Rembrandt; <http://rembrandt.nci.nih.gov>).

Sample preparation. DNA from wild-type IDH1, R132H IDH1 and parental astrocytes was extracted with the Puregene Cell and Tissue Kit (Qiagen) at various passages (passages 2, 5, 10, 15, 20, 25, 30, 40 and 50) and RNA was extracted with Trizol (Invitrogen) according to the manufacturer's directions. All experiments with the astrocytes were performed in duplicate, each with two corresponding technical (microarray) replicates. Genomic DNA and RNA from human tumours were extracted from frozen primary tumours for the methylation and expression studies. Frozen samples were snap frozen in liquid nitrogen and stored at -80°C . Each sample was examined histologically with haematoxylin-and-eosin-stained sections by a neuropathologist and representative sections were microdissected from the slides. Genomic DNA was extracted with the Qiagen DNeasy Blood and Tissue Kit using the manufacturer's instructions. RNA was extracted with Qiagen RNeasy Lipid Tissue Mini Kit using the manufacturer's instructions. Nucleic acid quality was determined with the Agilent 2100 Bioanalyzer.

Genomic analysis. Expression analysis of astrocytes and tumours was performed using the Affymetrix U133 2.0 microarray (Affymetrix). Genome-wide methylation analysis was performed using the Infinium HumanMethylation450 bead array (Illumina). Processing of the arrays was per the manufacturer's protocol. Methylation data were extracted using GenomeStudio software (Illumina). Methylation values for each site are expressed as a β value, representing a continuous measurement from 0 (completely unmethylated) to 1 (completely methylated). This value is based on following calculation: $\beta \text{ value} = (\text{signal intensity of methylation-detection probe}) / (\text{signal intensity of methylation-detection probe} + \text{signal intensity of non-methylation detection probe})$.

Data analysis. For methylation analysis, Illumina data were imported into Partek software. β Values were logit-transformed and adjusted for batch effects before analysis. Analysis of variance (ANOVA) with false discovery correction (FDR) was used to identify genes that were differentially methylated between the astrocytes expressing wild-type IDH1, mutant IDH1, and control astrocytes. Significant changes were defined as genes having an FDR-corrected P value < 0.05 . In human tumours, unsupervised consensus clustering of the β values was performed with K -means clustering ($K_{\text{max}} = 5$) with Euclidean distance and average linkage over 1,000 resampling iterations with random restart on the top 2% of the most variant probes (9,750 probes) using Gene Pattern v.2.0³¹. This identified an optimal number of $K = 2$ groups. This was repeated using unsupervised hierarchical clustering using Pearson dissimilarity. The cluster of samples that exhibited a large degree of hypermethylation was identified as CIMP+, and the remaining group CIMP-. ANOVA with FDR correction was used to identify genes that were differentially methylated between the CIMP groups. Significant changes were defined as genes having an FDR-corrected P value < 0.05 .

For gene expression analysis of astrocytes, Affymetrix CEL files were imported into the R statistical software (v.2.13.0; <http://www.R-project.org>). Normalization was performed with the AffyPLM package in BioConductor (v.2.4), using RMA background correction, quantile normalization, and the Tukey biweight summary method. Differential expression was detected using the limma package and P values were adjusted for multiple testing using the FDR approach. A probe set is considered differentially expressed if the FDR-adjusted P value < 0.05 . For gene

expression analysis of the human tumours, the Affymetrix data were imported into the Partek Genomics Suite (Partek) as Affymetrix CEL files. The data were RMA normalized and median-scaled for analysis. ANOVA followed by FDR was used to identify genes that were differentially expressed between the CIMP groups. To derive the 17-gene mutant IDH1 repression signature, we identified 605 unique genes that had either statistically significant hypermethylation at promoter-associated CpG islands and decreased gene expression, or had hypomethylation at promoter-associated CpG Islands and increased gene expression in CIMP+ versus CIMP- tumours. We identified common genes in a comparison of this gene set with that derived from mutant IDH1-expressing astrocytes versus wild type. Differential methylation in the cell lines was defined as an FDR-adjusted P value < 0.05 , and differential expression was defined as a P value < 0.05 with concordant fold change of at least 1.5 fold.

The 17-gene expression signature was used to predict CIMP in the Rembrandt data set. Unsupervised hierarchical clustering using Pearson dissimilarity identified two unique clusters that were categorized as 'predicted CIMP+' and 'predicted CIMP-'. The 17-gene expression signature was also used to identify subgroups from the TCGA GBM data set of 173 patients²⁷. Unsupervised consensus clustering using Pearson dissimilarity was performed on each of the subclasses identified by the TCGA to identify clusters³². Rembrandt data sets were obtained at <http://caintegrator-info.nci.nih.gov/rembrandt>.

Functional analysis of gene lists was performed using the PANTHER database and categories with adjusted P values (Benjamini-Hochberg) < 0.05 were considered as significantly over-represented in our gene lists³³. Concepts module mapping was performed as follows. The hypermethylation signature identified from our analysis of differentially methylated genes in IDH1 mutants compared to IDH1 wild-type was imported into OncoPrint (<http://www.oncoprint.org>) to identify associations with molecular concepts signatures derived from independent cancer profiling studies. Statistically significant concordances of our methylation gene signature with the pre-defined concepts were identified and Q value was calculated as previously described³⁴.

Methylation data of parental, wild-type IDH1-expressing astrocytes, and mutant IDH1-expressing astrocytes were clustered using self-organizing maps and visualized with the Gene Expression Dynamics Inspector (GEDI; v.2.1). For GEDI analysis, methylation data were normalized as a group across all passages and genotypes. Further hierarchical clustering (average-linkage) of GEDI map centroids was performed in R using the *hclust* library in the stats package. GSEA was performed using GSEA software v.2.0 and MSigDB database v.2.5. We assessed the significance of the curated gene sets (MSigDB collection c2) with the following parameters: number of permutations = 1,000 and permutation_type = phenotype, with an FDR Q -value cut-off of 5% (ref. 35).

G-CIMP was compared to MGMT methylation and MGMT expression in 52 LGG samples in the MSKCC cohort. We identified the Illumina 450K methylation probe ID (cg12981137) that corresponded to the MGMT MSP primer sequence as identified previously³⁶ and the Affymetrix probe ID (204880_at) that corresponds to MGMT expression.

Clinical and pathological characteristics between cohorts were compared using the χ^2 test. Overall survival was calculated from the date of surgery to death from any cause. Patients were censored at the time they were last known to be alive. Overall survival was assessed using the Kaplan-Meier method and the log-rank test was used for comparison between groups. Multivariate analysis was performed using a Cox proportional hazards model to assess the independent effect of prognostic variables on outcome, and using binary logistic regression to predict the probability of occurrence of CIMP+. An ROC curve was generated to graph the sensitivity and specificity of CIMP, MGMT methylation, and MGMT expression to predict survival ≥ 3 years. MGMT methylation and MGMT expression was considered continuous variables, and CIMP a categorical variable (defined by unsupervised hierarchical analysis as described above). Patients that were alive and had less than 3 years of follow-up were excluded from this analysis. Data was analysed using SPSS software (IBM SPSS statistics version 19.0).

Quantitative DNA methylation analysis using mass spectrometry. DNA methylation analysis was performed using the EpiTYPER system (Sequenom). The EpiTYPER assay is a tool for the detection and quantitative analysis of DNA methylation using base-specific cleavage of bisulphite-treated DNA and matrix-assisted laser desorption/ionization time-of-flight mass spectrometry (MALDI-TOF MS)³⁷. For primer sequences, target chromosomal sequence, and EpiTYPER-specific tags, see Supplementary Table 17. SpectroCHIPs were analysed using a Bruker Biflex III MALDI-TOF mass spectrometer (SpectroREADER, Sequenom). Results were analysed using the EpiTYPER Analyzer software, and manually inspected for spectra quality and peak quantification. CIMP positivity was defined as a mean methylated allelic frequency of $> 50\%$ or a twofold increase over normal breast tissue and the CIMP- state.

PCR amplification and sequencing. Exonic regions for the *IDH1* and *IDH2* genes (NCBI Human Genome Build 36.1) were broken into amplicons of 500 bp or less, and specific primers were designed using Primer3. Standard M13 tails were added to the primers to facilitate Sanger sequencing. PCR reactions were carried out in 384-well plates in a Duncan DT-24 water bath thermal cycler with 10 ng of whole-genome amplified DNA (REPLI-g Midi, Qiagen) as a template, using a touchdown PCR protocol with KAPA Fast HotStart (Kapa Biosystems). The touchdown PCR method consisted of: 1 cycle of 95 °C for 5 min; 3 cycles of 95 °C for 30 s, 64 °C for 15 s, 72 °C for 30 s; 3 cycles of 95 °C for 30 s, 62 °C for 15 s, 72 °C for 30 s; 3 cycles of 95 °C for 30 s, 60 °C for 15 s, 72 °C for 30 s; 37 cycles of 95 °C for 30 s, 58 °C for 15 s, 72 °C for 30 s; 1 cycle of 70 °C for 5 min. Templates were purified using AMPure (Agencourt Biosciences). The purified PCR reactions were split into two and sequenced bidirectionally with M13 forward and reverse primer and the Big Dye Terminator Kit v.3.1 (Applied Biosystems) at Agencourt Biosciences. Dye terminators were removed using the CleanSEQ kit (Agencourt Biosciences), and sequence reactions were run on ABI PRISM 3730xl sequencing apparatus (Applied Biosystems). Sanger sequencing of *IDH1* and *IDH2* produced an average coverage of 96.1% of coding sequence nucleotides across all samples.

Mutation detection. Passing reads were assembled against reference sequences, containing all coding exons including 5 kb upstream and downstream of the gene, using command line Consed 16.0³⁷. Assemblies were passed on to Polyphred 6.02b³⁸, which generated a list of putative candidate mutations, and to Polyscan 3.0³⁹, which generated a second list of putative mutations. The lists were merged together into a combined report, and the putative mutation calls were normalized to '+' genomic coordinates and annotated using the Genomic Mutation Consequence Calculator⁴⁰. The resulting list of annotated putative mutations was loaded into a Postgres database along with select assembly details for each mutation call (assembly position, coverage, and methods supporting mutation call). To reduce the number of false positives generated by the mutation detection software packages, only point mutations that were supported by at least one bi-directional read pair and at least one sample mutation called by Polyphred were considered, and only the putative mutations that were annotated as having non-synonymous coding effects, occurred within 1 bp of an exon boundary, or had a conservation score > 0.699 were included in the final candidate list. Indels were manually reviewed and included in the candidate list if found to hit an exon. All putative mutations were confirmed by a second PCR and sequencing reaction, in parallel with amplification and sequencing of matched normal tissue DNA.

ChIP. Cells were fixed with 1% formaldehyde for 10 min at room temperature (21 °C) and formaldehyde was inactivated by the addition of 125 mM glycine. ChIP assays were performed using a protocol recommended by the manufacturer of a commercially available ChIP assay kit (17-371, Millipore). Chromatin extracts were immunoprecipitated using anti-H3K9me3 (Ab8898, Abcam) or anti-H3K27me3 (07-449, Millipore) antibodies. After washing, ChIPed DNA was eluted from the beads and analysed on an Eppendorf Realplex using SYBR Green (Applied Biosystems). Relative occupancy values were calculated by determining ratios of the amount of immunoprecipitated DNA to that of the input sample (2% of total).

Flow cytometry and 5hmC assay. HEK 293T cells were transiently transfected with Flag-TET2 in pCMV6-ENTRY vector with Lipofectamine 2000 (GIBCO). For two-colour flow cytometry, 10⁶ cells were washed with ice-cold PBS, permeabilized and fixed using BD Cytoperm/Cytofix solution (BD, PharMingen), and incubated with anti-Flag (1:200, Sigma) and anti-5hmC (1:400, Active Motif #39770) antibodies for 30 min at room temperature. Cells were washed with PBS and incubated with secondary antibodies conjugated with Alexa Fluor 488 or Cy5 (Invitrogen) for 30 min in the dark. For single-colour flow cytometry, parental and *IDH1* mutant astrocytes were stained using anti-5hmC (1:400) followed by Alexa Fluor 488 secondary antibody. Cells were washed in PBS and analysed using the FACScan flow cytometer (Becton Dickinson). FACS data were analysed using FLOWJo Software (TreeStar).

Neurosphere assay. *IDH1*(R123H)-expressing astrocytes and parental controls were grown in media permissive of neural stem cell growth as previously described^{41,42}. Briefly, immortalized human astrocyte (IHA) cells stably expressing wild-type or R123H mutant *IDH1* at passage 15 were seeded in 6-well plates at 200,000 cells per well. The next day, proliferation medium (DMEM plus 10% FCS) was replaced with neural stem cell medium made from serum-free DMEM supplemented with B27 and N2 supplements (all from Invitrogen), bFGF, EGF and PDGFAA (all at 20 ng ml⁻¹, all from PeproTech). Medium was replaced every 2–3 days. Neurospheres were quantified using microscopy. Experiments were performed in triplicate.

31. Reich, M. *et al.* GenePattern 2.0. *Nature Genet.* **38**, 500–501 (2006).
32. Verhaak, R. G. *et al.* Integrated genomic analysis identifies clinically relevant subtypes of glioblastoma characterized by abnormalities in *PDGFRA*, *IDH1*, *EGFR*, and *NF1*. *Cancer Cell* **17**, 98–110 (2010).
33. Thomas, P. D. *et al.* PANTHER: a library of protein families and subfamilies indexed by function. *Genome Res.* **13**, 2129–2141 (2003).
34. Rhodes, D. R. *et al.* Molecular concepts analysis links tumors, pathways, mechanisms, and drugs. *Neoplasia* **9**, 443–454 (2007).
35. Subramanian, A. *et al.* Gene set enrichment analysis: a knowledge-based approach for interpreting genome-wide expression profiles. *Proc. Natl Acad. Sci. USA* **102**, 15545–15550 (2005).
36. Vlassenbroeck, I. *et al.* Validation of real-time methylation-specific PCR to determine O⁶-methylguanine-DNA methyltransferase gene promoter methylation in glioma. *J. Mol. Diagn.* **10**, 332–337 (2008).
37. Gordon, D., Abajian, C. & Green, P. Consed: a graphical tool for sequence finishing. *Genome Res.* **8**, 195–202 (1998).
38. Nickerson, D. A., Tobe, V. O. & Taylor, S. L. PolyPhred: automating the detection and genotyping of single nucleotide substitutions using fluorescence-based resequencing. *Nucleic Acids Res.* **25**, 2745–2751 (1997).
39. Chen, K. *et al.* PolyScan: an automatic indel and SNP detection approach to the analysis of human resequencing data. *Genome Res.* **17**, 659–666 (2007).
40. Major, J. E. Genomic mutation consequence calculator. *Bioinformatics* **23**, 3091–3092 (2007).
41. Galli, R. *et al.* Isolation and characterization of tumorigenic, stem-like neural precursors from human glioblastoma. *Cancer Res.* **64**, 7011–7021 (2004).
42. De Filippis, L. *et al.* A novel, immortal, and multipotent human neural stem cell line generating functional neurons and oligodendrocytes. *Stem Cells* **25**, 2312–2321 (2007).

Transformation by the (R)-enantiomer of 2-hydroxyglutarate linked to EGLN activation

Peppi Koivunen^{1*}, Sungwoo Lee^{2*}, Christopher G. Duncan³, Giselle Lopez³, Gang Lu², Shakti Ramkissoon^{2,4,5}, Julie A. Losman², Päivi Joensuu⁶, Ulrich Bergmann⁷, Stefan Gross⁸, Jeremy Travins⁸, Samuel Weiss⁹, Ryan Looper¹⁰, Keith L. Ligon^{2,4,5,11}, Roel G. W. Verhaak¹², Hai Yan³ & William G. Kaelin Jr^{2,13}

The identification of succinate dehydrogenase (SDH), fumarate hydratase (FH) and isocitrate dehydrogenase (IDH) mutations in human cancers has rekindled the idea that altered cellular metabolism can transform cells. Inactivating SDH and FH mutations cause the accumulation of succinate and fumarate, respectively, which can inhibit 2-oxoglutarate (2-OG)-dependent enzymes, including the EGLN prolyl 4-hydroxylases that mark the hypoxia inducible factor (HIF) transcription factor for polyubiquitylation and proteasomal degradation¹. Inappropriate HIF activation is suspected of contributing to the pathogenesis of SDH-defective and FH-defective tumours but can suppress tumour growth in some other contexts. IDH1 and IDH2, which catalyse the interconversion of isocitrate and 2-OG, are frequently mutated in human brain tumours and leukaemias. The resulting mutants have the neomorphic ability to convert 2-OG to the (R)-enantiomer of 2-hydroxyglutarate ((R)-2HG)^{2,3}. Here we show that (R)-2HG, but not (S)-2HG, stimulates EGLN activity, leading to diminished HIF levels, which enhances the proliferation and soft agar growth of human astrocytes. These findings define an enantiomer-specific mechanism by which the (R)-2HG that accumulates in IDH mutant brain tumours promotes transformation and provide a justification for exploring EGLN inhibition as a potential treatment strategy.

To study the role of IDH mutations in brain tumours, we stably infected immortalized human astrocytes with retroviral vectors encoding haemagglutinin (HA)-tagged versions of wild-type IDH1, a tumour-derived mutant (IDH1 R132H)^{2,3}, or an IDH1 R132H variant in which three conserved aspartic acid residues within the IDH1 catalytic domain were replaced with asparagines (R132H/3DN) (Fig. 1a and Supplementary Fig. 1). As expected, (R)-2HG levels, but not (S)-2HG levels, were markedly increased in the cells producing IDH1 R132H but not in cells producing the R132H/3DN variant (Fig. 1b and Supplementary Fig. 2). In multiple independent experiments the IDH1 R132H cells acquired a proliferative advantage relative to cells producing the other versions of IDH1 beginning around passage 14, manifested as increased proliferation at confluence (Fig. 1c) and the ability to form macroscopic colonies in soft agar (Fig. 1d, e).

Consistent with recent reports, we found that both (R)-2HG and (S)-2HG inhibit a number of 2-OG-dependent enzymes *in vitro*^{4–6}, including the collagen prolyl 4-hydroxylases, the TET1 and TET2 methyl cytosine hydroxylases, the HIF asparaginyl hydroxylase FIH1 (also known as HIF1AN) and the JMJD2D (also known as KDM4D) histone demethylase, with (S)-2HG being a more potent inhibitor than (R)-2HG (Supplementary Fig. 3 and data not shown). (S)-2HG was

also a micromolar to low millimolar inhibitor of the three mammalian HIF prolyl 4-hydroxylases (EGLN1, EGLN2 and EGLN3) under standard assay conditions, which included 10 μ M 2-OG (Supplementary Fig. 4). In contrast, (R)-2HG was not an effective EGLN inhibitor (half-maximum inhibitory concentration (IC₅₀) values > 5 mM; Supplementary Fig. 4). Moreover, we discovered unexpectedly that (R)-2HG, but not (S)-2HG, promoted EGLN1 and EGLN2 activity, and to a lesser extent EGLN3 activity, at tumour-relevant concentrations (low mM) in reactions that lacked exogenous 2-OG (Fig. 2a, c, d and Supplementary Fig. 5a, b). This was specific because (R)-2HG did not promote collagen prolyl 4-hydroxylase activity (Fig. 2b) or JMJD2D histone demethylase activity (data not shown). Similar results were obtained with EGLN1 purified from either insect cells or *Escherichia coli* and with a heat-inactivated HIF polypeptide substrate (Supplementary Fig. 6), making it unlikely that the ability of (R)-2HG to promote EGLN activity required a contaminating enzyme.

To determine how (R)-2HG might promote EGLN activity, we monitored the EGLN1 prolyl 4-hydroxylase reaction using liquid

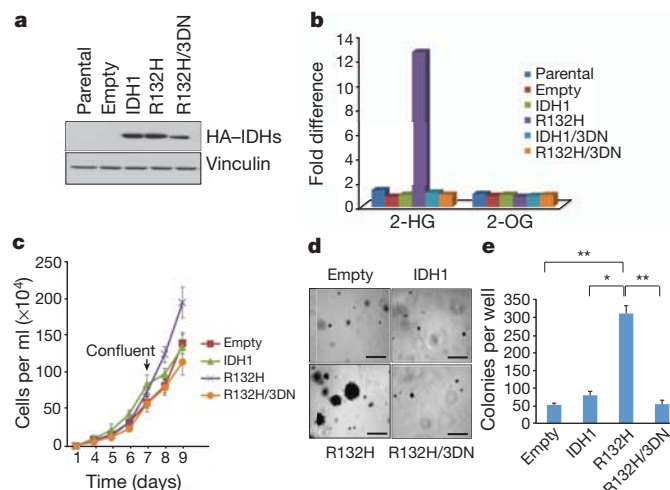


Figure 1 | Oncogenic properties of IDH1 R132H. **a**, **b**, Anti-HA immunoblot (**a**) and LC-MS analysis (**b**) of immortalized human astrocytes (passage 4) infected with retroviruses encoding HA-tagged versions of the indicated IDH1 variants. **c**, **d**, *In vitro* proliferation under standard culture conditions (**c**) or in soft agar (**d**) (passage 23). Scale bars, 0.5 mm. **e**, Number of macroscopic soft agar colonies in **d** (* P < 0.01, ** P < 0.005). Error bars show standard deviation (s.d.); n = 3.

¹Biocenter Oulu, Department of Medical Biochemistry and Molecular Biology, Oulu Center for Cell-Matrix Research, University of Oulu, FIN-90014 Oulu, Finland. ²Department of Medical Oncology, Dana-Farber Cancer Institute and Brigham and Women's Hospital, Boston, Massachusetts 02215, USA. ³The Preston Robert Tisch Brain Tumor Center at Duke, The Pediatric Brain Tumor Foundation Institute & The Department of Pathology, Duke University Medical Center, Durham, North Carolina 27710, USA. ⁴Department of Pathology, Brigham and Women's Hospital, Boston, Massachusetts 02115, USA.

⁵Department of Pathology, Harvard Medical School, Boston, Massachusetts 02115, USA. ⁶Department of Chemistry, University of Oulu, FIN-90014 Oulu, Finland. ⁷Biocenter Oulu, Mass Spectrometry Core Facility, Department of Biochemistry, University of Oulu, FIN-90014 Oulu, Finland. ⁸Agios Pharmaceuticals, Cambridge, Massachusetts 02139, USA. ⁹Hotchkiss Brain Institute, Departments of Cell Biology and Anatomy, University of Calgary Faculty of Medicine, Calgary, Alberta T2N 4N1, Canada. ¹⁰Department of Chemistry, University of Utah, Salt Lake City, Utah 84112, USA. ¹¹Department of Pathology, Children's Hospital Boston, Boston, Massachusetts 02115, USA. ¹²Department of Bioinformatics and Computational Biology, University of Texas MD Anderson Cancer Center, Houston, Texas 77030, USA.

¹³Howard Hughes Medical Institute, Chevy Chase, Maryland 20815, USA.

*These authors contributed equally to this work.

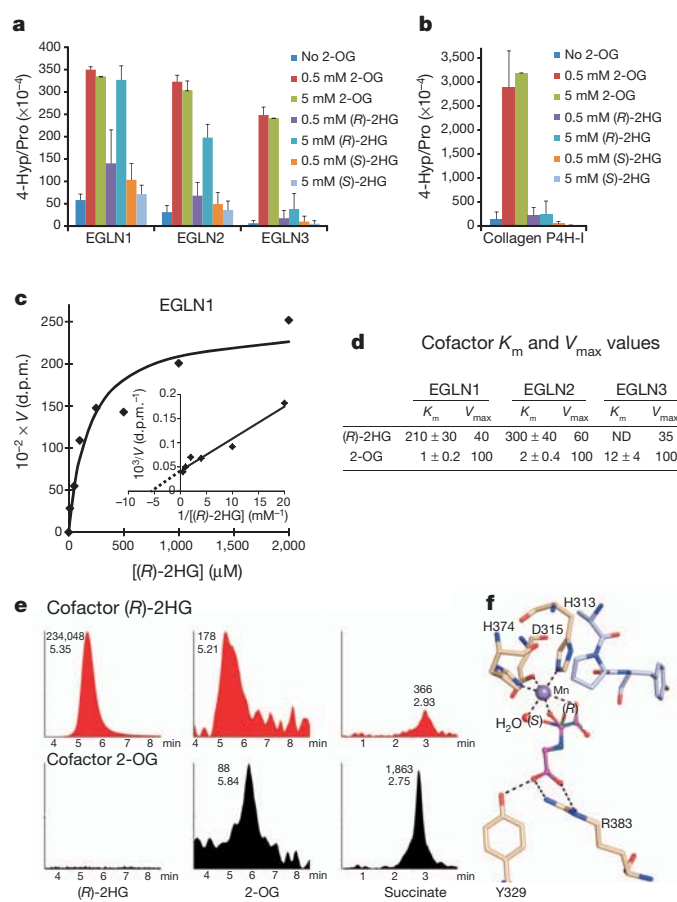


Figure 2 | (R)-2HG can serve as an EGLN cosubstrate. **a, b**, *In vitro* prolyl 4-hydroxylation assays conducted with recombinant EGLN proteins (**a**) and collagen P4H-I (**b**) in the presence of the indicated amounts of 2-OG or 2HG. 4-Hyp/Pro, ratio of 4-hydroxyproline to proline. L-[2,3,4,5- ^3H]proline-labelled HIF-1 α oxygen-dependent degradation domain (ODDD) (**a**) and [^{14}C]proline-labelled procollagen (**b**) were used as substrates. Enzymes were produced in insect cells using baculoviruses and affinity purified. Error bars, s.d.; $n = 3$ –4. **c, d**, K_m (in μM) and maximum enzyme velocity (V_{max} ; percentage of that obtained with 2-OG) values for (R)-2HG for EGLN family members. K_m and V_{max} values for 2-OG²¹ are included for comparison. d.p.m., disintegrations per minute. N.D., not defined. **e**, LC-MS analysis of succinate, 2-OG and (R)-2HG from enzymatic reactions with EGLN1, HIF-1 α ODDD polypeptide and either 5 mM (R)-2HG (red) or 80 μM 2-OG (black) as cofactors. Numbers next to each peak indicate elution times (bottom) and peak areas (top). No peaks above background were detected in samples in which 2-OG and (R)-2HG were both omitted (data not shown). **f**, Model of (R)-2HG (green) and (S)-2HG (cyan) bound to the active site of EGLN1. N-oxalylglycine (magenta) bound in the original structure²⁹ is shown for comparison. The active-site water molecule, which has been shown to be the O_2 -binding site³⁰, is shown in red and the peptide substrate in light blue. Hydrogen bonds are indicated by dash lines.

chromatography-mass spectrometry (LC-MS). 2-OG and succinate were detected when catalytically active EGLN1 was incubated with 5 mM (R)-2HG and a recombinant HIF-1 α polypeptide, suggesting that EGLN1 can oxidize (R)-2HG to 2-OG, which is then decarboxylated to succinate during the hydroxylation reaction (Fig. 2e and Supplementary Fig. 5c). In support of this model, ^{13}C -labelled succinate was generated in EGLN hydroxylation assays that contained uniformly labelled ^{13}C -(R)-2HG (Supplementary Fig. 5d).

Consistent with the idea that (R)-2HG can substitute for 2-OG as a cosubstrate, the addition of increasing amounts of (R)-2HG to EGLN1 assays containing 10 μM 2-oxo-[1- ^{14}C]glutamate progressively decreased the release of $^{14}\text{CO}_2$ without decreasing the prolyl hydroxylation of HIF-1 α , even at concentrations as high as 100 mM (Supplementary Fig. 7). Modelling of 2HG bound to the active site of EGLN1 predicts that binding of the (S)-enantiomer, but not the (R)-enantiomer, would

prevent the subsequent recruitment of oxygen to the active site, perhaps accounting for the qualitatively different effects of the two enantiomers on EGLN activity (Fig. 2f and Supplementary Fig. 5e).

To investigate whether these findings were relevant *in vivo* we examined HIF levels in IDH1 mutant cells. In keeping with our biochemical results, HIF-1 α and HIF-2 α protein levels were reproducibly lower in mid-passage (passage 9–15) human astrocytes producing IDH1 R132H relative to control astrocytes (Fig. 3a), due at least partly to increased HIF-1 α and HIF-2 α hydroxylation and diminished protein stability (Supplementary Figs 8 and 9), and were associated with lower levels of the HIF-responsive messenger RNAs encoding *VEGF*, *GLUT1* and *PDK1* (Supplementary Fig. 10a). Oxygen consumption and reactive oxygen species production, which can also affect HIF levels and the HIF response, were not measurably altered in the IDH1 mutant cells (Supplementary Fig. 11). IDH1(R132H)-expressing cells were relatively resistant to the 2-OG competitive antagonist dimethylxalylglycine (DMOG), but not to the iron chelator deferoxamine (DFO) (Fig. 3b), consistent with (R)-2HG acting as a 2-OG agonist in intact cells. In later passages (more than passage 20), HIF levels in IDH1(R132H)-expressing immortalized human astrocytes began to normalize despite persistent production of the exogenous IDH1 protein and (R)-2HG (Supplementary Fig. 12), possibly due to adaptive HIF-responsive feedback loops such as those involving EGLN3 and microRNA miR-155 (refs 1, 7). These cells, however, retained the ability to form colonies in soft agar (data not shown) and remained addicted to EGLN activity (see later).

Similarly, the induction of HIF-1 α and HIF-responsive mRNAs by hypoxia was diminished in two independent cell lines derived from two IDH1 R132H, 1p/19q-codeleted oligodendrogliomas compared to a control IDH1 wild-type, 1p/19q-codeleted oligodendroglioma line that had been generated in a similar fashion (Fig. 3c and Supplementary Fig. 10b). Although these three cell lines have similar growth kinetics *in vitro* (data not shown) they are not isogenic. We therefore also tested two HCT116 colorectal cancer cell sublines wherein the R132H mutation was introduced into the endogenous *IDH1* locus by homologous recombination. These sublines also showed a diminished HIF response compared to wild-type cells unless EGLN was pharmacologically (DFO) or genetically (short hairpin (sh)RNA) inactivated (Fig. 3d, e and Supplementary Fig. 13).

Finally, we asked whether IDH mutational status influenced HIF activity in primary patient astrocytoma samples using the TCGA expression data set⁸ and a previously defined HIF-responsive gene expression signature⁹. The HIF signature was diminished in proneural tumours—which is the subtype most often associated with IDH mutations⁸—relative to other gene-expression-defined subtypes of brain cancer (Supplementary Fig. 14a, b) and, notably, was diminished in IDH mutant proneural tumours relative to wild-type proneural tumours (Fig. 3f and Supplementary Fig. 14c). Similar results were obtained with other previously published HIF gene sets and with a manually curated data set (Supplementary Fig. 14a, d).

Downregulating HIF-1 α with three independent shRNAs promoted soft agar growth by immortalized human astrocytes after approximately 15 passages (Fig. 4a, b and Supplementary Fig. 15), as did overproduction of wild-type, but not catalytic-defective, EGLN1 (Fig. 4c, d and Supplementary Fig. 16). Conversely, downregulation of EGLN1 with multiple shRNAs inhibited the proliferation of late passage IDH1 R132H cells (Fig. 4e, f and Supplementary Fig. 17) unless HIF-1 α was concurrently ablated (Fig. 4g, h and Supplementary Fig. 18).

Collectively, these data suggest that EGLN activation by (R)-2HG, and subsequent downregulation of HIF-1 α , contributes to the pathogenesis of IDH mutant gliomas. Our data do not, however, exclude the possibility that (R)-2HG has additional targets, including TET2 and JmJc-containing histone demethylases, which contribute to its ability to transform cells^{4–6}. Indeed, we found that downregulation of TET2 in human astrocytes also promotes soft agar growth (Supplementary

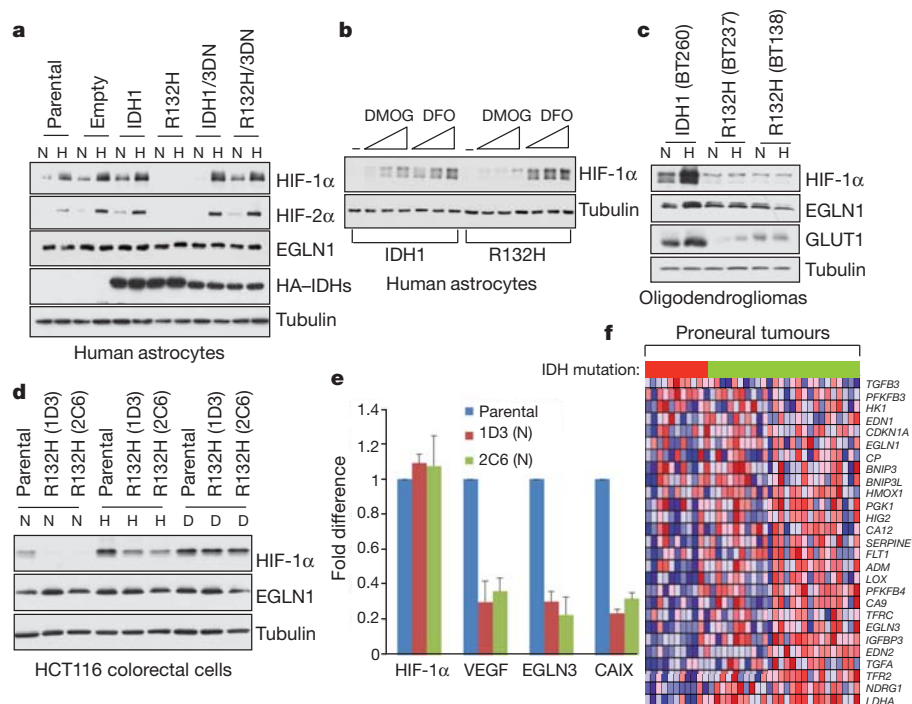


Figure 3 | HIF activity is diminished in IDH mutant cells. a–d, Immunoblot analysis of immortalized human astrocytes (passage 10) (**a, b**), oligodendrogloma cells (**c**) and HCT116 colorectal cells (**d**) expressing the indicated IDH1 variants grown under 21% (N) or 7.5% (H) oxygen for 24 h before lysis or under 21% oxygen in the presence of DFO (D). Names of cell lines are indicated in brackets. In **b**, cells grown under 21% oxygen were treated

with increasing amounts of DMOG or DFO for 16 h before lysis. **e**, Quantitative real-time PCR analysis of cells in **d** under normoxic conditions. Error bars, s.d. $n = 3$. **f**, Heat map depicting expression of HIF target genes (blue, lower expression; red, higher expression) in proneural tumours clustered based on IDH status (in the horizontal bar above the matrix, red indicates mutant; green, wild type).

Fig. 19). Nonetheless, our finding that (R)-2HG and (S)-2HG are qualitatively different with respect to EGLN might explain the apparent selection for (R)-2HG in adult tumours, despite the fact that (S)-2HG is a more potent inhibitor of most of the 2-OG-dependent enzymes tested so far. It should be noted, however, that (S)-2HG has been linked to neurological abnormalities and brain tumours in children and young adults with germline (S)-2-HG dehydrogenase mutations^{10–12}. The pathogenesis of (R)-2HG-driven tumours linked to somatic IDH mutations in adults and (S)-2HG-driven tumours linked to inborn errors of metabolism conceivably differ, with the latter possibly reflecting the perturbation of one or more neurodevelopmental programs during embryogenesis.

Nor are our data incompatible with the finding that HIF-1α protein levels are increased in IDH mutant tumours relative to normal brain¹³. Our data simply suggest that (R)-2HG quantitatively shifts the dose-response linking HIF activation to hypoxia, leading to a blunted HIF response for a given level of hypoxia. In support of this idea, HIF elevation in IDH mutant tumours is usually confined to areas of necrosis and presumed severe hypoxia¹⁴.

Although HIF is typically viewed as an oncoprotein it can behave as a tumour suppressor in embryonic stem cells^{15,16}, leukaemic cells¹⁷ and brain tumour cells^{18,19}. For example, HIF-1α has been shown to score as an oncoprotein when transformed murine astrocytes are grown subcutaneously but as a tumour suppressor when such cells are grown orthotopically¹⁹. This finding, together with our results, raises the possibility that pharmacological inhibition of EGLN activity (and the resulting increase in HIF activity) would impair the growth of IDH1 mutant tumours. A caveat, however, is that IDH mutant tumours tend to be relatively indolent²⁰. It is possible that low levels of HIF-1α, although promoting some aspects of transformation, simultaneously suppress other hallmarks of cancer required for aggressive behaviour (such as angiogenesis).

The published 2-OG Michaelis constant (K_m) values for the EGLN family members are below the estimated intracellular 2-OG concentration^{21,22}, suggesting that 2-OG should not be limiting for EGLN activity and that EGLN activity would not be enhanced further by (R)-2HG. A caveat is that a considerable amount of intracellular 2-OG appears to be sequestered in mitochondria and might also be bound by other 2-OG-dependent enzymes²². Moreover, these 2-OG K_m values were determined under idealized conditions with purified enzymes and substrates in the absence of endogenous inhibitors such as reactive oxygen species, nitric oxide and 2-OG competitive molecules such as succinate and fumarate¹. Studies in model organisms suggest that many metabolic enzymes are saturated *in vivo* with a mixture of substrate and competitive inhibitors and thus are sensitive to changes in substrate concentrations that are far above their nominal K_m values^{23,24}. We confirmed that succinate and fumarate increase the 2-OG requirement for the EGLN reaction and that their inhibitory activity, like that of DMOG (Fig. 3b) and its active derivative 2-oxalyl glycine, is blunted in the presence of (R)-2HG (Supplementary Fig. 20).

We have not yet formally proven that (R)-2HG is sufficient to downregulate HIF in intact cells. It is possible, for example, that additional metabolic changes in IDH mutant cells sensitize them to the HIF modulatory effects of (R)-2HG²⁵. Another, potentially related, observation is that both downregulation of HIF and transformation by mutant IDH in immortalized human astrocytes, although highly reproducible, was only noted after multiple passages. HIF activates a number of genes, including genes that participate in feedback regulation of the HIF response and genes that modify chromatin structure¹. It is possible that modulation of the HIF response over time, perhaps in conjunction with alterations in other enzymes affected by 2-HG, leads to epigenetic changes that ultimately are responsible for transformation. If so, it will be important to determine the degree to which such changes are reversible.

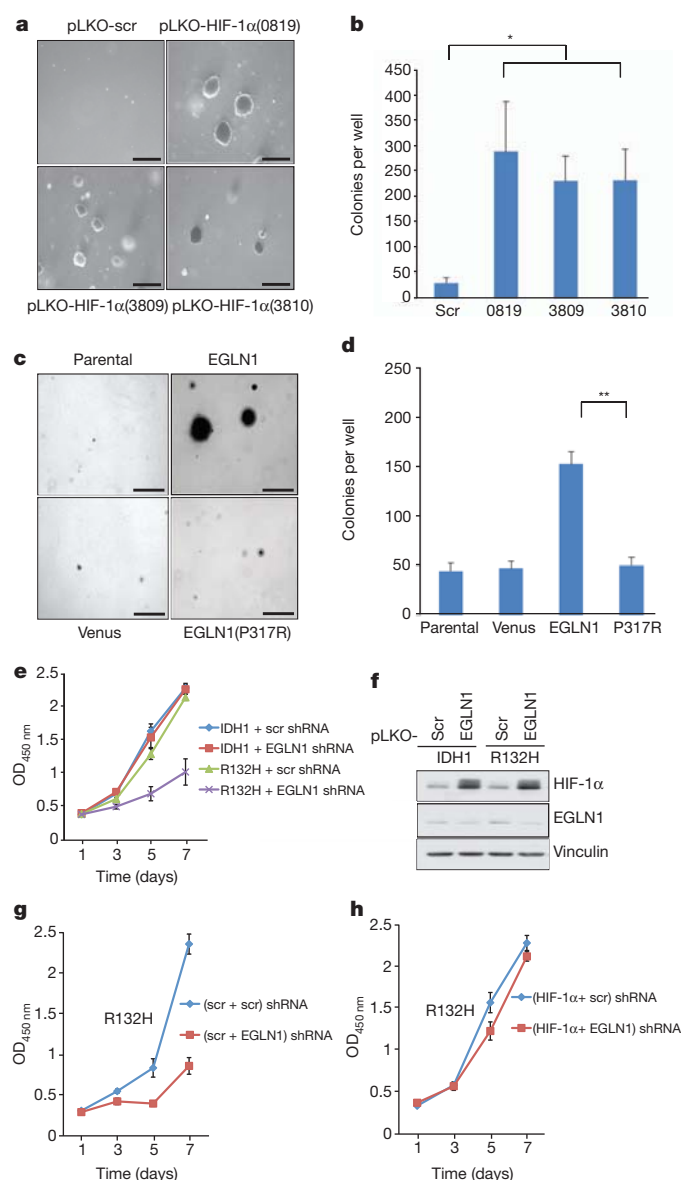


Figure 4 | Decreased HIF activity contributes to transformation by mutant IDH. **a, c**, Soft agar colony formation by human astrocytes after stable infection with lentiviruses encoding the indicated HIF-1α shRNAs or scrambled (scr) shRNA (**a**) or lentiviruses encoding EGLN1, EGLN1 (P317R), or Venus fluorescent protein (**c**; RNAi Consortium shRNA clone identifiers are indicated in brackets). Scale bars, 0.5 mm. **b, d**, Number of macroscopic soft agar colonies in **a** and **c**, respectively. * $P < 0.05$, ** $P < 0.005$. Error bars, s.d. $n = 3$. **e, f**, Proliferation (**e**) and immunoblot analysis (**f**) of human astrocytes expressing wild-type or R132H IDH1 and an shRNA against EGLN1 (10578) (or scrambled control). **g, h**, Proliferation of human astrocytes expressing IDH1 R132H and shRNAs against HIF-1α (0819), EGLN1 (10578), or both.

METHODS SUMMARY

NHAs immortalized with E6/E7/hTERT have been described elsewhere²⁶ and were subsequently infected with IDH retroviruses. IDH1 R132H HCT116 colorectal cancer cells were made by homologous recombination as previously described²⁷. Anaplastic oligodendroglioma cell lines were derived from resection material obtained at surgeries performed at the Brigham and Women's Hospital. Lentiviral shRNA vectors were from the Broad Institute. Immunoblots were performed with anti-HIF-1α monoclonal antibody (BD Transduction Laboratories), anti-HIF-2α polyclonal antibody (NB 100-122, Novus), anti-Flag monoclonal antibody (M2, Sigma-Aldrich), monoclonal anti-HA (HA-11, Covance Research Product), anti-EGLN1 monoclonal antibody (D31E11, Cell Signaling), anti-GLUT1 polyclonal antibody (NB300-666, Novus Biologicals), monoclonal anti-tubulin (B-512, Sigma-Aldrich) or anti-vinculin monoclonal antibody (V9131, Sigma-Aldrich). Metabolite levels were determined by LC-MS as previously

described². Enzyme activity assays were performed with affinity-purified human EGLN1, 2 and 3, collagen P4H-I and FIH, and murine Tet1 and Tet2 produced in insect cells using baculoviral vectors. (R)-2HG and (S)-2HG were from Sigma. (R)-2HG was free of contaminating 2-OG as determined by LC-MS under conditions that could detect 0.37 μM exogenous 2-OG in 5 mM (R)-2HG (data not shown). Human brain tumour mRNA expression data were obtained from The Cancer Genome Atlas and processed as described^{8,28}. Cell proliferation assays were performed using XTT assays (Cell Proliferation Kit II, Roche) according to the manufacturer's instructions or by direct counting of viable cells using an automated cell counter (Invitrogen). For soft agar assays ~8,000 cells were suspended in a top layer of 0.4% soft agar (SeaPlaque Agarose, BMA products) and plated on a bottom layer of 1% soft agar containing DMEM supplemented with 10% fetal bovine serum. For real-time qPCR analysis total RNAs were first extracted with Trizol reagent (Invitrogen). cDNA synthesis and PCR amplification were performed with Superscript One-Step RT-PCR (Invitrogen).

Full Methods and any associated references are available in the online version of the paper at www.nature.com/nature.

Received 26 May 2011; accepted 26 January 2012.

Published online 15 February 2012.

- Majmudar, A. J., Wong, W. J. & Simon, M. C. Hypoxia-inducible factors and the response to hypoxic stress. *Mol. Cell* **40**, 294–309 (2010).
- Dang, L. *et al.* Cancer-associated IDH1 mutations produce 2-hydroxyglutarate. *Nature* **462**, 739–744 (2009).
- Jin, G. *et al.* 2-Hydroxyglutarate production, but not dominant negative function, is conferred by glioma-derived NADP⁺-dependent isocitrate dehydrogenase mutations. *PLoS ONE* **6**, e16812 (2011).
- Figuerola, M. E. *et al.* Leukemic IDH1 and IDH2 mutations result in a hypermethylation phenotype, disrupt TET2 function, and impair hematopoietic differentiation. *Cancer Cell* **18**, 553–567 (2010).
- Xu, W. *et al.* Oncometabolite 2-hydroxyglutarate is a competitive inhibitor of α-ketoglutarate-dependent dioxygenases. *Cancer Cell* **19**, 17–30 (2011).
- Chowdhury, R. *et al.* The oncometabolite 2-hydroxyglutarate inhibits histone lysine demethylases. *EMBO Rep.* **12**, 463–469 (2011).
- Bruning, U. *et al.* MicroRNA-155 promotes resolution of hypoxia-inducible factor-1α activity during prolonged hypoxia. *Mol. Cell. Biol.* **31**, 4087–4096 (2011).
- Verhaak, R. G. *et al.* Integrated genomic analysis identifies clinically relevant subtypes of glioblastoma characterized by abnormalities in *PDGFRA*, *IDH1*, *EGFR*, and *NF1*. *Cancer Cell* **17**, 98–110 (2010).
- Nickols, N. G., Jacobs, C. S., Farkas, M. E. & Dervan, P. B. Modulating hypoxia-inducible transcription by disrupting the HIF-1-DNA interface. *ACS Chem. Biol.* **2**, 561–571 (2007).
- Aghili, M., Zahedi, F. & Rafiee, E. Hydroxyglutaric aciduria and malignant brain tumor: a case report and literature review. *J. Neurooncol.* **91**, 233–236 (2009).
- Moroni, I. *et al.* L-2-hydroxyglutaric aciduria and brain malignant tumors: a predisposing condition? *Neurology* **62**, 1882–1884 (2004).
- Özişik, P. A., Akalan, N., Palaoglu, S. & Topcu, M. Medulloblastoma in a child with the metabolic disease L-2-hydroxyglutaric aciduria. *Pediatr. Neurosurg.* **37**, 22–26 (2002).
- Zhao, S. *et al.* Glioma-derived mutations in IDH1 dominantly inhibit IDH1 catalytic activity and induce HIF-1α. *Science* **324**, 261–265 (2009).
- Williams, S. C. *et al.* R132H-mutation of isocitrate dehydrogenase-1 is not sufficient for HIF-1α upregulation in adult glioma. *Acta Neuropathol.* **121**, 279–281 (2011).
- Carmeliet, P. *et al.* Role of HIF-1α in hypoxia-mediated apoptosis, cell proliferation and tumour angiogenesis. *Nature* **394**, 485–490 (1998).
- Mack, F. A. *et al.* Loss of pVHL is sufficient to cause HIF dysregulation in primary cells but does not promote tumor growth. *Cancer Cell* **3**, 75–88 (2003).
- Song, L. P. *et al.* Hypoxia-inducible factor-1α-induced differentiation of myeloid leukemic cells is its transcriptional activity independent. *Oncogene* **27**, 519–527 (2008).
- Acker, T. *et al.* Genetic evidence for a tumor suppressor role of HIF-2α. *Cancer Cell* **8**, 131–141 (2005).
- Blouw, B. *et al.* The hypoxic response of tumors is dependent on their microenvironment. *Cancer Cell* **4**, 133–146 (2003).
- Christensen, B. C. *et al.* DNA methylation, isocitrate dehydrogenase mutation, and survival in glioma. *J. Natl. Cancer Inst.* **103**, 143–153 (2011).
- Koivunen, P. *et al.* Inhibition of hypoxia-inducible factor (HIF) hydroxylases by citric acid cycle intermediates: possible links between cell metabolism and stabilization of HIF. *J. Biol. Chem.* **282**, 4524–4532 (2007).
- Pritchard, J. B. Intracellular α-ketoglutarate controls the efficacy of renal organic anion transport. *J. Pharmacol. Exp. Ther.* **274**, 1278–1284 (1995).
- Bennett, B. D. *et al.* Absolute metabolite concentrations and implied enzyme active site occupancy in *Escherichia coli*. *Nature Chem. Biol.* **5**, 593–599 (2009).
- Yuan, J. *et al.* Metabolomics-driven quantitative analysis of ammonia assimilation in *E. coli*. *Mol. Syst. Biol.* **5**, 302 (2009).
- Reitman, Z. J. *et al.* Profiling the effects of isocitrate dehydrogenase 1 and 2 mutations on the cellular metabolome. *Proc. Natl Acad. Sci. USA* **108**, 3270–3275 (2011).

26. Sonoda, Y. *et al.* Formation of intracranial tumors by genetically modified human astrocytes defines four pathways critical in the development of human anaplastic astrocytoma. *Cancer Res.* **61**, 4956–4960 (2001).
27. Rago, C., Vogelstein, B. & Bunz, F. Genetic knockouts and knockins in human somatic cells. *Nature Protocols* **2**, 2734–2746 (2007).
28. Wang, X. V., Verhaak, R. G., Purdom, E., Spellman, P. T. & Speed, T. P. Unifying gene expression measures from multiple platforms using factor analysis. *PLoS ONE* **6**, e17691 (2011).
29. Chowdhury, R. *et al.* Structural basis for binding of hypoxia-inducible factor to the oxygen-sensing prolyl hydroxylases. *Structure* **17**, 981–989 (2009).
30. Koski, M. K. *et al.* The active site of an algal prolyl 4-hydroxylase has a large structural plasticity. *J. Biol. Chem.* **282**, 37112–37123 (2007).

Supplementary Information is linked to the online version of the paper at www.nature.com/nature.

Acknowledgements We thank R. P. Hausinger and J. D. Rabinowitz for helpful suggestions and critical reading of the manuscript, C. Schofield and Y. Zhang for reagents, S. Chen and Y. Shi for JMJD2D assays, K. Koski for modelling and T. Aatsinki and E. Lehtimäki for technical assistance. W.G.K. is a Doris Duke Distinguished Clinical Scholar and a Howard Hughes Medical Institute (HHMI) Investigator. Supported by the

National Institutes of Health (W.G.K.), HHMI (W.G.K.), Doris Duke Foundation (W.G.K.), Academy of Finland Grants 120156, 140765 and 218129 (P.K.) and S. Juselius Foundation (P.K.).

Author Contributions P.K., S.L. and W.G.K. initiated the project, analysed the data and wrote the manuscript. P.K. performed the *in vitro* enzyme assays. S.L. generated astrocyte cell lines stably expressing various IDH1 proteins. C.G.D., G. Lo. and H.Y. generated the HCT116 subclones. S.R., K.L.L. and S.W. provided oligodendrogloma cell lines. G. Lu generated and validated the reporter plasmids encoding HIF-1 α -luciferase fusion proteins. P.J., U.B. and S.G. performed the LC-MS analysis. J.T. synthesized ¹³C-(R)-2HG and R.L. synthesized and purified different 2-OG and 2-HG derivatives. R.G.W.V. performed the bioinformatics. P.K. and S.L. performed all other experiments with the help of G. Lu, J. A. L. and P.J. All the authors discussed the results and commented on the manuscript.

Author Information Reprints and permissions information is available at www.nature.com/reprints. The authors declare competing financial interests: details accompany the full-text HTML version of the paper at www.nature.com/nature. Readers are welcome to comment on the online version of this article at www.nature.com/nature. Correspondence and requests for materials should be addressed to W.G.K. (william_kaelin@dfci.harvard.edu).

METHODS

Cell lines. The NHA cell line immortalized with E6/E7/hTERT has been described elsewhere²⁶ and was maintained in DMEM containing 10% fetal bovine serum (FBS) and 1% penicillin/streptomycin in the presence of 10% CO₂ at 37 °C. Following retroviral infection, cells were maintained in the presence of hygromycin (100 µg ml⁻¹).

Introduction of the IDH1 R132H mutation into HCT116 colon cancer cell lines by homologous recombination was as previously described²⁷. Briefly, targeting constructs were designed using the pSEPT rAAV shuttle vector³¹. Homology arms for the targeting vector were PCR amplified from HCT116 genomic DNA using Platinum *Taq* HiFi polymerase (Invitrogen). The R132H hotspot mutation was introduced in the targeting construct using the Quickchange II site-directed mutagenesis kit (Stratagene). An infectious rAAV stock harbouring the targeting sequence was generated and applied to parental HCT116 cells as previously described³², and clones were selected in 0.5 mg ml⁻¹ geneticin (Invitrogen). Excision of the selectable element was achieved with an adenovirus encoding Cre recombinase (Vector Biolabs). Genomic DNA and total RNA were isolated from cells using QIAmp DNA Blood Kit and RNeasy kit (Qiagen). First strand cDNA was synthesized using iScript cDNA Synthesis Kit (BioRad). Successful homologous recombination and Cre-mediated excision were verified using PCR-based assays and by direct sequencing of genomic DNA and cDNA.

Anaplastic oligodendroglioma cell lines expressing wild-type IDH1 (BT260) or IDH1 R132H (BT237 and BT138) were derived from surgical resection material acquired from patients undergoing surgery at the Brigham and Women's Hospital on an Institutional Review Board approved protocol. Briefly, tumour resection samples were mechanically dissociated and tumospheres were established and propagated in Human NeuroCult NS-A Basal media (StemCell Technologies) supplemented with EGF, FGFb and heparin sulphate. All lines were obtained from the DF/BWCC Living Tissue Bank and confirmed to be derived from recurrent and progressive anaplastic oligodendrogliomas, World Health Organization grade III, at the time of cell-line isolation, and to have chromosome 1p/19q codeletion. The presence of IDH R132H mutation was confirmed by mutant specific antibody staining via immunohistochemistry and direct DNA sequencing.

Vectors. Human IDH1 cDNAs (wild type and R132H) were subcloned as BamHI-EcoRI fragments into pBabe-HA-hygro. Aspartic acid residues 273, 275 and 279 were mutated to asparagines (N) by site-directed mutagenesis and confirmed by DNA sequencing. *EGLN1*, *EGLN2* and *EGLN3* cDNAs were subcloned into pLenti6-Flag expression vector after restriction with XbaI and EcoRI. pLenti6-Flag-EGLN1 P317R³³ was prepared by QuikChange Mutagenesis (Stratagene) using pLenti6-Flag EGLN1 as a template and the following oligonucleotides: 5'-GTACGTCATGTTGATAATCGAAATGGAGATGGAAGATCTG-3' and 5'-CACATGTTCCATCTCCATTTTCGATTATCAACATGACGTAC-3'. The entire EGLN1 coding region was sequenced to verify its authenticity.

Lentiviral (pLKO.1) HIF-1α shRNA vectors (TRCN0000003810, target sequence: 5'-GTGATGAAAGAATTACCGAAT-3'; TRCN0000010819, target sequence: 5'-TGCTCTTTGTGGTTGGATCTA-3'; TRCN0000003809, target sequence: 5'-CCAGTTATGATTGTGAAGTTA-3'), EGLN1 (PHD2) shRNA vectors (TRCN0000001042, target sequence: 5'-CTGTTATCTAGCTGAGTTCAT-3'; TRCN0000001043, target sequence: 5'-GACGACCTGATACGCCACTGT-3'; TRCN00000010578, target sequence: 5'-TGCACGACACCGGGAAGTTCAT-3') and TET2 shRNA vectors (TRCN0000122172 (122), target sequence: 5'-GCGTTTATCCAGAATTAGCAA-3'; TRCN0000144344 (145), target sequence: 5'-CTTATATGACACCATGAAA-3') were obtained from the Broad Institute TRC shRNA library. pLKO.1 shRNA with target sequence 5'-GCAAGCTGACCTGAAGTTCAT-3' was used as negative control shRNA.

Immunoblot analysis. Cells extracts were prepared with 1× lysis buffer (50 mM Tris (pH 8.0), 120 mM NaCl, 0.5% NP-40) supplemented with a protease inhibitor cocktail (Complete, Roche Applied Science), resolved on 10% SDS-PAGE gels and transferred to nitrocellulose membranes (Bio-Rad). Membranes were blocked in TBS with 5% non-fat milk and probed with anti-HIF-1α monoclonal antibody (BD Transduction Laboratories), anti-HIF-2α polyclonal antibody (NB 100-122, Novus), anti-Flag monoclonal antibody (M2, Sigma-Aldrich), mouse monoclonal anti-HA (HA-11, Covance Research Product), anti-EGLN1(PHD2) monoclonal antibody (D31E11, Cell Signaling), anti-GLUT1 polyclonal antibody (NB300-666, Novus Biologicals), mouse monoclonal anti-tubulin (B-512, Sigma-Aldrich) or anti-vinculin monoclonal antibody (Sigma-Aldrich). Bound proteins were detected with horseradish-peroxidase-conjugated secondary antibodies (Pierce) and Immobilon western chemiluminescent horseradish peroxidase substrate (Millipore).

LC-MS. Metabolite levels in samples were determined by negative mode electrospray LC-MS as previously described². Briefly, metabolites were extracted from exponentially growing cells using 80% aqueous methanol (-80 °C) and were profiled by LC-MS. (R)-2HG, 2-oxolutarate and succinate were quantified by

LC-MS in negative mode using multiple reaction monitoring (MRM) on a Quattro micro triple quadrupole mass spectrometer (Waters). Samples were diluted with equal amounts of 25% acetonitrile and 10 µl aliquots were analysed in triplicate. The HPLC column (Luna NH2, 3 µm, 2.0 × 100 mm, Phenomenex) was operated isocratically with 130 mM ammonium acetate pH 5.0 in 37% acetonitrile/water. The MRM transitions were: 117 > 73, 117 > 93 (succinate), 145 > 57, 145 > 101 (2-OG) and 147 > 85, 147 > 129 ((R)-2HG), 0.2 s dwell time for all transitions. Calibration curves were set up with Quant Lynx, using standards dissolved in reaction buffer.

Enzyme activity assays. (R)-2HG (H8378) and (S)-2HG (S765015) were from Sigma. (R)-2HG was free of contaminating 2-OG as determined by LC-MS under conditions that could detect 0.37 µM exogenous 2-OG in 5 mM (R)-2HG (data not shown). Human EGLN1, 2 and 3, collagen P4H-I and FIH, and murine Tet1 and Tet2 were produced in insect cells and purified as described earlier³⁴⁻³⁷. The plasmids to generate the baculoviruses coding for Tet1 and 2 were a gift from Y. Zhang (University of North Carolina). IC₅₀ values for (R)-2HG and (S)-2HG were determined based on the hydroxylation-coupled stoichiometric release of ¹⁴CO₂ from 2-oxo-[1-¹⁴C]glutamate using synthetic peptides or double stranded oligonucleotides representing the natural targets of the studied enzymes as substrates. These were DLDLEMLAPYIPMDDDFQL (DLD19) for EGLN1, 2 and 3, (PPG)₁₀ for collagen P4H-I, DESGLPQLTSYDCEVNAPIQSGSRNLLQGEELRLAL for FIH and 5'-CTATACCTCCTCAACTT(mC)GATCACCGTCTCCGGCG-3' for Tet1 and 2. The K_m values for (S)-2HG for EGLN1, 2 and 3 were determined by adding (S)-2HG in four constant concentrations while varying the concentration of 2-oxo-[1-¹⁴C]glutamate.

To study whether (R)-2HG, which failed to efficiently inhibit EGLN activity, could promote EGLN activity by acting as a cofactor in the place of 2-OG, we determined the amount of 4-hydroxy[³H]proline formed by a specific radiochemical procedure³⁸ using a L-[2,3,4,5-³H]proline-labelled HIF-1α ODDD as a substrate. Collagen P4H-I and a [¹⁴C]-proline-labelled protocollagen³⁹ substrate were used as controls (detecting 4-hydroxy[¹⁴C]proline), and 2-OG (non-labelled) and (S)-2HG were assayed for comparison. The K_m values of EGLN1 and EGLN2 were determined by adding increasing amounts of (R)-2HG while the concentration of the substrate and other cofactors were kept constant.

Generation of a recombinant HIF-1α substrate. The HIF-1α ODDD substrate, spanning residues 356–603 of human HIF-1α, was produced in a BL21(DE3) *E. coli* strain (Novagen) in the presence of L-[2,3,4,5-³H]proline (75 Ci mmol⁻¹, PerkinElmer Life Sciences) and affinity purified in a chelating Sepharose column charged with Ni²⁺ (ProBond, Invitrogen) exploiting a C-terminal His tag⁴⁰. Concentration of the purified substrate was measured by RotiQuant (Carl Roth GmbH) and it was used at K_m concentrations for the distinct EGLN enzymes⁴⁰.

Modelling. EGLN1 active site structure (PDB accession 3HQ9²⁹) with N-oxalylglycine (NOG, magneta), Mg²⁺ and a peptide substrate (light blue), was used to model (R)-2HG (green) and (S)-2HG (cyan) into the active site.

Gene expression profiling and gene-set enrichment analysis. Expression data from human brain tumour samples were obtained from The Cancer Genome Atlas (<http://tcga-data.nci.nih.gov/tcga/tcgaHome2.jsp>) and processed as described^{8,28}. In short, 200 expression profiles from glioblastoma multiforme and two non-neoplastic brain samples were generated using three platforms (Agilent 244K, Affymetrix HT-HG-U133A, Affymetrix HuEx), preprocessed using gene centric probe sets and three expression values were integrated through factor analysis. After consensus clustering using 1,740 variably expressed genes, profiles with a negative silhouette metric were identified and removed from the data set, leaving expression profiles from 173 glioblastoma tumour samples. IDH1 mutation status was established for 116 out of the 173 samples.

Eleven gene sets representing response to induced hypoxia were reported in supplementary table 6 from ref. 41. One gene set was from figure 4C in ref. 9. A final set was assembled by one of us (W.G.K.) based on a literature review of genes upregulated by HIF in a wide variety of cell types (CA9, EGLN1, EGLN3, SLC2A1, BNIP3, ADM, VEGF, PDK1, LOX, PLOD1, CXCR4, P4HA1, ANKRD37). Single-sample gene-set enrichment analysis (GSEA) was applied as reported previously⁸. Briefly, genes were ranked by their expression values. The empirical cumulative distribution functions (ECDF) of both the genes in the signature as well as the remaining genes were calculated. An enrichment score was obtained by a sum of the difference between a weighted ECDF of the genes in the signature and the ECDF of the remaining genes. This calculation was repeated for all signatures and samples. Z-score transformation was applied to be able to make scores from different gene sets comparable. A positive score indicates gene set activation. A negative value does not indicate inactivation, but rather a lack of effect.

Cell proliferation assays. Cells were plated in 96-well plates (~700 cells per well) with a media change every 3 days. The number of viable cells per well at each time point was measured using an XTT assay (Cell Proliferation Kit II, Roche)

according to the manufacturer's instructions. Spectrophotometrical absorbance at 450 nm was measured 5–6 h after adding the XTT labelling reagent/electron coupling reagent using a microtiter plate reader (Perkin Elmer Life and Analytical Science). For direct cell counting, cells were plated in p60 dishes (~50,000 cells per dish) with a media change every 3 days. The number of viable cells at each time point was measured after trypan blue staining by using an automated cell counter (Invitrogen) according to the manufacturer's instructions.

Soft agar colony formation assay. Approximately 8,000 cells were suspended in a top layer of 0.4% soft agar (SeaPlaque Agarose, BMA products) and plated on a bottom layer of 1% soft agar containing complete DMEM supplemented with 10% FBS in 6-well plates. After 3–4 weeks, colonies were stained with 0.1% iodinitrotetrazolium chloride (Sigma-Aldrich).

Real-time qPCR analysis. Total RNAs were extracted with Trizol reagent (Invitrogen). cDNA synthesis and PCR amplification were performed with Superscript One-Step RT-PCR (Invitrogen) with 2 µg total RNA. *EGLN3* cDNA was amplified with sense primer (5'-GCGTCTCCAAGCGACA-3') and antisense primer (5'-GTCTTCAGTGAGGGCAGA-3'). *VEGF* cDNA was amplified with sense primer 5'-CGAAACCATGAACCTTCTGC-3') and antisense primer 5'-CCTGAGTGGGCACACACTCC-3'). *HIF1A* cDNA was amplified with sense primer (5'-TATTGCACTGCACAGGCCACATTC-3') and antisense primer (5'-TGATGGGTGAGGAATGGGTTCACA-3'). *HIF2A* was amplified with sense primer (5'-ACAAGCTCCTCTCCTCAGTTTGCT-3') and antisense primer (5'-ACCCTCCAAGGCTTTCAGGTACAA-3'). *GLUT1* *CAIX* cDNA was amplified with sense primer (5'-TGGAAGAAATCGCTGAGGAAGGCT-3') and antisense primer (5'-AGCACTCAGCATCACTGTCTGGTT-3'). *PDK1* cDNA was amplified with sense primer (5'-ATGATGTCATTCCCACAATGGCCC-3') and antisense primer (5'-TGAACATTCTGGCTGGTGACAGGA-3'). As a control, β -actin cDNA was amplified with sense primer (5'-ACCACTGGGACGACA

TGGAGAAA-3') and antisense primer (5'-TAGCACAGCCTGGATAGCAACGTA-3')

31. Topaloglu, O., Hurley, P. J., Yildirim, O., Civin, C. I. & Bunz, F. Improved methods for the generation of human gene knockout and knockin cell lines. *Nucleic Acids Res.* **33**, e158 (2005).
32. Kohli, M., Rago, C., Lengauer, C., Kinzler, K. W. & Vogelstein, B. Facile methods for generating human somatic cell gene knockouts using recombinant adeno-associated viruses. *Nucleic Acids Res.* **32**, e3 (2004).
33. Percy, M. J. *et al.* A family with erythrocytosis establishes a role for prolyl hydroxylase domain protein 2 in oxygen homeostasis. *Proc. Natl Acad. Sci. USA* **103**, 654–659 (2006).
34. Hirsila, M. *et al.* Effect of desferrioxamine and metals on the hydroxylases in the oxygen sensing pathway. *FASEB J.* **19**, 1308–1310 (2005).
35. Koivunen, P., Hirsila, M., Gunzler, V., Kivirikko, K. I. & Myllyharju, J. Catalytic properties of the asparaginyl hydroxylase (FIH) in the oxygen sensing pathway are distinct from those of its prolyl 4-hydroxylases. *J. Biol. Chem.* **279**, 9899–9904 (2004).
36. Ito, S. *et al.* Role of Tet proteins in 5mC to 5hmC conversion, ES-cell self-renewal and inner cell mass specification. *Nature* **466**, 1129–1133 (2010).
37. Annunen, P. *et al.* Cloning of the human prolyl 4-hydroxylase α subunit isoform α (II) and characterization of the type II enzyme tetramer. The α (I) and α (II) subunits do not form a mixed α (I) α (II) β 2 tetramer. *J. Biol. Chem.* **272**, 17342–17348 (1997).
38. Juva, K. & Prockop, D. J. Modified procedure for the assay of H³- or C¹⁴-labeled hydroxyproline. *Anal. Biochem.* **15**, 77–83 (1966).
39. Kivirikko, K. I. & Myllyla, R. Posttranslational enzymes in the biosynthesis of collagen: intracellular enzymes. *Methods Enzymol.* **82**, 245–304 (1982).
40. Koivunen, P., Hirsila, M., Kivirikko, K. I. & Myllyharju, J. The length of peptide substrates has a marked effect on hydroxylation by the hypoxia-inducible factor prolyl 4-hydroxylases. *J. Biol. Chem.* **281**, 28712–28720 (2006).
41. Benita, Y. *et al.* An integrative genomics approach identifies hypoxia inducible factor-1 (HIF-1)-target genes that form the core response to hypoxia. *Nucleic Acids Res.* **37**, 4587–4602 (2009).

Crystal structure of a concentrative nucleoside transporter from *Vibrio cholerae* at 2.4 Å

Zachary Lee Johnson¹, Cheom-Gil Cheong¹ & Seok-Yong Lee¹

Nucleosides are required for DNA and RNA synthesis, and the nucleoside adenosine has a function in a variety of signalling processes^{1,2}. Transport of nucleosides across cell membranes provides the major source of nucleosides in many cell types and is also responsible for the termination of adenosine signalling. As a result of their hydrophilic nature, nucleosides require a specialized class of integral membrane proteins, known as nucleoside transporters (NTs), for specific transport across cell membranes. In addition to nucleosides, NTs are important determinants for the transport of nucleoside-derived drugs across cell membranes^{3–5}. A wide range of nucleoside-derived drugs, including anticancer drugs (such as Ara-C and gemcitabine) and antiviral drugs (such as zidovudine and ribavirin), have been shown to depend, at least in part, on NTs for transport across cell membranes^{4,6–13}. Concentrative nucleoside transporters, members of the solute carrier transporter superfamily SLC28, use an ion gradient in the active transport of both nucleosides and nucleoside-derived drugs against their chemical gradients. The structural basis for selective ion-coupled nucleoside transport by concentrative nucleoside transporters is unknown. Here we present the crystal structure of a concentrative nucleoside transporter from *Vibrio cholerae* in complex with uridine at 2.4 Å. Our functional data show that, like its human orthologues, the transporter uses a sodium-ion gradient for nucleoside transport. The structure reveals the overall architecture of this class of transporter, unravels the molecular determinants for nucleoside and sodium binding, and provides a framework for understanding the mechanism of nucleoside and nucleoside drug transport across cell membranes.

Humans have three isoforms of concentrative nucleoside transporter (hCNT), and the substrate specificities and tissue distributions of these isoforms are different^{14–16}. Knowledge of the mechanism of these transporters would help us not only to understand physiological processes associated with nucleosides but also to provide a framework for future drug design to improve nucleoside drug delivery. The major barrier to achieving a mechanistic understanding is the lack of atomic structures that reveal the origins of nucleoside specificity and the principles of function of CNTs. For structure determination and functional studies we chose a CNT homologue from *Vibrio cholerae* (vcCNT) because of its high sequence homology to hCNTs (39% identical to hCNT3; Supplementary Fig. 1) and optimal biochemical stability.

To test whether vcCNT can transport nucleosides, and if so what ion gradient vcCNT uses, we performed a radioactive nucleoside uptake assay using recombinant vcCNT-reconstituted liposomes. Studies have shown that the human CNTs use Na⁺ ions and the *Escherichia coli* CNT uses H⁺ for nucleoside transport^{17–19}. Transport activity was measured by monitoring the uptake of [5,6-³H]uridine in both the presence and the absence of a Na⁺ gradient (Fig. 1a). We chose uridine because all of the CNTs that have been characterized so far transport uridine^{14,17–19}. When a Na⁺ gradient was present, vesicles containing vcCNT accumulated radioactive uridine significantly more than the control empty vesicles. When a Na⁺ gradient was not present (Na⁺ was replaced with choline in the solution), uridine uptake was significantly decreased.

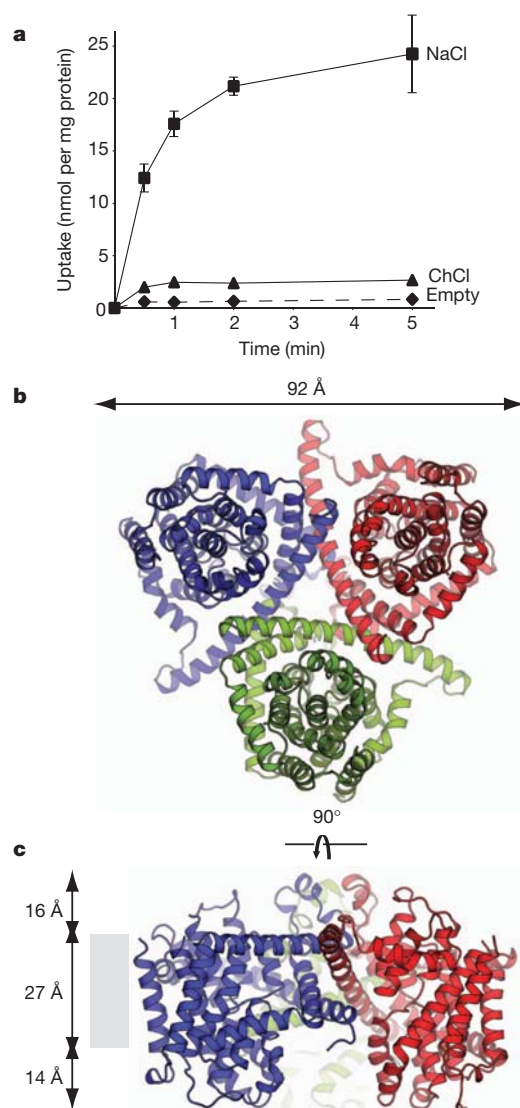


Figure 1 | vcCNT is a Na⁺-coupled nucleoside transporter with a trimeric architecture. **a**, Time course of the uptake of 2.4 μM [5,6-³H]uridine into vesicles containing vcCNT in the presence of a Na⁺ gradient (squares, NaCl), in the absence of a Na⁺ gradient (triangles, choline chloride), and the control empty vesicles in the presence of Na⁺ (diamonds, empty). Results are means ± s.d. (n = 3). **b**, Cartoon representation of the vcCNT trimer viewed from the cytoplasm. Individual protomers are coloured blue, red and green. **c**, Cartoon representation for the vcCNT trimer viewed parallel to the membrane. The putative membrane bilayer is indicated in c with grey boxes. The dimensions of the putative membrane bilayer, extracellular region, and intracellular region are shown.

¹Department of Biochemistry and Ion Channel Research Unit, Duke University Medical Center, 2 Genome Court, Durham, North Carolina 27710, USA.

Further characterization showed that uridine uptake was electrogenic and independent of pH gradients (Supplementary Fig. 2). These data clearly show that vcCNT, like human CNTs, uses a Na^+ gradient to transport nucleosides.

We crystallized and solved the structure of vcCNT at 2.4 Å (Supplementary Table 1). Experimental phases to 3.5 Å were obtained by single anomalous dispersion (SAD) from a platinum-soaked crystal (see Methods). The final model contains a single protomer in the asymmetric unit and is of good quality with a free *R* factor of 22.8% (Supplementary Table 1).

vcCNT crystallizes as a homotrimer that is shaped like an inverted triangular basin with its mouth facing the intracellular side and a knob-like structure facing the extracellular side (Fig. 1b, c). The three-fold axis coincides with the crystallographic six-fold axis and is perpendicular to the membrane. When viewed from the intracellular side, each side of the triangle formed by the trimer is about 92 Å, and when viewed parallel to the membrane the trimer is about 57 Å in height (Fig. 1). The membrane-embedded region lies roughly in the middle of the transporter, judging from the positions of three amphipathic helices on each protomer. On the basis of the predicted location of the membrane bilayer, the mouth of the basin penetrates into the membrane plane (Fig. 1c and Supplementary Fig. 3). The presence of several polar amino acids on the basin surface probably allows bulk aqueous solution to reach deep into the membrane bilayer and access this surface of the transporter.

The structure reveals that each protomer contains eight transmembrane helices (TM1–TM8), two re-entrant helix–turn–helix hairpins (HP1 and HP2) with opposite orientations in the membrane, and three interfacial helices (IH1–IH3) that run parallel to the membrane (Fig. 2a). The orientation of the structure relative to the

membrane is consistent with previous accessibility studies^{20–22} and conforms to the positive-inside rule (Supplementary Fig. 4). hCNTs are predicted to contain three more amino-terminal transmembrane helices than prokaryotic CNTs, suggesting an 11-TM topology for hCNTs²⁰.

Each protomer can be grouped into two subdomains on the basis of their locations (at the outer and inner regions) relative to the centre of the protomer. TM1, TM2, IH1, EH (a short stretch of extracellular helices), TM3 and TM6 are located at the outer part of the transporter, and they seem to be important for maintaining the overall architecture of the transporter. These helices in the outer region form a scaffold for the transporter (hereafter termed the scaffold domain) (Fig. 2). Trimerization contacts are mediated by part of the scaffold domain: IH1, EH, TM3 and TM6 (Fig. 2b). IH1 is an amphipathic helix 40 Å long that is most probably situated at the water/membrane interface, and TM6 is about 60 Å long and tilted almost 60° with respect to the membrane normal. EH protrudes into the extracellular solution and is about 16 Å in length. Because IH1 is involved in trimerization, is constrained to be at the membrane/water interface and interacts with many TMs (TM2–TM5), it is most probably important in building and maintaining the overall structure of vcCNT.

Surrounded by the scaffold domain, many conserved amino acids implicated in nucleoside transport are localized at the inner domain (hereafter termed the transport domain). The transport domain is composed of two structural groups that are related by an internal two-fold pseudo-symmetry. The first group is composed of IH2, HP1, TM4a/b and TM5 (pink background in Fig. 2a), and the second group is composed of IH3, HP2, TM7a/b and TM8 (cyan background in Fig. 2a). These two groups, separated by TM6 in sequence, can be superimposed with a root mean squared deviation of 3.3 Å, with the two-fold symmetry operator running through the middle of TM6 and

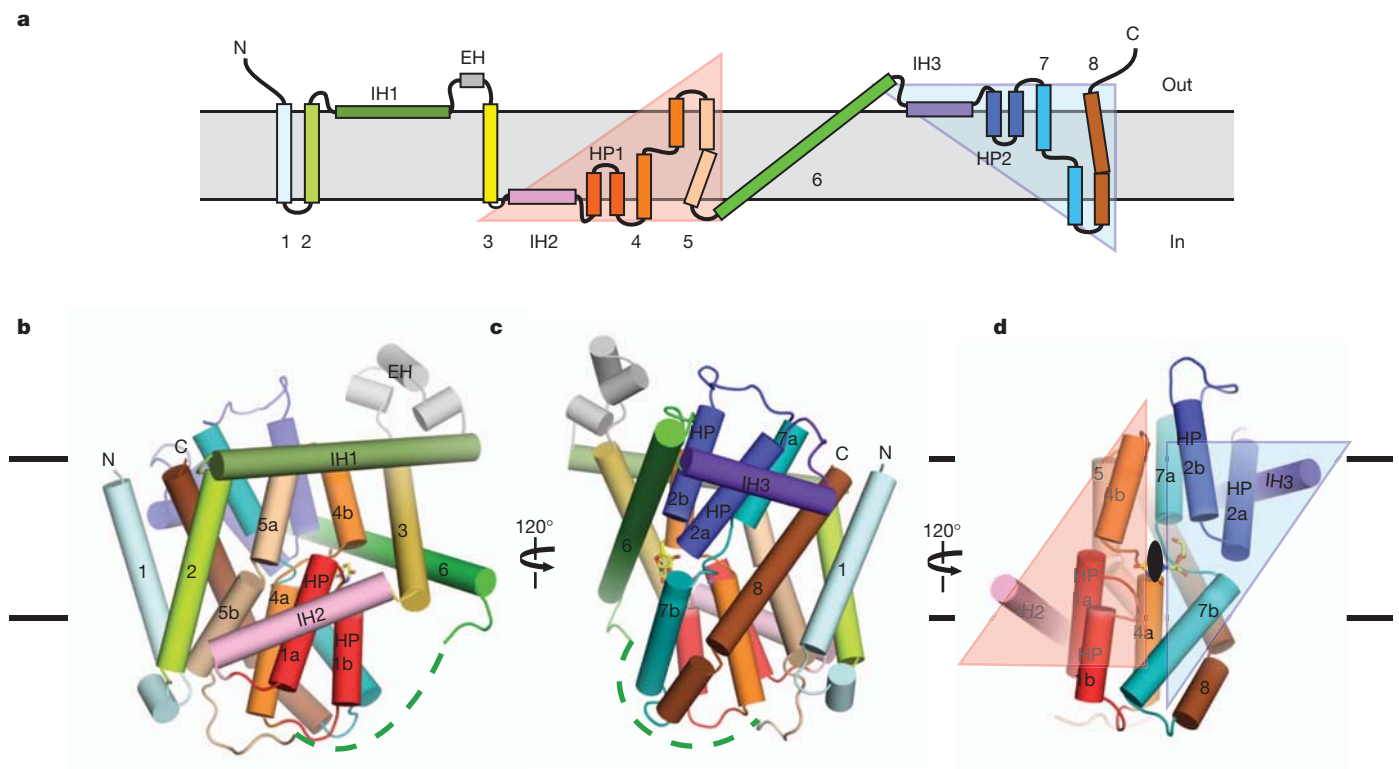


Figure 2 | Topology and fold of the vcCNT protomer. **a**, Schematic representation of vcCNT topology. The group of helices under the pink triangular background is related to the group of helices under the cyan triangular background by two-fold pseudo-symmetry, with the symmetry axis parallel to the membrane. **b**, Cartoon representation of the vcCNT protomer fold. Only helices comprising the scaffold domain and the group of helices under the pink triangular background are labelled. **c**, As in **b** but rotated

through 120°. Only TM1, TM6 and helices comprising the group of helices under the cyan triangular background are labelled. **d**, As in **c** but rotated through 120°. The scaffold domain has been removed to show the pseudo-two-fold relationship between the two groups of helices, coloured as pink and cyan triangular backgrounds. The two-fold symmetry axis runs through the nucleoside at the centre of the transporter.

parallel to the membrane (Fig. 2d). There is no significant amino-acid sequence homology between these two groups (roughly 10% sequence identity). This two-fold symmetry relationship positions the tips of HP1, HP2 and unwound regions of TM4 and TM7 at the centre of the transport domain, which is located slightly below the middle of the membrane plane (Fig. 2d). Sequence alignment of hCNTs and vcCNT reveals high sequence conservation around HP1, HP2 and the two unwound helices (TM4 and TM7), indicating the functional importance of this region (Supplementary Fig. 1).

To the best of our knowledge, the overall fold of vcCNT is novel, although local structural elements such as helical hairpins and unwound helices have been observed previously^{23,24}.

The crystal structure suggests that vcCNT adopts a trimeric configuration. To test whether the stoichiometry of vcCNT is trimeric and further validate the physiological relevance of our crystal structure, we performed structure-guided disulphide bridge crosslinking experiments (Supplementary Fig. 5). Our cysteine mutants readily form disulphide-crosslinked trimers in both detergent micelles and cell membranes under oxidizing conditions; therefore our crystal structure reflects a physiologically relevant oligomerization state. Given the sequence conservation of most of the amino acids involved in trimerization, we propose that the stoichiometry of both eukaryotic and prokaryotic CNT family members is trimeric (Supplementary Fig. 1).

The structure contains three deep clefts (one per subunit) at the intracellular side facing the centre of the trimer (Fig. 3a). A simulated-annealing OMIT map clearly shows that the electron density in the cleft is that of uridine (Fig. 3b). The bound uridine in the cleft faces the intracellular basin of the transporter; however, it is not free to be

released into the intracellular solution because TM6 and TM7b partly cover the binding site (Fig. 3a, b and Supplementary Fig. 6).

The nucleoside-binding site is located at the centre of the internal two-fold symmetry and lined by the tips of HP1 and HP2 and the unwound regions of TM4 and TM7 (Fig. 3b, c). Inspection of the interactions between uridine and the binding site shows that many polar or charged amino acids from HP1, HP2, TM4 and TM7 interact with the uracil base and ribose. HP1 and TM4b are responsible for interacting with the uracil base. The side chains of Gln 154, Thr 155 and Glu 156 from HP1 interact with the uracil base either directly (Gln 154) or indirectly through a water molecule (Thr 155 and Glu 156; Fig. 3c). Val 188 from TM4b interacts with the uracil base by means of van der Waals interactions. The involvement of these amino-acid residues in the interactions with the nucleoside is consistent with previous mutational studies^{25–27}: the residue corresponding to Gln 154, together with that corresponding to Val 188, is important for nucleoside specificity of hCNTs; Glu 156 is critical for Na⁺-nucleoside coupled transport.

HP2 and TM7 are responsible for the interactions with ribose. The side chains of Glu 332 (HP2), Asn 368 (TM7) and Ser 371 (TM7) interact with the ribose either directly (Glu 332, Asn 368 and Ser 371) or indirectly through a water molecule (Asn 368). Mutation of the residue corresponding to Glu 332 in hCNTs has been shown to have significant functional effects on both nucleoside binding and the rate of transport^{21,26}.

Because vcCNT is a Na⁺-coupled transporter, it must contain at least one Na⁺-binding site. Initial hints regarding the location of the Na⁺-binding site came from an $F_o - F_c$ map that shows a strong peak

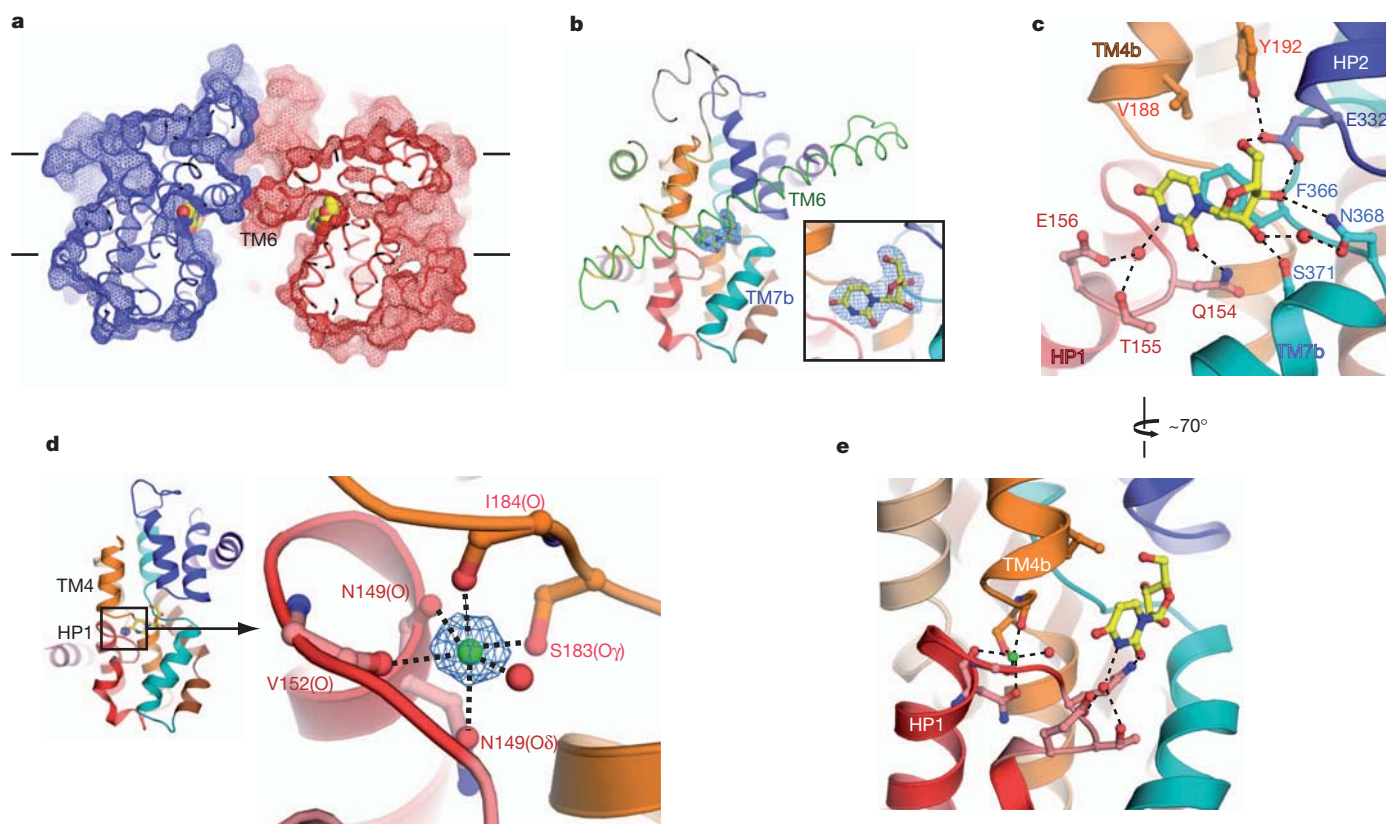


Figure 3 | Nucleoside-binding site and Na⁺-binding site. **a**, Cut-away surface representation of vcCNT viewed parallel to the membrane. The putative membrane bilayer is shown by horizontal lines. Uridine is shown as spheres. **b**, The vcCNT protomer viewed from the centre of the trimer. The scaffold domain is shown in ribbon representation; the transport domain is shown in cartoon representation. The blue mesh, covered by TM6 (green), is an $F_o - F_c$ simulated annealing OMIT map, contoured at 4 σ , showing density for uridine.

The inset is a zoomed-in image of the simulated annealing OMIT electron density. **c**, The nucleoside-binding site, showing HP1 (red), TM4b (orange), HP2 (blue) and TM7b (cyan). Hydrogen bonds are shown as dashed lines. **d**, The Na⁺-binding site is located between HP1 (red) and the unwound region of TM4 (orange). The blue mesh is an $F_o - F_c$ simulated annealing OMIT map, contoured at 6 σ , showing density for Na⁺. Coordination of the Na⁺ ion is shown as dashed lines. **e**, The Na⁺-binding site is near the nucleoside-binding site.

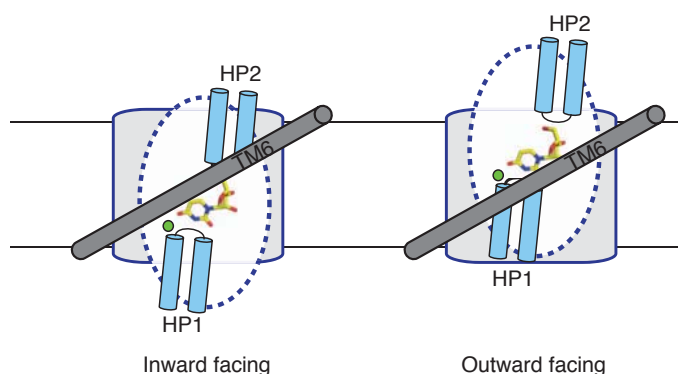


Figure 4 | Hypothetical mechanism of nucleoside transport. Only a single protomer is shown for simplicity, viewed from the centre of the trimer (same orientation as in Fig. 3b). On the left, the transporter adopts an inward-facing conformation. On the right, the transporter adopts an outward-facing conformation. Uridine is bound between the tips of HP1 and HP2, and TM6 (grey), serving as a hydrophobic barrier, partly covers uridine. The blue dotted lines demarcate the mobile part of the transport domain, and the grey region denotes the scaffold domain. Green circles represent sodium ions. A rigid-body motion of the nucleoside-binding site across TM6 can expose the binding site to the extracellular side.

(about 8σ) between the tip of HP1 and the unwound region of TM4. Further inspection reveals that this site is octahedrally coordinated by three backbone carbonyl groups, two side-chain hydroxyl groups and a water molecule (Fig. 3d) with the typical distances (about 2.4 Å) for Na^+ coordination by protein²⁸. Because it is difficult to distinguish Na^+ from H_2O on the basis of electron density alone, we performed the valence test that was used to identify the Na^+ sites in the crystal structure of LeuT^{28,29}. The result ($v = 1.02$) is consistent with Na^+ as the bound ion in this site. Therefore we suggest that vcCNT has at least one Na^+ -binding site at this position between HP1 and the unwound region of TM4.

The Na^+ -binding site is near the nucleoside-binding site, but the Na^+ does not interact directly with the nucleoside (Fig. 3e). What is the functional role of Na^+ binding at this site? Because key amino-acid residues for the interactions with the nucleoside base are localized on HP1 and TM4b, we propose that the role of Na^+ -binding is to bring HP1 close to TM4 to complete the formation of the nucleoside-binding site.

In the field of Na^+ -coupled secondary transporters, the prevailing model for ion-coupled transport is described by the alternating-access mechanism³⁰. If we assume that the alternating-access model is used, our crystal structure probably represents an inward-facing occluded conformation (Fig. 3a and Supplementary Fig. 6). On the basis of our crystal structure, previous accessibility studies of hCNTs, and studies of the Na^+ -coupled aspartate transporter Glt_{Ph}, which shares certain structural features with vcCNT (Supplementary Fig. 7), we propose a hypothetical model to explain Na^+ -coupled nucleoside transport by vcCNT (Fig. 4). A rigid-body movement of the transport domain across TM6 while the scaffold domain is held in place could permit the transition from an inward-facing to an outward-facing conformation. Our reasoning in proposing this mechanism is provided in Supplementary Information.

The crystal structure provides an important step towards understanding the mechanism of nucleoside transport by the CNT family. However, many important issues remain to be elucidated, including the structural basis for nucleoside and nucleoside-drug specificity and the conformational changes associated with each step along the transport cycle.

METHODS SUMMARY

vcCNT was expressed in *E. coli* C41 cells. Cells were lysed and protein was solubilized with dodecyl maltoside. Protein was purified by Co^{2+} -affinity chromatography followed by gel-filtration chromatography in the presence of decyl maltoside and uridine.

vcCNT was crystallized in the presence of 100 mM CaCl_2 , 37–42% PEG400 and 100 mM Tris-HCl pH 9.0 or 100 mM glycine pH 9.5. Platinum derivatives were prepared by soaking the crystals in $\text{K}_2\text{Pt}(\text{CNS})_6$. A partial poly-Ala model was built with phases to 5.0 Å from single isomorphous replacement with anomalous scattering (SIRAS). A complete model was built by combining phases from single anomalous dispersion using a new platinum derivative with molecular replacement phases from the partial model (MR-SAD) to 3.5 Å. Structure refinement was then performed against the 2.4-Å native data. The final model is of good quality with good Ramachandran statistics (98% favoured and 2% allowed). The model contains residues 2–416 (residues 230–240 missing), a uridine, 5 decylmaltosides (1 full and 4 partial), a Na^+ ion and 43 bound waters. Disordered residues Lys 226 and Glu 345 were modelled as Ala.

For the flux assay, protein was reconstituted into lipid vesicles and then vesicles were diluted into buffer containing either choline chloride or NaCl. Flux was initiated by the addition of 2.4 μM [5,6- ^3H]uridine and 1 μM valinomycin.

Full Methods and any associated references are available in the online version of the paper at www.nature.com/nature.

Received 24 August 2011; accepted 20 January 2012.

Published online 11 March 2012.

- King, A. E., Ackley, M. A., Cass, C. E., Young, J. D. & Baldwin, S. A. Nucleoside transporters: from scavengers to novel therapeutic targets. *Trends Pharmacol. Sci.* **27**, 416–425 (2006).
- Rose, J. B. & Coe, I. R. Physiology of nucleoside transporters: back to the future. *Physiology (Bethesda)* **23**, 41–48 (2008).
- Cano-Soldado, P. *et al.* Compensatory effects of the human nucleoside transporters on the response to nucleoside-derived drugs in breast cancer MCF7 cells. *Biochem. Pharmacol.* **75**, 639–648 (2008).
- Damaraju, V. L. *et al.* Nucleoside anticancer drugs: the role of nucleoside transporters in resistance to cancer chemotherapy. *Oncogene* **22**, 7524–7536 (2003).
- Jordheim, L. P. & Dumontet, C. Review of recent studies on resistance to cytotoxic deoxynucleoside analogues. *Biochim. Biophys. Acta* **1776**, 138–159 (2007).
- Errasti-Murugarren, E. & Pastor-Anglada, M. Drug transporter pharmacogenetics in nucleoside-based therapies. *Pharmacogenomics* **11**, 809–841 (2010).
- Mackey, J. R., Baldwin, S. A., Young, J. D. & Cass, C. E. Nucleoside transport and its significance for anticancer drug resistance. *Drug Resist. Updat.* **1**, 310–324 (1998).
- Mackey, J. R. *et al.* Immunohistochemical variation of human equilibrative nucleoside transporter 1 protein in primary breast cancers. *Clin. Cancer Res.* **8**, 110–116 (2002).
- Mackey, J. R. *et al.* Functional nucleoside transporters are required for gemcitabine influx and manifestation of toxicity in cancer cell lines. *Cancer Res.* **58**, 4349–4357 (1998).
- Nagai, K., Nagasawa, K. & Fujimoto, S. Uptake of the anthracycline pirarubicin into mouse M5076 ovarian sarcoma cells via a sodium-dependent nucleoside transport system. *Cancer Chemother. Pharmacol.* **55**, 222–230 (2005).
- Pastor-Anglada, M., Felipe, A. & Casado, F. J. Transport and mode of action of nucleoside derivatives used in chemical and antiviral therapies. *Trends Pharmacol. Sci.* **19**, 424–430 (1998).
- Pastor-Anglada, M. *et al.* Nucleoside transporters in chronic lymphocytic leukaemia. *Leukemia* **18**, 385–393 (2004).
- Zhang, J. *et al.* The role of nucleoside transporters in cancer chemotherapy with nucleoside drugs. *Cancer Metastasis Rev.* **26**, 85–110 (2007).
- Gray, J. H., Owen, R. P. & Giacomini, K. M. The concentrative nucleoside transporter family, SLC28. *Pharmacol. Ther.* **447**, 728–734 (2004).
- Molina-Arcas, M., Casado, F. J. & Pastor-Anglada, M. Nucleoside transporter proteins. *Curr. Vasc. Pharmacol.* **7**, 426–434 (2009).
- Ritzel, M. W. *et al.* Molecular identification and characterization of novel human and mouse concentrative Na^+ -nucleoside cotransporter proteins (hCNT3 and mCNT3) broadly selective for purine and pyrimidine nucleosides (system cib). *J. Biol. Chem.* **276**, 2914–2927 (2001).
- Loewen, S. K. *et al.* Functional characterization of a H^+ /nucleoside co-transporter (CaCNT) from *Candida albicans*, a fungal member of the concentrative nucleoside transporter (CNT) family of membrane proteins. *Yeast* **20**, 661–675 (2003).
- Loewen, S. K. *et al.* Transport of physiological nucleosides and anti-viral and anti-neoplastic nucleoside drugs by recombinant *Escherichia coli* nucleoside- H^+ cotransporter (NupC) produced in *Xenopus laevis* oocytes. *Mol. Membr. Biol.* **21**, 1–10 (2004).
- Xiao, G., Wang, J., Tangen, T. & Giacomini, K. M. A novel proton-dependent nucleoside transporter, CeCNT3, from *Caenorhabditis elegans*. *Mol. Pharmacol.* **59**, 339–348 (2001).
- Hamilton, S. R. *et al.* Subcellular distribution and membrane topology of the mammalian concentrative Na^+ -nucleoside cotransporter rCNT1. *J. Biol. Chem.* **276**, 27981–27988 (2001).
- Slugoski, M. D. *et al.* Substituted cysteine accessibility method analysis of human concentrative nucleoside transporter hCNT3 reveals a novel discontinuous region of functional importance within the CNT family motif (G/A)XXK3NEFVA(Y/M/F). *J. Biol. Chem.* **284**, 17281–17292 (2009).
- Zhang, J. *et al.* Cysteine-accessibility analysis of transmembrane domains 11–13 of human concentrative nucleoside transporter 3. *Biochem. J.* **394**, 389–398 (2006).

23. Cao, Y. *et al.* Crystal structure of a phosphorylation-coupled saccharide transporter. *Nature* **473**, 50–54 (2011).
24. Yernool, D., Boudker, O., Jin, Y. & Gouaux, E. Structure of a glutamate transporter homologue from *Pyrococcus horikoshii*. *Nature* **431**, 811–818 (2004).
25. Loewen, S. K. *et al.* Identification of amino acid residues responsible for the pyrimidine and purine nucleoside specificities of human concentrative Na⁺ nucleoside cotransporters hCNT1 and hCNT2. *J. Biol. Chem.* **274**, 24475–24484 (1999).
26. Slugoski, M. D. *et al.* Conserved glutamate residues Glu-343 and Glu-519 provide mechanistic insights into cation/nucleoside cotransport by human concentrative nucleoside transporter hCNT3. *J. Biol. Chem.* **284**, 17266–17280 (2009).
27. Yao, S. Y. *et al.* Conserved glutamate residues are critically involved in Na⁺/nucleoside cotransport by human concentrative nucleoside transporter 1 (hCNT1). *J. Biol. Chem.* **282**, 30607–30617 (2007).
28. Nayal, M. & Di Cera, E. Valence screening of water in protein crystals reveals potential Na⁺ binding sites. *J. Mol. Biol.* **256**, 228–234 (1996).
29. Yamashita, A., Singh, S. K., Kawate, T., Jin, Y. & Gouaux, E. Crystal structure of a bacterial homologue of Na⁺/Cl[−]-dependent neurotransmitter transporters. *Nature* **437**, 215–223 (2005).
30. Krishnamurthy, H., Piscitelli, C. L. & Gouaux, E. Unlocking the molecular secrets of sodium-coupled transporters. *Nature* **459**, 347–355 (2009).

Supplementary Information is linked to the online version of the paper at www.nature.com/nature.

Acknowledgements Data for this study were collected at beamlines SER-CAT BM22/ID22 and NE-CAT ID 24-C at the Advanced Photon Source. We thank R. MacKinnon and J. Butterwick for critical reading; R. Lefkowitz and A. Shukla for providing access and technical support for the radioactive flux assay; S. Lockless for advice on experiments; and C. Pemble for help with remote data collection. This work was supported by start-up funds from the Duke University Medical Center, the McKnight Endowment Fund for Neuroscience, the Alfred P. Sloan Foundation, the Klingenstein Fund, the Mallinckrodt foundation, the Basil O'Connor Starter Scholar Research Award 5-FY10-473 from the March of Dimes Foundation, and the National Institutes of Health Director's New Innovator Award 1 DP2 OD008380-01 (all to S.-Y.L.).

Author Contributions Z.J. expressed, purified and crystallized vcCNT. Z.J. performed radioactive flux and crosslinking experiments. C.-G.C. participated in part of the vcCNT crystallization and generated mutants for crystallization and functional studies. Z.J. and S.-Y.L. collected and processed the data, solved the structure, and wrote the paper. S.-Y.L. designed the study. All authors discussed the results and commented on the manuscript.

Author Information Atomic coordinates and structure factors for the reported crystal structure are deposited in the Protein Data Bank under accession code 3TIJ. Reprints and permissions information is available at www.nature.com/reprints. The authors declare no competing financial interests. Readers are welcome to comment on the online version of this article at www.nature.com/nature. Correspondence and requests for materials should be addressed to S.-Y.L. (sylee@biochem.duke.edu).

METHODS

Expression and purification. The gene encoding vcCNT was cloned from *Vibrio cholerae* genomic DNA into a modified pET26 vector that contains a pelB leader sequence and a PreScission Protease cleavable His₁₀-maltose-binding protein fusion. The original vector was a gift from R. Dutzler (University of Zurich) and was further modified. The vector containing vcCNT was expressed in *E. coli* C41 (DE3) cells. Cells were lysed with a homogenizer (Avestin) and protein was solubilized with 30 mM dodecyl maltoside (DDM) for 2 h at 4 °C. Solubilized lysates were spun down to remove the insoluble fraction, and supernatants were applied to Talon Co²⁺ affinity resin. After binding, protein was eluted with imidazole and digested overnight with PreScission Protease. The digestion mixture was concentrated and applied to a Superdex 200 size-exclusion column in the presence of 5 mM decyl maltoside (DM), 1 mM uridine, 150 mM NaCl, 20 mM Tris-HCl pH 8.0, 2 mM dithiothreitol. Peak fractions corresponding to vcCNT were collected for further experiments.

Crystallization. Initial crystallization conditions were obtained at the high-throughput crystallization-screening laboratory at the Hauptman-Woodward Institute³¹. Protein was concentrated to about 10 mg ml⁻¹ and mixed 1:1 with crystallization solution containing 100 mM CaCl₂, 37–42% PEG400 and 100 mM buffer. Crystals grew over a wide pH range (5.6–9.5), but data for structure solution were collected on crystals grown at pH 9.0 (100 mM Tris-HCl) and pH 9.5 (100 mM glycine). Crystals were grown by using the microbatch-under-oil method. After 10–14 days, crystals were harvested, transferred to cryo solution containing 32.5% PEG400, and flash-frozen in liquid nitrogen. Platinum derivatives were prepared by soaking for 2–4 h in 2.5 mM K₂Pt(CNS)₆ and then transferring them to cryo solution and flash-freezing.

Structure determination. The data were collected on beamlines 22ID, 22BM and 24ID-C at the Advanced Photon Source. The data were processed with HKL2000 (ref. 32). Crystals of vcCNT diffract to 2.4 Å Bragg spacings and belong to the space group *P*₆₃. Extensive screening of crystals was performed because roughly 70% of crystals are merohedrally twinned, with the twinning operator perpendicular to the crystallographic six-fold axis, leading to the apparent space group *P*₆₃22. We found that SeMet-substituted crystals were almost always twinned with significant twinning fractions (20–45%), which necessitated heavy-atom-soaked crystals as the choice for a *de novo* phasing method for the vcCNT structure. Initial phases to 5.0 Å were obtained by single isomorphous replacement with anomalous scattering (SIRAS) from a platinum-soaked crystal. Platinum sites were found by SHELXD³³; phasing was calculated to 5.0 Å Bragg spacings by using SOLVE³⁴ with the figure of merit 0.34, and the density was modified by solvent flattening with RESOLVE³⁵. A partial model was built by manually placing idealized poly-Ala helices into the solvent-flattened electron density map by using COOT³⁶. After further extensive screening of platinum derivatives, we found a derivative that diffracted to 3.1 Å with significant anomalous signal but was non-isomorphous with any of our native data. Platinum sites were found from an anomalous difference Fourier map by using the partial model phases. Combined phases of single anomalous dispersion from the platinum derivative and molecular replacement

from the partial model (MR-SAD) were calculated at 4.0 Å with the figure of merit 0.35 and extended to 3.5 Å by solvent flattening with PHASER³⁷ and RESOLVE³⁵ with the use of the PHENIX interface³⁸. After iterative cycles of manual adjustment of poly-Ala helices and calculation of combined MR-SAD phases, the electron density map was of excellent quality and allowed us to place side chains into the partial model. We also collected native data to 2.4 Å at a long wavelength (1.6 Å) and identified sulphur sites by using an anomalous difference Fourier map, which helped guide the model building. After about 70% of manual model building was complete, molecular replacement was performed with the partial model against the 2.4 Å native data for further model building and refinement. Structure refinement was performed with PHENIX³⁸. An anomalous difference Fourier map with the native data to 2.4 Å collected at a long wavelength (1.6 Å) identified six sulphur sites and helped guide the model building. The final model is of good quality with $R_{\text{work}}/R_{\text{free}} = 19.6/22.8\%$ and good Ramachandran statistics (98% favoured and 2% allowed), and contains residues 2–416 (residues 230–240 missing), a uridine, 5 DMs (1 full and 4 partial), a Na⁺ ion and 43 bound waters.

Vesicle reconstitution and flux assay. Protein was reconstituted into lipid vesicles containing 10 mg ml⁻¹ of 1-Palmitoyl-2-oleoyl-sn-glycero-3-phosphoethanolamine (POPE) and 1-Palmitoyl-2-oleoyl-sn-glycero-3-phosphoglycerol (POPG) (3:1 ratio of POPE:POPG) at a mass ratio of 1:500 protein:lipid, as described previously³⁹. Vesicles were reconstituted in the presence of 200 mM KCl, 20 mM HEPES pH 7.4, 100 mM choline chloride. Reconstituted vesicles were then flash-frozen and thawed three times, then extruded through a 1.0-µm filter with the use of the Avanti Mini-Extruder.

For the flux assay, vesicles were diluted 1:20 into buffer containing 200 mM KCl, 20 mM HEPES pH 7.4, and either 100 mM choline chloride or 100 mM NaCl. Flux was initiated by the addition of 2.4 µM [5,6-³H]uridine and 1 µM valinomycin. All experiments were performed in triplicate at 30 °C. Vesicles were harvested on GF/B glass microfibre filters (Whatman) and counted by scintillation on the following day.

- Kozelak-Rosenblum, M. *et al.* Determination and application of empirically derived detergent phase boundaries to effectively crystallize membrane proteins. *Protein Sci.* **18**, 1828–1839 (2009).
- Otwinowski, Z. & Minor, W. Processing of X-ray diffraction data collected in oscillation mode. *Methods Enzymol.* **276**, 307–326 (1997).
- Sheldrick, G. M. A short history of SHELX. *Acta Crystallogr. A* **64**, 112–122 (2008).
- Terwilliger, T. C. & Berendzen, J. Automated MAD and MIR structure solution. *Acta Crystallogr. D Biol. Crystallogr.* **55**, 849–861 (1999).
- Terwilliger, T. C. Maximum-likelihood density modification. *Acta Crystallogr. D Biol. Crystallogr.* **56**, 965–972 (2000).
- Emsley, P. & Cowtan, K. Coot: model-building tools for molecular graphics. *Acta Crystallogr. D Biol. Crystallogr.* **60**, 2126–2132 (2004).
- McCoy, A. J. *et al.* Phaser crystallographic software. *J. Appl. Cryst.* **40**, 658–674 (2007).
- Adams, P. D. *et al.* PHENIX: a comprehensive Python-based system for macromolecular structure solution. *Acta Crystallogr. D Biol. Crystallogr.* **66**, 213–221 (2010).
- Lee, S. Y., Letts, J. A. & MacKinnon, R. Functional reconstitution of purified human Hv1 H⁺ channels. *J. Mol. Biol.* **387**, 1055–1060 (2009).

Identification and characterization of a bacterial hydrosulphide ion channel

Bryan K. Czyzewski^{1,2} & Da-Neng Wang^{1,3}

The hydrosulphide ion (HS^-) and its undissociated form, hydrogen sulphide (H_2S), which are believed to have been critical to the origin of life on Earth¹, remain important in physiology and cellular signalling². As a major metabolite in anaerobic bacterial growth, hydrogen sulphide is a product of both assimilatory and dissimilatory sulphate reduction^{2–4}. These pathways can reduce various oxidized sulphur compounds including sulphate, sulphite and thiosulphate. The dissimilatory sulphate reduction pathway uses this molecule as the terminal electron acceptor for anaerobic respiration, in which process it produces excess amounts of H_2S (ref. 4). The reduction of sulphite is a key intermediate step in all sulphate reduction pathways. In *Clostridium* and *Salmonella*, an inducible sulphite reductase is directly linked to the regeneration of NAD^+ , which has been suggested to have a role in energy production and growth, as well as in the detoxification of sulphite³. Above a certain concentration threshold, both H_2S and HS^- inhibit cell growth by binding the metal centres of enzymes and cytochrome oxidase⁵, necessitating a release mechanism for the export of this toxic metabolite from the cell^{5–9}. Here we report the identification of a hydrosulphide ion channel in the pathogen *Clostridium difficile* through a combination of genetic, biochemical and functional approaches. The HS^- channel is a member of the formate/nitrite transport family, in which about 50 hydrosulphide ion channels form a third subfamily alongside those for formate^{10,11} (FocA) and for nitrite¹² (NirC). The hydrosulphide ion channel is permeable to formate and nitrite as well as to HS^- ions. Such polyspecificity can be explained by the conserved ion selectivity filter observed in the channel's crystal structure. The channel has a low open probability and is tightly regulated, to avoid decoupling of the membrane proton gradient.

Because H_2S is a weak acid with a pK_a of 6.8 and a second pK_a of 19, in a biological system more than 80% of it will exist in its ionized form as HS^- (refs 2, 13). To account for membrane permeation of intracellularly produced H_2S (refs 6, 9), a channel for HS^- or H_2S has been suggested^{5,7}, with the water channel aquaporins as possible candidates⁸. Whereas studies in planar lipid bilayers indicate that the aquaporin from *Archaeoglobus fulgidus* is not permeable to H_2S and that the lipid bilayer provides little resistance to H_2S permeation⁹, in the vent worm *Riftia pachyptila* it has been shown that HS^- ions, but not H_2S , are selectively transported through its outer epithelium into its vasculature⁵.

Despite the high permeability of H_2S across the lipid bilayer, we argue that its weak acidity necessitates a release mechanism for its ionized form, HS^- (Fig. 1a). As a weak acid with a pK_a of 6.8, H_2S can diffuse readily across the lipid bilayer. Therefore, the distribution of H_2S and HS^- on the two sides of the cell membrane is directly proportional to the pH differential as described by the Henderson–Hasselbalch equation¹⁴. Because cellular pH is kept at neutral levels, and extracellular pH is typically one to two units more acidic, at equilibrium the HS^- concentration will be 10–100-fold greater on the inside of the cell than on the outside in the absence of a release

mechanism for the HS^- anions. Therefore, given its significant toxicity, it would be beneficial to directly expel this ion across the membrane by the quickest mechanism available: an ion channel.

Recently, a novel family of anion channels for short-chain acids has been functionally characterized^{11,15,16}. Members of the formate/nitrite transport (FNT) family transport various anions during anaerobic bacterial growth^{10,12,17}. Judging from sequence homology, however, only about half of its 2,000 identified members clearly belong to either the FocA or the NirC subfamily (Figs 1b, c and Supplementary Figs 1 and 2). Notably, for both FocA and NirC, each channel gene is genetically linked to its reductase partner: *focA* to the formate reductase *pflB*¹⁰ and *nirC* to the nitrate reductase *nirBD*¹² (Fig. 1b). Our phylogenetic analysis of bacterial genes suggests the existence of additional

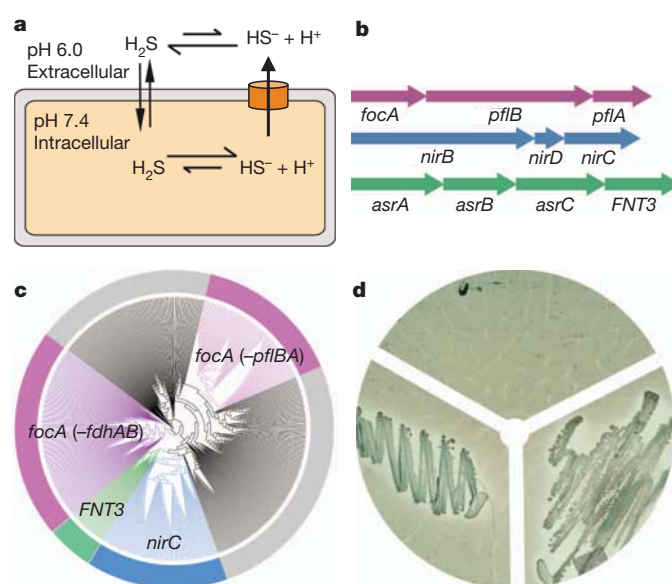


Figure 1 | Genetic analyses and functional characterization of FNT3 and the *asrABC* operon. About 50 FNT genes from *Clostridium* are linked to the sulphite reductase gene *asrABC*, and they form a third subfamily (FNT3) in the FNT family. **a**, Model of the intracellular anion concentrative effect for the weak acid H_2S . **b**, Genomic organization of three types of FNT gene and their metabolically related reductase genes. Representatives are shown for *focA*, *nirC* and *FNT3* with their respective linked operons. **c**, Phylogenetic tree of 474 bacterial and archaeal members of the FNT family. Branches are coloured on the basis of genetic linkage to metabolic enzymes: genes linked to pyruvate formate lyase (*pflBA*) or formate dehydrogenase (*fdhAB*; *fdhA* and *fdhB* also known as *selA* and *selD*, respectively) are coloured pink, genes linked to nitrite reductase (*nirBD*) are coloured blue and genes linked to sulphite reductase (*asrABC*) are coloured green. The FocA protein in archaea is encoded by *fdhC* (*selC*). The grey areas represent FNT family members with no assigned function based on genetic linkage. **d**, Bismuth sulphide agar plate assay: vector control (top); *asrA*, *asrB* and *asrC* (left); *asrA*, *asrB*, *asrC* and *FNT3* (right).

¹The Helen L. and Martin S. Kimmel Center for Biology and Medicine at the Skirball Institute of Biomolecular Medicine, New York University School of Medicine, 540 First Avenue, New York, New York 10016, USA. ²Molecular Biophysics Graduate Program, New York University School of Medicine, 540 First Avenue, New York, New York 10016, USA. ³Department of Cell Biology, New York University School of Medicine, 540 First Avenue, New York, New York 10016, USA.

channel subfamilies in the FNT family (Fig. 1c and Supplementary Fig. 1). One such subfamily is a group of ~50 homologous genes, temporarily termed FNT3, found in various species of *Clostridium* that are major human pathogens grown under strictly anaerobic conditions. As it is linked to a reductase gene, the *asrABC* operon¹⁸ (Fig. 1b), we proposed that FNT3 genes might encode a channel for HS^- or related ions. AsrABC reduces sulphite (SO_3^{2-}) to sulphide (S^{2-}), which is rapidly converted into H_2S and HS^- under physiological conditions.

Salmonella asrABC is the only such operon that has been characterized thus far. Its overexpression in *Escherichia coli*, which lacks this biochemical pathway, was previously shown to reduce SO_3^{2-} to H_2S (ref. 19). To verify first whether the homologous *asrABC* operon from *C. difficile* also encodes an SO_3^{2-} reductase, we tested the growth of *E. coli* transformed with the *C. difficile asrABC* genes, plated on bismuth sulphite agar^{19,20}. When *C. difficile asrABC* was induced, *E. coli* was able to overcome the expected growth inhibition by reducing SO_3^{2-} to H_2S (Fig. 1d and Supplementary Fig. 3). Darkening along the edges of the colonies, formed by the precipitation of bismuth and iron sulphide, further indicated that H_2S gas was being produced. This showed that the *asrABC* genes from *C. difficile* do indeed encode for an SO_3^{2-} reductase, which in turn supports the notion that the FNT3 gene ('FNT3') in the *asrABC* operon may encode a channel for SO_3^{2-} or for its reduced product, HS^- .

To determine whether the FNT3 protein from *C. difficile* functions as a channel for HS^- or SO_3^{2-} , we then carried out whole-cell transport, ion-protein binding in solution and transport-inhibition assays in reconstituted proteoliposomes. First we transformed sulphide-producing *Salmonella typhimurium*, which lacks an HS^- channel, with the *C. difficile FNT3*. In SO_3^{2-} -supplemented minimal medium, the FNT3-expressing *S. typhimurium* released a high concentration of HS^- ions into the culture medium (Fig. 2a and Supplementary Fig. 4). This increase in extracellular HS^- was specific to HS^- produced by the endogenous cytoplasmic AsrABC; when the other sulphide-producing reductase in the cell, the periplasmic thiosulphate reductase, was engaged with its substrate thiosulphate, little effect on the extracellular concentration of HS^- was observed. This indicates that the measured HS^- was generated by SO_3^{2-} reduction by the cytoplasmic AsrABC and then exported. Such an FNT3-linked increase in HS^- production in *S. typhimurium* can be attributed to either increased import of SO_3^{2-} or increased export of HS^- from the cell. It follows that an FNT3 protein could be an ion channel for SO_3^{2-} or HS^- .

An ion channel protein is often stabilized by its permeating ions through their direct interaction with its selectivity filter²¹. Therefore, we tested whether purified FNT3 protein interacts with the monovalent HS^- or the divalent SO_3^{2-} . Using size-exclusion chromatography of purified protein samples incubated at different temperatures, we found that at pH 8.0 the presence of HS^- ions was able to increase the nominal melting temperature of the FNT3 protein by 8 °C, whereas SO_3^{2-} had little effect (Fig. 2b and Supplementary Table 1). This result is consistent with the hypothesis that FNT3 protein functions as an HS^- channel but is probably impermeable to SO_3^{2-} . Notably, three other monovalent anions, formate, nitrite and chloride, also increased the melting temperature of the FNT3 protein, but to a lesser degree (3–4 °C).

We went on to identify the permeable ions of the FNT3 protein *in vitro*. As channels in the FNT family are expected to have low conductance rates¹¹, we measured the transport activity of FNT3 protein using a concentrative uptake assay^{11,22}. Given that HS^- ions at concentrations needed to set up a sufficient electrochemical gradient (~150 mM) are severely disruptive to the membrane, we chose to measure the permeability of FNT3 protein using another interacting ion, formate (Fig. 2b). Proteoliposomes reconstituted at pH 8.0 from purified *C. difficile* FNT3 protein were found to be permeable to formate, although at a lower rate than FocA from *Vibrio cholerae* (Fig. 2c). This permeability to formate by FNT3 protein allowed us to search for other ions that directly compete with formate for transport. Indeed, when HS^- or nitrite was present in the buffer outside the proteoliposomes,

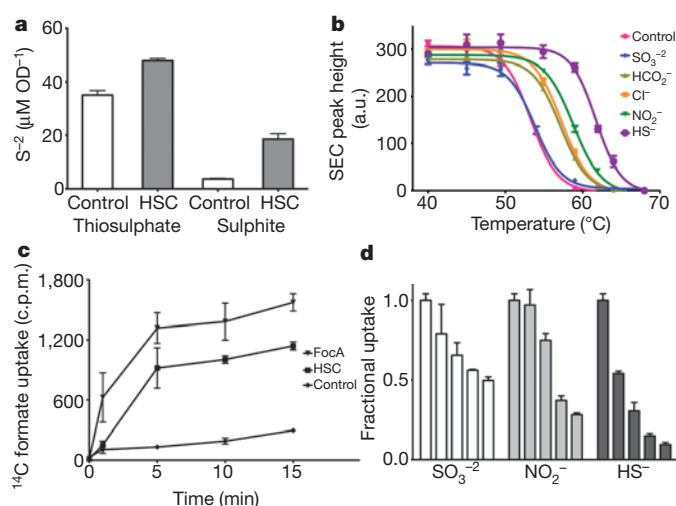


Figure 2 | Binding and transport activity of HSC in reconstituted proteoliposomes. **a**, Measurements of sulphide concentrations in the media of *Salmonella* transformed with vector control or vector encoding HSC. Minimal media were supplemented with either sulphite or thiosulphate to induce the production of hydrogen sulphide from either periplasmic thiosulphate reductase or cytoplasmic sulphite reductase. OD, optical density. **b**, Binding of detergent-solubilized and purified HSC to various anions was determined by using thermostability coupled size-exclusion chromatography. Peak heights of recovered samples are plotted against temperature and fitted to a Boltzmann sigmoidal model to determine nominal melting temperatures. **c**, Radiolabelled formate uptake in proteoliposomes reconstituted with purified HSC at pH 8.0 was monitored in a concentrative uptake assay and compared with FocA activity or vesicle controls. c.p.m., counts per minute. **d**, Inhibition of radiolabelled concentrative uptake of formate by the addition of various anions at increasing concentrations. The graph shows the amount of radiolabelled formate measured at the 10-min time point for each concentration of anion tested. The concentrations of the competing anions were 0, 0.15, 0.6, 3 and 15 mM (left to right). Error bars, s.e.m. ($N = 3$).

the uptake of formate was drastically inhibited (Fig. 2d). In the physiological sulphide concentration range (1–2 mM), ~70% inhibition was observed, whereas at the highest concentration tested (15 mM), HS^- and nitrite inhibited the uptake of formate by 90% and 70%, respectively.

Such direct competitive inhibition (Fig. 2c), coupled with whole-cell transport assays (Fig. 2a) and *in vitro* binding assays (Fig. 2b), collectively indicates that the FNT3 protein from *C. difficile* is likely to be a channel for the hydrosulphide ion, HS^- . Although the channel is also permeable to formate and nitrite ions, the FNT3 gene is directly linked to the *asrABC* sulphite reductase operon (Fig. 1b); we have therefore tentatively named the FNT3 protein a hydrosulphide ion channel (HSC). A definite understanding of the physiological role of these channels will need to be confirmed by *in vivo* experiments such as genetic deletion studies.

To understand the transport mechanism of the HSC protein from *C. difficile* (Supplementary Fig. 5), we determined its crystal structure at high pH (pH 9.0) to a resolution of 2.2 Å (Fig. 3a and Supplementary Table 2). The HSC adopts the aquaporin/FocA fold^{11,23} and forms a pentamer like FocA, with the five protomers having the same structure (Supplementary Figs 6–8). The two-fold inverted symmetry between the two halves of the protein is greater than that observed in FocA and extends to the pore-lining transmembrane helices TM2b and TM5b (Supplementary Fig. 8b), two salt-bridge triads on the periplasmic and the cytoplasmic sides (Lys 148-Glu 200-Asn 205 and Lys 16-Glu 81-Asn 86) (Fig. 4a–c), and the two short helices parallel to the membrane (helix P on the periplasmic surface and helix N at the amino terminus on the cytoplasmic surface) (Supplementary Fig. 8b). This helix N, by means of the Lys 16-Glu 81-Asn 86 salt-bridge triad, buttresses TM2b and TM5a, making the cytoplasmic side of the protein more closed and rigid than that in FocA¹¹.

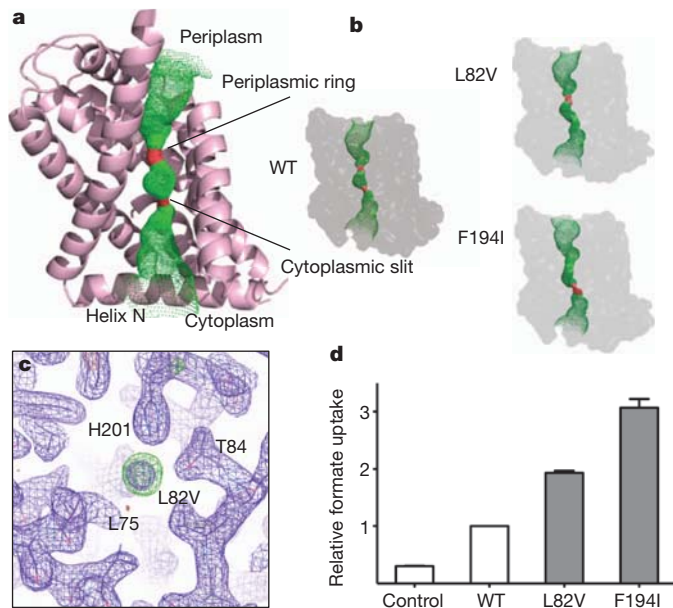


Figure 3 | Structural and functional characterization of the ion permeation pathway. **a**, Structure of a protomer of HSC overlaid with the pore diameter calculations made using HOLE, coloured to indicate permeability to water: green, permeable; red, impermeable. Transmembrane helix 2 has been removed for clarity. **b**, Pore diameter calculations from HOLE of the crystal structures for each of the two permeation pathway mutations, Leu 82 Val and Phe 194 Ile and wild type (WT). **c**, Close-up of the electron density observed at the selectivity filter for the Leu 82 Val mutant. The $2F_o - F_c$ electron density map contoured at 1.1σ is coloured purple and the $F_o - F_c$ difference density map contoured at 3σ is coloured green. **d**, Relative uptake of proteoliposomes reconstituted with purified HSC and pathway mutations. The graph shows the 10-min time point of each concentrative uptake experiment. Error bars, s.e.m. ($N = 3$).

The pore for ion permeation, which is located at the centre of each protomer, contains the selectivity filter formed by a cytoplasmic slit and a periplasmic ring in the middle of the membrane (Fig. 3a, b). The radius of the cytoplasmic slit is 0.8 \AA , which is too small for an HS^- ion (radius, 1.7 \AA ; ref. 24) to pass through (Supplementary Figs 9–11).

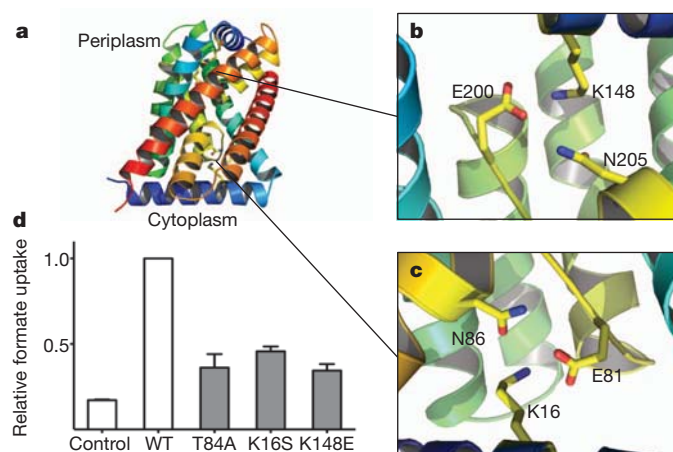


Figure 4 | Structural and functional characterization of possible gating mechanisms. **a**, Structure of the HSC protomer representing possible gating regions. The structure is coloured to show the two-fold inverted topology. **b**, **c**, The Glu-Lys-Asn salt-bridge triads, related by a pseudo-two-fold symmetry, help to stabilize helix P at the periplasmic side (**b**) and helix N at the cytoplasmic side (**c**) of the protein. The rotamer that each residue adopts is conserved. **d**, Relative uptake of proteoliposomes reconstituted with purified HSC and gating mutations. The graph shows the 10-min time point of each concentrative uptake experiment. Error bars, s.e.m. ($N = 3$).

Therefore, the HSC protein in the crystal structure is probably in a closed state. As expected from the sequence similarity between HSC and FocA in the selectivity filter (Supplementary Fig. 2), the positions or orientations of key residues changed only slightly in HSC (Supplementary Fig. 10). Such conservation explains the permeability of HSC to HS^- , as well as to formate and nitrite. When a residue at the cytoplasmic slit or the periplasmic ring is mutated into a smaller residue, for example Leu 82 to Val or Phe 194 to Ile, the pore size is increased, as shown in the crystal structures of the mutant protein (Fig. 3b and Supplementary Table 2), and the formate transport rate of the channel is significantly increased (Fig. 3d). We note that in the crystal structure of the Leu 82 Val mutant, electron density was observed in the cytoplasmic slit (Fig. 3c). This density, which is greater than that of a water molecule—as inferred from a B-factor fourfold lower than those of the surrounding atoms—could be accounted for by a Cl^- or an HS^- ion. Owing to their similar sizes and chemical properties, it has been previously observed that Cl^- and HS^- ions often bind to the same site in protein crystal structures²⁵.

The observed polyspecificity of HSC is typical for anion channels^{26–28}, and is most probably shared by the FocA and NirC channels as well. Such polyspecific anion recognition is at least partly due to the diffuse nature of the electron cloud of anions²⁹. By contrast, cation channels often show a high degree of selectivity, which is made possible by the point-like charge properties of such ions. Because different FNT channels in this ancient protein family are coupled with their specific metabolic pathways, each channel is expected to have its own preference for permeating ions, and that preference is probably due to the small structural variations in the selectivity filter that we observed here (Supplementary Fig. 10).

The expulsion of toxic concentrations of HS^- from the cytoplasm through HSC needs to be balanced against the potential risk of the uncoupling of the membrane proton gradient. Freely diffusible H_2S and other weak, short-chain acids will dissociate into an anion and a proton in the cytoplasm (Fig. 1a). As the anion is expelled, there will be an intracellular net accumulation of protons. Therefore, the ground state of HSC is likely to be closed and its opening tightly regulated.

Indeed, the HSC structure we determined at high pH is in its closed state (Fig. 3 and Supplementary Figs 9–11). We then considered how easily the channel could be opened. Because the homologous FocA channel can be gated by an appropriate change in pH or cytoplasmic formate concentration^{11,16}, we first investigated possible pH-dependent structural changes of HSC by determining its crystal structure at pH 7.5 (resolution, 3.2 \AA) and at pH 4.5 (3.0 \AA) (Supplementary Table 2). The protein structures obtained at these neutral and low pH values were the same as the structure at 2.2 \AA and pH 9.0 (Supplementary Fig. 12), and the channel remained closed. We then studied the two salt-bridge triads, both of which contain a glutamate residue that could potentially function as a pH sensor (Fig. 4a–c). When either of the salt bridges was broken, by mutating Lys 16 to Ser or Lys 148 to Glu, the HSC crystal structure did not change and the channel still remained closed (Supplementary Fig. 13 and Supplementary Table 2). Consistent with these structural results, the transport rates of these mutants did not increase (Fig. 4d).

To determine whether HSC is gated by anion concentration in a similar manner to *V. cholerae* FocA¹¹, in which the competition of formate with Thr90 from the Ω -loop for hydrogen bonding to His208 in the selectivity filter opens the channel, we mutated the equivalent threonine in HSC, Thr 84, to an Ala and determined its crystal structure at 2.4 \AA (Supplementary Table 2). This mutant structure did not differ from the closed wild-type channel, and no increase in transport was detected (Fig. 4d and Supplementary Fig. 14). Because Thr 84, Lys 16 and Lys 148 all line the ion permeation pathway, mutation of these residues slightly reduced the ion permeation rate of the channel. Therefore, we conclude that the opening of HSC is indeed tightly regulated and the channel has a much lower open probability than FocA^{11,16}.

The low open probability of HSC observed here is consistent with its physiological role in the cell. The opening of HSC probably requires significant movement of TM2b. As TM2b is 'held' in space by the cytoplasmic helix N (Fig. 4a), the movement of the latter, for example by direct interaction with a cytoplasmic enzyme in the same metabolic pathway, can trigger the opening of the channel. We have no evidence for such a hypothesis, and it can be validated only by further experimentation, which we expect would reveal greater variations in both the gating mechanism and the anionic preference of FNT channels.

METHODS SUMMARY

Bismuth sulphite agar plate assay. *FNT3* was isolated from *C. difficile* strain 630. *Escherichia coli* BL21(DE3) transformed with vector pCDFduet-1-asrA-asrB, pACYCduet-1-asrC, or pACYCduet-1-asrC-FNT3 were plated on bismuth sulphite agar²⁰ and allowed to develop for 48 h.

Whole-cell *in vivo* transport. *Salmonella typhimurium* transformed with pBAD-FNT3 were assayed for their ability to generate sulphide from either thiosulphate or sulphite using a silver-sulphide probe following modification of a previously published protocol¹⁹.

Proteoliposome reconstitution and *in vitro* transport assay. Proteoliposomes were formed from *E. coli* total lipids and Ni²⁺-NTA-purified proteins and assayed by a method modified from a previously published concentrative uptake assay^{11,22}.

Protein-ion interaction assay. Ion-induced thermostability of HSC was monitored using analytical size-exclusion chromatography. Purified protein was incubated at increasing temperatures and its recovery was monitored by size-exclusion chromatography using a high-performance liquid chromatograph. Candidate permeating ions were incubated at a concentration of 20 mM and protein was monitored for thermostabilization.

Protein purification and crystallization and structure determination. HSC was expressed as a carboxy-terminal FLAG-10×His fusion in *E. coli* BL21. The protein was purified using Ni²⁺-NTA affinity chromatography, followed by size-exclusion chromatography. The protein was crystallized by hanging-drop vapour diffusion and the crystal structure was solved by molecular replacement.

Full Methods and any associated references are available in the online version of the paper at www.nature.com/nature.

Received 2 August 2011; accepted 20 January 2012.

Published online 11 March 2012.

1. Wächtershäuser, G. Groundworks for an evolutionary biochemistry: the iron-sulphur world. *Prog. Biophys. Mol. Biol.* **58**, 85–201 (1992).
2. Kabil, O. & Banerjee, R. Redox biochemistry of hydrogen sulfide. *J. Biol. Chem.* **285**, 21903–21907 (2010).
3. Dhillon, A., Goswami, S., Riley, M., Teske, A. & Sogin, M. Domain evolution and functional diversification of sulfite reductases. *Astrobiology* **5**, 18–29 (2005).
4. Rabus, R., Hansen, T. & Widdel, F. in *The Prokaryotes: Ecophysiology and Biochemistry* Vol. 2 (eds Dworkin, M. et al.) 659–768 (Springer, 2006).
5. Goffredi, S. K., Childress, J. J., Desaulniers, N. T. & Lallier, F. J. Sulfide acquisition by the vent worm *Riftia pachyptila* appears to be via uptake of HS[−], rather than H₂S. *J. Exp. Biol.* **200**, 2609–2616 (1997).
6. Jacques, A. G. The kinetics of penetration: XII. Hydrogen sulfide. *J. Gen. Physiol.* **19**, 397–418 (1936).
7. Freytag, J. K. et al. A paradox resolved: sulfide acquisition by roots of seep tubeworms sustains net chemoautotrophy. *Proc. Natl Acad. Sci. USA* **98**, 13408–13413 (2001).
8. Lee, J. K. et al. Structural basis for conductance by the archaeal aquaporin AqpM at 1.68 Å. *Proc. Natl Acad. Sci. USA* **102**, 18932–18937 (2005).
9. Mathai, J. C. et al. No facilitator required for membrane transport of hydrogen sulfide. *Proc. Natl Acad. Sci. USA* **106**, 16633–16638 (2009).
10. Suppmann, B. & Sawers, G. Isolation and characterization of hypophosphite-resistant mutants of *Escherichia coli*: identification of the FocA protein, encoded by the pfl operon, as a putative formate transporter. *Mol. Microbiol.* **11**, 965–982 (1994).
11. Waight, A. B., Love, J. & Wang, D. N. Structure and mechanism of a pentameric formate channel. *Nature Struct. Mol. Biol.* **17**, 31–37 (2010).

12. Jia, W., Tovell, N., Clegg, S., Trimmer, M. & Cole, J. A single channel for nitrate uptake, nitrite export and nitrite uptake by *Escherichia coli* NarU and a role for NirC in nitrite export and uptake. *Biochem. J.* **417**, 297–304 (2009).
13. Hughes, M. N., Centelles, M. N. & Moore, K. P. Making and working with hydrogen sulfide: the chemistry and generation of hydrogen sulfide *in vitro* and its measurement *in vivo*: a review. *Free Radic. Biol. Med.* **47**, 1346–1353 (2009).
14. Hirshfield, I. N., Terzulli, S. & O'Byrne, C. Weak organic acids: a panoply of effects on bacteria. *Sci. Prog.* **86**, 245–269 (2003).
15. Wang, Y. et al. Structure of the formate transporter FocA reveals a pentameric aquaporin-like channel. *Nature* **462**, 467–472 (2009).
16. Lu, W. et al. pH-dependent gating in a FocA formate channel. *Science* **332**, 352–354 (2011).
17. Das, P., Lahiri, A. & Chakravorty, D. Novel role of the nitrite transporter NirC in *Salmonella* pathogenesis: SPI2-dependent suppression of inducible nitric oxide synthase in activated macrophages. *Microbiology* **155**, 2476–2489 (2009).
18. Crane, B. R. & Getzoff, E. D. The relationship between structure and function for the sulfite reductases. *Curr. Opin. Struct. Biol.* **6**, 744–756 (1996).
19. Hallenbeck, P. C., Clark, M. A. & Barrett, E. L. Characterization of anaerobic sulfite reduction by *Salmonella typhimurium* and purification of the anaerobically induced sulfite reductase. *J. Bacteriol.* **171**, 3008–3015 (1989).
20. Wilson, W. J. & Blair, E. M. v. A combination of bismuth and sodium sulphite affording an enrichment and selective medium for the typhoid-paratyphoid groups of bacteria. *J. Pathol. Bacteriol.* **29**, 310–311 (1926).
21. Doyle, D. A. et al. The structure of the potassium channel: molecular basis of K⁺ conduction and selectivity. *Science* **280**, 69–77 (1998).
22. Middleton, R. E., Pheasant, D. J. & Miller, C. Purification, reconstitution, and subunit composition of a voltage-gated chloride channel from *Torpedo* electroplax. *Biochemistry* **33**, 13189–13198 (1994).
23. Savage, D. F., O'Connell, J. D. III, Miercke, L. J., Finer-Moore, J. & Stroud, R. M. Structural context shapes the aquaporin selectivity filter. *Proc. Natl Acad. Sci. USA* **107**, 17164–17169 (2010).
24. Feth, S., Gibbs, G. V., Boisen, M. B. Jr & Myers, R. H. Promolecule radii for nitrides, oxides, and sulfides. A comparison with effective ionic and crystal radii. *J. Phys. Chem.* **97**, 11445–11450 (1993).
25. Tai, C. H. et al. Characterization of the allosteric anion-binding site of O-acetylserine sulfhydrylase. *Biochemistry* **40**, 7446–7452 (2001).
26. Hille, B. *Ionic Channels of Excitable Membranes* 362–389 (Sinauer, 1992).
27. Yasui, M. et al. Rapid gating and anion permeability of an intracellular aquaporin. *Nature* **402**, 184–187 (1999).
28. Rychkov, G. Y., Pusch, M., Roberts, M. L., Jentsch, T. J. & Bretag, A. H. Permeation and block of the skeletal muscle chloride channel, ClC-1, by foreign anions. *J. Gen. Physiol.* **111**, 653–665 (1998).
29. Simons, J. & Jordan, K. D. Ab initio electronic structure of anions. *Chem. Rev.* **87**, 535–555 (1987).

Supplementary Information is linked to the online version of the paper at www.nature.com/nature.

Acknowledgements We are grateful the staff at beamlines X25 and X29 of the National Synchrotron Light Source at Brookhaven National Laboratory and at beamline 23ID of the Advanced Photon Source at Argonne National Laboratory for assistance in X-ray diffraction experiments. We thank A. B. Waight for suggesting the project; J. J. Marden for assistance with cloning of mutants; T. Neubert and S. Blais for mass spectrometry measurements; the 2010 CCP4 Workshop for assistance in processing diffraction data; and A. David, H. Jackson, N. K. Karpowich, J. J. Marden, R. L. Mancuso, Y. Pan and M. Zhou for discussions. This work was financially supported by the NIH (R01-GM093825, R01-DK073973, R01-MH083840 and U54-GM075026). B.K.C. was partly supported by a NIH Supplement Grant to Promote Diversity in Health-Related Research (R01-DK053973-08A1S1) and an NIH pre-doctoral fellowship (F31-AI086072).

Author Contributions B.K.C. did the experiments. B.K.C. and D.-N.W. wrote the manuscript.

Author Information The atomic coordinates and structure factors of HSC for high, medium and low pH have been deposited in the Protein Data Bank under accession codes 3TDO, 3TDR and 3TDP, respectively, and those of the Lys 16 Ser, Leu 82 Val, Thr 84 Ala, Lys 148 Glu and Phe 194 Ile mutants have been deposited under the codes 3TE2, 3TDX, 3TE1, 3TE0 and 3TDS, respectively. Reprints and permissions information is available at www.nature.com/reprints. The authors declare no competing financial interests. Readers are welcome to comment on the online version of this article at www.nature.com/nature. Correspondence and requests for materials should be addressed to D.N.W. (wang@saturn.med.nyu.edu).

METHODS

Phylogenetic analysis. Phylogenetic data for 474 bacterial and archaeal members of the FNT family were obtained from the HOGENOM database³⁰, aligned using the program JALVIEW³¹ and plotted using the program ARCHAEOPTERYX³². Genomic sequences and operon annotations were derived from the NCBI GenBank nucleotide database³³.

Bismuth sulphite agar plate assay. Gene *FNT3* was isolated from *C. difficile* strain 630. The genes for *C. difficile* *asrA* (NCBI gene ID, 4915353) and *asrB* (4915352) were cloned into pCDFDuet-1 (EMD Biosciences) and the genes for *C. difficile* *asrC* (4915351) and *FNT3* (4915350) were cloned into pACYCDuet-1 (EMD Biosciences). Bismuth sulphite agar plates²⁰ were freshly prepared following the manufacturer's protocol and supplemented with 1 mM isopropyl β -D-1-thiogalactopyranoside and the antibiotics chloramphenicol and spectinomycin. *E. coli* BL21(DE3) cells were transformed with the indicated vectors and streaked, and colonies were allowed to grow at 37 °C for 48 h. The bismuth sulphite agar²⁰ contained the ATP synthase inhibitor brilliant green¹⁹ and high concentrations of SO_3^{2-} . When *C. difficile* *asrABC* was induced, *E. coli* were able to overcome the growth inhibition by producing ATP through glycolysis by reducing SO_3^{2-} to H_2S .

Whole-cell *in vivo* transport assay. *Salmonella typhimurium* LT2 was transformed with the *FNT3* cloned into a pBAD vector (Invitrogen). Cells were adapted in MOPS medium supplemented with 10 mM glucose and thiamine at $1 \mu\text{g ml}^{-1}$. A fraction of each culture (5 ml) was centrifuged and resuspended in fresh media supplemented with ampicillin, 0.2% arabinose and either 6 mM sodium sulphite or 6 mM sodium thiosulphate. Aliquots were incubated at 37 °C for 6 h and then centrifuged to pellet bacteria. Medium was gently poured into an equal volume of sulphide antioxidant buffer. Exported sulphide was measured using a combination silver sulphide electrode (Cole-Palmer). The concentration of sulphide in the medium was determined using standards of known sodium sulphide concentrations in the same antioxidant buffer.

Protein purification. *FNT3* was cloned into a modified pBAD vector (Invitrogen), creating a C-terminal TEV-FLAG-10 \times His fusion protein, and transformed into *E. coli* BL21 pLysS (Sigma-Aldrich) cells^{11,34,35}. Transformed cells were grown at 37 °C to $D_{600 \text{ nm}}$ 1.0 and induced with 0.2% of arabinose for 4 h. Cells were collected and lysed by passing twice through an Emulsiflex cell disrupter (Avestin). Lysate was clarified by a low-speed spin at 12,000g and solubilized with 1% β -dodecyl-maltopyranoside (DDM, Anatrace). Solubilized lysate was incubated with Ni^{+2} -NTA resin (Qiagen) and the bound protein was eluted with buffer containing 1.1% β -octyl-glucopyranoside (OG, Anatrace), 50 mM Tris 8.0, 200 mM NaCl, 300 mM imidazole and 10% glycerol. The protein sample was incubated with TEV protease overnight to remove the tags and then underwent size-exclusion chromatography in a Superdex 200 in 25 mM Tris, pH 6.8, 100 mM NaCl and 1.1% OG.

Mass spectrometry. The mass of purified HSC was determined using matrix-assisted laser desorption/ionization time-of-flight mass spectrometry in the laboratory of Dr T. Neubert following published protocols^{36–38}.

Protein-ion interaction assay. Ion-binding-induced thermostability of purified protein samples was measured using size-exclusion chromatography. Aliquots of 100 mg of Ni^{+2} -NTA-purified protein were incubated for 10 min in a thermocycler at increasing temperatures. Samples were injected onto a Shodex KW804 analytical size-exclusion chromatography column (Thomson) on a high-performance liquid chromatograph (Shimadzu) equilibrated in 200 mM Na_2SO_4 , 50 mM Tris, pH 8.0, 3 mM NaN_3 and 0.05% DDM. The height of the monodisperse peak was used to quantify the amount of remaining sample. The nominal melting temperature, T_m , defined as the temperature at which 50% of the protein remained soluble, was calculated by fitting the data to a Boltzmann sigmoidal model in PRISM5 (GraphPad Software). For screening of various compounds, 20 mM of each sodium salt was added before incubation.

Proteoliposome reconstitution and *in vitro* transport assay. Transport of radiolabelled formate was measured in a concentrative uptake assay^{11,22}. *Escherichia coli* total lipids were aliquoted in chloroform and dried under nitrogen. Following resuspension in intraliposomal buffer (150 mM sodium formate and 50 mM Tris, pH 8.0), lipids were overlaid with nitrogen, freeze-thawed ten times,

vortexed and sonicated to homogeneity. Proteoliposomes were formed by the addition of 1% OG and Ni^{+2} -NTA-purified HSC at a protein-to-lipid ratio of 1:10,000 (w/w). OG detergent was removed by incubation with 400 mg ml^{-1} Bio-Beads SM2 (Bio-Rad) overnight. Proteoliposomes were then extruded through a 400-nm membrane filter and frozen at -20°C until use. Concentrated re-uptake of formate was initiated by buffer-exchanging 200 ml of thawed proteoliposomes over 2 ml of G50 Sephadex swollen in extraliposomal buffer (150 mM glutamate, 50 mM Tris, pH 8.0). Carbon-14-labelled sodium formate (450 μM , American Radiolabelled Chemical) was added to the collected proteoliposomes, and the assays were terminated by centrifuging a 20-ml sample at 1,000g for 1 min at each time point through a G-50 Probequant Micro-column (GE Healthcare) to remove the external radiolabelled formate. The amount of transported radiolabelled formate was quantified by adding 1 ml of scintillation fluid to each sample and emitted photons were counted using a Wallac scintillation counter. For competition assays, increasing concentrations of sodium sulphite, sodium nitrite or sodium hydrosulphide (0, 0.15, 0.6, 3 and 15 mM), were added before the addition of radiolabelled formate.

Protein crystallization. High-pH, primitive orthorhombic crystals of HSC were grown using the vapour diffusion method, by mixing protein at a concentration of 11 mg ml^{-1} in a 1:1 ratio with reservoir solution containing 25–27% (v/v) PEG 400, 100 mM Tris, pH 7.0–9.0, and 100 mM sodium sulphite, with or without 50 mM sodium hydrosulphide. Medium-pH, monoclinic crystals were grown in reservoir solution containing 25–27% (v/v) PEG 400, 100 mM Tris, pH 7.5, and 100 mM sodium nitrite. Low-pH, C-centred orthorhombic crystals were grown in buffer containing 100 mM sodium sulphite, 100 mM sodium nitrite, 8–10% (w/v) PEG 6000, 100 mM zinc acetate and 100 mM sodium acetate, pH 4.5.

Structure determination. X-ray diffraction data were collected at beamlines X25 and X29 of the National Synchrotron Light Source at Brookhaven National Laboratory and beamline 23ID of the Advanced Photon Source at Argonne National Laboratory. Images were processed and scaled using the HKL2000 suite³⁹. The structure was solved by molecular replacement using the *V. cholerae* FocA structure¹¹ (PDB code: 3KLY) as a search model. Models were built using PHENIX Autobuild⁴⁰ and manually adjusted using COOT⁴¹. Refinement was carried out using PHENIX Refine⁴⁰. The pore size of the channel was calculated using HOLE⁴², and structure figures were generated using PYMOL⁴³.

- Penel, S. *et al.* Databases of homologous gene families for comparative genomics. *BMC Bioinformatics* **10** (suppl. 6), S3 (2009).
- Clamp, M., Cuff, J., Searle, S. M. & Barton, G. J. The Jalview Java alignment editor. *Bioinformatics* **20**, 426–427 (2004).
- Han, M. V. & Zmasek, C. M. phyloXML: XML for evolutionary biology and comparative genomics. *BMC Bioinformatics* **10**, 356 (2009).
- Benson, D. A., Karsch-Mizrachi, I., Lipman, D. J., Ostell, J. & Sayers, E. W. GenBank. *Nucleic Acids Res.* **39**, D32–D37 (2011).
- Auer, M. *et al.* High-yield expression and functional analysis of *Escherichia coli* glycerol-3-phosphate transporter. *Biochemistry* **40**, 6628–6635 (2001).
- Wang, D. N. *et al.* Practical aspects of overexpressing bacterial secondary membrane transporters for structural studies. *Biochim. Biophys. Acta* **1610**, 23–36 (2003).
- Cadene, M. & Chait, B. A robust, detergent friendly method for mass spectrometry analysis of integral membrane proteins. *Anal. Chem.* **72**, 5655–5658 (2000).
- Li, X. D. *et al.* Monomeric state and ligand binding of recombinant GABA transporter from *Escherichia coli*. *FEBS Lett.* **494**, 165–169 (2001).
- Safferling, M. *et al.* The TetL tetracycline efflux protein from *Bacillus subtilis* is a dimer in the membrane and in detergent solution. *Biochemistry* **42**, 13969–13976 (2003).
- Otwinowski, Z. & Minor, W. Processing of X-ray diffraction data collected in oscillation mode. *Methods Enzymol.* **276A**, 307–326 (1997).
- Adams, P. D. *et al.* PHENIX: building new software for automated crystallographic structure determination. *Acta Crystallogr. D* **58**, 1948–1954 (2002).
- Emsley, P. & Cowtan, K. Coot: model-building tools for molecular graphics. *Acta Crystallogr. D* **60**, 2126–2132 (2004).
- Smart, O. S., Neduelil, J. G., Wang, X., Wallace, B. A. & Sansom, M. S. HOLE: a program for the analysis of the pore dimensions of ion channel structural models. *J. Mol. Graph.* **14**, 354–360, 376 (1996).
- DeLano, W. L. The PyMOL Molecular Graphics System (<http://www.pymol.org>) (2002).

CORRECTIONS & AMENDMENTS

CORRIGENDUM

doi:10.1038/nature10976

Corrigendum: Functional complementation between FADD and RIP1 in embryos and lymphocytes

Haibing Zhang, Xiaohui Zhou, Thomas McQuade, Jinghe Li, Francis Ka-Ming Chan & Jianke Zhang

Nature **471**, 373–376 (2011)

In Fig. 3b of this Letter, the plot for the NP205 epitope response in the *Fadd*^{-/-}*Rip1*^{-/-} double-knockout (DKO) splenocytes was a duplicate of that for the NP38 epitope response. The correct figure panel is shown below. The panel has been corrected in the HTML and PDF versions online.

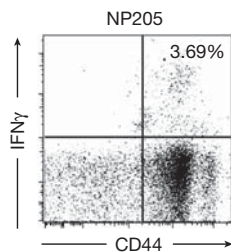


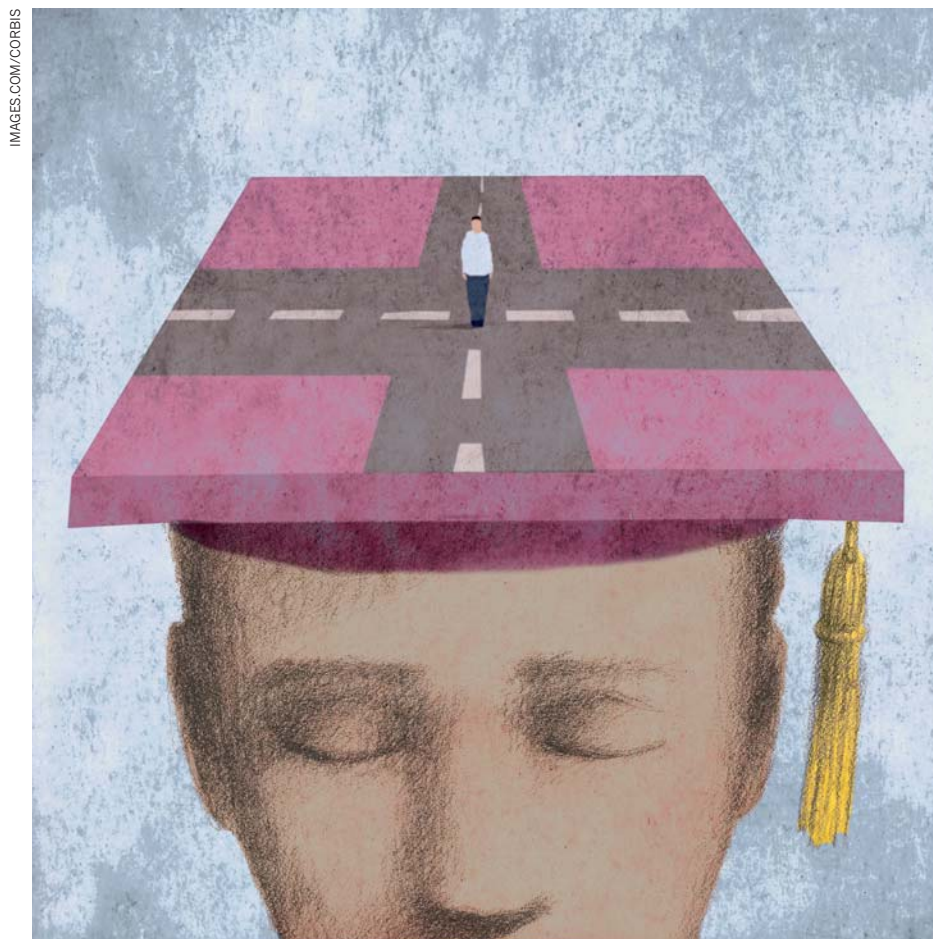
Figure 1 | This is the correct panel from Fig. 3b of the original Letter.

CAREERS

TURNING POINT Climate scientist devises mission statement for her lab **p.501**

ACADEMIA Private and public US faculty receive higher pay rise this year **p.501**

NATUREJOBS For the latest career listings and advice www.naturejobs.com



IMAGES.COM/CORBIS

RESEARCH

Postdoc or not?

Life-sciences graduates interested in academic research typically need to do at least one postdoc. For physics students, there are multiple caveats to consider.

BY KAREN KAPLAN

Björn Flatt had always assumed that he would become an academic physicist. After earning his PhD in particle physics from Johannes Gutenberg University Mainz in Gernersheim, Germany, he was happy to land a postdoctoral fellowship at Stanford University in Palo Alto, California.

But things deteriorated rapidly. The two-year fellowship was extended by a further two years so that Flatt could complete time-intensive experiments, but the delay hampered his efforts to break into the permanent-job market. By the time he started looking for an academic position in 2009, the effect of the recession was already widespread. He received no interview offers.

Flatt came to realize that he did not want to pursue an academic career after all, and set his sights on industry. However, he could not find a permanent research post, and ended up starting another postdoc, this time in mass spectrometry and instrumentation physics at Agilent Technologies in Santa Clara, California, which was at least a way to get his foot in the door. "It wasn't exactly my field, but my theses had been on instrumentation development," Flatt says. "It was actually a pretty good match." Last March, several months before the postdoc was due to end, Flatt heard about an opening in the company for a senior research and development scientist, a permanent position. Flatt applied for it and got the job.

Today, after a year in his new post, Flatt says that his two postdocs offered little value other than confirming that he did, in fact, want to pursue industrial research. They were neither crucial for building his research portfolio nor obligatory for landing his permanent position at Agilent.

Science postgraduates, especially those in the biological sciences, often see postdocs as a way to continue and refine their research, learn to run a laboratory and develop a broad, deep collaborative network. Flatt is one of many early-career physicists in the United States who dismiss that idea. Although researchers in the biological sciences may have to take multiple postdocs before landing their first permanent post, the landscape is shifting for physicists. Nearly 70% of physicists who earned their degree in 2004 took a postdoc, but the proportion had fallen to 56% in the classes of 2007 and 2008, according to the Statistical Research Center of American Institute of Physics (AIP) in College Park, Maryland.

One reason for the decline is that fewer people with physics PhDs are pursuing an academic research career. This is in part because there are, and have been, fewer positions to pick from. Academic hiring has been flat since 2003, says Crystal Bailey, the education and careers programme manager for the American Physical Society (APS), also in College Park. Between 2006 and 2007, about 350 faculty members left their job in physics, but in 2008, about 450 people with physics PhDs were seeking positions. Of those with physics PhDs in the United States from the classes of 2007 and 2008 who did not take a postdoc directly after earning their degree, 62% accepted private-sector positions, according to the AIP Statistical Research Center. Another 10% accepted government positions, such ▶

► as at one of the US Department of Energy's 21 labs and technology centres. About one-quarter accepted academic posts.

Few private-sector or industry positions require an applicant to have completed a postdoc — even if those posts involve research. Bailey says that she rarely advises physics graduate students to pursue a postdoc, unless they are certain they want a career in academia or they need a job while they consider their options. Physics postgraduates are, she says, far more likely to get full-time permanent employment in the private sector, for which a postdoc is largely irrelevant.

About 12 industrial employers in the United States are currently advertising jobs for people with physics PhDs on a members-only section of the APS website, but none of them lists a postdoc as a prerequisite.

The applied-research nature of physics-related professions often makes a stint in academia less than useful. "A lot of physicists are just as comfortable doing engineering as engineers are," says James Duderstadt, president emeritus at the University of Michigan in Ann Arbor. "If they go to work for IBM, they're going to be doing applied research. If they work at the Large Hadron Collider, they're going to be doing applied physics," says Duderstadt, who was also a member of a National Academies panel that, in 2000, analysed the US postdoctoral experience. "Overall, it is not necessary, unless they have some experimental thing they need to learn in someone's lab that they can't learn in a PhD."

A postdoc could even be a drawback for physicists considering the private sector. Many of Europe's industrial employers prefer to hire applicants who have a PhD and a 'clean slate', says Maria Allegrini, a physicist at University of Pisa in Italy and a member of the APS Committee on International Scientific Affairs. "They want to train you in their own field," she says.

Physicists with experience in US industry warn that a CV with three or more academic postdocs can create the impression that the applicant had hoped for a career in academia and does not really want one in industry. "We want to find someone who's charged up with enthusiasm to work for our company," says Jim Hollenhorst, Agilent's senior director of technology, who regularly hires physics postgraduates. "So don't do three postdocs, not find an academic job, and then apply here."

Having multiple industrial postdocs could also be detrimental in some cases. If a researcher completes a two- or three-year postdoc at a company — requiring a significant training commitment from a senior researcher — and then leaves to do the same

thing somewhere else, he or she may be viewed negatively by subsequent industrial hiring committees. But the outlook is also employer- and location-dependent, notes Dipali Bhatt-Chauhan, international-relations manager at the Institute of Physics in London. British industrial employers often view candidates



Anne Goodsell says a postdoc can help young physicists expand their network and publish more.

with several industrial postdocs as having greater skills and knowledge than those who have done one or none, she says. "Employers would be more likely to hire that postdoc."

SMART PURSUIT

The requirements are different for those seeking a government or academic research post, including at US liberal-arts colleges. Catherine Crouch, a materials physicist at Swarthmore College in Pennsylvania, completed two postdocs at Harvard University in Cambridge, Massachusetts, where she earned her PhD. In the first, she focused on physics-education research, with some teaching duties; in the second, she specialized in experimental research in a liberal-arts environment — important at Swarthmore, a liberal-arts college that heavily weights faculty research. As well as honing her research, she says, the fellowships taught her how to run a lab independently — and signalled to potential employers that she was capable of such. "When academic hiring committees are reviewing job applications, they look for a postdoc as evidence that you've had this kind of responsibility — how to run a research programme, how to pick good projects, how to decide what equipment will serve you well," she says. "There are all these meta-questions that don't necessarily come into your arena as a graduate student."

A postdoc expands young physicists' networks far beyond what they can typically achieve as a doctoral student, says Eric Jensen, chair of Swarthmore's physics and astronomy department. "It gives you the chance to build more collaborations and develop a network of colleagues at other institutions that you can be in touch with and work with," he says.

Postdocs can also be useful for those who are uncertain of their pathway or who want to pursue academia but are out of sync with the academic year hiring cycle. Anne Goodsell, an atomic and optical physicist at Middlebury College in Vermont, says that people who earn their PhD around June, for example, and are aiming for a career in academia, can generally apply for posts starting only during the following semester. In the meantime, she says, such postgraduates, as well as those who are not sure of their direction, can take a postdoc to maintain existing contacts, establish new ones, publish more, gain expertise in a subfield and sustain research momentum while waiting to apply or deciding what path to take. "It makes a lot of sense to take a postdoc to fill that gap," Goodsell says.

A postdoctoral fellowship at federal labs in Europe and the United States may sometimes lead directly to a full-time permanent position. Mary Anne With, a postdoctoral adviser at Los Alamos National Laboratory in New Mexico, says that 80–90% of the lab's technical positions are filled by former postdocs. Joseph Bernstein, an astrophysicist and postdoc at Argonne National Laboratory in Illinois, who is on his second renewal and fourth year, is considering either a consulting position or a third extension of his postdoc. The extension, he says, would be equivalent to a tenure-track assistant-professor post and is likely to lead to a permanent position at Argonne — and it pays well for a postdoc position. He declined an offer a couple of years ago for an assistant-professor position that would have meant taking a 10% pay cut. By extending his postdoc, Bernstein believes he will develop the technical computing and programming expertise necessary to become staff. "It's a good opportunity," he says.

So how does a student decide whether to pursue the postdoc path? If postgraduates are planning for a career in academia, it is still a requirement, acknowledges Bailey. But for those who remain uncertain, doing one postdoc is unlikely to damage anyone's budding career, even if they decide to head for industry, says APS executive officer Kate Kirby. "It increases the number of connections you have in your field," she says. "It makes it possible to get further letters of recommendation from a broader constituency — a tremendous advantage that can help you collaborate, get a grant or get a position." ■

Karen Kaplan is assistant Careers editor at Nature.

C. GRAINGER

TURNING POINT

Jessica Hellman

M.CASHORE

Conservation biologist Jessica Hellman studies the effects of climate change at the University of Notre Dame in Indiana. She was inspired by her one-year fellowship from the Aldo Leopold Leadership Program in Stanford, California to do something that few scientific laboratories do — create a mission and vision statement for her research group.

What is the best piece of career advice you have received?

My PhD adviser was Paul Ehrlich, a population biologist at Stanford University, and a public face of science. I studied with him because I wanted to have something to say about natural-resource management or how to deal with climate change. He was an ideal role model. But what he told me, and what I tell my students now, is “it’s all about science”. Concrete data, experience and knowledge are what give you a voice in the public sphere. If you bring nothing substantial to the table, you are just another voice.

You have a fear of being labelled a ‘butterfly’ person. Why?

I examine how climate change affects endangered species — an issue that has an inherent complexity because of the dynamics of temperature effects and species interactions. One of the species I’ve studied is the endangered Bay Checkerspot butterfly (*Euphydryas editha bayensis*), which runs out of food when high temperatures or drought cause its host plant to dry out. I don’t want people to miss the point: I study butterflies not because I am more fascinated with them than with other creatures but because, with so much data available, they serve as a useful proxy for insects in general. But one thing I learned from my leadership fellowship is to be comfortable in my own skin and recognize what distinguishes me as a researcher — I’m learning to embrace my inner butterfly.

Why are you trying to ‘brand’ your research?

There are two dimensions to branding: communicating to the world who you are and what you are about, and helping you to decide what you want to be doing. I wanted to be the person to study how populations are locally adapted to climate, which my group does.

Do you think every scientist should brand themselves?

I think it is a worthwhile exercise. When we first hire a researcher, we want a solid idea of who they are going to be, and it is important



for them to think strategically about how they can set themselves apart — so it is helpful to develop a plan that makes that clear.

Why did you decide to write a mission and vision statement for your laboratory?

I wanted to know who we were as a group and what we should focus on. Once you get tenure, there are a million things to do — collaborations, committees and grant applications to write. I decided that one way to be thoughtful about our work, and what to work on, would be to collectively write our mission and vision. I found some instructions and group exercises aimed at businesses, and then we had a retreat to strategically discuss how we could match our strengths, priorities and goals for making our research relevant to larger issues. We’ll put a copy in the lab for new students.

Will you continue to have retreats?

Yes. My research group should have regular retreats. We have lab meetings to talk about science, but retreats focus on broader topics, such as professional development. I want to brainstorm with everybody about what they can be best at. Retreats are also a great way to build morale. Everybody wants to be part of something.

Why did you start blogging and tweeting?

I want to make science relevant to the rest of the world, be it landowners or government agencies — but I want to do it with transparency and honesty. Social media opens the shop doors a bit more. I would never tell students that their time is better spent on a blog than on a published paper, but it is a great way to be more open. ■

INTERVIEW BY VIRGINIA GEWIN

WORK-LIFE BALANCE

Stress survey

Scientists’ work obligations conflict with their personal lives three or more times a week, finds a poll of 4,225 scientists by the Association for Women in Science (AWIS) in Alexandria, Virginia. A third of respondents to the global work–life satisfaction survey said that achieving work–life balance damages their careers. “There’s a lot of stress out there; it’s global and not gender-specific,” says AWIS past-president Joan Herbers, who blames the dissatisfaction in part on rigid tenure timelines and requirements. Extending the tenure clock to allow for birth or adoption, and asking tenure committees to rate candidates on the basis of their publications’ impact rather than total number, would ease stress, says Herbers.

ACADEMIA

Increasing salaries

Faculty members at US doctorate-granting institutions received an average 1.7% salary increase for 2011–2012, 41.7% higher than the average 1.2% the previous year, according to a survey of 224,693 faculty members at 813 four-year colleges and universities. The survey conducted by the College and University Professional Association for Human Resources in Knoxville, Tennessee, found that faculty members at public doctoral institutions received a 1.2% average pay rise for 2011–2012, three times higher than the year before. Private institutions awarded a 2.4% rise for 2011–2012, up from last year’s 2.2%. Assistant professors in biology and biomedicine earned US\$59,907 in 2011–2012, and those in physical sciences earned \$58,771, up 2% and 2.3%, respectively.

RESEARCH

NASA to award grants

As part of an inaugural space-technology research programme, NASA is seeking grant proposals from early-career scientists. Ten researchers in areas such as communication and navigation systems; materials, structures and mechanical systems; and human health, life support and habitation systems will receive up to US\$200,000 per year for up to three years. The programme aims to improve its future space-exploration and discovery capabilities by focusing on early-stage research and seeding innovation, says a NASA spokesperson. Notices of intent to submit are due on 30 March and the deadline for final proposals is 3 May.

VISITING BOB

Life insurance.

BY JOHN GILBEY

One of the great advantages of being a writer is the fascinating folk you meet. Take Bob, for example. I first talked to him in Palo Alto about eight years ago. We chatted, got on, shared some bizarre and unlikely anecdotes — but like so many chance encounters, I didn't think much more about it. Then, out of the blue, I was invited to write Bob's biography. He'd read my published stuff, liked it, and asked me to document his career in the Valley. To say I was pleased would be a major understatement.

A week later I was ensconced in a wood-panelled corner office at Bob's host institute, overlooking the coffee shops of University Avenue, with an expenses-paid contract to extract from Bob all his tales of the old days that were fit to print — a constraint that probably reduced the size of the book by half. It was one of the most enjoyable and intriguing jobs I've ever had.

Bob and I hadn't talked for several months when the call came, and I felt a sinking feeling when I realized that the caller wasn't Bob but Emily, one of the cloud of crazily bright postdocs that he employs as assistants. Like all of us, Bob wasn't getting any younger.

"Hi John, I thought I'd better call you about Bob..." Here it comes, I thought. "He's got some fairly serious health problems, and he's been asking for you."

I thought about this. "Can't you put him on the line?" There was a regretful, apologetic pause. "I'm afraid not, he can't interpret low-bandwidth AV now. Would you be able to visit him?" I was still pondering when she added: "Just one thing, don't leave it too long..."

After the ten-hour flight, what I really wanted was beer, food and sleep. At a pinch, I'd skip the food. Emily, however, was insistent that I talk to Bob first. Looking into his room from an observation window, it seemed more chaotic than I remembered, but it was the primal waft of organic decay — nauseating even from the next room — that shocked me. I glanced across at Emily, who gave a slow nod of the head.

"Hi, Bob, how are you doing?" The response was slow, like someone waking

from an anaesthetic. "John? Is that you?" The voice was stretched and blurred, but the sensory unit rotated and waddled towards the window like an inebriated desk lamp.

"I really appreciate you coming over," muttered Bob. "As you can see, things aren't going too well... I don't know how much Emily has told you, but it looks like I only

We found a bar, drank several beers, and tried to sketch out a budget for a rebuild. The numbers were astronomical, and it was clear from Emily's terse analysis that all attempts to gather funding through the usual channels had failed.

Sleep wasn't an option. As headlights panned across the ceiling of my motel room I fought to find a solution. "Follow the money," Bob had said. Bob — the 'Bucket of Brains' they used to call him, much to his annoyance. There were no physical brains in the system. Instead, the reasoning power of 20 top scientists of the day had been distilled into a semi-organic structure that — to everyone's surprise — had fought schizophrenia and paranoia to emerge as the composite personality of Bob. The first, and last, of his kind. "Follow the money." Easy to say, but why me?

The coffee was so strong that my vision took on the character of a shaky film noir — but it fought the jet lag. Emily toyed with her green tea and tried not to look concerned. I asked the critical question: "When I was here last, I left a set of notebook files — stuff that Bob wouldn't let me use in the book, or even have copies of. Are they still here?"

Emily shrugged slightly. "We never throw anything away, that's part of our culture."

I smiled with relief, thinking of all the doors — and bank accounts — that were about to open.

Emily looked puzzled. "I'll have to check," I qualified carefully, "but from memory, those notes cover every major scandal — personal, corporate and political — in the Valley between 2015 and 2035. Bob's component consciousnesses were deeply involved — more to the point, the other folk implicated are now in very senior posts and definitely won't want this stuff made public... 'Follow the money...'"

The mug of tea dropped to the table top. "You mean, he wants to blackmail people to raise the money?" Emily exclaimed in shock.

"It certainly looks like it," I replied with a smile. "I'm just beginning to realize how human Bob is." ■

John Gilbey (gilbey@bcs.org.uk) is a writer who knows a thing or two about mysterious inner rottings — but not blackmail, honest...



have a month or so left. I've already lost some peripheral stuff — that's why I can't use remote comms — but it is creeping into my long-term memory and... heck, I'm scared.

"I need you to buy me a few more years... Just a few..." His voice faded. "Sorry, I'm going to have to rest for a while now — just follow the money..." When I looked round, I found that Emily had tears in her eyes — which made two of us.

"What does he need?" I asked Emily. She sighed and referred to an internal list — a long one. Many of Bob's systems were well beyond their technical 'end of life': the organic wet-ware circuits that formed most of his unique design were literally rotting, and had only ever been made as research tools, not production systems. No one seemed to know whether the technology could be replicated with the skills now available — or even

if it would be legal — but there seemed no way that Bob's consciousness could be ported to another infrastructure.

Follow Futures on Facebook at: go.nature.com/mtoodm

Structure of the mitotic checkpoint complex

William C. H. Chao^{1*}, Kiran Kulkarni^{1*}, Ziguo Zhang¹, Eric H. Kong¹ & David Barford¹

In mitosis, the spindle assembly checkpoint (SAC) ensures genome stability by delaying chromosome segregation until all sister chromatids have achieved bipolar attachment to the mitotic spindle. The SAC is imposed by the mitotic checkpoint complex (MCC), whose assembly is catalysed by unattached chromosomes and which binds and inhibits the anaphase-promoting complex/cyclosome (APC/C), the E3 ubiquitin ligase that initiates chromosome segregation. Here, using the crystal structure of *Schizosaccharomyces pombe* MCC (a complex of mitotic spindle assembly checkpoint proteins Mad2, Mad3 and APC/C co-activator protein Cdc20), we reveal the molecular basis of MCC-mediated APC/C inhibition and the regulation of MCC assembly. The MCC inhibits the APC/C by obstructing degron recognition sites on Cdc20 (the substrate recruitment subunit of the APC/C) and displacing Cdc20 to disrupt formation of a bipartite D-box receptor with the APC/C subunit Apc10. Mad2, in the closed conformation (C-Mad2), stabilizes the complex by optimally positioning the Mad3 KEN-box degron to bind Cdc20. Mad3 and p31^{comet} (also known as MAD2L1-binding protein) compete for the same C-Mad2 interface, which explains how p31^{comet} disrupts MCC assembly to antagonize the SAC. This study shows how APC/C inhibition is coupled to degron recognition by co-activators.

The fidelity of chromosome separation in mitosis is governed by an evolutionarily conserved cell-cycle checkpoint mechanism called the SAC^{1,2}. The SAC arrests the mitotically dividing cell to allow complete chromosome attachment to the bipolar mitotic spindle. The essence of the SAC is to block the onset of anaphase by inhibiting APC/C-mediated ubiquitin-dependent degradation of securin and mitotic cyclin. Components of the SAC that are responsible for detecting unattached kinetochores and for propagating signals to the APC/C have been identified^{3,4}, but the molecular basis underlying these processes is only partially understood^{1,2}. Mad2 and Mad3 (BubR1 in metazoans) mediate APC/C inhibition through their association with its co-activator subunit Cdc20 (refs 5–12). Mad2, Mad3 and Cdc20 (together with mitotic checkpoint protein Bub3) form the MCC that directly binds the APC/C to inhibit substrate recognition^{13,14}. Mad2 and Mad3 cooperate to antagonize Cdc20-dependent activation of the APC/C¹², with Mad3–Cdc20 interactions requiring the pre-assembly of a Cdc20–Mad2 complex^{12,15–18}. Thus, SAC signalling occurs through the generation of the Cdc20–Mad2 complex, a process initiated by Mad1, which is the Mad2 receptor at unattached kinetochores. Central to the association of Mad2 with Cdc20 is the inter-conversion of Mad2 between the open (O-Mad2) and closed (C-Mad2) structural states^{1,19}. These states of Mad2 differ in the topology of a carboxy-terminal β -sheet that repositions in C-Mad2 to enable binding to its protein ligands, Mad1 or Cdc20 (refs 20–22). In the template model for SAC activation, Mad1 interacts with C-Mad2, generating the C-Mad2–Mad1 complex that subsequently recruits O-Mad2 through the C-Mad2 dimerization interface. By inducing the conformational transition of O-Mad2 to C-Mad2, the Mad1-bound C-Mad2 subunit catalyses the binding of Mad2 to Cdc20 (refs 17, 23).

APC/C activity and its substrate recruitment are dependent on its co-activators (Cdc20 and Cdh1)²⁴, which recognize APC/C substrates through two destruction motifs (degrons); the D box²⁵ and the KEN (Lys–Glu–Asn) box²⁶. Mad3 contains a KEN box that is essential for MCC assembly^{15,27,28}, suggesting that Mad3 may act as a pseudosubstrate

to block substrate recognition by APC/C^{Cdc20}. However, other studies showing that the promotion of ubiquitin-mediated degradation of Cdc20 by the SAC is dependent on the KEN box of Mad3 (refs 18, 27, 29) indicate that there is a more complex mechanism controlling APC/C^{Cdc20} activity. The mechanisms underlying APC/C activation after SAC silencing are also poorly understood. In metazoans, p31^{comet} antagonizes the SAC³⁰ by functioning as a structural mimic of Mad2 that binds at the Mad2 dimerization interface to inhibit the conformational activation of O-Mad2 (ref. 31). Ubch10, assisted by p31^{comet}, catalyses Cdc20 ubiquitination, which leads to the disassembly of the MCC³².

To understand the molecular mechanisms underlying the mitotic checkpoint complex, we determined the crystal structure of the fission yeast MCC. The structure shows how Mad2 and Mad3 cooperatively inhibit Cdc20, and indicates how p31^{comet} would antagonize MCC assembly. The structure of Cdc20 in the context of the MCC offers the first opportunity to visualize degron recognition by co-activators. The interaction between Mad2 and Mad3 positions the Mad3 KEN box towards the KEN-box receptor of the Cdc20 WD40 domain. Additionally, an unexpected D-box mimic of the Mad3 C terminus reveals the D-box-binding site on Cdc20, thus demonstrating the structural basis of D-box recognition by co-activators.

Overall structure of the MCC

We generated the fission yeast MCC by co-expressing Cdc20, Mad2 and Mad3 in insect cells. The complex comprises Cdc20 with all functional domains (C box, Mad2-binding motif, WD40 domain and Ile–Arg tail (Supplementary Fig. 1)), Mad2 locked in its closed conformation that facilitates binding to Cdc20 (ref. 31), and Mad3 truncated after the tetratricopeptide repeat (TPR) domain³³ and thus lacking its C-terminal KEN box. Bub3 was omitted from the complex because previous studies indicated that Bub3 was not an integral part of MCC in fission yeast²⁸ and was not required for MCC-mediated inhibition of human APC/C³⁴.

¹Division of Structural Biology, Institute of Cancer Research, Chester Beatty Laboratories, 237 Fulham Road, London, SW3 6JB, UK.

*These authors contributed equally to this work.

The crystal structure of the MCC, at 2.3 Å resolution, shows that Cdc20, Mad2 and Mad3 assemble into a triangular heterotrimer (Fig. 1 and Supplementary Table 1). Mad3 coordinates the overall organization of the complex by forming numerous inter-subunit interactions with Mad2 and Cdc20, whereas Cdc20 and Mad2 interact primarily through the sequestering of the Mad2-binding motif of Cdc20 by the Mad2 ‘safety belt’ (refs 21, 22). The core architecture of Mad3 is a contiguous TPR superhelix with three TPR motifs flanked by capping α -helices that resembles the BubR1 amino terminus³³. In addition, not present in the BubR1 structure, the conserved N terminus of Mad3 that incorporates the N-terminal KEN box that is essential for MCC assembly^{15,27,28} adopts a helix–loop–helix (HLH) motif (Fig. 1 and Supplementary Fig. 2). The HLH motif simultaneously binds Mad2 and Cdc20, orienting the KEN box towards its receptor on Cdc20 (Fig. 1a, b). Mad3 also contacts Mad2 and Cdc20 through its TPR domain (Fig. 1a, c).

The WD40 domain of Cdc20 conforms to a canonical seven-bladed β -propeller (Fig. 1a). The Mad2-binding motif, N-terminal to the WD40 domain, is structurally well defined, engaging the safety belt^{21,22} of Mad2 and adopting a conformation that is similar to the Mad2-binding motif of Mad1 bound to Mad2 (ref. 22) (Fig. 2a). The linker connecting the Mad2-binding motif with the N terminus of the WD40 domain is disordered, as are the two APC/C interacting motifs: a conserved C box that is immediately N-terminal to the Mad2-binding motif⁵, and the C-terminal Ile–Arg tail that interacts with the TPR subunit Cdc27³⁶ (Supplementary Fig. 1).

Mad2 is an α/β -HORMA-class protein²⁰ (Fig. 1a and Supplementary Fig. 3). Its C-Mad2 conformation enables interactions with the

Mad2-binding motifs of Cdc20 and Mad1 and, as revealed in the MCC crystal structure, is the only state of Mad2 that can recognize Mad3. Mad2 interacts through its α -C helix and $\beta 8'$ – $\beta 8''$ hairpin with the HLH motif of Mad3 (Fig. 2b). Notably, such Mad2 interactions resemble those between C-Mad2 and p31^{comet} (ref. 31.) (Fig. 2c), and C-Mad2 in an asymmetric C-Mad2–O-Mad2 dimer³⁷ (Fig. 2d). The involvement of the $\beta 8'$ – $\beta 8''$ hairpin—a region of Mad2 that undergoes substantial conformational change upon transition from the open to closed states²¹—at the Mad2–Mad3 interface indicates that Mad3 binds exclusively to C-Mad2.

Mutations of the Mad2 α -C helix disrupt C-Mad2–Mad3 interactions³⁸, consistent with our structure. To test the Mad3 interface, we replaced Met 13 with Arg (Fig. 2b). This mutation dissociated Mad3 from a Cdc20–C-Mad2 heterodimer when size-exclusion chromatography was performed (Supplementary Fig. 4). Together, these data confirm the physiological relevance of the C-Mad2–Mad3 interface and show that C-Mad2 is required to confer high-affinity binding of Mad3 to Cdc20, consistent with studies showing that Mad3 association with Cdc20 *in vivo* is synergistic with Mad2 (refs 12, 15, 16).

The Cdc20 WD40 domain is a receptor for KEN and D box

We identified two highly conserved surfaces on the Cdc20 WD40 domain, and these are responsible for APC/C degron recognition: the KEN-box²⁶ receptor, situated on the top side of the WD40 domain at the centre of the β -propeller (Fig. 3a), and the D-box²⁵ co-receptor lying in a channel between blades 1 and 7 (Fig. 4a). The KEN-box residues of Mad3 (Lys 20, Glu 21 and Asn 22) emerge from the C

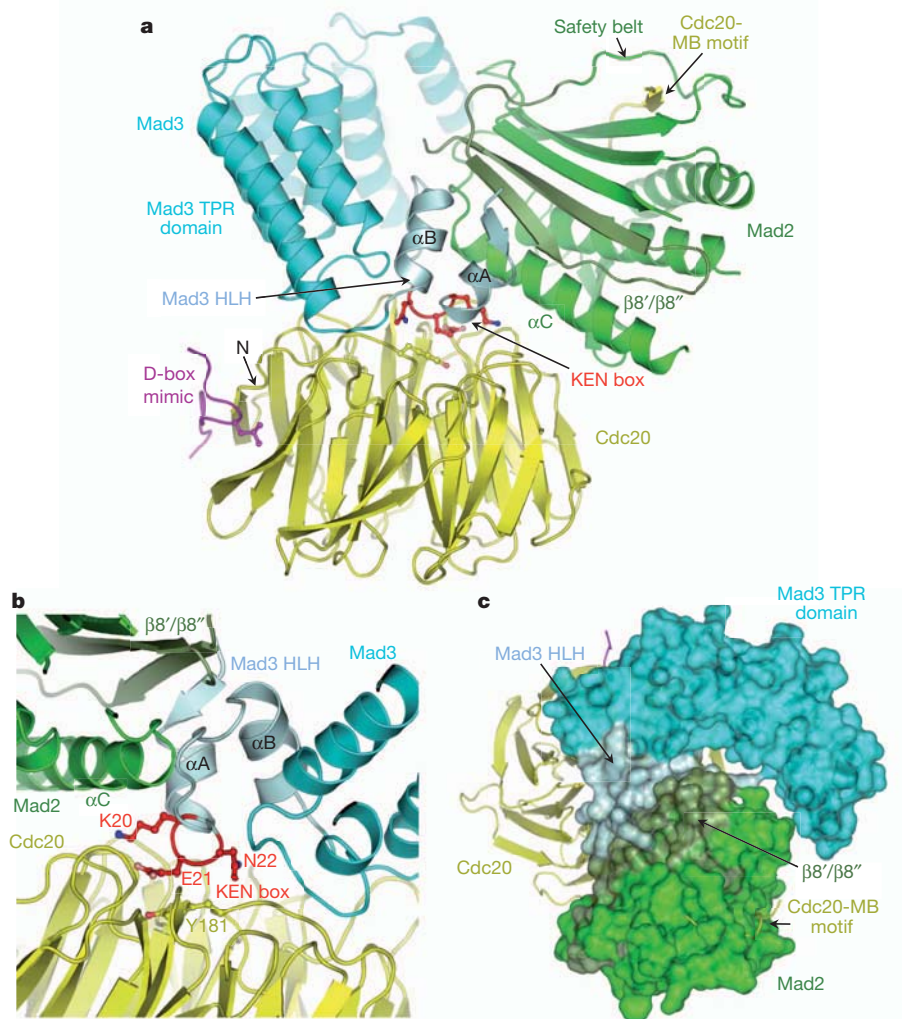


Figure 1 | Structure of *S. pombe* MCC trimer. **a**, Cartoon representation of the complex of Mad2 (green), Mad3 (cyan) and Cdc20 (yellow). Mad2 is in the C-Mad2 conformation. The KEN box is shown in red, located in the HLH motif of Mad3. The D-box mimic (magenta) that is bound to Cdc20 is from the C terminus of Mad3 from a symmetry-related molecule. The Mad2 $\beta 8'$ – $\beta 8''$ hairpin (dark green) that forms the Mad2–Mad3 interface, repositions on conversion from O-Mad2 to C-Mad2. The N terminus of the WD40 domain is indicated. **b**, Details of the Mad3 HLH interaction with Mad2 and Cdc20. **c**, Surface representation of the MCC. The interaction between Mad2 and Mad3 positions the Mad3 KEN box at the KEN-box receptor, which is located at the centre of the top side of Cdc20's WD40 domain. MB, Mad2-binding.

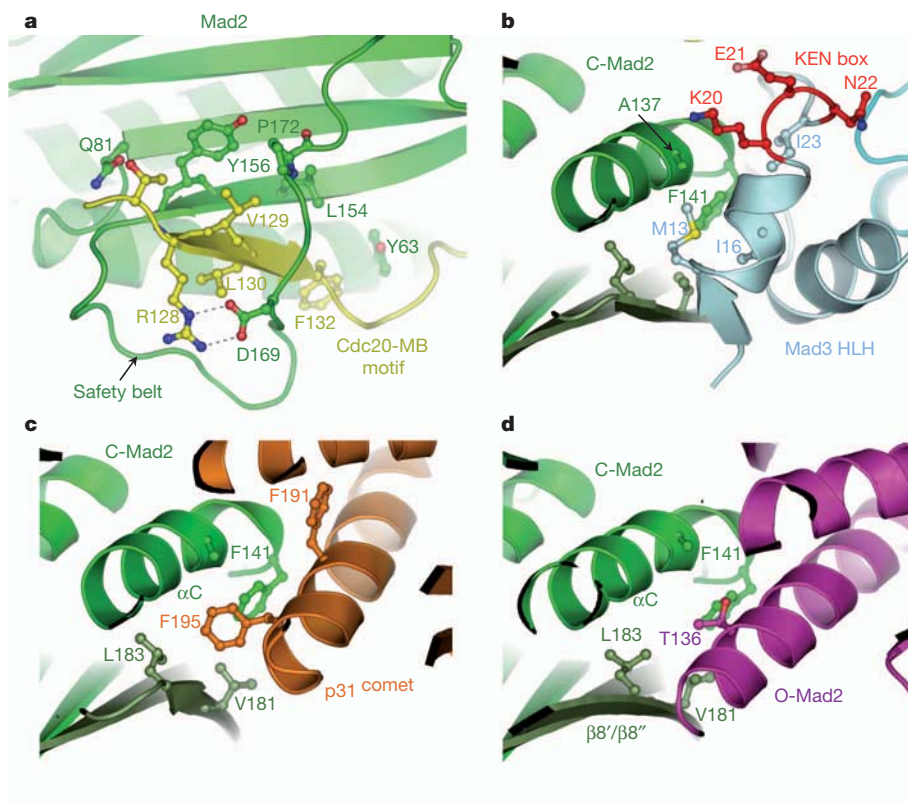


Figure 2 | Details of Cdc20–Mad2–Mad3 interactions. **a**, Mad2-binding motif of Cdc20 bound to the Mad2 safety belt. **b**, A universal Mad2 dimer interface contacts Mad3, p31^{comet} and O-Mad2. Mad2–Mad3 interactions. **c**, Mad2–p31^{comet} (ref. 31) (Protein Data Bank (PDB) accession 2QYF). **d**, C-Mad2–O-Mad2 (ref. 37) (PDB accession 2V64).

terminus of the α -A helix of the HLH as an underground turn of α -helix (Figs 1 and 3b). Their conformation resembles a 'U', with Glu 21 at the turn dipping into a depression at the centre of the Cdc20 β -propeller toroid. Tyr 181 of Cdc20, situated on an extended loop connecting blade 1 with blade 7, acts as a platform to support the aliphatic moiety of the Glu 21 side chain. Apart from this single hydrophobic interaction, the KEN box forms entirely polar contacts involving its side-chain and main-chain groups with conserved polar and charged residues of loops on four blades of the Cdc20 β -propeller. Notably, the five residues of Cdc20 that contribute side-chain interactions to the KEN box (Asp 180, Asn 326, Thr 368, Gln 392

and Arg 438) are invariant in both Cdc20 and Cdh1, indicating a universal mode of co-activator–KEN box interaction (Supplementary Fig. 5). A proline (Pro 25) positioned three residues C-terminal to the Mad3 KEN box—well conserved in KEN-box motifs—acts to break the α -helix and orient the polypeptide chain away from the Cdc20 surface.

The Mad3 KEN box has been proposed to function as a pseudo-substrate inhibitor, blocking access of Cdc20 to KEN-box degrons in APC/C substrates¹⁵. Thus, the mode of binding of the Mad3 KEN box to Cdc20 should serve as a model for understanding how co-activators recognize APC/C substrates. Consistent with this idea, mutating the

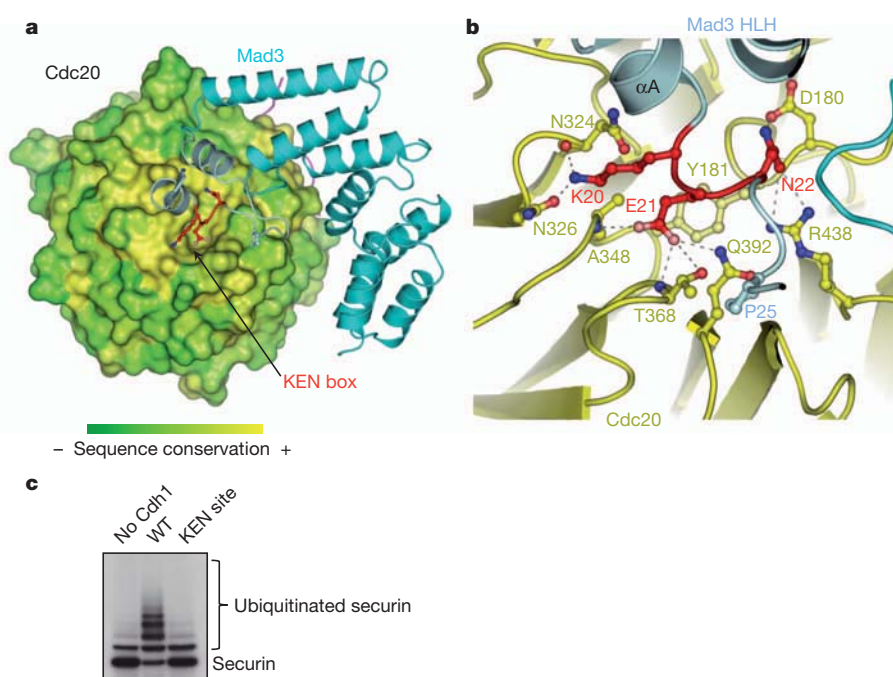


Figure 3 | The KEN box binds to a conserved surface at the centre of the top side of the WD40 domain. **a**, Cdc20 shown with surface representation coloured according to the sequence conservation of Cdc20 and Cdh1 (yellow (invariant) to green (less conserved)) (Supplementary Fig. 5). Mad3 diagram with KEN box in red. **b**, Details of KEN-box interactions with the Cdc20 WD40 domain. **c**, Mutation of the KEN-box-binding site abolishes *S. cerevisiae* APC/C^{Cdh1}-mediated ubiquitination of securin as indicated by an *in vitro* transcription or translation (IVT)-based ubiquitination assay. KEN-box mutants: N405A, N407A, Q473A, R517L (*S. pombe* Cdc20: N324, N326, Q392, R438).

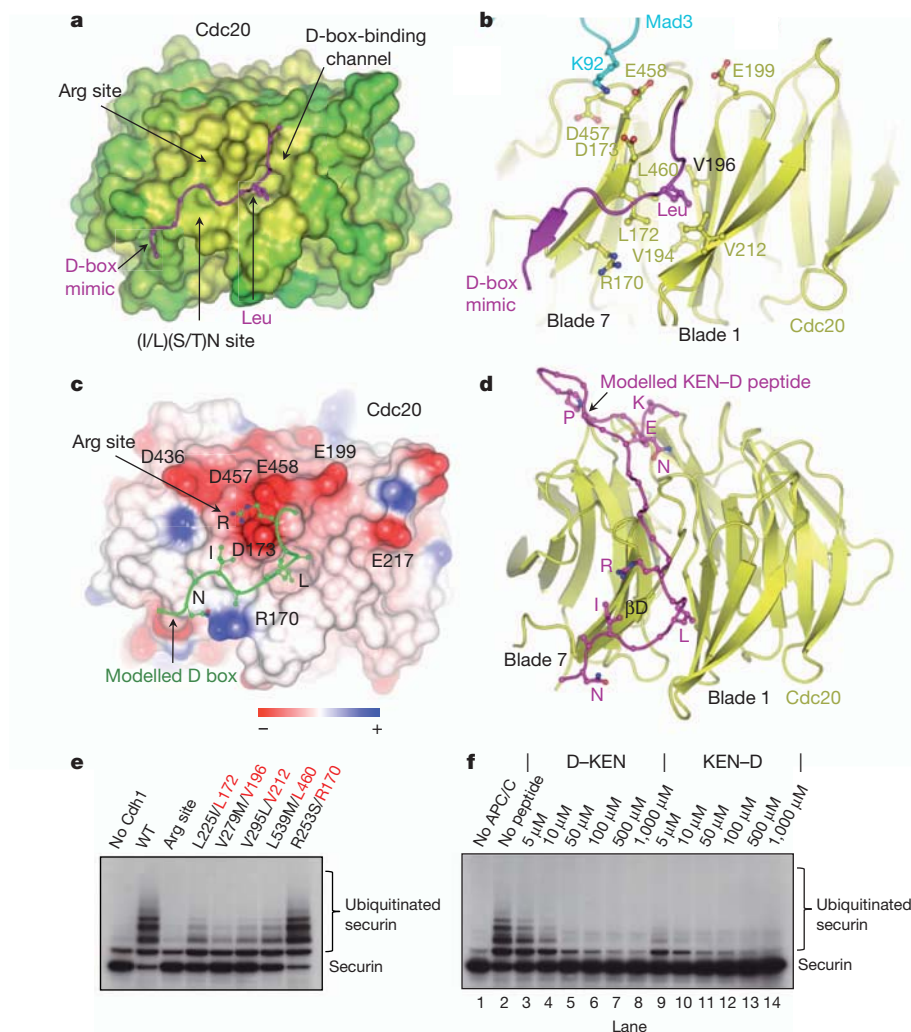


Figure 4 | The D box binds in an extended conformation to a conserved inter-blade channel on the Cdc20 WD40 domain. **a**, Cdc20 shown with surface representation coloured according to sequence conservation of Cdc20 and Cdh1 (yellow (invariant) to green (less conserved)). (Supplementary Fig. 5). D-box mimic (C terminus of Mad3) is shown in purple. **b**, D-box mimic bound through a peptide-in-channel mechanism to Cdc20. Lys 92 of Mad3 contacts the negatively charged D-box Arg-binding site of Cdc20, sterically hindering the D-box receptor of Cdc20. **c**, Negative electrostatic potential of Cdc20 in the vicinity of the Arg-binding site of modelled D box. **d**, Model of a KEN–D peptide bound to KEN and D-box sites of Cdc20. **e**, Mutation of the D-box-binding site abolishes *S. cerevisiae* APC/C^{Cdh1}-mediated ubiquitination of securin as indicated by an IVT-based ubiquitination assay. D-box Arg-binding-site mutants: D256S, D536S, E537S (*S. pombe* Cdc20: D173, D457, E458). Mutated *S. cerevisiae* Cdh1 residues are indicated in black with equivalent residues of *S. pombe* in red. At the D-box Leu-binding site, mutation of *S. pombe* Cdc20 Val 196 had the most notable effect, with little loss of activity for Leu460Met. Mutation of Arg 170, located distal to the Arg and Leu sites (Fig. 4c), did not affect APC/C^{Cdh1} activity. **f**, Ubiquitination competition assay. The KEN–D box peptide inhibits *S. cerevisiae* APC/C^{Cdh1}-mediated securin ubiquitination fivefold more efficiently than does the D-box–KEN-box peptide (compare lanes 5 and 10). Blocking the Leu-binding pocket by small molecules ligands may be a potential mechanism to inhibit APC/C-co-activator activity.

equivalents of the Cdc20 residues Asn 326, Thr 368, Gln 392 and Arg 438 in *Saccharomyces cerevisiae* Cdh1 abolished APC/C^{Cdh1}-catalysed ubiquitination of the KEN-box and D-box-dependent APC/C substrates securin and Clb2 (Fig. 3c and Supplementary Fig. 6). Co-migration of APC/C and Cdh1 on a native gel confirmed that the inactivation was not due to misfolding of the mutant co-activator (Supplementary Fig. 7). Our findings that the KEN box of Mad3 is embedded within a segment of ordered structure, possibly stabilized on the Mad3 HLH motif through contacts to Mad2 (Fig. 1), suggest that degons do not need to be disordered to allow substrate recognition by ubiquitin ligases.

The WD40 domain of co-activators interacts with the D-box degon (RXXLXX(I/L)(S/T)N)^{25,39}, acting as a co-receptor with the APC/C subunit Apc10 (refs 40, 41). However, the molecular details of co-activator–D box interactions have not been established. In the crystal structure of the MCC, an unexpected crystal packing contact, in which the C terminus of a neighbouring Mad3 subunit partially mimics a D box and contacts Cdc20, provides detailed molecular insights of co-activator–D box recognition. The D box mimic of Mad3 was found in an extended conformation engaged within a conserved channel located between blades 1 and 7 on the rim of the β -propeller toroid (Fig. 4b and Supplementary Fig. 8). The interaction is dominated by the burial of the aliphatic side chain of Leu 215 of Mad3, mimicking the Leu of the D-box RXXL motif, within a deep pocket perfectly matching a Leu side chain, and created by non-polar residues invariant in Cdc20 and Cdh1 (Fig. 4a and Supplementary Fig. 5). Other consensus residues of the D box—the essential and

invariant Arg and less-well-conserved (I/L)(S/T)N motif⁴²—are not represented in the Mad3 D-box mimic. However, a candidate recognition site for the Arg side chain of the D box can be assigned to a cluster of negatively charged residues (Asp 173, Asp 457 and Glu 458) located on two adjacent β -strands of blade 7 on the top side of the D-box-binding channel. These residues are suitably positioned to interact with an Arg residue that is N-terminal to the anchored Leu residue, and are conserved in Cdh1 (Fig. 4b, c and Supplementary Fig. 5).

To test whether the putative D-box-binding site that was identified on Cdc20 is responsible for recognizing the D box of APC/C substrates, we generated mutants to abolish individually the equivalent Arg- and Leu-binding sites in Cdh1. Disrupting the Leu-binding pocket by replacing Val 196 with a bulky methionine, and substituting Ser for the Cdh1 equivalents of Asp 173, Asp 457 and Glu 458 at the putative Arg-binding site, eliminated the ability of Cdh1 to stimulate APC/C activity (Fig. 4e and Supplementary Fig. 6) but had no effect on co-activator binding to the APC/C (Supplementary Fig. 7). These results are consistent with the inter-blade channel of Cdc20 functioning as the D-box-binding site. The region of this channel that probably contacts the D-box (I/L)(S/T)N motif is less well conserved between Cdc20 and Cdh1 (Fig. 4a), possibly explaining the differential affinity of the two co-activators for D-box degons.

Substrate and inhibitor recognition by co-activators

To characterize further the APC/C degon-binding sites on co-activators, we designed peptides that incorporate both KEN-box and D-box motifs and tested their ability to inhibit APC/C^{Cdh1}.

Examination of the Cdc20 structure suggested that a peptide with KEN and D boxes linked by 17 residues (KEN–D peptide) would enable cooperative binding of both degrons to their respective binding sites, thereby conferring higher-affinity binding than peptides with either degron alone (Fig. 4d). In contrast, a peptide with the reverse orientation of KEN and D boxes (D–KEN peptide), also connected by a 17-residue linker, would only permit a single degron to bind. When we compared the potential of these peptides to competitively inhibit securin ubiquitination by APC/C^{Cdh1}, we found that the KEN–D peptide was five times more potent as an inhibitor than the D–KEN peptide (Fig. 4f). Because D–KEN peptide inhibited APC/C^{Cdh1} with the same efficiency as a D-box peptide (Supplementary Fig. 9a), these results indicate that cooperative degron binding to Cdh1 was conferred by the specific spatial arrangement of the KEN and D boxes of the KEN–D peptide, in agreement with our assignment of the KEN- and D-box-binding sites on co-activators.

The spatial arrangement of KEN and D boxes in the KEN–D inhibitory peptide is markedly similar to the organization of KEN and D boxes in two APC/C inhibitors: Acm1 and Mes1 (refs 43–45) (Supplementary Fig. 10). Both proteins inhibit the APC/C co-activators through a pseudosubstrate-based mechanism that is dependent on their D and KEN boxes, and it seems reasonable to assume that the spacing of 18 and 24 residues between the KEN and D box degrons of Acm1 and Mes1, respectively, optimizes inhibitor-co-activator affinity. Here we show one mechanism by which a KEN- and D-box-containing protein would bind co-activators. However, because of the diverse configuration and relative separation of KEN- and D-box motifs in APC/C substrates, several modes of co-activator–substrate recognition probably exist. Our assignment of the D-box recognition site to an inter-blade channel of the co-activator β -propeller was recently confirmed by a Cdh1–Acm1 crystal structure (W.C.H.C., D.B. and J. He, unpublished observations).

KEN- and D-box motifs adopt different conformations when bound to Cdc20; the KEN box is an underwound helix (Fig. 3b), whereas the D box assumes an extended structure (Fig. 4b). This important distinction means that the three residues of the KEN motif are presented to the same surface of Cdc20, whereas in the D box alternative amino acid side chains are oriented in opposite directions. Thus, with the Leu side chain of the D box anchored by the co-activator, conserved Arg, Ile/Leu and Asn side chains at positions 1, 7 and 9 of the D box⁴², respectively, would be accessible to generate a composite D-box-co-activator recognition surface for the D-box co-receptor Apc10 (refs 40, 41). This is consistent with the identification of the D-box co-receptor at the interface of co-activator and Apc10 in an APC/C^{Cdh1-D box} ternary complex⁴¹.

Implications for MCC-mediated inhibition of the APC/C

The processes underlying MCC-mediated inhibition of APC/C are incompletely defined, and probably involve several mechanisms. Mad3, which is dependent on its N-terminal KEN box, blocks Cdc20-mediated substrate recognition¹⁵, consistent with our structure showing that the Mad3 KEN box binds to the KEN-box recognition site of Cdc20. Notably, the same KEN box also promotes Mad3-dependent APC/C-mediated degradation of Cdc20 (refs 18, 27, 29), which suggests that Mad3 has a role in positioning Cdc20 for ubiquitination by the APC/C's catalytic centre. To understand this function of Mad3, we docked our MCC coordinates into the electron-microscope-derived molecular envelope of the APC/C–MCC complex¹⁴ (Fig. 5). Interpretation of this structure was based on our previous subunit assignment and pseudo-atomic model of budding yeast APC/C^{Cdh1-D box} (ref. 46). The MCC crystal structure corresponds closely to the assigned MCC density of APC/C^{MCC}, with Cdc20, Mad2 and Mad3 clearly recognizable. Mad2 contacts the TPR subunits Cdc23 and Apc5, whereas Mad3 interacts with Apc1. There is insufficient unassigned density to account for the C-terminal kinase domain of BubR1 and Bub3, suggesting their structural disorder. Notably, the

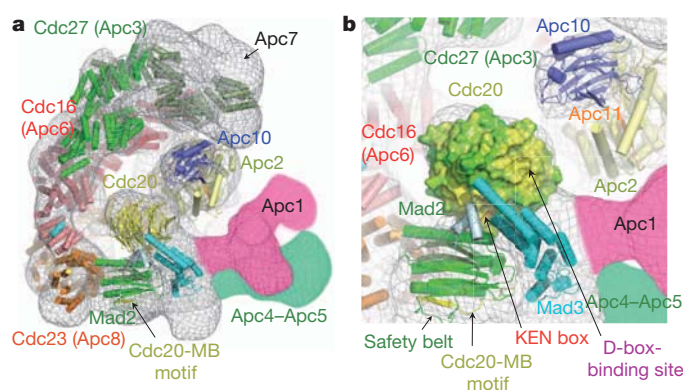


Figure 5 | Pseudo-atomic structure of human APC/C^{MCC}. **a**, Docking of MCC coordinates into a human APC/C^{MCC} electron microscope map¹⁴. APC/C subunit coordinates are based on the pseudo-atomic structure of *S. cerevisiae* APC/C⁴⁶. In the context of the APC/C^{MCC}, Cdc20 is in a downwards position relative to APC/C^{Cdh1} (ref. 41). **b**, Details of MCC interactions with APC/C showing the position of the D-box co-receptor on Cdc20 relative to Apc10 and the catalytic centre of Apc2 and Apc11. The downwards position of Cdc20 prevents interaction with Apc10. Surface representation of Cdc20 is colour-coded from yellow (invariant) to green (less conserved).

KEN-box-binding site of Cdc20 is blocked by Mad3, whereas the D-box site is directed towards, but not in contact with, its co-receptor Apc10 (Fig. 5b). Compared with APC/C^{Cdh1-D box}, in the APC/C^{MCC} complex, Cdc20 is displaced downwards towards Apc5. This position may facilitate Cdc20 ubiquitination. Furthermore, the lower position of co-activator prevents its D-box-binding site from generating a bipartite D-box co-receptor with Apc10 (ref. 41). This, together with a partial steric blockade of the arginine site of the D-box co-receptor of Cdc20 by Lys 92 of the Mad3 TPR domain (Fig. 4b), explains the inability of APC/C^{MCC} to recognize and ubiquitinate D-box-dependent substrates¹⁴. In APC/C^{MCC}, a region of the Cdc20 D-box-binding site for the Leu anchor and C-terminal residues, is accessible (Fig. 5b), suggesting that a non-consensus D-box sequence (that is, lacking an Arg residue and not dependent on the co-receptor Apc10) could engage this site.

In addition to the interactions of Mad2 and Mad3 with APC/C subunits, the position and activity of Cdc20 in the context of APC/C^{MCC} might also be influenced by the sequestration of its N-terminal APC/C recognition motifs by Mad2. The Mad2-binding motif of Cdc20 also mediates APC/C interactions⁴⁷, which would be blocked by the Mad2 safety belt (Fig. 5b). Furthermore, constraining the Cdc20 N terminus by Mad2 might also prevent the neighbouring C box from accessing its APC/C-binding site, which is necessary for Cdc20-dependent stimulation of APC/C catalytic activity⁴⁸.

The SAC is antagonized by p31^{comet} (refs 30,49), and the structure of the C-Mad2–p31^{comet} complex showed that p31^{comet} binds to the Mad2 dimerization interface to inhibit the conformational activation of O-Mad2 (ref. 31). However, it is clear from our MCC structure that because Mad3 and p31^{comet} bind to a common Mad2 interface, p31^{comet} would compete for Mad3 interactions with Mad2 (Fig. 2c), explaining how p31^{comet} both antagonizes the assembly of the MCC³¹ and promotes its disassembly^{32,50}.

Here we show how the molecular basis for APC/C inhibition by its regulators is coupled to degron recognition by co-activators. APC/C activity is modulated by sterically blocking substrate recognition and through conformational changes that disrupt the substrate-binding site, reminiscent of modes of protein kinase regulation. This contrasts with the SCF complex whose activity is regulated at the level of substrate recognition through degron phosphorylation.

METHODS SUMMARY

Expression, purification and crystallization of *S. pombe* MCC. The *S. pombe* MCC (involving Cdc20, Mad2 and Mad3) was generated by co-expressing

Cdc20-Slp1 (residues 87–488), Mad2 (with Leu12Ala and Arg133Ala mutations) and Mad3 (residues 1–223) in the baculovirus and insect cell systems. Crystallization, crystal structure determination, mutagenesis, enzyme assays and other procedures were performed as described in the Methods. Diffraction data were collected at beamline I02 at the Diamond Light Source.

Full Methods and any associated references are available in the online version of the paper at www.nature.com/nature.

Received 26 September 2011; accepted 25 January 2012.

Published online 21 March 2012.

- Musacchio, A. & Salmon, E. D. The spindle-assembly checkpoint in space and time. *Nature Rev. Mol. Cell Biol.* **8**, 379–393 (2007).
- Kim, S. & Yu, H. Mutual regulation between the spindle checkpoint and APC/C. *Semin. Cell Dev. Biol.*, (2011).
- Hoyt, M. A., Totis, L. & Roberts, B. T. *S. cerevisiae* genes required for cell cycle arrest in response to loss of microtubule function. *Cell* **66**, 507–517 (1991).
- Li, R. & Murray, A. W. Feedback control of mitosis in budding yeast. *Cell* **66**, 519–531 (1991).
- Li, Y., Gorbea, C., Mahaffey, D., Rechsteiner, M. & Benezra, R. MAD2 associates with the cyclosome/anaphase-promoting complex and inhibits its activity. *Proc. Natl Acad. Sci. USA* **94**, 12431–12436 (1997).
- Fang, G., Yu, H. & Kirschner, M. W. The checkpoint protein MAD2 and the mitotic regulator CDC20 form a ternary complex with the anaphase-promoting complex to control anaphase initiation. *Genes Dev.* **12**, 1871–1883 (1998).
- Hwang, L. H. *et al.* Budding yeast Cdc20: a target of the spindle checkpoint. *Science* **279**, 1041–1044 (1998).
- Kim, S. H., Lin, D. P., Matsumoto, S., Kitazono, A. & Matsumoto, T. Fission yeast Slp1: an effector of the Mad2-dependent spindle checkpoint. *Science* **279**, 1045–1047 (1998).
- Kallio, M., Weinstein, J., Daum, J. R., Burke, D. J. & Gorbsky, G. J. Mammalian p55CDC mediates association of the spindle checkpoint protein Mad2 with the cyclosome/anaphase-promoting complex, and is involved in regulating anaphase onset and late mitotic events. *J. Cell Biol.* **141**, 1393–1406 (1998).
- Hardwick, K. G., Johnston, R. C., Smith, D. L. & Murray, A. W. MAD3 encodes a novel component of the spindle checkpoint which interacts with Bub3p, Cdc20p, and Mad2p. *J. Cell Biol.* **148**, 871–882 (2000).
- Tang, Z., Bharadwaj, R., Li, B. & Yu, H. Mad2-Independent inhibition of APC^{Cdc20} by the mitotic checkpoint protein BubR1. *Dev. Cell* **1**, 227–237 (2001).
- Fang, G. Checkpoint protein BubR1 acts synergistically with Mad2 to inhibit anaphase-promoting complex. *Mol. Biol. Cell* **13**, 755–766 (2002).
- Sudakin, V., Chan, G. K. & Yen, T. J. Checkpoint inhibition of the APC/C in HeLa cells is mediated by a complex of BUBR1, BUB3, CDC20, and MAD2. *J. Cell Biol.* **154**, 925–936 (2001).
- Herzog, F. *et al.* Structure of the anaphase-promoting complex/cyclosome interacting with a mitotic checkpoint complex. *Science* **323**, 1477–1481 (2009).
- Burton, J. L. & Solomon, M. J. Mad3p, a pseudosubstrate inhibitor of APC^{Cdc20} in the spindle assembly checkpoint. *Genes Dev.* **21**, 655–667 (2007).
- Davenport, J., Harris, L. D. & Goorha, R. Spindle checkpoint function requires Mad2-dependent Cdc20 binding to the Mad3 homology domain of BubR1. *Exp. Cell Res.* **312**, 1831–1842 (2006).
- Kulukian, A., Han, J. S. & Cleveland, D. W. Unattached kinetochores catalyze production of an anaphase inhibitor that requires a Mad2 template to prime Cdc20 for BubR1 binding. *Dev. Cell* **16**, 105–117 (2009).
- Nilsson, J., Yekezare, M., Minshull, J. & Pines, J. The APC/C maintains the spindle assembly checkpoint by targeting Cdc20 for destruction. *Nature Cell Biol.* **10**, 1411–1420 (2008).
- Luo, X. & Yu, H. Protein metamorphosis: the two-state behavior of Mad2. *Structure* **16**, 1616–1625 (2008).
- Luo, X. *et al.* Structure of the Mad2 spindle assembly checkpoint protein and its interaction with Cdc20. *Nature Struct. Biol.* **7**, 224–229 (2000).
- Luo, X., Tang, Z., Rizo, J. & Yu, H. The Mad2 spindle checkpoint protein undergoes similar major conformational changes upon binding to either Mad1 or Cdc20. *Mol. Cell* **9**, 59–71 (2002).
- Sironi, L. *et al.* Crystal structure of the tetrameric Mad1–Mad2 core complex: implications of a ‘safety belt’ binding mechanism for the spindle checkpoint. *EMBO J.* **21**, 2496–2506 (2002).
- De Antoni, A. *et al.* The Mad1/Mad2 complex as a template for Mad2 activation in the spindle assembly checkpoint. *Curr. Biol.* **15**, 214–225 (2005).
- Barford, D. Structure, function and mechanism of the anaphase promoting complex (APC/C). *Q. Rev. Biophys.* **44**, 153–190 (2011).
- Glotzer, M., Murray, A. W. & Kirschner, M. W. Cyclin is degraded by the ubiquitin pathway. *Nature* **349**, 132–138 (1991).
- Pfleger, C. M. & Kirschner, M. W. The KEN box: an APC recognition signal distinct from the D box targeted by Cdh1. *Genes Dev.* **14**, 655–665 (2000).
- King, E. M., van der Sar, S. J. & Hardwick, K. G. Mad3 KEN boxes mediate both Cdc20 and Mad3 turnover, and are critical for the spindle checkpoint. *PLoS ONE* **2**, e342 (2007).
- Sczaniecka, M. *et al.* The spindle checkpoint functions of Mad3 and Mad2 depend on a Mad3 KEN box-mediated interaction with Cdc20-anaphase-promoting complex (APC/C). *J. Biol. Chem.* **283**, 23039–23047 (2008).
- Pan, J. & Chen, R. H. Spindle checkpoint regulates Cdc20p stability in *Saccharomyces cerevisiae*. *Genes Dev.* **18**, 1439–1451 (2004).
- Habu, T., Kim, S. H., Weinstein, J. & Matsumoto, T. Identification of a MAD2-binding protein, CMT2, and its role in mitosis. *EMBO J.* **21**, 6419–6428 (2002).
- Yang, M. *et al.* p31^{comet} blocks Mad2 activation through structural mimicry. *Cell* **131**, 744–755 (2007).
- Reddy, S. K., Rape, M., Margansky, W. A. & Kirschner, M. W. Ubiquitination by the anaphase-promoting complex drives spindle checkpoint inactivation. *Nature* **446**, 921–925 (2007).
- D’Arcy, S., Davies, O. R., Blundell, T. L. & Bolanos-Garcia, V. M. Defining the molecular basis of BubR1 kinetochore interactions and APC/C-CDC20 inhibition. *J. Biol. Chem.* **285**, 14764–14776 (2010).
- Malureanu, L. A. *et al.* BubR1 N terminus acts as a soluble inhibitor of cyclin B degradation by APC/C(Cdc20) in interphase. *Dev. Cell* **16**, 118–131 (2009).
- Schwab, M., Neutzner, M., Mockler, D. & Seufert, W. Yeast Hct1 recognizes the mitotic cyclin Clb2 and other substrates of the ubiquitin ligase APC. *EMBO J.* **20**, 5165–5175 (2001).
- Vodermaier, H. C., Gieffers, C., Maurer-Stroh, S., Eisenhaber, F. & Peters, J. M. TPR subunits of the anaphase-promoting complex mediate binding to the activator protein CDH1. *Curr. Biol.* **13**, 1459–1468 (2003).
- Mapelli, M., Massimiliano, L., Santaguida, S. & Musacchio, A. The Mad2 conformational dimer: structure and implications for the spindle assembly checkpoint. *Cell* **131**, 730–743 (2007).
- Tipton, A. R. *et al.* BUBR1 and closed MAD2 (C-MAD2) interact directly to assemble a functional mitotic checkpoint complex. *J. Biol. Chem.* **286**, 21173–21179 (2011).
- Kraft, C., Vodermaier, H. C., Maurer-Stroh, S., Eisenhaber, F. & Peters, J. M. The WD40 propeller domain of Cdh1 functions as a destruction box receptor for APC/C substrates. *Mol. Cell* **18**, 543–553 (2005).
- Carroll, C. W., Enquist-Newman, M. & Morgan, D. O. The APC subunit Doc1 promotes recognition of the substrate destruction box. *Curr. Biol.* **15**, 11–18 (2005).
- da Fonseca, P. C. *et al.* Structures of APC/C(Cdh1) with substrates identify Cdh1 and Apc10 as the D-box co-receptor. *Nature* **470**, 274–278 (2011).
- King, R. W., Glotzer, M. & Kirschner, M. W. Mutagenic analysis of the destruction signal of mitotic cyclins and structural characterization of ubiquitinated intermediates. *Mol. Biol. Cell* **7**, 1343–1357 (1996).
- Choi, E., Dial, J. M., Jeong, D. E. & Hall, M. C. Unique D box and KEN box sequences limit ubiquitination of Acm1 and promote pseudosubstrate inhibition of the anaphase-promoting complex. *J. Biol. Chem.* **283**, 23701–23710 (2008).
- Ostapenko, D., Burton, J. L., Wang, R. & Solomon, M. J. Pseudosubstrate inhibition of the anaphase-promoting complex by Acm1: regulation by proteolysis and Cdc28 phosphorylation. *Mol. Cell Biol.* **28**, 4653–4664 (2008).
- Kimata, Y. *et al.* A mutual inhibition between APC/C and its substrate Mes1 required for meiotic progression in fission yeast. *Dev. Cell* **14**, 446–454 (2008).
- Schreiber, A. *et al.* Structural basis for the subunit assembly of the anaphase-promoting complex. *Nature* **470**, 227–232 (2011).
- Zhang, Y. & Lees, E. Identification of an overlapping binding domain on Cdc20 for Mad2 and anaphase-promoting complex: model for spindle checkpoint regulation. *Mol. Cell Biol.* **21**, 5190–5199 (2001).
- Kimata, Y., Baxter, J. E., Fry, A. M. & Yamano, H. A role for the Fizzy/Cdc20 family of proteins in activation of the APC/C distinct from substrate recruitment. *Mol. Cell* **32**, 576–583 (2008).
- Xia, G. *et al.* Conformation-specific binding of p31(comet) antagonizes the function of Mad2 in the spindle checkpoint. *EMBO J.* **23**, 3133–3143 (2004).
- Westhorpe, F. G., Tighe, A., Lara-Gonzalez, P. & Taylor, S. S. p31 comet-mediated extraction of Mad2 from the MCC promotes efficient mitotic exit. *J. Cell Sci.* **124**, 3905–3916 (2011).

Supplementary Information is linked to the online version of the paper at www.nature.com/nature.

Acknowledgements This work was funded by a Cancer Research UK grant to D.B. and an ICR studentship to W.C.H.C. We thank J. Yang and J. He for advice, and staff at the Diamond Light Source beamline I02 for help with data collection.

Author Contributions W.C.H.C. cloned, purified and crystallized the *S. pombe* MCC, and performed the biochemistry and mutagenesis experiments. W.C.H.C., K.K. and D.B. collected the X-ray diffraction data. K.K. determined the complex structure and modelled the D-box and KEN–D peptides. Z.Z. advised on cloning strategies of the MCC. E.H.K. provided purified endogenous APC/C. W.C.H.C., K.H.K. and D.B. docked crystal coordinates into the human APC/C^{MCC} electron-microscope map. W.C.H.C. and D.B. wrote the manuscript and the others authors provided editorial input.

Author Information The MCC coordinates have been deposited in the Protein Data Bank under accession number 4aez. Reprints and permissions information is available at www.nature.com/reprints. The authors declare no competing financial interests. Readers are welcome to comment on the online version of this article at www.nature.com/nature. Correspondence and requests for materials should be addressed to D.B. (david.barford@icr.ac.uk).

METHODS

Cloning, expression and purification of the MCC complex.

Schizosaccharomyces pombe CDC20–SLP1 (residues 87–488), MAD2 (residues 1–203) and MAD3 (residues 1–223) genes were amplified by polymerase chain reaction (PCR) using an *S. pombe* complementary DNA library pTN–TH7 (a gift from T. Nakamura) as a template and cloned into a modified pFBDM vector⁵¹ (Z.Z. & D.B., unpublished observations). A double Strep-tag II (ds) together with a tobacco etch virus (TEV) cleavage site were introduced into the N terminus of Cdc20–Slp1 and mutations of Leu12Ala and Arg133Ala were introduced into Mad2 (ref. 31). A previous study showed that the Arg133Ala mutant was fully capable of inducing a mitotic arrest⁵². The resultant protein expression cassettes were recombined with the DH10MultiBac cells to create a bacmid by transposition⁵¹. The ds–Cdc20–Mad2–Mad3 complex was expressed using the baculovirus and insect cell (High 5 cells) systems, and purified by a combination of Strep-Tactin (Qiagen), anion exchange chromatography Resource Q and Superdex 200 size-exclusion chromatography (GE Healthcare). The identities of the purified complex subunits were confirmed by antibody labelling and N-terminal sequencing. Mutagenesis was performed to generate the Mad2–Mad3 interface mutant, Cdc20–Mad2(A137Y)–Mad3(M13R).

Crystallization, data collection and structure determination. Crystals were obtained in a hanging-drop fashion by pre-incubating 1:1 v/v of 4.5 mg ml^{−1} of protein with the crystallization solution, 100 mM Tris–HCl pH 8.8, 21% PEG 3350, 30% ethylene glycol, 5 mM dithiothreitol (DTT), and 5 mM EDTA at 20 °C for 24 h, followed by streak seeding. Crystals grew to full size after 2 weeks and were mounted in 0.2–0.3 mm cryoloops and frozen in liquid nitrogen. Native crystals diffracted to a minimum Bragg spacing (d_{\min}) of about 2.1 Å. The diffraction data set was collected at the I02 beamline of Diamond Light Source from a single crystal, processed with XDS and scaled to 2.3 Å with SCALA⁵³. Phase information was obtained by molecular replacement with AMoRe⁵⁴. Monomeric coordinates from the crystal structures of human MAD2(L13A) (PDB 2VFX)⁵⁵, human BUBR1 (PDB 2WV1)³³ and human WDR5 (PDB 3EMH)⁵⁶ were used as search models. All three trimeric complexes (MCC complexes) that are present in the asymmetric unit were assembled with repeated runs of AMoRe. Iterative model building and refinements were carried out with COOT⁵⁷ and PHENIX⁵⁸, respectively. Simulated annealing composite omit maps were systematically calculated at several stages of model building and refinement, and examined to minimize the effects of model bias. TLS parameters that were generated from the TLS motion determination server⁵⁹ (<http://skuld.bmsc.washington.edu/~tksmd/>) were used throughout the refinement. Water molecules were added towards the end of the refinement. The structure was validated with MolProbity⁶⁰. Data collection and refinement statistics are given in Supplementary Table 1.

APC/C ubiquitination assays with wild-type and mutant Cdh1. *Saccharomyces cerevisiae* Cdh1 mutants were generated using PCR-based mutagenesis and cloned into a linearized pRSET vector. A functional T7 promoter and the Cdh1 sequences were confirmed by DNA sequencing. APC/C ubiquitination assays were adopted and modified from ref. 61. ³⁵S-labelled Clb2p and securin (Pds1p) and unlabelled Cdh1 mutants were prepared using TNT T7 Quick-coupled *in vitro* transcription (or translation) (IVT; Promega). Each ubiquitination reaction contains approximately 10 ng of *S. cerevisiae* APC/C, 1 µl of ³⁵S-labelled substrate and 2 µl of Cdh1 in a 10-µl reaction volume with 40 mM Tris–HCl pH 7.5, 10 mM MgCl₂, 0.6 mM DTT, 2.7 mM ATP, 6.6 µg of methyl ubiquitin, 500 ng of Ubc4, 200 ng of ubiquitin aldehyde (Enzo Life Science), 2 µM

LLnL (*N*-acetyl-Leu-Leu-Norleu-aldehyde) (Sigma). Reactions were incubated at room temperature for 15 min and were analysed using 8% SDS–PAGE. Gels were fixed and stained with Coomassie blue, then dried and exposed to BioMax MR Film (Kodak).

Native gel electrophoresis. Correct folding of *S. cerevisiae* Cdh1 mutants was assessed by their co-migration with the APC/C in native gel electrophoresis. 50 ng of apoAPC/C was mixed with 2 µl of ³⁵S-labelled IVT-produced Cdh1 and 0.7 µl of 100 mM CaCl₂ in a volume of 14 µl with 10 mM Tris pH 8.0, 150 mM NaCl, 3 mM DTT, 1 mM magnesium acetate and 2 mM EGTA. Samples were incubated at room temperature for 15 min before adding 1 µl of native gel loading buffer (125 mM Tris pH 8.0, 84% (v/v) glycerol) to each reaction. The entire reaction was loaded onto a 5.25% non-denaturing polyacrylamide gel run at 4 °C, 110 V for 2 h. Gels were fixed and stained with Coomassie blue, then dried and exposed to film.

KEN–D peptide competition assays. The KEN–D (Ac–NKENEGPASGASGASGASGAQRAALSDITNS–NH₂), D–KEN (Ac–QRAALSDITNSGASGASGASGASGASGASGAQRAALSDITNS–NH₂), KEN–D^{mut} (Ac–NKENEGPASGASGASGASGAQSAASDITSS–NH₂) and KEN^{mut}–D (Ac–NSASEGPASGASGASGASGAQRAALSDITNS–NH₂) peptides were designed with a 17-residue linker between the KEN-box sequence (NKENEGPA) and the D-box sequence (QRAALSDITNS), or between their respective mutant sequences (NSASEGPA and QSAASDITSS). The peptides were synthesized by Cambridge Peptides. APC/C ubiquitination reactions were performed in the same way as described above using the co-purified APC/C^{Cdh1} complex⁴¹. Peptides were added into the reaction to a final concentration ranging from 5 µM to 1000 µM. Reactions were incubated at room temperature for 15 min and were analysed using 8% SDS–PAGE. Gels were fixed and stained with Coomassie blue, then dried and exposed to film.

Fitting structure coordinates into the human APC/C^{MCC} EM map. The structure coordinates of *S. pombe* Cdc16–Cdc26 complex (PDB 2XPI), Cdc27 (PDB 3KAE), Apc10 (PDB 1GQP), modelled Apc2 and MCC were fitted into the human APC/C^{MCC} map (EMD–1591) based on the *S. cerevisiae* APC/C assignment⁴⁶, using UCSF Chimera.

51. Berger, I., Fitzgerald, D. J. & Richmond, T. J. Baculovirus expression system for heterologous multiprotein complexes. *Nature Biotechnol.* **22**, 1583–1587 (2004).
52. Sironi, L. *et al.* Mad2 binding to Mad1 and Cdc20, rather than oligomerization, is required for the spindle checkpoint. *EMBO J.* **20**, 6371–6382 (2001).
53. Evans, P. Scaling and assessment of data quality. *Acta Crystallogr. D* **62**, 72–82 (2006).
54. Navaza, J. Implementation of molecular replacement in AMoRe. *Acta Crystallogr. D* **57**, 1367–1372 (2001).
55. Yang, M. *et al.* Insights into mad2 regulation in the spindle checkpoint revealed by the crystal structure of the symmetric mad2 dimer. *PLoS Biol.* **6**, e50 (2008).
56. Song, J. J. & Kingston, R. E. WDR5 interacts with mixed lineage leukemia (MLL) protein via the histone H3-binding pocket. *J. Biol. Chem.* **283**, 35258–35264 (2008).
57. Emsley, P. & Cowtan, K. Coot: model-building tools for molecular graphics. *Acta Crystallogr. D* **60**, 2126–2132 (2004).
58. Adams, P. D. *et al.* PHENIX: building new software for automated crystallographic structure determination. *Acta Crystallogr. D* **58**, 1948–1954 (2002).
59. Painter, J. & Merritt, E. A. Optimal description of a protein structure in terms of multiple groups undergoing TLS motion. *Acta Crystallogr. D* **62**, 439–450 (2006).
60. Davis, I. W. *et al.* MolProbity: all-atom contacts and structure validation for proteins and nucleic acids. *Nucleic Acids Res.* **35**, W375–W383 (2007).
61. Passmore, L. A., Barford, D. & Harper, J. W. Purification and assay of the budding yeast anaphase-promoting complex. *Methods Enzymol.* **398**, 195–219 (2005).

Role of corin in trophoblast invasion and uterine spiral artery remodelling in pregnancy

Yujie Cui^{1*†}, Wei Wang^{1*†}, Ningzheng Dong^{2,3*}, Jinglei Lou^{1*}, Dinesh Kumar Srinivasan^{1†}, Weiwei Cheng⁴, Xiaoyi Huang⁴, Meng Liu², Chaodong Fang², Jianhao Peng¹, Shenghan Chen¹, Shannon Wu¹, Zhenzhen Liu², Liang Dong², Yiqing Zhou² & Qingyu Wu^{1,2}

In pregnancy, trophoblast invasion and uterine spiral artery remodelling are important for lowering maternal vascular resistance and increasing uteroplacental blood flow. Impaired spiral artery remodelling has been implicated in pre-eclampsia, a major complication of pregnancy, for a long time but the underlying mechanisms remain unclear^{1,2}. Corin (also known as atrial natriuretic peptide-converting enzyme) is a cardiac protease that activates atrial natriuretic peptide (ANP), a cardiac hormone that is important in regulating blood pressure³. Unexpectedly, corin expression was detected in the pregnant uterus⁴. Here we identify a new function of corin and ANP in promoting trophoblast invasion and spiral artery remodelling. We show that pregnant corin- or ANP-deficient mice developed high blood pressure and proteinuria, characteristics of pre-eclampsia. In these mice, trophoblast invasion and uterine spiral artery remodelling were markedly impaired. Consistent with this, the ANP potently stimulated human trophoblasts in invading Matrigels. In patients with pre-eclampsia, uterine *Corin* messenger RNA and protein levels were significantly lower than that in normal pregnancies. Moreover, we have identified *Corin* gene mutations in pre-eclamptic patients, which decreased corin activity in processing pro-ANP. These results indicate that corin and ANP are essential for physiological changes at the maternal-fetal interface, suggesting that defects in corin and ANP function may contribute to pre-eclampsia.

Pregnancy poses a serious challenge for maintaining normal blood pressure. Pregnancy-induced hypertension, a major cause of maternal and fetal deaths, occurs in approximately 10% of pregnancies^{5,6}. During pregnancy, the uterus undergoes profound morphological changes, including trophoblast invasion and spiral artery remodelling. In pre-eclampsia, impaired spiral artery remodelling is common, but the underlying mechanisms are unclear^{1,2,7-9}. Studies indicate that vascular growth factor receptors, angiotensin and oestradiol are involved in the disease¹⁰⁻¹⁴.

Corin is a cardiac protease that activates ANP, which is a cardiac hormone that regulates blood pressure and sodium homeostasis¹⁵. In mice, lack of CORIN prevents ANP generation and causes hypertension¹⁶. In humans, CORIN variants are associated with hypertension¹⁷. Interestingly, *Corin* expression was detected in the pregnant mouse⁴ (Fig. 1A) and human uterus (Supplementary Fig. 1). As a transmembrane protein, CORIN is expected to act at the expression sites, suggesting a possible function in the pregnant uterus.

To understand the role of CORIN in pregnancy, we created a mouse model in which a *Corin* transgene was expressed under a cardiac promoter (Fig. 1B). The transgenic and *Corin* knockout mice were crossed to generate mice expressing *Corin* only in the heart ('knockout/transgenic mice'; Fig. 1C, D). In knockout/transgenic mice, transgenic *Corin* expression restored pro-ANP processing in the heart (Supplementary Fig. 2) and normalized blood pressure (Fig. 1E),

indicating that cardiac CORIN was sufficient to maintain normal blood pressure in non-pregnant mice.

In pregnant *Corin* knockout mice, blood pressure increased at approximately 17 days post coitus and rose further before returning to the non-pregnant blood pressure level after delivery (Fig. 1F), which resembled late gestational hypertension in pre-eclamptic women. In *Corin* knockout/transgenic mice, which were normotensive, blood pressure increased similarly during pregnancy (Fig. 1G), indicating that cardiac *Corin* expression did not prevent pregnancy-induced hypertension. The data also show that in these mice, hypertension in pregnancy was not due to pre-existing high blood pressure. As well as in the uterus, *Corin* mRNA was detected in the umbilical cord and placenta (Supplementary Fig. 3). To distinguish the role of maternal *Corin* from that of placental or other fetal organs, *Corin* knockout females were mated with either wild-type or knockout males. The resulting fetuses carried one or no copy of the functional *Corin* gene. Normally, enzymes that are encoded by one gene copy are able to function. As shown in Fig. 1H, pregnant *Corin* knockout females that were mated with either wild-type or knockout males had similarly increased blood pressure, indicating that lack of maternal, but not fetal, *Corin* caused hypertension in pregnancy.

Proteinuria is a hallmark of pre-eclampsia. Wild-type, *Corin* knockout and knockout/transgenic mice had similar urinary protein levels before pregnancy and at mid gestation. However, the levels increased in *Corin* knockout and knockout/transgenic mice at late gestation (Fig. 1I), consistent with reported proteinuria in mouse models of pre-eclampsia¹⁸. Ischaemic glomeruli, indicated by fewer red blood cells, were found in pregnant *Corin* knockout and knockout/transgenic mice (Fig. 1J, a–f) but not in non-pregnant mice (Supplementary Fig. 4). Periodic acid–Schiff staining revealed increased extracellular matrices and collapsed glomerular capillaries in pregnant *Corin* knockout and knockout/transgenic mice (Fig. 1J, g–i). Electron microscopy showed narrow glomerular capillary lumens and thick basement membranes (Fig. 1K), suggesting endotheliosis and increased extracellular matrices. Additional pathological features such as necrotic cells and calcium deposits in the placental labyrinth also existed in these mice (Supplementary Fig. 5), indicating insufficient uteroplacental perfusion. Consistent with this, *Corin* knockout and knockout/transgenic mice had smaller litters (7.1 ± 2.3 ($n = 28$) and 6.8 ± 2.7 ($n = 28$) pups per litter, respectively, versus wild-type mice, which had 9.1 ± 1.2 ($n = 21$) pups per litter; $P < 0.001$ in both cases).

We examined embryos at embryonic day 12.5 (E12.5), an early time point before blood pressure increase in *Corin* knockout and knockout/transgenic mice, and E18.5 (two days before delivery). Wild-type E12.5 embryos showed obvious trophoblast invasion, shown by cytokeratin staining (Fig. 2a), and large vessels mostly in the deep decidua, shown by smooth-muscle α -actin (SMA) staining (Fig. 2b), indicating that

¹Molecular Cardiology, Nephrology and Hypertension, Lerner Research Institute, Cleveland Clinic, 9500 Euclid Avenue, Cleveland, Ohio 44195, USA. ²Cyrus Tang Hematology Center, Jiangsu Institute of Hematology, the First Affiliated Hospital, Soochow University, 199 Ren Ai Road, Suzhou 215123, China. ³Key Lab of Thrombosis and Hemostasis, Jiangsu Institute of Hematology, the First Affiliated Hospital, Soochow University, 188 Shi Zhi Street, Suzhou 215006, China. ⁴The International Peace Maternity and Child Health Hospital, Shanghai Jiaotong University School of Medicine, 910 Hengshan Road, Shanghai 200030, China. [†]Present address: School of Laboratory Science, Tianjin Medical University, Tianjin 300203, China (Y.C.); Department of Cardiology, Peking Union Medical College, Beijing 100730, China (W.W.); Lee Kong Chian School of Medicine, Singapore 637553 (D.K.S.).

*These authors contributed equally to this work.

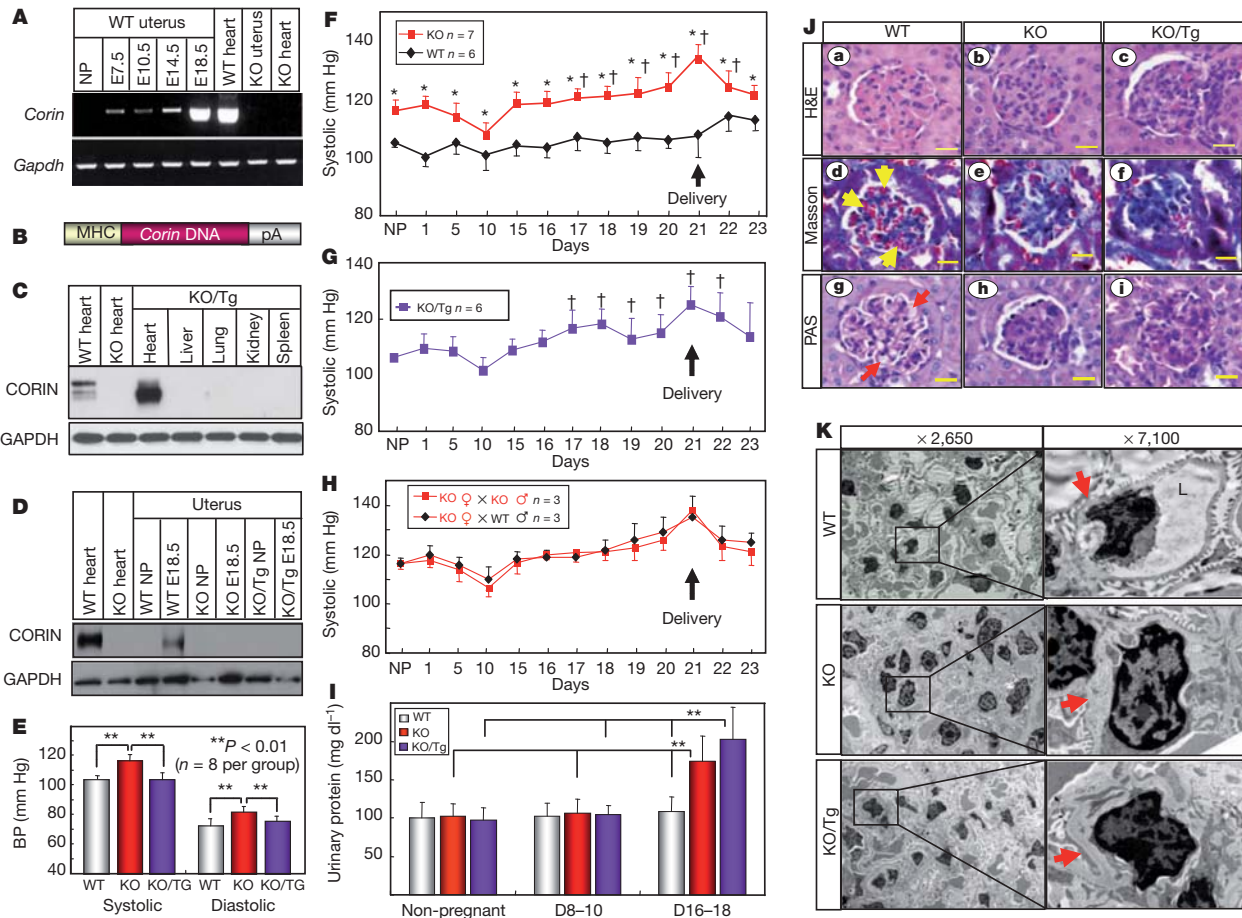


Figure 1 | Hypertension, proteinuria and renal pathology in pregnant *Corin* knockout and knockout/transgenic mice. **A**, *Corin* mRNA expression in mouse uterus. **B**, *Corin* transgenic (Tg) construct. **C**, **D**, Western blot analysis of CORIN protein in wild-type (WT), *Corin* knockout (KO) and knockout/transgenic mice. **E**, Blood pressure (BP, mean \pm s.d.) in non-pregnant females. **F**, **G**, Blood pressure increased in *Corin* knockout (F) and knockout/transgenic (G) mice in pregnancy. Data are mean \pm s.d. $^{*}P < 0.05$ versus WT of the same time point. $^{\dagger}P < 0.05$ versus non-pregnant level of the same genotype. **H**, Similar blood-pressure changes in *Corin* knockout females mated with knockout or WT males. **I**, Late gestational proteinuria in *Corin*

knockout and knockout/transgenic mice. Data are mean \pm s.d. $^{**}P < 0.01$, $n = 7$ or 8 per group. **J**, **a–i**, Renal ischaemia in pregnant *Corin* knockout and knockout/transgenic mice. E18.5 sections are stained with haematoxylin and eosin (H&E), Masson trichrome or periodic acid–Schiff (PAS). Scale bar, 20 μ m. Red blood cells (yellow arrows) and open capillaries (red arrows) in WT glomeruli are shown. **K**, Narrow glomerular capillary lumen (L) and thick basement membranes (red arrows) in *Corin* knockout and knockout/transgenic mice at E18.5 shown by electron microscopy. GAPDH, glyceraldehyde 3-phosphate dehydrogenase; NP, non pregnant; pA, poly A.

smooth muscles in the superficial decidua were replaced by invading trophoblasts. In contrast, trophoblast invasion in *Corin* knockout and knockout/transgenic embryos was markedly reduced (Fig. 2a) and smaller arteries were found in both superficial and deep decidua (Fig. 2b). In E18.5 wild-type embryos, more abundant trophoblasts were found in the decidua and myometrium compared with those in *Corin* knockout and knockout/transgenic mice (Fig. 2c, d). By haematoxylin and eosin staining, larger and more abundant decidual spiral arteries were observed in wild-type than in *Corin* knockout or knockout/transgenic mice (Fig. 2e). Figure 2f–h shows strong cytokeratin (trophoblasts) staining but weak von Willebrand factor (endothelial) and SMA (smooth muscle) staining in wild-type decidual and myometrial arteries. These data indicate that trophoblast invasion and spiral artery remodelling were impaired in *Corin* knockout and knockout/transgenic mice, and that this defect occurred before blood pressure increased in these mice.

CORIN activates ANP in the heart¹⁵ but it was unknown whether the CORIN function in pregnancy was also mediated by ANP. Pro-ANP is expressed in the non-pregnant and pregnant uterus (Supplementary Fig. 6). If CORIN acts on pro-ANP to promote trophoblast invasion and spiral artery remodelling, thereby preventing hypertension in pregnancy, ANP (also known as *Nppa*) and *Corin* knockout mice should have similar phenotypes. ANP knockout mice are hypertensive (Fig. 3a)

but their blood pressure was not monitored during pregnancy¹⁹. We found similarly increased blood pressure in pregnant ANP knockout mice (Fig. 3b). The mice also had late gestational proteinuria (Fig. 3c) and smaller litters (4.4 ± 1.7 ($n = 25$) versus wild-type, 9.1 ± 1.2 ($n = 21$) pups per litter, $P < 0.001$). By immunostaining, impaired trophoblast invasion and smaller spiral arteries were observed in E12.5 embryos (Fig. 3d, e). In E18.5 embryos, ANP knockout mice had far fewer trophoblasts (Fig. 3f, g) and smaller arteries (Fig. 3h) in the decidua and myometrium than those in wild-type mice. Consistent with this, weak cytokeratin-staining but strong von Willebrand factor-staining were found in arteries in ANP knockout mice (Fig. 3i). Thus, ANP and *Corin* knockout mice had very similar phenotypes, indicating that the role of CORIN in pregnancy is probably mediated by ANP.

In the heart, CORIN produces ANP, which then regulates blood pressure by promoting natriuresis and vasodilation³. Here we found that lack of CORIN and ANP impaired trophoblast invasion and spiral artery remodelling, which was not rescued by cardiac *Corin* expression in *Corin* knockout/transgenic mice. ANP is known to relax vascular smooth muscles. Recently, ANP and its downstream cyclic GMP-dependent protein kinase were shown to be important in angiogenic processes by promoting endothelial regeneration^{20,21}. Thus, ANP may function locally to remodel uterine arteries. Our results also indicate that ANP may directly promote trophoblast invasion (Fig. 4a), and we

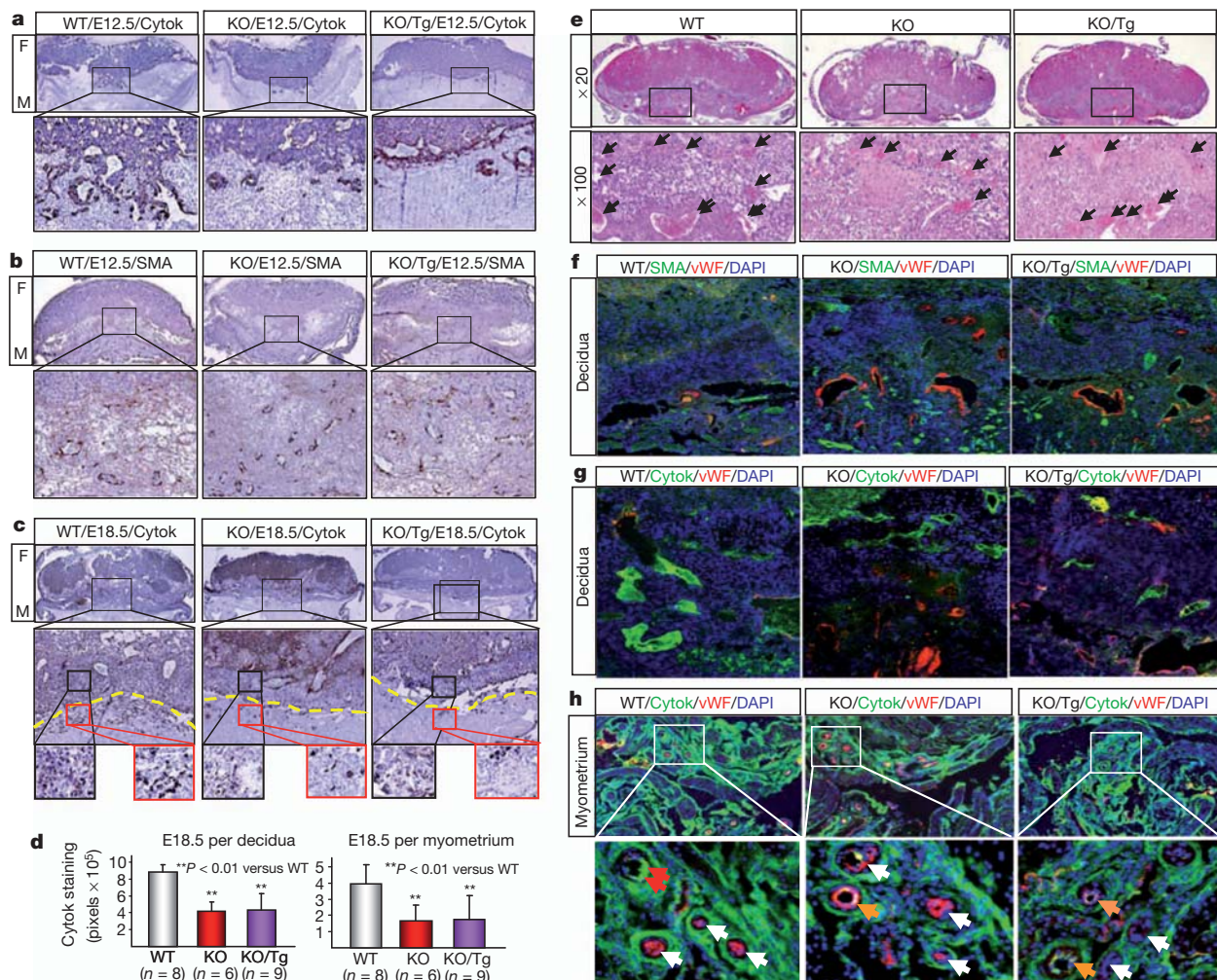


Figure 2 | Impaired trophoblast invasion and spiral artery remodelling in *Corin* knockout and knockout/transgenic mice. **a, b,** E12.5 embryo sections were stained for trophoblasts (**a**) or smooth muscles (**b**). Fetal (F) and maternal (M) sides are indicated. Boxed areas in top panels are shown at a higher magnification ($\times 200$). **c,** E18.5 embryo sections were stained for trophoblasts. In lower panels ($\times 100$), yellow lines show the decidua and myometrium boundary.

therefore tested this idea. We found that ANP markedly stimulated human trophoblasts to invade Matrigels (Fig. 4b) (Supplementary Fig. 7a). In these cells, ANP receptor (also known as atrial natriuretic peptide receptor 1) mRNA expression was confirmed (Supplementary Fig. 7b) and ANP-stimulated intracellular cGMP production was detected (Fig. 4c) (Supplementary Fig. 7c).

Our findings emphasize the importance of local ANP production by CORIN, which acts on trophoblasts and vascular cells in the uterus. Because heart-derived ANP circulates inside the vessel, our model may explain why cardiac CORIN failed to promote trophoblast invasion and uterine artery remodelling, as shown in *Corin* knockout/transgenic mice. To verify this hypothesis, we quantified *Corin* mRNA and protein in human uteruses by polymerase chain reaction with reverse transcription (RT-PCR) and enzyme-linked immunosorbent assay (ELISA). The levels were low in non-pregnant women but increased in pregnant women (Fig. 4d, e). In pre-eclamptic women, the levels were significantly lower than in normal pregnancies. Similar results were found by immunostaining (Fig. 4d and Supplementary Fig. 8). Consistent with this, pro-ANP levels in uterine tissues were significantly higher in pre-eclamptic women than in normal pregnant women (Fig. 4f), indicating that reduced uterine *Corin* expression impaired pro-ANP processing in these patients. *Corin* is a membrane-bound protein^{4,15}, and recent studies showed that CORIN can be shed from

cardiomyocytes and that soluble CORIN is found in human plasma^{22,23}. We found that plasma CORIN levels were higher in pre-eclamptic patients than non-pregnant or normal pregnant women (Fig. 4g). Thus, CORIN levels in plasma did not reflect the levels in tissues, indicating that plasma CORIN was probably derived from the heart, where *Corin* expression increased in response to high blood volume and high blood pressure in pregnancy. These results provide further support for a local function of CORIN in the pregnant uterus.

We next sequenced the *CORIN* gene²⁴ in pre-eclamptic patients and identified a mutation that alters Lys to Glu at position 317 in low-density lipoprotein receptor repeat 2 in one woman (Fig. 4h, j) and another mutation altering Ser to Gly at position 472 in the frizzled 2 domain in two women from the same family who had pre-eclampsia (Fig. 4i, j). In functional studies, Lys317Glu and Ser472Gly mutations did not affect CORIN expression in HEK293 cells but markedly reduced CORIN activity in processing pro-ANP (Fig. 4k–n). The data were consistent with previous findings that Low-density lipoprotein receptor repeats and frizzled domains are critical for CORIN activity²⁵, suggesting that the mutations may impair CORIN function in the patients, thereby contributing to pre-eclampsia. Interestingly, CORIN variants in the frizzled 2 domain that impaired CORIN function have been reported in African American people^{17,26}, a high-risk population for pre-eclampsia.

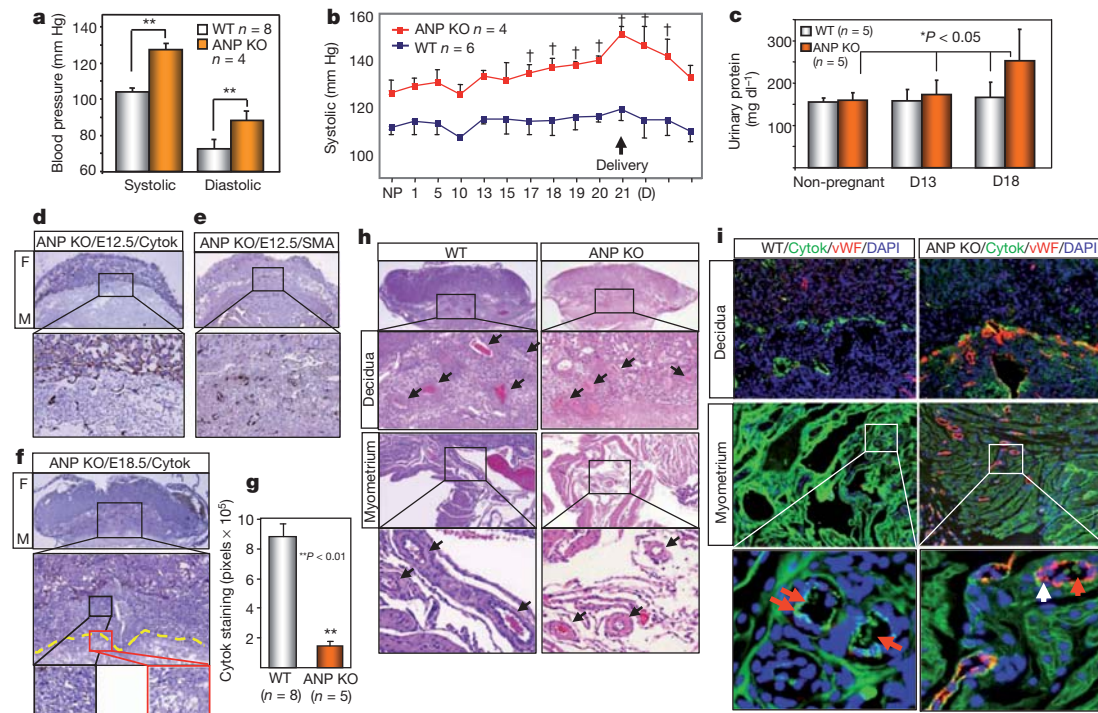


Figure 3 | Hypertension, proteinuria and uteroplacental pathology in pregnant ANP knockout mice. **a**, Blood pressure (mean \pm s.d.) in non-pregnant females, $**P < 0.01$. **b**, Elevated blood pressure (mean \pm s.d.) in pregnant ANP knockout mice. $\dagger P < 0.05$ versus non-pregnant level. **c**, Gestational proteinuria in ANP knockout mice. Data are mean \pm s.d. **d**, **e**, Impaired trophoblast invasion and smooth muscle remodelling in E12.5 embryos stained for cytokeratin (**d**) or SMA (**e**). Boxed areas in top panels are

shown at a higher magnification ($\times 200$). **f**, Impaired trophoblast invasion in E18.5 embryos stained for cytokeratin. **g**, Quantitative data (mean \pm s.d.) of cytokeratin staining in E18.5 ANP knockout embryos. **h**, Impaired decidual and myometrial artery remodelling (arrows) in H&E-stained E18.5 ANP knockout embryos. **i**, Co-staining of cytokeratin, von Willebrand factor and nuclei in E18.5 ANP knockout embryos. Red arrows indicate cytokeratin (green) signals and white arrows indicate von Willebrand factor (red) signals.

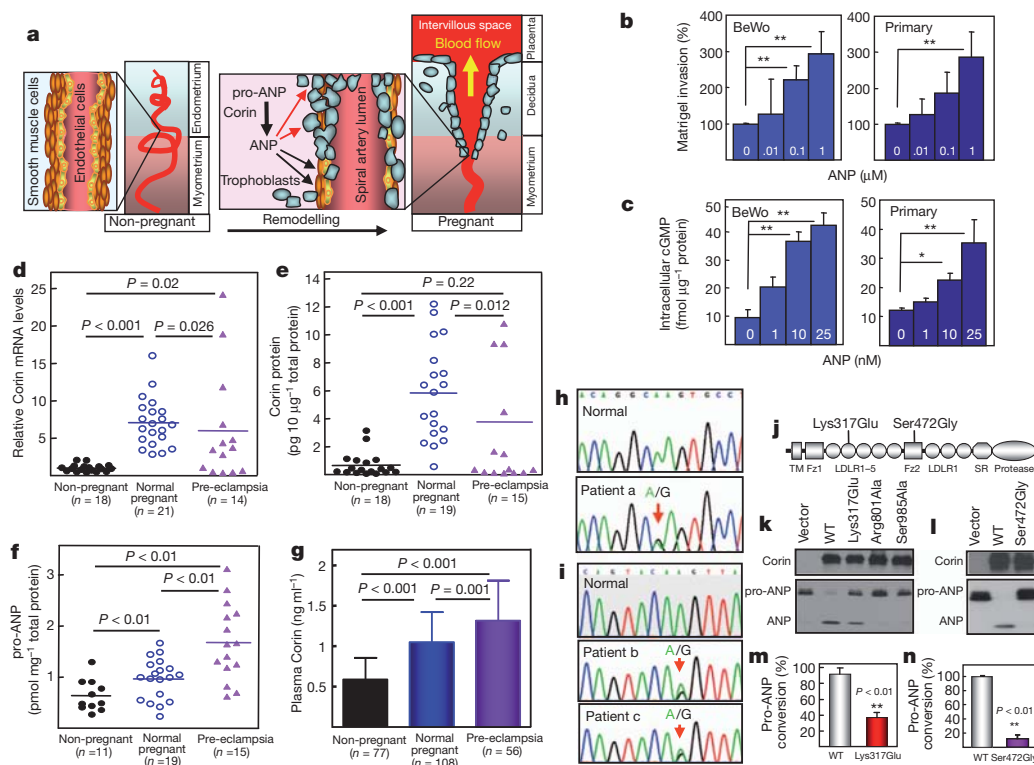


Figure 4 | ANP-stimulated human trophoblast invasion, and impaired uterine Corin expression and Corin mutations in pre-eclamptic patients. **a**, A model showing that CORIN-produced ANP in the pregnant uterus promotes trophoblast invasion (red arrows) and vascular-wall remodelling (black arrows). **b**, **c**, ANP-stimulated human BeWo trophoblasts and primary trophoblasts in Matrigel invasion (**b**) and intracellular cGMP production (**c**). Data are mean \pm s.d. $*P < 0.05$; $**P < 0.01$ versus control. **d**–**f**, Corin mRNA (**d**) and protein (**e**), and pro-ANP levels (**f**) in human uterus samples. Horizontal lines indicate mean values. **g**, Plasma-soluble CORIN levels (mean \pm s.d.) in pre-eclamptic patients and normal controls. **h**–**j**, CORIN gene mutations causing Lys317Glu (**h**) and Ser472Gly (**i**) changes in CORIN (**j**). **k**, **l**, Expression of Lys317Glu and Ser472Gly mutants in HEK293 cells (top panels). Vector, WT CORIN and inactive CORIN Arg801Ala and Ser985Ala mutants were controls. Lys317Glu and Ser472Gly mutations reduced pro-ANP processing activity (bottom panels). **m**, **n**, Quantitative data (mean \pm s.d.) from three experiments or more. Fz, frizzled; LDLR, LDL receptor; SR, scavenger receptor; TM, transmembrane.

Previously, high levels of plasma pro-ANP or ANP were detected in pre-eclamptic patients^{27,28}. As shown by our plasma soluble CORIN data, plasma protein levels may not reflect those in tissues. Taken together, our data show a novel local function of CORIN and ANP in promoting trophoblast invasion and spiral artery remodelling to prevent hypertension in pregnancy. The data suggest that impaired *Corin* expression or function in the pregnant uterus may be an important mechanism underlying pre-eclampsia. Studies to better understand impaired uterine *Corin* expression in pre-eclamptic patients may help to develop new strategies to enhance the CORIN-ANP pathway and prevent or treat this life-threatening disease.

METHODS SUMMARY

Corin and ANP knockout mice have been described previously^{16,19}. Transgenic mice with cardiac *Corin* expression were generated using a heart-specific promoter. Blood pressure was measured by radiotelemetry¹⁶. Tissue sections from non-pregnant and pregnant mice were stained with haematoxylin and eosin, Masson's trichrome, periodic acid-Schiff or von Kossa, or immunostained with antibodies against cytokeratin, SMA, von Willebrand factor or CORIN. Renal sections were also examined by electron microscopy. Trans-well invasion assay was carried out with human primary villous trophoblasts (ScienCell) and trophoblastic JEG3, BeWo, JAR cell lines (ATCC) in Matrigel Invasion Chambers (BD Biosciences). ANP-stimulated cGMP production in trophoblasts was assayed in 96-well plates. Intracellular cGMP levels were determined using an enzyme immunoassay kit (Enzo Life Sciences). *Corin* levels in human blood and uterus tissue samples were measured using ELISA²². Pro-ANP levels in human uterus tissues were also measured using ELISA (Alpco Diagnostics). *Corin* gene exons²⁴ from pre-eclamptic patients were PCR-amplified and sequenced directly. *Corin* gene mutations that were identified were studied by expressing mutant CORIN proteins in HEK293 cells and testing their activities in pro-ANP processing assays, as described previously²⁶.

Full Methods and any associated references are available in the online version of the paper at www.nature.com/nature.

Received 21 May 2010; accepted 25 January 2012.

Published online 21 March 2012.

- Pijnenborg, R., Vercruysse, L. & Hanssens, M. The uterine spiral arteries in human pregnancy: facts and controversies. *Placenta* **27**, 939–958 (2006).
- Red-Horse, K. *et al.* Trophoblast differentiation during embryo implantation and formation of the maternal-fetal interface. *J. Clin. Invest.* **114**, 744–754 (2004).
- Wu, Q., Xu-Cai, Y. O., Chen, S. & Wang, W. *Corin*: new insights into the natriuretic peptide system. *Kidney Int.* **75**, 142–146 (2009).
- Yan, W., Sheng, N., Seto, M., Morser, J. & Wu, Q. *Corin*, a mosaic transmembrane serine protease encoded by a novel cDNA from human heart. *J. Biol. Chem.* **274**, 14926–14935 (1999).
- Lain, K. Y. & Roberts, J. M. Contemporary concepts of the pathogenesis and management of preeclampsia. *J. Am. Med. Assoc.* **287**, 3183–3186 (2002).
- Sibai, B., Dekker, G. & Kupferminc, M. Pre-eclampsia. *Lancet* **365**, 785–799 (2005).
- Brosens, I. A., Robertson, W. B. & Dixon, H. G. The role of the spiral arteries in the pathogenesis of preeclampsia. *Obstet. Gynecol. Annu.* **1**, 177–191 (1972).
- Kaufmann, P., Black, S. & Huppertz, B. Endovascular trophoblast invasion: implications for the pathogenesis of intrauterine growth retardation and preeclampsia. *Biol. Reprod.* **69**, 1–7 (2003).
- Norwitz, E. R., Schust, D. J. & Fisher, S. J. Implantation and the survival of early pregnancy. *N. Engl. J. Med.* **345**, 1400–1408 (2001).
- Kanasaki, K. *et al.* Deficiency in catechol-O-methyltransferase and 2-methoxyoestradiol is associated with pre-eclampsia. *Nature* **453**, 1117–1121 (2008).
- Levine, R. J. *et al.* Circulating angiogenic factors and the risk of preeclampsia. *N. Engl. J. Med.* **350**, 672–683 (2004).
- Redman, C. W. & Sargent, I. L. Latest advances in understanding preeclampsia. *Science* **308**, 1592–1594 (2005).
- Venkatesha, S. *et al.* Soluble endoglin contributes to the pathogenesis of preeclampsia. *Nature Med.* **12**, 642–649 (2006).
- Zhou, C. C. *et al.* Angiotensin receptor agonistic autoantibodies induce pre-eclampsia in pregnant mice. *Nature Med.* **14**, 855–862 (2008).
- Yan, W., Wu, F., Morser, J. & Wu, Q. *Corin*, a transmembrane cardiac serine protease, acts as a pro-atrial natriuretic peptide-converting enzyme. *Proc. Natl Acad. Sci. USA* **97**, 8525–8529 (2000).
- Chan, J. C. *et al.* Hypertension in mice lacking the proatrial natriuretic peptide convertase *corin*. *Proc. Natl Acad. Sci. USA* **102**, 785–790 (2005).
- Dries, D. L. *et al.* *Corin* gene minor allele defined by 2 missense mutations is common in blacks and associated with high blood pressure and hypertension. *Circulation* **112**, 2403–2410 (2005).
- Davison, R. L. *et al.* Discovery of a spontaneous genetic mouse model of preeclampsia. *Hypertension* **39**, 337–342 (2002).
- John, S. W. *et al.* Genetic decreases in atrial natriuretic peptide and salt-sensitive hypertension. *Science* **267**, 679–681 (1995).
- Kuhn, M. *et al.* The natriuretic peptide/guanylyl cyclase—a system functions as a stress-responsive regulator of angiogenesis in mice. *J. Clin. Invest.* **119**, 2019–2030 (2009).
- Tokudome, T. *et al.* Impaired recovery of blood flow after hind-limb ischemia in mice lacking guanylyl cyclase-A, a receptor for atrial and brain natriuretic peptides. *Arterioscler. Thromb. Vasc. Biol.* **29**, 1516–1521 (2009).
- Dong, N. *et al.* Plasma soluble *corin* in patients with heart failure. *Circ. Heart Fail.* **3**, 207–211 (2010).
- Jiang, J. *et al.* Ectodomain shedding and autocleavage of the cardiac membrane protease *corin*. *J. Biol. Chem.* **286**, 10066–10072 (2011).
- Pan, J. *et al.* Genomic structures of the human and murine *corin* genes and functional GATA elements in their promoters. *J. Biol. Chem.* **277**, 38390–38398 (2002).
- Knappe, S., Wu, F., Madlansacay, M. R. & Wu, Q. Identification of domain structures in the propeptide of *corin* essential for the processing of proatrial natriuretic peptide. *J. Biol. Chem.* **279**, 34464–34471 (2004).
- Wang, W. *et al.* *Corin* variant associated with hypertension and cardiac hypertrophy exhibits impaired zymogen activation and natriuretic peptide processing activity. *Circ. Res.* **103**, 502–508 (2008).
- Irons, D. W., Baylis, P. H., Butler, T. J. & Davison, J. M. Atrial natriuretic peptide in preeclampsia: metabolic clearance, sodium excretion and renal hemodynamics. *Am. J. Physiol.* **273**, F483–F487 (1997).
- Tihtonen, K. M., Koobi, T., Vuolteenaho, O., Huhtala, H. S. & Uotila, J. T. Natriuretic peptides and hemodynamics in preeclampsia. *Am. J. Obstet. Gynecol.* **196**, 328.e1–328.e7 (2007).

Supplementary Information is linked to the online version of the paper at www.nature.com/nature.

Acknowledgements We thank J. Robbins for the α -myosin heavy chain promoter construct and L. Zhang for help with statistical analysis. This work was partly supported by grants from the Ralph Wilson Medical Foundation, the Bakken Heart-Brain Institute and the National Institutes of Health (HL089298, HD064634), and by grants from the National Natural Science Foundation of China (31070716, 81170247 and 31161130356) and the Priority Academic Program Development of Jiangsu Higher Education Institutions.

Author Contributions Y.C., W.W., N.D., J.L., D.K.S., M.L., C.F., J.P., S.C., S.W., Z.L. and L.D. designed and performed experiments. N.D., W.C. and X.H. collected patient samples and analysed clinical data. Q.W. conceived the study and designed experiments. Y.Z. and Q.W. wrote the manuscript. All authors analysed and interpreted data, and critically read the manuscript.

Author Information Reprints and permissions information is available at www.nature.com/reprints. The authors declare no competing financial interests. Readers are welcome to comment on the online version of this article at www.nature.com/nature. Correspondence and requests for materials should be addressed to Q.W. (wuq@ccf.org).

METHODS

Knockout and transgenic mice. Corin knockout mice were described previously¹⁶. ANP knockout mice (B6.129P2-*Nppa*^{tm1Umc/J})¹⁹ were from the Jackson Laboratory. To make transgenic mice expressing *Corin* in the heart, the full-length mouse *Corin* cDNA was inserted into a construct driven by the mouse α -myosin heavy chain (α -MHC) promoter. Pro-nuclear microinjection and breeding of transgenic mice were carried out at the Case Western Reserve University Transgenic Core. Corin knockout and transgenic mice were crossed to generate knockout/transgenic mice. Littermates were used as controls. The animal study was conducted in accordance with the National Institutes of Health guidelines and approved by the Institutional Animal Care and Use Committee at the Cleveland Clinic.

Blood-pressure monitoring. Radiotelemetry was used for real-time blood-pressure monitoring in conscious and unrestrained mice¹⁶. Female mice (8–12 weeks old) were chronically instrumented in the left carotid artery with a PA-C10 device (Data Sciences International) and rested for at least 7 days to recover from the surgery. The mice were mated and checked for vaginal plugs to establish gestation timing. The day on which a plug was observed was defined as E0.5. The mating mice were homozygous except for those in the fetal testing experiment. Telemetry receivers (model RPC-1) were placed under individual cages for data acquisition using the Dataquest A.R.T. 4.0 Gold System (Data Sciences International). Data presented were from continuous recording of at least 6 h per day (10:00 to 16:00).

Urinary protein measurement. Urine samples were collected from non-pregnant mice and pregnant mice at mid (8–10 days post coitus) and late (16–18 days post coitus) gestational stages. Urinary protein levels were measured using a colorimetric assay based on a modified Bradford method (Bio-Rad).

RT-PCR, western blot analysis and ELISA. Total RNAs were isolated from cultured cells or mouse and human tissues using TRIzol reagent (Invitrogen) or an RNeasy kit (Qiagen), and were used to synthesize the first strand cDNAs. RT-PCR was carried out using oligonucleotide primers that were specific for the mouse or human CORIN, mouse ANP, or human ANP receptor genes. Quantitative RT-PCR for human CORIN mRNA expression in uterus tissues was carried out using the PRISM 7500 System (Applied Biosystems). The β -actin gene was used as an internal control. Quantitative RT-PCR for mouse ANP mRNA in uteruses was carried out using the iCycler system (Bio-Rad). For western blot analysis of CORIN protein, membrane fractions from tissue homogenates were isolated by ultracentrifugation, as described previously²⁹. Proteins were analysed by SDS-polyacrylamide agarose gel electrophoresis (SDS-PAGE) and western blot using a polyclonal antibody (Berlex Biosciences). Western blot analysis of pro-ANP in heart samples was carried out using a polyclonal antibody (Santa Cruz). Processing pro-ANP by CORIN in transfected cells was analysed by western blot analysis, as described previously³⁰. Pro-ANP in human uterus tissues was measured by an amino-terminal (NT) pro-ANP ELISA kit from Alpco Diagnostics. Human CORIN in uterus tissues or plasma was measured by ELISA, as described previously³¹.

Histology and immunohistochemistry. Tissues were fixed with 4% paraformaldehyde and embedded in paraffin. Sections were stained with H&E, Masson's trichrome, PAS or von Kossa. For immunohistochemical or immunofluorescent analysis, antibodies against SMA (Sigma-Aldrich), von Willebrand factor (Sigma-Aldrich) and cytokeratin (Dako) were used to label smooth muscle cells, endothelial cells and trophoblasts, respectively. For human CORIN, an antibody from Berlex Biosciences was used. Secondary antibodies were conjugated with horseradish peroxidase or Alexa Fluor 488 (green) or Alexa Fluor 594 (red) (Invitrogen). Tissue sections were mounted with or without DAPI-containing (blue) mounting medium (Dako). For ANP expression in mouse uterus tissues, a polyclonal antibody from Millipore was used. Control sections were treated similarly but without the primary antibodies. Photographs were taken with a light or fluorescent microscope equipped with a digital camera (Olympus). Data are from experiments using five or more mice per study group.

For immunohistochemical analysis of trophoblast invasion in mouse embryos, tissue samples from at least five mice per group, and at least two implant sites per mouse were used. Serial sections (>50 per embryo) of 5 μ m in thickness were prepared. The position of the maternal artery was used as a guide to orient section positions. At least 4–6 sections from the centre of the placenta of each embryo were used for immunohistochemical analysis. Slides that were stained for cytokeratin were examined by two individuals. The sections that showed the deepest trophoblast invasion are presented. These sections were also analysed by ImagePro software to quantify cytokeratin staining. For each section that was analysed, the entire area of the decidua and myometrium was scanned by the software.

Electron microscopy. Kidneys from pregnant mice at E18.5 were fixed in 3% glutaraldehyde, treated with 1% osmium tetroxide and embedded in an Araldite-Epon mixture. Semi-thin sections (0.6 μ m) were prepared and examined with a transmission electron microscope (JEOL JEM-1210) at the Lerner Image Core of the

Cleveland Clinic. Data are from experiments using at least three mice per study group.

Trans-well invasion assay. Human trophoblastic JEG3, BeWo and JAR cells from the American Type Culture Collection were cultured in Minimum Essential Medium (JEG3), RPMI1640 (JAR) and F-12K (BeWo) medium, respectively, with 10% FBS at 37 °C. Primary human villous trophoblasts from ScienCell Research Labs (Carlsbad) were cultured in the Trophoblast Medium (ScienCell) with 10% FBS. Transwell invasion assays were carried out using the BioCoat Growth Factor Reduced Matrigel Invasion Chambers (pore size of 8 μ m) and control inserts (no Matrigel coating) (BD Biosciences) in 24-well plates. Culture medium containing human ANP (Calbiochem) was added to the bottom wells, and cell suspension (5×10^4) was added to the top wells and incubated at 37 °C for 24 h. Non-invading cells were removed from the upper surface of the Matrigel layer by gentle scrubbing. The cells on the lower surface of the membrane were stained using Diff-Quick staining solutions. The membranes were excised and mounted onto glass slides. Invasion indices were determined by counting the number of stained cells on the membrane under a light microscope. The assay was carried out in duplicate in at least three independent experiments.

cGMP assay. ANP-stimulated intracellular cGMP production assay was performed with JEG3, JAR and BeWo cells and primary human trophoblasts using a method described previously³². The cells were grown in 96-well plates. Confluent cells were washed once with serum-free medium. Human ANP was added to serum-free medium and incubated with cells at 37 °C for 30 min. In these experiments, ANP was more potent in stimulating intracellular cGMP production when serum-free medium was used (data not shown). The cells were lysed with 0.1 M HCl. Intracellular cGMP levels in ANP-stimulated cells were determined using an EIA kit (Enzo Life Sciences). Each experimental condition was assayed in duplicate in at least three independent experiments.

Human blood and tissue samples. The study was approved by local ethics committees and participants gave informed consent. Women of normal pregnancy or with pre-eclampsia, and age-matched non-pregnant normal controls who underwent routine medical check-ups were recruited. All participants were ethnic Han Chinese. Hypertension was defined as diastolic pressure >90 mm Hg and/or systolic pressure >140 mm Hg on at least two occasions. Pre-eclampsia was defined as hypertension that appeared after 20 weeks of gestation with proteinuria (>300 mg urinary protein per 24 h). Patients with chronic hypertension, chronic kidney disease, diabetes and heart disease were excluded. Uterus tissues were obtained during caesarean sections in pregnant women or operations for uterine leiomyoma in non-pregnant women. Clinical characteristics of women who provided blood and those who provided uterus tissue samples are summarized in Supplementary Tables 1 and 2, respectively.

CORIN gene sequences in patients. Blood samples from 56 patients with pre-eclampsia were collected into tubes containing EDTA as an anticoagulant. Genomic DNA was extracted from white blood cells using the QIAamp DNA Mini kit (Qiagen) and used in PCR to amplify exon sequences of the *CORIN* gene²⁴. PCR products were used for direct DNA sequencing. Mutations that were identified were verified by independent PCR and DNA sequencing. Additional PCR and DNA sequencing were carried out with DNA samples from more than 100 normal controls to verify that mutations that were identified in patients did not exist in the normal population.

Expression and functional analysis of *Corin* mutants. Plasmids expressing human wild-type *Corin* and two inactive mutants Arg801Ala and Ser985Ala, in which the activation cleavage site and catalytic site residues were mutated, respectively, were described previously³³. Plasmids expressing *Corin* mutants Lys317Glu or Ser472Gly were constructed by PCR-based mutagenesis. Recombinant CORIN proteins that were expressed by these plasmids contained a carboxy-terminal V5 tag to be detected by an anti-V5 antibody (Invitrogen)³⁰. Plasmids were transfected into HEK293 cells using Lipofectamine 2000 (Invitrogen). Cells were lysed and proteins were analysed by western blot using an anti-V5 antibody. To analyse the function of CORIN, recombinant human pro-ANP in conditioned medium was added to HEK293 cells expressing *Corin* wild-type or mutants and incubated at 37 °C for 2 h. Pro-ANP and ANP in the medium were immunoprecipitated and analysed by western blot. Protein bands on X-ray films were scanned by densitometry. The percentage of pro-ANP to ANP conversion was calculated as described previously³⁰.

Statistical analysis. Results are presented as mean \pm s.d. Differences between two groups were analysed with the Student's *t*-test. Data involving more than two groups were analysed by analysis of variance followed by the Tukey multiple comparison test. Comparisons for *Corin* mRNA and protein and pro-ANP levels in human uterus samples were carried out using the Mann-Whitney-Wilcoxon test. A *P* value of less than 0.05 was considered statistically significant.

29. Chen, S. *et al.* Protease corin expression and activity in failing hearts. *Am. J. Physiol. Heart Circ. Physiol.* **299**, H1687–H1692 (2010).

30. Liao, X., Wang, W., Chen, S. & Wu, Q. Role of glycosylation in corin zymogen activation. *J. Biol. Chem.* **282**, 27728–27735 (2007).
31. Dong, N. *et al.* Effects of anticoagulants on human plasma soluble corin levels measured by ELISA. *Clin. Chim. Acta* **411**, 1998–2003 (2010).
32. Wu, F., Yan, W., Pan, J., Morser, J. & Wu, Q. Processing of pro-atrial natriuretic peptide by corin in cardiac myocytes. *J. Biol. Chem.* **277**, 16900–16905 (2002).
33. Qi, X., Jiang, J., Zhu, M. & Wu, Q. Human corin isoforms with different cytoplasmic tails that alter cell surface targeting. *J. Biol. Chem.* **286**, 20963–20969 (2011).

Spontaneous coherence in a cold exciton gas

A. A. High¹, J. R. Leonard¹, A. T. Hammack¹, M. M. Fogler¹, L. V. Butov¹, A. V. Kavokin^{2,3}, K. L. Campman⁴ & A. C. Gossard⁴

If bosonic particles are cooled down below the temperature of quantum degeneracy, they can spontaneously form a coherent state in which individual matter waves synchronize and combine. Spontaneous coherence of matter waves forms the basis of a number of fundamental phenomena in physics, including superconductivity, superfluidity and Bose–Einstein condensation^{1,2}. Spontaneous coherence is the key characteristic of condensation in momentum space³. Excitons—bound pairs of electrons and holes—form a model system to explore the quantum physics of cold bosons in solids^{4,5}. Cold exciton gases can be realized in a system of indirect excitons, which can cool down below the temperature of quantum degeneracy owing to their long lifetimes⁶. Here we report measurements of spontaneous coherence in a gas of indirect excitons. We found that spontaneous coherence of excitons emerges in the region of the macroscopically ordered exciton state⁷ and in the region of vortices of linear polarization. The coherence length in these regions is much larger than in a classical gas, indicating a coherent state with a much narrower than classical exciton distribution in momentum space, characteristic of a condensate. A pattern of extended spontaneous coherence is correlated with a pattern of spontaneous polarization, revealing the properties of a multicomponent coherent state. We also observed phase singularities in the coherent exciton gas. All these phenomena emerge when the exciton gas is cooled below a few kelvin.

There are intriguing theoretical predictions for a range of coherent states in cold exciton systems, including the Bose–Einstein condensate⁴, a BCS-like condensate⁵, the charge-density wave⁸, and a condensate with spontaneous time-reversal symmetry breaking⁹. Because excitons are much lighter than atoms, quantum degeneracy can be achieved in excitonic systems at temperatures orders of magnitude higher than the microkelvin temperatures needed in atomic vapours^{1,2}. Exciton gases need be cooled down to a few kelvin to enter the quantum regime.

Although the temperature of the semiconductor crystal lattice (T_l) can be lowered well below 1 K in helium refrigerators, lowering the temperature of the exciton gas (T_X) to even a few kelvin is challenging^{10,11}. Owing to recombination, excitons have a finite lifetime that is too short to allow cooling to low temperatures in usual semiconductors. In order to create a cold exciton gas with T_X close to T_l , the exciton lifetime should considerably exceed the exciton cooling time. As well as this, the realization of a cold and dense exciton gas requires an excitonic state to be the ground state and to have lower energy than the electron–hole liquid¹².

A gas of indirect excitons fulfils these requirements. An indirect exciton can be formed by an electron and a hole confined in separate quantum-well layers (Fig. 1a, b). The spatial separation allows the overlap of electron and hole wavefunctions to be controlled. In this way, indirect excitons can be produced with radiative lifetimes and spin relaxation times orders of magnitude longer than those of direct excitons^{13–15}.

In earlier studies, evidence for spontaneous coherence was obtained for indirect excitons in coupled quantum wells (CQWs)¹⁶ and for indirect excitons in quantum Hall bilayers^{17,18}. The onset of spontaneous coherence was evidenced by a strong enhancement of the rates of recombination¹⁶ and tunnelling¹⁷, respectively. The results of other transport and optical experiments were also consistent with spontaneous coherence of indirect excitons^{6,16–22}. However, no direct measurement of coherence was performed in these studies.

Exciton coherence is evidenced by coherence of their light emission, which can be studied by interferometry. In our earlier work, we reported an enhancement of the exciton coherence length in the macroscopically ordered exciton state^{23,24} (MOES). However, these experiments used a single-pinhole interferometric technique, which does not measure the coherence function, and the derivation of the exciton coherence length in refs 23 and 24 was based on a mathematical analysis of the data.

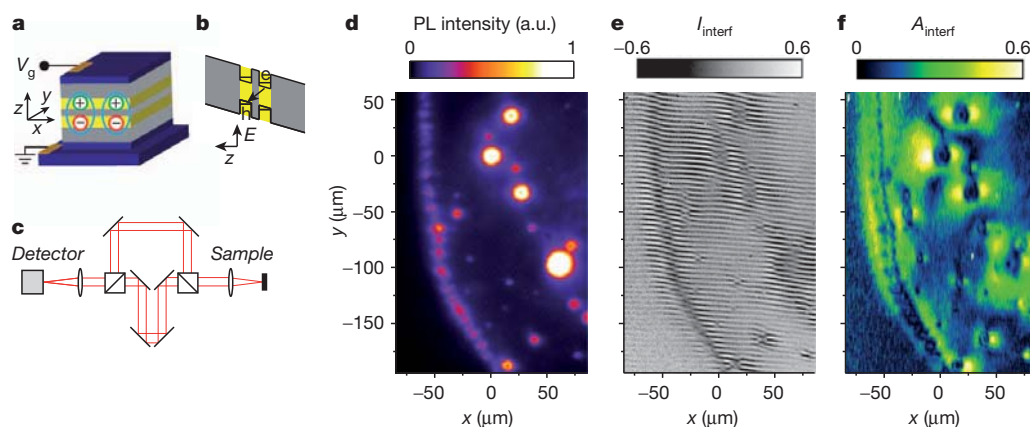


Figure 1 | Emission, interference and coherence patterns of indirect excitons. **a**, Diagram of CQW structure: n^+ -GaAs (blue), $\text{Al}_{0.33}\text{Ga}_{0.67}\text{As}$ (grey), GaAs quantum well (yellow). V_g is applied voltage. Ellipses indicate indirect excitons composed of electrons (–) and holes (+). **b**, CQW band diagram; e, electron; h, hole; E , energy. The arrow indicates an indirect exciton.

c, Diagram of the interferometric set-up. **d**, Emission pattern (luminescence). **e**, Interference pattern $I_{\text{interf}}(x, y)$ for $\delta x = 2 \mu\text{m}$. **f**, Pattern of the amplitude of the interference fringes $A_{\text{interf}}(x, y)$, presenting a map of coherence. The temperature in the refrigerator at the sample is $T_{\text{bath}} = 0.1 \text{ K}$.

¹Department of Physics, University of California at San Diego, La Jolla, California 92093-0319, USA. ²School of Physics and Astronomy, University of Southampton, Southampton SO17 1BJ, UK. ³Spin Optics Laboratory, State University of Saint Petersburg, 1, Uljanovskaya, 198504, Russia. ⁴Materials Department, University of California at Santa Barbara, Santa Barbara, California 93106-5050, USA.

Here we report the direct measurement of spontaneous coherence in a gas of indirect excitons in CQWs. These indirect excitons may have four spin projections on the z direction normal to the CQW plane: $J_z = -2, -1, +1, +2$. The states $J_z = -1$ and $+1$ contribute to left- and right-circularly polarized emission and their coherent superposition to linear polarized emission, whereas the states $J_z = -2$ and $+2$ are dark^{9,15}. The exciton condensate is a four-component coherent state in general. The build-up of exciton coherence should manifest itself in an increase of the coherence length and of the degree of polarization of the exciton emission. The former phenomenon is general for both one- and multicomponent condensates³, whereas the latter is specific to multi-component condensates²⁵. In this work, we report the emergence of both long-range spontaneous coherence of excitons and spontaneous polarization. A pattern of extended spontaneous coherence, measured by shift interferometry (see below), is correlated with a pattern of spontaneous polarization, measured by polarization-resolved imaging. These two experiments reveal the properties of a multi-component coherent state.

The pattern of the first-order coherence function $g_1(\delta x)$ is measured by shift interferometry: the emission images produced by each of the two arms of the Mach–Zehnder interferometer (Fig. 1c) are shifted with respect to each other to measure the interference between the emission of excitons spatially separated by δx . Details of the experiment are given in Supplementary Information.

Extended spontaneous coherence is observed in the region of rings in the exciton emission pattern. Exciton rings—including the inner ring, external ring and localized bright spot (LBS) rings—were observed earlier⁷. The external and LBS rings form on the boundaries between electron-rich and hole-rich regions; the former is created by current through the structure (specifically, by the current filament at the LBS centre in the case of the LBS ring), whereas the latter is created by optical excitation^{26,27}. The external and LBS rings are sources of cold excitons. In the area of these rings coherence forms spontaneously. Figure 1d shows a segment of the exciton emission pattern, with a section of the external ring and smaller LBS rings.

The pattern of interference fringes is shown in Fig. 1e and the map of their amplitude, A_{interf} in Fig. 1f. The quantity A_{interf} describes the degree of coherence of excitons, as detailed below. The regions of extended spontaneous coherence of excitons correspond to the green colour in Fig. 1f.

Figure 2 presents the patterns of coherence of emission from indirect excitons in regions of an LBS and the external ring. The observed

properties of exciton coherence are qualitatively similar around both these sources of cold excitons. We first consider an LBS region. At low temperatures, a strong enhancement of A_{interf} is observed at distance $r \approx r_0 = 7 \mu\text{m}$ away from the LBS centre (Fig. 2b, c, i). This enhancement of the degree of coherence shows the emergence of extended spontaneous coherence of excitons.

Furthermore, the phase of the interference fringes, ϕ_{interf} experiences a shift at $r \approx r_0 = 7 \mu\text{m}$, which defines a phase domain boundary (Fig. 2b). The shift in phase correlates with the enhancement of A_{interf} (Fig. 2b, c). Its magnitude $\delta\phi = \phi_{\text{interf}}^{\text{outer}} - \phi_{\text{interf}}^{\text{inner}}$ increases with δx (Fig. 2j). The interference pattern in the shift-interferometry experiment with shift δx can be simulated using the formula $I_{\text{interf}} = |\Psi(\mathbf{r}) + e^{iq_t y} \Psi(\mathbf{r} + \delta \mathbf{x})|^2$, where $q_t = 2\pi\alpha/\lambda$ sets the period of interference fringes (α is a small tilt angle between the image planes of the interferometer arms, λ is the emission wavelength) and the complex function $\Psi(\mathbf{r})$ represents the source amplitude at point \mathbf{r} . For a flow of excitons with momentum \mathbf{q} , $\Psi(\mathbf{r}) = e^{iq\mathbf{r}}$, so that $I_{\text{interf}} = 2 + 2\cos(q_t y + \mathbf{q}\delta\mathbf{x})$ and the shift in the phase of the interference fringes means a jump in (average) measured exciton momentum $\delta q \approx \delta\phi_{\text{interf}}/\delta x \approx 2 \mu\text{m}^{-1}$ at $r = r_0$.

Figure 2d presents a pattern of linear polarization around an LBS. It spatially correlates with the pattern of the amplitude and phase of the interference fringes: compare Fig. 2b, c and d. At $r \gtrsim r_0$ a vortex of linear polarization with the polarization perpendicular to the radial direction is observed. Such polarization vortices appear owing to precession of the Stokes vector for excitons propagating out of the LBS origin (see Supplementary Information for details).

To summarize, close to the heating sources within the LBS ring the exciton gas is hot, and no spontaneous coherence forms there (the heating of the exciton gas is due to the current filament at the LBS centre and the binding energy released at the exciton formation in the ring²⁶). This is revealed by the small amplitude of the interference fringes. Excitons cool down with increasing distance r away from the heating sources so that they can approach the transition temperature to a coherent state. At $r = r_0$, the (average) exciton momentum reduces and the coherence degree sharply rises, indicating the emergence of extended spontaneous coherence of excitons. This is revealed by the shift in the phase of the interference fringes and the strong enhancement of the amplitude of the interference fringes, respectively. The polarization vortex emerges along with extended spontaneous coherence at $r = r_0$, revealing the properties of a multicomponent coherent state.

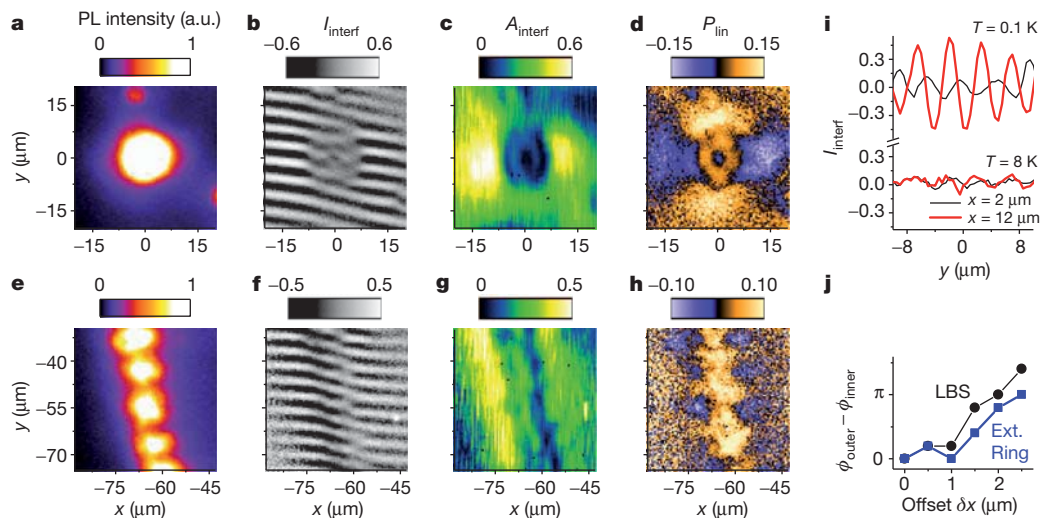


Figure 2 | Coherence of indirect excitons in regions of an LBS and the external ring. **a–d**, A region of an LBS; **e–h**, a region of the external ring. Shown are the emission pattern (**a**, **e**), the interference pattern at shift $\delta x = 2 \mu\text{m}$ (**b**, **f**), the amplitude $A_{\text{interf}}(x, y)$ of interference fringes (**c**, **g**), and the linear polarization of exciton emission $P_{\text{lin}} = (I_x - I_y)/(I_x + I_y)$ (**d**, **h**). **i**, y -axis

cross-sections of $I_{\text{interf}}(x, y)$ at $x = 2 \mu\text{m}$ (black lines) and $x = 12 \mu\text{m}$ (red lines) at $T_{\text{bath}} = 0.1 \text{ K}$ and 8 K . **j**, The shift in the phase of interference fringes in **b** at $r \approx 7 \mu\text{m}$ (black) and in **f** at $\sim 4 \mu\text{m}$ away from the centre of the external ring (blue) versus δx . $T_{\text{bath}} = 0.1 \text{ K}$ for **a–h**, **j**.

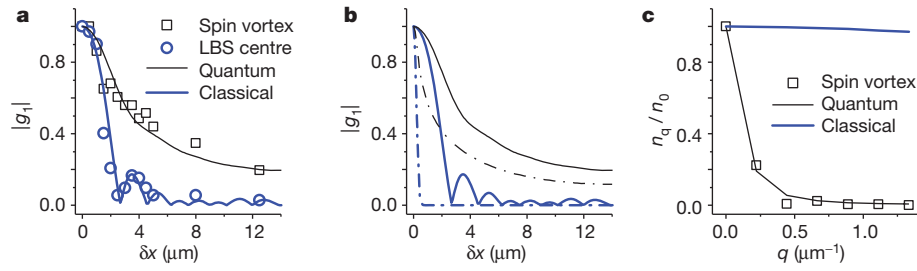


Figure 3 | First-order coherence function and distribution in momentum space. **a**, Measured $|g_1(\delta x)|$ for the polarization vortex (squares) and LBS centre (circles), and simulated $|g_1(\delta x)|$ for a quantum (black line) and classical (blue line) gas. **b**, Simulated $|g_1(\delta x)|$ for a quantum (black) and classical (blue)

gas with (solid) and without (dashed) convolution with the PSF. **c**, Distribution in momentum space obtained by the Fourier transform of g_1 in **b** for a quantum (black line) and a classical (blue line) gas. See main text for details.

Similar phenomena are observed in the external ring region. At low temperature, the MOES forms in the external ring⁷ (Figs 1d and 2e) and a periodic polarization texture forms around the periodic array of beads in the MOES (Fig. 2h). Figure 2f and g shows the extended spontaneous coherence of excitons observed in the MOES. It emerges at low temperatures, along with the spatial order of exciton beads and periodic polarization texture.

We now discuss the measurements of the first-order coherence function. Coherence of the exciton gas is directly characterized by coherence of exciton emission, described by the first-order coherence function $g_1(\delta \mathbf{r})$. In turn, this function is given by the amplitude of the interference fringes $A_{\text{interf}}(\delta \mathbf{r})$ in ‘the ideal experiment’ with perfect spatial resolution. In practice, the measured $A_{\text{interf}}(\delta \mathbf{r})$ is given by the convolution of $g_1(\delta \mathbf{r})$ with the point-spread function (PSF) of the optical system used in the experiment²⁴. The PSF width corresponds to the spatial resolution of the optical system ($\sim 1.5 \mu\text{m}$ in our experiments).

The measurements of $A_{\text{interf}}(\delta x)$ in the polarization vortex and in the LBS centre are presented in Fig. 3a. In the hot LBS centre, A_{interf} quickly drops with δx and the shape $A_{\text{interf}}(\delta x)$ fits well to the PSF, which is shown by the blue line. In the polarization vortex, $g_1(\delta x)$ extends to large δx , demonstrating extended spontaneous coherence. A fit to the experimental points computed using a model described below is shown by the black line (Fig. 3a).

Figure 3b and c demonstrates the relation between the first-order coherence function and the particle distribution in momentum space. Figure 3b presents $g_1(\delta x)$ for a classical gas (blue dashed line) and for a quantum gas (black dashed line); both curves are for a spatially homogeneous gas of non-interacting particles with a quadratic dispersion (see Supplementary Information). Both gases are at 0.1 K; the occupation number of the $q = 0$ momentum state (n_0) is $\ll 1$ for the classical gas, but is 5,000 for the quantum gas. The convolution of these $g_1(\delta x)$ with the PSF produces data shown as black and blue solid lines, which fit to $A_{\text{interf}}(\delta x)$ in the spin polarization vortex and in the LBS centre, respectively (Fig. 3a, b). The Fourier transform of $g_1(\delta x)$ in Fig. 3b gives the momentum occupation factor n_q shown in Fig. 3c.

Figure 3b and c illustrates that a classical gas is characterized by a broad distribution in momentum space n_q and a narrow first-order coherence function $g_1(r)$, whereas a quantum gas is characterized by a narrow n_q and an extended $g_1(r)$. For a classical gas, $g_1(r)$ reduces substantially within the thermal de Broglie wavelength λ_{dB} , which scales $\propto T^{-1/2}$ and is about $0.5 \mu\text{m}$ at 0.1 K. The extension of $g_1(r)$ well beyond λ_{dB} indicates a coherent exciton state.

Figure 3a also illustrates why $\delta x = 2 \mu\text{m}$ is selected for mapping extended spontaneous coherence of excitons. The shift $\delta x = 2 \mu\text{m}$ is chosen to exceed both λ_{dB} and the PSF width. At such δx , only weak coherence given by the PSF value at $\delta x = 2 \mu\text{m}$ can be observed for a classical gas. The regions of enhanced coherence exceeding such a background level reveal the regions with extended spontaneous coherence of excitons.

Next, we present a pattern of coherence length. The spatial extension of $g_1(\delta \mathbf{r})$ can be characterized by a coherence length ξ . To consider

all the points in the pattern on an equal footing, we evaluate ξ as that value of δr at which the interference visibility drops e times. We measured the exciton interference pattern at different δr to produce the spatial map of $g_1(\delta \mathbf{r})$ and, in turn, ξ . Figure 4a and b shows the pattern of ξ for the shift between the interfering excitons along x and y , respectively. Figure 4c and d presents the cross-sections of $\xi(x, y)$ in the region of the polarization vortex (Fig. 4c) and MOES (Fig. 4d).

The regions of a classical gas in the $\xi(x, y)$ pattern correspond to the smallest observed coherence length, which is given by the PSF width. Long-range spontaneous coherence of excitons is observed in the polarization vortices and in the macroscopically ordered exciton state (Fig. 4). The coherence length in these regions is much larger than in a classical gas, indicating a coherent state with a much narrower-than-classical exciton distribution in momentum space, characteristic of a condensate.

The observed coherence length in the polarization vortex exceeds $\lambda_{\text{dB}} = 0.5 \mu\text{m}$ at 0.1 K by more than an order of magnitude (Fig. 4). The coherence length in the MOES is smaller than in the polarization vortex. This may be related to fluctuations of the exciton density wave in the external ring. Such fluctuations were observed recently, and their studies will be reported in future work.

The patterns of coherence length are different for the shifts along x and y , revealing a directional property of exciton coherence. In the

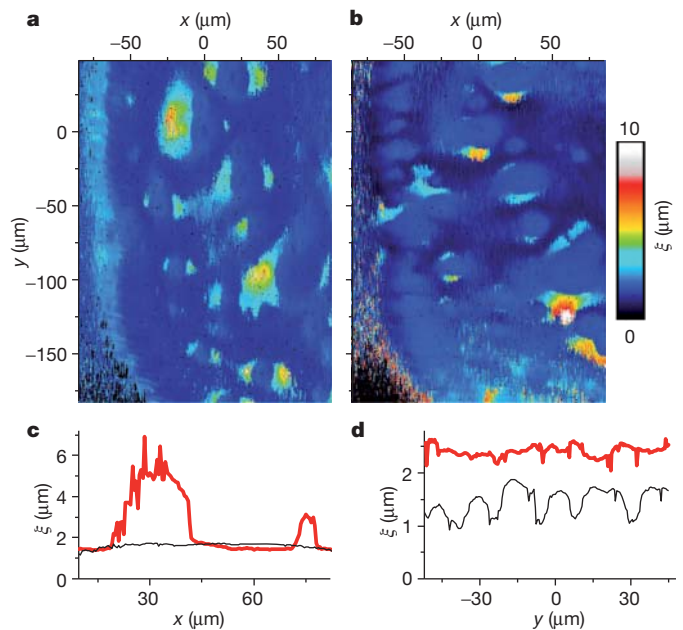


Figure 4 | Patterns of the coherence length of excitons, $\xi(x, y)$. **a**, **b**, $\xi(x, y)$ for a shift along x (**a**) and y (**b**). **c**, **d**, Cross-section of $\xi(x, y)$ through LBS ($y = -90 \mu\text{m}$; **c**) and along the external ring ($x = -70 \mu\text{m}$; **d**) for a shift along x (red) and y (black). $T_{\text{bath}} = 0.1 \text{ K}$.

region of the polarization vortices, ξ is higher in the direction along the shift between the interfering excitons (that is, the x direction for the δx shift (Fig. 4a), and the y direction for the δy shift (Fig. 4b)). In the region of the MOES, ξ is higher for the δx shift (that is, for the shift along the direction of exciton propagation away from the external ring in Fig. 4a). These data indicate that the extension of $g_1(\mathbf{r})$ is greater when the exciton propagation direction is along vector \mathbf{r} .

Finally, we present observations of phase singularities. A well known example of a phase singularity is a quantized vortex. In a singly quantized vortex, the phase of the wavefunction winds by 2π around the singularity point, which can be revealed as a fork-like defect in a phase pattern. Fork-like defects in interference patterns have been reported for optical vortices, vortices in atom condensates, and polariton vortices (see refs 28–30 and references therein).

We observed a number of fork-like defects in the interference pattern of a cold exciton gas. For example, more than 20 such defects are present in Fig. 1e. Information on an enlarged scale is presented in Fig. 5. Figure 5a shows forks in the interference pattern, indicating the presence of phase singularities. We have studied the properties of this phenomenon and show below that its origin is different from that of a quantized vortex.

The forks in the interference pattern are observed at low temperatures in a quantum exciton gas (Fig. 5a) and vanish at high temperatures in a classical exciton gas (Fig. 5d). At low temperatures, a closed contour around the fork crosses an odd number of interference fringes, so the phase of the interference fringes winds by 2π , indicating a phase singularity (Fig. 5e). Similar properties are observed for quantized vortices.

However, the distance between the left- and right-facing forks in the interference pattern is different from the shift $\delta x = 2\mu\text{m}$ in the shift-interferometry experiment, and depends on the excitation power (Fig. 5a–c). This indicates the difference between the observed phase singularity and a quantized vortex. Indeed, straightforward simulations show that a quantized vortex is characterized by a pair of opposite forks separated by a distance equal to the shift in the shift-interferometry experiment (see Supplementary Information).

Simulations of the interference pattern produced by a ring-shaped source, such as an LBS ring, result in an interference pattern with opposite forks separated by a distance much larger than δx , in qualitative agreement with the experiment (see Supplementary Information).

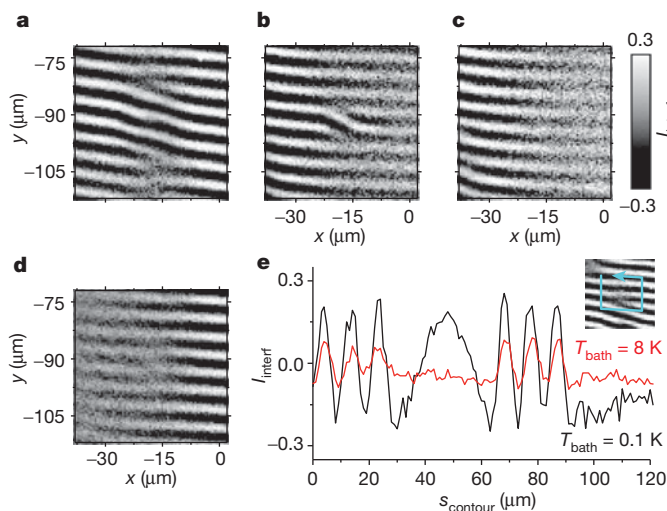


Figure 5 | Fork-like defects in exciton interference patterns. **a–d**, Interference pattern $I_{\text{interf}}(x, y)$ around an LBS; for **a–c**, T_{bath} is constant (0.1 K) and P_{ex} varies (7, 1.2 and 0.7 mW, respectively); for **a** and **d**, P_{ex} is constant (7 mW) and T_{bath} varies (0.1 and 5 K, respectively). **e**, I_{interf} along a closed contour (shown in inset) for $T_{\text{bath}} = 0.1$ K (black) and 8 K (red). $\delta x = 2\mu\text{m}$.

A ring-shaped source with particles propagating away from their origin on the ring produces a more complicated phase pattern than a vortex, yet both objects are characterized by the spreading of particle velocities over all directions. The observed phase singularities constitute the properties of a quantum exciton gas with extended spontaneous coherence (Fig. 5a), and no such phase singularity is observed at high temperatures in a classical gas (Fig. 5d).

METHODS SUMMARY

Experiments are performed on a $n^+ - i - n^+$ GaAs/AlGaAs CQW structure. The i region consists of a single pair of 8-nm GaAs quantum wells separated by a 4-nm $\text{Al}_{0.33}\text{Ga}_{0.67}\text{As}$ barrier and surrounded by 200-nm $\text{Al}_{0.33}\text{Ga}_{0.67}\text{As}$ barrier layers. The n^+ layers are Si-doped GaAs with Si concentration $N_{\text{Si}} = 5 \times 10^{17} \text{ cm}^{-3}$. The electric field in the z direction is controlled by the external voltage applied between n^+ layers. The small in-plane disorder in the CQW is indicated by the emission linewidth of 1 meV. Long lifetimes of the indirect excitons allow them to cool to temperatures within about 0.1 K of the lattice temperature, which can be lowered to 0.1 K in an optical dilution refrigerator. This allows the realization of a cold exciton gas with temperature well below the temperature of quantum degeneracy, which is in the range of a few kelvin for typical exciton densities $\sim 10^{10} \text{ cm}^{-2}$ for the CQW⁶. The laser excitation is performed by a HeNe laser at excitation wavelength $\lambda_{\text{ex}} = 633 \text{ nm}$ with an excitation power $P_{\text{ex}} = 1.2$ (2.9) mW for the data in Figs 1–3 (Fig. 4). The photoexcitation is more than 400 meV above the energy of indirect excitons, and the 10- μm -wide excitation spot is farther than 80 μm away from both the LBS and the external ring. The x -polarization is along the sample cleavage direction within the experimental accuracy. The data have been acquired on a timescale of the order of 100 s. During the measurements, the LBS rings are static while the exciton density wave in the external ring fluctuates on a length scale of few micrometres (such fluctuations may be responsible for a smaller coherence length in the MOES than in the polarization vortex, as discussed in the text). The coherence length is generally smaller than the distance between the LBS and MOES, or between different LBS. The spatial resolution of the optical system is $\sim 1.5 \mu\text{m}$.

Received 9 September 2011; accepted 17 January 2012.

Published online 21 March 2012.

- Cornell, E. A. & Wieman, C. E. Bose-Einstein condensation in a dilute gas, the first 70 years and some recent experiments. *Rev. Mod. Phys.* **74**, 875–893 (2002).
- Ketterle, W. When atoms behave as waves: Bose-Einstein condensation and the atom laser. *Rev. Mod. Phys.* **74**, 1131–1151 (2002).
- Penrose, O. & Onsager, L. Bose-Einstein condensation and liquid helium. *Phys. Rev.* **104**, 576–584 (1956).
- Keldysh, L. V. & Kozlov, A. N. Collective properties of excitons in semiconductors. *Sov. Phys. JETP* **27**, 521–528 (1968).
- Keldysh, L. V. & Kopaev, Yu V. Possible instability of the semimetallic state toward Coulomb interaction. *Sov. Phys. Solid State* **6**, 2219–2224 (1965).
- Butov, L. V. *et al.* Stimulated scattering of indirect excitons in coupled quantum wells: signature of a degenerate Bose-gas of excitons. *Phys. Rev. Lett.* **86**, 5608–5611 (2001).
- Butov, L. V., Gossard, A. C. & Chemla, D. S. Macroscopically ordered state in an exciton system. *Nature* **418**, 751–754 (2002).
- Chen, X. M. & Quinn, J. J. Excitonic charge-density-wave instability of spatially separated electron-hole layers in strong magnetic fields. *Phys. Rev. Lett.* **67**, 895–898 (1991).
- Wu, C., Shem, I. M. & Exciton condensation with spontaneous time-reversal symmetry breaking. Preprint at <http://arXiv.org/abs/0809.3532v1> (2008).
- Tikhodeev, S. G., Kopelevich, G. A. & Gippius, N. A. Exciton transport in Cu_2O : phonon wind versus superfluidity. *Phys. Status Solidi B* **206**, 45–53 (1998).
- Jang, J. I. & Wolfe, J. P. Auger recombination and biexcitons in Cu_2O : a case for dark exciton matter. *Phys. Rev. B* **74**, 045211 (2006).
- Keldysh, L. V. The electron-hole liquid in semiconductors. *Contemp. Phys.* **27**, 395–428 (1986).
- Lozovik, Yu E & Yudson, V. I. A new mechanism for superconductivity: pairing between spatially separated electrons and holes. *Sov. Phys. JETP* **44**, 389–397 (1976).
- Fukuzawa, T., Kano, S. S., Gustafson, T. K. & Ogawa, T. Possibility of coherent-light emission from Bose condensed states of SEHPs. *Surf. Sci.* **228**, 482–485 (1990).
- Maialle, M. Z., de Andrade e Silva, E. A. & Sham, L. J. Exciton spin dynamics in quantum wells. *Phys. Rev. B* **47**, 15776–15788 (1993).
- Butov, L. V. & Filin, A. I. Anomalous transport and luminescence of indirect excitons in AlAs/GaAs coupled quantum wells as evidence for exciton condensation. *Phys. Rev. B* **58**, 1980–2000 (1998).
- Spielman, I. B., Eisenstein, J. P., Pfeiffer, L. N. & West, K. W. Resonantly enhanced tunneling in a double layer quantum Hall ferromagnet. *Phys. Rev. Lett.* **84**, 5808–5811 (2000).
- Eisenstein, J. P. & MacDonald, A. H. Bose-Einstein condensation of excitons in bilayer electron systems. *Nature* **432**, 691–694 (2004).

19. Butov, L. V., Zrenner, A., Abstreiter, G., Böhm, G. & Weimann, G. Condensation of indirect excitons in coupled AlAs/GaAs quantum wells. *Phys. Rev. Lett.* **73**, 304–307 (1994).
20. Tutuc, E., Shayegani, M. & Huse, D. A. Counterflow measurements in strongly correlated GaAs hole bilayers: evidence for electron-hole pairing. *Phys. Rev. Lett.* **93**, 036802 (2004).
21. Tiemann, L. *et al.* Exciton condensate at a total filling factor of one in Corbino two-dimensional electron bilayers. *Phys. Rev. B* **77**, 033306 (2008).
22. Karmakar, B., Pellegrini, V., Pinczuk, A., Pfeiffer, L. N. & West, K. W. First-order quantum phase transition of excitons in quantum hall bilayers. *Phys. Rev. Lett.* **102**, 036802 (2009).
23. Sen, Yang, Hammack, A. T., Fogler, M. M., Butov, L. V. & Gossard, A. C. Coherence length of cold exciton gases in coupled quantum wells. *Phys. Rev. Lett.* **97**, 187402 (2006).
24. Fogler, M. M., Sen Yang, Hammack, A. T., Butov, L. V. & Gossard, A. C. Effect of spatial resolution on the estimates of the coherence length of excitons in quantum wells. *Phys. Rev. B* **78**, 035411 (2008).
25. Read, D., Liew, T. C. H., Rubo, Y. G. & Kavokin, A. V. Stochastic polarization formation in exciton-polariton Bose-Einstein condensates. *Phys. Rev. B* **80**, 195309 (2009).
26. Butov, L. V. *et al.* Formation mechanism and low temperature instability of exciton rings. *Phys. Rev. Lett.* **92**, 117404 (2004).
27. Rapaport, R. *et al.* Charge separation of dense two dimensional electron-hole gases: mechanism for exciton ring pattern formation. *Phys. Rev. Lett.* **92**, 117405 (2004).
28. Scheuer, J. & Orenstein, M. Optical vortices crystals: spontaneous generation in nonlinear semiconductor microcavities. *Science* **285**, 230–233 (1999).
29. Hadzibabic, Z., Krüger, P., Cheneau, M., Battelier, B. & Dalibard, J. Berezinskii-Kosterlitz-Thouless crossover in a trapped atomic gas. *Nature* **441**, 1118–1121 (2006).
30. Lagoudakis, K. G. *et al.* Quantized vortices in an exciton-polariton condensate. *Nature Phys.* **4**, 706–710 (2008).

Supplementary Information is linked to the online version of the paper at www.nature.com/nature.

Acknowledgements We thank L. Levitov, T. Ostatnický, L. Sham, B. Simons and C. Wu for discussions. This work was supported by the DOE Office of Basic Energy Sciences (DE-FG02-07ER46449). The development of spectroscopy in a dilution refrigerator was supported by ARO and NSF. M.M.F. was supported by the UCOP. A.V.K. was supported by the Royal Society (UK).

Author Contributions All authors contributed to the work presented in this paper.

Author Information Reprints and permissions information is available at www.nature.com/reprints. The authors declare no competing financial interests. Readers are welcome to comment on the online version of this article at www.nature.com/nature. Correspondence and requests for materials should be addressed to A.A.H. (alex.high@gmail.com).

Endospore abundance, microbial growth and necromass turnover in deep sub-seafloor sediment

Bente Aa. Lomstein¹, Alice T. Langerhuus¹, Steven D'Hondt², Bo B. Jørgensen³ & Arthur J. Spivack²

Two decades of scientific ocean drilling have demonstrated widespread microbial life in deep sub-seafloor sediment, and surprisingly high microbial-cell numbers. Despite the ubiquity of life in the deep biosphere, the large community sizes and the low energy fluxes in this vast buried ecosystem are not yet understood^{1,2}. It is not known whether organisms of the deep biosphere are specifically adapted to extremely low energy fluxes or whether most of the observed cells are in a dormant, spore-like state³. Here we apply a new approach—the D,L-amino-acid model—to quantify the distributions and turnover times of living microbial biomass, endospores and microbial necromass, as well as to determine their role in the sub-seafloor carbon budget. The approach combines sensitive analyses of unique bacterial markers (muramic acid and D-amino acids) and the bacterial endospore marker, dipicolinic acid, with racemization dynamics of stereo-isomeric amino acids. Endospores are as abundant as vegetative cells and microbial activity is extremely low, leading to microbial biomass turnover times of hundreds to thousands of years. We infer from model calculations that biomass production is sustained by organic carbon deposited from the surface photosynthetic world millions of years ago and that microbial necromass is recycled over timescales of hundreds of thousands of years.

Deep sub-surface sediment material was obtained from the eastern tropical Pacific during the Ocean Drilling Program (ODP) Leg 201 expedition with DS JOIDES Resolution. Coring sites ranged from the continental shelf off the coast of Peru to ocean depths of 5,000 m. The expedition recovered sediment at depths of up to 420 metres below the sea floor (mbsf), and this sediment was found to be up to 35 million years old.

We report estimates of high bacterial endospore numbers in the order of 10^7 endospores per cm^3 (Fig. 1) in deep sediment and sediment that is up to 10 million years old. We used two different analyses to quantify endospores: muramic acid, which is a unique building block in cell walls of both bacteria and endospores; and dipicolinic acid, which is uniquely formed by endospores. In the first analysis, muramic acid of endospores is calculated as the total muramic acid (Supplementary Fig. 1) minus muramic acid from vegetative cells. Vegetative cells (and intact but recently dead cells) were quantified by acridine orange direct counts (AODCs)⁴. Endospore muramic acid is converted to endospore numbers by the use of cell-specific conversion factors that are obtained from the literature (Supplementary Information). It remains unclear whether bacteria or archaea predominate in the studied sediment^{5,6}. We therefore use two extreme scenarios for our estimates of endospore abundance, either that bacteria completely dominate⁶ (bacterial dominance) or that 90% are archaea⁵ (archaeal dominance). Archaea do not contain muramic acid in the cell wall. We also assume that 35% of the bacteria are Gram positive and 65% are Gram negative, as was found throughout the sediment column at Site 1229 (ref. 7).

Muramic-acid-based endospore numbers are 0.2×10^7 to 3×10^7 endospores per cm^3 . Archaeal or bacterial dominance did not affect the estimated endospore numbers because muramic acid levels calculated from AODC only marginally contributes to the measured

muramic acid concentrations (Fig. 1). At Site 1227 we also estimated endospore numbers from dipicolinic acid concentrations assuming an average dipicolinic-acid content of 2.2×10^{-16} mol spore⁻¹ (ref. 8). Dipicolinic-acid-based endospore numbers are 0.3×10^7 to 1.0×10^7 endospores per cm^3 and confirmed the muramic-acid-based estimates by a mean deviation factor of 4.6. There was a significant positive correlation between the two endospore estimates from muramic acid and dipicolinic acid as judged from a statistical analysis of their depth trend (regression of muramic acid and dipicolinic acid; $P = 0.0008$; $R^2 = 0.7297$). To our knowledge, this is the first time that such comparative data are published for endospores in environmental samples.

This discovery of high endospore abundances raises the question of why endospores have not been detected previously and whether total cell abundance in the deep biosphere, including endospores, has been globally underestimated. Previous studies of the deep biosphere did not quantify endospores. Endospores are unlikely to be stained by fluorescent DNA dyes such as acridine orange^{9,10} or by ribosomal RNA staining techniques such as catalysed reporter deposition fluorescence in situ hybridization because endospore walls are impermeable⁶. In this study we processed samples with 3 N HCl (for 4 h at 95 °C), which completely extracts muramic acid and dipicolinic acid from endospores¹¹. Our results suggest that endospores are as abundant as vegetative prokaryotes in this deep marine biosphere. Studies in other oceanographic regions are needed to clarify how the earlier global estimate of 3.5×10^{30} cells¹² should be adjusted to account for this.

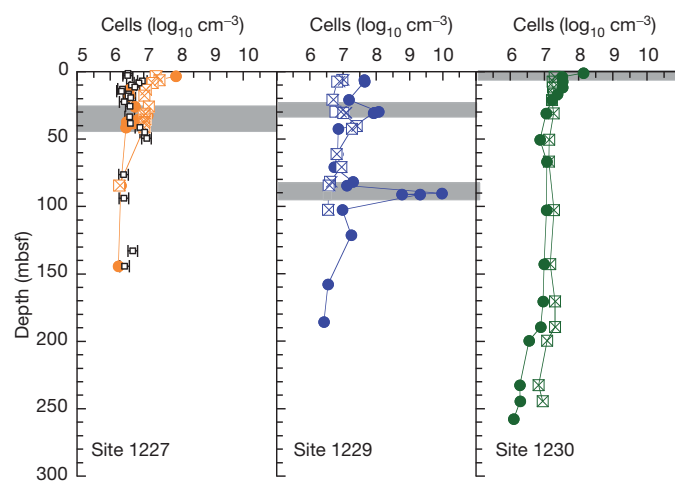


Figure 1 | Profiles of AODCs and estimated endospore numbers on the Peruvian continental shelf (sites 1227 and 1229) and in the Trench in Peru (site 1230). Filled circles, AODC; coloured open squares, muramic-acid-based estimated number of endospores (bacterial dominance); crosses, muramic-acid-based estimated number of endospores (archaeal dominance); black open squares, dipicolinic-acid-based estimated number of endospores ($n = 6$). Grey shading, sulphate-methane transition zones. Error bars, s.d.

¹Department of Bioscience, Section for Microbiology, Aarhus University, Building 1540, Ny Munkegade 114, DK-8000 Aarhus C, Denmark. ²Graduate School of Oceanography, University of Rhode Island, 100A, Horn Building, Narragansett, Rhode Island 02882, USA. ³Center for Geomicrobiology, Department of Bioscience, Aarhus University, Building 1535, Ny Munkegade 114, DK-8000 Aarhus C, Denmark.

It has been suggested that bacterial necromass production is responsible for enhanced organic matter preservation in highly productive regions such as the upwelling system off the coast of Peru¹³. Hence, whether microbial necromass is a major component¹³ or an insignificant component¹⁴ of sedimentary organic matter is an important question. We address this question by comparing the total measured amino acid carbon with the amino acid carbon estimated from vegetative cells and endospores, based on published cellular protein contents (Supplementary Information) and AODCs. Independent of whether bacteria or archaea dominate the microbial community, vegetative cells and endospores contribute less than 3% and 1% to amino acid carbon, respectively (Supplementary Fig. 2). As expected, microbial necromass accounts for the remaining >96% of amino acid carbon. The concentration of bulk organic matter progressively decreases with sediment depth and age. Amino acids contribute 4–5% to the total organic carbon in the youngest sediment and <0.1% in sediment that is several millions of years old (Supplementary Fig. 3), thus showing the preferential degradation of amino acids compared to bulk organic matter. Hence, the down-core decrease in amino acid concentrations is the result of a dynamic amino acid turnover in which amino acid degradation slightly exceeds amino acid formation. Our data suggest that the original amino acids that are derived from the water column are degraded soon after deposition and that sub-surface amino acids are produced *in situ* by new microbial biomass formation.

Almost all of the amino acids in living cells are present in the L-isomeric configuration. The only known exception is in bacteria, as they uniquely produce specific D-amino acids for incorporation into their cell-wall complex¹⁵. In marine sediment there is an additional source of D-amino acids derived from racemization, which is the slow stereo-chemical conversion of L-amino acids to D-amino acids and vice versa (see Supplementary Information). Bacterial cultures isolated from the deep sub-seafloor have been screened for D- and L-forms of aspartic acid. The D:L-Asp ratios are relatively constant with an average of 0.09 (s.e.m. = 0.02) (Supplementary Table 2). The half-life of abiotic chemical racemization (D:L = 0.33 is the ratio obtained when chemical racemization is half way to unity¹⁶) is 0.1–0.4 million years for Asp at the *in situ* temperature (Fig. 2a and Supplementary Information).

D:L-Asp ratios for sites 1227, 1229 and 1230 are higher than D:L-Asp ratios in cultures and increase in sediment that is older than 4 million years (Fig. 2a). This indicates that D-Asp is produced both biologically and by chemical racemization in sediment that is up to 10 million years old. Thus, the turnover time of Asp in the sediment is of a similar magnitude to the half-life for chemical racemization between L-Asp and D-Asp.

Constant low D:L ratios of Asp have been reported previously from vent systems¹⁷ and Holocene-epoch sediments¹⁸. In those studies low D:L ratios were considered evidence of bacterial activity, but the data were not used quantitatively.

We present a D:L model from which the turnover time of amino acids in living cells and microbial necromass, as well as their role in sedimentary carbon cycling, can be quantified (Fig. 2b; see the mathematical model in Supplementary Information). Inputs to the model are the measured mean D:L-Asp ratios in cultured bacteria from the deep biosphere (Fig. 2a and Supplementary Table 2), the fraction of Asp associated with living microorganisms (Supplementary Information), and the racemization half-life of the Asp¹⁶. We use Asp because the D:L-Asp ratio in bacterial cultures varies within a limited range (Fig. 2a) and because all of our measured D:L-Asp ratios deviate from the average ratios in bacterial cultures. Such a deviation is a prerequisite for accurate model calculations of turnover time.

The primary output of the D:L model is the turnover time of microbial necromass, which can be used to model microbial biomass turnover time (Supplementary Information equation (25)). A quasi-steady state in microbial biomass is assumed because AODC cell numbers are relatively constant within the 5-m intervals used in the model (Fig. 1). Total carbon oxidation rates of amino acids and uncharacterized total organic carbon, and the total carbon incorporation into microbial biomass (Fig. 2b), are estimated from necromass degradation rates and an assumed growth yield (carbon incorporation efficiency). In our calculations we use an 11% growth yield, which is the average growth yield for anaerobic heterotrophic bacteria¹⁹. At steady state, when microbial biomass production is equal to necromass degradation (Supplementary equation (5)), carbon must be incorporated into vegetative cells from uncharacterized total organic carbon to maintain balance (Fig. 2b). All model estimates are performed for two extremes in microbial community composition; that is, for bacterial dominance and archaeal dominance.

The biomass turnover time, T_b , of vegetative cells is equal to cell carbon divided by the rate of cellular carbon incorporation. We use biomass-turnover time instead of generation time, because we do not know whether the cells are dividing (as indicated by the term generation time) or whether they are turning over their biomass and persist without dividing. The T_b values of vegetative cells estimated from the D:L model are less than 0.2×10^3 to 4.0×10^3 years, irrespective of whether bacteria or archaea dominate (Fig. 3a). These results are supported by estimates of the T_b of sulphate-reducing bacteria (SRB; less than 0.1×10^3 to 1.5×10^3 years) at sites 1227 and 1229 (with one exception at site 1229 at which the T_b is 12×10^3 years; Fig. 3b). The T_b of SRB is estimated from sulphate-reduction rates modelled from

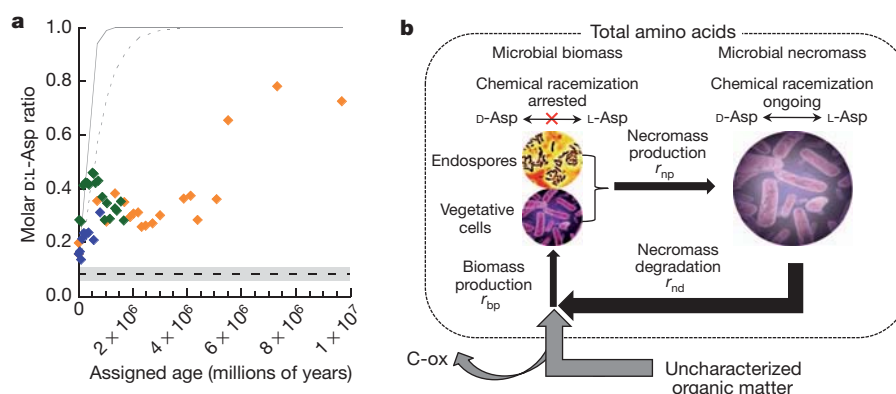


Figure 2 | D:L-Asp model. **a, b,** Turnover of amino acids in microbial biomass and necromass are quantified by application of the time constant (k_i) for chemical racemization of Asp in necromass and the known constant D:L-Asp in bacteria. **a,** D:L-Asp versus assigned age of the sediment (Supplementary Information): orange, site 1227; blue, site 1229; green, site 1230. Mean D:L-Asp in bacterial cultures (dashed line in the shaded box; Supplementary Table 2)

and s.e.m. (shaded box; $n = 7$). Curves show D:L-Asp generated by chemical racemization at the highest (solid line) and lowest (dotted line) temperatures encountered. **b,** Visualizes additional outputs of the D:L model: necromass production, necromass degradation, carbon oxidation (C-ox) and biomass production rates.

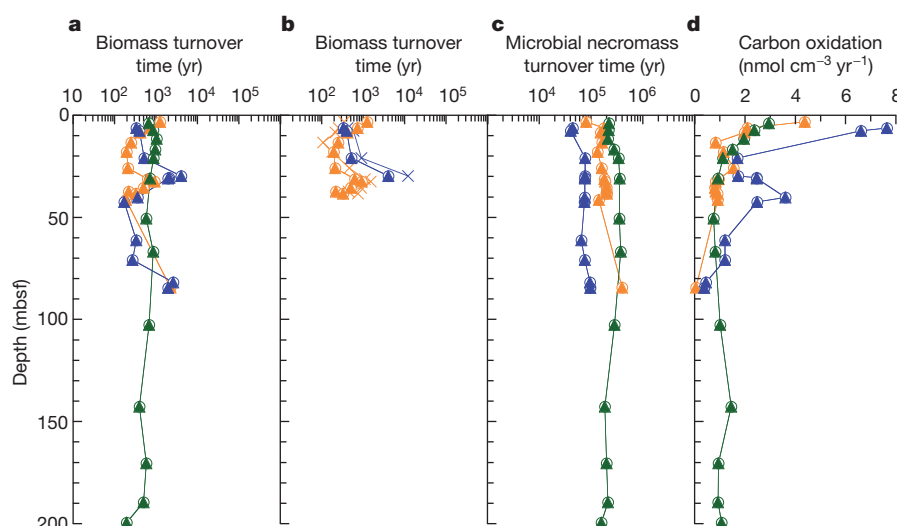


Figure 3 | D:L-model estimates of microbial biomass turnover times, necromass turnover times and carbon-oxidation rates. **a**, Microbial-biomass turnover times. **b**, Comparison between D:L-modelled biomass turnover times, and modelled biomass turnover times of sulphate reducing bacteria (crosses).

c, Necromass turnover times. **d**, Carbon-oxidation rates. Orange, site 1227; blue, site 1229; green, site 1230. Open circles, bacterial dominance; filled triangles, archaeal dominance of the microbial community (the two symbols overlap).

sulphate profiles and a 13% contribution of SRB to the microbial community in the sulphate zone²⁰ (Supplementary Information). The two independent estimates of T_b , from D:L modelling and from sulphate modelling, show almost identical down-core changes at sites 1227 and 1229 (Fig. 3b), and this underscores the capability of our new D:L modelling approach. At site 1230 we have only two estimates of T_b based on sulphate reduction and they were considerably shorter than the D:L modelled T_b (data not shown).

Previous estimates of microbial generation times in deep sub-seafloor sediment are in the range of 1×10^3 to 2×10^3 years (ref. 12). These estimates are based on the rates of organic carbon supply and an assumed 20% growth yield. If an 11% growth yield is applied, as in our D:L model, this gives longer generation times of 2×10^3 to 3×10^3 years, and these generation times are still consistent with results of the present study. Irrespective of the approach used to estimate mean generation times in the deep sub-seafloor, these times are far longer than the generation times found in any other ecosystem¹².

Sub-seafloor necromass is turned over on timescales that are 100-fold longer than the turnover of living biomass. Necromass turnover times are in the range of 0.4×10^5 to 4.0×10^5 years, irrespective of whether bacteria or archaea are assumed to dominate. This is still 10–100-fold shorter than the age of the oldest sediment (6.9 million years; Fig. 3c) and is consistent with our assumption of a quasi-steady state. It has been suggested that bacterial necromass may be an important source of recalcitrant, and hence preserved, organic matter in sediments of high-productivity regions^{13,21,22}. This apparent contradiction between previous studies and our results is probably due to differences in timescales among studies, which range from less than a few thousand years in earlier studies^{13,21,22} to several millions of years in the present study. Hence, preservation of sub-seafloor necromass on a shorter timescale does not preclude efficient mineralization on a longer timescale.

At all sites, D:L-Asp-modelled carbon oxidation rates decrease steeply in the upper part of the sediment (Fig. 3d). In the deeper part of site 1230 (70–200 mbsf), carbon oxidation rates remain relatively high compared to sites 1227 and 1229 (Fig. 3d). Site 1230 is located in the subduction zone and differed from the two other sites by the presence of gas hydrates at depths below 70 mbsf (ref. 23). The accumulation of methane hydrate and the more compressed sulphate-methane zonation at site 1230 compared to the other sites indicate that site 1230 has a higher carbon and energy flux in the deeper parts of the sediment.

Areal carbon oxidation rates in the sulphate zone are $1\text{--}9 \mu\text{mol cm}^{-2} \text{yr}^{-1}$ (irrespective of bacterial or archaeal dominance) based on D:L modelling. These rates are remarkably similar to independently determined carbon oxidation rates based on sulphate profiles¹ ($2\text{--}5 \mu\text{mol cm}^{-2} \text{yr}^{-1}$; Table 1). This supports the validity of the D:L model and gives confidence that the model is reliable also in zones below the depth of sulphate depletion.

The growth yields of the sulphate-reducing community can be estimated from biomass-production rates derived from D:L modelling, a 13% contribution of sulphate-reducing bacteria to the microbial community²⁰ and the carbon flux (carbon oxidation rate plus carbon incorporation into microbial biomass) to the sulphate-reducing bacteria, modelled from sulphate profiles (Supplementary equation (27)). The resultant average growth yield for sulphate-reducing bacteria is $13 \pm 8\%$, which is in agreement with the average growth yield of 11% derived from data in the literature and applied to the entire bacterial community. At the exceedingly low metabolic rates found in the present study (Fig. 3) it is unknown whether this growth yield leads to net growth and cell division or instead to turnover of the microbial-cell mass without division.

It is generally assumed that microbial communities in deep sub-surface sediments primarily rely on energy from the photosynthetic

Table 1 | Estimated carbon oxidation rates at ODP Leg 201 sites

ODP Leg 201 site	Water depth (m)	Relevant depth interval for sulphate reduction (mbsf)	Potential C-ox by net sulphate reduction ¹ ($\mu\text{mol cm}^{-2} \text{yr}^{-1}$)	Integration depth (D:L-modelled C-ox in sulphate zone (mbsf))	D:L-modelled C-ox in sulphate zone (bacterial dominance)* ($\mu\text{mol cm}^{-2} \text{yr}^{-1}$)	D:L-modelled C-ox in sulphate zone (archaeal dominance)† ($\mu\text{mol cm}^{-2} \text{yr}^{-1}$)	Integration depth (total D:L-modelled C-ox) (mbsf)	Total D:L-modelled C-ox (bacterial dominance)* ($\mu\text{mol cm}^{-2} \text{yr}^{-1}$)	Total D:L-modelled C-ox (archaeal dominance)† ($\mu\text{mol cm}^{-2} \text{yr}^{-1}$)
1227	427	1–34	1.8	5–35	3.9	4.0	5–85	6.6	6.7
1229	151	1–30	1.8 ‡	5–30	8.9	9.0	5–80	18.1	18.4
1230	5,086	1–10	5.0	5–10	1.2	1.2	5–200	21.3	21.4

* It is assumed that all living cells belong to Bacteria

† It is assumed that 10% of all living cells belong to the Bacteria and 90% to the Archaea

‡ At site 1229 carbon oxidation (C-ox) by sulphate reduction was assumed to be similar to that at site 1227 because sulphate penetrated to approximately the same depth at the two sites.

surface world¹. We estimate the minimum turnover time of the buried total organic carbon pool by dividing the total organic carbon concentration by the D:L-modelled carbon oxidation rates at all depths and sites. The total organic carbon turnover time is less than 43 million years, irrespective of whether bacteria or archaea dominate the microbial community. The total organic-carbon turnover times increase with approximately an order of magnitude from the upper and youngest sediment layers to the base of the cores. This suggests that buried organic carbon is indeed sufficient to fuel microbial activities over timescales of millions of years.

METHODS SUMMARY

Sediment handling and analysis. Samples were obtained from sites 1227, 1229 and 1230 of ODP Leg 201 (ref. 23). Sub-samples were taken from the central part of the cores immediately after these were brought on deck. Samples were stored at -20°C until analysis. Concentrations of muramic acid, D- and L-Asp, and individual amino acids were analysed by high-performance liquid chromatography (HPLC) following the method described in a previous study²² with the exception that in cases in which one of the samples was spiked, muramic acid was analysed twice in each sample. Dipicolinic-acid concentrations were analysed by HPLC and calibrated by standard additions to samples²⁴. Total organic carbon was determined in a Carlo Erba analyser after removal of carbonates by acidification with H_2SO_3 (5–6% w/w). Total organic carbon was estimated from five-point standard curves and flour containing 44.39% carbon was used as a standard.

Cell-specific concentrations of D- and L-amino acids. Seven pure cultures, isolated from ODP Leg 201, were analysed for D- and L-Asp. Cultures were washed twice in saline before acid hydrolysis to remove amino acids from the growth medium. Cultures (2 ml) were added to 2 ml of 12 mol l^{-1} HCl and hydrolysed at 105°C for 24 h under N_2 . Concentrations of the respective D- and L-amino acids were analysed as described earlier. Cell numbers in the different cultures were determined by epifluorescence microscopy after DNA staining with 4'-6-diamidino-2-phenylindole.

Standardization of data. Samples for the present study were not obtained from exactly the same depths as AODC⁴. Hence, concentrations were read from profiles at the depth of AODC to make comparisons to AODC. No attempt was made to standardize profiles in the lower part of site 1229 because our samples did not cover the depths of elevated AODC. Moisture and density data were obtained from the IODP database (<http://iodp.tamu.edu/janusweb/physprops/maddat.cgi>).

Received 27 October 2011; accepted 27 January 2012.

Published online 18 March 2012.

1. D'Hondt, S. *et al.* Distributions of microbial activities in deep subseafloor sediments. *Science* **306**, 2216–2221 (2004).
2. Jørgensen, B. B. & D'Hondt, S. A starving majority deep beneath the seafloor. *Science* **314**, 932–934 (2006).
3. Schrenk, M. O., Huber, J. A. & Edwards, K. J. Microbial provinces in the subseafloor. *Annu. Rev. Mar. Sci.* **2**, 279–304 (2010).
4. Jørgensen, B. B., D'Hondt, S. & Miller, D. J. (eds) Leg 201 synthesis: controls on microbial communities in deeply buried sediments. *Proc. ODP Sci. Res.* 1–45 (2006).
5. Lipp, J. S., Morono, Y., Inagaki, F. & Hinrichs, K. U. Significant contribution of Archaea to extant biomass in marine subsurface sediments. *Nature* **454**, 991–994 (2008).
6. Schippers, A. *et al.* Prokaryotic cells of the deep sub-seafloor biosphere identified as living bacteria. *Nature* **433**, 861–864 (2005).
7. Biddle, J. F., Fitz-Gibbon, S., Schuster, S. C., Brenchley, J. E. & House, C. H. Metagenomic signatures of the Peru Margin subseafloor biosphere show a genetically distinct environment. *Proc. Natl Acad. Sci. USA* **105**, 10583–10588 (2008).
8. Fichtel, J., Koster, J., Rullkotter, J. & Sass, H. Spore dipicolinic acid contents used for estimating the number of endospores in sediments. *FEMS Microbiol. Ecol.* **61**, 522–532 (2007).

9. Madigan, M. T. & Martinko, J. M. *Brock Biology of Microorganisms* 11th edn (Prentice Hall, 2006).
10. Schichnes, D., Nemson, J. A. & Ruzin, S. E. Fluorescent staining method for bacterial endospores. *Microscope* **54**, 91–93 (2006).
11. Hsieh, L. K. & Vary, J. C. Germination and peptidoglycan solubilization in *Bacillus megaterium* spores. *J. Bacteriol.* **123**, 463–470 (1975).
12. Whitman, W. B., Coleman, D. C. & Wiebe, W. J. Prokaryotes: the unseen majority. *Proc. Natl Acad. Sci. USA* **95**, 6578–6583 (1998).
13. Parkes, R. J. *et al.* A quantitative study of microbial decomposition of biopolymers in Recent sediments from the Peru Margin. *Mar. Geol.* **113**, 55–66 (1993).
14. Hartgers, W. A. *et al.* Evidence for only minor contributions from bacteria sedimentary carbon. *Nature* **369**, 224–227 (1994).
15. Schleifer, K. H. & Kandler, O. Peptidoglycan types of bacterial cell walls and their taxonomic implications. *Bacteriol. Rev.* **36**, 407–477 (1972).
16. Bada, J. L. Racemization of amino acids in nature. *Interdiscip. Sci. Rev.* **7**, 30–46 (1982).
17. Takano, Y., Sato, R., Kaneko, T., Kobayashi, K. & Marumo, K. Biological origin for amino acids in a deep subterranean hydrothermal vent, Toyoha mine, Hokkaido, Japan. *Org. Geochem.* **34**, 1491–1496 (2003).
18. Er, C., Nagy, B. & Riser, E. C. Analysis of muramic acid in holocene microbial environments by gas chromatography, electron impact, and fast atom bombardment mass spectrometry. *Geomicrobiol. J.* **5**, 57–78 (1987).
19. Heijnen, J. J. & van Dijken, J. P. In search of a thermodynamic description of biomass yields for the chemotrophic growth of microorganisms. *Biotechnol. Bioeng.* **39**, 833–858 (1992).
20. Leloup, J. *et al.* Sulfate-reducing bacteria in marine sediment (Aarhus Bay, Denmark): abundance and diversity related to geochemical zonation. *Environ. Microbiol.* **11**, 1278–1291 (2009).
21. Lomstein, B., Aa, Jørgensen, B. B., Schubert, C. J. & Niggemann, J. Amino acid biogeo- and stereochemistry in coastal Chilean sediments. *Geochim. Cosmochim. Acta* **70**, 2970–2989 (2006).
22. Lomstein, B., Aa, Jørgensen, B. B. & Langerhuus, A. T. Accumulation of prokaryotic remains during organic matter diagenesis in surface sediments off Peru. *Limnol. Oceanogr.* **54**, 1139–1151 (2009).
23. Shipboard Scientific Party. Leg 201 summary *Proc. ODP Init. Rep.* **201**, 1–81 (2003).
24. Lomstein, B. A. & Jørgensen, B. B. Pre column liquid chromatographic determination of dipicolinic acid from bacterial endospores. *Limnol. Oceanogr. Methods* (in the press).

Supplementary Information is linked to the online version of the paper at www.nature.com/nature.

Acknowledgements Bacterial cultures were provided by H. Cypionka. We thank members of the Leg 201 cruise for assistance in obtaining and processing samples. This research used samples and data provided by the Ocean Drilling Program (http://www-odp.tamu.edu/publications/201_IR/201ir.htm). The ODP was sponsored by the US National Science Foundation and participating countries under the management of Joint Oceanographic Institutions. We thank R. O. Holm and L. Poulsen for technical assistance and guidance with high-performance liquid chromatographic analyses. We thank D. L. Valentine for comments and suggestions to improve the manuscript. Financial support was provided by the Max Planck Society, the Danish National Research Foundation, the Danish National Science Research Council, the Danish Agency for Science, Technology and Innovation, the Faculty of Science and Technology at the University of Aarhus, and the US National Science Foundation.

Author Contributions A.J.S. and B.Aa.L. developed ideas and performed the project planning. B.Aa.L. performed the analysis and data processing of total organic carbon, amino acid composition, dipicolinic acid and D- and L-amino acids. A.T.L. performed the muramic acid analysis and data processing. B.B.J. developed the mathematical formulation of the D:L model together with A.T.L. and B.Aa.L. Estimation of sulphate reduction rates from sulphate profiles was carried out by B.B.J. and S.D. The manuscript was written by B.Aa.L., A.T.L. and B.B.J. All authors participated in early stages of data interpretation and provided editorial comments on the manuscript.

Author Information Reprints and permissions information is available at www.nature.com/reprints. The authors declare no competing financial interests. Readers are welcome to comment on the online version of this article at www.nature.com/nature. Correspondence and requests for materials should be addressed to B.Aa.L. (bente.lomstein@biology.au.dk).

Wild-type microglia arrest pathology in a mouse model of Rett syndrome

Noël C. Derecki^{1,2}, James C. Cronk^{1,2,3}, Zhenjie Lu¹, Eric Xu^{1,4}, Stephen B. G. Abbott⁵, Patrice G. Guyenet⁵ & Jonathan Kipnis^{1,2,3}

Rett syndrome is an X-linked autism spectrum disorder. The disease is characterized in most cases by mutation of the *MECP2* gene, which encodes a methyl-CpG-binding protein^{1–5}. Although *MECP2* is expressed in many tissues, the disease is generally attributed to a primary neuronal dysfunction⁶. However, as shown recently, glia, specifically astrocytes, also contribute to Rett pathophysiology. Here we examine the role of another form of glia, microglia, in a murine model of Rett syndrome. Transplantation of wild-type bone marrow into irradiation-conditioned *Mecp2*-null hosts resulted in engraftment of brain parenchyma by bone-marrow-derived myeloid cells of microglial phenotype, and arrest of disease development. However, when cranial irradiation was blocked by lead shield, and microglial engraftment was prevented, disease was not arrested. Similarly, targeted expression of *MECP2* in myeloid cells, driven by *Lysm*^{cre} on an *Mecp2*-null background, markedly attenuated disease symptoms. Thus, through multiple approaches, wild-type *Mecp2*-expressing microglia within the context of an *Mecp2*-null male mouse arrested numerous facets of disease pathology: lifespan was increased, breathing patterns were normalized, apnoeas were reduced, body weight was increased to near that of wild type, and locomotor activity was improved. *Mecp2*^{+/-} females also showed significant improvements as a result of wild-type microglial engraftment. These benefits mediated by wild-type microglia, however, were diminished when phagocytic activity was inhibited pharmacologically by using annexin V to block phosphatidylserine residues on apoptotic targets, thus preventing recognition and engulfment by tissue-resident phagocytes. These results suggest the importance of microglial phagocytic activity in Rett syndrome. Our data implicate microglia as major players in the pathophysiology of this devastating disorder, and suggest that bone marrow transplantation might offer a feasible therapeutic approach for it.

The role of glia in Rett syndrome has recently been recognized^{7–9}. *Mecp2*-null astrocytes were unable to support the normal dendritic ramification of wild-type neurons growing in culture⁷, and expression of wild-type *MECP2* protein in astrocytes of *Mecp2*-null hosts dramatically ameliorated disease pathology⁹. *Mecp2*-null microglia were reported to be toxic to neurons *in vitro* through production of high levels of glutamate¹⁰.

Microglia, the brain-resident macrophages, are of haematopoietic origin¹¹. Still, the idea of repopulation of brain microglia from bone-marrow-derived cells in adult mice under normal physiological conditions is controversial¹². However, when bone marrow transplantation is preceded by irradiation-mediated immune ablation, bone-marrow-derived cells with microglia-like morphology and phenotype (expressing low levels of CD45 and high levels of CD11b) are found in the brain^{13,14}. Microglia have received increasing attention in the pathophysiology of several neurodegenerative and neuropsychiatric diseases^{14–18}.

We first studied microglial function in the context of *Mecp2*^{-/-} male mice. Males possess a single mutant X chromosome, and thus manifest

a severe phenotype that includes markedly retarded growth, apnoeas, tremor, impaired gait and locomotor function, and a postnatal life expectancy of approximately 8 weeks^{4,19} (Fig. 1a, b and Supplementary Movie 1).

To address the role of hematopoietically derived cells in the pathophysiology of Rett, *Mecp2*^{-/-} (*Mecp2*^{tm1.1Jae} and *Mecp2*^{tm2Bird}) mice were subjected to lethal split-dose irradiation at postnatal day (P)28 (the approximate age at which neurological signs appear⁴). Mice were then injected intravenously with syngeneic bone marrow from C57Bl/6J mice ubiquitously expressing green fluorescent protein (GFP). Control groups were injected with autologous (*Mecp2*^{-/-}) bone marrow, or left naive. Surprisingly, the lifespan of *Mecp2*-null recipients of wild-type bone marrow (wild type → *Mecp2*^{-/-}) was significantly extended compared with *Mecp2*^{-/-} mice receiving autologous bone marrow (*Mecp2*^{-/-} → *Mecp2*^{-/-}) or to naive *Mecp2*^{-/-} mice (Fig. 1b and Supplementary Movie 2). Our oldest living wild-type → *Mecp2*^{-/-} mice were over 48 weeks of age (Supplementary Movie 3); most experimental mice were euthanized at the age of ~16 weeks for tissue analysis.

Although *Mecp2*^{-/-} mice on the C57Bl/6J background are undersized^{4,19}, within 4 weeks of transplantation, wild-type → *Mecp2*^{-/-} (but not *Mecp2*^{-/-} → *Mecp2*^{-/-}) mice approached the size of wild-type littermates (Fig. 1c, d). Wild-type → *Mecp2*^{-/-} mice also exhibited an increase in brain weight (Fig. 1e, f), which was probably caused by general growth of the mouse, because the reduced soma size characteristic of *Mecp2*-null neurons was not changed by bone marrow transplantation (Fig. 1g, h) and the brain to body weight ratio was normalized (Supplementary Fig. 1a). Spleens of *Mecp2*^{-/-} mice were also smaller than normal and their size normalized after transplantation (Supplementary Fig. 1b–d).

Growth retardation is a characteristic feature of Rett pathology. Along these lines, treatment with insulin-like growth factor (IGF)-1 benefits survival and behavioural outcomes in *Mecp2*-null mice²⁰. Indeed, peripheral macrophages from wild-type mice expressed significantly higher levels of IGF-1 *in vitro* in response to immunological stimuli than macrophages from *Mecp2*-null (*Mecp2*^{tm1.1Jae/y}) mice (Supplementary Fig. 2); this difference may contribute to the increased body growth seen in *Mecp2*-null mice after bone marrow transplantation.

The general appearance of wild-type → *Mecp2*^{-/-} mice was improved compared with that of naive *Mecp2*^{-/-} or *Mecp2*^{-/-} → *Mecp2*^{-/-} mice. The severe involuntary tremors normally seen in mutant mice were absent following wild-type bone marrow transplantation (Fig. 2a), and gait was improved. Interestingly, no detectable benefit on hindlimb clasping phenotype was observed.

Breathing irregularities and apnoeas are cardinal signs of Rett syndrome. We used whole-body plethysmography to compare the breathing patterns of *Mecp2*^{-/-} mice with or without bone marrow transplantation to those of control mice (Fig. 2b). As expected, *Mecp2*^{-/-} mice developed apnoeas progressively with age (data not shown). However, wild type → *Mecp2*^{-/-} exhibited significantly reduced apnoeas and fewer breathing irregularities than either naive *Mecp2*^{-/-} or

¹Department of Neuroscience, School of Medicine, University of Virginia, Charlottesville, Virginia 22908, USA. ²Graduate Program in Neuroscience, School of Medicine, University of Virginia, Charlottesville, Virginia 22908, USA. ³Medical Scientist Training Program, School of Medicine, University of Virginia, Charlottesville, Virginia 22908, USA. ⁴Undergraduate School of Arts and Sciences, University of Virginia, Charlottesville, Virginia 22908, USA. ⁵Department of Pharmacology, School of Medicine, University of Virginia, Charlottesville, Virginia 22908, USA.

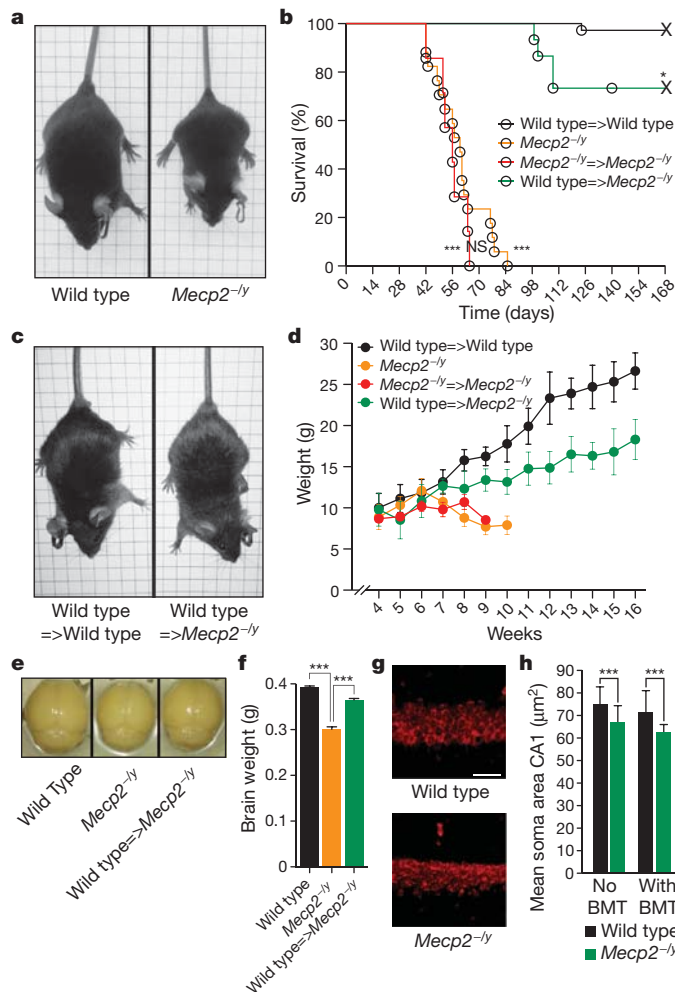


Figure 1 | Wild-type bone marrow transplantation (BMT) at P28 arrests disease progression in *Mecp2*^{-/-} mice. **a**, Representative images of wild-type and *Mecp2*^{-/-} littermates at P56. **b**, Lifespan of *Mecp2*^{-/-} mice receiving wild-type bone marrow at P28 (wild type → *Mecp2*^{-/-}; *n* = 15) compared with naive *Mecp2*^{-/-} (*n* = 17), *Mecp2*^{-/-} receiving *Mecp2*^{-/-} bone marrow (*Mecp2*^{-/-} → *Mecp2*^{-/-}; *n* = 9) and wild-type mice receiving wild-type bone marrow (wild type → wild type; *n* = 29) (***P* < 0.0001, log rank (Mantel-Cox)). **c**, Representative images of wild-type → wild-type compared with wild-type → *Mecp2*^{-/-} mice are shown at P56 (4 weeks after bone marrow transplantation). **d**, Weights (mean ± s.e.m.) of wild-type → wild-type, *Mecp2*^{-/-}, *Mecp2*^{-/-} → *Mecp2*^{-/-} and wild-type → *Mecp2*^{-/-} mice (*n* = 15, 15, 7, 15 mice per group) are shown over time. **e**, Representative images of brains isolated from P56 wild-type → wild-type and wild-type → *Mecp2*^{-/-} mice transplanted at P28 and naive *Mecp2*^{-/-} mice. **f**, Brain weight (mean ± s.e.m.) for each group (***P* < 0.001; one-way analysis of variance (ANOVA); *n* = 4 each group). **g**, Representative images of Nissl staining in hippocampal slices (CA1 area) of wild-type and *Mecp2*^{-/-} mice (scale bar, 40 μm). **h**, Soma area (mean ± s.d.) of CA1 hippocampal cells. For each group of mice, a set of cells was created by randomly selecting 100 cells per mouse, three mice per group (***P* < 0.001; two-way ANOVA with Bonferroni *post hoc* test).

Mecp2^{-/-} → *Mecp2*^{-/-} mice (Fig. 2c, d). Wild-type → *Mecp2*^{-/-} mice also displayed significantly increased mobility in the open field compared with naive *Mecp2*^{-/-} or *Mecp2*^{-/-} → *Mecp2*^{-/-} mice (Fig. 2e, f).

We also performed bone marrow transplantation in heterozygous female mice at 2 months of age, and animals were examined at 9 months. The disease in *Mecp2*^{+/-} mice develops slowly, with behavioural abnormalities becoming clear at 4–6 months of age. Weights of treated *Mecp2*^{+/-} mice were comparable to wild-type controls (Fig. 2g). Moreover, there was significant improvement in motor function, as examined on rotarod (Fig. 2h), and time spent in the centre of the open field arena was significantly increased (Fig. 2i).

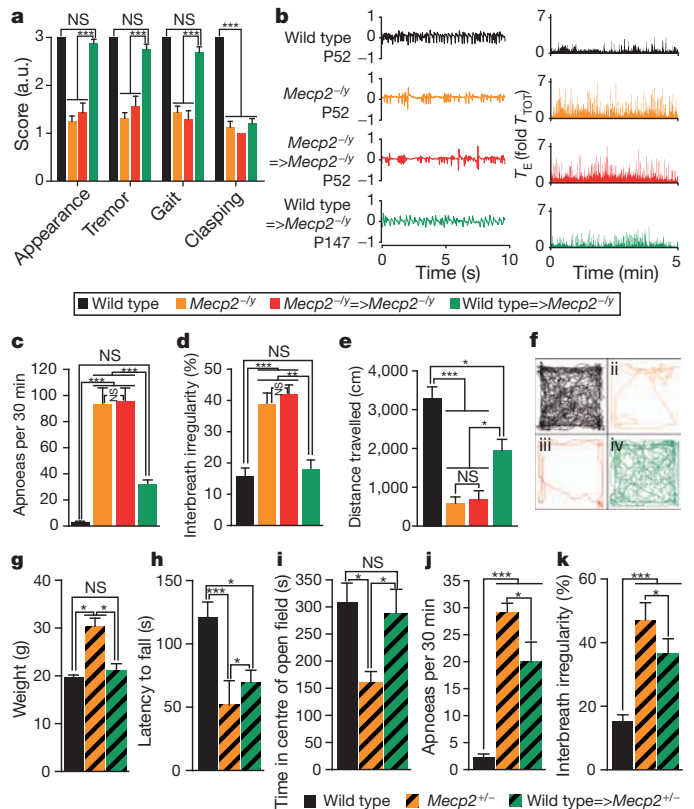


Figure 2 | Bone marrow transplantation effects on general appearance, breathing and locomotion of *Mecp2*^{-/-} and *Mecp2*^{+/-} mice. **a**, Neurological scores at P56 for wild-type → wild-type, *Mecp2*^{-/-} naive, *Mecp2*^{-/-} → *Mecp2*^{-/-} and wild-type → *Mecp2*^{-/-} mice. Behaviours (mean ± s.e.m.) are scored as indicated in Methods (***P* < 0.001; one-way ANOVA; *n* = 16, 16, 7, 16); NS, not significant; a.u., arbitrary units. **b**, Left, representative plethysmograph recordings of animals from each group; right, expiratory time (*T_E*) for representative wild-type, *Mecp2*^{-/-}, *Mecp2*^{-/-} → *Mecp2*^{-/-} and wild-type → *Mecp2*^{-/-} mice (transplantation at P28 and examination at indicated ages for all groups) as measured over 5 min; *T_E* is normalized to mean breath duration for each mouse. **c**, Apnoeas (mean ± s.e.m.) per 30 min as measured in all four groups (***P* < 0.001; one-way ANOVA with Bonferroni *post hoc* test; *n* = 5 mice per group; for the entire figure, all mice were age P56 except for wild-type → *Mecp2*^{-/-} at 12 weeks of age; that is, 8 weeks after bone marrow transplantation). **d**, Interbreath irregularity (mean percentage ± s.e.m.) calculated as absolute ($(T_{\text{total},n} - T_{\text{total},n+1})/T_{\text{total},n+1}$) for all four groups (***P* < 0.01; ****P* < 0.001; one-way ANOVA with Bonferroni *post hoc* test; *n* = 5 mice per group). **e**, Distance travelled (mean ± s.e.m.) in an open field (**P* < 0.05; ****P* < 0.001; one-way ANOVA, *n* = 5 mice per group). **f**, Representative traces of the path travelled by mice in an open field during 20 min test time. **g–k**, *Mecp2*^{+/-} mice were transplanted with wild-type bone marrow at P56 and were examined for disease symptoms at 9 months of age. **g**, Weight (mean ± s.e.m.); **h**, latency to fall (mean ± s.e.m.) in the rotarod task; **i**, time (mean ± s.e.m.) spent in the centre of the open field; **j**, apnoeas (mean ± s.e.m.) measured by whole-body plethysmography in 30 min; **k**, interbreath irregularity (mean ± s.e.m.): all were improved in the treated mice compared with non-treated controls (**P* < 0.05; ****P* < 0.001; one-way ANOVA, *n* = 6 mice per group; *post hoc* Bonferroni test was used for individual comparisons).

Apnoeas in bone marrow transplanted mice were reduced (Fig. 2j) and their overall breathing patterns were improved compared with their non-treated controls (Fig. 2k).

The peripheral immune system of *Mecp2*^{-/-} hosts was repopulated by donor bone marrow (Supplementary Fig. 3a). Additionally, it has been previously shown that bone marrow transplantation after whole-body irradiation results in engraftment of microglia-like myeloid cells into the brain parenchyma¹³. Indeed, GFP⁺ cells in the parenchyma of bone marrow transplanted mice expressed CD11b (Fig. 3a) but not GFAP or NeuN (data not shown). Twelve weeks after bone marrow transplantation, mice were perfused and their brains dissected into

sub-areas, prepared in single-cell suspensions and analysed using flow cytometry to determine percentages of bone-marrow-derived (GFP⁺) cells in the haematopoietic (CD45⁺) cell fractions in the brain (Supplementary Fig. 3b, c).

Interestingly, in mice in which bone marrow transplantation was performed later (P40 or P45), only slight improvements in disease pathology were observed (Supplementary Fig. 4a). No microglial engraftment was evident, although substantial numbers of GFP⁺ cells were found in the meningeal spaces (Supplementary Fig. 4b). These results may suggest that when disease progression is faster than microglial engraftment, full rescue cannot be achieved. The moderate results observed, however, may have been due to a yet-unknown mechanism, perhaps through soluble factors produced by meningeal immune cells, or peripherally-expressed IGF-1 (Supplementary Fig. 2). When bone marrow transplantation was performed at P2 without irradiation, minimal peripheral chimaerism was achieved without detectable microglial engraftment and no lifespan extension was observed (Supplementary Fig. 4a, c).

Newly engrafted microglia expressed detectable levels of wild-type *Mecp2* (data not shown) but nearby cells did not show any *Mecp2*

labelling, arguing against the possibility of protein or messenger RNA transfer from engrafted microglia into nearby cells as an underlying mechanism for the beneficial effect of bone marrow transplantation.

To substantiate the specific role of microglia in bone marrow transplantation-mediated disease arrest, we repeated transplantation experiments, again at P28, but with the addition of lead shielding to block cranial irradiation, which results in repopulation of peripheral immunity (Fig. 3b, c) but no parenchymal engraftment (Fig. 3d), supporting previously published work^{13,18}. Disease was not arrested in 'head-covered' mice (Fig. 3e), suggesting that peripheral immune reconstitution without microglial engraftment is insufficient to arrest pathology in *Mecp2*^{-/-} mice.

To substantiate further the role of myeloid cells in arrest of Rett pathology, we used a genetic approach. We employed the widely used *Lysm*^{Cre} mouse—which results in a high degree of recombination in myeloid cells, granulocytes and in significant numbers of microglia^{21–23}—in cross with *Mecp2*^{lox-stop} mice. Male progeny, *Mecp2*^{lox-stop/y}*Lysm*^{Cre}, express wild-type *Mecp2* in myeloid cells on an otherwise *Mecp2*-null background. These animals exhibited improvements in overall appearance and growth (Fig. 3f, g and Supplementary Movie 4) and their lifespans were significantly increased (Fig. 3h). The oldest *Mecp2*^{lox-stop/y}*Lysm*^{Cre} animals were 31 weeks of age, with survival of 100%; *n* = 6 mice per group. Apnoeas and interbreath irregularity of these mice were also significantly reduced compared with control mice (Fig. 3i, j), and their open field activity was not significantly different from wild-type counterparts (Fig. 3k). These results cannot be interpreted by cre leakiness, because no cre-mediated recombination was evident in either astrocytes or neurons in *Lysm*^{Cre} crossed to a reporter strain (data not shown), in line with previous publications^{22,23}.

Microglia from *Mecp2*-null mice were deficient in their response to immunological stimuli (Supplementary Fig. 5) and in phagocytic capacity, as examined by feeding cultured microglia with pre-labelled ultraviolet-irradiated neural progenitor cells, used as apoptotic targets²⁴ (Fig. 4a–c). Thus, it is possible that apoptotic debris would accumulate over time in the *Mecp2*-null brain, contributing to neuronal malfunction and accelerating disease progression. Along these lines, supplementation of wild-type microglia could reduce debris levels and allow improved neuronal function. Indeed, in mice transplanted with GFP⁺

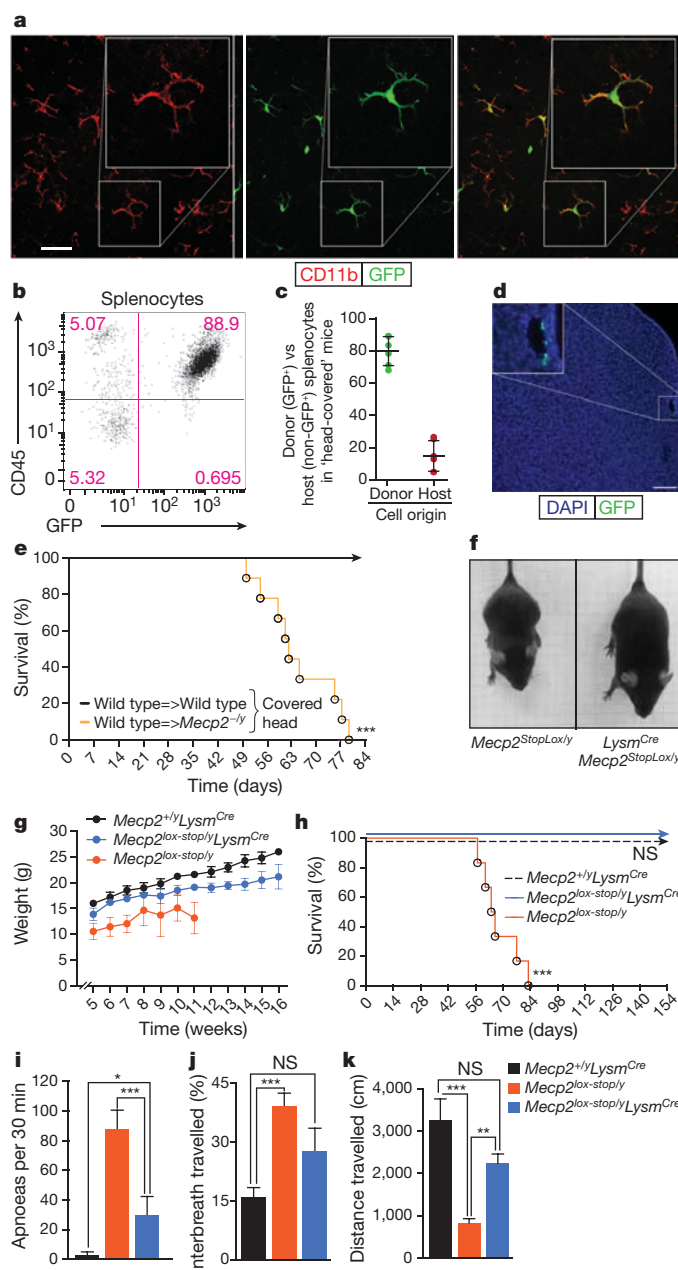


Figure 3 | Brain parenchymal engraftment of cells after bone marrow transplantation is required to arrest Rett syndrome. **a**, Representative confocal images of brain parenchyma from cerebellum of wild-type → *Mecp2*^{-/-} mice 8 weeks after transplantation (at P28), immunolabelled for CD11b and GFP (scale bar, 20 μm). **b–e**, *Mecp2*^{-/-} mice underwent bone marrow transplantation at P28 with their heads lead-protected. Mice were examined at their end-point, about 7 weeks after bone marrow transplantation. **b**, Representative dot plot of splenocytes obtained from bone-marrow-transplanted mouse with lead-protected head. **c**, Distribution of 'peripheral chimaerism' in mice with lead-protected heads after bone marrow transplantation. **d**, Representative micrograph from mice with lead-protected heads after bone marrow transplantation, immunolabelled for GFP. Coronal cortical slice is presented showing sporadic cells found in meningeal spaces, but not in the parenchyma. **e**, Lifespan of *Mecp2*^{-/-} mice with wild-type bone marrow transplantation with lead-covered heads compared with wild-type → wild-type controls with lead-covered heads (****P* < 0.0001, log rank (Mantel-Cox); *n* = 9 mice per group). **f–k**, Genetic approach for expressing MECP2 protein in myeloid cells. *Mecp2*^{lox-stop} mice were bred to *Lysm*^{Cre} mice and their progeny (*Mecp2*^{lox-stop/y}*Lysm*^{Cre} mice) were analysed for disease progression. **f**, Representative image of mice at P56. **g**, Weights (mean ± s.e.m.) of mice as they progress with age. **h**, Lifespan for indicated groups (****P* < 0.0001, log rank (Mantel-Cox); *n* = 6 mice per group). **i**, Apnoeas (mean ± s.e.m.) measured by whole-body plethysmography in 30 min for the three groups at 9 weeks. **j**, Interbreath irregularity (mean % ± s.e.m.) measured at 9 weeks. **k**, Distance travelled (mean ± s.e.m.) in an open field at 9 weeks (***P* < 0.01; ****P* < 0.001; one-way ANOVA, *n* = 5 mice per group; Bonferroni *post hoc* test was used for individual comparisons).

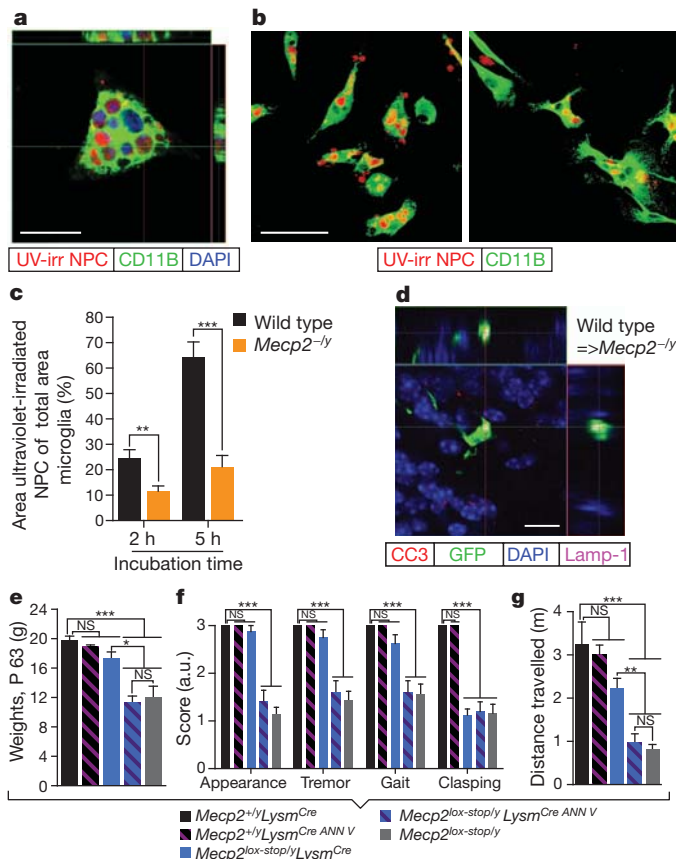


Figure 4 | Microglial phagocytic activity is necessary for their beneficial effect in *Mecp2*^{-ly} mouse brains. **a**, Representative micrograph of phagocytosing microglia in orthogonal projections of confocal z-stacks. Scale bar, 25 μ m. **b**, Wild-type (left) or *Mecp2*^{-ly} (right) microglia incubated for 2 or 5 h with fluorescently labelled ultraviolet-irradiated neural progenitor cells and stained with anti-CD11b. Scale bar, 50 μ m. **c**, Bar graphs comparing surface area of ultraviolet-irradiated neural progenitor cells (NPC) to total surface area (mean \pm s.e.m.) of wild-type or *Mecp2*^{-ly} microglia (** P < 0.01; *** P < 0.001; one-way ANOVA; representative experiment shown out of three independently performed). **d**, Representative micrograph of phagocytosing microglia *in situ* containing cleaved caspase-3 debris co-localized with lysosomal marker, Lamp-1. Scale bar, 50 μ m. **e–g**, *Mecp2*^{lox-stop/y}*Lysm*^{Cre} mice and the appropriate controls were treated with annexin V to inhibit phagocytic activity pharmacologically. **e**, Weights (mean \pm s.e.m.) of *Mecp2*^{+/y}*Lysm*^{Cre}, *Mecp2*^{lox-stop/y}*Lysm*^{Cre}, *Mecp2*^{lox-stop/y}*Lysm*^{Cre} ANN V and *Mecp2*^{lox-stop/y}*Lysm*^{Cre} mice treated with annexin V are shown at the end point for *Mecp2*^{lox-stop/y} and *Mecp2*^{lox-stop/y}*Lysm*^{Cre} treated with annexin V groups (~P63). **f**, Neurological scores (mean \pm s.e.m.) at P56 are presented (** P < 0.001; one-way ANOVA; n = at least seven mice per group; Bonferroni *post hoc* test was used for individual comparisons). **g**, Distance travelled (mean \pm s.e.m.) in an open field by mice from all the above groups (** P < 0.001; one-way ANOVA, n = 5 mice per group; Bonferroni *post hoc* test was used for individual comparisons).

bone marrow, only GFP⁺ parenchymal cells were consistently found containing cleaved caspase-3-positive debris within lysosomes (Fig. 4d).

It has been previously shown that annexin V (a protein that binds phosphatidylserine on apoptotic cells and inhibits engulfment) injected intravenously can reach the central nervous system²⁵. Moreover, we have recently shown that intravenous injection of annexin V results in substantial blockade of phagocytic activity in the brain²⁴. Indeed, treatment of wild-type mice with annexin V resulted in significant accumulation of terminal deoxynucleotidyl transferase (TdT)-mediated dUTP nick end labelling (TUNEL)⁺ fragments (Supplementary Fig. 6).

We attempted to inhibit brain phagocyte activity pharmacologically in *Mecp2*^{lox-stop/y}*Lysm*^{Cre} mice and compare disease progression with

controls. Long-term treatment of *Mecp2*^{lox-stop/y}*Lysm*^{Cre} mice with annexin V abolished the amelioration of the disease normally seen in these mice (Fig. 4e–g). Wild-type mice treated with annexin V were not significantly affected. This is probably because, unlike in *Mecp2*^{lox-stop/y}*Lysm*^{Cre} mice, neurons and astrocytes in wild-type mice are fully functional, expressing wild-type MECP2. It is conceivable, however, that a longer treatment of wild-type mice with annexin V might result in neurological pathology. Overall, these results suggest active engagement of wild-type microglia in clearance of apoptotic cells or cell remnants within the context of otherwise *Mecp2*-null brain—a task that probably cannot be sufficiently performed by *Mecp2*-null microglia.

Neuropathologists have observed gliosis and cell loss in the cerebellum of deceased patients who had Rett syndrome²⁶, but this work has not received much attention, presumably because the disease is generally considered non-neurodegenerative. Our results do not claim that neurodegeneration underlies the pathology of the disease. Rather, they suggest that *Mecp2*-null microglia, deficient in phagocytic function, may be unable to keep pace in clearing debris left behind from the normal process of neural cell death or membrane shedding. This, in turn, would lead to a crowded and sub-optimal central nervous system milieu within which neurons, already challenged by loss of *Mecp2*, might be further impaired in function. The inability of *Mecp2*-null microglia to clear debris as effectively as wild-type microglia has the potential to contribute to the underlying neuropathology and/or the time course of appearance of symptoms in *Mecp2*-null mice^{4,27}.

Future studies should be aimed at understanding the connections between glial phagocytic activity and neuronal function, and possible interactions between microglia and astrocytes in the pathology of Rett syndrome. Phagocytic activity per se is almost certainly just one aspect of glial involvement in the pathophysiology of the disease. It is conceivable that glia, including astrocytes—which are also capable phagocytes²⁸—release soluble factors in connection with their own phagocytic activity, in turn benefiting neuronal function. Therefore, removal of debris itself may not be as primarily relevant to disease progression as a secondary response of glia to the phagocytic process. Accordingly, inhibition of phagocytosis might result in exacerbation of pathology of the disease through these as yet unknown processes, even in the absence of deposits of easily observable cellular debris.

Our present findings support previous publications describing the potential for clinical treatment of Rett pathology^{6,29}, while also suggesting the possibility of achieving this goal through augmentation or repopulation of brain phagocytes, or improvement of their phagocytic activity. These results open the possibility for a new approach in the amelioration of the pathology of Rett syndrome.

METHODS SUMMARY

Animals. Male and female C57Bl/6-Tg(UBC-GFP)30Scha/J, C57Bl/6J, B6.129P2(C)Mecp2^{tm1.1Bird}/J, B6.129P2-Lyz2^{tm1(cres)}/J (*Lysm*^{Cre}), B6.129P2-Mecp2^{tm2Bird}/J, *Mecp2*^{lox-stop/y} and C57Bl/6J mice were purchased from Jackson Laboratories; B6.Cg-Mecp2^{tm1.1Jae/Mmcd} mice were a gift from A. Pieper and maintained in our laboratory on C57Bl/6J background. All procedures complied with regulations of the Institutional Animal Care and Use Committee at The University of Virginia.

Irradiation and bone marrow transfer. Four-week-old mice were subjected to lethal split-dose γ -irradiation (300 rad followed 48 h later by 950 rad). Four hours after the second irradiation, mice were injected with 5×10^6 bone marrow cells. After irradiation, mice were kept on drinking water fortified with sulphamethoxazole for 2 weeks to limit infection by opportunistic pathogens.

Full Methods and any associated references are available in the online version of the paper at www.nature.com/nature.

Received 3 May 2011; accepted 27 January 2012.

Published online 18 March 2012.

1. Van den Veyver, I. B. & Zoghbi, H. Y. Mutations in the gene encoding methyl-CpG-binding protein 2 cause Rett syndrome. *Brain Dev.* **23** (suppl. 1), S147–S151 (2001).

2. Van den Veyver, I. B. & Zoghbi, H. Y. Genetic basis of Rett syndrome. *Ment. Retard. Dev. Disabil. Res. Rev.* **8**, 82–86 (2002).
3. Amir, R. E. *et al.* Rett syndrome is caused by mutations in X-linked MECP2, encoding methyl-CpG-binding protein 2. *Nature Genet.* **23**, 185–188 (1999).
4. Guy, J., Hendrich, B., Holmes, M., Martin, J. E. & Bird, A. A mouse *Mecp2*-null mutation causes neurological symptoms that mimic Rett syndrome. *Nature Genet.* **27**, 322–326 (2001).
5. Nan, X. & Bird, A. The biological functions of the methyl-CpG-binding protein MeCP2 and its implication in Rett syndrome. *Brain Dev.* **23** (suppl. 1), S32–S37 (2001).
6. Luikenhuis, S., Giacometti, E., Beard, C. F. & Jaenisch, R. Expression of MeCP2 in postmitotic neurons rescues Rett syndrome in mice. *Proc. Natl Acad. Sci. USA* **101**, 6033–6038 (2004).
7. Ballas, N., Lioy, D. T., Grunseich, C. & Mandel, G. Non-cell autonomous influence of MeCP2-deficient glia on neuronal dendritic morphology. *Nature Neurosci.* **12**, 311–317 (2009).
8. Maezawa, I., Swanberg, S., Harvey, D., LaSalle, J. M. & Jin, L. W. Rett syndrome astrocytes are abnormal and spread MeCP2 deficiency through gap junctions. *J. Neurosci.* **29**, 5051–5061 (2009).
9. Lioy, D. T. *et al.* A role for glia in the progression of Rett's syndrome. *Nature* **475**, 497–500 (2011).
10. Maezawa, I. & Jin, L. W. Rett syndrome microglia damage dendrites and synapses by the elevated release of glutamate. *J. Neurosci.* **30**, 5346–5356 (2010).
11. Ginhoux, F. *et al.* Fate mapping analysis reveals that adult microglia derive from primitive macrophages. *Science* **330**, 841–845 (2010).
12. Ajami, B., Bennett, J. L., Krieger, C., Tetzlaff, W. & Rossi, F. M. Local self-renewal can sustain CNS microglia maintenance and function throughout adult life. *Nature Neurosci.* **10**, 1538–1543 (2007).
13. Mildner, A. *et al.* Microglia in the adult brain arise from Ly-6ChiCCR2⁺ monocytes only under defined host conditions. *Nature Neurosci.* **10**, 1544–1553 (2007).
14. Boissonneault, V. *et al.* Powerful beneficial effects of macrophage colony-stimulating factor on β -amyloid deposition and cognitive impairment in Alzheimer's disease. *Brain* **132**, 1078–1092 (2009).
15. Chen, S. K. *et al.* Hematopoietic origin of pathological grooming in *Hoxb8* mutant mice. *Cell* **141**, 775–785 (2010).
16. Hoogerbrugge, P. M. *et al.* Donor-derived cells in the central nervous system of twitcher mice after bone marrow transplantation. *Science* **239**, 1035–1038 (1988).
17. Simard, A. R., Soulet, D., Gowing, G., Julien, J. P. & Rivest, S. Bone marrow-derived microglia play a critical role in restricting senile plaque formation in Alzheimer's disease. *Neuron* **49**, 489–502 (2006).
18. Shechter, R. *et al.* Infiltrating blood-derived macrophages are vital cells playing an anti-inflammatory role in recovery from spinal cord injury in mice. *PLoS Med.* **6**, e1000113 (2009).
19. Chen, R. Z., Akbarian, S., Tudor, M. & Jaenisch, R. Deficiency of methyl-CpG binding protein-2 in CNS neurons results in a Rett-like phenotype in mice. *Nature Genet.* **27**, 327–331 (2001).
20. Tropea, D. *et al.* Partial reversal of Rett syndrome-like symptoms in MeCP2 mutant mice. *Proc. Natl Acad. Sci. USA* **106**, 2029–2034 (2009).
21. Willemsen, H. L. *et al.* Microglial/macrophage GRK2 determines duration of peripheral IL-1 β -induced hyperalgesia: contribution of spinal cord CX3CR1, p38 and IL-1 signaling. *Pain* **150**, 550–560 (2010).
22. Nijboer, C. H. *et al.* Cell-specific roles of GRK2 in onset and severity of hypoxic-ischemic brain damage in neonatal mice. *Brain Behav. Immun.* **24**, 420–426 (2010).
23. Cho, I. H. *et al.* Role of microglial IKK β in kainic acid-induced hippocampal neuronal cell death. *Brain* **131**, 3019–3033 (2008).
24. Lu, Z. *et al.* Phagocytic activity of neuronal progenitors regulates adult neurogenesis. *Nature Cell Biol.* **13**, 1076–1083 (2011).
25. Zhang, X. *et al.* A minimally invasive, translational biomarker of ketamine-induced neuronal death in rats: microPET imaging using 18F-annexin V. *Toxicol. Sci.* **111**, 355–361 (2009).
26. Oldfors, A. *et al.* Rett syndrome: cerebellar pathology. *Pediatr. Neurol.* **6**, 310–314 (1990).
27. McGraw, C. M., Samaco, R. C. & Zoghbi, H. Y. Adult neural function requires MeCP2. *Science* **333**, 186 (2011).
28. Park, D. *et al.* BAI1 is an engulfment receptor for apoptotic cells upstream of the ELMO/Dock180/Rac module. *Nature* **450**, 430–434 (2007).
29. Guy, J., Gan, J., Selfridge, J., Cobb, S. & Bird, A. Reversal of neurological defects in a mouse model of Rett syndrome. *Science* **315**, 1143–1147 (2007).

Supplementary Information is linked to the online version of the paper at www.nature.com/nature.

Acknowledgements We thank S. Smith for editing the manuscript. We thank the members of the Kipnis laboratory as well as the members of the University of Virginia Neuroscience Department for their comments during multiple discussions of this work. We also thank S. Feldman for injection of neonatal mice, I. Smirnov for tail vein injections, and B. Tomlin and J. Jones for their animal care. N.C.D. is a recipient of a Hartwell Foundation post-doctoral fellowship. This work was primarily supported by a grant from the Rett Syndrome Research Trust (to J.K.) and in part by HD056293 and AG034113 (to J.K.).

Author Contributions N.C.D. performed most of the experiments, analysed the data and prepared it for presentation, and contributed to experimental design and manuscript writing. J.C.C. performed the experiments with phagocytic activity of microglia *in vivo* and assisted with additional immunohistochemistry experiments along with data analysis and presentation, and contributed to experimental design and manuscript editing. Z.L. assisted with *in vitro* phagocytic activity experiments. E.X. assisted with animal behaviour scoring. S.B.G.A. assisted with plethysmography experiments and data analysis. P.G.G. assisted with plethysmography experimental design, data analysis and presentation of plethysmography-related data, and contributed to manuscript editing. J.K. designed the study, assisted with data analysis and presentation, and wrote the manuscript.

Author Information Reprints and permissions information is available at www.nature.com/reprints. The authors declare no competing financial interests. Readers are welcome to comment on the online version of this article at www.nature.com/nature. Correspondence and requests for materials should be addressed to J.K. (kipnis@virginia.edu).

METHODS

Animals. Male and female C57Bl/6-Tg(UBC-GFP)30Scha/J, C57Bl/6J, B6.129P2(C)Mecp2^{tm1.1Bird}/J, B6.129P2-Lyz2^{tm1.1cre}/Jf/J (*Lysm*^{cre}), B6.129P2-Mecp2^{tm2Bird}/J, *Mecp2*^{lox-stop/y} and C57Bl/6J mice were purchased from Jackson Laboratories; B6.Cg-Mecp2^{tm1.1Jae/Mmcd} mice were a gift from A. Pieper (Southwestern Medical School, Dallas, Texas, USA) and were maintained in our laboratory on C57Bl/6J background. All animals were housed in temperature and humidity controlled rooms, maintained on a 12 h/12 h light/dark cycle (lights on at 7:00) and age-matched in each experiment. All strains were kept in identical housing conditions. All procedures complied with regulations of the Institutional Animal Care and Use Committee at The University of Virginia.

Neurological assays. Mice were weighed on a laboratory scale and weights recorded to the nearest tenth of a gram; all other assays were scored on a scale from 3 to 1, with '3' being wild type (normal), and '1' being severe, as follows: gait '1', wide-spread hind limbs, severe 'waddling gait,' hopping or (unintentional) reverse locomotion; claspings '1', clenching of both rear hindlimbs tightly across ventral body aspect; tremor '1', visible involuntary shaking, particularly during or after handling; appearance '1', greasy and/or unkempt fur, clear signs of severe self-neglect in terms of grooming; kyphosis, hunched posture; eyes sunken, partly or fully closed, watery or crusted over. Scores of '2' were assigned to any phenotypes in between wild type and severe.

Bone marrow isolation. Mice were killed using CO₂ saturated with 70% alcohol. Skin was removed from the lower part of the body. Tissue was removed from hindlimbs with scissors and dissected away from body. Remaining tissue was cleaned from the tibial and femoral bones and bones were separated at the knee joint. Bone ends were cut off. Cells were forced out of bones with a stream of pH 7.4 0.1 M PBS containing 10% fetal calf serum using a 10 ml syringe with 25 gauge needle. Cells were centrifuged and re-suspended at the concentration of 2×10^7 cells per millilitre in PBS (250 µl cell suspension was injected intravenously in each animal through the tail vein).

Irradiation and bone marrow transfer. Four-week-old wild-type C57Bl/6J, B6.129P2(C)Mecp2^{tm1.1Bird}–/y, or B6.Cg-Mecp2^{tm1.1Jae/Mmcd}–/y mice were subjected to lethal split-dose γ -irradiation (300 rad followed 48 h later by 950 rad). Four hours after the second irradiation, mice were injected with 5×10^6 bone-marrow cells freshly isolated from C57Bl/6-Tg(UBC-GFP)30Scha/J, CBySmn.CB17-Prkdc^{scid}/J or B6.Cg-Mecp2^{tm1.1Jae/Mmcd}–/y mice. After irradiation, mice were kept on drinking water fortified with sulphamethoxazole for 2 weeks to limit infection by opportunistic pathogens.

Fluorescence-activated cell sorting (FACS) of brain isolates. Mice were perfused with 0.1 M PBS for 5 min. Heads were removed and skulls were quickly stripped of all flesh. Mandibles were next removed, as was all skull material rostral to maxillae. Surgical scissors (Fine Science Tools) were used to remove tops of skulls, cutting clockwise, beginning and ending inferior to the right post-tympanic hook. Brains were immediately placed in ice-cold FACS buffer (pH 7.4 0.1 M PBS, 1 mM EDTA, 1% BSA). Meninges (dura mater, arachnoid mater and pia mater) were carefully removed from the interior aspect of skulls and surfaces of brains with Dumont #5 forceps (Fine Science Tools). Brains were separated into sections (neocortex, hippocampus, striatum, cerebellum, brainstem) and sections from each group ($n = 3$ mice per group) were pooled. Brain tissue was homogenized with three gentle strokes in 10 ml FACS buffer in a 15 ml Tenbroeck Homogenizer (Lowell) then gently pressed through 70 µm nylon mesh cell strainers with sterile plastic plungers (BD Biosciences) to yield a single cell suspension. Cells were then centrifuged at 280g at 4 °C for 10 min, the supernatant removed and cells re-suspended in ice-cold FACS buffer. Myelin was removed using AutoMACS and myelin removal beads (Miltenyi Biotech). Cells were stained for extracellular markers with antibodies to CD11b conjugated to Alexa 780, CD45 conjugated to APC, CD4 conjugated to PE and MHC-II conjugated to Alexa 700 (eBioscience). All cells were fixed in 1% PFA in 0.1 M pH 7.4 PBS. Fluorescence data were collected with a CyAn ADP High-Performance Flow Cytometer (Dako) then analysed using FlowJo software. To obtain equivalent and accurate cell counts, cells were gated first using the LIVE/DEAD Fixable Dead Cell Stain Kit as per the manufacturer's instructions (Invitrogen), pulse width versus area to select singlet cells, forward scatter versus side scatter to eliminate debris, then by appropriate markers for cell type (for example, CD11b for myeloid-derived cells, or CD3 for T cells). Experiments were repeated twice with brains from $n = 3$ mice each group (total of $n = 6$ mice at 12 weeks after bone marrow transplantation).

Floating section immunohistochemistry. Free-floating sections were incubated with 10% normal serum (either goat or chicken) for 1 h at room temperature in PBS containing 0.1% Triton X-100 (Sigma), followed by incubation with appropriate dilutions of primary antibodies (anti-CD11b (eBioscience), 1:100; anti-MECp2 1:200 (Cell Signaling Technology); anti-cleaved caspase-3 (Cell Signaling Technology) 1:300; anti-GFP (Abcam) 1:2,000; anti-GFAP (Abcam) 1:1,000; anti-IGF-1 (R&D Systems) 1:100; anti-Lamp-1 (Abcam) 1:1000) for

24–48 h at 4 °C in the same buffer but without serum. Sections were then washed for 10 min three times at room temperature in 0.1% Triton X-100 (Sigma) in PBS followed by incubation with Alexa-fluor 488, 546, 594, 633 or 647 chicken/goat anti-mouse/rat/goat/chicken IgG antibodies (1:1,000, Invitrogen) for 1 h at room temperature. After 30 s in 1:20,000 DAPI reagent, sections were washed again with 0.1% Triton X-100 in 0.1 M PBS (3 × 10 min) and mounted with Aqua-Mount (Lerner Laboratories) under coverslips.

Analysis of Nissl staining. Three mice were analysed per group (wild type, *Mecp2*^{–/y}, wild type → wild type, wild type → *Mecp2*^{–/y}). Three coronal brain sections containing hippocampus were selected per mouse. Sections were incubated in 0.1% Triton X-100 (Sigma) in PBS for 10 min at 25 °C. Two washes were performed in PBS for 5 min each at 25 °C. Sections were then incubated in 1:40 Neurotrace Fluorescent Nissl Stain 530/615 Red (Molecular Probes), diluted in PBS, for 20 min at 25 °C. Sections were again incubated in 0.1% Triton X-100 (Sigma) in PBS for 10 min at 25 °C, and two washes were performed in PBS for 5 min each at 25 °C. After a final wash, sections were mounted on glass slides using Aqua-Mount (Thermo Scientific), coverslipped and visualized by confocal microscopy. Each hippocampal CA1 region (two per tissue section) was imaged, and quantified using the free hand tool in ImageJ. A Wacom computer graphics tablet was used to outline the somas of CA1 neurons, and the 'Measure and Label' function in ImageJ was used to quantify the area of each soma. After quantification, 100 soma measurements were randomly selected per mouse. This resulted in data sets of 300 soma measurements per group. GraphPad Prism was used to calculate two-way ANOVAs with Bonferroni *post-hoc* test.

Phagocytosis assay and analysis. To determine the phagocytic ability of microglial cells, we chose apoptotic neural cells as targets, because they would most closely approximate natural targets *in vivo*. Accordingly, dissociated neural progenitor cells were treated with ultraviolet light for 15 min, stained with 5(6)-TAMRA, succinimidyl ester (Invitrogen), and washed thoroughly with cold PBS before they were used for incubation with cell culture and fed on to wild-type or *Mecp2*^{–/y} microglial cells. After 2 or 5 hours at 37 °C and 5% CO₂, cells were removed, then washed and fixed with 4% PFA O/N. Coverslips were blocked in 10% chicken serum in 0.1 M PBS containing 0.3% Triton X-100 and 0.5% BSA, followed by incubation with anti-CD11b (eBioscience, 1:100) for 1 h at room temperature. Coverslips were then washed for 10 min three times at room temperature in 0.1% Triton X-100 (Sigma) in PBS, followed by incubation with Alexa-fluor 488 chicken anti-rat IgG antibodies (1:1,000, Invitrogen) for 1 h at room temperature. Coverslips were washed again with 0.1% Triton X-100 in 0.1 M PBS (10 min, three times) and mounted with Aqua-Mount (Lerner Laboratories) on slides. Slides were analysed using confocal microscopy and ImageJ software.

Whole-animal plethysmography. Plethysmography was performed during the dark phase of the diurnal cycle from 9:30 to 12:30 to assess normal waking respiratory parameters. Respiratory parameters were assessed by whole-animal plethysmography in unrestrained C57Bl/6J (wild-type), *Mecp2*^{–/y}, wild-type → *Mecp2*^{–/y}, *Mecp2*^{–/y} → *Mecp2*^{+/y}, *Lysm*^{cre}, *Mecp2*^{lox-stop/y}*Lysm*^{cre} and *Mecp2*^{lox-stop/y} mice. Animals were placed individually into 1,000 cm³ Plexiglas chambers (Buxco) and allowed 15 min to acclimate. The chamber was continuously flushed with dry room-temperature air (24 ± 0.5 °C) delivered by three computer-driven mass-flow regulators connected to pure O₂, N₂ and CO₂ (total flow: 1 l min^{–1}). The flow signal was recorded and analysed using EMKA IOX 2.7 (EMKA Technologies) and Spike 5.21 (CED) software. Breathing parameters were calculated from a calibrated flow signal derived from a differential pressure sensor connected to the plethysmography chamber using the equation of Drorbaugh and Fenn³⁰. Real-time chamber conditions (temperature and humidity) and atmospheric pressure were continuously measured and the calculation of tidal volume was automatically adjusted to account for changes in these variables. Inspiration and expiration were detected using a pressure transducer calibrated before each experiment by injecting 1 ml of air. The pressure signal was amplified, digitized and recorded using IOX software (EMKA Technologies) and Spike2 software (Cambridge Electronic Design), concurrently. Animals were left in chambers until sufficient data representing periods of quiescent breathing were collected to allow analysis. Animals were then returned to home cages.

Analysis of plethysmography. For apnoea scoring, plethysmography traces were hand-scored for apnoeas using the following criteria: expiratory time, $T_E > 1$ s measured exclusively during periods free of grooming, sniffing or locomotor behaviour, such that false positives were excluded.

Interbreath irregularity. Interbreath variability was derived from the absolute value of $((T_{\text{total},n} - T_{\text{total},n+1})/T_{\text{total},n+1})$, where $T_{\text{total},n}$ is the duration of the breathing cycle during the n th breath. In each mouse this variable was determined over 100 consecutive breaths during periods when the animals were quiescent (no locomotion or sniffing) and the average value produced a single score per mouse.

This score was averaged for each group of mice and expressed as a percentage (\pm s.e.m.).

Open-field activity. Behavioural testing in a novel open field was also performed during the dark phase of the diurnal cycle from 21:30 to 23:30 in the vivarium, such that measured locomotion would most closely correspond to normal waking activity. Animals were brought to the testing location within the vivarium and allowed to acclimate for 30 min before beginning the assay. Open field behaviour was measured using a Versamax activity monitor (AccuScan Instruments). Each mouse was placed initially in the centre of the monitoring cage, and allowed to roam freely for 20 min before being returned to the home cage. Animal activity levels were examined using Versamax software.

Accelerating rotarod. Motor coordination and balance were assessed on an Economex accelerating rotarod (Columbus Instruments) that had the capacity to test four mice simultaneously. The testing procedure consisted of two training phases and a testing phase: stationary training on a non-rotating rod, constant-speed training on a rod rotating at a speed of 2.0 r.p.m. and testing on an accelerating rotarod (acceleration = 0.1 r.p.m.). Latency to fall from the rotarod was recorded. For stationary training, the mouse was placed on the non-rotating rod facing the back side of the apparatus. The mouse was required to remain on the rod for 60 s before it was removed from the apparatus. If the mouse fell before the 60 s cutoff per trial, the animal was placed back onto the rod. This procedure was repeated for two trials with no inter-trial interval. For constant-speed training, the rod was adjusted to spin at a constant speed of 2.0 r.p.m. The mouse was placed on the rod facing the back side of the apparatus, and was required to remain on the rotating rod for 60 s before it was removed from the apparatus. If the mouse fell before the 60 s cutoff per trial, the animal was placed back onto the rod. This procedure was repeated for a total of two trials with no inter-trial interval. For accelerating rotarod testing, the rod was adjusted to spin at a constant speed of 2.0 r.p.m. The acceleration (acceleration = 0.1 r.p.m.) was started and the latency to fall recorded.

Microglia primary culture. Mouse mixed glia cultures were prepared from P2 mouse neonates as follows. Brains were excised and placed in ice-cold HBSS. Neocortical tissue was removed, meninges discarded and minced with forceps. Minced tissue was then incubated in 2 mg ml⁻¹ papain (Sigma) in HBSS at 37 °C for 30 min. After adding cold heat-inactivated fetal bovine serum, and DNase, the tissue was washed twice with cold HBSS by re-suspending the tissue and then pelleting in a 4 °C centrifuge. To obtain a single-cell suspension, the tissue was triturated gently by pipetting through a 5 ml serological pipette 20 times and then filtered through a 70 µm nylon filter (BD Biosciences). Mixed glial cells were cultured with culture medium consisting of DMEM/F12 with 10% fetal bovine serum (Invitrogen), GlutaMAX (Invitrogen) and 1% penicillin/streptomycin in a 5% CO₂/37 °C incubator, changing medium after 7 days, for a total of 14 days. To

obtain microglia, flasks were shaken at 120 r.p.m. for 12 h at 37 °C. Supernatants were collected, spun at 300g for 7 min, and then washed twice by re-suspending the cells in fresh medium and centrifuging at 25 °C. Cell pellets were re-suspended in culture medium and seeded at 5×10^5 cells per millilitre onto 24-well inserts (5×10^5 cells per well). Microglia were allowed to rest for 48 h before MHCII and cytokine expression assays.

Bone-marrow-derived macrophage culture. Macrophage cultures were prepared from bone marrow as follows: bone marrow was isolated as above. Five hundred thousand cells were pipetted into each well of a 24-well plate in 1 ml culture medium consisting of DMEM/F12 with 10% fetal bovine serum (Invitrogen), 10 ng ml⁻¹ rMCSF (eBioscience) and 1% penicillin/streptomycin in a 5% CO₂/37 °C incubator, changing 500 µl medium after 3 days and 6 days. At 9 days, mature macrophages were washed three times with 37 °C 0.1 M PBS to remove all non-adherent cells, then placed in 1 ml culture medium consisting of DMEM/F12 with 10% fetal bovine serum (Invitrogen) and 1% penicillin/streptomycin. Cells were allowed to rest for 6 h before further treatment.

Enzyme-linked immunosorbent assay of bone-marrow-derived macrophage supernatants. Bone-marrow-derived macrophages were prepared as above. Cells were treated in triplicate wells with cytokines (50 ng ml⁻¹ rIL4 or rIFNγ), or plain medium (control) and placed in a 5% CO₂/37 °C incubator for 72 h. If cells were subsequently treated with lipopolysaccharide (LPS; 100 ng ml⁻¹), they were removed from the incubator at 48 h, LPS was added and cells replaced for the final 24 h of incubation. At 72 h, 1 ml supernatant was removed from each well and frozen immediately at -80 °C. Samples were thawed simultaneously, an aliquot of each diluted 1:5 in manufacturer's diluent and enzyme-linked immunosorbent assay was performed with triplicate samples, according to the manufacturer's instructions (R&D).

TUNEL. Sections (20 µm) were sliced by cryostat and assayed the same day. Sections were permeabilized for 1 h using neuropore reagent (Trevigen) then labelled using the *In situ* Cell Death Detection Kit, Fluorescein (Roche) according to the manufacturer's instructions (using floating sections). Sections were washed 3×10 min in 0.1 M PBS, incubated for 30 s in 1:20,000 DAPI reagent, washed 1×10 min in 0.1 M PBS, mounted on slides with Aqua-Mount (Lerner) and coverslipped. Images were taken using a Zeiss LSM 700 confocal microscope. Six total slices from the cerebellum of three mice were imaged per group. Five images were taken per slice, and a randomly selected 100 µm \times 100 µm section of the granular layer was sampled for each image. The area of staining was measured for each field. The staining per field was used to calculate statistics by two-way ANOVA with Bonferroni *post hoc* test using GraphPad Prism.

30. Drorbaugh, J. E. & Fenn, W. O. A barometric method for measuring ventilation in newborn infants. *Pediatrics* **16**, 81–87 (1955).

Notch-dependent VEGFR3 upregulation allows angiogenesis without VEGF–VEGFR2 signalling

Rui Benedito^{1,2}, Susana F. Rocha^{1,2}, Marina Woeste^{1,2}, Martin Zamykal^{1,2}, Freddy Radtke³, Oriol Casanovas⁴, Antonio Duarte⁵, Bronislaw Pytowski⁶ & Ralf H. Adams^{1,2}

Developing tissues and growing tumours produce vascular endothelial growth factors (VEGFs), leading to the activation of the corresponding receptors in endothelial cells. The resultant angiogenic expansion of the local vasculature can promote physiological and pathological growth processes¹. Previous work has uncovered that the VEGF and Notch pathways are tightly linked. Signalling triggered by VEGF-A (also known as VEGF) has been shown to induce expression of the Notch ligand DLL4 in angiogenic vessels and, most prominently, in the tip of endothelial sprouts^{2,3}. DLL4 activates Notch in adjacent cells, which suppresses the expression of VEGF receptors and thereby restrains endothelial sprouting and proliferation^{2,4–6}. Here we show, by using inducible loss-of-function genetics in combination with inhibitors *in vivo*, that DLL4 protein expression in retinal tip cells is only weakly modulated by VEGFR2 signalling. Surprisingly, Notch inhibition also had no significant impact on VEGFR2 expression and induced deregulated endothelial sprouting and proliferation even in the absence of VEGFR2, which is the most important VEGF-A receptor and is considered to be indispensable for these processes. By contrast, VEGFR3, the main receptor for VEGF-C, was strongly modulated by Notch. VEGFR3 kinase-activity inhibitors but not ligand-blocking antibodies suppressed the sprouting of endothelial cells that had low Notch signalling activity. Our results establish that VEGFR2 and VEGFR3 are regulated in a highly differential manner by Notch. We propose that successful anti-angiogenic targeting of these receptors and their ligands will strongly depend on the status of endothelial Notch signalling.

Angiogenesis is prominently controlled by the activity of Notch in the endothelium of developing mice, zebrafish embryos and tumour models^{6–9}. Although the precise mechanisms linking the Notch and VEGF pathways remain incompletely understood, the activation of DLL4–Notch by VEGFR2 and the repression of VEGFR2 expression downstream of Notch activation are seen as two crucial processes regulating endothelial sprouting and angiogenesis^{1,4,5,10,11}. To study the role of VEGFR2 *in vivo* and circumvent the embryonic lethality of a global knockout of *Vegfr2* (also known as *Flk1* and *Kdr*) in mice, we generated inducible endothelial-cell-specific loss-of-function mutants (*Vegfr2*^{iAEC}) by combining *loxP*-flanked (floxed) *Vegfr2* alleles (*Vegfr2*^{flxed/flxed})¹² and tamoxifen-inducible Cre (*CreERT2*) transgenes^{13,14}. Following tamoxifen administration from postnatal day 3 (P3) to P5, analysis of the retinal vasculature at P7 confirmed that endothelial sprouting and vessel density were strongly reduced in *Vegfr2*^{iAEC} mutants (Fig. 1a, b).

Surprisingly, blocking Notch activation (for 48 h before analysis) with the γ -secretase inhibitor DAPT (*N*-[*N*-(3,5-difluorophenacetyl)-*L*-alanine]-*S*-phenylglycine *t*-butyl ester) strongly enhanced angiogenesis even in these mutant animals (Fig. 1a, b and Supplementary Fig. 2a, b). Because Notch is not the only substrate of γ -secretase and because

DAPT acts on all cell types, we combined *Vegfr2*^{flxed/flxed} and *Dll4*^{flxed/flxed} mice¹⁵ to generate endothelial-cell-specific double mutants. Deletion of the *Dll4* gene between P1 and P3 prominently increased sprout formation and vascular density (Fig. 1c), the latter of which reflects the known suppression of endothelial cell proliferation by Notch^{3,6,7}. Confirming the DAPT data, this increase in angiogenesis was not abolished by also targeting *Vegfr2*, even though both gene products were no longer detectable at the protein level (Fig. 1c and Supplementary Fig. 2c, d). The outgrowth and density of the *Dll4*^{iAEC}/*Vegfr2*^{iAEC} vasculature were slightly reduced compared with those of *Dll4*^{iAEC} mutants, whereas the numbers of sprouts and filopodia at the angiogenic front (that is, the distal region of the growing vasculature) were similar (Fig. 1e and Supplementary Fig. 2c, f). We also compared angiogenesis in the retinas of mice with different combinations of floxed *Notch1* and *Vegfr2* alleles and did not observe any significant differences in vascular density or sprouting between *Notch1*^{iAEC} and *Notch1*^{iAEC}/*Vegfr2*^{iAEC} retinas (Supplementary Fig. 2e, f).

The *Rbpj* gene encodes the transcription factor RBP-J κ , which binds to the intracellular domain of activated Notch (NICD) and is indispensable for Notch signalling¹⁶. The phenotype of inducible endothelial-cell-specific *Rbpj*^{iAEC} mutants manifests itself only after P4, which enabled us to study the effects of VEGFR2 and VEGF-A inhibition in this model from P4 to P7 (Fig. 1d). Like the targeting of the *Vegfr2* gene, the administration of VEGF-A- or VEGFR2-blocking antibodies efficiently reduced endothelial cell sprouting and vessel density in the retinas of control mice but did not significantly impair the deregulated angiogenic growth in *Rbpj*^{iAEC} mutants (Fig. 1d, e and Supplementary Fig. 3). This finding further supported the idea that angiogenesis in Notch-deficient vessels can occur in the absence of VEGF-A or VEGFR2 activity. Moreover, despite the high vessel density and extensive sprouting in the *Rbpj*^{iAEC} and *Dll4*^{iAEC} vasculature, vessel outgrowth towards the VEGF-A-rich (avascular) retinal periphery was strongly reduced (Fig. 1d, e). Thus, in contrast to the existing models of the crosstalk between VEGF and Notch, these results suggest that endothelial responses to the tissue-derived VEGF-A gradient are not enhanced by the loss of Notch activity.

Previous studies have reported that VEGF-A–VEGFR2 signalling is important for the upregulation of *Dll4* expression in sprouting endothelial tip cells^{2,3}, which, in turn, is thought to activate Notch signalling in adjacent (stalk) cells and thereby suppress sprouting behaviour. However, the strong effects of *Dll4* or *Notch* inactivation in the *Vegfr2*^{iAEC} background (Fig. 1a–e) suggested that a substantial level of endothelial Notch signalling was maintained without VEGFR2 function. Indeed, control and *Vegfr2*^{iAEC} sprouting tip cells and arteries displayed similar anti-DLL4 antibody staining (Fig. 2a and Supplementary Fig. 4), and weaker protein signals were only seen within the mutant capillary network. *Dll4* and *Hey1* messenger RNA levels were also only partially reduced in *Vegfr2*^{iAEC} lungs, a tissue that was

¹Max Planck Institute for Molecular Biomedicine, Department of Tissue Morphogenesis, D-48149 Münster, Germany. ²University of Münster, Faculty of Medicine, D-48149 Münster, Germany. ³Ecole Polytechnique Fédérale de Lausanne (EPFL), Swiss Institute for Experimental Cancer Research (ISREC), CH-1015 Lausanne, Switzerland. ⁴Translational Research Laboratory, Catalan Institute of Oncology, IDIBELL, 08907 L'Hospitalet de Llobregat, Spain. ⁵The Interdisciplinary Centre of Research in Animal Health (CIISA), Faculty of Veterinary Medicine, Technical University of Lisbon, 1300-474 Lisbon, Portugal. ⁶ImClone Systems, 180 Varick Street, New York, New York 10014, USA.

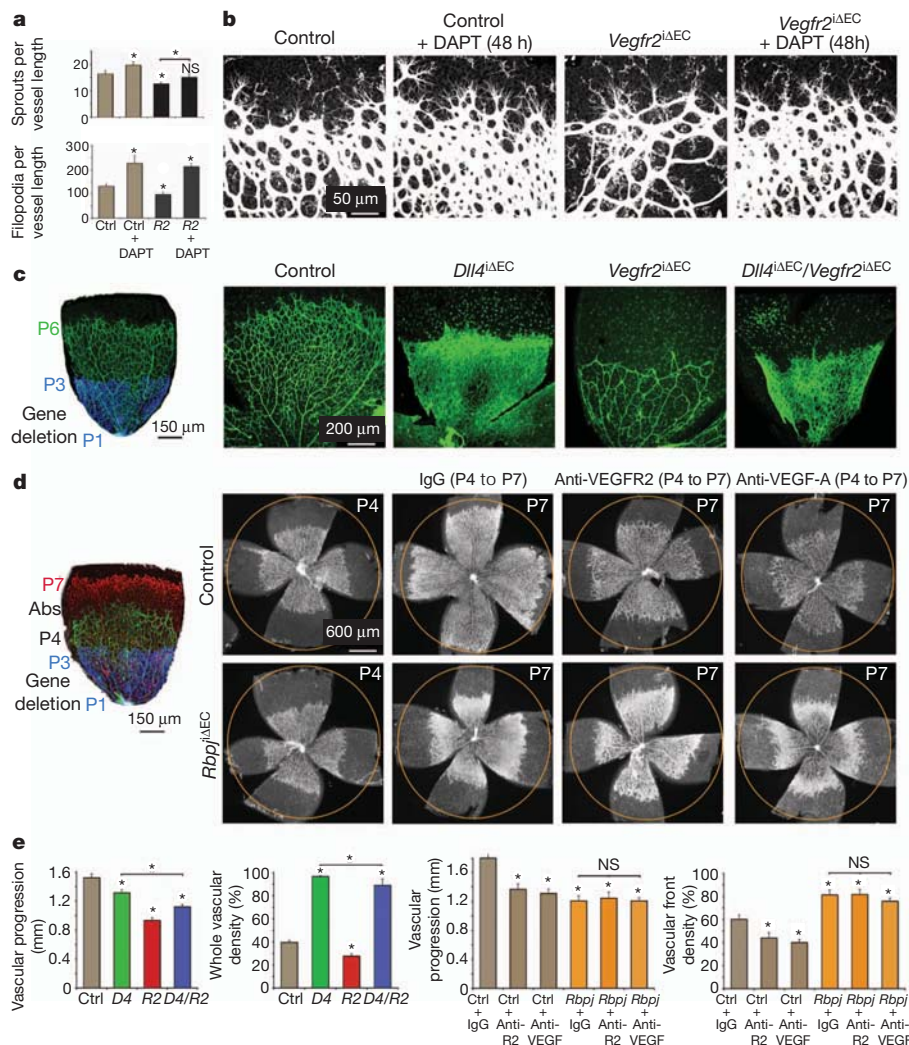


Figure 1 | Notch inhibition promotes angiogenesis independently of VEGFR2.

a, b, Quantification of sprouting defects and representative confocal images of the islectin-B4-stained angiogenic front of *Vegfr2*^{ΔEC} mutants, as well as the effect of DAPT treatment (see also Supplementary Fig. 2a, b). Ctrl, control; R2, *Vegfr2*^{ΔEC}. **c**, Induction of endothelial-cell-specific *Dll4* or *Vegfr2* deletion from P1 to P3 and analysis at P6. Note the strongly enhanced angiogenesis in *Dll4*^{ΔEC} and *Dll4*^{ΔEC}/*Vegfr2*^{ΔEC} mutants compared with control and *Vegfr2*^{ΔEC} retinas. **d**, Isolectin-B4-stained control and *Rbpj*^{ΔEC} P4 and P7 retinas (tamoxifen administration from P1 to P3) treated with control IgG, or anti-VEGFR2 or anti-VEGF-A antibodies (Abs) from P4 to P7. The orange circles facilitate the comparison of vascular progression. **e**, Quantification of vascular parameters of retinas in **c** and **d**. See Supplementary Figs 2 and 3 for additional data. D4, *Dll4*^{ΔEC}; D4/R2, *Dll4*^{ΔEC}/*Vegfr2*^{ΔEC}; *Rbpj*^{ΔEC}. **a, e**, Data are presented as mean + s.e.m.; $n \geq 12$. *, $P < 0.05$ compared with the left-most histogram bar unless otherwise indicated; NS, not significant.

chosen for analysis because of its particularly high endothelial cell content (Fig. 2c). The level of NICD protein was lower in *Vegfr2*^{ΔEC} lungs, but NICD was still readily detectable by immunoblotting (Fig. 2c). By contrast, VEGFR3, which has previously been shown to be positively regulated by VEGFR2 signalling⁵, showed the expected decrease in expression in the *Vegfr2*^{ΔEC} endothelium (Fig. 2b, c and Supplementary Fig. 4c). These results indicate that substantial DLL4 expression is maintained in the absence of VEGFR2, while the VEGFR3 protein levels are strongly reduced.

Active Notch is widely seen as a potent negative regulator of VEGFR2 and VEGFR3 expression^{4,11}, but published reports provide an inconsistent picture. For example, overexpression of DLL4 or NICD in cultured human umbilical vein endothelial cells (HUVECs) was shown to repress *VEGFR2* transcription^{17,18}. By contrast, DAPT treatment of HUVECs did not lead to significant changes in VEGFR2 protein or *VEGFR2* transcript levels, despite increased proliferation and sprouting^{17,19} (Supplementary Fig. 5a). In the mouse retina, both *Vegfr2* and *Vegfr3* mRNAs have been found to be only slightly upregulated in *Dll4*^{+/-} heterozygotes or after DAPT administration^{2,5}. In zebrafish, *vegfr3* (also known as *flt4*) mRNA expression has been shown to be increased in *rbpj* morphants but not in *dll4* morphants^{6,20}. Our own data indicate the selective regulation of VEGFR3 but not VEGFR2 downstream of Notch. In arteries, in which Notch is more active, DLL4 was strongly expressed; however, the endogenous levels of the VEGFR3 protein were low. By contrast, VEGFR2 was present in arteries and veins (Supplementary Fig. 5b–d).

Furthermore, we found a strong increase in the VEGFR3 protein but not the VEGFR2 protein in the *Rbpj*^{ΔEC} angiogenic front (Fig. 2e).

Upregulation of the VEGFR3 protein was also observed in lung lysates and sections from *Rbpj*^{ΔEC} and *Dll4*^{ΔEC} mutants, whereas the VEGFR2 level was not significantly altered (Figs 2d and 3c and Supplementary Fig. 6). Interestingly, this difference was not mirrored at the mRNA level: the levels of *Vegfr2* and *Vegfr3* mRNA were not substantially increased, which hints at post-transcriptional regulation of VEGFR3 levels by Notch (Fig. 2d). The differential regulation of VEGFR protein levels was also mirrored by the activity levels of these receptors. The level of phosphorylated VEGFR3 (phospho-VEGFR3) was strongly increased in *Rbpj*^{ΔEC} lung lysates, whereas the increase in phospho-VEGFR2 was more modest and mirrored the increase in vascular endothelial cadherin (CDH5) (which reflects the number of endothelial cells) in the *Rbpj*^{ΔEC} mutant model (Figs 2d and 3a–c). VEGFR2 and Notch play opposing roles in the regulation of VEGFR3 levels. Their actions seem to be independent because the combined deletion of *Dll4* and *Vegfr2* (*Dll4*^{ΔEC}/*Vegfr2*^{ΔEC}) or the administration of DAPT to *Vegfr2*^{ΔEC} pups led to a significant increase in VEGFR3 protein compared with control or *Vegfr2*^{ΔEC} mutant pups (Fig. 3c, d; see also Fig. 2b).

To investigate the functional consequences of high levels and activity of VEGFR3 protein in endothelial cells with low or compromised Notch signalling, we first used a monoclonal antibody that specifically blocks ligand binding to VEGFR3 (mF4-31C1). Daily injection from P4 to P7 with 50 mg kg day⁻¹ of mF4-31C1 did not impair vessel growth in control or *Rbpj*^{ΔEC} mutants (Fig. 3e, f), suggesting that the ligand-dependent activation of VEGFR3 is not important for developmental angiogenesis, which is consistent with previous reports^{21,22}. We then carried out short-term administration (24 h) of DAPT and the kinase inhibitor MAZ51. MAZ51 potently inhibits VEGF-C- or

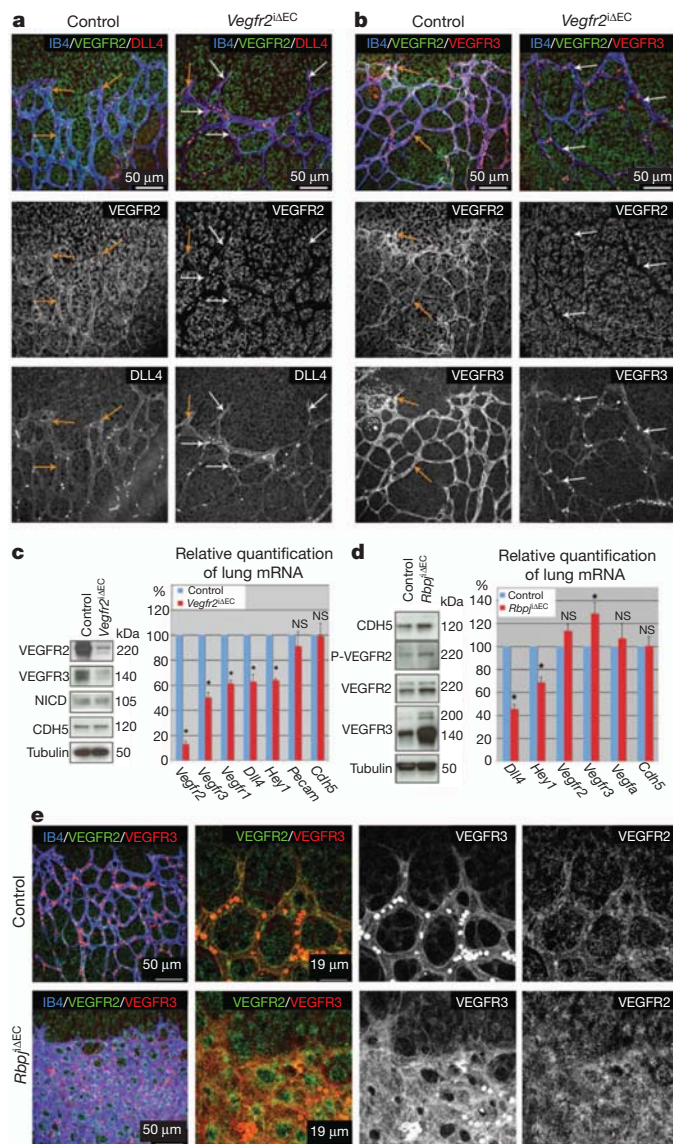


Figure 2 | VEGFR2 strongly regulates VEGFR3 protein levels but not DLL4 at the angiogenic front. **a, b**, Whole-mount triple immunofluorescence for DLL4 or VEGFR3 (red), VEGFR2 (green) and islectin B4 (IB4; blue) of P6 control and *Vegfr2*^{ΔEC} retinas. The deletion of *Vegfr2* for 5 days strongly compromised angiogenesis and the expression of VEGFR3 but not of DLL4 in tip endothelial cells. The arrows indicate endothelial cells expressing VEGFR2 (orange) and devoid of VEGFR2 (white). **c, d**, Immunoblotting (left) and quantitative PCR analysis with reverse transcription (qRT-PCR; right) of *Vegfr2*^{ΔEC} and *Rbpj*^{ΔEC} P6 mouse lungs for the indicated proteins and transcripts. The CDH5 protein levels reflect endothelial cell content. Data are presented as mean ± s.e.m.; *n* = 4. *, *P* < 0.001 compared with control group data (blue bars) unless otherwise indicated; NS, not significant. P-VEGFR2, phospho-VEGFR2. **e**, Whole-mount triple immunofluorescence for VEGFR3 (red), VEGFR2 (green) and islectin B4 (blue), showing upregulated VEGFR3 but not VEGFR2 protein in *Rbpj*^{ΔEC} vessels. **a, b, e**, Autofluorescent red blood cells are visible as round spots inside the vessels.

VEGF-D-induced activation of VEGFR3 but only weakly impairs VEGFR2 activation by VEGF-A²³. In contrast to the VEGFR3-blocking antibody, MAZ51 strongly inhibited both VEGF-C-dependent and VEGF-C-independent VEGFR3 phosphorylation in cultured cells (Supplementary Fig. 7). Although MAZ51 alone only weakly affected the number of filopodia and sprouts at the angiogenic front of the control retinal vasculature, this inhibitor strongly suppressed the enhanced sprouting caused by DAPT (Fig. 4a, b). MAZ51 also reduced the phosphorylation of VEGFR3 in *Rbpj*^{ΔEC} lung lysates (Fig. 4c).

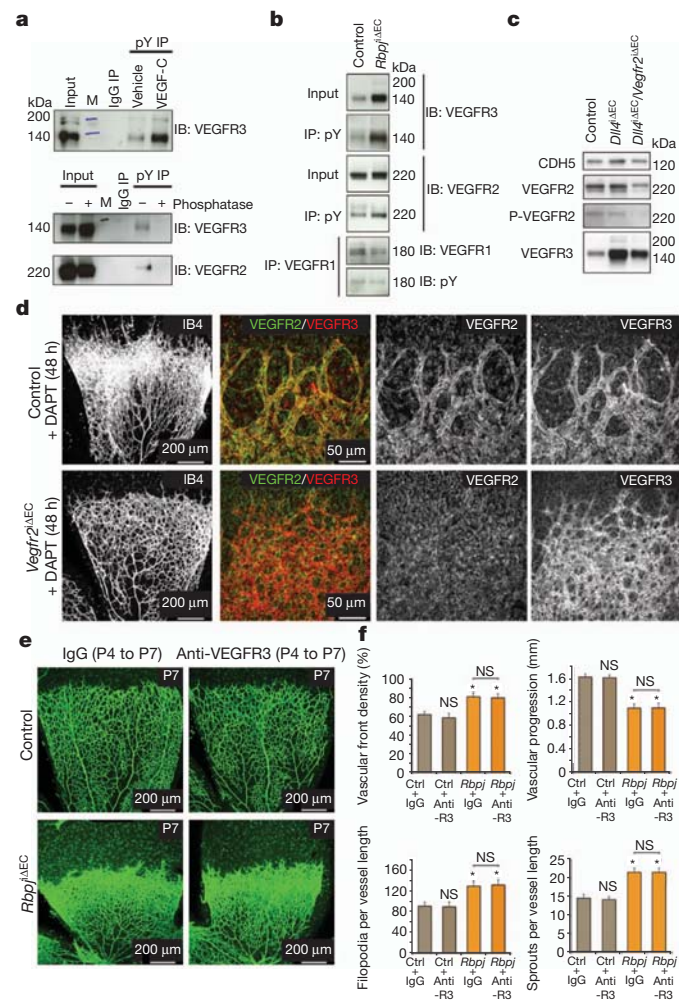


Figure 3 | Notch regulates VEGFR3 activity independently of VEGFR2.

a, Controls for VEGFR3 and VEGFR3 phosphotyrosine (pY) immunoprecipitation (IP) from P6 lungs. Phospho-VEGFR3 is present at increased levels in VEGF-C-injected P6 pups. The specificity was confirmed by lambda protein phosphatase pre-incubation. IB, immunoblotting antibody; M, molecular weight markers. **b**, Phosphotyrosine immunoprecipitation from lung lysates, showing strongly increased phospho-VEGFR3 in *Rbpj*^{ΔEC} mutants. Smaller changes were observed for phospho-VEGFR2, total VEGFR1 and phospho-VEGFR1. **c**, Immunoblot analysis, showing strongly increased VEGFR3 protein levels in *Dll4*^{ΔEC} and *Dll4*^{ΔEC}/*Vegfr2*^{ΔEC} P6 lung lysates, which was only partly attenuated in the absence of endothelial VEGFR2. **d**, Isolectin B4 combined with VEGFR2 (green) and VEGFR3 (red) staining of control and *Vegfr2*^{ΔEC} retinas. DAPT administration for 48 h before dissection restored high VEGFR3 protein levels at the *Vegfr2*^{ΔEC} angiogenic front (compare with Fig. 2b). **e**, Confocal images of islectin-B4-stained P7 control and *Rbpj*^{ΔEC} retinas (with tamoxifen administration from P1 to P3) injected with control IgG or anti-VEGFR3 antibody from P4 to P7. **f**, Quantification of vascular parameters in control and *Rbpj*^{ΔEC} mice treated with VEGFR3-blocking antibody (anti-R3) or IgG, as indicated. Data are presented as mean ± s.e.m.; *n* ≥ 12. *, *P* < 0.05 compared with control group data shown to the left of each graph unless otherwise indicated; NS, not significant.

These results point to a crucial role for VEGFR3 in the regulation of sprouting in endothelial cells with low Notch signalling activity, which is also in agreement with previous reports using morpholino targeting of *vegfr3* in zebrafish^{6,20}.

By contrast, the DAPT-induced increase in endothelial cell density at the angiogenic front was not significantly altered by the addition of MAZ51 (Fig. 4a and Supplementary Fig. 8). Providing further evidence for the important role of VEGFR3 in Notch-controlled angiogenesis, the injection of *Vegfr2*^{ΔEC} pups with DAPT and MAZ51 (at P5 for 24 h) led to a striking decrease in the number of sprouts and filopodia

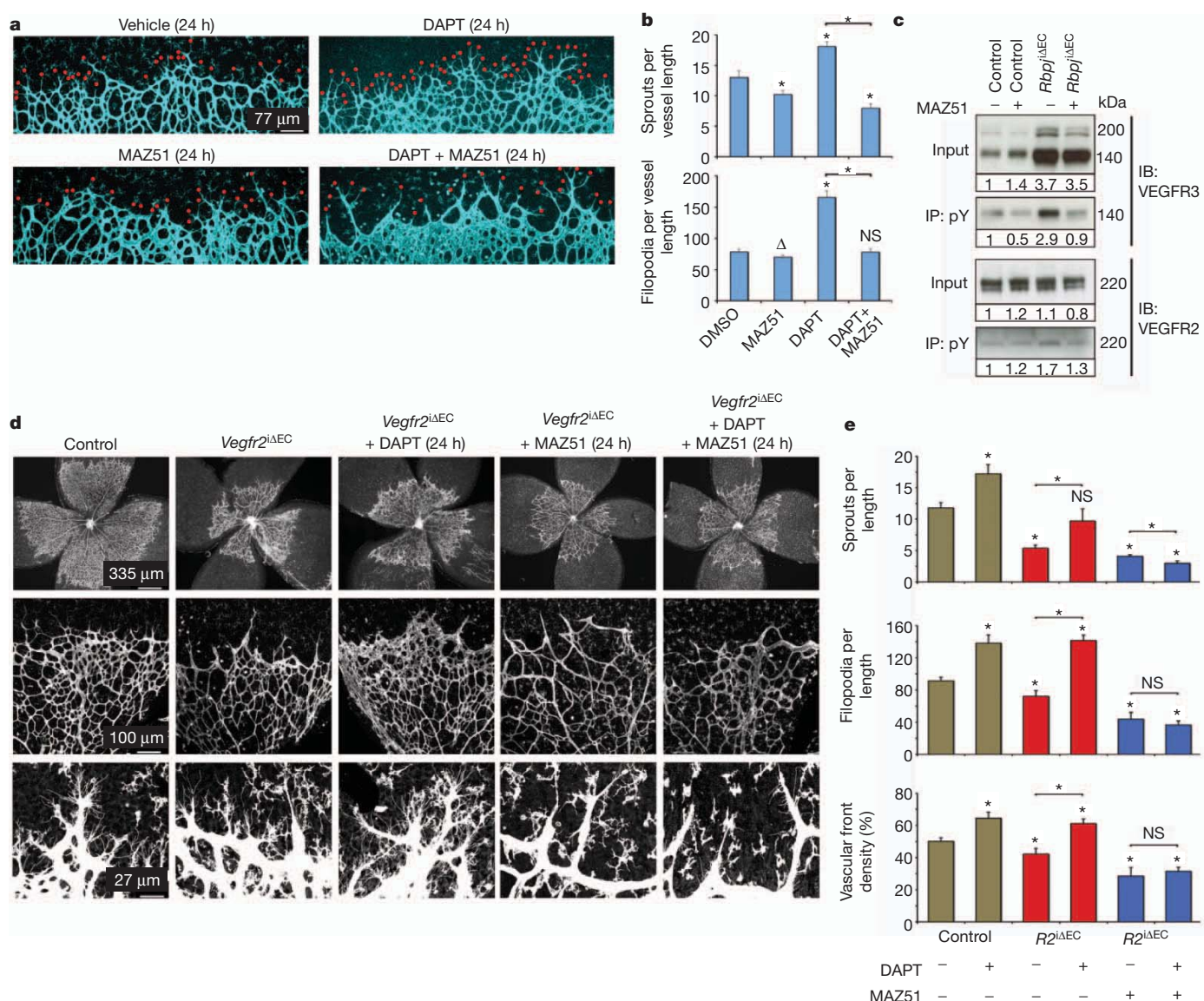


Figure 4 | Inhibition of VEGFR3 kinase activity suppresses Notch-regulated sprouting. **a, b**, Retina whole-mount immunostaining for isolectin B4 (blue) after 24 h treatment (P5 to P6) with the indicated inhibitors. MAZ51 efficiently blocked sprouting (red dots) of DAPT-treated endothelial cells without having an overt effect on vessel density (see also Supplementary Fig. 8). Vehicle, dimethylsulphoxide (DMSO). **c**, MAZ51 had strong effects on VEGFR3 but not VEGFR2 phosphorylation *in vivo*. Lungs from pups with the indicated genotypes and treatments were subjected to phosphotyrosine

and the vascular density compared with DAPT-treated *Vegfr2^{ΔEC}* littermates (Fig. 4d, e). Moreover, administration of AAL-993, a kinase inhibitor that blocks all VEGFRs, led to a significant decrease in vascular density and endothelial sprouting in DAPT-treated retinas (Supplementary Fig. 9). These results indicate that the inhibition of Notch signalling allows vessel growth in the absence of VEGF-A-VEGFR2 signalling, and this vessel growth requires the kinase activity of VEGFR3 but not the binding of VEGF-C. This is consistent with recent reports proposing ligand-independent VEGFR3 activation^{24,25}.

The initially simplistic models describing the molecular crosstalk between the VEGF and Notch pathways need to be revised. It has been reported that endothelial-cell-specific deletion of the *Vegfr3* gene postnatally in mice leads to enhanced angiogenesis²⁴. The authors of this report proposed that VEGFR3 has 'active' (ligand-dependent and pro-angiogenic) and 'passive' (ligand-independent and anti-angiogenic) signalling modes, among which the passive mode is mediated by

immunoprecipitation followed by VEGFR3 and VEGFR2 immunoblotting. The numbers below the blots indicate the relative quantification of the signals. **d, e**, Isolectin-B4-stained control and *Vegfr2^{ΔEC}* P5 retinas after 24 h treatment with the indicated chemical inhibitors. Inhibition of the kinase activity of VEGFR3 strongly impaired angiogenesis in DAPT-treated *Vegfr2^{ΔEC}* mutants. **b, e**, Data are presented as mean + s.e.m.; $n \geq 12$. *, $P < 0.05$; Δ, $P = 0.1$; NS, not significant; compared with control group data shown to the left of each graph unless otherwise indicated.

Notch activation. Our own data indicate that VEGFR3 activity is pro-angiogenic in endothelial cells with low or no Notch signalling activity. Both findings are not incompatible and might reflect a dynamic, Notch-controlled switching of VEGFR3 function in growing blood vessels.

Our results also fundamentally change the understanding of the crosstalk between Notch and VEGFR2 in angiogenesis (Supplementary Fig. 1). VEGFR2 is not essential for *Dll4* expression in tip cells, suggesting that other upstream regulators, such as cell-matrix signalling, have important roles^{26,27}. Although VEGFR2 is not regulated or only weakly regulated by Notch, both Notch and VEGFR2 modulate VEGFR3 protein and activation levels independently and in opposite directions. In settings with low Notch activity, VEGFR3 upregulation allows strong, ligand-independent and highly deregulated angiogenesis even in the absence of VEGF-VEGFR2 signalling, which mimics aspects of growth-factor-independent (autocrine) cancer cell growth²⁸. This mode of vessel growth might contribute to the excessive and

deregulated angiogenesis that is observed in tumours treated with Notch inhibitors⁹. Probing the status of vascular Notch or VEGFR3 activation might be relevant for patients who do not respond to anti-VEGF treatment, a complicating factor in the therapy of cancer and age-related macular degeneration^{29,30}. This information could yield valuable clues for selecting suitable therapeutic strategies that could reduce the resistance to current anti-angiogenic therapies.

METHODS SUMMARY

Mutant mice, inducible genetic experiments and pharmacological inhibition. For inducible and endothelial-cell-specific genetic loss-of-function experiments, we interbred *Vegfr2*^{flxed} (ref. 12), *Dil4*^{flxed} (ref. 15), *Notch1*^{flxed} (see Methods) or *Rbpj*^{flxed} (ref. 16) mice with transgenic mice expressing the tamoxifen-inducible recombinase CreERT2 under the control of the endothelial *Cdh5* (ref. 14) or *Pdgfrb* (ref. 13) promoter.

Cre activity and gene deletion were induced by intraperitoneal injections of 50 µg (P1–P3) or 100 µg (P3–P5) tamoxifen (Sigma, T5648; 2 mg ml⁻¹). In some experiments, Notch signalling was inhibited in half of the pups by subcutaneous injection with 100 mg kg⁻¹ DAPT (Calbiochem). The kinase activity of VEGFR3 was inhibited with 10 mg kg⁻¹ MAZ51 (Sigma). For simultaneous inhibition of the kinase activity of all VEGFRs, we used 25 mg kg⁻¹ AAL-993 (Enzo Life Sciences). To block signalling with monoclonal antibodies, daily intraperitoneal injections with 50 mg kg⁻¹ anti-VEGFR2 (ImClone Systems, DC101), anti-VEGFR3 (ImClone Systems, mF4-31C1), anti-VEGF-A (Genentech, G6-31) or control mouse or rat IgG antibodies (Jackson ImmunoResearch) were given at P4, P5 and P6.

Ethical review. All animal experiments were performed in compliance with the relevant laws and institutional guidelines and were approved by local animal ethics committees.

Full Methods and any associated references are available in the online version of the paper at www.nature.com/nature.

Received 1 December 2010; accepted 26 January 2012.

Published online 18 March 2012.

- Lohela, M., Bry, M., Tammela, T. & Alitalo, K. VEGFs and receptors involved in angiogenesis versus lymphangiogenesis. *Curr. Opin. Cell Biol.* **21**, 154–165 (2009).
- Suchting, S. *et al.* The Notch ligand Delta-like 4 negatively regulates endothelial tip cell formation and vessel branching. *Proc. Natl Acad. Sci. USA* **104**, 3225–3230 (2007).
- Lobov, I. B. *et al.* Delta-like ligand 4 (Dll4) is induced by VEGF as a negative regulator of angiogenic sprouting. *Proc. Natl Acad. Sci. USA* **104**, 3219–3224 (2007).
- Phng, L. K. & Gerhardt, H. Angiogenesis: a team effort coordinated by Notch. *Dev. Cell* **16**, 196–208 (2009).
- Tammela, T. *et al.* Blocking VEGFR-3 suppresses angiogenic sprouting and vascular network formation. *Nature* **454**, 656–660 (2008).
- Siekmann, A. F. & Lawson, N. D. Notch signalling limits angiogenic cell behaviour in developing zebrafish arteries. *Nature* **445**, 781–784 (2007).
- Benedito, R. *et al.* The Notch ligands Dll4 and Jagged1 have opposing effects on angiogenesis. *Cell* **137**, 1124–1135 (2009).
- Hellström, M. *et al.* Dll4 signalling through Notch1 regulates formation of tip cells during angiogenesis. *Nature* **445**, 776–780 (2007).
- Noguera-Troise, I. *et al.* Blockade of Dll4 inhibits tumour growth by promoting non-productive angiogenesis. *Nature* **444**, 1032–1037 (2006).
- Siekmann, A. F., Covassin, L. & Lawson, N. D. Modulation of VEGF signalling output by the Notch pathway. *Bioessays* **30**, 303–313 (2008).
- Thurston, G. & Kitajewski, J. VEGF and Delta–Notch: interacting signalling pathways in tumour angiogenesis. *Br. J. Cancer* **99**, 1204–1209 (2008).
- Haigh, J. J. *et al.* Cortical and retinal defects caused by dosage-dependent reductions in VEGF-A paracrine signalling. *Dev. Biol.* **262**, 225–241 (2003).

- Claxton, S. *et al.* Efficient, inducible Cre-recombinase activation in vascular endothelium. *Genesis* **46**, 74–80 (2008).
- Wang, Y. *et al.* Ephrin-B2 controls VEGF-induced angiogenesis and lymphangiogenesis. *Nature* **465**, 483–486 (2010).
- Koch, U. *et al.* Delta-like 4 is the essential, nonredundant ligand for Notch1 during thymic T cell lineage commitment. *J. Exp. Med.* **205**, 2515–2523 (2008).
- Han, H. *et al.* Inducible gene knockout of transcription factor recombination signal binding protein-J reveals its essential role in T versus B lineage decision. *Int. Immunol.* **14**, 637–645 (2002).
- Harrington, L. S. *et al.* Regulation of multiple angiogenic pathways by Dll4 and Notch in human umbilical vein endothelial cells. *Microvasc. Res.* **75**, 144–154 (2008).
- Taylor, K. L., Henderson, A. M. & Hughes, C. C. Notch activation during endothelial cell network formation *in vitro* targets the basic HLH transcription factor HESR-1 and downregulates VEGFR-2/KDR expression. *Microvasc. Res.* **64**, 372–383 (2002).
- Sainson, R. C. *et al.* Cell-autonomous notch signaling regulates endothelial cell branching and proliferation during vascular tubulogenesis. *FASEB J.* **19**, 1027–1029 (2005).
- Hogan, B. M. *et al.* Vegfc/Flt4 signalling is suppressed by Dll4 in developing zebrafish intersegmental arteries. *Development* **136**, 4001–4009 (2009).
- Zhang, L. *et al.* VEGFR-3 ligand-binding and kinase activity are required for lymphangiogenesis but not for angiogenesis. *Cell Res.* **20**, 1313–1331 (2010).
- Pytowski, B. *et al.* Complete and specific inhibition of adult lymphatic regeneration by a novel VEGFR-3 neutralizing antibody. *J. Natl Cancer Inst.* **97**, 14–21 (2005).
- Kirkin, V. *et al.* Characterization of indolinones which preferentially inhibit VEGF-C- and VEGF-D-induced activation of VEGFR-3 rather than VEGFR-2. *Eur. J. Biochem.* **268**, 5530–5540 (2001).
- Tammela, T. *et al.* VEGFR-3 controls tip to stalk conversion at vessel fusion sites by reinforcing Notch signalling. *Nature Cell Biol.* **13**, 1202–1213 (2011).
- Galvagni, F. *et al.* Endothelial cell adhesion to the extracellular matrix induces c-Src-dependent VEGFR-3 phosphorylation without the activation of the receptor intrinsic kinase activity. *Circ. Res.* **106**, 1839–1848 (2010).
- Stenzel, D. *et al.* Endothelial basement membrane limits tip cell formation by inducing Dll4/Notch signalling *in vivo*. *EMBO Rep.* **12**, 1135–1143 (2011).
- Estrach, S. *et al.* Laminin-binding integrins induce Dll4 expression and Notch signaling in endothelial cells. *Circ. Res.* **109**, 172–182 (2011).
- Lemmon, M. A. & Schlessinger, J. Cell signaling by receptor tyrosine kinases. *Cell* **141**, 1117–1134 (2010).
- Lux, A., Llacer, H., Heussen, F. M. & Joussen, A. M. Non-responders to bevacizumab (Avastin) therapy of choroidal neovascular lesions. *Br. J. Ophthalmol.* **91**, 1318–1322 (2007).
- Jubb, A. M. & Harris, A. L. Biomarkers to predict the clinical efficacy of bevacizumab in cancer. *Lancet Oncol.* **11**, 1172–1183 (2010).

Supplementary Information is linked to the online version of the paper at www.nature.com/nature.

Acknowledgements We thank M. Schiller, M. Ehling, M. Pitulescu and M. Nakayama for the help with experiments and discussions, and G. Breier and T. Honjo for floxed *Vegfr2* and *Rbpj* mutant mice, respectively. Funding was provided by the Max Planck Society, the University of Münster and the German Research Foundation (programmes SFB 629 and SPP 1190).

Author Contributions R.B. and R.H.A. designed the experiments, interpreted the results and wrote the manuscript. R.B. generated and characterized the mutant mouse lines. R.B. directed M.W. and M.Z. and carried out the immunohistochemistry, immunoblots, qRT-PCR, confocal imaging and quantifications. S.F.R. developed the immunoprecipitation and immunoblotting assays and carried out the confocal imaging and quantifications. A.D. and F.R. provided the *Dil4*^{flxed} and *Notch1*^{flxed} mice, respectively. O.C. and B.P. generated and provided the monoclonal VEGFR2- and VEGFR3-blocking antibodies (ImClone Systems).

Author Information Reprints and permissions information is available at www.nature.com/reprints. The authors declare competing financial interests: details accompany the full-text HTML version of the paper at www.nature.com/nature. Readers are welcome to comment on the online version of this article at www.nature.com/nature. Correspondence and requests for materials should be addressed to R.H.A. (ralf.adams@mpi-muenster.mpg.de) and R.B. (ruibenedito@mpi-muenster.mpg.de).

METHODS

Mutant mice, inducible genetic experiments and pharmacological inhibition.

To delete *Vegfr2* in the postnatal vasculature, we interbred *Vegfr2*^{flxed} mice¹² with transgenic mice expressing the tamoxifen-inducible recombinase CreERT2 under the control of the endothelial *Cdh5* promoter¹⁴. *Vegfr2*^{flxed/flxed} *Cdh5*(PAC)-*CreERT2*^{T/+} males were interbred with *Vegfr2*^{flxed/flxed} females to generate litters containing *Vegfr2*^{flxed/flxed} *Cdh5*(PAC)-*CreERT2*^{T/+} (*Vegfr2*^{ΔEC}) and control (*Vegfr2*^{flxed/flxed}) littermates. Cre activity and gene deletion were induced by intraperitoneal injections with 100 μg tamoxifen (Sigma, T5648; 2 mg ml⁻¹) in every pup of the litter, every 24 h at P3, P4 and P5 (Fig. 1). Notch signalling was inhibited in half of the pups by subcutaneous injection at P5 and P6 with 100 mg kg⁻¹ DAPT (Calbiochem) dissolved in 10% ethanol and 90% peanut oil. Retinas were collected at P7, 48 h after the first injection of DAPT. Control mice were injected with vehicle only. We also induced *Vegfr2* deletion from P1 to P3 and analysed tissues at P6 (Figs 2 and 3). In addition, Notch signalling was inhibited in half of the pups by subcutaneous injection of DAPT at P4 and P5 (Fig. 3d).

For combined endothelial-cell-specific loss-of-function of *Dll4* and *Vegfr2*, we interbred *Dll4*^{flxed} (ref. 15) with *Vegfr2*^{flxed} (ref. 12) and *Pdgfrb-iCre* mice¹³. Because *Dll4* is a haploinsufficient gene^{2,31}, it was necessary to compare the vascular phenotypes of animals from two different types of breeding. Specifically, we interbred *Dll4*^{flxed/+} *Vegfr2*^{flxed/+} *Pdgfrb-iCre*^{T/+} males with *Dll4*^{flxed/flxed} *Vegfr2*^{flxed/+} females to generate control (*Pdgfrb-iCre*^{T/+}), *Dll4*^{flxed/flxed} *Vegfr2*^{T/+} *Pdgfrb-iCre*^{T/+} (*Dll4*^{ΔEC}), and *Dll4*^{flxed/flxed} *Vegfr2*^{flxed/flxed} *Pdgfrb-iCre*^{T/+} (*Dll4*^{ΔEC} *Vegfr2*^{ΔEC}) littermates. To generate *Dll4*^{+/+} *Vegfr2*^{flxed/flxed} *Pdgfrb-iCre*^{T/+} (*Vegfr2*^{ΔEC} in Fig. 1c) and matching littermate control animals (*Pdgfrb-iCre*^{T/+}), we interbred *Dll4*^{flxed/+} *Vegfr2*^{flxed/+} *Pdgfrb-iCre*^{T/+} males with *Dll4*^{+/+} *Vegfr2*^{flxed/flxed} females in the same genetic background. For the combined endothelial-cell-specific loss-of-function of *Notch1* and *Vegfr2*, we interbred *Notch1*^{flxed} mice³², *Vegfr2*^{flxed} and *Cdh5*(PAC)-*CreERT2* mice to obtain the animals with the genotypes described in Supplementary Fig. 2e. To induce Cre recombinase activity and gene deletion, animals were injected with 50 μg tamoxifen (1 mg ml⁻¹), every 24 h, at P1, P2 and P3 and dissected at P6.

To disrupt transcriptional responses downstream of activated Notch in endothelial cells, we interbred *Rbpj*^{flxed} mice¹⁶ with the *Pdgfrb-iCre* transgenics. *Rbpj*^{flxed/flxed} *Pdgfrb-iCre*^{T/+} males were interbred with *Rbpj*^{flxed/flxed} females to generate litters containing *Rbpj*^{flxed/flxed} *Pdgfrb-iCre*^{T/+} (*Rbpj*^{ΔEC}) and control (*Rbpj*^{flxed/flxed}) littermates. All pups were injected with 50 μg tamoxifen (1 mg ml⁻¹), every 24 h, from P1 to P3 and dissected at P6 (Fig. 2) or P7 (Figs 1 and 3).

For the combined pharmacological inhibition of Notch and VEGFR signalling *in vivo*, we subcutaneously injected the indicated combinations of vehicle (dimethylsulphoxide (DMSO)), the Notch signalling inhibitor DAPT (Calbiochem; 100 mg kg⁻¹), the VEGFR3 inhibitor²³ (MAZ51, Sigma; 10 mg kg⁻¹) or the pan-VEGFR tyrosine kinase inhibitor (AAL-993, Enzo Life Sciences; 25 mg kg⁻¹)^{33,34}. Injections of the vehicle and inhibitors DAPT and MAZ51 were done twice, at P5 and 8 h before dissecting the animals at P6; that is, for a 24-h period (16 h + 8 h) in total. Injection of the vehicle and inhibitors DAPT and AAL-993 was done at P5, 24 h before collecting the retinas at P6. When *Vegfr2* deletion was combined with chemical inhibition (Fig. 4), all of the control and *Vegfr2*^{ΔEC} litter pups were injected with 50 μg tamoxifen (1 mg ml⁻¹) from P1 to P3 before receiving the inhibitor injections at P4 as described above.

For the combined deletion of *Rbpj* and inhibition of VEGFR signalling *in vivo*, we injected 50 μg tamoxifen (1 mg ml⁻¹) from P1 to P3 and then injected the monoclonal antibodies anti-VEGFR2 (ImClone Systems, DC101)³⁵, anti-VEGFR3 (ImClone Systems, mF4-31C1)²², anti-VEGF-A (Genentech, G6-31)³⁶ or control mouse or rat IgG antibodies (Jackson ImmunoResearch) at 50 mg kg day⁻¹ from P4 to P6.

Immunohistochemistry. All of the immunostaining was carried out with littermate tissues processed simultaneously under the same conditions. With the exception of the isolectin B4 staining of the retinas from *Dll4/Vegfr2*^{flxed/flxed} litters (see explanation in the previous section), no comparisons have been made between animals from different litters or processed on different days.

To analyse (and quantify) the retina vascular phenotype and to preserve intact endothelial filopodia and sprouts at the angiogenic front, whole animal eyes were fixed in 4% paraformaldehyde (PFA) at 4 °C overnight. The following day, the eyes were washed in PBS before the retinas were dissected and partially cut in four quadrants to allow subsequent flat mounting. After blocking/permeabilization in 1% BSA with 0.3% Triton for some hours at room temperature or overnight at 4 °C, the retinas were washed two times in Pblec buffer (1% Triton X-100, 1 mM CaCl₂, 1 mM MgCl₂ and 1 mM MnCl₂ in PBS, pH 6.8) for 20 min and then incubated for 2 h in Pblec buffer containing biotinylated isolectin B4 (Vector Labs, 1:50). Following five washes (each 20 min) in blocking solution, retinas were incubated with Alexa-Fluor-streptavidin-conjugated antibodies (Molecular Probes, 1:100)

for 2 h, washed three times further and flat-mounted on microscope glass slides with Fluoromount-G (SouthernBiotech, 0100-01). Double or triple whole-mount immunohistochemistry was performed in retinas fixed for 2 h on ice in 2% PFA or at -20 °C in methanol. After fixation, retinas were blocked for 1 h in 1% BSA with 0.05% Tween and incubated overnight or for 2 h with isolectin B4 (1:50) and the following primary antibodies: rat anti-VEGFR2 (1:200, 555307, BD Pharmingen), goat anti-VEGFR3 (1:200, AF743, R&D Systems) or goat anti-DLL4 (1:200, AF1389, R&D Systems) antibody. For detection, suitable species-specific Alexa-Fluor-coupled secondary antibodies (1:500) were used. To detect proteins in P6 mouse lungs, organs were fixed in 4% PFA. Immunohistochemistry was performed on 100-μm vibratome sections as described above for the retinas. The following additional antibodies were used: rat anti-endothelium (from D. Vestweber) and rabbit anti-GFP-Alexa Fluor 488 (1:500, A21311, Invitrogen).

Immunoprecipitation, immunoblotting and qRT-PCR of lung lysates. For immunoprecipitations, freshly dissected or snap frozen lungs were lysed in lysis buffer (20 mM Tris, 1 mM EDTA, 1 mM dithiothreitol (DTT), 1% NP-40, 0.1% SDS, 0.1% deoxycholate, 150 mM NaCl, 1 mM PMSF, 1 mM Na₃VO₄, 5 mM NaF, phosphatase inhibitor cocktail SetV (Calbiochem, 524629) and protease inhibitor cocktail (Sigma, P2714)). Lysates were centrifuged at 4 °C for 30 min at 20,000g, and aliquots were set aside for direct input blot analysis. For the immunoprecipitation, the remaining lysates were pre-cleared for 1 h at 4 °C with protein-G-sepharose or protein-A-sepharose beads. Pre-cleared lysates were incubated with primary antibody for 2 h at 4 °C, after which the beads were added and incubated for an additional 2 h at 4 °C. Immunocomplexes were washed five times with lysis buffer (without SDS and deoxycholate) and analysed by SDS-PAGE. For the detection of phosphotyrosine after VEGFR1 immunoprecipitation, membranes were blocked with BSA, and 1 mM Na₃VO₄ was added during the blocking and washing steps. The following primary antibodies were used for immunoprecipitations: control mouse or goat IgG, mouse anti-phosphotyrosine (4G10, 05-321, Millipore) and goat anti-VEGFR1 (AF471, R&D Systems). Subsequent detection of the immunoprecipitated protein was done with the antibodies described below. As a positive control for the detection of phospho-VEGFR3 after phosphotyrosine immunoprecipitation, P5 pups received an intraperitoneal injection of 200 ng g⁻¹ body weight VEGF-C (Peprotech) or vehicle (PBS) at 30 min before tissue dissection. As a negative control to confirm the specificity of the phospho-tyrosine immunoprecipitation, a sample was treated with lambda protein phosphatase (New England Biolabs) before incubation of the pre-cleared lysate with anti-phosphotyrosine antibodies. To determine the ligand requirement for VEGFR3 phosphorylation after deletion of *Rbpj* in endothelial cells, we intraperitoneally injected 25 mg kg⁻¹ mouse VEGFR3-Fc (743-R3-100, R&D Systems) at P5 and collected the tissue 24 h later.

For the analysis of protein levels in mutant mouse pups, the inferior left lobe or the whole lung was dissected out, transferred to a reagent tube and frozen in liquid nitrogen. On the day of the immunoblot analysis, the tissue was lysed in PL buffer (20 mM Tris-HCl, pH 8.0, 1 mM EDTA, 1 mM DTT, phosphatase inhibitor cocktail SetV, 1 mM Na₃VO₄, protease inhibitor cocktail (1:10), 1% Triton X-100 and 150 mM NaCl) and homogenized with a cylindrical glass pestle (Potter-Elvehjem). Tissue debris was removed by centrifugation, and the supernatant was diluted in loading buffer and analysed by SDS-PAGE and immunoblotting. The following antibodies were used for immunoblotting: rabbit anti-VEGFR2 (2479, Cell Signaling Technology), rabbit anti-phospho-VEGFR2 (2478, Cell Signaling Technology), rat anti-VEGFR3 (14-5988, eBioscience), rabbit anti-VEGFR1 (sc-316, Santa Cruz Biotechnology), rabbit anti-cleaved-Notch1 (2421, Cell Signaling Technology), rat anti-CDH5 (555289, BD Biosciences), mouse anti-phosphotyrosine (4G10, 05-321, Millipore) and rabbit anti-tubulin (T5168, Sigma).

All of the immunoblot images shown represent the average result obtained from a minimum of two different lung extracts for each group, and each extract was blotted in duplicate. The blots shown in Fig. 4c were quantified with the gel analysis function in the program ImageJ.

For the analysis of mRNA relative expression levels, total RNA was isolated with the RNeasy Mini Kit (QIAGEN), and 500 ng per reaction was used to generate cDNA with the SuperScript III First-Strand Synthesis System (Invitrogen) and oligo(dT) primers. Quantitative PCR with reverse transcription (qRT-PCR) was performed by using an ABI PRISM 7900HT Sequence Detection System. TaqMan gene expression assays for murine *Gapdh*, *Dll4*, *Hey1*, *Vegfr2*, *Vegfr3*, *Pecam1*, *Cdh5*, *Pdgfrb* and *Vegfa* were used in combination with TaqMan Gene Expression Master Mix (Applied Biosystems). Gene expression was normalized to the endogenous control *Gapdh*. The relative expression differences obtained represent the average of the results obtained for two independent animals per group from two independent litters. For each animal/cDNA, two separate qRT-PCR plates were used, with duplicate reactions for each gene.

A fraction of *Vegfr2*^{ΔEC} *Cdh5*(PAC)-*CreERT2* mutant lungs showed reduced deletion of *Vegfr2* in the lungs and were therefore excluded from the analysis. The results shown represent mutants for which the deletion of *Vegfr2* was most efficient (around 90%, Fig. 2c).

Quantitative analysis of the retinal vasculature. All of the images shown are representative of the vascular phenotype observed in at least eight retinas from four pups from two distinct litters per group. All quantifications were done with Volocity (Improvion) software on high-resolution confocal images representing a thin *z* section of the retina stained with isolectin B4. The numbers of endothelial sprouts and filopodial extensions were quantified at the retina angiogenic front in a minimum of 12 fields (sized 1,550 μm × 1,550 μm for sprouts and 387 μm × 387 μm for filopodia) and four retinas per group. The total number of sprouts or filopodia was normalized for a standard endothelial vessel length of 1,000 μm that was measured and defined according to published protocols³⁶. The proportion of endothelial cell area coverage was calculated in a minimum of eight fields per group. Regions of quantification were selected in 1,550 μm × 1,550 μm fields, including the whole vascular plexus, for genetic deletions starting at P1, or in only the angiogenic front (around 1,550 μm × 250 μm) for 24–72 h experiments. The isolectin-B4-stained endothelial network was selected based on the strong intensity of the fluorescent signal. For each vascularized field, the ratio of the isolectin-B4-positive area to the total area was calculated and defined as the percentage of the vascularized retina area covered by endothelial cells. Vascular progression was measured by defining a straight line from the angiogenic front to the centre of the retina for each retina quadrant in low magnification stereomicroscope pictures. A minimum of 16 quadrants belonging to four retinas per group was used for quantification. The *P* values in all figures were calculated using a two-tailed Student's *t*-test.

Image acquisition and processing. Stained and flat-mounted retinas were analysed at high resolution with a TCS SP5 confocal microscope (Leica) or at lower resolution with an MZ16F stereomicroscope (Leica) coupled to a digital camera (Hamamatsu C4742-95). Volocity, Photoshop (Adobe) and Illustrator (Adobe) software were used for image acquisition and processing, in compliance with *Nature's* guide for digital images. All of the images shown in which the immunostaining levels were compared are representative of at least six different images from three different retina immunostainings per group, where the laser excitation and confocal scanner detection settings were the same between groups.

Cell culture and *in vitro* assays. HUVECs and immortalized mouse endothelial cells (MECs) were isolated and cultured as described previously⁷. Cells (5 × 10⁵) were plated in each well of six-well plates coated with PBS containing 5 μg ml⁻¹ fibronectin. To some wells, 1.44 μg ml⁻¹ recombinant DLL4-His (1389-D4, R&D Systems) was added to the coating solution. DMSO or an equal volume of DAPT (10 μM) dissolved in DMSO was added to the culture medium in some wells. Cells were incubated overnight and starved for 5 h before stimulation with vehicle or 50 ng ml⁻¹ VEGF-A (Peprotech) for 8 min. Cells were lysed in 200 μl 1× SDS sample buffer and subjected to immunoblotting with rabbit anti-VEGFR2 (2479, Cell Signaling Technology), rabbit anti-phospho-VEGFR2 (478, Cell Signaling Technology), rat anti-VEGFR3 (14-5988, eBioscience), rabbit anti-cleaved-Notch1 (2421, Cell Signaling Technology), rat anti-CDH5 (555289, BD Biosciences) or rabbit anti-tubulin (T5168, Sigma) antibody.

To generate human embryonic kidney 293 (HEK293) cells stably expressing mouse VEGFR3 (R3) or a tyrosine-kinase dead version (R3^{TK-}), we first subcloned in-frame the mouse *Vegfr3* cDNA without the 3' untranslated region (UTR) into the vector pcDNA3.1 membrane-Tomato-2A. A single point mutation

(Ile1053Phe) in VEGFR3 was generated following the procedures described in the QuikChange II Site-Directed Mutagenesis Kit (Stratagene). To generate HEK293 cells stably expressing mouse VEGFR2 (R2), we first subcloned in-frame the mouse *Vegfr2* cDNA without the 3' UTR and stop codon in the vector pcDNA3.1-2A-MYFP. HEK293 cells were transfected with one of the three constructs by using Lipofectamine 2000 (Invitrogen) and selected in 500 μg ml⁻¹ G418 (neomycin) for 2 weeks. Following selection, isolated red or yellow fluorescent clones were picked and expanded. Immunoblot analysis was subsequently performed to confirm the expression of VEGFR3 or VEGFR2. For stimulation assays, 5 × 10⁵ cells were plated in each well of six-well plates, cultured for 1 day to attach and then, on the following day, starved overnight (18 h). Starved cells were stimulated with 500 ng ml⁻¹ VEGF-C, VEGF-A (Peprotech) or vehicle, in the absence or presence of the indicated concentrations of anti-VEGFR3 (mF4-31C1) or MAZ51. Cells were lysed in 1× lysis buffer (9803, Cell Signaling Technology), and after removing the residual cell debris, the extracts were used for immunoblotting as described previously or for enzyme-linked immunosorbent assays (ELISAs). ELISA plates (96 wells) were coated overnight in capture antibody solution (PBS containing 1 μg ml⁻¹ goat-anti mouse VEGFR3 (AF743, R&D Systems) or PBS containing 1 μg ml⁻¹ goat-anti mouse VEGFR2 (AF644, R&D Systems)). The next day, the solution was removed, and blocking solution (PBS containing 0.5% BSA and 0.05% Tween 20) was added for 1 h. After three washes with wash buffer (PBS containing 0.05% Tween 20), 100 μl lysate was added in triplicate to the coated plates, which were then incubated for 2 h. The plates were washed four times in wash buffer, and primary antibodies diluted in blocking buffer were added for 2 h. For the detection of the captured phosphorylated VEGFR3 or VEGFR2 proteins, biotinylated mouse anti-phosphotyrosine (16-103, Millipore) was used. For the detection of all captured VEGFR3 and VEGFR2, we used rat anti-VEGFR3 (14-5988, eBioscience) and rat anti-VEGFR2 (2479, Cell Signaling Technology), respectively. Following four additional washing steps, species-specific or streptavidin horseradish-peroxidase-conjugated secondary antibodies were diluted in blocking solution and then incubated with the plates for 30 min. The washing procedure was repeated and TMB substrate (7004S, Cell Signaling Technology) was used to obtain the detection signal. Absorbance measurements at 450 nm and 650 nm and the relative quantification were performed on a Synergy 2 Biotek microplate reader. The ELISAs were performed in triplicate and for three times per condition. The ratio of the detected phosphorylated VEGFR3 to the total VEGFR3 (and the VEGFR2 ratio) was determined for each condition, and the relative difference from the non-treated condition was calculated. The *P* values were calculated using a two-tailed Student's *t*-test.

31. Duarte, A. *et al.* Dosage-sensitive requirement for mouse Dll4 in artery development. *Genes Dev.* **18**, 2474–2478 (2004).
32. Radtke, F. *et al.* Deficient T cell fate specification in mice with an induced inactivation of Notch1. *Immunity* **10**, 547–558 (1999).
33. Manley, P. W. *et al.* Advances in the structural biology, design and clinical development of VEGF-R kinase inhibitors for the treatment of angiogenesis. *Biochim. Biophys. Acta* **1697**, 17–27 (2004).
34. Manley, P. W. *et al.* Anthranilic acid amides: a novel class of antiangiogenic VEGF receptor kinase inhibitors. *J. Med. Chem.* **45**, 5687–5693 (2002).
35. Prewett, M. *et al.* Antivascular endothelial growth factor receptor (fetal liver kinase 1) monoclonal antibody inhibits tumor angiogenesis and growth of several mouse and human tumors. *Cancer Res.* **59**, 5209–5218 (1999).
36. Liang, W. C. *et al.* Cross-species vascular endothelial growth factor (VEGF)-blocking antibodies completely inhibit the growth of human tumor xenografts and measure the contribution of stromal VEGF. *J. Biol. Chem.* **281**, 951–961 (2006).

A new understanding of the decoding principle on the ribosome

Natalia Demeshkina^{1*}, Lasse Jenner^{1*}, Eric Westhof², Marat Yusupov¹ & Gulnara Yusupova¹

During protein synthesis, the ribosome accurately selects transfer RNAs (tRNAs) in accordance with the messenger RNA (mRNA) triplet in the decoding centre. tRNA selection is initiated by elongation factor Tu, which delivers tRNA to the aminoacyl tRNA-binding site (A site) and hydrolyses GTP upon establishing codon–anticodon interactions in the decoding centre^{1–9}. At the following proofreading step the ribosome re-examines the tRNA and rejects it if it does not match the A codon^{2,3,10–14}. It was suggested that universally conserved G530, A1492 and A1493 of 16S ribosomal RNA, critical for tRNA binding in the A site^{15–17}, actively monitor cognate tRNA¹⁸, and that recognition of the correct codon–anticodon duplex induces an overall ribosome conformational change (domain closure)¹⁹. Here we propose an integrated mechanism for decoding based on six X-ray structures of the 70S ribosome determined at 3.1–3.4 Å resolution, modelling cognate or near-cognate states of the decoding centre at the proofreading step. We show that the 30S subunit undergoes an identical domain closure upon binding of either cognate or near-cognate tRNA. This conformational change of the 30S subunit forms a decoding centre that constrains the mRNA in such a way that the first two nucleotides of the A codon are limited to form Watson–Crick base pairs. When U•G and G•U mismatches, generally considered to form wobble base pairs, are at the first or second codon–anticodon position, the decoding centre forces this pair to adopt the geometry close to that of a canonical C•G pair. This by itself, or with distortions in the codon–anticodon mini-helix and the anticodon loop, causes the near-cognate tRNA to dissociate from the ribosome.

We determined six X-ray structures of the 70S ribosome at 3.1–3.4 Å resolution (Supplementary Tables 1 and 2) programmed by 30-nucleotide-long mRNAs with the AUG codon and tRNA^{fMet} in the peptidyl tRNA-binding site (P site) and the A site occupied by tRNA₂^{Leu} or tRNA^{Tyr} (Fig. 1a and Methods). In one set of experiments, tRNA₂^{Leu} and tRNA^{Tyr} were bound to their respective cognate codons CUC and UAC in the A site. In a second set of experiments, we modelled near-cognate states of the ribosome (Supplementary Fig. 1). These states of the ribosome naturally occur during protein synthesis but with low probability because binding of cognate tRNA is kinetically

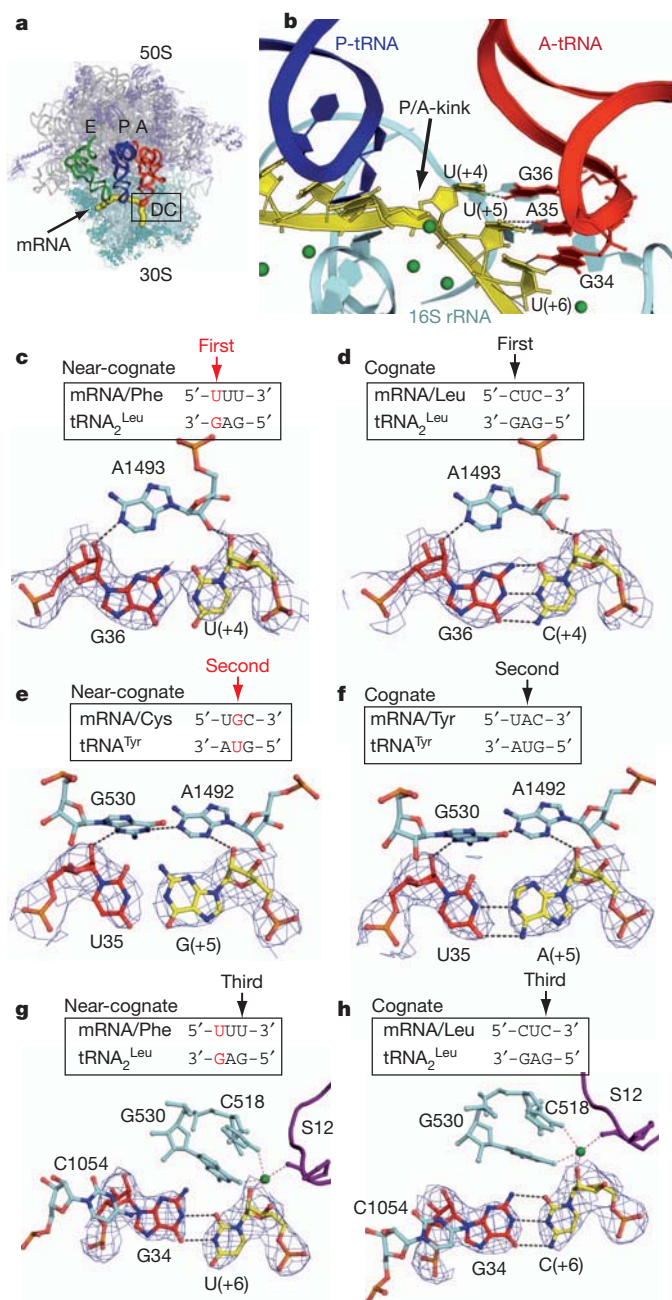


Figure 1 | Codon–anticodon interactions in the decoding centre on the 70S ribosome. **a**, The mRNA path on the 70S ribosome with the decoding (DC) area indicated. **b**, Close-up view of the mRNA P/A kink with near-cognate tRNA₂^{Leu}. Magnesium ions are in green. **c**, **d**, The first base pairs of the near-cognate (**c**) and cognate (**d**) codon–anticodon duplexes and their interactions with A1493 of 16S rRNA. **e**, **f**, The second base pairs of the near-cognate (**e**) and cognate (**f**) codon–anticodon duplexes and their interactions with G530 and A1492 of 16S rRNA. **g**, **h**, A classical wobble U•G pair (**g**) versus canonical C•G interactions (**h**); a magnesium ion interacting with the base pair is coordinated by protein S12 and part of 16S rRNA. All graphical representations were prepared with PyMol. Probable hydrogen bonds within 3 Å distance are indicated by dashed lines; 2F_o – F_c electron density maps are contoured at 1.2 sigma.

¹Département de Biologie et de Génétique Structurales, Institut de Génétique et de Biologie Moléculaire et Cellulaire, Illkirch 67400, France; CNRS, UMR7104, Illkirch 67400, France; INSERM, U964, Illkirch 67400, France; Université de Strasbourg, Strasbourg 67000, France. ²Architecture et Réactivité de l'ARN, Université de Strasbourg, Institut de Biologie Moléculaire et Cellulaire, CNRS, Strasbourg 67084, France.

*These authors contributed equally to this work.

favoured. We made the ribosome accept near-cognate tRNA by giving it only one type of tRNA carrying a mismatch to the A codon along with tRNA^{fMet} for the P site. In these complexes the A site was filled either by tRNA₂^{Leu} and codon UUU with a U•G mismatch in the first position of the codon–anticodon helix or by tRNA^{Tyr} and codon UGC with a G•U mismatch in the second position.

As shown earlier, the mRNA forms a kink between the P and A codons (P/A kink), a universal feature of the mRNA path on the 70S ribosome that is stabilized by the P site tRNA, 16S ribosomal RNA (rRNA) and magnesium ions^{7,20,21} (Fig. 1b and Supplementary Fig. 2). The single mismatch states described above represent bona fide near-cognate complexes expected to have standard wobble U•G and G•U base pairs. At our data resolution (3.1–3.5 Å) we can confidently assign the general base pairing (Supplementary Figs 3 and 4). The electron density maps unambiguously demonstrate that U4 and G5 of the A codons UUU and UGC do not show the anticipated wobble interactions with G36 in tRNA₂^{Leu} and U35 in tRNA^{Tyr}, respectively. Instead, U4•G36 and G5•U35 at the first and second positions of

the codon–anticodon duplexes form base pairs similar to a standard Watson–Crick G•C pair (Fig. 1c, e and Supplementary Fig. 5). G•C-like G•U or G•T pairs have been shown earlier for RNA and DNA in other X-ray structures^{22,23}. When U•G is at the third codon–anticodon position we observe standard U•G wobble pairing (Fig. 1g, h). Unexpectedly, nucleotides A1493, A1492 and G530 of 16S rRNA in helix 44 (h44), which contact the first and the second pairs of the codon–anticodon helix, interact with these unusual U4•G36 and G5•U35 pairs identically to the way they interact with canonical Watson–Crick base pairs C4•G36 and A5•U35 (Fig. 1c–f). These findings are in contradiction with studies where these nucleotides were given a role as monitors and discriminators of canonical Watson–Crick pairs in the decoding process^{18,19}. Our structures show that G530, A1492 and A1493 form a static part of the decoding centre, defining its spatial and stereochemical properties (Fig. 2a, b).

The observed non-wobble U•G differs from previous X-ray studies that were based on the 30S subunit alone¹⁹ (Fig. 2c and Supplementary Figs 5 and 6). For example, for the study of the mismatch at the first

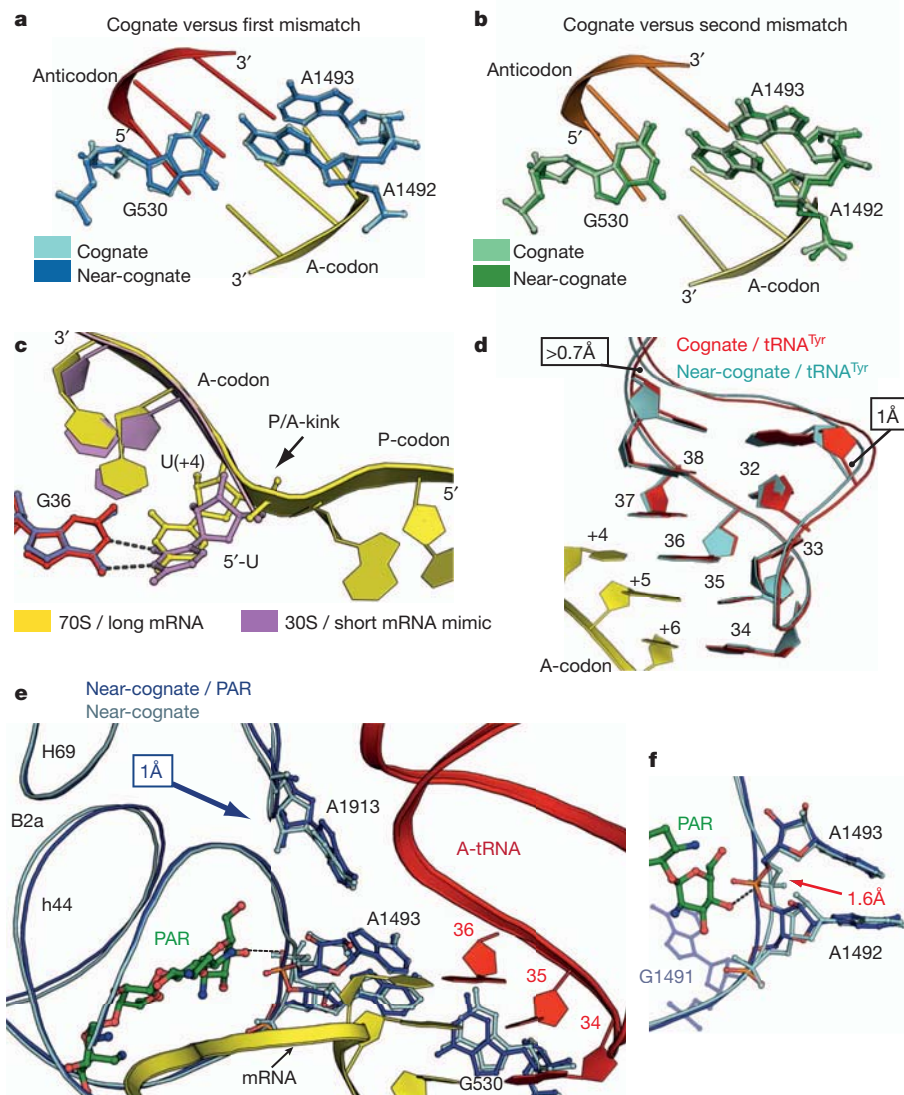


Figure 2 | The nature of the decoding centre. **a, b**, The overall conformations of universally conserved G530, A1492 and A1493 of 16S rRNA in the cognate structures are identical to those in the near-cognate models when the mismatches are at the first (**a**) or second (**b**) codon–anticodon positions. **c**, Differences between the position of the first uridine in the UUU codon base-paired to the GAG anticodon of tRNA₂^{Leu} from our 70S structure and from the 30S model¹⁹. **d**, Comparison of the anticodon loops of tRNA^{Tyr} in the cognate

(red) and near-cognate (cyan) states. **e**, Rearrangements of rRNA helices h44 and H69 in the near-cognate state upon binding of the aminoglycoside paromomycin (PAR). The near-cognate structures with tRNA^{Tyr} are shown (a similar effect of PAR is observed with tRNA₂^{Leu}, see also Supplementary Fig. 10). **f**, Magnified view of the changes in the A1493 phosphate position induced by PAR. Superimpositions in **d**, **e** and **f** were performed using 23S rRNA as reference.

position, 30S crystals soaked with an anticodon stem-loop of tRNA^{Leu}₂ and a hexauridine (U₆) mRNA displayed a classical wobble U•G pair. There the P codon was mimicked by the 3'-end of 16S rRNA, so the U₆ mRNA could only bind to the A site and downstream, leading to a situation where the mRNA was not covalently linked between the P and A codons. By superimposing the A site GAG anticodons from our near-cognate tRNA^{Leu}₂ structure and the 30S model we found that the first nucleotide of the A codon is positioned differently (Fig. 2c and Supplementary Fig. 6). Because it does not have the natural restraint coming from being covalently bound to the P codon, this first nucleotide in the A codon has the freedom to move so it can form a wobble U•G pair. However, in our structure the P/A mRNA kink specifically directs the first nucleotide of the A codon to form Watson–Crick like interactions with G36 of tRNA^{Leu}₂ (Fig. 1c).

The positional restrictions imposed by the decoding centre on the first two near-cognate U•G codon–anticodon pairs may result in differences in geometry compared with the corresponding cognate helices (Supplementary Figs 7 and 8). Although, the resolution of the data sets does not allow us to determine the exact value for these deviations in the base pairs, the tendencies are clear. A noticeable change is an increase in buckling at the first and third codon–anticodon positions with the U4•G36 mismatch (Supplementary Fig. 7) and at the second and third positions with the G5•U35 mismatch (Supplementary Fig. 8). These deviations could disturb the base stacking network within the near-cognate codon–anticodon helices and deform the entire anticodon loop structure²⁴ (Fig. 2d, Supplementary Fig. 9 and Supplementary Movie 1). This deformation might influence the position of helix 69 (H69) of 23S rRNA, whose universally conserved A1913 protrudes into the decoding centre^{20,21} (Fig. 2e).

Additional structures of the near-cognate states determined in the presence of the miscoding aminoglycoside paromomycin (Supplementary Tables 1 and 2) reveal a movement of H69 accompanied by

rearrangements of the intersubunit bridge B2a between h44 and H69 (Fig. 2e and Supplementary Movie 2). These distortions are most probably caused by binding of the antibiotic that strongly shifts the A1493 phosphate group (Fig. 2f). Although this shift does not alter much the interactions of A1493 with U4•G36 and A1492/G530 with G5•U35 (Supplementary Figs 7g and 8h), these local changes modulate the B2a bridge. H69 is displaced towards the tRNA, which probably enhances the interaction surface of H69 with the tRNA D-stem. In the presence of paromomycin the position of H69 is closer to that observed for the cognate state (Supplementary Fig. 10). Furthermore, displacement of the A1493 phosphate group relaxes the decoding pocket from the side of the A codon (Fig. 2e) and changes the deformation of the near-cognate codon–anticodon helix (Supplementary Movie 2). This novel understanding of the paromomycin action therefore differs from the previously suggested mechanism in decoding where it was proposed to influence the monitoring capabilities of A1492 and A1493 (ref. 18). The observed moderate structural rearrangements with paromomycin are consistent with its measured effect at the proofreading step²⁵.

We find that both near-cognate tRNAs induce rearrangements of the 30S subunit known as domain closure¹⁹ (that is, shoulder movement and head rotation) as described for cognate tRNA²¹ (Fig. 3a). This implies that domain closure is an inherent quality of the ribosome in response to binding of any tRNA to the A site¹² and is prerequisite for formation of the decoding pocket.

Initially, the mechanism underlying the decoding process was deduced from pioneer X-ray structures of the isolated 30S subunit where crystals were soaked with U₆ and anticodon stem-loop mimicking mRNA and tRNA^{18,19}. Besides those limitations, all attempts to model near-cognate states on the 30S subunit were performed in the presence of paromomycin, which, on the one hand, stimulated an ordered binding of the near-cognate tRNA analogs, but, on the other,

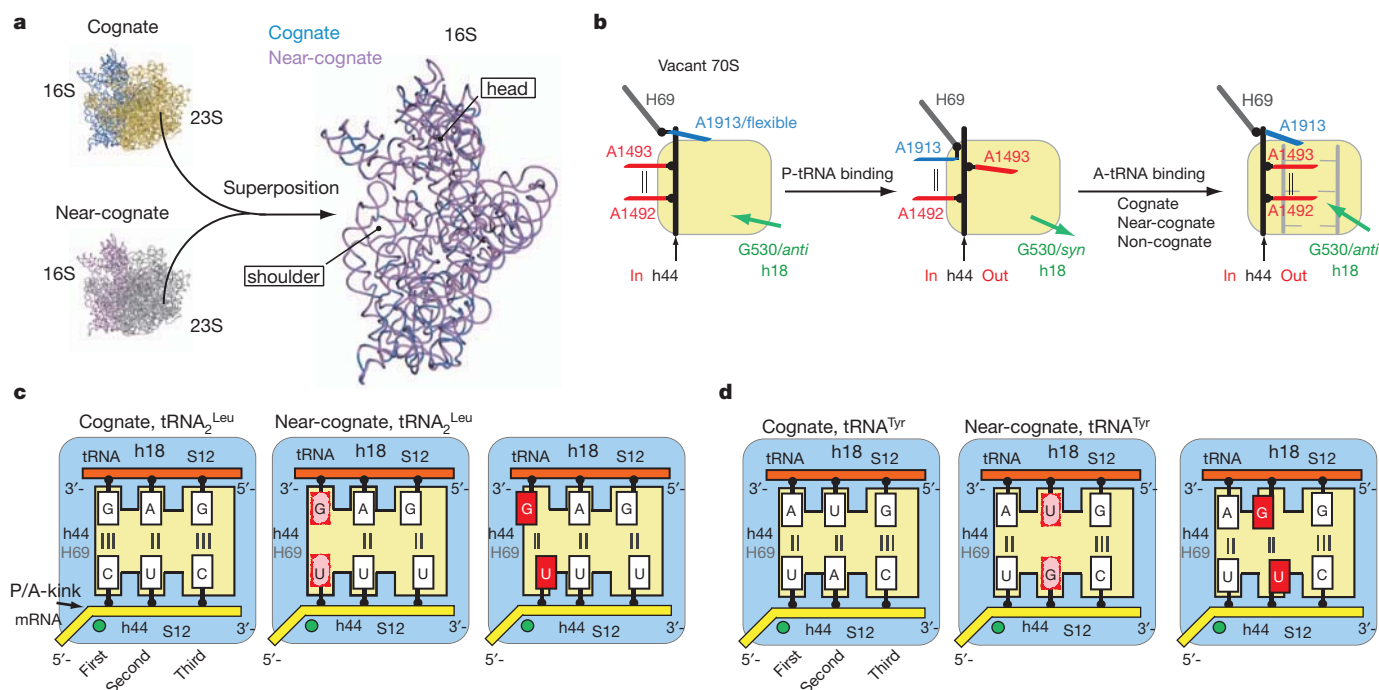


Figure 3 | The principle of decoding. **a**, Superposition of 23S rRNA from near-cognate and cognate structures with tRNA^{Leu}₂ shows identical domain closure in the near-cognate and cognate states. **b**, Representation of conformations of the core nucleotides composing the decoding centre depending on its functional states (data with the vacant 70S ribosome are unpublished). **c**, **d**, Illustration of the decoding principle: together with the constraints imposed on the A codon by the P/A kink coordinated by a magnesium ion (green sphere), the DC (h18, h44 and protein S12 from the

small subunit and H69 from the large subunit) restricts the allowed geometry of the first two nucleotides of the codon. No such restraints are imposed on the third base pair. A near-cognate tRNA with G•U in the first or second position is forced to form Watson–Crick-like base pairs (middle panels). This creates repulsion or requires energy for tautomerization (shown in pink), which by itself can be the source of the tRNA discrimination. The right panels illustrate the impossible situation when standard wobble base pairs (shown in red) occur in either the first or second positions of the codon–anticodon duplexes.

made it difficult to distinguish the independent effect of the mismatch on the 30S decoding centre¹⁹. The cognate and near-cognate models of the 70S ribosome described here, with or without paromomycin, together with our previous structures^{12,21}, give rise to novel insights into decoding with revisited roles for universally conserved nucleotides G530, A1492 and A1493 of 16S rRNA (Fig. 3b). Although these nucleotides form extensive contacts to the A-minor groove of a codon–anticodon helix, G530, A1492 and A1493 do not actively sense the correct Watson–Crick base-pairing geometry and thus do not discriminate against near-cognate tRNA.

We propose that upon binding of cognate or near-cognate tRNA to the 70S ribosome, the small subunit undergoes domain closure around the anticodon loop of the tRNA. The closure results in formation of a tight decoding centre that restricts the first two nucleotides of the A codon to form exclusively Watson–Crick base pairs with the tRNA anticodon (Fig. 3c, d). Owing to our current data resolution, we cannot precisely identify the hydrogen bond pattern of the mismatches in the near-cognate codon–anticodon helices, but tautomerism is a plausible chemical mechanism. An alternative explanation for the tRNA discrimination source could be repulsion in the U•G pair (Fig. 1c, e). Energy expenditure for formation of tautomers (or repulsion energy) could constitute the sole cause for the very efficient rejection of near-cognate tRNAs by the ribosome^{3,4}. Additionally, the observed deformation of the anticodon may lead to alterations in the codon–anticodon mini-helix and propagate through the rest of the near-cognate tRNA molecule, destabilizing it and causing the tRNA to dissociate from the ribosome (Supplementary Fig. 11). This corroborates the idea that evolutionarily tuned sequences of tRNAs play an active role in the tRNA selection process^{26–28}. Recent X-ray structures of the 70S ribosome with cognate tRNA and elongation factor Tu^{7,28} demonstrated that binding of an anticodon loop of tRNA in the decoding centre is nearly identical to that shown for accommodated tRNA. This information prompts us to hypothesize that the same mechanism described here for the proofreading step governs the initial tRNA selection step.

METHODS SUMMARY

Ribosomes were purified from *Thermus thermophilus* cells as described before²¹. For all complexes, mRNA, tRNA^{fMet} and tRNA^{Leu} (or tRNA^{Tyr}) were present in fivefold stoichiometric excess of the ribosome concentration. Complexes with paromomycin were obtained by including the antibiotic (30 µM) into the incubation mixture. Crystals were grown at 24 °C by sitting-drop vapour diffusion as described before³⁰. All crystals belonged to space group *P*2₁2₁2₁ and contained two molecules per asymmetric unit. A very low dose mode with high redundancy was used for data collection²⁹. The structure²¹, with tRNAs, mRNA and metal ions removed, was used for refinement with Phenix³⁰. Throughout refinement, no base-pair restraints were used between tRNAs and mRNAs to avoid bias towards standard base-pair geometry.

Full Methods and any associated references are available in the online version of the paper at www.nature.com/nature.

Received 25 August 2011; accepted 1 February 2012.

Published online 21 March 2012.

1. Rodnina, M. V. & Wintermeyer, W. Fidelity of aminoacyl-tRNA selection on the ribosome: kinetic and structural mechanisms. *Annu. Rev. Biochem.* **70**, 415–435 (2001).
2. Rodnina, M. V., Gromadski, K. B., Kothe, U. & Wieden, H. J. Recognition and selection of tRNA in translation. *FEBS Lett.* **579**, 938–942 (2005).
3. Zaher, H. S. & Green, R. Fidelity at the molecular level: lessons from protein synthesis. *Cell* **136**, 746–762 (2009).
4. Gromadski, K. B., Daviter, T. & Rodnina, M. V. A uniform response to mismatches in codon–anticodon complexes ensures ribosomal fidelity. *Mol. Cell* **21**, 369–377 (2006).
5. Lee, T. H., Blanchard, S. C., Kim, H. D., Puglisi, J. D. & Chu, S. The role of fluctuations in tRNA selection by the ribosome. *Proc. Natl Acad. Sci. USA* **104**, 13661–13665 (2007).

6. Li, W. *et al.* Recognition of aminoacyl-tRNA: a common molecular mechanism revealed by cryo-EM. *EMBO J.* **27**, 3322–3331 (2008).
7. Schmeing, T. M. *et al.* The crystal structure of the ribosome bound to EF-Tu and aminoacyl-tRNA. *Science* **326**, 688–694 (2009).
8. Schuetz, J. C. *et al.* GTPase activation of elongation factor EF-Tu by the ribosome during decoding. *EMBO J.* **28**, 755–765 (2009).
9. Voorhees, R. M., Schmeing, T. M., Kelley, A. C. & Ramakrishnan, V. The mechanism for activation of GTP hydrolysis on the ribosome. *Science* **330**, 835–838 (2010).
10. Ehrenberg, M., Kurland, C. G. & Ruusala, T. Counting cycles of EF-Tu to measure proofreading in translation. *Biochimie* **68**, 261–273 (1986).
11. Voorhees, R. M., Weixlbaumer, A., Loakes, D., Kelley, A. C. & Ramakrishnan, V. Insights into substrate stabilization from snapshots of the peptidyl transferase center of the intact 70S ribosome. *Nature Struct. Mol. Biol.* **16**, 528–533 (2009).
12. Jenner, L., Demeshkina, N., Yusupova, G. & Yusupov, M. Structural rearrangements of the ribosome at the tRNA proofreading step. *Nature Struct. Mol. Biol.* **17**, 1072–1078 (2010).
13. Geggier, P. *et al.* Conformational sampling of aminoacyl-tRNA during selection on the bacterial ribosome. *J. Mol. Biol.* **399**, 576–595 (2010).
14. Whitford, P. C. *et al.* Accommodation of aminoacyl-tRNA into the ribosome involves reversible excursions along multiple pathways. *RNA* **16**, 1196–1204 (2010).
15. Moazed, D. & Noller, H. F. Binding of tRNA to the ribosomal A and P sites protects two distinct sets of nucleotides in 16 S rRNA. *J. Mol. Biol.* **211**, 135–145 (1990).
16. Powers, T. & Noller, H. F. Selective perturbation of G530 of 16 S rRNA by translational miscoding agents and a streptomycin-dependence mutation in protein S12. *J. Mol. Biol.* **235**, 156–172 (1994).
17. Yoshizawa, S., Fourmy, D. & Puglisi, J. D. Recognition of the codon–anticodon helix by ribosomal RNA. *Science* **285**, 1722–1725 (1999).
18. Ogle, J. M. *et al.* Recognition of cognate transfer RNA by the 30S ribosomal subunit. *Science* **292**, 897–902 (2001).
19. Ogle, J. M., Murphy, F. V., Tarry, M. J. & Ramakrishnan, V. Selection of tRNA by the ribosome requires a transition from an open to a closed form. *Cell* **111**, 721–732 (2002).
20. Selmer, M. *et al.* Structure of the 70S ribosome complexed with mRNA and tRNA. *Science* **313**, 1935–1942 (2006).
21. Jenner, L. B., Demeshkina, N., Yusupova, G. & Yusupov, M. Structural aspects of messenger RNA reading frame maintenance by the ribosome. *Nature Struct. Mol. Biol.* **17**, 555–560 (2010).
22. BPS Database of RNA Base-pair Structures. <http://bps.rutgers.edu/bps> (2008).
23. Bebenek, K., Pedersen, L. C. & Kunkel, T. A. Replication infidelity via a mismatch with Watson–Crick geometry. *Proc. Natl Acad. Sci. USA* **108**, 1862–1867 (2011).
24. Auffinger, P. & Westhof, E. An extended structural signature for the tRNA anticodon loop. *RNA* **7**, 334–341 (2001).
25. Pape, T., Wintermeyer, W. & Rodnina, M. V. Conformational switch in the decoding region of 16S rRNA during aminoacyl-tRNA selection on the ribosome. *Nature Struct. Biol.* **7**, 104–107 (2000).
26. Cochella, L. & Green, R. An active role for tRNA in decoding beyond codon:anticodon pairing. *Science* **308**, 1178–1180 (2005).
27. Dale, T. & Uhlenbeck, O. C. Amino acid specificity in translation. *Trends Biochem. Sci.* **30**, 659–665 (2005).
28. Schmeing, T. M., Voorhees, R. M., Kelley, A. C. & Ramakrishnan, V. How mutations in tRNA distant from the anticodon affect the fidelity of decoding. *Nature Struct. Mol. Biol.* **18**, 432–436 (2011).
29. Mueller, M., Wang, M. & Schulze-Briese, C. Optimal fine ϕ -slicing for single-photon-counting pixel detectors. *Acta Crystallogr. D* **68**, 42–56 (2012).
30. Adams, P. D. *et al.* PHENIX: a comprehensive Python-based system for macromolecular structure solution. *Acta Crystallogr. D* **66**, 213–221 (2010).

Supplementary Information is linked to the online version of the paper at www.nature.com/nature.

Acknowledgements We are grateful to C. Schulze-Briese and the staff at the Swiss Light Source (Switzerland) for help during synchrotron X-ray data collection. We thank S. Duclaud for ribosome preparation and the staff of the Structural Biology Department core facility at Institut de Génétique et de Biologie Moléculaire et Cellulaire, Université de Strasbourg. This work was supported by ANR BLAN07-3_190451 (to M.Y.), ANR-07-PCVI-0015-01 (to G.Y.), Fondation pour la Recherche Médicale en France (to N.D.) and by the European Commission SPINE2.

Author Contributions N.D. and L.J. conducted experiments and performed analysis. All authors discussed the results and commented on the manuscript.

Author Information The atomic coordinates and structure factors for the determined crystal structures are deposited in the Protein Data Bank under accession numbers 3TVF and 3TVE (cognate tRNA^{Leu} complex), 3UYE and 3UYD (near-cognate tRNA^{Leu} complex), 3UZ3 and 3UZ1 (near-cognate tRNA^{Leu} complex with paromomycin), 3UZ6 and 3UZ9 (cognate tRNA^{Tyr} complex), 3UZG and 3UZF (near-cognate tRNA^{Tyr} complex), and 3UZL and 3UZK (near-cognate tRNA^{Tyr} complex with paromomycin). Reprints and permissions information is available at www.nature.com/reprints. The authors declare no competing financial interests. Readers are welcome to comment on the online version of this article at www.nature.com/nature. Correspondence and requests for materials should be addressed to M.Y. (marat@igbmc.fr) or G.Y. (gula@igbmc.fr).

METHODS

Complex formation and crystallization. Ribosomes were purified from *Thermus thermophilus* cells as described before²¹. The 30-nucleotide-long mRNA constructs I–IV (see below) were purchased from Dharmacon. In all sequences the AUG start codon is underlined and the A codons are in bold. Purified native uncharged *Escherichia coli* tRNA^{Met}, tRNA^{Leu} and tRNA^{Tyr} were supplied by Chemical Block. Aminoglycoside antibiotic paromomycin was purchased from Sigma-Aldrich.

The cognate and near-cognate complexes were formed in 10 mM tris-acetate, pH 7.0, 40 mM KCl, 7.5 mM Mg(Ac)₂, 0.5 mM DTT by incubating 70S ribosomes (3 µM) with mRNA-I, -II, -III or -IV and tRNA^{Met} for 10 min at 37 °C. Then tRNA^{Leu} and tRNA^{Tyr} were added to the mixtures with mRNA-I or -II and mRNA-III or -IV, respectively, and the complexes were further incubated for 30 min. For all complexes mRNA, tRNA^{Met} and tRNA^{Leu} (or tRNA^{Tyr}) were present in fivefold stoichiometric excess of the ribosome concentration. Complexes with paromomycin were obtained by including the antibiotic (30 µM) into the incubation mixture containing mRNA-II with tRNA^{Leu} and mRNA-IV with tRNA^{Tyr}. Crystals were grown at 24 °C by sitting-drop vapour diffusion as described before²⁰. In agreement with previous results, initiator tRNA^{Met} was found in the P site of all complexes and either tRNA^{Leu} or tRNA^{Tyr} was found in the A site (tRNA^{Met} was easily distinguishable from tRNA^{Leu} and tRNA^{Tyr} based on the large variable loops in those tRNAs). In the complexes with mRNA III and IV, the E site was occupied by tRNA^{Tyr}. However, in complexes with mRNA I and II, the quality of the density did not allow identification of the E site tRNA which was then modelled as tRNA^{Met}. mRNA-I 5'-GGCAAGGAGGU(U)₄AUGCC(U)₉-3' (cognate for tRNA^{Leu}). mRNA-II 5'-GGCAAGGAGGU(U)₄AUGUU(U)₉-3' (near-cognate for tRNA^{Leu}). mRNA-III 5'-GGCAAGGAGGU(A)₄AUGUAC(A)₉-3' (cognate for tRNA^{Tyr}). mRNA-IV 5'-GGCAAGGAGGU(A)₄AUGUGC(A)₉-3' (near-cognate for tRNA^{Tyr}).

Data collection, processing and structure determination. All crystals belong to space group P2₁2₁2₁ and contain two molecules per asymmetric unit. Data on all six complexes were collected at 100 K at the Synchrotron Light Source,

Switzerland, using the Pilatus 6M detector. A very low dose mode was used and huge redundancy was collected²⁹. The structure²¹, with tRNAs, mRNA and metal ions removed, was used for refinement with Phenix³⁰. The initial model was correctly placed within each data set by rigid body refinement with each molecule as a rigid body. This was followed by rigid body refinement of individual subunits. After positional and B-factor refinement, the resulting electron density maps were inspected and the tRNAs and mRNA ligands were built in these unbiased maps. In all of these and the following refinement rounds, no base-pair restraints were used between tRNAs and mRNAs to avoid bias towards perfect base-pair geometry. After several cycles of manual rebuilding followed by positional and individual isotropic B-factor refinement, magnesium ions were added and a final refinement round took place. A summary of the crystallographic data and refinement statistics is given in Supplementary Tables 1 and 2. Supplementary Table 3 shows the average B-factor for the entire structure as well as average B-factors for the decoding centre and the codon–anticodon helix. From this table it is seen that the average B-factors for the substructure comprising the decoding centre (G530, A1492, A1493 from 16S and G1913 from 23S), as well as the codon–anticodon helices (nucleotides 34–36 of tRNA in the A site and the corresponding codon of mRNA), are less than the overall B-factor for the entire ribosome structure. Therefore it is clear that the decoding centre is part of the most accurately determined parts of these models.

To verify that the base-pair geometry described in the paper is correct, we performed a many extra independent refinement rounds with base-pair geometries restrained to various standards (Watson–Crick, wobble, etc.) so that we could be confident about the reported geometries. Supplementary Figs 3 and 4 show OMIT-averaged kick maps^{30,31} of the G•U mismatch for the two near-cognate complexes. These unbiased maps show that a wobble conformation of these base pairs would not fit into the electron density and clearly demonstrate that a Watson–Crick conformation is the only plausible fit.

31. Praeenikar, J., Afonine, P. V., Guncar, G., Adams, P. D. & Turk, D. Averaged kick maps: less noise, more signal and probably less bias. *Acta Crystallogr. D* **65**, 921–931 (2009).

MAP and kinesin-dependent nuclear positioning is required for skeletal muscle function

Thomas Metzger^{1,2*}, Vincent Gache^{3*}, Mu Xu¹, Bruno Cadot³, Eric S. Folker¹, Brian E. Richardson¹, Edgar R. Gomes^{3,4*} & Mary K. Baylies^{1,2*}

The basic unit of skeletal muscle in all metazoans is the multinucleate myofibre, within which individual nuclei are regularly positioned¹. The molecular machinery responsible for myonuclear positioning is not known. Improperly positioned nuclei are a hallmark of numerous diseases of muscle², including centronuclear myopathies³, but it is unclear whether correct nuclear positioning is necessary for muscle function. Here we identify the microtubule-associated protein *ensconsin* (*Ens*)/microtubule-associated protein 7 (*MAP7*) and kinesin heavy chain (*Khc*)/*Kif5b* as essential, evolutionarily conserved regulators of myonuclear positioning in *Drosophila* and cultured mammalian myotubes. We find that these proteins interact physically and that expression of the *Kif5b* motor domain fused to the *MAP7* microtubule-binding domain rescues nuclear positioning defects in *MAP7*-depleted cells. This suggests that *MAP7* links *Kif5b* to the microtubule cytoskeleton to promote nuclear positioning. Finally, we show that myonuclear positioning is physiologically important. *Drosophila ens* mutant larvae have decreased locomotion and incorrect myonuclear positioning, and these phenotypes are rescued by muscle-specific expression of *Ens*. We conclude that improper nuclear positioning contributes to muscle dysfunction in a cell-autonomous fashion.

To identify the mechanisms governing nuclear positioning in muscle, we performed an F₃ recessive ethylmethane sulphonate mutagenesis screen using the *apterous*ME-NLS::dsRed transgenic line (*apRed*)⁴, which expresses dsRed in the nuclei of the four lateral transverse muscles of the *Drosophila* embryo. At the end of embryogenesis, the myonuclei are distributed throughout the muscles (Fig. 1a, b). One mutation resulted in clustered nuclei near the ventral end of each lateral transverse muscle. Within each hemisegment these clusters resembled the Nike trademark, so we named the mutant *swoosh* (*swo*) (Fig. 1a).

Further analysis of *swo* mutant embryos indicated that myoblast specification⁵, fusion⁵, muscle elongation^{6,7} and attachment⁷ occur normally. The only notable difference in *swo* mutant muscles is a ventral bulge in the cell body that correlates with the cluster of nuclei (Supplementary Figs 1 and 2). These data suggest that the clustering of nuclei in *swo* mutants is a genuine nuclear positioning defect.

To examine nuclear movement, we performed *in vivo* time-lapse imaging on *apRed* control and *swo,apRed* mutant embryos (Fig. 1b). In stage 14 *apRed* control embryos (10.5 h after egg laying (AEL)), nuclei in the four lateral transverse muscles group near the ventral end of each growing myotube in the hemisegment. During stage 15 (11.5 h AEL) after the completion of myoblast fusion and muscle attachment, the nuclei within each myotube begin to separate into distinct dorsal and ventral clusters. These clusters finish their migration during stage 16 (15 h AEL) and each cluster resides at an opposite end of the myotube. Finally, during stage 17 (18 h AEL), the six to eight nuclei in each lateral transverse muscle move from the clusters and distribute evenly throughout each lateral transverse muscle. The entire process of nuclear movement spans 7 h (Supplementary Movie 1). Time-lapse

imaging of *swo,apRed* mutant embryos demonstrated that the nuclei fail to undergo the initial separation into dorsal and ventral clusters during stage 15 and remain clustered at stage 17, indicating that *swo* does not simply cause a delay in myonuclear positioning (Supplementary Movie 2). In addition, the nuclei in every other somatic muscle examined in *swo* mutant embryos also failed to separate (Supplementary Fig. 1e).

We determined that the *swo* flies carry a nonsense mutation in *ensconsin* (*ens*), a gene encoding a MAP. Expression of haemagglutinin-tagged *Ens* specifically in the developing mesoderm and muscle rescued the nuclear positioning phenotype in *swo* embryos, confirming that the mutation in *ens* is responsible for the nuclear positioning defect. Depletion of *ens* solely in the developing mesoderm and muscle by RNA-mediated interference recapitulated the phenotype we observed in the *swo* mutant (renamed *ens^{swo}*), and known *ens* mutant alleles failed to complement *ens^{swo}* (Supplementary Figs 1c and 2a, and data not shown). These results indicate that *ens* is required autonomously within muscle for proper myonuclear positioning. We also found that nuclear position was disrupted in *ens^{swo}* oocytes⁸ (Supplementary Fig. 3a, b), but not in *ens^{swo}* photoreceptor cells (Supplementary Fig. 3c, and data not shown)⁹, indicating that *Ens* is necessary for some, but not all, nuclear positioning processes in *Drosophila*.

Four different genes in the mouse genome encode *Ens* orthologues: *Map7* (*E-MAP-115*, *Ensconsin*), *Map7D1*, *Map7D2* and *Map7D3* (Supplementary Fig. 2c). Using cultures of C2C12 myoblasts and primary mouse myoblasts, we examined the effect on nuclear positioning in myotubes depleted of each *Ens* orthologue by short interfering RNA (siRNA) (Fig. 1 and Supplementary Fig. 4). *MAP7* depletion caused a significant increase in the aggregation of nuclei within a myotube but did not affect myoblast fusion or myotube differentiation (Fig. 1c, d, Supplementary Fig. 4d, e and Supplementary Movies 3–6). Depletion of *MAP7D1*, *MAP7D2* or *MAP7D3* did not affect nuclear positioning (Supplementary Fig. 4b). Expression of full-length *MAP7* in *MAP7*-depleted myotubes restored nuclear alignment (Fig. 1d and Supplementary Fig. 6h). Thus, *MAP7* is required for nuclear positioning in both *Drosophila* muscles and cultured mammalian myotubes.

No major defects on the microtubule network were observed in *ens^{swo}* mutant embryos or *MAP7*-depleted myotubes (Supplementary Figs 2g–h and 6g). Therefore, to gain mechanistic insight, we conducted a yeast two-hybrid screen to find *Ens*-binding proteins and identified kinesin heavy chain (*Khc*) (Supplementary Fig. 5). Both a *kinesin*-null mutation (*khc*⁸) and a motor-dead mutation (*khc*⁴)¹⁰ disrupted myonuclear positioning without affecting muscle elongation and attachment (Fig. 2a and Supplementary Fig. 5a). Likewise, siRNA-mediated depletion of the mammalian *Khc* orthologue *Kif5b* (ref. 11) in primary and C2C12 myotubes disrupted nuclear alignment similarly to *MAP7* depletion without affecting myotube formation or differentiation (Fig. 2b, c, Supplementary Figs 4d–e

¹Program in Developmental Biology, Sloan-Kettering Institute, New York, New York 10065, USA. ²Weill Graduate School of Medical Sciences of Cornell University, New York, New York 10065, USA. ³UMR S 787 INSERM, Université Pierre et Marie Curie Paris 6, 75634 Paris, France. ⁴Groupe Hospitalier Pitié-Salpêtrière, Institut de Myologie, 75013 Paris, France.

*These authors contributed equally to this work.

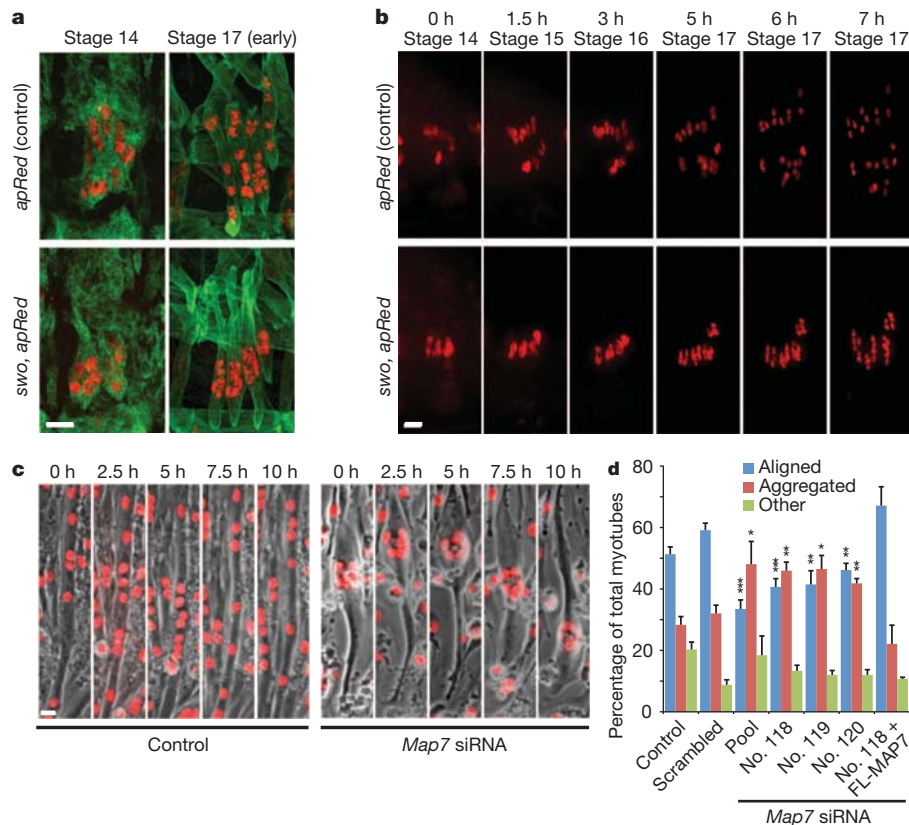


Figure 1 | Myonuclear positioning requires ensconsin/MAP7.

a, Hemisegments from control and *ens^{sw/o}* embryos at the beginning (stage 14) and end (stage 17) of nuclear migration. Muscles are immunostained for tropomyosin (green); nuclei are immunostained for dsRed (red). Scale bar, 10 μ m. **b**, Time-lapse images of nuclear migration in hemisegments of control and *ens^{sw/o}* embryos. Elapsed imaging times are shown along the top. Scale bar, 10 μ m. **c**, Time-lapse images of nuclear migration in control and *Map7*-

and 6, and Supplementary Movies 7 and 8). Expression of full-length Kif5b in Kif5b-depleted myotubes restored nuclear alignment (Fig. 2c and Supplementary Fig. 6h). These data indicate that Khc, with a

depleted C2C12-H1B-GFP myotubes. Elapsed imaging times are shown along the top. Nuclei are stained red. Scale bar, 15 μ m. **d**, Nuclear distribution in C2C12 myotubes that were untreated (control) or treated with the indicated siRNA and *Map7*-depleted cells expressing full-length MAP7 (no. 118 + FL-MAP7). Error bars indicate s.e.m. Asterisk, $P < 0.05$; two asterisks, $P < 0.01$; three asterisks, $P < 0.001$ (scrambled versus experimental condition).

functional motor domain, is required for proper nuclear positioning in both *Drosophila* muscles and cultured mammalian myotubes.

We next examined whether Ens and Khc interact functionally to position myonuclei. Embryos heterozygous for *ens* or *khc* position their myonuclei normally. However, embryos that were doubly heterozygous for *ens^{sw/o}* and *khc* showed defective nuclear positioning similar to that in the homozygous *ens* embryos (Supplementary Fig. 5). This demonstrates that *ens* and *khc* interact functionally and that the dosage of these genes is important for proper nuclear positioning.

We next tested whether Ens/MAP7 and Khc/Kif5b interact physically. Endogenous Kif5b co-immunoprecipitated with expressed full-length green fluorescent protein (GFP)-tagged MAP7, independently of microtubules (Fig. 3a, b). Using fragments of MAP7, we mapped the Kif5b interaction to the carboxy-terminal coiled-coil domain of MAP7 (CC2), which was confirmed by reciprocal co-immunoprecipitation (Fig. 3a–c). Similarly, fragments of Kif5b were used to identify the C-terminal region (Kif5b-motorless) as the MAP7-interacting domain (Fig. 3a, d, e). The C-terminal coiled-coil domain of MAP7 therefore interacts with the C-terminal region of Kif5b (Fig. 3).

To test whether the specific interaction identified above between Ens/MAP7 and Khc/Kif5b is required for nuclear positioning, we expressed chimaeras consisting of the Kif5b motor domain¹² fused to fragments of MAP7 that contained (K-EMTB and K-EMTB-M) or lacked (K-N-term) the microtubule-binding domain (EMTB)¹³ in *Map7* siRNA-depleted myotubes (Fig. 3a, f, g). Expression of chimaeras that contained the MAP7 EMTB rescued the alignment of nuclei in MAP7-depleted myotubes, whereas expression of the EMTB domain alone, or a chimaera that lacked the MAP7 EMTB (K-N-term) did not

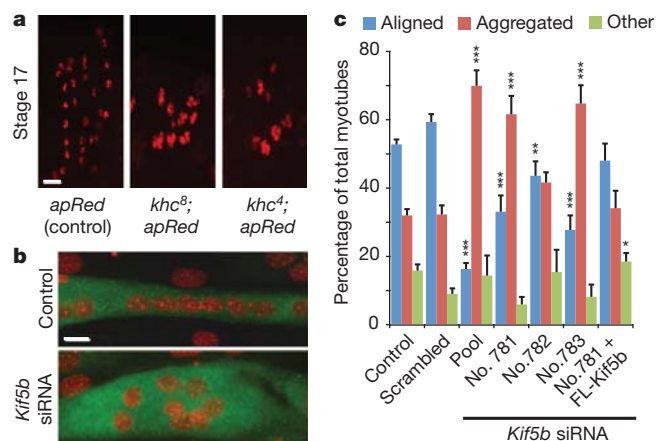


Figure 2 | Kinesin is required for myonuclear positioning. **a**, Single hemisegments from stage 17 (22 h AEL) embryos of indicated genotypes. Scale bar, 10 μ m. **b**, Representative immunofluorescence images of control and *Kif5b*-depleted C2C12 myotubes differentiated for 4 days and immunostained for myosin heavy chain (green) and 4',6-diamidino-2-phenylindole (red). Scale bar, 15 μ m. **c**, Histogram of nuclear distribution in C2C12 myotubes that were untreated (control) or treated with the indicated siRNA or *Kif5b*-depleted cells expressing full-length Kif5b (no. 781 + FL-Kif5b). Error bars indicate s.e.m. Asterisk, $P < 0.05$; two asterisks, $P < 0.01$; three asterisks, $P < 0.001$ (scrambled versus experimental condition).

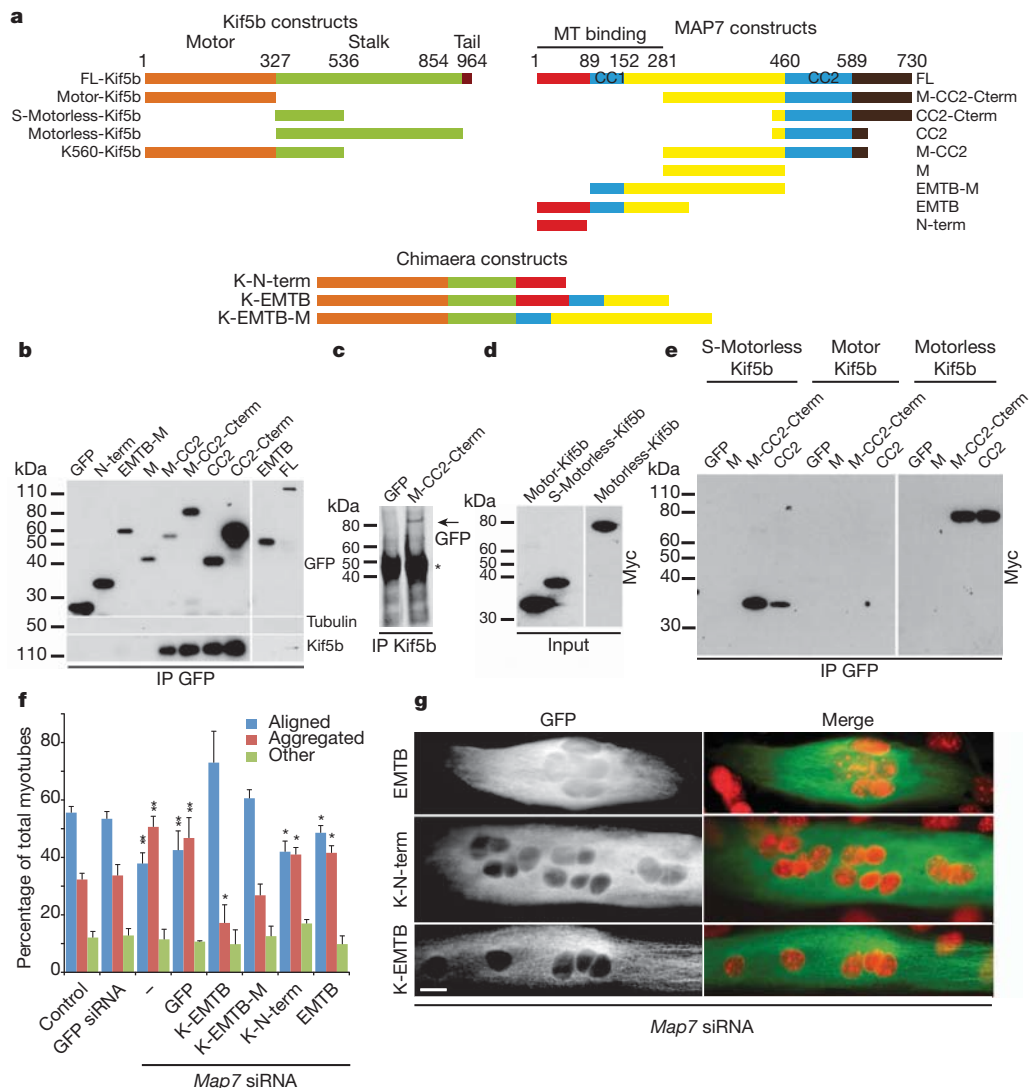


Figure 3 | Kinesin and ensconsin/MAP7 interact to regulate nuclear position. **a**, Kif5b, MAP7 and chimaera constructs amino-terminally tagged with GFP (MAP7 and chimaeras) or c-Myc (Kif5b). Numbers indicate amino acids. **b**, Western blot with indicated antibodies (right) of GFP–MAP7 (top) immunoprecipitations (IP). **c**, Anti-GFP Western blot of Kif5b immunoprecipitations from C2C12 cells expressing indicated constructs (top). Asterisk indicates anti-Kif5b IgG. **d**, Anti-c-Myc Western blot from C2C12 cells

expressing Kif5b constructs. **e**, Anti-c-Myc Western blot from GFP immunoprecipitations with C2C12 myotubes expressing the indicated constructs. **f**, Nuclear distribution in *Map7*-depleted C2C12 myotubes expressing the indicated chimaeras. Error bars indicate s.e.m. Asterisk, $P < 0.05$; two asterisks, $P < 0.01$. **g**, *Map7*-depleted C2C12s expressing indicated chimaeras. Anti-GFP is shown in green; nuclei are shown in red (stained with 4',6-diamidino-2-phenylindole). Scale bar, 15 μ m.

(Fig. 3f, g). These results indicate that the function of MAP7 in nuclear positioning is to link Kif5b to microtubules.

To investigate the physiological impact of mispositioned nuclei on muscle function *in vivo*, we examined larval motility¹⁴. *ens* mutant larvae move significantly more slowly than controls (Fig. 4b and Supplementary Fig. 7d). Moreover, analysis of the muscle structure in tracked larvae revealed that the myonuclei in *ens*^{sw} mutants were 33% closer together than in controls (Fig. 4a, c and Supplementary Fig. 7a, e). Sarcomere structure¹⁵, t-tubules¹⁶, neuromuscular junctions¹⁷, nuclei number (Supplementary Fig. 7c, e, f, h, i) and mitochondrial localization (Supplementary Fig. 8) were unchanged in *ens* mutants compared with controls. Expression of *Ens* in the mesoderm and muscle during embryonic development or in muscle starting at the L2 larval stage in *ens* mutants rescued the nuclear positioning and motility defects in L3 larvae (Fig. 4a–c and Supplementary Fig. 7a, d, g), demonstrating a strong correlation between aberrant myonuclear position and decreased muscle function.

These experiments define a subset of the nuclear behaviours that occur during muscle differentiation, and demonstrate conservation

across species at both the cellular and molecular levels. We find that *Ens*/MAP7 and *Khc*/Kif5b are critical for myonuclear positioning and are not required for fusion and myofibre formation. Moreover, these proteins interact genetically and physically, and the physical interaction is necessary for proper nuclear positioning. Furthermore, our results argue that the correct spacing of myonuclei is required for proper muscle function.

Within a myotube, distinct microtubule networks emanate from each myonucleus, producing regions of overlapping antiparallel microtubules^{18–20}. Furthermore, *Ens*/MAP7 functions to load *Khc*/Kif5b onto microtubules⁸. The results presented here therefore suggest a molecular mechanism for nuclear positioning. Adjacent nuclei could be positioned relative to each other by *Ens*/MAP7 and *Khc*/Kif5b interacting with and sliding antiparallel microtubules that have their minus ends anchored to the nuclear envelope, in a similar manner to the mechanism by which the Eg5 kinesin facilitates spindle elongation²¹ (Supplementary Fig. 10). This mechanism is distinct from the kinesin-1-dependent nuclear position in the *Caenorhabditis elegans* hypodermis, in which *Khc* is anchored to the nucleus by kinesin light

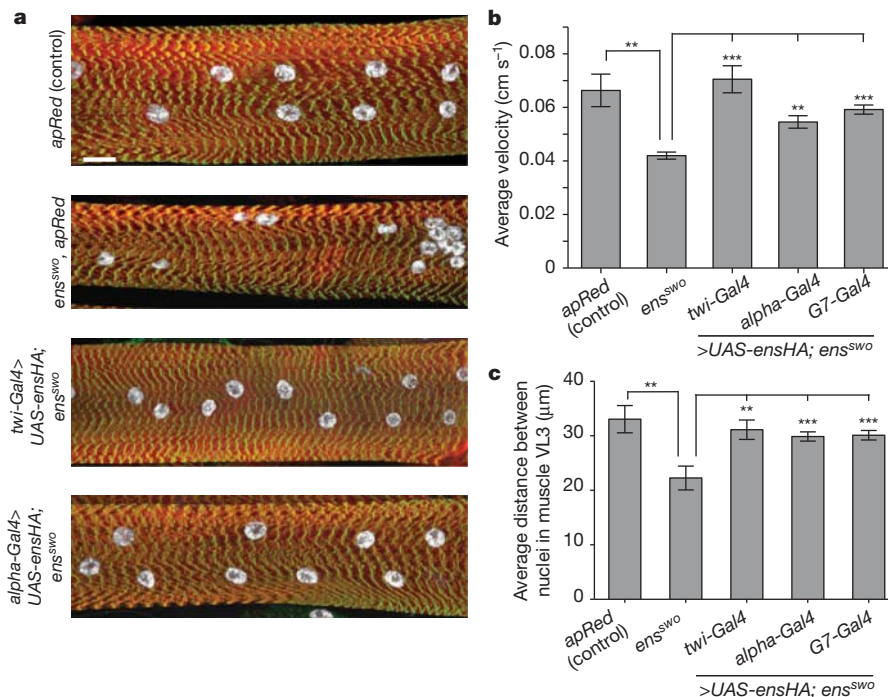


Figure 4 | Ensconsin/MAP7 is required for intracellular muscle organization and efficient larval locomotion. **a**, Maximum-intensity xy projections of muscle VL3 from segment A3 of L3 larvae from the indicated genotypes stained for actin (red), nuclei (white) and Z-bands (green). Scale bar, 20 μm. **b**, Average velocity of migration for L3 larvae of the indicated genotypes.

chain (Klc) and the KASH-domain protein Unc-83, which drive the nucleus unidirectionally on microtubules²². We find that *klc* mutants in *Drosophila* do not show defects in the positioning of nuclei that we describe here. Additionally, overexpression of dominant-negative (dn)-KASH-domain constructs in C2C12 myotubes that remove KASH proteins from the nuclear envelope and disrupt the function of the LINC (linker of nucleoskeleton and cytoskeleton) complex and nuclear anchoring^{23,24} does not affect nuclear positioning (Supplementary Fig. 9). Taken together, these results suggest that kinesin is not interacting directly with the nucleus; they therefore provide evidence for the sliding mechanism.

Patients suffering from various muscle diseases, including centronuclear myopathies, show muscle weakness with mislocalized myonuclei³. However, it remains unclear whether these mispositioned nuclei contribute to muscle weakness or are simply a result of impaired myofibre function³. Our results show that the ability to position myonuclei correctly correlates with better muscle function. Because nuclear misposition is the first observable defect in zygotic *ens* mutant embryos, we speculate that this is a cause of the observed muscle weakness. Mispositioned nuclei might lead to the observed muscle weakness as a result of a disruption in the size and spacing of myonuclear domains throughout the muscle²⁵ or in the distribution of subcellular structures whose positioning depends on correct nuclear spacing. We rescue nuclear position, muscle function, and viability not only by supplying *Ens* during embryogenesis but also by expressing *Ens* solely in mature muscles later in larval development. We therefore propose that correcting nuclear positioning defects in patients with muscle diseases might benefit muscle strength and improve muscle function. The model systems that we present here provide a platform with which to identify additional nuclear positioning genes and assess their function, and to screen for potential drugs to alleviate muscle weakness due to disease.

METHODS SUMMARY

Drosophila stocks used included *apME-NLS::dsRed* (ref. 4), *Df(3L)GN34* (ref. 26), *ens^{HP36480}* (Bloomington), *ens⁰⁷¹²¹* (Harvard), *Df-ens^{A3277}*, *ens^{AN}*, *ens^{AC}* (ref. 8),

Each of the indicated Gal4 drivers is expressing *UAS-ensHA* in a homozygous *ens^{swo}* mutant background. Error bars, s.e.m. Two asterisks, $P < 0.01$; three asterisks, $P < 0.001$. **c**, Nearest-neighbour analysis of nuclei within muscle VL3 from segment A3 from L3 larvae of the indicated genotypes. Error bars indicate s.e.m. Asterisk, $P < 0.05$; three asterisks, $P < 0.001$.

khc⁸, *khc⁴*, *khc²³* (ref. 10), *klc^{8ex94}* (ref. 27), *twi-Gal4* (ref. 4), *alpha-Gal4*, *G7-Gal4* (ref. 28) (from K. Broadie), and *UAS-ens-IR* lines 106207 and 18491 (VDRC). *UAS-ensHA* transgenic flies were generated by BestGene Inc. Mouse cells were transfected with siRNA using Lipofectamine RNAiMAX (Invitrogen) or with DNA using Lipofectamine 2000 (Invitrogen). Primary antibodies used were rabbit anti-dsRed (Clontech), rat anti-tropomyosin (Abcam), mouse anti-myosin heavy chain (from S. Abmayr), rabbit anti-Zasp (from F. Schöck), chicken anti-β-gal (Abcam), mouse anti-α-tubulin (Sigma), rat anti-ensconsin (from P. Rørth), guinea pig anti-Krüppel (from J. Reinitz), rabbit anti-Eve (from M. Frasch), mouse anti-β-PS integrin (DSHB), rabbit anti-vestigial (from S. Carroll), fluorescein isothiocyanate-conjugated anti-horseradish peroxidase (Jackson ImmunoResearch), mouse anti-discs large (DSHB), rabbit anti-ATP synthase²⁹ (from H. Duan), rat anti-DE-cadherin (DSHB), mouse anti-chaoptin 24B10 (DSHB), rat anti-elav (DSHB), Alexa Fluor 488-conjugated wheatgerm agglutinin (Invitrogen), MF20 (DSHB), rabbit anti-KHC (Santa Cruz), mouse anti-c-Myc (Roche) and rabbit anti-GFP (Invitrogen). Secondary antibodies were either biotinylated (Vector Laboratories and Jackson ImmunoResearch) or conjugated to Alexa Fluor 488, 555 or 647. The fusion index³⁰, sarcomere length¹⁵, bouton number¹⁷ and larval velocity¹⁴ were quantified as described, with minor modifications (see Methods). The yeast two-hybrid screen was performed with full-length *Ens* by Hybrigenics SA Services using a 0–24-h *Drosophila* complementary DNA library. Standard protocols were used for immunoprecipitation, western blotting and quantitative polymerase chain reaction experiments and are described in Methods.

Full Methods and any associated references are available in the online version of the paper at www.nature.com/nature.

Received 30 March 2011; accepted 31 January 2012.

Published online 18 March 2012.

1. Bruusgaard, J. C., Liestøl, K., Ekmark, M., Kollstad, K. & Gundersen, K. Number and spatial distribution of nuclei in the muscle fibres of normal mice studied *in vivo*. *J. Physiol. (Lond.)* **551**, 467–478 (2003).
2. Cohn, R. D. & Campbell, K. P. Molecular basis of muscular dystrophies. *Muscle Nerve* **23**, 1456–1471 (2000).
3. Jungbluth, H., Wallgren-Pettersson, C. & Laporte, J. Centronuclear (myotubular) myopathy. *Orphanet J. Rare Dis.* **3**, 26 (2008).
4. Richardson, B. E., Beckett, K., Nowak, S. J. & Baylies, M. K. SCAR/WAVE and Arp2/3 are crucial for cytoskeletal remodeling at the site of myoblast fusion. *Development* **134**, 4357–4367 (2007).

5. Beckett, K. & Baylies, M. K. The development of the *Drosophila* larval body wall muscles. *Int. Rev. Neurobiol.* **75**, 55–70 (2006).
6. Prokop, A., Martín-Bermudo, M. D., Bate, M. & Brown, N. H. Absence of PS integrins or laminin A affects extracellular adhesion, but not intracellular assembly, of hemiadherens and neuromuscular junctions in *Drosophila* embryos. *Dev. Biol.* **196**, 58–76 (1998).
7. Volk, T. Singling out *Drosophila* tendon cells: a dialogue between two distinct cell types. *Trends Genet.* **15**, 448–453 (1999).
8. Sung, H.-H. *et al.* *Drosophila* ensconsin promotes productive recruitment of Kinesin-1 to microtubules. *Dev. Cell* **15**, 866–876 (2008).
9. Fischer-Vize, J. A. & Mosley, K. L. Marbles mutants: uncoupling cell determination and nuclear migration in the developing *Drosophila* eye. *Development* **120**, 2609–2618 (1994).
10. Brendza, K. M., Rose, D. J., Gilbert, S. P. & Saxton, W. M. Lethal kinesin mutations reveal amino acids important for ATPase activation and structural coupling. *J. Biol. Chem.* **274**, 31506–31514 (1999).
11. Vale, R. D., Reese, T. S. & Sheetz, M. P. Identification of a novel force-generating protein, kinesin, involved in microtubule-based motility. *Cell* **42**, 39–50 (1985).
12. Vale, R. D. *et al.* Direct observation of single kinesin molecules moving along microtubules. *Nature* **380**, 451–453 (1996).
13. Masson, D. & Kreis, T. E. Identification and molecular characterization of E-MAP-115, a novel microtubule-associated protein predominantly expressed in epithelial cells. *J. Cell Biol.* **123**, 357–371 (1993).
14. Louis, M., Huber, T., Benton, R., Sakmar, T. P. & Vosshall, L. B. Bilateral olfactory sensory input enhances chemotaxis behavior. *Nature Neurosci.* **11**, 187–199 (2008).
15. Bai, J., Hartwig, J. H. & Perrimon, N. SALS, a WH2-domain-containing protein, promotes sarcomeric actin filament elongation from pointed ends during *Drosophila* muscle growth. *Dev. Cell* **13**, 828–842 (2007).
16. Razzaq, A. *et al.* Amphiphysin is necessary for organization of the excitation-contraction coupling machinery of muscles, but not for synaptic vesicle endocytosis in *Drosophila*. *Genes Dev.* **15**, 2967–2979 (2001).
17. McCabe, B. D. *et al.* The BMP homolog Gbb provides a retrograde signal that regulates synaptic growth at the *Drosophila* neuromuscular junction. *Neuron* **39**, 241–254 (2003).
18. Tassin, A. M., Maro, B. & Bornens, M. Fate of microtubule-organizing centers during myogenesis *in vitro*. *J. Cell Biol.* **100**, 35–46 (1985).
19. Guerin, C. M. & Kramer, S. G. RacGAP50C directs perinuclear γ -tubulin localization to organize the uniform microtubule array required for *Drosophila* myotube extension. *Development* **136**, 1411–1421 (2009).
20. Bugnard, E., Zaal, K. J. M. & Ralston, E. Reorganization of microtubule nucleation during muscle differentiation. *Cell Motil. Cytoskeleton* **60**, 1–13 (2005).
21. Glotzer, M. The 3Ms of central spindle assembly: microtubules, motors and MAPs. *Nature Rev. Mol. Cell Biol.* **10**, 9–20 (2009).
22. Meyerzon, M., Fridolfsson, H. N., Ly, N., McNally, F. J. & Starr, D. A. UNC-83 is a nuclear-specific cargo adaptor for kinesin-1-mediated nuclear migration. *Development* **136**, 2725–2733 (2009).
23. Grady, R. M., Starr, D. A., Ackerman, G. L., Sanes, J. R. & Han, M. Syne proteins anchor muscle nuclei at the neuromuscular junction. *Proc. Natl Acad. Sci. USA* **102**, 4359–4364 (2005).
24. Lei, K. *et al.* SUN1 and SUN2 play critical but partially redundant roles in anchoring nuclei in skeletal muscle cells in mice. *Proc. Natl Acad. Sci. USA* **106**, 10207–10212 (2009).
25. Pavlath, G. K., Rich, K., Webster, S. G. & Blau, H. M. Localization of muscle gene products in nuclear domains. *Nature* **337**, 570–573 (1989).
26. Feng, G., Deák, P., Kasbekar, D. P., Gil, D. W. & Hall, L. M. Cytogenetic and molecular localization of tipE: a gene affecting sodium channels in *Drosophila melanogaster*. *Genetics* **139**, 1679–1688 (1995).
27. Gindhart, J. G., Desai, C. J., Beushausen, S., Zinn, K. & Goldstein, L. S. Kinesin light chains are essential for axonal transport in *Drosophila*. *J. Cell Biol.* **141**, 443–454 (1998).
28. Zhang, Y. Q. *et al.* *Drosophila* fragile X-related gene regulates the MAP1B homolog Futsch to control synaptic structure and function. *Cell* **107**, 591–603 (2001).
29. Peña, P. & Garesse, R. The β subunit of the *Drosophila melanogaster* ATP synthase: cDNA cloning, amino acid analysis and identification of the protein in adult flies. *Biochem. Biophys. Res. Commun.* **195**, 785–791 (1993).
30. Mitchell, K. J. *et al.* Identification and characterization of a non-satellite cell muscle resident progenitor during postnatal development. *Nature Cell Biol.* **12**, 257–266 (2010).

Supplementary Information is linked to the online version of the paper at www.nature.com/nature.

Acknowledgements We thank K. Anderson, K. Hadjantonakis, A. Hall and D. Sassoon for comments on the manuscript. We thank the Baylies and Gomes Laboratories for discussions, and R. Fernandez-Gonzalez for his assistance in computational analysis. The initial screens in *Drosophila* were supported by National Institutes of Health (NIH) grants GM056989 and GM0781318 to M.B.; the *Drosophila* nuclear positioning analysis was supported by a Muscular Dystrophy Association (MDA) grant to M.B. T.M. was supported initially by NIH Training Grant T32 BM008539. B.C. was supported initially by a Fondation pour la Recherche Médicale (FRM) fellowship. V.G. was supported initially by a Région Île-de-France fellowship. Mammalian work was supported by Muscular Dystrophy Association (MDA), INSERM Avenir programme and Agence Nationale de la Recherche (ANR) grants to E.R.G.

Author Contributions T.M. and V.G. are joint first authors. E.G. and M.B. are joint senior authors. M.B., M.X., T.M., E.G., V.G. and B.C. conceived, designed and analysed the experiments. T.M., M.X., E.S. and B.R. conducted the *Drosophila* experimental work. V.G. and B.C. conducted the mouse primary cultures and C2C12 experimental work. The manuscript was written by T.M., E.S., V.G., E.G. and M.B. with assistance from other authors.

Author Information Reprints and permissions information is available at www.nature.com/reprints. The authors declare no competing financial interests. Readers are welcome to comment on the online version of this article at www.nature.com/nature. Correspondence should be addressed to E.G. (edgar.gomes@upmc.fr) or M.B. (m-baylies@ski.mskcc.org).

METHODS

Flies and husbandry. Stocks were grown and maintained under standard conditions on standard cornmeal medium. Crosses were performed at 25 °C. *Drosophila* stocks: *apME-NLS::dsRed* (ref. 4), *Df(3L)GN34* (ref. 26), *ens*^{HP36480} (Bloomington), *ens*⁷⁰⁷¹²¹ (Harvard), *ens*^{AN}, *ens*^{AC}, *Df-ens*^{A3277} (ref. 8), *UAS-ensHA* (this study), *khc*⁸, *khc*⁴, *khc*²³ (ref. 10), *klc*^{8ex94} (ref. 27), and *UAS-ens-IR* lines 106207 and 18491 (VDRC). Mutant alleles were balanced and identified using *CyO P[w+en1lacZ]* or *CTG [CyO,twi-GAL4,UAS-2xeGFP]* (ref. 26), *TM3 Sb1Dfd-lacZ* or *TTG [TM3,twi-GAL4,UAS-2xeGFP]* (ref. 31). Gal4 lines used in this work were *twi-Gal4* (ref. 4), which is specifically expressed in the mesoderm and developing muscle (2.5–13 h AEL), and *alpha-Gal4* and *G7-Gal4* (ref. 28) (gift from K. Broadie), which are specifically expressed in the larval muscles beginning at the late L1 and early L2 larval stages and perdures until pupation.

Ethylmethane sulphonate mutagenesis and screening. A detailed description of the screen and its findings are available from the authors. In brief, males from an isogenized stock carrying the *apME-NLS::dsRed* transgene on the third chromosome were mutagenized with 35 mM ethylmethane sulphonate dissolved in 1% sucrose in accordance with a standard protocol³². Individual mutant lines were established over the TTG balancer. Live F₃ progeny were screened under fluorescence, and embryos homozygous for the mutant chromosome were identified by an absence of the balancer GFP. Deficiency mapping, complementation and sequencing were used to identify the genetic lesion.

Phylogenetic analysis. *Drosophila*, human and mouse MAP7 orthologues were aligned using LALIGN (http://www.ch.embnet.org/software/LALIGN_form.html) and the phylogenetic tree was created using Vector NTI (Invitrogen).

Cell culture. C2C12 myoblasts were grown and differentiated for 4 days as described³³. Primary myoblasts were isolated and differentiated for 3 days as described^{30,34}.

Constructs. *Map7* fragments were cloned from a C2C12 cDNA library into pEGFP-C1 vector (Invitrogen), using the following primers: *N-term* (1–244), 5'-ATGGCGGAGCAGGGAGC-3' (forward) and 5'-CTAGCTGTTTTCTCG TTCCTC-3' (reverse); *EMTB-M* (261–1351), 5'-ATGTGGCTAGAGAGAGAA GAACGAG-3' (forward) and 5'-TAGGAACACACCGACAGTCACAG-3' (reverse); *M-CC2-Cterm* (859–2187), 5'-ATGACCATTCATGGACTAGCG AG-3' (forward) and 5'-AACTTCTGCGGTCTGTGT-3' (reverse); *M-CC2* (859–1806), 5'-ATGACCATTCATGGACTAGCGAG-3' (forward) and 5'-TT TCTTATCAGCGGTCTGTCTC-3' (reverse); *CC2-Cterm* (1337–2187), 5'-ATGGGCGGTGTAGTTCCTAAGACTTCTG-3' (forward) and 5'-AACTT CTGCGGTCTGTGTG-3' (reverse); *CC2* (1337–1806), 5'-ATGGGCGGTGT AGTTCCTAAGACTTCTG-3' (forward) and 5'-TTTCTTATCAGCGGTCTCT GTCCTC-3' (reverse); *M* (859–1351), 5'-ATGACCATTCATGGACTAGC GAG-3' (forward) and 5'-TAGGAACACACCGACAGTCACAG-3' (reverse).

Full-length *Map7* (NM_008635) was made from the *Map7* fragments and was cloned into pEGFP-C1. *EMTB-Map7* was made by cloning the fragment consisting of base pairs 1–947 from full-length *Map7* into the pEGFP-C1 vector. *K-N-term*, *K-EMTB* and *K-EMTB-M* chimera constructs were made by cloning the K560 fragment from pET17b-K560–GFP (gift from R. Vale) into *N-Term*, *EMTB* and *EMTB-M Map7* pEGFP constructs, respectively. *Motor-Kif5b*, *S-Motorless-Kif5b* and *Motorless-Kif5b* c-Myc were a gift from G. Kreitzer. FL-Kif5b was made by cloning the K560 fragment with a C-terminal region of full-length Kif5b (gift from C. C. Hoogenraad) into pEGFP C1 construct. EGFP–KASH2 and EGFP–KASH2ext were a gift from D. Hodzic³⁵.

siRNA sequences (Ambion): *Map7*, 5'-CAGAUUAGAUGUACACCAUTT-3' (no. 118), 5'-CCAUGAAUUCUGAAACATT-3' (no. 119) and 5'-ACUUAUCUGUUGGAUCAAATT-3' (no. 120); *Map7D1*, 5'-GGAACAGAGGGAACG CGAATT-3' (no. 710), 5'-ACGUGGACUCUAUAAUCAAATT-3' (no. 711) and 5'-GCAAUCCAGCGGUCAGUAGATT-3' (no. 712); *Map7D2*, 5'-CUUUAAC AUCAACCAUGATT-3' (no. 436), 5'-CUUGAUGACUGUAAACAAATT-3' (no. 437) and 5'-GGUCUCCUGUGAAGUAUUAATT-3' (no. 438); *Map7D3*, 5'-GGACGACAUCUCUAAAGUUTT-3' (no. 000), 5'-GAACUAUCCUCCAU AGUGATT-3' (no. 001) and 5'-CUGAUGAGGUUGAUACCAATT-3' (no. 002); *Kif5b*, 5'-GCAAGAAGUAGACCGGAUATT-3' (no. 781), 5'-GCUGUAAU UAUGAUCAGATT-3' (no. 782) and 5'-GACAUGUCGAGUUAACAAATT-3' (no. 783).

Transfections. Myoblasts were transfected with siRNA using Lipofectamine RNAiMAX (Invitrogen) or DNA using Lipofectamine 2000 (Invitrogen). H1B–GFP stable cell line was made by transfecting cells with H1B–GFP (gift from R. Vallee).

qPCR. Messenger RNA from C2C12 cells was isolated with the RNeasy Micro Kit (Qiagen), and cDNA was prepared with the Transcriptor first-strand cDNA synthesis kit (Roche). Quantitative analyses (qPCR) were performed using CyberGreen kit in a LightCycler 480 II system (Roche), using the following primers: *Kif5b*-F, 5'-GGAGGCAAGCAGTCGTAAAC-3'; *Kif5b*-R, 5'-TCTAG

TGTTGGGAAGCAGCA-3'; *Map7*-F, 5'-TGAAACCAATTTTGGCCTTT-3'; *Map7*-R, 5'-AAAACAGAGGGAGGAGCTG-3'; *Hprt1*-F, 5'-GTTAAGCAG TACAGCCCCAAA-3'; *Hprt1*-R, 5'-AGGGCATATCCAACAACAACTT-3'.

Immunoprecipitations. C2C12 cells were transfected with GFP-tagged or c-Myc-tagged constructs. After 24 h, cell lysates were prepared using lysis buffer (10 mM Tris-HCl pH 7.4, 150 mM NaCl, 0.5 mM EDTA, 0.5% Nonidet P40, 1 mM phenylmethylsulphonyl fluoride) containing protease inhibitor cocktail (Roche) and 0.6 μM nocodazole (Sigma). Immunoprecipitation of GFP-fusion proteins or endogenous Kif5b was performed at 4 °C using the magnetic GFP-Trap kit (Chromotek) or Protein A magnetic beads (Millipore) coated with Khc antibody, respectively.

Western blot. Extracts were loaded on a 4–12% gradient gel (Invitrogen) and transferred using iBlot (Invitrogen).

Immunohistochemistry, immunofluorescence, microscopy, and image analysis. Embryos were collected at 25 °C on apple-juice agar plates and were fixed as described⁴ except for tubulin staining, for which the embryos were fixed in equal volumes of 10% formalin (Sigma) and heptane (Fisher Scientific). Larvae were dissected and fixed in 4% paraformaldehyde (Electron Microscopy Sciences) in relaxing buffer as described previously^{15,36,37}. Eye discs were dissected from wandering third-instar larvae and fixed in 4% paraformaldehyde. Ovaries from females that were fed on fresh yeast for 2 days were dissected in PBS and fixed in 4% paraformaldehyde. All fluorescent stainings were mounted in Prolong Gold (Molecular Probes); otherwise, embryos were mounted in Araldite.

Mouse cells were fixed using 3.7% paraformaldehyde (Sigma) and permeabilized with 0.5% Triton. All fluorescent stainings were mounted in Fluoromount G (Southern Biotech).

Antibodies were preabsorbed (PA) where noted, and used at the specified final dilutions: rabbit anti-dsRed (1:400; Clontech), rat anti-tropomyosin (1:1,000; Abcam), mouse anti-myosin heavy chain (1:400; gift from S. Abmayr), rabbit anti-Zasp (1:400; gift from F. Schöck), chicken anti-β-gal (1:1,000; Abcam), mouse anti-α-tubulin (1:500; Sigma), rat anti-ensconsin (1:100; gift from P. Rörth), guinea pig anti-Krüppel (PA; 1:2,000; gift from J. Reintz), rabbit anti-Eve (PA; 1:3,000; gift from M. Frasch), mouse anti-β-PS integrin (1:50; DSHB), rabbit anti-vestigial (PA; 1:50; gift from S. Carroll), fluorescein isothiocyanate-conjugated anti-horseshoe peroxidase (1:500; Jackson ImmunoResearch), mouse anti-discs large (1:200; DSHB), rabbit anti-ATP synthase²⁹ (1:100; gift from H. Duan), rat anti-DE-cadherin (1:100; DSHB), mouse anti-chaptin 24B10 (1:200; DSHB), rat anti-elav (1:50; DSHB), mouse anti-myosin heavy chain MF20 (1:500; DSHB), rabbit anti-KHC (1:2,500; Santa Cruz), mouse anti-c-Myc (1:5,000; Roche) and rabbit anti-GFP (1:2,500; Invitrogen). Biotinylated secondary antibodies (Vector Laboratories and Jackson ImmunoResearch) and the Vectastain ABC kit (Vector Laboratories) were applied for non-fluorescent stainings. Alexa Fluor 488-conjugated, Alexa Fluor 555-conjugated and Alexa Fluor 647-conjugated secondary antibodies, Alexa Fluor 546-conjugated and Alexa Fluor 647-conjugated phalloidin, Alexa Fluor 488-conjugated wheatgerm agglutinin (Invitrogen), and Hoechst 33342 or 4',6-diamidino-2-phenylindole were used for fluorescent staining (Invitrogen).

Fluorescent images of *Drosophila* were acquired on a Leica SP5 laser scanning confocal microscope running the LAS AF 2.2 software (objectives used: 20× 0.70 numerical aperture (NA) HC PL APO multi-immersion, 40× 1.25 NA, 63× 1.4 NA or 100× 1.43 NA HCX PL APO oil-immersion). Non-fluorescent images were acquired on a Zeiss Axiophot microscope. Image stacks were analysed and processed using Volocity (Improvision), ImageJ, and Photoshop CS4 (Adobe).

Fluorescent images of mouse cells were acquired with a Nikon Ti microscope equipped with a CoolSNAP HQ2 camera (Roper Scientific), an xy motorized stage (Nikon) and a 40× 1.0 NA PL APO oil-immersion objective, using Metamorph Software (Molecular Devices).

Quantification methods. Nuclear positioning was quantified in mammalian myotubes containing at least three nuclei, and myotubes were classified as follows: 'aligned', more than 70% of the nuclei in a myotube aligned along the same axis; 'aggregated', more than 70% of the nuclei did not align along the same axis; 'other', nuclei in a myotube did not fall into either category. Fusion index was quantified as described³⁰.

A nearest-neighbour analysis in *Drosophila* was conducted to determine the average distance between a nucleus and its single closest neighbour within a muscle. To identify the closest neighbour for each nucleus in a muscle, the distance between the centre of a nucleus and the centre of each of the closely surrounding nuclei (usually four to eight) was measured. The shortest distance identified the closest nucleus or 'nearest neighbour' and this distance was recorded. A nearest neighbour was identified for each nucleus in every muscle analysed and the nearest neighbour distances were averaged to give an average 'nearest-neighbour' distance for the average space between one nucleus and the next closest nucleus in a muscle.

Sarcomere length was defined as the distance between the Z-lines labelled with the anti-ZASP antibody¹⁵. Sarcomere length was measured at five separate regions per muscle and in the same five regions for each muscle examined.

Neuromuscular junctions were revealed by staining with horseradish peroxidase or Dlg, and quantified as previously described¹⁷.

The position of the oocyte nucleus was determined by measuring the distance from the anterior border of the oocyte to the centre of the nucleus.

Time-lapse imaging. *Drosophila* embryos were prepared as described^{4,38}. Time-lapse sequences were acquired using a Zeiss Axio Imager.Z1 with a 20× 0.75 NA Plan-Apochromat dry objective. All time-lapse series were taken as a set of z-stacks over time (four-dimensional imaging) with optical sections every 3 µm. Only a single z-section with the greatest number of nuclei in focus was selected for each time point. Images were processed with ImageJ and compiled into movie by using Apple Quicktime. Single images of live embryos were acquired on a Zeiss Axiophot microscope.

Time-lapse imaging of mouse cells was done as reported³⁰.

Yeast two-hybrid screen. Yeast two-hybrid screening was based on a full-length Ens as bait and performed by Hybrigenics S.A Services using a 0–24-h embryonic *Drosophila* cDNA library; 99 million interactions were analysed, and 10% of the high-confidence clones that were recovered from the screen were Khc.

Larval behaviour. Larval behaviour was assessed as described previously, with minor modifications^{14,39}. In brief, embryos (stages 16 and 17) were selected for the presence of clustered *apRed* nuclei and/or the absence of the fluorescent balancer. Selected embryos were placed on a yeast-coated apple-juice plate overnight at 25 °C, and L1 larvae were selected on the following day and placed into vials of standard food containing bromophenol blue. Larvae were picked from the vial 3 days later and tracked. Larvae were tracked individually as they migrated towards a single odour source (0.25 M ethyl butyrate; Sigma) and recorded for 5 min with a charge-coupled device camera until they reached the odour source or until they contacted any of the walls of the apparatus. Images were processed by Ethovision software (Noldus).

Germline transformation and constructs. *UAS-ensHA* DNA was constructed by PCR-amplifying the full-length cDNA from the *ens* RA transcript with primers to add a haemagglutinin tag to the C-terminal end of the protein followed by an *EcoRI* restriction site. Primers used were 5'-GCCGAATTCCACCATGGCGA GTCTTGGGGGC-3' (5') and 5'-GCCGAATTCTTATCAAGCGTAATCTGGA ACATCGTATGGGTACAGCAGCGATATATCTTTATTTTCGTG-3' (3'). Amplified cDNA was introduced into the Uni-ZAP XR vector (a derivative of pBlueScript SK[−]; Stratagene) using *EcoRI/XhoI*. This DNA was used by BestGene Inc. to generate transgenic flies.

Statistics. Statistical analysis was performed with Prism (GraphPad Software Inc.). Pairwise comparisons were made with Student's *t*-test, and group comparisons were made by analysis of variance followed by Tukey's posthoc analysis. In nuclear positioning analysis in C2C12 cells, Student's *t*-tests were performed between scrambled siRNA and experimental condition for each category (aligned, aggregated and other).

31. Halfon, M. S. *et al.* New fluorescent protein reporters for use with the *Drosophila* Gal4 expression system and for vital detection of balancer chromosomes. *Genesis* **34**, 135–138 (2002).
32. Lewis, E. *Method of Feeding Ethane Methylsulfonate (EMS) to Drosophila Males*. (Drosophila Information Service, 1968).
33. Parlakian, A. *et al.* Skeletal muscle phenotypically converts and selectively inhibits metastatic cells in mice. *PLoS ONE* **5**, e9299 (2010).
34. De Palma, C. *et al.* Nitric oxide inhibition of Drp1-mediated mitochondrial fission is critical for myogenic differentiation. *Cell Death Differ.* **17**, 1684–1696 (2010).
35. Khatau, S. B. *et al.* A perinuclear actin cap regulates nuclear shape. *Proc. Natl Acad. Sci. USA* **106**, 19017–19022 (2009).
36. Brent, J., Werner, K. & McCabe, B. *Drosophila* larval NMJ dissection. *J. Vis. Exp.* 10.3791/1107 (2009).
37. Brent, J., Werner, K. & McCabe, B. D. *Drosophila* larval NMJ immunohistochemistry. *J. Vis. Exp.* (25) e1108, doi:10.3791/1108 (2009).
38. Richardson, B. E., Beckett, K. & Baylies, M. K. Live imaging of *Drosophila* myoblast fusion. *Methods Mol. Biol.* **475**, 263–274 (2008).
39. Louis, M., Piccinotti, S. & Vosshall, L. B. High-resolution measurement of odor-driven behavior in *Drosophila* larvae. *J. Vis. Exp.* (11) e638, doi:10.3791/638 (2008).

Trans-synaptic Teneurin signalling in neuromuscular synapse organization and target choice

Timothy J. Mosca^{1*}, Weizhe Hong^{1*}, Vardhan S. Dani¹, Vincenzo Favaloro¹ & Liqun Luo¹

Synapse assembly requires trans-synaptic signals between the pre- and postsynapse¹, but our understanding of the essential organizational molecules involved in this process remains incomplete². Teneurin proteins are conserved, epidermal growth factor (EGF)-repeat-containing transmembrane proteins with large extracellular domains³. Here we show that two *Drosophila* Teneurins, Ten-m and Ten-a, are required for neuromuscular synapse organization and target selection. Ten-a is presynaptic whereas Ten-m is mostly postsynaptic; neuronal Ten-a and muscle Ten-m form a complex *in vivo*. Pre- or postsynaptic Teneurin perturbations cause severe synapse loss and impair many facets of organization trans-synaptically and cell autonomously. These include defects in active zone apposition, release sites, membrane and vesicle organization, and synaptic transmission. Moreover, the presynaptic microtubule and postsynaptic spectrin cytoskeletons are severely disrupted, suggesting a mechanism whereby Teneurins organize the cytoskeleton, which in turn affects other aspects of synapse development. Supporting this, Ten-m physically interacts with α -Spectrin. Genetic analyses of *teneurin* and *neuroligin* reveal that they have differential roles that synergize to promote synapse assembly. Finally, at elevated endogenous levels, Ten-m regulates target selection between specific motor neurons and muscles. Our study identifies the Teneurins as a key bi-directional trans-synaptic signal involved in general synapse organization, and demonstrates that proteins such as these can also regulate target selection.

Vertebrate teneurins are enriched in the developing brain^{4,5}, localize to synapses in culture⁶, and pattern visual connections⁷. Both *Drosophila* Teneurins, Ten-m and Ten-a, function in olfactory synaptic partner matching⁸ and were further identified in neuromuscular junction (NMJ) defect screens^{9,10}, with Ten-m also affecting motor axon guidance¹¹. We examine their roles and the underlying mechanisms involved in synapse development.

Both Ten-m and Ten-a were enriched at the larval NMJ (Fig. 1a and Supplementary Fig. 1a). Ten-a was detected at neuronal membranes; this staining was undetectable beyond background in *ten-a* null mutants (Supplementary Fig. 1b) and barely detectable after neuronal *ten-a* RNA interference (RNAi; Supplementary Fig. 1c), indicating that Ten-a is predominantly presynaptic. Partial co-localization was observed between Ten-a and the periaxial zone marker Fasciclin 2 (ref. 12) as well as the active zone marker Bruchpilot¹³ (Fig. 1b, c), suggesting that Ten-a is localized to the junction between the periaxial zone and the active zone. Ten-m appeared strongly postsynaptic and surrounded each bouton (Fig. 1a and Supplementary Fig. 1a, d). Muscle-specific *ten-m* RNAi eliminated the postsynaptic staining, but uncovered weak presynaptic staining (Supplementary Fig. 1e) that ubiquitous *ten-m* RNAi eliminated (Supplementary Fig. 1f). Thus, the Ten-m signal was specific and, although partly presynaptic, enriched postsynaptically. Consistently, muscle Ten-m colocalized extensively with Dlg (Fig. 1d) and completely with α -Spectrin (Fig. 1e) and is thus probably coincident with all postsynaptic membranes.

The localization of Ten-a and Ten-m suggested their trans-synaptic interaction. To examine this, we co-expressed Myc-tagged Ten-a in nerves using the Q system¹⁴ and haemagglutinin (HA)-tagged Ten-m in muscles using GAL4. Muscle Ten-m was able to co-immunoprecipitate nerve Ten-a from larval synaptosomes (Fig. 1f), suggesting that the Teneurins form a heterophilic trans-synaptic receptor pair at the NMJ.

To determine Teneurin function at the NMJ, we examined the *ten-a* null allele and larvae with neuron or muscle RNAi of *ten-a* and/or *ten-m*. Following such perturbations, bouton number and size were altered: the quantity was reduced by 55% (Fig. 2a–c, g and Supplementary Fig. 2)

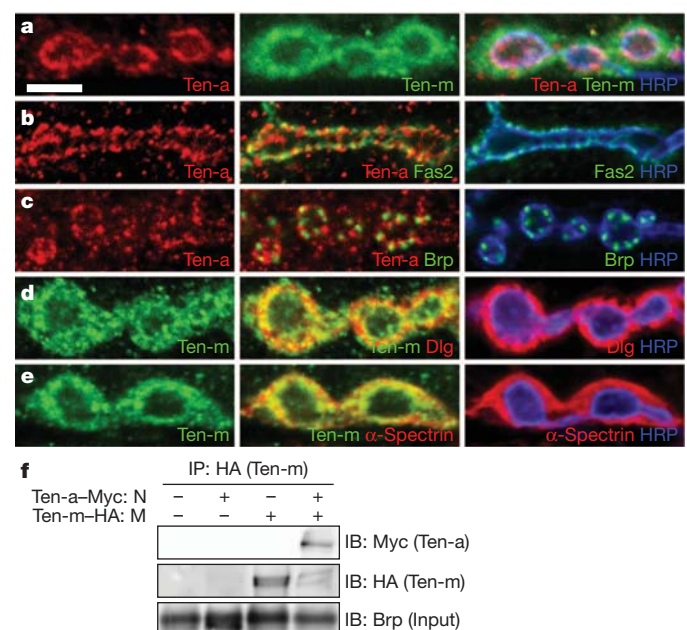


Figure 1 | Teneurins are enriched at and interact across *Drosophila* neuromuscular synapses. a–e, Representative single confocal sections of synaptic boutons stained with antibodies against Ten-a (red) or Ten-m (green), horseradish peroxidase (HRP) to mark the neuronal membrane (blue), and a synaptic marker as indicated. a, Ten-a is associated with presynaptic membranes and Ten-m largely with the surrounding postsynapse (a). b, c, Ten-a shows limited co-localization with the periaxial zone marker Fasciclin 2 (b), and Bruchpilot (Brp), an active zone marker (c). d, e, Ten-m co-localizes with, and extends beyond, Dlg (d) and completely co-localizes with muscle α -Spectrin (e). f, Immunoblots (IB) of larval synaptosomes expressing neuronal Flag-Myc-tagged Ten-a (N) and muscle Flag-HA-tagged Ten-m (M) and immunoprecipitated (IP) using antibodies to HA. Ten-a is detected in the pull-down, indicating that nerve Ten-a and muscle Ten-m interact across the NMJ. This is not seen in control lanes. Owing to low expression, neither transgene product is detectable in input lysates, which are enriched in Brp. Scale bar, 5 μ m.

¹Department of Biology, Howard Hughes Medical Institute, Stanford University, Stanford, California 94305, USA.

*These authors contributed equally to this work.

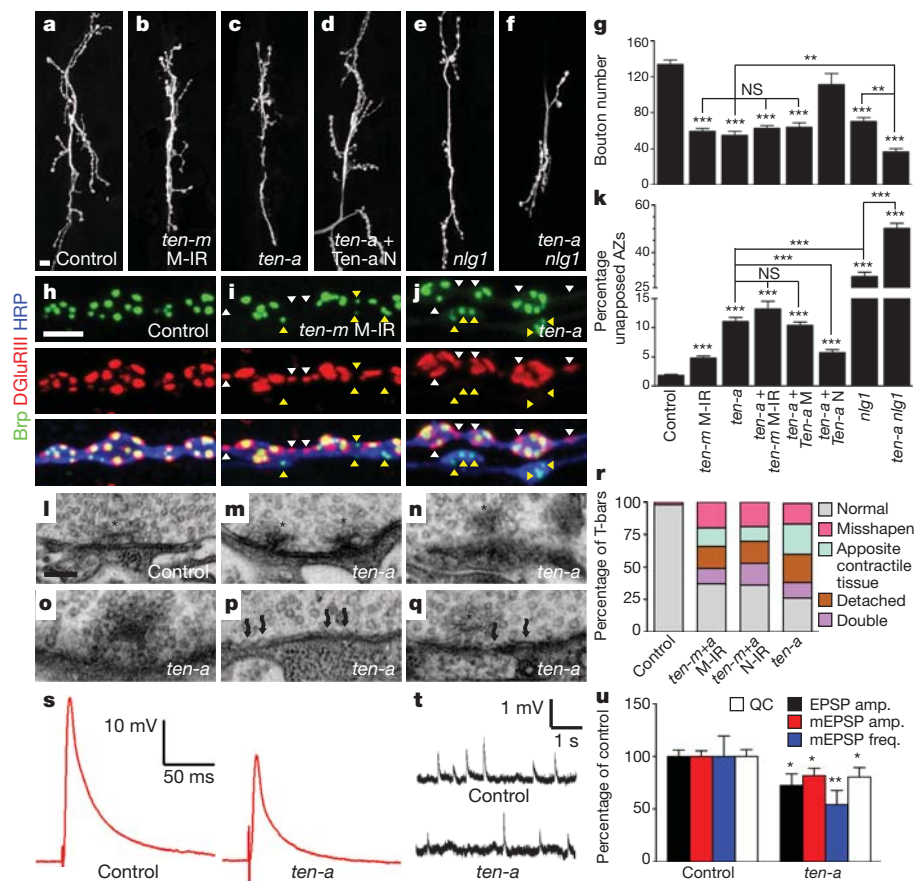


Figure 2 | Teneurins affect the structure and function of the neuromuscular synapse. **a–f**, Representative NMJs stained with antibodies to HRP. Muscle-specific *ten-m* RNAi (M-IR) and lots of *ten-a* decrease bouton number. Neuronal (Ten-a N) but not muscle (Ten-a M) restoration of *ten-a* expression rescues this phenotype. These defects resemble *nlg1* mutants and are enhanced in *ten-a nlg1* double mutants. **g**, Quantification of bouton number. **h–j**, Representative NMJs stained with antibodies to Brp (green), the glutamate receptor subunit DGluRIII (red) and HRP (blue). In control larvae (**h**), Brp and DGluRIII puncta properly appose. *teneurin* perturbations (**i**, **j**) disrupt this active zone (yellow arrowhead) and glutamate receptor apposition (white arrowhead). **k**, Quantification of unapposed active zone/glutamate receptor pairs. For each quantification, $n \geq 8$ larvae, 16 NMJs. **l–q**, Transmission electron microscopy of active zone T-bars (asterisks) in control larvae (**l**) and

ten-a mutants (**m–q**) showing double T-bars (**m**), detached T-bars (**n**), misshapen T-bars (**o**), membrane ruffling (**p**, wavy arrows) and T-bars facing contractile tissue (**q**). Some images show multiple defects. **r**, Distribution of T-bar defects as a percentage of the total T-bars. N-IR, neuronal RNAi. For each genotype, $n \geq 3$ larvae, 40 boutons. **s**, **t**, Representative evoked EPSP (**s**) and mEPSP (**t**) traces from control and *ten-a* mutant genotypes. **u**, Quantification of mean EPSP amplitude (black), mEPSP amplitude (red), mEPSP frequency (blue) and quantal content (QC, white) expressed as a percentage of the control average. For all genotypes, $n \geq 7$ larvae, 8 muscles. Error bars represent s.e.m. Scale bars, 10 μ m (**a–f**), 5 μ m (**h–j**), 100 nm (**l–q**). *** $P < 0.001$, ** $P < 0.01$, * $P < 0.05$, NS, not significant. Statistical comparisons are with control unless noted.

and the incidence of large boutons markedly increased (Supplementary Fig. 2k). Both changes indicate impaired synaptic morphogenesis. The reduction in bouton number was probably cumulative through development, as it was visible in first instar *ten-a* mutants and persisted (Supplementary Fig. 2k). In the *ten-a* mutant, bouton morphogenesis was rescued by restoring Ten-a expression in neurons, but not muscles (Fig. 2d, g and Supplementary Fig. 2). Neuronal Ten-m overexpression could not substitute for the lack of Ten-a, revealing their non-equivalence (Supplementary Fig. 2e, l). Neuronal knockdown of Ten-a or Ten-m resulted in fewer synaptic boutons (Supplementary Fig. 2f–h, l), indicating that both have a presynaptic function, although presynaptic Ten-a has a more predominant role (Supplementary Fig. 2l). Moreover, knocking down postsynaptic Ten-m in the *ten-a* mutant did not enhance the phenotype (Fig. 2g). Thus, presynaptic Ten-a (and, to a lesser extent, Ten-m) and postsynaptic Ten-m are required for synapse development.

teneurin perturbation also caused defects in the apposition between presynaptic active zones (release sites) and postsynaptic glutamate receptor clusters¹⁵ (Fig. 2h and Supplementary Fig. 3): up to 15% of the active zones/receptor clusters lacked their partner compared to 1.8% in controls (Fig. 2h–k). Under electron microscopy, active zones

are marked by electron-dense membranes and single presynaptic specializations called T-bars (Fig. 2l), which enable synapse assembly, vesicle release and Ca^{2+} -channel clustering¹⁶. Teneurin disruption caused defects (Fig. 2m–r and Supplementary Fig. 3) in T-bar ultrastructure (Fig. 2m–o), membrane organization, and apposition to contractile tissue (Fig. 2p, q). Teneurin perturbation also impaired postsynaptic densities while increasing membrane ruffling (Supplementary Table 1), further indicating organizational deficiency. These phenotypes resemble mutants with adhesion and T-bar biogenesis defects^{17,18}, suggesting a role for Teneurins in synaptic adhesion and stability. Synaptic vesicle populations similarly required Teneurins for clustering at the bouton perimeter and proper density (Supplementary Fig. 4). As these effects are not synonymous with active zone disruption¹⁹, Teneurins are also required for synaptic vesicle organization.

Synapses lacking *teneurin* were also functionally impaired. The mean amplitude of evoked excitatory postsynaptic potentials (EPSPs) in larvae was decreased by 28% in the *ten-a* mutant (Fig. 2s, u). Spontaneous miniature EPSPs showed a 20% decrease in amplitude, a 46% decrease in frequency (Fig. 2t, u), and an altered amplitude distribution compared with control (Supplementary Fig. 5a). These defects resulted in a 20% reduction in quantal content (Fig. 2u), which could be partly due to

fewer boutons and release sites. However, release probability may also be reduced, as suggested by an increased paired pulse ratio in *ten-a* mutants (Supplementary Fig. 5d, e). The decay kinetics of responses were faster in *ten-a* mutants, suggesting additional postsynaptic effects on glutamate receptors and/or intrinsic membrane properties (Supplementary Fig. 5b, c). Further, FM1-43 dye loading revealed markedly defective vesicle cycling in *ten-a* mutants (Supplementary Fig. 5f, h). Consistent with physiological impairment, *teneurin*-perturbed larvae exhibited profound locomotor defects (Supplementary Fig. 5i). In summary, Teneurins are required for multiple aspects of NMJ organization and function.

As a potential mechanism for synaptic disorganization following *teneurin* perturbation, we examined the pre- and postsynaptic cytoskeletons. In the presynaptic terminal, organized microtubules contain Futsch (a microtubule-binding protein)-positive 'loops', whereas disorganized microtubules possess punctate, 'unbundled' Futsch²⁰. Each classification normally represented ~10% (often distal) of boutons (Fig. 3a, d and Supplementary Fig. 6). Upon *teneurin* perturbation, many more boutons had unbundled Futsch (Fig. 3b, c and Supplementary Fig. 6) whereas those with looped microtubules were decreased by 62–95% (Fig. 3d). Therefore, proper microtubule organization requires pre- and postsynaptic Teneurins. In contrast to mild active zone/glutamate receptor apposition defects, most boutons displayed microtubule organizational defects.

teneurin perturbation also severely disrupted the postsynaptic spectrin cytoskeleton, with which Ten-m colocalized (Fig. 1e). Postsynaptic α -Spectrin normally surrounds the bouton (Fig. 3e). Perturbing neuronal or muscle Teneurins markedly reduced postsynaptic α -Spectrin without affecting Dlg (Fig. 3f–h and Supplementary Fig. 7). Postsynaptic β -Spectrin²¹, Adducin²² and Wsp were similarly affected (Supplementary Fig. 8). In muscle, α -Spectrin is coincident with and essential for the integrity of the membranous subsynaptic reticulum (SSR)^{21,23}. Consistent with this, *teneurin* disruption reduced SSR width up to 70% (Supplementary Fig. 9d–g) and increased the frequency of 'ghost' boutons, which are failures of postsynaptic membrane organization²³

(Supplementary Fig. 9a–d). Thus, Teneurins are involved in the organization of the pre- and postsynaptic cytoskeletons and postsynaptic membranes. Further, endogenous α -Spectrin co-immunoprecipitated with muscle-expressed, Flag-tagged Ten-m (Fig. 3i), suggesting that Ten-m physically links the synaptic membrane to the cytoskeleton.

Because the most severe defects following *teneurin* perturbation were cytoskeletal, we propose that Teneurins primarily organize the presynaptic microtubule and postsynaptic spectrin-based cytoskeletons (Fig. 3j), which then organize additional synaptic aspects^{20,21}. However, such a solitary role cannot fully explain the observed phenotypes. The reduction in bouton number associated with cytoskeletal disruption is milder than that following *teneurin* disruption^{20,21,24}. Also, although active zone dynamics are affected by cytoskeletal perturbation²¹, defects in apposition are not^{21,25}. Moreover, the T-bar structural defects more closely resemble synapse adhesion and active zone formation defects^{17,18}. Thus, Teneurins may regulate release site organization and synaptic adhesion independent of the cytoskeleton (Fig. 3j).

Our data also indicate that Teneurins act bi-directionally across the synaptic cleft. Ten-a acts predominantly in neurons, as evidenced by localization, phenotypes caused by neuronal (but not muscle) knock-down, and mutant rescue by neuronal (but not muscle) expression (Figs 2 and 3 and Supplementary Figs 2–4, 6, 7 and 9). Yet, in addition to the presynaptic phenotypes, many others were postsynaptic, including reduced muscle spectrin, SSR, and membrane apposition (Fig. 3 and Supplementary Figs 7–9). Similarly, although Ten-m is present both pre- and postsynaptically, muscle knockdown resulted in pre-synaptic defects, including microtubule and vesicle disorganization, reduced active zone apposition, and T-bar defects (Figs 2 and 3 and Supplementary Figs 3, 4, 6 and 7). Thus, Teneurins function in bi-directional trans-synaptic signalling to organize neuromuscular synapses. This may involve downstream pathways or simply establish an organizational framework by the receptors themselves. Moreover, as the results of single disruptions of neuronal *ten-a* or muscle *ten-m* were similarly severe and not enhanced by combination (Figs 2g and 3d, h and Supplementary Fig. 2k), both Ten-a and Ten-m probably

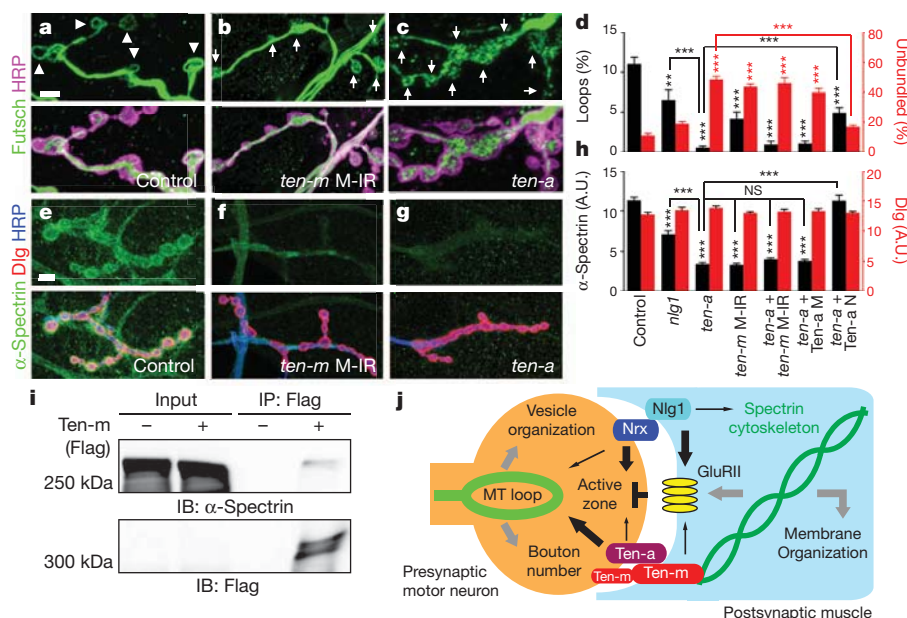


Figure 3 | Teneurin perturbation results in marked cytoskeletal disorganization. **a–c**, Representative NMJs stained with antibodies to Futsch (green) and HRP (magenta). Arrowheads indicate looped organization. Arrows indicate unbundled Futsch. **d**, Quantification of the percentage of total boutons with looped or unbundled microtubules. **e–g**, Representative NMJs stained with antibodies to α -Spectrin (green), Dlg (red) and HRP (blue). Following *teneurin* perturbation, α -Spectrin staining is largely lost. Axonal α -Spectrin is unaffected by muscle *teneurin* RNAi (**f**). **h**, Quantification of α -Spectrin (green)

and Dlg (red) fluorescence. A.U., arbitrary units. For all genotypes, $n \geq 6$ larvae, 12 NMJs. **i**, Immunoblots (IB) showing that α -Spectrin is detected in the Flag immunoprecipitates (IP) of larvae expressing muscle Flag-HA-tagged Ten-m but not in control larvae. Owing to low expression, Flag-HA-Ten-m is only detectable after enrichment by immunoprecipitation. **j**, Model showing the roles of Teneurins, Neurexin and Neuroigin at the NMJ. Arrow size represents the relative contribution of each pathway to the cellular process as inferred from mutant phenotypic severity. Scale bars, 5 μ m. *** $P < 0.001$, NS, not significant.

function in the same pathway. Our finding that Ten-a and Ten-m co-immunoprecipitate from different cells *in vitro*⁸ and across the NMJ *in vivo* (Fig. 1f) further suggests a signal via a trans-synaptic complex. Teneurin function, however, may not be solely trans-synaptic. In some cases (vesicle density, SSR width), cell-autonomous knockdown resulted in stronger phenotypes than knocking down in synaptic partners (Supplementary Figs 3, 4, 9 and Supplementary Table 1). This suggests additional cell-autonomous roles in addition to trans-synaptic Teneurin signalling.

Signalling involving the transmembrane proteins Neurexin and Neuroligin also mediates synapse development²⁶. In *Drosophila*, Neurexin (*nrx*) and Neuroligin 1 (*nlg1*) mutations cause phenotypes similar to *teneurin* perturbation: reductions in bouton number, active zone organization, transmission, and SSR width^{27,28}. *nlg1* and *nrx* mutations do not enhance each other, suggesting that they function in the same pathway²⁸. Consistently^{27,28}, we found that *nrx* and *nlg1* mutants exhibited largely similar phenotypes (data not shown). To investigate the relationship between the *teneurin* genes and *nrx* and *nlg1*, we focused on the *nlg1* null mutant. Both Nlg1 tagged with enhanced green fluorescent protein (Nlg1-eGFP) and endogenous Ten-m occupied a similar postsynaptic space (Supplementary Fig. 10a). *teneurin* and *nlg1* loss-of-function mutations also displayed similar bouton number reductions (Fig. 2e, g), vesicle disorganization (Supplementary Fig. 4), and ghost bouton frequencies (Supplementary Fig. 9). Other phenotypes showed notable differences in severity. In *nlg1* mutants, there was a 29% failure of active zone/glutamate receptor apposition (Fig. 2k and Supplementary Fig. 10d), compared to 15% for the strongest *teneurin* perturbation. The cytoskeleton of *nlg1* mutants, however, was only mildly impaired compared to that seen with *teneurin* perturbations (Fig. 3d, h and Supplementary Figs 6 and 7).

To examine further the interplay of *teneurin* and *nlg1*, we analysed *ten-a nlg1* double mutants. Both single mutants were viable, despite their synaptic defects. Double mutants, however, were larval lethal. We obtained rare escapers, which showed a 72% reduction in boutons, compared to a 50–55% decrease in single mutants (Fig. 2e). Active zone apposition in double mutants was enhanced synergistically over either single mutant (Fig. 2k and Supplementary Fig. 10e). Cytoskeletal defects in the double mutant resembled the *ten-a* mutant (Fig. 3 and Supplementary Figs 6 and 7). These data suggest that *teneurin* genes and *nrx* and *nlg1* act in partially overlapping pathways, cooperating to organize synapses properly, with Teneurins contributing more to cytoskeletal organization and Neurexin and Neuroligin to active zone apposition (Fig. 3j).

In the accompanying manuscript⁸, we showed that although the basal Teneurins are broadly expressed in the *Drosophila* antennal lobe, elevated expression in select glomeruli mediates olfactory neuron partner matching. At the NMJ, this basal level mediates synapse organization. Analogous to the antennal lobe, we found elevated *ten-m* expression at muscles 3 and 8 using the *ten-m-GAL4* enhancer trap (Fig. 4a). We confirmed this for endogenous *ten-m*, and determined that it was contributed by elevated Ten-m expression in both nerves and muscles (Fig. 4b–g). Indeed, *ten-m-GAL4* was highly expressed in select motor neurons, including MN3-Ib, which innervates muscle 3 (ref. 29; Supplementary Fig. 11c). This elevated larval expression also varied along the anterior–posterior axis (Supplementary Fig. 12), and was specific for Ten-m, as Ten-a expression did not differ within or between segments (data not shown).

To test whether elevated Ten-m expression in muscle 3 and MN3-Ib affects neuromuscular connectivity, we expressed *ten-m* RNAi using *ten-m-GAL4*. Wild-type muscle 3 was almost always innervated (Fig. 4h). However, after *ten-m* knockdown, muscle 3 innervation failed in 11% of hemisegments (Fig. 4i, j). This required Ten-m on both sides of the synapse, as the targeting phenotype persisted following neuronal or muscle RNAi suppression using tissue-specific *GAL80* transgenes (Fig. 4j). *ten-a* RNAi did not show this phenotype (Fig. 4j), consistent with homophilic target selection via Ten-m. The phenotype

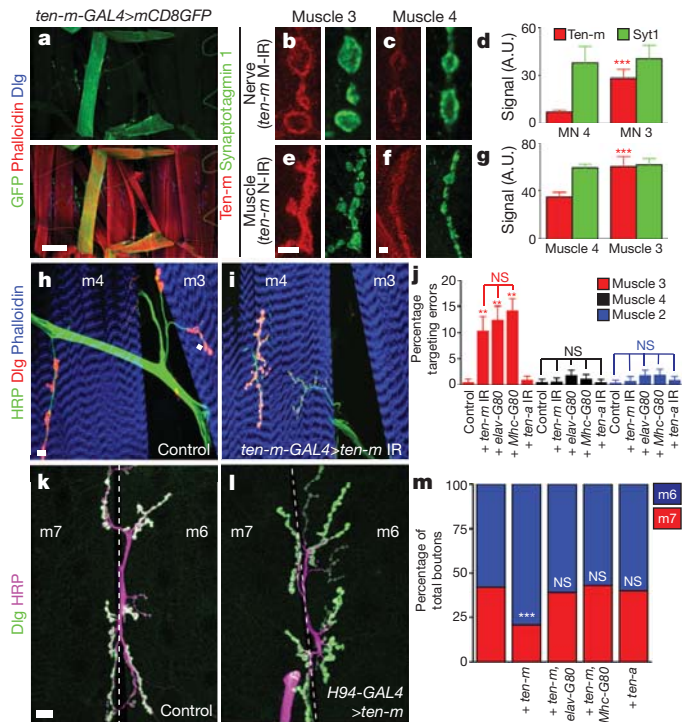


Figure 4 | High-level Ten-m expression regulates muscle target selection. **a**, Representative images of hemisegment A3 stained with antibodies to Dlg (blue), phalloidin (red), and expressing GFP via *ten-m-GAL4* (green). High-level expression is observed in muscles 3 and 8 and basally in all muscles. **b, c**, Muscle 3 (**b**) and 4 (**c**) NMJs show differential Ten-m (red) but similar Synaptotagmin 1 (Syt1; green) expression (from a *ten-m* muscle knockdown animal). **d**, Quantification of presynaptic Ten-m (red) and Syt1 (green) fluorescence at muscle 3 and 4 NMJs. MN, motor neuron. **e, f**, NMJs at muscles 3 (**e**) and 4 (**f**) show differential Ten-m (red) but similar Syt1 (green) expression in muscles (from a *ten-m* nerve knockdown). **g**, Quantification of postsynaptic Ten-m (red) and Syt1 (green) fluorescence at muscle 3 and 4 NMJs. **h, i**, Representative images stained with phalloidin (blue) and antibodies to HRP (green) and Dlg (red) to visualize motor neurons and muscles in control (**h**) or *ten-m-GAL4>ten-m* RNAi larvae (**i**). **m**, muscle. **j**, Quantification of the hemisegment percentage with failed muscle 3 (red), 4 (black) or 2 (blue) innervation. IR, interfering RNA. **k, l**, Representative images of the muscle 6/7 NMJ labelled with antibodies to Dlg (green) and HRP (magenta). The characteristic wild-type arrangement of boutons (**k**) is shifted towards muscle 6 when Ten-m is overexpressed in that muscle and the innervating motor neurons (**l**). **m**, Quantification of the total bouton percentage on muscles 6 (blue) and 7 (red). All genotypes contain *H94-GAL4*, additional transgenes are indicated (for details, see Methods). The Ten-m-mediated shift is abolished by neuronal or muscle *GAL80* transgenes. Scale bars, 100 μ m (**a**), 5 μ m (**b–i**), 10 μ m (**k, l**). In all cases, $n \geq 12$ larvae. *** $P < 0.001$, ** $P < 0.01$, NS, not significant.

was specific to muscle 3, as innervation onto the immediately proximal or distal muscle was unchanged (Fig. 4j). The low penetrance is probably due to redundant target selection mechanisms³⁰. Where innervation did occur, the terminal displayed similarly severe phenotypes to other NMJs (not shown). Thus, in addition to generally mediating synaptic organization, Ten-m also contributes to correct target selection at a specific NMJ.

To determine whether Ten-m overexpression could alter connectivity, we expressed Ten-m in muscle 6 (but not the adjacent muscle 7), and the motor neurons innervating both muscles using *H94-GAL4*. Normally, 60% of the boutons at muscles 6/7 are present on muscle 6 with 40% on muscle 7 (Fig. 4k, m). Ten-m overexpression caused a shift whereby 81% of boutons synapsed onto muscle 6 and only 19% onto muscle 7 (Fig. 4l, m). This shift also required both neuronal and muscle Ten-m, as neuronal or muscle *GAL80* abrogated it (Fig. 4m). The effect was specific because Ten-a overexpression did not alter this synaptic balance (Fig. 4m), nor was it secondary to altered bouton

number, which was unchanged (data not shown). Therefore, elevated Ten-m on both sides of the NMJ can bias target choice. This, combined with evidence that Ten-m can mediate homophilic interaction *in vitro*⁸, supports a trans-synaptic homophilic attraction model at the NMJ as in the olfactory system.

We identified a two-tier mechanism for Teneurin function in synapse development at the *Drosophila* NMJ. At the basal level, Teneurins are expressed at all synapses and engage in hetero- and homophilic bi-directional trans-synaptic signalling to organize synapses properly (Fig. 3j). Supporting this, Teneurins can mediate homo- and heterophilic interactions *in vitro*⁸ and heterophilic interactions *in vivo* (Fig. 1f). At the synapse, Teneurins organize the cytoskeleton, interact with α -Spectrin, and enable proper adhesion and release site formation. Further, elevated Ten-m expression regulates target selection in specific motor neurons and muscles via homophilic matching and functions with additional molecules³⁰ to mediate precise neuromuscular connectivity. Teneurin-mediated target selection at the NMJ is analogous to its role in olfactory synaptic partner matching⁸. As Teneurins are expressed broadly throughout the antennal lobe, it remains an attractive possibility that they also regulate synapse organization in the central nervous system.

METHODS SUMMARY

Details of *Drosophila* stocks, immunostaining, electron microscopy, functional assays, construction of epitope-tagged Teneurin constructs, immunoprecipitation, imaging and statistical analysis can be found in Methods.

Full Methods and any associated references are available in the online version of the paper at www.nature.com/nature.

Received 14 June 2011; accepted 7 February 2012.

Published online 18 March 2012.

- Williams, M. E., de Wit, J. & Ghosh, A. Molecular mechanisms of synaptic specificity in developing neural circuits. *Neuron* **68**, 9–18 (2010).
- Giagtzoglou, N., Ly, C. V. & Bellen, H. J. Cell adhesion, the backbone of the synapse: “vertebrate” and “invertebrate” perspectives. *Cold Spring Harb. Perspect. Biol.* **1**, a003079 (2009).
- Young, T. R. & Leamey, C. A. Teneurins: important regulators of neural circuitry. *Int. J. Biochem. Cell Biol.* **41**, 990–993 (2009).
- Kenzelmann, D., Chiquet-Ehrismann, R., Leachman, N. T. & Tucker, R. P. Teneurin-1 is expressed in interconnected regions of the developing brain and is processed *in vivo*. *BMC Dev. Biol.* **8**, 30 (2008).
- Li, H., Bishop, K. M. & O’Leary, D. D. Potential target genes of EMX2 include *Odz/Ten-M* and other gene families with implications for cortical patterning. *Mol. Cell. Neurosci.* **33**, 136–149 (2006).
- Silva, J. P. *et al.* Latrophilin 1 and its endogenous ligand Lasso/teneurin-2 form a high-affinity transsynaptic receptor pair with signaling capabilities. *Proc. Natl Acad. Sci. USA* **108**, 12113–12118 (2011).
- Leamey, C. A. *et al.* Ten-m3 regulates eye-specific patterning in the mammalian visual pathway and is required for binocular vision. *PLoS Biol.* **5**, e241 (2007) CrossRef.
- Hong, W., Mosca, T. J. & Luo, L. Teneurins instruct synaptic partner matching in an olfactory map. *Nature* <http://dx.doi.org/10.1038/nature10926> (this issue).
- Liebl, F. L. *et al.* Genome-wide P-element screen for *Drosophila* synaptogenesis mutants. *J. Neurobiol.* **66**, 332–347 (2006).
- Kurusu, M. *et al.* A screen of cell-surface molecules identifies leucine-rich repeat proteins as key mediators of synaptic target selection. *Neuron* **59**, 972–985 (2008).
- Zheng, L. *et al.* *Drosophila* Ten-m and Filamin affect motor neuron growth cone guidance. *PLoS ONE* **6**, e22956 (2011).
- Sone, M. *et al.* Synaptic development is controlled in the periaxial zones of *Drosophila* synapses. *Development* **127**, 4157–4168 (2000).
- Wagh, D. A. *et al.* Bruchpilot, a protein with homology to ELKS/CAST, is required for structural integrity and function of synaptic active zones in *Drosophila*. *Neuron* **49**, 833–844 (2006).
- Potter, C. J., Tasic, B., Russler, E. V., Liang, L. & Luo, L. The Q system: a repressible binary system for transgene expression, lineage tracing, and mosaic analysis. *Cell* **141**, 536–548 (2010).
- Marrus, S. B., Portman, S. L., Allen, M. J., Moffat, K. G. & DiAntonio, A. Differential localization of glutamate receptor subunits at the *Drosophila* neuromuscular junction. *J. Neurosci.* **24**, 1406–1415 (2004).
- Wichmann, C. & Sigrist, S. J. The active zone T-bar—a plasticity module? *J. Neurogenet.* **24**, 133–145 (2010).
- Aberle, H. *et al.* *wishful thinking* encodes a BMP type II receptor that regulates synaptic growth in *Drosophila*. *Neuron* **33**, 545–558 (2002).
- Owald, D. *et al.* A Syd-1 homologue regulates pre- and postsynaptic maturation in *Drosophila*. *J. Cell Biol.* **188**, 565–579 (2010).
- Kittel, R. J. *et al.* Bruchpilot promotes active zone assembly, Ca²⁺ channel clustering, and vesicle release. *Science* **312**, 1051–1054 (2006).
- Roos, J., Hummel, T., Ng, N., Klambt, C. & Davis, G. W. *Drosophila* Futsch regulates synaptic microtubule organization and is necessary for synaptic growth. *Neuron* **26**, 371–382 (2000).
- Pielage, J., Fetter, R. D. & Davis, G. W. A postsynaptic spectrin scaffold defines active zone size, spacing, and efficacy at the *Drosophila* neuromuscular junction. *J. Cell Biol.* **175**, 491–503 (2006).
- Pielage, J., Bulat, V., Zuchero, J. B., Fetter, R. D. & Davis, G. W. Hts/Adducin controls synaptic elaboration and elimination. *Neuron* **69**, 1114–1131 (2011).
- Mosca, T. J. & Schwarz, T. L. The nuclear import of Frizzled2-C by Importins- β 1 and α 2 promotes postsynaptic development. *Nature Neurosci.* **13**, 935–943 (2010).
- Featherstone, D. E., Davis, W. S., Dubreuil, R. R. & Broadie, K. *Drosophila* α - and β -spectrin mutations disrupt presynaptic neurotransmitter release. *J. Neurosci.* **21**, 4215–4224 (2001).
- Miech, C., Pauer, H. U., He, X. & Schwarz, T. L. Presynaptic local signaling by a canonical wingless pathway regulates development of the *Drosophila* neuromuscular junction. *J. Neurosci.* **28**, 10875–10884 (2008).
- Craig, A. M. & Kang, Y. Neurexin-neuroigin signaling in synapse development. *Curr. Opin. Neurobiol.* **17**, 43–52 (2007).
- Li, J., Ashley, J., Budnik, V. & Bhat, M. A. Crucial role of *Drosophila* Neurexin in proper active zone apposition to postsynaptic densities, synaptic growth, and synaptic transmission. *Neuron* **55**, 741–755 (2007).
- Banovic, D. *et al.* *Drosophila* Neuroigin 1 promotes growth and postsynaptic differentiation at glutamatergic neuromuscular junctions. *Neuron* **66**, 724–738 (2010).
- Landgraf, M., Roy, S., Prokop, A., VijayRaghavan, K. & Bate, M. *even-skipped* determines the dorsal growth of motor axons in *Drosophila*. *Neuron* **22**, 43–52 (1999).
- Sanes, J. R. & Yamagata, M. Many paths to synaptic specificity. *Annu. Rev. Cell Dev. Biol.* **25**, 161–195 (2009).

Supplementary Information is linked to the online version of the paper at www.nature.com/nature.

Acknowledgements We thank H. Aberle, V. Budnik, A. DiAntonio, R. Dubreuil, D. Featherstone, N. Reist, T. Schwarz, S. Stowers, D. Van Vactor, R. Wides, the Bloomington Stock Center and the Developmental Studies Hybridoma Bank for fly stocks, antibodies and reagents; J. Perrino and D. Luginbuhl for technical assistance; K. Shen, K. Zinn, D. Banovic, D. Berns, Y. Chou, C. A. Frank, X. Gao, S. Hippenmeyer, K. Miyamichi, K. Sillar, B. Tasic, X. Yu and S. Zosimus for critiques. Supported by a National Institutes of Health (NIH) grant (R01 DC-005982 to L.L.), and Epilepsy, Neonatology and Developmental Biology Training Grants (NIH 5T32 NS007280 and HD007249 to T.J.M.). L.L. is an investigator of the Howard Hughes Medical Institute.

Author Contributions T.J.M. designed and performed all experiments (apart from electrophysiology). W.H. characterized and provided new reagents, and assisted in some experiments. V.S.D. and T.J.M. designed and V.S.D. performed electrophysiology experiments with assistance from T.J.M. V.F. provided new reagents. L.L. supervised the project. T.J.M. wrote the manuscript with feedback from all authors.

Author Information Reprints and permissions information is available at www.nature.com/reprints. The authors declare no competing financial interests. Readers are welcome to comment on the online version of this article at www.nature.com/nature. Correspondence and requests for materials should be addressed to T.J.M. (tmosca@stanford.edu).

METHODS

Drosophila stocks. All *Drosophila* strains and controls were raised at 29 °C to maximize GAL4 expression. All mutants and transgenes were maintained over GFP balancer chromosomes to enable larval selection. *Mhc-GAL4* or *Mef2-GAL4* (ref. 31) was used to drive expression in all somatic muscles. *Nrv2-GAL4* (ref. 32) and *elav-GAL4* (ref. 33) were used to drive expression in all neurons. *H94-GAL4* was used to drive expression in muscles 6, 13 and 4 and their corresponding motor neurons³⁴. *daughterless-GAL4* was used to drive expression ubiquitously³⁵. *Synj-QF*³⁶ was used to drive expression in all nerves. *NP6658-GAL4* (*ten-m-GAL4*) was used to drive expression in the pattern of endogenous *Ten-m* expression⁸. The *Df(X)ten-a* deletion was used as a *ten-a* null mutant⁸. For *nlg1* mutants, the 1960 and ex2.3 alleles were used in *trans*²⁸ and double mutant larvae with *ten-a* and *nlg1* mutations were obtained using optimized rearing conditions³⁷. Because of the early lethality of the *ten-m* mutant¹¹, and to assess independently *ten-a*, tissue-specific RNAi was used to examine *teneurin* perturbation using the following RNAi transgenic strains: for *ten-m*, *UAS-ten-m*^{RNAi-V51173} and for *ten-a* (ref. 8), *UAS-ten-a*^{RNAi-V32482}. The following transgenic strains were used: *UAS-Dcr2* (ref. 38), *UAS-Fas2* (ref. 34), *UAS-mCD8GFP* (ref. 39), *UAS-Nlg1-eGFP* (ref. 28), *UAS-Ten-a* (ref. 8), *P[GS]9267* for *ten-m* overexpression⁸. In all cases, the efficacy of RNAi transgenes, overexpression transgenes and the *ten-a* deletion mutant were assessed and verified by the alteration of antibody staining (loss, reduction or increase) using tissue-specific *GAL4* drivers. For all cases, N-IR indicates neuronal RNAi, M-IR indicates muscle RNAi, U-IR indicates ubiquitous RNAi. For rescuing *ten-a* mutants, Ten-a N indicates neuronal overexpression with *elav-GAL4* of *UAS-ten-a* and Ten-a M indicates muscle overexpression of *UAS-ten-a* with *Mef2-GAL4*.

Immunostaining. Wandering third instar larvae were processed as previously described²³. The following primary antibodies were used: mouse antibody to *Ten-m* (mAb20, 1:500)⁴⁰, guinea pig antibody to *Ten-a* (1:100)⁴¹, mouse antibody to Brp (mAbnc82, 1:250)⁴², rabbit antibody to Synaptotagmin 1 (1:4,000)⁴³, mouse antibody to Cysteine String Protein (mAb6D6, 1:100)⁴⁴, mouse antibody to Dlg (mAb4F3, 1:500)⁴⁵, rabbit antibody to Dlg (1:40,000)⁴⁶, mouse antibody to α -Spectrin (mAb3A9, 1:50)⁴⁷, mouse antibody to Fasciclin 2 (mAb1D4, 1:20)⁴⁸, rabbit antibody to Fasciclin 2 (1:5,000)⁴⁶, mouse antibody to Futsch (mAb22C10, 1:50)²⁰, rabbit antibody to DGluRIII (1:2,500)¹⁵, rat antibody to Elav (mAb7E8A10, 1:25)⁴⁹, mouse antibody to Even-skipped (mAb3C10, 1:100)⁵⁰, rabbit antibody to β -Spectrin (1:1,000)⁵¹, mouse antibody to Hts (1:500)²², guinea pig antibody to Wsp (1:1,000)⁵². Alexa488-, Alexa546- or Alexa647-conjugated secondary antibodies were used at 1:250 (Invitrogen). Texas-Red-conjugated Phalloidin was used at 1:300. FITC-, Cy3- or Cy5-conjugated antibodies to HRP were used at 1:100 (Jackson ImmunoResearch).

Electron microscopy. Wandering third instar larvae were processed and sectioned as described²³. Sections were imaged on a JEM-1400 (JEOL) transmission electron microscope at $\times 3,000$ to $\times 20,000$ magnification.

Electrophysiology. Larvae were dissected in HL3 saline⁵³ containing 0 mM Ca^{2+} and 4 mM Mg^{2+} . They were then transferred to saline containing 0.6 mM Ca^{2+} and recordings conducted by impaling larval muscle 6 in body wall segments A3 and A4 using sharp intracellular electrodes (10–20 M Ω), fabricated from borosilicate glass capillaries and filled with 3 M KCl solution. For evoked EPSPs, severed nerve bundles were stimulated using a suction electrode connected to a linear stimulus isolated (A395, World Precision Instruments). Data, acquired using Multiclamp 700B amplifiers (Molecular Devices), were low-pass filtered at 3 kHz and digitized at 10 kHz. Recordings were acquired and analysed using Igor Pro software (Wavemetrics) and custom-written programs. All recordings in which the resting membrane potential was higher than -60 mV and/or whose resting potential, input resistance or access resistance changed by more than 20% during the duration of data acquisition were excluded from analysis. All recordings and data analyses were performed blind to the genotype. Quantal content was corrected for nonlinear summation⁵⁴.

Larval locomotion. Crawling assays were conducted as described⁵⁵.

FM1-43 dye loading. FM1-43 (Invitrogen) dye loading was conducted as described⁵⁶ with the following modifications: loading was conducted in 1.5 mM Ca^{2+} , 90 mM K^{+} saline for 1 min followed by six 2-min washes in 0 mM Ca^{2+} saline. Imaging was conducted on a Zeiss LSM 510 Meta Confocal (Carl Zeiss) with a $\times 40$, PlanApo NA 1.0 water immersion lens (Carl Zeiss).

Construction of epitope-tagged teneurin transgenes. The *ten-m* and *ten-a* coding sequences lacking the stop codon were cloned into *pENTR-D/TOPO* (Invitrogen) from *pENTR-ten-m* and *pENTR-ten-a*. *pENTR-ten-m* (stop) and *pENTR-ten-a* (stop) were recombined into the destination vectors *pUASTattB-gtw-tFHAH* and *pQUASTattB-gtw-tFMH*, respectively, using LR Clonase II (Invitrogen). *pUASTattB-gtw-tFHAH* is a *pUAST-Gateway-attB* based vector with a C-terminal TEV recognition site and 3 \times Flag, 3 \times HA and 10 \times His tags. *pQUASTattB-gtw-tFMH* is a *pQUAST-Gateway-attB*⁸ based vector with a

C-terminal TEV recognition site and 3 \times Flag, 6 \times Myc and 10 \times His tags. The resulting constructs were verified by restriction digest and sequencing and integrated into the *attP24* or *86Fb* landing sites on the second and third chromosomes⁵⁷. Transgenic flies were verified by immunoprecipitation on western blot and overexpression experiments.

Immunoprecipitation, western blots and SDS-PAGE analysis. For *Ten-m* and *Ten-a*, *QUAS-Ten-a-Flag-Myc* was expressed in nerves using *Synj-QF* and *UAS-Ten-m-Flag-HA* in muscles using *mhc-GAL4*. Larval synaptosomes were prepared from larval body wall fillets as described⁵⁸. For *Ten-m* and α -Spectrin, control larvae consisted of *Mef2-GAL4* without *UAS-Ten-m-Flag-HA* whereas experimental flies combined the two. Immunoprecipitation was conducted as described using M2-anti-Flag-conjugated agarose (Sigma) or Affi-Prep Protein A beads (Bio-Rad) and rat antibodies to HA (Roche)²³. Proteins were separated on NuPAGE 3–8% Tris-Acetate Gels (Invitrogen) and transferred to nitrocellulose. Primary antibodies were applied overnight at 4 °C and secondary antibodies at 21 °C for 1 h. The following primary antibodies were used: mouse antibody to α -Spectrin (mAb3A9, 1:2,000), mouse antibody to Brp (mAbnc82, 1:100), mouse antibody to Flag (M2, 1:5,000, Sigma-Aldrich), mouse antibody to Myc (3E10, 1:1,500, Santa Cruz Biotechnology), rat antibody to HA (3F10, 1:1,500, Roche). HRP-conjugated secondary antibodies (Jackson ImmunoResearch) were used at 1:10,000. Blots were developed using the SuperSignal West Femto Maximum Sensitivity Substrate (ThermoScientific).

Imaging analysis. Larvae were imaged with a Zeiss LSM 510 Meta laser-scanning confocal microscope (Carl Zeiss) using either a $\times 63$ 1.4 NA or a $\times 40$ 1.0 NA objective. NMJ images were taken as confocal z-stacks with the upper and lower bounds defined by HRP staining unless otherwise noted. For all metrics, boutons were assessed in segment A3 at muscle 6/7 and muscle 4 on both the left and right sides. Fluorescence intensity measurements were taken from terminals on muscle 4. All phenotypes, however, were observed at all synapses regardless of muscle fibre or segment. For membrane organization, vesicle distribution and Teneurin colocalization, NMJ images were taken as single optical sections at the precise centre of the bouton as determined by HRP staining. Images were processed with the LSM software and Adobe Photoshop CS4. Bouton number, active zone/glutamate receptor apposition, fluorescent intensity and microtubule organization were quantified as previously described²³. Targeting errors for each larva were quantified as the percentage of hemisegments from A1 to A7 in a single animal with a failure of target innervation. There was no difference in targeting errors based on body wall segment. Experiments using *H94-GAL4* were conducted as described³⁴, and their effects confirmed using Fasciclin 2 overexpression (control = 58.1% of boutons on muscle 6, 41.9% on muscle 7; Fas 2 overexpression = 73.0% on muscle 6, 27.0% on muscle 7; $n = 8$ animals for each, $P < 0.0001$)³⁴.

In electron micrographs, parameters were quantified as previously described using ImageJ (NIH)²³. T-bar defects were classified into one of five categories: normal (no discernible defect), double (two T-bars were observed in the same, continuous active zone), detached (where the T-bar was clearly visible but was not explicitly connected to the membrane associated with the nearest PSD), apposite contractile tissue (where the T-bar was not apposed to the SSR, but rather, the contractile tissue of the muscle), misshapen (where an electron-dense T-bar was visible but did not conform to the 'T' shape. Often, the T-bars were 'X' shaped). For Fig. 2r, each defect is expressed as a percentage of the total number of T-bars observed in a particular genotype.

For *Ten-m* gradient calculation, single optical sections were taken through the centre of the NMJ on muscle 3 or muscle 4, as determined by HRP immunoreactivity. The GFP signal (*ten-m-GAL4*) or antibody signal was then measured using ImageJ (NIH). For each larva, measurements were taken on the right and left sides of each indicated segment. The fluorescence for each segment was expressed as a percentage of the fluorescence from segment A1 in the same animal, on the same side of the larvae. For all larvae, segment A1 represented the maximal fluorescence. **Statistical analysis.** Statistical analysis used GraphPad Prism 5 (Graphpad Software). In all cases involving more than two samples, significance was calculated using ANOVA followed by a Dunnett post-hoc test to the control sample and a Bonferroni post-hoc test among all samples. For two-sample cases, an unpaired Student's *t*-test was used to assess significance, unless otherwise indicated. In all cases, both methods provided similar significance measurements. In all figures, significance is with respect to control genotypes unless otherwise noted.

- Lilly, B. et al. Requirement of MADS domain transcription factor D-MEF2 for muscle formation in *Drosophila*. *Science* **267**, 688–693 (1995).
- Sun, B., Xu, P. & Salvaterra, P. M. Dynamic visualization of nervous system in live *Drosophila*. *Proc. Natl Acad. Sci. USA* **96**, 10438–10443 (1999).
- Luo, L., Liao, Y. J., Jan, L. Y. & Jan, Y. N. Distinct morphogenetic functions of similar small GTPases: *Drosophila* Drac1 is involved in axonal outgrowth and myoblast fusion. *Genes Dev.* **8**, 1787–1802 (1994).
- Davis, G. W. & Goodman, C. S. Synapse-specific control of synaptic efficacy at the terminals of a single neuron. *Nature* **392**, 82–86 (1998).

35. Wodarz, A., Hinz, U., Engelbert, M. & Knust, E. Expression of crumbs confers apical character on plasma membrane domains of ectodermal epithelia of *Drosophila*. *Cell* **82**, 67–76 (1995).
36. Petersen, L. K. & Stowers, R. S. A Gateway MultiSite recombination cloning toolkit. *PLoS ONE* **6**, e24531 (2011).
37. Loewen, C. A., Mackler, J. M. & Reist, N. E. *Drosophila* synaptotagmin I null mutants survive to early adulthood. *Genesis* **31**, 30–36 (2001).
38. Dietzl, G. *et al.* A genome-wide transgenic RNAi library for conditional gene inactivation in *Drosophila*. *Nature* **448**, 151–156 (2007).
39. Lee, T. & Luo, L. Mosaic analysis with a repressible cell marker for studies of gene function in neuronal morphogenesis. *Neuron* **22**, 451–461 (1999).
40. Levine, A. *et al.* odd Oz: a novel *Drosophila* pair rule gene. *Cell* **77**, 587–598 (1994).
41. Rakovitsky, N. *et al.* *Drosophila* Ten-a is a maternal pair-rule and patterning gene. *Mech. Dev.* **124**, 911–924 (2007).
42. Laissue, P. P. *et al.* Three-dimensional reconstruction of the antennal lobe in *Drosophila melanogaster*. *J. Comp. Neurol.* **405**, 543–552 (1999).
43. Mackler, J. M., Drummond, J. A., Loewen, C. A., Robinson, I. M. & Reist, N. E. The Ca^{2+} -binding motif of synaptotagmin is required for synaptic transmission *in vivo*. *Nature* **418**, 340–344 (2002).
44. Zinsmaier, K. E., Eberle, K. K., Buchner, E., Walter, N. & Benzer, S. Paralysis and early death in cysteine string protein mutants of *Drosophila*. *Science* **263**, 977–980 (1994).
45. Parnas, D., Haghighi, A. P., Fetter, R. D., Kim, S. W. & Goodman, C. S. Regulation of postsynaptic structure and protein localization by the Rho-type guanine nucleotide exchange factor dPix. *Neuron* **32**, 415–424 (2001).
46. Koh, Y. H., Popova, E., Thomas, U., Griffith, L. C. & Budnik, V. Regulation of DLG localization at synapses by CaMKII-dependent phosphorylation. *Cell* **98**, 353–363 (1999).
47. Byers, T. J., Dubreuil, R., Branton, D., Kiehart, D. P. & Goldstein, L. S. *Drosophila* spectrin. II. Conserved features of the alpha-subunit are revealed by analysis of cDNA clones and fusion proteins. *J. Cell Biol.* **105**, 2103–2110 (1987).
48. Van Vactor, D., Sink, H., Fambrough, D., Tsao, R. & Goodman, C. S. Genes that control neuromuscular specificity in *Drosophila*. *Cell* **73**, 1137–1153 (1993).
49. O'Neill, E. M., Rebay, I., Tjian, R. & Rubin, G. M. The activities of two Ets-related transcription factors required for *Drosophila* eye development are modulated by the Ras/MAPK pathway. *Cell* **78**, 137–147 (1994).
50. Patel, N. H., Schafer, B., Goodman, C. S. & Holmgren, R. The role of segment polarity genes during *Drosophila* neurogenesis. *Genes Dev.* **3**, 890–904 (1989).
51. Byers, T. J., Husain-Chishti, A., Dubreuil, R. R., Branton, D. & Goldstein, L. S. Sequence similarity of the amino-terminal domain of *Drosophila* beta spectrin to alpha actinin and dystrophin. *J. Cell Biol.* **109**, 1633–1641 (1989).
52. Ben-Yaacov, S., Le Borgne, R., Abramson, I., Schweisguth, F. & Schejter, E. D. *Wasp*, the *Drosophila* Wiskott-Aldrich syndrome gene homologue, is required for cell fate decisions mediated by *Notch* signaling. *J. Cell Biol.* **152**, 1–13 (2001).
53. Stewart, B. A., Atwood, H. L., Renger, J. J., Wang, J. & Wu, C. F. Improved stability of *Drosophila* larval neuromuscular preparations in haemolymph-like physiological solutions. *J. Comp. Physiol. A Neuroethol. Sens. Neural Behav. Physiol.* **175**, 179–191 (1994).
54. Martin, A. R. A further study of the statistical composition on the end-plate potential. *J. Physiol. (Lond.)* **130**, 114–122 (1955).
55. Lnenicka, G. A., Spencer, G. M. & Keshishian, H. Effect of reduced impulse activity on the development of identified motor terminals in *Drosophila* larvae. *J. Neurobiol.* **54**, 337–345 (2003).
56. Verstreken, P., Ohyama, T. & Bellen, H. J. FM 1-43 labeling of synaptic vesicle pools at the *Drosophila* neuromuscular junction. *Methods Mol. Biol.* **440**, 349–369 (2008).
57. Markstein, M., Pitsouli, C., Villalta, C., Celniker, S. E. & Perrimon, N. Exploiting position effects and the gypsy retrovirus insulator to engineer precisely expressed transgenes. *Nature Genet.* **40**, 476–483 (2008).
58. Higashi-Kovtun, M. E., Mosca, T. J., Dickman, D. K., Meinertzhagen, I. A. & Schwarz, T. L. Importin- β 11 regulates synaptic phosphorylated mothers against decapentaplegic, and thereby influences synaptic development and function at the *Drosophila* neuromuscular junction. *J. Neurosci.* **30**, 5253–5268 (2010).

Teneurins instruct synaptic partner matching in an olfactory map

Weizhe Hong¹, Timothy J. Mosca¹ & Liqun Luo¹

Neurons are interconnected with extraordinary precision to assemble a functional nervous system. Compared to axon guidance, far less is understood about how individual pre- and postsynaptic partners are matched. To ensure the proper relay of olfactory information in the fruitfly *Drosophila*, axons of ~50 classes of olfactory receptor neurons (ORNs) form one-to-one connections with dendrites of ~50 classes of projection neurons (PNs). Here, using genetic screens, we identified two evolutionarily conserved, epidermal growth factor (EGF)-repeat containing transmembrane Teneurin proteins, Ten-m and Ten-a, as synaptic-partner-matching molecules between PN dendrites and ORN axons. Ten-m and Ten-a are highly expressed in select PN-ORN matching pairs. Teneurin loss- and gain-of-function cause specific mismatching of select ORNs and PNs. Finally, Teneurins promote homophilic interactions *in vitro*, and Ten-m co-expression in non-partner PNs and ORNs promotes their ectopic connections *in vivo*. We propose that Teneurins instruct matching specificity between synaptic partners through homophilic attraction.

The chemoaffinity hypothesis was proposed nearly 50 years ago to explain the target specificity of regenerating optic nerves: developing neurons “must carry individual identification tags, presumably cytochemical in nature, by which they are distinguished one from another almost, in many regions, to the level of the single neuron”¹. Many molecules are now known that guide axons to their target areas^{2,3}, but few may mediate mutual selection and direct matching between individual pre- and postsynaptic partners. Here we show that the transmembrane Teneurin proteins instruct the selection of specific synaptic partners in the *Drosophila* olfactory circuit (Supplementary Fig. 1).

In *Drosophila*, individual classes of ORN axons make one-to-one connections with individual classes of second-order PN dendrites within one of ~50 discrete glomeruli in the antennal lobe. We refer to this specific one-to-one connection as PN-ORN synaptic partner matching. Olfactory circuit assembly takes place in sequential steps before sensory activity begins^{4–6}. PN dendrites first elaborate within and pattern the developing antennal lobe^{7–9}, which is followed by invasion of ORN axons^{10–14}. Importantly, re-positioning PN dendrites redirects their partner ORN axons without disrupting the connections¹⁵, suggesting that proper PN-ORN connections probably involve direct recognition and matching between partners.

Matching screens identified Ten-m and Ten-a

To identify potential PN-ORN matching molecules, we simultaneously labelled select PN dendrites and ORN axons in two colours and performed two complementary genetic screens (Fig. 1a, d). We overexpressed 410 candidate cell-surface molecules, comprising ~40% of the potential cell-recognition molecules in *Drosophila*¹⁶. In the first screen, we used *Mz19-GAL4* to label DA1, VA1d and DC3 PNs (hereafter Mz19 PNs), and *Or47b-rCD2* to label Or47b ORNs (Fig. 1a, b). Or47b ORN axons normally project to the VA1m glomerulus and are adjacent to Mz19 PN dendrites without overlap. We overexpressed candidate cell-surface molecules only in Mz19 PNs to identify those that promoted ectopic connections between Or47b axons and Mz19 dendrites (Fig. 1a). We found that overexpression of *ten-m* (*P{GS}9267*; Supplementary Fig. 2b) produced ectopic connections (Fig. 1c).

In the second screen, we labelled Mz19 PNs as above and Or88a ORNs using *Or88a-rCD2* (Fig. 1d, e). Or88a ORN axons normally project to the VA1d glomerulus, intermingling extensively with VA1d PN dendrites (Fig. 1e). We overexpressed candidate cell-surface molecules in Mz19 PNs (Fig. 1d) as above and found that overexpression of *ten-a* (*P{GE}1914*, Supplementary Fig. 2a) partially disrupted the intermingling of Or88a axons and Mz19 dendrites (Fig. 1f).

In addition to impairing PN-ORN matching, *ten-m* and *ten-a* overexpression shifted Mz19 PN dendrite position (Fig. 1c, f). However, mismatching was not a secondary consequence of axon or dendrite mispositioning; mispositioning alone, caused by perturbation of other genes, does not alter PN-ORN matching^{9,13,15}. Furthermore, among 410 candidate molecules, only *ten-m* and *ten-a* overexpression exhibited mismatching defects, suggesting their specificity in PN-ORN matching.

Both *ten-m* and *ten-a* appear to encode type II transmembrane proteins^{17–19}. They possess highly similar domain compositions and amino acid sequences; each contains eight EGF-like and multiple YD (tyrosine-aspartate) repeats within its large carboxy-terminal extracellular domain (Fig. 1g). Ten-m and Ten-a were initially identified as tenascin-like molecules^{20,21}, but vertebrate teneurins were later identified as their true homologues based on sequence and domain similarity (Fig. 1h). Thus, we refer to Ten-m and Ten-a as *Drosophila* Teneurins. Teneurins are present in nematodes, flies and vertebrates. In human, teneurin-1 and teneurin-2 are located in chromosomal regions associated with intellectual disability¹⁷, and teneurin-4 is linked to susceptibility to bipolar disorder²².

Drosophila ten-m was originally identified as a pair-rule gene required for embryonic patterning^{21,23}, but this function was recently shown to be unrelated to *ten-m*²⁴. Teneurins were implicated in synapse development at the neuromuscular junction^{16,25} (see ref. 26), and Ten-m also regulates motor axon guidance²⁴. Neither the underlying mechanisms nor their potential roles in the central nervous system are known. Vertebrate teneurins are widely expressed in the nervous system^{18,27} and interact homophilically *in vitro*^{28,29}, suggesting their potential role as homophilic cell adhesion molecules in patterning neuronal connectivity.

¹Department of Biology, Howard Hughes Medical Institute, Stanford University, Stanford, California 94305, USA.

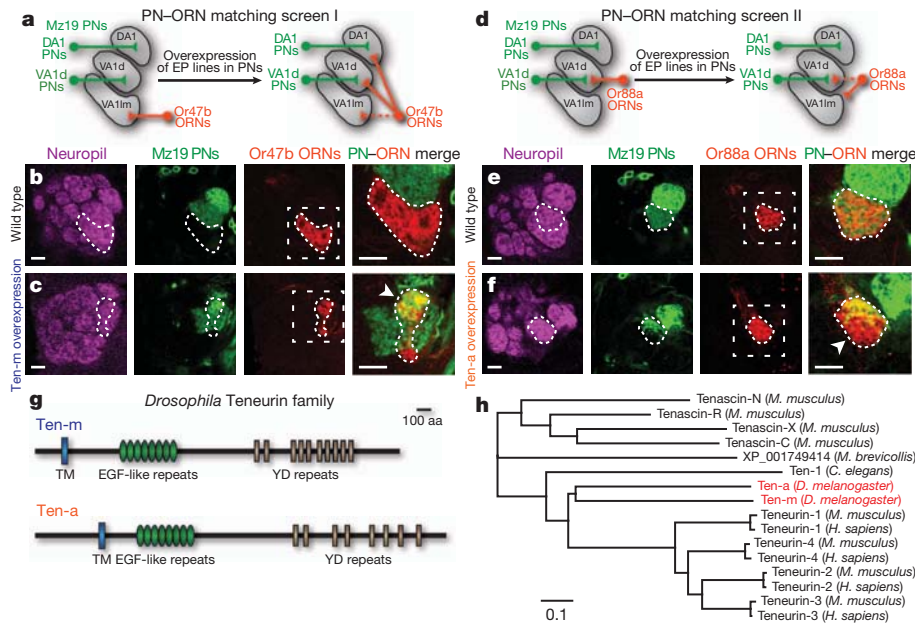


Figure 1 | PN-ORN synaptic matching screens identify two Teneurins.

a, d, Schematics showing two PN-ORN matching screens. PN dendrites are labelled by *Mz19-GAL4* driving mCD8GFP and ORN axons by *Or47b-rCD2* (**a**) or *Or88a-rCD2* (**d**). Each EP line has a transposable element insertion that places *UAS* 5' to a gene encoding a predicted cell-surface protein, which can be overexpressed using *Mz19-GAL4*. **b, c**, Or47b axons and Mz19 dendrites do not overlap in control (**b**), but form ectopic connections following *Ten-m* overexpression (**c**), as seen by axon-dendrite intermingling (arrowhead). **e, f**, Or88a axons and Mz19 dendrites connect at the VA1d glomerulus in control (**e**), but the connection is partially lost following *Ten-a* overexpression, as some of the Or88a axons no longer intermingle with Mz19 dendrites

Matching expression of *Ten-m* and *Ten-a*

Both *Drosophila* Teneurin proteins were endogenously expressed in the developing antennal lobe (Fig. 2a and Supplementary Fig. 3). At 48 h after puparium formation (APF), when individual glomeruli just become identifiable, elevated Teneurin expression was evident in select glomeruli. The subset of glomeruli expressing elevated *Ten-m* was distinct but partially overlapping with that expressing elevated *Ten-a* (Fig. 2a, e). Teneurin proteins were also detected at a low level in all glomeruli. Both basal and elevated Teneurin expressions were eliminated by pan-neuronal RNA interference (RNAi) targeting the corresponding gene (Fig. 2b, c), suggesting that Teneurin proteins are produced predominantly by neurons. In a *ten-a* null mutant we generated (Supplementary Fig. 2a), all *Ten-a* expression was eliminated, confirming antibody specificity (Fig. 2d).

The antennal lobe consists of ORN axons as well as PN and local interneuron dendrites. We used intersectional analysis to determine the cellular source for elevated Teneurin expression. For *ten-m*, we screened *GAL4* enhancer traps near the *ten-m* gene, and identified NP6658 (hereafter *ten-m-GAL4*; Supplementary Fig. 2b) that recapitulated the glomerulus-specific *Ten-m* staining pattern (Supplementary Fig. 4a–c). We used a FLPout reporter *UAS>stop>mCD8GFP* to determine the intersection of *ten-m-GAL4* and an ORN-specific *ey-Flp* (Fig. 2f and Supplementary Fig. 4d–f) or a PN-specific *GH146-Flp* (Fig. 2g and Supplementary Fig. 4g–i). We found that *ten-m-GAL4* was selectively expressed in a subset of ORNs and PNs. Owing to reagent availability, we focused our analysis on five glomeruli (DA1, VA1d, VA1lm, DC3 and DA3), adjacently located on the lateral and anterior side of the antennal lobe. In these five glomeruli, *Ten-m* expression in PN and ORN classes matched: high levels in PNs corresponded to high levels in ORNs and vice versa (Fig. 2f, g).

To determine the cellular origin of elevated *Ten-a* expression, we performed tissue-specific RNAi of endogenous *Ten-a*, as no *GAL4*

(arrowhead). Target areas of Or47b (**b, c**) or Or88a (**e, f**) axons are outlined. Mismatching phenotypes are quantified in Supplementary Figs 9k and 10q. The first three columns in **b, c, e, f** show separate channels of the same section; the fourth shows higher magnification of the dashed squares (as in Figs 3, 4, 5d–g). Unless indicated, all images in this and subsequent figures are single confocal sections and all scale bars are 10 μ m. **g**, Domain composition of *Drosophila* *Ten-m* and *Ten-a*. aa, amino acids; TM, transmembrane domain. **h**, Phylogeny of the *Drosophila* Teneurins and related proteins in other species. Branch lengths represent units of substitutions per site of the sequence alignment. Teneurins are evolutionarily conserved in bilaterians and a unicellular choanoflagellate *Monosiga brevicollis*, but not in cnidarians.

enhancer trap is available near *ten-a*. To isolate *Ten-a* expression in ORNs, we drove pan-neuronal *ten-a* RNAi while specifically suppressing RNAi in ORNs using *tubP>stop>GAL80* and *ey-Flp* (Fig. 2h). To restrict *Ten-a* expression to central neurons, we expressed *ten-a* RNAi in all ORNs (Fig. 2i). We found that *Ten-a* was highly expressed in a subset of ORNs and central neurons, and also showed a matching expression in the five glomeruli we focused on (Fig. 2h, i). The glomerular-specific differential *Ten-a* expression in central neurons probably arises mainly from PNs as they target dendrites to specific glomeruli, and punctate *Ten-a* staining was observed in PN cell bodies (Supplementary Fig. 5). In summary, *Ten-m* and *Ten-a* are each highly expressed in a distinct, but partially overlapping, subset of matching ORNs and PNs (Fig. 2j).

Teneurins are required for PN-ORN matching

To examine whether Teneurins are required for proper PN-ORN matching, we performed tissue-specific RNAi (Fig. 3 and Supplementary Fig. 2c) in all neurons using *C155-GAL4*, in PNs using *GH146-GAL4*, or in ORNs using *peb-GAL4*. To label specific subsets of PN dendrites independent of *GAL4*-UAS, we used the Q binary expression system³⁰, and converted *Mz19-GAL4* to *Mz19-QF* by bacterial artificial chromosome (BAC) recombineering (Supplementary Fig. 2d). We could thus perform *GAL4*-based RNAi knockdown while labelling PN dendrites and ORN axons in two colours independent of *GAL4*. We focused our analysis on Mz19 dendrites and Or47b axons, which innervate neighbouring glomeruli but never intermingle in wild type (Figs 1b and 3a, b).

Pan-neuronal RNAi of both *teneurin* genes shifted Or47b axons to a position between two adjacent Mz19 glomeruli, DA1 and VA1d (Fig. 3c). Moreover, Mz19 dendrites and Or47b axons intermingled without a clear border (Fig. 3c, d), reflecting a PN-ORN matching defect. We confirmed this using independent RNAi lines targeting

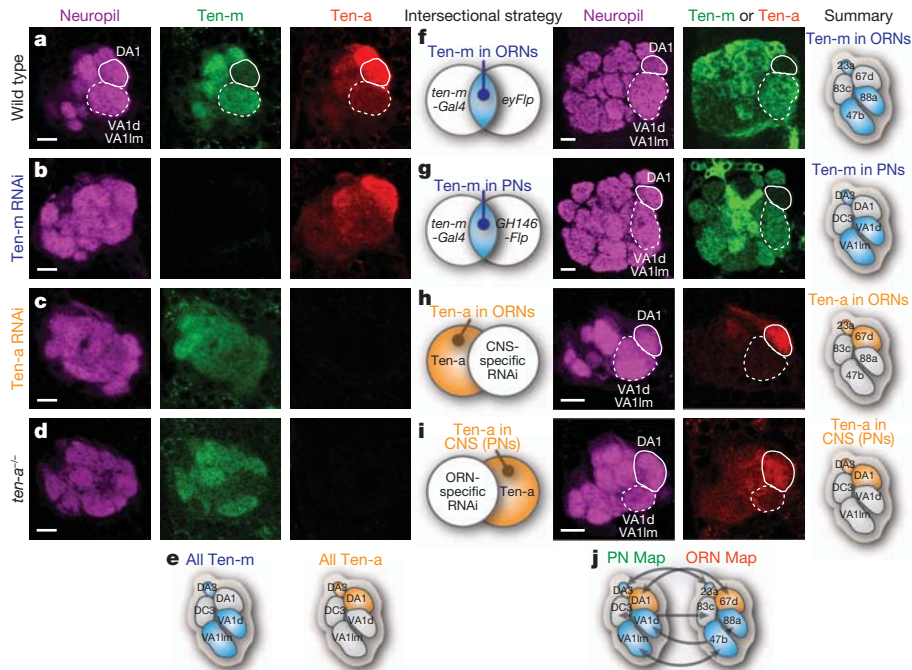


Figure 2 | Ten-m and Ten-a are differentially expressed in matching PN and ORN classes. **a**, Developing antennal lobes at 48 h APF stained by antibodies against Ten-m, Ten-a, and a neuropil marker, N-cadherin. Solid lines encircle the DA1 glomerulus (Ten-m low, Ten-a high). Dashed lines encircle the VA1d/VA1lm glomeruli (Ten-m high, Ten-a low). **b, c**, Ten-m and Ten-a proteins are undetectable following pan-neuronal RNAi of *ten-m* (**b**) and *ten-a* (**c**), respectively. **d**, A *ten-a* homozygous mutant eliminated the Ten-a antibody staining. **e**, Summary of elevated Ten-m and Ten-a expression in five select

glomeruli. **f, g**, Expression of the Flp-out GFP reporter *UAS>stop>mCD8GFP* at the intersection of *ten-m-GAL4* with ORN-specific *ey-Flp* (**f**) or with PN-specific *GHI46-Flp* (**g**) in adult. **h, i**, Antibody staining of Ten-a in central nervous system (CNS)-neuron-specific RNAi (**h**) or in ORN-specific RNAi (**i**) at 48 h APF. **f-i**, Right, individual cell-type-specific Teneurin expression patterns are schematically summarized. **j**, Combined expression patterns of Teneurin proteins in PNs (left) and ORNs (right). Blue, Ten-m high; orange, Ten-a high. Scale bars, 10 μ m.

different regions of the *ten-m* and *ten-a* transcripts (Supplementary Fig. 6). Further, knocking down *ten-m* and *ten-a* only in PNs or only in ORNs also led to Mz19-Or47b intermingling (Fig. 3e and Supplementary Fig. 7a, d), indicating that Teneurins are required in both PNs and ORNs to ensure proper matching.

Next, we examined the contribution of each Teneurin by individual RNAi knockdown in ORNs. Knocking down *ten-m* and, to a lesser extent, *ten-a*, caused mild mismatching (Fig. 3e and Supplementary Fig. 7). This was greatly enhanced by simultaneous knockdown of both *ten-m* and *ten-a* (Fig. 3e), probably because Mz19-Or47b

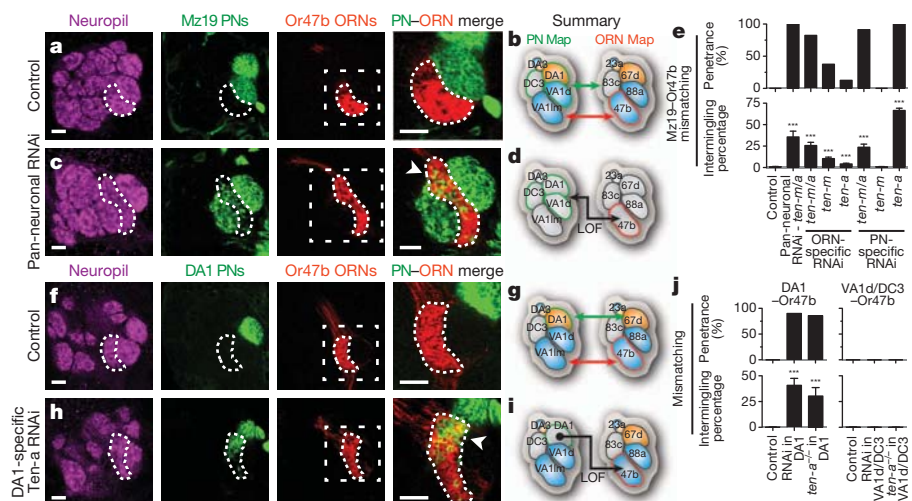


Figure 3 | Loss of Teneurins causes PN–ORN mismatching. **a**, Normally, Mz19 dendrites (green) innervate glomeruli adjacent to the VA11m glomerulus, which is itself innervated by Or47b axons (red). The dashed line encircles Or47b axons. DC3 PNs are located posterior to DA1/VA1d PNs and Or47b ORNs, and are not visible in these sections. **c**, Mismatching phenotypes in *ten-m* and *ten-a* RNAi driven by the pan-neuronal driver *C155-GAL4*. Dashed lines encircle Or47b ORN axons, showing intermingling with Mz19 PN dendrites (arrowhead). **e**, Quantification of Mz19–Or47b mismatching phenotypes. For

all genotypes, $n \geq 15$. **f**, In control, DA1 PN do not intermingle with Or47b ORNs. **h**, MARCM expression of *ten-a* RNAi in DA1 PN causes dendrite intermingling with Or47b axons (arrowhead). **j**, Quantification of mismatching phenotypes. For all genotypes, $n \geq 6$. Error bars represent s.e.m. ***, $P < 0.001$ compared to control. **b**, **d**, **g**, **i**, Summary showing normal connectivity in control (**a**, **f**) and mismatching phenotypes following *teneurin* RNAi (**c**, **h**). Blue, Ten-m high; orange, Ten-a high. Green outlines, labelled PN. Red outlines, labelled ORNs. Scale bars, 10 μ m.

mismatching requires weakening connections with their respective endogenous partners (Supplementary Fig. 7g). This synergy implies that multiple matching molecules can enhance partner matching robustness.

We also tested the functions of individual Teneurins in PNs. We found that the Mz19–Or47b mismatching was caused by PN-specific knockdown of *ten-a*, but not *ten-m* (Fig. 3e and Supplementary Fig. 7). As VA1d/DC3 and DA1 PNs arise from separate neuroblast lineages³¹, we used mosaic analysis with a repressible cell marker (MARCM) to generate neuroblast clones to label and knockdown *ten-a* in DA1 or VA1d/DC3 PNs (Fig. 3f–j; see Methods). *ten-a* knockdown only in DA1 PNs (normally Ten-a high) caused their dendrites to mismatch with Or47b axons (Fig. 3h–j). By contrast, *ten-a* knockdown in VA1d/DC3 PNs (normally Ten-a low) did not cause mismatching (Fig. 3j and Supplementary Fig. 8a, b). Similarly, MARCM loss-of-function of *ten-a* mutant in DA1 but not in VA1d/DC3 PNs resulted in mismatching with Or47b ORNs (Fig. 3j and Supplementary Fig. 8c, d). Thus, removal of *ten-a* from Ten-a-high DA1 PNs caused their dendrites to mismatch with Ten-a-low Or47b ORNs (Fig. 3i). The differential requirements of Ten-m and Ten-a in ORNs or PNs in preventing Mz19–Or47b mismatching probably reflect differential expression of Ten-m and Ten-a in the mismatching partners.

Our finding that loss of *ten-a* caused Ten-a-high PNs to mismatch with Ten-a-low ORNs (Fig. 3i, j), together with the matching expression of Teneurin proteins in PNs and ORNs, raised the possibility that Teneurins instruct class-specific PN–ORN connections through homophilic attraction: PNs expressing high-level Ten-m or Ten-a connect to ORNs with high-level Ten-m or Ten-a, respectively.

Teneurins instruct matching specificity

This homophilic attraction hypothesis predicts that overexpression of a given Teneurin in PNs (1) should preferentially affect PNs normally

expressing low levels of that Teneurin, causing their dendrites to lose endogenous connections with their cognate ORNs, and (2) should cause these PNs to make ectopic connections with ORNs expressing high levels of that Teneurin.

To test the first prediction, we examined whether Teneurin overexpression in Mz19 PNs impaired their endogenous connections with cognate ORNs. Consistent with our prediction, Ten-m overexpression specifically disrupted the connections of DA1 PNs and Or67d ORNs, a PN–ORN pair expressing low-level Ten-m (Supplementary Fig. 9b, e). Connections of the other two pairs were unaffected (Supplementary Fig. 9a, c, d, f). Likewise, Ten-a overexpression specifically disrupted connections between VA1d PNs and Or88a ORNs, a PN–ORN pair expressing low-level Ten-a (Supplementary Fig. 9g), but not between the other two PN–ORN pairs (Supplementary Fig. 9h, i).

To test the second prediction, we examined the specificity of ectopic connections made by Mz19 PNs overexpressing Teneurins, and sampled five non-partner ORN classes that project axons to the vicinity of Mz19 dendrites (Supplementary Fig. 10). We found that Ten-m overexpression in Mz19 PNs caused their dendrites to mismatch only with Or47b ORNs (Supplementary Fig. 10f). To examine additional mismatching phenotypes that may occur within Mz19 glomeruli and to determine whether DA1 or VA1d/DC3 PNs contribute to the ectopic connections, we used MARCM to overexpress Ten-m in individual PN classes. We found that Ten-m overexpression in DA1 PNs (Ten-m low) caused their dendrites to mismatch with Or47b (Fig. 4a, b) and (to a lesser extent) Or88a ORNs (Fig. 4b, c), both endogenously expressing high-level Ten-m. By contrast, Ten-m overexpression in VA1d/DC3 PNs did not produce ectopic connections with any non-matching ORNs tested (Fig. 4d–f).

Likewise, Ten-a overexpression in Mz19 PNs caused their dendrites to mismatch only with Or23a ORNs among all non-matching ORN classes sampled outside the Mz19 region (Supplementary Fig. 10l).

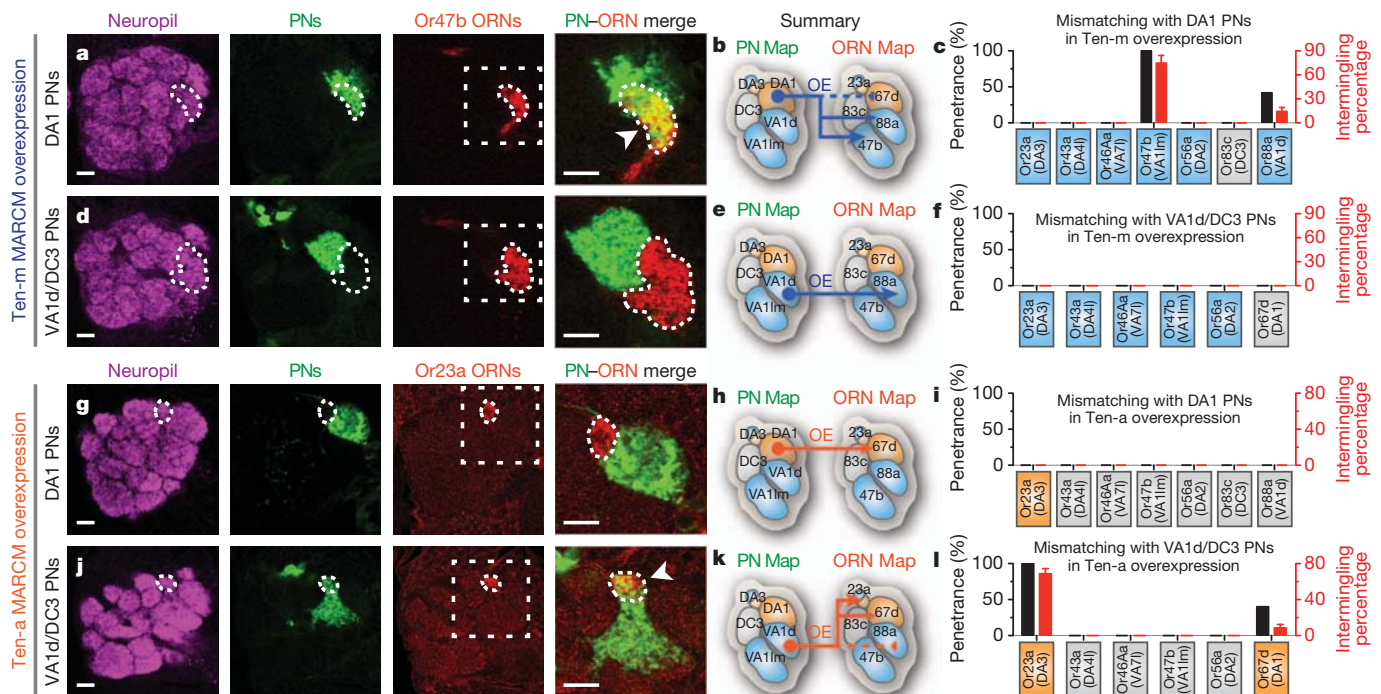


Figure 4 | Teneurin overexpression in specific PN classes causes mismatching. a–f, Mismatching phenotypes following Ten-m (a–f) or Ten-a (g–l) overexpression in different PN classes. Specific PN classes are labelled by MARCM with *Mz19-GAL4* and ORN axons using *Or47b-rCD2* (a, d) or *Or23a-mCD8GFP* (g, j). In control, Mz19 PNs do not intermingle with Or47b ORNs (Fig. 1b). MARCM overexpression of Ten-m in DA1 PNs (a, arrowhead), but not VA1d/DC3 PNs (d), causes dendrite mismatching with Or47b axons. MARCM overexpression of Ten-a in VA1d/DC3 PNs (j, arrowhead), but not in DA1 PNs (g), causes their dendrites to mismatch with Or23a axons. *P[GS]9267* and *P[GE]1914* (Supplementary Fig. 2) are used to overexpress Ten-m and Ten-a, respectively. c, f, i, l, Quantification of mismatching phenotypes ($n = 9$ for each). Error bars represent s.e.m. See Supplementary Fig. 10 for details on some genotypes quantified here. b, e, h, k, Schematic summarizing the mismatching phenotypes in Fig. 4 and Supplementary Figs 9 and 10. Blue, Ten-m high; orange, Ten-a high. Scale bars, 10 μ m.

DA1 PNs (g), causes their dendrites to mismatch with Or23a axons. *P[GS]9267* and *P[GE]1914* (Supplementary Fig. 2) are used to overexpress Ten-m and Ten-a, respectively. c, f, i, l, Quantification of mismatching phenotypes ($n = 9$ for each). Error bars represent s.e.m. See Supplementary Fig. 10 for details on some genotypes quantified here. b, e, h, k, Schematic summarizing the mismatching phenotypes in Fig. 4 and Supplementary Figs 9 and 10. Blue, Ten-m high; orange, Ten-a high. Scale bars, 10 μ m.

Further, MARCM overexpression of Ten-a in VA1d/DC3 PNs (Ten-a low) caused their dendrites to mismatch specifically with Or23a (Fig. 4j, k) and (to a lesser extent) Or67d ORNs (Fig. 4k, l), both endogenously expressing high-level Ten-a (Fig. 4l). By contrast, Ten-a overexpression in DA1 PNs (Ten-a high) did not produce ectopic connections with any non-matching ORNs tested (Fig. 4g–i). Thus, both Ten-m and Ten-a overexpression analyses support the homophilic attraction hypothesis.

Our data also suggest that additional molecule(s) are required to determine completely the wiring specificity of the five PN–ORN pairs examined. For example, VA1d–Or88a and VA1m–Or47b have indistinguishable Ten-m/Ten-a expression patterns (Fig. 2j), and may require additional molecules to distinguish target choice. Indeed, Ten-a knockdown (Fig. 3h–j and Supplementary Fig. 8e, f) or Ten-m overexpression (Fig. 4b, c) caused DA1 PNs to mismatch preferentially with Or47b as opposed to Or88a axons. This suggests that the non-adjacent DA1 and VA1m share a more similar Teneurin-independent cell-surface code than the adjacent VA1d and VA1m. Likewise, Ten-a overexpression caused VA1d PNs to mismatch with the non-adjacent Or23a more so than the adjacent Or67d ORNs, even though both ORNs express high-level Ten-a (Fig. 4k, l). Finally, Ten-m overexpression in DC3 PNs, which express low-level Ten-m, did not change its matching specificity (Fig. 4f and Supplementary Fig. 9f), suggesting that Teneurin-independent mechanisms are involved in matching DC3 PNs and Or83c ORNs.

In summary, we showed that Teneurin overexpression in Teneurin-low PNs caused their dendrites to lose endogenous connections with Teneurin-low ORNs and mismatch with Teneurin-high ORNs (Fig. 4b, k). However, Teneurin overexpression in Teneurin-high PNs did not disrupt their proper connections (Fig. 4e, h). These data indicate that Teneurins instruct connection specificity, probably through homophilic attraction, by matching Ten-m or Ten-a levels in PN and ORN partners.

Ten-m promotes PN–ORN homophilic attractions

To test whether Teneurins interact *in vitro*, we separately transfected two populations of *Drosophila* S2 cells with Flag- and haemagglutinin (HA)-tagged Teneurins, and performed co-immunoprecipitations from lysates of these cells after mixing. We detected strong homophilic interactions between Flag- and HA-tagged Ten-m proteins and, to a lesser extent, between Flag- and HA-tagged Ten-a proteins (Fig. 5a). Ten-m and Ten-a also exhibited heterophilic interactions (Fig. 5a), which may account for their role in synapse organization²⁶.

Next, we tested whether Teneurins can homophilically promote *in vivo* trans-cellular interactions between PN dendrites and ORN axons. We simultaneously overexpressed Ten-m in Mz19 PNs using *Mz19-QF*, and Or67a and Or49a ORNs using *AM29-GAL4* (ref. 32; Fig. 5b). This enabled us to label and manipulate independently Mz19 dendrites and AM29 axons with distinct markers and transgenes. We chose *AM29-GAL4* because of its early onset of expression, whereas other class-specific ORN drivers start to express only after PN–ORN connection is established^{5,6}. AM29 axons do not normally connect with Mz19 dendrites (Fig. 5c, d).

Simultaneous overexpression of Ten-m in both Mz19 PNs and AM29 ORNs produced ectopic connections between them (Fig. 5c, g), suggesting that Ten-m homophilically promotes PN–ORN attraction. By contrast, Ten-m overexpression only in PNs or ORNs did not produce any ectopic connections, despite causing dendrite or axon mistargeting, respectively (Fig. 5c, e, f). These data ruled out the involvement of heterophilic partners in Ten-m-mediated attraction. Simultaneous overexpression of Ten-a in Mz19 PNs and AM29 ORNs did not produce ectopic connections (data not shown), possibly due to lower expression or weaker Ten-a homophilic interactions (Fig. 5a). Although heterophilic interactions between Ten-m and Ten-a also occur *in vitro* (Fig. 5a), heterophilic overexpression of Ten-m and

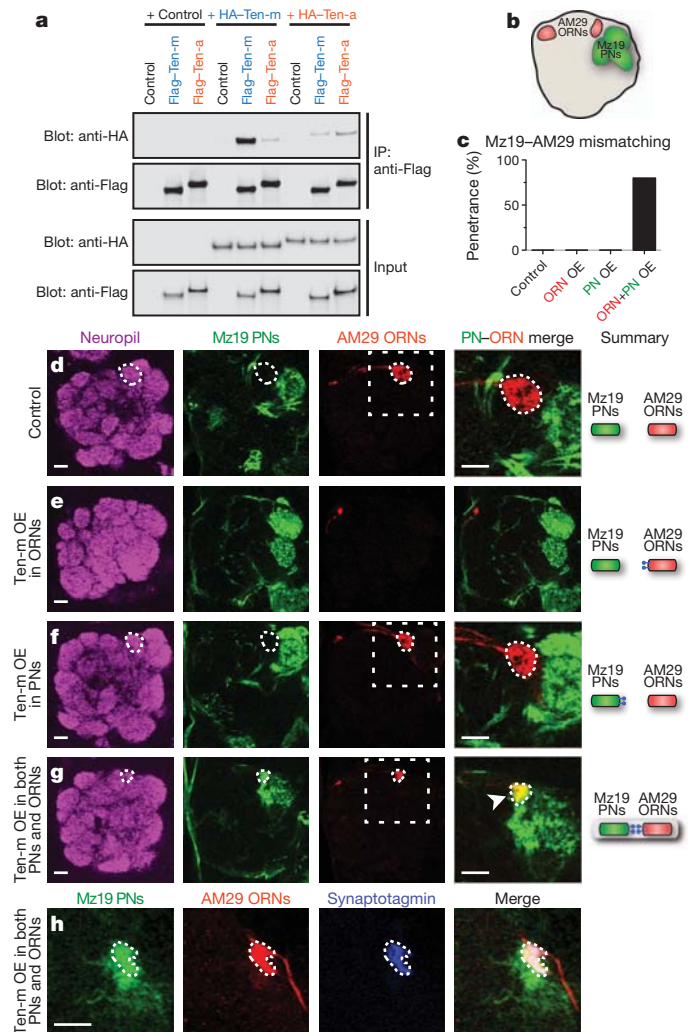


Figure 5 | Ten-m promotes homophilic interactions *in vitro* and *in vivo*.

a, Co-immunoprecipitation of Flag- and HA-tagged Teneurin proteins from separately transfected S2 cells. Co-immunoprecipitated HA-tagged Teneurin proteins are detected by anti-HA antibody and immunoprecipitated Flag-tagged Teneurin proteins by anti-Flag antibody (top two blots). The input lysates are immunoblotted for HA and Flag (bottom two blots). **b**, Schematic showing the relative positions of glomeruli targeted by Mz19 PN dendrites (green) and AM29 ORN axons (red). **c**, Quantification of mismatching between Mz19 PNs and AM29 ORNs ($n = 10$ for each condition). OE, overexpression. **d**, In control, Mz19 dendrites do not connect with AM29 axons. **e, f**, Overexpression of Ten-m only in AM29 ORNs (e) or Mz19 PNs (f) does not produce mismatching between them. Following Ten-m overexpression, AM29 axons mistarget posteriorly to Mz19 dendrites and are therefore not visible in e. **g**, Simultaneous overexpression of Ten-m in both PNs and ORNs produces ectopic Mz19–AM29 connections (arrowhead). Schematics on the right show the Mz19–AM29 connectivity in different conditions. **h**, The synaptic vesicle marker Synaptotagmin is enriched at these Mz19–AM29 ectopic connections. AM29 axons are labelled by *AM29-Gal4* with *UAS-mtdT* to visualize the entire axonal processes and *UAS-synaptotagmin-HA* to visualize synaptic vesicles in axon terminals. Mz19 dendrites are labelled by *Mz19-QF* driving *QUAS-mCD8GFP*. To overexpress Ten-m, *P{GS}9267* and *QUAS-ten-m* (Supplementary Fig. 2) are driven by *AM29-GAL4* and *Mz19-QF*, respectively. Scale bars, 10 μ m.

Ten-a in AM29 ORNs and Mz19 PNs did not produce ectopic connections (data not shown).

Finally, we examined whether these ectopic connections lead to the formation of synaptic structures. Indeed, the ectopic connections between Mz19 dendrites and AM29 axons were enriched in synaptotagmin–HA expressed from AM29 ORNs (Fig. 5h), suggesting that these connections can aggregate synaptic vesicles and could

be functional. We propose that Teneurins promote attraction between PN–ORN synaptic partners through homophilic interactions, eventually leading to synaptic connections.

Discussion

Compared to axon guidance, relatively little is known about synaptic target selection mechanisms^{2–4}. Among the notable examples, the graded expressions of vertebrate EphA and ephrin-A instruct the topographic targeting of retinal ganglion cell axons^{4,33–35}. Chick DSCAM and Sidekick promote lamina-specific arborization of retinal neurons³⁶. *Drosophila* Capricious promotes target specificity of photoreceptor and motor axons^{16,37–39}. *Caenorhabditis elegans* SYG-1 and SYG-2 specify synapse location through interaction between pre-synaptic axons and intermediate guidepost cells⁴⁰. However, it is unclear whether any of these molecules mediate direct, selective interactions between individual pre- and postsynaptic partners. Indeed, in complex neural circuits, it is not clear a priori whether molecular determinants mediate such interactions. For example, the final retinotopic map is thought to result from both ephrin signalling and spontaneous activity^{41,42}. Mammalian ORN axon targeting involves extensive axon–axon interactions through activity-dependent and independent modes^{43,44}, with minimal participation of post-synaptic neurons identified thus far.

Here, we show that Teneurins instruct PN–ORN matching through homophilic attraction. Although each glomerulus contains many synapses between cognate ORNs and PNs, these synapses transmit the same information and can be considered identical with regard to specificity. Thus, Teneurins represent a strong case in determining connection specificity directly between pre- and postsynaptic neurons. We further demonstrate that molecular determinants can instruct connection specificity of a moderately complex circuit at the level of individual synapses.

Our study reveals a requirement for PN–ORN attraction in the stepwise assembly of the olfactory circuit. PN dendrites and ORN axons first independently project to appropriate regions using global cues, dendrite–dendrite and axon–axon interactions^{8,9,12–14}. The initial, independent targeting of PN dendrites and ORN axons is eventually coordinated in their final one-to-one matching. We identified Teneurins as the first molecules to mediate this matching process, through direct PN–ORN attraction. Our analyses have focused on a subset of PN–ORN pairs involving trichoid ORNs⁴⁵, including Or67d, Or88a and Or47b that have been implicated in pheromone sensation⁴⁶. The partially overlapping expressions of Teneurins in other PN and ORN classes (Fig. 2 and Supplementary Fig. 4) suggest a broader involvement of Teneurins. At the same time, additional cell-surface molecules are also needed to determine completely connection specificity of all 50 PN–ORN pairs.

Teneurins are present throughout Animalia (Fig. 1h). Different vertebrate teneurins are broadly expressed in distinct and partially overlapping patterns in the nervous system¹⁸. Teneurin-3 is expressed in the visual system and is required for ipsilateral retinogeniculate projections⁴⁷. Our study suggests that differential Teneurin expression may have a general role in matching pre- and postsynaptic partners. Indeed, high-level Ten-m is involved in matching select motor neurons and muscles²⁶. Furthermore, Ten-m and Ten-a also trans-synaptically mediate neuromuscular synapse organization²⁶. This suggests that the synapse partner matching function of Teneurins may have evolved from their basal role in synapse organization. Interestingly, synaptic partner matching only involves homophilic interactions (this study and ref. 26), whereas synapse organization preferentially involves heterophilic interactions²⁶. This could not be fully accounted for by the different strength of their homophilic and heterophilic interactions *in vitro* (Fig. 5a). We speculate that these dual functions of Teneurins *in vivo* may engage signalling mechanisms that further distinguish homophilic versus heterophilic interactions.

METHODS SUMMARY

Detailed methods on fly stocks, generation of the *ten-a* allele, construction of transgenic flies, clonal analysis, histology, imaging, quantification and statistical analysis, epitope-tagged constructs, and co-immunoprecipitation can be found in Methods.

Full Methods and any associated references are available in the online version of the paper at www.nature.com/nature.

Received 14 June 2011; accepted 6 February 2012.

Published online 18 March 2012.

- Sperry, R. W. Chemoaffinity in the orderly growth of nerve fiber patterns and connections. *Proc. Natl Acad. Sci. USA* **50**, 703–710 (1963).
- Dickson, B. J. Molecular mechanisms of axon guidance. *Science* **298**, 1959–1964 (2002).
- Zipursky, S. L. & Sanes, J. R. Chemoaffinity revisited: dscams, protocadherins, and neural circuit assembly. *Cell* **143**, 343–353 (2010).
- Luo, L. & Flanagan, J. G. Development of continuous and discrete neural maps. *Neuron* **56**, 284–300 (2007).
- Komiyama, T. & Luo, L. Development of wiring specificity in the olfactory system. *Curr. Opin. Neurobiol.* **16**, 67–73 (2006).
- Brochtrup, A. & Hummel, T. Olfactory map formation in the *Drosophila* brain: genetic specificity and neuronal variability. *Curr. Opin. Neurobiol.* **21**, 85–92 (2011).
- Jefferis, G. S. X. E. *et al.* Developmental origin of wiring specificity in the olfactory system of *Drosophila*. *Development* **131**, 117–130 (2003).
- Komiyama, T., Sweeney, L. B., Schuldiner, O., Garcia, K. C. & Luo, L. Graded expression of semaphorin-1a cell-autonomously directs dendritic targeting of olfactory projection neurons. *Cell* **128**, 399–410 (2007).
- Hong, W. *et al.* Leucine-rich repeat transmembrane proteins instruct discrete dendrite targeting in an olfactory map. *Nature Neurosci.* **12**, 1542–1550 (2009).
- Hummel, T. *et al.* Axonal targeting of olfactory receptor neurons in *Drosophila* is controlled by Dscam. *Neuron* **37**, 221–231 (2004).
- Hummel, T. & Zipursky, S. L. Afferent induction of olfactory glomeruli requires N-cadherin. *Neuron* **42**, 77–88 (2004).
- Sweeney, L. B. *et al.* Temporal target restriction of olfactory receptor neurons by Semaphorin-1a/PlexinA-mediated axon-axon interactions. *Neuron* **53**, 185–200 (2007).
- Lattmann, M. *et al.* Semaphorin-1a controls receptor neuron-specific axonal convergence in the primary olfactory center of *Drosophila*. *Neuron* **53**, 169–184 (2007).
- Chou, Y.-H., Zheng, X., Beachy, P. A. & Luo, L. Patterning axon targeting of olfactory receptor neurons by coupled Hedgehog signaling at two distinct steps. *Cell* **142**, 954–966 (2010).
- Zhu, H. *et al.* Dendritic patterning by Dscam and synaptic partner matching in the *Drosophila* antennal lobe. *Nature Neurosci.* **9**, 349–355 (2006).
- Kurusu, M. *et al.* A screen of cell-surface molecules identifies leucine-rich repeat proteins as key mediators of synaptic target selection. *Neuron* **59**, 972–985 (2008).
- Tucker, R. P. & Chiquet-Ehrismann, R. Teneurins: a conserved family of transmembrane proteins involved in intercellular signaling during development. *Dev. Biol.* **290**, 237–245 (2006).
- Tucker, R. P., Kenzelmann, D., Trzebiatowska, A. & Chiquet-Ehrismann, R. Teneurins: transmembrane proteins with fundamental roles in development. *Int. J. Biochem. Cell Biol.* **39**, 292–297 (2007).
- Young, T. R. & Leamey, C. A. Teneurins: important regulators of neural circuitry. *Int. J. Biochem. Cell Biol.* **41**, 990–993 (2009).
- Baumgartner, S. & Chiquet-Ehrismann, R. *Ten^a*, a *Drosophila* gene related to tenascin, shows selective transcript localization. *Mech. Dev.* **40**, 165–176 (1993).
- Baumgartner, S., Martin, D., Hagios, C. & Chiquet-Ehrismann, R. *Tenm*, a *Drosophila* gene related to tenascin, is a new pair-rule gene. *EMBO J.* **13**, 3728–3740 (1994).
- Psychiatric GWAS Consortium Bipolar Disorder Working Group. Large-scale genome-wide association analysis of bipolar disorder identifies a new susceptibility locus near *ODZ4*. *Nature Genet.* **43**, 977–983 (2011).
- Levine, A. *et al.* *odd Oz*: a novel *Drosophila* pair rule gene. *Cell* **77**, 587–598 (1994).
- Zheng, L. *et al.* *Drosophila* *Ten-m* and *Filamin* affect motor neuron growth cone guidance. *PLoS ONE* **6**, e22956 (2011).
- Liebl, F. L. W. *et al.* Genome-wide *P*-element screen for *Drosophila* synaptogenesis mutants. *J. Neurobiol.* **66**, 332–347 (2006).
- Mosca, T. J., Hong, W., Dani, V. S., Favaloro, V. & Luo, L. Trans-synaptic Teneurin signalling in neuromuscular synapse organization and target choice. *Nature* <http://dx.doi.org/10.1038/nature10923> (this issue).
- Li, H., Bishop, K. M. & O'Leary, D. D. M. Potential target genes of *EMX2* include *Odz/Ten-M* and other gene families with implications for cortical patterning. *Mol. Cell. Neurosci.* **33**, 136–149 (2006).
- Rubin, B. P., Tucker, R. P., Brown-Luedi, M., Martin, D. & Chiquet-Ehrismann, R. Teneurin 2 is expressed by the neurons of the thalamofugal visual system *in situ* and promotes homophilic cell-cell adhesion *in vitro*. *Development* **129**, 4697–4705 (2002).
- Oohashi, T. *et al.* Mouse *Ten-m/Odz* is a new family of dimeric type II transmembrane proteins expressed in many tissues. *J. Cell Biol.* **145**, 563–577 (1999).

30. Potter, C. J., Tasic, B., Russler, E. V., Liang, L. & Luo, L. The Q system: a repressible binary system for transgene expression, lineage tracing, and mosaic analysis. *Cell* **141**, 536–548 (2010).
31. Jefferis, G. S., Marin, E. C., Stocker, R. F. & Luo, L. Target neuron prespecification in the olfactory map of *Drosophila*. *Nature* **414**, 204–208 (2001).
32. Endo, K., Aoki, T., Yoda, Y., Kimura, K.-I. & Hama, C. Notch signal organizes the *Drosophila* olfactory circuitry by diversifying the sensory neuronal lineages. *Nature Neurosci.* **10**, 153–160 (2007).
33. Drescher, U. *et al.* *In vitro* guidance of retinal ganglion cell axons by RAGS, a 25 kDa tectal protein related to ligands for Eph receptor tyrosine kinases. *Cell* **82**, 359–370 (1995).
34. Cheng, H. J., Nakamoto, M., Bergemann, A. D. & Flanagan, J. G. Complementary gradients in expression and binding of ELF-1 and Mek4 in development of the topographic retinotectal projection map. *Cell* **82**, 371–381 (1995).
35. Feldheim, D. A. *et al.* Genetic analysis of ephrin-A2 and ephrin-A5 shows their requirement in multiple aspects of retinocollicular mapping. *Neuron* **25**, 563–574 (2000).
36. Yamagata, M. & Sanes, J. R. Dscam and Sidekick proteins direct lamina-specific synaptic connections in vertebrate retina. *Nature* **451**, 465–469 (2008).
37. Shinza-Kameda, M., Takasu, E., Sakurai, K., Hayashi, S. & Nose, A. Regulation of layer-specific targeting by reciprocal expression of a cell adhesion molecule, Capricious. *Neuron* **49**, 205–213 (2006).
38. Shishido, E., Takeichi, M. & Nose, A. *Drosophila* synapse formation: regulation by transmembrane protein with Leu-rich repeats, CAPRICIOUS. *Science* **280**, 2118–2121 (1998).
39. de Wit, J., Hong, W., Luo, L. & Ghosh, A. Role of leucine-rich repeat proteins in the development and function of neural circuits. *Annu. Rev. Cell Dev. Biol.* **27**, 697–729 (2011).
40. Shen, K., Fetter, R. D. & Bargmann, C. I. Synaptic specificity is generated by the synaptic guidepost protein SYG-2 and its receptor, SYG-1. *Cell* **116**, 869–881 (2004).
41. McLaughlin, T., Torborg, C. L., Feller, M. B. & O'Leary, D. D. M. Retinotopic map refinement requires spontaneous retinal waves during a brief critical period of development. *Neuron* **40**, 1147–1160 (2003).
42. Pfeifferberger, C., Yamada, J. & Feldheim, D. A. Ephrin-As and patterned retinal activity act together in the development of topographic maps in the primary visual system. *J. Neurosci.* **26**, 12873–12884 (2006).
43. Imai, T. *et al.* Pre-target axon sorting establishes the neural map topography. *Science* **325**, 585–590 (2009).
44. Serizawa, S. *et al.* A neuronal identity code for the odorant receptor-specific and activity-dependent axon sorting. *Cell* **127**, 1057–1069 (2006).
45. Couto, A., Alenius, M. & Dickson, B. J. Molecular, anatomical, and functional organization of the *Drosophila* olfactory system. *Curr. Biol.* **15**, 1535–1547 (2005).
46. van der Goes van Naters, W. & Carlson, J. R. Receptors and neurons for fly odors in *Drosophila*. *Curr. Biol.* **17**, 606–612 (2007).
47. Leamey, C. A. *et al.* Ten_m3 regulates eye-specific patterning in the mammalian visual pathway and is required for binocular vision. *PLoS Biol.* **5**, e241 (2007).

Supplementary Information is linked to the online version of the paper at www.nature.com/nature.

Acknowledgements We thank V. Favaloro for advice on biochemistry and D. Luginbuhl for technical assistance; K. Zinn for the EP collection; H. Zhu for the initial contribution; R. Wides and S. Baumgartner for *teneurin* reagents; B. Zhang, Bloomington, Kyoto, Harvard and Vienna Stock Centers for fly stocks; BestGene for injection service; and K. Shen, T. Clandinin, D. Berns, V. Favaloro, X. Gao, S. Hippenmeyer, C. Liu, K. Miyamichi and X. Yu for critiques. Supported by a National Institutes of Health (NIH) grant (R01 DC-005982 to L.L.), and Epilepsy, Neonatology and Developmental Biology Training Grants (NIH 5T32 NS007280 and HD007249 to T.J.M.). L.L. is an investigator of the Howard Hughes Medical Institute.

Author Contributions W.H. designed and performed all experiments. T.J.M. assisted in some experiments. L.L. supervised the project. W.H. and L.L. wrote the manuscript with feedback from T.J.M.

Author Information Reprints and permissions information is available at www.nature.com/reprints. The authors declare no competing financial interests. Readers are welcome to comment on the online version of this article at www.nature.com/nature. Correspondence and requests for materials should be addressed to L.L. (lluo@stanford.edu).

METHODS

Fly stocks. *Mz19-GAL4* (ref. 7) was used to label PNs. *Or-rCD2* lines^{15,48} (*Or47b-rCD2* and *Or88a-rCD2*), *Or-mCD8GFP* lines⁴⁵ (*Or23a-mCD8GFP*, *Or43a-mCD8GFP*, *Or46Aa-mCD8GFP*, *Or56a-mCD8GFP* and *Or83c-mCD8GFP*), *Or67d-GAL4* (ref. 49) and *AM29-GAL4* (ref. 32) were used to label ORNs. *GH146-Flp* (ref. 9), *ey-Flp* (ref. 50), *UAS>stop>mCD8GFP* (ref. 9) and *tubP>stop>GAL80* (ref. 51) were used to perform the intersectional expression analysis. *P{GS}9267* (*ten-m*) was generated by the *Drosophila* Gene Search Project (Metropolitan University)⁵² and *P{GE}1914* (*ten-a*)¹⁶ was from the GenExel collection of EP lines generated by the Korean Advanced Institute of Science and Technology. Their ability to drive the overexpression of each respective Teneurin was verified by elevated antibody staining.

All RNAi lines targeting *ten-m* or *ten-a* from the Vienna *Drosophila* RNAi Center (*UAS-ten-m*^{RNAi-V51173} and *UAS-ten-a*^{RNAi-V32482}), the Bloomington *Drosophila* Stock Center (*UAS-ten-m*^{RNAi-JF03323} and *UAS-ten-a*^{RNAi-JF03375}), and the National Institute of Genetics Fly Stock Center (*UAS-ten-m*^{RNAi-5723R} and *UAS-ten-a*^{RNAi-2590R}) were collected. The efficiency of all RNAi lines was tested by pan-neuronal expression using *C155-GAL4* followed by Ten-m or Ten-a antibody staining. *UAS-ten-m*^{RNAi-V51173} and *UAS-ten-m*^{RNAi-JF03323} targeting *ten-m*, and *UAS-ten-a*^{RNAi-V32482} and *UAS-ten-a*^{RNAi-JF03375} targeting *ten-a* were able to eliminate respective antibody staining beyond detection. *UAS-ten-m*^{RNAi-V51173} and *UAS-ten-a*^{RNAi-V32482} were used in all the experiments except Supplementary Fig. 6, in which *UAS-ten-m*^{RNAi-JF03323} and *UAS-ten-a*^{RNAi-JF03375} were used to confirm the RNAi phenotypes. *UAS-Dcr2* (ref. 53) was used to enhance RNAi efficiency.

To identify *ten-m-GAL4*, we collected a group of GAL4 enhancer traps⁵⁴ located near the 5' end of the *ten-m* gene. Their expression patterns were determined using a membrane-tagged GFP reporter *UAS-mCD8GFP* gene from the *Drosophila* Genetic Resource Center. *NP6658-GAL4*, which recapitulated the glomerulus-specific Ten-m staining pattern, was identified and referred to as *ten-m-GAL4*.

Generation of the *ten-a* allele. A small deficiency of *ten-a* was generated by FRT-mediated excision. This deficiency allele is homozygous viable and contains a deletion between *P{XP}d07540* and *P{Bac}WHJf01428*, which flanks the entire *ten-a* genomic region (~140 kb) and four additional predicted genes (Supplementary Fig. 2a), and is referred to as *Df(X)ten-a*. The deletion was verified by both PCR and antibody staining against Ten-a. The loss-of-function phenotypes were due to the loss of *ten-a* rather than the four additional predicted genes, as they mimicked the RNAi phenotypes.

Construction of UAS and QUAS transgenic flies. Ten-m and Ten-a coding sequences were amplified from the cDNA constructs^{23,55,56}. One primer amplified from the start codon and added a CACC overhang for the TOPO reaction and a Kozak sequence. The other primer amplified to the stop codon. The PCR products were subcloned into *pENTR-D/TOPO* (Invitrogen). A 46-bp irrelevant fragment was found in the middle of the *ten-m* coding sequence in the original cDNA construct, and was removed by replacing a small region containing this fragment with the corresponding region in the *ten-m* genomic DNA. To make *UAS-ten-m*, *UAS-ten-a*, *QUAS-ten-m* and *QUAS-ten-a*, *pENTR-ten-m* and *pENTR-ten-a* were recombined into destination vector *pUAS-Gateway-attB*⁵⁷ and *pQUAS-Gateway-attB* using LR Clonase II (Invitrogen). The destination vector *pQUAS-Gateway-attB* was constructed by replacing the UAS site in *pUAS-Gateway-attB* with a QUAS site. All constructs were sequence verified. All the UAS and QUAS transgenes were integrated into both *attP24* and *86Fb* landing sites^{58,59} on second and third chromosomes, respectively. All transgenic flies were verified by PCR and overexpression followed by antibody staining. The UAS and QUAS transgenes inserted in the *86Fb* site were used in this paper.

BAC recombineering to construct *Mz19-QF*. A 110-kb BAC (#CH321-85L03) in the *attB-P[acman]-CmR* vector⁶⁰, which contains genomic DNA that covers the *Mz19-GAL4* enhancer trap insertion site, was collected from the BACPAC Resources Center. The QF coding sequence, with a P-element minimal promoter and an hsp70 polyA, was amplified using primers containing 50-bp arm sequences allowing site-specific recombination. The 5-kb PCR product was recombined into the 110-kb genomic BAC using bacterial BAC recombineering and was verified by sequencing. The 115-kb *Mz19-QF* BAC was further verified by digestion pattern analysis and used to produce transgenes at the VK37 landing site⁶¹ on the second chromosome by BestGene. The *Mz19-QF* transgenic flies were verified by PCR and the expression of reporters *QUAS-mCD8GFP* or *QUAS-mTdt3HA*.

Clonal analysis. To determine the contribution of individual PNs to the ectopic connections with ORNs, the MARCM method⁶² was applied. Briefly, heat-shock-induced Flp activity caused mitotic recombination of the FRT chromosome arm such that one of the daughter cells lost *GAL80*. This cell (and its progeny) can therefore be labelled by the *GALA-UAS* system. For generating neuroblast clones, flies were heat-shocked between 24–48 h after egg laying for 1 h at 37 °C. *Mz19-GAL4* labels VA1d

and DC3 from the anterodorsal neuroblast and DA1 from the lateral neuroblast⁷. By generating neuroblast clones at 24–48 h after egg laying, we used *MZ19-GAL4* to specifically label DA1 or VA1d/DC3 PNs and simultaneously express RNAi targeting *ten-a*, or overexpress Ten-m or Ten-a in the labelled neurons.

In the *ten-a* mutant analysis, *Df(X)ten-a* was placed in *trans* to *GAL80* on the FRT chromosome arm. Upon Flp-induced mitotic recombination, one of the daughter cells became homozygous for *ten-a* and simultaneously lost *GAL80*. We used *MZ19-GAL4* to specifically label DA1 or VA1d/DC3 mutant PNs.

Different classes of ORNs, except for Or67d, were labelled by *Or-mCD8GFP* transgenes in a GAL4-independent manner, allowing the visualization of the specific matching between the labelled PNs and ORNs. Owing to the lack of an Or67d-*mCD8GFP*, Or67d ORNs were labelled by *Or67d-GAL4* and Ten-m overexpression was achieved by using *Mz19-QF* to drive *QUAS-ten-m* (Supplementary Fig. 9). In Teneurin overexpression by *Mz19-QF*, Or67d-*GAL4* expression was found unchanged compared with the control, and co-localized with Ncad staining in the DA1 glomerulus, which can be unambiguously identified (Supplementary Fig. 9). Therefore, Ncad staining in the DA1 glomerulus was used to determine the location of Or67d ORNs in Fig. 4f, l, in which Teneurins were overexpressed by *Mz19-GAL4*.

Histology. The procedures used for fixation and immunostaining were described previously⁶³. For primary antibodies, we used mouse nc82 (1:30), rat antibody to N-cadherin (1:40), rat antibody to mCD8 (1:100), mouse antibody to rCD2 (1:200), chicken antibody to GFP (1:1,000), mouse antibody to HA (1:1,000), rabbit antibody to HA (1:1,000), rabbit antibody to DsRed (1:500), mouse antibody (mAb20) to Ten-m (1:3,000)²³, and guinea pig antibody to Ten-a (1:100)⁶⁴. Neuropil staining indicates the antennal lobe, where PN dendrites and ORN axons are located. Fluorescent labelling outside the antennal lobe may come from labelled PN cell bodies or non-specific tissues.

Imaging, quantification and statistical analysis. Immunostained brains were imaged with a Zeiss LSM 510 Meta laser-scanning confocal microscope. Images of antennal lobes were taken as confocal stacks with 1-μm-thick sections. Representative single sections were shown to illustrate the matching and mismatching between PN dendrites and ORN axons. Penetration of phenotypes represents the percentage of animals in which at least one antennal lobe showed a given phenotype among the total animals examined. Percentage of intermingling represents the fraction of labelled dendrites located within the axonal area of a given ORN class, and was measured by dividing dendritic area by total axonal area in a single confocal plane that shows maximum intermingling between dendrites and axons. Statistical significance between two samples was determined by the unpaired Student's *t*-test.

Flag- and HA-tagged constructs. To express Flag- and HA-tagged proteins in S2 cells, the Gateway destination vectors *pUAS-Flag-Gateway(-w)* and *pUAS-HA-Gateway(-w)* were generated by removing a ~4.5-kb non-essential fragment between two DraIII sites that contains the *white* gene from the original Gateway vectors pTFW and pTHW (*Drosophila* gateway collection, DGRC, Bloomington), respectively. The modified destination vectors are ~40% smaller than the original ones while preserving all the essential components for S2 cell expression, and showed greater transfection and expression efficiency in S2 cells. To express Flag- and HA-tagged Teneurin proteins in S2 cells, *pENTR-ten-m* and *pENTR-ten-a* were recombined into modified destination vectors *pUAS-Flag-Gateway(-w)* and *pUAS-HA-Gateway(-w)* using LR Clonase II (Invitrogen). All expression constructs, including *UAS-Flag-ten-m*, *UAS-Flag-ten-a*, *UAS-HA-ten-m* and *UAS-HA-ten-a*, were sequence verified.

Co-immunoprecipitation assay. S2 cells were cultured in Schneider's insect medium (Sigma) according to the manufacturer's description. *UAS-Flag-ten-m*, *UAS-Flag-ten-a*, *UAS-HA-ten-m* or *UAS-HA-ten-a* constructs were separately transfected into S2 cells, along with an *Actin5c-GAL4* vector, using the Effectene transfection reagent (QIAGEN). The amount of each construct and the number of cells used for transfection were adjusted to ensure comparable expression levels of Ten-m and Ten-a proteins. Three days after transfection, separately transfected cells were harvested, mixed together, and incubated for 1 h at room temperature (25 °C). Equivalent amounts of untransfected cells were used as controls, and the final mixtures contained the same total amount of cells under all co-immunoprecipitation conditions. The mixed cells were lysed in lysis buffer (50 mM Tris-HCl pH 7.4, 10 mM MgCl₂, 150 mM NaCl, 1 mM EGTA, 10% glycerol) supplemented with 0.5% Nonidet P-40 and protease inhibitor cocktail (Sigma). The cell lysates were then incubated with EZview Red anti-Flag M2 affinity gel (Sigma) for 3 h at 4 °C with rotation. The samples were washed extensively in lysis buffer. The proteins were eluted in 2% SDS elution buffer, and were detected using western blot analysis using rat antibody to HA (1:1,000, Roche), mouse antibody to Flag (1:5,000, Sigma), and HRP-conjugated-goat antibodies to rat or mouse primaries (both at 1:20,000, Jackson ImmunoResearch).

48. Zhu, H. & Luo, L. Diverse functions of N-cadherin in dendritic and axonal terminal arborization of olfactory projection neurons. *Neuron* **42**, 63–75 (2004).

49. Kurtovic, A., Widmer, A. & Dickson, B. J. A single class of olfactory neurons mediates behavioural responses to a *Drosophila* sex pheromone. *Nature* **446**, 542–546 (2007).
50. Newsome, T. P., Asling, B. & Dickson, B. J. Analysis of *Drosophila* photoreceptor axon guidance in eye-specific mosaics. *Development* **127**, 851–860 (2000).
51. Bohm, R. A. *et al.* A genetic mosaic approach for neural circuit mapping in *Drosophila*. *Proc. Natl Acad. Sci. USA* **107**, 16378–16383 (2010).
52. Toba, G. *et al.* The gene search system. A method for efficient detection and rapid molecular identification of genes in *Drosophila melanogaster*. *Genetics* **151**, 725–737 (1999).
53. Dietzl, G. *et al.* A genome-wide transgenic RNAi library for conditional gene inactivation in *Drosophila*. *Nature* **448**, 151–156 (2007).
54. Hayashi, S. *et al.* GETDB, a database compiling expression patterns and molecular locations of a collection of Gal4 enhancer traps. *Genesis* **34**, 58–61 (2002).
55. Fascetti, N. & Baumgartner, S. Expression of *Drosophila* Ten-a, a dimeric receptor during embryonic development. *Mech. Dev.* **114**, 197–200 (2002).
56. Kinel-Tahan, Y., Weiss, H., Dgany, O., Levine, A. & Wides, R. *Drosophila* *odz* gene is required for multiple cell types in the compound retina. *Dev. Dyn.* **236**, 2541–2554 (2007).
57. Tea, J. S., Chihara, T. & Luo, L. Histone deacetylase Rpd3 regulates olfactory projection neuron dendrite targeting via the transcription factor Prospero. *J. Neurosci.* **30**, 9939–9946 (2010).
58. Markstein, M., Pitsouli, C., Villalta, C., Celniker, S. E. & Perrimon, N. Exploiting position effects and the gypsy retrovirus insulator to engineer precisely expressed transgenes. *Nature Genet.* **40**, 476 (2008).
59. Bischof, J., Maeda, R. K., Hediger, M., Karch, F. & Basler, K. An optimized transgenesis system for *Drosophila* using germ-line-specific ϕ C31 integrases. *Proc. Natl Acad. Sci. USA* **104**, 3312–3317 (2007).
60. Venken, K. J. T. *et al.* Versatile P[acman] BAC libraries for transgenesis studies in *Drosophila melanogaster*. *Nature Methods* **6**, 431–434 (2009).
61. Venken, K. J. T., He, Y., Hoskins, R. A. & Bellen, H. J. P[acman]: a BAC transgenic platform for targeted insertion of large DNA fragments in *D. melanogaster*. *Science* **314**, 1747–1751 (2006).
62. Lee, T. & Luo, L. Mosaic analysis with a repressible cell marker for studies of gene function in neuronal morphogenesis. *Neuron* **22**, 451–461 (1999).
63. Wu, J. S. & Luo, L. A protocol for dissecting *Drosophila melanogaster* brains for live imaging or immunostaining. *Nature Protocols* **1**, 2110–2115 (2006).
64. Rakovitsky, N. *et al.* *Drosophila* *Ten-a* is a maternal pair-rule and patterning gene. *Mech. Dev.* **124**, 911–924 (2007).

Transcription factor PIF4 controls the thermosensory activation of flowering

S. Vinod Kumar^{1*}, Doris Lucyshyn^{1†*}, Katja E. Jaeger¹, Enriqueta Alós¹, Elizabeth Alvey¹, Nicholas P. Harberd^{1,2} & Philip A. Wigge^{1†}

Plant growth and development are strongly affected by small differences in temperature¹. Current climate change has already altered global plant phenology and distribution^{2,3}, and projected increases in temperature pose a significant challenge to agriculture⁴. Despite the important role of temperature on plant development, the underlying pathways are unknown. It has previously been shown that thermal acceleration of flowering is dependent on the florigen, FLOWERING LOCUS T (FT)^{5,6}. How this occurs is, however, not understood, because the major pathway known to upregulate FT, the photoperiod pathway, is not required for thermal acceleration of flowering⁶. Here we demonstrate a direct mechanism by which increasing temperature causes the bHLH transcription factor PHYTOCHROME INTERACTING FACTOR4 (PIF4) to activate FT. Our findings provide a new understanding of how plants control their timing of reproduction in response to temperature. Flowering time is an important trait in crops as well as affecting the life cycles of pollinator species. A molecular understanding of how temperature affects flowering will be important for mitigating the effects of climate change.

Arabidopsis thaliana, like many higher plants, responds to warmer ambient temperatures by increasing its growth rate and accelerating the floral transition^{1,5,7}. *Arabidopsis* is a facultative long-day plant, and plants grown under short photoperiods are dramatically delayed in flowering. Interestingly, late flowering in short days can be overcome by growth at higher temperatures⁶. The underlying mechanism is, however, unknown. The flowering response to temperature is dependent on the floral pathway integrator gene *FT*⁶, indicative of a thermosensory pathway that upregulates FT expression independently of daylength. Because the bHLH transcription factor PIF4 has been shown to regulate architectural responses to high temperature^{8,9}, we tested if PIF4 is required for the induction of flowering at high temperature in short photoperiods. Although *pif4-101* was slightly delayed in flowering at 22 °C, *pif4-101* mutants showed a striking loss of thermal induction of flowering at 27 °C (Fig. 1a, b). To test if *pif4-101* perturbed floral induction by affecting FT expression, we examined the thermal induction of FT in Col-0 and *pif4-101*. Although FT expression was strongly thermally inducible in Col-0, this response was largely abolished in *pif4-101* at 27 °C (Fig. 1c), indicating that PIF4 is necessary for the thermal acceleration of flowering in short days. By contrast, PIF4 is not required for the thermosensory induction of flowering under continuous light⁸, suggesting that the photoperiod pathway also interacts with the ambient temperature sensing pathway. The reduced role of PIF4 under continuous light probably reflects the instability of PIF4 in light¹⁰ coupled with the fact that the output of the photoperiod pathway, CONSTANS (CO) protein, is stabilized by light¹¹, shifting the balance of floral induction from PIF4 to the photoperiod pathway. Because PIF4 is necessary for the thermal induction of flowering in short days, we tested if it is sufficient to trigger flowering when overexpressed. 35S::PIF4 caused extremely early flowering

(Fig. 1d, e), similar to the effect of overexpressing a related gene, PHYTOCHROME INTERACTING FACTOR5 (ref. 12), suggesting that PIF4 is limiting for the acceleration of flowering at lower temperature in short photoperiods. Consistently, 35S::PIF4 plants showed elevated levels of FT (Fig. 1f). Furthermore, 35S::PIF4 *ft-3* showed a complete suppression of the early flowering phenotype, indicating that the induction of flowering by 35S::PIF4 was dependent on FT (Fig. 1g, h). This activation of FT appears to be independent of the established

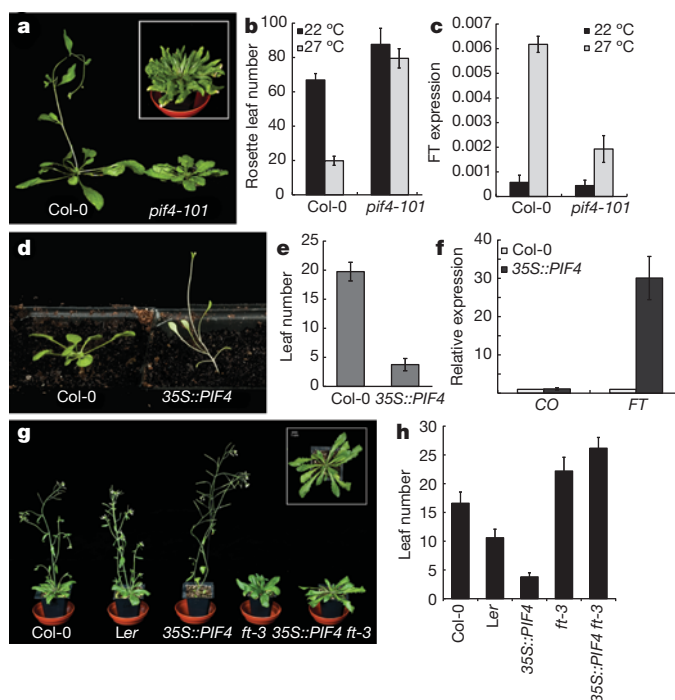


Figure 1 | PIF4 is necessary for the thermal induction of flowering in short photoperiods. **a**, *pif4-101* plants do not show acceleration of flowering at 27 °C compared with Col-0. Inset, a 16-week-old *pif4-101* plant grown at 22 °C. **b**, Rosette leaf numbers at flowering for Col-0 and *pif4-101* grown at 22 and 27 °C in short-photoperiod conditions (error bars, SD; *n* = 6). **c**, FT expression as measured by quantitative polymerase chain reaction (qPCR) in 4-week-old plants at 22 and 27 °C under short photoperiods in a PIF4-dependent manner (data from three biological replicates; error bars, SD). **d**, 35S::PIF4 overexpression triggers very early flowering. **e**, Leaf numbers at flowering for Col-0 and 35S::PIF4 in long photoperiods (error bars, SD; *n* = 5). **f**, CO and FT gene expression data measured by qPCR in Col-0 and 35S::PIF4 at 21 °C in long photoperiods (samples taken 2 weeks after sowing; data from three biological replicates; all error bars, SD). **g**, FT is required for the early flowering phenotype of 35S::PIF4 plants. When crossed into the *ft-3* background, the early flowering of 35S::PIF4 is completely suppressed. Inset, top view of the 35S::PIF4 *ft-3* plant showing that petiole elongation growth is retained. **h**, Flowering time data for Col-0, *Ler*, 35S::PIF4, *ft-3* and 35S::PIF4 *ft-3* plants (error bars, SD; *n* = 5).

¹Department of Cell and Developmental Biology, John Innes Centre, Norwich NR4 7UH, UK. ²Department of Plant Sciences, University of Oxford, South Parks Road, Oxford OX1 3RB, UK. [†]Present addresses: Institute for Applied Genetics and Cell Biology, BOKU–University for Applied Life Sciences and Natural Resources, Muthgasse 18, 41190 Vienna, Austria (D.L.); Sainsbury Laboratory, Cambridge University, Bateman Street, Cambridge CB2 1LR, UK (P.A.W.).

*These authors contributed equally to this work.

photoperiod pathway because *CO* did not change in response to *35S::PIF4* (Fig. 1f). Finally, although *co-9* mutants are late flowering^{6,13}, we found *35S::PIF4 co-9* plants were early flowering, indicating that *PIF4* acts largely independently of *CO* (Supplementary Information and Supplementary Fig. 1), consistent with the thermal induction of flowering being independent of the photoperiod pathway (Fig. 1f).

Although *PIF4* has been shown to be important for high-temperature responses, long-term increases in either *PIF4* transcript or *PIF4* protein levels in response to higher ambient temperature that can account for the observed growth responses have not been detected^{8,9}. To examine if variation of *PIF4* transcription under our experimental conditions might account for the increases in *PIF4* activity with temperature, we measured *PIF4* transcript levels at 12, 17, 22 and 27 °C in seedlings (Fig. 2a). *PIF4* transcript levels increased from 12 °C to 22 °C, whereas the difference between 22 °C and 27 °C was not statistically significant. Plants at 27 °C, compared with 22 °C, showed a very large *PIF4*-dependent response, suggesting that variation in the *PIF4* transcript is not sufficient to account for the acceleration of flowering at 27 °C compared with 22 °C. To test whether temperature-mediated changes in *PIF4* transcription are rate limiting for the biological response, we analysed the behaviour of plants constitutively expressing *PIF4*. Although *35S::PIF4* plants at 22 °C were extremely early flowering, this phenotype could be largely suppressed at 12 °C (Fig. 2b and Supplementary Fig. 2), indicating that even when *PIF4* transcript is abundant, lower temperatures are inhibitory for *PIF4* activity. A possible explanation for this difference is that *PIF4* protein is destabilized by low temperature. Indeed, *PIF4* protein levels have already been shown to be strongly regulated by light¹⁰, and growth in red and blue photocycles destabilizes *PIF4* protein at low temperatures¹⁴. The *PIF4* over-expression lines contain a fusion to the haemagglutinin (HA) epitope (*35S::PIF4:HA*). We therefore examined the levels of *PIF4:HA*, protein at 12, 17, 22 and 27 °C under the same light conditions used for our flowering time assays. Consistent with previous studies¹⁰ we saw a strong accumulation of *PIF4* at the end of the night period, which was subsequently degraded during the day. Despite the suppression of early flowering in *35S::PIF4* at 12 °C compared with 22 °C (Fig. 2b), we did not observe an appreciable difference in *PIF4* protein levels at

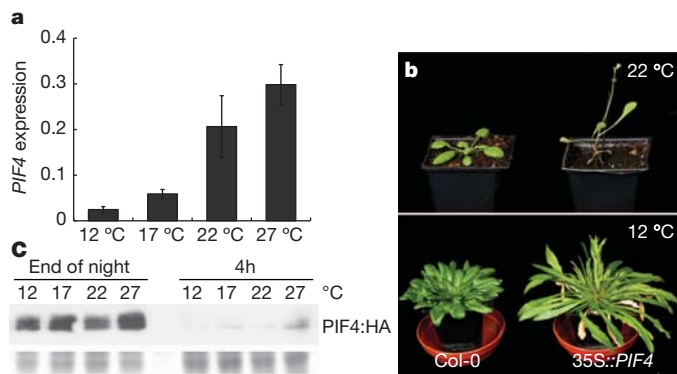


Figure 2 | Regulation of *PIF4* by temperature. **a**, Transcriptional regulation of *PIF4* by temperature. Ten-day-old Col-0 seedlings grown at 12, 17, 22 and 27 °C under short photoperiods were analysed for *PIF4* expression by qPCR. Data shown are from three biological replicates. Error bars, s.d. **b**, Flowering phenotype of *35S::PIF4* is temperature dependent. Although *35S::PIF4* plants (right) flower very early at 22 °C (upper panel) compared with Col-0 (left), this phenotype is largely suppressed by growth at 12 °C (lower panel). **c**, *PIF4* protein levels in *35S::PIF4* plants are not affected by growth temperature. Seven-day-old *35S::PIF4:HA* seedlings grown at 17 °C were transferred to 12, 17, 22 and 27 °C under short photoperiods for 2 days and samples were collected at the end of night before light and after 4 h under illumination. Although *PIF4:HA* protein levels are independent of growth temperatures, the protein is robustly degraded in presence of light. *PIF4:HA* protein was detected by horseradish peroxidase (HRP)-conjugated HA antibody. Stained lower half of the gel used for immunoblot is shown as loading control.

these two temperatures that was likely to account for these different phenotypes (Fig. 2c and Supplementary Fig. 3). Slightly higher levels of *PIF4:HA* appeared to be present at 27 °C (Fig. 2c), suggesting high-temperature stabilization of *PIF4* may also contribute to higher *PIF4* activity at 27 °C.

Taken together, these data indicate that *PIF4* regulates *FT* in a temperature-dependent manner. To determine if this is probably the case *in planta*, we analysed the spatial expression of *FT* and *PIF4*. *FT* has a distinctive pattern of expression in the vasculature of the leaf^{15,16}, and significantly *PIF4* was expressed in the same domain (Fig. 3a). Because the regulation of *FT* by *PIF4* could be either direct or indirect, we used chromatin immunopurification (ChIP) to analyse if *PIF4* binds directly to the *FT* promoter proximal to the transcriptional start site. This region of the promoter was chosen because it has been shown to be both phylogenetically conserved and the site for light-mediated regulation of *FT* expression^{16,17}. We observed robust enrichment of *PIF4* near to the transcriptional start site (Fig. 3b), indicating that *PIF4* binds this region *in vivo* to activate *FT* expression.

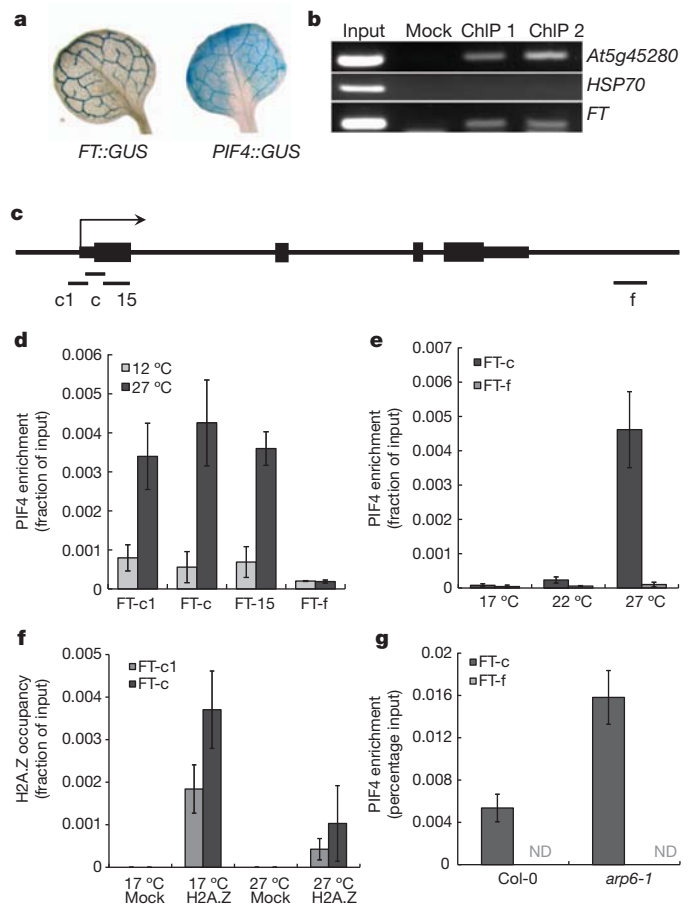


Figure 3 | *PIF4* directly binds the *FT* promoter in a temperature-dependent manner. **a**, β -Glucuronidase (GUS) histochemical analysis of the expression domains of *FT* and *PIF4* in rosette leaves. **b**, ChIP analysis shows *PIF4* binding to the *FT* locus *in vivo* in seedlings. The *At5g45280* promoter is a positive control for *PIF4*-binding activity²¹, the *HSP70* promoter was used as a negative control. **c**, Summary of the structure of the *FT* promoter and positioning of qPCR amplicons for ChIP analysis. **d**, ChIP analysis of *35S::PIF4:HA* at 12 and 27 °C (2-week-old seedlings, short photoperiods). **e**, ChIP analysis of *PIF4::PIF4:ProA* at 17, 22 and 27 °C (4-week-old soil-grown plants, short photoperiods). **f**, Analysis of H2A.Z occupancy at the *FT* locus at 17 and 27 °C (3-week-old plate-grown plants, short photoperiods). **g**, ChIP analysis of *PIF4* binding to *FT* in Col-0 and *arp6-1* (3-week-old soil-grown plants, 22 °C short photoperiod). (For all ChIP experiments, plant materials were collected at the end of dark period before lights came on and were protected from light until frozen. All data presented are from two independent ChIP experiments; all error bars, SD.)

Given the striking effect of ambient temperature on PIF4 activity, which occurs even when *PIF4* is constitutively expressed, we hypothesized that the ability of PIF4 to bind the *FT* promoter may be temperature dependent. To test this, we performed ChIP experiments using 35S::*PIF4* plants grown at 12 and 27 °C with primers flanking an E-box in the *FT* promoter (Fig. 3c). Strikingly, we observed a very strong temperature dependence for this binding, with an approximately fivefold increase in binding at 27 °C compared with 12 °C (Fig. 3d). This indicates that the later flowering of 35S::*PIF4* at 12 °C is caused by a decrease in PIF4 binding to *FT*. Because the 35S promoter causes strong ectopic expression of PIF4, we sought to confirm that PIF4 protein expressed at endogenous levels displays similar temperature-dependent binding to the *FT* promoter. We therefore performed ChIP experiments on a *pif4-101* line complemented with *PIF4_{pro}::PIF4:ProteinA* (Supplementary Fig. 4). Consistent with the overexpression studies, we observed a strong increase in PIF4 binding to *FT* as a function of temperature. Reduced binding was observed at 17 °C, consistent with the very late flowering of plants under short days at low temperature, but this binding increased at 22 °C and was even higher at 27 °C (Fig. 3e). The temperature-dependent binding of PIF4 to *FT* could be due to growth temperature influencing the affinity of the PIF4 transcription factor for its binding site, or the efficiency of the ChIP could be affected by the temperature at which tissues were grown. To test these possibilities, we analysed another recently described PIF4 target locus¹⁸, *CYP79B2* (At4g39950), which is upregulated in 35S::*PIF4* (Supplementary Fig. 5a). We found PIF4 binding to occur constitutively at both 12 and 27 °C at a region in the first exon (Supplementary Fig. 5b). Another region further upstream in the promoter showed a temperature-dependent binding of PIF4, and, in both cases, no enrichment was seen for a control locus (Supplementary Fig. 5b). This indicates that the abundant PIF4 protein we observed at 12 °C is active and able to bind target sites, and confirms that the ChIP method per se is not influenced by the temperature at which the sample is grown, consistent with other studies¹⁹. The ability of PIF4 to bind loci in a more temperature-independent manner might explain why 35S::*PIF4* at 12 °C maintains hypocotyl and petiole elongation, while early flowering is strongly suppressed. We do not exclude that temperature may also influence PIF4 activity post-translationally.

Temperature signals are mediated through H2A.Z-nucleosomes in *Arabidopsis*²⁰, suggesting that temperature may be increasing the accessibility of the PIF4-binding site at the *FT* promoter. Consistent with this hypothesis, we found that H2A.Z-nucleosomes were present at the PIF4-binding site in the *FT* promoter. Furthermore, we found that the levels of H2A.Z-nucleosomes at the *FT* promoter decreased with higher temperature (Fig. 3f). These results suggest that the presence of H2A.Z-nucleosomes is limiting for PIF4 binding to *FT*, and that the PIF4 binding we observed at higher temperature is due to the greater accessibility of chromatin containing H2A.Z-nucleosomes at higher temperature. This suggests that in the absence of H2A.Z-nucleosomes, PIF4 should bind *FT* more strongly. We therefore compared the ability of PIF4 expressed under its own promoter to bind to the *FT* promoter in wild type and *arp6-1*, a background lacking incorporation of H2A.Z-nucleosomes. Interestingly, we observed considerably greater binding of PIF4 in *arp6-1* (Fig. 3g), indicating that H2A.Z-nucleosomes are rate limiting for PIF4 to activate *FT* expression. The eviction of H2A.Z-nucleosomes by higher temperature therefore provides a direct mechanism for the temperature-regulated expression of *FT* (Fig. 4c). Consistent with our previous results and the established role of H2A.Z in regulating temperature-dependent gene expression, we found that there is increased PIF4 messenger RNA in *arp6-1* background (Supplementary Fig. 6). However, our results for 35S::*PIF4* suppression by 12 °C indicate that transcriptional upregulation of PIF4 is not the rate-limiting step in regulating PIF4-mediated flowering at higher temperatures.

Our results indicate that the temperature-dependent regulation of *FT* by PIF4 is controlled at the level of chromatin accessibility of the

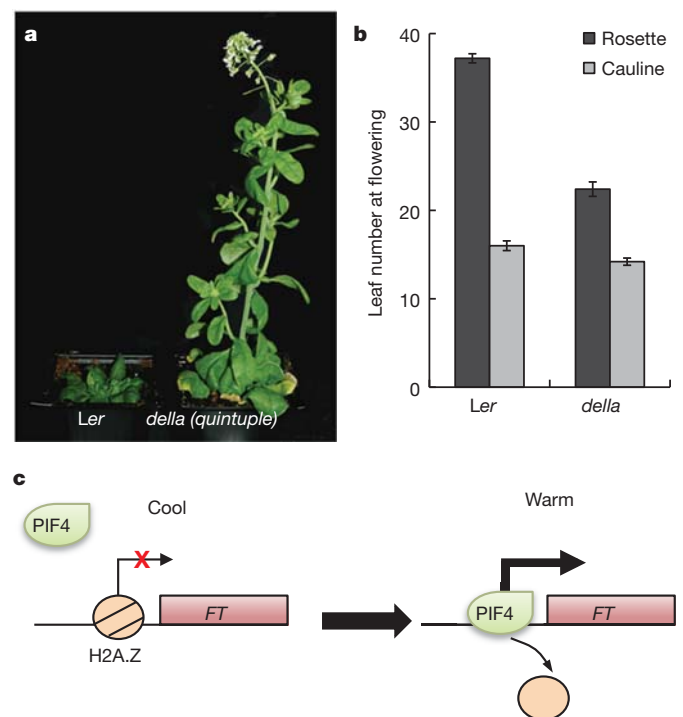


Figure 4 | PIF4 integrates environmental signals. **a**, Suppression of flowering at 12 °C is significantly repressed in the absence of DELLA-mediated repression. **b**, Leaf number at flowering for *della* global is reduced compared with *Ler* at 12 °C (error bars, SD; $n = 6$). **c**, Representation of temperature-dependent *FT* regulation by PIF4. Temperature-induced H2A.Z nucleosome dynamics can regulate PIF4 binding to target loci for transcriptional activation.

FT promoter and possibly at the level of PIF4 protein activity. PIF4 activity is controlled through the repressive activity of DELLA proteins that prevent PIF4 binding DNA^{21,22}.

Consistently, plants having reduced or absent DELLA function are early flowering²³. We hypothesized that delay in flowering at lower temperatures might at least in part be due to DELLA-mediated repression of PIF4 activity. If so, it would be expected that absence of DELLAs should cause accelerated flowering at lower temperatures. In accord with this expectation, we found that a mutant lacking DELLAs flowered much earlier than wild type when grown at 12 °C (Fig. 4a, b). The phytohormone gibberellin triggers DELLA protein degradation, and plays a key permissive role for *FT* induction, because in a gibberellin-deficient background, gibberellin application increases *FT* expression 15-fold²⁴. Although it was proposed more than 50 years ago that gibberellins are upstream of florigen²⁵, the mechanism has not been clear. As DELLA proteins have been shown to be key regulators by which gibberellin influences PIF4, our finding that PIF4 is able to activate *FT* directly suggests a possible mechanism by which changes in gibberellin levels may influence flowering.

Climate change has already caused measurable changes in plant phenology and behaviour², and plants that incorporate temperature information into their life cycles appear to be able to adapt to warmer conditions more effectively than those that primarily rely on photoperiod to synchronize their lifestyles³. The importance of the effects of climate change on yield are highlighted by the significant detrimental effects of increasing temperatures on yield⁴. *PIF4* is a central integrator of environmental information in the plant and our finding that it activates *FT* at higher temperatures suggests it will be a key node for breeding crops resilient to climate change. This importance is suggested by the recent discovery that natural variation at *PIF4* plays a major role in key ecological traits²⁶.

METHODS SUMMARY

Detailed descriptions of the plant growth conditions, growth assays, transgenic constructs and ChIP techniques are provided in the Supplementary materials.

Full Methods and any associated references are available in the online version of the paper at www.nature.com/nature.

Received 26 July 2010; accepted 6 February 2012.

Published online 21 March 2012.

- Samach, A. & Wigge, P. A. Ambient temperature perception in plants. *Curr. Opin. Plant Biol.* **8**, 483–486 (2005).
- Fitter, A. H. & Fitter, R. S. Rapid changes in flowering time in British plants. *Science* **296**, 1689–1691 (2002).
- Willis, C. G., Ruhfel, B., Primack, R. B., Miller-Rushing, A. J. & Davis, C. C. Phylogenetic patterns of species loss in Thoreau's woods are driven by climate change. *Proc. Natl Acad. Sci. USA* **105**, 17029–17033 (2008).
- Battisti, D. S. & Naylor, R. L. Historical warnings of future food insecurity with unprecedented seasonal heat. *Science* **323**, 240–244 (2009).
- Halliday, K. J., Salter, M. G., Thingnaes, E. & Whitelam, G. C. Phytochrome control of flowering is temperature sensitive and correlates with expression of the floral integrator FT. *Plant J.* **33**, 875–885 (2003).
- Balasubramanian, S., Sureshkumar, S., Lempe, J. & Weigel, D. Potent induction of *Arabidopsis thaliana* flowering by elevated growth temperature. *PLoS Genet.* **2**, e106 (2006).
- Blazquez, M. A., Ahn, J. H. & Weigel, D. A thermosensory pathway controlling flowering time in *Arabidopsis thaliana*. *Nature Genet.* **33**, 168–171 (2003).
- Koini, M. A. et al. High temperature-mediated adaptations in plant architecture require the bHLH transcription factor PIF4. *Curr. Biol.* **19**, 408–413 (2009).
- Stavang, J. A. et al. Hormonal regulation of temperature-induced growth in *Arabidopsis*. *Plant J.* **60**, 589–601 (2009).
- Nozue, K. et al. Rhythmic growth explained by coincidence between internal and external cues. *Nature* **448**, 358–361 (2007).
- Valverde, F. et al. Photoreceptor regulation of CONSTANS protein in photoperiodic flowering. *Science* **303**, 1003–1006 (2004).
- Lorrain, S., Allen, T., Duek, P. D., Whitelam, G. C. & Fankhauser, C. Phytochrome-mediated inhibition of shade avoidance involves degradation of growth-promoting bHLH transcription factors. *Plant J.* **53**, 312–323 (2008).
- Wenkel, S. et al. CONSTANS and the CCAAT box binding complex share a functionally important domain and interact to regulate flowering of *Arabidopsis*. *Plant Cell* **18**, 2971–2984 (2006).
- Foreman, J. et al. Light receptor action is critical for maintaining plant biomass at warm ambient temperatures. *Plant J.* **65**, 441–452 (2011).
- Takada, S. & Goto, K. Terminal flower2, an *Arabidopsis* homolog of heterochromatin protein1, counteracts the activation of flowering locus T by constans in the vascular tissues of leaves to regulate flowering time. *Plant Cell* **15**, 2856–2865 (2003).
- Adrian, J. et al. cis-regulatory elements and chromatin state coordinately control temporal and spatial expression of FLOWERING LOCUS T in *Arabidopsis*. *Plant Cell* **22**, 1425–1440 (2010).
- Liu, H. et al. Photoexcited CRY2 interacts with CIB1 to regulate transcription and floral initiation in *Arabidopsis*. *Science* **322**, 1535–1539 (2008).
- Franklin, K. A. et al. PHYTOCHROME-INTERACTING FACTOR 4 (PIF4) regulates auxin biosynthesis at high temperature. *Proc. Natl Acad. Sci. USA* **108**, 20231–20235 (2011).
- Angel, A., Song, J., Dean, C. & Howard, M. A Polycomb-based switch underlying quantitative epigenetic memory. *Nature* **476**, 105–108 (2011).
- Kumar, S. V. & Wigge, P. A. H2A.Z-containing nucleosomes mediate the thermosensory response in *Arabidopsis*. *Cell* **140**, 136–140 (2010).
- de Lucas, M. et al. A molecular framework for light and gibberellin control of cell elongation. *Nature* **451**, 480–484 (2008).
- Feng, S. et al. Coordinated regulation of *Arabidopsis thaliana* development by light and gibberellins. *Nature* **451**, 475–479 (2008).
- Mutasa-Gottgens, E. & Hedden, P. Gibberellin as a factor in floral regulatory networks. *J. Exp. Bot.* **60**, 1979–1989 (2009).
- Hisamatsu, T. & King, R. W. The nature of floral signals in *Arabidopsis*. II. Roles for FLOWERING LOCUS T (FT) and gibberellin. *J. Exp. Bot.* **59**, 3821–3829 (2008).
- Brian, P. W. Role of gibberellin-like hormones in regulation of plant growth & flowering. *Nature* **181**, 1122–1123 (1958).
- Brock, M. T., Maloof, J. N. & Weinig, C. Genes underlying quantitative variation in ecologically important traits: PIF4 (phytochrome interacting factor 4) is associated with variation in internode length, flowering time, and fruit set in *Arabidopsis thaliana*. *Mol. Ecol.* **19**, 1187–1199 (2010).

Supplementary Information is linked to the online version of the paper at www.nature.com/nature.

Acknowledgements We thank S. Prat, C. Fankhauser, K. Franklin, K. Goto, G. Coupland and D. Weigel for seeds. We are grateful to members of the Wigge laboratory for discussions. This work was supported in part by award No. KUK-I1-002-03 (to N.P.H.) made by King Abdullah University of Science and Technology and a Biotechnology and Biological Sciences Research Council (BBSRC) grant BB/I019022/1 (to S.V.K.). D.L. was supported by an Erwin Schrödinger Fellowship from the Austrian Science Fund FWF. P.A.W. was supported by start-up funds from the John Innes Centre and BBSRC, a BBSRC grant (BB/D0100470/1) and a European Research Council Starting Grant (ERC 243140).

Author Contributions S.V.K., D.L., K.E.J. and E.A. performed the experiments. N.P.H. and P.A.W. designed the study and supervised the work. All authors discussed the results and made substantial contributions to the manuscript.

Author Information Reprints and permissions information is available at www.nature.com/reprints. The authors declare no competing financial interests. Readers are welcome to comment on the online version of this article at www.nature.com/nature. Correspondence and requests for materials should be addressed to P.A.W. (philip.wigge@slcu.cam.ac.uk).

METHODS

Plant material and growth conditions. All plant lines used were in Col-0 background unless otherwise specified. *pif4-101* mutant was provided by C. Fankhauser, HA-tagged 35S::PIF4 by S. Prat¹². All references to '35S::PIF4' and 'PIF4:HA' refer to this line: that is, 35S::PIF4:HA. FT::GUS was obtained from K. Goto¹⁵. 35S::PIF4:HA *co-9* was obtained by crossing. The crosses were genotyped for presence of the 35S::PIF4 construct by PCR on genomic DNA using primers 2362 and 2363, resulting in two products of different size representing the complementary DNA (cDNA) transgene and the genomic DNA fragment, respectively. *co-9* was genotyped with primers 3650 and 3652 for insertion, and 3291 and 3292 for the wild-type fragment. For genotyping *phyb-9*, DNA was amplified using oligonucleotides 2137 and 2138 followed by MnlI digestion to distinguish between wild-type and mutant alleles. The global *della* mutant is in the *Ler* background and was described previously⁸. PIF4::PIF4:ProteinA and PIF4::PIF4:GUS were constructed by amplifying the genomic fragment of PIF4 including the promoter with oligonucleotides 1534 and 1535. The PCR product was cloned into pENTR/D-TOPO (Invitrogen) and inserted into the binary plasmids PW889 (carboxy-terminal ProteinA) and PW395 (carboxy-terminal GUS), respectively, using Gateway technology (Invitrogen). Transgenic plants were obtained by transforming *pif4-101* by floral dip. For hypocotyl measurements, seeds were surface sterilized, sown on ½ MS media, stratified for 2 days at 4 °C in the dark and germinated for 24 h at 22 °C. The plates were then transferred to short-day conditions (8/16 h photoperiod) at 22 and 27 °C respectively, and grown vertically for 10 days before being imaged and the hypocotyl length measured using the ImageJ software (<http://rsbweb.nih.gov/ij/>). Oligonucleotide sequences are provided in Supplementary Table 1.

Transcript analysis. Samples from plants grown in long days (16/8 h photoperiod) were collected and total RNA was extracted using Trizol Reagent (Invitrogen). RNA (2 µg) was treated with DnaseI (Roche) and used for cDNA synthesis (First strand cDNA synthesis kit, Fermentas). cDNA was diluted 1:8 and used for qPCR with a Roche Lightcycler 480 and the corresponding Sybr Green master mix. To detect *FT* transcript levels, oligonucleotides 3180 and 3181 were used; for *CO*, oligonucleotides 2951 and 2952. PIF4 transcript levels were analysed using oligonucleotides 3952 and 3953. Oligonucleotides 3247 and 3408 amplifying *TUB6* (At5g12250) were used for normalization.

Immunoblot analysis. To analyse the possible effect of temperature on PIF4 protein stability, plants overexpressing PIF4:HA (35S::PIF4:HA) were used. Seven-day-old 35S::PIF4:HA seedlings grown in short days at 17 °C were transferred to 12, 17, 22 and 27 °C in short days for 2 days. Samples were collected at end of night and

thereafter 30 min, 1 h and 4 h under illumination. Protein samples were separated by SDS–polyacrylamide gel electrophoresis and transferred on to nitrocellulose membrane. PIF4:HA was detected using HRP-conjugated HA antibody (Miltenyi Biotech) and visualized by chemiluminescent detection using Immobilon Chemiluminescent HRP substrate (Millipore).

GUS histochemical assay. For GUS-staining, plants were grown on ½ MS plates in long days (16/8 h photoperiods) for 10 days and kept in the dark for 24 h before collecting. Plants were stained in buffer containing 100 mM phosphate buffer, pH 7, 10 mM EDTA, 0.1% Triton-X100, 0.5 mM K-ferrocyanide and 1 mM X-Gluc at 37 °C for 24 h before de-staining in ethanol.

ChIP. ChIP was performed as described²⁰ with minor modifications. 35S::PIF4:HA seedlings were grown on ½ MS plates for 10 days and kept in the dark for 24 h at respective temperatures before collecting. Plant tissue (1.5 g) and 4 µg of antibody (HA-tag antibody ab9110 from Abcam) were used for ChIP. To analyse the dynamics of PIF4::PIF4:ProteinA, plants were grown in respective temperatures under short-day conditions for 4 weeks. Aerial parts of the plants were collected and cross-linked before being used for chromatin preparations. ChIP was done using magnetic beads (Dynabeads M-270 Epoxy, Invitrogen) coated with rabbit IgG (Sigma, I5006) as described (<http://www.ncdir.org/protocols/Rout/Conjugation%20of%20Dynabeads.pdf>). To analyse H2A.Z dynamics at the *FT* locus in response to temperature, we used 3-week-old seedlings of *HTA11::HTA11:GFP* grown at 17 and 27 °C. ChIP was done using anti-GFP antibody (Abcam, ab290). To analyse PIF4 binding in Col-0 and *arp6-1* backgrounds, respective genotypes with PIF4::PIF4:3XFLAG were grown on soil at 22 °C under short photoperiods for 3 weeks before samples were fixed by formaldehyde cross-linking. ChIP was performed using anti-Flag M2 affinity gel (Sigma A2220). Immuno-complexes were eluted using 3× Flag peptide (Sigma F4799) according to the manufacturer's instructions. Immunoprecipitated DNA was eluted after reverse cross-linking by boiling at 95 °C for 1 min in the presence of 10% Chelex (BioRad laboratories) followed by treatment with Proteinase K. Oligonucleotides 3255 and 3256 for FT-15 region, 3613 and 3614 for FT-c1, 3607 and 3608 for FT-c and 3261 and 3262 for FT-f were used for detecting PIF4 binding to the *FT* locus. As a positive control for PIF4 binding, At5g45280 was analysed using oligonucleotides 2857 and 2958. *HSP70* was used as a negative control using oligonucleotides 1862 and 1865. To analyse PIF4 binding at At4g39950, oligonucleotides 4240 and 4241 was used for region 1, and oligonucleotides 4246 and 4247 were used for region 2. Oligonucleotides 1860 and 1861 were used for *HSP70* as a negative control. Oligonucleotide sequences are provided in Supplementary Table 1.

Small-molecule inhibitors of the AAA+ ATPase motor cytoplasmic dynein

Ari J. Firestone^{1*}, Joshua S. Weinger^{2*}, Maria Maldonado², Kari Barlan³, Lance D. Langston², Michael O'Donnell², Vladimir I. Gelfand³, Tarun M. Kapoor² & James K. Chen¹

The conversion of chemical energy into mechanical force by AAA+ (ATPases associated with diverse cellular activities) ATPases is integral to cellular processes, including DNA replication, protein unfolding, cargo transport and membrane fusion¹. The AAA+ ATPase motor cytoplasmic dynein regulates ciliary trafficking², mitotic spindle formation³ and organelle transport⁴, and dissecting its precise functions has been challenging because of its rapid timescale of action and the lack of cell-permeable, chemical modulators. Here we describe the discovery of ciliobrevins, the first specific small-molecule antagonists of cytoplasmic dynein. Ciliobrevins perturb protein trafficking within the primary cilium, leading to their malformation and Hedgehog signalling blockade. Ciliobrevins also prevent spindle pole focusing, kinetochore-microtubule attachment, melanosome aggregation and peroxisome motility in cultured cells. We further demonstrate the ability of ciliobrevins to block dynein-dependent microtubule gliding and ATPase activity *in vitro*. Ciliobrevins therefore will be useful reagents for studying cellular processes that require this microtubule motor and may guide the development of additional AAA+ ATPase superfamily inhibitors.

The AAA+ superfamily of enzymes couples ATP hydrolysis with the generation of mechanical force to regulate diverse aspects of prokaryote and eukaryote biology¹. ATP-dependent conformational changes can propagate through these molecular machines to complete cellular processes within seconds, and chemical inhibitors that act rapidly and reversibly are much-needed tools for investigating the cellular functions of individual superfamily members. Yet, so far, only one AAA+ ATPase mechanoenzyme has been selectively targeted by a small molecule⁵.

We recently conducted a high-throughput screen for inhibitors of the Hedgehog (Hh) pathway (Fig. 1a)⁶, a key mediator of embryonic development and oncogenesis⁷. Our study was designed to identify compounds that act downstream of Smoothened (Smo), a transmembrane Hh signalling protein, and one of the small molecules, HPI-4 (Fig. 1b; 1), blocked Hh pathway activation in cells lacking the negative regulator Suppressor of Fused (Sufu)⁶. Prolonged treatment of cells with this benzoyl dihydroquinazolinone also reduced the number and size of primary cilia, a microtubule-based extension of the plasma membrane that is required for Hh signalling⁸. Intrigued by these cellular phenotypes, we investigated the biochemical mechanism of HPI-4.

We first synthesized a series of analogues (Fig. 1b; 2–9) and evaluated their effects on Hh signalling and primary cilia formation (Fig. 1c, d and Supplementary Figs 1–3). Chemical derivatives lacking either a 3- or 4-chloro substituent on the benzoyl ring system (2 and 6) or the acyclic ketone (9) were significantly less active in either assay (Fig. 1b, d). The other small molecules segregated into 2,4-dichlorobenzoyl dihydroquinazolinones that inhibit both Hh signalling and primary cilia formation (1, 3–5), which we henceforth name 'ciliobrevins A–D', and monochlorobenzoyl analogues that can block Hh target gene expression without inducing ciliary defects (7 and 8) (Fig. 1b, d).

Hh signalling is primarily mediated by the transcription factors Gli2 and Gli3, which exist in a pathway state-dependent balance of amino (N)-terminal repressors (Gli2/3R), full-length polypeptides (Gli2/3FL) and transcriptional activators (Gli2/3A) (Fig. 1a)⁷. Both repressor and activator formation require the primary cilium⁸, and accordingly ciliobrevins altered the Gli3FL/Gli3R ratio in cells stimulated with the N-terminal domain of Sonic Hedgehog (Shh-N) (Fig. 1e; 30 μ M doses of each compound). Shh-N-dependent Gli3FL phosphorylation was also reduced by these compounds, perhaps reflecting loss of Gli3A⁹. In contrast, none of the other analogues had a significant effect on the Gli3 processing or phosphorylation state (Fig. 1e).

To understand better the basis of these phenotypes, we took advantage of the temporal control afforded by chemical perturbations. Although prolonged exposure to these compounds causes defects in axonemal morphology, shorter treatments can divulge ciliobrevin-sensitive processes within structurally intact cilia. Because Hh pathway activation coincides with Gli2 accumulation at the distal ciliary tip¹⁰, we examined the effect of ciliobrevins on Gli2 localization (Fig. 1f). We incubated Hh-responsive cells with individual compounds at a 30 μ M concentration in the absence or presence of Shh-N-conditioned medium for 4 h. Gli2 localization was unchanged by derivatives that do not significantly perturb ciliogenesis (2 and 8), whereas ciliobrevins A and D (1 and 5) induced ciliary Gli2 levels comparable to that in Shh-N-stimulated cells.

The ability of ciliobrevins to increase ciliary Gli2 levels suggests that these compounds might target protein trafficking mechanisms within this organelle. Intraflagellar transport (IFT) can be resolved into anterograde trafficking, which requires the plus-end-directed motor kinesin-2 and the IFTB multisubunit complex, and retrograde trafficking, which uses the minus-end-directed motor cytoplasmic dynein 2 and the IFTA complex⁸. Loss of the primary cilia-specific cytoplasmic dynein 2 heavy chain (Dync2h1) alters cilia morphology¹¹, reduces Hh target gene expression¹¹ and increases ciliary levels of Gli2¹⁰. Similarities between these genetic phenotypes and the effects of ciliobrevins led us to hypothesize that these small molecules might inhibit cytoplasmic dynein 2. We therefore examined the effect of ciliobrevins on the subcellular localization of IFTB component IFT88, which requires cytoplasmic dynein 2-dependent retrograde transport for its return to the basal body. Treating cells for 1 hour with ciliobrevin D (5) but not DMSO or an inactive analogue (2) significantly increased IFT88 levels at the distal tip of primary cilia (Supplementary Fig. 4), providing further evidence that ciliobrevins inhibit cytoplasmic dynein 2 function.

Cytoplasmic dynein complexes have other cellular functions, including the crosslinking and focusing of microtubule minus ends within the mitotic spindle³. These actions create the fusiform shape and localize γ -tubulin-containing complexes to the spindle poles³. Cytoplasmic dynein 1 inhibition by blocking antibodies or dominant-negative constructs perturbs spindle assembly, resulting in disorganized poles and reduced γ -tubulin recruitment^{3,12–14}. To determine whether

¹Department of Chemical and Systems Biology, Stanford University School of Medicine, Stanford, California 94305, USA. ²Laboratory of Chemistry and Cell Biology, Rockefeller University, New York City, New York 10021, USA. ³Department of Cell and Molecular Biology, Northwestern University School of Medicine, Chicago, Illinois 60611, USA.

*These authors contributed equally to this work.

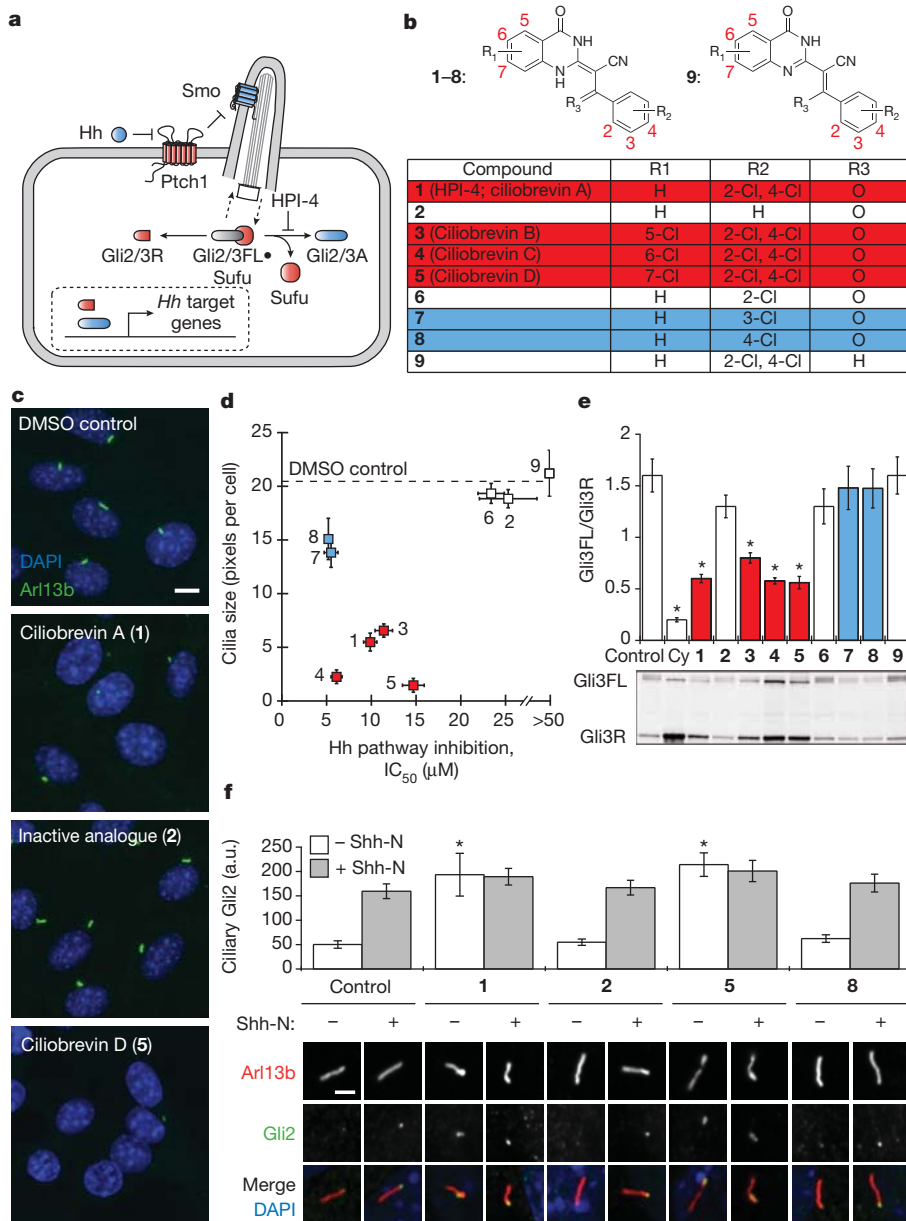


Figure 1 | Ciliobrevins disrupt primary cilium-dependent Gli regulation.
a, Depiction of Hh signalling with positive (blue) and negative (red) regulators.
b, Dihydroquinazolinone structures. **c**, Ciliary phenotypes after treatment with individual compounds (30 μ M) for 24 h. Scale bar, 10 μ m. **d**, Compound effects on Hh target gene expression in Shh-LIGHT2 cells³⁰ and cilia size in Shh-EGFP cells⁶. Half-maximum inhibitory concentration (IC₅₀) values are the average of three independent experiments \pm s.d., and cilia size is defined as the average number of Arl13b-positive pixels per nuclei for ten micrographs \pm s.d., each containing approximately 150 cells. Small molecules that block Hh signalling alone (blue) and those that inhibit both Hh pathway activity and ciliogenesis

(ciliobrevins; red) are highlighted. **e**, Gli3FL and Gli3R levels in Shh-EGFP cells treated with Shh-N and either individual dihydroquinazolinones (30 μ M), 3 μ M cyclopamine or DMSO for 16 h. Average Gli3FL/Gli3R ratios for five independent experiments \pm s.e.m. and a representative immunoblot are shown, with asterisks indicating $P < 0.005$ for individual compounds versus DMSO and cyclopamine (Cy). **f**, Ciliary Gli2 levels (a.u., arbitrary units) in Shh-EGFP cells treated with selected ciliobrevins (**1** and **5**), inactive analogues (**2** and **8**) or DMSO for 4 h. Average Gli2 levels in the distal end of at least 25 cilia \pm s.e.m. and representative confocal micrographs are shown. Asterisks indicate $P < 0.005$ for individual compounds versus DMSO. Scale bar, 2 μ m.

ciliobrevins recapitulate these phenotypes, we treated a metaphase-enriched population of NIH-3T3 cells with 50 μ M of either ciliobrevin D (**5**) or an inactive analogue (**2**) for 1 hour and examined their mitotic structures. Cells treated with ciliobrevin D showed abnormal (unfocused, multipolar or collapsed) spindles with disrupted γ -tubulin localization (Fig. 2a, b and Supplementary Fig. 5a), whereas cells incubated with the non-cilia-disrupting analogue or vehicle alone showed normal spindle morphologies. Similar ciliobrevin-induced spindle defects were observed in HeLa cells, although to a lesser extent (Fig. 2b). Cytoplasmic dynein 1 is also required for establishing stable kinetochore-microtubule interactions¹⁵, and ciliobrevin D treatment disrupted the formation of

cold-stable microtubules that mediate proper spindle-chromosome attachments (Fig. 2c).

To investigate if these spindle-disruptive effects were associated with altered dynein localization, we examined binding partners that recruit or co-localize with this motor. Immunofluorescence microscopy showed that p150-Glued, a dynactin component proposed to recruit dynein to kinetochores and spindle poles during mitosis¹⁶, was localized to the disorganized spindle poles of ciliobrevin D-treated cells (Fig. 2d and Supplementary Fig. 5b). Kinetochores targeting of p150-Glued was also unaffected by ciliobrevin D, as assessed in nocodazole-treated cells to obviate effects due to microtubule-attachment status

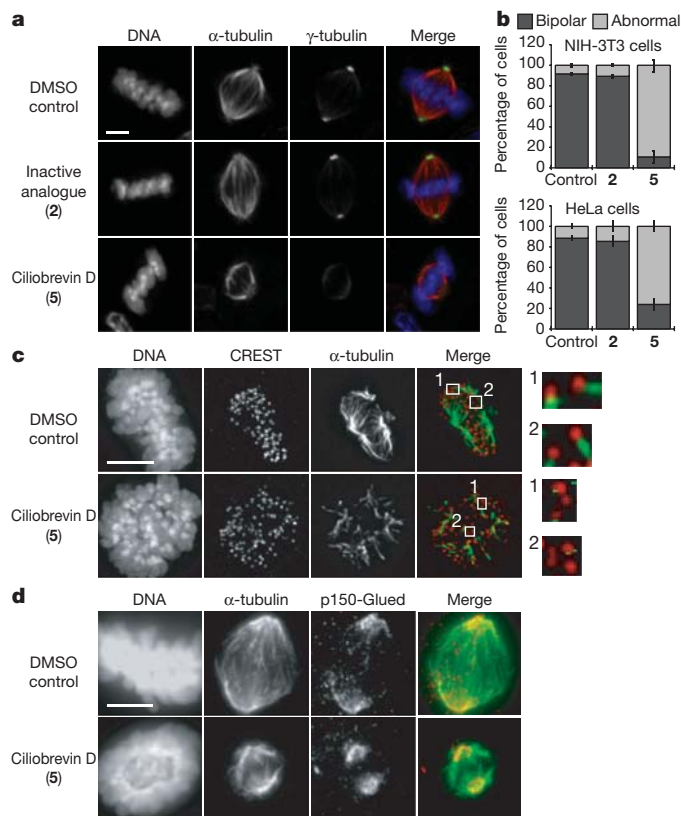


Figure 2 | Ciliobrevins disrupt spindle pole assembly and kinetochore-microtubule attachment. **a**, Mitotic spindles observed in NIH-3T3 cells treated with MG132 for 90 min and subsequently cultured with either an inactive analogue (2) or ciliobrevin D (5) at a 50 μ M dose or DMSO for 1 h. Staining for DNA, α -tubulin and γ -tubulin is shown. **b**, Quantification of spindle phenotypes in NIH-3T3 and HeLa cells treated as described above and scored for either bipolar or abnormal morphologies. Data are the average of three independent experiments \pm s.e.m., each including at least 150 spindles. **c**, Kinetochore-microtubule interactions analysed in metaphase-arrested NIH-3T3 cells treated with DMSO or 50 μ M 5 and then incubated on ice for 10 min. Staining for DNA, the kinetochore marker CREST and α -tubulin is shown. Insets highlight individual kinetochore-microtubule attachments or untethered kinetochores (400 \times magnification). **d**, Localization of p150-Glued in metaphase-arrested NIH-3T3 cells treated with DMSO or 50 μ M 5. Staining for DNA, α -tubulin and p150-Glued is shown. Scale bars: **a**, 4 μ m; **c**, **d**, 5 μ m.

(Supplementary Fig. 6). We similarly observed that Zeste white 10 (Zw10), a component of the Rod/Zw10/Zwlich complex that recruits cytoplasmic dynein 1 to kinetochores¹⁷, and the kinetochore-associated protein Centromere protein E (CENP-E)¹⁸ correctly localized to kinetochores under these conditions (Supplementary Fig. 6), indicating that their recruitment and the kinetochore structure itself are not disrupted by ciliobrevins. Thus, ciliobrevin-induced spindle phenotypes most likely result from dynein inhibition rather than mislocalization.

To characterize further the mitotic defects associated with ciliobrevin treatment, we conducted real-time confocal microscopy of green fluorescent protein (GFP)-tubulin-expressing NIH-3T3 cells (Supplementary Figs 7, 8). Within minutes of ciliobrevin D treatment, spindles collapsed, bipolarity was lost and spindle poles appeared disorganized (Supplementary Fig. 7b). Upon compound washout, bipolar spindles quickly re-emerged and chromosomes segregated at anaphase without any pronounced defects (Supplementary Fig. 7c, d). Ciliobrevin D addition also reversibly disrupted the pre-formed spindles of metaphase-arrested cells (Supplementary Fig. 8b, c) and reduced overall microtubule levels (Supplementary Fig. 8d). These latter effects are mitosis-specific, as microtubule levels in non-dividing cells were unaffected by inhibitor treatment (Supplementary Fig. 7e, f). Taken together, these results reveal that cytoplasmic dynein is not only

required for spindle pole assembly but also actively participates in its maintenance.

Cytoplasmic dynein 1 also regulates organelle trafficking, such as the melatonin-induced aggregation of melanosomes in *Xenopus* melanophores¹⁹. To determine if melanosome trafficking is sensitive to ciliobrevins, we cultured *Xenopus* melanophores with melanocyte-stimulating hormone to disperse these pigment granules and then treated the cells with melatonin and various concentrations of ciliobrevin D (5) or an inactive analogue (2). Ciliobrevin D reversibly inhibited melanosome aggregation, but the non-cilia-disrupting derivative had no discernible effect at comparable doses (Fig. 3a, b and Supplementary Movies 1–3). Ciliobrevin D similarly abrogated the movement of peroxisomes in *Drosophila* S2 cells (Fig. 3c–e and Supplementary Movies 4 and 5), consistent with the role of cytoplasmic dynein in their bidirectional motility²⁰.

Collectively, these results indicate that ciliobrevins are specific, reversible inhibitors of disparate cytoplasmic dynein-dependent processes. Ciliobrevins do not perturb cellular mechanisms that are independent of dynein function, including actin cytoskeleton organization (Supplementary Fig. 9) and the mitogen-activated protein kinase and phosphoinositol-3-kinase signalling pathways⁶. To examine more directly whether cytoplasmic dynein is the direct target of ciliobrevins, we evaluated their effects on dynein-dependent microtubule gliding *in vitro*. Ciliobrevins A and D (1 and 5) retarded the ATP-dependent

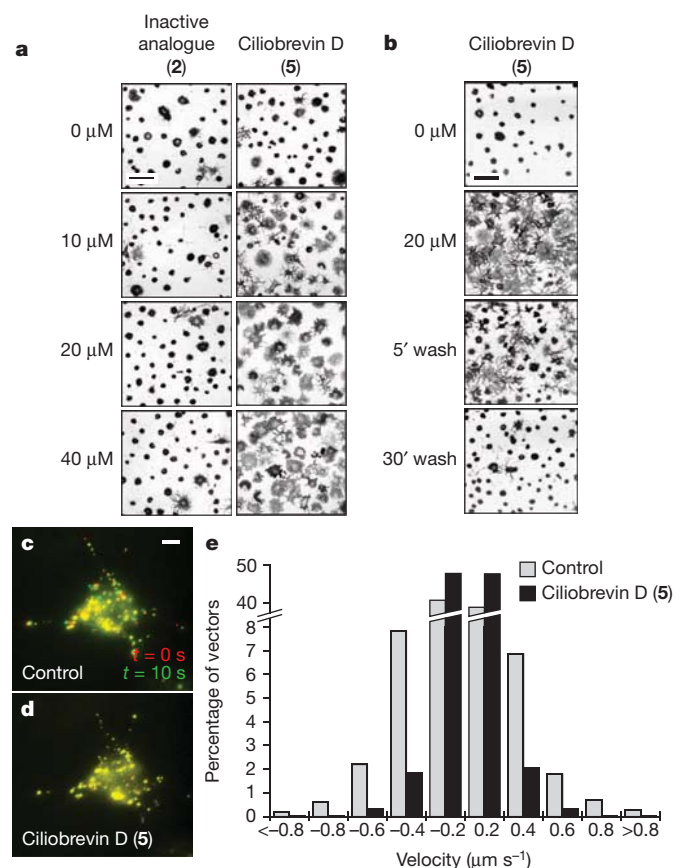


Figure 3 | Ciliobrevins inhibit melanosome aggregation and peroxisome motility. **a**, Brightfield images of *Xenopus* melanophores treated with various concentrations of ciliobrevin D (5) or an inactive derivative (2) for 10 min, stimulated with melatonin in the presence of the compounds for 30 min, and then paraformaldehyde-fixed. **b**, Melanophores treated with 5 as before, washed in medium containing melatonin alone, and then imaged. Scale bars, 100 μ m. **c**, **d**, Motility of GFP-labelled peroxisomes in *Drosophila* S2 cells cultured in the absence (**c**) or presence (**d**) of 5. Overlays of videomicroscopy frames at $t = 0$ s (red) and $t = 10$ s (green) are shown. Scale bar, 5 μ m. **e**, Vector distributions for the GFP-labelled peroxisomes with movement towards and away from the cell centre denoted by negative and positive bin values, respectively.

movement of fluorescently labelled microtubules on bovine cytoplasmic dynein-coated glass slides in a reversible and dose-dependent manner (Fig. 4a–c, Supplementary Fig. 10 and Supplementary Movies 6–8); analogues that did not perturb cytoplasmic dynein-dependent processes in our cell-based assays (2 and 8) had minimal effects (Fig. 4a, b and Supplementary Movie 9). The conserved structure–activity relationships of dihydroquinazolinones in the microtubule gliding and cell-based assays confirm cytoplasmic dynein as the ciliobrevin target, and neither ciliobrevin A nor D significantly affected K560/kinesin-1-dependent microtubule gliding *in vitro* at 100 μM concentrations (Fig. 4d and Supplementary Movies 10–12). The compounds do not broadly target members of the AAA+ ATPase family either, as they have no effect on p97-dependent degradation of endoplasmic-reticulum-associated proteins (Supplementary Fig. 11) or Mcm2–7-mediated DNA unwinding (Supplementary Fig. 12).

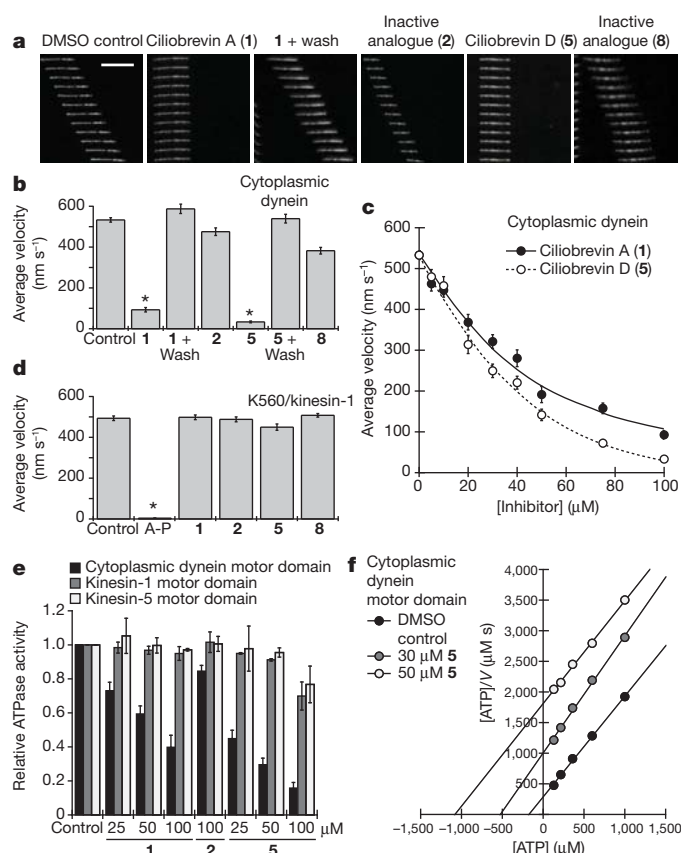


Figure 4 | Ciliobrevins inhibit cytoplasmic dynein-dependent microtubule gliding and ATPase activity. **a**, Montages of fluorescent microtubules moving on bovine dynein-coated glass slides in the presence of ATP and either DMSO, ciliobrevin A (1), ciliobrevin D (5) or non-cilia-disrupting analogues (2 and 8). All compounds were tested at a 100 μM concentration and the vertically stacked images were acquired 2 s apart. Scale bar, 10 μm . **b**, Quantification of the compounds' effects on dynein-dependent microtubule gliding. Data are the average velocities for at least 56 microtubules \pm s.e.m. Asterisks indicate $P < 10^{-6}$ and at least 30% inhibition for individual compounds versus DMSO. **c**, Dose responses of 1 and 5 in the dynein-dependent assay. Data are the average velocities for at least 45 microtubules \pm s.e.m. **d**, Effects of 1, 2, 5, 8 and the competitive ATP antagonist adenyllyl imidodiphosphate (A-P) on microtubule gliding driven by the K560 N-terminal fragment of kinesin-1. Dihydroquinazolinones and AMP-PNP were tested at a 100 μM and 1 mM concentrations, respectively. Data are the average velocities for at least 34 microtubules \pm s.e.m., and asterisks indicate $P < 0.01$ for individual compounds versus DMSO. **e**, Effects of 1, 2 and 5 on the ATPase activities of recombinant motor domains derived from rat cytoplasmic dynein, human kinesin-1 and human kinesin-5. Compound concentrations in micromolar units are shown, and data are the average ATPase activities for two independent experiments \pm s.d. **f**, Hanes–Woolf plot of rat dynein motor ATPase velocity (V) suggesting the nucleotide-competitive activity of 5.

We next investigated how ciliobrevins abrogate cytoplasmic dynein function. Neither ciliobrevin A nor D was able to disrupt the association between ADP-bound dynein and microtubules, as determined in a co-sedimentation assay (Supplementary Fig. 13). Both small molecules, however, were able to inhibit the ATPase activity of bovine brain cytoplasmic dynein in a concentration-dependent manner, whereas their inactive analogue (2) could not (Supplementary Fig. 14). The compounds had analogous effects on the ATPase activity of recombinant rat dynein motor domain, but none significantly inhibited the ATPase activities of recombinant motor domains derived from human kinesin-1 or kinesin-5 (Fig. 4e). Ciliobrevin efficacies at various ATP concentrations suggest that these small molecules act in a nucleotide-competitive manner (Fig. 4f). Consistent with this mechanism, ciliobrevin A also inhibited ultraviolet-light-induced cleavage of the cytoplasmic dynein motor domain in the presence of sodium vanadate and ATP (Supplementary Fig. 15).

Our studies establish ciliobrevins as the first small molecules known specifically to inhibit cytoplasmic dynein *in vitro* and in live cells. Although the ATP analogue erythro-9-[3-(2-hydroxynonyl)]adenine²¹ and the antioxidant nordihydroguaiaretic acid²² have been previously reported to abrogate dynein function, these compounds are promiscuous enzyme antagonists^{23,24}. The natural product purealin can partly inhibit dynein ATPase activity *in vitro*²⁵, but its ability to block cytoplasmic dynein-dependent cellular processes has not been demonstrated. Our studies indicate that ciliobrevins can inhibit both cytoplasmic dynein 1 and 2, and, accordingly, the compounds will be broadly applicable probes of dynein-dependent processes. Further development of ciliobrevin-like molecules could lead to isoform-selective inhibitors of this minus-end-directed microtubule motor and perhaps specific antagonists of other AAA+ ATPase superfamily members.

METHODS SUMMARY

Hh signalling assays. Hh signalling and Gli3 processing assays were performed as described^{6,9}.

Cell imaging. Cilia were immunostained with anti-Arl13b antibody (T. Caspari), and cilia size was determined by dividing the number of Arl13b-positive pixels by the number of nuclei per image. Ciliary levels of Gli2 and IFT88 were determined by immunostaining cells with anti-Gli2 (R&D Systems) or anti-IFT88 (ProteinTech Group) antibodies. Analyses of mitotic spindles and kinetochore–microtubule attachments in fixed cells were performed as described²⁶, and real-time confocal microscopy was conducted with NIH-3T3 cells stably expressing GFP-tubulin. Melanosome and peroxisome motility studies were conducted as reported^{19,20}.

Dynein activity assays. Bovine brain dynein was purified as described²⁷, and its microtubule gliding activity was assayed as reported²⁸ with modifications. Recombinant rat cytoplasmic dynein motor domain was heterologously expressed and purified as described²⁹. ATPase activities were determined using a Malachite Green assay (Novus Biologicals).

Full Methods are in the Supplementary Information.

Received 15 June 2011; accepted 1 February 2012.

Published online 18 March 2012.

- White, S. R. & Lauring, B. AAA+ ATPases: achieving diversity of function with conserved machinery. *Traffic* **8**, 1657–1667 (2007).
- Scholey, J. M. Intraflagellar transport. *Annu. Rev. Cell Dev. Biol.* **19**, 423–443 (2003).
- Merdes, A., Ramyar, K., Vechio, J. D. & Cleveland, D. W. A complex of NuMA and cytoplasmic dynein is essential for mitotic spindle assembly. *Cell* **87**, 447–458 (1996).
- Akhmanova, A. & Hammer, J. A. III. Linking molecular motors to membrane cargo. *Curr. Opin. Cell Biol.* **22**, 479–487 (2010).
- Chou, T. F. *et al.* Reversible inhibitor of p97, DBE9, impairs both ubiquitin-dependent and autophagic protein clearance pathways. *Proc. Natl Acad. Sci. USA* **108**, 4834–4839 (2011).
- Hyman, J. M. *et al.* Small-molecule inhibitors reveal multiple strategies for Hedgehog pathway blockade. *Proc. Natl Acad. Sci. USA* **106**, 14132–14137 (2009).
- Jiang, J. & Hui, C.-C. Hedgehog signaling in development and cancer. *Dev. Cell* **15**, 801–812 (2008).
- Goetz, S. C. & Anderson, K. V. The primary cilium: a signalling centre during vertebrate development. *Nature Rev. Genet.* **11**, 331–344 (2010).

9. Humke, E. W., Dorn, K. V., Milenkovic, L., Scott, M. P. & Rohatgi, R. The output of Hedgehog signaling is controlled by the dynamic association between Suppressor of Fused and the Gli proteins. *Genes Dev.* **24**, 670–682 (2010).
10. Kim, J., Kato, M. & Beachy, P. A. Gli2 trafficking links Hedgehog-dependent activation of Smoothened in the primary cilium to transcriptional activation in the nucleus. *Proc. Natl Acad. Sci. USA* **106**, 21666–21671 (2009).
11. Huangfu, D. & Anderson, K. V. Cilia and Hedgehog responsiveness in the mouse. *Proc. Natl Acad. Sci. USA* **102**, 11325–11330 (2005).
12. Heald, R. *et al.* Self-organization of microtubules into bipolar spindles around artificial chromosomes in *Xenopus* egg extracts. *Nature* **382**, 420–425 (1996).
13. Gaglio, T., Dionne, M. A. & Compton, D. A. Mitotic spindle poles are organized by structural and motor proteins in addition to centrosomes. *J. Cell Biol.* **138**, 1055–1066 (1997).
14. Young, A., Dichtenberg, J. B., Purohit, A., Tuft, R. & Doxsey, S. J. Cytoplasmic dynein-mediated assembly of pericentriolar and gamma tubulin onto centrosomes. *Mol. Biol. Cell* **11**, 2047–2056 (2000).
15. Varma, D., Monzo, P., Stehman, S. A. & Vallee, R. B. Direct role of dynein motor in stable kinetochore-microtubule attachment, orientation, and alignment. *J. Cell Biol.* **182**, 1045–1054 (2008).
16. King, S. J., Brown, C. L., Maier, K. C., Quintyne, N. J. & Schroer, T. A. Analysis of the dynein-dynactin interaction *in vitro* and *in vivo*. *Mol. Biol. Cell* **14**, 5089–5097 (2003).
17. Starr, D. A., Williams, B. C., Hays, T. S. & Goldberg, M. L. ZW10 helps recruit dynactin and dynein to the kinetochore. *J. Cell Biol.* **142**, 763–774 (1998).
18. Yen, T. J., Li, G., Schaar, B. T., Szilak, I. & Cleveland, D. W. CENP-E is a putative kinetochore motor that accumulates just before mitosis. *Nature* **359**, 536–539 (1992).
19. Gross, S. P. *et al.* Interactions and regulation of molecular motors in *Xenopus* melanophores. *J. Cell Biol.* **156**, 855–865 (2002).
20. Kim, H. *et al.* Microtubule binding by dynactin is required for microtubule organization but not cargo transport. *J. Cell Biol.* **176**, 641–651 (2007).
21. Bouchard, P., Penningroth, S. M., Cheung, A., Gagnon, C. & Bardin, C. W. erythro-9-[3-(2-Hydroxynonyl)]adenine is an inhibitor of sperm motility that blocks dynein ATPase and protein carboxylmethylase activities. *Proc. Natl Acad. Sci. USA* **78**, 1033–1036 (1981).
22. Arasaki, K., Tani, K., Yoshimori, T., Stephens, D. J. & Tagaya, M. Nordihydroguaiaretic acid affects multiple dynein-dynactin functions in interphase and mitotic cells. *Mol. Pharmacol.* **71**, 454–460 (2007).
23. Schliwa, M., Ezzell, R. M. & Euteneuer, U. Erythro-9-[3-(2-hydroxynonyl)]adenine is an effective inhibitor of cell motility and actin assembly. *Proc. Natl Acad. Sci. USA* **81**, 6044–6048 (1984).
24. Park, S., Lee, D. K. & Yang, C. H. Inhibition of fos-jun-DNA complex formation by dihydroguaiaretic acid and *in vitro* cytotoxic effects on cancer cells. *Cancer Lett.* **127**, 23–28 (1998).
25. Zhu, G. *et al.* Synthesis and biological evaluation of purealin and analogues as cytoplasmic dynein heavy chain inhibitors. *J. Med. Chem.* **49**, 2063–2076 (2006).
26. Maldonado, M. & Kapoor, T. M. Constitutive Mad1 targeting to kinetochores uncouples checkpoint signalling from chromosome biorientation. *Nature Cell Biol.* **13**, 475–482 (2011).
27. Woehlke, G. *et al.* Microtubule interaction site of the kinesin motor. *Cell* **90**, 207–216 (1997).
28. Kapoor, T. M. & Mitchison, T. J. Allele-specific activators and inhibitors for kinesin. *Proc. Natl Acad. Sci. USA* **96**, 9106–9111 (1999).
29. Hook, P. *et al.* Long range allosteric control of cytoplasmic dynein ATPase activity by the stalk and C-terminal domains. *J. Biol. Chem.* **280**, 33045–33054 (2005).
30. Taipale, J. *et al.* Effects of oncogenic mutations in Smoothened and Patched can be reversed by cyclopamine. *Nature* **406**, 1005–1009 (2000).

Supplementary Information is linked to the online version of the paper at www.nature.com/nature.

Acknowledgements We thank T. Caspary for anti-Arl13b antibodies, W. Brinkley for human CREST anti-serum, T. Yen for anti-CENP-E antibodies, U. Peters for purified bovine dynein, S. Wacker for human kinesin-5 motor domain, R. Vallee for a pVL1393 baculovirus expression vector containing the rat dynein motor domain, and K. Bersuker and R. Kopito for TCR- α -GFP-expressing cells. This work was supported by funding from the National Institutes of Health (R01 CA136574 to J.K.C.; R01 GM65933 to T.M.K.; R01 GM71772 to T.M.K. and V.I.G.; R01 GM52111 to V.I.G.).

Author Contributions J.K.C. and T.M.K. conceived and directed the study. A.J.F. performed chemical syntheses and assays of Hedgehog signaling, primary cilia formation and function, ATPase activity, vanadate-dependent dynein photocleavage and p97-dependent protein degradation. A.J.F. and M.M. performed mitotic spindle analyses. K.B. and V.I.G. designed and interpreted the melanophore and peroxisome trafficking assays. J.S.W. performed microtubule gliding and dynein/microtubule binding assays. L.D.L. and M.O. designed and interpreted the Mcm2–7 helicase assays. A.J.F. and J.K.C. wrote the manuscript with contributions from all other authors.

Author Information Reprints and permissions information is available at www.nature.com/reprints. The authors declare no competing financial interests. Readers are welcome to comment on the online version of this article at www.nature.com/nature. Correspondence and requests for materials should be addressed to J.K.C. (jameschen@stanford.edu) or T.M.K. (kapoor@rockefeller.edu).

A murine lung cancer co-clinical trial identifies genetic modifiers of therapeutic response

Zhao Chen^{1,2,3}, Katherine Cheng^{2,3}, Zandra Walton^{2,3}, Yuchuan Wang^{4,5,6}, Hiromichi Ebi^{1,7}, Takeshi Shimamura⁸, Yan Liu^{1,2,3}, Tanya Tupper⁴, Jing Ouyang², Jie Li⁹, Peng Gao^{2,3}, Michele S. Woo², Chunxiao Xu^{1,2,3}, Masahiko Yanagita², Abigail Altabef², Shumei Wang¹⁰, Charles Lee¹⁰, Yuji Nakada¹¹, Christopher G. Peña¹¹, Yanping Sun^{4,5}, Yoko Franchetti¹², Catherine Yao², Amy Saur⁴, Michael D. Cameron¹³, Mizuki Nishino^{5,6}, D. Neil Hayes¹⁴, Matthew D. Wilkerson¹⁴, Patrick J. Roberts¹⁴, Carrie B. Lee¹⁴, Nabeel Bardeesy⁷, Mohit Butaney², Lucian R. Chirieac¹⁰, Daniel B. Costa¹⁵, David Jackman², Norman E. Sharpless¹⁴, Diego H. Castrillon¹¹, George D. Demetri³, Pasi A. Jänne^{1,2,16}, Pier Paolo Pandolfi¹⁷, Lewis C. Cantley^{18,19}, Andrew L. Kung^{4,20}, Jeffrey A. Engelman^{1,7} & Kwok-Kin Wong^{1,2,3,16}

Targeted therapies have demonstrated efficacy against specific subsets of molecularly defined cancers^{1–4}. Although most patients with lung cancer are stratified according to a single oncogenic driver, cancers harbouring identical activating genetic mutations show large variations in their responses to the same targeted therapy^{1,3}. The biology underlying this heterogeneity is not well understood, and the impact of co-existing genetic mutations, especially the loss of tumour suppressors^{5–9}, has not been fully explored. Here we use genetically engineered mouse models to conduct a ‘co-clinical’ trial that mirrors an ongoing human clinical trial in patients with *KRAS*-mutant lung cancers. This trial aims to determine if the MEK inhibitor selumetinib (AZD6244)¹⁰ increases the efficacy of docetaxel, a standard of care chemotherapy. Our studies demonstrate that concomitant loss of either *p53* (also known as *Tp53*) or *Lkb1* (also known as *Stk11*), two clinically relevant tumour suppressors^{6,9,11,12}, markedly impaired the response of *Kras*-mutant cancers to docetaxel monotherapy. We observed that the addition of selumetinib provided substantial benefit for mice with lung cancer caused by *Kras* and *Kras* and *p53* mutations, but mice with *Kras* and *Lkb1* mutations had primary resistance to this combination therapy. Pharmacodynamic studies, including positron-emission tomography (PET) and computed tomography (CT), identified biological markers in mice and patients that provide a rationale for the differential efficacy of these therapies in the different genotypes. These co-clinical results identify predictive genetic biomarkers that should be validated by interrogating samples from patients enrolled on the concurrent clinical trial. These studies also highlight the rationale for synchronous co-clinical trials, not only to anticipate the results of ongoing human clinical trials, but also to generate clinically relevant hypotheses that can inform the analysis and design of human studies.

Activating *KRAS* mutations are found in 15–30% of all patients with non-small cell lung cancer (NSCLC), and predict poor outcome in response to conventional treatment regimens^{13,14}. Preclinical studies have suggested that inhibition of MAPK/ERK kinase (MEK) may be effective against *KRAS*-mutant NSCLC¹⁵, prompting an ongoing

human clinical trial comparing docetaxel monotherapy (standard of care) to docetaxel combined with the MEK inhibitor selumetinib (AZD6244). Although the sole genetic entry criteria for patients on this trial is the presence of *KRAS* mutations, the complexity of NSCLC dictates that many tumours will harbour concomitant genetic alterations that may modulate response to therapy. To mirror this human clinical trial in a murine co-clinical trial, and to investigate the modulating effects of concomitant tumour suppressor loss, we generated cohorts of genetically engineered mice with either *Kras*, *Kras* and *p53* (*Kras/p53*) or *Kras/Lkb1* mutant lung cancers. Activation of *Kras*(G12D) and inactivation of *p53* or *Lkb1* in the lung epithelium was achieved using nasal instillation of adenovirus encoding the CRE recombinase⁷. Mice with established disease, defined by tachypnoea, hypoxaemia on pulse oximetry¹⁶, and bulk disease on magnetic resonance imaging (MRI)¹⁷, were randomized to receive either docetaxel 16 mg kg^{−1} every other day by intraperitoneal injection¹⁸ (Supplementary Table 1), selumetinib at 25 mg kg^{−1} daily by oral gavage¹⁹, or docetaxel in combination with selumetinib. Treatment response was determined by serial MRI. Tumour volumes were reconstructed from the MRI images (Supplementary Fig. 1a) with a high level of inter-operator reliability (Supplementary Fig. 1b; 95% confidence interval, −25.6% to +31.4%). On the basis of these performance metrics, and paralleling human response criteria, we used a threshold of 30% change in tumour volume to define progressive disease and partial response.

For tumours with only *Kras* mutation, treatment with docetaxel monotherapy resulted in a modest rate of response, with 30% of mice achieving a partial response (Fig. 1a, c). Mice bearing *Kras* tumours with concurrent loss of *p53* or *Lkb1* had markedly lower response rates to docetaxel treatment (5% and 0%, respectively), and more of these animals demonstrated progressive disease on MRI or progression to morbidity (Fig. 1a and Supplementary Table 2). The addition of selumetinib to docetaxel treatment provided substantial benefit (Fig. 1b, c), with the overall response rate increased to 92% in *Kras*-mutant cancers ($P = 2.8 \times 10^{-5}$, Fisher exact test compared to docetaxel alone) and 61% in *Kras/p53* mice ($P = 2.7 \times 10^{-4}$). In contrast, for

¹Department of Medicine, Harvard Medical School, Boston, Massachusetts 02115, USA. ²Department of Medical Oncology, Dana-Farber Cancer Institute, Boston, Massachusetts 02115, USA. ³Ludwig Center at Dana-Farber/Harvard Cancer Center, Dana-Farber Cancer Institute, Boston, Massachusetts 02115, USA. ⁴Lurie Family Imaging Center, Dana-Farber Cancer Institute, Boston, Massachusetts 02115, USA. ⁵Department of Imaging, Dana-Farber Cancer Institute, Boston, Massachusetts 02115, USA. ⁶Department of Radiology, Brigham and Women's Hospital, Boston, Massachusetts 02115, USA. ⁷Department of Medical Oncology, Massachusetts General Hospital Cancer Center, Boston, Massachusetts 02114, USA. ⁸Department of Molecular Pharmacology and Therapeutics, Oncology Institute, Loyola University Chicago Stritch School of Medicine, Maywood, Illinois 60153, USA. ⁹Center for Survey Statistics & Methodology, Department of Statistics & Statistical Laboratory, Iowa State University, Ames, Iowa 50010, USA. ¹⁰Department of Pathology, Brigham and Women's Hospital, Boston, Massachusetts 02115, USA. ¹¹Department of Pathology and Simmons Comprehensive Cancer Center, UT Southwestern Medical Center, Dallas, Texas 75390, USA. ¹²Department of Biostatistics and Computational Biology, Dana-Farber Cancer Institute, Department of Biostatistics, Harvard School of Public Health, Boston, Massachusetts 02115, USA. ¹³Translational Research Institute, The Scripps Research Institute, Jupiter, Florida 33458, USA. ¹⁴The Lineberger Comprehensive Cancer Center, University of North Carolina, Chapel Hill, North Carolina 27599, USA. ¹⁵Division of Hematology/Oncology, Beth Israel Deaconess Medical Center, Harvard Medical School, Boston, Massachusetts 02115, USA. ¹⁶Lowe Center for Thoracic Oncology, Dana-Farber Cancer Institute, Boston, Massachusetts 02115, USA. ¹⁷Cancer Genetics Program, Beth Israel Deaconess Cancer Center, Department of Medicine and Pathology, Beth Israel Deaconess Medical Center, Harvard Medical School, Boston, Massachusetts 02115, USA. ¹⁸Department of Systems Biology, Harvard Medical School, Boston, Massachusetts 02115, USA. ¹⁹Division of Signal Transduction, Beth Israel Deaconess Medical Center, Boston, Massachusetts 02115, USA. ²⁰Department of Pediatric Oncology, Dana-Farber Cancer Institute and Children's Hospital, Boston, Massachusetts 02115, USA.

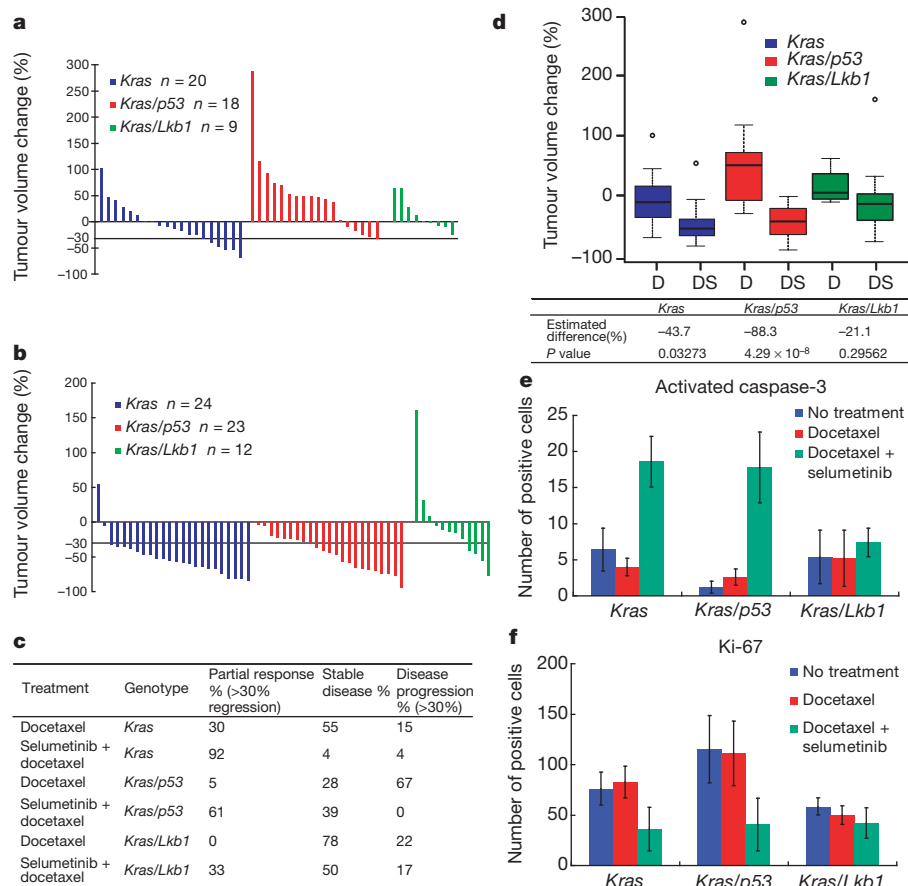


Figure 1 | Docetaxel and selumetinib combination therapy is more efficacious than docetaxel monotherapy in *Kras* and *Kras/p53* lung cancers. **a**, Waterfall plot showing tumour response after 2 weeks of docetaxel treatment at 16 mg kg⁻¹ every 2 days. Each column represents one individual mouse, with data expressed relative to the pre-treatment tumour volume. **b**, Waterfall plot showing tumour response after 2 weeks of docetaxel treatment at 16 mg kg⁻¹ every 2 days in combination with daily selumetinib at 25 mg kg⁻¹. **c**, Response rate of docetaxel and selumetinib combination therapy and docetaxel only in mice bearing tumours with different genotypes. **d**, Box plot showing tumour response for different genotypes with either docetaxel monotherapy (D) or combination treatment (DS). Lines depict median response, small circles indicate outliers. Estimated magnitude of difference between single and combination treatment within each genotype and corresponding one-sided *P* values obtained by likelihood ratio test. **e**, **f**, Number of activated caspase-3 (**e**) and Ki-67 (**f**) positive cells per microscopic field in mice of different genotypes after short-term treatment. Data represent the average of 5 different fields ± standard deviation (s.d.) from 1–3 different mice (see Supplementary Table 6 for detailed information).

Kras/Lkb1 mutant cancers the addition of selumetinib to docetaxel led to only a modest improvement in overall response, with 33% of the mice achieving a partial response (Fig. 1b, c). Compared to the other genotypes, *Kras/Lkb1* mice had a significantly lower rate of response to combined treatment with selumetinib and docetaxel (*P* = 0.0009, 3 × 2 contingency Fisher exact test).

The magnitude of change in volume confirmed that tumours with *Kras* or *Kras/p53* mutations were considerably more responsive to combination therapy compared to docetaxel alone. In contrast, the addition of selumetinib did not significantly reduce the volume of tumours with compound *Kras/Lkb1* mutations (Fig. 1d and Supplementary Fig. 1c, d). Concordantly, histopathological assessments of tumours collected after two doses of treatment revealed that the combination treatment increased apoptosis (Fig. 1e and Supplementary Fig. 2a) and reduced proliferation (Fig. 1f and Supplementary Fig. 2b) in the *Kras* and *Kras/p53* tumours compared to docetaxel alone, but this was not observed in *Kras/Lkb1* tumours (Fig. 1e, f and Supplementary Fig. 2a, b). These results demonstrate that combined treatment with selumetinib and docetaxel induces apoptosis and decreases proliferation in *Kras* and *Kras/p53* tumours, leading to antitumour efficacy, but that concomitant mutation of *Lkb1* confers primary resistance to the combination treatment.

Because repeated tumour biopsies are difficult in patients, we explored the use of ¹⁸F-fluoro-2-deoxy-glucose PET (FDG-PET) as an early response indicator that could be used in the clinic. Comparison of FDG avidity, quantified by standardized uptake value (SUV)^{20,21} in lung cancers across the three different genotypes showed an overall higher FDG uptake in both *Kras/p53* and *Kras/Lkb1* tumours compared to *Kras* tumours (Fig. 2a; *P* = 0.02, one-way ANOVA). Expression of the glucose transporter GLUT1 (also known as SLC2A1) was elevated in *Kras/Lkb1* mutant tumours (Supplementary Fig. 3a), consistent with the increased baseline FDG-PET signal. To determine if this finding was applicable to human patients, we determined the pre-treatment

FDG avidity in nine patients with *KRAS*-mutated lung cancer. Tumours from three patients positive for LKB1 immunostaining had a mean maximum SUV (SUV_{max}) of 2.33, whereas tumours from six patients negative for LKB1 immunostaining had a mean SUV_{max} of 8.75 (Fig. 2b; *P* = 0.048, two-sided Wilcoxon).

We next used FDG-PET to assess early tumour metabolic changes after initiation of therapy. Treatment with docetaxel alone did not result in significant changes in tumour hypermetabolism in *Kras*-, *Kras/p53*- or *Kras/Lkb1*-tumour-bearing mice (Fig. 2c, d). Of note, some of the murine *Kras* lung cancer nodules were not FDG avid (Fig. 2a) and these were the most sensitive to single-agent docetaxel (data not shown). In contrast, within 24 h of the first dose of treatment with docetaxel and selumetinib, tumour hypermetabolism was markedly suppressed in both *Kras* and *Kras/p53* mice (Fig. 2c, d). However, *Kras/Lkb1*-mutant tumours had no appreciable decrease in FDG avidity when treated with the combination (Fig. 2c, d). Together, these results demonstrate that early changes in tumour metabolism measured by FDG-PET (Fig. 2c, d) are concordant with histopathological analysis of apoptosis and proliferation (Fig. 1e, f) and predict antitumour efficacy (Fig. 1a–c) of docetaxel and selumetinib in treating *Kras*-mutant lung cancers.

To assess the pharmacodynamic effects of treatment on the MEK–ERK signalling axis, we assayed pathway activation using phospho-ERK immunostaining of lung cancer nodules. At baseline, the ERK pathway was most activated in *Kras/p53*-mutant tumours (Fig. 3a, b). We observed substantially less phospho-ERK staining in *Kras/Lkb1* tumours, suggesting that the MEK–ERK pathway is not highly activated in these cancers. Treatment with docetaxel did not alter phospho-ERK staining, but, as expected, the addition of selumetinib decreased MEK–ERK signalling in the *Kras* and *Kras/p53* tumours (Fig. 3a, b).

We further evaluated cellular signalling from short-term-treated lung cancer nodules by immunoblotting tumour lysates. Concordant with immunostaining (Fig. 3a), elevated phospho-ERK and phospho-90RSK were observed in *Kras/p53* tumours relative to the other genotypes

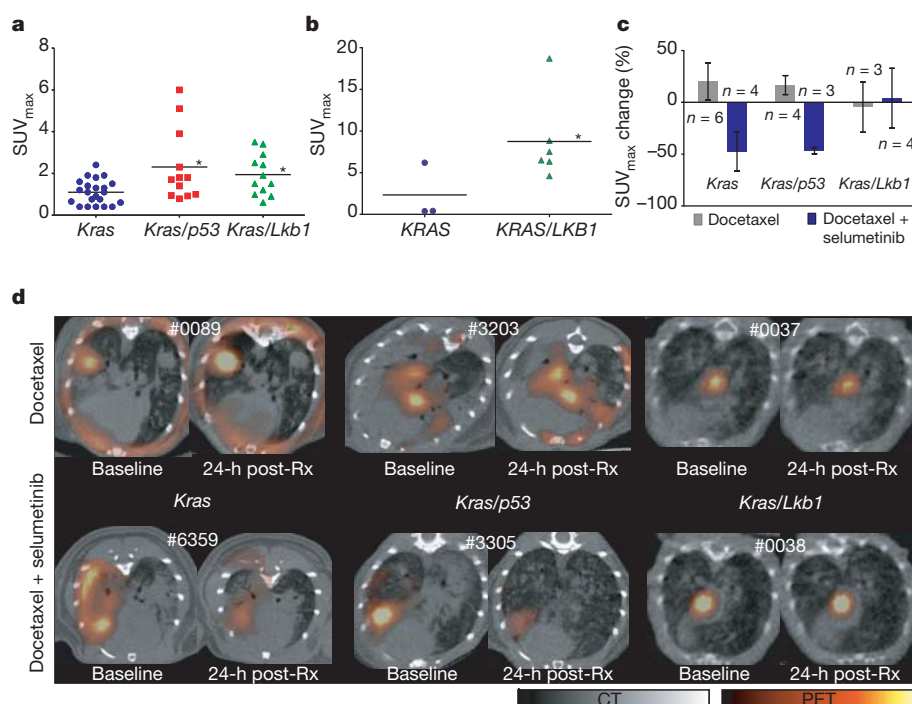


Figure 2 | FDG-PET predicts treatment response. **a**, FDG-PET signal intensity (SUV_{max}) in *Kras*, *Kras/p53* and *Kras/Lkb1* mutant mice. Statistical significance determined by rank sum test, with $*P < 0.05$ for *Kras* compared to *Kras/p53* mutant mice ($P = 0.019$), and *Kras* compared to *Kras/Lkb1* mutant mice ($P = 0.014$). **b**, FDG-PET signal intensity in patients with *KRAS* or *KRAS/LKB1* mutant tumours. Statistical significance determined by two-sided Wilcoxon with $*P = 0.048$. **c**, Comparisons of changes in FDG uptake by PET imaging after 1 day of treatment. Data are represented as mean \pm s.d. **d**, Representative FDG-PET/CT images of mice from different genotypes at baseline and 1 day after initiation of treatment. For each animal, the baseline and post-treatment (post-Rx) PET images are depicted with identical scales. The pseudocoloured FDG-PET images are fused with the grey-scale cross-sectional CT images.

(Fig. 3c and Supplementary Fig. 4a). *Kras/Lkb1* tumours displayed low basal activation of the MEK–ERK pathway (Fig. 3c and Supplementary Fig. 4a), consistent with immunostaining (Fig. 3a). Treatment with docetaxel had no discernable impact on the MEK–ERK pathway in any genotype (Fig. 3a–c and Supplementary Fig. 4b). Although selumetinib alone resulted in decreased phospho-ERK, residual activity was still present (Fig. 3c and Supplementary Fig. 4b). Treatment with both docetaxel and selumetinib more effectively eradicated phospho-ERK activity (Fig. 3c and Supplementary Fig. 4b). Pharmacokinetic studies suggested that selumetinib levels were elevated in the serum

and tumours of mice treated with selumetinib combined with docetaxel compared to selumetinib alone (Supplementary Table 3), perhaps providing a mechanism for the more potent suppression of MEK–ERK signalling by the combination (Fig. 3c). The potential relevance of these findings to human disease was investigated by assessing phospho-ERK staining in a set of 57 human NSCLC tumour samples with known *KRAS*, *p53* and *LKB1* mutation status. Consistent with our findings in murine tumours, of seven patients harbouring the *KRAS* activating mutation, the three patients with concurrent *p53* loss showed higher phospho-ERK activity (Fig. 3d).

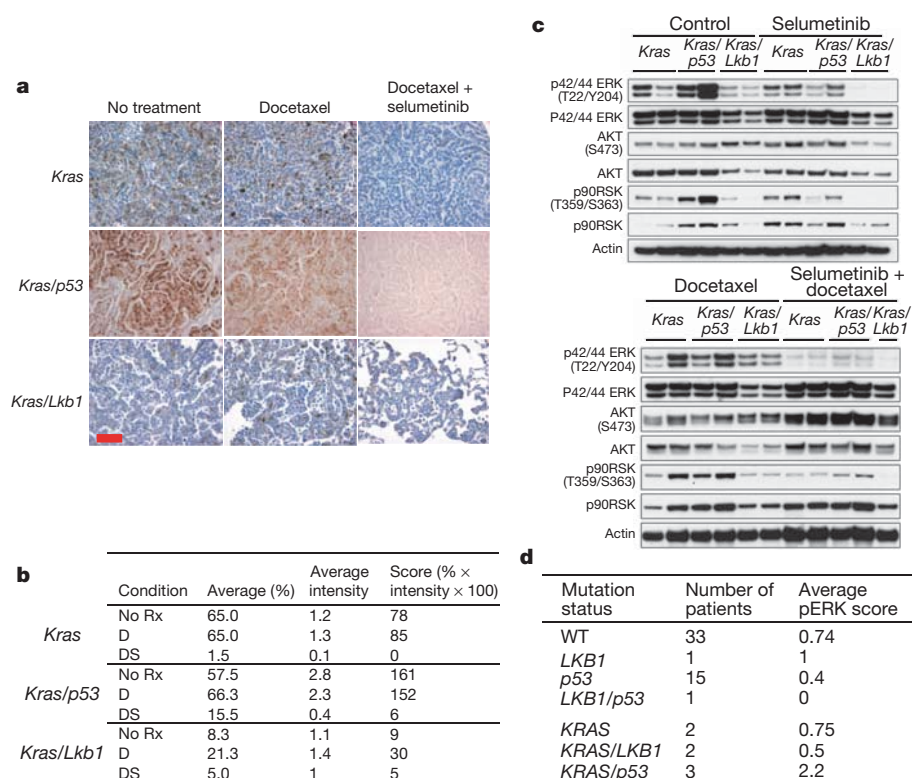


Figure 3 | Modulation of the MEK–ERK pathway in response to treatment is different across the three genotypes. **a**, Immunostaining of phospho-ERK before and after treatment with docetaxel alone or in combination with selumetinib. Scale bar, 50 μ m. **b**, Pathology score of phospho-ERK staining of mouse tumours shown in **a**. Both percentage of phospho-ERK positive cells and average intensity of phospho-ERK staining were scored for individual nodules, with a composite score derived by multiplying phospho-ERK positive percentage and average intensity. All samples were stained in the same batch. **d**, Human NSCLC patients grouped by mutation status as indicated in the first column. Mean phospho-ERK (pERK) score from immunostaining is shown for each subset.

The decreased activation of ERK phosphorylation in *Kras/Lkb1* tumours suggests that the proliferation of these tumours may be driven through other signalling pathways. On the basis of our prior studies^{19,22}, we investigated the activity of AKT and SRC in *Kras/Lkb1* mutant tumours. Immunoblotting with activation-state-specific antibodies revealed that *Kras/Lkb1*-mutant tumours have heightened activation of both AKT and SRC (Supplementary Fig. 3a, b), consistent with the finding of increased FDG avidity in *Kras/Lkb1* tumours (Fig. 2a, b), because PI3K regulates expression of GLUT1 (Supplementary Fig. 3a). These results suggest that concomitant mutation of *Kras* and *Lkb1* may alter the signalling circuitry in tumour cells from one dependent on MEK–ERK (in *Kras* and *Kras/p53* tumours) to one that has more active AKT and SRC pathways, resulting in primary resistance to docetaxel and selumetinib.

The concurrent human clinical trial does not include a treatment arm in which patients are treated with selumetinib alone, based on lack of efficacy in a phase II clinical trial in patients with NSCLC²³, and on our preclinical data in *Kras* genetically engineered mice¹⁹. In mice with *Kras*, *Kras/p53* and *Kras/Lkb1* tumours, treatment with selumetinib alone resulted in a heterogeneous reduction in FDG-PET uptake (Supplementary Fig. 5a), consistent with pharmacodynamic evidence that selumetinib alone partially attenuates MEK–ERK signalling within tumours (Fig. 3c and Supplementary Fig. 7c). However, no partial responses were achieved in any genotype with selumetinib monotherapy, although there was attenuation of tumour growth compared to untreated controls (Supplementary Fig. 5b). Together, these data suggest that selumetinib as monotherapy modulates MEK–ERK signalling in *Kras*-driven tumours, but is insufficient for clinical benefit in mice and humans.

We determined the long-term benefit of combined treatment with docetaxel and selumetinib in the *Kras*- and *Kras/p53*-mutant mice compared to chronic treatment with docetaxel monotherapy. We did not assess long-term treatment outcome in *Kras/Lkb1* animals given the primary resistance to both treatments in these animals (Figs 1–3). In mice with *Kras* tumours, treatment with docetaxel alone stabilized disease for several weeks, whereas the addition of selumetinib caused frank tumour regression and slower tumour re-growth (Fig. 4a and Supplementary Fig. 6a, b). Accordingly, the addition of selumetinib to docetaxel significantly prolonged progression-free survival (Fig. 4b). In mice with *Kras/p53* tumours, treatment with docetaxel alone largely resulted in progressive disease, whereas animals treated with a combination of docetaxel and selumetinib had initial disease regression before progression (Fig. 4a and Supplementary Fig. 6c), resulting in prolonged progression-free survival (Fig. 4c). These results demonstrate that the enhanced response to treatment with combined therapy translates to improved progression-free survival, albeit not outright cure, in mice bearing *Kras*- and *Kras/p53*-mutant tumours.

To investigate mechanisms of resistance upon disease progression, tumour nodules were isolated from moribund animals after long-term treatment with docetaxel and selumetinib. In all animals examined (5/5 in *Kras/p53* and 11/11 in *Kras*), tumour nodules showed recrudescence of ERK phosphorylation (Fig. 4d and Supplementary Fig. 7a), suggesting that acquired resistance could be partly due to reactivation of MEK–ERK signalling despite ongoing treatment with selumetinib. We evaluated treatment-resistant nodules for ERK amplification (Supplementary Fig. 7b), activation of parallel signalling pathways (Supplementary Fig. 7c), and drug pharmacokinetics (Supplementary Fig. 7d), and did not find consistent changes, suggesting more than one mechanism for pathway reactivation. Efforts to identify the diversity of mechanisms responsible for acquired resistance are ongoing.

This co-clinical study provides several insights and predictions that affect the interpretation of the concurrent human clinical trial. First, these results predict that combination therapy with docetaxel and selumetinib will be more effective than docetaxel alone in several subclasses of *KRAS*-mutant NSCLC. These data are consistent with the results of the human phase II clinical trial described in a recent

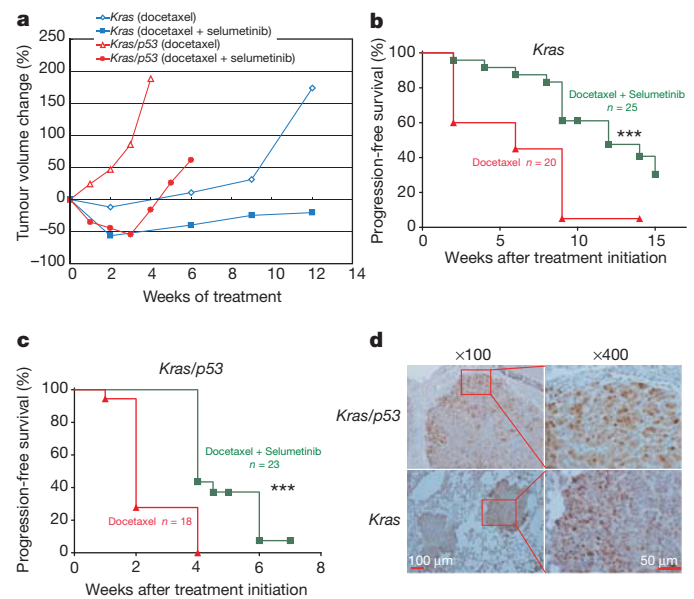


Figure 4 | Long-term treatment outcome in *Kras* and *Kras/p53* mice.

a, Tumour volume was longitudinally assessed by MRI imaging in *Kras* and *Kras/p53* mice treated with either docetaxel or docetaxel plus selumetinib. Data points represent median tumour volume relative to start of treatment for all available data at the indicated time point. **b**, Progression-free survival for *Kras* mice treated with either docetaxel or docetaxel plus selumetinib. Median survival for single and combination treatments was 6 weeks and 12 weeks respectively, with $***P = 0.0003$ by log-rank test. **c**, Progression-free survival for *Kras/p53* mice treated with either docetaxel or docetaxel plus selumetinib. Median survival for single and combination treatments was 2 weeks and 4 weeks, respectively, with $***P < 0.0001$ by log-rank test. Progression was defined as the time point when total tumour volume exceeded the baseline volume. **d**, Immunostaining of activation-specific phospho-ERK of tumours from *Kras/p53* and *Kras* mice with acquired resistance to docetaxel and selumetinib treatment.

press release (<http://phx.corporate-ir.net/phoenix.zhtml?c=123810&p=irol-newsArticle&ID=1611800>). However, our studies predict that concurrent mutation of *LKB1* will confer primary resistance to combination therapy, possibly through activation of parallel signalling pathways such as AKT and SRC. As *LKB1* status is not being prospectively assessed in the ongoing human clinical trial, inclusion of patients with cancers harbouring concurrent *LKB1* mutations may blunt differences between treatment arms based solely on *KRAS* status. These results suggest that a retrospective analysis of *p53* and *LKB1* status in samples from the concurrent human clinical trial is warranted, and lead us to advocate prospective analysis in future clinical trials with sufficient enrolment to all strata to enable sufficiently powered sub-group analyses.

Beyond assessing genetic modulators, co-clinical studies allow for validation of biomarker strategies and discovery of mechanisms of resistance that may benefit future clinical trials. In this study, we observed the potential utility of FDG-PET imaging as a biomarker strategy for identifying an enriched responder population and predicting long-term outcome. Prior studies have suggested that lung tumour hypermetabolism at the time of diagnosis predicts poor outcome in response to conventional therapies^{20,24}, our current study further suggests that high baseline FDG avidity may predict poor response to targeted therapy with selumetinib combined with docetaxel. Specifically, loss of *LKB1* function appears to confer increased FDG avidity, probably through upregulated expression of glucose transporters. As current approaches for assessing *LKB1* status are not comprehensive, FDG-PET imaging may represent a practicable patient stratification strategy. Furthermore, the current preclinical study suggests a role for repeat FDG-PET imaging early in the course of treatment as a potential predictor of outcome, as metabolic changes may be apparent within 24 h of initiating therapy. In these studies, we also observed reactivation of the MEK–ERK

signalling pathway in mice that became resistant to the combination of selumetinib and docetaxel. Although the exact mechanisms responsible for pathway reactivation remain to be elucidated, mechanisms of resistance discovered in co-clinical studies should be confirmed in human clinical trials by examining biopsy samples from patients who relapse on therapy. The ability to assess mechanisms of resistance in the preclinical setting may uncover rational combinatorial strategies that can be implemented in future clinical studies.

Building upon prior success using genetically engineered mouse models^{25–27}, the current study demonstrates that co-clinical trials can provide data that has value beyond predicting the outcome of clinical trials, and can rapidly generate new clinically relevant hypotheses that can affect how the concurrent human clinical trial is analysed, and inform the design of future clinical studies. As similar efforts are undertaken in other cancer disease types, we anticipate that murine co-clinical trials will enable more effective oncology drug development.

METHODS SUMMARY

Mice. Mouse strains harbouring a conditional activating mutation (G12D) at the endogenous *Kras* locus, conditional *Lkb1* knockout, and conditional *p53* knockout were described previously⁷. Genotypes were confirmed by PCR (Supplementary Fig. 8). All studies were performed on protocols approved by Dana-Farber Cancer Institute and University of North Carolina Animal Care and Use Committees, and all mice used are listed in Supplementary Table 4.

MRI quantification. 3D Slicer was used to reconstruct MRI volumetric measurements^{28,29} (Supplementary Fig. 1a). To assess variation between independent operators, Bland–Altman analysis was performed using quantification results from the two operators on a total of 16 MRI scan images (Supplementary Fig. 1b).

Pharmacokinetics. Docetaxel concentrations in serum, lung, and tumour nodules was determined using published doses (8 and 16 mg kg^{−1}). Drug concentration was determined 3 h after the last dose (Supplementary Table 1). All serum concentrations were within the range found in the clinical setting³⁰. Selumetinib was administered as previously described¹⁹, and pharmacokinetics in mice were also documented (Supplementary Table 3).

PET/CT studies. All murine FDG-PET/CT studies were performed with a pre-clinical small animal PET/CT system (Siemens Inveon) after injection with 14 MBq of ¹⁸F-FDG. Mice used for PET/CT studies are listed in Supplementary Table 5.

Human samples and clinical information. All human samples and clinical information were obtained under Institutional Review Board approved protocols (02-180 and 07-0120), and patient information is listed in Supplementary Tables 7 and 8. A tissue microarray (TMA) was generated from genotyped human lung cancer samples as previously described⁷. The TMA was immunostained for phospho-ERK and scored by a pathologist blinded to patient information.

Immunohistochemistry staining. Immunohistochemical analyses assessing phospho-ERK, activated caspase 3, and Ki-67 were performed as previously described¹⁹. Scoring was done by a pathologist, using the same parameters used for scoring human specimens.

Received 11 August 2011; accepted 9 February 2012.

Published online 18 March 2012.

- Demetri, G. D. *et al.* Efficacy and safety of imatinib mesylate in advanced gastrointestinal stromal tumors. *N. Engl. J. Med.* **347**, 472–480 (2002).
- Huang, M. E. *et al.* Use of all-trans retinoic acid in the treatment of acute promyelocytic leukemia. *Blood* **72**, 567–572 (1988).
- Maemondo, M. *et al.* Gefitinib or chemotherapy for non-small-cell lung cancer with mutated EGFR. *N. Engl. J. Med.* **362**, 2380–2388 (2010).
- Mok, T. S. *et al.* Gefitinib or carboplatin-paclitaxel in pulmonary adenocarcinoma. *N. Engl. J. Med.* **361**, 947–957 (2009).
- Ahrendt, S. A. *et al.* p53 mutations and survival in stage I non-small-cell lung cancer: results of a prospective study. *J. Natl. Cancer Inst.* **95**, 961–970 (2003).
- Gill, R. K. *et al.* Frequent homozygous deletion of the *LKB1/STK11* gene in non-small cell lung cancer. *Oncogene* **30**, 3784–3791 (2011).
- Ji, H. *et al.* LKB1 modulates lung cancer differentiation and metastasis. *Nature* **448**, 807–810 (2007).
- Nagata, Y. *et al.* PTEN activation contributes to tumor inhibition by trastuzumab, and loss of PTEN predicts trastuzumab resistance in patients. *Cancer Cell* **6**, 117–127 (2004).
- Steels, E. *et al.* Role of p53 as a prognostic factor for survival in lung cancer: a systematic review of the literature with a meta-analysis. *Eur. Respir. J.* **18**, 705–719 (2001).

- Yeh, T. C. *et al.* Biological characterization of ARRY-142886 (AZD6244), a potent, highly selective mitogen-activated protein kinase kinase 1/2 inhibitor. *Clin. Cancer Res.* **13**, 1576–1583 (2007).
- Matsumoto, S. *et al.* Prevalence and specificity of *LKB1* genetic alterations in lung cancers. *Oncogene* **26**, 5911–5918 (2007).
- Weir, B. A. *et al.* Characterizing the cancer genome in lung adenocarcinoma. *Nature* **450**, 893–898 (2007).
- Douillard, J. Y. *et al.* Molecular predictors of outcome with gefitinib and docetaxel in previously treated non-small-cell lung cancer: data from the randomized phase III INTEREST trial. *J. Clin. Oncol.* **28**, 744–752 (2010).
- Mascaux, C. *et al.* The role of RAS oncogene in survival of patients with lung cancer: a systematic review of the literature with meta-analysis. *Br. J. Cancer* **92**, 131–139 (2005).
- Ji, H. *et al.* Mutations in BRAF and KRAS converge on activation of the mitogen-activated protein kinase pathway in lung cancer mouse models. *Cancer Res.* **67**, 4933–4939 (2007).
- Verhoeven, D., Teijaro, J. R. & Farber, D. L. Pulse-oximetry accurately predicts lung pathology and the immune response during influenza infection. *Virology* **390**, 151–156 (2009).
- Li, D. *et al.* Bronchial and peripheral murine lung carcinomas induced by T790M-L858R mutant EGFR respond to HKI-272 and rapamycin combination therapy. *Cancer Cell* **12**, 81–93 (2007).
- Dykes, D. J., Bissery, M. C., Harrison, S. D. Jr & Waud, W. R. Response of human tumor xenografts in athymic nude mice to docetaxel (RP 56976, Taxotere). *Invest. New Drugs* **13**, 1–11 (1995).
- Engelman, J. A. *et al.* Effective use of PI3K and MEK inhibitors to treat mutant Kras G12D and PIK3CA H1047R murine lung cancers. *Nature Med.* **14**, 1351–1356 (2008).
- Berghmans, T. *et al.* Primary tumor standardized uptake value (SUV_{max}) measured on fluorodeoxyglucose positron emission tomography (FDG-PET) is of prognostic value for survival in non-small cell lung cancer (NSCLC): a systematic review and meta-analysis (MA) by the European Lung Cancer Working Party for the IASLC Lung Cancer Staging Project. *J. Thorac. Oncol.* **3**, 6–12 (2008).
- Vansteenkiste, J. F. *et al.* Prognostic importance of the standardized uptake value on ¹⁸F-fluoro-2-deoxy-glucose-positron emission tomography scan in non-small-cell lung cancer: an analysis of 125 cases. Leuven Lung Cancer Group. *J. Clin. Oncol.* **17**, 3201–3206 (1999).
- Carretero, J. *et al.* Integrative genomic and proteomic analyses identify targets for *Lkb1*-deficient metastatic lung tumors. *Cancer Cell* **17**, 547–559 (2010).
- Hainsworth, J. D. *et al.* A phase II, open-label, randomized study to assess the efficacy and safety of AZD6244 (ARRY-142886) versus pemetrexed in patients with non-small cell lung cancer who have failed one or two prior chemotherapeutic regimens. *J. Thorac. Oncol.* **5**, 1630–1636 (2010).
- Erasmus, J. J., Rohren, E. & Swisher, S. G. Prognosis and reevaluation of lung cancer by positron emission tomography imaging. *Proc. Am. Thorac. Soc.* **6**, 171–179 (2009).
- Singh, M. *et al.* Assessing therapeutic responses in Kras mutant cancers using genetically engineered mouse models. *Nature Biotechnol.* **28**, 585–593 (2010).
- Tuveson, D. & Hanahan, D. Translational medicine: cancer lessons from mice to humans. *Nature* **471**, 316–317 (2011).
- Politi, K. & Pao, W. How genetically engineered mouse tumor models provide insights into human cancers. *J. Clin. Oncol.* **29**, 2273–2281 (2011).
- Nishino, M. *et al.* CT tumor volume measurement in advanced non-small-cell lung cancer: Performance characteristics of an emerging clinical tool. *Acad. Radiol.* **18**, 54–62 (2011).
- Zhao, B. *et al.* A pilot study of volume measurement as a method of tumor response evaluation to aid biomarker development. *Clin. Cancer Res.* **16**, 4647–4653 (2010).
- LoRusso, P. M. *et al.* Phase I and pharmacokinetic study of lapatinib and docetaxel in patients with advanced cancer. *J. Clin. Oncol.* **26**, 3051–3056 (2008).

Supplementary Information is linked to the online version of the paper at www.nature.com/nature.

Acknowledgements This work is supported by the National Institutes of Health (CA122794, CA140594, CA137181, CA137008, CA147940, CA137008-01, 1U01CA141576, Lung SPOR P50CA090578), United against Lung Cancer Foundation, American Lung Association and Susan Spooner Research Fund.

Author Contributions Z.C., K.C., Z.W., Y.W., H.E., T.S., Y.L., T.T., J.O., J.L., P.G., M.S.W., C.X., M.Y., A.A., S.W., C.L., Y.N., C.G.P., Y.S., Y.F., C.Y., A.S., M.D.C., D.N.H., M.D.W., P.J.R., C.B.L., N.B., N.E.S., D.H.C., G.D.D., P.A.J., L.C.C., C.B.L., M.N. and P.P.P. performed experimental work and data analyses. M.B., L.R.C., D.B.C. and D.J. collected data and provided patient materials. A.L.K., J.A.E. and K.-K.W. conceived and supervised all aspects of the project. All authors contributed to the final manuscript.

Author Information Reprints and permissions information is available at www.nature.com/reprints. The authors declare competing financial interests: details accompany the full-text HTML version of the paper at www.nature.com/nature. Readers are welcome to comment on the online version of this article at www.nature.com/nature. Correspondence and requests for materials should be addressed to K.-K.W. (kwong1@partners.org), J.A.E. (jengelman@partners.org) or A.L.K. (andrew_kung@dfci.harvard.edu).

Structure of the human κ -opioid receptor in complex with JD_{Tic}

Huixian Wu¹, Daniel Wacker¹, Mauro Mileni¹, Vsevolod Katritch¹, Gye Won Han¹, Eyal Vardy², Wei Liu¹, Aaron A. Thompson¹, Xi-Ping Huang², F. Ivy Carroll³, S. Wayne Mascarella³, Richard B. Westkaemper⁴, Philip D. Mosier⁴, Bryan L. Roth², Vadim Cherezov¹ & Raymond C. Stevens¹

Opioid receptors mediate the actions of endogenous and exogenous opioids on many physiological processes, including the regulation of pain, respiratory drive, mood, and—in the case of κ -opioid receptor (κ -OR)—dysphoria and psychotomimesis. Here we report the crystal structure of the human κ -OR in complex with the selective antagonist JD_{Tic}, arranged in parallel dimers, at 2.9 Å resolution. The structure reveals important features of the ligand-binding pocket that contribute to the high affinity and subtype selectivity of JD_{Tic} for the human κ -OR. Modelling of other important κ -OR-selective ligands, including the morphinan-derived antagonists norbinaltorphimine and 5'-guanidinonaltrindole, and the diterpene agonist salvinorin A analogue RB-64, reveals both common and distinct features for binding these diverse chemotypes. Analysis of site-directed mutagenesis and ligand structure-activity relationships confirms the interactions observed in the crystal structure, thereby providing a molecular explanation for κ -OR subtype selectivity, and essential insights for the design of compounds with new pharmacological properties targeting the human κ -OR.

The four opioid receptors, μ , δ , κ and the nociceptin/orphanin FQ peptide receptor, belong to the class A (rhodopsin-like) γ subfamily of G-protein-coupled receptors (GPCRs)¹ with a common seven-transmembrane helical architecture, and are coupled predominantly to heterotrimeric G_i/G_o proteins. Activation of these receptors by endogenous or exogenous ligands is linked to a number of neuro-psychiatric sequelae, including analgesia, sedation, depression, dysphoria and euphoria². The three closely related subtypes, μ -OR, δ -OR and κ -OR, share ~70% sequence identity in their seven transmembrane helices (I–VII), with more variations in the extracellular loops (ECLs) and very little similarity in their amino and carboxy termini². The majority of endogenous opioid peptides have a defined preference for specific subtypes, for example, endorphins act via δ -ORs and μ -ORs, whereas dynorphins preferentially activate κ -ORs. However, most exogenous and synthetic opioid ligands interact promiscuously (see the K_i Database; <http://pdsp.med.unc.edu/pdsp.php>), probably owing to the high degree of similarity among binding pockets of opioid receptors. Although decades of focused medicinal chemistry efforts have yielded reasonably selective ligands for all four ORs (see the K_i Database), there remains substantial interest in the development of subtype-selective agonists and antagonists.

Recent breakthroughs in elucidating high-resolution structures of GPCRs in complex with small-molecule^{3–7} and peptide⁸ ligands are providing details of their function⁹, leading to numerous rational ligand discovery studies^{10,11}. However, whereas most of these structures belong to the α subfamily of class A GPCRs¹, the highly diverse peptide-binding γ subfamily is represented only by the CXCR4 chemokine receptor⁸; additional structural coverage is needed to elucidate the repertoire of features¹² that define the pharmacological profile of this subfamily. The κ -OR, identified based on studies with the κ -type prototypic agonist ketocyclazocine¹³, represents an attractive target for structure determination. Several κ -OR-selective partial agonists and antagonists have been developed as potential

antidepressants, anxiolytics and anti-addiction medications¹⁴, whereas a widely abused, naturally occurring hallucinogen—salvinorin A (SaA)—was also found to be a highly selective κ -OR agonist¹⁵. Although many κ -OR agonists and antagonists have not demonstrated desirable pharmacological properties, lacking specificity or displaying frank psychotomimetic actions in humans^{14,16}, some have been shown to be viable drug candidates. A κ -OR ligand in early stages of clinical development, JD_{Tic} (3R)-1,2,3,4-tetrahydro-7-hydroxy-N-[(1S)-1-[[[(3R,4R)-4-(3-hydroxyphenyl)-3,4-dimethyl-1-piperidinyl]methyl]-2-methylpropyl]-3-isoquinolinecarboxamide), was originally designed as a novel selective κ -OR antagonist¹⁷ that blocks the κ -OR agonist U50,488-induced antinociception, while not antagonizing μ -OR agonist-induced analgesia¹⁸. JD_{Tic} also displays robust activity in rodent models of depression, anxiety, stress-induced cocaine relapse, and nicotine withdrawal^{18,19}. Here we report the crystal structure of a human κ -OR construct, κ -OR-T4 lysozyme (T4L), in complex with JD_{Tic} at 2.9 Å resolution. The results provide structural insights into the atomic details of molecular recognition and subtype selectivity of the κ -OR and related ORs, and should catalyse the structure-based design of advanced human κ -OR agonists and antagonists with improved pharmacological profiles and enhanced therapeutic efficacies.

Overall architecture of the κ -OR

Structural studies were carried out using an engineered human κ -OR construct (see Methods and Supplementary Fig. 1) and crystallized in cholesterol-doped monoolein lipidic cubic mesophase (see Methods). The construct used showed pharmacological behaviour similar to that of a native receptor expressed in HEK293T cells (Supplementary Tables 2 and 3). Data collection and refinement statistics are shown in Supplementary Table 1.

The structure of κ -OR-JD_{Tic} was determined at 2.9 Å in the P2₁2₁2₁ space group. The asymmetric unit consists of two receptors forming a parallel dimer (Fig. 1a). The dimer interface with ~1,100 Å²

¹Department of Molecular Biology, The Scripps Research Institute, 10550 North Torrey Pines Road, La Jolla, California 92037, USA. ²National Institute of Mental Health Psychoactive Drug Screening Program, Department of Pharmacology and Division of Chemical Biology and Medicinal Chemistry, University of North Carolina Chapel Hill Medical School, 4072 Genetic Medicine Building, Chapel Hill, North Carolina 27599, USA. ³Center for Organic and Medicinal Chemistry, Research Triangle Institute, P.O. Box 12194, Research Triangle Park, North Carolina 27709, USA. ⁴Department of Medicinal Chemistry, Virginia Commonwealth University, 800 E. Leigh Street, Richmond, Virginia 23298, USA.

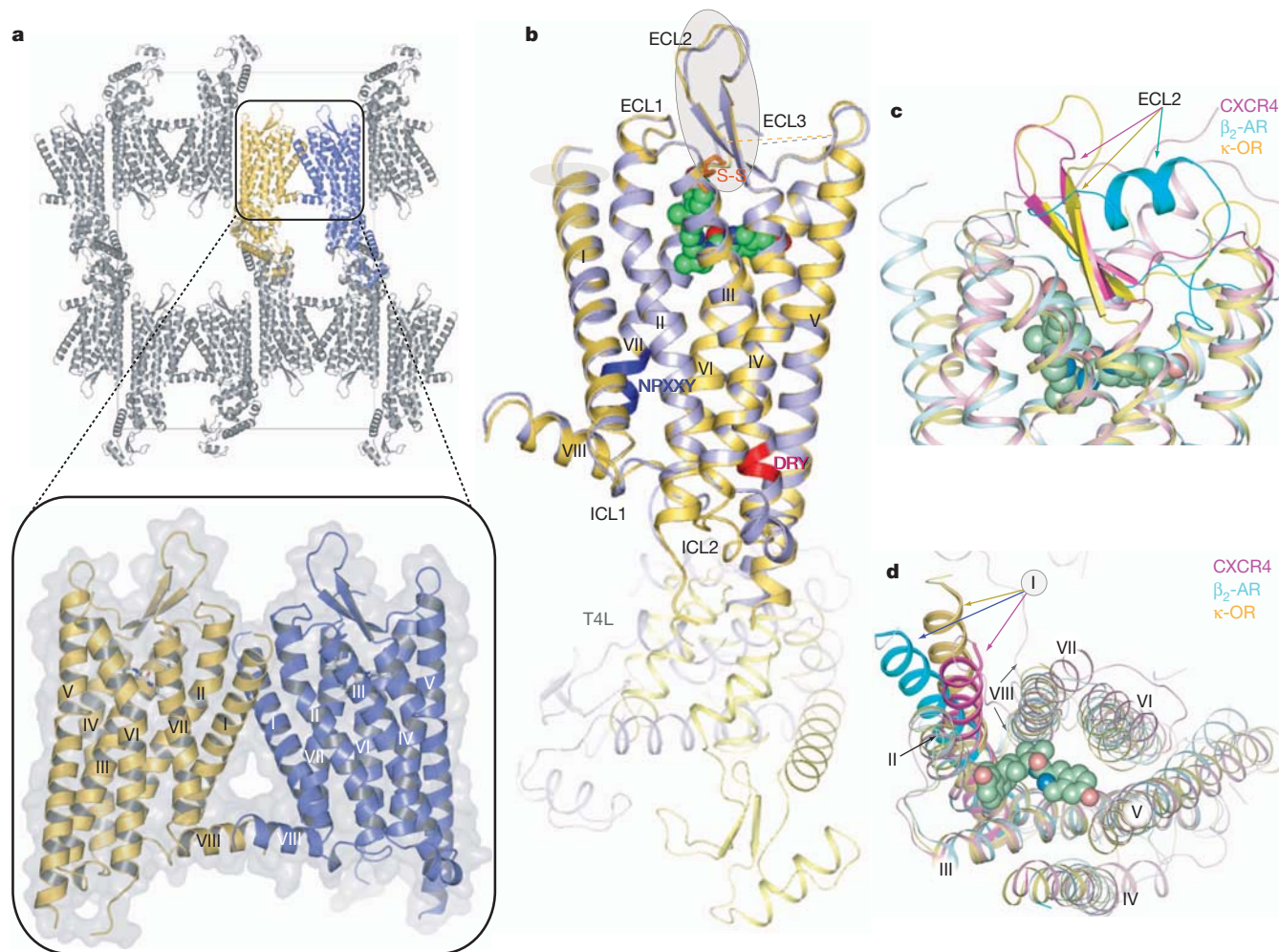


Figure 1 | Crystal packing and overview of the human κ -OR structure in complex with JD1c, and comparison with the inactive CXCR4 and β_2 -AR structures. **a**, κ -OR-T4L crystal packing. The parallel dimer in one asymmetric unit is highlighted by the insert. **b**, Overall architecture of κ -OR-T4L in complex with JD1c. The A molecule (yellow) and B molecule (blue) from one asymmetric unit are aligned through the receptor part. The DRY and

buried surface area is formed through contacts among helices I, II and VIII (Fig. 1a, insert). Previously, parallel receptor dimers have been identified in crystal structures of activated rhodopsin (involving helices I, II and VIII)²⁰, the β_2 adrenergic receptor (β_2 -AR; cholesterol mediated)³ and CXCR4 (involving helices IV, V and VI)⁸. Consistent with these crystallographic data, recent biochemical studies have suggested the existence of two dimerization interfaces: along helices IV and V (sensitive to receptor activation) and along helix I (insensitive to the state of activation)²¹. Although the orientations of the two T4L copies in the receptor monomers in one asymmetric unit differ by $\sim 60^\circ$ rotation, both copies of the receptor are highly similar (Fig. 1b) and will be treated identically except where otherwise noted.

The main fold of the human κ -OR consists of a canonical seven-transmembrane bundle of α -helices followed by an intracellular helix VIII that runs parallel to the membrane (Fig. 1a, b), resembling previously solved GPCR structures^{3–8}. Structural comparison with other GPCRs suggests that human κ -OR has marked similarities in the ECL region with CXCR4, another peptide-binding receptor in the γ subfamily. In the seven-transmembrane region, however, the κ -OR structure is closer to aminergic receptors belonging to the α subfamily (alpha carbon root mean squared deviation (r.m.s.d.) ~ 2.3 Å for the β_2 -AR, ~ 1.9 Å for the dopamine D3 receptor (D3R) and ~ 2.7 Å for CXCR4). The structure reveals distinctive features of the human κ -OR, including the following. First, conformation of the extracellular end of

NPXXY motifs are highlighted in red and blue, respectively. JD1c is shown in a green sphere representation and the disulphide bond is coloured orange.

c, d, Side (**c**) and extracellular (**d**) views of a structural alignment of the human κ -OR (yellow); CXCR4 (PDB accession 3ODU; magenta) and β_2 -AR (PDB accession 2RH1; cyan). The graphics were created by PyMOL.

helix I deviates from the position observed in CXCR4, where the tip of helix I is pulled towards the transmembrane bundle by a disulphide bond between the N terminus and ECL3. Second, ECL2, the largest extracellular loop of the human κ -OR, forms a β -hairpin similar to that observed in CXCR4, despite the low sequence similarity in this domain between the two receptors. Conservation of this feature between these peptide receptors suggests that the β -hairpin could be a common motif in the ECL2 of other γ subfamily receptors, where interactions between ECL2 and their endogenous peptide ligands are deemed important for ligand recognition and selectivity²². Third, unlike other solved non-rhodopsin class A GPCRs that have more than one disulphide bond, the human κ -OR has only one formed between Cys 131^{3,25} (supercripts indicate residue numbering using the Ballesteros-Weinstein nomenclature²³) and Cys 210, bridging ECL2 to the end of helix III. These two cysteines are conserved in all opioid receptors and this disulphide bond is the canonical one shared by most other solved class A GPCRs. Fourth, intracellular loop 2 (ICL2) adopts slightly different structures in the two κ -OR molecules in the asymmetric unit, involving a two-turn α -helix in molecule B, and only a one-turn α -helix in molecule A (Supplementary Fig. 2), possibly reflecting the conformational plasticity of this region⁵. Last, ECL3 of the κ -OR is disordered. Of the approximately 11 residues in this loop (residues 300–310), 6 residues in molecule A and 3 in molecule B do not have interpretable electron density.

A common feature of the class A GPCRs is the presence of a conserved sequence motif Asp/Glu^{3.49}-Arg^{3.50}-Tyr^{3.51} (D/ERY) located at the cytoplasmic end of helix III. A salt bridge interaction between Arg^{3.50} and Asp/Glu^{6.30} from the cytoplasmic end of helix VI constitutes an 'ionic lock', which is thought to stabilize the inactive conformation of rhodopsin and other rhodopsin-like class A GPCRs^{5,24}, whereas its absence can enhance constitutive activity^{6,23}. Although the human κ -OR lacks either of the acidic residues Asp/Glu at position 6.30, Arg 156^{3.50} forms a hydrogen bond to another helix VI residue, Thr 273^{6.34} (Supplementary Fig. 3a) in this inactive κ -OR structure, thereby conceivably stabilizing the inactive receptor conformation. The NPXXY motif located at the cytoplasmic side of helix VII, which is composed of Asn 326^{7.49}, Pro 327^{7.50}, Ile 328^{7.51}, Leu 329^{7.52} and Tyr 330^{7.53} in the κ -OR, is another highly conserved functional motif that is proposed to act as one of the molecular switches responsible for class A GPCR activation^{25,26}. Comparison of the human κ -OR with inactive β_2 -AR and A_{2A} adenosine receptor (A_{2A}AR) structures (Supplementary Fig. 3b) reveals a similar conformation of this motif in these receptors, thereby supporting the hypothesis that the observed κ -OR-JDTic complex structure corresponds to the inactive state. To establish further that JDTic stabilizes an inactive conformation, we evaluated its ability to modulate G_i/G_o-mediated and β -arrestin-mediated signalling in transfected HEK293T cells. We found that JDTic was devoid of agonist activity at both canonical and non-canonical pathways and completely blocked the effects of the prototypic agonist U69593 (Supplementary Fig. 4).

The κ -OR ligand-binding pocket

The κ -OR ligand-binding pocket displays a unique combination of key characteristics both shared with and distinct from those in the chemokine and aminergic receptor families. Although the human κ -OR binding pocket is comparatively large and partially capped by the ECL2 β -hairpin, as in CXCR4, it is also much narrower and deeper than in CXCR4 (Fig. 2c, d and Supplementary Fig. 5). In addition to a

different set of side chains lining the pocket, the shape differences result from an approximately 4.5 Å inward shift of the extracellular tip of helix VI in the κ -OR as compared to CXCR4. The electron density clearly shows the position of the JDTic ligand (Supplementary Fig. 6), which reaches deep into the pocket to form ionic interactions with the Asp 138^{3.32} side chain (Fig. 2a). The Asp^{3.32} residue is conserved in all aminergic GPCRs, thereby having a critical role in the selectivity of aminergic receptors towards protonated amine-containing ligands. Likewise, Asp^{3.32} is conserved in all opioid receptors, and modelling and mutagenesis studies²⁷ suggest that it has an essential role in anchoring positively charged κ -OR ligands.

Structural basis of JDTic selectivity

JDTic, developed as a derivative of the *trans*-(3R,4R)-4-(3-hydroxyphenyl)-3,4-dimethyl-1-piperidine scaffold¹⁷, has exceptionally high affinity ($K_i = 0.32$ nM), potency ($K_i = 0.02$ nM in GTP γ S assays)^{17,28}, long duration of action and a more than 1,000-fold selectivity for the human κ -OR as compared to other opioid receptor subtypes²⁸. Extensive structure-activity relationship (SAR) analyses performed on JDTic analogues have yielded important insights into key determinants of JDTic activity^{28–30}, although reliable identification of the interaction mode(s) and contact residues of these ligands has not been feasible without a receptor crystal structure.

The crystal structure of κ -OR-JDTic shows a tight fit of the ligand in the bottom of the binding cleft (Fig. 2a), forming ionic, polar and extensive hydrophobic interactions with the receptor (Fig. 2b). The protonated amines in both piperidine and isoquinoline moieties of the ligand form salt bridges to the Asp 138^{3.32} side chain (3.0 and 2.8 Å nitrogen-oxygen for molecule A, and 2.7 and 2.3 Å for molecule B, respectively). The piperidine amine is part of the original *trans*-(3R,4R)-dimethyl-4-(3-hydroxyphenyl)piperidine scaffold and is essential for opioid receptor antagonist activity³¹. SAR studies of JDTic analogues show that the isoquinoline nitrogen can be replaced by carbon, oxygen or sulphur atoms with only a ~10- to 50-fold

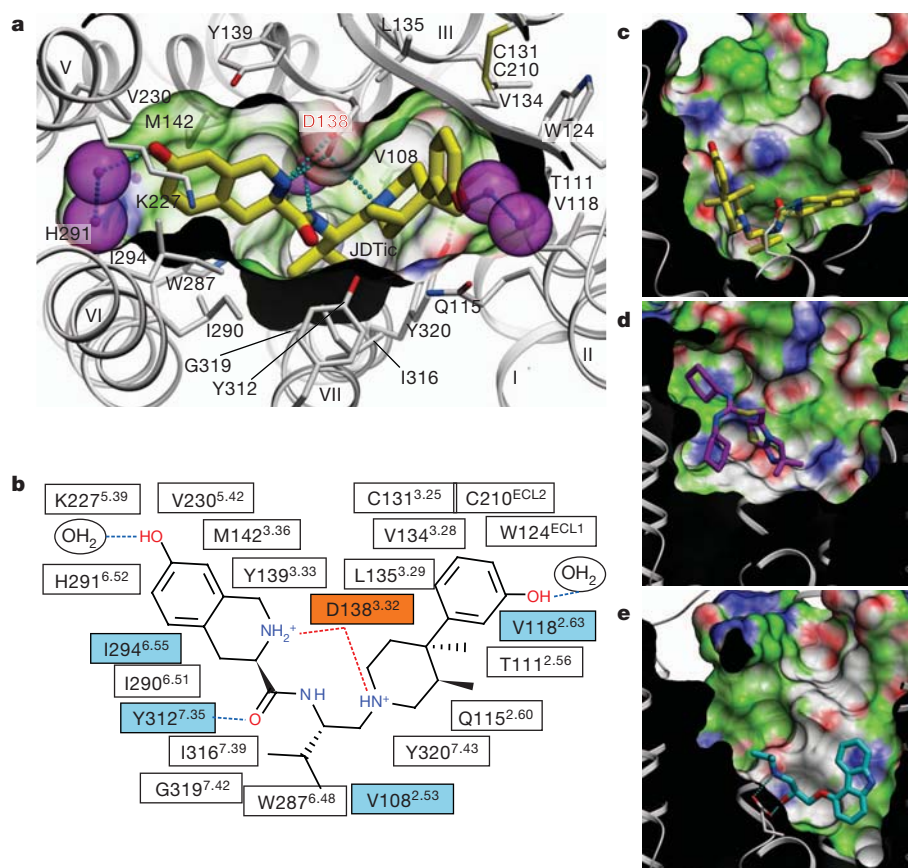


Figure 2 | Binding of the high-affinity selective antagonist JDTic in the human κ -OR crystal structure. **a**, Conformation of the binding pocket with JDTic shown by sticks with yellow carbons. The protein is displayed in cartoon representation looking down from the extracellular side, with the 22 contact residues within 4.5 Å from the ligand shown by white sticks. The pocket surface is shown as a semitransparent surface coloured according to binding properties (green: hydrophobic; blue: hydrogen-bond donor; red: hydrogen-bond acceptor). Salt bridges and hydrogen bonds are shown as dotted lines. Structured water molecules are shown as large magenta spheres. **b**, Diagram of ligand interactions in the binding pocket side chains at 4.5 Å cut-off. Salt bridges are shown in red and direct hydrogen bonds in blue dashed lines. Ballesteros-Weinstein numbering is shown as superscript. Residues that vary among the μ -OR, δ -OR and κ -OR subtypes are highlighted in cyan, and residue Asp 138^{3.32} implicated in κ -OR-ligand binding by mutagenesis data, is highlighted orange. **c–e**, Side views of the sliced binding pocket in κ -OR-JDTic (**c**), CXCR4-IT1t (**d**) and β_2 -AR-carazolol (**e**) complexes. The pocket surfaces are coloured as in panel **a**, the protein interior is black and the extracellular space is white. Ligands are shown as capped sticks with carbons coloured yellow (JDTic), magenta (IT1t) and cyan (carazolol). Asp^{3.32} side chains in κ -OR-JDTic and β_2 -AR-carazolol complexes are shown by thin sticks with grey carbons. The graphics were prepared using the ICM molecular modelling package (Molsoft LLC).

reduction in affinity³⁰. Similar to the observed JD_{Tic} conformation in the κ -OR–JD_{Tic} complex, a V-shaped conformation was found in the small molecule X-ray crystal structure of JD_{Tic}, which showed its amino groups coordinating a water molecule (Supplementary Fig. 7a). Although several rotatable bonds within the JD_{Tic} molecule allow for the sampling of different conformations (see Supplementary Fig. 7b) and facilitate the ligand passage through the narrow binding pocket entrance, the anchoring-type interaction of two amino groups with Asp 138^{3,32} probably fixes the ligand in this characteristic V shape.

SAR studies have also underscored the importance of the distal hydroxyl groups on both the piperidine and isoquinoline moieties of JD_{Tic}, the removal of which did result in about a 100-fold reduction of affinity. A much smaller effect was observed upon methylation of these hydroxyls or their replacement by other polar groups²⁸. These SAR results suggest the importance of water-mediated interactions between these two hydroxyl groups and the receptor. Indeed, although the crystal structure does not show direct hydrogen bonding with the receptor for both hydroxyl groups, there is clear electron density for several structured water molecules that mediate their polar interactions (Supplementary Fig. 6).

The κ -OR structure provides important clues for understanding the structural basis of the exceptional subtype selectivity of JD_{Tic}. Among many extensive contacts, JD_{Tic} interacts with four residues in the binding pocket that differ in other closely related opioid receptors, which are thought to contribute to the subtype selectivity of JD_{Tic} and other κ -OR-selective ligands³² (human μ -OR and δ -OR amino acids are shown in parentheses, respectively): Val 108^{2,53} (Ala and Ala), Val 118^{2,63} (Asn and Lys), Ile 294^{6,55} (Val and Val) and Tyr 312^{7,35} (Trp and Leu) (Fig. 2b and Supplementary Fig. 8). Analysis of JD_{Tic} binding into κ -OR-based μ -OR and δ -OR homology models, as well as JD_{Tic} SAR results^{17,28,30} (Supplementary Fig. 9), suggest that all described residues can contribute to the JD_{Tic} selectivity profile. Thus, changes in the Val 118^{2,63} side chain, where larger hydrophilic residues Asn^{2,63} and Lys^{2,63} are found in the human μ -OR and δ -OR, respectively, are likely to introduce unfavourable contacts with JD_{Tic}. Additionally, changing Tyr 312^{7,35} to the Trp^{7,35} and Leu^{7,35} residues found in the human μ -OR and δ -OR, respectively, is likely to result in the loss of an important polar interaction with the JD_{Tic} amide. The remaining two hydrophobic side-chain replacements, Val to Ala at position 2.53 and Ile to Val at position 6.55, may cause a reduction of the hydrophobic contact between JD_{Tic} and the receptor.

The isopropyl group of JD_{Tic} reaches deep into the orthosteric pocket to form a hydrophobic interaction with a conserved Trp 287^{6,48} side chain, possibly having a critical role in the pharmacological properties of this ligand. Trp^{6,48} is thought to be a key part of the activation mechanism in many class A GPCRs, including rhodopsin²⁶ and the A_{2A}AR²⁵, and similar hydrophobic contacts have been implicated in blocking activation-related conformational changes in the dark state visual rhodopsin by 11-*cis* retinal, and by inverse agonists in the A_{2A}AR and D3R.

Binding of κ -OR-selective morphinans

Prior mutagenesis and modelling studies suggested that many small-molecule opioid ligands can interact with the κ -OR, as well as with the μ -OR and δ -OR, by forming a salt bridge with the highly conserved Asp^{3,32} (refs 33, 34). This is consistent with our mutagenesis studies (Supplementary Table 3) and flexible docking³⁵ of a series of morphine analogues, including selective κ -OR antagonists norbinaltorphimine (nor-BNI) and 5'-guanidinonaltrindole (GNTI) (Fig. 3 and Supplementary Fig. 10). To assess the compatibility of these bulky and rigid ligands with the observed κ -OR protein backbone conformation, we performed global energy optimizations of nor-BNI and GNTI in the binding cavity of κ -OR, keeping side chains of the binding pocket fully flexible. Multiple independent runs consistently resulted in low energy conformations with essentially identical poses and receptor contacts

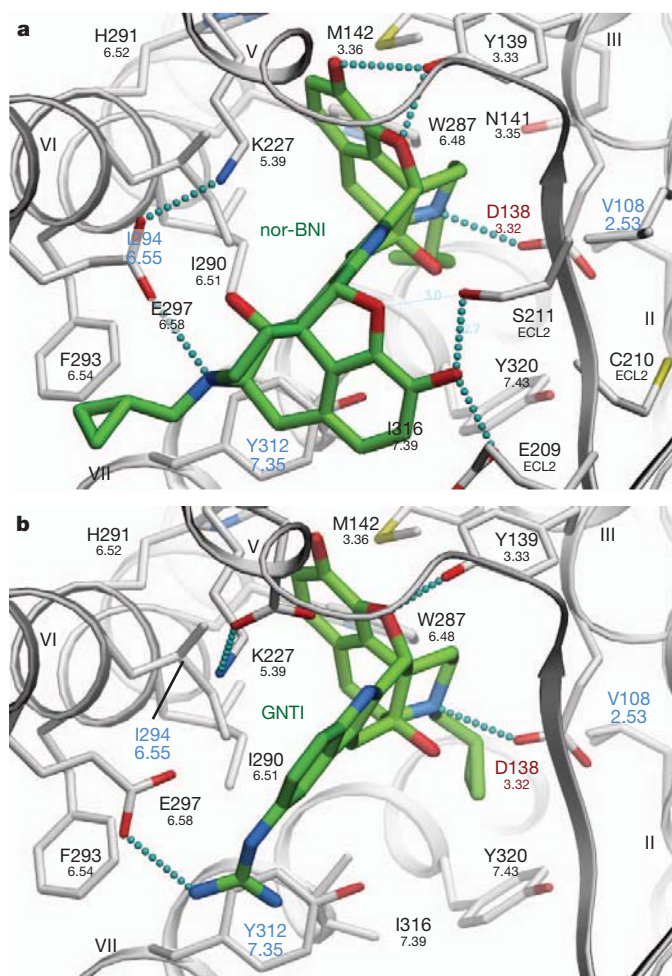


Figure 3 | Putative interaction modes of morphine-based high-affinity κ -OR-selective antagonists nor-BNI and GNTI. **a, b,** Interaction modes of nor-BNI (**a**) and GNTI (**b**). Ligands are depicted as capped sticks with green carbons, and contact side chains of the receptor within 4 Å from the ligand are shown with grey carbons. Key hydrogen bonds and salt bridges are indicated with small cyan spheres and residues unique to the κ -OR are labelled in blue. Residue Asp 138^{3,32}, which also shows critical impact on GNTI and nor-BNI binding in mutagenesis studies, is highlighted in red. Ballesteros–Weinstein residue numbers are shown under the κ -OR residue numbers. The graphics were prepared using the ICM molecular modelling package (Molsoft LLC).

for the common naltrexone moieties of both nor-BNI and GNTI (r.m.s.d. 0.85 Å). In addition to a highly complementary van der Waals interface, both compounds formed an amino group salt bridge to the Asp 138^{3,32} side chain and a hydrogen bond to the Tyr 139^{3,33} side chain, both of which are important anchoring points for binding of morphine-based ligands, as supported by previous mutagenesis studies³⁴.

Moreover, unlike JD_{Tic}, both nor-BNI and GNTI compounds have a second basic moiety located more than 10 Å away from the first amino group (the second morphine moiety in nor-BNI and the guanidine moiety in GNTI). In the predicted models of κ -OR–nor-BNI/GNTI complexes, these additional amino groups of both ligands form a salt bridge with Glu 297^{6,58} located at the entrance to the ligand-binding pocket, which was previously characterized as a residue critical for subtype selectivity of κ -OR-selective morphinan derivatives³⁶. This interaction is also supported by our mutagenesis results (Supplementary Table 3), where a Glu297Ala mutation induced a significant drop in both nor-BNI and GNTI binding affinity, but did not affect JD_{Tic} affinity. Hydrophobic interactions at the κ -OR-specific residue Ile 294 were also found for both nor-BNI and GNTI; consistent with our mutagenesis results (Supplementary

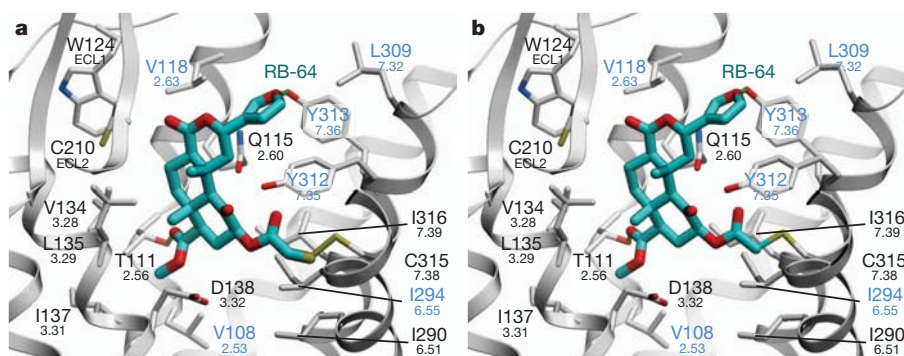


Figure 4 | Model of covalently bound RB-64. **a, b,** Putative binding mode of the RB-64 + 463 AMU (**a**) and the RB-64 + 431 AMU (**b**) adduct. Residues within 4 Å of the ligand are shown. Ligand, capped sticks/cyan carbons; κ -OR side chains, capped sticks; hydrogen bonds, small green spheres; κ -OR-unique

residues are labelled in blue. Ballesteros–Weinstein residue numbers are shown under the κ -OR residue numbers. The graphics were prepared using the ICM molecular modelling package (Molsoft LLC).

Table 3) and suggesting that Ile294 may also be important for developing human κ -OR-subtype-selective morphinan derivatives. Additional polar interactions with κ -OR-specific residues, Glu 209 and Ser211 in ECL2, are found for nor-BNI, which may further enhance the κ -OR selectivity of this bulky ligand. Another side chain of the pocket, His291^{6,52}, which is involved in the highly conserved aromatic cluster around Trp^{6,48} and thought to have a critical role in the receptor activation process³⁷, forms hydrophobic contacts with JDTic, nor-BNI and GNTI. His291^{6,52} can be mutated to another aromatic residue, phenylalanine, without disrupting binding of these antagonists (Supplementary Table 3). The non-conservative His291^{6,52}Lys mutation, however, abolished binding of all tested ligands, probably because of the disruption of the aromatic cluster induced by the lysine side chain. Interestingly, the cyclopropyl moiety of both nor-BNI and GNTI in these binding poses has the same position as the isopropyl moiety of JDTic, making hydrophobic contact with the conserved residue Trp287^{6,48}. This cyclopropyl moiety is generally implicated in conversion of opioid agonists into antagonists (for example, agonist oxymorphone into antagonist naltrexone), and this effect may be partially explained by a direct interaction with the Trp287^{6,48} side chain.

Overall, these structure-based docking results support the ‘message–address’ model³⁸ for morphine-based ligands nor-BNI and GNTI³⁶, which points to Glu297^{6,58} as a key side chain that controls κ -OR selectivity by anchoring the ‘address’ moieties of these compounds. The crystal structure of the κ -OR–JDTic complex (Figs 2 and 3), however, demonstrates that even without an ‘address’ interaction with Glu297^{6,58}, more than a 1,000-fold subtype-selectivity to κ -OR can be achieved for JDTic and some of its derivatives. Importantly, then, the message–address hypothesis does not uniformly apply to all κ -OR-selective antagonists.

Binding of salvinorins

SalA, a naturally occurring diterpene from the widely abused hallucinogenic plant *Salvia divinorum*, represents an exceedingly potent (half-maximum effective concentration (EC₅₀) = 1 nM) and selective κ -OR agonist (>1,000-fold)¹⁵. SalA is unique compared to other κ -OR ligands in that it lacks a charged or polar nitrogen atom to anchor it in the binding pocket. Extensive site-directed mutagenesis, substituted cysteine-accessibility mutagenesis (SCAM) and SAR studies on SalA and its analogues have been performed, indicating (among others) that the 2-acetoxy moiety interacts with Cys315^{7,38} (ref. 39). Possible modes of interaction between the cysteine-reactive and ultrapotent agonist and SalA analogue 22-thiocyanatosalvinorin A (RB-64; K_i = 0.59 nM; EC₅₀ = 0.077 nM)³⁹, and the human κ -OR structure were thus evaluated. Exposure of κ -OR to RB-64 produces irreversibly bound, wash-resistant adducts that are tethered to Cys315^{7,38} (ref. 39). As the thiocyanate group contains two electrophilic centres, two

distinct adducts may be formed, increasing the mass by either 463 or 431 AMU. Docking studies using GOLD⁴⁰ predict that the salvinorin 2-position can access Cys315^{7,38} while maintaining many of the interactions implicated by site-directed mutagenesis for SalA, providing a possible mechanism for the formation of the κ -OR–RB-64 adduct (Fig. 4, Supplementary Tables 4 and 5, and Supplementary Figs 11 and 12). Additionally, the docking results serve as a model of the initial recognition process of SalA-related agonists of the human κ -OR in an inactive state, although additional studies will be needed to fully elucidate the nature of the SalA-induced activation mechanism.

Conclusions

The κ -OR–JDTic crystal structure has uncovered a combination of key features shared with chemokine and aminergic GPCRs along with unique structural details characteristic of the opioid subfamily. The human κ -OR was crystallized as a parallel dimer with contacts involving helices I, II and VIII. Although the existence of GPCR dimers *in vivo* and their physiological relevance remain highly debatable, several distinct potential dimer interfaces are starting to emerge from crystallographic and biochemical studies. Such multiple dimerization interfaces may serve to support different functional pathways, as well as to promote oligomeric assembly of GPCRs. Analysis of ligand–receptor interactions has revealed important molecular details of the exceptionally high affinity and subtype selectivity of JDTic, a small-molecule antagonist with a broad therapeutic potential. The elucidation of a large binding cavity with a multitude of potential anchoring points begins to explain both the broad structural diversity of drugs targeting the human κ -OR and differences in their receptor interaction modes, as supported by differential effects of various site-directed mutations on the binding properties of chemically diverse prototypic ligands. The human κ -OR structure provides a long anticipated molecular framework for understanding opioid drug action, and thereby affords valuable new opportunities for the structure-based discovery of new drugs with ideal pharmacological properties.

METHODS SUMMARY

κ -OR–T4L was expressed in *Spodoptera frugiperda* (Sf9) cells. Ligand-binding and functional assays were performed as described in Methods. Receptor–ligand complexes were solubilized from washed Sf9 membranes using 1% (w/v) *n*-dodecyl- β -D-maltopyranoside (DDM) and 0.2% (w/v) cholesteryl hemisuccinate (CHS), and purified by immobilized metal ion affinity chromatography (IMAC), followed by reverse IMAC after cleaving N-terminal Flag–10×His tags by His-tagged tobacco etch virus (TEV) protease. The purified protein solution was mixed with monoolein and cholesterol in a ratio of 40%:54%:6% (w/w) to form lipidic cubic phase (LCP) from which the receptor was crystallized. Crystals were grown at 20 °C in 45 nl protein-laden LCP boluses overlaid by 800 nl of precipitant solutions as described in Methods. Crystals were harvested from the LCP matrix and flash frozen in liquid nitrogen. X-ray diffraction data were collected on the 23ID-B/D beamline (GM/CA CAT) at the Advanced Photon Source, Argonne, using a 10 μ m minibeam at a wavelength of 1.0330 Å. Data collection, processing, structure solution and refinement are described in Methods. Modelling of JDTic analogues and κ -OR-selective

morphine derivatives nor-BNI and GNTI was performed using ICM-Pro; SYBYL-X 1.3 and GOLD Suite 5.1 were used to model RB-64 complexes, as described in Methods.

Full Methods and any associated references are available in the online version of the paper at www.nature.com/nature.

Received 31 December 2011; accepted 10 February 2012.

Published online 21 March 2012.

- Fredriksson, R., Lagerstrom, M. C., Lundin, L. G. & Schioth, H. B. The G-protein-coupled receptors in the human genome form five main families. Phylogenetic analysis, paralogon groups, and fingerprints. *Mol. Pharmacol.* **63**, 1256–1272 (2003).
- Waldhoer, M., Bartlett, S. E. & Whistler, J. L. Opioid receptors. *Annu. Rev. Biochem.* **73**, 953–990 (2004).
- Cherezov, V. *et al.* High-resolution crystal structure of an engineered human β_2 -adrenergic G protein-coupled receptor. *Science* **318**, 1258–1265 (2007).
- Jaakola, V. P. *et al.* The 2.6 angstrom crystal structure of a human A_{2A} adenosine receptor bound to an antagonist. *Science* **322**, 1211–1217 (2008).
- Chien, E. Y. *et al.* Structure of the human dopamine D3 receptor in complex with a D2/D3 selective antagonist. *Science* **330**, 1091–1095 (2010).
- Warne, T. *et al.* Structure of a β_1 -adrenergic G-protein-coupled receptor. *Nature* **454**, 486–491 (2008).
- Shimamura, T. *et al.* Structure of the human histamine H_1 receptor complex with doxepin. *Nature* **475**, 65–70 (2011).
- Wu, B. *et al.* Structures of the CXCR4 chemokine GPCR with small-molecule and cyclic peptide antagonists. *Science* **330**, 1066–1071 (2010).
- Rasmussen, S. G. *et al.* Crystal structure of the β_2 adrenergic receptor–Gs protein complex. *Nature* **477**, 549–555 (2011).
- Katritch, V., Cherezov, V. & Stevens, R. C. Diversity and modularity of G protein-coupled receptor structures. *Trends Pharmacol. Sci.* **33**, 17–27 (2011).
- Congreve, M., Langmead, C. J., Mason, J. S. & Marshall, F. H. Progress in structure based drug design for G protein-coupled receptors. *J. Med. Chem.* **54**, 4283–4311 (2011).
- Kufareva, I., Rueda, M., Katritch, V., Stevens, R. C. & Abagyan, R. Status of GPCR modeling and docking as reflected by community-wide GPCR Dock 2010 assessment. *Structure* **19**, 1108–1126 (2011).
- Martin, W. R., Eades, C. G., Thompson, J. A., Huppler, R. E. & Gilbert, P. E. The effects of morphine- and nalorphine- like drugs in the nondependent and morphine-dependent chronic spinal dog. *J. Pharmacol. Exp. Ther.* **197**, 517–532 (1976).
- Carlezon, W. A. Jr, Beguin, C., Knoll, A. T. & Cohen, B. M. Kappa-opioid ligands in the study and treatment of mood disorders. *Pharmacol. Ther.* **123**, 334–343 (2009).
- Roth, B. L. *et al.* Salvinorin A: a potent naturally occurring nonnitrogenous κ opioid selective agonist. *Proc. Natl Acad. Sci. USA* **99**, 11934–11939 (2002).
- Walsh, S. L., Strain, E. C., Abreu, M. E. & Bigelow, G. E. Enadoline, a selective kappa opioid agonist: comparison with butorphanol and hydromorphone in humans. *Psychopharmacology (Berl.)* **157**, 151–162 (2001).
- Thomas, J. B. *et al.* Identification of the first trans-(3R,4R)- dimethyl-4-(3-hydroxyphenyl)piperidine derivative to possess highly potent and selective opioid κ receptor antagonist activity. *J. Med. Chem.* **44**, 2687–2690 (2001).
- Carroll, F. I. *et al.* Pharmacological properties of JDTC: a novel κ -opioid receptor antagonist. *Eur. J. Pharmacol.* **501**, 111–119 (2004).
- Jackson, K. J., Carroll, F. I., Negus, S. S. & Damaj, M. I. Effect of the selective kappa-opioid receptor antagonist JDTC on nicotine antinociception, reward, and withdrawal in the mouse. *Psychopharmacology (Berl.)* **210**, 285–294 (2010).
- Salom, D. *et al.* Crystal structure of a photoactivated deprotonated intermediate of rhodopsin. *Proc. Natl Acad. Sci. USA* **103**, 16123–16128 (2006).
- Mancia, F., Assur, Z., Herman, A. G., Siegel, R. & Hendrickson, W. A. Ligand sensitivity in dimeric associations of the serotonin 5HT $_2c$ receptor. *EMBO Rep.* **9**, 363–369 (2008).
- Wang, J. B., Johnson, P. S., Wu, J. M., Wang, W. F. & Uhl, G. R. Human κ opiate receptor second extracellular loop elevates dynorphin's affinity for human μ/κ chimeras. *J. Biol. Chem.* **269**, 25966–25969 (1994).
- Ballesteros, J. A. & Weinstein, H. Integrated methods for the construction of three-dimensional models and computational probing of structure-function relations in G protein-coupled receptors. *Methods Neurosci.* **25**, 366–428 (1995).
- Palczewski, K. *et al.* Crystal structure of rhodopsin: a G protein-coupled receptor. *Science* **289**, 739–745 (2000).
- Xu, F. *et al.* Structure of an agonist-bound human A_{2A} adenosine receptor. *Science* **332**, 322–327 (2011).
- Standfuss, J. *et al.* The structural basis of agonist-induced activation in constitutively active rhodopsin. *Nature* **471**, 656–660 (2011).
- Subramanian, G., Paterlini, M. G., Larson, D. L., Portoghese, P. S. & Ferguson, D. M. Conformational analysis and automated receptor docking of selective arylacetamide-based κ -opioid agonists. *J. Med. Chem.* **41**, 4777–4789 (1998).
- Cai, T. B. *et al.* Synthesis and *in vitro* opioid receptor functional antagonism of analogues of the selective kappa opioid receptor antagonist (3R)-7-hydroxy-N-[(1S)-1-[(3R,4R)-4-(3-hydroxyphenyl)-3,4-dimethyl-1-piperidinyl]methyl]-2-methylpropyl]-1,2,3,4-tetrahydro-3-isoquinolinecarboxamide (JDTC). *J. Med. Chem.* **51**, 1849–1860 (2008).
- Thomas, J. B. *et al.* Importance of phenolic address groups in opioid kappa receptor selective antagonists. *J. Med. Chem.* **47**, 1070–1073 (2004).
- Runyon, S. P. *et al.* Analogues of (3R)-7-hydroxy-N-[(1S)-1-[(3R,4R)-4-(3-hydroxyphenyl)-3,4-dimethyl-1-piperidinyl]methyl]-2-methylpropyl]-1,2,3,4-tetrahydro-3-isoquinolinecarboxamide (JDTC). Synthesis and *in vitro* and *in vivo* opioid receptor antagonist activity. *J. Med. Chem.* **53**, 5290–5301 (2010).
- Zimmerman, D. M., Nickander, R., Horng, J. S. & Wong, D. T. New structural concepts for narcotic antagonists defined in a 4-phenylpiperidine series. *Nature* **275**, 332–334 (1978).
- Vortherms, T. A., Mosier, P. D., Westkaemper, R. B. & Roth, B. L. Differential helical orientations among related G protein-coupled receptors provide a novel mechanism for selectivity. Studies with salvinorin A and the κ -opioid receptor. *J. Biol. Chem.* **282**, 3146–3156 (2007).
- Surraatt, C. K. *et al.* -mu opiate receptor. Charged transmembrane domain amino acids are critical for agonist recognition and intrinsic activity. *J. Biol. Chem.* **269**, 20548–20553 (1994).
- Befort, K. *et al.* The conserved aspartate residue in the third putative transmembrane domain of the delta-opioid receptor is not the anionic counterpart for cationic opiate binding but is a constituent of the receptor binding site. *Mol. Pharmacol.* **49**, 216–223 (1996).
- Totrov, M. & Abagyan, R. Flexible protein-ligand docking by global energy optimization in internal coordinates. *Proteins* **29**, 215–220 (1997).
- Metzger, T. G., Paterlini, M. G., Portoghese, P. S. & Ferguson, D. M. Application of the message-address concept to the docking of naltrexone and selective naltrexone-derived opioid antagonists into opioid receptor models. *Neurochem. Res.* **21**, 1287–1294 (1996).
- Chen, S. *et al.* Mutation of a single TMVI residue, Phe²⁸², in the β_2 -adrenergic receptor results in structurally distinct activated receptor conformations. *Biochemistry* **41**, 6045–6053 (2002).
- Chavkin, C. & Goldstein, A. Specific receptor for the opioid peptide dynorphin: structure–activity relationships. *Proc. Natl Acad. Sci. USA* **78**, 6543–6547 (1981).
- Yan, F. *et al.* Structure-based design, synthesis, and biochemical and pharmacological characterization of novel salvinorin A analogues as active state probes of the κ -opioid receptor. *Biochemistry* **48**, 6898–6908 (2009).
- Verdonk, M. L., Cole, J. C., Hartshorn, M., Murray, C. W. & Taylor, R. Improved protein-ligand docking using GOLD. *Proteins* **52**, 609–623 (2003).

Supplementary Information is linked to the online version of the paper at www.nature.com/nature.

Acknowledgements This work was supported by PSI: Biology grant U54 GM094618 (V.K., V.C., R.C.S.) for biological studies and structure production, NIH Roadmap grant P50 GM073197 (V.C., R.C.S.) for technology development and R01 DA017624 (B.L.R., E.V., R.B.M., P.D.M.), R01 DA027170 (B.L.R.), the NIMH Psychoactive Drug Screening Program Contract (B.L.R., X.-P.H.), the Michael Hooker Distinguished Chair of Pharmacology (B.L.R.), and the NIH grant R01 DA009045 (F.I.C.). D.W. is supported by a Boehringer Ingelheim Fonds PhD Fellowship. The JDTC X-ray structure was determined by C. George at the Laboratory for the Structure of Matter, Naval Research Laboratory. We thank J. Velasquez for help on molecular biology; T. Trinh, K. Allin and M. Chu for help on baculovirus expression; V. Setola for help with functional activity assays; J. Evans for help acquiring compounds; the National Institute of Drug Abuse Drug Supply Program for supplying JDTC and other opioid ligands used in these studies; K. Kadyshchik for assistance with figure preparation; E. Abola for assistance with manuscript preparation; A. Walker for assistance with manuscript preparation; J. Smith, R. Fischetti and N. Sanishvili for assistance in the development and use of the minibeam and beamtime at GM/CA-CAT beamline 23-ID at the Advanced Photon Source, which is supported by National Cancer Institute grant Y1-CO-1020 and National Institute of General Medical Sciences grant Y1-GM-1104.

Author Contributions H.W. assisted with protein expression, optimized the constructs, purified and crystallized the receptor in LCP, optimized crystallization conditions, grew crystals for data collection, collected the data and processed diffraction data, and prepared the manuscript. D.W. assisted with protein expression, purified the receptor, performed the thermal stability assay and assisted with preparing the manuscript. M.M. assisted with protein expression, purified the receptor, tested the JDTC compound, and performed the thermal stability assay. V.K. performed nor-BNI/GNTI-receptor docking and prepared the manuscript. G.W.H. processed diffraction data, solved and refined the structure and assisted with preparing the manuscript. E.V. created the initial tagged human κ -OR constructs and E.V. and X.-P.H. performed the ligand-binding and site-directed mutagenesis studies. W.L. assisted with construct optimization and crystallization in LCP. A.A.T. refined the structure and assisted with preparing the manuscript. F.I.C. and S.W.M. provided JDTC crystal structure, performed conformational studies of JDTC, and assisted with preparing the manuscript. R.B.W. and P.D.M. performed RB-64-receptor docking and prepared the manuscript. V.C. assisted with the crystallization in LCP, processed diffraction data, refined the structure and prepared the manuscript. B.L.R. suggested the JDTC compound for structural studies, supervised the pharmacology and mutagenesis studies and prepared the manuscript. R.C.S. was responsible for the overall project strategy and management and led the manuscript preparation and writing.

Author Information The coordinates and structure factors have been deposited in the Protein Data Bank under accession code 4DJH. Reprints and permissions information is available at www.nature.com/reprints. The authors declare competing financial interests: details accompany the full-text HTML version of the paper at www.nature.com/nature. Readers are welcome to comment on the online version of this article at www.nature.com/nature. Correspondence and requests for materials should be addressed to R.C.S. (stevens@scripps.edu).

METHODS

Protein engineering for structural studies. Human κ -OR was engineered for structural studies by fusing lysozyme from T4 phage (T4L) into ICL3 (Gly 261–Arg 263) and further modified by N/C-terminal truncations (Δ Glu2–Ala42, Δ Arg359–Val380) and a single point mutation Ile135^{3,29}Leu (see Supplementary Information). The resulting κ -OR–T4L construct was subsequently expressed in baculovirus-infected *Spodoptera frugiperda* (Sf9) insect cells.

Generation of κ -OR constructs for Sf9 expression. The human κ -OR (I135L) cDNA provided by the NIMH Psychoactive Drug Screening Program was cloned into a modified pFastBac1 vector (Invitrogen), designated as pFastBac1-833100, which contained an expression cassette with a haemagglutinin (HA) signal sequence followed by a Flag tag, a 10 \times His tag³, and a TEV protease recognition site at the N terminus before the receptor sequence. Subcloning into the pFastBac1-833100 was achieved using PCR with primer pairs encoding restriction sites BamHI at the 5' and HindIII at the 3' termini of κ -OR wild type with subsequent ligation into the corresponding restriction sites found in the vector.

The κ -OR–T4L gene, based on the human κ -OR (I135L) and cysteine-free lysozyme from bacteriophage T4 (T4L C54T, C97A) sequences⁴¹, included the following additional features: (1) residue Ser 262 at ICL3 of κ -OR was deleted by using standard QuickChange PCR; (2) Asn 2–Tyr 161 of T4L were inserted between Gly 261 and Arg 263 within the ICL3 region; and (3) N-terminal residues 2–42 and C-terminal residues 359–380 of κ -OR were truncated.

Expression and purification of κ -OR constructs. High-titre recombinant baculovirus (>10⁹ viral particles per ml) was obtained using the Bac-to-Bac Baculovirus Expression System (Invitrogen) as previously described^{5,8}. 25 μ M of the antagonist naltrexone (NTX) and 5% Protein Boost Additive (PBA) were added to the system during expression. Cell suspensions were incubated for 4 days while shaking at 27 °C. Production of high-titre baculovirus stocks was performed as described before^{5,8}. Sf9 cells at a cell density of 2–3 \times 10⁶ cells ml^{−1} were infected with P2 virus at a m.o.i. (multiplicity of infection) of 2. Cells were harvested by centrifugation at 48 h post-infection and stored at −80 °C until use.

Insect cell membranes were disrupted by thawing frozen cell pellets in a hypotonic buffer containing 10 mM HEPES, pH 7.5, 10 mM MgCl₂, 20 mM KCl and EDTA-free complete protease inhibitor cocktail tablets (Roche). Extensive washing of the raw membranes was performed by repeated centrifugation in the same hypotonic buffer (two to three times), and then in a high osmotic buffer containing 1.0 M NaCl, 10 mM HEPES, pH 7.5, 10 mM MgCl₂, 20 mM KCl and EDTA-free complete protease inhibitor cocktail tablets (three to four times), thereby separating soluble and membrane associated proteins from integral transmembrane proteins.

Washed membranes were resuspended into buffer containing 40 μ M NTX, 2 mg ml^{−1} iodoacetamide, 150 mM NaCl and EDTA-free complete protease inhibitor cocktail tablets, and incubated at 4 °C for 1 h before solubilization. The membranes were then solubilized in 50 mM HEPES, pH 7.5, 150 mM NaCl, 1% (w/v) *n*-dodecyl- β -D-maltopyranoside (DDM, Anatrace), 0.2% (w/v) cholesteryl hemisuccinate (CHS, Sigma) and 20 μ M NTX for 3 h at 4 °C. The supernatant was isolated by centrifugation at 160,000g for 40 min, and incubated in 30 mM buffered imidazole (pH 7.5), 1 M NaCl with TALON IMAC resin (Clontech) overnight at 4 °C. After binding, the resin was washed with 10 column volumes of Wash I Buffer (50 mM HEPES, pH 7.5, 800 mM NaCl, 10% (v/v) glycerol, 0.1% (w/v) DDM, 0.02% (w/v) CHS, 10 mM ATP, 10 mM MgCl₂ and 50 μ M JDTic), followed by 6 column volumes of Wash II Buffer (50 mM HEPES, pH 7.5, 500 mM NaCl, 10% (v/v) glycerol, 0.05% (w/v) DDM, 0.01% (w/v) CHS, 50 mM imidazole and 50 μ M JDTic). The protein was then eluted by 3 column volumes of Elution Buffer (50 mM HEPES, pH 7.5, 300 mM NaCl, 10% (v/v) glycerol, 0.03% (w/v) DDM, 0.006% (w/v) CHS, 250 mM imidazole and 50 μ M JDTic). PD MiniTrap G-25 column (GE healthcare) was used to remove imidazole. The protein was then treated overnight with His-tagged AcTEV protease (Invitrogen) to cleave the N-terminal His-tag and Flag-tag. AcTEV protease and cleaved N-terminal fragment were removed by TALON IMAC resin incubation at 4 °C for 2 h for binding. The tag-less protein was collected as the TALON IMAC column flow-through. The protein was then concentrated to 40 mg ml^{−1} with a 100 kDa molecular weight cut-off Vivaspin centrifuge concentrator (GE healthcare). Protein purity and monodispersity were tested by SDS–PAGE and analytical size-exclusion chromatography (aSEC). Typically, the protein purity exceeded 95%, and the aSEC profile showed a single peak, indicative of receptor monodispersity.

Lipidic cubic phase crystallization. Protein samples of κ -OR in complex with JDTic were reconstituted into lipidic cubic phase (LCP) by mixing with molten lipid in a mechanical syringe mixer⁴². LCP crystallization trials were performed using an NT8-LCP crystallization robot (Formulatrix) as previously described⁴³. 96-well glass sandwich plates (Marienfeld) were incubated and imaged at 20 °C using an automated incubator/imager (RockImager 1000, Formulatrix). Initial

crystal hits were found from precipitant condition containing 100 mM sodium citrate pH 6.0, 30% (v/v) PEG400, 400 mM potassium nitrate. After extensive optimization, crystals of 30 μ m \times 10 μ m \times 5 μ m to 60 μ m \times 20 μ m \times 10 μ m size were obtained in 100 mM sodium citrate pH 5.8–6.4, 28–32% (v/v) PEG400, 350–450 mM potassium nitrate. Crystals were harvested directly from LCP matrix using MiTeGen micromounts and flash frozen in liquid nitrogen.

Data collection, structure solution and refinement. X-ray data were collected at the 23ID-B/D beamline (GM/CA CAT) at the Advanced Photon Source, Argonne, using a 10 μ m minibeam at a wavelength of 1.0330 Å and a MarMosaic 300 CCD detector. Most crystals were invisible after flash freezing in liquid nitrogen, and a similar alignment and data-collection strategy was followed as previously described⁴⁴. Among the several hundred crystal samples screened, most crystals diffracted to 2.8–3.5 Å resolution when exposed to 1–5 s of unattenuated beam using 1° oscillation. Data collection was limited to 5–10 frames per crystal, due to the fast onset of radiation damage in the microcrystals. Data were integrated, scaled and merged using HKL2000⁴⁵. A 97% complete data set of κ -OR–T4L/JDTic (space group *P*2₁2₁) at 2.9 Å resolution was obtained by merging data collected from 60 crystals. Initial phase information was obtained by molecular replacement with the program PHASER⁴⁶ using two independent search models of the polyaniline seven-transmembrane α -helices of CXCR4–IT1t (PDB accession 3ODU) and ensemble T4L models of β_2 -AR–T4L (PDB accession 2RH1), A_{2A}AR–T4L (PDB accession 3EML), CXCR4–T4L (PDB accession 3ODU), D3R–T4L (PDB accession 3PBL) and H_{1R}–T4L (PDB accession 3RZE). Electron density refinement was performed with REFMAC5⁴⁷, autoBUSTER⁴⁸, and PHENIX⁴⁹ followed by manual examination and rebuilding of the refined coordinates in the program COOT⁵⁰ using both $|2F_o| - |F_c|$ and $|F_o| - |F_c|$ maps, as well as omit maps. The final model includes 287 residues of A chain (Ser 55–Gly 261, Arg 263–Ser 301, Ala 307–Pro 347) and 288 residues of B chain (Ser 55–Gly 261, Arg 263–Gly 300, Ser 305–Pro 347) of the κ -OR, and residues Asn 2–Tyr 161 of both A and B chains of T4L.

Ligand-binding assay. Membrane preparations, radioligand binding assays using ³H-diprenorphine and data analyses were performed as previously described³⁹.

Modelling of high-affinity analogues of JDTic and morphine. Docking of high-affinity κ -OR-specific ligands was performed using an all-atom flexible receptor docking algorithm in ICM-Pro (MolSoft LLC) molecular modelling package as described previously³⁵. Internal coordinate (torsion) movements were allowed in the side chains of the binding pocket, defined as residues within 10 Å distance of JDTic in the crystal structure. Other side chains and the backbone of the protein were kept as in the crystal structure. An initial conformation for each of the ligands was generated by Cartesian optimization of the ligand model in Merck Molecular Force Field. Docking was performed by placing the ligand in a random position within 5 Å from the entrance to the binding pocket and global conformational energy optimization of the complex^{39,40}. To facilitate side-chain rotamer switches in flexible κ -OR models, the first 10⁶ steps of the Monte Carlo (MC) procedure used 'soft' van der Waals potentials and high MC temperature, followed by another 10⁶ steps with 'exact' van der Waals method and gradually decreasing temperature. A harmonic 'distance restraint' applied between an amino group of the ligand and carboxyl of Asp 138 side chain in the initial 10⁶ steps was removed in the final 10⁶ steps. At least 10 independent runs of the docking procedure were performed for each κ -OR ligand. The docking results were considered 'consistent' when at least 80% of the individual runs resulted in conformations clustered within a r.m.s.d. of <1 Å to the overall best energy pose of the ligand. All calculations were performed on a 12-core Linux workstation.

Modelling of RB-64. Modelling of RB-64 was performed using SYBYL-X 1.3 (Tripos) and GOLD 5.1 (Cambridge Crystallographic Data Centre)⁴⁰. Default parameters were used except where noted. The structures of RB-64 and its κ -OR complexes were energy minimized using the Tripos Force Field (Gasteiger–Hückel charges, distance-dependent dielectric constant $\epsilon = 4$, non-bonded interaction cut-off = 8 Å, energy gradient termination = 0.05 kcal/(mol \times Å)). The κ -OR C315^{7,38} χ_1 torsion angle was modified ($\chi_1 = +60.0^\circ$), orienting the sulfhydryl group towards the binding cavity. A docking distance constraint was used (C315 SG atom to thiocyanate sulphur atom distance, 2.0–6.0 Å; spring constant = 5.0). The Q115^{2,60}, D138^{3,32}, I290^{6,51}, I294^{6,55}, Y313^{7,36} and I316^{7,39} side chains were allowed to flex via rotamer library. The GoldScore fitness function was used with early termination disabled for 30 genetic algorithm runs. Poses were selected based on their GoldScore and ability to explain the relevant observed biochemical data. Stereochemical quality was assessed using PROCHECK.

41. Rosenbaum, D. M. *et al.* GPCR engineering yields high-resolution structural insights into β_2 -adrenergic receptor function. *Science* **318**, 1266–1273 (2007).

42. Caffrey, M. & Cherezov, V. Crystallizing membrane proteins using lipidic mesophases. *Nature Protocols* **4**, 706–731 (2009).
43. Cherezov, V., Peddi, A., Muthusubramaniam, L., Zheng, Y. F. & Caffrey, M. A robotic system for crystallizing membrane and soluble proteins in lipidic mesophases. *Acta Crystallogr. D* **60**, 1795–1807 (2004).
44. Cherezov, V. *et al.* Rastering strategy for screening and centring of microcrystal samples of human membrane proteins with a sub-10 μm size X-ray synchrotron beam. *J. R. Soc. Interface* **6** (Suppl. 5), S587–S597 (2009).
45. Otwinowski, Z. & Minor, W. Processing of X-ray diffraction data collected in oscillation mode. *Methods Enzymol.* **276**, 307–326 (1997).
46. McCoy, A. J. *et al.* Phaser crystallographic software. *J. Appl. Cryst.* **40**, 658–674 (2007).
47. Murshudov, G. N., Vagin, A. A. & Dodson, E. J. Refinement of macromolecular structures by the maximum-likelihood method. *Acta Crystallogr. D* **53**, 240–255 (1997).
48. Bricogne, G. *et al.* BUSTER v. 2.8.0 (Global Phasing, 2009).
49. Adams, P. D. *et al.* PHENIX: a comprehensive Python-based system for macromolecular structure solution. *Acta Crystallogr. D* **66**, 213–221 (2010).
50. Emsley, P., Lohkamp, B., Scott, W. G. & Cowtan, K. Features and development of Coot. *Acta Crystallogr. D* **66**, 486–501 (2010).

Crystal structure of the μ -opioid receptor bound to a morphinan antagonist

Aashish Manglik¹, Andrew C. Kruse¹, Tong Sun Kobilka¹, Foon Sun Thian¹, Jesper M. Mathiesen¹, Roger K. Sunahara², Leonardo Pardo³, William I. Weis^{1,4}, Brian K. Kobilka¹ & Sébastien Granier^{1,5}

Opium is one of the world's oldest drugs, and its derivatives morphine and codeine are among the most used clinical drugs to relieve severe pain. These prototypical opioids produce analgesia as well as many undesirable side effects (sedation, apnoea and dependence) by binding to and activating the G-protein-coupled μ -opioid receptor (μ -OR) in the central nervous system. Here we describe the 2.8 Å crystal structure of the mouse μ -OR in complex with an irreversible morphinan antagonist. Compared to the buried binding pocket observed in most G-protein-coupled receptors published so far, the morphinan ligand binds deeply within a large solvent-exposed pocket. Of particular interest, the μ -OR crystallizes as a two-fold symmetrical dimer through a four-helix bundle motif formed by transmembrane segments 5 and 6. These high-resolution insights into opioid receptor structure will enable the application of structure-based approaches to develop better drugs for the management of pain and addiction.

Opium extracts from the plant *Papaver somniferum* have been used for therapeutic and recreational purposes for thousands of years. Opioid alkaloids and related pharmaceuticals are the most effective analgesics for the treatment of acute and chronic pain. They also represent one of the largest components of the illicit drug market worldwide, generating revenue of approximately \$70 billion in 2009, much of which supports crime, wars and terrorism (UNODC World Drug Report 2011). Intravenous use of opioid drugs is a leading cause of death by overdose in Europe and North America, and a major contributing factor to the worldwide AIDS epidemic.

Morphine and codeine are the main active opioid alkaloids in opium. In humans, they act on the central nervous system to produce a wide range of effects including analgesia, euphoria, sedation, respiratory depression and cough suppression, and have peripheral effects such as constipation¹. Gene disruption studies in mice show that the target for the majority of the effects of opioid alkaloids, whether beneficial or adverse, is the μ -OR². The μ -OR belongs to the γ subfamily of class A G-protein-coupled receptors (GPCRs) with two closely related family members known as the δ - and κ -opioid receptors³. The μ -OR constitutes the main opioid target for the management of pain, acute pulmonary oedema, cough, diarrhoea and shivering¹. However, opioid drugs are highly addictive, with the acetylated form of morphine, heroin, being the best-known example. Because of this, the clinical efficacy of opioid drugs is often limited by the development of tolerance and dependence.

Although both beneficial and adverse effects are attributable to activation of the μ -OR, they seem to be mediated by different downstream signalling and regulatory pathways. The μ -OR couples predominantly to Gi, the inhibitory G protein for adenylyl cyclase. μ -OR signalling through Gi is responsible for its analgesic properties⁴. After activation, the μ -OR undergoes phosphorylation and subsequently couples to arrestins, which have both regulatory and signalling functions⁵. Studies suggest that ligands with the greatest addictive potential, such as morphine, promote interactions with Gi more strongly than they promote interactions with arrestins⁶. These studies suggest

that it may be possible to develop safer and more effective therapeutic agents targeting the μ -OR.

To understand better the structural basis for μ -OR function, we performed a crystallographic study of this receptor using the T4 lysozyme (T4L) fusion protein strategy developed previously⁷ (Supplementary Fig. 1). Using the *in meso* crystallization method, we obtained crystals and collected diffraction data from 25 crystals of *Mus musculus* μ -OR–T4L protein bound to the irreversible morphinan antagonist β -funaltrexamine (β -FNA). The structure was solved by molecular replacement from a 2.8 Å data set.

Transmembrane architecture

The lattice for the μ -OR receptor shows alternating aqueous and lipidic layers with receptors arranged in parallel dimers tightly associated through transmembrane (TM) helices 5 and 6. More limited parallel interdimeric contacts through TM1, TM2 and helix 8 are observed between adjacent dimers (Supplementary Fig. 2).

As in other GPCRs, the structure of the μ -OR consists of seven TM α -helices that are connected by three extracellular loops (ECL1–3) and three intracellular loops (ICL1–3) (Fig. 1a). TM3 is connected to ECL2 by a conserved disulphide bridge between C140^{3,25} (superscripts indicate Ballesteros–Weinstein numbers⁸) and C217. The morphinan ligand β -FNA (Fig. 1b, c) makes contacts with TM3, TM5, TM6 and TM7 (Fig. 1a), and the electron density observed in the structure confirms previous data identifying the K233^{5,39} side chain as the site of covalent attachment⁹ (Fig. 1c and Supplementary Fig. 3).

The intracellular face of the μ -OR closely resembles rhodopsin with respect to the relative positions of TM3, TM5 and TM6 (Supplementary Fig. 4). Nevertheless, like the β_2 -adrenergic receptor (β_2 -AR), there is no ionic bridge between the DRY sequence in TM3 and the cytoplasmic end of TM6. As with the β_2 -AR, R165^{3,50} forms a salt bridge with the adjacent D164^{3,49} of the DRY sequence. D164^{3,49} also engages in a polar interaction with R179 in ICL2, a feature that is similar to an interaction observed between D130^{3,49} and S143 in ICL2

¹Department of Molecular and Cellular Physiology, Stanford University School of Medicine, Stanford, California 94305, USA. ²Department of Pharmacology, University of Michigan Medical School, Ann Arbor, Michigan 48109, USA. ³Laboratori de Medicina Computacional, Unitat de Bioestadística, Universitat Autònoma de Barcelona, Barcelona 08193, Spain. ⁴Department of Structural Biology, Stanford University School of Medicine, Stanford, California 94305, USA. ⁵CNRS UMR 5203, INSERM U661, and Université Montpellier 1 et 2, Institut de Génétique Fonctionnelle, Montpellier 34094, France.

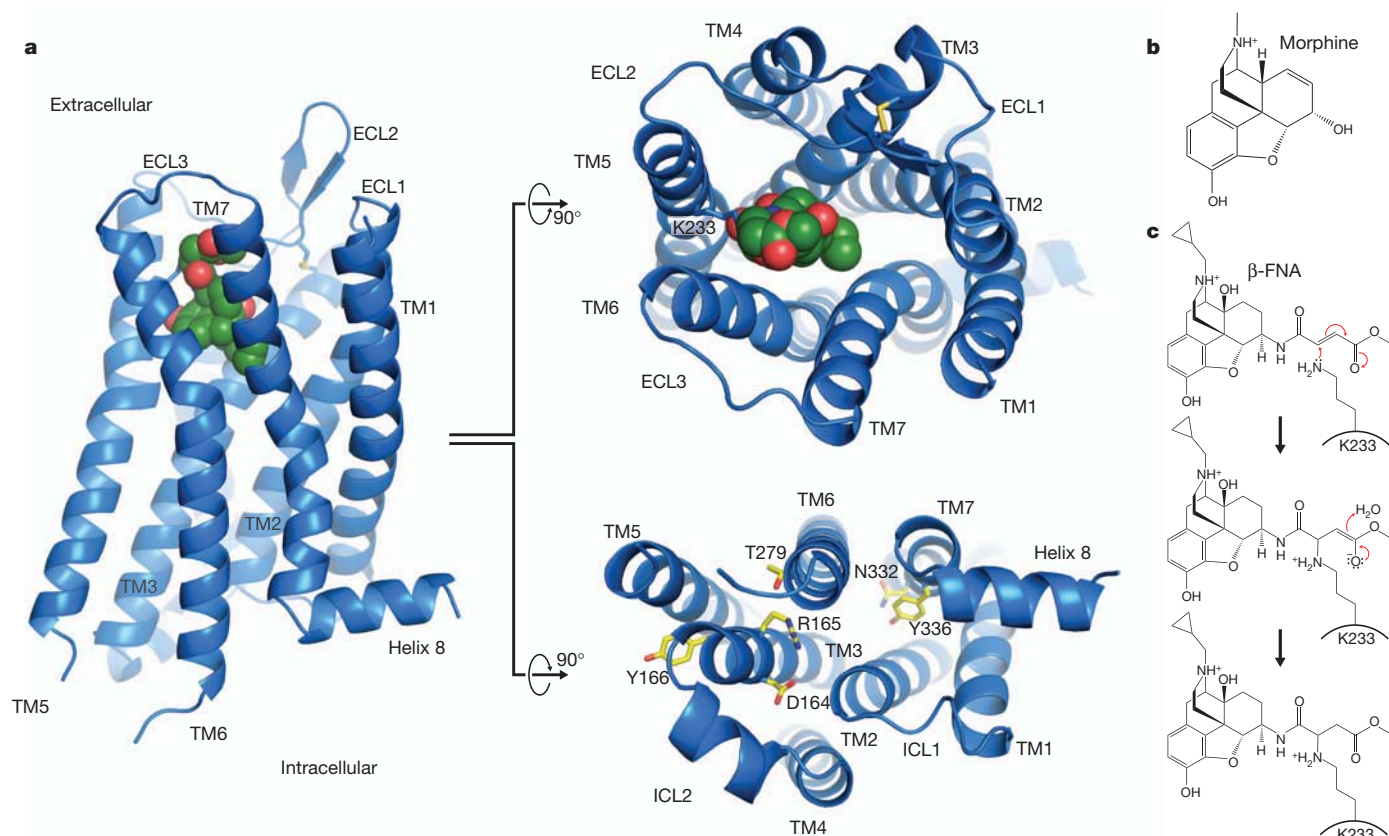


Figure 1 | Overall view of the μ -OR structure. **a**, Views from within the membrane plane (left), extracellular side (top) and intracellular side (bottom) show the typical seven-pass transmembrane GPCR architecture of the μ -OR. The ligand, β -FNA, is shown in green spheres. **b**, The chemical structure of

morphine. **c**, The chemical structure of β -FNA and the chemical reaction with the side chain of K233^{5,39} in the receptor are shown. β -FNA is a semisynthetic opioid antagonist derived from morphine, shown in **b**.

of the β_2 -AR (Supplementary Fig. 4). In the μ -OR, it has been shown that the mutation of T279^{6,34} to a lysine results in a constitutively active receptor¹⁰. This may be explained by a polar interaction observed in the crystal structure of the μ -OR between T279^{6,34} and R165^{3,50} (Supplementary Fig. 4). This interaction may stabilize the receptor in an inactive state.

An exposed ligand-binding pocket

In most available GPCR structures, the ligand is partially buried within the helical bundle by more superficial residues in TM segments and ECL2. The most extreme examples are the M2 and M3 muscarinic receptors^{11,12}, in which the ligand is covered with a layer of tyrosines (Fig. 2). This provides a structural basis for the very slow dissociation

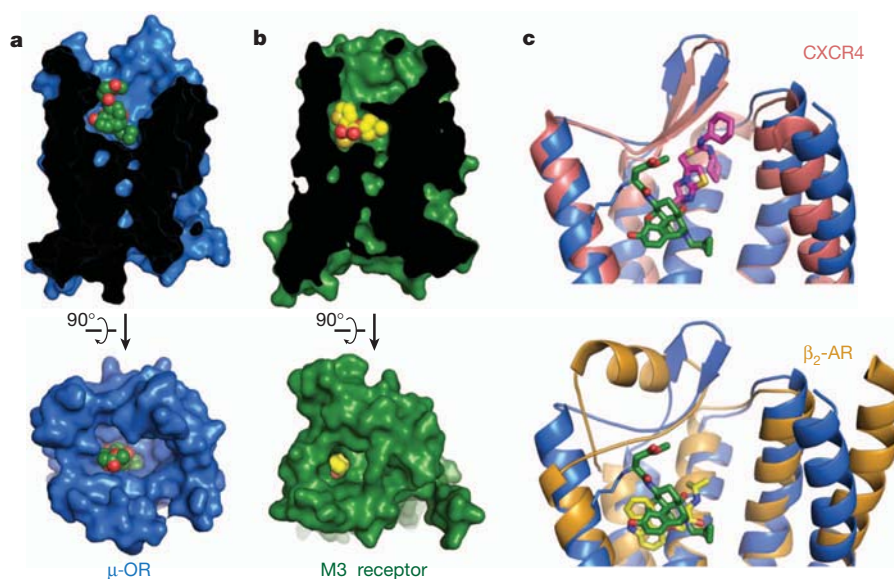


Figure 2 | Comparison of ligand-binding pockets. **a**, **b**, The binding pocket of the μ -OR (**a**) is wide and open above the ligand, in stark contrast to the deeply buried binding pocket of the muscarinic receptors, as exemplified by the M3 receptor (**b**). **c**, Top, the small-molecule antagonist IT1t (magenta) occupies a

binding pocket closer to the extracellular surface of CXCR4 than β -FNA in μ -OR. Bottom, β -FNA is positioned more similarly to the distantly related aminergic receptors for the binding site of carazolol (yellow) in the β_2 -AR.

kinetics of muscarinic antagonists. For example, the dissociation half-life of the clinically used drug tiotropium at the M3 receptor is 34.7 h and its dissociation constant (K_d) is 40 pM (ref. 13). By contrast, the binding pocket for β -FNA in the μ -OR is largely exposed to the extracellular surface (Fig. 2a). This may explain why extremely potent opioids such as buprenorphine, with an inhibition constant (K_i) of 740 pM, diprenorphine (K_i 72 pM), alvimopan (K_i 350 pM) and etorphine (K_i 230 pM) present rapid dissociation half-lives of 44 min, 36 min, 30 min¹⁴ and less than 1 min (ref. 15), respectively. Therefore, although the affinity of high-affinity opioid ligands is comparable to tiotropium, the dissociation kinetics are considerably different. This feature of opioid ligands may explain why heroin overdoses are rapidly reversible by naloxone¹⁶. In addition, the extremely high potency and fast kinetics of etorphine agonism and diprenorphine antagonism allows for a system that is capable of rapid anaesthesia and prompt reversal in veterinary use. As a result, etorphine is a preferred anaesthetic (dose in the range of 5–20 $\mu\text{g kg}^{-1}$) for valuable racehorses and for captive and free-ranging mammals¹⁷.

The μ -OR belongs to a subgroup of peptide GPCRs, and the closest published structure is that of the CXCR4 chemokine receptor¹⁸ (root mean squared deviation (r.m.s.d.) value of 1.35 Å). In the μ -OR the morphinan ligand β -FNA binds much more deeply than the small-molecule CXCR4 antagonist IT1t and occupies a similar position as agonists and antagonists for the β_2 -AR (r.m.s.d. value of 1.52 Å) and other monoamine receptors (Fig. 2c).

Binding pocket and opioid specificity

There are 14 residues within 4 Å of β -FNA. Nine of these have more direct interactions with the ligand (Fig. 3a–c), and are conserved in the κ -OR and δ -OR. D147^{3,32} engages in a charge–charge interaction with the amine moiety of the ligand and hydrogen bonds with Y326^{7,43} (both residues are strictly conserved in all the opioid receptor subtypes). Although D147^{3,32} occupies the same position as the counterion in aminergic receptors, a sequence comparison shows that it is not conserved in other peptide receptors. H297^{6,52} interacts with the aromatic ring of the morphinan group, but does not directly hydrogen bond with β -FNA as has been previously suggested¹⁹. However, the electron density suggests the presence of two water molecules that are well positioned to form a hydrogen-bonding network between H297^{6,52} and the phenolic hydroxyl of the morphinan group (Fig. 3b, c).

A direct comparison with the δ -OR sequence also shows that of the 14 residues within 4 Å of the ligand, 11 are identical between μ -OR and δ -OR. The three differences are at μ -OR positions E229^{ECL2}, K303^{6,58} and W318^{7,35}, which are Asp, Trp and Leu in the δ -OR, respectively. The substitution of leucine in δ -OR for W318^{7,35} is highlighted in Fig. 3d. W318^{7,35} was shown to be responsible for the binding selectivity of naltrindole, a δ -OR-selective antagonist and of [D-Pen2,D-Pen5]enkephalin (DPDPE), a δ -OR-selective peptide agonist²⁰. In particular, the point mutation W318L markedly increases the affinity of both these ligands at the μ -OR. Positioning naltrindole (represented in Fig. 3d) into the μ -OR-binding pocket by

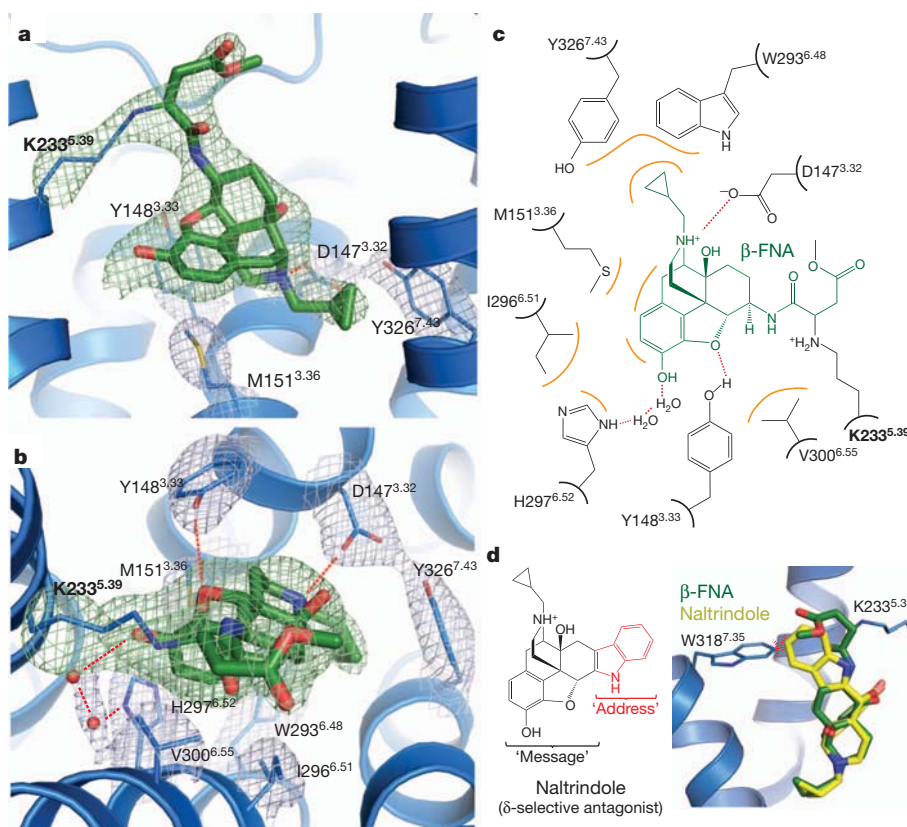


Figure 3 | Structural basis for morphinan ligand binding to the μ -OR. **a**, Side view of the ligand-binding pocket with polar interactions shown. TM6 is excluded from this view. The electron density used to position interacting side chains is shown in light blue coloured mesh depicting the $2F_o - F_c$ electron density contoured at 1.3σ . Green mesh depicts an omit map of β -FNA and K233^{5,39} side-chain atoms contoured at 3.0σ . **b**, Binding pocket viewed from the extracellular surface. Water molecules are shown as red spheres, with the accompanying electron density shown in light blue mesh. **c**, The binding site is diagrammed, showing the chemical structure of β -FNA (green) covalently

bound to the receptor through K233^{5,39} (bold). Hydrophobic interactions are shown in orange and polar contacts with red dotted lines. V300^{6,55} and I296^{6,51} form extensive hydrophobic contacts with the back face of the ligand (not shown). Two water molecules are positioned between H297^{6,52} and the phenolic group of β -FNA. **d**, The δ -OR-selective ligand naltrindole includes an indole group that would clash with W318^{7,35} in μ -OR, but not with the leucine found in the equivalent position in δ -OR. The indole has been described as an 'address' to target the ligand to δ -OR, whereas its efficacy ('message') is determined by the morphinan group on the left⁴⁰.

superimposition of its morphinan group on that of β -FNA shows that naltrindole would clash with the W318 side chain in μ -OR (Fig. 3d), whereas the leucine in this position of δ -OR would probably accommodate naltrindole without requiring structural rearrangement.

Endomorphins 1 and 2 are small peptides isolated from brain that were shown to have the highest affinity (low nM range) and the highest selectivity profile for the μ -OR receptor²¹. For instance, endomorphin 1 exhibits 4,000- and 15,000-fold selectivity for μ -OR over δ -OR and κ -OR, respectively²¹. Although little is known about the determinants of endomorphin binding, mutagenesis studies suggest that the μ -OR-selective synthetic peptide agonist [D-Ala2,N-MePhe4,Gly-ol5] enkephalin (DAMGO) occupies a space that overlaps with the β -FNA-binding pocket but also extends beyond this site²². Sites of mutations that impair DAMGO binding include H297^{6,52}, positioned near the bottom of the β -FNA pocket, as well as K303^{6,58}, W318^{7,35} and H319^{7,36}, positioned above the β -FNA-binding pocket (Supplementary Fig. 5). Given the residues involved in DAMGO binding to μ -OR, opioid peptides probably make both polar and non-polar contacts within the μ -OR-binding pocket. This feature of opioid peptide binding is also reflected in the lack of a highly charged surface within the μ -OR-binding pocket compared with that of the CXCR4 receptor¹⁸.

Oligomeric arrangement of μ -OR

The structure of μ -OR shows receptor molecules intimately associated into pairs along the crystallographic two-fold axis through two different interfaces (Fig. 4a, b). The first interface is a more limited parallel association mediated by TM1, TM2 and helix 8, with a buried surface area of 615 Å² (Fig. 4d and Supplementary Fig. 6). The second and more prominent interface observed in the μ -OR crystal structure is comprised of TM5 and TM6 (Fig. 4c). In this case, within each μ -OR- μ -OR pair, the buried surface area for a single protomer is 1,492 Å². This represents 92% of the total buried surface between μ -OR-T4L molecules, indicating that the comparatively small 114 Å² buried surface contributed by T4L is unlikely to drive the contact (Supplementary Fig. 7). This suggests that the pairwise association of receptor monomers may represent a physiological opioid receptor dimer or higher-order oligomer, the existence of which is supported by previous biochemical, pharmacological and cell biological studies²³.

Recent computational and biochemical studies have indicated the potential role of TM4 and TM5 in the interaction between δ -OR receptors²⁴. More generally, oligomers have been observed for a large number of GPCRs (recently reviewed in ref. 25). Some of these studies have shown that TM5 and TM6 peptides can disrupt dimers of the β_2 -AR and V2 vasopressin receptor^{26,27}, and recent crosslinking experiments with the M3 muscarinic receptor suggest a direct dimeric contact mediated by TM5 of each monomer²⁸. The potential involvement of the alternative TM1–TM2–H8 (where H8 is helix 8) interface in GPCR oligomerization has previously been indicated by several different biochemical studies²⁵ and, more recently, by the structure of opsin (Protein Data Bank (PDB) accession 3CAP)²⁹. In the case of opioid receptors, it has been shown that a μ -OR TM1 domain fused to a polybasic TAT sequence could disrupt the μ -OR- δ -OR interaction in the mouse spinal cord, resulting in an enhancement of morphine analgesia and a reduction in morphine tolerance³⁰.

The more prominent interface observed in the μ -OR crystal structure is comprised of TM5 and TM6 of each protomer arranged in a four-helix bundle motif (Fig. 5a). This interface is formed by an extensive network of interactions involving 28 residues in TM5 and TM6 (Fig. 5c and Supplementary Fig. 8). These surface packing interactions are highly complementary and are maintained all along the receptor membrane plane from the extracellular to the intracellular side of the μ -OR (Fig. 5c, d). The T279^{6,34} residue described earlier as having a role in maintaining the receptor in an inactive state is also part of the dimer interface, with the methyl of the threonine contacting I256^{5,62} of the adjacent protomer. It is thus tempting to speculate

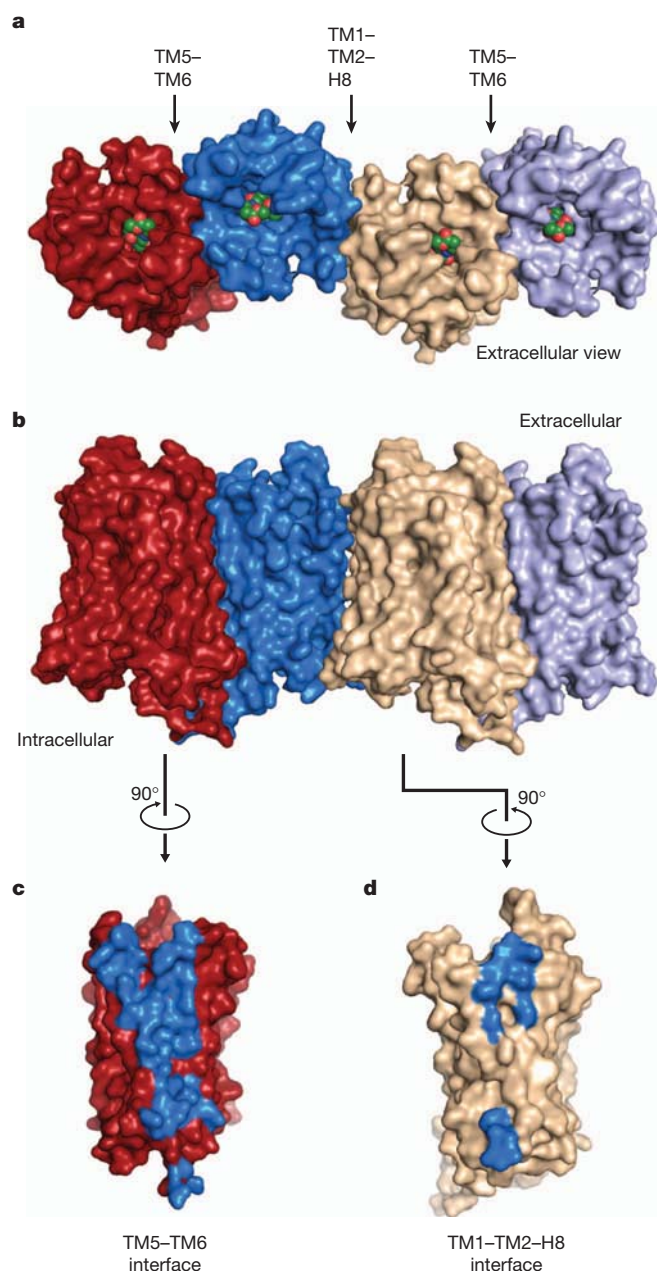


Figure 4 | μ -OR oligomeric arrangement. a, b, μ -OR crystallized as intimately associated pairs, with two different interfaces as defined in the text. c, d, The interface defined by TM5 and TM6 (c) is much more extensive than for the one defined by TM1–TM2–H8 (d).

that dimerization of the μ -OR could have a role in regulating receptor signalling.

The observed dimer is of interest because of existing evidence for both homo- and heterodimers (or oligomers) involving the μ -OR³¹. It has been suggested that opioid agonists such as DAMGO and methadone reduce tolerance to morphine *in vivo* by facilitating morphine-induced endocytosis through μ -OR oligomerization^{32,33}. These studies implicate allosteric interactions between a protomer bound to DAMGO or methadone and an adjacent protomer bound to morphine. Co-expressing μ -OR and δ -OR in cells results in pharmacological profiles distinct from either receptor expressed alone³⁴. Of interest, morphine is more efficacious in cells expressing both μ -OR and δ -OR in the presence of a δ -OR-selective antagonist, suggesting an allosteric interaction between μ -OR and δ -OR protomers³⁵. Hetero-oligomerization between μ -OR and non-opioid receptors has

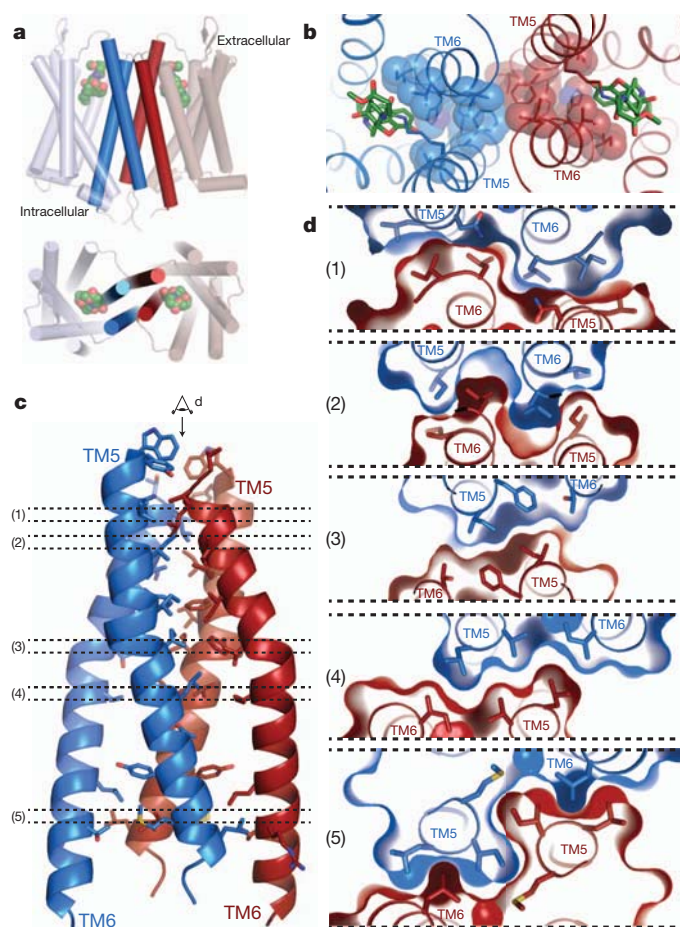


Figure 5 | The four-helix bundle interface. **a**, Schematic showing the four-helix bundle architecture of the TM5–TM6 interface. **b**, Viewed from the extracellular surface, the binding pocket shows tight association between the ligand (green sticks) and residues that are involved directly or indirectly in forming the dimeric interface (blue spheres). **c**, The four-helix bundle is expanded and shown in detail with interacting residues within 4.2 Å shown as sticks. **d**, Tomographic representation along the dimer interface viewed from the extracellular side (as indicated in panel **c**) showing the high surface complementarity within the four-helix bundle interface.

also been reported²³. For example, the α_{2a} adrenergic receptor was shown to modulate receptor μ -OR structure and signalling³⁶.

Consistent with a role for oligomerization in μ -OR function, we observed that the amino acids involved in the dimer interface display a high degree of homology with the δ -OR (Supplementary Figs 9 and 10). Replacing the residues of μ -OR with the corresponding residues from δ -OR would not be predicted to interfere with dimer formation (Supplementary Figs 9 and 10). This analysis also suggests that a μ -OR– δ -OR dimer could share the same interface. Interestingly, in the μ -OR TM5–TM6 dimer, the two binding sites are coupled through a network of packing interactions at the dimeric interface (Fig. 5b). This network could provide a structural explanation for the distinct pharmacological profiles obtained for μ -OR heterodimers and for the allosteric effects of one protomer on the pharmacological properties of the other. This dimeric interface thus provides potential insights into the mechanism of allosteric regulation of one GPCR protomer by the other.

Parallel dimers have also been observed in other GPCR crystal structures, most notably in CXCR4–T4L¹⁸. Interestingly, the CXCR4 dimer is also related by a two-fold rotational symmetry axis with a receptor arrangement similar but not identical to that seen in μ -OR (Supplementary Fig. 8). However, for the five different CXCR4–T4L crystal structures, the largest calculated contact area between the

two CXCR4 protomers is smaller (1,077 Å² for PDB accession 3OE0) than in the μ -OR structure (Supplementary Fig. 7), and it presents a comparatively less extensive network of interactions (Supplementary Fig. 8).

The dimeric arrangement of μ -OR across the TM5–TM6 interface observed in the crystal structure would probably preclude either protomer from coupling to G proteins. This is based on structural changes in TM5 and TM6 observed in the recent crystal structure of the β_2 -AR–G_s complex³⁷. This is also consistent with the observation that inverse agonists stabilize β_2 -AR oligomers, while the G protein G_s reduced the extent of oligomerization³⁸. However, we were able to model an active structure of μ -OR in complex with G protein based on the crystal structure of the β_2 -AR–G_s complex. Here, we observed that a tetramer formed by the association of two dimers through a TM5–TM6 interface would accommodate two G proteins in interaction with the two distal protomers (Supplementary Fig. 11). This model of an activated μ -OR–G-protein oligomeric complex is highly speculative but is compatible with results from a recent biophysical study suggesting that the G-protein G_i remains associated with a μ -OR tetramer stabilized by the agonist morphine³⁹.

The μ -OR is perhaps the most economically important GPCR in terms of the combined legal and illicit drug market. Although there are a number of effective drugs targeting the μ -OR on the market, the ideal agonist has yet to be developed. The structure of the μ -OR presented here provides the first high-resolution insight, to our knowledge, into a peptide receptor that can also be activated by small-molecule agonist ligands, some of which are the oldest used drugs in human history. This structure will enable the application of structure-based approaches to complement more conventional drug discovery programs. In addition, it may provide novel insights into the role of oligomerization in GPCR function.

METHODS SUMMARY

The μ -OR–T4L fusion protein was expressed in Sf9 insect cells and purified by nickel affinity chromatography followed by Flag antibody affinity chromatography and size-exclusion chromatography. It was crystallized using the lipidic cubic phase technique, and diffraction data were collected at GM/CA-CAT beamline 23ID-D at the Advanced Photon Source at Argonne National Laboratory. The structure was solved by molecular replacement using merged data from 25 crystals.

Full Methods and any associated references are available in the online version of the paper at www.nature.com/nature.

Received 18 December 2011; accepted 9 February 2012.

Published online 21 March 2012.

- Katzung, B. G. *Basic and Clinical Pharmacology* 10th edn (LANGE McGraw Hill Medical, 2007).
- Matthres, H. W. *et al.* Loss of morphine-induced analgesia, reward effect and withdrawal symptoms in mice lacking the μ -opioid-receptor gene. *Nature* **383**, 819–823 (1996).
- Lord, J. A., Waterfield, A. A., Hughes, J. & Kosterlitz, H. W. Endogenous opioid peptides: multiple agonists and receptors. *Nature* **267**, 495–499 (1977).
- Raffa, R. B., Martinez, R. P. & Connelly, C. D. G-protein antisense oligodeoxynucleotides and μ -opioid supraspinal antinociception. *Eur. J. Pharmacol.* **258**, R5–R7 (1994).
- Shukla, A. K., Xiao, K. & Lefkowitz, R. J. Emerging paradigms of β -arrestin-dependent seven transmembrane receptor signaling. *Trends Biochem. Sci.* **36**, 457–469 (2011).
- Molinari, P. *et al.* Morphine-like opiates selectively antagonize receptor-arrestin interactions. *J. Biol. Chem.* **285**, 12522–12535 (2010).
- Rosenbaum, D. M. *et al.* GPCR engineering yields high-resolution structural insights into β_2 -adrenergic receptor function. *Science* **318**, 1266–1273 (2007).
- Ballesteros, J. A. & Weinstein, H. *Integrated Methods for the Construction of Three Dimensional Models and Computational Probing of Structure Function Relations in G Protein-Coupled Receptors* Vol. 25 366–428 (Academic, 1995).
- Chen, C. *et al.* Determination of the amino acid residue involved in [³H] β -funaltrexamine covalent binding in the cloned rat μ -opioid receptor. *J. Biol. Chem.* **271**, 21422–21429 (1996).
- Huang, P. *et al.* Functional role of a conserved motif in TM6 of the rat μ opioid receptor: constitutively active and inactive receptors result from substitutions of Thr6.34(279) with Lys and Asp. *Biochemistry* **40**, 13501–13509 (2001).

11. Haga, K. *et al.* Structure of the human M2 muscarinic acetylcholine receptor bound to an antagonist. *Nature* **482**, 547–551 (2012).
12. Kruse, A. C. *et al.* Structure and dynamics of the M3 muscarinic acetylcholine receptor. *Nature* **482**, 552–556 (2012).
13. Disse, B. *et al.* Ba 679 BR, a novel long-acting anticholinergic bronchodilator. *Life Sci.* **52**, 537–544 (1993).
14. Cassel, J. A., Daubert, J. D. & DeHaven, R. N. [³H]Alvimopan binding to the μ opioid receptor: comparative binding kinetics of opioid antagonists. *Eur. J. Pharmacol.* **520**, 29–36 (2005).
15. Kurowski, M., Rosenbaum, J. S., Perry, D. C. & Sadee, W. [³H]-etorphine and [³H]-diprenorphine receptor binding *in vitro* and *in vivo*: differential effect of Na⁺ and guanylyl imidodiphosphate. *Brain Res.* **249**, 345–352 (1982).
16. Sporer, K. A. Acute heroin overdose. *Ann. Intern. Med.* **130**, 584–590 (1999).
17. Alford, B. T., Burkhardt, R. L. & Johnson, W. P. Etorphine and diprenorphine as immobilizing and reversing agents in captive and free-ranging mammals. *J. Am. Vet. Med. Assoc.* **164**, 702–705 (1974).
18. Wu, B. *et al.* Structures of the CXCR4 chemokine GPCR with small-molecule and cyclic peptide antagonists. *Science* **330**, 1066–1071 (2010).
19. Mansour, A. *et al.* Key residues defining the μ -opioid receptor binding pocket: a site-directed mutagenesis study. *J. Neurochem.* **68**, 344–353 (1997).
20. Bonner, G., Meng, F. & Akil, H. Selectivity of μ -opioid receptor determined by interfacial residues near third extracellular loop. *Eur. J. Pharmacol.* **403**, 37–44 (2000).
21. Zadina, J. E., Hackler, L., Ge, L. J. & Kastin, A. J. A potent and selective endogenous agonist for the μ -opioid receptor. *Nature* **386**, 499–502 (1997).
22. Seki, T. *et al.* DAMGO recognizes four residues in the third extracellular loop to discriminate between μ - and κ -opioid receptors. *Eur. J. Pharmacol.* **350**, 301–310 (1998).
23. Rozenfeld, R., Gomes, I. & Devi, L. In *The Opiate Receptors* Vol. 23 (ed. Pasternak, G. W.) Ch. 15 407–437 (Humana, 2011).
24. Johnston, J. M. *et al.* Making structural sense of dimerization interfaces of δ opioid receptor homodimers. *Biochemistry* **50**, 1682–1690 (2011).
25. Fanelli, F. & De Benedetti, P. G. Update 1 of: computational modeling approaches to structure-function analysis of G protein-coupled receptors. *Chem. Rev.* **111**, PR438–PR535 (2011).
26. Hebert, T. E. *et al.* A peptide derived from a β_2 -adrenergic receptor transmembrane domain inhibits both receptor dimerization and activation. *J. Biol. Chem.* **271**, 16384–16392 (1996).
27. Granier, S. *et al.* A cyclic peptide mimicking the third intracellular loop of the V2 vasopressin receptor inhibits signaling through its interaction with receptor dimer and G protein. *J. Biol. Chem.* **279**, 50904–50914 (2004).
28. Hu, J. *et al.* Structural aspects of M3 muscarinic acetylcholine receptor dimer formation and activation. *FASEB J.* **26**, 604–616 (2011).
29. Park, J. H., Scheerer, P., Hofmann, K. P., Choe, H. W. & Ernst, O. P. Crystal structure of the ligand-free G-protein-coupled receptor opsin. *Nature* **454**, 183–187 (2008).
30. He, S. Q. *et al.* Facilitation of μ -opioid receptor activity by preventing δ -opioid receptor-mediated codegradation. *Neuron* **69**, 120–131 (2011).
31. Jordan, B. A. & Devi, L. A. G-protein-coupled receptor heterodimerization modulates receptor function. *Nature* **399**, 697–700 (1999).
32. He, L., Fong, J., von Zastrow, M. & Whistler, J. L. Regulation of opioid receptor trafficking and morphine tolerance by receptor oligomerization. *Cell* **108**, 271–282 (2002).
33. He, L. & Whistler, J. L. An opiate cocktail that reduces morphine tolerance and dependence. *Curr. Biol.* **15**, 1028–1033 (2005).
34. George, S. R. *et al.* Oligomerization of μ - and δ -opioid receptors. Generation of novel functional properties. *J. Biol. Chem.* **275**, 26128–26135 (2000).
35. Gomes, I., Ijzerman, A. P., Ye, K., Maillet, E. L. & Devi, L. A. G protein-coupled receptor heteromerization: a role in allosteric modulation of ligand binding. *Mol. Pharmacol.* **79**, 1044–1052 (2011).
36. Vilardaga, J. P. *et al.* Conformational cross-talk between α_{2A} -adrenergic and μ -opioid receptors controls cell signaling. *Nature Chem. Biol.* **4**, 126–131 (2008).
37. Rasmussen, S. G. *et al.* Crystal structure of the β_2 adrenergic receptor–G_s protein complex. *Nature* **477**, 549–555 (2011).
38. Fung, J. J. *et al.* Ligand-regulated oligomerization of β_2 -adrenoceptors in a model lipid bilayer. *EMBO J.* **28**, 3315–3328 (2009).
39. Golebiewska, U., Johnston, J. M., Devi, L., Filizola, M. & Scarlata, S. Differential response to morphine of the oligomeric state of μ -opioid in the presence of δ -opioid receptors. *Biochemistry* **50**, 2829–2837 (2011).
40. Portoghese, P. S., Sultana, M. & Takemori, A. E. Design of peptidomimetic δ opioid receptor antagonists using the message-address concept. *J. Med. Chem.* **33**, 1714–1720 (1990).

Supplementary Information is linked to the online version of the paper at www.nature.com/nature.

Acknowledgements We acknowledge support from INSERM (S.G.), the Stanford Medical Scientist Training Program (A.M.), the National Science Foundation (A.C.K.), the Lundbeck Foundation (J.M.M.), the National Institutes of Health Grants NS028471 (B.K.K.) and DA031418 (B.K.K. and R.K.S.), and the Mathers Foundation (B.K.K. and W.I.W.).

Author Contributions A.M., A.C.K. and S.G. designed experiments, performed research and analysed data. T.S.K. and F.S.T. expressed and purified receptor. J.M.M. performed preliminary biochemical experiments with wild-type μ -OR. R.K.S. contributed to the effort of μ -OR crystallization and writing of the manuscript. W.I.W. supervised diffraction data analysis and model refinement. L.P. built the tetramer model and helped with the analysis of the dimer interfaces. A.M., A.C.K., S.G. and B.K.K. prepared the manuscript. S.G. and B.K.K. supervised the research.

Author Information Coordinates and structure factors for μ -OR–T4L are deposited in the Protein Data Bank under accession code 4DKL. Reprints and permissions information is available at www.nature.com/reprints. The authors declare no competing financial interests. Readers are welcome to comment on the online version of this article at www.nature.com/nature. Correspondence and requests for materials should be addressed to S.G. (granier@stanford.edu) or B.K.K. (kobilka@stanford.edu).

METHODS

Expression and purification. Previously crystallized GPCRs show little density for the poorly ordered amino- and carboxy-terminal domains. Although these domains are not critical for maintaining high ligand affinity, these flexible regions may inhibit crystallogenesis⁷. We therefore removed these regions in the receptor construct used for crystallography. Specifically, a TEV protease recognition site was introduced after residue G51 in the amino terminus and the C terminus was truncated after Q360. The short third intracellular loop of μ -OR, consisting of residues 264–269, was replaced with T4L residues 2–161 in a manner described previously⁷. To facilitate receptor purification, a Flag M1 tag was added to the N terminus and an octa-histidine tag was appended to the C terminus. Finally, a proline residue was introduced N-terminal to the octahistidine tag to allow efficient removal of C-terminal histidines by carboxypeptidase A. For these studies, we used the *M. musculus* μ -OR sequence because it is expressed at higher levels. The mouse and human μ -OR share 94% sequence identity and there are only four residues in the resolved part of the structure that differ between the mouse and human μ -OR. These include residues 66, 137, 187 and 306, which are all in the extracellular or intracellular loops of μ -OR and do not make contacts in the ligand-binding pocket. The final crystallization construct (μ -OR–T4L) is shown in a representative snake diagram in Supplementary Fig. 1a.

We compared the pharmacological properties of μ -OR–T4L to those of the wild-type receptor (Supplementary Fig. 1b). Both constructs showed identical affinity for the radiolabelled antagonist [³H]-diprenorphine ([³H]DPN).

The μ -OR–T4L construct was expressed in Sf9 cells using the baculovirus system. Culture media was supplemented with 10 μ M naloxone to stabilize the receptor during expression. Cells were infected at a density of 4×10^6 cells per ml and culture flasks were shaken at 27 °C for 48 h. After harvesting, cells were lysed by osmotic shock in a buffer comprised of 10 mM Tris-HCl pH 7.5, 1 mM EDTA, 100 μ M TCEP, 1 μ M naloxone and 2 mg ml^{−1} iodoacetamide to block reactive cysteines. Extraction of μ -OR–T4L from Sf9 membranes was done with a Dounce homogenizer in a solubilization buffer comprised of 0.5% dodecyl maltoside (DDM), 0.3% 3-[(3-Cholamidopropyl) dimethylammonio]-1-propanesulphonate (CHAPS), 0.03% cholesterol hemisuccinate (CHS), 20 mM HEPES pH 7.5, 0.5 M NaCl, 30% v/v glycerol, 2 mg ml^{−1} iodoacetamide, 100 μ M TCEP and 1 μ M naloxone. After centrifugation, nickel-NTA agarose was added to the supernatant, stirred for 2 h, and then washed in batch with 100g spins for 5 min each with a washing buffer of 0.1% DDM, 0.03% CHAPS, 0.01% CHS, 20 mM HEPES pH 7.5 and 0.5 M NaCl. The resin was poured into a glass column and bound receptor was eluted in washing buffer supplemented with 300 mM imidazole.

We used anti-Flag M1 affinity resin to purify μ -OR–T4L further and to exchange the ligand with the covalent antagonist β -FNA. Nickel-resin eluate was loaded onto anti-Flag M1 resin and washed extensively in the presence of 10 μ M β -FNA. The detergent DDM was then gradually exchanged over 1 h into a buffer with 0.01% lauryl maltose neopentyl glycol (MNG) and the NaCl concentration was lowered to 100 mM. Receptor was eluted from the anti-Flag M1 affinity resin with 0.2 mg ml^{−1} Flag peptide and 5 mM EDTA in the presence of 1 μ M β -FNA. To remove the N terminus of μ -OR–T4L, TEV protease was added at 1:3 w/w (TEV: μ -OR–T4L) and incubated at room temperature (23 °C) for 1 h. Receptor was then treated with carboxypeptidase A (1:100 w/w) and incubated overnight at 4 °C to remove the octa-histidine tag. The final purification step separated TEV and carboxypeptidase A from receptor by size exclusion chromatography on a Sephadex S200 column (GE Healthcare) in a buffer of 0.01% MNG, 0.001% CHS, 100 mM NaCl, 20 mM HEPES pH 7.5 and 1 μ M β -FNA. After size exclusion, β -FNA was added to a final concentration of 10 μ M.

The resulting receptor preparation was pure and monodisperse (Supplementary Fig. 12).

Crystallization and data collection. Purified μ -OR–T4L receptor was concentrated to 30 mg ml^{−1} using a Vivaspin sample concentrator with a 50 kDa molecular weight cut-off (GE Healthcare) and crystallization was performed using the *in meso* method⁴¹. Concentrated μ -OR–T4L was reconstituted into 10:1 monoolein:cholesterol (Sigma) in a ratio of 1:1.5 parts by weight receptor:lipid mixture. Reconstitution was done by the two-syringe method⁴¹. The resulting mesophase was dispensed onto glass plates in 80-nl drops and overlaid with 700 nl precipitant solution by a Gryphon LCP robot (Art Robbins Instruments). Crystals grew in precipitant solution consisting of 30–38% PEG 400, 100 mM HEPES pH 7.0, 7.5% DMSO and 300 mM lithium sulphate. Crystals were observed after 24 h and grew to full size after 5 days. Typical crystals before harvesting are shown in Supplementary Fig. 2.

Diffraction data were collected at Advanced Photon Source GM/CA-CAT beamline 23ID-D using a beam size of 10 μ m. Owing to radiation damage, the diffraction quality decayed during exposure. Wedges of 10–20 degrees were collected and merged from 25 crystals using HKL2000⁴². Diffraction quality ranged from 2.4–3.5 Å in most cases. The structure of the μ -OR was solved by molecular replacement in Phaser⁴³ using the CXCR4 receptor as a search model. We improved the initial model by iteratively building regions of the receptor in Coot⁴⁴ and refining in Phenix⁴⁵. We used translation libration screw-motion (TLS) refinement with groups generated within Phenix. Electron density suggested the presence of a cholesterol molecule and a monoolein lipid within the lipidic layer. These were subsequently incorporated into the model. To assess the overall quality of the final structure, we used MolProbity⁴⁶. The resulting statistics for data collection and refinement are shown in Supplementary Table 1. Figures were prepared in PyMOL⁴⁷.

Saturation binding experiments. Membrane homogenates were prepared from Sf9 cells expressing either wild-type μ -OR or μ -OR–T4L. Membranes containing μ -OR or μ -OR–T4L were incubated with the opioid antagonist, [³H]DPN for 1 h at 22 °C in 0.5 ml of binding buffer containing 75 mM Tris-HCl pH 7.4, 1 mM EDTA, 5 mM MgCl₂, 100 mM NaCl. To determine the affinity for diprenorphine, we used [³H]DPN concentrations ranging from 0.1 to 13.5 nM. High concentrations of un-labelled naloxone (1 μ M) were used to determine non-specific binding. To separate unbound [³H]-ligand, binding reactions were rapidly filtered over GF/C Brandel filters. The filters were then washed three times with 5 ml ice-cold binding buffer. Radioactivity was assayed by liquid scintillation counting. The resulting data were analysed using Prism 5.0 (GraphPad Software). [³H]DPN (specific activity: 55.0 Ci mmol^{−1}) was obtained from PerkinElmer Life Sciences.

41. Caffrey, M. & Cherezov, V. Crystallizing membrane proteins using lipidic mesophases. *Nature Protocols* **4**, 706–731 (2009).
42. Otwinowski, Z. & Minor, W. Processing of X-ray diffraction data collected in oscillation mode. *Methods Enzymol.* **276**, 307–326 (1997).
43. McCoy, A. J. *et al.* Phaser crystallographic software. *J. Appl. Cryst.* **40**, 658–674 (2007).
44. Emsley, P. & Cowtan, K. Coot: model-building tools for molecular graphics. *Acta Crystallogr. D* **60**, 2126–2132 (2004).
45. Afonine, P. V., Grosse-Kunstleve, R. W. & Adams, P. D. A robust bulk-solvent correction and anisotropic scaling procedure. *Acta Crystallogr. D* **61**, 850–855 (2005).
46. Chen, V. B. *et al.* MolProbity: all-atom structure validation for macromolecular crystallography. *Acta Crystallogr. D* **66**, 12–21 (2010).
47. Schrodinger, L. The PyMOL Molecular Graphics System v.1.3r1. (2010).

QUANTUM OPTICS

An entangled walk of photons

By harnessing the quantum nature of light and guiding the light through a network of circuits integrated in a glass chip, it is possible to mimic fundamental particles undergoing a quantum walk.

JONATHAN C. F. MATTHEWS
& MARK G. THOMPSON

Quantum mechanics is the most successful model of nature that we have, accurately describing fundamental physical processes. Although quantum effects such as entanglement and superposition are counterintuitive and often described as ‘spooky’, they are being observed and characterized in laboratories worldwide. Writing in *Physical Review Letters*, Sansoni *et al.*¹ describe how they have designed and built an optical network, integrated in a glass chip, that manipulates photons to simulate a process known as a discrete-time quantum walk. Furthermore, using a particular kind of entanglement, the authors simulated different classes of fundamental particles undergoing the quantum-walk process². The results are a step towards the development of quantum-mechanical machines that promise to outperform conventional supercomputers, which operate according to the laws of classical physics.

Perhaps the most far-reaching applications of quantum technologies will be based on the American physicist Richard Feynman’s proposal that an efficient way to simulate one quantum system is to use another. Such simulators could be used to study complex quantum systems that are computationally hard to simulate or difficult to physically control. We are currently witnessing initial demonstrations of these simulators in the form of purpose-built quantum devices that mimic other, less readily accessible quantum systems.

Developments in quantum simulation are still at the stage of mimicking systems simple enough to be handled with classical computers. However, photonics is an attractive candidate for reaching the point at which quantum machines could outperform state-of-the-art supercomputers for particular tasks. This is partly thanks to the complexity and stability of quantum networks realized with integrated optics, and to the nature of multiple identical photons interfering in a sufficiently complicated optical network³.

In classical physics, the analogue of Sansoni and colleagues’ discrete-time quantum walk would be a form of random walk, a tool already used in a broad range of fields from

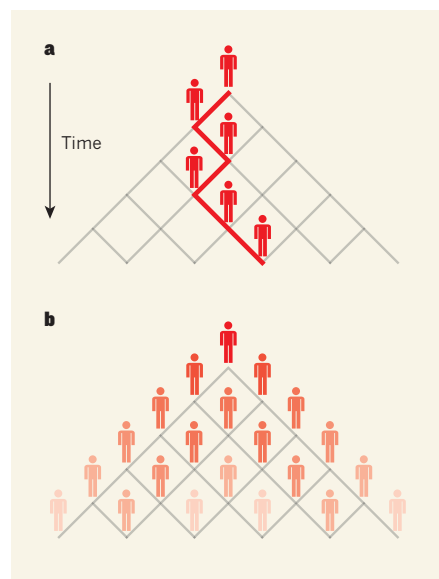


Figure 1 | Classical and quantum walks. **a**, In a classical random walk, a walker must make a choice (randomly) of moving either left or right at each step. After many trials of a fixed number of steps, the walker is most probably found close to its initial starting point. **b**, In a quantum walk, the walker uses a ‘quantum coin’ mechanism that allows it to move in a superposition of both left and right. The probability distribution of its position after many steps is therefore starkly different from that of a classical random walk, with the walker most likely to be found far from its initial starting point.

animal behaviour to economics, for example in modelling the path of a foraging animal or fluctuating prices in the stock market. The simplest random walk is on a line, and is conducted by repeatedly flipping a coin and walking left if the coin lands on heads, and right if it lands on tails — on average, the walker remains close to where it started. By contrast, if the walker is endowed with quantum properties (for example, in the case of a photon), it moves in a superposition of both left and right at each coin flip, with these multiple possibilities undergoing interference and giving rise to completely different behaviour from that of a classical random walk (Fig. 1).

Such quantum walks were initially conceived as an abstract computer-science model for developing ideas in quantum computation.

But now researchers are interested in using quantum walks to mimic real systems that exhibit local coupling. Examples of such systems are materials in which particles with spin are coupled or excitons travelling around large molecules (an exciton is a particle-like entity formed by an electron and the ‘hole’ left by a missing electron).

So far, all demonstrations of quantum walks (including those based on cold atoms, nuclear magnetic resonance and photonics) have sidestepped the requirement of a quantum computer by constructing purpose-built systems that exhibit quantum-walk dynamics. These demonstrations have allowed tests of quantum phenomena to be performed ahead of building a full-scale quantum computer. The first walks to be realized were of single quantum walkers, which display classical wave-like behaviour⁴. Multiple quantum walkers lead to behaviour that cannot be explained with wave phenomena alone, and have been reported⁵ using two indistinguishable photons launched into integrated optical circuits. Sansoni and colleagues’ demonstration¹ goes further by entangling the walkers in a discrete-time quantum-walk network⁶ achieved using an integrated network of waveguide beam splitters.

The particles of choice for Sansoni *et al.* are photons, which show great promise for quantum technologies⁷. They are readily manipulated at the single-photon level and experience negligible noise — in effect, they ‘leak’ very little quantum information to the environment. Working with photons also allows the deployment of integrated quantum photonics⁸ to make reconfigurable, complex miniature circuits that are inherently stable within fractions of an optical wavelength (about 10 nanometres)⁹. The authors fabricated their circuits using a laser ‘direct-write’ technique that allows three-dimensional optical circuits to be written into a solid block of borosilicate glass using a tightly focused beam of laser pulses¹⁰.

Sansoni and colleagues’ optical network¹ consisted of ten waveguide beam splitters at discrete points in a centimetre-scale glass circuit. Each beam splitter provided the ‘quantum coin’ mechanism that repeatedly placed the photons in quantum superposition as they progressed through the network (Fig. 2). Moreover, thanks to the type of entanglement they

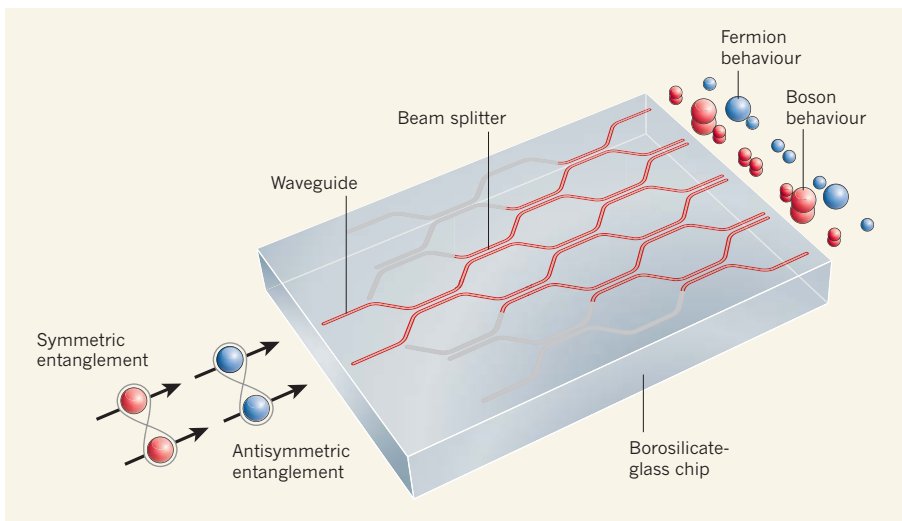


Figure 2 | Discrete quantum walk on a photonic chip. Sansoni *et al.*¹ fabricated a network of ten waveguide beam splitters in a borosilicate-glass chip using a focused pulsed laser (not shown) and launched two entangled photons (spheres) into the network. The photons underwent a quantum walk and were detected at the chip's output. The output depends on the symmetry of the entanglement between the photons. A symmetric entangled input leads to boson-like behaviour (the photons can occupy the same waveguide and so can exit the waveguides together), whereas an antisymmetrically entangled input yields fermion-like behaviour (the photons cannot occupy the same waveguide and therefore exit through separate waveguides). The size of the spheres at the output illustrates the probability of the photons leaving each of the waveguides, with a bigger size corresponding to a larger probability.

used and the fact that their device preserves photon polarization, the authors were able to simulate quantum walks not just for photons (and therefore the boson class of particles) but also fundamentally different classes of particles (the fermion and intermediate-type families). This approach can be generalized for any quantum network (not just quantum walks) and can be scaled-up to simulate any number of particles².

The scalability of integrated-optics circuits

allows for incredible flexibility: waveguide networks, consisting of hundreds of waveguides and beam splitters, could be implemented in future experiments to simulate more complex dynamics than those demonstrated by the authors. So far, only two non-interacting quantum particles have been simulated undergoing relatively simple quantum walks. Large numbers of photons will be required for any practical quantum-photonics technology, and future developments could include the

simulation of interacting quantum particles (such as charged particles) through implementation of photon–photon nonlinearities⁷ using auxiliary photon measurement or light–matter interaction, for example.

However, a recent, and perhaps surprising, theoretical result³ is that a large number of identical photons themselves pose computationally difficult problems due to their bosonic nature, even in the absence of interaction. Using just tens of photons guided in a circuit with hundreds of waveguides could lead to the first quantum computation competitive with the equivalent calculation performed with the best classical computers currently available. Sansoni and colleagues' study is a development in this direction, and paves the way for using integrated quantum circuits to build a practical quantum simulator. ■

Jonathan C. F. Matthews and Mark G. Thompson are at the Centre for Quantum Photonics, H. H. Wills Physics Laboratory and the Department of Electrical and Electronic Engineering, University of Bristol, Bristol BS8 1UB, UK.

e-mail: mark.thompson@bristol.ac.uk

1. Sansoni, L. *et al.* *Phys. Rev. Lett.* **108**, 010502 (2012).
2. Matthews, J. C. F. *et al.* preprint at arxiv.org/abs/1106.1166v1 (2011).
3. Aaronson, S. & Arkhipov, A. *Proc. 43rd Annu. ACM Symp. Theory Comput.* 333–342 (2011).
4. Knight, P. L., Roldán, E. & Sipe, J. E. *Phys. Rev. A* **68**, 020301(R) (2003).
5. Peruzzo, A. *et al.* *Science* **329**, 1500–1503 (2010).
6. Omar, Y., Paunković, N., Sheridan, L. & Bose, S. *Phys. Rev. A* **74**, 042304 (2006).
7. O'Brien, J. L., Furusawa, A. & Vučković, J. *Nature Photon.* **3**, 687–695 (2009).
8. Politi, A. *et al.* *Science* **320**, 646–649 (2008).
9. Shadbolt, P. *et al.* *Nature Photon.* **6**, 45–49 (2012).
10. Sansoni, L. *et al.* *Phys. Rev. Lett.* **105**, 200503 (2010).